Earth Observation:
Data, Processing and Applications

Volume 3B: Applications—Surface Waters



This publication is available in PDF format at *eopublications.au*.
We welcome your comments regarding the readability and usefulness of this report.
To provide feedback, please email *feedback@eopublications.au*.

Publisher:
Australia and New Zealand CRC for Spatial Information

ISBN [ONLINE]:
978-0-6482278-3-0

Copyright:
All material in this publication is licensed under a Creative Commons Attribution 4.0 Australia Licence, save for content supplied by third parties, and logos. Creative Commons Attribution 4.0 Australia Licence is a standard form licence agreement that allows you to copy, distribute, transmit, and adapt this publication provided you attribute the work. The full licence terms are available from *https://creativecommons.org/licenses/by/4.0/legalcode*. A summary of the licence terms is available from *https://creativecommons.org/licenses/by/4.0/*.



Disclaimer:
While every effort has been made to ensure its accuracy, the CRCSI does not offer any express or implied warranties or representations as to the accuracy or completeness of the information contained herein. The CRCSI and its employees and agents accept no liability in negligence for the information (or the use of such information) provided in this report.

Recommended Citation for Volume 3B:
CRCSI (2021). *Earth Observation: Data, Processing and Applications. Volume 3B: Applications—Surface Waters*. (Eds. Harrison, B.A., Anstee, J.M., Dekker, A.G., King, E.A., Griffin, D.A., Mueller, N., Phinn, S.R., Kovacs, E., and Byrne, G.) CRCSI, Melbourne.

The recommended citation for each contributed chapter is given on the first page of the chapter.

Latest Revision:
October 2025

Background image on previous page: Sentinel-2A imagery acquired on 8 June 2020 over the eastern portion of the Wide Bay Burnett region in southeast Queensland. This region includes the cities of Bundaberg in the northeast and Maryborough, west of Fraser Island. In addition to tourism and fishing, this district supports a variety of agricultural production, principally beef, citrus, sugarcane, and forestry.
Source: Norman Mueller, Geoscience Australia

Acknowledgements

Production of this series of texts would not have been possible without the financial support of CSIRO, CRCSI, GA, BNHCRC and FrontierSI, input from members of the editorial panels and direction from members of the various advisory panels.

Volumes 1 and 2 of this series are based on text originally published in Harrison and Jupp (1989, 1990, 1992, and 1993)[1]. Many illustrations and some text from these publications have been reproduced with permission from CSIRO.

The following authors are thanked for their contributed chapters:

- 11. **Extent**: Norman Mueller (Geoscience Australia)
- 12. **Level**: Edward King (CSIRO)
- 13. **Bathymetry**: Kim Picard (Geoscience Australia), Janet Anstee (CSIRO), and Barbara Harrison (CSIRO)
- 14. **Temperature**: Helen Beggs (Bureau of Meteorology)
- 15. **Ice**: Rob Massom (Australian Antarctic Division and Australian Antarctic Program Partnership)
- 16. **Wind and Waves**: Mark Hemer (CSIRO) and Salman Khan (CSIRO)
- 17. **Circulation**: David Griffin (CSIRO)
- 18. **Colour**: Janet Anstee (CSIRO)
- 19. **Quality**: Arnold Dekker (Satdek), Janet Anstee (CSIRO), Barbara Harrison (CSIRO), and Edward King (CSIRO)
- 20. **Ecology**: Janet Anstee (CSIRO), Chris Roelfsema (University of Queensland), Eva Kovacs (University of Queensland), and Stuart Phinn (University of Queensland)
- 21. **Looking Ahead**: Barbara Harrison (CSIRO), Edward King (CSIRO), Arnold Dekker (Satdek), David Hudson (Geoscience Australia), and Stuart Phinn (University of Queensland)

Chapter 13 is published with the permission of the CEO, Geoscience Australia.

Other contributors are gratefully acknowledged:

- excursus authors: Paul Tregoning (Excursus 1.1), Paul Irving (Excursus 2.1 and Excursus 19.4), Edward King (Excursus 2.2 and Excursus 12.1), Rachael Thomas (Excursus 3.1), Mark Baird (Excursus 5.1), Helen Beggs (Excursus 14.1), Madeleine Cahill (Excursus 14.2), Rob Massom (Excursus 15.1), Mark Hemer and Salman Khan (Excursus 16.1), David Griffin (Excursus 17.2), Chari Pattiaratchi (Excursus 17.3), Klaus Joehnk and Tapas Biswas (Excursus 18.1), Janet Anstee (Excursus 19.3 and Excursus 20.2)
- reviewers: Rachael Thomas (Section 3), Marian Wiltshire (Excursus 5.1), Phillip Ford (parts of Section 5), Kim Picard (Sections 6 and 10), Sean Chua (Section 11), David Griffin (Sections 12 and 16), Nick Crosbie (Excursus 19.3),
- illustrations: Elizabeth Fredericks, Carl Davies (CMDphotographics), Edward King, Matt Chamberlain, Tony Sparks, Ron Hoeke, Rachael Thomas, Joanne Ocok, Paul Packard, Vince Bicello, James Dyer, Simon Hunter, Bill Johnson, Carmon Amos, Sharon Bowen, Nathan Drayson, Janet Anstee, Vittorio Brando, Arnold Dekker, Lesley Clementson, Bozena Wojtasiewicz, Bruce Forster, Linlin Ge, Peter Harrison, Kim Picard, Andrew Carroll, Norman Mueller, Benoit Legresy, Helen Beggs, Leon Majewski, Phillip Reid, Christopher Griffin, Madeleine Cahill, Salman Khan, David Griffin, Susan Wijffels, Nearmap, Erin Hester, Yi Qin, Daniel Haines, Paul Irving, Chris Roelfsema

We thank those owners of copyrighted illustrative material for permission to reproduce their work. Credits for individual illustrations are provided below the relevant graphic.

All volumes in this series are covered by the copyright provisions of CC BY 4.0 AU.

1 Harrison, B.A., and Jupp, D.L.B. (1989) Introduction to Remotely Sensed Data: Part ONE of the microBRIAN Resource Manual. CSIRO, Melbourne. 156 p.
Harrison, B.A., and Jupp, D.L.B. (1990) Introduction to Image Processing: Part TWO of the microBRIAN Resource Manual. CSIRO, Melbourne. 256 p.
Harrison, B.A., and Jupp, D.L.B. (1992) Image Rectification and Registration: Part FOUR of the microBRIAN Resource Manual. MPA, Melbourne.
Harrison, B.A., and Jupp, D.L.B. (1993) Image Classification and Analysis: Part THREE of the microBRIAN Resource Manual. MPA, Melbourne.

Table of Contents

Volume 3B: Applications—Surface Waters a

Acknowledgements i

Introduction 1

1 The Blue Planet 3
- **1.1** The Hydrological Cycle 5
- **1.2** Categories of Surface Waters 7
  - **1.2.1** Oceans 7
  - **1.2.2** Coastal waters 9
  - **1.2.3** Inland waters 11
- **1.3** Physical Layers within Waterbodies 11
  - **1.3.1** Water surface 11
  - **1.3.2** Water column 11
  - **1.3.3** Substratum 12
- **1.4** Global Water Circulation 12
  - **1.4.1** Currents 13
  - **1.4.2** Gyres 14
  - **1.4.3** Eddies 15
  - **1.4.4** Langmuir circulation 15
- **1.5** Global Carbon Cycle 16
- **1.6** Further Information 18
- **1.7** References 19

2 Australia's Surface Water Environment 21
- **2.1** Marine Jurisdiction 21
  - **2.1.1** Territorial Sea Baseline 26
  - **2.1.2** Territorial Sea 26
  - **2.1.3** Coastal Waters 26
  - **2.1.4** Contiguous Zone 26
  - **2.1.5** Exclusive Economic Zone 26
  - **2.1.6** Australian Fishing Zone 27
  - **2.1.7** Continental Shelf 27
- **2.2** Marine Geomorphology and Bioregionalisation 27
- **2.3** Regional Water Circulation 29
- **2.4** Australian Marine Environment 34
- **2.5** Antarctica 35
- **2.6** Australia's Inland Water Resources 37
- **2.7** Australian Water Usage 39
- **2.8** Further Information 39
- **2.9** References 40

3 Aquatic Ecosystems 43
3.1 Aquatic Ecosystem Zones 43
3.2 Aquatic Habitats 45
3.3 Aquatic Organisms 54
3.3.1 Microorganisms 55
3.3.2 Algae 56
3.3.3 Plants 59
3.3.4 Animals 60
3.4 Further Information 60
3.5 References 61

Measureable Properties of Surface Waters 65

4 Attributes of Water Surface 67
4.1 Level 67
4.2 Shape 68
4.3 Texture 71
4.4 Surface Tension 74
4.5 Temperature 74
4.6 Floating Layers 74
4.7 Ice cover 75
4.8 Further Information 76
4.9 References 76

5 Attributes of Water Column 77
5.1 Physical 77
5.1.1 Water depth 77
5.1.2 Density and stratification 81
5.1.3 Temperature 82
5.1.4 EMR absorption and transmission 83
5.1.5 Transparency and suspended particles 86
5.2 Chemical 88
5.2.1 Salinity 88
5.2.2 pH 89
5.2.3 Dissolved matter 89
5.3 Biological 93
5.3.1 Microorganisms 93
5.3.2 Macroalgae and macrophytes 94
5.4 Further Information 95
5.5 References 95

6 Attributes of Substratum 99
6.1 Waterbody Depth 99
6.2 Geomorphic Features 99
6.3 Composition 102
6.4 Benthos 103
6.5 Further Information 104
6.6 References 104

7 Attributes of Waterbodies 105
7.1 Observed Colour 105
7.2 Extent and Permanence 105
7.3 Depth and Volume 106
7.4 Carbon Cycling 108
7.5 Dynamics 110
7.6 Further Information 112
7.7 References 112

EO Data and Models 115

8 Optical EO 117
8.1 Optical EO Framework 122
8.1.1 Scattering 124
8.1.2 Fluorescence 125
8.1.3 Water surface effects 125
8.1.4 Radiative transfer theory 128
8.1.5 Atmospheric correction 128
8.2 Optically Active Constituents of Water 129
8.2.1 Pure water 130
8.2.2 Phytoplankton and cyanobacteria pigments 130
8.2.3 Non-algal particles (NAP) 133
8.2.4 Coloured dissolved organic matter (CDOM) 133
8.2.5 Coloured dissolved inorganic matter (CDIM) 134
8.3 Optical Properties of Water 134
8.3.1 Inherent Optical Properties 134
8.3.2 Apparent Optical Properties 135
8.3.3 Optical properties of substratum 137
8.4 Optical EO Models 140
8.4.1 Radiative Transfer Modelling 142
8.4.2 Water column 143
8.4.3 Substratum factors 144
8.4.4 Integrated models 145
8.5 Optical EO sensors 146
8.6 Further Information 150
8.7 References 150

9 Microwave EO 155
9.1 Microwave EO Framework 158
9.1.1 Review of microwave EMR 158
9.1.2 Observing microwave EMR 160
9.2 Passive Microwave 161
9.3 Imaging Radar 162
9.4 SAR Interferometry 164
9.5 Radar Altimetry 165
9.6 Microwave Scatterometry 166
9.7 Further Information 167
9.8 References 167

10 Acoustic EO 169
10.1 Acoustic EO Framework 170
10.2 Echosounders 171
10.2.1 Single beam echosounders 172
10.2.2 Sidescan sonar 172
10.2.3 Multibeam echosounders 173
10.3 Acoustic Surveys and Platforms 175
10.4 Acoustic Data Processing 176
10.5 Further Information 177
10.6 References 177

Observing Surface Water Dimensions 179

11 Extent 181
Norman Mueller
11.1 Extent of Australian Surface Waters 182
11.2 EO Sensors for Water Extent 183
11.3 Delineating Shorelines 186
11.3.1 Passive optical analysis 186
11.3.2 Synthetic Aperture Radar 191
11.4 Monitoring Floods 191
11.4.1 The International Charter for Space and Major Disasters 191
11.4.2 The Copernicus Emergency Management Service 192
11.5 Permanent/Temporary water 193
11.6 Further Information 193
11.7 References 194

12 Level 197
Edward King
12.1 Level of Australian Surface Waters 198
12.2 EO Sensors for Sea Level 199
12.2.1 Radar altimetry 200
12.2.2 EO sensor calibration 203
12.3 Causes of Change in Sea Level 205
12.3.1 Short term change 206
12.3.2 Seasonal to decadal change 207
12.3.3 Longer term change 209
12.4 Measuring Sea Level 210
12.4.1 Paleo indicators 210
12.4.2 Tide gauges 210
12.4.3 Satellite altimetry 213
12.5 Monitoring Sea Level 215
12.5.1 In geological ages 215
12.5.2 In recent centuries 216
12.5.3 In recent decades 216
12.6 Modelling Future Sea Level 217
12.7 Further Information 219
12.8 References 220

13 Bathymetry 223
Kim Picard, Janet Anstee, and Barbara Harrison

13.1 Bathymetry of Australian Surface Waters 225
13.2 EO Sensors for Bathymetry 231
13.3 Seafloor Mapping 231
13.3.1 Satellite radar altimetry 232
13.3.2 Echosounders 233
13.4 Coastal Monitoring 234
13.4.1 Lidar bathymetry 234
13.4.2 Satellite-derived bathymetry (SDB) 235
13.5 Further Information 238
13.6 References 238

Observing Surface Water Energy 243

14 Temperature 245
Helen Beggs

14.1 Temperature of Australian Surface Waters 245
14.2 EO Sensors for Water Temperature 246
14.2.1 Infrared sensors 247
14.2.2 Passive microwave sensors 250
14.3 Sea Surface Temperature 250
14.3.1 Retrieval of satellite SST 252
14.3.2 Validation of satellite SST 253
14.3.3 'GHRSST' satellite SST products 254
14.4 Global Sea Surface Temperature Products 258
14.4.1 Numerical Weather Prediction model input 262
14.4.2 Climate monitoring 262
14.4.3 Feature resolution 262
14.4.4 Coral bleaching nowcasting 263
14.4.5 Verification 263
14.5 Regional SST Products 263
14.5.1 IMOS satellite SST products 266
14.5.2 High resolution SST climatologies and extreme events 271
14.6 Inland Water Temperature 271
14.7 Further Information 273
14.8 References 274

15 Ice 281
Rob Massom

15.1 Ice in Australian Surface Waters 281
15.1.1 Antarctic Ice Sheet 283
15.1.2 Antarctic sea ice 285
15.2 EO Sensors for Ice 289
15.3 EO of the Antarctic Ice Sheet 290
15.3.1 Ice sheet surface morphology and areal change 290
15.3.2 Icebergs 291

15.3.3 Ice surface temperature 292
15.3.4 Surface melt 293
15.3.5 Ice sheet velocity 293
15.3.6 Surface elevation 294
15.3.7 Ice sheet mass balance 296
15.4 EO of Sea Ice 297
15.4.1 Sea ice concentration, extent, and seasonality, and their variability 297
15.4.2 Coastal landfast sea ice (fast ice) distribution 299
15.4.3 Sea ice motion and dynamics 300
15.4.4 Sea ice and snow cover thickness 301
15.5 Outlook: Future Opportunities and Needs 302
15.6 Further Information 303
15.7 References 304

16 Winds and Waves 311
Mark Hemer and Salman Khan
16.1 Winds and Waves in Australian Surface Waters 313
16.2 EO Sensors for Winds 314
16.2.1 ***In situ*** wind measurements 315
16.2.2 Scatterometers 315
16.2.3 Passive microwave radiometers 317
16.2.4 Satellite altimeters 317
16.2.5 Synthetic Aperture Radar 318
16.2.6 GNSS Reflectometry 319
16.3 EO Sensors for Waves 320
16.3.1 ***In situ*** wave measurements 320
16.3.2 Satellite altimeters 321
16.3.3 SAR imagery 322
16.3.4 Emerging platforms 324
16.4 Further Information 324
16.5 References 325

17 Circulation 329
David Griffin
17.1 Circulation of Australian Surface Waters 331
17.2 EO Sensors for Water Circulation 334
17.2.1 Radar altimeters 334
17.2.2 Passive optical 335
17.3 Circulation Patterns 337
17.4 Ocean Fronts 339
17.5 Further Information 340
17.6 References 341

Observing the Waterscape 343

18 Colour 345
Janet Anstee
18.1 Colour of Australian Surface Waters 347

18.2 EO Sensors for Water Colour 348
18.3 Classifications of Water Colour 348
18.3.1 Classifications based on AOP 349
18.3.2 Classifications based on IOP 350
18.3.3 Optical Water Types (OWT) 351
18.4 Transparency 351
18.5 Dissolved Matter 354
18.5.1 CDOM 354
18.5.2 DOC 354
18.6 Chlorophyll Content 357
18.7 Substratum 359
18.8 Further Information 361
18.9 References 361

19 Quality 367
Arnold Dekker, Janet Anstee, Barbara Harrison, and Edward King
19.1 Quality of Australian Surface Waters 368
19.2 EO Sensors for Water Quality 368
19.3 Inland Water Quality 371
19.3.1 Traditional methods 372
19.3.2 EO approaches 372
19.4 Pollution 378
19.4.1 Plastic debris 378
19.4.2 Shipping 379
19.4.3 Oil spills 380
19.5 Algal Blooms 385
19.6 Marine Heatwaves 386
19.7 Salinity 387
19.8 Further Information 388
19.9 References 389

20 Ecology 395
Janet Anstee, Chris Roelfsema, Eva Kovacs, and Stuart Phinn
20.1 Ecology of Australian Surface Waters 397
20.2 EO Sensors for Water Ecology 400
20.3 Coastal Wetlands 403
20.3.1 Seagrass meadows 404
20.3.2 Mangrove forests 405
20.3.3 Saltmarshes 407
20.4 Estuarine Ecosystems 408
20.5 Coastal waters 409
20.6 Coral Reefs 410
20.6.1 Structural characteristics 411
20.6.2 Optical properties 412
20.6.3 EO datasets and applications 412
20.6.4 Mapping biophysical properties 416
20.7 Marine Fauna 421
20.7.1 Fisheries 422

20.7.2 Animal counts 423
20.8 Further Information 424
20.9 References 425

Looking Ahead 437

21 Over the Horizon 439
Barbara Harrison, Edward King, Arnold Dekker, David Hudson, and Stuart Phinn
21.1 The Global Picture 439
21.2 From Data to Information 443
21.3 Smart Management of Surface Water Resources 445
21.4 The Human Factor 445
21.5 Further Information 447
21.6 References 447

Glossary 449

List of Figures

Figure 1.1 Gravity Recovery and Climate Experiment (GRACE) 3

Figure 1.2 Murray-Darling Basin total water storage 4

Figure 1.3 Water mass anomalies 4

Figure 1.4 The global water cycle 5

Figure 1.5 River catchment 6

Figure 1.6 Artesian well 6

Figure 1.7 ETOPO1 global relief model 8

Figure 1.8 Oceans of the world 8

Figure 1.9 Major marine geomorphic features 9

Figure 1.10 Large scale atmospheric circulation 12

Figure 1.11 Major non-tidal currents 14

Figure 1.12 Eddies in waters around Tasmania 15

Figure 1.13 Langmuir circulation 15

Figure 1.14 Ocean carbon pumps 16

Figure 1.15 Biological pump 17

Figure 2.1 Names and limits of oceans and seas around Australia 22

Figure 2.2 Australian Charting Area 23

Figure 2.3 UNCLOS marine zone boundaries 23

Figure 2.4 Australia's Maritime Zones 24

Figure 2.5 Australian Search and Rescue Region 25

Figure 2.6 Seafloor morphology around Australia 28

Figure 2.7 Provincial marine bioregions 28

Figure 2.8 Three-dimensional model of water masses defined by pelagic regionalisation 29

Figure 2.9 Example of global forecast 31

Figure 2.10 BRAN 2020 reanalysis 32

Figure 2.11 Sample ocean temperature 33

Figure 2.12 Littoral forecast example 34

Figure 2.13 Types of ice in polar regions 35

Figure 2.14 Australian Antarctic Territory 36

Figure 2.15 Australia's average annual rainfall 37

Figure 2.16 Australian inland waterbodies 38

Figure 2.17 Major drainage divisions in Australia 38

Figure 3.1 Aquatic zones for marine waters 44
Figure 3.2 Inland floodplain wetland distribution in the MDB 46
Figure 3.3 Mosaics of inland floodplain wetland types 47
Figure 3.4 Longitudinal, lateral and vertical hydrological pathways 48
Figure 3.5 Inundation patterns 49
Figure 3.6 Conceptual models of common inland floodplain wetlands in MDB 50
Figure 3.7 Examples of common inland floodplain wetlands in the MDB 52
Figure 3.8 Simple food chain 54
Figure 3.9 Phytoplankton forms 57
Figure 4.1 Global-mean sea level (GMSL) estimates 67
Figure 4.2 Change in sea surface topography 1993–2019 68
Figure 4.3 Tidal forces due to the Moon 69
Figure 4.4 Spring and neap tides 69
Figure 4.5 Lunar cycle of tides 69
Figure 4.6 Types of tides 70
Figure 4.7 Global distribution of tide cycles 70
Figure 4.8 Tidal range 71
Figure 4.9 Water wave 72
Figure 4.10 Energy spectrum of ocean waves 72
Figure 4.11 Algal bloom 75
Figure 5.1 Argo global array 78
Figure 5.2 Bathymetry of Bass Strait 79
Figure 5.3 Ocean glider transect 80
Figure 5.4 Thermohaline circulation patterns 81
Figure 5.5 Stratification of water column 82
Figure 5.6 Lake stratification 82
Figure 5.7 Electromagnetic spectrum 84
Figure 5.8 Atmospheric opacity 84
Figure 5.9 Reflectance from different water colours 85
Figure 5.10 Light attenuation in water 85
Figure 5.11 Turbidity caused by flocculation 86
Figure 5.12 Secchi disk 87
Figure 5.13 pH scale 89
Figure 5.14 Separation of dissolved and particulate matter 90
Figure 5.15 Deep chlorophyll maximum for northeast Pacific Ocean 93

Figure 6.1 Morphological features 100
Figure 6.2 Global Seafloor Geomorphic Feature map (GSFM) 102
Figure 7.1 Proposed waterbody depth regions for Seabed 2030 107
Figure 7.2 Aquatic carbon in freshwater system 109
Figure 7.3 Earth System Science 111
Figure 8.1 Measurement and analysis of image features 117
Figure 8.2 Polar angles 118
Figure 8.3 Solid angle 118
Figure 8.4 Geometric framework for optical studies 119
Figure 8.5 Radiative transfer process 120
Figure 8.6 Specular reflection 120
Figure 8.7 Radiance definitions 121
Figure 8.8 Cosine law 121
Figure 8.9 Downwelling and upwelling irradiance 121
Figure 8.10 EMR reflectance from water 124
Figure 8.11 Scattering directions 124
Figure 8.12 Internal reflection and refraction 126
Figure 8.13 Sun-sensor geometry of example images 127
Figure 8.14 Impact of sun-sensor geometry on image quality 128
Figure 8.15 Absorption spectrum of pure water 130
Figure 8.16 Effect of salinity on scattering by water 130
Figure 8.17 Absorption spectra of algal pigments 131
Figure 8.18 Water colour variations due to phytoplankton 131
Figure 8.19 Absorption spectra for phytoplankton 132
Figure 8.20 CDOM Absorption spectra 133
Figure 8.21 Simulation of substratum reflectance at different water depths 138
Figure 8.22 Modelled subsurface irradiance reflectance 139
Figure 8.23 Relationship underlying optical EO models 140
Figure 9.1 Blackbody radiation 156
Figure 9.2 Radar wavelengths 157
Figure 9.3 Radar penetration in ice/snow cover 158
Figure 9.4 Electromagnetic wave 159
Figure 9.5 Bragg scattering 163
Figure 9.6 SAR composite images 163
Figure 9.7 InSAR operation 164

Figure 9.8 Operation of radar altimeter 165
Figure 9.9 Global wind power 166
Figure 10.1 Longitudinal or compression waves 169
Figure 10.2 Speed of sound varies with water depth 170
Figure 10.3 Hull-mounted sonar system 171
Figure 10.4 Beam patterns of sonar systems 172
Figure 10.5 Comparison of sonar systems 172
Figure 10.6 Sidescan sonar image of shipwreck 173
Figure 10.7 Multibeam mapping 174
Figure 10.8 Swath overlap for backscatter data 175
Figure 10.9 Relationship between reference ellipsoid, antenna, water line, and chart datum 175
Figure 11.1 Scales of observing ocean changes 181
Figure 11.2 A selection of hydrologic features of Australia from the Geofabric 182
Figure 11.3 Region north of Lake Eyre during flooding 184
Figure 11.4 Sentinel-1a SAR image of Lake Sorrell in Tasmania, acquired on the 7 May 2015 185
Figure 11.5 NIDEM process 187
Figure 11.6 GLOWABO overview 188
Figure 11.7 GLOWABO estimates 189
Figure 11.8 Distribution of lakes by latitude and elevation 190
Figure 11.9 Charter Activation 192
Figure 12.1 Reference frames and measurements for sea level observation 198
Figure 12.2 Variability of Australian tides 199
Figure 12.3 Operation of SWOT 201
Figure 12.4 Simulated SWOT measurements 202
Figure 12.5 SWOT fast sampling swaths 202
Figure 12.6 *In situ* measurement sites 203
Figure 12.7 Example calibration site 204
Figure 12.8 Converting mooring measurements into datum 205
Figure 12.9 Factors affecting sea level at a range of spatial and temporal scales 205
Figure 12.10 Tropic Cyclone Yasi 206
Figure 12.11 Wave setup 207
Figure 12.12 Mean sea level 208
Figure 12.13 Ocean-climate system variability 208
Figure 12.14 Tide gauge records 209
Figure 12.15 PSMSL tide gauge stations 211

Figure 12.16 GLOSS network of tide gauge stations 211
Figure 12.17 TOPEX/Poseidon altimeter coverage 214
Figure 12.18 Ground tracks of several altimeter missions 215
Figure 12.19 The past three centuries of the global sea level record 216
Figure 12.20 The satellite era mean sea level record 216
Figure 12.21 Historical sea level change 217
Figure 12.22 Projected sea level changes around Australia in 2090 218
Figure 13.1 Improvements in GEBCO over time 224
Figure 13.2 Search for MH370 relative to available bathymetric datasets 226
Figure 13.3 Australian Bathymetric and Topographic Grid 227
Figure 13.4 Primary bathymetric units 228
Figure 13.5 Distribution of geomorphic features around Australia's continental margin 229
Figure 13.6 Satellite altimetry versus acoustic datasets 231
Figure 13.7 Example of bathymetric data improvements 232
Figure 13.8 Global map of marine gravity 233
Figure 13.9 AusSeabed bathymetry holdings (by survey) in January 2020 234
Figure 13.10 Lidar bathymetry 235
Figure 14.1 Average SST around Australia 246
Figure 14.2 AVHRR/3 GAC grid resolution and sampling 248
Figure 14.3 Nighttime SST maps 249
Figure 14.4 Near-surface oceanic temperature gradients 251
Figure 14.5 Nighttime SST maps for 13 March 2019 over the Queensland region 256
Figure 14.6 Australian AVHRR ground stations 266
Figure 14.7 Skin SST maps 267
Figure 14.8 SST maps 268
Figure 14.9 IMOS nighttime, 6-day AVHRR L3S SST around Tasmania 269
Figure 14.10 Argo temperature profile and SST 270
Figure 14.11 Daytime SWT map from VIIRS 272
Figure 15.1 Satellite-derived map of the Antarctic Ice Sheet and surrounding sea ice 282
Figure 15.2 Plan view and cross section profiles across Antarctica 283
Figure 15.3 Schematic of an Antarctic ice shelf 284
Figure 15.4 Schematic of an ice sheet and its individual mass balance components 285
Figure 15.5 Extent of Antarctic sea ice in 2015/2016 286
Figure 15.6 Photographs of Antarctic pack ice and fast ice 287
Figure 15.7 Portion of Mosaic of Antarctica (MOA) map 291

Figure 15.8 Warming trend of Antarctica from 1957 through 2006 292
Figure 15.9 Byrd Glacier velocity 294
Figure 15.10 Antarctic ice shelf thickness changes 295
Figure 15.11 DEM of the Antarctic Ice Sheet 296
Figure 15.12 Extent of Arctic versus Antarctic sea ice 298
Figure 15.13 Fast ice coverage and persistence 299
Figure 15.14 Mean monthly (March through November) ice drift for 1982-2015. 300
Figure 16.1 Example wave spectrum 312
Figure 16.2 Significant wave height 313
Figure 16.3 Australian Marine Energy Atlas 314
Figure 16.4 Scatterometer missions 316
Figure 16.5 GNSS-R system 319
Figure 16.6 Australian wave buoy network 320
Figure 16.7 Global buoys for March 2016 321
Figure 16.8 Australasian SAR database 323
Figure 17.1 Mean surface currents around Australia 331
Figure 17.2 Speed of Antarctic Circumpolar Current 335
Figure 17.3 Temperature variations 336
Figure 17.4 Detailed view of temperature variation 336
Figure 17.5 Circulation in EAC 338
Figure 17.6 MODIS Chlorophyll a OC3 29 May 2018 339
Figure 17.7 Frontal systems on Australian northwest shelf 340
Figure 18.1 Characteristic reflectance features of water colour constitutents 345
Figure 18.2 Simulations of waterbody reflectance 346
Figure 18.3 Variations in surface water colour 347
Figure 18.4 Hue angle conversion 348
Figure 18.5 The Forel-Ule colour scale 349
Figure 18.6 Ternary diagrams 350
Figure 18.7 Non-algal particulates 352
Figure 18.8 Simulated EO reflectance for different substrates 353
Figure 18.9 Blackwater plume 355
Figure 18.10 Blackwater event 356
Figure 18.11 MODIS chlorophyll a concentration products 358
Figure 18.12 Epiphytic growth on seagrass blades 359
Figure 18.13 Impact of water depth on substrate spectra 360

Figure 19.1 Great Barrier Reef shown in true colour 370

Figure 19.2 Effect of spatial resolution on Lake Burley Griffin, Canberra 374

Figure 19.3 Cyanobacteria bloom 375

Figure 19.4 *In situ* measurement locations 376

Figure 19.5 HydraSpectra installation 376

Figure 19.6 HydraSpectra reflectance data 377

Figure 19.7 Weathering processes associated with an oil spill 380

Figure 19.8 Duration of oil weathering processes 381

Figure 19.9 Beach profile showing potential oil spill deposits 381

Figure 19.10 AMSA oil spill response process 384

Figure 19.11 MODIS image of algal bloom 386

Figure 19.12 Defining marine heatwaves 387

Figure 19.13 Global salinity image composites 388

Figure 20.1 Great Barrier Reef Marine Park 398

Figure 20.2 Australia's other marine parks 399

Figure 20.3 EO data resolutions for seagrass and mangrove features in coastal environments 401

Figure 20.4 Wetland habitat zones 403

Figure 20.5 Seagrass spatial and organisational scales 404

Figure 20.6 Mangrove features versus image resolution 407

Figure 20.7 Coral diversity 410

Figure 20.8 Coral reef hierarchical scales 411

Figure 20.9 Comparison of spatial resolution and extent for four EO sensors 413

Figure 20.10 Exposure (directional) filtering 414

Figure 20.11 Approaches to reef mapping 417

Figure 20.12 Automated classification of geomorphic zones 418

Figure 20.13 Mapping reef biophysical properties 419

Figure 20.14 eReefs modelling extent 420

Figure 20.15 Pelagic sampling methods 422

Figure 21.1 Spectral characteristics of hyperspectral PACE OCI compared with heritage spaceborne ocean colour sensors 440

Figure 21.2 Pressures and drivers on global ocean biology 443

List of Tables

Table 1.1 Dimensions of oceans 7

Table 1.2 Geomorphological categories of coastal landforms 10

Table 2.1 Australia's maritime zones 24

Table 2.2 Area of Australian Exclusive Economic Zones 26

Table 2.3 Categories of waterbodies in Australia 39

Table 3.1 The plant kingdom 55

Table 3.2 Most common phytoplankton groups 57

Table 3.3 Most frequently occurring algal groups 58

Table 3.4 Classification of macrophytes 59

Table 4.1 Beaufort scale 71

Table 4.2 Categories of waves 73

Table 4.3 WMO Sea State tables for waves and swells 73

Table 5.1 Factors impacting ocean water density 81

Table 5.2 Trophic status categories for freshwater lakes 92

Table 6.1 Generic geomorphic features 100

Table 7.1 Seabed 2030 minimum mapping resolutions 107

Table 7.2 Modelled scenarios for Antarctica and Southern Ocean in 2070 110

Table 8.1 Terminology for EO geometry 119

Table 8.2 Light behaviour in different media 120

Table 8.3 Impact of cosine law on irradiance 121

Table 8.4 Hydrologic optics terms 122

Table 8.5 Inherent optical properties 123

Table 8.6 Apparent Optical Properties 123

Table 8.7 Some fluorescence features in waterbodies 125

Table 8.8 Major photo pigments for phytoplankton taxonomic classes 132

Table 8.9 Commonly used Inherent Optical Properties 135

Table 8.10 Commonly used Apparent Optical Properties 136

Table 8.11 Optical depth 137

Table 8.12 Forward and inverse models 141

Table 8.13 Mathematical inversion models for aquatic ecosystem variables 141

Table 8.14 Optical EO sensors for aquatic mapping 147

Table 8.15 Recommended spectral bands for assessing water quality and characterising benthos 149

Table 8.16 Recommended spectral bands for atmospheric and air-interface correction 150
Table 9.1 Spectral regions observed by EO sensors 155
Table 9.2 Radar bands used for EO 157
Table 9.3 Effects of EMR on matter 159
Table 9.4 Wave-matter interactions relevant to EO 159
Table 9.5 Polarisation options for radar signals 161
Table 10.1 MBES footprint 173
Table 10.2 Examples of sounding accuracy and TPU 176
Table 11.1 EO sensors relevant to water extent 183
Table 12.1 EO sensors relevant to water level 199
Table 12.2 Satellite missions providing data from a radar altimeter instrument 200
Table 12.3 Predicted temperature variations 217
Table 13.1 Surface areas of primary bathymetric units 228
Table 13.2 Geomorphic features of Australian continental margin 230
Table 13.3 EO sensors relevant to bathymetry 231
Table 13.4 Examples of neural network and machine learning models 236
Table 13.5 Examples of semi-analytical models 238
Table 14.1 EO sensors relevant to water temperatures 247
Table 14.2 AVHRR/3 channels 247
Table 14.3 Global, Daily, Multi-Sensor SST analysis products in GHRSST L4 format 258
Table 14.4 GHRSST products 263
Table 15.1 EO sensors relevant to ice 289
Table 16.1 EO sensors relevant to water waves 314
Table 17.1 Water circulation terms 329
Table 17.2 Names and abbreviations of major currents 332
Table 17.3 EO sensors relevant to water circulation 334
Table 18.1 EO sensors relevant to water colour 348
Table 19.1 Suitability of optical EO sensors to map water quality variables 369
Table 19.2 EO sensors relevant to water quality 370
Table 19.3 Size distribution of waterbodies in Australia 373
Table 19.4 National water quality system based on EO 374
Table 19.5 Major EO sensors for oil spill detection 382
Table 19.6 Environmental limitations on oil spill detection 383
Table 20.1 Commonwealth Marine Reserves IUCN protected area management categories 400
Table 20.2 EO sensors relevant to coastal and marine water ecology 401

Table 20.3 Suitability of optical EO sensors for mapping aquatic ecosystem features 402

Table 20.4 Backscatter from mangroves 406

Table 20.5 Four reef differentiation scales 412

Table 21.1 Global monitoring systems 441

Table 21.2 Essential Ocean Variables 442

Table 21.3 Big Earth data challenges 444

Table 21.4 Target variables for pressures and drivers in the aquatic biological environment 446

List of Excurses

Excursus 1.1—Global Freshwater Resources 3

Excursus 1.2—Coriolis Force and Ferrel's Law 13

Excursus 2.1—Australian Maritime Safety Authority (AMSA) 25

Excursus 2.2—Bluelink Ocean Forecasting 30

Excursus 3.1—Inland Floodplain Wetlands 46

Excursus 3.2—Phytoplankton Groups 57

Excursus 4.1—Astronomical Tides 69

Excursus 4.2—Water Waves 72

Excursus 5.1—Ocean Profile Sensors 78

Excursus 7.1—Nippon Foundation-GEBCO Seabed 2030 Project 107

Excursus 7.2—The Global System 111

Excursus 8.1—Optics Review 118

Excursus 9.1—Radar 156

Excursus 11.1—GLOWABO 188

Excursus 12.1—Surface Water and Ocean Topography (SWOT) 201

Excursus 12.2—The National Operations Centre (NOC) Tidal Unit 212

Excursus 13.1—Australian Bathymetric and Topographic Grid 227

Excursus 14.1—Selecting a Satellite SST Product 257

Excursus 14.2—Sea Surface Temperature around Tasmania 269

Excursus 15.1—The Importance of EO for Sea Ice 287

Excursus 16.1—Marine Surface Winds and Waves 312

Excursus 17.1—Major Currents around Australia 332

Excursus 17.2—Example Circulation Study 337

Excursus 17.3—Ocean Fronts 339

Excursus 18.1—Blackwater Events 355

Excursus 19.1—Australian Inland Water Quality 371

Excursus 19.2—Assessing Inland Water Quality using Optical EO 373

Excursus 19.3—Western Treatment Plant, Werribee 375

Excursus 19.4—Operational Oil Spill Response 384

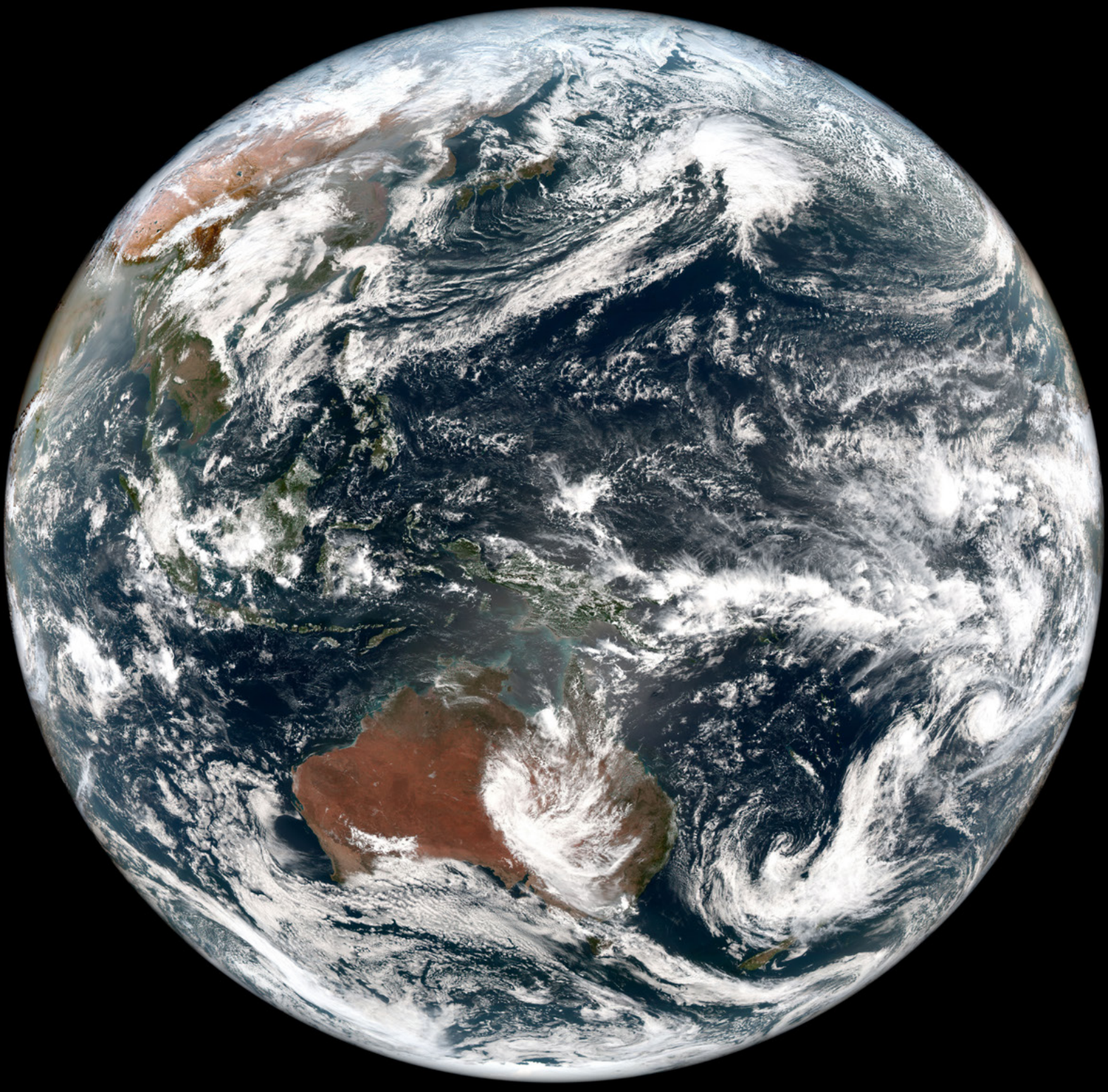
Excursus 20.1—Biodiversity 396

Excursus 20.2—Marine Protected Areas 398

Excursus 20.3—Coral Bleaching 415

Excursus 21.1—Essential Ocean Variables 442

Introduction



This series of publications, *Earth Observation: Data, Processing and Applications*, comprises three volumes. Volume 1 in this series is presented as three sub-volumes, which together outline the basics of Earth Observation (EO) in terms of energy sources, data acquisition, sampling characteristics, image availability, data interpretation and usage. Volume 2 (six sub-volumes) describes the various options involved with image representation, analysis, transformation, integration and modelling, including details of relevant algorithms, with emphasis on their underlying mathematical and statistical principles. These volumes provide valuable background information for understanding specific applications of EO. They also define terminology used in Volume 3, which currently comprises two sub-volumes: 3A, Terrestrial Vegetation, and 3B, Surface Waters.

Volume 3B details how EO methods are used to map, monitor and model various characteristics of Australia's inland, coastal and marine waters. In this context, surface waters include sea ice, ice sheets and shelves, and icebergs in Antarctica and the Southern Ocean. The introductory sections in this sub-volume describe background topics that are relevant to understanding EO studies of these surface waters:

- water on Earth—the hydrological cycle, categories of surface water, physical layers within waterbodies, global water circulation, and the global carbon cycle (see Section 1);
- surface waters in the Australian environment—legislative and environmental zones, waterbody characteristics, and water distribution and usage (see Section 2); and
- aquatic ecosystems—relevant characteristics of ecological zones, habitats and organisms within the Australian marine environment (see Section 3).

Sections 4 to 7 respectively summarise attributes of the water surface, water column, substratum and waterbodies that are relevant to EO-based studies. Sections 8 to 10 review characteristics of optical, microwave and acoustic EO datasets. Sections 11 to 20 introduce specific application areas where EO datasets are being used to observe Australian surface waters. Section 21 concludes this sub-volume by considering some potential future challenges in this area.

Contents

1 The Blue Planet 3

2 Australia's Surface Water Environment 21

3 Aquatic Ecosystems 43

Background image on previous page: Full disk image captured by Himawari-8 geostationary satellite on 1 January 2016, displayed as natural colour composite. **Source:** © Bureau of Meteorology/JMA



1 The Blue Planet

With over 70% of the Earth's surface being covered by water, our planet can reasonably be called the 'Blue Planet'. The total volume of water of Earth has been estimated as 1,386 million km^3, 96.5% of which occurs in the oceans (Shiklomanov and Rodda, 2003). Of the 2.53% that is freshwater, nearly 69% is frozen in permanent ice and glaciers, and around 30% exists as groundwater. Thus, only a very small proportion of the total water on Earth is available for routine use. Estimates of global freshwater reserves are now being refined and monitored using integrated EO technologies (see Excursus 1.1).

The following subsections provide an overview of global water characteristics:

- water movement around the planet, that is, the hydrological cycle (see Section 1.1);
- categories of surface waters (see Section 1.2)
- physical layers within surface waterbodies (see Section 1.3);
- global circulation of surface waters (see Section 1.4); and
- the global 'blue' carbon cycle (see Section 1.5).

Excursus 1.1—Global Freshwater Resources

Source: Paul Tregoning, Australian National University

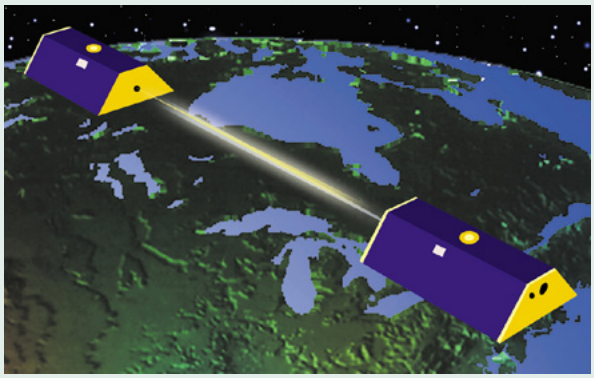
Changes in Earth's gravity are caused by mass movements of water, due to:

- ocean circulation and currents;
- the exchange between continents and oceans through the hydrological cycle; and also
- through the current melting of glaciers and ice sheets in polar regions.

Measurements from the Gravity Recovery and Climate Experiment (GRACE) inferred gravity changes over the Earth. The GRACE mission (operational from 2002 to 2017) used microwave ranging to measure the precise change in distance between two spacecraft, which is affected by changes in the Earth's gravitational field (see Figure 1.1). The GRACE Follow-on mission, launched in May 2018, includes a laser ranging system to deliver these measurements with substantially greater accuracy.

Figure 1.1 Gravity Recovery and Climate Experiment (GRACE)

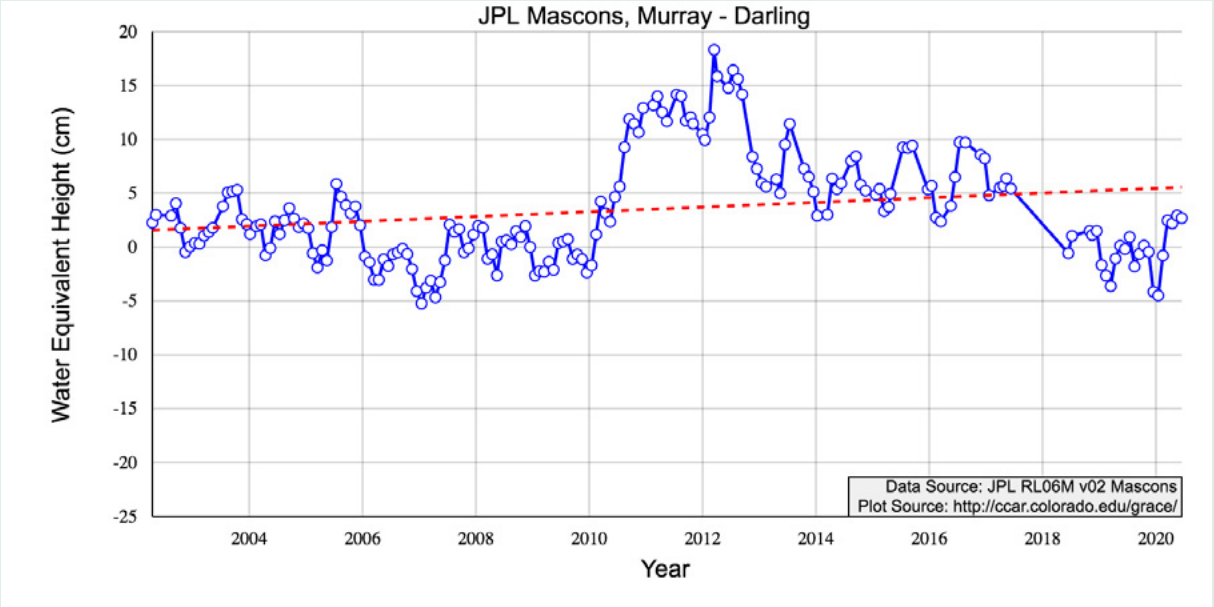
The GRACE mission measured the precise distance between twin satellites accurate to about 1/10 of the thickness of a human hair. Slight changes in the distance between these satellites occur over time as differences in the Earth's gravity field cause the speeds of the satellites to vary as they orbit around Earth.



Background image: Portion of the Southern Hemisphere from 'one million miles' (1.6 million km) away, taken by NASA's Earth Polychromatic Imaging Camera (EPIC) on 6 July 2015 from the Deep Space Climate Observatory (DSCOVR). This image uses the red, green and blue channels. **Source:** NASA. Retrieved from *http://www.nasa.gov/press-release/nasa-satellite-camera-provides-epic-view-of-earth*

Figure 1.2 Murray-Darling Basin total water storage

Time series of the changes in total water storage, averaged over the entire Murray-Darling Basin system, from April 2002 to June 2020, showing the annual variations and long term trends of droughts and wet times during this period.



An integrated NASA study that monitored the availability of freshwater in 34 regions globally has been able to distinguish changes due to natural climatic factors from those due to anthropogenic causes (Rodell *et al.,* 2018). This study involved analysis of:

- 14 years of data from GRACE;
- Landsat imagery;
- satellite precipitation data from the Global Precipitation Climatology Project;
- irrigation maps; and
- published reports of agricultural, mining and reservoir operations.

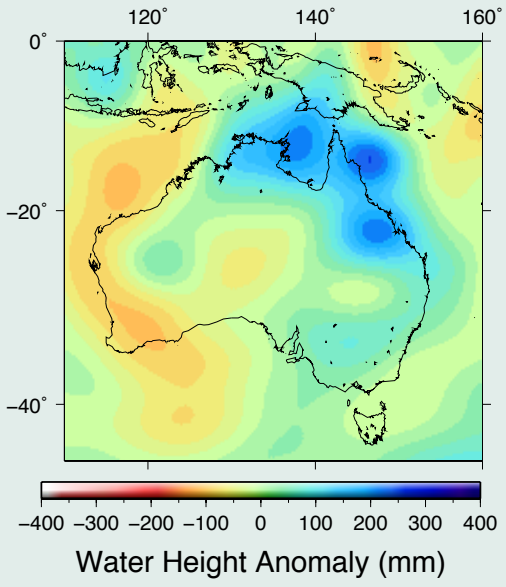
Distinct patterns emerged of wet areas becoming wetter, especially in polar and tropical regions, and dry areas becoming drier, often due to groundwater depletion.

At a national scale, GRACE data provides the potential to estimate changes in total water storage in Australian drainage basins at monthly intervals and to quantify the severity of droughts and floods. For example, water storage in the Murray-Darling Basin was estimated using GRACE and GRACE Follow-On data (see Figure 1.2). These results showed that an average of 5.52 Gt per year of water were lost from surface and subsurface storage during the Millenium Drought (ending in 2009), comprising soil moisture, surface waters (from rivers, dams, reservoirs) and groundwater. The breaking of the drought is clearly visible, with significant water mass increase occurring between 2010 and 2012. Unfortunately, another drought occurred in the subsequent years, as captured by GRACE data (2012–2017) and GRACE Follow-On data (2018–2019).

Similarly, water anomalies (expressed in terms of an equivalent water height, or the height of water as a column or disk required to equal the mass change) were estimated from 30 days of GRACE data during the January 2011 floods in northeastern Australia. In Figure 1.3, the southernmost blue region near Rockhampton indicates the start of flooding, while the blue regions near Cairns and in the Gulf of Carpentaria are related to mass changes caused by wind-driven water movement associated with Tropical Cyclone Yasi.

Figure 1.3 Water mass anomalies

Estimates of water height anomaly (mm) based on 30 days of GRACE data show higher water volumes in northeastern Australia after the January 2011 floods.



1.1 The Hydrological Cycle

The hydrosphere comprises all the water on the Earth's surface, inside the Earth and in its atmosphere. Water constantly moves:

- between locations on the Earth's surface;
- between the surface and subsurface storage; and
- between the surface and the atmosphere (see Figure 1.4).

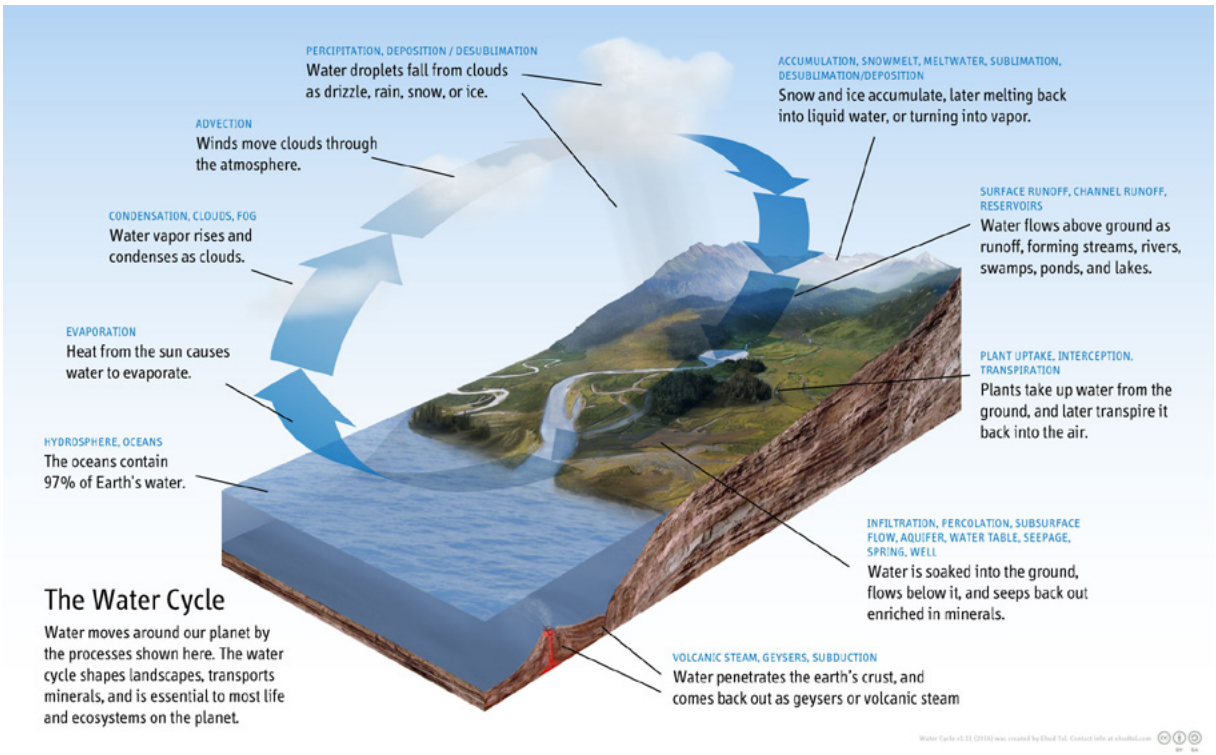
Water can exist in the form of liquid water, water vapour, ice, or snow, and may be nearly pure or contain dissolved and/or suspended substances. As surface water is heated by the Sun, it evaporates to become water vapour in the atmosphere. Plants also release water vapour to the atmosphere by transpiration (see Volume 3A). As water vapour rises in the atmosphere, it cools and condenses, forming clouds. Global air currents move clouds until they release their water as precipitation, in the form of rain, hail or snow. This sub-volume focuses on surface waters.

Water on the surface of the Earth is stored in the natural depressions of oceans and lakes, or the man-made storage facilities of reservoirs and dams. Some surface water is frozen, in the form of polar ice caps and their glaciers, in millennial time scales. Other frozen surface water regularly melts with seasonal changes. This includes sea ice that covers a vast, though seasonally-variable, area of the high-latitude Southern Ocean.

Water running on the Earth's surface, or runoff, can come directly from precipitation or melting sources. Rivers obey the laws of gravity and transport water from higher to lower elevations, generally delivering it to larger storage, such as a lake or an ocean. Many changes occur in rivers between its source and the outlet to a larger waterbody. Near the source, river water is generally clear, cold, and low in nutrients, and hence most likely low in phytoplankton. At this point, the river channel is likely to be narrow, shallow, and lined with rock. Further along, the river typically widens and deepens, runs through softer soils, and may include marshes and wetlands. The water in midstream sections of rivers is generally warmer and more turbid than near the source. Higher populations of phytoplankton would live in these waters.

Figure 1.4 The global water cycle

Each year, more than half a million cubic kilometres of water is moved around the Earth's surface, mostly between the oceans and the atmosphere, and some between the surface and subsurface storage.



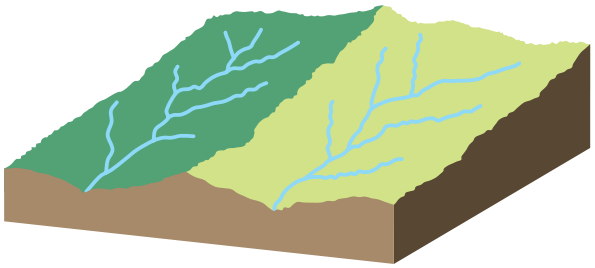
Source: Ehud Tal, Wikimedia. Retrieved from *https://upload.wikimedia.org/wikipedia/commons/b/b1/Diagram_of_the_Water_Cycle.jpg*

Most rivers meet the sea via estuaries or deltas. Estuaries are semi-enclosed waterbodies at the river mouth where river flow and tides mix fresh and saltwater. These areas are typically turbid and nutrient rich, which provides valuable habitat for marine and bird life. Deltas result from settling river sediment, which creates shallower riverbeds. Deltas can occur where one river meets another, a river meets a lake or reservoir, or a river meets an open sea that has weak tidal currents. The formation of deltas gradually slows down the flow of rivers and lengthens its journey through meanders. Inland rivers can also flow into dry salt lakes, as occurs in Central Australia.

The area of land draining into a river is referred to as its catchment or watershed. Characteristics of the catchment area, or drainage basin, determine the size and flow rate of the river, as well as sources of organic and inorganic inputs to flows, which impact water quality (see Figure 1.5). A hierarchical system of catchments often exists such that catchments drain into other catchments.

Figure 1.5 River catchment

This schematic shows two drainage basins divided by a ridge. Individual basins drain into a network of streams and rivers which carry surface flow downhill.



Before flowing towards a drainage channel, precipitation can be intercepted by vegetation, buildings, or small surface depressions within a catchment. Interception of rainfall allows some precipitation to soak into the ground rather than flow away. Water can infiltrate into the soil layer and be stored as soil moisture or percolate through the soil until it reaches the water table. Beneath the Earth's surface, soil and/or rock are typically layered in two distinct zones. The upper zone is aerated, that is, it contains some air. Water in this zone is available to plants. In the lower, rocky zone, air pockets are saturated with water. This saturated zone is called an aquifer. The boundary between these zones is called the water table. The depth of the water table varies with the volume of water that is added to (recharge) and/or removed from (discharge) the aquifer. A spring occurs when groundwater naturally overflows onto the land surface. Groundwater is often extracted from aquifers artificially by installing a well or bore. Unconfined aquifers require a pump to raise groundwater to the surface from a bore. Confined aquifers, however, exist above layers of relatively impermeable rock such that natural internal pressures spontaneously eject the groundwater to (or above) the surface. Such waters are called artesian waters (see Figure 1.6).

Figure 1.6 Artesian well

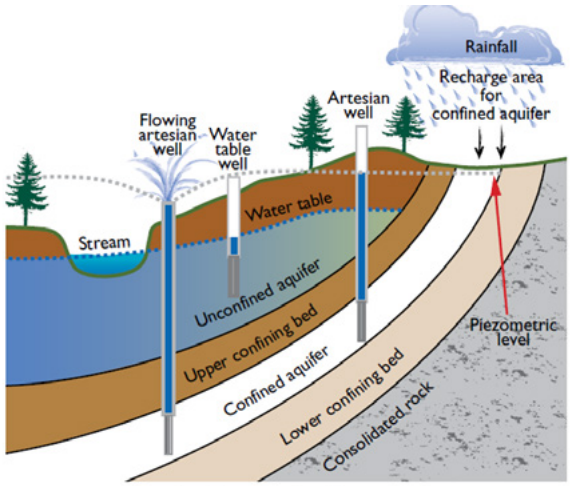


Figure 1. Geological and topographical controls affecting artesian and flowing artesian wells.

Source: UGSG (2018). Retrieved from: *https://www.usgs.gov/media/images/artesian-wells-can-bring-water-land-surface-naturally*

1.2 Categories of Surface Waters

Bodies of water on the Earth's surface can be categorised in several ways. The most basic division of waterbodies (non-frozen) relates to their salt content, with marine waters being salty, and freshwater systems, as the name implies, generally containing low levels of salt. For practical purposes, it is also common to subdivide marine waters into oceans and coastal waters. Accordingly, to discuss surface waters in this text, three broad categories will be used:

- inland: freshwater rivers and lakes located within continental boundaries;
- coastal: shallow marine waters adjacent to continental boundaries; and
- oceans: deeper marine waters bordering coastal waters.

Accepted legislative definitions for marine zones in Australia are introduced in Section 2.1. These zones are located relative to the Territorial Sea Baseline (TSB), a reference boundary that effectively defines a border between land and sea. In most cases, the TSB corresponds to the Lowest Astronomical Tide (LAT; GA, 2021). For administrative purposes, these definitions allow our three water categories to be described more precisely as:

- inland waters: fresh waterbodies located within the TSB;
- coastal waters: marine waters within 3 nautical miles (M) from TSB (where 1 M≈1.8 km); and
- oceans: marine waters more than 3 M from TSB.

Unfortunately, these precise definitions do not always correlate with the physical characteristics of these three water classes, such as their constituents, optical properties, or variations in water depth. For the purposes of the following discussion, these terms will be defined as:

- oceans: deeper marine waters at least 3 M away from the TSB. These large waterbodies are saline and subject to tidal variations (see Section 1.2.1).
- coastal waters: shallower marine waters adjacent to the TSB. These include estuaries, beaches, salt marshes, mudflats, and mangrove swamps, as well as the shallow waters on the fringe of oceans that contain coral reefs and lagoons, seagrass meadows and kelp forests (see Section 1.2.2); and
- inland waters: freshwater rivers and lakes located within the TSB. Most inland waterbodies have low levels of dissolved salt, but some salt lakes can contain higher concentration of salts than seawater. Ponds, dams, and lakes feature standing water while rivers and streams have flowing water (see Section 1.2.3).

1.2.1 Oceans

Our oceans constitute a contiguous saline waterbody that covers around 70% of the Earth's surface. This single mass is sometimes called the 'world ocean'. For convenience it is divided into five major regions, here listed in order of increasing area:

- Arctic;
- Southern;
- Indian;
- Atlantic; and
- Pacific Oceans (see Figure 1.8).

The ETOPO1 is a 1 arc-minute digital representation of Earth's solid surface that integrates land topography and ocean bathymetry using global and regional datasets (Amante and Eakins, 2009; see Figure 1.7). The area and volume of each ocean have been estimated from this model (Eakins and Sharman, 2010; see Table 1.1).

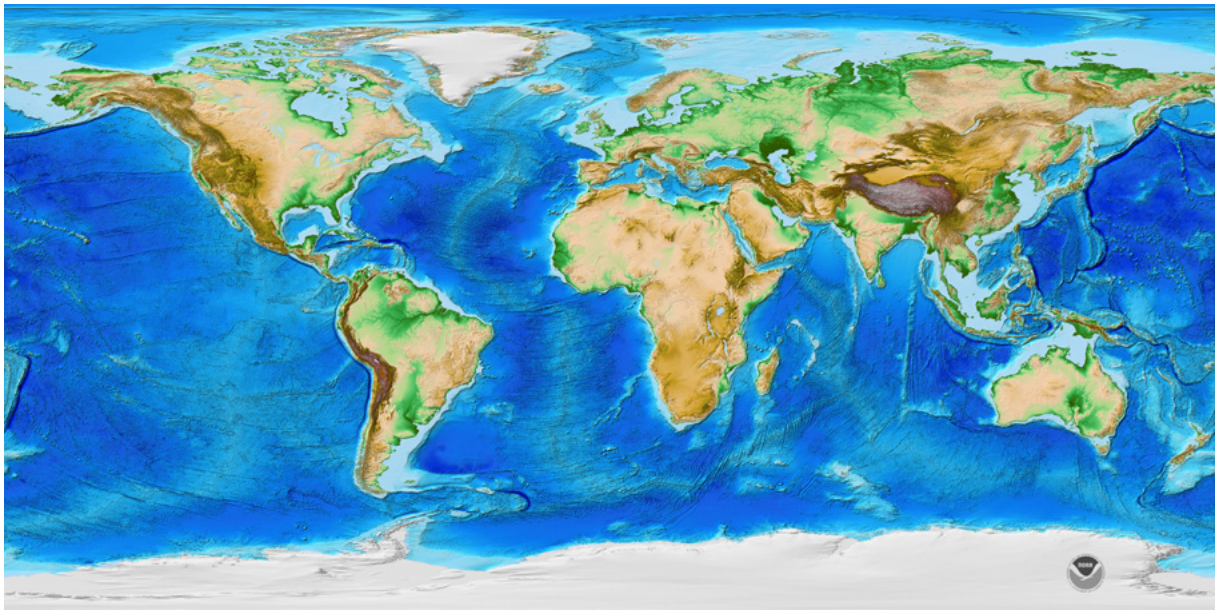
Table 1.1 Dimensions of oceans

Estimates based on ETOPO1 Ice Surface global relief model with error estimates 0.1% for area and 1% for volume.

Ocean	Area (km^2)	Volume (km^3)	Average Depth (m)	Maximum Depth (m)
Arctic	15,558,000	18,750,000	1,205	5,567
Atlantic	85,133,000	310,410,900	3,646	8,486
Indian	70,560,000	264,000,000	3,741	7,906
Pacific	161,760,000	660,000,000	4,080	10,803
Southern	21,960,000	71,800,000	3,270	7,075

Source: Eakins and Sharman (2010).

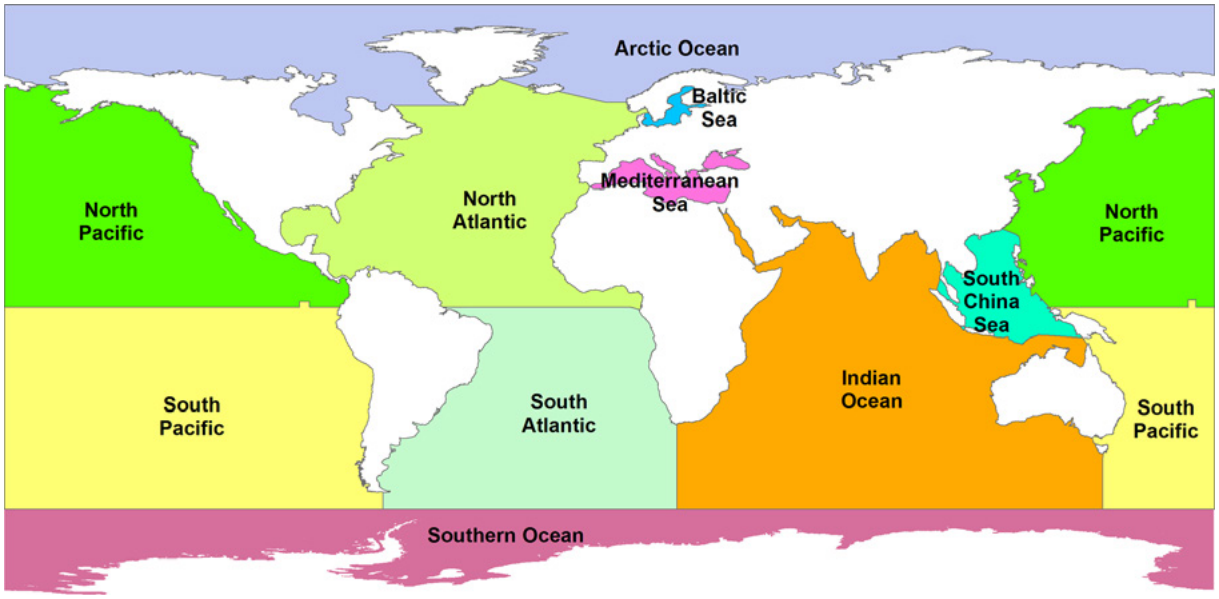
Figure 1.7 ETOPO1 global relief model



Source: NOAA. Retrieved from: *https://www.ngdc.noaa.gov/mgg/global/global.html*

Figure 1.8 Oceans of the world

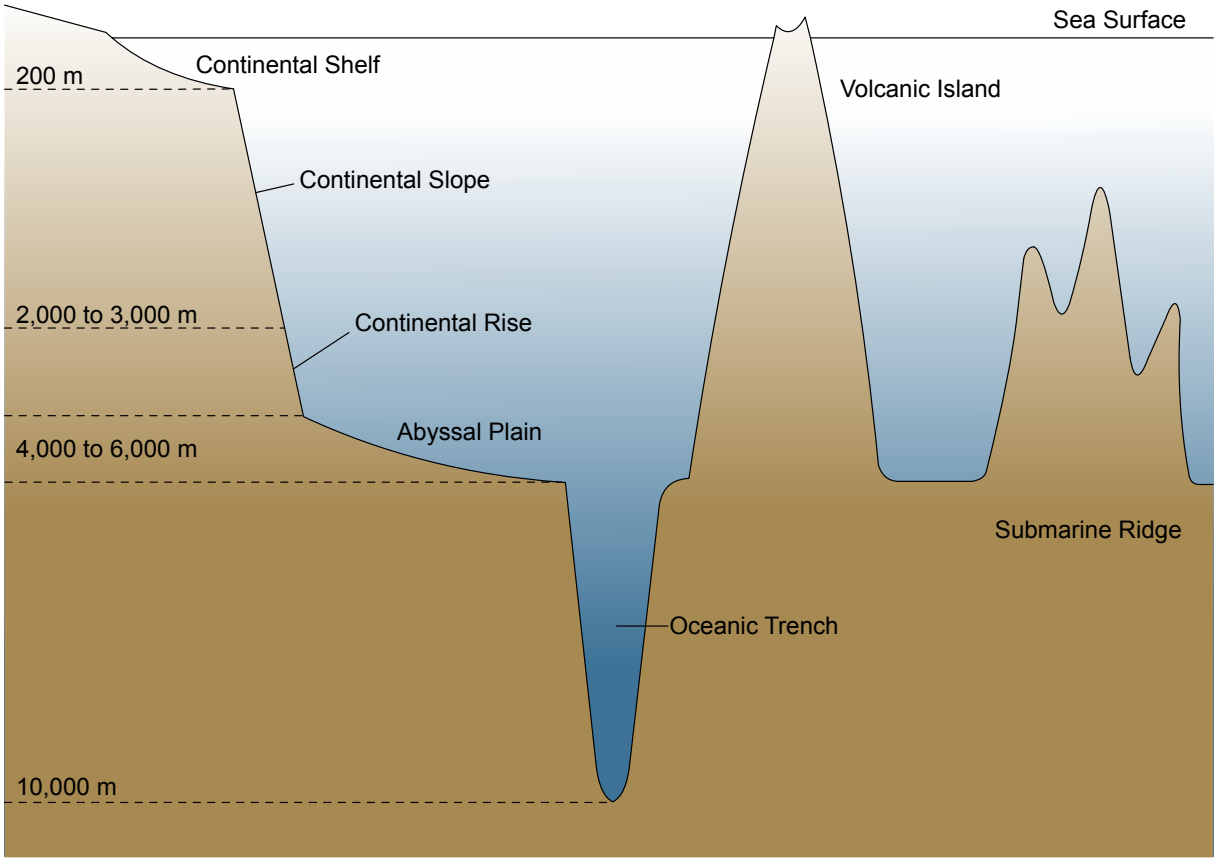
Note that the precise boundaries between oceans may vary with jurisdictions. In this map, ocean boundaries were modified from IHO (1953) to include major oceans and marginal seas.



Source: NOAA. Retrieved from: *https://www.ngdc.noaa.gov/mgg/global/etopo1_ocean_volumes.html*

The average depth of the ocean is 3,720 m with the deepest point found in the Mariana Trench (11,033 m). In total, oceans cover around 362 million km^2 and comprise 1.335 million km^3 of water. The topography of the ocean floor is similar to that of land masses, featuring mountains, volcanoes, plateaus and deep trenches. As introduced in Section 2.1, shallow, sloping seas called 'continental shelves' surround most continents. At their edge, the 'continental slope' leads to the deeper parts of the ocean, where volcanoes, abysses, oceanic ridges, abyssal plains, fracture zones, guyots, trenches and seamounts occur (see Figure 1.9). Underwater plains, usually between 3,000 m and 6,000 m depth, called abyssal plains cover over 50% of the Earth's surface. The abyssal rise, which links the abyssal plain and the continental slope, is also called the continental rise.

Figure 1.9 Major marine geomorphic features



Source: Wikimedia. Retrieved from *https://upload.wikimedia.org/wikipedia/commons/1/13/Oceanic_basin.svg*

Ocean waters provide a significant heat store for our planet and are in constant motion (see Sections 1.4 and 17). They also act as a long term sink for atmospheric carbon dioxide (CO_2). As atmospheric carbon levels increase with deforestation and burning of fossil fuels, the amount of CO_2 being absorbed by the oceans has increased, making these waters more acidic.

Long term climate records indicate the global sea temperatures have risen over the past half century (see Sections 4.5, 5.1.3 and 14), especially in the upper water layers (few hundred metres). This change has prompted movement of marine species from their traditional territories to cooler waters. Since water expands as it warms, sea levels have also been observed to rise 20 cm in the last century leaving 70% of the global shorelines on higher ground (see Sections 4.1 and 12). Moreover, as ocean waters increase in temperature, ice sheets and glaciers melt (see Sections 4.7 and 15), thus adding stored water to the circulating surface waters and further contributing to sea level rise.

Productivity in oceans refers to photosynthetic activity, primarily of phytoplankton, which is the source of the marine food chain (see Section 3.3). Location, season and depth can all affect the productivity of ocean waters (see Section 18.6). Ocean productivity has obvious relevance to several marine industries, including fishing, aquaculture and tourism.

1.2.2 Coastal waters

A coastline marks the dynamic boundary between land and sea. Since this boundary moves with marine tides, the coastal, or littoral, zone is commonly defined as intertidal and subtidal fringes of land, extending from the high tide mark to the continental shelf (see Section 2.1.7). The supralittoral (or supratidal or splash) zone is the narrower, transient area above the spring high tide line that is often splashed by seawater, but is not submerged, and therefore not part of the littoral zone.

Estuaries are the interface region where freshwater from inland rivers and streams mixes with saltwater from the ocean. The biota of estuaries is suited to variations in salt concentrations and temperatures. They also benefit from the nutrient-rich soils transported by rivers, which create one of the most productive ecosystems on Earth. Estuaries provide valuable breeding grounds for many invertebrates, fish, and birds. Estuary habitats in Australia include seagrasses, mangroves, saltmarshes, melaleuca swamps, open waters, muddy and sandy basins, coastal floodplains, intertidal mudflats, coral reefs, sandy shoals and beaches, rocky shores, and macroalgae (Turner *et al*., 2004). The hydrological processes between these habitats include:

- precipitation from atmosphere;
- surface water flows from catchments;
- flow changes due to biota, e.g. burrowing crabs;
- tidal flows and mixing of freshwater and salt waters in estuaries;
- runoff from tides, storms, and floods between wetland pools and estuaries;
- evapotranspiration from vegetation;
- evaporation from waterbodies; and
- surface water exchange with groundwater (OzCoasts, 2018).

Numerous environmental factors, such as climate, topography, tectonic setting, geology, sediments, tidal currents, wave action, river flow and biota, shape estuaries and coastal waterways (Ryan *et al*., 2003). When tectonic and sea level conditions are stable, the geomorphology of coastal waterways is controlled by waves, tides, and rivers to form seven coastal landform classes (see Table 1.2). Two immature categories, embayments and drowned river valleys, evolve into tide-dominated or wave-dominated estuaries, which, with sediment infilling, subsequently become tide-dominated deltas or wave-dominated deltas respectively. The water, nutrient and sediment dynamics of these coastal landform categories are furthered detailed in Ryan *et al*. (2003).

The dynamics and stability of estuaries directly impact the condition of coastal marine waters. Sediment entering coastal waters from estuaries can negatively influence beaches and coral reefs, as well as local industries, for example, fishing, aquaculture, and tourism. Various activities in coastal catchments, such as forestry, agriculture, and urban development, can change the nutrient status or sediment load of coastal rivers, with a direct impact on coastal ecosystems. There is also increasing evidence illustrating the benefit of coastal subtidal and intertidal vegetation as an ecosystem-based defence against climate change impacts and sea level rise (Temmerman *et al.,* 2013).

Coastal environments are productive. In some cases, the standing biomass of the substratum (the material comprising the seabed surface) can be greater than that of the water column (Mazel, 2001). Of particular relevance to coastal studies is the capricious nature of some substratum features in both space and time. Not only can substratum type change abruptly, but the impact of some substratum types on the optical properties of water can also change with water movement (see Section 8.4.3).

Table 1.2 Geomorphological categories of coastal landforms

Coastal Landform	Sediment Trapping	Turbidity	Circulation	Sediment risk to habitat	Dominant Feature
Wave-dominated Estuary	High	Low	Partly mixed	High	Central basin
Coastal Lagoons	Low	Low	Partly mixed	Low	Intertidal flats, barriers and channels
Strandplain					
Tide-dominated estuary	Moderate	High	Well mixed	Moderate	Mangroves, salt marshes and channels
Tidal creek and flat	Low	High	Well mixed	Low	Mangroves and salt marshes
Wave-dominated delta	Low	Low	Partly mixed	Low	Mangroves and channels
Tide-dominated delta	Low	High	Well mixed	Low	Mangroves
Embayments	Low	Low	Partly mixed	Low	Rocky coastal indentation; immature landform enroute to wave- or tide-dominated estuary or delta
Drowned river valleys					

Source: Turner *et al.* (2004) and OzCoasts (2018). Retrieved from: *http://www.ozcoasts.gov.au/conceptual_mods/science_models.jsp*

1.2.3 Inland waters

Inland waters include dams, rivers, lakes, reservoirs, and estuaries, which contain standing or flowing freshwater. They also exist beneath the land surface as groundwater. All water in the biosphere circulates through the oceans and atmosphere over time. As introduced in Section 1.1, less than 1% of the total amount of water in the biosphere exists as inland water. Nonetheless, it supports a diverse range of ecosystems, which are distinctly different from marine and terrestrial ecosystems.

The habitats supported by inland waters can be classified as either lotic (flowing water) or lentic (still water). Five major types of inland waterbodies can be defined, based on the permanency, salt content and circulation of the water:

- lotic—flowing water (rivers, streams or creeks):
  - permanently freshwater;
  - temporarily freshwater; or
  - permanently saline;
- lentic—relatively still waters (lakes, ponds and wetlands)
  - permanent; or
  - temporary.

The distribution of these inland waterbody types varies with climatic region. For example, permanent waters are more common in temperate and tropical climates, while salt lakes characterise arid environments.

The movement of inland waters create drainage systems, which can be categorised as:

- exoheric—open systems that drain into the ocean via lakes, rivers and streams;
- endorheic—closed systems that drain to inland termini (such as temporary or permanent salt lakes), where they evaporate into the atmosphere or percolate into groundwater; or
- arheic—small quantities of unpredictable rainfall that form haphazard drainage patterns.

Lentic waterbodies tend to occur in basins created by volcanoes, glaciers, and tectonic activity, or depressions resulting from water, wind, and chemical erosion, while lotic waters occur in areas of low elevation, which have possibly resulted from water erosion.

Lotic: flowing water (from Latin: lotus meaning washed)
Lentic: still water (from Latin: lentus meaning slow)

1.3 Physical Layers within Waterbodies

All waterbodies can be considered to comprise three fundamental layers, namely the:

- water surface—the boundary between the waterbody and the atmosphere (see Section 1.3.1);
- water column—the layer of water between the water surface and the lithosphere or seabed (see Section 1.3.2); and
- substratum—the topmost layer of consolidated or unconsolidated material of the seabed beneath the waterbody (see Section 1.3.3).

1.3.1 Water surface

The surface of a waterbody is also referred to as the air/water interface as it forms a boundary between the atmosphere and the water column (see Section 4). Different waterbodies have different surface characteristics, depending on biogeography, topography, water flow, atmospheric conditions, chemical and/or biological composition, and temperature (e.g. ice in the form of both glacial ice and sea ice—see Section 15.1).

1.3.2 Water column

The body of water extending from the water surface to the seabed can be viewed as a water column (see Section 5). All solar radiation (both direct and diffuse) is either reflected or refracted by the water surface. Solar and sky radiation intercepted by the surface is refracted into the water column, then transmitted, scattered, or absorbed (see Excursus 8.1). The scattering and absorption characteristics of the water column depend on those of pure water and the specific chemical and biological composition of the waterbody (see Section 8). In the terminology of aquatic zones (see Section 3.1), the pelagic zone corresponds to the water column.

1.3.3 Substratum

Below the water column lies the seabed—the solid base of the waterbody (see Section 6). The substratum layer rests on the seabed (or lithosphere) and may comprise sand, silt, mud, rocks, and live and/or dead coral. Aquatic macroalgae (seaweeds), seagrasses, and benthic microalgae (BMA; also called 'microphytobenthos', Cahoon, 1999), may grow in this layer (Pennesi *et al.,* 2015). Most macroalgae are attached to the substratum whereas seagrasses prefer to grow in an unconsolidated substrate.

Significant changes can occur in substratum features over small intervals of space, depth, and time. The substratum surface can also vary abruptly in depth, slope, composition, and texture. The geomorphology of the substratum influences movement of water in the water column.

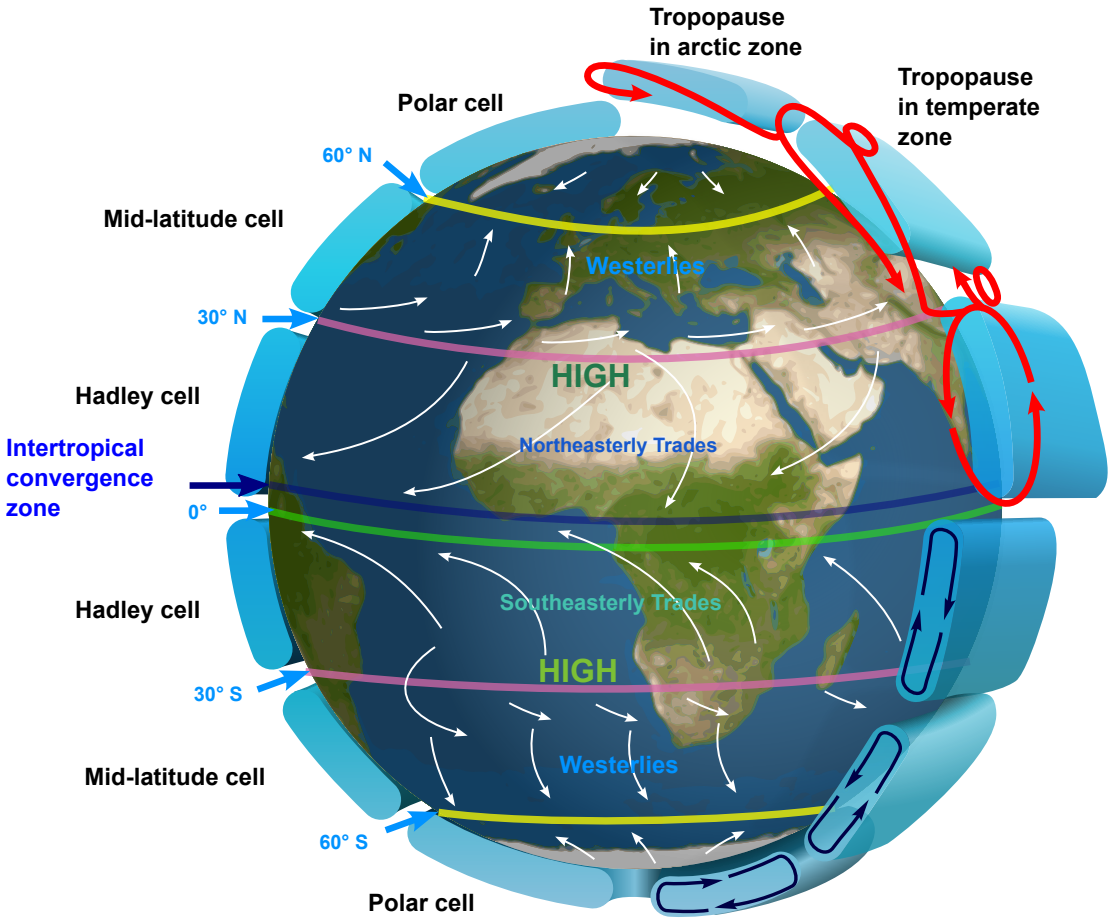
Depending on the depth and scattering/absorption properties of the water column above it, this layer may also reflect some of the radiation refracted by the water column from the water surface (see Section 8.3.3). In this case, the colour and texture of the substratum, and those of any vegetation it supports, will form part of the spectral characteristics of the reflected energy.

1.4 Global Water Circulation

The horizontal movement of the surface layers of a waterbody, particularly in oceans, is closely related to atmospheric patterns of surface winds. While the large scale movement of air around our planet varies with small scale weather systems, its global structure can be represented as a series of latitude-based wind bands that form the Hadley, Ferrel and Polar cells in each hemisphere (see Figure 1.10). Fluctuations in wind velocity, however, happen across the full range of time scales, from seconds to years (see Excursus 4.2).

Figure 1.10 Large scale atmospheric circulation

Three latitude-based belts of surface winds encircle each hemisphere: 0°–30° (trade winds or Hadley cell); 30°–60° (westerlies or Ferrel cell); and 60°–90° (polar easterlies or Polar cell), with the lower latitude and subantarctic bands having greatest impact on surface water movement.



Source: Wikimedia. Retrieved from: *https://commons.wikimedia.org/wiki/File:Earth_Global_Circulation_-_en.svg*

1.4.1 Currents

A current is a continuous, directed movement of water generated by a range of forces. Surface currents are driven by global wind patterns, while slower deep ocean currents result from thermohaline circulation (see Sections 5.1.2). Due to Earth's rotation, both winds and currents are influenced by the Coriolis Effect, which causes them to turn in a clockwise direction in the Northern Hemisphere and an anticlockwise direction in the Southern Hemisphere (see Excursus 1.2). The geomorphology of ocean and coastal features also modifies the location, direction, and velocity of currents. Both atmospheric winds and water circulation help to compensate for differential solar heating of our planet, by drawing surplus heat from equatorial regions to the polar regions (see Volume 1A—Section 4).

Current: A non-periodical, generally horizontal movement of water (or other fluid) due to many causes such as prevalent winds, temperature differential etc., but not to gravitational forces of the Moon and Sun. (Australian Hydrographic Office Glossary)

Excursus 1.2—Coriolis Force and Ferrel's Law

Source: NOAA SciJinks (*https://scijinks.gov/coriolis/*)
Further Information: NOAA National Ocean Service Education: *https://oceanservice.noaa.gov/education/tutorial_currents/04currents1.html*

Coriolis force, first described by Gustave-Gaspard de Coriolis in 1835, is an inertial force that applies upon any object moving relative to a rotating reference frame. It acts in a direction that is perpendicular to the axis of the object and its strength varies with the object's mass and rotation rate. For objects rotating in a clockwise direction, the Coriolis force acts to the left of the object's motion, while for objects rotating in an anticlockwise direction, it acts to the right.

The rotation of Earth on its axis from west to east creates an inertial force which tends to redirect the flow of fluids around it. The impact of this force is described by Ferrel's law:

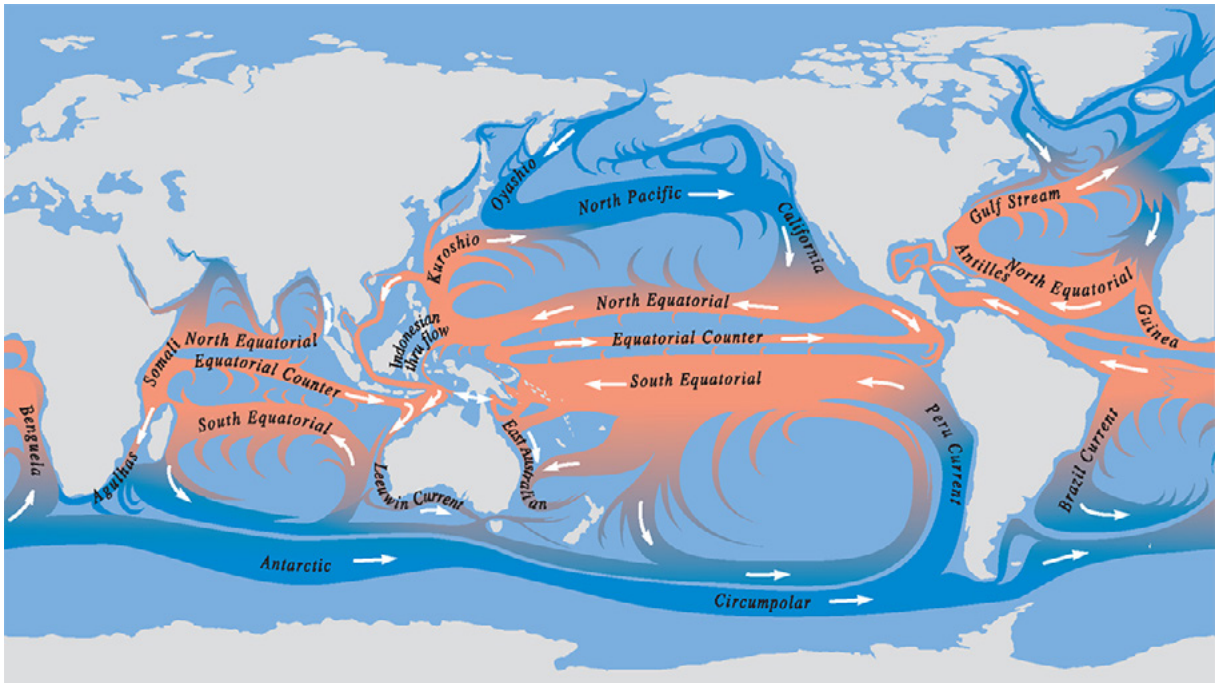
If a body moves in any direction
on the Earth's surface,
there is a deflecting force arising
from the Earth's rotation,
which deflects it to the right
in the northern hemisphere
and to the left
in the southern hemisphere.
(William Ferrel, 1856)

This pattern of deflection of objects that is caused by the Coriolis force is called the Coriolis Effect. On Earth, the Coriolis force influences the direction of both winds and water currents and has a major influence on storm systems and the trajectories of objects flying long distances (including aeroplanes), the Coriolis Effect results in the latitude-related deflection gradients of:

- no deflection at the equator;
- deflection to the right in the Northern Hemisphere;
- deflection to the left in the Southern Hemisphere; and
- maximum deflecton at the poles (Strahler, 1975).

Figure 1.11 Major non-tidal currents

Red shading indicate warmer currents and blue shading indicate colder currents.



Source: Veron (2000a). Retrieved from: *http://www.coralsoftheworld.org/page/distributions/*

Time-dependent movements of global waters occur at a variety of space and time scales, from the water surface to the deepest layers. Only a small part of this movement can be explained by 'predictable' frequency variations such as tides and inertial motion (Wells, 1986). The horizontal movement of water that is generated by astronomical tides is called a tidal current (see Excursus 4.1).

Thus, the movement of surface water is largely determined by the distribution of surface winds, with seasonal changes in wind distribution modifying surface water circulation (see Sections 16 and 17). Non-tidal currents can be permanent or temporary, depending on variations in local weather conditions. Distribution, circulation and temperature of the major global non-tidal currents are shown in Figure 1.11.

Many aquatic species rely on currents to provide transport, deliver sustenance, and distribute offspring. Upwelling currents move colder nutrient-rich waters fom the ocean floor to the surface, thus supporting a range of life forms in the marine food chain (see Section 3). Downwelling currents push dense, oxygen-rich surface waters to lower depths, which enables deep ocean ventilation. Currents also transport salt and other chemicals around the globe, sculpt shorelines, and impact shipping routes (NOS, 2021a).

1.4.2 Gyres

A large system of rotating ocean currents, largely formed by wind and Coriolis forces, is called a gyre (NOS, 2021b). These permanent systems span thousands of kilometres and form a significant component of global weather patterns. Sea level in the centre of gyres is higher than global mean sea level. As illustrated in Figure 1.11, there are five major ocean gyres:

- North Pacific—clockwise;
- South Pacific—anticlockwise;
- North Atlantic—clockwise;
- South Atlantic—anticlockwise; and
- Indian—anti-clockwise.

Two smaller gyres also exist in the two subpolar regions.

Gyres are bounded by permanent ocean currents, called boundary currents, that travel alongside continental boundaries. Boundary currents are classified into two groups based on their location relative to ocean basins:

- eastern boundary currents—occur along the west coast of continents or the eastern side of ocean basins, and tend to be cooler, slower, wider and shallower, transporting water from higher to lower latitudes. These currents are often enriched by coastal upwelling, so are considered productive. Off the WA coast, however, instead of a 'classical'

equatorward, cold, productive eastern boundary current, the warm Leeuwin Current flows southward with a general absence of upwelling, which fundamentally impacts the ecology of the region. The northward flowing current near WA that is shown in Figure 1.11 is the weaker West Australian Current.

- western boundary currents—occur along the east coast of continents or the western side of ocean basins. They tend to be warmer, faster, narrower, and deeper, transporting water from lower to higher latitudes. The East Australia Current is a western boundary current that flows southward along the east coast of Australia (see Excursus 17.1).

1.4.3 Eddies

Temporary features of contained, swirling water are called eddies (NOS, 2021c). Smaller than gyres, these looping currents can also travel long distances. They may form in currents or mid-ocean, but are most obvious in western boundary currents. Such movement is important for circulating nutrients from deeper waters to the surface. Eddies are visible in EO imagery and provide valuable information on ocean circulation patterns, meteorological conditions, and fishing potential (see Figure 1.12 and Section 17).

Figure 1.12 Eddies in waters around Tasmania



Source: NOAA. Retrieved from: *http://oceanservice.noaa.gov/facts/eddy.html*

1.4.4 Langmuir circulation

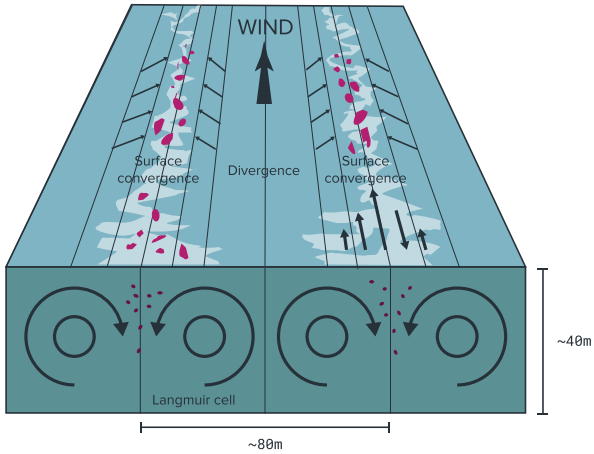
Another local water circulation feature that can be observed by its impact on floating material is called Langmuir circulation, which comprises tubes of circulating water, parallel with the surface and mostly aligned with the wind direction. First studied by Irving Langmuir, these cells are visible in many waterbodies, including oceans, seas, lakes and rivers, as lines of floating material (such as seaweed, algae, oil and debris) collected on the water surface (see Figure 1.13a). As each tube in a pair rotates towards the other, water circulates past the surface forcing surface material into a line between the cells (see Figure 1.13b). These cells typically form parallel lines of floating material, or windrows, which typically have a horizontal spacing and depth of 4–6 m but can have much greater separation and depth. They act as a natural 'clean-up' mechanism for a range of buoyant materials, including plastic particles (van Sebille *et al.*, 2020), and attract a variety of wildlife.

Figure 1.13 Langmuir circulation

a. Lines of sargassum can stretch for miles along the water surface in the Sargasso Sea



b. Formation of Langmuir cells



Source: a. NOAA. Retrieved from: *https://commons.wikimedia.org/wiki/File:Lines_of_sargassum_Sargasso_Sea.jpg* b. van Sebille *et al.* (2020) Figure 3

1.5 Global Carbon Cycle

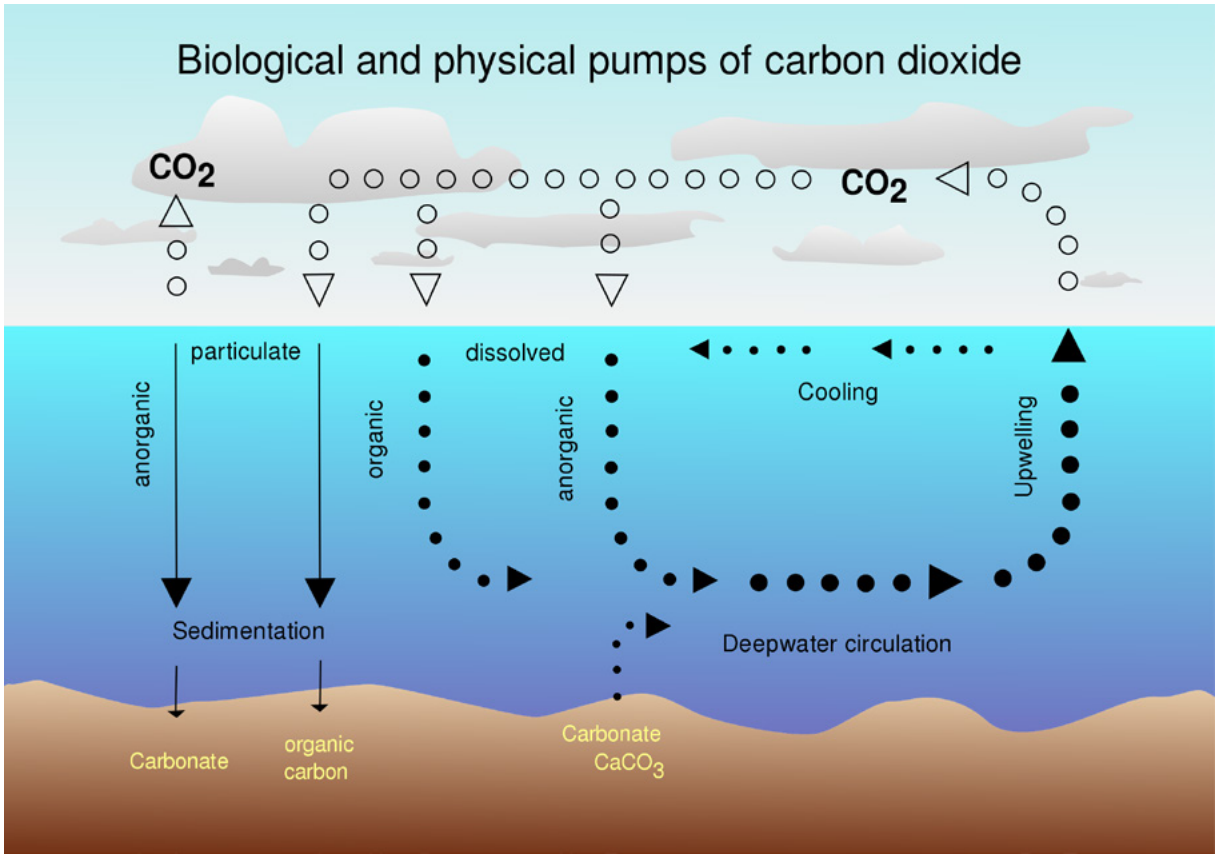
The carbon cycle is introduced in Volume 1—Section 4.2.4 and Volume 3A—Section 17. Surface waters play an important role in the global cycling of carbon, from readily available carbon in the form of atmospheric CO_2 to carbon stored in 'sinks', such as fossil fuels beneath the seafloor. The carbon stored in coastal and marine ecosystems, either in the plants or the sediment below, is called 'blue carbon' (The Blue Carbon Initiative, 2020; see Section 7.4). In conjunction with field studies and modelling, a wide range of EO sensors are being employed to track and interpret current changes in the global carbon cycle and understand its principal driving forces (NASA, 2020; see Sections 7.4 and 7.5).

At a global scale, when atmospheric CO_2 dissolves in surface waters, the level of CO_2 in the atmosphere is lowered; when carbon is released from carbon sinks, such as burning of fossil fuels, it is released back to the atmosphere as CO_2 (see Figure 1.14). Current estimates indicate that around 50 times more carbon is stored in the ocean than in the atmosphere, and nearly half the carbon emissions being released by burning of fossil fuels returning to the ocean via the 'ocean carbon pump' (NASA, 2020). The 'ocean carbon pump' comprises two fundamental transfer mechanisms:

- a biological pump, which moves carbon from the atmosphere to the seabed via aquatic organisms (Volk and Hoffert, 1985; see Section 3.3); and
- a physical pump, which transports water and dissolved inorganic carbon from the surface to the deep sea (see Section 1.4).

While the physical pump is slow and robust, the biological pump is directly impacted by climatic and geographic variables (see Figure 1.15). These carbon pumps relate to coupled physical-biogeochemical processes that are influenced by (change in) ocean properties and structure (stratification), and sea ice. The high-latitude Southern Ocean plays an immensely important role in the ocean uptake (and subsequent storage) of anthropogenic CO_2 and heat from the atmosphere (Rintoul *et al.*, 2019). Marine habitats, such as mangroves, seagrass beds and salt marshes also form effective carbon sinks, but in a shorter time scale than fossil fuels, and with more vulnerability to degraded water quality and environmental conditions (see Section 20).

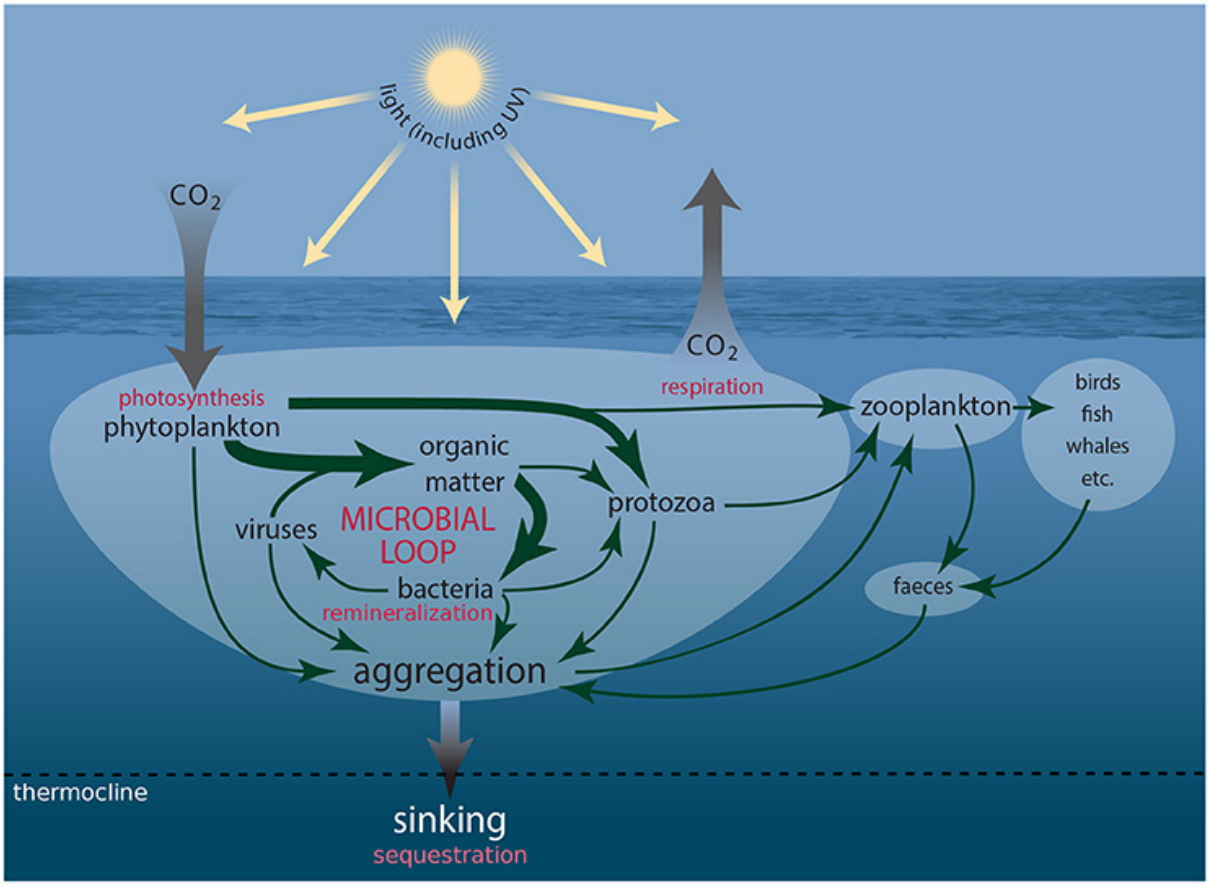
Figure 1.14 Ocean carbon pumps



Source: Hannes Grobe and McSush, Wikimedia. Retrieved from: *https://commons.wikimedia.org/wiki/File:CO2_pump_hg.svg*

Figure 1.15 Biological pump

CO_2 is converted into organic matter during photosynthesis by phytoplankton growth in the surface ocean. A small amount of this material reaches the deep sea where it is sequestered from the atmosphere, either as organic carbon, or dissolved CO_2 after bacterial remineralisation. The overall effect is known as the 'biological pump'. The deeper the carbon is transported into the ocean interior, the longer it remains isolated from the atmosphere.



Source: Deppeler and Davidson (2017) Figure 1

Aquatic organisms use carbon for:

- photosynthesis—phytoplankton converts atmospheric and dissolved carbon into organic matter (and also return 0_2 and CO_2 to the atmosphere via respiration); and
- calcification—marine organisms containing calcium (principally coccolithophores, unicellar algae) use dissolved carbon to create calcium carbonate for their structural components. As these organisms decay, their structure decomposes and sinks to form sediments, and ultimately rocks, on the seafloor.

As expanded in Section 7.4, a balance is required between these processes. The concentration of CO_2 in ocean water has been observed to vary with both atmospheric CO_2 concentration and water temperature, with both increasing in recent centuries. Since the ocean absorbs around 30% of the CO_2 that is released into the atmosphere, increased levels of atmospheric CO_2 also increases the amount of CO_2 absorbed by the ocean, making it more acidic. Thus, as the CO_2 concentration of oceans increases, the pH of these waters decreases (see Section 5.2.2), potentially leading to broad scale ocean acidification. At the current rate of 22 million tons per day it is estimated that at least 25% of atmospheric CO_2 is dissolved into the ocean, resulting in these waters now being 30% more acidic than they were 200 years ago.

However, lower pH levels in surface waters, including coastal estuaries and waterways, means that there are more hydrogen ions and fewer carbonate ions for calcifying organisms, such as crustaceans and corals, to use for growing shells and skeletons. As pH levels in these waters continue to fall, these organic structures may even dissolve. Such changes in the ecology of aquatic habitats could have significant implications for the stability of the ocean food web and global carbon cycle (see Sections 3 and 7.4).

One marine geoengineering solution intended to accelerate the growth of phytoplankton, and thus increase the rate of CO_2 transfer from the atmosphere to the oceans, has been ocean fertilisation. This process involves stimulating primary productivity by 'fertilising' ocean waters with nutrients, such as iron, nitrogen or phosphorus. While it is uncertain that the increased phytoplankton growth from ocean fertilisation will actually sequester carbon in the deep sea in the longer term, there is evidence that it may result in undesirable changes to the marine food chain and various marine ecosystems. It may also decrease subsurface oxygen and further increase ocean pH (ACE CRC, 2008, 2016).

1.6 Further Information

The Hydrosphere

https://www.pbslearningmedia.org/resource/buac17-35-sci-ess-waterdistribute/saltwater-and-freshwater-distribution-on-earth/

http://education.nationalgeographic.com/education/activity/our-hydrosphere/?ar_a=1

Tides

NOAA National Ocean Service: Tides and Water Levels: *https://oceanservice.noaa.gov/education/tutorial_tides/*

Currents

CSIRO Australasian currents: *https://www.csiro.au/en/Research/Environment/Oceans-and-coasts/Australasian-ocean-currents*

NOAA National Ocean Service:

Currents: *https://oceanservice.noaa.gov/education/tutorial_currents/welcome.html*

Ocean currents *http://www.noaa.gov/resource-collections/ocean-currents*

NASA: Ocean Motion and Surface Currents: *http://oceanmotion.org/html/introduction-general.htm*

NOAA National Ocean Service: *https://oceanservice.noaa.gov/welcome.html*

Oceana: *http://oceana.org*

Sea Ice

Biogeochemical Exchange Processes at Sea Ice Interfaces (BEPSII): *https://sites.google.com/site/bepsiiwg140/vision*

Nomenclature

IHO-IOC (2018). GEBCO (General Bathymetric Chart of the Oceans) Gazetteer of Undersea Feature Names: *https://www.gebco.net/data_and_products/undersea_feature_names/*

Sea Level Rise

NOAA: *https://oceanservice.noaa.gov/education/sea-level-rise/welcome.html*

CSIRO: *https://research.csiro.au/slrwavescoast/sea-level/*

Australian Water Industry

Australian Water Association: *www.awa.asn.au*

Australian Water Storages

Bureau of Meteorology: *http://www.bom.gov.au/akamai/https-redirect.html#/water-storages/about*

Australian Inland Waters

Topographic Drainage Divisions and River Regions: *http://www.bom.gov.au/water/about/riverBasinAuxNav.shtml*

Australian Coasts

CSIRO: *https://research.csiro.au/slrwavescoast/extremes/causes-extreme-sea-levels/*

OzCoasts: *http://www.ozcoasts.gov.au/*

Australian Oceans

Ross (1995)

Offshore Constitutional Settlement: *https://www.ag.gov.au/Internationalrelations/InternationalLaw/Pages/TheOffshoreConstitutionalSettlement.aspx*

GA: Australian Marine Spatial Information System (AMSIS): *http://www.ga.gov.au/scientific-topics/marine/jurisdiction/amsis*

CAWCR (Collaboration for Australian Weather and Climate Research): *https://www.cawcr.gov.au/publications/*

IMOS:

Australian Ocean Data Network (AODN): *https://portal.aodn.org.au/*

Ocean Current: *http://oceancurrent.imos.org.au*

Bluelink: *https://www.csiro.au/en/Research/OandA/Areas/Oceans-and-climate/Bluelink*

Oceanwatch Australia: *http://www.oceanwatch.org.au*

1.7 References

ACE CRC (2008). *Position Analysis: Ocean Fertilisation*: *Science and Policy Issues*. The Antarctic Climate and Ecosystems Cooperative Research Centre, Hobart. *http://acecrc.org.au/wp-content/uploads/2015/03/2008-ACE-PA-Ocean-Fertilisation.pdf*

ACE CRC (2016). *Position Analysis: Ocean Fertilisation*. The Antarctic Climate and Ecosystems Cooperative Research Centre, Hobart. ISSN: 1835-7911. *http://acecrc.org.au/wp-content/uploads/2016/07/ACE106_Position-Analysis_Ocean-Fert_April-2016_WEB.pdf*

AHS (2017) *Names and Limits of Oceans and Seas around Australia*. Australian Hydrographic Service Fact sheet: *http://www.hydro.gov.au/factsheets/WFS_Names_and_Limits_of_Oceans_and_Seas_Around_Australia.pdf*

Amante, C., and Eakins, B.W. (2009). *ETOPO1 1 Arc-Minute Global Relief Model: Procedures, Data Sources and Analysis*. NOAA Technical Memorandum NESDIS NGDC-24, 19 pp, March 2009. *http://www.ngdc.noaa.gov/mgg/global/relief/ETOPO1/docs/ETOPO1.pdf*

Cahoon, L. (1999). The role of benthic microalgae in neritic ecosystems. *Oceanography and marine biology*, 37, 47–86.

Deppeler, S.L., and Davidson, A.T. (2017). Southern Ocean Phytoplankton in a Changing Climate. *Frontiers in Marine Science*, 4, 40. *https://www.frontiersin.org/article/10.3389/fmars.2017.00040*

Eakins, B.W. and Sharman, G.F. (2010). *Volumes of the World's Oceans from ETOPO1*. NOAA National Geophysical Data Center, Boulder, CO, 2010: *https://www.ngdc.noaa.gov/mgg/global/etopo1_ocean_volumes.html*

IHO (1953). *The Limits of Oceans and Seas*. International Hydrographic Organisation Special Publication 23, 3rd Edition, Monte Carlo. *http://www.iho-ohi.net/*

IHO-IOC (2018). *GEBCO (General Bathymetric Chart of the Oceans) Gazetteer of Undersea Feature Names*. *https://www.gebco.net/data_and_products/undersea_feature_names/*

Mazel, C.H. (2001). Optics of the Seafloor. *Oceanography*, 14(3), 54–63.

NASA (2020). *NASA Science. Carbon Cycle* webpage: *https://science.nasa.gov/earth-science/oceanography/ocean-earth-system/ocean-carbon-cycle*

NOS (2021b). *What is a gyre?* webpage, NOAA National Ocean Service website: *https://oceanservice.noaa.gov/facts/gyre.html*

NOS (2021a). *Currents* webpage, National Ocean Service (NOAA) website: *https://oceanservice.noaa.gov/education/tutorial_currents/welcome.html*

NOS (2021c). *What is an eddy?* webpage, NOAA National Ocean Service website: *http://oceanservice.noaa.gov/facts/eddy.html*

OzCoasts (2018). *OzCoasts Australian Online Coastal Information* website: *https://ozcoasts.org.au/*

Pennesi, C., Rindi, F., Totti, C., and Beolchini, F. (2015). Marine Macrophytes: Biosorbents. In *Springer Handbook of Marine Biotechnology*. (Ed: Kim S.K.) Springer Handbooks. Springer, Berlin, Heidelberg.

Rintoul, S., Bindoff, N., and Hobbs, W. (2019). *Position Analysis: Causes and Consequences of Southern Ocean Change*. The Antarctic Climate and Ecosystems Cooperative Research Centre, Hobart.

Rodell, M., Famiglietti, J.S., Wiese, D.N., Reager, J.T., Beaudoing, H.K., Landerer, F.W., and Lo, M.-H. (2018). Emerging trends in global freshwater availability. *Nature*, 557, 651–659. doi:10.1038/s41586-018-0123-1

Ross, D.A. (1995). *Introduction to Oceanography*. HarperCollins, New York. pp. 236–242.

Ryan, D.A., Heap, A.D., Radke, L., and Heggie, D.T. (2003). *Conceptual models of Australia's estuaries and coastal waterways: applications for coastal resource management*. Geoscience Australia, Record 2003/09, 136 pp.

Shiklomanov, I.A., and Rodda, J.C. (2003). *World Water Resources at the Beginning of the Twenty-First Century*. United Nations Educational, Scientific and Cultural Organization (UNESCO). Cambridge University Press, Cambridge. ISBN 0 521 82085 5 *http://catdir.loc.gov/catdir/samples/cam034/2002031201.pdf*

SOE (2011). *State of Environment Report 2011*. *http://155.187.2.69/soe/2011/report/inland-water/index.html*

SOE (2017). *State of Environment Report 2016*. Australia's water resources: Inland water (2016): *https://soe.environment.gov.au/theme/inland-water/topic/2016/australias-water-resources*

Strahler, A.N. (1975). *Physical Geography*. Wiley, New York.

Symonds, P., Alcock, M., and French, C. (2009). Setting Australia's Limits: Understanding Australia's marine jurisdiction. *AusGeo News* 93, March 2009, Geoscience Australia.

Temmerman, S., Meire, P., Bouma, T.J., Herman, P.M., Ysebaert, T., De Vriend, H.J. (2013). Ecosystem-based coastal defence in the face of global change. *Nature*, 504(7478), 79–83. doi:10.1038/nature12859

The Blue Carbon Initiative (2020). *The Blue Carbon Initiative* website: *https://www.thebluecarboninitiative.org/*

Turner, L., Tracy, D., Tilden, J., and Dennison, W.C. (2004). *Where river meets sea: Exploring Australia's estuaries*. CRC for Coastal Zone Estuary and Waterway Management, Brisbane.

USGS (2018). *United States Geological Survey* website: *https://www.usgs.gov/science/science-explorer/Water*

van Sebille, E., Aliani, S., Law, K.L., Maximenko, N., Alsina, J., Bagaev, A., Bergmann, M., Chapron, B., Chubarenko, I., Cózar, A., Delandmeter, P., Egger, M., Fox-Kemper, B., Garaba, S.P., Goddijn-Murphy, L., Hardesty, B.D., Hoffman, M., Isobe, A., Jongedijk, C., Kaandorp, M., Khatmullina, L., and Koelmans, A.A. (2020). The physical oceanography of the transport of floating marine debris. *Environmental Research Letters*, 15(2), [023003]. *https://doi.org/10.1088/1748-9326/ab6d7d*

Veron, J.E.N. (2000a). *Corals of the World*. Australian Institute of Marine Science, Townsville. Volumes 1–3. 1410 p.

Volk, T., and Hoffert, M.I. (1985). Ocean carbon pumps: Analysis of relative strengths and efficiencies in ocean-driven atmospheric CO_2 changes. In *The Carbon Cycle and Atmospheric CO2: Natural Variations Archean to Present*. pp 99–110. (Eds: Sundquist, E., and Broecker, W.S.). Geophysical Monograph 32, American Geophysical Union, Washington, D.C.

Wells, N. (1986). *The Atmosphere and Ocean. A Physical Introduction*. Taylor and Francis, London.



2 Australia's Surface Water Environment

This section provides an overview of the surface water environment within and surrounding the Australian land masses. The Australian continent and its islands are described in Volume 3A. The following topics are covered below:

- marine jurisdiction, including names of marine territories and entitlements of zones (see Section 2.1);
- geomorphology of marine waters (see Section 2.2);
- circulation of marine waters in the Australasian region (see Section 2.3);
- environmental factors affecting marine waters (see Section 2.4);
- Antarctica (see Section 2.5);
- characteristics of inland waters (see Section 2.6); and
- water storage and consumption (see Section 2.7).

2.1 Marine Jurisdiction

In addition to its land areas, Australia regulates vast marine areas extending from its continental coastline and encircling its many islands (GA, 2021a). The total confirmed area of marine jurisdiction is 13.86 million km^2, nearly twice its continental landmass (Symonds *et al.,* 2009). This makes Australia custodian of around 3.8% of the Earth's oceans, and, with both land and marine jurisdictions combined, around 5.4% of the Earth's surface. For cartographic and hydrographic (rather than legal) purposes, the names and limits of marine waters around Australia are defined by The Australian Hydrographic Service (AHS) as illustrated in Figure 2.1. In addition to its marine jurisdiction zones, Australia has obligations within its charting area (see Figure 2.2) as specified by the:

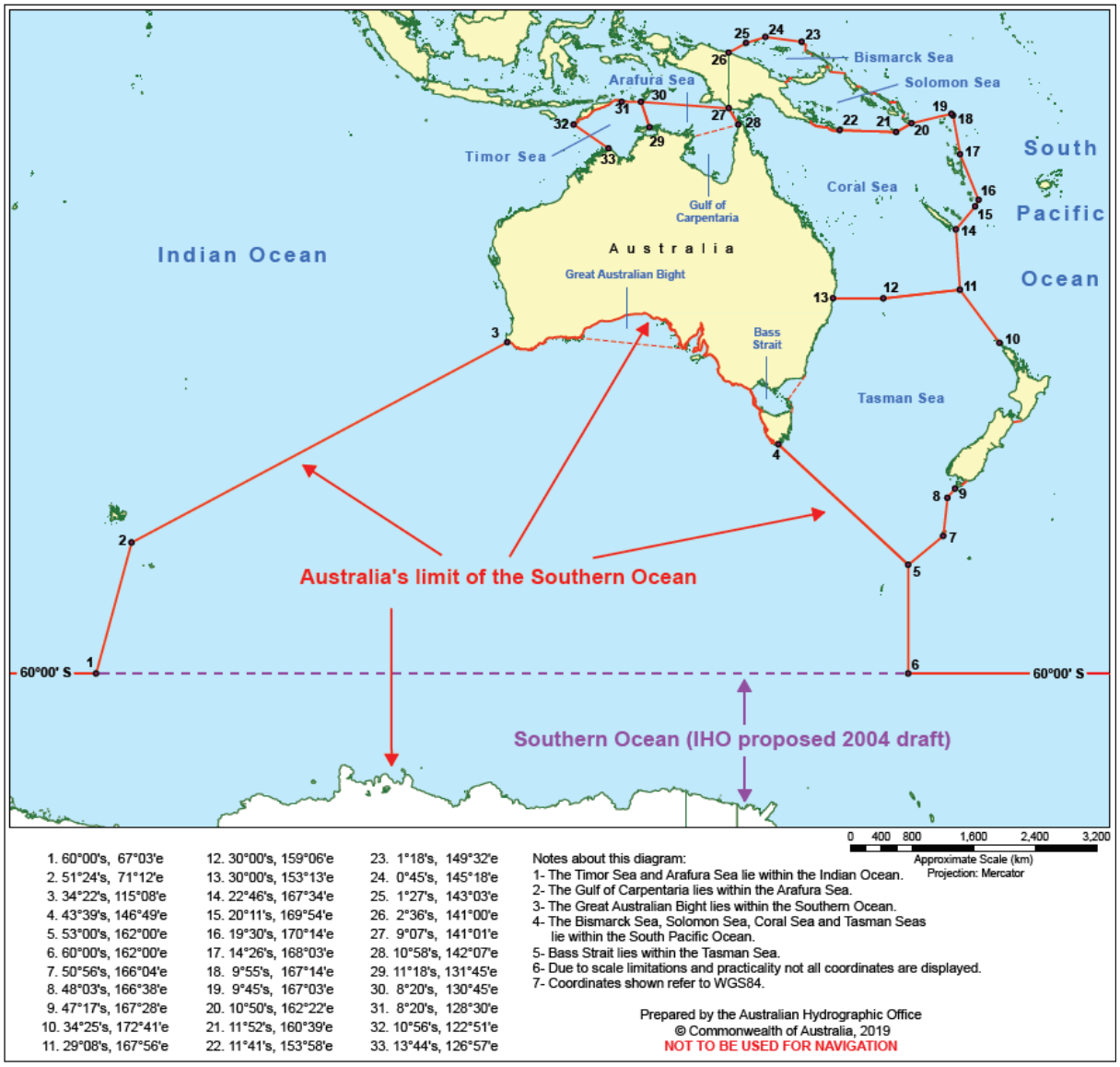
- International Convention for the Safety of Life at Sea (SOLAS) convention;
- United Nations Convention on the Law of the Sea (UNCLOS); and the
- Australian Navigation Act 2012.

This charting area obligates Australia to provide hydrographic services to the international maritime community, including surveying, charting, and publishing nautical information and International Series (IS) Charts, as specified by the International Hydrographic Organisation (IHO). Australia also supports hydrographic services in Papua New Guinea and the Solomon Islands (AHS, 2017a).

The coastline of Australia is an old one. For long ages there has been none of the major convulsions of the earth's crust that have resulted in the peculiar contours of many other great land-masses. There have been inland seas in past ages but they have dried up and are now part of the land. There have been deep gulfs penetrating far into the interior, but they too have long since gone.
(Charles F. Laseron, 1953)

Background image: Australian land mass surrounded by portion of its marine jurisdiction. **Source:** Blue Marble World topography and bathymetry composition, November 2004, NASA.

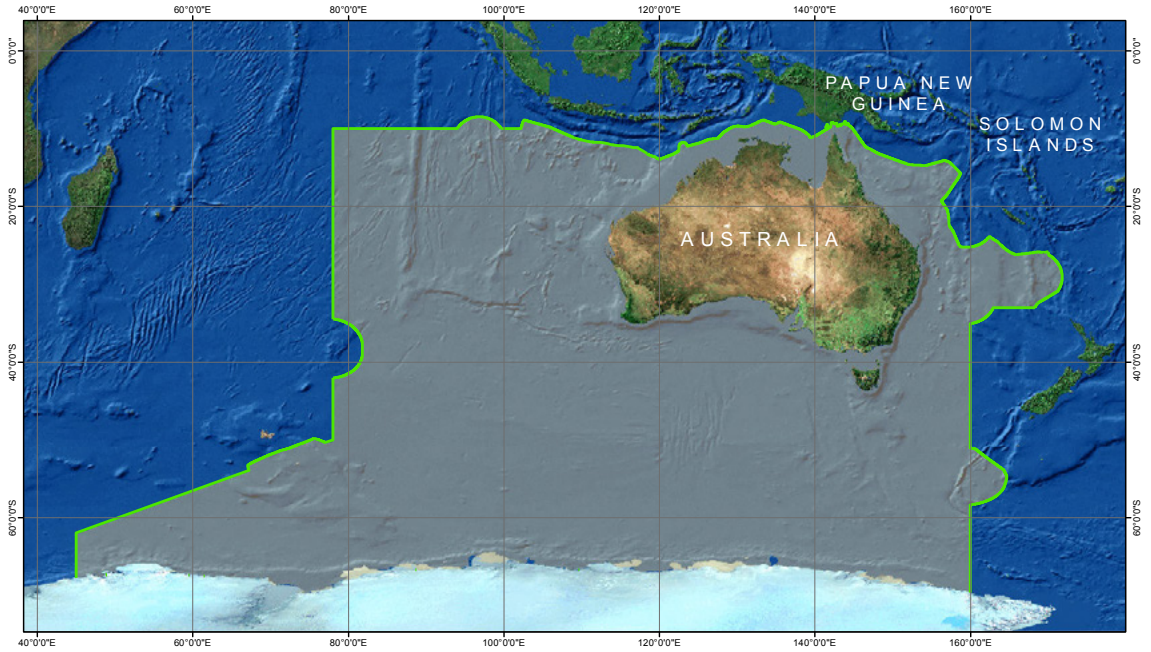
Figure 2.1 Names and limits of oceans and seas around Australia



Source: AHS (2017b). Retrieved from: *https://www.hydro.gov.au/factsheets/FS_Hydrographic_Surveying-Limits_of_oceans_and_seas_around_Aus.pdf*

Within Australian waters (3–200 M from the Territorial Sea Baseline, TSB), the Australian Marine Safety Authority (AMSA) is responsible for navigation safety and protection of the marine environment, including surveillance of ship-sourced pollution (see Section 19.4). AMSA also maintains a national search and rescue service for maritime and aviation traffic (see Excursus 2.1).

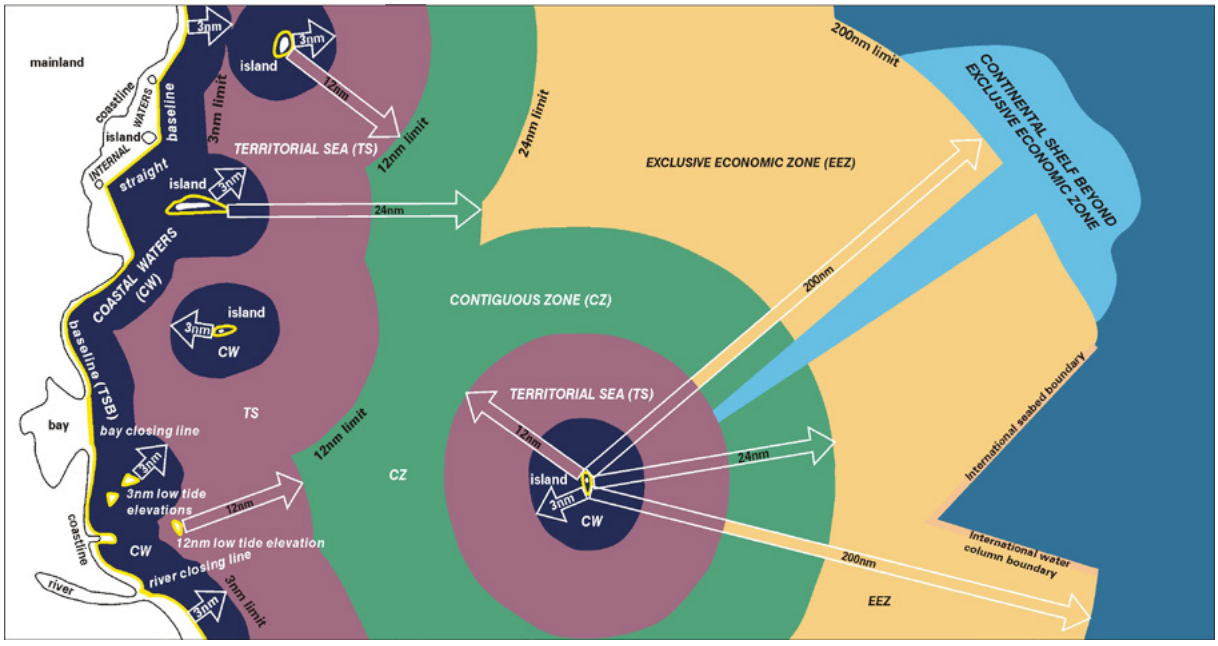
Figure 2.2 Australian Charting Area



Source: AHS (2017a). Retrieved from: *http://www.hydro.gov.au/business-publications/HydroScheme_2017-2020_WEB_20171103.pdf* page 3

UNCLOS established a legal order to distinguish national and international government of seas and oceans. This convention determines the location of several marine zones, relative to a precisely defined interface between land and sea (UN, 1982). In combination with Australian legislation, six marine zones have been defined around Australian land. The relative extents of these zones, as measured from the official baseline (TSB; see Section 2.1.1), and the rights they bestow to Australia, are summarised in Table 2.1 and illustrated in Figure 2.3. Each zone is described below and the extents of most of these zones are shown in Figure 2.4.

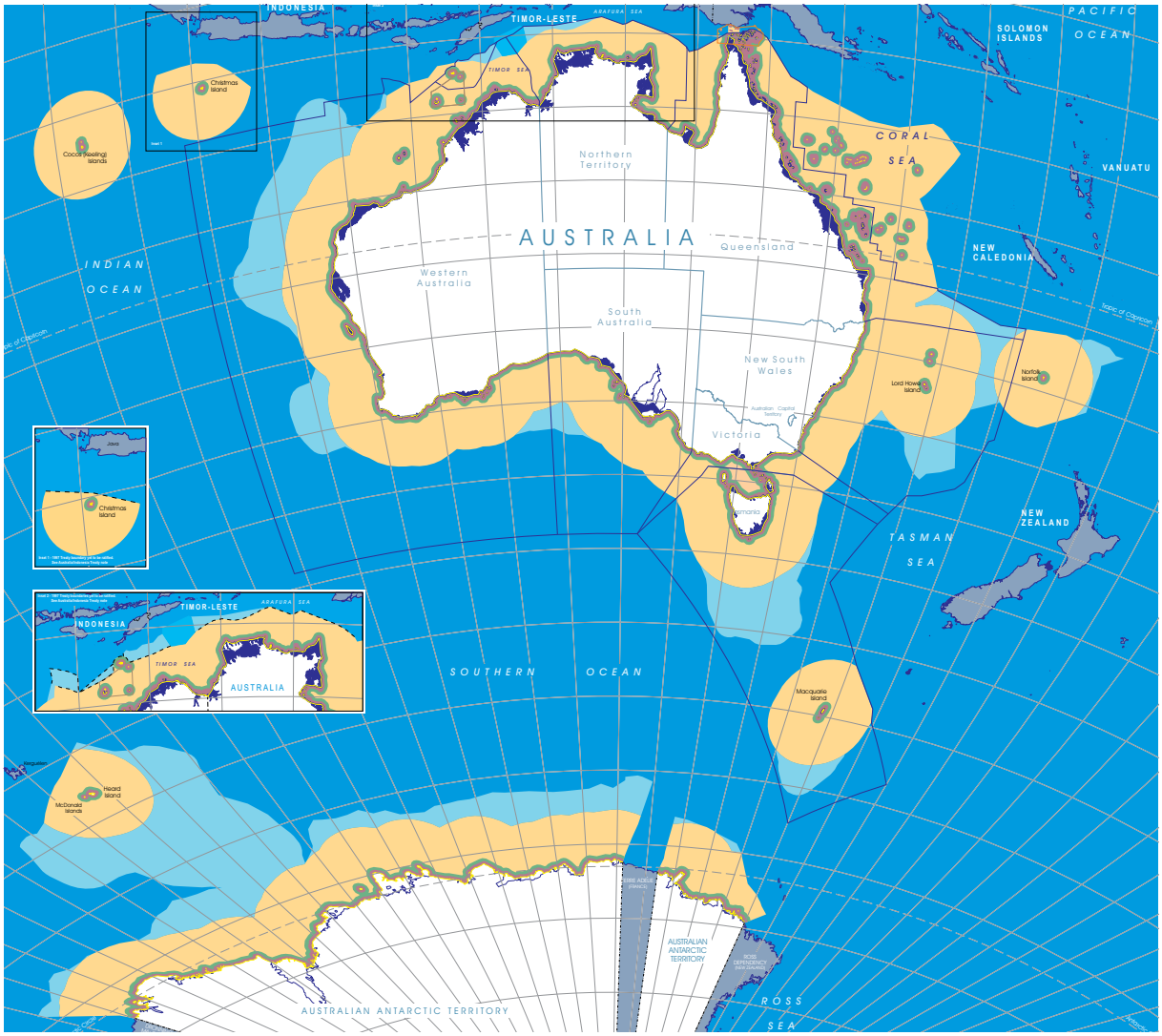
Figure 2.3 UNCLOS marine zone boundaries



Source: GA (2021a)

Figure 2.4 Australia's Maritime Zones

Refer to Figure 2.3 for colour codes.



Source: GA (2021a). Note that this map was produced in 2005 (GeoGat 63690) and updated regional maps are available at 1:500,000 from *http://www.ga.gov.au/scientific-topics/marine/jurisdiction/map-series*

Table 2.1 Australia's maritime zones

1 M: 1 nautical mile (≈1,852 m); TSB: Territorial Sea Baseline

From TSB	To						Area (million km²)	Sovereign Rights to		
	Distance from TSB (M)					Nearest EEZ		Air	Water	Seabed and subsoil
	3	12	24	200	350 (max.)					
Coastal Waters							0.15	Full		
Territorial Waters – limit of sovereign territory							0.85			
			Contiguous Zone				n/a	Customs, immigration, quarantine		
			Exclusive Economic Zone				10.19		Economic and conservation activities	
		Australian Fishing Zone							Fishing	
			Continental Shelf (generally only extends to 200 M from TSB)				2.56			Exploration, exploitation
					High Seas		n/a			

Source: Content derived from GA (2021a)

Excursus 2.1—Australian Maritime Safety Authority (AMSA)

Source: Paul Irving, AMSA
Further Information: *https://www.amsa.gov.au/*

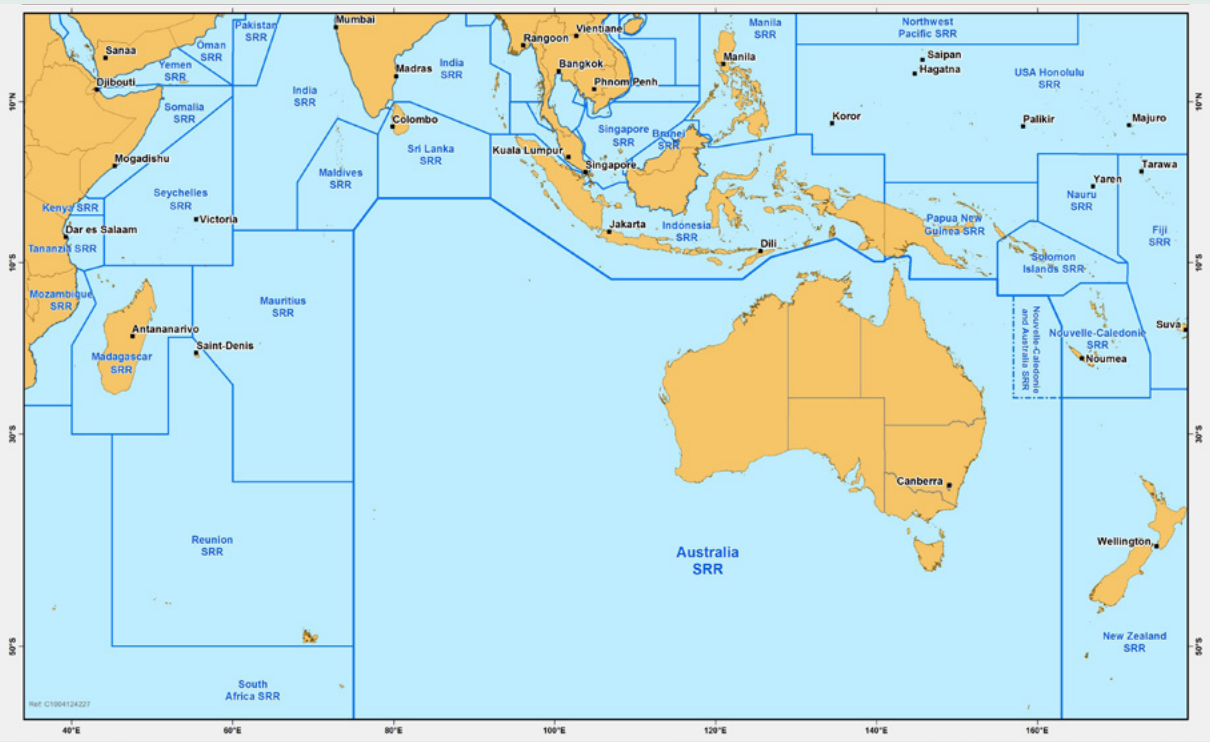
AMSA promotes the safety and protection of our marine environment and combats ship-sourced pollution. Often in partnership with individual states and territories, AMSA provides much of the infrastructure for safety of navigation in Australian waters, and maintains a national search and rescue service for the maritime and aviation sectors. Spaceborne and airborne technologies are now a fundamental means of delivering these functions across the nearly 53 million sq. km (around 10% of the Earth's surface) that makes up Australia's search and rescue region. This covers the Australian continent and large areas of the Indian, Pacific and Southern Oceans, as well the Australian Antarctic territories (see Figure 2.5). AMSA's use of satellite technologies extends from communications to Earth Observation.

Inmarsat and Iridium provide Australia's Global Maritime Distress and Safety Services (GMDSS). This allows distress beacons to be detected and information distributed through the Cospas-Sarsat system. AMSA also works with partners, such as NASA and the new Australian SmartSAT CRC to explore possible future enhancements to the distress beacon system, which will provide more sensitivity and potentially two-way communications.

The satellite automatic identification system (S-AIS) provides AMSA with real time information transmitted from ships about their facilities, location, and voyage. This augments shore-based VHF AIS stations, that work best close to land. The S-AIS data is used to monitor ships around Australia, building a dynamic picture for maritime domain awareness. This provides information to undertake oil spill prosecutions, ship-reporting Synthetic Aperture Radar (SAR), and casualty management. Through Airservices Australia, AMSA also receives aviation reporting and provides safety services for aviation search and rescue functions.

AMSA uses satellite-based SAR data from various international service providers to identify illegal maritime oil spills, and to support oil spill response functions (see Excursus 19.4). In particular, AMSA has been collaborating with CSIRO Oceans and Atmosphere, as they develop new capabilities to improve oil spill identification using direct acquisitions from new satellite constellations and the use of artificial intelligence in image analysis.

Figure 2.5 Australian Search and Rescue Region



Source: AMSA. Retrieved from *https://www.amsa.gov.au/sites/default/files/2017-05-sar-australia-search-rescue-region.jpg*

2.1.1 Territorial Sea Baseline

The Territorial Sea Baseline (TSB) is defined as the 'low water' along the coastline (GA, 2021a). The Australian TSB is based on the Lowest Astronomical Tide (LAT) and interpolates bays, rivers, islands and, where necessary, deeply indented coastlines. Derivation of the LAT relies on EO, topographic and bathymetric maps, and hydrological charts. The distance between high and low tide can be particularly significant for small islands such as atolls.

2.1.2 Territorial Sea

Each nation implicitly retains sovereignty over adjacent marine areas up to 12 nautical miles (M) from its coastline[2]. Jurisdiction includes the air space above these marine areas, and their seabed and subsoil. The landward boundary of the Territorial Sea is defined by the TSB and its extent is determined by extrapolating from the TSB.

Australia's area of Territorial Sea covers 0.85 million km^2 (including Coastal Waters—see Section 2.1.3). The federal government administers activities within its 0.70 million km^2 of Territorial Sea, including mining, fishing, shipping, navigation and conservation.

2.1.3 Coastal Waters

Within the Territorial Sea, Australian states and territories govern their adjacent coastal waters up to 3 M from the TSB, excluding low tide elevations more than 3 M from the coastline. Their jurisdiction includes the water column and subjacent seafloor, and totals 0.15 million km^2. Within these regions activities such as fishing and exploration are regulated by the relevant state or territory, as permitted in the Offshore Constitutional Settlement (AGD, 1980).

2.1.4 Contiguous Zone

Another marine zone defined by UNCLOS is the Contiguous Zone, which lies directly on the seaward side of the territorial zone, and extends up to 24 M from the TSB. Within this zone, Australia is permitted to prevent and punish infringement of relevant laws, including those relating to customs, immigration, taxes, and health.

Table 2.2 Area of Australian Exclusive Economic Zones

Note: Excluding Antartica EEZ

EEZ	Area (km^2)
Mainland Australia (including Tasmania and minor islands)	6,048,681
Macquarie Island	471,837
Cocos Island	463,371
Norfolk Island	428,618
Heard and McDonald Islands	410,722
Christmas Islands	325,021
Total	8,148,250

Source: Geoscience Australia

2.1.5 Exclusive Economic Zone

Also extending further seaward from the Territorial Sea is the Exclusive Economic Zone (EEZ), whose outer limit is defined by UNCLOS as being within 200 M from the TSB. The boundaries of the Australian EEZ were defined by the Seas and Submerged Land Act (1973) and the Maritime Legislation Amendment Act (1994) and this maritime territory is the third largest in the world (after USA and France). The areas of EEZ for Australia's major land areas are listed in Table 2.1.

Within this zone, Australia has sovereign rights for specific economic activities within the water, seabed and subsoil. These rights allow exploration, exploitation, conservation, and management of both living and non-living natural resources within and below those waters, as well as production of energy and installation of observation facilities for research, protection, and preservation.

Marine waters between defined EEZ are referred to as the High Seas. Subject to regulations of UNCLOS, these waters are shared by all nations for peaceful purposes, including navigation, overflight, submarine cable and pipelines, installation of observation facilities, fishing, and scientific research.

2 1 nautical mile (M) = 1,852 metres. This approximates the mean length of 1 minute of latitude.

2.1.6 Australian Fishing Zone

The federal government of Australia manages fisheries in Commonwealth waters, that is, those marine areas within the Territorial Sea and EEZ, but excluding Coastal Waters and defined 'excepted waters'. The latter occur in the Torres Strait and adjacent to the Australian Antarctic Territory. The Australian Fishing Zone is established via the Fisheries Management Act 1991 and covers 8 milllion km^2.

2.1.7 Continental Shelf

UNCLOS defines the Continental Shelf of a nation as comprising the seabed and subsoil of its submarine areas from the seaward boundary of its Territorial Sea to the outer edge of its continental margin, or up to 200 M from the TSB where the continental margin terminates at less than this distance. In general, the continental shelf cannot extend further than 350 M from the TSB and covers the same area as the EEZ. Within the Continental Shelf, the sovereign nation has exclusive rights to explore and exploit the natural resources of the seabed and subsoil, and/or authorise and regulate these activities by other nations, but must cooperate with other nations with regard to navigation through the waters above the Continental Shelf and infrastructure (such as cables) on the marine floor. In 2008, the Commission on the Limits of the Continental Shelf (established under UNCLOS) extended the area of Australia's Continental Shelf by 2.56 million km^2. This extension was based on the geomorphology of the continental margins surrounding the Australian land mass (Symonds *et al*., 2009).

2.2 Marine Geomorphology and Bioregionalisation

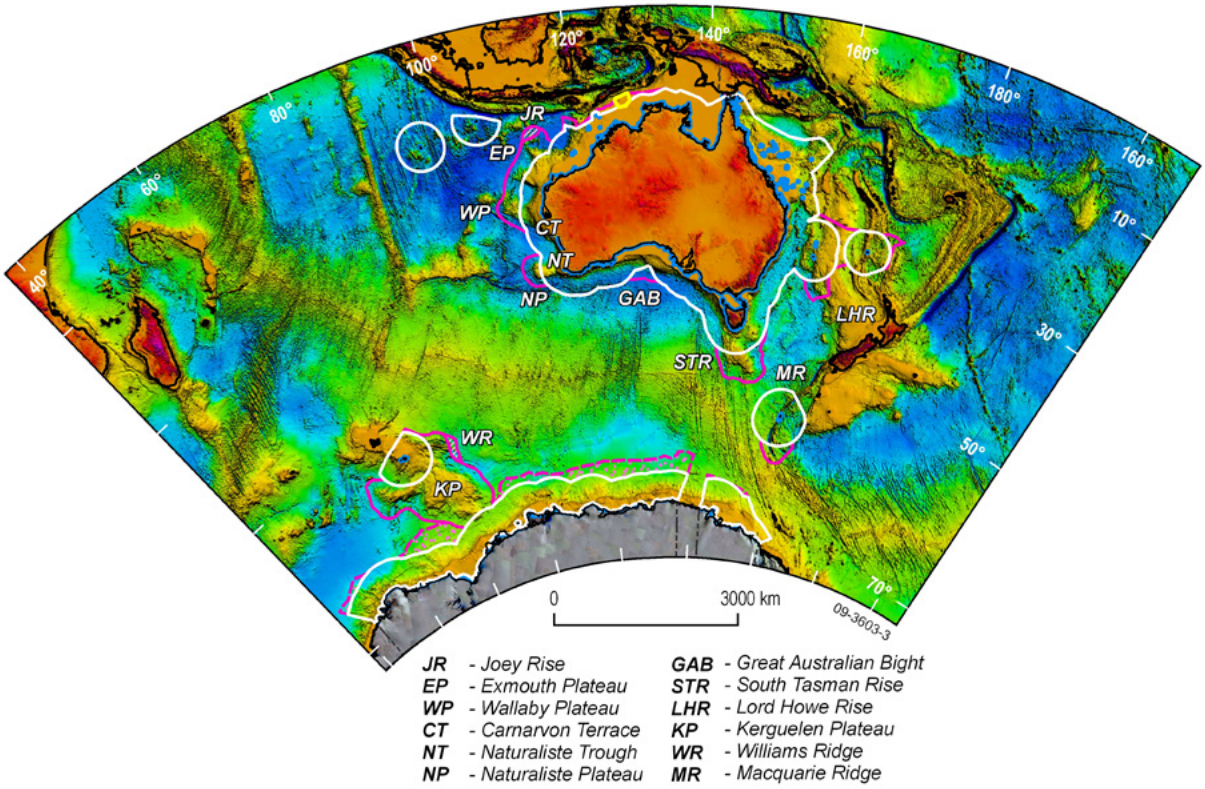
With the launch of Australia's Ocean Policy in 1998, the Australian federal government committed to an integrated, ecosystem-based approach to the planning and management of all ocean uses (CoA, 1998). Although this policy proved to be shortlived, being disbanded in 2005, it gave impetus to a number of valuable investigations into the Australian marine environment (Vince *et al*., 2015). In order to effectively manage maritime areas, an understanding of bathymetry (shape of the seabed) and geomorphic features (type of seabed forms) is fundamental.

The geomorphology of the Australian continental margin has been detailed in Harris *et al*. (2005) and Heap and Harris (2008), including systematic collation of available data sources to enable measurement of the surface area and distribution of geomorphic features within the limits of the EEZ (see Excursus 13.1). Major geomorphological features around Australia are shown with recognised maritime zones in Figure 2.6).

Broadscale mapping of seabed environments into a series of 'seascapes' has uncovered great diversity in Australia's marine jurisdiction, including aspects of the seabed that may be important for conservation and biodiversity management. These seascapes combine aspects of water depth, sediment type, geomorphology, sea-floor temperature, disturbance by tides and waves, slope of the seabed and amount of primary production. These parameters are related in complex ways to the distribution of biodiversity, so areas where there are many seascapes might also be areas with a high diversity of species or ecological communities (SOE, 2011; Whiteway et al., 2007)

Figure 2.6 Seafloor morphology around Australia

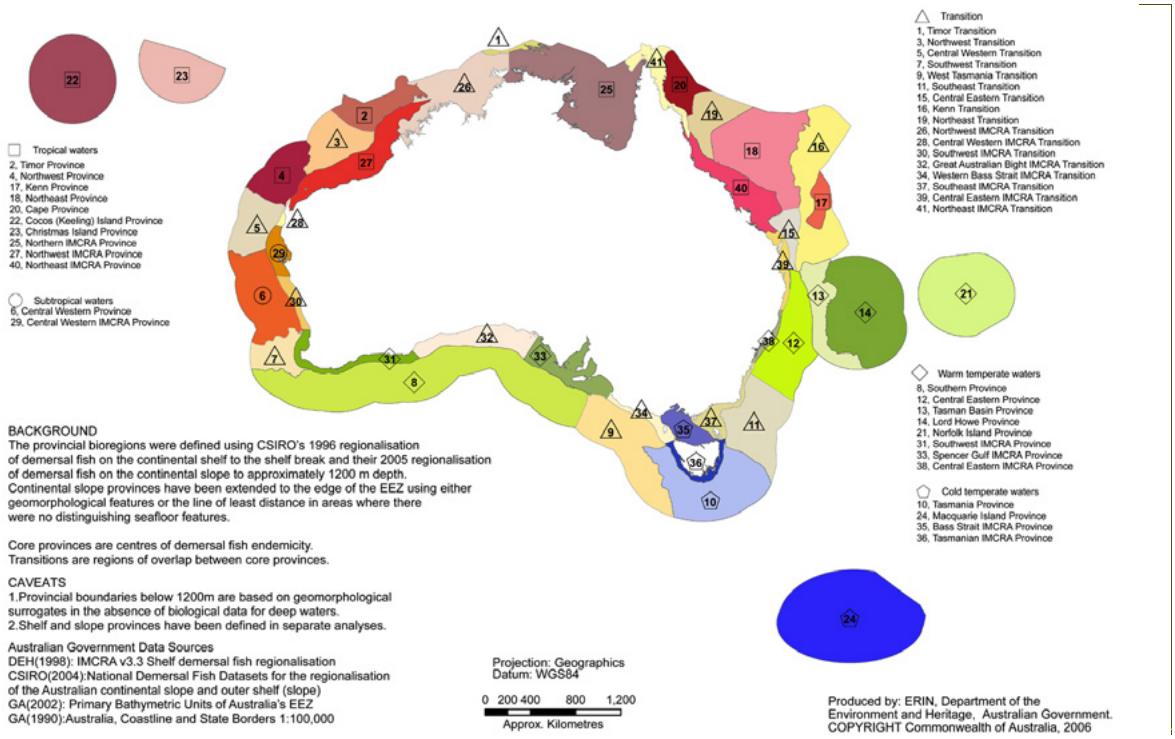
Major geomorphological features around the Australian continent are overlaid with maritime zones.



Source: Symonds *et al.* (2009) Figure 3. Retrieved from: *http://www.ga.gov.au/ausgeonews/ausgeonews200903/limits.jsp*

Figure 2.7 Provincial marine bioregions

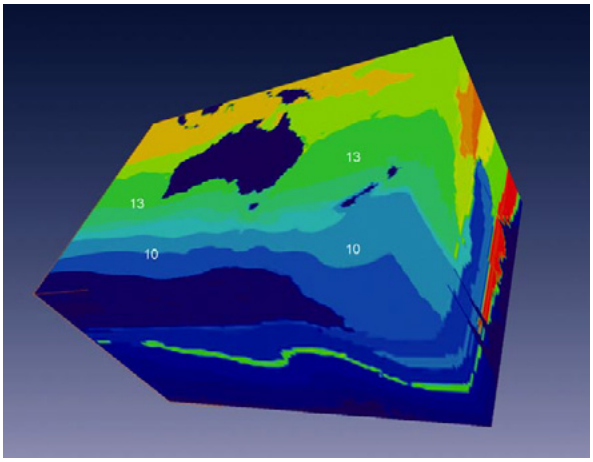
IMCRA v4.0 defines 41 provincial bioregions in Australia's waters, comprising 24 provinces (with biotic endemism) and 17 transitional zones. These reflect biogeographic patterns in the distribution of demersal (bottom-dwelling) fish.



Source: CoA (2006) Map 1.

Figure 2.8 Three-dimensional model of water masses defined by pelagic regionalisation

25 three-dimensional water masses have been defined around Australia based largely on latitudinal oceanographic processes. Water mass 13 (green) is Pacific Central-South subtropical water, which extends to a depth of 250 m. Water mass 10 (light blue) is the southern Subtropical Convergence, which extends down to 800 m depth, and is part of the Southern Ocean.



Source: CoA (2006) Figure 1

To simplify the process of regional planning within the Australian EEZ, the Interim Marine and Coastal Regionalisation of Australia (IMCRA v4.0) delineates 'bioregions' (areas that are ecologically similar; see Volume 3A). IMCRA v4.0 combines IMCRA v3.3, which covered inshore waters, and the National Marine Bioregionalisation (NMB; CoA, 2005), which described off-shelf waters. It comprises two regionalisations:

- benthic—based on biogeography of fish, which uses geomorphology as a proxy (Heap *et al*., 2005; Last *et al*., 2005; see Figure 2.7); and
- pelagic—based on three-dimensional oceanographic characteristics of defined waterbodies (Lyne and Hayes, 2005; see Figure 2.8).

2.3 Regional Water Circulation

The Australian continent is bounded by three oceans and four seas (see Figure 2.1). The closest land mass to the south is Antarctica. While the impact of currents varies with the seasons, the most significant ocean and coastal major currents in the Australasian region are the:

- East Australian Current (EAC)—carrying subtropical warmth down the eastern coastline of Australia from Cairns to Tasmania. This western boundary current is driven by the South Pacific Gyre, which in turn, is triggered by seasonal changes in the upper atmosphere over Antarctica. Eddies are frequent and can be recurrent, commonly spanning 200–300 km in diameter (CSIRO, 2018).
- Leeuwin Current (LC)—forming near the North West Shelf of WA coastline and traveling south to Cape Leeuwin, across the southern shelf as the South Australia Current, then down the west coast of Tasmania as the Zeehan Current, this 5,000 km current is the longest coastal current in the world. It forms an unusual eastern boundary current for the Indian Ocean gyre and a northern boundary current for the Southern Ocean.
- Antarctic Circumpolar Current (ACC)—connecting the southern Atlantic, Pacific and Indian Oceans this powerful current flows eastward around Antarctica and is highly significant in the global climate system.
- Indonesian Throughflow (ITF)—flowing westward through the Indonesian Archipelago, this system of currents transports water from the Pacific Ocean to the Indian Ocean, warms the waters carried south by the Leeuwin current, and contributes to monsoonal weather in Asia and Australia. Without the ITF, Australia would have a classical northward flowing eastern boundary current instead of the LC.
- Zeehan Current (ZC)—the final stage of the Leeuwin Current, moving southeastward along the edge of the continental shelf of western Bass Strait and western Tasmania (see Section 16 for details).

The CSIRO Atlas of Regional Seas (CARS) records mean ocean properties and average seasonal properties for Australian waters derived from historical subsurface ocean property measurements (Ridgway *et al*., 2002). This atlas can be used to generate valuable insights into regional water circulation characteristics (see Section 16). Water circulation patterns infer bioenergetics and can be used to model regional water productivity (CoA, 2006; see Section 16). The collaborative Bluelink partnership (see Excursus 2.2) models ocean dynamics to deliver improved operational forecasts for a range of ocean users.

Excursus 2.2—Bluelink Ocean Forecasting

Source: Edward King, CSIRO
Further Information: *https://research.csiro.au/bluelink*; Brassington *et al.* (2007); Schiller *et al.* (2019)

The ocean is an energetic, stratified, saline fluid in which currents, eddies, fronts and other three-dimensional structures form, evolve and dissipate over time in response to forcing at the surface through wind friction, solar radiation (including loss via evaporation), ice formation and melt, and terrestrial freshwater inflow. Knowledge of the surface and near-surface conditions is important information for decision makers for a wide range of maritime industries and Defence operations. Applications include:

- understanding the subsea acoustic environment (e.g. sonar ranges and shadow zones);
- tactical decision making, including:
  - optimum navigation;
  - safe operating conditions;
  - surface and coastal wave environments; and
  - limits of knowledge/uncertainty;
- maritime incident response (e.g. oil spills, people, objects adrift);
- sea level variations for ports and coastal management; and
- planning for coastal infrastructure.

Bluelink is a partnership, established in 2001, between the CSIRO (Australia's national research organisation), the Bureau of Meteorology (BoM, Australia's operational forecasting agency) and the Department of Defence, to deliver operational forecasts of ocean properties globally. Although the original focus was on global forecasts, today they are produced across three scales: globally, regionally, and in the littoral zone. The global forecasts are produced routinely on a daily basis, with the regional and littoral forecasts at higher resolution over smaller areas nested within the global forecast when and as required.

Global forecasts

Global ocean forecasts, like meteorological forecasts, combine knowledge of the physics of ocean hydrodynamics (encoded in an ocean model) with *in situ* and remotely sensed (satellite) observations of the ocean state to capture the existing conditions and evolve them forward over time. The observations are sparse in both time and space, and the model cannot capture the ocean dynamics at all scales, so the model state is always an approximation of the true conditions in the ocean. A mathematical technique called data assimilation is used to continuously update and correct the model with the most recent observations so that forecasts are always based on a combination of best available historical observations and physical knowledge of the ocean.

Three technological developments have been key to making global ocean forecasting practical:

- satellite observations of the global ocean surface, primarily sea surface height from altimetry missions (see Section 12) since 1993, but also sea surface temperature (see Section 14) from even earlier, provide a frequent measurement of the surface boundary conditions. Remotely sensed height and temperature give important information about integrated column density and surface density respectively;
- since the start of the 21st century, the Argo robotic float program (*https://argo.ucsd.edu/*) has provided observations of the subsurface physical oceanography (temperature and salinity) to a depth of 2000 m (see Excursus 5.1). Around the globe, approximately 4,000 floats each report once every 10 days yielding about 400 ocean depth profiles daily; and
- high performance computing has reached a scale and capability in the past 20 years that enables the physical ocean models to be run with grid spacings sufficient to resolve the key mesoscale features of the ocean that are important for maritime operations.

In combination, these developments, together with the incorporation of data assimilation techniques, underpins the production of ocean forecasts.

The Bluelink partnership developed a system to produce global ocean forecasts at sub-mesoscale scales (10s of km), resolving the important structures, at short to medium-range (days to weeks). The BoM now runs the operational forecast model (known as OceanMAPS) daily, covering the globe between latitudes 75°S and 75°N. The model provides temperature, salinity, and current estimates at approximately 50 depths from the surface to the deep ocean, with higher density (more closely spaced layers) in the 500 m closest to the surface. Sea surface height (without tides or the pressure component of storm surge) is also produced. Output for the Australasian region can be explored at the BoM website (see Figure 2.9).

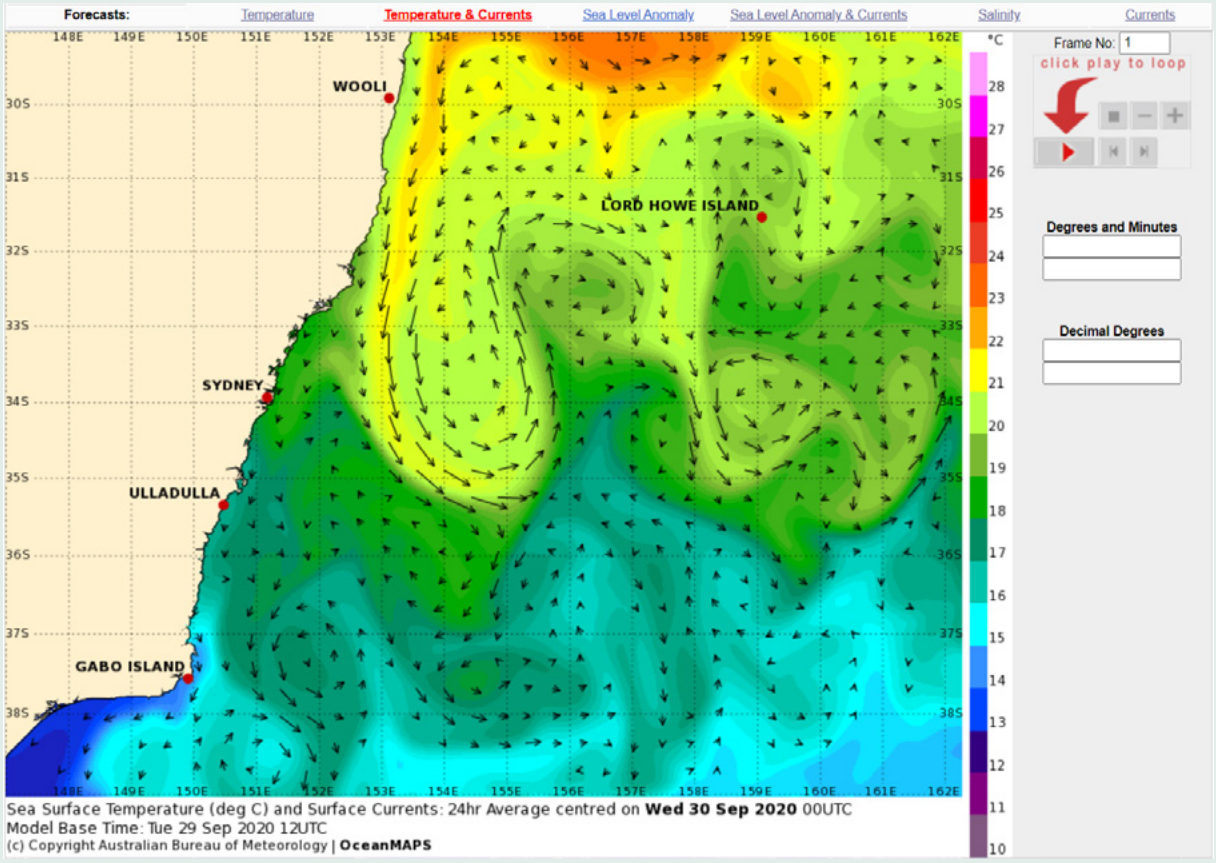
Ongoing development of the model and data assimilation scheme occurs through a range of national and international partnerships. Notably the Cosima partnership (*cosima.org.au*) is incorporating a sea ice capability to the core model that will extend the forecast reach to higher latitudes to make it truly global. CSIRO is responsible for the Bluelink Reanalysis (BRAN), a multi-decadal historical run of the model that uses all of the best available observations (which may not be either available, or fully quality-controlled, at the time that the BoM runs its daily forecast; see Figure 2.10). Thus, BRAN provides a historical record of the global ocean, and is also a testbed for innovations in the model and data assimilation, which enables thorough evaluation before they are incorporated into the forecast system. OceanMAPS and BRAN are both very resource (memory and compute) intensive and run on supercomputers operated by the BoM and the National Computational Infrastructure (NCI) respectively.

Regional forecasts

The second tier of the Bluelink modelling suite is the Relocateable Ocean Atmosphere Model (ROAM), which enables a higher resolution ocean model to be run in a region of interest specified interactively by a forecaster via a web interface. Runs of the ROAM-Ocean model typically provide forecasts with a horizontal spatial resolution of 1–2 km over an area of several hundred km (see Figure 2.11), for between two and four days ahead. Constraining the area of modelling and nesting within the global model makes the computational demand of the higher resolution tractable. The higher resolution model captures the sub-mesoscale physics, including internal tides, fine scale fronts and filaments, recirculations around headlands, coastal sea level, and coastal or open ocean upwellings. The ROAM ocean model is nested within the global model and so incorporates all the benefits of the assimilated observations. The regional modelling suite also includes ROAM-Atmosphere and ROAM-Wave models that can be run in restricted regions to provide higher resolution forecasts of parameters relevant to marine operations.

Figure 2.9 Example of global forecast

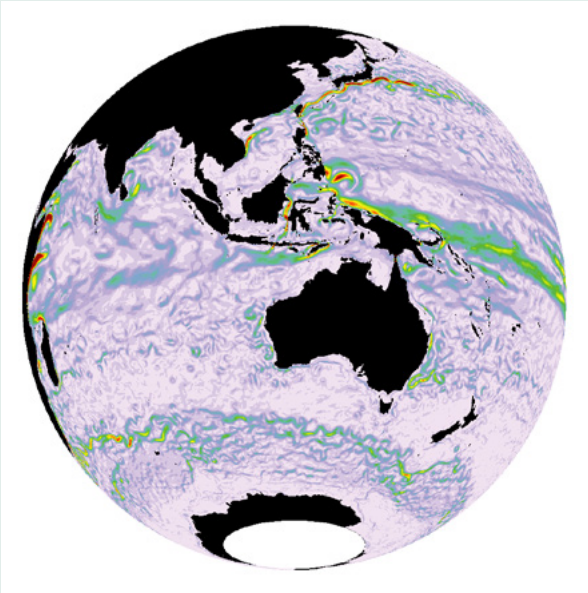
An example of Bluelink forecasting for daily average surface temperature and current strength and direction in the Tasman Sea on 28 September 2020.



Source: Bureau of Meteorology. Retrieved from *http://www.bom.gov.au/oceanography/forecasts/index.shtml*

Figure 2.10 BRAN 2020 reanalysis

The BRAN 2020 reanalysis captures the evolving historical state of the ocean every day since 1993 until the recent present. The example shown here is surface current speed from mid-2010, with colours ranging through the visible spectrum for low to high current speeds.



Source: Matt Chamberlain, CSIRO

Litttoral forecasts

Littoral forecasts are an emerging focus for Bluelink and comprise the third tier of the system known as ROAM-Surf. These use the mature Simulating Waves Nearshore (SWAN) spectral wave model, and the fully phase-resolved XBeach model to provide information on conditions to be expected in the littoral zone, where the interaction of the surface waves and currents with the seafloor becomes significant. These forecasts include wave propagation and breaking, currents, rip-currents, and sediment transport right up to the beach face at spatial resolutions down to a few metres (see Figure 2.12). In combination with ROAM Atmosphere, they enable operational decision making and risk control for nearshore activities, such as amphibious landings operations.

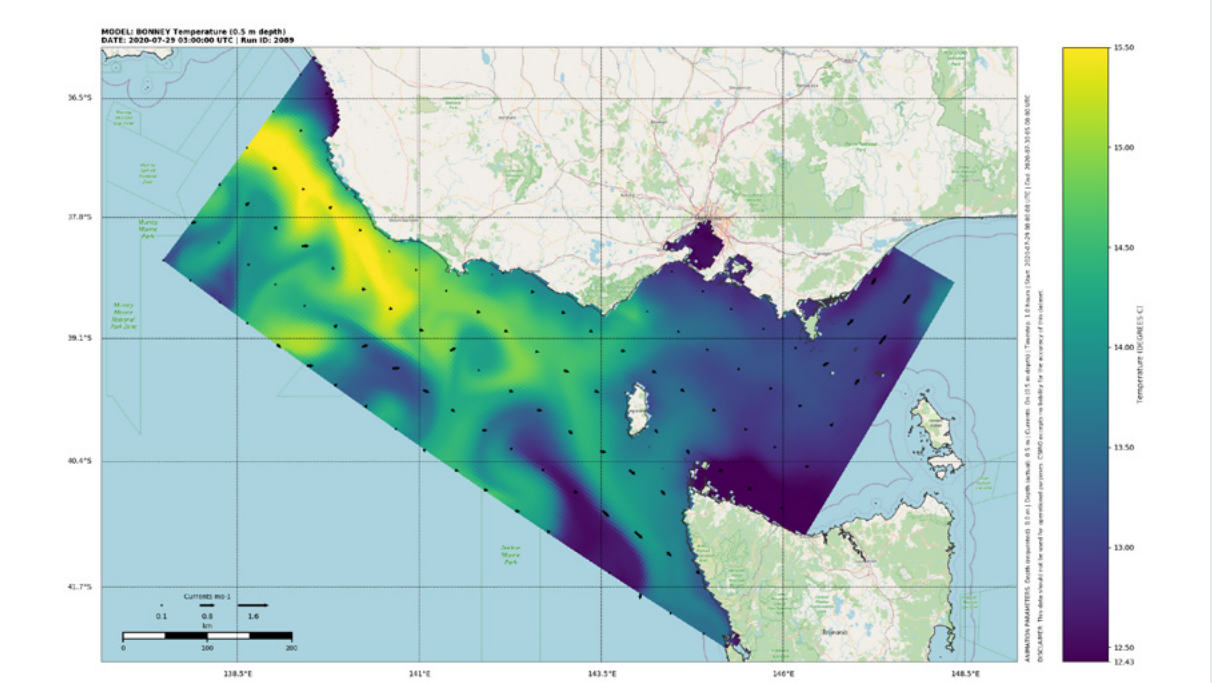
Although the Bluelink partnership has been in place for nearly two decades, the forecast system it has developed remains under active development. Some areas of focus are:

- extension to a fully global forecast including sea ice;
- inclusion of biogeochemistry in order to forecast water clarity;
- improvements in littoral forecasts, including techniques for remotely determining near-shore bathymetry; and
- employment of unstructured grids in the ROAM-Ocean models to improve representation in complex bathymetric environments and computational efficiency.

Figure 2.11 Sample ocean temperature

Relocateable Ocean Atmosphere Model (ROAM) forecasts for coastal waters bordering southwest Victoria on 29 July 2020

a. At 0.5 m water depth (temperature range 12.43–15.5°C)



b. At 105 m water depth (temperature range 12.68–15.35°C)

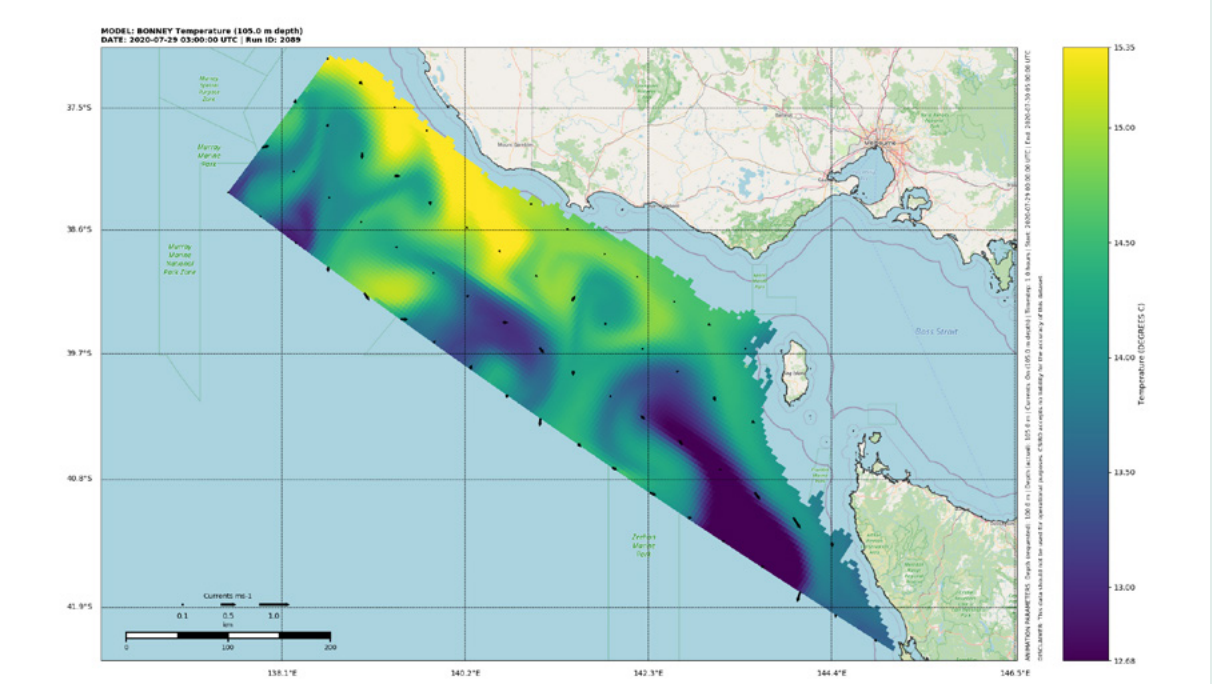


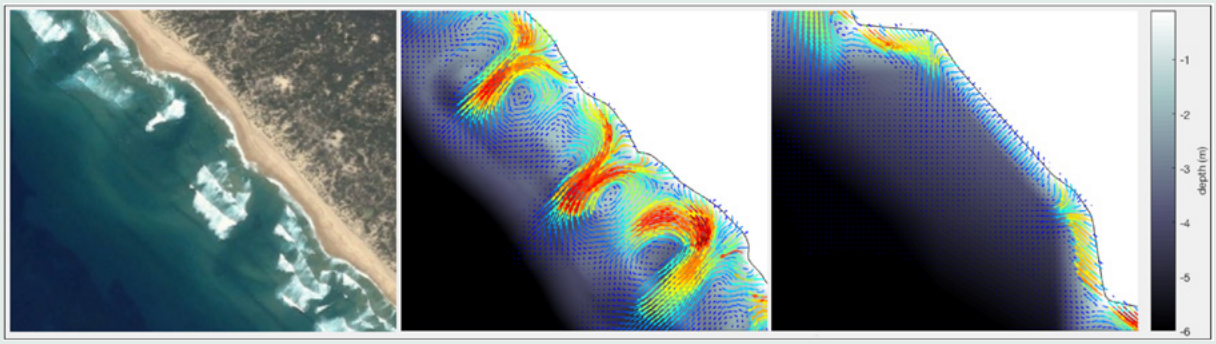
Figure 2.12 Littoral forecast example

Gunnamatta Beach , Mornington Peninsular, Victoria

a. True colour image of beach

b. Forecast currents in the presence of a wave field

c. Underlying bathymetry



Source: Ron Hoeke, CSIRO

2.4 Australian Marine Environment

Coastal zone mapping and monitoring are increasingly important in Australia given that around half its population live within 7 km of its shores, and up to 85% of Australians live within 50 km of the coast (NMSP, 2015). The coastline of the Australian mainland is estimated to span around 34,000 km and includes more than 1,000 estuaries (GA, 2021b). While the states and territories manage coastal resources, the federal government defines maritime boundaries, monitors shoreline location, assesses environmental condition, coordinates natural disaster mitigation efforts, develops shallow water bathymetric models, and evaluates the potential impact of groundwater extraction on coastal aquifers.

Most Australian coastal waters are considered to contain low levels of nutrients, and are therefore not very productive, due to limited mixing with ocean waters (SOE, 2011). However, seasonal variations in water condition, driven by river outflows and coastal runoff, mean that coastal waters can vary from clear, with low nutrients, to turbid, and more productive. Many marine species tend to be locally endemic, particularly in southern regions, grouping into unique ecosystems in a diverse range of habitats.

As part of the international, decadal project entitled 'Census of Marine Life' (see Section 2.8), and using species counts from four primary databases[3], Butler *et al.* (2010) estimated that Australian marine waters supported more than 33,000 marine species, mostly animals (130 of these species were introduced, and another 58 are listed as threatened), but the total number of macroscopic species could be as high as 250,000. Database records confirmed the existence of:

- 8525 species of molluscs;
- 6,365 species of crustaceans; and
- 5,184 species of fish.

While, the major economic return from Australian marine waters comes from the oil and gas industry (see Section 19.4), coastal fisheries and aquaculture comprise the most profitable renewable industry. Australian oceans do not support the same volumes of fish and related species as occur in waters around other continents in the Southern Hemisphere at comparable latitudes. Areas of upwelling currents, and related higher productivity, do occur, however, in selected locations (see Section 16; SOE, 2011).

3 Australian Faunal Directory, Codes for Australian Aquatic Biota, Online Zoological Collections of Australian Museums, and Australian node of the Ocean Biogeographic Information System (OBIS).

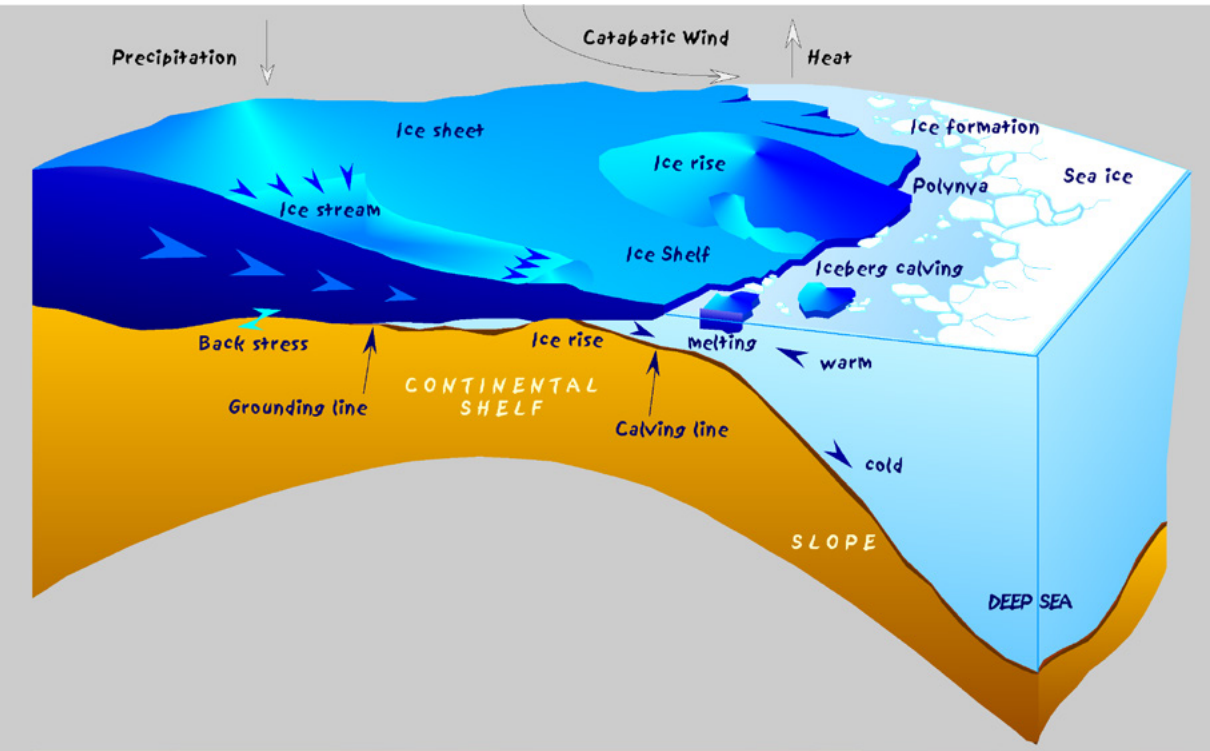
2.5 Antarctica

Antarctica warrants numerous superlatives: the world's largest cold desert; coldest, windiest, driest and highest continent; and largest store of ice (90% of global total) and freshwater (that is, the potentially largest source of sea level rise). It is also home to the world's deepest continental shelf; largest wind-driven currents (circling around it in the circumpolar Southern Ocean); and the oldest and most detailed climate records in continental ice. Moreover, Antarctica is the only continent without a native human population (SOE, 2011).

Continental Antarctica, with its islands and ice shelves, comprises an area of 13.7 million km^2 (AAD, 2018), which is roughly equivalent to that of Australia's marine jurisdiction. The Antarctic continent is further surrounded by sea ice that covers an approximate area of 19 million km^2 at its maximum annual extent each September to October (spring) and melts back to a summer minimum of around 3 million km^2 each February (Parkinson, 2019). As introduced in Section 1.3.1, two dynamic, though distinctly different, forms of ice occur in polar regions (see Figure 2.13):

- ice sheets—over prolonged periods of time, snow accumulates and compacts on land to form extensive sheets of glacial ice. Far from being static, the ice flows under gravity towards the surrounding ocean in the form of glaciers and ice streams. On reaching the ocean and in certain places, the ice continues to advance in the form of floating glacier tongues and ice shelves, which can reach hundreds of metres in thickness. Subsequent breakages (termed 'calvings') from floating ice sheet margins form icebergs.
- sea ice—when ocean water freezes (at ~-1.8°C), it forms floating crystals of ice that subsequently coalesce into buoyant sheets of ice and acquire a snow cover, that is, the ice intercepts and accumulates snowfall that would otherwise have fallen directly into the ocean. Sea ice that is constantly in motion under the influence of winds and ocean currents is referred to as 'pack ice', which is made up of contiguous parcels of ice termed 'floes'. In contrast, sea ice that remains stationary when attached to the coastline, the seafloor, or icebergs grounded on the seafloor is called 'fast ice'. Although generally up to a metre or so thick, sea ice can attain thicknesses in excess of 10 m in places, due to either its great age (thermodynamic growth) or by deformation (dynamic thickening where two pieces of ice collide). In certain key coastal locations, areas of open water surrounded by sea ice can recur seasonally or persist for longer time periods. These are called polynyas, and influence global ocean circulation and biological production.

Figure 2.13 Types of ice in polar regions



Source: Hannes Grobe, Wikimedia. Retrieved from: *https://commons.wikimedia.org/wiki/File:Antarctic_shelf_ice_hg.png*

In the Arctic, a greater proportion of the sea ice coverage persists into summer than in Antarctica,

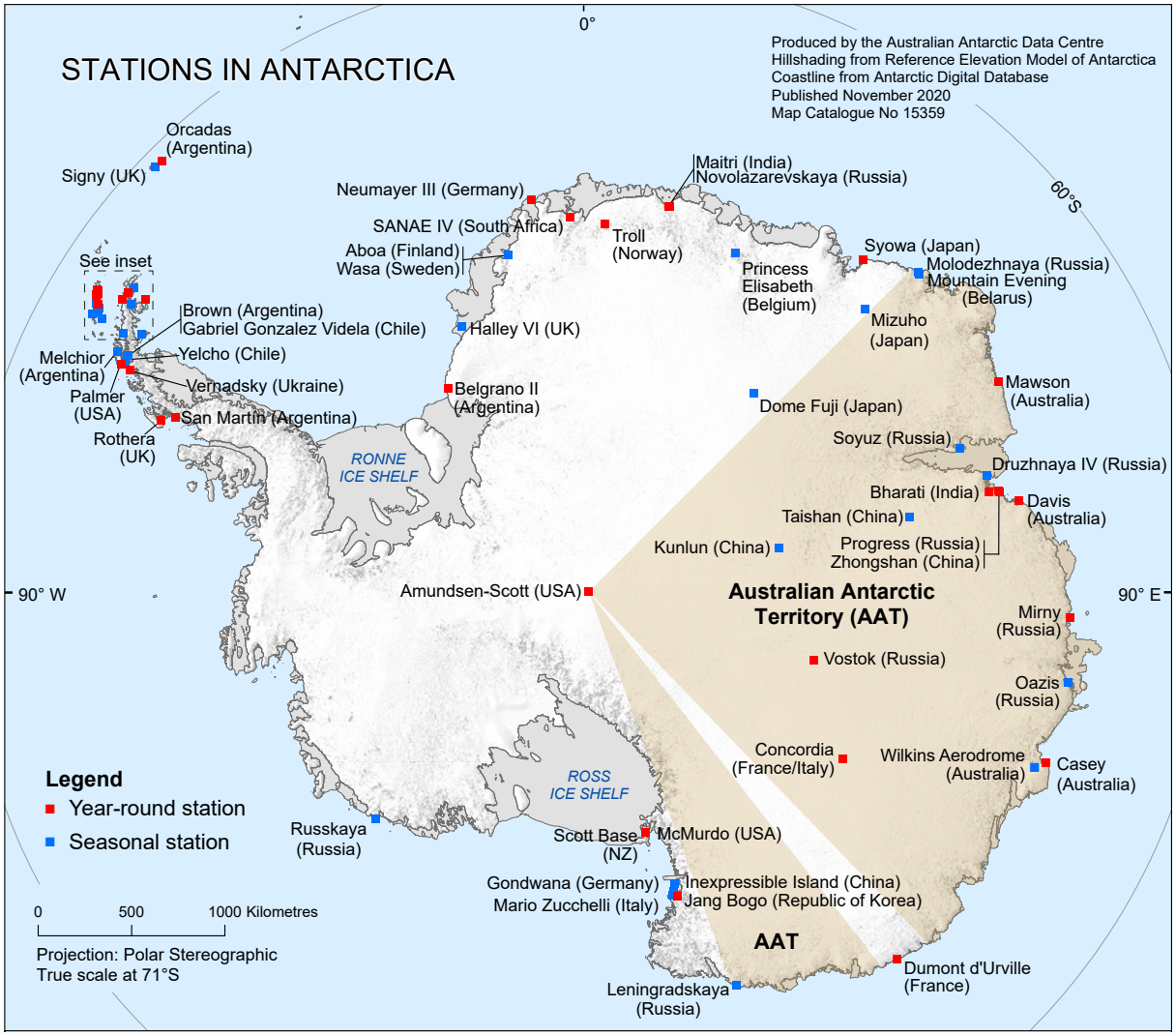
where most sea ice melts back each spring-summer—although this situation is changing as the Arctic Ocean loses much of its perennial sea ice cover, which is being replaced by more of a seasonal ice cover (see Section 15). Arctic sea ice also occurs closer to the pole (mostly above 70°N) than Antarctic sea ice, which only extends south of about 70°S in the great embayments of the Ross and Weddell seas.

Significantly, 70% of Earth's available freshwater is stored in the Antarctic Ice Sheet, which, if melted, is sufficient to elevate sea levels by 60 m (SOE, 2011; Fretwell *et al.*, 2013). The Antarctic environment directly impacts global weather patterns and climate, and acts as a sensitive indicator of climate change, with recent observations confirming that polar ice coverage is melting at a faster rate than expected (Scott *et al.*, 2009). EO datasets play a crucial role in monitoring this vast and remote region (see Section 15).

Seven countries, including Australia, claim territory in Antarctica. The Australian Antarctic Territory comprises 42% of Antarctica, covering all land/ice sheet and islands south of 60°S and from longitude 45°E to 138°E, and from 142°E to 160°E (see Figure 2.14). Australia's subantarctic islands (namely, Macquarie, Heard and McDonald Islands) are included on the World Heritage List.

Despite territorial claims, Antarctica is effectively governed by the Antarctic Treaty System, which is jointly signed by 48 member countries to manage the area south of the 60°S parallel as a 'natural reserve, devoted to peace and science' (The Madrid Protocol, 1998). The Convention on the Conservation of Antarctic Marine Living Resources (CCAMLR) regulates fishing in this region, with the stated goal of sustaining relevant ecosystems, rather than industries (CCAMLR, 1984).

Figure 2.14 Australian Antarctic Territory



Source: Australian Antarctic Data Centre. Retrieved from *https://data.aad.gov.au/aadc/mapcat/display_map.cfm?map_id=15359*

2.6 Australia's Inland Water Resources

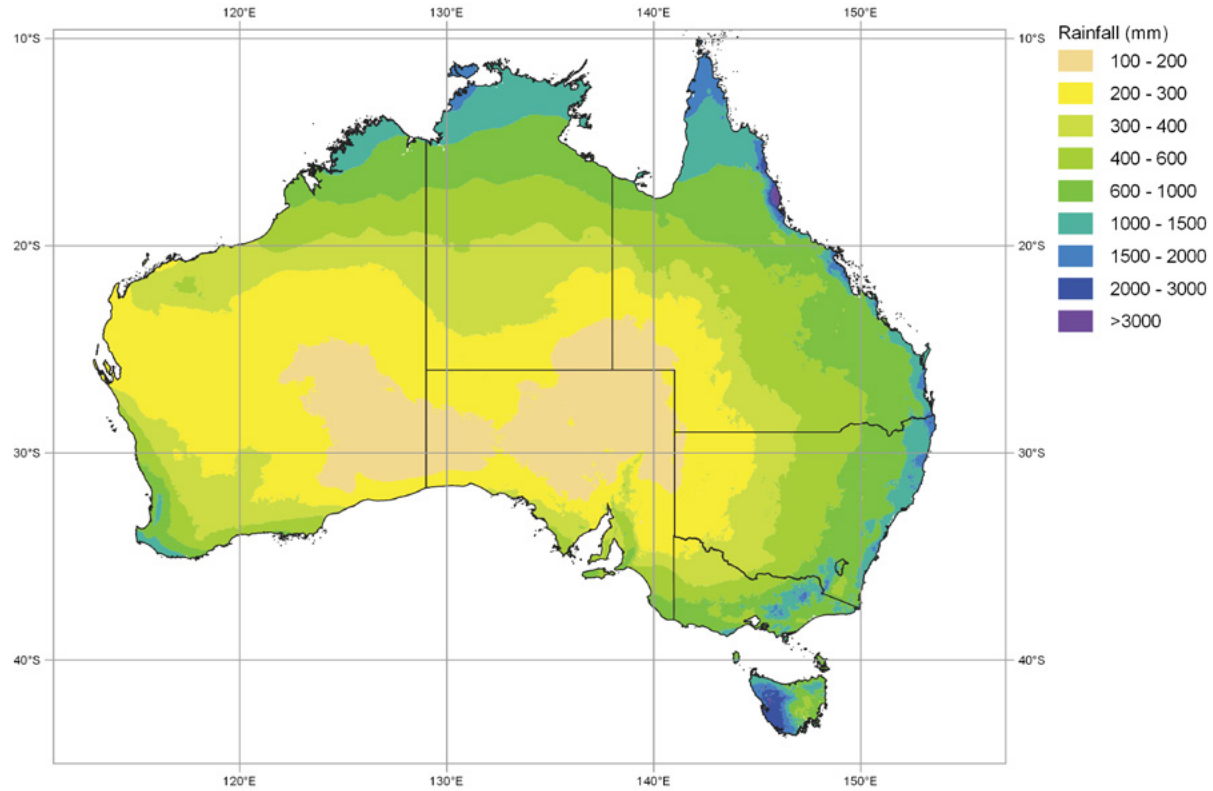
Australia's average annual rainfall is 430 mm, with regional variations ranging from less than 100 mm in inland deserts to over 3,000 mm in the tropical north (see Figure 2.15 and Volume 3A—Section 2). 88% of this rainfall is subsequently lost through evapotranspiration, leaving an estimated 383,000 GL to enter Australia's water environment (SOE, 2017). Although both the timing and volume of rainfall is variable, largely due to the El Niño Southern Oscillation (ENSO), distribution can be described in terms of two broad seasonal regimes:

- monsoonal northern regions, with significant rainfall from October through April only; and
- temperate southern regions, with maximum rainfall from April through November (SOE, 2011).

These rainfall patterns mean that inland surface waterbodies in Australia (see Figure 2.16) have fluctuating flow conditions, and many are dry for much of the time. Even when water is permanently stored, large changes can occur in flow regimes, which impact aquatic ecosystems and other water users. Given their fragiility and importance, many Australian rivers and wetlands are protected under federal or state legislation (EPBC Act, 1999). Additionally, 66 Australian wetlands, covering more than 8.3 million ha, are listed under the Ramsar Convention for Wetlands of International Importance (DAWE, 2021).

Based on surface water flows, 13 drainage divisions have been defined within Australia (see Figure 2.17). Most of these divisions are sufficiently extensive to contain the boundaries of recharge and discharge for their associated aquifers, with the exception of the Great Artesian Basin, which spans three drainage divisions (SOE, 2017; see Volume 3A—Section 2). The number and extent of inland waterbodies in Australia is summarised in Table 2.2.

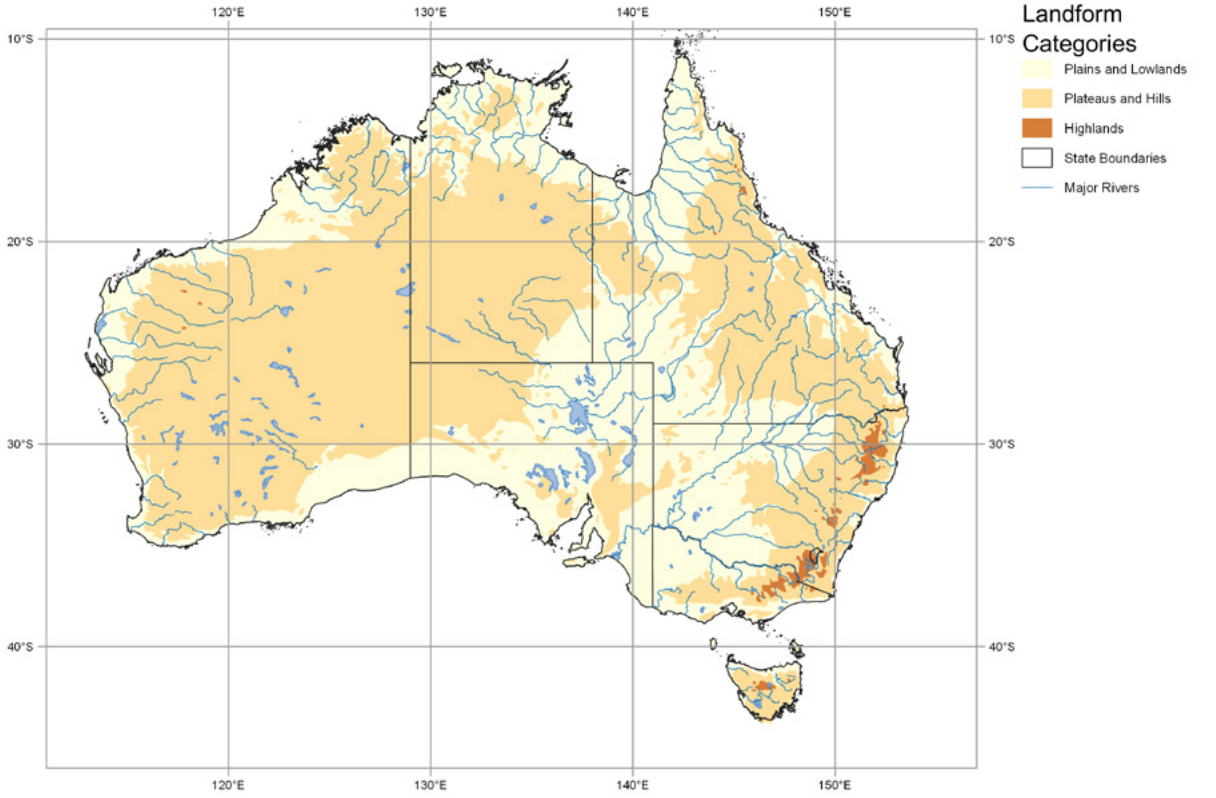
Figure 2.15 Australia's average annual rainfall



Source: Tony Sparks, Icon Water, using gridded data from BoM (2020a) based on a standard 30-year climatology (1961–1990)

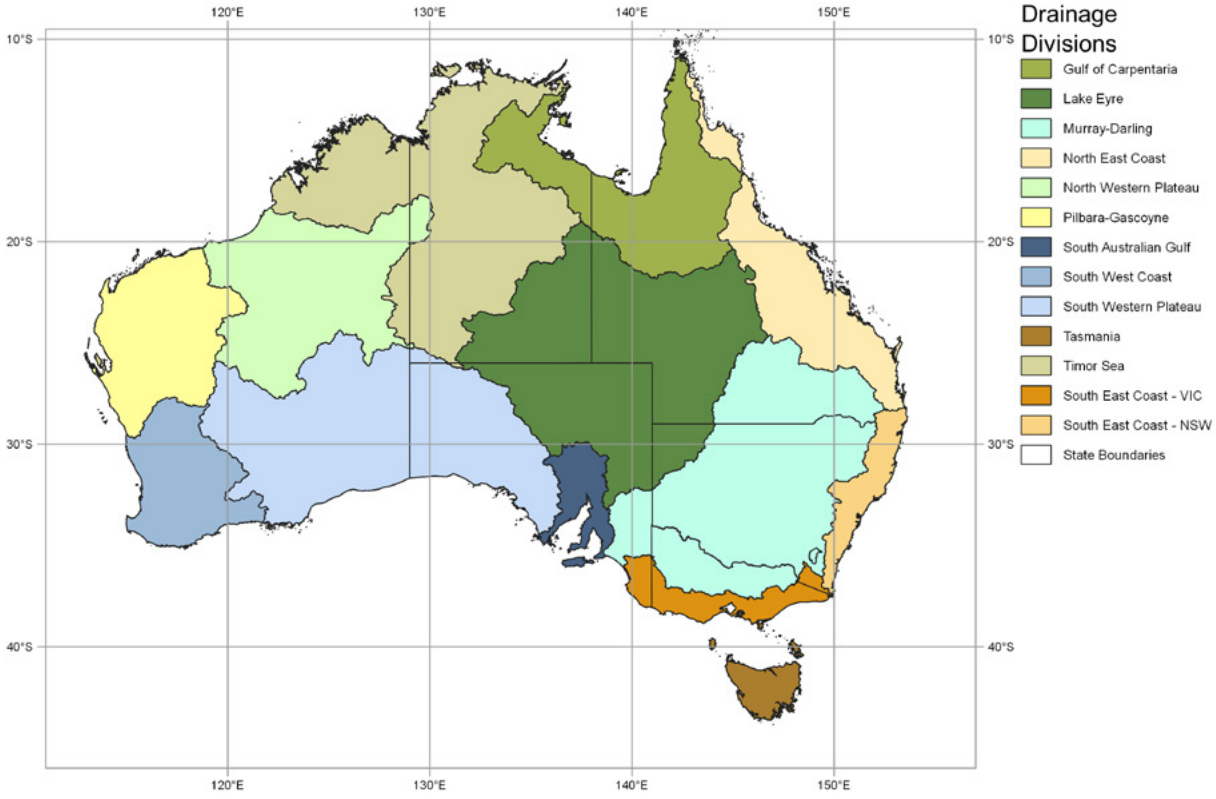
Figure 2.16 Australian inland waterbodies

While this map implies a dense network of rivers and waterbodies in many parts of Australia, most are ephemeral, and the waterbodies shown as blue in central Australia are salt lakes.



Source: Tony Sparks, Icon Water, using data from GA (2002) for waterbodies

Figure 2.17 Major drainage divisions in Australia



Source: Tony Sparks, Icon Water, using data derived from the Geofabric Hydrology Reporting Catchments product (BoM, 2020b)

Table 2.3 Categories of waterbodies in Australia

Type of Waterbody	Number	Area (km²)	Comment
Lake	108,830	188,085	Over half occur in WA with greater area in NT
Watercourse Area	10,965	40,265	Over half occur in WA with greater area in NT
Land Subject to Inundation	17,458	406,887	Around a quarter occur in each of NT and Qld, with greater area in NT
Swamp	9,342	42,809	Nearly half occur in Qld with greatest area in NT
Town Rural Storage	2,347	16,936	Nearly half occur in Qld with greatest area in NT
Settling Pond	264	441	Highest numbers in WA and Qld with greatest area in WA nd NT
Total	149,000	695,423	Distribution varies widely between states

Source: Dekker and Hestir (2012)

2.7 Australian Water Usage

Understandably, as the driest inhabited continent on Earth, Australia manages the largest area of surface water storage per capita (BoM, 2020c). Our 305 publicly-owned lakes, reservoirs and weirs have a total storage capacity of 80.8 million ML. Water levels in these storages are routinely monitored by relevant authorities and standardised by the BoM for publication (see Section 1.6).

Australia's annual water consumption (domestic and industrial) in 2015–16 was estimated as 16,132 GL (ABS, 2017), with agriculture being the largest single user (consuming 9,604 GL). During this time period, environmental extraction of water was estimated as 75,544 GL, of which 65,238 GL was ultimately discharged back to the environment.

2.8 Further Information

Australian Marine Waters

Australian Hydrographic Service: *http://www.hydro.gov.au*

Australian Marine Spatial Information System (AMSIS)

http://maps.ga.gov.au/interactive-maps/#/theme/amsis

National Marine Science Plan

http://www.marinescience.net.au/fileadmin/user_upload/documents/National_Marine_Science_Plan_2015_Factsheet_20150807.pdf

Seasonal Ocean Water Properties

CSIRO Atlas of Regional Seas (CARS): *http://www.marine.csiro.au/~dunn/cars2009/*

Coastal Change

https://www.coastalrisk.com.au/home

https://coastadapt.com.au/tools/coastadapt-datasets#future-datasets

https://ecat.ga.gov.au/geonetwork/srv/eng/catalog.search#/metadata/104160

Antarctica

Australian Antarctic Commission: *http://www.antarctica.gov.au*

Committee for Environmental Protection: 25 Years of the Protocol on Environmental Protection to the Antarctic Treaty. Secretariat of the Antarctic Treaty, Buenos Aires, 2016. *https://www.ats.aq/documents/atcm39/ww/atcm39_ww007_e.pdf*

2.9 References

ABS (2017). *Water Account, Australia 2015–16*: *http://www.abs.gov.au/ausstats/abs@.nsf/mf/4610.0*

AAD (2018). *Antarctic environment* webpage on Australian Antarctic Division website: *http://www.antarctica.gov.au/about-antarctica/environment*

AGD (1980). *Offshore constitutional settlement. A milestone in cooperative federalism*. Attorney-General's Department. AGPS, Canberra.

AHS (2017a). *Hydroscheme 2017–2020*. Australian Hydrographic Office, Department of Defence. *http://www.hydro.gov.au/business-publications/HydroScheme_2017-2020_WEB_20171103.pdf*

AHS (2017b). *Names and Limits of Oceans and Seas around Australia*. Australian Hydrographic Service Fact sheet: *http://www.hydro.gov.au/factsheets/WFS_Names_and_Limits_of_Oceans_and_Seas_Around_Australia.pdf*

BoM (2020a). *Long-range weather and climate* webpage. Bureau of Meteorology website: *http://www.bom.gov.au/climate/averages/maps.shtml*

BoM (2020b). *Topographic Drainage Basins and River Regions* webpage. Bureau of Meteorology website: *http://www.bom.gov.au/water/about/riverBasinAuxNav.shtml*

BoM (2020c). *Water Information* webpage, Bureau of Meteorology website: *http://www.bom.gov.au/water/dashboards/#/water-storages/summary/state*

Brassington, G.B., Pugh, T. Spillman, C. Schulz, E. Beggs, H. Schiller, A. and Oke, P.R. (2007). BLUElink> Development of operational oceanography and servicing in Australia. Journal of Research and Practice in Information Technology, 39, 151–164.

Butler, A.J., Rees, T., Beesley, P., and Bax, N.J. (2010). Marine biodiversity in the Australian region. *Plos One*, 5(8), e11831.

CCAMLR (1984). *Report of the third meeting of the scientific committee*. Commission for the Conservation of Antarctic Marine Living Resources, Hobart.

CoA (1998). *Australia's Oceans Policy*. Commonwealth of Australia. ISBN 0 642 54580 4. *http://www.environment.gov.au/archive/coasts/oceans-policy/publications/pubs/policyv1.pdf*

CoA (2005). *National Marine Bioregionalisation of Australia. Summary*. Commonwealth of Australia. Department of Environment and Heritage, Canberra, Australia.

CoA (2006). *A Guide to the Integrated Marine and Coastal Regionalisation of Australia Version 4.0*. Commonwealth of Australia. Department of the Environment and Heritage, Canberra, Australia.

CSIRO (2018). *Causes of extreme sea levels* webpage, Commonwealth Scientific and Industrial Research Organisation website: *https://research.csiro.au/slrwavescoast/extremes/causes-extreme-sea-levels/*

DAWE (2021). *Australian Ramsar Wetlands* webpage, Department of Agriculture, Water and the Environment website: *https://www.environment.gov.au/water/wetlands/australian-wetlands-database/australian-ramsar-wetlands*

DE (2013). *Australia's Ramsar Sites*. Department of Environment website: *http://www.environment.gov.au/water/wetlands/publications/factsheet-australias-ramsar-sites*

Dekker, A.G., and Hestir, E.L. (2012). *Evaluating the Feasibility of Systematic Inland Water Quality Monitoring with Satellite Remote Sensing*. Water for a Healthy Country National Research Flagship, CSIRO.

EPBC Act (1999). *Environment Protection and Biodiversity Conservation Act*. Department of Environment and Energy Website: *http://www.environment.gov.au/epbc/about*

Fretwell, P., Pritchard, H.D., Vaughan, D.G., Bamber, J.L., Barrand, N.E., Bell, R., Bianchi, C., Bingham, R.G., Blankenship, D.D., Casassa, G., Catania, G., Callens, D., Conway, H., Cook, A.J., Corr, H.F.J., Damaske, D., Damm, V., Ferraccioli, F., Forsberg, R., Fujita, S., Gim, Y., Gogineni, P., Griggs, J.A., Hindmarsh, R.C.A., Holmlund, P., Holt, J.W., Jacobel, R.W., Jenkins, A., Jokat, W., Jordan, T., King, E.C., Kohler, J., Krabill, W., Riger-Kusk, M., Langley, K.A., Leitchenkov, G., Leuschen, C., Luyendyk, B.P., Matsuoka, K., Mouginot, J., Nitsche, F.O., Nogi, Y., Nost, O.A., Popov, S.V., Rignot, E., Rippin, D.M., Rivera, A., Roberts, J., Ross, N., Siegert, M.J., Smith, A.M., Steinhage, D., Studinger, M., Sun, B., Tinto, B.K., Welch, B.C., Wilson, D., Young, D.A., Xiangbin, C., and Zirizzotti, A. (2013). Bedmap2: improved ice bed, surface and thickness datasets for Antarctica. *Cryosphere*, 7(1), 375–393.

GA (2002). *GEODATA TOPO 10M 2002* webpage, Geoscience Australia website: *https://ecat.ga.gov.au/geonetwork/srv/eng/catalog.search#/metadata/60803*

GA (2021a). *Maritime Boundary Definitions* webpage, Geoscience Australia website: *https://www.ga.gov.au/scientific-topics/marine/jurisdiction/maritime-boundary-definitions#:~:text=The%20term%20Territorial%20Sea%20Baseline,some%20cases%2C%20the%20continental%20shelf*.

GA (2021b). *Australia's Coasts and Estuaries* webpage, Geoscience Australia website: *https://www.ga.gov.au/scientific-topics/marine/coasts-estuaries#:~:text=The%20Australian%20coastline%20extends%20approximately,includes%20more%20than%201000%20estuaries*.

Harris, P., Heap, A., Passlow, V., Shaffi, L., Fellows, M., Porter-Smith, R., Buchanan, C., and Daniell, J. (2005). *Geomorphic Features of the Continental Margin of Australia*. Geoscience Australia, Canberra.

Heap, A.D., and Harris, P.T. (2008). Geomorphology of the Australian margin and adjacent seafloor. *Australian Journal of Earth Sciences*, 55(4), 555–585. doi:10.1080/08120090801888669

Heap, A.D., Harris, P.T., Last, P., Lyne, V., Hinde, A., and Woods, M. (2005). *Draft Benthic Marine Bioregionalisation of Australia's Exclusive Economic Zone*. Geoscience Australia Report to the National Oceans Office. Geoscience Australia, Canberra.

Last, P., Lyne, V., Yearsley, G., Gledhill, D., Gomon, M., Rees, T., and White, W. (2005). *Validation of National Demersal Fish Datasets for the Regionalisation of the Australian Continental Slope and Outer Shelf*. CSIRO Report to the National Oceans Office. CSIRO Marine Research, Hobart.

Lyne, V., and Hayes, D. (2005). *Pelagic Regionalisation: National Marine Bioregionalisation Integration Project*. CSIRO Report to the National Oceans Office. CSIRO Marine Research, Hobart.

NMSP (2015). *National Marine Science Plan 2015–2025*: *http://www.marinescience.net.au/national-marine-science-plan/*

Parkinson, C.L. (2019). A 40-y record reveals gradual Antarctic sea ice increases followed by decreases at rates far exceeding the rates seen in the Arctic. *Proceedings of National Academy of Science*, 116, 14414–14423. *https://doi.org/10.1073/pnas.1906556116*

Ridgway K.R., Dunn, J.R., and Wilkin, J.L. (2002). Ocean interpolation by four-dimensional least squares—Application to the waters around Australia. *Journal of Atmospheric and Oceanic Technology*, 19(9), 1357–1375.

Scott, J.B.T., Gudmundsson, G.H., Smith, A.M., Bingham, R.G., Pritchard, H.D., and Vaughan, D.G. (2009). Increased rate of acceleration on the Pine Island Glacier strongly coupled to changes in gravitational driving stress. *The Cryosphere*, 3, 125–131.

Schiller, A., Brassington, G., Oke, P., Cahill, M., Divakaran, P., Entel, M., Freeman, J., Griffin, D., Herzfeld, M., ; Hoeke, R., Huang, X., Jones, E., King, E., Parker, B., Pitman, T., Rosebrock, U., Sweeney, J., Taylor, A., Thatcher, M., Woodham, R., and Zhong, A. (2019). Bluelink Ocean Forecasting Australia: 15 Years of Operational Ocean Service Delivery with Societal, Economic and Environmental Benefits. *Journal of Operational Oceanography*, 13(1), 1–18. *https://doi.org/10.1080/1755876X.2019.1685834*

SOE (2011). *State of Environment Report 2011*. *http://155.187.2.69/soe/2011/report/inland-water/index.html*

SOE (2017). *State of Environment Report 2016*. Australia's water resources: Inland water (2016): *https://soe.environment.gov.au/theme/inland-water/topic/2016/australias-water-resources*

Symonds, P., Alcock, M., and French, C. (2009). Setting Australia's Limits: Understanding Australia's marine jurisdiction. *AusGeo News* 93, March 2009, Geoscience Australia.

The Madrid Protocol (1998). *The Protocol on Environmental Protection to the Antarctic Treaty*. Secretariat of the Antarctic Treaty. *https://www.ats.aq/e/ep.htm*

UN (1982) *United Nations Convention on the Law of the Sea*. United Nations Treaty Series. *http://www.un.org/depts/los/convention_agreements/convention_overview_convention.htm*

Vince, J., Smith, A.D.M., Sainsbury, K.J., Cresswell, I.D., Smith, D.C., and Haward, M. (2015). Australia's Ocean Policy: Past, present and future. *Marine Policy*, 57, 1–8. *https://doi.org/10.1016/j.marpol.2015.02.014*

Whiteway, T., Heap, A.D., Lucieer, V., Hinde, A., Ruddick, R., Harris, P.T. (2007). *Seascapes of the Australia margin and adjacent seafloor: methodology and results*. Geoscience Australia, Canberra.



3 Aquatic Ecosystems

Ecology is the science that looks at interactions between organisms and their environment. As detailed in Volume 3A, an ecosystem describes the assemblage of organisms living in a particular environment, and their connections in terms of energy and nutrient recycling. Aquatic ecosystems, by definition, exist in aquatic environments—both natural and man-made—including oceans (and sea ice), coastal waters, rivers, wetlands, dams, and lakes.

As with all ecosystems, the specific characteristics of aquatic habitats determine the organisms that live there. Relevant characteristics include food and nutrient availability, water and air temperature, water circulation, shelter, and water depth.

3.1 Aquatic Ecosystem Zones

A number of related, but overlapping, terms are used to describe specific regions of surface water as they relate to aquatic ecosystems. In this context, waterbodies are divided into zones based on: distance from the shore, light penetration, and/or the depth of the substrate (see Figure 3.1).

The **Benthic Zone** is the lowest level of any aquatic ecosystem, extending from the shoreline to deep water. This zone consists of rock, sand, and sediment on the floor of an ocean, sea, lake, or river. As such, the conditions of the benthic zone can vary significantly between shallow coastal waters and deep ocean. It supports a wide range of benthic organisms, or 'benthos', depending on local conditions, such as the amount of light that reaches it, the ambient temperature, and available nutrients.

The **Intertidal Zone** spans between the high and low tide marks and describes the coastal land that is exposed to changing tides. It is impacted by waves at high tide, and Sun and wind at low tide. Benthos living in the intertidal zone, such as barnacles, are adapted to these harsh, cyclic conditions.

The **Neritic Zone** occurs along coastlines between the low tide mark and the continental shelf. Since some sunlight reaches the bottom of this relatively shallow zone, it fosters photosynthetic organisms, such as phytoplankton, benthic microalgae, and macroalgae. Most coral reefs occur in this zone. Organisms such as molluscs, sponges, crustaceans, and worms can live on the seafloor of this zone.

Freshwater ecosystems are a foundation of our social, cultural, spiritual and economic well being.
*(Likens **et al.**, 2009)*

Background image: Phytoplankton—the foundation of the oceanic food chain. **Source:** NOAA MESA Project. Retrieved from *https://commons.wikimedia.org/wiki/File:Phytoplankton_-_the_foundation_of_the_oceanic_food_chain.jpg*

The **Photic Zone** refers to water that is close enough to the surface to admit sufficient light for photosynthesis. In lakes, this region is referred to as the **Limnetic Zone**.

The Photic Zone can be further divided into the **Euphotic**, or sunlit, zone and the **Dysphotic**, or twilight, zone. The lower extent of the Euphotic zone is defined as that water depth where only 1% of the photosynthetically active radiation (PAR) penetrating the water surface is 'visible'. Thus, as little as 1% of light entering the Euphotic zone reaches the Dysphotic Zone. The Euphotic zone includes shallow, coastal waters and the upper part of deeper, ocean waters. In clear water, this zone can extend down to 200 m. The Euphotic zone supports phytoplankton, microscopic algae and cyanobacteria as well as water plants and zooplankton, and the vast majority of marine life. Most photosynthesis on Earth occurs in the Euphotic Zone.

The **Aphotic Zone** (or midnight zone) refers to the darker, deeper waters below 1000 m in which light levels are too low for photosynthesis. This zone is also called **Deep Sea** in oceans and the **Profundal Zone** in lakes. The Aphotic Zone comprises 90% of the total area of oceans on Earth.

The **Oceanic Zone** spans between the continental shelves of different land masses.

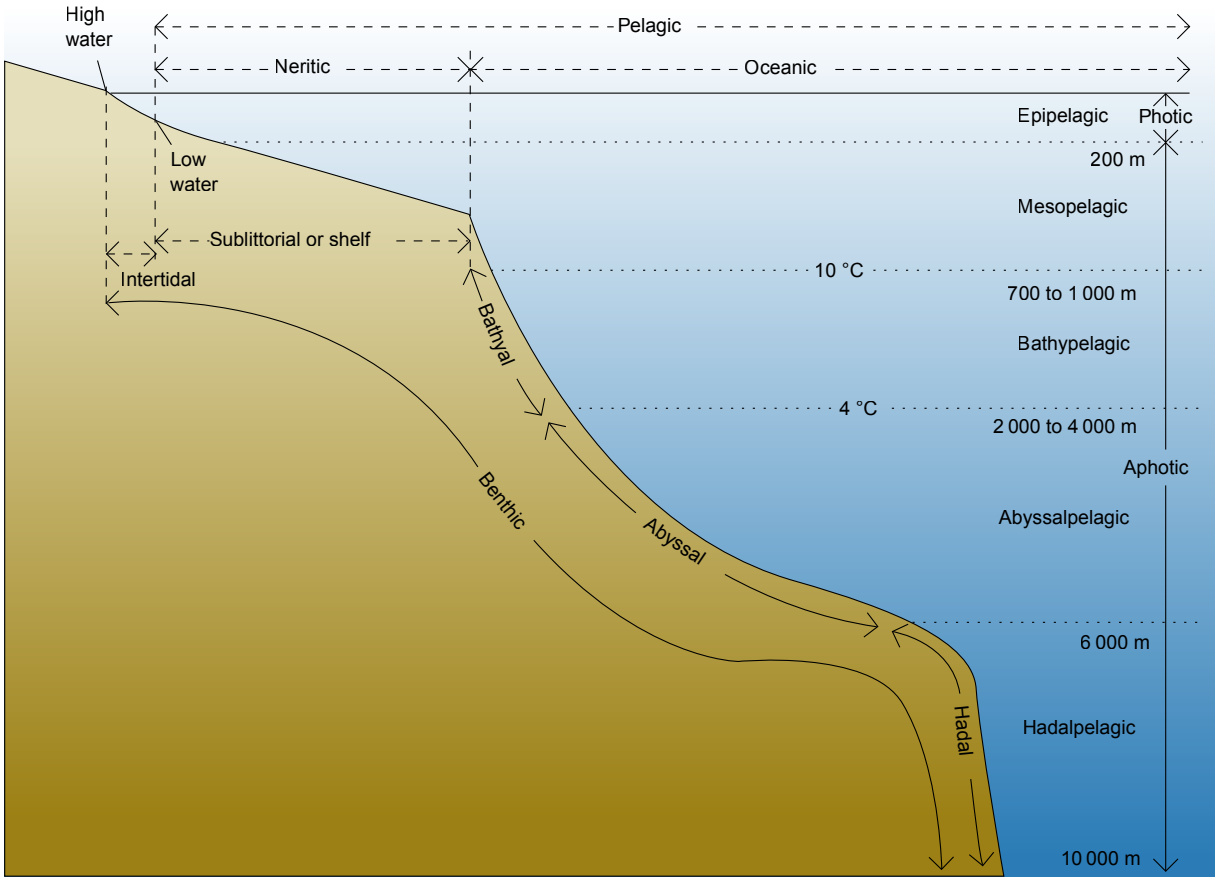
The **Pelagic Zone** describes open water in oceans that is both away from the coast and above the seafloor, and includes both photic and aphotic waters.

The **Demersal Zone** includes water near the seabed, but below the pelagic zone.

The **Littoral Zone** extends from the high tide mark to the continental shelf and thus includes the intertidal and neritic zones defined above.

The **Riparian** zone occurs along the edges of rivers or streams and includes the riverbed, banks, and floodplains.

Figure 3.1 Aquatic zones for marine waters



Source: Wikimedia. Retrieved from *https://commons.wikimedia.org/wiki/File:Oceanic_divisions.svg*

3.2 Aquatic Habitats

A range of aquatic habitats exist in surface waters, including:

- seas and oceans—contiguous waterbodies containing saltwater and covering around 70% of the globe. At high latitudes, this includes habitats covered by sea ice;
- coastal waters—aquatic fringes along land masses;
- estuaries—the interface between rivers and open sea, containing a fluctuating mix of freshwater and saltwater as determined by tidal water movement;
- rivers and streams—flowing waterbodies containing freshwater;
- lakes—permanent waterbodies at least 2 m deep and covering more than 0.25 ha. The largest supply of available freshwater on Earth is contained in lakes (Kalff, 2002); and
- inland floodplain wetlands—habitats reliant on variable flow and flooding regimes, including lakes and lagoons, grass-sedge-herb swamps, floodplain shrublands, and eucalypt forests and woodlands (see Excursus 3.1).

All aquatic habitats vary in terms of inflows, outflows, shoreline extent, water depth, geology, geomorphology, climate, and surrounding vegetation. In turn, these characteristics impact the physical, chemical, and biological attributes of the habitat, including resident organisms. To protect coastal and ocean habitats, numerous Marine Protected Areas (MPA) have been defined around Australia in recent decades to ensure that these unique and valuable regions are managed sustainably (see Excursus 20.2). Similarly, RAMSAR wetlands, and other nature reserves containing wetlands, rivers, and lakes, have been established to protect inland aquatic habitats.

While the precise definitions of wetlands and riparian zones can vary, both these terms describe the occurrence of vegetation in the transition zone between surface waterbodies, such as streams, rivers or lakes, and higher ground. The term 'wetlands' refers to areas that are partially or fully inundated on a periodic basis, and includes the soil, flora, and fauna existing in these areas, whereas the riparian zone describes the terrestrial or aquatic vegetation that fringes watercourses. In both cases, the presence of water promotes the growth of plants that are adapted to these environments and these plants impact the ecology of the watercourses. For example, riparian vegetation provides habitat for a wide range of faunal species, stabilises river banks, filters sediment, reduces floodwater velocity, and modulates water temperature (DWER, 2021; WaterNSW, 2021). Both wetlands and riparian zones are sensitive to land management practices that change surface water flows, and actively help to maintain water quality and waterbody health (see Excursus 3.1).

The National Intertidal Subtidal Benthic (NISB) Habitat Classification Scheme (Mount and Bricher, 2008a) defines a common set of identifiers for national reporting of aquatic habitats in Australia. NISB was used to produce nationally consistent Estuarine, Coastal and Marine (ECM) maps for seagrass, mangrove, saltmarsh, rocky reef, coral reef, macroalgae, shorelines (beaches), coastal wetlands, and estuaries (Mount and Bricher, 2008b), which "contribute to vulnerability and risk assessments of coastal ecosystems and human infrastructure" (DAWE, 2015). These maps show detailed habitat extent and distribution at local, state, and regional scales, and more general habitat distribution at regional and national scales.

Clearly, coasts and oceans face pressures from multiple human uses, and conflicts exist between competing human uses and between these uses and imperatives to protect the ocean environment and ecosystems (Vince ***et al.****, 2015).*

Excursus 3.1—Inland Floodplain Wetlands

Source: Rachael Thomas, NSW Department of Planning, Industry and Environment

Introduction

Floodplains are part of the riverine landscape formed as a result of alluvial processes. They are inherently heterogeneous and among the most biologically productive and diverse ecosystems in the world (Thoms *et al.*, 2016; Ward *et al.*, 2002; Tockner and Stanford, 2002). EO-based monitoring approaches for wetlands are considered in Section 20.

The Murray-Darling Basin (MDB) in southeastern Australia is a large (1 million km^2) complex system of rivers that rise in the high rainfall areas of the southeastern dividing ranges and flow westward for long distances (see Figure 2.15, Figure 2.16 and Figure 3.2). These rivers flow across the semi-arid to arid inland regions where rainfall is low (annual < 406 mm) and evaporation is high (exceeding 2000 mm)—and ultimately into the Southern Ocean. The rivers of the MDB exhibit high flow variability, which is primarily determined by the El Niño Southern Oscillation (ENSO) climate phenomenon (Walker *et al.*, 1995; van Dijk *et al.*, 2013).

Large floodplains, or 'floodscapes', are formed on the lowlands of these large alluvial rivers where the valley floor widens in a downstream direction and river flow velocity decreases to form low energy environments (Thoms *et al.*, 2016). Floodplain complexity is characterised by a diverse mosaic of landforms (such as channels, flats and basins), which provide the physical template for wetland habitats (Semeniuk and Semeniuk, 2011; Thoms and Parsons, 2016). The presence of water drives the productivity of floodplain wetlands as floodplains are variably inundated by the lateral overflow of their associated rivers producing a dynamic mosaic of wet and dry habitats. Vegetation communities of the floodplain landscape also reveal a heterogenous mosaic distribution which together with landform and variable inundation patterns begin to characterise inland floodplain wetlands (see Figure 3.3).

Figure 3.2 Inland floodplain wetland distribution in the MDB

Insets show locations of example inland floodplain wetlands: A: 1.Gwydir wetlands, 2. Narran Lakes, 3. Macquarie Marshes, and B: 4. Booligal wetlands, 5. Great Cumbung Swamp, 6. Lower Murrumbidgee (Lowbidgee floodplain), 7. Barmah-Millewa Forest Swamps

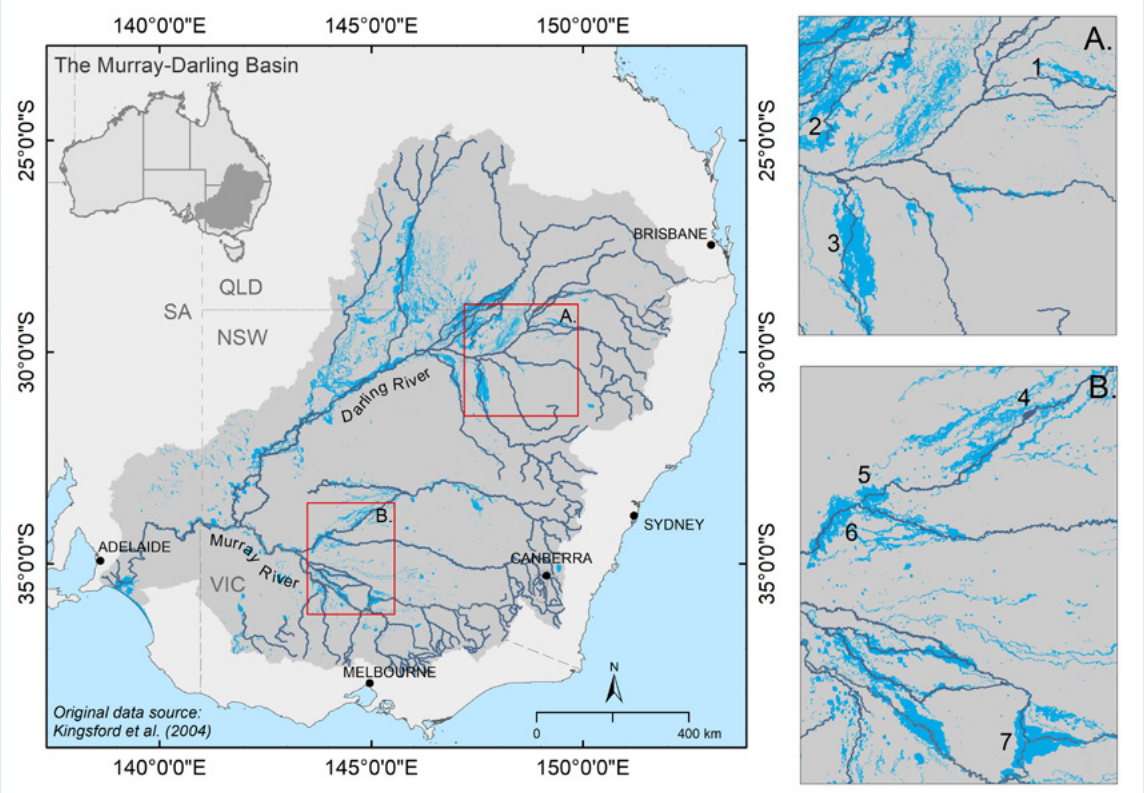


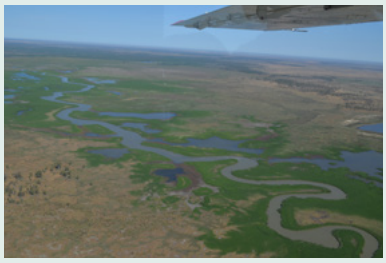
Figure 3.3 Mosaics of inland floodplain wetland types

a. Grassland-sedgeland-herbland swamps with open water lakes and lagoons

1. Common reed grasslands in the Macquarie Marshes



2. Common reed grasslands in the Great Cumbung Swamp at the terminus of the Lachlan River



3. Rushlands in and around Moira Lake in Millewa Forest of the Murray River

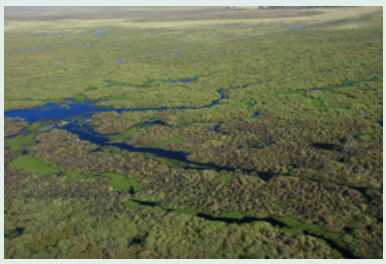


b. Lignum shrubland swamps with open water lakes and lagoons

1. Narran Lakes system



2. Booligal wetlands



3. Lowbidgee floodplain



c. river red gum forest and woodlands with open water lakes and lagoons

1. Lowbidgee floodplain including Piggery Lake



2. Mid-Murrumbidgee Yarradda Lagoon, an oxbow lagoon amongst river red gum woodlands



3. Macquarie Marshes



Source: Copyright © to photographers: Rachael Thomas (a1, b1); Joanne Ocok (a2); Paul Packard (b2, b3); Vince Bicello (a3);James Dyer (c2); Simon Hunter (c1); Bill Johnson (c3)

High variability of flows drives the ecological 'boom' and 'bust' of these floodplain systems. Flooding of habitats triggers a series of dynamic ecological processes that produces a huge increase in species biodiversity and abundance for which inland floodplain wetlands are recognised (Bunn *et al.*, 2006; Kingsford *et al.*, 1999). Accordingly, many are in protected areas (such as National Parks or Nature Reserves) and some are also recognised as Wetlands of International Importance under the Ramsar Convention for supporting unique wetland habitat, rare and threatened species, and providing important habitat for waterbirds (Pittock *et al.*, 2015; see Section 2.6). Many of the MDB rivers are regulated by large dams and weirs built to support agricultural production and this has altered flows and impacted the ecology of inland floodplain wetlands (Kingsford, 2000; Kingsford *et al.*, 2015). Environmental flows are managed in the MDB to mitigate the impacts of river regulation by restoring flow and flooding regimes for the ecological requirements of the system (Arthington, 2012; Swirepik *et al.*, 2016).

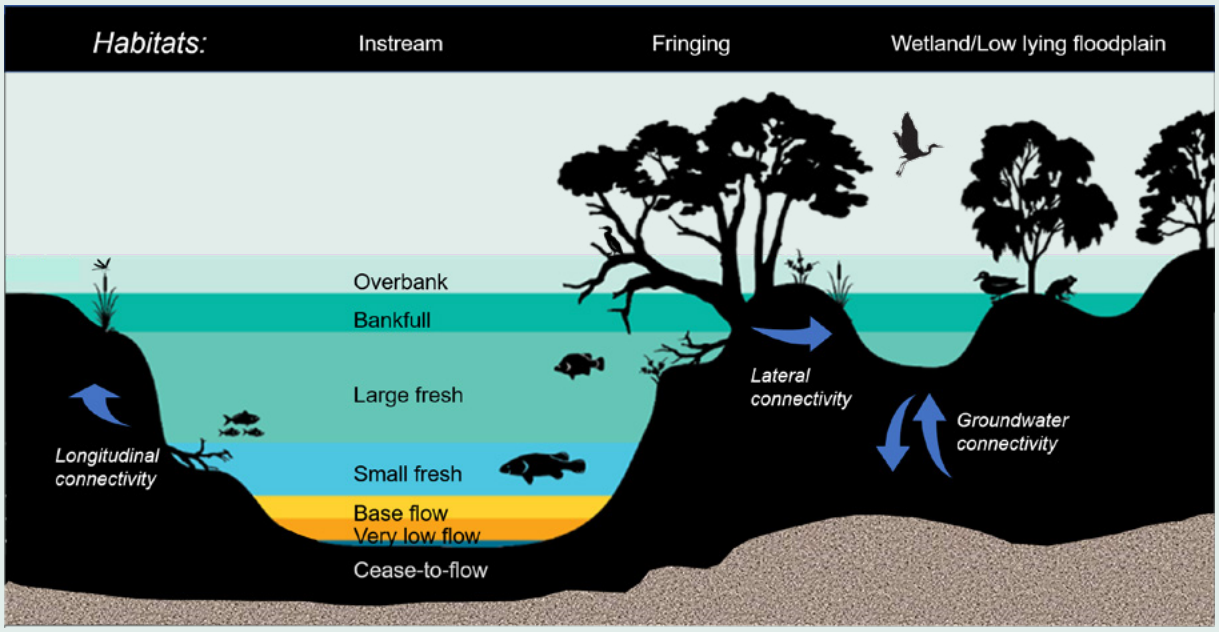
Hydrology

Highly variable river flows, or flow regimes, drive the dynamics of hydrological connectivity in riverine landscapes, influencing the longitudinal (in-channel river flows), lateral (overbank floodplain and wetland inundation) and vertical connectivity (groundwater) pathways that shape and sustain the riverine landscape (Walker *et al*., 1995; see Figure 3.4). Flow regimes connect instream and fringing habitats longitudinally along rivers, and laterally across wetland and low-lying floodplain habitats through the variable nature of hydrological connectivity: from low flows, to small and large freshes, to bankfull and overbank wetland inundating flows.

Ecologically important aspects of the flow regime are characterised by the magnitude (extent), duration, timing and flood frequency (Poff *et al*., 1997). Flow and flooding regimes describe the hydrological variability in relation to the ecological function they support, for example, nutrient cycling, growth, breeding, migration, and dispersal of plants and animals. The most influential driver of inland floodplain wetland ecosystems is variations in flooding regime (lateral connectivity), which produce a dynamic heterogeneous mosaic of wet and dry habitats across the floodplain (Bunn and Arthington, 2002; see Figure 3.5).

Figure 3.4 Longitudinal, lateral and vertical hydrological pathways

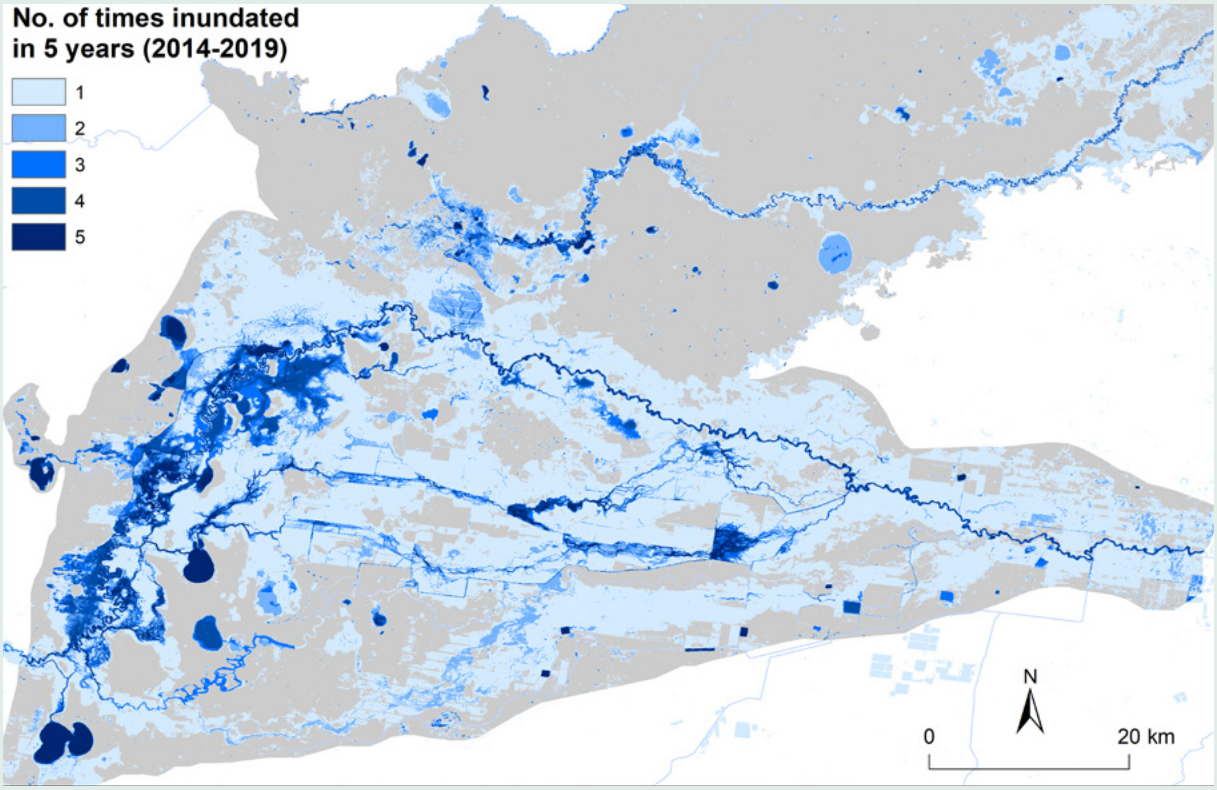
Hydrological pathways connect inland floodplain habitats with the variations of the flow regime.



Adapted from: DPIE Long-term Water Plans (DPIE, 2020)

Figure 3.5 Inundation patterns

The distribution of variable inundation patterns during a five year period (2014–2019) across the inland floodplains of the Lower Murrumbidgee (Lowbidgee) and Lower Lachlan is shown below. This is based on annual inundation maps derived from satellite imagery using mapping methods modified from Thomas *et al.* (2015).



Floodplain wetland types

The components that characterise floodplain wetlands are diverse landforms, the inundation regime, and vegetation cover types (see Figure 3.6). Vegetation in the inland floodplains of the MDB is distributed as a mosaic with low tree diversity and a high diversity of understorey/wetland plant species that transition from dry- to wet-adapted species when inundated (Roberts *et al.*, 2016). Different types of inland floodplain wetland vegetation rely on specific ecological water regimes for their growth, survival, and reproduction.

As detailed below, four common types of inland floodplain wetlands in the MDB (see Figure 3.6) are:

- floodplain lakes and lagoons, which retain areas of open water and include aquatic plant species;
- herbaceous swamps, which include aquatic plants, forbs, grasslands, sedgelands, and rushlands;
- floodplain shrubland swamps; and
- tree swamps (Eucalypt forests and woodlands).

The resulting vegetation mosaic provides many functional fauna habitats for waterbirds, fish, frogs, turtles, and invertebrates.

Figure 3.6 Conceptual models of common inland floodplain wetlands in MDB

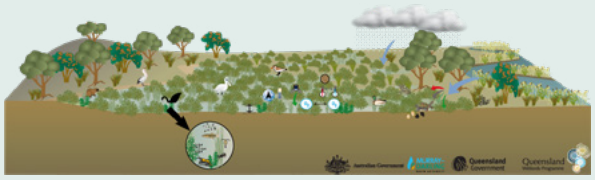
a. Floodplain lakes and lagoons (e.g. lagoons of the Mid-Murrumbidgee, Narran Lakes, Macquarie Marshes, Lachlan)



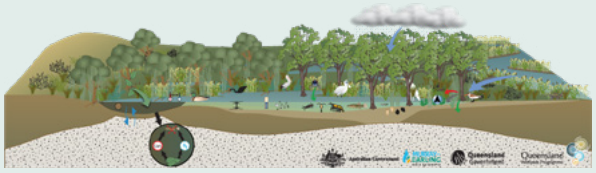
b. Grassland-sedgeland-herbland swamps (e.g Gwydir, Great Cumbung Swamp, Macquarie Marshes)



c. Floodplain shrubland (lignum) swamps (e.g. Lowbidgee floodplain, Narran Lakes system, Booligal wetlands)



d. Tree swamps (Eucalypt forests and woodlands; e.g. Macquarie Marshes, Lowbidgee, Barmah-Millewa forests)



Source: QDES (2013) © WetlandInfo, Department of Environment and Science, Queensland

Lakes and lagoons

Naturally occurring lakes and lagoons on inland floodplains are a basin landform and vary in size (from a few to thousands of hectares), shape (e.g. circular, oxbow), and depth (< 1–5 m deep; see Figure 3.3 and Figure 3.7). Together, the varying connectivity with associated creeks, overland flows, and lake geomorphology influence the flooding regime dynamics of lakes and lagoons. These waterbodies provide a wide variety of habitat types in patches of deep and shallow open water, submerged aquatic vegetation, mudflats along the shoreline, and a vegetated littoral zone of emergent grasses, sedges, shrubs, or trees, which enable diverse and abundant communities of invertebrates, fish, frogs, and waterbirds to shelter, feed and breed. Waterbirds that are commonly found in lakes and lagoons are those that dive for food (e.g. cormorants), or forage on aquatic plants in deep water (e.g. black swans, ducks) or along the shoreline (e.g. shorebirds). The debris from floating and submergent aquatic plants provide breeding habitats for duck species. When flooded, lakes and lagoons provide open water habitat, retaining water in an otherwise dry floodplain landscape after floodwaters have receded in adjacent areas to function as important refugia between flood events.

Grassland-sedgeland-herbland swamps

Inland floodplain wetlands dominated by grassland, sedgelands, or herblands occur on varied landforms, including basins, flats, and channel networks, which influence lateral connectivity, water depth, and subsequent inundation regime dynamics (see Figure 3.3). There is a high diversity of grassland, sedgeland, and herbland plant species found in inland floodplain wetlands, which can be individually widespread across the MDB, but their species assemblage distribution is primarily in response to water availability and the variations in depth, duration, and frequency of flooding (see Figure 3.7). Many of these plant species are functionally related in their response to water regimes: terrestrial (dry, damp), amphibious (tolerator, responder), and submerged (emergent, submerged; Casanova, 2011). After flooding there is an increase in habitat heterogeneity, plant species, cover, and height. Plant communities can be monospecific or heterogenous in their species assemblage composition. They provide the architectural habitat structure for fauna to shelter, take refuge, forage, and breed.

Grassland plant species typically found in inland floodplain wetlands are usually perennial and morphologically diverse:

- tall (1–3 m, such as the common reed, *Phragmites australis*)—can form vast and dense monospecific grassland swamps, most notably in the Macquarie Marshes and the Great Cumbung Swamp (see Figure 3.3). Tall and dense emergent cover in shallow water provides structural habitat for cryptic waterbird species, such as the Australasian bittern, and nesting substrate for coots and grebes. When adjacent to open water lagoons, common reed is an important waterbird breeding habitat for colonial nesters.
- mat-forming—occur on most riverbanks of western MDB rivers, but sometimes they can form extensive grasslands as occur on the Gwydir floodplain and in the Macquarie Marshes (see Figure 3.3).
- tussock—grow as isolated clumps typically in flat, shallow wetlands with turbid waters and are distributed most extensively in the hotter and drier parts of the north and west of the MDB (see Figure 3.3); and

- aquatic—grow in flooded wetlands with long buoyant stems floating on the water surface (Roberts and Marston, 2011).

Sedgelands are a diverse plant group that occurs in the inland floodplain wetlands of the MDB (Roberts and Marston, 2011). They can occur in a range of shallow water and wet-dry habitats and form dense stands of entire wetlands or understories of forests and woodlands. Sedgelands provide important refuge habitat for frogs, foraging grounds for swamp hens and ducks, and breeding habitat for brolgas. For example, Marsh Club-rush (*Bolboschoenus fluviatilis*) is a tall (1–2 m) perennial sedge, which occurs as small patches or as extensive monospecific stands. It is listed in NSW as a critically endangered ecological community with the most significant stand occurring in the inland floodplain wetlands of the Gwydir River (see Figure 3.2). The widespread perennial tall (2–3 m) emergent rush species of Cumbungi (*Typha domingensis* and *T.orientalis*) are widely spread across most inland floodplain wetlands because they grow in the water or on the mudflats of wetlands that have permanent, near-permanent, or seasonal water regimes. Cumbungi typically forms dense mono-specific stands in patches or as a littoral fringe around lakes, lagoons, and in rivers, and provides suitable refuge habitat for a range of cryptic waterbirds, shelter for small fish fish and frogs, and breeding habitat for cryptic waterbirds or colonially nesting waterbirds.

Herblands comprise a diverse and dynamic group of plants that transition from dry- to wet-adapted species when inundated so can be aquatic, amphibious, or terrestrial. Aquatic plants grow while inundated, whereas amphibious plants tolerate wetting and drying and persist during the drying phase as floods recede. Terrestrial plants also develop during the drying phase and then dominate the dry phase. Herblands can occur on the lakebeds or shoreline, in riverbanks or riverbeds, or can be part of the larger vegetation mosaic that includes forests, woodlands, and shrublands.

Shrubland (lignum) swamps

Lignum (*Duma florulenta*), a multi-stemmed shrub, is the most ecologically significant inland floodplain shrub species occurring on the floodplains of most major rivers in the MDB (Roberts and Marston, 2011). Flooding is the main influencer of lignum growth, and flood frequency strongly affects the size and vigour of individual shrubs, which can grow to 3 m in height, diameter and width to form extensive and dense shrublands. Lignum is often associated with other shrub species and is also an important structural component of the understorey of many woodland communities, especially those of river cooba (*Acacia stenophylla*), river red gum (*Eucalyptus camaldulensis*), black box (*E. largiflorens*), and coolibah (*E. coolabah*). During extensive flooding the structure of lignum shrublands is flattened and becomes significant habitat for colonial-nesting waterbirds, by providing a nesting platform that protects them from rising floodwaters whilst near foraging habitat (Brandis *et al*., 2011). During flooding, lignum shrubland swamps also provide important sheltering habitat for fish, frogs, and aquatic invertebrates, whereas during dry periods they provide niche habitat for understorey herbs to grow (Freestone *et al*., 2017).

Eucalypt forests and woodlands

In the riverine systems of the MDB, the most widely distributed tree is the river red gum (*E. camaldulensis*) which forms extensive forest and woodland habitat across the entire Basin (Roberts and Marston, 2011). The other woodland tree species that dominate inland floodplain wetlands are black box (*E. largiflorens*), distributed from the central Basin to southwestern rivers, and coolibah (*E. coolabah*), which is distributed from central to northwest regions. Forests tend to be confined to frequently flooded locations, whereas woodlands are located in more variably flooded regions. River red gum forests and woodlands growing along the riverine habitat of the main rivers and tributaries that connect wetlands provide important corridors for movement of fauna especially waterbirds. They also provide important fish habitat within channels through fallen trees and branches, providing cover from predatory birds and other fish, feeding and breeding locations, and refuge from the current. Tree canopies of river red gums moderate temperature by providing shade over rivers and swamps (see Figure 3.7). River red gum litter provides one of the most important biologically accessible carbon sources to inland floodplain habitats that are influenced by highly variable flow regimes (Francis and Sheldon, 2002). Forest and woodland tree canopies and hollows provide important habitat for roosting and breeding waterbirds. Woodland trees are important habitats for a range of fauna because they provide canopy, hollows, and fallen logs, which are not otherwise available in adjacent shrublands or grasslands (Roberts and Marston, 2011). Understorey composition of river red gum, coolibah, and black box forests and woodlands varies with inundation regimes (e.g. aquatic plant species, sedgelands, grassy-herblands), which provides the ecological character of the tree habitat.

Figure 3.7 Examples of common inland floodplain wetlands in the MDB

a. Inundated lagoon with aquatic vegetation species in the Murrumbidgee River system



b. Inundated sedgeland swamp in the Gwydir wetlands



c. Lignum shrubland swamp in the Lowbidgee floodplain



d. Inundated river red gum forest with an aquatic plant species understorey in the Macquarie Marshes



Copyright © to photographers a. Carmon Amos; b. Joanne Ocock; c. Sharon Bowen; d. Rachael Thomas

Fauna

The mosaic of inland floodplain wetland habitats supports a diversity of fauna, sometimes in high abundance, and often at critical life cycle stages (Roberts and Marsden, 2011). Waterbirds, fish, frogs, and other dependent fauna, including freshwater crabs and mussels, snails, water rats, and snakes, rely on these important habitats, so are often found throughout the inland floodplain wetlands of the MDB.

Waterbirds

Inland floodplain wetlands across the MDB form a large landscape of strategically located diverse habitats to which waterbirds will travel large distances to find temporary wetland resources so they can breed, feed, and take refuge in an otherwise dry landscape (Kingsford *et al*., 2010). These wetland habitats are critical for supporting a high diversity of waterbirds (> 165 species in the Murray-Darling).

During times of increased water availability (flooding) inland floodplain wetlands (vegetated swamps, floodplains and lakes) support high abundances of waterbirds (e.g. 300,000 waterbirds; Kingsford and Thomas, 1995) and when water is scarce, rivers and lake habitats provide critical refugia (Bino *et al*., 2015). Waterbird species have similar feeding and habitat preferences and can be grouped on the basis of these ecological requirements (Kingsford *et al*., 2010; Spencer *et al*., 2010):

- dabbling and diving ducks—feed on small invertebrates and plant material in shallow water or the littoral zone;
- herbivores—forage on plants in either deep water or at the edge of the wetlands, or in grasslands;
- piscivores—feed on fish in the main body of water of lakes, lagoons, and swamps;
- large wading birds—feed in wetlands with shallow water, grasslands, and sedgelands; while

- small wading birds (shorebirds)—are restricted to the shoreline of a wetland where there are mudflats (Kingsford *et al*., 2010; Spencer *et al*., 2010).

Several waterbird species are listed as threatened through state and Commonwealth legislations (NSW Biodiversity Conservation Act, 2016; Environmental Protection and Biodiversity Conservation Act, 1999) and migratory waterbird species that utilise inland floodplain habitats are listed under international migratory bird agreements (JAMBA, CAMBA and RoKAMBA[4]; OEH, 2012).

Diverse inland floodplain wetland habitats support waterbird nesting habitat preferences for a range of different types of waterbirds. Several inland floodplain wetlands of the MDB are globally significant Ramsar sites for waterbirds that breed in colonies (e.g. Narran Lakes, Macquarie Marshes, Gwydir wetlands, Barmah Forest; see Figure 3.2) and include some of Australia's largest waterbird breeding events ever recorded (e.g. in the Macquarie Marshes; Kingsford and Johnson, 1998). Waterbirds species can also breed in rookeries using the tree canopy of eucalypt trees in or over water, and herbivores will breed in common reeds and cumbungi.

Frogs, fish and other fauna

The variety of inland floodplain habitats supports an equally diverse range of dependent faunal species, including turtles, crustaceans, and frogs.

Frogs are an important part of these ecosystems as they are a food source for waterbirds, fish and reptiles as well as being a predator. They are a diverse faunal group but different species share similarities in their behaviours and habitat preferences (Ocock *et al*., 2016):

- marsh frogs prefer well vegetated wetlands and floodplain creeks where water levels rise when they are seasonally (or intermittently) inundated providing refuge and breeding habitat;
- tree frogs prefer woodland habitat; while
- burrowing frogs also occur in inland floodplain wetlands and are active after periods of high rainfall.

Aquatic vegetation is important for the entire frog life cycle as it provides a substrate for attaching eggs, tadpole feeding, metamorphosis, and shelter from predators (Wassens and Maher, 2011).

The inland floodplain wetland and connected river habitats of the MDB support a native fish community estimated at 46 species (Lintermans, 2007). Native fish communities respond to different conditions and so have different distributions through the MDB system. Some are restricted to the warmer water in the north, or to southern locations with access to the sea, or they vary with altitude. Fish diversity is highest in inland floodplains habitats where there are slow-flowing turbid rivers surrounded by open water lagoons, vegetated swamps, and river red gum forests.

Groups of fish species (known as guilds) have similar life spans, flow responses and habitat preferences (DPIE, 2020). The extent and condition of fish populations in the MDB have been in decline due to river regulation, impediments to fish passage, habitat degradation, and poor water quality, and many native fish species are listed as threatened or vulnerable under State or National legislation (Riches *et al*., 2016). Significant declines occurred after 2007 when there was an extreme reduction in water availability during the Millennium drought.

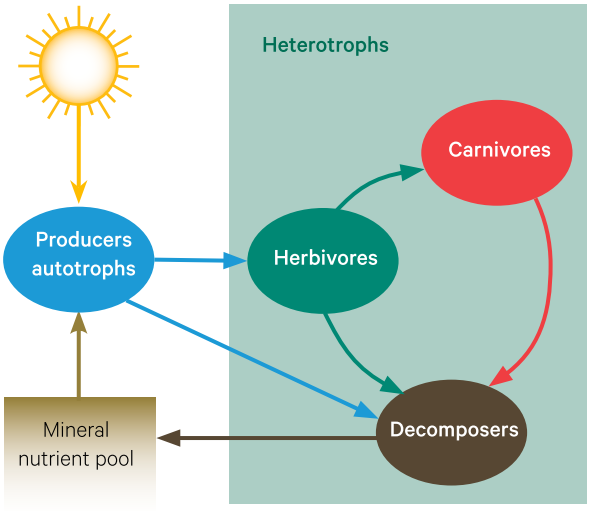
4 JAMBA: Japan-Australia Migratory Bird Agreement; CAMBA: China-Australia Migratory Bird Agreement; RoKAMBA: Republic of Korea-Australia Migratory Bird Agreement

3.3 Aquatic Organisms

A diverse range of organisms live in water—both freshwater and seawater. Most aquatic organisms require water, energy, carbon, and oxygen, plus the nutrients nitrogen, phosphorus, potassium, iron, sulphur, and selenium. For example, when the availability of nitrogen and phosphorus is limited, aquatic plant growth can become inhibited. The interdependence of organisms within an ecosystem can be represented in terms of a simple food chain, (see Figure 3.8). As detailed in Volume 3A, primary producers synthesise organic matter from raw ingredients via photosynthesis, so include plants and photosynthesing microorganisms. Secondary producers (herbivores, carnivores, and decomposers) assimilate organic material from other organims (living or dead).

Organisms can also be differentiated in terms of their biomass production, that is, the increase in biomass over a given time period. A productive environment accumulates biomass as living plant or animal tissue over time. The marine food chain depends on phytoplankton, which is estimated to be responsible for around 40% of the global photosynthetic activity (Falkowski, 1994). As such, the concentration of phytoplankton is viewed as an indicator of marine ecosystem health, with consequent impact on global climate stability.

Figure 3.8 Simple food chain



Microphytobenthos, microscopic algae, and cyanobacteria living in intertidal and aquatic sediment, are also important in aquatic ecosystems (see Section 3.3.2.1). While the productivity of phytoplankton is widely recognised, the productive capacity of the seemingly 'unvegetated' habitats that support microphytobenthos has only been investigated in recent decades (MacIntyre *et al.*, 1996). The distribution and concentration of phytoplankton, microphytobenthos, and cyanobacteria are directly related to the temperature, circulation, and nutrient content of the photic zone (see Excursus 3.2).

One approach to classifying living organisms defines three domains based on evolutionary development: Bacteria, Archaea, and Eukaryota. Species in Bacteria and Archaea are collectively known as prokaryotes, which are single-celled organisms with cell size 1–10 μm (such as cyanobacteria), whereas eukaryotes have a more complex and larger (10–100 μm) cell structure. The Plant Kingdom has also been sub-divided on the basis of reproductive characteristics and morphology (see Table 3.1; see also Volume 3A—Excursus 1.1;).

In this sub-volume, aquatic organisms will be considered in terms of four broad groupings:

- microorganisms—an imprecise label for microscopic life forms, including viruses, bacteria, fungi, and protozoa (see Section 3.3.1);
- algae—photosynthesising plant-like organisms (without roots, stems, or leaves), both microscopic and individually visible, that are either attached to the substratum or suspended in the water column (see Section 3.3.2);
- plants—photosynthesising organisms, which may be attached to the substratum or suspended in water (see Section 3.3.3); and
- animals—both vertebrates and invertebrates (see Section 3.3.4).

Aquatic biota that occur in the water column are further discussed in Section 5.3.

Table 3.1 The plant kingdom

Angiosperm class names are based on the Cronquist system. Note that since cyanobacteria is classified as bacteria, it is not included in this table.

Sub-Kingdom	Division	Major sub-groups
Cryptogamae (non-flowering and non-seeding plants; reproduce via spores)	Thallophyta (algae and fungi; non-vascular)	Bacillariophyta (diatoms)
		Charophyta (stoneworts)
		Chlorophyta (green algae, ~8,000 species)
		Chrysophyta (golden brown algae)
		Haptophyta/ Prymnesiophyta (e.g. Coccolithophorids)
		Pyrrophyta/Dinophyta (dinoflagellates, ~200 species)
		Phaephyta (brown algae—kelp)
		Rhodophyta (red algae, ~6,000 species)
		Glaucophyta (rare freshwater algae)
		Tribophyta (yellow-green algae)
	Bryophyta (non-vascular)	Hepaticae (liverworts)
		Anthocerotae (hornworts)
		Musci (mosses)
	Pteidophyta (vascular)	Psilopsida (two small genera of fern-like plants)
		Lycopsida (club mosses; five genera with > 1000 species)
		Equisetopsida (horsetail; one genus)
		Pteridopsida (ferns; ~9,000 species)
Phanerogamae (or Spermatophyta: seeding plants with roots, stems, and leaves)	Gymnospermae (non-flowering; seed not enclosed in fruit)	Cycadophyta (one genus: *Cycadaceae*; < 200 species)
		Ginkgophyta (one genus and species: *Ginkgo biloba*)
		Coniferophyta (two orders: Pinales and Taxale; ~200 species)
		Gnetophyta (three genera; ~ 100 species)
	Angiospermae (flowering plants)	Liliopsida (monocotyledons—one seed leaf; ~60,000 species)
		Magnoliopsida (dicotyledons—two seed leaves; ~200,000 species)

3.3.1 Microorganisms

By definition, individual microorganisms are too small to see with the naked eye, but colonies can become visible. These organisms exist in large quantities in all ecosystems. They play an essential role in aquatic ecosystems via photosynthesis and/or decomposition.

3.3.1.1 Viruses

Viruses are prevalent in surface waters, just as they are in terrestrial environments, with the highest abundance appearing to occur in coastal waters and sediments. They comprise the greatest genetic diversity in the ocean and can migrate between inland and marine waters.

Viruses catalyse the movement of nutrients from a range of organisms (phytoplankton, grazers, carnivores and bacteria) to the 'pools' of dissolved organic matter (DOM) and particulate organic matter (POM). While their importance in aquatic environments has only been recognised in recent decades (Suttle, 2005), they have significant impacts on the composition of planktonic communities (Weinbauer and Rassoulzadegan, 2004), as well as cycling nutrients and energy from living organisms to dissolved forms (Wilhelm and Suttle, 1999). Such cycling is significant for the global carbon cycle (see Section 1.5).

3.3.1.2 Bacteria

Bacteria are abundant in most aquatic environments (both marine and inland waters), and often enter a waterbody in runoff from adjacent land. Bacteria include some of the smallest known organisms and can reproduce very rapidly. They inhabit decaying material and hard surfaces, or suspend in water. Photosynthesising bacteria are predominantly prokaryotic cyanobacteria. While these organisms are commonly called blue-green algae, they are not true plants but belong to the kingdom Monera (see Section 3.3.2.1 and Excursus 3.2). Non-photosynthesising bacteria absorb dissolved organic compounds from their surroundings.

3.3.1.3 Fungi

Fungi can be single-celled organisms or filaments (hyphae). These non-photosynthesing organisms are also abundant in aquatic ecosystems and help to decompose plant material, especially material containing cellulose and lignin, by dissolving the absorbing organic compounds.

3.3.1.4 Protozoa

Protozoa are single-celled organisms that consume bacteria, algae, and other protists (see Volumes 1 and 3A). Some protozoa are parasites and induce disease.

3.3.2 Algae

The non-taxonomic term 'algae' is used to describe a variety of plant-like organisms without vascular tissue to internally transfer water and nutrients (that is, without true roots, stems, or leaves). While not classified as plants botanically, for convenience algae are often included in aquatic plant groupings. These photosynthesising organisms grow in both marine and inland waterbodies and can be considered in terms of two size groups:

- microalgae—diverse group of unicellular aquatic organisms, such as cyanobacteria, that exist in the water column or benthos (see Section 3.3.2.1); and
- macroalgae—eukaryotic organisms with compartmentalised cells and simple plant-like structures, such as kelp (see Section 3.3.2.2).

3.3.2.1 Microalgae

Microscopic algae, such as phytoplankton, can exist as single cells, chains, or colonies (see Section 5.3.1). The structure of these microorganisms allows them to suspend in calm water, or propel through the water column (Biocyclopedia, 2019). Their rapid production mechanisms supply most of the world's oxygen via photosynthesis, and help to absorb nutrients and heavy metals. In excess, however, they can result in algal blooms and deterioration of water quality (Entwisle *et al.*, 1997; see Sections 4.6 and 19.5).

The term microalgae encompasses both phytoplankton and microscopic algae living in the benthos, with the same classes of algae occurring in each group (see Excursus 3.2). The term 'microphytobenthos' encompasses photosynthesising microorganisms that inhabit the surface layers of intertidal, subtidal and submerged sediments, and includes unicellular eukaryotic algae (Baccilariophyceae, Chlorophyceae and Dinophyceae) and prokaryotic Cyanobacteria (MacIntyre *et al.*, 1996). However, depending on water depth, movement and particulate content, the distinction between phytoplankton and microphytobenthos can become unclear (MacIntyre *et al.*, 1996).

Rising ocean temperatures will likely increase stratification of the water column and reduce nutrient input into the photic zone. This will increase the likelihood of nutrient limitation in marine microalgae, leading to changes in the abundance and composition of phytoplankton communities, which in turn will affect global biogeochemical cycles.
Gerecht et al. (2014)

Excursus 3.2—Phytoplankton Groups

The most common groups of phytoplankton are listed in Table 3.2 and some of their diverse forms are illustrated in Figure 3.9. Over 5,000 species of marine phytoplankton have been identified globally (Sournia *et al.*, 1991).

Cyanbacteria, or blue-green algae, have the cell structure of primitive bacteria. They prefer calm, warm nutrient-rich water with high pH, as occurs during drought conditions, and can multiply extremely rapidly in suitable conditions to form a thick, green scum. While some species are sometimes toxic, all can produce contact irritants, and some change the colour and taste of water. As such, they present a threat to livestock and recreational water users.

The largest and most diverse phytoplankton group is diatoms, which are generally coloured brown or yellow. These organisms require silica for their cell wall. Their abundant presence has little impact on the taste or smell of water. They have been estimated to account for up to 20% of the global carbon fixation via photosynthesis, more than the combined contribution from tropical rainforests (Mann, 1999).

Dinoflagellates are capable of independent movement and will alter the taste and odour of water in large numbers. Some species are toxic, as occasionally occur in red tides. Green algae do not usually impact the taste of water unless a large population is present.

Table 3.2 Most common phytoplankton groups

Group	Description			
	Form	Occurrence	Trophic mode	Example
Cyanobacteria	Bacteria	Marine, freshwater, and terrestrial	Autotrophic	Blue-green algal blooms; spirulina
Diatoms	Unicellular or colonial coccoid algae	Marine, freshwater, and terrestrial	Autotrophic and heterotrophic	Ubiquitous in moist habitats; commonly used for environmental assessment
Dinoflagellates	Flagellate protists	Marine and Freshwater	Autotrophic and mixotrophic	*Noctiluca scintillans*, which can cause red tides
Chlorophyta (Green algae)	Unicellular colonial flagellates	Marine and Freshwater	Autotrophic	Chlorella
Coccolithophores	Unicellular eukaryote	Marine waters	Autotrophic	Important primary producers that thrive in warm, nutrient-poor waters

Figure 3.9 Phytoplankton forms

Phytoplankton are extremely diverse, varying from photosynthesizing bacteria (cyanobacteria), to plant-like diatoms, to armor-plated coccolithophores. Note: drawings are not to scale.

a. Cyanobacteria b. Diatom c. Dinoflagellate d. Green algae e. Cocolithophore



Source: Sally Bensusen, NASA. Retrieved from *https://upload.wikimedia.org/wikipedia/commons/archive/8/8a/20190514231026%21Phytoplankton_types.jpg*

Macroalgae ('seaweeds') are an ancient class of large multicellular plants that resemble vascular plants but lack the complex array of tissues used for reproduction and water transport.
OzCoasts (2018)

3.3.2.2 Macroalgae

This term 'macroalgae' collectively applies to algae that are visible to the naked eye (Diaz-Pulido and McCook, 2008). These multi-celled organisms feature a variety of shapes, sizes, and structures, and can occupy a variety of habitats. They extract nutrients from the water column and can be anchored to hard surfaces in the benthos by simple root-like structures called holdfasts (Entwisle *et al.*, 1997).

Macroalgae are traditionally described in terms of their photosynthetic pigments, and include (see Table 3.3):

- green algae (Division Chlorophyta), for example *Ulva lactuca* (sea lettuce);
- brown algae (Class Phaeophyceae in Division Heterokontophyta), including large kelps; and
- red algae (Division Rhodophyta), such as crustose coralline algae (Diaz-Pulido and McCook, 2008).

As indicated in Table 3.3, a range of photosynthetic pigments have been found in algae. These pigments are located as macromolecular complexes within the chloroplast (Jeffrey and Vesk, 1997). For example, the pigments phycoerythrin and phycocyanin are phycobilins, efficient light-trapping molecules that occur in some algal species (see Table 3.3). These pigments are bonded to water-soluble proteins called phycobiliproteins, which transfer the light energy to chlorophyll pigments for photosynthesis. This mechanism allows red algal species to grow at greater water depths than other algae. Red coralline algae, for example, grow at water depths of 268 m, the deepest of any photosynthetic organism (OzCoasts, 2018).

Many species of algae have economic value for their pigments and other components (alginates, agar, and carrageenan), which are extracted for industrial use from the flexible cell wall components. Algae provide food sources for fish, crustaceans, indigenous gourmands, food supplements (such as wakame for human and animal consumption), and fertilisers for terrestrial vegetation (Entwisle *et al.*, 1997). They are also cultivated for use in aquaculture and aquariums.

Table 3.3 Most frequently occurring algal groups

Life Form	Plants			Bacteria
Common Name	Red Algae	Green Algae	Brown Algae	Blue-Green Algae
Botanical Division	Rhodophyta	Chlorophyta	Heterokontophyta; (Class Phaeophyceaae)	Cyanophyta
Distribution	Marine habitats	Marine, freshwater and terrestrial habitats	Predominantly marine habitats	Almost every marine, freshwater, and terrestrial habitats
Diversity (Approximate # species)	5,000–5,500 globally; 1,300 in Australia	8,000 globally; 2,000 in Australia	1,500–2,000 globally; 350 in Australia	2,698 described species; over 6,000 estimated[5]
Appearance	Small and inconspicuous; diverse reddish forms growing in limited beds	Grass-green, sometimes with greyish hue	Most conspicuous; large and brown	Small and inconspicuous, unless present as algal bloom in marine or freshwater; predominantly greenish-blue, but may appear as other colours
Chlorophyll pigments	Chlorophyll a	Chlorophyll a Chlorophyll b	Chlorophyll a Chlorophyll c	Mostly Chlorophyll a; some genera have Chlorophyll b instead
Masking/accessory pigments	Phycoerythrin	Carotenoids and Xanthophylls	Fucoxanthan	Phycocyanin; Phycoerythrin
Extracts	Agar; Carrageenan	None	Alginates	Potential for biofuel

Source for most entries: Huisman (2000)

5 Nabout *et al.* (2013)

Macrophyte (from) Greek: makro meaning 'large' and phuton meaning 'plant'

3.3.3 Plants

Non-algal aquatic plants include angiosperms (flowering plants), pteridophytes (ferns), and bryophytes (mosses, hornworts and liverworts; see Table 3.1 and Volume 3A). Since all plant life forms require light for photosynthesis, the distribution of aquatic vegetation is restricted to either the upper water layers of a waterbody where light can penetrate (the photic zone—see Section 3.1) or, in shallow waters, the seafloor. The major types of aquatic plant life are commonly differentiated by their attachment to the substratum or to other plants or animals (Huisman, 2000; see Section 5.3.2).

Large aquatic plants (visible to the naked eye), or 'vascular plants in which specialised cells transport water and minerals from true roots' (Bowden *et al.,* 2017), are commonly termed macrophytes. These plants need to grow in standing water, where the water level is at or above the soil surface, or near a waterlogged environment. Being supported by water, they typically develop much less structural tissue than terrestrial plants, but contain additional air spaces to increase buoyancy. Macrophytes are traditionally described in terms of their growth habit (see Table 3.4). The form of some macrophytes can change between these categories during the seasonal cycle and/or the life cycle. Submerged plants and macroalgae are collectively known as submerged aquatic vegetation (SAV).

Commonly encountered examples of macrophytes include mangroves, seagrasses, lilies, rushes, and reeds. For example, seagrasses are vascular plants growing in coastal and inland waters that derive nutrients from the benthos via roots. While seagrass flowers are inconspicuous, seagrasses are true flowering plants (Division Magnoliophyta). They are considered to be closely related to terrestrial plants, having vascular tissue and green foliage resembling grass or leaves. Around 60 species are known worldwide, with about half of those occurring in Australia (see Section 20.3.1). While the distribution of tropical seagrasses is typically sparse, in other locations seagrasses can form dense, extensive beds in shallow coastal waters, which are important for stabilising sediments and furnishing nurseries for juvenile fish and invertebrates (Huisman, 2000).

Bryophytes lack true roots and xylem tissue. They tend to occur in faster and shallower streams than macrophytes, with harder substrates. These plants require less light than macrophytes and have been used as biomonitors for water quality (Gecheva and Yurukova, 2014).

Aquatic vegetation is vulnerable to seasonal water level changes and heavy rains. While they provide valuable habitat and food for animals and microorganisms, invasive growth can threaten ecosystem health, and reduce accessibility and the aesthetic appearance of the waterbody (Bowden *et al.,* 2017).

Table 3.4 Classification of macrophytes

Classification	Example	Characteristic of plant
Emergent (rooted)	mangroves, rushes, reeds, seagrass, cumbungi, sedges, cattails	normally erect and standing above the water surface, but some species tolerate submergence; all produce aerial reproductive organs
Floating leaved (rooted)	waterliliy, alligator weed, nardoo	permanently submerged and produce floating leaves that differ in morphology from submerged leaves in still and slow-flowing water; produce floating or aerial reproductive organs
Submerged (rooted)	mosses, bladderwort, ribbonweed, sea tassel,arrowhead, water plantain	permanently submerged; produce floating, aerial, or submerged reproductive organs
Free-floating (not rooted)	duckweed, azolla, liverwort, salvinia	not attached to the substrate; produce floating, aerial, or very rarely submerged reproductive organs

Source: Bowden *et al.* (2017) Table 13.1; Aquatic Technologies: *https://aquatictechnologies.com.au/Free+Floating+Aquatic+Weeds+Australia*

3.3.4 Animals

Aquatic animal life forms are diverse, abundant, and exist at all water depths. Aquatic animals can be grouped into three broad categories:

- benthos—those animals that live on the seafloor. As well as microscopic organisms collectively called 'microphytobenthos', benthos include immobile sponges and corals, creeping crabs and snails, burrowing worms, crustaceans and bivalves, plus barnacles and sea squirts;
- nekton—swimming animals including fish, serpents, seals, dolphins, and whales; and
- plankton—minute animals called zooplankton, most of which do not have the ability to move themselves around so tend to drift and float with water movement.

3.4 Further Information

Marine Parks

Parks Australia: *https://parksaustralia.gov.au/marine/parks/*

Australian Marine Parks Science Atlas: *https://atlas.parksaustralia.gov.au/amps*

Marine Life

Phytoplankton: *https://earthobservatory.nasa.gov/Features/Phytoplankton*

Aquatic plants and algae: *https://manoa.hawaii.edu/exploringourfluidearth/biological/aquatic-plants-and-algae/what-are-aquatic-plants-and-algae*

Algae, Phytoplankton and Chlorophyll: *https://www.fondriest.com/environmental-measurements/parameters/water-quality/algae-phytoplankton-chlorophyll/*

Macroalgae: *https://thefishsite.com/articles/macroalgae-the-facts*

Aquatic Macrophytes: *https://environment.des.qld.gov.au/__data/assets/pdf_file/0027/90783/biological-assessment-background-to-aquatic-macrophytes-collecting-data-along-a-belt-transect.pdf*

Exploring our Fluid Earth: *https://manoa.hawaii.edu/exploringourfluidearth/*

Sea Ice Ecosystems: Thomas (2017)

Marine Food Webs

NZ Science Learning Hub: *https://www.sciencelearn.org.nz/resources/143-marine-food-webs*

Marine Habitats

National Intertidal Subtidal Benthic (NISB) Habitat Classification Scheme:

Mount and Bircher (2008a, 200b);

https://www.environment.gov.au/fed/catalog/search/resource/details.page?uuid=5c6b3f45-dfce-4859-9af3-08d175e24881

Blue Habitats: *http://www.bluehabitats.org*

Regional Aquatics Monitoring Program (RAMP): *http://www.ramp-alberta.org/RAMP.aspx*

Wetlands

https://wetlandinfo.des.qld.gov.au/wetlands/ecology/aquatic-ecosystems-natural/

https://www.environment.nsw.gov.au/topics/water/water-for-the-environment

Systems for Marine Biota

Census of Marine Life: *http://www.coml.org/*

This international projection records the diversity, distribution and abundance of life in the ocean, and spawned OBIS (see below).

Global Oean Observing System for Marine Life: *https://www.goosocean.org/*

Ocean Biogeographic Information System (OBIS): *http://www.iobis.org/about/*

OBIS is a global open-access data and information clearing-house on marine biodiversity for science, conservation and sustainable development.

Online Zoological Collections of Australian Museums (OZCAM): *https://www.ozcam.org.au/*

Australia's Marine Biodiversity Hub: *http://www.marinehub.org/index.php/site/home/*

CSIRO Atlas of Regional Seas (CARS)/Oceanographic database (CSIRO Marine and Atmospheric Research)

Australian Biological Resources Study (ABRS): Numbers of Living Species in Australia and the World (Chapman, 2006, 2009)

The Codes for Australian Aquatic Biota database maintained by CSIRO Marine and Atmospheric Research (*www.cmar.csiro.au/caab*)

The Australian Faunal Directory: *https://biodiversity.org.au/afd/home*

NIMPIS (National Introduced Marine Pest Information System—part of the National System for the Prevention and Management of Marine Pest Incursions (Sliwa *et al.*, 2009)

3.5 References

Arthington, A.H. (2012). *Environmental flows: saving rivers in the third millennium*. Vol 4. University of California Press, Berkley.

Bino, G., Kingsford, R.T., and Porter, J. (2015). Prioritizing Wetlands for Waterbirds in a Boom and Bust System: Waterbird Refugia and Breeding in the Murray-Darling Basin. *PLoS ONE*, 10(7), e0132682. doi:10.1371/journal.pone.0132682

Biocyclopedia (2019). *How Algae Move* webpage: *https://biocyclopedia.com/index/algae/anatomy/how_algae_move.php*

Bowden, W.B., Glime, J.M., and Riis, T. (2017). Macrophytes and Bryophytes. Ch 13 in *Methods in Stream Ecology (Vol. 1)* 3rd *edn*. Elsevier Inc. pp. 243–271. *http://dx.doi.org/10.1016/B978-0-12-416558-8.00013-5*

Brandis, K.J., Kingsford, R.T., Ren, S., and Ramp, D. (2011). Crisis Water Management and Ibis Breeding at Narran Lakes in Arid Australia. *Environmental Management*, 48, 489–498.

Bunn, S.E., and Arthington, A.H. (2002). Basic principles and ecological consequences of altered flow regimes for aquatic biodiversity. *Environmental Management*, 30, 492–507.

Bunn, S.E., Thoms, M.C., Hamilton, S.K., and Capon, S.J. (2006). Flow variability in dryland rivers: boom, bust and the bits in between. *River Research and Applications*, 22, 179–186.

Casanova, M.T. (2011). Using water plant functional groups to investigate environmental water requirements. *Freshwater Biology*, 56, 2637–2652.

Chapman, A.D. (2006). Numbers of living species in Australia and the world. *Australian Biological Resources Study*. Canberra. 60 p.

Chapman, A.D. (2009). *Numbers of living species in Australia and the world*. 2nd edn. Australian Biological Resources Study, Canberra. 80 p. *http://www.environment.gov.au/biodiversity/abrs/publications/other/species-numbers/2009/index.html*.

DAWE (2015). *National Intertidal Subtidal Benthic (NISB) Habitat Classification Scheme* webpage, Department of Agriculture, Water and the Environment website: *https://www.environment.gov.au/fed/catalog/search/resource/details.page?uuid=5c6b3f45-dfce-4859-9af3-08d175e24881*

Diaz-Pulido, G., and McCook, L.J. (2008). Macroalgae (Seaweeds). In *The State of the Reef Report. Environmental Status of the Great Barrier Reef*. (Ed: Chin, A.). Great Barrier Reef Marine Park Authority, Townsville. ISBN: 1 876945 34 6 *http://www.gbrmpa.gov.au/__data/assets/pdf_file/0019/3970/SORR_Macroalgae.pdf*

DPIE (2020). *Long-term Water Plans for nine river catchments in NSW* webpage, NSW Government Department of Planning, Industry and Environment website: *https://www.environment.nsw.gov.au/topics/water/water-for-the-environment/planning-and-reporting/long-term-water-plans*

DWER (2021). *Aquatic and riparian vegetation* webpage, WA Department of Water and Environmental Regulation website: *https://www.water.wa.gov.au/water-topics/waterways/values-of-our-waterways/aquatic-and-riparian-vegetation*

Entwisle, T.J., Sonneman, J.A., and Lewis, S.H. (1997). *Freshwater algae in Australia. A guide to conspicuous genera*. Sainty and Associates, Sydney. ISBN 0646314084.

Falkowski, P.G. (1994). The role of phytoplankton photosynthesis in global biogeochemical cycles. *Photosynthesis Research*, 39(3), 235–258. doi:10.1007/BF00014586

Francis, C., and Sheldon, F. (2002). River Red Gum (*Eucalyptus camaldulensis* Dehnh.) organic matter as a carbon source in the Lower Darling River, Australia. *Hydrobiologia*, 481, 113–124.

Freestone, F. L., Brown, P., Campbell, C.J., Wood, D.B., Nielsen, D.L., and Henderson, M.W. (2017). Return of the lignum dead: Resilience of an arid floodplain shrub to drought. *Journal of Arid Environments*, 138, 9–17.

Gecheva, G., and Yurukova, L. (2014). Water pollutant monitoring with aquatic bryophytes: a review *Environmental Chemistry Letters*, 12, 49–61.

Gerecht, A.C., Šupraha, L., Edvardsen, B., Probert, I., and Henderiks, J. (2014). High temperature decreases the PIC / POC ratio and increases phosphorus requirements in Coccolithus pelagicus (Haptophyta). *Biogeosciences*, 11, 3531–3545. *https://doi.org/10.5194/bg-11-3531-2014*

Huisman, J. (2000). *Marine Plants of Australia*. University of Western Australia Press/Australian Biological Resources Study.

Jeffrey, S.W., and Vesk, M. (1997). Introduction to marine phytoplankton and their pigment signatures. Ch 2 in *Phytoplankton pigments in oceanography: guidelines to modern methods*. (Eds: Jeffrey, S.W., Mantoura, R.F.C., and Wright, S.W.) UNESCO, Paris.

Kalff, J. (2002). *Limnology: inland water ecosystems*. Prentice Hall, New Jersey.

Kingsford, R. (2000). Ecological impacts of dams, water diversions and river management on floodplain wetlands in Australia. *Austral Ecology*, 25, 109–127.

Kingsford, R., and Thomas, R. (1995). The Macquarie Marshes in Arid Australia and Their Waterbirds: A 50- Year History of Decline. *Environmental Management*, 19, 867–878.

Kingsford, R.T., and Johnson, W.J. (1998). The impact of water diversions on colonially nesting waterbirds in the Macquarie Marshes in arid Australia. *Colonial Waterbirds*, 21, 159–170.

Kingsford, R.T., Curtin, A.L., and Porter, J.L. (1999). Water flows on Cooper Creek in arid Australia determine 'boom' and 'bust' periods for waterbirds. *Biological Conservation*, 88, 231–248.

Kingsford, R.T., Roshier, D.A., and Porter, J.L. (2010). Australian waterbirds - time and space travellers in dynamic desert landscapes. *Marine and Freshwater Research*, 61, 875–884.

Kingsford, R.T., MacNally, R., King, A., Walker, K.F., Bino, G., Thompson, R., Wassens, S., and Humphries, P. (2015). A commentary on 'Long-term ecological trends of flow-dependent ecosystems in a major regulated river basin', by Matthew J. Colloff, Peter Caley, Neil Saintilan, Carmel A. Pollino and Neville D. Crossman. *Marine and Freshwater Research*, 66, 970–980.

Likens, G.E., Walker, K.F., Davies, P.E., Brookes, J., Olley, J., Young, W.J., Thoms, M.C., Lake, P. S., Gawne, B., Davis, J., Arthington, A.H., Thompson, R., and Oliver, L. (2009). Ecosystem science: toward a new paradigm for managing Australia's inland aquatic ecosystems. *Marine and Freshwater Research*, 60, 271–279. *https://doi.org/10.1071/MF08188*

Lintermans, M. (2007). *Fishes of the Murray-Darling Basin: An introductory guide*. MDBC Publication No. 10/07. MDBA, Canberra.

MacIntyre, H L., Geider, R.J., and Miller, D.C. (1996). Microphytobenthos: the ecological role of the Secret Garden of unvegetated, shallow-water marine habitats. 1. Distribution, abundance and primary production. *Estuaries*, 19(2A), 186–201.

Mann, D.G. (1999). The species concept in diatoms. *Phycologia*, 38, 437–495.

Mount, R.E., and Bricher, P.J. (2008a). *Estuarine, Coastal and Marine (ECM) National Habitat Map Series User Guide Version 1 February 2008*. Spatial Science Group, School of Geography and Environmental Studies, University of Tasmania. Report to the Department of Climate Change and the National Land and Water Resources Audit, Canberra, ACT.

Mount, R.E., and Bricher, P.J. (2008b). *Estuarine, Coastal and Marine (ECM) National Habitat Map Series Project Report February 2008*. Spatial Science Group, School of Geography and Environmental Studies, University of Tasmania. Report to the Department of Climate Change and the National Land and Water Resources Audit, Canberra, ACT.

Nabout, J.C., da Silva Rocha, B., Carneiro, F.M., and Sant'Anna, C.L. (2013). How many species of Cyanobacteria are there? Using a discovery curve to predict the species number. B*iodiversity and Conservation*, 22, 2907–2918. *https://doi.org/10.1007/s10531-013-0561-x*

OEH (2012). *Macquarie Marshes Ramsar Site—Ecological character description Macquarie Marshes Nature Reserve and U-block components*. Office of Environment and Heritage, Sydney.

Ocock, J., Kingsford, R.T., Penman, T.D., and Rowley, J.J.L. (2016). Amphibian abundance and detection trends during a large flood in a semi-arid floodplain wetland. *Herpetological Conservation and Biology*, 11, 408–425

OzCoasts (2018). *OzCoasts Australian Online Coastal Information* website: *https://ozcoasts.org.au/*

Pittock, J., Finlayson, M., Arthington, A. H., Roux, D., Matthews, J. H., Biggs, H., Harrison, I., Blom, E., Flitcroft, R., Froend, R., Hermoso, V., Junk, W., Kumar, R., Linke, S., Nel, J., Nunes da Cunha, C., Pattnaik, A., Pollard, S., Rast, W., Thieme, M., Turak, E., Turpie, J., van Niekerk, L., Willems, D., and Viers, J. (2015) Managing freshwater, river, wetland and estuarine protected areas. In *Protected Area Governance and Management*. (Eds: G. L. Worboys, M. Lockwood, A. Kothari, S. Feary and I. Pulsford) pp. 569–608. ANU Press, Canberra.

Poff, N., Allan, J., Bain, M., Karr, J., Prestegaard, K., Richter, B., Sparks, R., and Stromberg, J. (1997). The natural flow regime. *BioScience*, 47, 769–784.

QDES (2013). *Wetland (aquatic ecosystem) types* webpage, Wetland Info website, Queensland Department of Environment and Science: *https://wetlandinfo.des.qld.gov.au/wetlands/ecology/aquatic-ecosystems-natural/*

Riches, M., Gilligan, D., Danaher, K., and Pursey, J. (2016). *Fish communities and threatened species distributions of NSW*. NSW Department of Primary Industries, Tamworth. *https://www.dpi.nsw.gov.au/__data/assets/pdf_file/0007/669589/fish-communities-and-threatened-species-distributions-of-nsw.pdf*

Roberts, J., and Marston, F. (2011). *Water regime for wetland and floodplain plants. A source book for the Murray-Darling Basin*. National Water Commission, Canberra.

Roberts, J., Colloff, M., and Doody, T. (2016). Riverine vegetation of inland south-eastern Australia. In *Vegetation of Australian Riverine Landscapes. Biology, ecology and management*. (Eds: Capon, S., James, C., and Reid, M.) CSIRO Publishing. Clayton South, Australia

Semeniuk, C.A., and Semeniuk, V. (2011). A comprehensive classification of inland wetlands of Western Australia using the geomorphic-hydrologic approach. *Journal of the Royal Society of Western Australia*, 94, 449–464

Sliwa, C., Migus, S., McEnnulty, F., and Hayes, K.R. (2009). Marine bioinvasions in Australia. Ch 25 in *Biological invasions in marine systems*. (Eds: Rilov, G., Crooks, J.A.) Ecological Studies 204. Berlin, Heidelberg: Springer-Verlag. pp 425–437.

Sournia, A., Chrdtiennot-Dinet, M.-J., and Ricard, M. (1991). Marine phytoplankton: how many species in the world ocean? *Journal of Plankton Research*, 13, 1093–1099.

Spencer, J.A., Heagney, E.C., and Porter, J.L. (2010). *Final report on the Gwydir waterbird and fish habitat study. NSW Wetland Recovery Program*. Rivers and Wetlands Unit, Department of Environment, Climate Change and Water NSW.

Suttle, C.A. (2005). Viruses in the sea. *Nature*, 437, 356–361.

Swirepik, J.L., Burns, I.C., Dyer, F.J., Neave, I.A., O'Brien, M.G., Pryde, G.M., and Thompson, R.M. (2016). Establishing Environmental Water Requirements for the Murray–Darling Basin, Australia's Largest Developed River System. *River Research and Applications*, 32, 1153–1165.

Thomas, D.N. (Ed.) (2017). *Sea Ice*, 3rd edn. Wiley-Blackwell, New York (USA) and Oxford (UK). ISBN: 978-1-118-77838-8 664 pp.

Thomas, R.F., Kingsford, R.T., Lu, Y., Cox, S.J., Sims, N.C., and Hunter, S.J. (2015). Mapping inundation in the heterogeneous floodplain wetlands of the Macquarie Marshes, using Landsat Thematic Mapper. *Journal of Hydrology*, 524, 194–213.

Thoms, M., and Parsons, M. (2016). The physical template of Australia's floodplain landscapes. In *Vegetation of Australian Riverine Landscapes. Biology, ecology and management*. (Eds: Capon, S., James, C., and Reid, M.) CSIRO Publishing, Clayton South, Australia.

Thoms, M., Parsons, M., and Southwell, M. (2016). The physical template of Australia's rivers. In *Vegetation of Australian Riverine Landscapes. Biology, ecology and management*. (Eds: Capon, S., James, C., and Reid, M.) CSIRO Publishing, Clayton South, Australia.

Tockner, K., and Stanford, J.A. (2002). Riverine flood plains: present state and future trends. *Environmental Conservation*, 29(3), 308–330.

van Dijk, A.I.J.M., Beck, H.E., Crosbie, R.S., de Jeu, R.A.M., Liu, Y.Y. Podger, G.M., Timbal, B., and Viney, N.R. (2013). The Millennium Drought in southeast Australia (2001–2009): Natural and human causes and implications for water resources, ecosystems, economy, and society. *Water Resources Research*, 49, 1040–1057.

Vince, J., Smith, A.D.M., Sainsbury, K.J., Cresswell, I.D., Smith, D.C., and Haward, M. (2015). Australia's Ocean Policy: Past, present and future. *Marine Policy*, 57, 1–8. *https://doi.org/10.1016/j.marpol.2015.02.014*

Walker, K.F., Sheldon, F., and Puckridge, J.T. (1995). An ecological perspective on large dryland rivers. *Regulated Rivers: Research and Management*, 11, 85–104.

Ward, J.V., Tockner, K., Arscott, D.B., and Claret, C. (2002). Riverine landscape diversity. *Freshwater Biology*, 47, 517–539.

Wassens, S., and Maher, M. (2011). River regulation influences the composition and distribution of inland frog communities. *River Research and Applications*, 27(2), 238–246

WaterNSW (2021). *Riparian Zones* webpage, Water NSW website: *https://www.waternsw.com.au/water-quality/catchment/living/managing-land/riparian*

Weinbauer, M.G., and Rassoulzadegan, F. (2004). Are viruses driving microbial diversification and diversity? *Environmental Microbiol*ogy, 6, 1–11.

Wilhelm, S.W., and Suttle, C.A. (1999). Viruses and nutrient cycles in the sea. *Bioscience*, 49, 781–788.

Measureable Properties of Surface Waters



The three major categories of waterbodies (inland, coastal, and ocean) share a number of measurable properties (see Section 1.2), such as the waterbody size, surface, water column, substratum, or history. For example, some properties of the water column that can be measured in relative or precise terms include depth, temperature, transparency, and composition (chemical and/or biological). In addition to these properties of the water itself, waterbodies can vary in terms of their substratum characteristics, emergent vegetation, and the dynamics of the water surface.

The following sections introduce the variations that can occur in, and the measurement methods used for, these generic characteristics of waterbodies:

- water surface attributes—level, shape, texture, surface tension, surface temperature, floating layers, and ice cover (see Section 4);
- water column attributes—physical, chemical and biological (see Section 5);
- water substratum attributes—waterbody depth, geomorphology, composition, and benthos (see Section 6); and
- waterbody attributes—observed colour, extent and permanence, waterbody depth, carbon cycling, and dynamics (see Section 7).

Contents

4 Attributes of Water Surface 67

5 Attributes of Water Column 77

6 Attributes of Substratum 99

7 Attributes of Waterbodies 105

Background image on previous page: Sentinel-2 true colour composite image acquired on 10 February 2019 showing muddy floodwaters from the Burdekin River entering the Coral Sea, off the northern Queensland coast, potentially impacting the Great Barrier Reef. **Source:** ESA (CC-BY-SA 3.0). Retrieved from *http://www.esa.int/ESA_Multimedia/Images/2019/04/Queensland_floods*



4 Attributes of Water Surface

The most visible feature of a waterbody—from land, air, or space—is its surface layer. If the water surface is essentially transparent, features of the water column may also be visible and, for shallow waterbodies, it may also be possible to discern attributes of the substratum.

Characteristics of the water surface can both inform and belie characteristics of the waterbody. The interaction between incident radiation and the water surface is particularly important for EO of surface waters that are not covered by ice. Unlike the reflectance from terrestrial surfaces, the radiation reflected from a water surface is generally considered as 'noise', with the useful information originating below the surface. In some studies, waves or currents 'visible' on or below the water surface are used to infer water dynamics or locate floating objects (see Sections 1.4, 4.3, and 16). Typically, however, direct solar reflectance from the water surface, such as sunglint, is best avoided for optical EO of surface waters, which can be achieved by selecting imagery with appropriate illumination and sensor geometry (see Volume 1B—Section 3.5 and 2A—Section 3.2.1).

Water surfaces can vary in terms of:

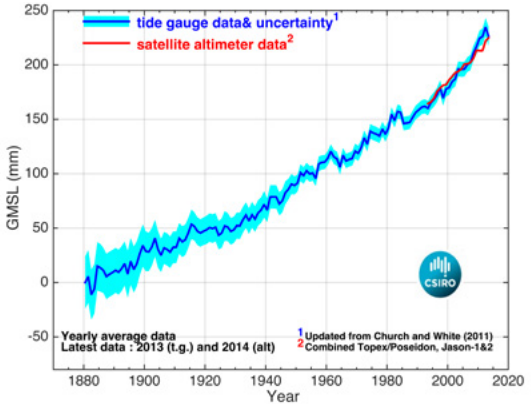
- level (see Section 4.1);
- shape (see Section 4.2);
- texture (see Section 4.3);
- surface tension (see Section 4.4);
- temperature (see Section 4.5);
- floating layers (see Section 4.6); and
- ice cover (see Section 4.7).

4.1 Level

Sea level varies both in space and time, due to a range of factors including tides, waves, storm surges, and tectonic activity. Other sources of sea level variation include extraction of groundwater, seepage into aquifers, construction of reservoirs that reduce surface runoff, changes in water temperature, and melting of glaciers and ice sheets (see Sections 12.3 and 15). Sea level is also known to cycle with the seasons (see Section 12.3.2).

Traditionally the tidal datum called mean sea level (MSL) was defined as "the arithmetic mean of hourly heights of the sea at the tidal station observed over a period of time (preferably 19 years)" (AHO, 2020). Historically MSL was used as a standard geodetic reference point, from which other elevations and water depths were measured. Since space-based geodetic methods have become available (see Volume 1A—Section 3.3), the topography of our planet—including sea surface topography—has been measured and monitored more accurately and consistently, both spatially and temporally.

Figure 4.1 Global-mean sea level (GMSL) estimates

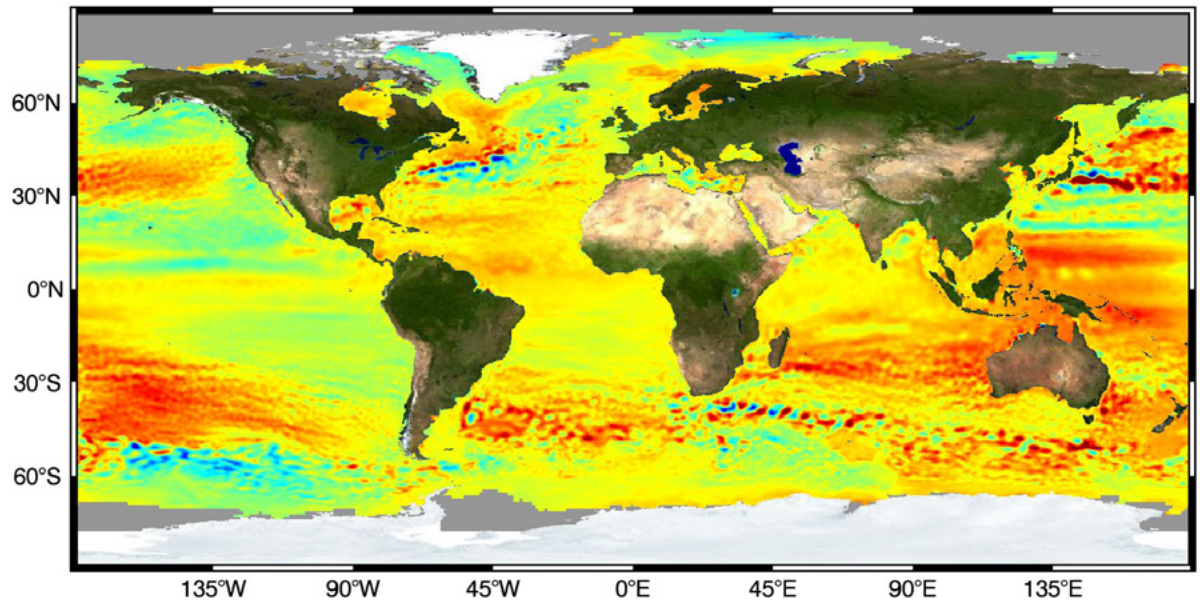


Source: Church and White (2011). Retrieved from: *https://research.csiro.au/slrwavescoast/sea-level/measurements-and-data/sea-level-data/*

Background image: An artifical inlet called the Dawesville channel, WA, links the rough water of Indian Ocean (left) to the smooth surface of the Peel-Harvey estuary (right). The difference between these water surfaces is varying Fresnel reflectance (see Section 8.1.3) of sunglint and skyglint due to ocean swell. This pseudo true colour composite image was acquired on 23 December 2014. Source: Planet Labs Inc. (CC-BY-SA 4.0). Retrieved from *https://www.planet.com/gallery/#!/post/dawesville-channel*

Figure 4.2 Change in sea surface topography 1993–2019

Colour spectrum ranges from sea surface height changes of -10 mm/yr (blue) to 10 mm/yr (red).



Source: NASA. Retrieved from: *https://sealevel.nasa.gov/internal_resources/185*

Traditional estimates of changes in sea level with respect to a defined datum have relied on long term averages of tide gauge measurements (see Section 12.4.2) and, in some cases, the midpoint between the mean high and low tide marks was used as a surrogate. These estimates were necessarily localised and sparse, therefore difficult to interpolate over large areas, or track with certainty through time.

The global perspective of EO sensors now allows variations in the sea surface topography to be analysed for the whole planet and compared over time. In particular, as described in Sections 9.5 and 12, satellite altimetry provides valuable data for estimating the average height of the entire ocean surface, or global-mean sea level (GMSL; see Figure 4.1).

Analyses of sea level records indicate that GMSL has been rising globally for several centuries, and predictions suggest that this trend is likely to continue and possibly accelerate (see Sections 12.5 and 12.6). For example, between 1880 and 2014, GMSL increased by 230 mm (Church and White, 2011; see Figure 4.1). The natural consequences of this trend include flooding of low-lying land and a reduction in land area, most significantly on islands (Nicholls and Lowe, 2006). In the last few decades, satellite altimetry has enabled global monitoring of sea surface height, or mean dynamic topography (see Figure 4.2). The use of EO datasets acquired by microwave sensors to map and monitor sea level is further discussed in Section 12.

4.2 Shape

Being a fluid, the shape of a water surface can vary considerably with forces within, on, above, or below the water column. There are several types of movement that can change the surface shape of natural waterbodies, including:

- tides—underlying surface rhythms for marine waters resulting from the gravitational forces of the Moon and the Sun, combined with the rotation of the Earth, that cause sea level to rise and fall (see Excursus 4.1);
- waves—generated either by water molecules on the surface being dragged along by air molecules in atmospheric winds, or by seismic activity (see Excursus 4.2);
- ripples, or capillary waves, result from some external body or pressure impacting the surface (these are quickly corrected by surface tension when the external influence is removed; see Excursus 4.2);
- internal waves—subsurface movement between layers in the water column with differing densities;
- flow—the effect of gravity on water encouraging downhill movement in rivers and streams; and
- wake—trail of recirculating water that has been impacted by a moving or stationary body.

The shape of a water surface is rarely static and can strongly influence its texture and observed colour. Resonances within partially or fully bounded waterbodies can result in oscillating standing waves called seiches. These oscillations literally cause the water to 'sway back and forth' between shores creating short term variations in water levels that can last for days, gradually diminishing back to equilibrium. Seiches typically result from atmospheric disturbances, but can also be related to seismic activity (USGS, 2018).

Excursus 4.1—Astronomical Tides

Further Information: NOAA: *https://oceanservice.noaa.gov/education/tutorial_tides/*

Ocean tides are the response of Earth's waters to the gravitational forces exerted by the Moon and the Sun. Although the Sun is 27 times larger than the Moon, it is significantly further away from Earth, which reduces its tide-generating force to 46% of the Moon's (NOAA, 2018). Since proximity matters to gravitational forces, when the Moon is closer to one side of the Earth, its pull has more impact on water on that side of the planet, creating a surface 'bulge'. On the opposite side of Earth, however, inertia creates a counter-bulge (Ross, 1995). Elsewhere, the Moon's gravitational force is balanced by inertial forces (see Figure 4.3). These tidal bulges follow the position of the Moon relative to the equator, allowing highest tides to occur at different latitudes.

During the lunar cycle, the gravitational forces of our Moon and the Sun either work together to create spring tides (at new moon or full moon) or against each other to form neap tides (at first and third quarter moons; see Figure 4.4). The balance of these forces changes gradually between two spring tides and two neap tides within each lunar cycle (see Figure 4.5).

Figure 4.3 Tidal forces due to the Moon

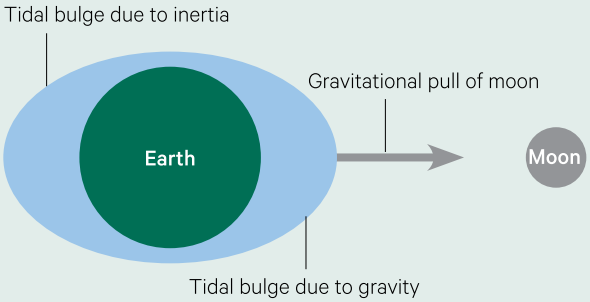
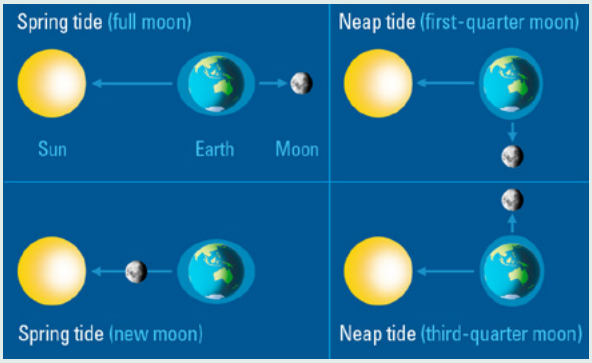
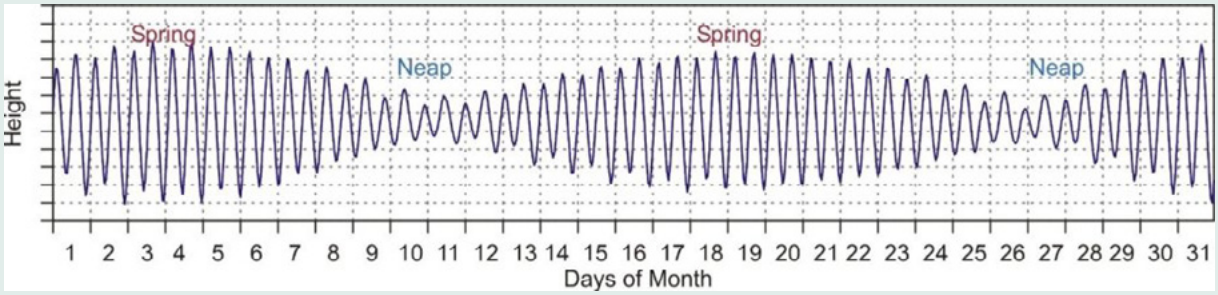


Figure 4.4 Spring and neap tides



Source: COSPPar (2014)

Figure 4.5 Lunar cycle of tides

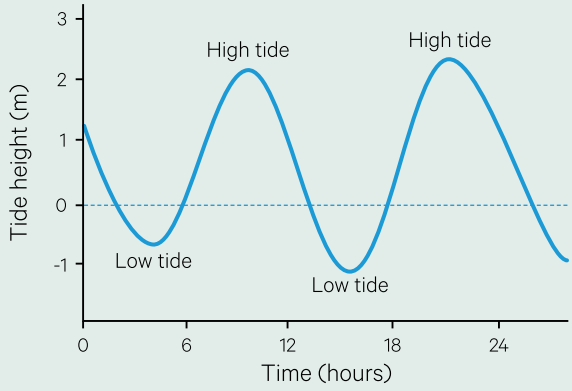


Source: CSIRO. Retrieved from: *https://research.csiro.au/slrwavescoast/extremes/causes-extreme-sea-levels/*

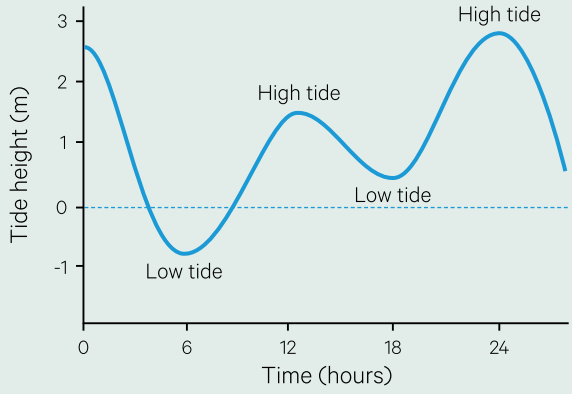
Tide: 1. The periodic rise and fall of the water of oceans, seas, bays, etc., caused mainly by the gravitational interactions between the Earth, Moon and Sun. (Australian Hydrographic Office Glossary)
2. A tide is a distortion in the shape of one body induced by the gravitational pull of another nearby object. (Morrison and Owen, 1996)

Figure 4.6 Types of tides

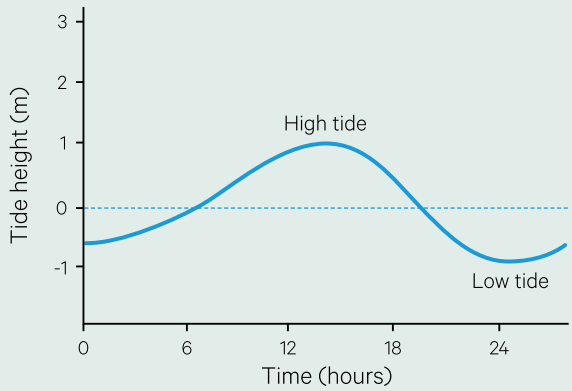
a. Semidiurnal



b. Mixed semidiurnal



c. Diurnal



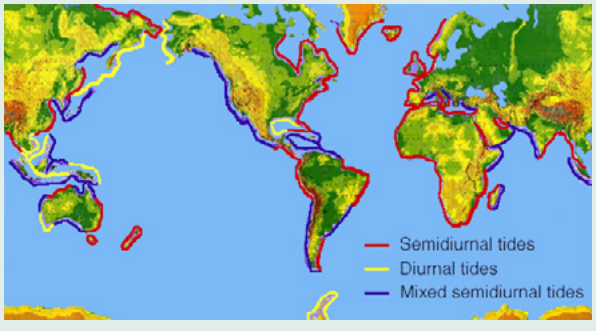
Without any topography on the Earth's surface, all locations across the globe would experience two equivalent high and low tides each lunar day. Instead, larger continents obstruct the flow of tidal bulges from west to east with Earth's rotation, resulting in complex patterns of tidal movement within each ocean basin. Accordingly, depending on the proximity of a shoreline to open ocean waters, three basic tidal patterns may be observed at a given location during each lunar day (see Figure 4.7):

- semidiurnal—the most common pattern of two high tides and two low tides of similar height;
- mixed semidiurnal—two pairs of high and low tides with different heights; or
- diurnal—only one high tide and one low tide (see Figure 4.6).

The global distribution of these three tidal patterns is illustrated in Figure 4.7.

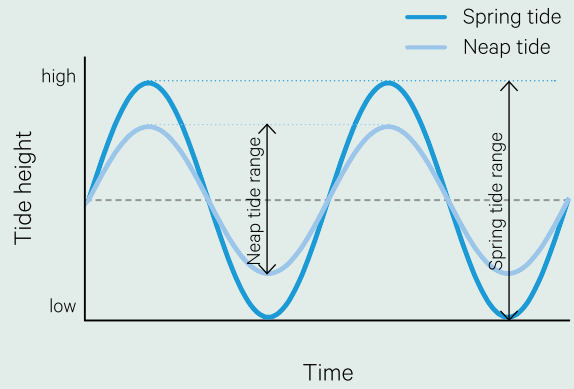
The term tidal range is used to define the difference between high and low tide heights (see Figure 4.8), which can vary from a few centimetres in deep ocean to several metres in coastal areas (CSIRO, 2018). Tide height can also be modified by the shape and geomorphology of coastlines, bays and estuaries, tidal rivers, and local weather patterns. Since the boundary between sea and land varies with the tides, the line corresponding to the lowest astronomical tide (LAT; or, more colloquially, low tide mark) is used to define the shoreline.

Figure 4.7 Global distribution of tide cycles



Source: NOAA (see Section 4.8)

Figure 4.8 Tidal range



Tidal currents and tidal height are both manifestations of tides. A tidal current is said to flow (or flood), as it moves towards the high tide mark, and ebb, as it recedes to the low tide mark. Tidal currents are most noticeable when water has to flow through restrictions, as occur at the edge of the continental shelf or in passageways into bays.

Attributes of Australian tides are monitored by the National Operations Centre (NOC) Tidal Unit (see Excursus 12.2).

4.3 Texture

Water texture changes the way light is reflected from the surface. This can result in sunglint when the angle at which sunlight is reflected from the water surface is the same as the angle used to view the surface (see banner image for Section 4). Sunglint causes the water surface to appear as a mirror (bright silver, see Section 7.1). Skyglint is also reflected from the surface, but as it is mostly diffuse downwelling irradiance, the resulting surface reflectance is also diffuse. It is still affected by the angles of the water surface (due to swell, waves, and wavelets) to the incident irradiance field (as illustrated in the Section 4 banner image of the Peel-Harvey inlet on page 67.

Table 4.1 Beaufort scale

Beaufort number	Descriptive term	Wind speed (km/hr)	Description on sea	Description land
0	Calm	0	Sea surface like a mirror	Smoke rises vertically
1	Light winds	1–5	Small wavelets, ripples formed but do not break; glassy appearance maintained	Wind felt on face: leaves rustle; ordinary vanes moved by wind
2		6–11		
3		12-19		
4	Moderate winds	20–29	Small waves, becoming longer; fairly frequent white horses	Raises dust and loose paper; small branches are moved
5	Fresh winds	30–39	Moderate waves, taking a more pronounced form: many white horse are formed—chance of spray	Small trees in leaf begin to sway; crested wavelets form on inland waters
6	Strong winds	40–50	Large waves begin to form; the white foam crests are more extensive with probably some spray	Large branches in motion; whistling heard in telephone wires; umbrellas used with difficulty.
7	Near gale	51–62	Sea heaps up and white foam from breaking waves begins to be blown in streaks along direction of wind.	Whole trees in motion; inconvenience felt when walking against wind.
8	Gale	63–75	Moderately high waves of greater length; edges of crests begin to break into spindrift; foam is blown in well-marked streaks along the direction of the wind.	Twigs break off trees; progress generally impeded.
9	Strong gale	76–87	High waves; dense streaks of foam; crests of waves begin to topple, tumble and roll over; spray may affect visibility.	Slight structural damage occurs, roofing dislodged; larger branches break off.
10	Storm	88–102	Very high waves with long overhanging crests; the resulting foam in great patches is blown in dense white streaks; the surface of the sea takes on a white appearance; the tumbling of the sea becomes heavy with visibility affected.	Seldom experienced inland; trees uprooted; considerable structural damage.
11	Violent storm	103–117	Exceptionally high waves; small and medium sized ships occasionally lost from view behind waves; the sea is completely covered with long white patches of foam; the edges of wave crests are blown into froth.	Very rarely experienced - widespread damage
12	Hurricane	>118	The air is filled with foam and spray. Sea completely white with driving spray; visibility very seriously affected	Very rarely experienced - widespread damage

Source: BoM (2018b); MetOffice (2018)

The texture or roughness on the surface of a waterbody can be created by waves (see Excursus 4.2), currents, and tides (see Excursus 4.1), as well as the movement of water vehicles and recreational water users. As waves travel, refract, and break, both their texture and observed colour changes. The spatial scale of surface texture will vary with many factors, including wave height and velocity, water composition, and temperature and atmospheric influences.

Traditionally, mariners used observations of water surface roughness to estimate wind speed. Various qualitative scales were devised for this purpose until the Beaufort scale was adopted as the official, if somewhat subjective, gauge in the early 1800s. Modern versions of this scale indicate wind speed for 12 categories of surface texture (see Table 4.1). By contrast, the Douglas scale that was adopted by WMO describes wave height (see Table 4.3). More recently, however, WMO advocates the use of instruments such as wave buoys and anemometers to directly quantify wind characteristics (WMO, 2018). EO technologies that can be used to map and monitor wave activity are detailed in Section 16.

Excursus 4.2—Water Waves

Wave: 1. A periodic disturbance which moves through or over the surface of the medium (eg. water) with speed dependent upon the properties of the medium. It is characterised by frequency, length, and amplitude. 2. A ridge-like deformation, or undulation of a liquid or solid surface. (Australian Hydrographic Office Glossary)

Wind blowing over a water surface creates waves. While the wave moves horizontally, the water in the wave does not move with the wave—it just oscillates in a vertical, circular pattern. A wave 'breaks' when its base is unable to support its top, as frequently occurs in shallow water along shorelines, or when two waves collide.

Figure 4.9 Water wave

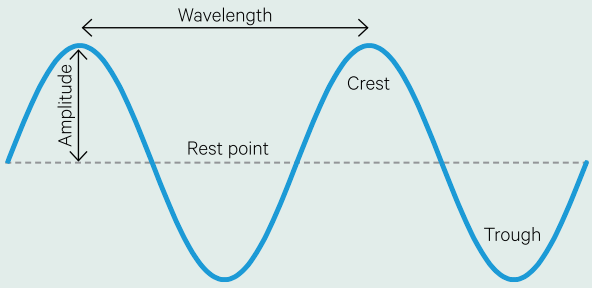
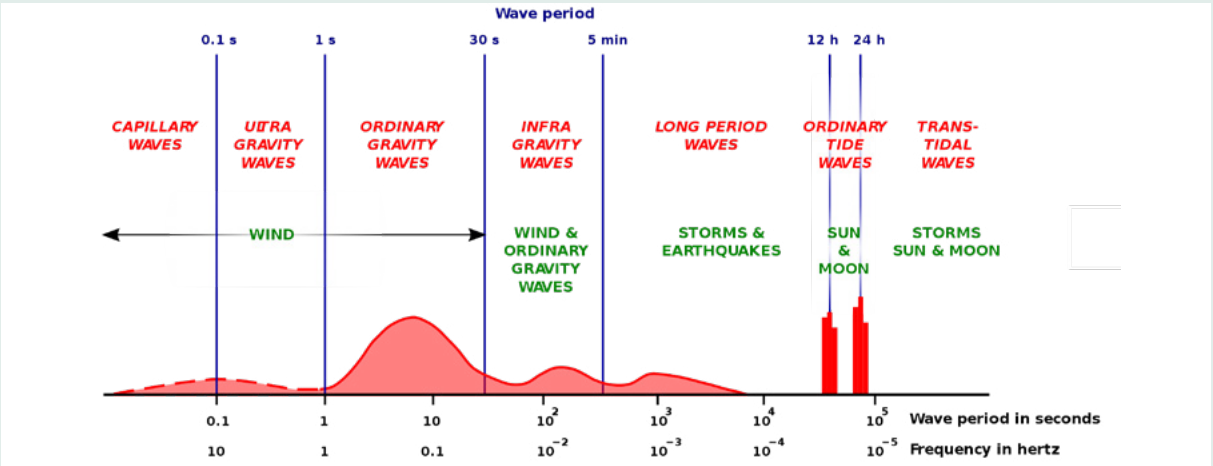


Figure 4.10 Energy spectrum of ocean waves



Adapted from: Munk (1950) Figure 1. Retrieved from *https://commons.wikimedia.org/wiki/File:Munk_ICCE_1950_Fig1.svg*

Table 4.2 Categories of waves

Name	Wave length (m)	Wave period (sec)	Wave phase velocity (m/sec)	Description
Capillary wave	< 0.0173	0.1	> 0.023	Ripples generated by gusts and dissipated by gravity and surface tension in less than 30 seconds by viscosity.
Wind wave	1.6–39	1–5	1.6–7.8	Generated by friction from surface winds and restored by gravity. Wave motion rapidly reduces with water depth.
Swell	156–624	10–20	15.6–31.2	Generated by turbulent surface winds and restored by gravity. Wave motion rapidly reduces with water depth.
Tsunami	200,000	1,000	200	Seismic waves have lower velocity but greater amplitude in shallow, coastal water. (Note: These figures apply to deep ocean water.)

Source: Wells (1986) Chapter 8

Wave height, the vertical distance from the wave crest to wave trough (twice the amplitude), varies with wind speed, duration, and fetch (or the distance it blows). While the wavelength is the horizontal distance between two successive crests or troughs (see Figure 4.9), the wave period is the time taken to travel one wavelength. The number of complete wave cycles in a given time unit is the wave frequency. A wave's energy or velocity is the product of its wavelength and frequency. These characteristics can be used to generate an energy spectrum for surface waves in the ocean (see Figure 4.10).

Wave characteristics are also used to classify various forms of water waves (see Table 4.2). Regular waves with longer periods are called swell waves, and result from distant weather systems (BOM, 2018a). Another type of water wave is a 'seiche', which is a standing wave that occurs in a confined space, such as an enclosed waterbody (see Section 4.2).

The term 'sea state' is used in oceanography to describe the condition of the surface of a waterbody. Sea state is determined qualitatively by observations of the surface conditions or quantified by measurements such as wave height and period. Wind waves and swell waves both contribute to sea state (BOM, 2018a). The combined effects of 'wind sea' (ten categories based on wave average height; see Table 4.3a) and swell (eight categories based on wave length, period and height; see Table 4.3b) were coded into the Douglas Scale, and adopted by the WMO.

Table 4.3 WMO Sea State tables for waves and swells

a. Ten categories based on wave height

Code	Description	Wave height (m)	Effect
0	Calm (glassy)	0	No waves breaking on beach
1	Calm (rippled)	0–0.1	No waves breaking on beach
2	Smooth	0.1–0.5	Slight waves breaking on beach
3	Slight	0.5–1.25	Waves rock buoys and small craft
4	Moderate	1.25–2.5	Sea becoming furrowed
5	Rough	2.5–4.0	Sea deeply furrowed
6	Very rough	4.0–6.0	Sea much disturbed with rollers having steep fronts
7	High	6.0–9.0	Sea much disturbed with rollers having steep fronts (damage to foreshore)
8	Very high	9.0–14.0	Towering seas
9	Phenomenal	> 14	Precipitous seas (experienced only in cyclones)

b. Eight categories based on wavelength, period and height

Description	Wave length (m)	Wave Period (sec)	Wave Height (m)
Low swell of short or average length	0–200	< 11	0–2
Long, low swell	> 200	>11	0–2
Short swell of moderate height	0–100	< 8	2–4
Average swell of moderate height	100–200	8–11	2–4
Long swell of moderate height	> 200	> 11	2–4
Short heavy swell	0–100	< 8	> 4
Average length heavy swell	100–200	8–11	> 4
Long heavy swell	> 200	> 11	> 4

Source: BoM (2018a)

4.4 Surface Tension

The intermolecular forces that hold a surface together are called surface tension. Such forces vary for different materials in different environments. The surface tension of water at 20°C is 72.8 mN/m. This is higher than most liquids and varies inversely with temperature.

The surface layer or skin of waterbodies, also known as the air-water interface, results from surface tension. This characteristic allows objects to float on the surface of fluids even when they are denser than the fluid itself. It also determines the shape of water droplets.

Pollutants, such as oil slicks and detergents, change the surface tension of water and impact its movement patterns and optical properties. Since capillary waves depend on surface tension, they are most impacted by surface films of oil and similar organic matter, and their absence can be indicative of these types of pollutants (see Section 19.4).

4.5 Temperature

Water temperature typically decreases with water depth (see Section 5.1.2). Near the water surface however, the water 'skin' experiences a miniscule region of slightly increased temperature (Donlon *et al.,* 2002; see Figure 14.4). The diurnal difference in skin temperature can vary between 0.6 K and 2.8 K (Zeng *et al.,* 1999; Heron *et al*., 2013).

Different wavelengths of electromagnetic radiation (EMR) penetrate the water surface to different water depths (see Section 5.1.4 and Volume 1B—Section 7). Thermal infrared (TIR) wavelengths only penetrate the upper 10 μm of the ocean (Sea Surface Temperature skin: SST skin), or the 'skin layer' (see Sections 5.1.3 and 14), whereas microwave sensors penetrate the upper 1 mm of the water column (SST subskin; see Section 9). Thus EO-based measurements from TIR sensors relate to the SST skin temperature, while measurements from microwave sensors represent the temperature at the lower boundary of the skin layer. Below the skin layer, temperatures vary with water column depth, and *in situ* measurements are required (and need to be recorded with the depth of acquisition; Heron *et al.,* 2013). Sea surface temperature is monitored operationally at regional and global scales using a range of EO datasets (see Section 14).

4.6 Floating Layers

The surface of a waterbody can support various types of material that float, such as algal blooms, seaweeds, sea ice, pollution, and flotsam (see Figure 1.13a). One growing source of floating matter in marine waterbodies globally is plastic debris (see Section 19.4.1). Floating layers can change the optical properties of the water surface (see Section 8.1.3) and may be indicative of local water circulation patterns (see Section 16).

The term 'algal bloom' describes a rapid increase in algae populations in freshwater or marine waters and are distinguished by discolouration of the water surface (see Section 19.5). Algal blooms occur as natural ecological responses to variations in ambient light, temperature, and nutrient levels in aquatic environments, and are most common in warm, calm, and stratified conditions in estuaries, and in coastal waters with high nutrient loads (OzCoasts, 2020).

These transient features manifest with differing speeds, extents, and intensities, depending on latitude, season, distance from shore, and the rate of grazing by zooplankton. They generally appear as coloured 'scum' on the surface of waterbodies (see Figure 4.11) but are not always visible. Some, but not all, algal blooms are harmful to other aquatic species and/or humans (see Section 19.5).

Figure 4.11 Algal bloom

An algal bloom was photographed on 10 February 2021 in the Murrray River, near its junction with the Darling River. This bloom in the foreground appears milky due to photo bleaching as it dies, in contrast with the clear water in the distance.



Source: Nathan Drayson, CSIRO

4.7 Ice cover

In polar regions, both landmasses and waterbodies may be covered with ice (and snow). Two main categories of surface ice can be defined in polar regions. These are:

- glacier ice, which accumulates (from snowfall and subsequent compaction) over a land mass and occurs in the extensive ice sheets in Antarctica and Greenland, the coastal margins of which can extend across the ocean in the form of floating glacier tongues and ice shelves; and
- sea ice, which is frozen seawater and occurs in the high-latitude waters of the Arctic region and the Southern Ocean around Antarctica (see Section 2.5. Note that sea ice also occurs in winter in certain lower-latitude regions, such as the Bohai Sea, Sea of Okhotsk, and the Baltic Sea).

While their ice-covered surfaces may appear to be similar, the formation and nature of ice in the Arctic region (around the North Pole) and the Antarctic region (around the South Pole) are quite different due to their different geographical settings and related formation and melt processes (for details see Massom, 2009). Antarctica is a frozen continent surrounded by a highly dynamic and stormy ocean, whereas the Arctic comprises a frozen ocean basin largely surrounded by land (NASA Earth Observatory, 2016).

Due to their high reflectance and strong insulative properties, the polar ice and snow masses substantially modify the surface radiation balance of ocean surface properties and the interaction of the ocean and its surface with the atmosphere. Moreover, the presence of a snow and ice surface significantly limits the input of solar radiation to heat the upper ocean, while sea ice formation and melt processes also modify the characteristics of the underlying ocean through injection of brine and freshwater respectively, and contribute in places to global ocean (thermohaline) circulation (see Section 5.1.2). As detailed in Section 15, EO has a crucially important role to play in the measurement and monitoring of polar snow and ice masses, which are vulnerable to climate change.

4.8 Further Information

Tides

NOAA: *https://oceanservice.noaa.gov/education/tutorial_tides/*

4.9 References

AHO (2020). *Tidal Glossary* webpage, Australian Hydrographic Office website: https://www.hydro.gov.au/prodserv/data/tides/tidal-glossary.htm

BOM (2018a). *Waves* webpage, Bureau of Meteorology website: *http://www.bom.gov.au/marine/knowledge-centre/reference/waves.shtml*

BOM (2018b). *Beaufort Wind Scale*, Bureau of Meteorology website glossary. *http://www.bom.gov.au/lam/glossary/beaufort.shtml*

Church, J.A. and White, N.J. (2011), Sea-level rise from the late 19th to the early 21st century. *Surveys in Geophysics*, 32, 585–602. doi:10.1007/s10712-011-9119-1.

COSPPar (2014). *Tides and extreme tide events* factsheet. Climate and Oceans Support Program in the Pacific, Commonwealth of Australia. *http://cosppac.bom.gov.au/assets/pdf/COSPPac-PSLM-Tide-Fact-Sheet.pdf*

CSIRO (2018). *Why Does Sea Level Change?* webpage, Sea Level Rise website: *https://www.cmar.csiro.au/sealevel/sl_drives_seas_dec.html*

Donlon, C.J., Minnett, P.J., Gentemann, C.L., Nightingale, T.J., Barton, I.J., Ward, B., Murry, M.J. (2002). Toward improved validation of satellite sea surface skin temperature measurements for climate research. *Journal of Climate,* 15(4), 353–369.

Heron, S.F., Heron, M.L., and Pichel, W.G. (2013). Thermal and Radar Overview. Ch 11 in *Coral Reef Remote Sensing*. (Eds: Goodman, J.A., Purkis, S.J., and Phinn, S.R.). Springer, Dordrecht. ISBN 978-90-481-9291-5.

MetOffice (2018). *Beaufort wind force scale* webpage, UK Meteorological Office website: *https://www.metoffice.gov.uk/guide/weather/marine/beaufort-scale*

Massom, R.A. (2009). Principal Uses of Remote Sensing in Sea-Ice Field Research. In *Handbook on Field Techniques in Sea-Ice Research* (Eds: H. Eicken *et al.,*). University of Alaska Press, Fairbanks, USA, pp. 405–466.

Morrison, D. and Owen, T. (1996). *The Planetary System*. Addison-Wesley. 570 p.

Munk, W.H. (1950). Origin and generation of waves. *Proceedings* 1st *International Conference on Coastal Engineering, Long Beach, California*. ASCE. pp. 1–4.

NASA Earth Observatory (2016). *Sea Ice* webpage, NASA Earth Observatory website: *https://earthobservatory.nasa.gov/features/SeaIce*

Nicholls, R.J. and Lowe, J.A. (2006). Climate stabilisation and impacts of sea level rise. In Avoiding Dangerous Climate Change (eds. H.J. Schellnhuber, W. Cramer, N. Nakicenovic, T.M.L. Wigley, and G. Yohe). Cambridge University Press, Cambridge. and Nicholls, R.J. and Tol, R.S.J. (2006). Impacts and responses to sealevel rise: a global analysis of the SRES scenarios over the twenty-first century. *Philosophical Transactions of the Royal Society, London A*, 364, 1073–1095.

NOAA (2018). *Tides and Water Levels* webpage, National Ocean Service website: https://oceanservice.noaa.gov/education/tutorial_tides/tides02_cause.html

OzCoasts (2020). *OzCoasts Australian Online Coastal Information (Geoscience Australia) website*: *http://www.ozcoasts.gov.au/index.jsp*

Ross, D.A. (1995). *Introduction to Oceanography*. HarperCollins, New York. pp. 236–242.

Wells, N. (1986). *The Atmosphere and Ocean. A Physical Introduction*. Taylor and Francis, London.

USGS (2018). *Seismic Seiches* webpage, United States Geological Survey website: *https://earthquake.usgs.gov/learn/topics/seiche.php*

WMO (2018). *Frequently Asked Questions* webpage, World Meteorological Organisation website. Marine Meteorology and Oceanography Programme: *http://www.wmo.int/pages/prog/amp/mmop/faq.html*

Zeng, X., Zhao, M., Dickinson, R.E., and He, Y. (1999). A multiyear hourly sea surface skin temperature data set derived from the TOGA TAO bulk temperature and wind speed over the tropical Pacific. *Journal of Geophysical Research,* 104, 1525–1536.



5 Attributes of Water Column

Water columns in surface waters can vary widely in terms of their physical (see Section 5.1), chemical (see Section 5.2), and biological (see Section 5.3) composition, both within and between waterbodies.

5.1 Physical

Physical characteristics of the water column that are relevant to EO studies include water depth (see Section 5.1.1), density and stratification (see Section 5.1.2), temperature (see Section 5.1.3), interactions with electromagnetic radiation (EMR; see Section 5.1.4), and transparency (see Section 5.1.5).

5.1.1 Water depth

When referencing waterbodies, depth can have two different meanings:

- the vertical distance between the water surface and the substrate—this is measured by bathymetric methods (see Section 13) and is referred to therein as the waterbody depth; and
- the vertical distance from the water surface within the waterbody—this is referenced therein as the water depth.

Bathymetry systematically measures waterbody depth to map the topography of submerged surfaces. Such measurements originally relied on sounding lines from ships or platforms, and now use various EO technologies, carried by ships, aircraft, or satellites, including:

- multispectral and hyperspectral sensors—infer waterbody depth in relatively shallow coastal and inland waters using light absorption properties (see Section 13.4.2, plus Volume 1);
- airborne bathymetric lidar—most cost-effective for surveying waterbody depth in small, relatively shallow areas with clear waters (see Section 13.4.1);
- satellite altimetry—sea surface mapping from satellite altimetry can be used to infer seafloor topography (see Section 13.3.1); and
- echosounders—single and multi-beam acoustic sensors for mapping waterbody depths in deep water (see Section 10.2).

Some measurable changes occur in the properties of water with increasing distance from the water surface. A region of water depth that involves rapid change in some property is referred to as a cline, such as temperature (thermocline), salinity (halocline), or density (pycnocline). Salinity and temperature gradients are further discussed in Sections 5.1.2 and 5.1.3). An array of autonomous *in situ* floating sensors routinely measure temperature, salinity, and other characteristics from the water surface to 2,000 m deep. This global operation of sensors is introduced in Excursus 5.1.

Background image: This photo shows the journey of Sun and skylight through the atmosphere, the air-water interface, and the water column to the benthos. Note the changes in colour and intensity from the sky to the bottom of the river. **Source**: Mel-nik, ©iStock photo ID 519368058

Excursus 5.1—Ocean Profile Sensors

Source: Mark Baird, CSIRO
Further information: Integrated Marine Observing System (IMOS) website: *https://imos.org.au/facilities/argofloats;* Volume 2D—Excursus 12.3; *http://biogeochemical-argo.org/*

Autonomous Underwater Vehicles (AUV), untethered and unmanned robotic platforms equipped with a range of sensors, are used to perform planned aquatic surveys (Monk *et al*., 2018). AUV either cruise along defined tracks at 2 m/sec or hover at precise locations and travel slowly (Huvenne *et al*., 2018) to acquire information about the water surface, water column, or substrate.

Every ten days nearly 4,000 profiling floats within the Argo network measure temperature and salinity around the globe, from the water surface down to water depths of 2000 m (see Figure 5.1). These autonomous sensors are cheap, reusable, and remotely-controlled, and can be equipped with a range of sensors to deliver ocean profile data in all weather conditions. Since 2003 these high resolution, hydrographic profiles have been instrumental in providing new information about the broad structure of our oceans. A new global network of biogeochemical sensors on Argo profiling floats is currently being developed by an international consortium called Biogeochemical-Argo to monitor a range of parameters related to nutrient and carbon cycling (see Section 1.5).

The operational cycle of an Argo float for one profile involves:

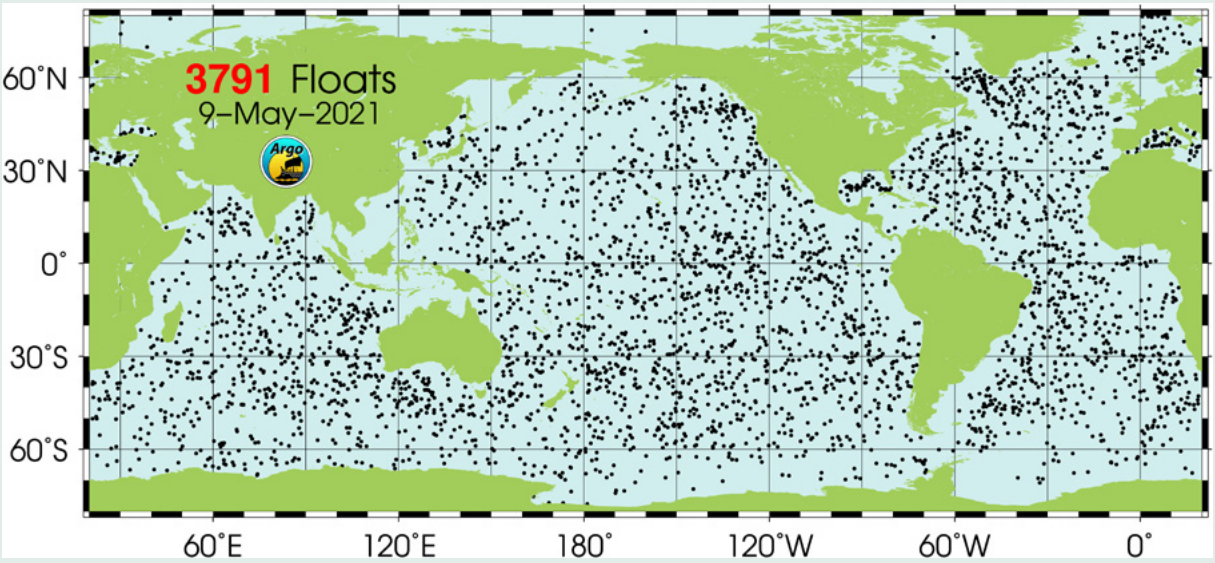
- deployment by ship or aircraft;
- slow descent to 2000 m takes 6 hours at 10 cm/s;
- float drifts with ocean currents for 9 days;
- oil is pumped from internal reservoir to inflate the external bladder causing the float to rise;
- water temperature and salinity profile is recorded during ascent; and
- at surface, for up to 12 hours, data is transmitted to satellite.

The bladder oil is then pumped back to an internal reservoir for the float to begin a new profile and uploaded data is sent to weather and climate forecasting centres around the world. In addition to profiling data, the movement of floats provides information about the direction and velocity of currents.

Observations from these floats have provided independent confirmation of global warming of ocean waters as deep as 2000 m. The greatest change was observed at latitudes below 20°S, attributed to the fact that oceans comprise a larger proportion of surface area in the Southern Hemisphere.

Figure 5.1 Argo global array

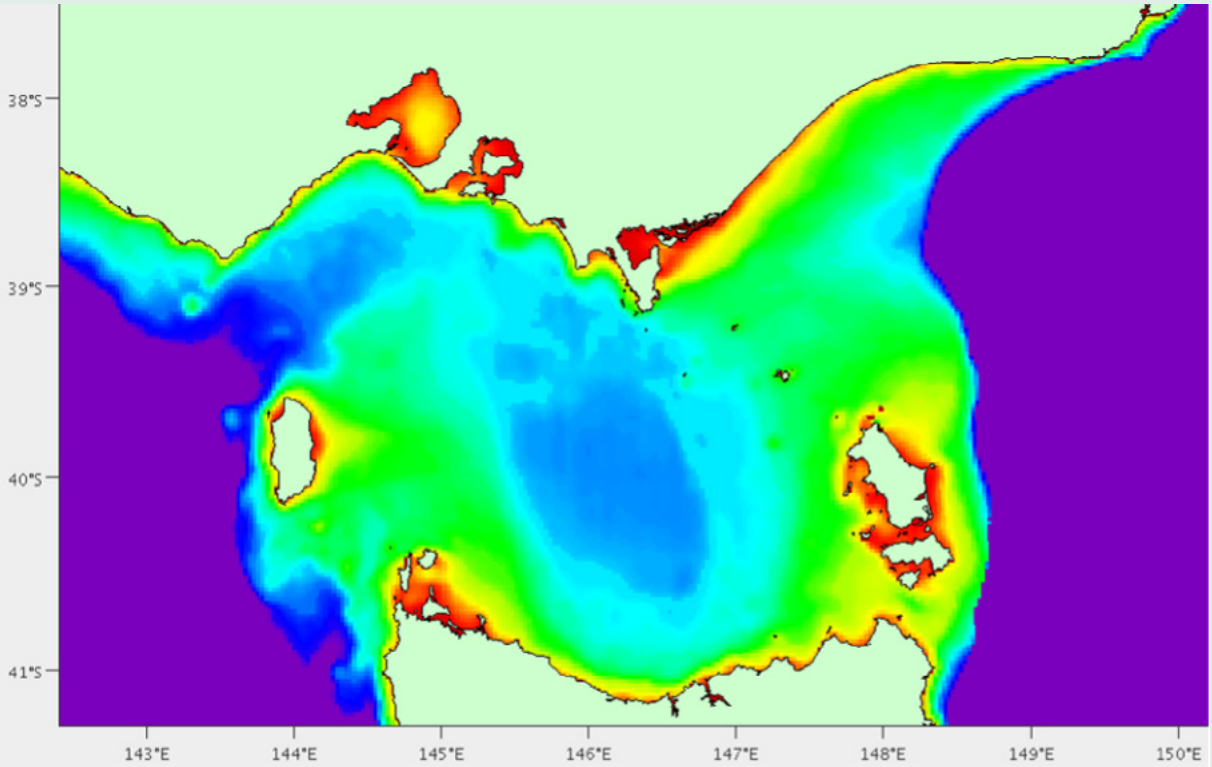
A growing array of Argo profiling floats deliver *in situ* measurements of ocean waters around the globe.



Source: Scripps Institution of Oceanography, University of California San Diego. Retrieved from: *https://argo.ucsd.edu/about/status/*

Figure 5.2 Bathymetry of Bass Strait

The colour spectrum shows depth of water in the Bass Strait, from red (0 m) to blue (100 m).



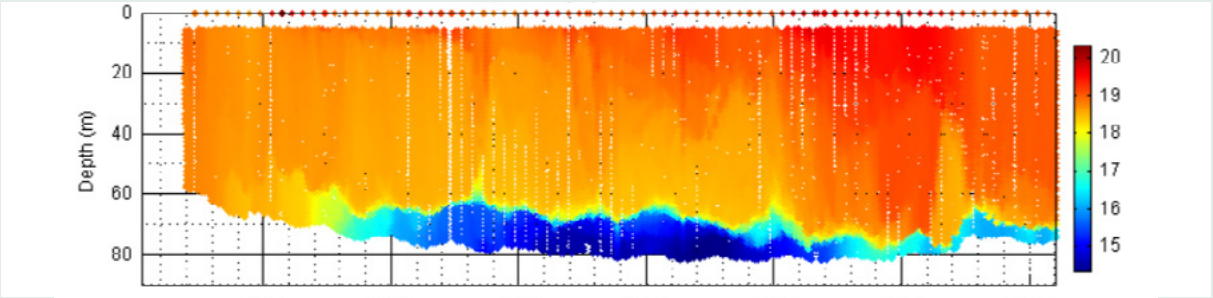
The Ocean Gliders facililty within IMOS (Integrated Marine Observing System—see Volume 2D) operates a fleet of underwater ocean gliders that undertake measurements from shelf and boundary currents in Australian waters. This unprecedented insight into ocean temperature and salinity is freely available online from IMOS. For example, in early 2018 the IMOS Ocean Glider Facility launched the third annual glider travelling from east to west across Bass Strait, the channel of water between the Australian mainland and Tasmania (Baird, 2018). The glider transect indicated the presence of a dense cold pool in the deepest part of Bass Strait, which is shown as a blue region in Figure 5.2. The centre of Bass Strait is deeper than its surrounds and would have formed a large freshwater lake when Bass Strait was exposed over 15,000 years ago. Nowadays the deepest part of Bass Strait is 80 m deep with the deepest outlet to the north at 70 m. Thus the ancient lake continues to act as a place where dense water can collect.

During winter, strong winds and surface cooling create a well-mixed, dense water mass in Bass Strait, which gradually becomes denser than the water in the Tasman Sea to the east because the cooling is confined to the depth of the strait. Once the density difference becomes large enough in the winter, the cold dense pool exits Bass Strait as a bottom density current at the northeastern side.

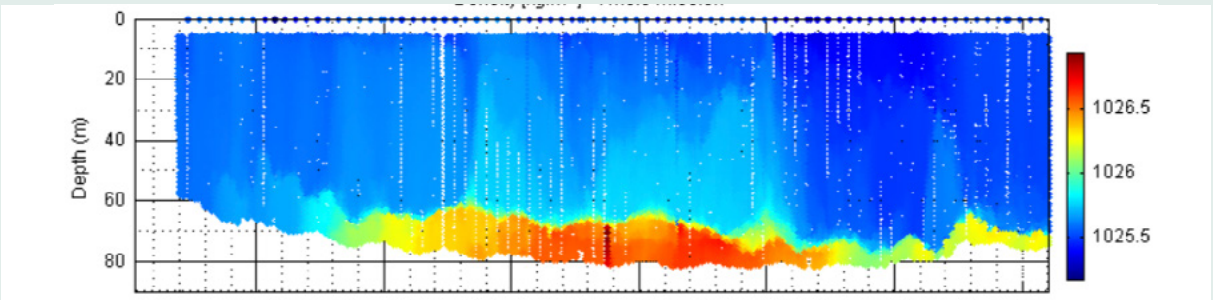
The cold, dense pool of water detected by the glider is low in oxygen, most likely a remnant of the previous winter (see Figure 5.3). This bottom layer at 70–80 m water depth was the portion of Bass Strait water that could not exit in the previous winter because of the 70 m deep ridge across the eastern edge of Bass Strait. High chlorophyll a levels indicate a bloom has occurred in the deep water where both nutrients and some light are present. The oxygen maximum just above the interface shows the bloom is growing. But once winter comes, they will be mixed to the surface and then flow northward out of Bass Strait. Only the unlucky ones will get trapped for another summer—perhaps to be seen by the next Bass Strait glider.

Figure 5.3 Ocean glider transect

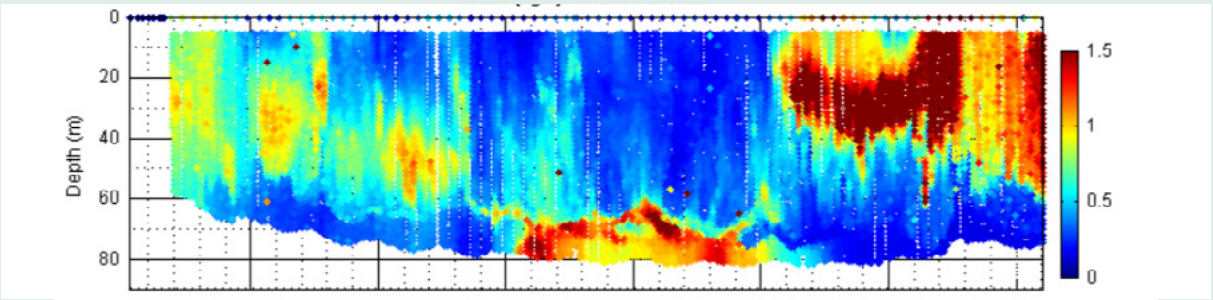
a. Temperature (°C)



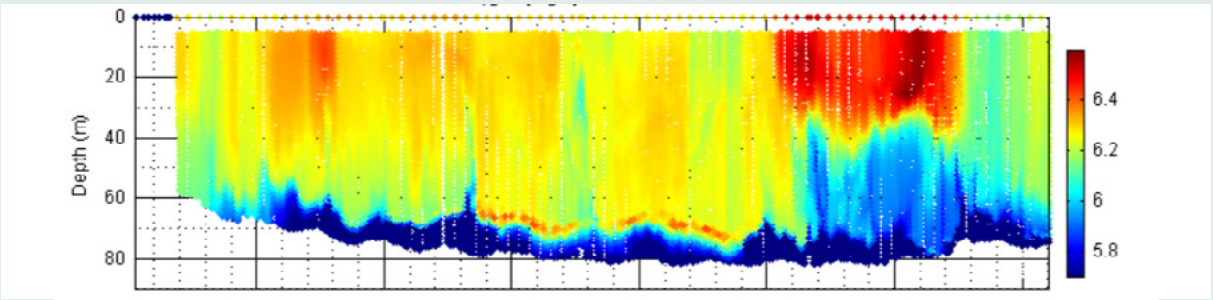
b. Density (kg/m^3)



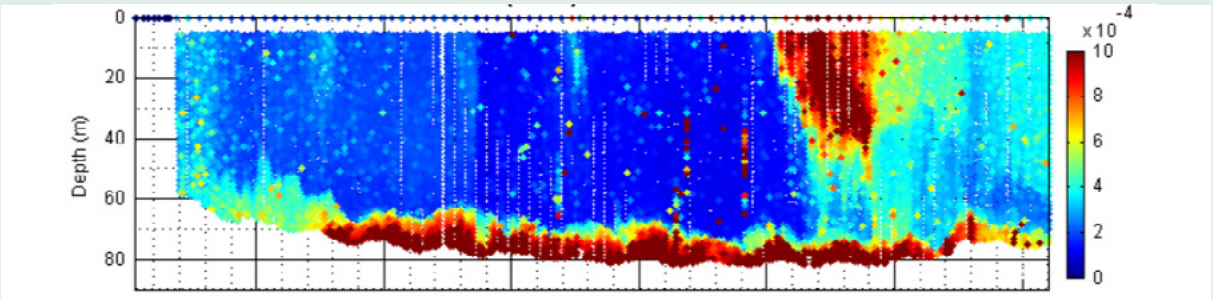
c. Chlorophyll a (µm/L)



d. Oxygen (mg/L)



e. b700 (light scattering coefficient at 700 nm; *m-1.sr*$^{-1}$)



5.1.2 Density and stratification

Density is defined as the mass of a substance per unit volume. At 4°C pure water has the approximate density of 1 g/ml. However, water density increases with increasing salinity or pressure, and with decreasing temperature (see Table 5.1). Since denser water tends to sink and less dense water tends to rise, water density enables water circulation in waterbodies (see Section 16).

In oceans, cold, dense water masses tend to sink at high latitudes, which draws warmer water from low latitudes towards the poles. This density-driven, or 'thermohaline', cycle results in global ocean circulation patterns, which redistribute heat, salt, and nutrients, and carry carbon from the surface ocean and atmosphere to the deep ocean (see Figure 5.4).

While temperature generally decreases with increasing water depth, the characteristics of salinity, density, and pressure all tend to increase. In some waterbodies, density transitions can result in stratification of the water column into three layers of water (see Figure 5.5):

- surface layer—relatively shallow, well-lit, moving, and least dense;
- transition layer—rapid temperature loss with increasing water depth; and
- deep zone—cold, dark, calm water, with highest density.

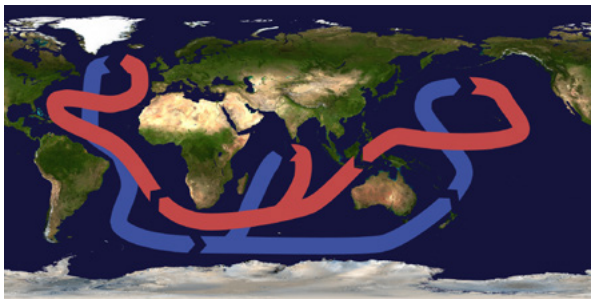
The transition zone effectively inhibits mixing of the circulating, surface ocean waters (about 20% by volume) with the cold, deeper waters (about 80% by volume). In both lakes and oceans, however, stratification can occur at water depths of 1 m.

A similar stratification of the water column can be observed in lakes (see Figure 5.6). In temperate climates lake water warms and cools with the seasonal change, which results in vertical cycling of water within the lake. Many Australian lakes are monomictic, where only one seasonal period of circulation occurs in winter (MacKinnon and Herbert, 1996) and during other times, there is thermal stratification with an obvious epilimnion (see Figure 5.6).

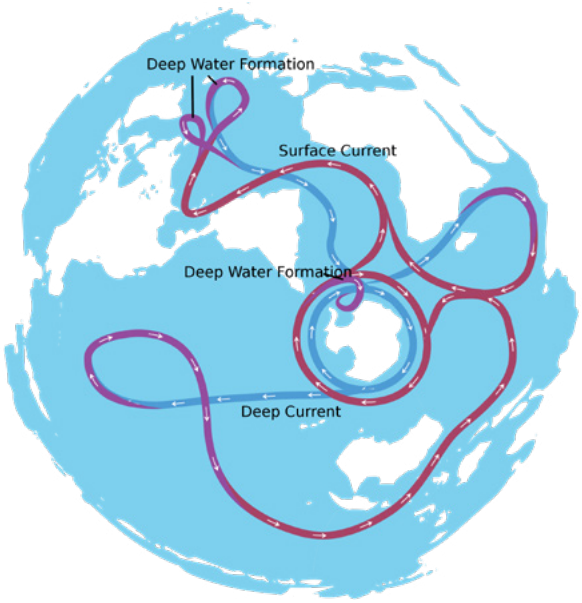
Figure 5.4 Thermohaline circulation patterns

These diagrams show the slow, large scale circulation pattern of ocean waters, one cycle of which takes nearly a millenium.

a. Warm, northward-moving waters in the North Altantic cool and sink into the deep ocean then resurface to warm in the Southern, Indian and North Pacific oceans. Surface currents then carry the warm water back through the Pacific, Indian, and South Atlantic oceans into the North Altantic.



b. Near polar perspective of thermohaline 'conveyor belt' which circulates ocean waters around the globe. This azimuthal equidistant projection (see Volume 2B) views the world ocean as a single unit.



Source: Wikimedia. a. Retrieved from: *https://upload.wikimedia.org/wikipedia/commons/b/b0/Thermohaline_circulation.png* b. *https://upload.wikimedia.org/wikipedia/commons/thumb/a/a6/Conveyor_belt.svg/1991px-Conveyor_belt.svg.png*

Table 5.1 Factors impacting ocean water density

Both temperature and salinity impact water density in oceans.

Climate	Density factors
Wet (low evaporation + high rainfall)	—> Lower salinity —> density decreases —> water rises
Dry (high evaporation + low rainfall)	—> higher salinity —> density increases —> water sinks
	High salinity + low temperature —> greater density increases —> water sinks more
Polar (less heat from sun)	—> temperature decreases —> density increases —> water sinks
Tropical (more heat from sun)	—> temperature increases —> density decreases —> water rises

Figure 5.5 Stratification of water column

Changes in temperature and salinity with increasing water depth result in changes to water density, which create three vertical layers within the water column:
1. A surface layer of lowest density, which is relatively shallow, well-lit and moving;
2. A transition layer, in which temperature decreases rapidly with increasing water depth; and
3. A lower layer of cold, stable, dark water, which has the highest density.

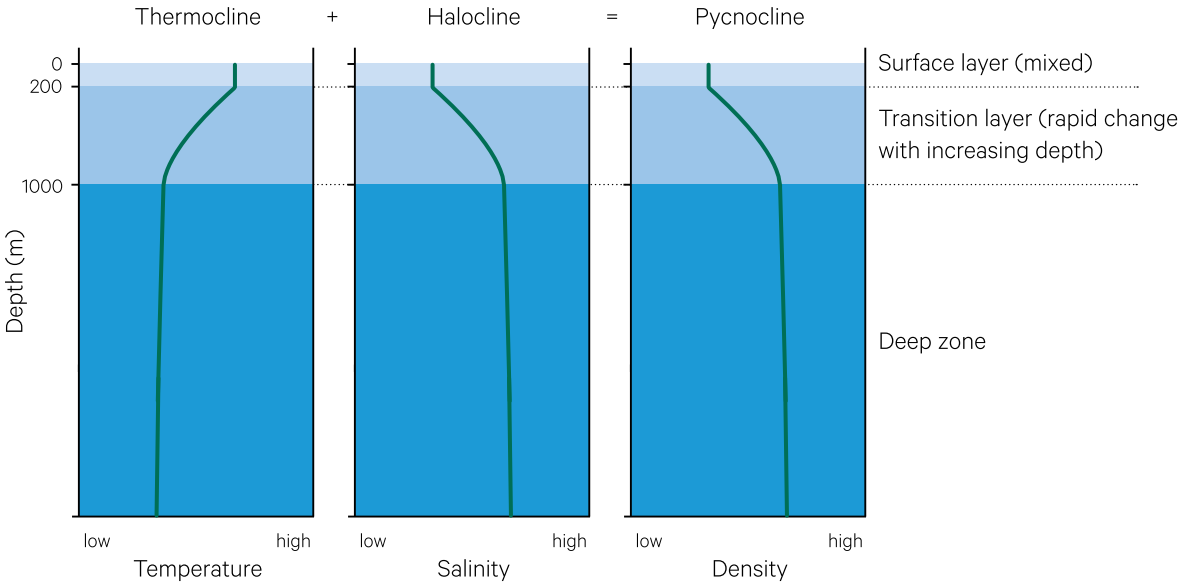
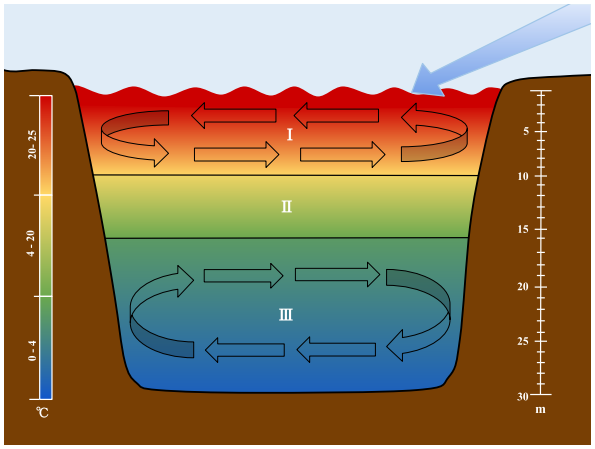


Figure 5.6 Lake stratification

In freshwater systems, temperature and density determine the separation of lakes into three layers:
I. Epilimnion—the top, warmer layer of the lake;
II. Metalimnion (or thermocline)—the middle layer that forms a thermal barrier between the upper and lower layers; and
III. Hypolimnion—the lower, cooler layer.
The scales associate each layer with their corresponding temperatures (right) and water depths (left). The top arrow indicates wind movement over the water surface, which initiates turnover in the epilimnion and hypolimnion.



Source: Mbrookings19, Wikimedia. Retrieved from *https://commons.wikimedia.org/wiki/File:Lake_Stratification_(11).svg*

5.1.3 Temperature

The temperature of water in a waterbody will vary with season, latitude, altitude, aspect, exposure, colour, and depth. Some of these factors, principally waterbody colour and depth, can also lead to variations in temperature within a waterbody (see Figure 5.5). The natural range of temperatures across all waterbodies varies from less than 0°C in polar areas, where water freezes into ice, to over 100°C in geothermal features, where water boils and condenses into steam (Te Ara, 2018). Water colour can impact temperature when solar energy is absorbed by darker, shallower waters, making them warmer than the equivalent depth in clear water. Similarly, solar energy penetrates to greater depths in clear water, distributing the heat across a larger depth range.

At sea level, pure water freezes at 0°C and boils at 100°C. Impurities, including salt, in water will slightly increase its boiling point and lower its freezing point. This has obvious implications for thermal analyses of water pollution and wastewater. At higher altitudes, with lower atmospheric pressure, both the freezing and boiling temperatures of water will be lowered.

Unless covered by ice, waterbodies are warmed by solar radiation and cooled by evaporation and surface winds, and shallow water is generally warmer than deep water due to absorption of solar energy. The resistance of a material to changes in temperature is described as its thermal inertia. This property controls diurnal and seasonal temperature variations of surface materials. Large waterbodies have high thermal inertia—they warm and cool slowly relative to their surroundings.

While 75% of ocean waters have temperatures in the range -1 to 6°C, the thermal properties of the ocean surface are very variable, ranging from sub-zero temperatures in extreme polar regions to over 34°C in tropical waters (BOM, 2018). This variation is largely driven by turbulence (Minnett and Kaiser-Weiss, 2012). Large waterbodies in non-polar regions develop a transition zone, or thermocline, in which the temperature of the water changes rapidly relative to the waters above or below (see Figure 5.5). The water depth, thickness and persistence of thermoclines varies with season, latitude, and turbulence. A thermocline in a waterbody tends to inhibit mixing of warmer, more turbulent surface waters and deeper, cooler, and calmer waters. Accordingly, only surface waters, comprising around 2% of all ocean water, tend to change in temperature with external heating. Upwelling fronts, where the thermocline breaks through the water surface, can also create vertical stratification of water temperature (Tomczak, 1998).

The temperature of water in rivers has been observed to be more closely related to the local air temperature than the upstream water temperature. The waters of the Murray River, for example, annually vary between 6–28°C at the headwaters, 7–30°C in the middle reaches and 9–30°C in South Australia (Shafron *et al.*, 1990). Reservoirs, however, introduce thermal stratification of stored water during summer in the same way that oceans develop thermoclines. In the Hume Reservoir, for example, the temperature of water discharged from outlets located below the reservoir's thermocline may be more than 5°C cooler than the surface water during spring and summer, with the temperature varying with water storage levels (Sherman, 2005). When this cooler, denser, deep water is released, it has been observed to reduce the temperature of river water downstream. Such sudden cooling has been termed 'cold water pollution' since it is likely to have adverse effects on water biota, particularly during spring when many species of native fish are spawning. Similarly, the release of wastewater, from industrial, agricultural, and/or domestic activities, can change the temperature of river water.

'Unnatural' changes in temperature within a waterbody can significantly impact a wide range of resident organisms, including native fish species. An increase in temperature of only 1°C lasting one month, for example, can initiate coral bleaching (see Excursus 20.3).

The temperature of a water surface can be measured by *in situ* sensors or remote thermal infrared (TIR) sensors. These sensors only measure the surface temperature of a waterbody, which is impacted by both Sun and wind (see Section 14). In Australian waters the lowest Sea Surface Temperatures (SST) typically occur in early spring while the highest temperatures occur in autumn. Changes in SST indicate water movement, which may be helpful to locate pelagic fish species (see Section 20.7.1). The temporal distribution of temperature measurements in inland waterbodies provides valuable insight into its thermal cycle (Lindell *et al.*, 1999; see Volume 1B—Section 7).

5.1.4 EMR absorption and transmission

Electromagnetic radiation (EMR) can be viewed as a continuous energy spectrum ranging from very short, high energy waves to longer waves with much lower energy, all of which travel at the speed of light (3×10^8 m/s through a vacuum; see Figure 5.7). Commonly accepted ranges for EMR spectral regions are:

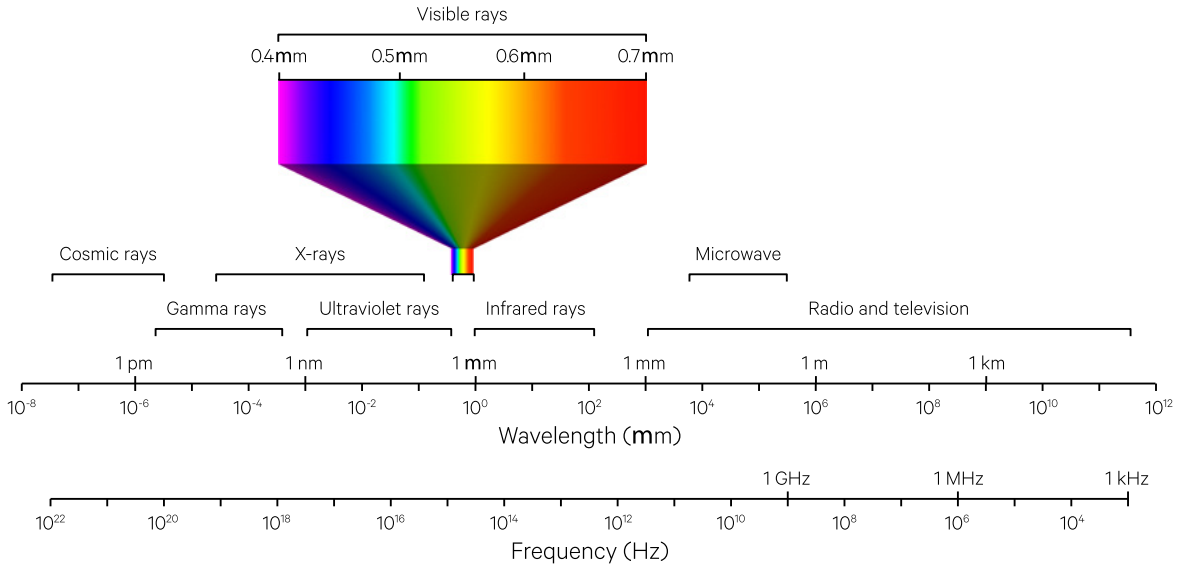
- ultraviolet (UV): 0.1–0.38 μm;
- visible: 0.38–0.7 μm;
- infrared (IR): 0.7–1,000 μm; and
- microwave: >1 mm–1 m.

Infrared wavelengths are often subdivided into the regions:

- near infrared (NIR): 0.7–1.3 μm;
- short wave infrared (SWIR): 1.3–3 μm;
- middle infrared (MIR) or mid-wavelength (or medium wave) infrared (MWIR): 3–8 μm;
- thermal infrared (TIR) or long wavelength infrared (LWIR): 8–15 μm; and
- far infrared (FIR): 15–1,000 μm.

Figure 5.7 Electromagnetic spectrum

Names are assigned to regions of the spectrum for convenience – there are no clearly defined divisions. Cosmic rays are high energy, charged particles that travel at close to the speed of light. They are not EMR but included for comparison. Note: scales are logarithmic.



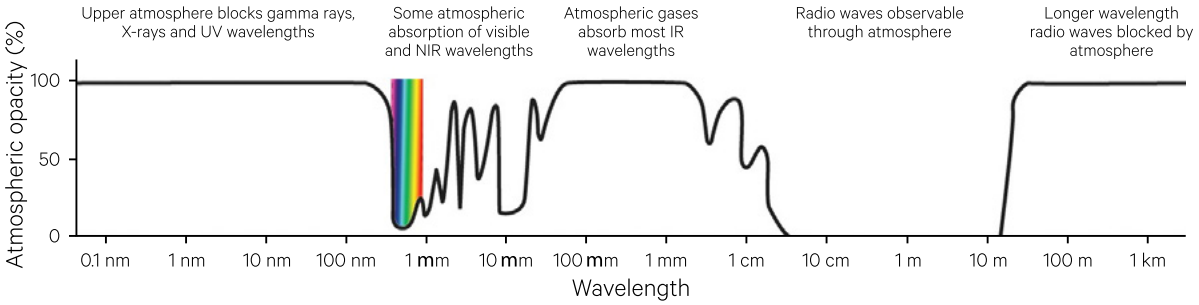
Adapted from: Harrison and Jupp (1989) Figure 2

Most EMR originates from the sun, particularly for shorter wavelengths. Some regions of the EMR spectrum are absorbed by atmospheric gases before they reach the surface of Earth (see Figure 5.8). The gradual reduction in intensity of EMR as it travels through a medium is called attenuation (see Volume 1B—Sections 4 and 5).

EMR radiation is attenuated by pure water and its constituent materials (due to absorption and backscattering), such that the intensity of energy in all wavelengths decreases exponentially with increasing water depth. Less than 1% of total EMR energy intercepted at the surface of a very clear and transparent waterbody will be detected at water depths greater than 100 m. In clear water, the Beer-Lambert Law (see Volume 1A—Section 2.9) can be used to estimate the intensity of light likely to reach a given water depth. For example, the EMR spectra corresponding to four typical Australian water colours are shown in Figure 5.9). The absorption of light by pure water also varies slightly with temperature (Pegau and Zaneveld, 1993).

Figure 5.8 Atmospheric opacity

Some wavelength regions of the EM spectrum are absorbed by atmospheric gases so cannot be used for EO of surface features on Earth. Note: Scale is logarithmic.



Adapted from: Wikimedia Commons at *https://commons.wikimedia.org/wiki/File:Atmospheric_electromagnetic_opacity.svg* (original source: NASA)

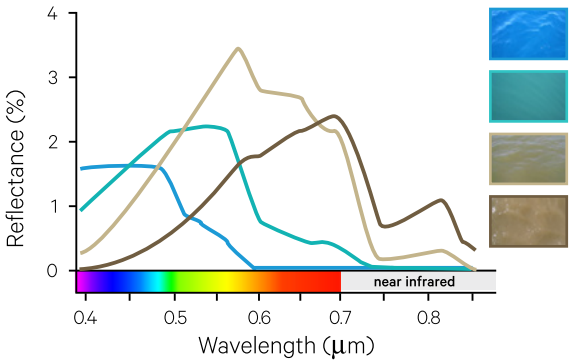
The extent of EMR attenuation in the visible and NIR range varies with wavelength, with shorter wavelengths reaching greater water depths before being absorbed or scattered (see Figure 5.10). In clear, calm, oligotrophic ocean water:

- blue wavelengths are mostly absorbed at a water depth around 60 m;
- green wavelengths are mostly absorbed at a water depth around 30 m;
- yellow wavelengths are mostly absorbed at a water depth around 20 m;
- orange wavelengths are mostly absorbed at a water depth around 10 m;
- red wavelengths are mostly absorbed at a water depth around 5 m; and
- near infrared wavelengths are mostly absorbed at a water depth around 0.5 m.

Optical properties of water as they relate to EO are reviewed in Excursus 8.1 and further detailed in Section 8.3

Figure 5.9 Reflectance from different water colours

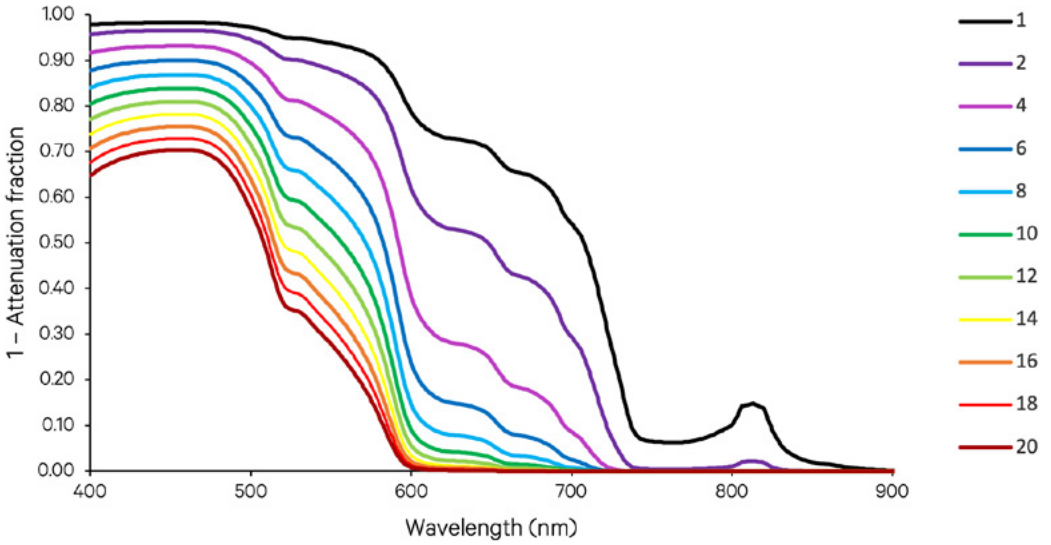
Variations in water colour result in varying spectral characteristics for waterbodies. This graph shows the spectra resulting from four different water colours.



Source: Vittorio Brando, ISAC-CNR

Figure 5.10 Light attenuation in water

The amount of downwelling light in the water column after attenuation by pure water is shown as a function of water depth from 1–20 m, presuming the white substrate reflects 100% of all wavelengths. Light attenuation increases with water depth and with wavelength due to increased molecular pure water absorption. The y-axis shows the amount of light at each water depth as a fraction of the surface downwelling irradiance.



Source: Arnold Dekker, SatDek

5.1.5 Transparency and suspended particles

The relative clarity of water is commonly described in terms of turbidity or transparency. The term turbidity is often used in an attempt to quantify the concentration of suspended sediments in water at a particular time. In this context, sediments may include any particulate matter of mineral or organic origins, such as clay or silt, or detritus and biomass from phytoplankton, macrophytes, or zooplankton. Coloured dissolved organic matter also influences transparency and vertical attenuation of light and thus need to be accounted for in the total light attenuation budget.

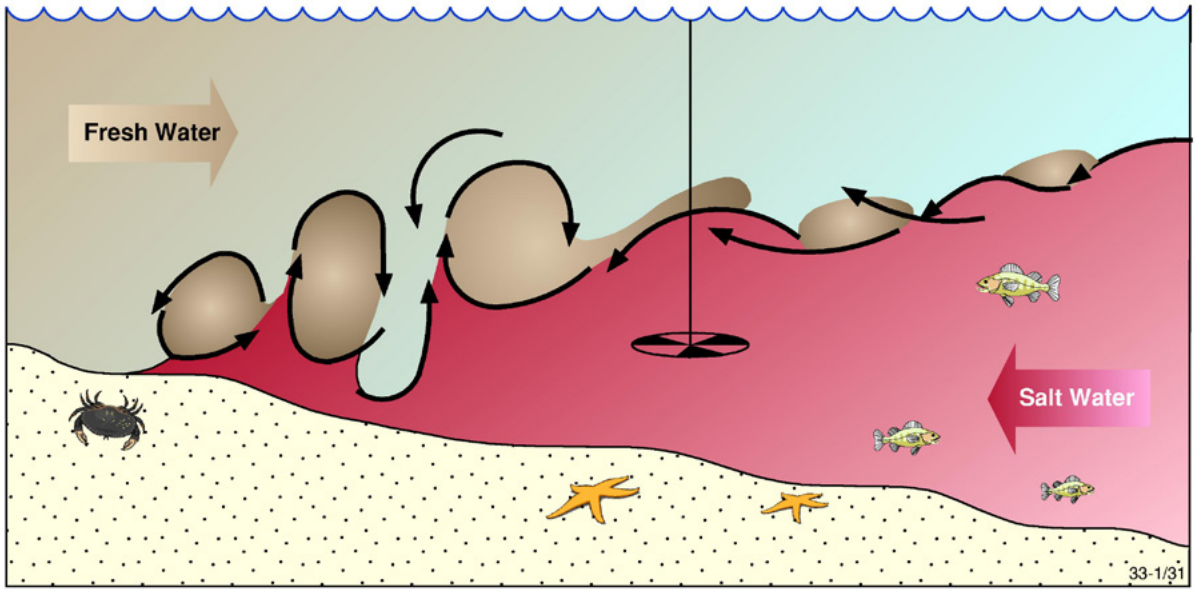
Turbidity levels are related to both water flow and available sediment and particle size. Water circulation encourages loose sediments to become suspended, and the extent of turbidity will depend on both the level of agitation within the waterbody and the buoyancy of loose particles. As such, the turbidity of water in a waterbody varies with the surrounding and underlying soil type, the erodibility of the soil, adjacent land activities, the geology and geography of its catchment area, and recent weather conditions. Runoff laden with nitrogen and phosphorus from fertilised soils, for example, (depending on other growth limiting factors such as light and temperature) encourages the growth of phytoplankton and macrophytes, which ultimately (through their breakdown products) increases the concentration of detritus. Weather conditions, such as wind- and wave-based resuspension of bottom sediments in shallow lakes, can also initiate water movement so that settled sediments become resuspended.

Turbidity in inland and coastal waters is strongly driven by runoff and river flow, so can increase dramatically during flooding. Conversely, by controlling flow rate, reservoirs on rivers act as sediment traps. A local maximum turbidity tends to occur where fresh and saltwater meet and tidal movements interact with river flow. At this interface, water mixing encourages fine particles to clump together, or flocculate, resulting in turbidity (see Figure 5.11). An example of this is visible in the image of floodwaters on the page before Section 4.

Most rivers transition from clear, fast-flowing highland headwaters running through gravel streambeds to slower, muddy-bottomed lowland sections with inflowing tributaries. In particular, rivers that travel through fine clay soils, such as the Darling River in western NSW, are more likely to be turbid, unless their flow rate is slow enough to allow suspended particles to settle out of the water (Shafron *et al.*, 1990).

Figure 5.11 Turbidity caused by flocculation

The interface between freshwater and saltwater encourages flocculation of fine particles. Maximum turbidity tends to occur in this region. Light attenuation in the water column is increased by turbidity. A Secchi depth is related to turbidity and measures the water transparency.

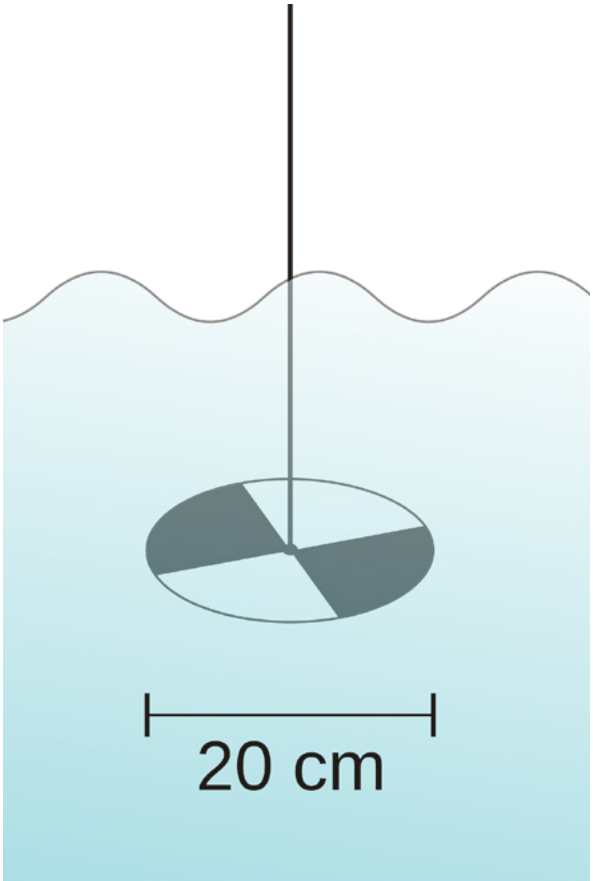


Source: OzCoasts (2018)

High levels of suspended sediment can impact aquatic biota, either directly by smothering benthic organisms, or indirectly by reducing light levels and photosynthetic activity. Elevated turbidity also affects water consumers and can disable water filtration apparatus. When fine clays are prevalent in riverbeds, as tends to occur in tropical regions, the river water is frequently turbid. Abnormally high levels of turbidity, however, can be transported into coastal marine areas in river plumes, and negatively impact fragile ecosystems such as coral reefs (see Section 20.6). The fine clay and colloidal particles of these sediments also carry nutrients as ions and organic molecules. This mechanism has been estimated to account for 40% of the nitrogen and 60–80% of the phosphorus leaving the Great Barrier Reef (GBR) catchment (Furnas, 2003).

Once turbid river waters reach the sea, their flow rate slows down and larger sediments are deposited. Saline marine waters encourage sediments to flocculate and settle. Over time, this transportation of sediment changes the geomorphology of coastlines (Furnas, 2003; see also Sections 1.1 and 1.2.2 above).

Figure 5.12 Secchi disk



Source: Mysid, Wikimedia. Retrieved from *https://commons.wikimedia.org/wiki/File:Secchi_disks.svg*

Blackwater events (see Excursus 18.1) can occur in waterbodies due to very high concentrations of dissolved organic carbon (DOC) and black particulates, which generally results from leaf litter decomposition (often from *Eucalyptus* species) and/or the presence of dark minerals. Significant quantities of ash can also enter waterbodies after fire, creating a range of water colours and impacting water quality.

The suspended sediment load of water samples is directly measured in terms of the Total Suspended Matter (TSM; also called Total Suspended Solids: TSS or Suspended Sediment Concentration: SSC), that is, the mass of suspended particles per unit volume of water that does not pass through a filter (Blackburn and Dekker, 2006). In this context, the nominal pore size for sediment filters is generally in the range 0.45–0.7 μm for optical purposes. Traditional measurement methods derive the dry weight of sediment from water samples at specific point locations.

TSM can be viewed as a collective term for the sum of phytoplankton, detritus, and mineral matter. The various suspended sediment particles that manifest as turbidity change the optical properties of the water. Turbid waters have a brighter reflectance across all wavelengths than clear waters (except when the mineral detritus is black, as can occur with particulate matter from fires or of volcanic origin), and this characteristic can be used to map the concentration of suspended sediment. Indirect optical measures of turbidity are based on the impact of turbidity on the interaction between light and water. Some of the methods that are used to quantify water transparency based on its optical behaviour include (Dekker and Hestir, 2012):

- visual measurements of water clarity or transparency—have traditionally relied upon the Secchi disk (see Volume 1B—Section 6.4). The black and white disk is lowered to the water depth at which the black and white segmentation can no longer be discriminated (the Secchi depth; see Figure 5.12). The limit of light penetration (K_d) is generally 2 to 3 times the Secchi depth;
- spectrophotometers—used for laboratory analyses of water samples to determine concentrations of non-algal particulates (NAP) and TSM;
- submersible laser scattering instruments (such as LISST-100)—measure *in situ* particle size distribution and optical transmission, as well as water pressure and temperature;
- submersible backscatterometers—measure *in situ* optical backscattering, with some instruments measuring multiple wavelengths (e.g. BB-9);
- submersible hyperspectral light absorption and beam attenuation meters—allow detailed *in situ* spectral measurements (e.g. AC-S); and
- *in situ* spectroradiometers—can measure above-water or in-water light reflectance

Various studies have demonstrated a strong relationship between TSM and optical measurements of turbidity (Brando *et al.,* 2006; Webster *et al.,* 2006). Similar correlations have been established between scattering in green, red or NIR wavelengths and TSM concentrations. These correlations have proved valuable for mapping turbidity in waterbodies (see Section 18.1).

The large variation in the concentration of suspended sediments, phytoplankton, and coloured dissolved organic matter (CDOM) in many inland, estuarine, and coastal waters results in a highly variable light climate (see Section 5.2.3). Optical models play a key role in understanding and quantifying the effect of water composition on optical variables obtained from either *in situ* or EO measurements (see Section 19). Further information on EO of inland waters is provided by Greb *et al.* (2018).

5.2 Chemical

The chemical composition of the water column can impact EO measurements in terms of salinity (see Section 5.2.1), pH (see Section 5.2.2), and both organic and inorganic dissolved matter (see Section 5.2.3).

5.2.1 Salinity

Salts in water lower its specific heat and freezing point and raise its boiling point. Seawater freezes at ~2°C. Salts are expelled from sea ice as it freezes, which increases the salinity and density of surrounding waters. Water can also become more saline via evaporation, whereas the addition of precipitation, runoff, and melting ice all reduce the salinity of a waterbody.

Seawater, on average, contains 3.5% salts, dissolved gases, organic substances, and suspended matter. The most common mineral constituents of sea salt are sodium, chloride, sulphate, magnesium, calcium, and potassium. Salt content affects other properties of water, such as absorption and scattering of light (see Section 8.2.5). The salinity of estuaries fluctuates with tidal penetration and typically decreases with distance inland from the coast. Many coastal lakes and lagoons, for example, are intermittently open and closed to the ocean (and termed ICOLL: Intermittently Open and Closed Lakes and Lagoons; NSW NPI, 2015). In Western Australia, some ICOLLs have salinity levels that are twice the concentration of seawater. Thus, salinity is an important indicator of circulation between marine and freshwater sources.

Dissolved salt concentration in river systems is primarily due to dryland salinity and typically involves chlorides, bicarbonates, and sulphates, of sodium, calcium, magnesium, and potassium. River salinity can often be traced to the combined impacts of reduced flow (due to river regulation or drought) and clearing of catchment vegetation. Where the groundwater, geology, and soils within a catchment area are naturally saline, its rivers and lakes are likely to have a naturally high salt concentration. Another mechanism for introducing salt to inland waterbodies can be seen with salt lakes. Lake Eyre in arid central Australia, for example, is 13 m below mean sea level at its deepest point and, as its water evaporates, a salt crust remains on the dried lake surface.

Salinity is measured in terms of electrical conductivity, which varies with the number of dissolved ions per volume and the mobility of the ions (which, in turn, varies with temperature and pressure). *In situ* sensors measure electrical conductivity as an indicator of Total Dissolved Salts (TDS). Officially, salinity is defined as the ratio of the electrical conductivity of a sample at 15°C and 1 atmosphere pressure to that of a standard solution with 32.4356 g of potassium chloride per kg of water (UNESCO, 1981a, 1981b). As such, salinity measurements do not have units. The standard salinity of seawater is 35 and 75% of ocean waters on Earth have salinity in the range 34 to 35. During the dry season, the salinity of tropical waters can increase to 36, but major flooding and heavy rain can reduce it to 33 (Furnas, 2003) or less (Schroeder *et al.*, 2012).

Saline waters affect the taste, hardness and corrosiveness of domestic water and can reduce plant growth. Both marine and freshwater aquatic organisms generally achieve optimal function within a relatively narrow salinity range, so would be adversely impacted by large or rapid variations. A global network of autonomous Argo floats have been collecting information on salinity and temperature profiles in ocean waters for over a decade (see Excursus 5.1).

5.2.2 pH

The acidity (low pH) or alkalinity (high pH) of natural waters varies with soil type, geology, vegetation, algal content, land use, and climatic conditions. pH indicates the activity of hydrogen ions expressed as moles per litre on a logarithmic scale from 0 to 14 (where 7.0 is considered neutral; see Figure 5.13). The pH of most natural freshwater systems varies in the range 6.5–9.0. The pH of seawater approximates 8.2.

Changes in pH are resisted by most natural waters by the interactions of other minerals with hydroxyl ions. The pH of waterbodies can change with environmental conditions including increased atmospheric CO^2 concentrations, salinity, temperature, photosynthetic activity, decomposition, soil disturbance, and industrial, agricultural, and domestic pollutants. Prolonged drought, for example, can expose acid sulphate soils in waterbodies and lead to the formation of sulphuric acids, which lowers the pH of the water after rain. Organic matter leaching into waterbodies can also raise their pH, while conversely land clearing and pollution can result in lowered pH levels.

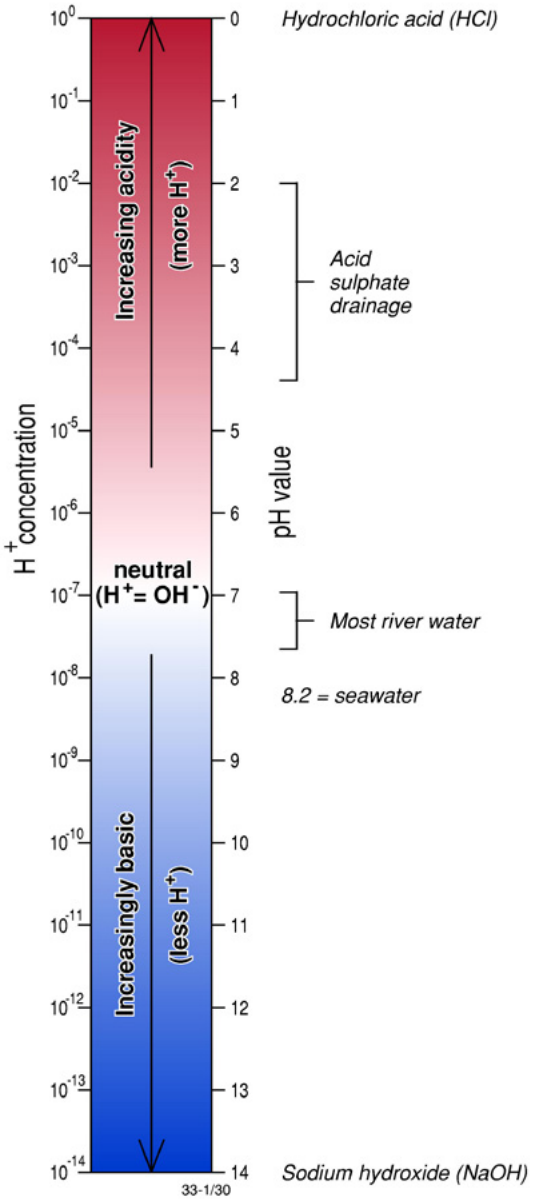
Nutrients and pollutants are more soluble in acidic water. Accordingly, the higher nutrient levels of waterbodies with acidic water encourage plant and algal growth, which in turn deoxygenates the water column. While some diurnal pH variation does occur in most waterbodies, aquatic organisms have mostly adapted to thrive within relatively narrow pH ranges, so rapid changes in acidity or alkalinity can adversely impact ecological balance.

pH of waterbodies is measured directly using *in situ* sensors. While pH cannot be directly measured using EO sensors, EO imagery can help to identify conditions resulting from acidic water. For example, while algal blooms initially increase water pH, the ensuing anaerobic conditions can cause water pH levels to decline (Dekker and Hestir, 2012).

The salinity of any water body is the result of an equilibrium between the environmental ionic inputs and removals. (Smyth and Elliot, 2016)

Figure 5.13 pH scale

The ph of example solutions is indicated beside this scale.



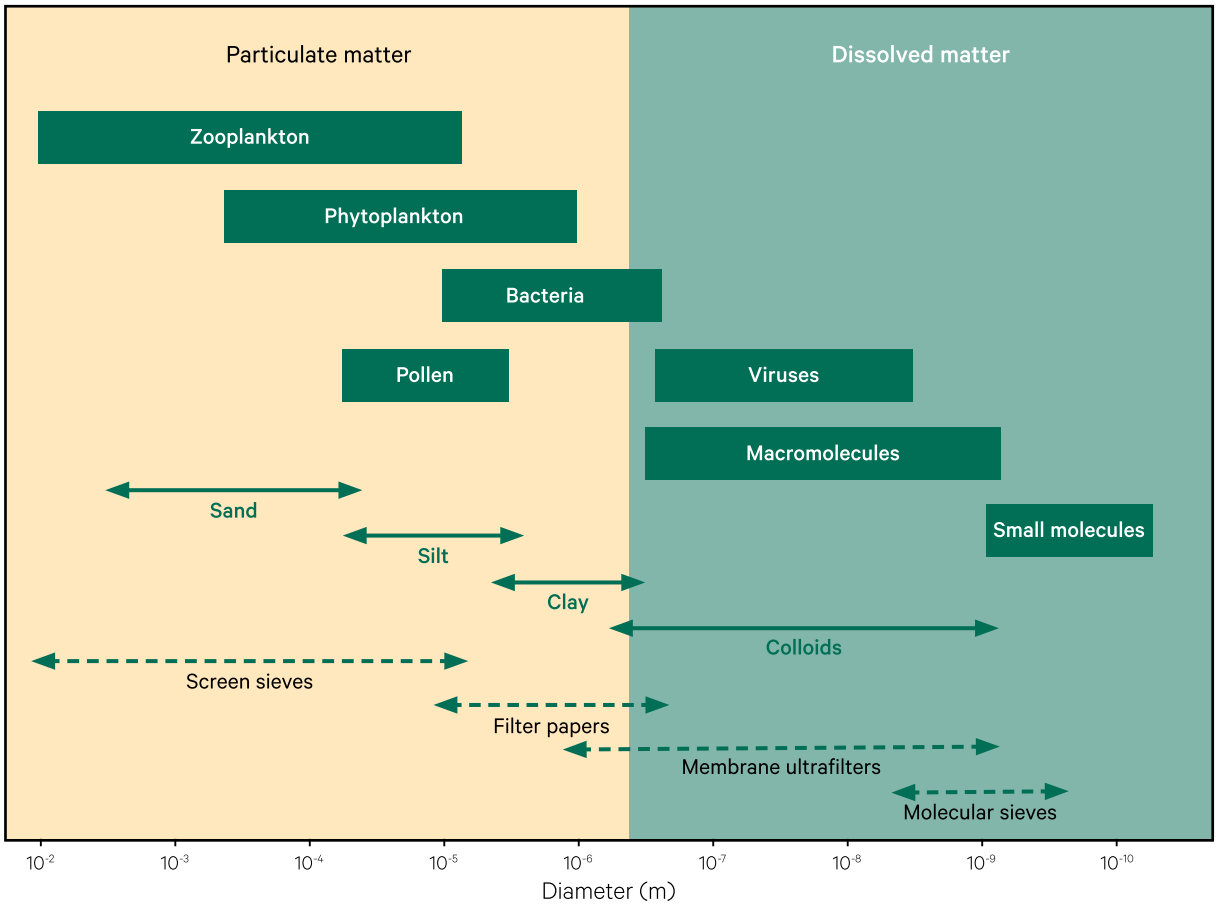
Source: *http://www.ozcoasts.gov.au/indicators/ph_coastal_waterways.jsp*

5.2.3 Dissolved matter

Dissolved materials have been traditionally separated from particulate matter by filtering water samples through glass fibre or membrane filters (see Figure 5.14). Dissolved matter in waterbodies originates from either organic (see Section 5.2.3.1) or inorganic (see Section 5.2.3.2) substances.

Figure 5.14 Separation of dissolved and particulate matter

The continuum of sizes and separation methods for organic matter in seawater are shown. Note scale is logarithmic.



Adapted from: Hedges (2002)

DOM concentration, composition, and chemistry are highly variable and depend on the sources of organic matter (allochthonous versus autochthonous); on the temperature, ionic strength, pH, major cation composition of the water; on the surface chemistry of sediment sorbents that act as solubility controls; and on the presence of photolytic and microbiological degradation processes.
Leenheer and Croué (2003)

5.2.3.1 Organic

Various organic substances, such as tannins from decaying tree bark and leaves or decomposing algae or macrophytes, dissolve in natural waters. Such substances (whether dissolved or colloidal) have become known as yellow substances (Bricauld *et al.*, 1981), Gelbstoff (Carder *et al.*, 1989), gilvin (Kirk, 1976), aquatic humus (Lindell *et al.*, 1999), or Coloured (or Chromophoric) Dissolved Organic Matter (CDOM).

While their colour varies with the parent material, which can derive from both aquatic and terrestrial origin, they can result in water colours from green to yellow to brown as concentration increases. Greater concentrations of CDOM occur in inland and coastal waters than in ocean waters. Origins of the dissolved organic matter can be either:

- autochthonous—found at the site; or
- allochthonous—found elsewhere.

The term 'dissolved' is meant to indicate all water and CDOM passing through a filter size of either 0.47 micron (μm) or 0.20 μm, the latter being preferred as it is half of the wavelength of the deepest blue visible light. Chemical methods can be used to determine the concentration of dissolved organic matter (DOM) in discrete water samples.

The presence of CDOM exponentially increases absorption of light with decreasing wavelengths (Pozdnyakov and Grassl (2003). The resulting colour can be measured using spectrophotometric readings. Often the spectral absorption of filtered water samples at 380 nm or 440 nm is provided if a single number is required (Lindell *et al.*, 1999).

Since carbon approximates half the DOM by weight, the concentration of DOM is generally expressed in terms of unit grams of carbon per unit volume. As such, the terms DOM and Dissolved Organic Carbon (DOC) are sometimes used interchangeably (Pozdnyakov and Grassl, 2003). DOC comprises 'a complex mixture of aromatic and aliphatic hydrocarbon structures that have attached functional groups', with the majority being humic substances (HS; Leenheer and Croué, 2003). HS derive from the non-bioconsumable residue of plant or animal matter and have relatively high molecular weights (Sachse *et al.,* 2005). HS decrease the transparency of water, especially in the blue and blue-green wavelengths (see Section 18.5), and thus reduce the depth of the euphotic zone. Accordingly, CDOM tends to limit photosynthesis (and hence phytoplankton production), slightly increases water acidity, and binds toxic metals and organic contaminants. The marine DOC also has a central role in the global carbon cycle, as it is the largest stores of carbon in the ocean and is the intermediatory pathway for carbon to be transferred into the food webs (Seritti, *et al.,* 2003).

5.2.3.2 Inorganic

Various minerals, such as phosphorus, nitrogen, and silica, are nutrients for aquatic plants. In excess, however, they encourage the growth of undesirable algae and bacteria. Increased nutrient levels in waterbodies have been observed to coincide with increased growth of ephemeral macroalgae, phytoplankton and epiphytes, and decreased growth of perennial macrophytes (Hardison *et al.*, 2013).

Wastewater from urban, industrial, and irrigation activities can contribute large quantities of nutrients to inland and coastal waters. The limited measurements available for waterways within largely pristine catchments indicate lower nutrient levels than for those rivers and streams impacted by land clearing and agriculture within the GBR catchment area (Furnas, 2003). Nutrient levels in waterbodies can also be increased after fire, due to extensive loss of vegetation and greater catchment erosion, or when water volume is reduced by drought conditions. Flushing of waterways by tides or freshwater flows both dilutes and transports nutrients. In the coastal rivers near the GBR, both the average nutrient concentrations and the relative abundances of individual nutrients vary both between and within rivers (Furnas, 2003), although the differences between rivers is generally less than the temporal variation within individual rivers.

Phosphorus can enter waterbodies from urban areas and agricultural land. It is considered a 'conservative' pollutant as it stays in the river water and does not leach into groundwater. Nitrogen, however, is not a conservative pollutant, and can infiltrate groundwater storages. Calcium and magnesium ions 'harden' water, that is, they increase surface tension and limit the efficacy of surfactants, such as cleaning products.

The oceanographic community's perception of DOM [Dissolved Organic Matter] has evolved from an emphasis on a dilute and largely separate pool of remarkably old and static substances to the current view of a dynamic assemblage of organic molecules that interact with each other, trace metals, and living organisms over a broad continuum of space and time scales. The sparingly reactive components of this molecular continuum that persist and change on time scales sampled by conventional oceanographic surveys represent a small molecular outcrop of a churning mass of molecules through which much of the total primary production of the ocean cycles.
Hedges (2002)

Table 5.2 Trophic status categories for freshwater lakes

Trophic Status	Nutrient Level	Productivity	Water Clarity	Dissolved Oxygen	Possible Causal Agents
Oligotrophic	Low	Low	High	High	Acid rain
Mesotrophic	Medium	Medium	Medium	Medium	Balanced conditions
Eutrophic	High	High	Low	Low	Fertiliser or faecal contamination
Hypertrophic	Super-saturated	Extremely high	Extremely low	Lacking	Excessive nutrients or low flow

Eutrophication describes the condition of a waterbody enriched by nutrients, which can result in excessive primary production[6], reduced secondary production[7], and lead to long term loss in species diversity. The natural process of eutrophication occurs slowly, due to long term weathering and leaching of nutrients from soils and vegetation. By increasing the volume of phytoplankton and aquatic plants, this enrichment results in more productive waters. Eutrophication can also occur rapidly, resulting from anthropogenic activities, such as forest clearing and agricultural practices, or following the addition of polluted wastewater. Relevant pollutants in wastewater may include polyphosphates from detergents, or fertiliser residues from irrigation. Rapid eutrophication encourages accelerated growth of phytoplankton, some types of which have a detrimental impact on water quality. Exhaustion of individual nutrients can also disrupt the balance of nutrients, leaving some in excess quantities.

Of the many parameters that have been used to classify lake habitats, trophic status is currently the most widely used. Several indices have been proposed to express the trophic status of lake water based on varying levels of dissolved oxygen, total phosphorus, total nitrogen, chlorophyll a, transparency, and/or organic matter in sediments. Table 5.2 summarises the relationships between nutrient levels and other water characteristics for four trophic status categories.

The classic method for assigning lake trophic level is that of Carlson (1977), which combines quantitative measurements of chlorophyll, total phosphorus, and the Secchi disk (see Section 5.1.5) into a single index. This is intuitively attractive as the chlorophyll content provides a measure of the standing crop of phytoplankton, while the total phosphorus defines the upper limit of biomass production (since most lake systems in the Northern Hemisphere are phosphorus limited). In the case where nitrogen is the limiting nutrient, as typically occurs in Australian inland waters, cyanobacteria often become the dominant phytoplankton class through their ability to fix nitrogen from the atmosphere. The deep, or subsurface, chlorophyll maximum (chl max) describes a layer of high chlorophyll in stratified marine and freshwater that may coincide with primary productivity and phytoplankton abundance (Moeller *et al.*, 2019).

Dissolved oxygen concentration is also a general indicator of lake trophic status. Photosynthesis fixes inorganic carbon from the water column and produces oxygen. The interpretation of dissolved oxygen measurement is complicated by the dynamics of photosynthesis during daytime illumination (when the oxygen concentration rises) and the respiration of the phytoplankton and sediments during the night (which consume oxygen and produce carbon dioxide). Ideally the 24-hour integral of the dissolved oxygen concentration and the day/night difference in dissolved oxygen offer the most representative measures of trophic status and of classifying trophic status. Positive dissolved oxygen integral indicates autotrophy while a negative dissolved oxygen integral indicates heterotrophy (Pace and Prairie, 2005).

Nutrient concentration is thus an important limiting factor in the production of phytoplankton quite apart from its significance for understanding the global biogeochemical cycling to which EO methods can contribute. The principal nutrients required by phytoplankton are the biologically available forms of nitrogen, phosphorus, and silicon, plus many other trace nutrients. Water composition is determined by chemical analysis of water samples collected from the waterbody. A strong distinction is made between the nutrient content of the filtered sample, which is assumed to be readily available for phytoplankton growth, and the total nutrient concentrations, which lumps together all the different chemical forms of nitrogen and phosphorus, and includes phosphorus containing minerals, some of which do not sustain phytoplankton growth, and the nitrogen and phosphorus that are already incorporated into phytoplankton. When using EO datasets, consideration must be given to the interplay between mixing dynamics, the optical depth of the water column in relation to the mixing depth, and the capability to support phytoplankton growth, especially in lakes (Wetzel, 2001).

6 Primary production refers to chemical energy directly produced by living organisms from 'new' organic materials, primarily via photosynthesis (see Volume 3A).
7 Secondary production refers to biomass generated by heterotrophic organisms by consuming matter created by primary producers (see Volume 3A).

5.3 Biological

The diversity of biological life forms in surface waters is immense. In this section we review the most relevant characteristics of aquatic biota in terms of:

- microorganisms (microalgae and other microbiota; see Section 5.3.1); and
- macroalgae and macrophytes (see Section 5.3.2).

5.3.1 Microorganisms

5.3.1.1 Phytoplankton and other microalgae

Despite the literal meaning of the term 'phytoplankton' (wandering plants), this collective noun is commonly used to encompass a diverse assemblage of microscopic organisms—bacteria, protists, or single-celled plants—that live in a wide range of aquatic environments (see Section 3.3.1). Myriad species of phytoplankton have adapted to specific water conditions, and can rapidly respond to changes in water clarity, nutrient content, salinity, and temperature (see Sections 5.1 and 5.2). Within the commonly accepted usage of the term, most—but not all—organisms included in the 'phytoplankton community' do photosynthesise (Ian Jameson[8], *pers. comm.*). Phytoplankton species can be differentiated into three groups in terms of the mechanism by which they obtain carbon:

- 'autotrophic'—obtain all their carbon via photosynthesis;
- 'mixotrophic'—consume other organisms as well as photosynthesising; and
- 'heterotrophic'—only derive carbon from other organisms (or zooplankton).

The most common groups of phytoplankton are introduced in Excursus 3.2. Phytoplankton perform a critical role in the aquatic food chain, providing the food supply for a wide range of aquatic animals, such as zooplankton, molluscs and crustaceans (see Figure 3.8). Both marine and freshwater phytoplankton oxygenate water (see Figure 1.15). Most species included in the phytoplankton community are denser than water, so require some water movement to stay suspended, but some species can move independently (see Section 3.3.2.1). Their growth is accelerated by light, heat, water, and nutrients, and decreased by turbidity and cool conditions. Deep outflows from water reservoirs generally do not transfer phytoplankton unless water levels are low, but they can seed the outflowing waters with spores, thus enabling blooms downstream if growing conditions are suitable. In the right conditions, rapid eutrophication can lead to visible algal blooms (see Section 19.5).

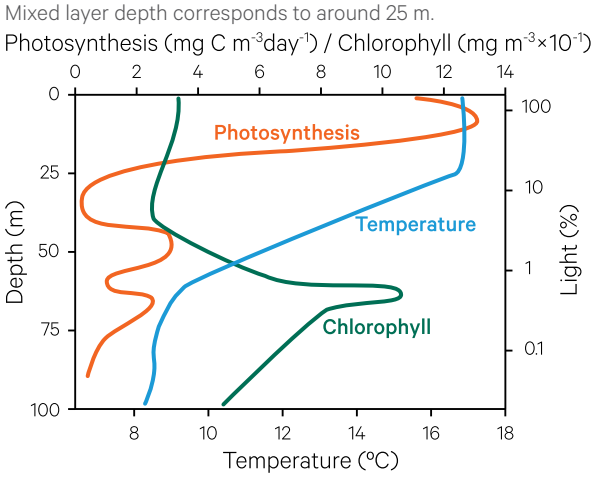
The circulating, surface waters, also called the mixed layer, define the region of greatest photosynthetic activity (see Figure 5.15). Phytoplankton can either fix CO_2 from the atmosphere or obtain it in its dissolved form in water (Hülse *et al.*, 2017). The most productive waters have been observed to be those with shallow mixed layers, either due to a shallow water column or a shallow mixed layer above the thermocline (Kirk, 1994). In seawaters, the mixed layer is typically 20–100 m deep, with the depth varying seasonally in temperate and polar latitudes. In ocean waters where the density gradient is stable, a deep chlorophyll layer also occurs, commonly 10 m thick, near the base of the euphotic zone. Its occurrence is possibly related to nutrient availability (Kirk, 1994).

Phyto—plant
plankton—wandering

A number of laboratory-based analyses can be used to estimate phytoplankton concentration in water samples (Dekker and Hestir, 2012):

- high performance liquid chromatography (HPLC)—accurately measures concentrations of chlorophyll, cyano-phycocyanin, cyano-phycoerythrin, and all other phytoplankton pigments;
- spectrophotometers—accurately identify chlorophyll based on spectral characteristics, with lowered accuracy for cyano-phycocyanin; and
- microscopic cell identification and counting methods—render exact counts for available samples but are time consuming and require expert taxonomic knowledge.

Figure 5.15 Deep chlorophyll maximum for northeast Pacific Ocean



Adapted from: Kirk (1994) Figure 11.1

8 Curator, Australian National Algae Culture Collection, CSIRO, 2014.

The concentration of pigments in natural waters can also be estimated *in situ* using fluorometers to measure fluorescence of chlorophyll and accessory pigments. Fluorometers transmit a light beam of a specific wavelength known to induce chlorophyll fluorescence (such as 443 nm for chlorophyll a) and measure the wavelength of the emitted return (between 650–700 nm, centred on 683 nm, for chlorophyll a.) The algal concentration can be inferred from these measurements (Xing *et al*., 2007). *In situ* optical measurements using submerged hyperspectral light absorption and beam attenuation meters and in-water or above-water spectroradiometers are increasingly popular for inferring phytoplankton concentration from the spectral characteristics of its major pigments (chlorophyll, cyano-phycocyanin, and cyano-phycoerythrin). Similar methods based on EO data have been developed to map phytoplankton based on its chlorophyll concentration (see Section 18.6).

5.3.1.2 Other microbiota

Pathogens, such as viruses, parasites, protozoa, and bacteria from human or animal origins, can be introduced into waterbodies either directly or from wastewater or runoff, and many occur naturally. These are typically identified by indicator species, such as *Escherichia coli* (*E. coli*). Since bacteria in water are generally associated with particulate matter, their concentration is determination in terms of 'clump' count, rather than individual organisms. Microbiological analyses involve incubation trials based on different regimes of medium, temperature, and time. Different groups of organisms can be identified based on their incubation characteristics under different regimes.

Environmental DNA (eDNA) methods are based on molecular analysis of the DNA present in environmental samples (such as sediment, water, faeces, etc), and offers an opportunity to identify the diversity and abundance of organisms using non-invasive sampling techniques (Stewart, 2019). For example, these techniques have been used to determine fish diets in freshwater environments to ultimately derive ecosystem food webs (Rees *et al*., 2019), and derive the composition and spatial patterns of wetland plant communities (Shackleton *et al*., 2019). Similarly, eDNA is relevant to assessing the bacterial and viral composition of natural waters.

5.3.2 Macroalgae and macrophytes

Macroalgae (algae that are visible to the naked eye) are introduced in Section 3.3.2.2. These organisms are important to the ecology of shallow coastal waterways and coral reefs, and are typically found growing attached to hard substrates such as rocks, shells, and coral skeletons (Diaz-Pulido and McCook, 2008; OzCoasts, 2018).

In Australia, macroalgae are valued for their intrinsic biodiversity, providing food and refuge for juvenile fish, crabs, and a wide range of herbivores. Macroalgae thrive in nutrient-rich waters to such an extent that the occurrence of particular types of macroalgae can be indicative of the nutrient status of water. Macroalgal blooms impact the natural environment directly, by reducing light available to macrophytes, or indirectly, where the presence of decomposing mats of macroalgae drastically lower the dissolved oxygen content of the water column, resulting in massive fish kills (Valeila *et al*., 1997; OzCoasts, 2018).

Large aquatic plants or macrophytes (see Section 3.3.2) are also important as primary producers (Pennesi *et al*., 2015) and have been called 'ecological engineers' (Jones *et al*., 1994), that is, organisms that directly or indirectly change the physical state in biotic or abiotic matter and consequently impact the availability of resources to other organisms. All macrophytes offer a diversity of habitats and shelter for aquatic organisms. Rooted macrophytes also help to stabilise the substratum, and by reducing the movement of water, they also increase sedimentation of suspended particles in waterbodies (Bowden *et al*., 2017).

A significant function of macrophytes is their direct uptake of dissolved nutrients (principally nitrogen and phosphorus) from water, and their indirect nutrient cycling via the denitrifying bacteria they support. Accordingly, some macrophytes are being used for biological filtration in sewerage treatment systems.

The condition of macrophyte and macroalgal communities is directly related to the water quality of their environment. Suspended sediments and/or growth of algae will reduce light levels and, in excess levels, can kill submerged vegetation. While such plants live in 'extreme' conditions, others do not re-colonise readily, so need to be managed with care. Anthropogenic disturbance presents the greatest threat to the sustainability of aquatic ecosystems (Wilcox, 1995; Short and Wyllie-Echeveria, 1996; Meinesz, 1999).

Aquatic carbon, particularly DOC, benefit plants by attenuating UVB radiation, binding heavy metals, and generating CO_2, but high concentrations can also retard growth. Humic substances (see Section 5.2.3.1) colour the water, thus reducing light transmission, and contain chemicals that disrupt biochemical processes in aquatic organisms, including photosynthesis of macrophytes (Steinberg *et al.,* 2008).

Recent studies have shown that the concentration of aquatic carbon is increasing in freshwater ecosystems, especially DOC, possibly due to climate change (Reitsema *et al.,* 2018). Changes have also been observed in the composition of DOM (with links to DOC), particularly near urban areas, which render it less susceptible to photodegradation (Williams *et al.,* 2016). Other potential changes related to climate variations, which are likely to impact aquatic organisms, include rising sea level, elevated water temperature, coastal erosion, and increased flow of water carrying anthropogenic sources of POC and DOC (IPCC, 2014).

Ground-based surveys of aquatic vegetation composition are usually in the form of quadrant surveys of very limited spatial scale, and have traditionally involved destructive sampling of biomass at selected locations. Mapping based on EO data has the obvious advantages of being non-destructive, faster, spatially-coherent and consistent, and more cost-effective (Mumby *et al*., 1997; Clark *et al*., 1997). The use of EO to map aquatic vegetation is considered in Section 20.

5.4 Further Information

Kirk (1976, 1994, 2010)

Tomczak (1998)

IMOS State and Trends of Australia's Ocean Report: 1. Physical and Chemical Environment: *https://www.imosoceanreport.org.au/time-series/environment/*

Oceans: *https://www.sciencelearn.org.nz/topics/oceans*

5.5 References

Baird, M. (2018). *Bass Strait Glider Reveals the Ancient Bassian Lake* . IMOS Marine Matters, 29. *https://imos.org.au/fileadmin/user_upload/shared/IMOS_General/documents/newsletters/IMOS_Marine_Matters_Issue_29_WEB.pdf*

Blackburn, D., and Dekker, A.G. (2006). *Remote Sensing study of marine and coastal features and interpretation of changes in relation to natural and anthropogenic processes*. Adelaide Coastal Waters Study Technical Report 6. Prepared for ACWS Steering Committee, Sept 2006. David Blackburn Env. P/L and CSIRO LW.

BOM (2018*). Bureau of Meteorology* website: *http://www.bom.gov.au/*

Bowden, W.B., Glime, J.M., and Riis, T. (2017). Macrophytes and Bryophytes. Ch 13 in *Methods in Stream Ecology* (Vol. 1) 3rd edn. Elsevier Inc. pp. 243–271. *http://dx.doi.org/10.1016/B978-0-12-416558-8.00013-5*

Brando, V., Dekker, A., Marks, A., Qin, Y and Oubelkheir, K. (2006). *Chlorophyll and suspended sediment assessment in a macrotidal tropical estuary adjacent to the Great Barrier Reef: spatial and temporal assessment using remote sensing*. Cooperative Research Centre for Coastal Zone, Estuary & Waterway Management Technical Report 74.

Bricaud, A., Morel, A., and Prieur, L. (1981). Absorption by dissolved organic matter of the sea (yellow substance) in the UV and visible domains, *Limnology and Oceanography*, 26, 43–53.

Carder, K.L., Steward, R.G., Harvey, G.R., and Ortner, P.B. (1989). Marine humic and fulvic acids: Their effects on remote sensing of ocean chlorophyll. *Limnology and Oceanography*, 34(1), 68–81.

Carlson, R.E. (1977) A trophic state index for lakes. *Limnology and Oceanography*, 22(2), 361–369.

Clark, C.D., Ripley, H.T., Green, E.P., Edwards, A.J., and Mumby, P.J. (1997). Mapping and measurement of tropical coastal environments with hyperspectral and high spatial resolution data. *International Journal of Remote Sensing*, 18, 237–242.

Dekker, A.G., and Hestir, E. L. (2012). *Evaluating the Feasibility of Systematic Inland Water Quality Monitoring with Satellite Remote Sensing*. Water for a Healthy Country National Research Flagship, CSIRO.

Diaz-Pulido, G., and McCook, L.J. (2008). Macroalgae (Seaweeds). In *The State of the Reef Report. Environmental Status of the Great Barrier Reef*. (Ed: Chin, A.). Great Barrier Reef Marine Park Authority, Townsville. ISBN: 1 876945 34 6 *http://www.gbrmpa.gov.au/__data/assets/pdf_file/0019/3970/SORR_Macroalgae.pdf*

Furnas, M. (2003). *Catchments and Corals. Terrestrial Runoff to the Great Barrier Reef*. AIMS, Townsville. 334pp.

Greb, S., Dekker, A.G., and Binding, C. (Eds) (2018). *Earth Observations in Support of Global Water Quality Monitoring. IOCCG Report Series, No. 17,* International Ocean Colour Coordinating Group, Dartmouth, Canada.

Hardison, A., Canuel, E., Anderson, I., Tobias, C., Veuger, B., and Waters, M. (2013). Microphytobenthos and benthic macroalgae determine sediment organic matter composition in shallow photic sediments. *Biogeosciences Discussions*, 10, 2791–2834. doi:10.5194/bgd-10-2791-2013.

Harrison, B.A., and Jupp, D.L.B. (1989) *Introduction to Remotely Sensed Data: Part ONE of the microBRIAN Resource Manual*. CSIRO, Melbourne. 156 p.

Hedges, J.I. (2002). Why Dissolved Organics Matter. Ch. 1 in *Biogeochemistry of marine organic matter*. (Eds: D. Hansell and C. Carlson). Academic Press, San Diego. ISBN: 0-12-323841-2

Hülse, D., Arndt, S., Wilson, J.D.;,Munhoven, G., and Ridgwell, A. (2017). Understanding the causes and consequences of past marine carbon cycling variability through models. *Earth Science Review*, 171, 349–382.

Huvenne, V.A.I., Robert, K., Marsh, L., Lo Iacono, C., Le Bas, T., Wynn, R.B. (2018). ROVs and AUVs. In *Submarine Geomorphology* (Eds: A. Micallef, S. Krastel, and A. Savini) Springer Geology. Springer, Switzerland. ISBN: 978-3-319-57851-4

IPCC (2014). Climate Change 2014: *Impacts, Adaptation, and Vulnerability. Part A: Global and Sectoral Aspects. Contribution of Working Group II to the Fifth Assessment Report of the Intergovernmental Panel on Climate Change* (Eds: Field, C.B., Barros, V.R., Dokken, D.J., Mach, K.J., Mastrandrea, M.D., Bilir, T.E., Chatterjee, M., Ebi, K.L., Estrada, Y.O., Genova, R.C., Girma, B., Kissel, E.S., Levy, A.N., MacCracken, S., Mastrandrea, P.R., and White, L.L.). Cambridge University Press, Cambridge, United Kingdom and New York, NY, USA, 1132 p.

Jones, C.G., Lawton, J.H., and Shachak, M. (1994). Organisms as ecosystem engineers. *Oikos,* 69, 373–386.

Kirk, J.T.O. (1976). *Light and Photosynthesis in Aquatic Ecosystems*. Cambridge University Press, Cambridge. 414 p.

Kirk, J.T.O. (1994). *Light and Photosynthesis in Aquatic Ecosystems*, 2nd Edn. Cambridge University Press, Cambridge. 509 p.

Kirk, J.T.O. (2010) *Light and Photosynthesis in Aquatic Ecosystems*, 3rd Edn. Cambridge University Press, Cambridge. 662 p.

Leenheer, J. A., and Croué, J. (2003). Characterizing dissolved aquatic organic matter. *Environmental Science and Technology*, 37, 18A–26A. doi:10.1021/es032333c

Lindell, T., Pierson, D., Premazzi, G., and Ziliolli, E. (1999). (Eds) *Manual for monitoring European lakes using remote sensing techniques*. Office for official publications of European Communities, Luxembourg. 161 p.

MacKinnon, M.R., and Herbert. B.W. (1996). Temperature, Dissolved Oxygen and Stratification in a Tropical Reservoir, Lake Tinaroo, Northern Queensland, Australia. *Marine Freshwater Research*, 47, 937–949.

Meinesz, A. (1999). *Killer algae: the true tale of a biological invasion*. University of Chicago Press, Chicago. 360 p.

Minnett, P., and Kaiser-Weiss, A. (2012). *Near-surface oceanic temperature gradients*. GHRSST Discussion document, version 12, Jan 2012. *https://www.ghrsst.org/wp-content/uploads/2021/04/SSTDefinitionsDiscussion.pdf*

Moeller, H.V., Laufkötter, C., Sweeney, E.M., and Johnson, M.D. (2019). Light-dependent grazing can drive formation and deepening of deep chlorophyll maxima. *Nature Communications*, 10, 1978. *https://doi.org/10.1038/s41467-019-09591-2*

Monk J, Barrett N, Bridge T, Carroll A, Friedman A, Ierodiaconou D, Jordan A, Kendrick G, and Lucieer V. (2018). Marine sampling field manual for autonomous underwater vehicles (AUVs). In *Field Manuals for Marine Sampling to Monitor Australian Waters*. (Eds: Przeslawski, R., Foster, S.). National Environmental Science Programme (NESP). pp. 65–81.

Mumby, P.J., Green, E.P., Edwards, A.J., and Clark, C.D. (1997). Measurement of seagrass standing crop using satellite and digital airborne remote sensing. *Marine Ecology Progress Series*, 159, 51–60.

NSW NPI (2015). *Management of coastal lakes and lagoons in NSW* webpage, NSW Department of Primary Industries website: *https://www.dpi.nsw.gov.au/fishing/habitat/aquatic-habitats/wetland/coastal-wetlands/management-of-coastal-lakes-and-lagoons-in-nsw*

OzCoasts (2018). *OzCoasts Australian Online Coastal Information (Geoscience Australia) website*: *http://www.ozcoasts.gov.au/index.jsp*

Pace, M.L., and Prairie, Y.T. (2005). Respiration in Lakes. Ch 7 in *Respiration in Aquatic Ecosystems* (Eds: P.A. del Giorgio and P.J. le B. Williams) Oxford University Press, Oxford. pp 103–121.

Pegau, W.S., and Zaneveld, J.R.V. (1993). Temperature-dependent absorption of water in the red and near-infrared portions of the spectrum. *Limnology and Oceanography*, 38 (1), 188–192.

Pennesi, C., Rindi, F., Totti, C., and Beolchini, F. (2015). Marine Macrophytes: Biosorbents. In: *Springer Handbook of Marine Biotechnology*. (Ed: Kim, S.K.) Springer Handbooks. Springer, Berlin, Heidelberg.

Pozdnyakov D.V., and Grassl, H. (2003). *Colour of inland and coastal waters: A methodology for its interpretation*. Springer-Praxis, Chichester.

Rees, G.N., Shackleton, M.E., Watson, G.O., Dwyer, G.K., and Stoffels, R.J. (2019). Metabarcoding demonstrates dietary niche partitioning in two coexisting blackfish species. *Marine and Freshwater Research*, 71, 512–517. *https://doi.org/10.1071/MF18491*

Reitsema, R.E., Meire, P., and Schoelynck, J. (2018). The Future of Freshwater Macrophytes in a Changing World: Dissolved Organic Carbon Quantity and Quality and Its Interactions With Macrophytes. *Frontiers in Plant Science*, 9, 629. doi:10.3389/fpls.2018.00629

Sachse, A., Henrion, R., Gelbrecht, J., and Steinberg, C. E. W. (2005). Classification of dissolved organic carbon (DOC) in river systems: Influence of catchment characteristics and autochthonous processes. *Organic Geochemistry*, 36, 923–935. doi:10.1016/j.orggeochem.2004.12.008

Schroeder, T, Devlin, M.J., Brando, V.E., Dekker, A.G., Brodie, J.E., Clementson, L.A., and McKinna, L. (2012). Inter-annual variability of wet season freshwater plume extent into the Great Barrier Reef lagoon based on satellite coastal ocean colour observations. *Marine Pollution Bulletin*, 65, 210–223. doi:10.1016/j.marpolbul.2012.02.022

Seritti A., Manca B.B., Santinelli C., Murru E., Boldrin A., and Nannicini L. (2003). Relationships between dissolved organic carbon (DOC) and water mass structures in the Ionian Sea (winter 1999). *Journal of Geophysical Research*, 108(C9), 8112. doi:10.1029/2002JC001345

Shackleton, M.E., Rees, G.N., Watson, G., Campbell, C., and Nielsen, D. (2019). Environmental DNA reveals landscape mosaic of wetland plant communities. *Global Ecology and Conversation*, 19, e00689. *https://doi.org/10.1016/j.gecco.2019.e00689*

Shafron, M., Croome, R., and Rolls, J. (1990). Water Quality. Ch 9 in *The Murray* (Eds: Mackay, N., and Eastburn, D.). Murray Daring Basin Commission, Canberra.

Sherman, B., (2005). *Hume Reservoir Thermal Monitoring and Modelling*. Final Report for State Water as agent for MDBC. CSIRO Land and Water Client Report, April 2005.

Short, F.T., and Wyllie-Echeveria, S. (1996). Natural and human-induced disturbance of seagrasses. *Environmental Conservation*, 23 (1), 17–27. doi:10.1017/S0376892900038212

Smyth, K., and Elliot, M. (2016). Effects of changing salinity on the ecology of the marine environment. In *Stressors in the Marine Environment* (Eds: Solan, M. and Whitely, N.M.). Oxford University Press, Oxford. doi:10.1093/acprof:oso/9780198718826.003.0009

Steinberg, C.E.W., Meinelt, T., Timofeyev, M.A., Bittner, M., and Menzel, R. (2008). Humic substances (review series). Part 2: Interactions with Organisms. *Environmental Science and Pollution Research*, 15, 128–135. doi:10.1065/espr2007.07.434

Stewart, K.A. (2019). Understanding the efects of biotic and abiotic factors on sources of aquatic environmental DNA. *Biodiversity and Conservation*, 28, 983–1001. *https://doi.org/10.1007/s10531-019-01709-8*

Te Ara (2018). *Unique geothermal fields* webpage, The Encyclopedia of New Zealand website: *https://teara.govt.nz/en/hot-springs-mud-pools-and-geysers/page-1*

Tomczak, M. (1998). *Shelf and Coastal Oceanography* website: *https://incois.gov.in/Tutor/ShelfCoast/index.html*

UNESCO (1981a). The Practical Salinity Scale 1978 and the International Equation of State of Seawater 1980. *UNESCO Technical Papers in Marine Science 36*. 25 p.

UNESCO (1981b). Background papers and supporting data on the Practical Salinity Scale 1978. *UNESCO Technical Papers in Marine Science 37*. 144 p.

Valeila, I., McClelland, J., Hauxwell, J., Behr, P.J., Hersh, D., and Foreman, K. (1997). Macroalgal blooms in shallow estuaries: Controls and ecophysiological and ecosystem consequences. *Limnology and Oceanography*, 42(5–2), 1105–1118.

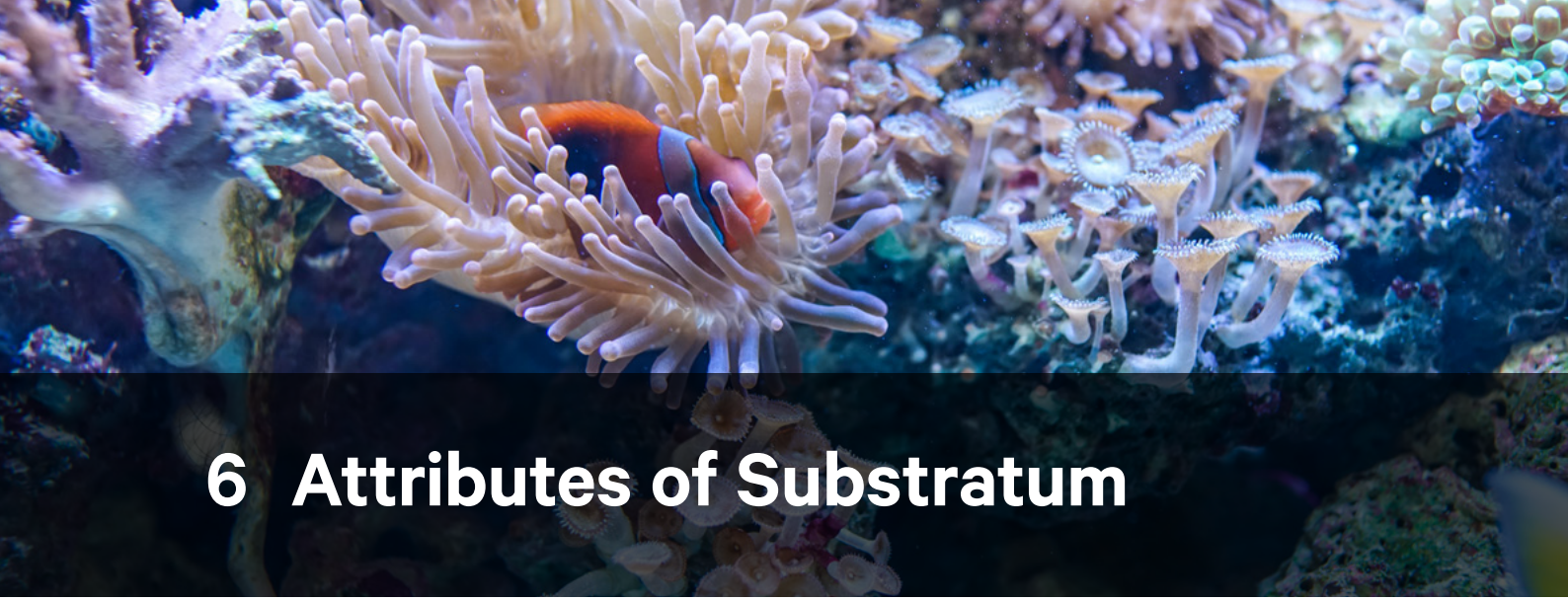
Webster, I.T., Atkinson, I., Bostock, H., Brooke, B., Douglas, G., Ford, P., Hancock, G., Herzfeld, M., Leeming, R., Lemckert, C., Margvelashvili, N., Noble, B., Oubelkheir, K., Radke, L., Revill, A., Robson, B., Ryan, D., Schacht, C., Smith, C., Smith, J., Vicente-Beckett, V., and Wild-Allen, K. (2006). *The Fitzroy Contaminants Project. A Study of the Nutrient and Fine-Sediment Dynamics of the Fitzroy Estuary and Keppel Bay.* Cooperative Research Centre for Coastal Zone, Estuary and Waterway Management Technical Report #42, Coastal CRC, Queensland. ISBN 1 921017 56 2

Wetzel, R.G. (2001). *Limnology.* 3rd Edn. Academic Press. ISBN 9780127447605

Wilcox, D.A. (1995). Wetland and aquatic macrophytes as indicators of anthropogenic hydrologic disturbance. *Natural Areas Journal,* 15(3), 240–248.

Williams, C.J., Frost, P.C., Morales-Williams, A.M., Larson, J.H., Richardson, W.B., Chiandet, A.S., and Xenopoulos, M.A. (2016). Human activities cause distinct dissolved organic matter composition across freshwater ecosystems. *Global Change Biology,* 22, 613–626. doi:10.1111/gcb.13094

Xing, X.-G., Zhao, D-Z., Liu, Y.-G., Yang, J._H., Xiu, P., and Wang, L. (2007). An overview of remote sensing of chlorophyll fluorescence. *Ocean Science Journal*, 42(1), 49–59.



6 Attributes of Substratum

The solid surface that underlies a waterbody is called the seabed or seafloor. The generic term substratum describes an underlying layer or substance beneath the ground surface. In an aquatic environment, the substratum layer rests on the seabed (or lithosphere) and may comprise a variety of materials such as sand, silt, mud, rocks, and coral (see Section 1.3.3). It forms the interface between the seabed and the water column and hosts a range of aquatic organisms, by providing both food and habitat (see Section 3).

Variations in the substratum can be described in terms of four interrelated attributes:

- waterbody depth (see Section 6.1);
- geomorphic features (see Section 6.2);
- composition (see Section 6.3); and
- benthos (see Section 6.4).

6.1 Waterbody Depth

Bathymetry measures the vertical distance from the water surface to the substrate in a waterbody (see Section 13). As introduced in Section 5, the depth of a waterbody impacts several physical, chemical, and biological attributes of the water column. Both light penetration and temperature decrease with increasing water depth in waterbodies (see Section 8). In oceans, light levels below 200 m are insufficient for photosynthesis, but this may decrease to 1 m water depth in very turbid waterbodies (see Section 5.1.5).

The depth of the substratum directly impacts the type of organisms, both plants and animals, which can exist there. Accordingly, classification of benthic animals is based on two primary depth regions:

- shallower littoral region—with more light and warmth, supporting primary producing organisms; and the
- deep region—with virtually no light, containing colder waters, accommodating organisms that do not rely on sight, comprising the bathyal, abyssal, and hadal zones (see Section 6.4).

However, it is not only the depth of the substratum but its shape that is ecologically significant (see Section 6.2). Water movement also tends to be reduced at greater water depths, which in turn impacts the materials that comprise the substratum (see Section 6.3).

6.2 Geomorphic Features

Marine geomorphology is the study of landforms, their processes, form and sediments at the seabed. Geomorphology is scale dependent, and significant for a range of marine activities, such as:

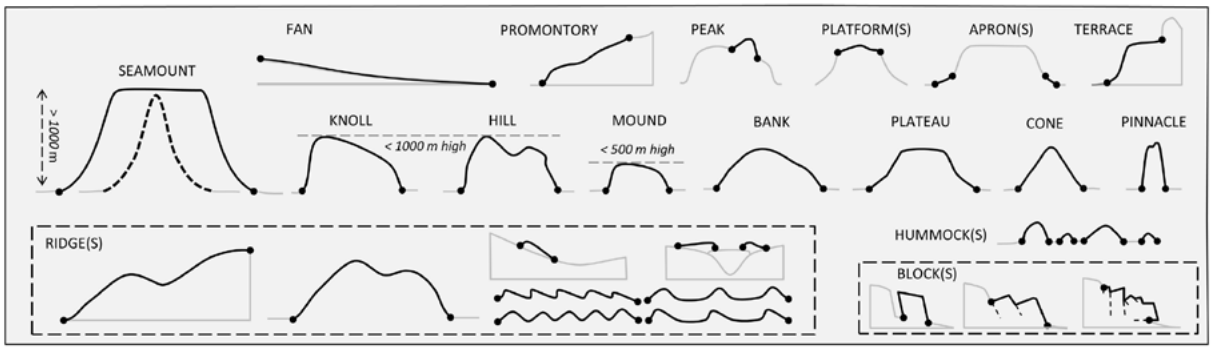
- designing and monitoring Marine Protected Areas (MPA; see Excursus 20.2);
- understanding benthic ecosystems and seafloor geology (see Sections 2.2, 3 and 20); and
- assessing living and non-living seabed resources, including those with economic value, such as seabed mining (Harris and Baker, 2012; Harris *et al.*, 2014).

The major geomorphic zones (continental shelf, the continental slope, the continental rise, and the abyssal plain) are continental in scale (see Figure 1.9). In bathymetric terms these broad zones are also called Primary Bathymetric Units (see Excursus 13.1). For most practical purposes, the continental zones are subdivided into distinct geomorphic features, which are regional and local in scale (Geo-Seas, 2012). Dove et al. (2020) defined 40 geomorphic features based on a two-part classification of morphology (bathymetric highs and lows, plus surfaces and lineaments; see Figure 6.1), and geomorphology. Definitions of these generic features are listed in Table 6.1.

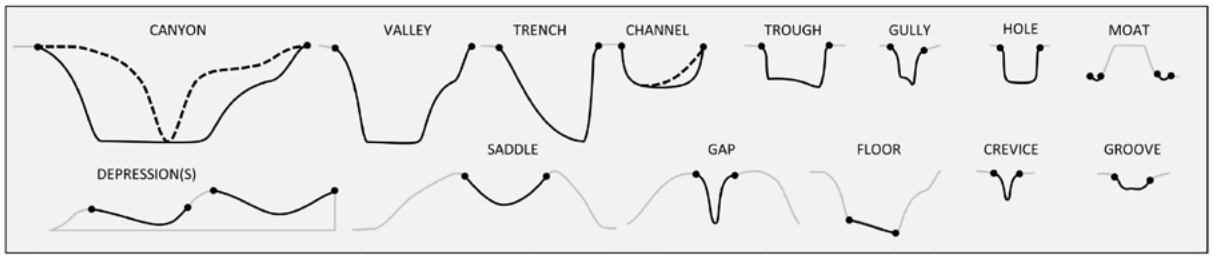
Background image: Coral substrate. **Source:** Michelle Raponi, Pixabay. Retrieved from *https://pixabay.com/photos/underwater-coral-reef-fish-ocean-3250644/*

Figure 6.1 Morphological features

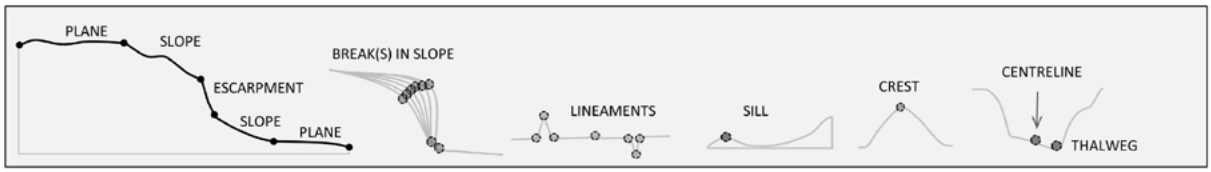
a. Bathymetric highs



b. Bathymetric lows



c. Planar surfaces, inclined planes and surfaces



Source: Dove *et al.* (2020) Figure 3

Table 6.1 Generic geomorphic features

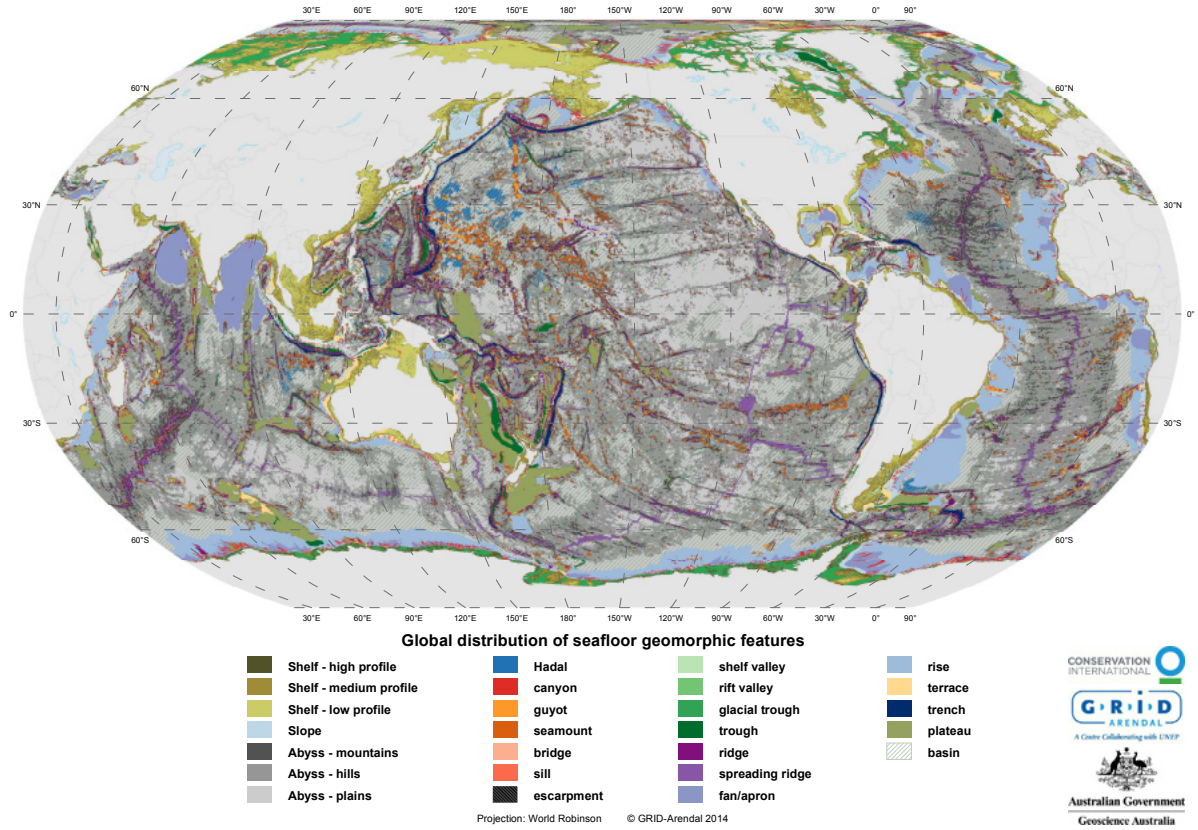
Term	Definition
APRON	A gently-dipping surface, occurring at the base of a bathymetric high, that is elevated relative to the adjacent seafloor.
BANK	An elevation of the seafloor, often found in water depths less than 200 m (adapted from IHO, 2019). *BANKS are lower elevation than SEAMOUNTS, and tend to occur in shallower water.*
BLOCK	A discrete, usually angular mass comprising at least two relatively flat surfaces.
BREAK IN SLOPE	A marked and/or abrupt change in slope. *BREAK IN SLOPE can be used to define the limit of other features (e.g. SHELF, PLATFORM, ESCARPMENT).*
CANYON	A typically elongated, steep-sided bathymetric low that generally deepens down-slope (modified from IHO, 2019). *CANYONS tend to be higher gradient and more complex features than CHANNELS and are larger and more sinuous than GULLIES. VALLEYS tend to have a more limited depth range than CANYONS.*
CENTRELINE	A line that represents the mid-line long axis of a feature. Contrast CENTRELINE with THALWEG and CREST, which define the lines of lowest and highest elevation, respectively, along an elongate feature.
CHANNEL	A general term for an elongated bathymetric low (adapted from IHO, 2019). *CHANNELS tend to have flatter and lower gradient FLOORS than GULLIES and CANYONS, and usually have more variable cross-sections than TROUGHS.*
CONE	A topographic high of generally conical shape, which may have a truncated peak. *CONES have more pointed peaks and are more symmetrical than KNOLLS.*
CREST	A line of highest elevation along a bathymetric high, the lateral position of which can vary longitudinally. *CRESTS contrast with CENTRELINES, which define mid-line axes along elongated features.*
CREVICE	An elongated narrow opening (adapted from Goudie, 2014). *Unlike CANYONS, CREVICES do not necessarily deepen downslope, and unlike TROUGHS, they are not flat bottomed.*

Term	Definition
DEPRESSION	A general term for a closed-contoured bathymetric low. *DEPRESSIONS vary in scale from small local features to larger basins. They generally have lower gradient sides than HOLES.*
ESCARPMENT	A steep slope, separating areas of relatively lower slope (modified from IHO, 2019).
FAN	An elevated feature which expands (and typically descends) from a locus to a commonly curved outer margin.
FLOOR	A relatively broad and lower gradient feature within a bathymetric low, flanked by higher and steeper gradient features.
GAP	A narrow break in an elevated feature (modified from IHO, 2019). *GAPS are generally narrower than SADDLES.*
GROOVE	An elongated, narrow and relatively shallow bathymetric low which commonly occurs in parallel or sub-parallel groups. *Unlike GAPS, GROOVES are elongated features, and often occur in groups. GROOVES tend to have higher length/width ratios than CREVICES*
GULLY	A steep-sided, low sinuosity, relatively high-gradient channel. *GULLIES are typically smaller than CANYONS.*
HILL	A distinct elevation generally of irregular shape, less than 1000 m above the surrounding relief as measured from the deepest isobath that surrounds most of the feature (IHO, 2019). *HILLS have more irregular profiles than KNOLLS, and their length generally exceeds their height (contrast with PEAKS). They are also smaller than SEAMOUNT, and larger than individual HUMMOCKS.*
HOLE	A sub-circular (in planform) bathymetric low with steep walls and a generally flat FLOOR (modified from IHO, 2019). HOLES generally have steeper sides than DEPRESSIONS.
HUMMOCK	A small KNOLL or MOUND, which commonly occurs in groups. HUMMOCKS are generally smaller than KNOLLS and HILLS
KNOLL	A distinct elevation with a smooth, commonly rounded profile, <1000 m above the surrounding relief (modified from IHO, 2019). *KNOLLS have more regular profiles than HILLS, and their width generally exceeds their height (contrast with PEAKS). They are also smaller than SEAMOUNTS, and larger than individual HUMMOCKS.*
LINEAMENT	A linear to curvilinear topographic feature of positive, negative or indeterminate relief. May be discontinuous with variable relief (positive to negative) along its length.
MOAT	An annular or partially annular bathymetric low typically located at the base of isolated elevation (modified from IHO).
MOUND	A distinct elevation with a variable, sometimes rounded profile which is generally less than 500 m above the surrounding seafloor (modified from IHO, 2019).
PEAK	A prominent, commonly pointed elevation rising from a larger feature (modified from IHO, 2019)
PINNACLE	A spire-shaped pillar, either isolated or rising from a larger feature (IHO, 2019).
PLANE	A flat, or sub-horizontal surface.
PLATEAU	A generally closed-contoured, relatively flat-topped bathymetric high with one or more relatively steep sides (modified from IHO, 2019).
PLATFORM	A generally broad, planar surface that is at least partially elevated, and lower gradient, than the surrounding areas (adapted from Goudie, 2014).
PROMONTORY	A protrusion extending from a bathymetric high into deeper water (adapted from IHO, 2019).
RIDGE	An elongated elevation of varying complexity, size and gradient (length > width) (modified from IHO, 2019).
SADDLE	A broad pass in an elevated feature (modified from IHO, 2019). *SADDLES are generally broader (relative to their height) than GAP*
SEAMOUNT	A prominent feature rising more than 1000 m above the surrounding relief (modified from IHO, 2019). *SEAMOUNTS are larger than KNOLLS and HILLS (<1000 m) and may incorporate PEAKS (and other features).*
SILL	A relatively shallow elevated feature between (or adjacent to) bathymetric lows (e.g. DEPRESSIONS) (modified from IHO, 2019).
SLOPE	An inclined surface.
TERRACE	A generally elongated and planar feature consisting of an upper planar surface, and relatively steeper descending slope. The planar surface is bounded on one side by a steeper ascending slope (modified from IHO, 2019). A TERRACE is not closed-contoured like a PLATEAU, and its lower-gradient surface can be mapped as a PLATFORM.
THALWEG	A line of lowest elevation along an elongate bathymetric low, the lateral position of which can vary longitudinally. *THALWEGS contrast with CENTRELINES, which define mid-line axes along bathymetric lows.*
TRENCH	A long, deep, asymmetrical bathymetric low with relatively steep sides (adapted from IHO, 2019). Unlike TROUGHS, TRENCHS are typically asymmetric in cross-section.
TROUGH	An elongate bathymetric low, generally wide and flat bottomed with symmetrical and sub-parallel sides (modified from IHO, 2019). Unlike DEPRESSIONS, TROUGHS are not necessarily closed-contoured, and unlike VALLEYS, they do not always deepen down-slope. Unlike TRENCHS, TROUGHS are typically symmetrical in cross-section
VALLEY	An elongated bathymetric low, typically occurring between prominent bathymetric highs, which generally widens and deepens down-slope (modified from IHO). *VALLEYS have more limited depth ranges than CANYONS.*

Source: Dove *et al.* (2020)

Figure 6.2 Global Seafloor Geomorphic Feature map (GSFM)

This is the first digital, global map showing the distribution of seafloor geomorphic features.



Source: Conservation International, GRID-Arsenal and Geoscience Australia. Retrieved from: *http://www.bluehabitats.org*

A classification of 29 geomorphic feature categories was used to produce the first digital Global Seafloor Geomorphic Feature map (GSFM; Harris *et al.*, 2014; see Figure 6.2). Based on Shuttle Radar Topography Mapping (SRTM30_PLUS) data and other datasets, this product has enabled global and regional estimates of physiographic characteristics, such as area, abundance, and size, for a range of geomorphic features, and comparisons of selected characteristics in different geographic regions.

6.3 Composition

The substratum may comprise rock, reefal material, sand, and/or sediment that have settled out of the water column. These components can occur in varying combinations, depending on local geology and water movement. Loose materials offer a medium for microbial and plant growth, and a wide range of habitats for animal life (see Section 3). The packing density of substrate materials is related to grain size, which regulates the flow of water and determines the availability of dissolved oxygen to benthic fauna. The quality of the benthic environment is essentially determined by the organic content of sediments and the size and shape of their particles.

Four types of seafloor substrates are recognised to support specific benthic organisms:

- sandy soft (psammon)—occurring along exposed shorelines, these loose sands and gravels are regularly moved by waves, facilitating circulation of oxygen and nutrients for corals, nematodes, echinodermata, and sponges;
- muddy soft (pelos)—offer more stable and anoxic conditions that are endured by bivalves and annelids, which can siphon oxygen and nutrients from the water column;
- hard—support stationary fauna with tentacles and mobile crinoidea;
- secondary hard—unconsolidated organic and inorganic materials accumulate on the ocean floor and coalesce to support annelid tube worms.

In Australia, Geoscience Australia (GA) is responsible for the national marine samples database (MARS), which quantifies and catalogues seabed sediment samples from Australian marine waters (Passlow *et al.*, 2005). MARS includes quantitative analyses of > 40,000 sediment samples, as well as subsample records of grain size, mud, sand, gravel, and/or carbonate concentrations (see Section 5.4). Sediment cores are analysed in terms of mineralogy, age, geochemical properties, bulk density, p-wave velocity, porosity, and magnetic susceptibility. Relationships between sediment properties and geomorphic features have contributed to the development of the national benthic bioregionalisation (CoA, 2005).

6.4 Benthos

Depending on waterbody depth and composition, the substratum may support a variety of plant and animal life, including microphytobenthos, seagrass, macroalgae, and corals. In favourable conditions, a rich community of organisms coexist on and in the substratum. Most of the sand and mud dwelling organisms live on detritus from decomposed plant material. In some environments, the patterns of benthic marine biodiversity are clearly related to abiotic attributes, such as latitude, waterbody depth, current velocity, and substrate type (Roff *et al.*, 2003; Post *et al.*, 2006), allowing relevant attributes to be used as surrogates of biodiversity (McArthur *et al.*, 2010). The Australian standardised nomenclature for benthic habitat classification is given in Butler *et al.* (2017).

The diverse group of benthic organisms is commonly divided into overlapping categories based on size:

- microbenthos—microscopic organisms, such as microphytobenthos (less than 0.1 mm);
- meiobenthos—tiny, motile fauna living in aquatic sediments (0.1–1.0 mm);
- macrobenthos—visible invertebrates and macroalgae living on or in submerged sediments (greater than 1.0 mm);

or location:

- endobenthos—smaller organisms living in sandy or muddy sediments; and
- epibenthos—larger organisms living on the seabed and comprising around 80% of all benthic fauna.

Ocean benthic biome definitions are based on the water column depth above the substratum (see Figure 3.1). Their substrata support varying aquatic organisms:

- sublittoral zone—substratum of the continental shelf with sufficient light penetration to allow photosynthesis, which supports a rich diversity of plant and animal life;
- bathyal zone—substratum of the continental slope, which supports fewer organisms;
- abyssal zone—substratum of the deep ocean, which supports hardy organisms that can survive on detritus sifted from sediments; and
- hadal zone—substratum of hydrothermal vents in deep ocean trenches, which only supports invertebrates such as tubeworms and clams that live in microscopic Archaea.

The National Marine Bioregionalisation (NMB) defines a benthic bioregionalisation of Australia's EEZ as well as a pelagic regionalisation of water column structure (CoA, 2005; see Section 2.2).

...spatial changes in seabed biota are strongly related to mud and gravel content, seabed disturbance from waves and currents, water depth, and geomorphology.
(Heap, 2006)

6.5 Further Information

Benthic bioregionalisation for Australian EEZ: CoA (2005)

Bentho-Pelagic Processes: Alfred Wegener Institute: *https://www.awi.de/en/science/biosciences/bentho-pelagic-processes.html*

Geo-Seas: *http://www.geo-seas.eu/; http://www.geo-seas.eu/documents/geoseas/html_page/Geo-Seas_D10_5_B.pdf*

Keene *et al.* (2008)

Marine Sediments Database (MARS): GA (2018), Passlow *et al.* (2005); *https://ecat.ga.gov.au/geonetwork/srv/eng/catalog.search?node=srv#/metadata/69869*

6.6 References

Butler, C., Lucieer, V., Walsh, P., Flukes, E., and Johnson, C. (2017). *Seamap Australia [Version 1.0] the development of a national benthic marine classification scheme for the Australian continental shelf*. Seamap Australia, University of Tasmania. ISBN: 978-1-925646-61-0

CoA (2005). *National Marine Bioregionalisation of Australia. Summary*. Department of Environment and Heritage, Canberra, Australia.

Dove, D., Nanson, R., Bjarnadóttir, L.R., Guinan, J., Gafeira, J., Post, A., Dolan, M.F.J., Stewart, H., Arosio, R., and Scott, G. (2020). *A two-part seabed geomorphology classification scheme: (v.2)*. Open Report Prepared by the MIM-GA Geomorphology Working Group. doi:10.5281/ZENODO.4075248

GA (2018) *Marine Sediments (MARS) Database* webpage, Geoscience Australia website: *https://ecat.ga.gov.au/geonetwork/srv/eng/catalog.search?node=srv#/metadata/a05f7892-eef2-7506-e044-00144fdd4fa6*

Geo-Seas (2012). *Pan-European infrastructure for management of marine and ocean geological and geophysical data. Deliverable 10.5: Standards for seabed habitat mapping (Part B: Terrain)*. *http://www.geo-seas.eu/documents/geoseas/html_page/Geo-Seas_D10_5_B.pdf*

Goudie, A. (2014). *Alphabetical glossary of geomorphology, version 1.0*. Electronic edition of the International Association of Geomorphologists (IAG). 2014. 84 p.

Harris, P.T., and Baker, E.K. (Eds.) (2012). *Seafloor Geomorphology as Benthic Habitat: GeoHab Atlas of Seafloor Geomorphic Features And Benthic Habitats*. Elsevier, Amsterdam, p. 947.

Harris, P.T., Macmillian-Lawler, M., Rupp, J., and Baker, E.K. (2014). Geomorphology of the oceans. *Marine Geology*, 352, 4–24.

Heap, A. (2006). Classifying Australia's seascapes for marine conservation. *AusGeo News 84*, March 2006. Geoscience Australia.

IHO (2019) *Standardization of Undersea Feature Names: Guidelines Proposal form Terminology*. (Edition 4.2.0 October, 2019). Monaco, International Hydrographic Bureau, IHO Publication B–6.

Keene, J., Baker, C., Tran, M. and Potter, A. (2008). *Geomorphology and Sedimentology of the East Marine Region of Australia*. Geoscience Australia, Record 2008/10. Geoscience Australia, Canberra. 262 p.

McArthur, M.A., Brooke, B.P., Przeslawski, R., Ryan, D.A., Lucieer, V.I., Nichol, S., McCallum, A.W., Mellin, C., Cresswell, I.D., Radke, L.C. (2010). On the use of abiotic surrogates to describe marine benthic biodiversity. *Estuarine, Coastal and Shelf Science*, 88, 21–32.

Passlow, V., Rogis, J., Hancock, A., Hemer, M., Glenn, K and Habib, A. (2005). *Final Report, National Marine Sediments Database and Seafloor Characteristics Project*. Geoscience Australia, Record 2005/08.

Post, A.L., Wassenberg, T.J., Passlow, V. (2006). Physical surrogates for macrofaunal distributions and abundance in a tropical gulf. *Marine and Freshwater Research*, 57, 469e483.

Roff, J.C., Taylor, M.E., and Laughren, J. (2003). Geophysical approaches to the classification, delineation and monitoring of marine habitats and their communities. *Aquatic Conservation: Marine and Freshwater Ecosystems*, 13(1), 77–90. doi:10.1002/aqc.525



7 Attributes of Waterbodies

Waterbodies can be described in terms of a number of attributes, including:

- observed colour (see Section 7.1);
- extent and permanence (see Section 7.2);
- depth and volume (see Section 7.3);
- carbon cycling (see Section 7.4); and
- dynamics (see Section 7.5).

7.1 Observed Colour

The colour of a waterbody, when observed from above its surface, critically depends on illumination and viewing conditions (see Sections 5.1.4 and 8). It can also vary with changes in:

- the shape, texture, and surface tension of the surface (see Sections 4.2, 4.3, and 4.4 respectively);
- the presence of floating matter (see Section 4.6) and ice cover (see Section 4.7);
- the colour of the water column (see Section 5); and/or
- the colour of the underlying water column and/or substratum (see Section 6).

Oil slicks and other pollutants can dampen wave action and increase reflectance of some wavelengths (see Section 19.4.3). Ocean surface waves create 'whitecaps' as they break, which change the observed water colour (Estep and Arnone, 1994). Algal blooms floating on the water surface can also dramatically change the apparent water colour (see Section 19.5).

Water surface roughness, or texture, changes the way light is reflected from the surface and can result in sunglint and skyglint (see Section 4.3). Skyglint is caused by diffuse blue skylight, or in cloudy conditions diffuse white to grey light, being reflected from the water surface, and only comprises a small proportion of diffuse upwelling radiation (see Section 8.1.3).

7.2 Extent and Permanence

Current knowledge about surface water extent is valuable for a wide range of applications, including:

- updating cartographic boundaries;
- monitoring floodwaters;
- assessing aquatic habitats;
- delineating wetland dynamics;
- determining minimum flow requirements of rivers; and
- modelling hydrology for water resource management.

Surface water is readily discernible from both bare and vegetated land by using near infrared (NIR) reflectance (see Section 5.1.4), since while NIR wavelengths are absorbed by pure water, they are strongly reflected by dry land surfaces and vegetation (see Volume 3A). In highly turbid waters the NIR reflectance may increase slightly (see Section 5.1.5).

Background image: The northeastern portion of Lake Carnegie, a large ephemeral lake in central WA, is imaged by the Flock-1 satellite on 26 January 2016.
Source: Planet Labs Inc. (CC-BY-SA 4.0). Retrieved from *https://www.planet.com/gallery/#!/post/lake-carnegie*

Most difficulties with delineating land-water boundaries in EO imagery are related to floating plants, algal scum, or overhanging riparian vegetation. The interface between land and water, however, generally involves varying water depth and colour, which may make the boundaries of waterbodies more difficult to delineate using optical imagery. Other forms of EO data, including TIR and radar imagery, can also be used to delineate surface water extent (see Section 11).

Many Australian waterbodies are ephemeral, and their permanence has been characterised by analysis of EO image time series (see Volume 1A—Excursus 5.1). EO methods for monitoring the permanence of waterbodies are described in Section 11.5.

7.3 Depth and Volume

The depth of a waterbody invariably changes across its extent. As well as obvious differences between shallow borders and deep, central areas, the topography of submerged zones can vary significantly due to features such as coral reefs, and underwater ridges and trenches (see Sections 2.2 and 6.2). Seafloor shape impacts water movement (see Section 16) and the distribution of marine biota (see Section 20).

The volume of water in a waterbody is a function of the depth of the water column (see Section 5.1.1), the extent of the water surface (see Section 11) and the depth profile(s) of the waterbody (see Section 12). The depth and extent of the water column, however, can change over time with precipitation, runoff, outflow, and evaporation. The depth profile of a waterbody also varies over time with the processes of sedimentation, erosion and dredging.

Depth measurements in water are called soundings. Originally measured using sounding lines from ships, a range of EO technologies can now be used to measure water depth in both shallow and deep waters (see Section 10). Such measurements at individual points can be processed into map or image form to create bathymetric charts. The Nippon Foundation-GEBCO Seabed 2030 project is coordinating and extending bathymetric datasets around the globe to create a public map of seafloor topography by 2030 (see Excursus 7.1).

Depth sounding instruments include lidar (based on laser) and sonar (based on sound; see Sections 10 and 13.3.2). Lidar is deemed more cost-effective than multi-beam acoustic surveys for coverages of less than 100 km^2 and water depths less than 50 m, although the cost of lidar surveys varies significantly with sampling density (Purkis and Brock, 2013; see Section 13.4.1). Shallow seafloor topographic maps have also been derived from synthetic aperture radar (SAR) imagery, although the processing requires imagery to be acquired under favourable conditions involving tidal flow and requires depth soundings for calibration (see Section 13.3.1).

Light attenuation in pure water increases with increasing water depth (see Figure 5.10). This relationship allows multispectral and hyperspectral imagery to be used to estimate water depth in optically shallow waters (that is, where there is a measurable amount of light being reflected from the benthos through the water column and through the air-water interface; Brando *et al.,* 2009). Such methods rely on the varying attenuation properties of different wavelengths of light through water (see Section 5.1.4). In shallow waters, changes in substrate colour also impact optical properties (see Section 8.4.3). While these estimates are not the same as depth sounding, and rarely achieve the same accuracy or maximum depth that may be obtained using depth sounding techniques, they are spatially comprehensive. Stereophotogrammetric methods using high resolution imagery with multi-angle sensors have been used in conjunction with multispectral and hyperspectral methods to determine water depth (Collings *et al*., 2018; see Section 13.4.2).

Excursus 7.1—Nippon Foundation-GEBCO Seabed 2030 Project

Source: GEBCO (2017)
Further Information: Mayer *et al.* (2018)

Seabed 2030, a collaborative project between the Nippon Foundation and the General Bathymetric Chart of the Oceans (GEBCO), intends to collate all current bathymetric data to create a 'definitive', publicly-available map of the world ocean floor by 2030. Launched in 2017 at the UN Ocean Conference, this project seeks to map the extensive areas of seafloor topography that are currently unmapped—these are estimated to be up to 80% of the global seafloor (Mayer *et al.*, 2018). It builds on more than 100 years of GEBCO's history of global seafloor mapping and coordinates inputs from academic, public and industry sources (Wölfl *et al.*, 2019). The expected mapping resolutions of this project are summarised in Table 7.1 and shown in Figure 7.1. Australia is contributing to this global effort through its national seabed mapping coordination program, AusSeabed (see Section 10.4).

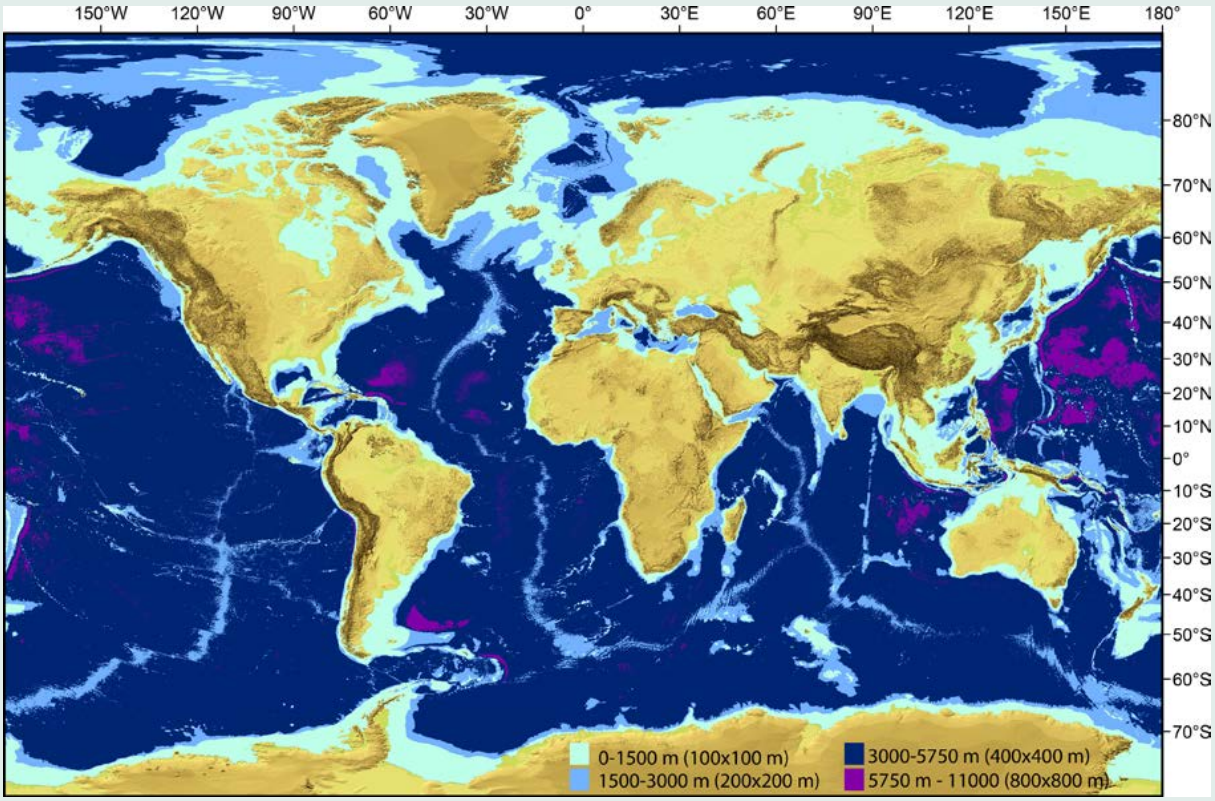
Table 7.1 Seabed 2030 minimum mapping resolutions

Waterbody depth range (m)	Grid cell size (m)	% world ocean
0–1500	100 x 100	13.7
1500–3000	200 x 200	11
3000–5750	400 x 400	72.6
5750–11,000	800 x 800	2.7

Source: Mayer *et al.* (2018) Table 2

Figure 7.1 Proposed waterbody depth regions for Seabed 2030

Depth regions based on 2°×2° deep water multibeam installed on surface vessels, calculated at 60° from nadir (see Table 7.1).



Source: Mayer *et al.* (2018) Figure 7

7.4 Carbon Cycling

The role of waterbodies in the global carbon cycle is briefly introduced in Section 1.5. The most comprehensive measure of carbon in an aqueous system is called Total Carbon (TC). The sources of carbon compounds in water are generally differentiated by their genesis in the aquatic carbon cycle:

- Total Organic Carbon (TOC)—amount of carbon detected in organic compounds, which originate from primary producers (see Volume 3A). In an aquatic environment, this is derived from photosynthesis via decaying plant life, bacterial growth, biological processes, or chemical activity:
  - Dissolved Organic Carbon (DOC)—an aquatic equivalent of soil humus, and that portion of the TOC remaining after filtering through a pore size of 0.2 µm (Laanen *et al.*, 2011; see Section 5.2.3.1); and
  - Particulate Organic Carbon (POC)—particulate matter resulting from photosynthetic processes.
- Total Inorganic Carbon (TIC)—dissolved CO_2 and carbonic acid salts derived from calcification and geological processes:
  - Dissolved Inorganic Carbon (DIC)—dissolved carbon resulting from calcification processes, mostly in the form of carbonates and bicarbonates, with a tiny proportion of carbonic acid (see Section 5.2.3.2); and
  - Particulate Inorganic Carbon (PIC)—particulate matter resulting from calcification processes, mostly comprising carbonates (see Section 1.5).

The actual proportions of these different forms, and their interactions, vary between waterbodies depending on local geography and biogeochemistry. A simplified view of these interactions within a freshwater system, and between that system and the surrounding environment, is illustrated in Figure 7.2. In higher latitudes, carbon cycling involves a complex interplay of oceanic and terrestrial systems, including seasonal sea ice (Capelle *et al.*, 2020). Carbon is transferred into and out of the freshwater system via several mechanisms:

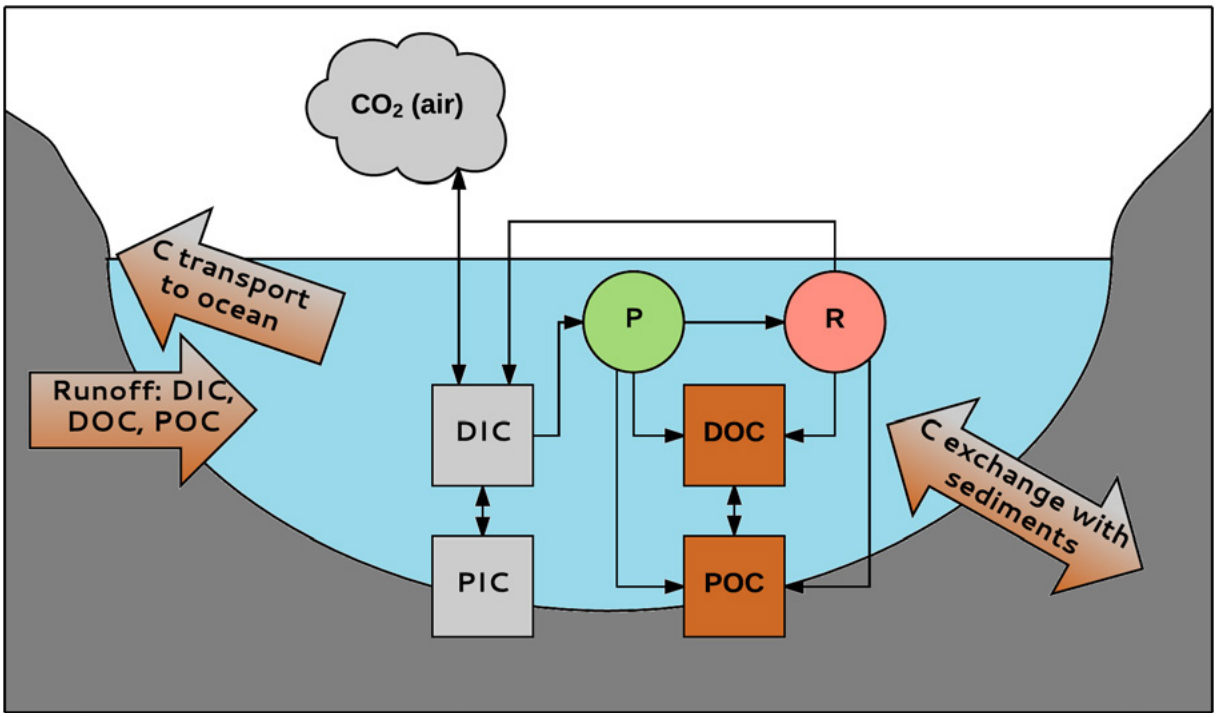
- runoff from land—carbon in the form of DIC, DOC and POC can enter the waterbody from terrestrial ecosystems. From there it may continue in the water cycle and be carried to the ocean, enter the food web by being consumed by organisms, be emitted into the atmosphere as CO_2, or sink to the substratum as sediment.
- atmospheric CO_2—enters the aquatic system via photosynthesis and is returned to the atmosphere via respiration. Dissolved CO_2 can also become carbonic acid for use by marine organisms in calcification.
- sediments—both organic and inorganic forms of carbon can sink from the water into the sediments of the substratum where it may be stored for millenia. Natural processes, such as tectonic activity, and human interventions, such as deep sea mining, can remove this stored carbon from the aquatic system.

Aquatic organisms are an important link between organic and inorganic forms of carbon. DOC comprises around 90% of TOC in most inland waterbodies, with concentrations in the range 0.1–332 mg/l (Sobek *et al.*, 2007). While flocculation, the process of clumping small particles together, may transform DOC into POC (see Figure 5.11), POC can also gradually degrade to become DOC. The water pH tends to determine the balance between inorganic carbon forms (Stumm and Morgan, 1996).

Carbon is transported continuously by rivers as particulate and dissolved organic carbon (POC, DOC) and as dissolved inorganic carbon (DIC) that functions in weathering reactions. Of the global carbon fluxes to the oceans from the continents, about 18% moves in riverine transport as POC, 37% as DOC, and 45% as DIC. Proportions of DIC, POC, and DOC in the rivers of the world are variable; differences emanate from lithology, which controls DIC levels, and differences in relief that control the DOC/POC ratios. DIC is very low in many tropical rivers of humid regions, and there DOC is the dominating form of exported carbon. Within the pelagic zone of lakes and reservoirs, however, the ratio of DOC/POC is ca. 10:1.
Wetzel (2001)

Figure 7.2 Aquatic carbon in freshwater system

C: carbon; P: photosynthesis; R: respiration; DIC: dissolved inorganic carbon; DOC: Dissolved organic carbon; PIC: particulate inorganic carbon; POC: particulate organic carbon



Source: Reitsema *et al.* (2018) Box 1

POC constitutes one of the major causes of surface water pollution, with the proportion of riverine POC increasing with the flow rate and size of the river. The ratio of PIC to POC production is an indicator of the ratio of calcification to photosynthesis in selected marine organisms, such as coccolithophores (calcifying algae such as *Emiliania huxleyi*). Since these organisms convert carbon into POC via photosynthesis, and remove carbon from water via calcification to form PIC, the PIC/POC ratio indicates whether they function as a source (high ratio) or sink (low ratio) of atmospheric CO_2 (Gerecht *et al.*, 2014). Changes in this ratio have been correlated with several environmental factors such as:

- higher CO_2 levels decreased the ratio of PIC/POC in *E. huxleyi* (Zondervan *et al.*, 2001; 2002);
- higher water temperatures decreased the ratio of PIC/POC in *E. huxleyi* (Gerecht *et al.*, 2014); and
- deficiencies in zinc and cobalt both increased the ratio of PIC/POC in *E. huxleyi* (Boye *et al.*, 2017).

Such results raise significant concerns about the future impact of increasing atmospheric CO_2 levels and surface water temperatures on aquatic environments, and the implications of ocean acidification on ocean chemistry (IPCC, 2014; see Section 1.5). Several algorithms have been developed to estimate surface concentrations of PIC (Balch *et al.*, 2005; Gordon *et al.*, 2001) and POC (Duforet-Gaurier *et al.*, 2010; Gardner *et al.*, 2006; Stramski *et al.*, 2008) for EO datasets and, when calibrated using ship-based observations, these levels can be mapped and monitored at global and regional scales (Swirgon and Stramska, 2015). EO-based algorithms have been developed to monitor other indicators of the ocean carbon cycle including primary productivity (Antoine *et al.*, 1996; Behrenfeld and Falkowski, 1997) and coloured dissolved and detrital organic materials (Maritorena *et al.*, 2002; Siegel *et al.*, 2002). These methods are further discussed in Sections 8 and 18.

7.5 Dynamics

Like all environmental features, waterbodies are not static, but change with diurnal, seasonal and longer term cycles. An important part of understanding dynamics in any natural feature is to separate the cyclic from longer term changes. Some of the features of waterbodies that change in human time frames include water extent, level, depth, temperature, ice cover, and movement, as well as their physical, chemical, and biological composition, which impact water colour, quality and ecology (see Sections 11 to 20 respectively). While seasonal meteorological cycles involving precipitation and evaporation determine the 'standard' characteristics of waterbodies, such as their extent, volume, and quality, extreme meteorological events (e.g. storms and floods) can radically modify these characteristics.

Water moves locally, regionally, and globally by various mechanisms, including transient currents, thermohaline circulation, and wind-driven circulation (see Section 17). In polar regions, the formation, presence, and subsequent melting of dynamic sea ice is a major feature that transforms the surface (and deeper) waters of the high-latitude oceans (including the Southern Ocean). Unlike the ice that forms on waterbodies in lower latitudes, coverage of sea ice is either annual or perennial depending on the location (see Section 15).

The environmental drivers of marine life differ with many factors, including an organism's position in the food web (see Section 3.2). For example, in the Southern Ocean, Boyd *et al.* (2019) identified different sets of drivers for the following trophic levels:

- phytoplankton at the base of the food web is driven by temperature, sunlight, pH, CO_2, nutrients, and trace elements;
- benthic organisms in the middle of the food web are driven by pH, CO_2, temperature, and oxygen; and
- pelagic organisms at the top of the food web are driven by CO_2, temperature, and pH (see Sections 3 and 5).

The response of particular biota to different drivers also varies with habitat, but changes in these drivers are likely to modify the distribution and prevalence of individual species. Global phenomena, such as ocean acidification, have implications not just for individual species (Collins *et al.*, 2014), but also for the aquatic food web, the carbon cycle, and global weather patterns (see Section 1.5).

Table 7.2 Modelled scenarios for Antarctica and Southern Ocean in 2070

For the two modelled scenarios of high and low CO_2 emissions, changes in eleven characteristics were predicted relative to a 1986–2005 reference period.

Data	Characteristic	Modelled scenario for 2070	
		Low emissions	High emissions
Atmosphere/ocean/ice differences (IPCC, 2013; DeConto and Pollard, 2016; Hauri *et al.*, 2016)	Global air temperature	+0.9°C	+2.9°C
	Antarctic contribution to sea level	6 cm	27 cm
	Antarctic air temperature	+0.9°C	+3.0°C
	Southern Ocean temperature	+0.7°C	+1.9°C
	Summer (February) sea ice extent	12% loss	43% loss
	Ice shelf volume	8% reduction	23% reduction
Ecosystem states and pressures (IPCC, 2013; Aronson *et al.*, 2015; Atkinson *et al.*, 2004; Chown *et al.*, 2012a, 2012b; Duffy *et al.*, 2017; Dodds *et al.*, 2017; Gutt *et al.*, 2015; Hauri *et al.*, 2016)	Ocean acidification/reduced calcification	Surface waters saturated	Surface waters corrosive to aragonite shells of pteropods
	Biological invaders	Double reference level	Ten times reference level
	Ecosystem structure	Penguins and krill	Crustaceans and salps
	Human presence	3 times reference level	8 times reference level
	Resource use	Small increase	Signficant increase

Source: Rintoul *et al.* (2018) Figure 2

By providing a series of consistent observations from a synoptic viewpoint, EO imagery offer a unique opportunity to monitor the timing and extent of environmental change. Long term change detection generally requires images that were acquired in the same season since some water features, such as macroalgae, change seasonally in terms of distribution and abundance. EO time series data in Analysis Ready format, such as Digital Earth Australia (DEA) imagery (see Volume 2D—Excursus 11.2), provides useful for modelling exercises (either as input or validation) for forecasting or predicting future conditions (see Volume 2D—Section 14), such as coral bleaching (see Excursus 20.3).

In conjunction with EO imagery, the Integrated Marine Observing System (IMOS) operates a variety of equipment in Australia's coastal and ocean waters to research the dynamic nature of these regions (see Excursus 5.1 above and Volume 2D—Excursus 12.3). Sophisticated systems such as eReefs have also been developed to integrate EO datasets with other environmental data to monitor regional biogeochemical cycles (see Volume 2D—Excursus 14.4). At a global scale, Earth System Science (ESS; see Excursus 7.2) offers an appropriately-scaled platform on which historical and current datasets can be analysed and integrated to model future environmental conditions on our dynamic planet.

One example of using global modelling to assess likely trajectories for future conditions in the Southern Ocean is given in Rintoul *et al.* (2018). This analysis considers two opposing scenarios of continued high CO_2 emissions versus a future with reduced emissions over the period from 2020 to 2070. The impacts of these scenarios are summarised in terms of eleven characteristics, relative to a 1986–2005 reference period (see Table 7.2). Further modelling indicated that continuing high CO_2 emissions until 2300 could result in nutrients being trapped in the Southern Ocean, which would reduce nutrient export to lower latitudes, decrease primary productivity by 24%, and potentially result in a 20% reduction in fishery yields (LaufKötter *et al.*, 2018; Moore *et al.*, 2018; Rintoul *et al.*, 2019). Such analyses demonstrate how current governance and lifestyle choices determine future environmental conditions, even in remote locations (Boyd *et al.*, 2019).

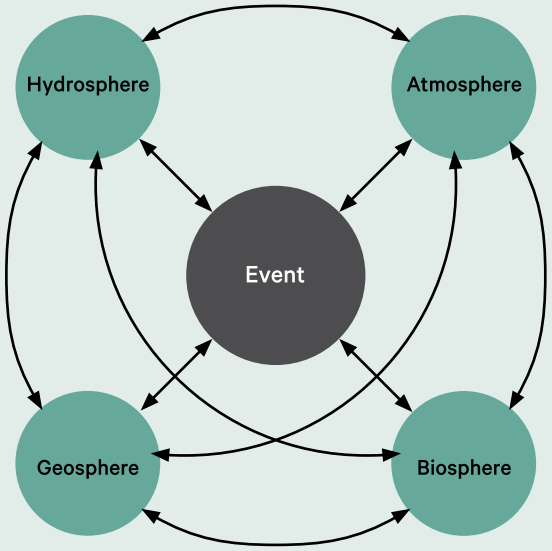
Excursus 7.2—The Global System

Earth System Science (ESS), a multidisciplinary approach to understanding the structure and function of Earth as an integrated system (Steffen *et al.*, 2020; see Volume 1A—Section 4.1 and Volume 3A—Excursus 1.2), describes events on Earth in terms of their interactions with four integrated spheres (see Figure 7.3):

- atmosphere—gaseous, protective layer around the Earth;
- hydrosphere—all surface waters, groundwater and atmospheric water in any state (see Section 1);
- geosphere—solid components of Earth on land and under water; and
- biosphere—all forms of life on Earth.

ESS analyses the dynamic geochemical processes and interactions occurring between these spheres to better understand the Earth—its past, present and future—at global to local scales. Of particular relevance to surface waters is the hydrological cycle, which circulates water—and energy—between these four spheres (see Section 1.1).

Figure 7.3 Earth System Science



To monitor changes within the integrated ESS framework requires consistent observations of unambiguous and agreed variables that minimally describe major states and trends. These criteria have become known as 'essential variables' (EV) and have been embraced by a wide range of international bodies to develop interchangeable data repositories to monitor our planet (see Volume 3A). Given the global scale of analysis, EO datasets are at the core of this approach. Examples of EV include:

- essential climate variables (ECV; see Volume 1A—Section 1.5.2);
- essential agricultural variables (EAV; see Volume 3A—Section 11.3);
- essential biodiversity variables (EBV; see Volume 3A—Section 19.3);
- essential water variables (EWV; GEOGLOWS, 2016); and
- essential ocean variables (EOV; see Excursus 21.1).

EOV describe the physics and biogeochemistry of the ocean system and its biological and ecological components (NASA Earthdata, 2020). Global monitoring of ocean properties based on EOV is further discussed in Section 21 in the context of marine biodiversity.

7.6 Further Information

General Bathymetric Chart of the Oceans (GEBCO): *https://www.gebco.net/*

Geomorphology: Dove *et al.* (2020)

7.7 References

Antoine, D., Andre, J.M., and Morel, A. (1996). Oceanic primary production: 2. Estimation at global scale from satellite (Coastal Zone Color Scanner) chlorophyll. *Global Biogeochemical Cycles*, 10(1), 56–69.

Aronson, R.B., Smith, K.E., Vos, S.C., McClintock, J.B., Amsler, M.O., Moksnes, P.O., Ellis, D.S., Kaeli, J.W., Singh, H., Bailey, J.W., Schiferl, J.C., van Woesik, R., Martin, M.A., Steffel, B.V., Deal, M.E., Lazarus, S.M., Havenhand, J.N., Swalethorp, R., Kjellerup, S. and Thatje, S. (2015) No barrier to emergence of bathyal king crabs on the Antarctic shelf. *Proceedings of the National Academy of Sciences*, 112 (42), 12997–13002. doi:10.1073/pnas.1513962112

Atkinson, A., Siegel, V., Pakhomov, E. A., and Rothery, P. (2004)Long-term decline in krill stock and increase in salps within the Southern Ocean. *Nature,* 432, 100–103.

Balch, W.M., Gordon, H.R., Bowler, B.C., Drapeau, D.T., and Booth, E.S. (2005). Calcium Carbonate Measurements in the Surface Global Ocean based on MODIS Data. *Journal of Geophysical Research,* 110, C07001. doi:10.1029/2004JC002560

Behrenfeld, M.J., and Falkowski, P.G. (1997). Photosynthetic rates derived from satellite-based chlorophyll concentration. *Limnology and Oceanography*, 42 (1), 1–20.

Boye, M., Adjou, M.A., Dulaquais, G., and Tréguer, P. (2017). Trace metal limitations (Co, Zn) increase PIC/POC ratio in cocolithophore *Emiliania huxleyi*. *Marine Chemistry*, 192, 22–31. doi.org/10.1016/j.marchem.2017.03.006

Boyd P.W., Kawaguchi, S. Strzepek, R. Meiners, K. Hallegraeff, G. McMinn, A., Swadling, K., and Reilly, D. (2019). *Report Card: Potential Tipping Points for life in the Southern Ocean*. Antarctic Climate and Ecosystems Cooperative Research Centre, Hobart, Australia. *http://dx.doi.org/10.25959/100.00031768*

Brando, V.E., Anstee, J.M., Wettle, M., Dekker, A.G., Phinn, S.R., and Roelfsema, C. (2009). A physics based retrieval and quality assessment of bathymetry from suboptimal hyperspectral data. *Remote Sensing of Environment*, 113, 755–770. doi:10.1016/j.rse.2008.12.003.

Capelle, D.W., Kuzyk, Z.Z.A., Papkyriakou, T., Guéguen, C., Miller, L.A., and Macdonald, R.W. (2020). Effect of terrestrial organic matter on ocean acidification and CO2 flux in an T Arctic shelf sea. *Progress in Oceanography*, 185, 102319. *https://doi.org/10.1016/j.pocean.2020.102319*

Chown, S.L., Lee, J.E., Hughes, K.A., Barnes, J., Barrett, P.J., Bergstrom, D.M., Convey, P., Cowan, D.A., Crosbie, K., Dyer, G., Frenot, Y., Grant, S.M., Herr, D., Kennicutt, M.C., Lamers, M., Murray, A., Possingham, H.P., Reid, K., Riddle, M.J., Ryan, P.G., Sanson, L., Shaw, J.D., Sparrow, M.D., Summerhayes, C.,Terauds, A., and Wall, D.H. (2012a). Challenges to the future conservation of the Antarctic. *Science*, 337(6091). 158–159. *https://doi.org/10.1126/science.1222821*

Chown, S.L., Huiskes, A.H., Gremmen, N.J., Lee, J.E., Terauds, A., Crosbie, K., Frenot, Y., Hughes, K.A., Imura, S., Kiefer, K., Lebouvier, M., Raymond, B., Tsujimoto, M., Ware, C., Van de Vijver, B., and Bergstrom, D.M. (2012b). Continent-wide risk assessment for the establishment of nonindigenous species in Antarctica. *Proceedings of the National Academy of Sciences*, 109(13), 4938–4943. doi:10.1073/pnas.1119787109

Collings, S., Botha, E.J., Anstee, J., and Campbell, N. (2018). Depth of Satellite Images: Depth Retrieval Using a Stereo and Radiative Transfer-based Hybrid Method. (2018). *Remote Sensing*, 8, 1247. *https://doi.org/10.3390/rs10081247*

Collins, S., Rost, B. and T.A. Rynearson. (2014). Evolutionary potential of marine phytoplankton under ocean acidification. *Evolutionary Applications*, 7, 140–155.

DeConto, R.M., and Pollard, D. (2016). Contribution of Antarctica to past and future sea-level rise. *Nature*, 531, 591–597.

Dodds, K., Hemmings, A.D., and Roberts, P. (2017). *Handbook on the Politics of Antarctica*. Edward Elgar, Cheltenham.

Dove, D., Nanson, R., Bjarnadóttir, L.R., Guinan, J., Gafeira, J., Post, A., Dolan, M.F.J., Stewart, H., Arosio, R., and Scott, G. (2020). *A two-part seabed geomorphology classification scheme: (v.2)*. Open Report Prepared by the MIM-GA Geomorphology Working Group. doi:10.5281/ZENODO.4075248

Duffy, G.A., Coetzee, B.W.T., Latombe, G., Akerman, A.H., McGeoch, M.A., and Chown, S.L. (2017). Barriers to globally invasive species are weakening across the Antarctic. *Diversity and Distributions*, 23, 982–996. *https://doi.org/10.1111/ddi.12593*

Duforet-Gaurier, L., Loisel, H., Dessailly, D., Nordkvist, K., Alvain., S. (2010). Estimates of particulate organic carbon over the euphotic depth from in situ measurements, Application to satellite data over the global ocean. *Deep Sea Research I*, 57 (3), 351–367.

Estep, L., and Arnone, R.A. (1994). Effect of whitecaps on determination of chlorophyll concentration from satellite data. *Remote Sensing of Environment,* 50, 328–334.

Gardner, W.D., Mishonov, A.V., and Richardson., M.J. (2006). Global POC concentrations from *in-situ* and satellite data. *Deep-Sea Research II*, 53, 718–740.

GEBCO (2017). *Seabed 2030: Roadmap for Future Ocean Floor Mapping*. The Nippon Foundation/GEBCO (General Bathymetric Chart of the Oceans), June 2017. *https://www.gebco.net/documents/seabed_2030_roadmap_v10_low.pdf*

GEOGLOWS (2016). *Working Group 3: Essential Water Variables and Observations* webpage, GEO Global Water Sustainability website: *https://www.geoglows.org/pages/workinggroup3*

Gerecht, A.C., Šupraha, L., Edvardsen, B., Probert, I., and Henderiks, J. (2014). High temperature decreases the PIC / POC ratio and increases phosphorus requirements in *Coccolithus pelagicus* (Haptophyta), *Biogeosciences*, 11, 3531–3545. *https://doi.org/10.5194/bg-11-3531-2014*

Gordon, H.R., Boynton, G.C., Balch, W.M., Groom, S.B., Harbour, D.S., and Smyth, T.J. (2001). Retrieval of coccolithophore calcite concentration from SeaWiFS imagery. *Geochemical Research Letters*, 28(8), 1587–1590.

Gutt, J., Bertler, N., Bracegirdle, T.J., Buschmann, A., Comiso, J., Hosie, G., Isla, E., Schloss, I.R., Smith, C.R., Tournadre, J., and Xavier, J.C. (2015). The Southern Ocean ecosystem under multiple climate change stresses—an integrated circumpolar assessment. *Global Change Biology*, 21(4), 1434–1453. doi:10.1111/gcb.12794

Hauri, C., Friedrich, T., and Timmermann, A. (2016). Abrupt onset and prolongation of aragonite undersaturation events in the Southern Ocean. *Nature Climate Change*, 6, 172–176.

IPCC (2013). *The Physical Science Basis. Contribution of Working Group I to the Fifth Assessment Report of the Intergovernmental Panel on Climate Change*. (Eds: Stocker, T.F. *et al.*) Cambridge University Press, Cambridge.

IPCC (2014). *Climate Change 2014: Impacts, Adaptation, and Vulnerability. Part A: Global and Sectoral Aspects. Contribution of Working Group II to the Fifth Assessment Report of the Intergovernmental Panel on Climate Change* (Eds: Field, C.B., Barros, V.R., Dokken, D.J. , Mach, K.J., Mastrandrea, M.D., Bilir, T.E., Chatterjee, M., Ebi, K.L., Estrada, Y.O., Genova, R.C., Girma, B., Kissel, E.S., Levy, A.N., MacCracken, S., Mastrandrea, P.R., and White, L.L.). Cambridge University Press, Cambridge, United Kingdom and New York, NY, USA, 1132 p.

Laanen, M.L., Peters, S.W.M., Dekker, A.G., and van der Woerd, H.J. (2011). Assessment of the scattering by sub-micron particles in inland waters. *Journal of the European Optical Society,* 6, 11046.

Laufko¨tter, C., and Gruber, N. (2018). Will marine productivity wane? *Science*, 359, 1103–1104.

Maritorena, S., Siegel, D.A., and Peterson. A.R. (2002). Optimal tuning of a semi-analytical model for global applications. *Applied Optics*, 41, 2705–2714.

Mayer, L., Jakobsson, M., Allen, G., Dorschel, B., Falconer, R., Ferrini, V., Lamarche, G., Snaith, H., and Weatherall, P. (2018). The Nippon Foundation—GEBCO Seabed 2030 Project: The Quest to See the World's Oceans Completely Mapped by 2030. *Geosciences*, 8, 63. *http://www.mdpi.com/2076-3263/8/2/63*

Moore, J.K., Fu, W., Primeau, F., Britten, G.L., Lindsay, K., Long, M., Doney, S.C., Mahowald, N., Hoffman, F., and Randerson, J.T. (2018). Sustained climate warming drives declining marine biological productivity, *Science*, 359(6380), 1139–1143.

NASA Earthdata (2020). *Essential Variables* webpage, NASA Earthdata website: *https://earthdata.nasa.gov/learn/essential-variables*

Purkis, S.J., and Brock, J.C. (2013). Lidar Overview. Ch 5 in *Coral Reef Remote Sensing*. (Eds: Goodman, J.A., Purkis, S.J., and Phinn, S.R.). Springer, Dordrecht. ISBN 978-90-481-9291-5.

Reitsema, R.E., Meire, P., and Schoelynck, J. (2018). The Future of Freshwater Macrophytes in a Changing World: Dissolved Organic Carbon Quantity and Quality and Its Interactions With Macrophytes. *Frontiers in Plant Science*, 9, 629. doi:10.3389/fpls.2018.00629

Rintoul, S.R., Chown, S.L., DeConto, R.M., England, M.H., Fricker, H.A., Mason-Delmotte, V., Naish, T.R., Siegert, M.J., and Xavier, J.C. (2018). Choosing the future of Antarctica. *Nature*, 558, 233–241. *https://doi.org/10.1038/s41586-018-0173-4*

Siegel, D.A., Maritorena, S., Nelson, N.B., Hansell, D.A., and Lorenzi-Kayser, M. (2002). Global distribution and dynamics of colored dissolved and detrital organic materials. *Journal of Geophysical Research*, 107, 3228. doi:10.1029/2001JC000965

Sobek, S., Tranvik, L.J., Prairie, Y.T., Kortelainen, P., and Cole, J.J. (2007). Patterns and regulation of dissolved organic carbon: an analysis of 7,500 widely distributed lakes. *Limnology and Oceanography,* 52, 1208–1219. *https://doi.org/10.4319/lo.2007.52.3.1208*

Steffen, W., Richardson, K., Rockström, J., Schellnhuber, H.J., Dube, O.P., Dutreuil, S., Lenton, T.M., and Lubchenco, J. (2020). The emergence and evolution of Earth System Science. *Nature Reviews Earth and Environment*, 1, 54–63. *https://doi.org/10.1038/s43017-019-0005-6*

Stramski, D., Reynolds, R. A., Babin, M., Kaczmarek, S., Lewis, M. R., Röttgers, R., Sciandra, A., Stramska, M., Twardowski, M. S., Franz, B. A., and Claustre, H. (2008). Relationships between the surface concentration of particulate organic carbon and optical properties in the eastern South Pacific and eastern Atlantic Oceans. *Biogeosciences*, 5, 171–201. *doi.org/10.5194/bg-5-171-2008*.

Stumm, W., and Morgan, J.J. (1996). *Aquatic Chemistry: Chemical Equilibria and Rates in Natural Waters. Environmental Science and Technology.* John Wiley and Sons Inc., New York.

Swirgon, M., and Stramska, M. (2015). Comparison of in situ and satellite ocean colour determinations of particulate organic carbon concentration in the global ocean. *Oceanologia*, 57, 25–31. *doi.org/10.1016/j.oceano.2014.09.002*

Wetzel, R.G. (2001). The Inorganic Carbon Complex. Ch 11 in *Limnology* 3rd Edn. (Ed: Wetzel, R.G.). Academic Press. pp 187–204. ISBN: 9780127447605

Wölfl, A.-C., Snaith, H., Amirebrahimi, S., Devey, C.W., Dorschel, B., Ferrini, V., Huvenne, V.A.I., Jakobsson, M., Jencks, J., Johnston, G., Lamarche, G., Mayer. L., Millar, D., Pedersen, T.H., Picard, K., Reitz, A., Schmitt, T., Visbeck, M., Weatherall, P., and Wigley, R. (2019). Seafloor Mapping—The Challenge of a Truly Global Ocean Bathymetry. *Frontiers in Marine Science*, 6, 283. doi:10.3389/fmars.2019.00283

Zondervan, I., Zeebe, R.E., Rost, B., and Riebesell, U. (2001). Decreasing marine biogenic calcification: A negative feedback on rising atmospheric pCO_2. *Global Biogeochemical Cycles*, 15(2), 507–516. doi.org/10.1029/2000GB001321

Zondervan, I., Rost, B., and Riebesell, U. (2002). Effect of CO_2 concentration on the PIC/POC ratio in the coccolithophore *Emiliania huxleyi* grown under light-limiting conditions and different daylengths. *Journal of Experimental Marine Biology and Ecology*, 272, 55–70.



EO Data and Models

Various EO technologies are appropriate for mapping and monitoring different aspects of surface waters, including:

- multispectral and hyperspectral sensors—water extent (see Section 11), depth (see Section 13.4.2), concentrations of optically active constituents in coastal and inland waters (see Sections 18 and 19), and occurrence of aquatic biota (see Section 20);
- thermal infrared sensors—accurate sea surface temperature and charts of coastal currents (see Sections 14, 15, and 16);
- microwave radiometers—ocean salinity and soil moisture (see Section 19);
- radar sensors—sea surface height, seafloor mapping, coastal currents, and ocean waves, (see Sections 12, 13.3.1, 16, and 17);
- lidar sensors—bathymetry, water column profiling, and fisheries (see Section 13.4.1); and
- sonar sensors—bathymetry and submerged geomorphology (see Sections 10 and 13.3.2).

Modes of EO data acquisition are introduced in Volume 1A—Sections 14 to 16. In the following three sections we focus of those properties of water that can be measured and modelled using EO sensors in the context of Australian surface waters. Specifically, these sections address:

- optical EO (see Section 8);
- microwave EO (see Section 9);
- acoustic EO (see Section 10).

Contents

8 Optical EO 117

9 Microwave EO 155

10 Acoustic EO 169

Background image on previous page: These tidal channels through the Great Barrier Reef system, Queensland, were imaged on 8 July 2016. **Source:** Planet Labs Inc. (CC-BY-SA 4.0). Retrieved from *https://www.planet.com/gallery/#!/post/reef-20160708*



8 Optical EO

An indirect relationship exists between features in an EO dataset and quantifiable attributes of the Earth's surface (see Figure 8.1). EO data processing operates on the 'data space', or observation domain, and relies on implicit assumptions within defined measurement and structure models that relate the data back to selected parameters of the surface, or the attribute domain (see Volume 2D—Section 1). This indirect relationship is particularly relevant to aquatic applications of EO and applies to all EO data sources (see Volume 1A—Section 1).

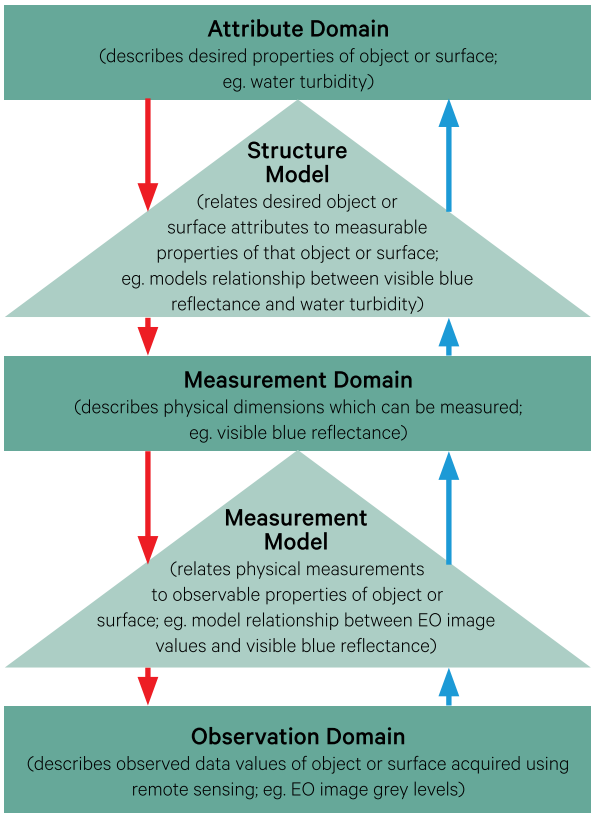
Optical wavelengths comprise the ultraviolet (UV), visible, near infrared (NIR), and short wave infrared (SWIR) regions of the electromagnetic spectrum (see Section 5.1.4). The behaviour of these 'reflective' wavelengths can be described in terms of geometric or ray optics (see Volume 1A—Section 2.8), since they are shorter than the lenses and sensors that detect them. Within the optical wavelength range, atmospheric absorption reduces solar transmission of some wavelength intervals (see Figure 5.8).

This section summarises some fundamental principles of using optical EO to observe surface waters. The basic principles of optics and lenses are introduced in Volume 1A—Section 2, some of which are reviewed in Excursus 8.1, and the underlying framework of optical EO is considered in Section 8.1. In subsequent subsections we describe:

- optically active constituents of water (see Section 8.2);
- optical properties of water (see Section 8.3);
- optical EO models (see Section 8.4); and
- optical EO sensors (see Section 8.5).

Figure 8.1 Measurement and analysis of image features

Interpreting imagery from EO sensors is an indirect process, whereby a measurement model is used to transform EO observations to measurements of some measurable property, and a structure model is used to relate those measurements to application-specific attributes.



Adapted from: Harrison and Jupp (1989) Figure 33

Background image: Optical image of Sydney Harbour acquired by Flock-1 satellites on 29 November 2015. **Source:** Planet Labs Inc. (CC BY SA 4.0). Retrieved from *https://medium.com/planet-stories/imaging-australian-flooding-from-space-b6f30b025e2d*

Excursus 8.1—Optics Review

Optics is the scientific study of light properties—how light interacts with matter and how it can be detected and measured by instruments. In the context of EO, optical wavelengths generally refer to those wavelengths whose behaviours are best described by ray optics (see Volume 1A—Section 2.8), namely ultraviolet (UV), visible, and infrared (IR: near, short wave, and thermal; see Section 5.1.4). An understanding of optics and optical laws underpins all optical EO studies and is relevant to an expanding range of engineering applications.

Geometric concepts

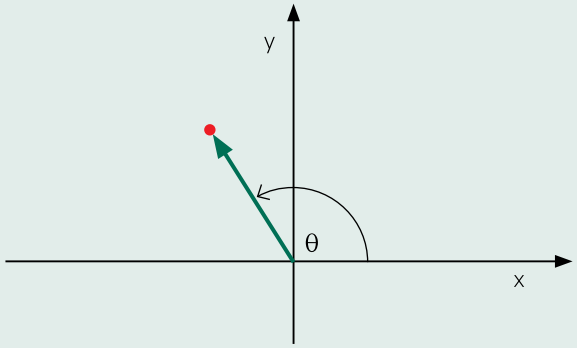
Some basic geometric concepts referenced in optics include:

- polar angle:
  - in two dimensions (on a plane), this angular measure is the counterclockwise angle between the X-axis and a point in the X-Y plane (see Figure 8.2a); and
  - in three dimensions (on a sphere), the polar angle is measured from the Z-axis (see Figure 8.2b); and
- solid angle (ω *or* Ω)—three-dimensional angle defined by a cone extracted from a sphere, derived from the surface area of the cone (A) and the radius of the sphere (R) (see Figure 8.3)

The terms used to define the position of celestial bodies, or airborne and spaceborne sensors, relative to locations on the Earth's surface are summarised in Table 8.1 and Figure 8.4a. The angles derived from these positions are used in EO to define the geometry between the illumination source, the target, and the viewing sensor (see Figure 8.4b). As illustrated in Figure 8.4c, the spherical coordinate system, locations are referenced in terms of the polar zenith and azimuth angles and denoted (θ, ϕ). The position of a light source is determined using the zenith and azimuth angles for light streaming downwards. Conversely, the nadir and azimuth angles are used to determine the position of a light source from which light streams upwards.

Figure 8.2 Polar angles

a. Polar angle in a plane



b. Polar angle in spherical coordinates

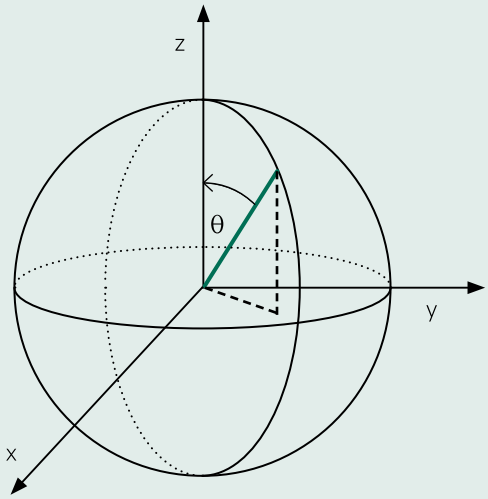


Figure 8.3 Solid angle

Solid angle $\Omega = A/R^2$ steradians, where A is the area on the surface of a sphere of radius R that is intersected by a cone originating from the centre of the sphere

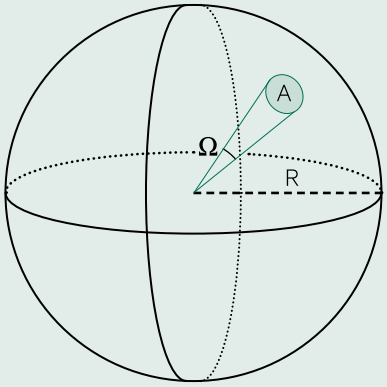
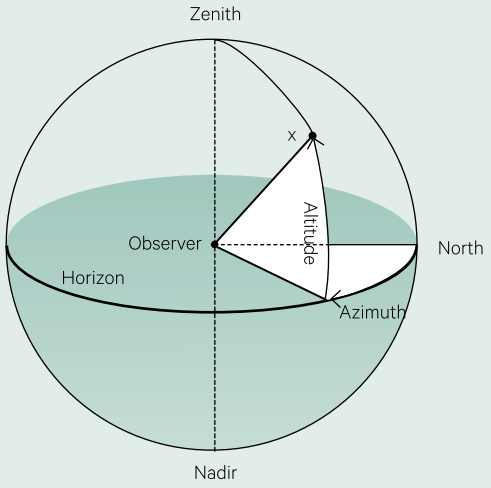
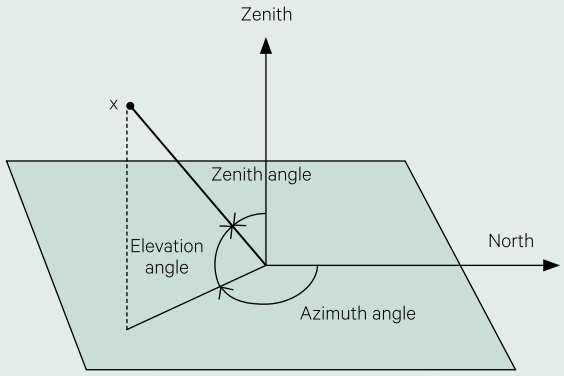


Figure 8.4 Geometric framework for optical studies

a. Defining positions



b. Defining angles



c. The basic geometry of a passive EO sensor viewing reflected solar radiation from an illuminated target surface is shown below.

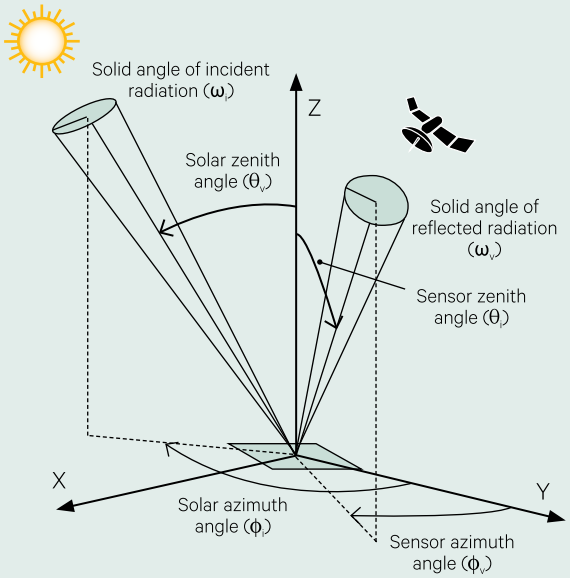


Table 8.1 Terminology for EO geometry

Position	Definition	Symbol
Zenith	Point directly above observer	*Z*
Nadir	Point directly below observer	*N*
Zenith angle	Angle between zenith and body measured on vertical plane through zenith, observer, and body	*z* or θ
Elevation or altitude	Angle between horizon and body measured on vertical plane through observer	*h* or α
Azimuth	Angle between reference direction (usually North) and horizontal projection of body measured clockwise from reference direction (usually North)	*a* or ϕ

Electromagnetic radiation

Visible light energy is loosely defined as that subset of electromagnetic radiation (EMR) with wavelengths in the range 380–700 nm. As introduced in Volume 1A—Section 5, EMR comprises streams of photons moving at the speed of light (c). While the speed of light is defined as 3×10^8 m/sec through a vacuum, it actually varies through different media (see Table 8.2). Under water, the spectral distribution of solar radiation also changes significantly with water depth (Kirk, 2010; see Figure 5.10).

Each photon has a wavelength (λ) and frequency (ν), which are related by:

$$c = \lambda \nu$$

Photon energy (ε) varies with its frequency, so that high frequency (short wavelength) photons contains more energy than lower frequency (longer wavelength) photons (see Volume 1A—Section 2.5).

Matter absorbs or transmits incoming, or incident, EMR depending on whether or not that energy excites physical processes in the matter's atoms and molecules. The nature of excitation varies with the wavelength or frequency of the energy and the molecular composition of the matter being irradiated. Thus, EM energy is selectively absorbed by materials depending on how different frequencies of EMR interact with the molecules, atoms, and nuclei of the material (see Volume 1A—Section 2.2). When the frequency of the incident EM energy does not match the energy levels required for absorption, that energy is transmitted through or scattered by the object. Thus, the transparency of an object (allowing transmission of incident radiation through the object) and its opacity (resulting in reflectance of incident radiation) are determined by the physical and chemical structure of the object, relative to the wavelength of the radiation.

Table 8.2 Light behaviour in different media

Medium	Refractive Index	Velocity of Light (m/sec)
Vacuum	1.0	~3 x 10^8 (=299,792,458)
Air	1.00028	~3 x 10^8 (=299,702,547)
Natural Waters	1.33	~2.25 x 10^8 (=225,407,863)

Source for refractive index data: Kirk (1994)

Figure 8.5 Radiative transfer process

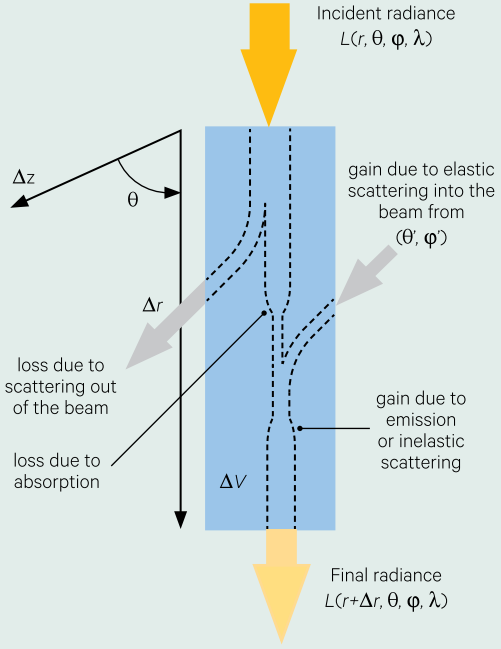
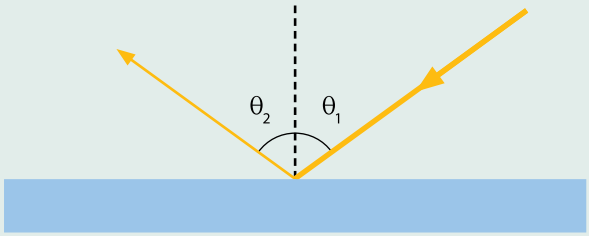


Figure 8.6 Specular reflection

The extent to which a surface obeys the law of reflection depends on its surface texture relative to the wavelength of incident radiation. In specular reflection from a smooth surface the angle of incidence (θ_1) equals the angle of reflection (θ_2).



Source: Harrison and Jupp (1989) Figure 7

Radiative Transfer (RT) describes the transfer of energy as photons through a medium and the interactions of photons with surface materials. Thus, RT models account for the impact of absorption, emission, and scattering on energy propagation through a medium. Figure 8.5 illustrates the processes that can affect a single beam travelling a distance Δr through a medium.

In terms of EO, the interaction of incoming radiation with surface features depends on both the spectral reflectance properties of the surface materials and the surface smoothness relative to the radiation wavelength (see Volume 1A—Section 2.5). A relatively 'smooth' surface, which reflects energy without any scattering (that is, where the angle of incidence equals the angle of reflection), is called a 'specular' or 'mirror' reflector. 'Diffuse' or 'Lambertian' reflectance occurs when the surface is rough relative to the wavelength(s) of the incoming radiation and causes the energy to be reflected equally in all directions (see Figure 8.6). While calm water can act as a specular reflector, most of the Earth's surface materials are diffuse reflectors in the visible wavelengths (especially at the spatial resolution of most EO imagery) but may display specular reflectance properties in the microwave wavelengths. Surface orientation relative to both the energy source and sensing device also affects the amount of radiation detected by the sensor. Other aspects of the interaction of EMR with the Earth's surface are discussed in Volume 1B—Sections 4 to 6.

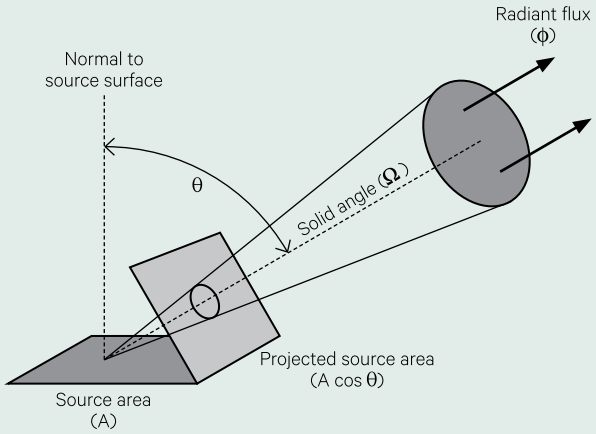
Measuring EMR

The energy associated with EMR can be measured in a number of ways:

- radiant flux (Φ)—number of photons per second (*J/sec* or *W*); this measures the rate of radiant energy flow;
- radiant intensity (*I*)—radiant flux per unit solid angle in a specified direction (*W/sr*);
- radiance (*L*)—radiant intensity per unit area on a plane perpendicular to the flow direction ($W/m^2/sr$; see Figure 8.7). This can be defined in terms of:
  - field radiance—radiant intensity intercepted by a point in space, or a point on a surface; and
  - surface radiance—radiant intensity emitted from a point on a surface; and
- irradiance (*E*)—radiant flux per unit area that is incident on a surface from any direction in a hemisphere (W/m^2).

Figure 8.7 Radiance definitions

The radiance (*L*) from a source area *A* is measured in terms of the radiant flux within a specified solid angle in a given direction.



Adapted from: Elachi and van Zyl (2006) Figure 2-10

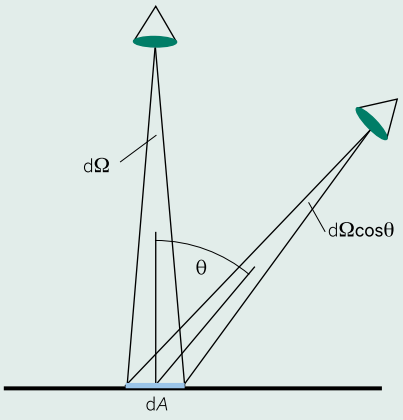
Table 8.3 Impact of cosine law on irradiance

Zenith angle (°)	Irradiance (%)
0	100
30	87
60	50
85	9

Data source: *http://www.intl-lighttech.com/support/basic-light-measurement-principles-chapter-6-light-measurement-tutorial*

Figure 8.8 Cosine law

For equal aperture observations (area *dA*), the observed solid angle reduces from dΩ at the normal to $d\Omega\cos(\theta)$ for θ° off-normal.



By Lambert's cosine law, the irradiance (*E*) is proportional to the cosine of the zenith angle (θ) for the light source (see Table 8.3):

$$E_\theta = E\cos\theta$$

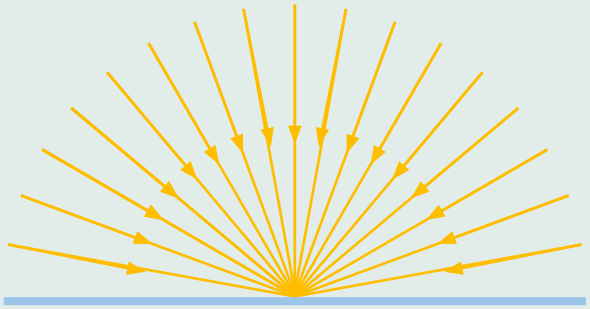
The same relationship applies to the light scattered (or emitted) from a diffuse (or Lambertian) surface. Thus maximum energy is intercepted, scattered, or emitted when the light stream is perpendicular to a surface. The number of photons per second emitted into equal angle wedges bounded by a circle is proportional to the area of each wedge, with the maximum rate into the wedge that is directed along the normal. When the light stream is directed to or from an off-normal direction, the number of photons is proportionally reduced by the cosine of the angle of the light stream away from the normal (see Figure 8.8). This has obvious implications for the energy detected by a sensor in normal and off-normal positions.

Irradiance onto a horizontal plane can be considered in terms of the upper and lower hemispheres of a sphere:

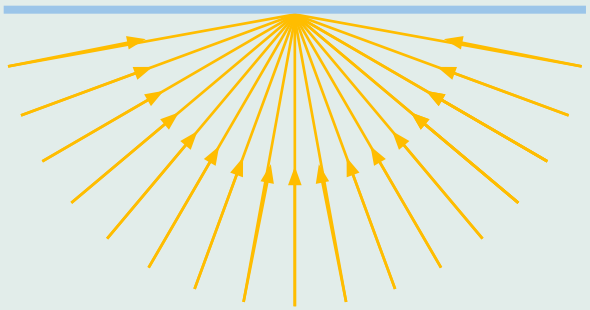
- downward irradiance (E_d)—downwelling light stream intercepted by the upper surface (see Figure 8.9a); and
- upward irradiance (E_u)—upwelling light stream intercepted by the lower surface (see Figure 8.9b).

Figure 8.9 Downwelling and upwelling irradiance

a. Downwelling irradiance: $E_d = \pi \times L_d$



b. Upwelling irradiance: $E_u = \pi \times L_u$



The total upward irradiance at a point on the lower surface is computed by integrating over all solid angles in the lower hemisphere with respect to the Cosine Law; likewise the total downward irradiance is determined by integration over the upper hemisphere. Scalar irradiance, however, integrates equally over all spherical directions about a point, so is always greater than the sum of E_d and E_u (Zimmerman and Dekker, 2006).

Upwelling radiance (L_u) effectively determines the appearance of waterbodies. It is significant for hydrological EO and important in primary productivity and radiative transfer (Ma *et al.*, 2011). Optical properties of waterbodies are further discussed in terms of inherent and apparent optical properties in Sections 8.3.1 and 8.3.2 respectively.

8.1 Optical EO Framework

The topics of water models and EO of waterbodies are introduced in Volume 1B—Section 5.2 and Volume 1B—Section 6.4 respectively. Hydrological optics are detailed in Jerlov (1976), Preisendorfer (1976), Kirk (2010), Mobley (1994), and Mobley (2020). These seminal texts endorse the symbols and definitions for relevant terms summarised in Table 8.4, Table 8.5, and Table 8.6.

Aquatic ecosystem applications of EO rely upon an understanding of the interactions between electromagnetic radiation (EMR) and the atmosphere, the water surface, the water column and, if visible, the substratum. Thus, as illustrated in Figure 8.10, the reflected EMR signal from a waterbody that is detected by the 'viewing cone' of an EO sensor (see Figure 8.4) is impacted by scattering and absorption within the atmosphere and within the water, and reflection and refraction from the water surface (or air/water interface) and possibly from the floor of the waterbody, or substratum.

Table 8.4 Hydrologic optics terms

Description and definition of the spectral radiometric variables. Ξ is the unit sphere (the set of all directions $\boldsymbol{s}$ with solid angle $d\boldsymbol{\Omega}$). μ is the cosine of the zenith angle of the horizontal plane. ∂ is the partial derivative. While all terms are wavelength-dependent, the notation (λ) has been omitted for simplicity. W: watts; m: metre; nm: nanometre; sr: steradian

a. Quantities

Type	Optical Term	Definition	Symbol/equation	Dimensions
Fundamental Quantities	Azimuth angle	see Table 8.1	ϕ	Degrees or radians
	Zenith polar angle	see Table 8.1	θ	Degrees or radians
	Solid angle	see Figure 8.3	ω (or $\boldsymbol{\Omega}$)	sr
	Cosine of polar angle	see Figure 8.8	$\mu \equiv \cos\theta$	n/a
	Water depth	Vertical distance from the water surface within the water column (see Section 5.1.1)	Z	m
Radiometric Quantities	Irradiance	Radiant flux per unit area that is incident on a surface from any direction in a hemisphere	E	W m^{-2} nm^{-1}
	Scalar irradiance	Integral of the radiance distribution at a point over all directions about that point, which measures the radiant intensity at the point	$E_0 = \int_{\Xi} L(\mathbf{s}) d\Omega$	W m^{-2} nm^{-1}
	Downwelling irradiance	See Figure 8.9a	$E_d = \int_{\Xi_d} \mu L(\mathbf{s}) d\Omega$	W m^{-2} nm^{-1}
	Upwelling irradiance	See Figure 8.9b	$E_u = \int_{\Xi_u} \lvert\mu\rvert L(\mathbf{s}) d\Omega$	W m^{-2} nm^{-1}
	Radiance	Radiant intensity per unit area on a plane perpendicular to the flow direction	$L \equiv \frac{\partial^4 Q}{\partial t \partial \boldsymbol{\Omega} \partial A \partial \lambda}$	W m^{-2} sr^{-1} nm^{-1}
	Upwelling radiance	Radiance directed from the downward hemisphere (see Figure 8.9b)	L_u	W m^{-2} sr^{-1} nm^{-1}
	Water-leaving radiance	Radiance that exits the water column at the air-water interface	L_w	W m^{-2} sr^{-1} nm^{-1}

Adapted from: Kirk (1994); Zimmerman and Dekker (2006); Ogashawara (2015)

Absorption occurs when the energy of photons is converted to another wavelength due to interaction with matter. As illustrated in Figure 8.10, an EO sensor detects the backscattered photons that survive the water surface, the water column, the substratum (if visible), and the atmosphere. In most cases, the goal of using EO methods is to reconstruct those constituents that affect (through absorption, backscattering, or fluorescence) the backscattered signal.

Table 8.5 Inherent optical properties

Definitions of Inherent optical properties (IOP) are relative to an infinitesimally thin layer of medium being orthogonally illuminated by a beam of monochromatic light (Kirk, 1994).

Optical Term	Definition	Symbol/equation	Dimensions
Absorptance	Fraction of incident radiation that is absorbed by the medium	A	n/a
Scatterance	Fraction of incident radiation that is scattered by the medium	B	n/a
Transmittance	Fraction of incident radiation that is transmitted by the medium	T	n/a
Attenuance	Fraction of radiant flux that is lost from the incident beam by absorption and scattering combined	C	n/a
Optical density	Measure of transmittance of radiation through an optical medium	D	n/a
Absorption coefficient	Fraction of incident flux that is absorbed divided by the thickness of the layer	a	m^{-1}
Scattering coefficient	Fraction of incident flux that is scattered divided by the thickness of the layer	b	m^{-1}
Attenuation coefficient	Fraction of incident flux that is absorbed and scattered, divided by the thickness of the layer	$c=a+b$	m^{-1}
Volume scattering function	Radiant intensity in a given direction from a volume element illuminated by a p	$\beta(\theta)$	$m^{-1} sr^{-1}$
Scattering phase function	Compares the shape of the angular distribution of scattering in different media with the absolute amount of scattering	$P(\theta)=\frac{\beta(\theta)}{b}$	sr^{-1}

Adapted from: Kirk (1994); Zimmerman and Dekker (2006); Ogashawara (2015)

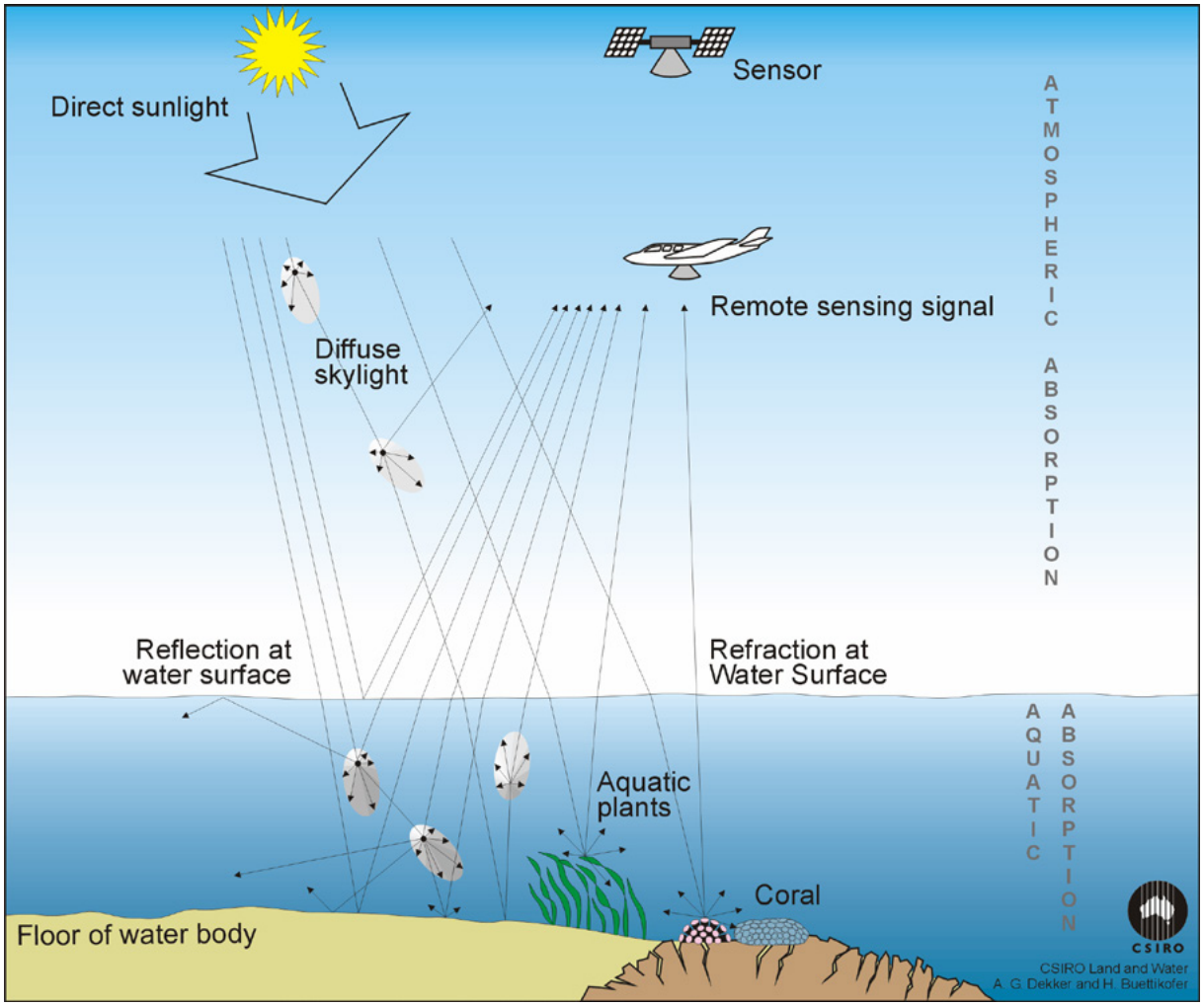
Table 8.6 Apparent Optical Properties

Optical Term	Definition	Symbol/equation	Dimensions
Irradiance reflectance	Hemispherical measure of irradiance from the water surface	$R \equiv \frac{E_u}{E_d}$	n/a
Subsurface irradiance reflectance	Hemispherical irradiance reflectance just below the water surface (0−)	$R(\lambda,0-)=\frac{E_u(\lambda,0-)}{E_d(\lambda,0-)}$	n/a
Remote sensing reflectance	Reflectance detected within the viewing 'cone' of EO sensor (see Figure 8.4c)	$R_{rs}(\mathbf{s})=\frac{L_u(\mathbf{s})}{E_d}$	sr^{-1}
Subsurface remote sensing reflectance	Reflectance detected within the viewing 'cone' of EO sensor just below the water surface (0−)	$r_{rs}(\lambda,\theta,\varphi,0-)=\frac{L_u(\lambda,\theta,\varphi,0-)}{E_d(\lambda,0-)}$	sr^{-1}
Coefficient of downwelling attenuation	Accounts for rate of change in radiant flux with increasing water depth as light beam travels down through the water column	$K_d \equiv -\frac{1}{E_d}\frac{dE_d}{dz}$	m^{-1}
Coefficient of upwelling attenuation	Accounts for rate of change in radiant flux with decreasing water depth as light beam travels up through the water column	$K_u \equiv -\frac{1}{E_u}\frac{dE_u}{dz}$	m^{-1}
Average cosine of downwelling irradiance	Average value, in an infinitesimally small volume element at that point in the field, of the cosine of the zenith angle of all downwelling photons in the volume element	$\overline{\mu}_d \equiv \frac{E_d}{E_{0d}}$	n/a
Average cosine of upwelling irradiance	Average value of the cosine of the nadir angle of all upwelling photons at a particular point	$\overline{\mu}_u \equiv \frac{E_u}{E_{0u}}$	n/a

Adapted from: Kirk (1994); Zimmerman and Dekker (2006); Ogashawara (2015)

Figure 8.10 EMR reflectance from water

For aquatic targets, four sources can contribute to the radiance detected by a remote sensor, namely the atmosphere, the interface between air and water (the surface), constituents of the water column and, in optically shallow waters, the substrate.



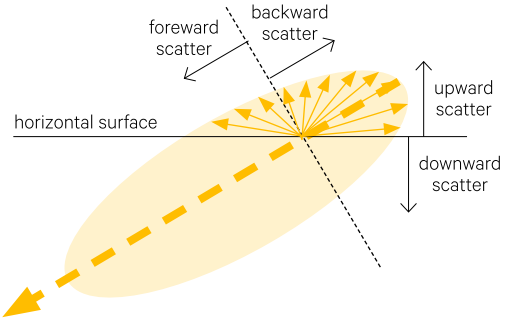
Source: Arnold Dekker, CSIRO

8.1.1 Scattering

Scattering is caused by photons that change direction and/or energy due to interaction with matter (see Volume 1B—Sections 3 and 4). Four fundamental scattering directions can be identified for incident light being intercepted by a waterbody. As depicted in Figure 8.11, forward and backward scattering directions describe the scattering processes with respect to the angle of the incident light, while upward and downward scattering describe the fractions of incident light that are scattered relative to the surface normal (that is, the water surface). Downwelling radiance comprises both direct sunlight and diffuse skylight (or scattered sunlight) at all altitudes within the atmosphere, and specifically just above the water surface.

Figure 8.11 Scattering directions

Forward and backward scattering are defined relative to the direction of the incident beam. Downward and upward scattering are defined relative to a horizontal surface. The upwelling light detected by EO may be derived from light scattered in both forward and backward directions, although the backward scattering will dominate.



Source: Zimmerman and Dekker (2006) Figure 4

Scattering can be either an elastic process, when the scattered photon has the same wavelength and polarisation as the incident photon, or an inelastic process, when the wavelength and/or polarisation of the scattered photon differ from the incident photon. In natural waters Raman scattering mostly results in the scattered photons having lower energy and thus longer wavelength. Scattering of sunlight off air molecules is called Rayleigh scattering, and results in the blue colour of the sky (see Volume 1B—Section 4.2.1). Mie scattering predominates where there are large air particles (larger than the wavelength of light; see Volume 1B—Section 4.2.2). Rayleigh and Mie scattering are elastic so the scattered photon's energy does not change. In natural waters, two types of inelastic scattering of relevance are Raman scattering and fluorescence (see Section 8.1.2. Raman scattering is virtually instantaneous and does not change incident polarisation. In natural waters, it is essentially due to the interaction of photons with water molecules, and is considered a relatively constant factor that slightly influences underwater light between 550 nm and 650 nm in very clear water.

8.1.2 Fluorescence

Fluorescence is an absorption-emission process that is relatively slow and results in unpolarised photons. In natural waters, dissolved organic matter and photosynthetic pigments (in phytoplankton, seagrasses, macrophytes, and symbiotic algae) contain fluorescent substances. Typically 1–5% of photons absorbed by chlorophyll via photosynthesis are emitted as fluorescence in a 25 nm band centred at 685 nm (Falkowski and Raven, 2007). Fluorescence effects are observed in features associated with both the water column and the substratum (see Table 8.7). Fluorescence imaging (such as the Fluorescence Image Laser line Scan: FILLS; Jaffe *et al*., 2001) can be used to distinguish between a wide variety of substratum features, including hard corals and zoanthids, soft corals, macroalgae, red algae and cyanobacteria, vase sponges, sand, shadow, and non-fluorescent features.

Table 8.7 Some fluorescence features in waterbodies

Example Feature	Description	Fluorescence
Chlorophyll	Photosynthetic pigment in organisms within water column and substratum	Red
Phycoerythrin	Photosynthetic accessory pigment in red algae and cyanobacteria within water column and substratum	Orange
Corals	Substratum fauna	–
Anemones		–
Some sponges		–
Carbonate sediment	Organic matter in calcium carbonate matrix	–
CDOM	Coloured Dissolved Organic Matter	Ultraviolet

Source for data: Mazel (2001); Para *et al.* (2010)

8.1.3 Water surface effects

Waterbody surfaces exhibit swell, waves, and capillary waves with heights or amplitude ranging from a few centimetres to tens of metres. Although their overall distribution can be predicted in a stochastic way, the inherently chaotic nature of these surface effects complicates their removal from surface reflectance. Oil slicks can dampen wave action and increase reflectance of some wavelengths. Ocean surface waves create 'whitecaps', that is bubbles and streaks on their breaking crests, which also change the observed water colour (Estep and Arnone, 1994). Air bubbles, which tend to occur in association with waves, increase reflectance in different wavelengths (Pozdnyakov and Grassl, 2003). These are easier to measure in oceans, but also occur in other natural waters.

At the surface of a waterbody, or the 'air-water interface', two processes can occur:

- downwelling irradiance may be reflected due to the specular or Fresnel reflectance of the water surface; or
- light is refracted (due to a density difference between air and water) and passes into the water column.

Thus, downwelling irradiance above the water surface is either reflected from the surface back into the atmosphere or refracted across the air-water interface into the water. 1–15% of the downwelling irradiance from the atmosphere is reflected from the surface of waterbodies, with most waterbodies reflecting 2–6%. For a flat water surface, these Fresnel reflectance and refraction values can easily be computed. When the situation is more complex, such as a rough water surface with swell, waves, and fractal wavelets, these values can still be computed, or derived through observations (Dekker *et al.*, 2006).

Snell's law describes the change in the angle of light and other waves as they pass through a boundary between two media, such as air and water (see Volume 1A—Section 2.5.2):

$$\frac{\sin\theta_{air}}{\sin\theta_{water}} = \frac{n_{water}}{n_{air}}$$

where

θ is the angle of incidence; and
n is the refractive index.

This equation is used to calculate refraction and reflection of incident light beams at the water surface. The refractive index is a function of the wavelength of the light, as well as the salinity, temperature, and pressure of the water (Parrish, 2020). For seawater the refractive index is generally 1.338 (Plass and Kattawar, 1972) to 1.34 (Mobley, 2020), while freshwater is generally slightly lower at 1.333.

Given the refractive index of seawater, irradiance intercepting a flat seawater surface from the atmosphere at all angles (potentially spanning 180°) only passes into the water column within a compressed cone (spanning a maximum of 97.6°). Conversely, any upwelling light that intercepts the surface at angles outside this cone will not penetrate the surface but becomes reflected internally within the water (see Figure 8.12). Surface roughness tends to slightly widen the solid angle of this cone.

In most studies of surface water, the surface reflected component is an unwanted signal in EO imagery whereas the surface refracted component becomes involved in cascades of absorption and scattering. The light-interaction-with-water processes involving refraction, refractive indices, internal reflection, sea roughness, sunglint, and wind-induced optics have been successfully explained and modelled by optical oceanographers for several decades. When remotely sensing natural waterbodies from satellite and/or aircraft altitudes, numerous techniques have been proposed to remove the impact of surface waves on downwelling solar and sky radiation (Cox and Munk, 1954). Wave energy issues that are a function of local climatic conditions, however, still present difficulties in rigorously detailing how radiation is transferred through the air-water interface.

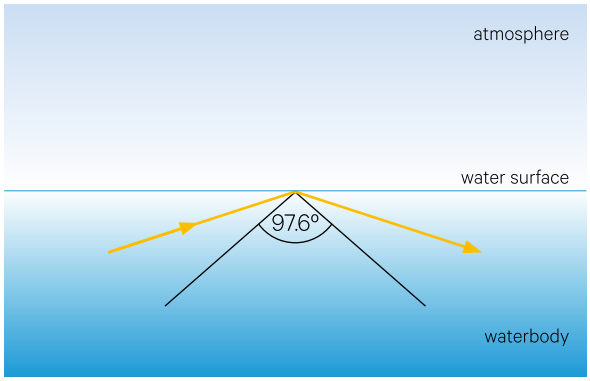
The extent of water surface reflection observed by a remote (airborne) sensor largely depends on Sun position. Image acquisition by airborne and 'agile' satellite borne sensors (such as Quickbird or WorldView-2/3 which are 'pointable' in space), therefore, would ideally consider the solar zenith angles and azimuths from which (given the field of view of the scanner) it is least likely to image sunglint from a water surface (Botha *et al.*, 2016). In general:

- solar zenith angles between 30° and 60° are optimal over water targets; and
- flight paths should be flown at 0° or 180° headings with respect to the solar azimuth (that is either directly towards or away from the Sun; Mustard *et al.*, 2001; Dekker *et al.*, 2003).

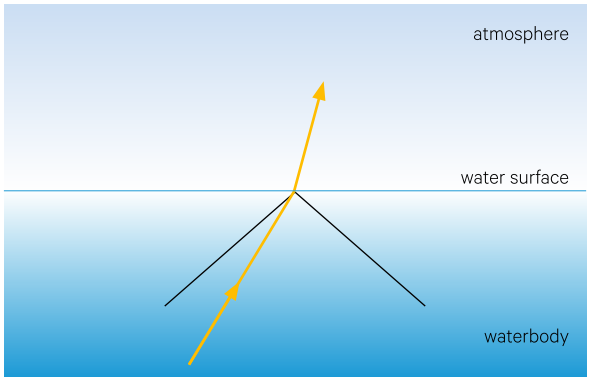
Figure 8.12 Internal reflection and refraction

The direction of travel of light beams from inside a water body (such as substratum reflectance, Raman fluorescence, or backscattering in the water column) determines whether, at the water surface, they are internally reflected back into the waterbody or refracted into the atmosphere.

a. Internal radiance intercepting the water surface outside the 97.6° refraction cone will be internally reflected into the waterbody.



b. Internal radiance intercepting the water surface inside the 97.6° cone will be refracted into the atmosphere.



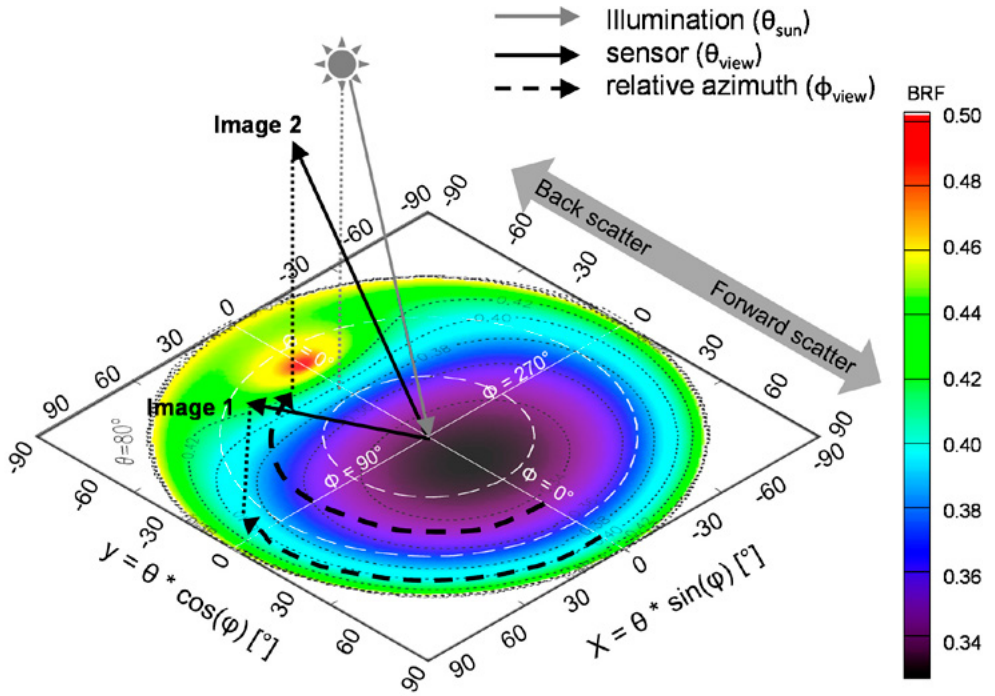
At high latitudes this will mean acquiring imagery in a short period of time around noon in summer to achieve a maximal amount of irradiance. At mid-latitudes the flight time will be dependent on the season since the maximum solar zenith angles increase from summer to winter. Accordingly, the mid-latitude flight time envelope decreases from approximately six to eight hours surrounding noon in summer to two hours surrounding noon in winter. At low latitudes the requirement to fly between 30° and 60° solar zenith angles means that solar noon must also be avoided to prevent sunspot effects (direct reflectance from horizontal water surfaces into the field of view). In this case, there are only two suitable image acquisition periods: one in the morning and one in the afternoon. These considerations are also relevant to ordering high spatial resolution satellite imagery since the new generation of satellite sensors offer selectable viewing angles (that is, in addition to nadir imaging). Off-nadir viewing is advantageous if sunglint and skyglint can be avoided but detrimental if these effects are enhanced.

Image processing methods exist to 'deglint' water surfaces in EO imagery (see Volume 2). While the deglinting process decreases the radiometric resolution of the image data, it may not increase the spectral separation between different substrata (Hedley, 2013). Shipborne, above-water EO sensors face particular challenges with respect to surface-reflected glint (Garaba and Zielinski, 2013) with no current correction methods offering a universal panacea.

One example of the impact of water surface effects in EO imagery is given by Botha et al. (2016), who compare two high spatial resolution EO images that were acquired one minute apart over an optically shallow coastal ecosystem in Tasmania. While the viewing and illumination geometries of the first image were optimal, resulting in minimal sunglint, the second image was acquired with significant sunglint and atmospheric scattering (see Figure 8.13 and Figure 8.14). When satellite-based bathymetry (see Section 13.4.2) was applied to both images, accurate results were obtained from the first image, but water depths were underestimated from the second image.

Figure 8.13 Sun-sensor geometry of example images

Two WorldView-2 images were acquired one minute apart over a shallow coastal lagoon in Tasmania, Australia (42.8211°S, 147.5508°E) on 22 October 2011. The position of the Sun, relative to the target, was constant, while the position of the sensor, relative to the target, changed. The resulting images are shown in Figure 8.14.



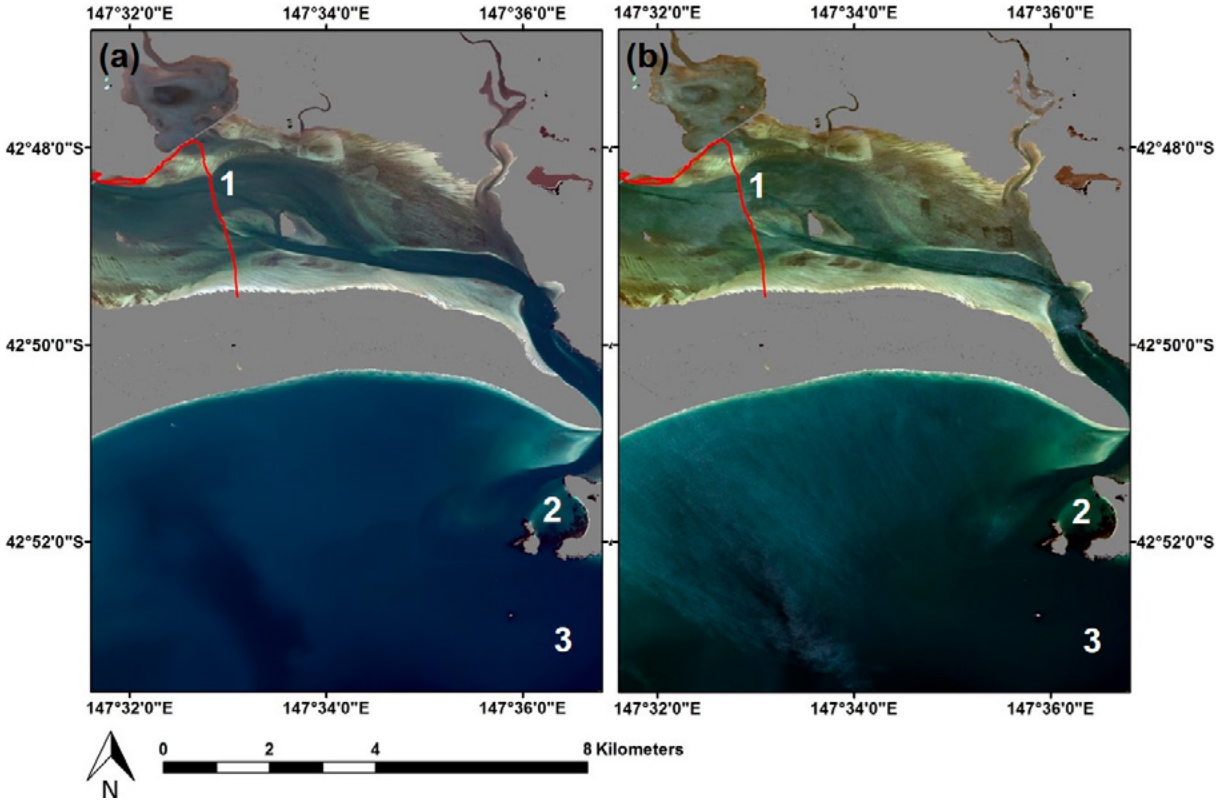
Source: Botha *et al.* (2016) Figure 1

Figure 8.14 Impact of sun-sensor geometry on image quality

These images were acquired using the sun-sensor geometry shown in Figure 8.13, during an outgoing tide with a gentle (16 km/h) southeasterly breeze. Gray mask: exposed land area; 1: location of the *in situ* depth observations (red dots) collected on 22 August 2013; 2: location of the least glint-affected image segment, selected for atmospheric correction inter-comparison; 3: location of an area of water (as homogenous and optically deep as possible) that was selected for the NEΔrsE (Environmental Noise Equivalent Remote Sensing Reflectance Difference) computation.

a. Image 1 (ϕ_{view} = 106°, θ_{view} = 77°) showed minimal sunglint and resulted in accurate water depth estimates.

b. Image 2 (ϕ_{view} = 175°, θ_{view} = 57°) showed significant sunglint and atmospheric path scattering and underestimated water depths.



Source: Botha *et al.* (2016) Figure 2

8.1.4 Radiative transfer theory

Scattering and absorption of light occurs as it passes through any medium. In the atmosphere, aerosols, gases, and water absorb or scatter light. Within a natural water column, the absorption and scattering of light depends on water depth, substratum type (if visible), and/or water constituents, (namely pure water, photosynthetic pigments, particulate matter, coloured dissolved organic matter (CDOM), and coloured dissolved inorganic matter (CDIM); see Section 8.1.3). Each of these constituents absorbs and scatters light in a spectral (that is, wavelength-dependent) manner. The light reaching a seagrass canopy, for example, is modified by the interaction of the downwelling irradiance with these water constituents and thus influences the quality of the light available for photosynthesis (see Zimmerman, 2006). The upwelling radiance, then, includes direct and diffuse sunlight that has been reflected by the water surface and/or scattered back through the water surface by the water column after penetrating the surface and interacting with water or benthic components.

As introduced in Volume 1B—Section 5, radiative transfer describes how radiant energy, such as light, is changed by any medium it passes through. Radiative Transfer theory approximates the loss of radiant energy of a beam due to absorption and scattering along a defined path, and any energy gain resulting from scattering into the path (see Figure 8.5). Radiative Transfer models for optical EO imagery of water are detailed in Section 8.4.1.

8.1.5 Atmospheric correction

While the atmospheric correction physics of optical EO data over waters is essentially the same as for terrestrial targets, a few practical differences need to be considered. On land, the signal reflected from the surface contains useful information about the surface, whereas for any waterbody, the signal coming from within the water is the desired signal. Moses *et al.* (2017) provide a useful overview of this process for inland waters.

In most studies of water properties, the signal reflected from the water surface is considered to be noise and comprises the reflected component of diffuse skylight and the direct sunlight impinging on the water surface (see Section 8.1.3). While methods for atmospheric correction of oceans are quite mature, the task is more complex for coastal and inland waters due to highly varying aerosol levels, adjacency effects, elevation issues, less predictable sunglint and skyglint, and local effects with finer spatial resolution data.

Although many atmospheric correction software packages are available, or are included in generic EO processing software, they only function over land targets. For atmospheric correction over waterbodies, various models have attempted to extract the unwanted atmospheric signal from water-leaving radiances. These models range from overly simplistic in attributing all the atmospheric return to a single NIR wavelength band (often incorrectly assuming the water reflectance to be zero) to diligently generating 'generic' atmospheres by practical combinations of air temperature, solar azimuth, terrain elevation, aerosol density, day of year, atmospheric composition, wind speed, and other atmospheric parameters such as visibility and meteorological range (Pahlevan *et al.*, 2021). Artificial neural networks have delivered promising results for atmospheric correction over the GBR (Goyens *et al.,* 2013; Singh *et al.*, 2019).

8.2 Optically Active Constituents of Water

All particulate matter (algae, dead organic matter, and mineral particles) scatters light, with the extent and type of scattering depending on the sizes and refractive indices of particles (see Section 8.1.1). When light is absorbed, however, it can no longer be elastically scattered, but may be emitted as fluorescence (inelastic scattering).

A variety of components that are present in natural waters collectively determine the optical properties of a waterbody. Historically, the terminology used to describe these components has differed between oceanographers studying marine waters and limnologists studying inland lakes. Further, the range of optical components, and their relative complexity, varies for different types of surface waters. Accordingly, the current terminology to describe the optical components of natural waterbodies can appear somewhat confusing. For example, limnological terms that may be encountered in research literature include:

- seston—total particulate matter including terrigeneous sediments, plankton, detritus, volcanic ash, chemical process particulates, and anthropogenic particles (Dekker, 1993; Lindell *et al.*, 1999); this is equivalent to Total Suspended Matter (TSM) and includes pigments and algal biomass; or
- tripton—all particulate matter except phytoplankton pigments, also called detritus; this is equivalent to non-algal particulates (NAP); or
- gilvin, gelbstoff, yellow substance—is equivalent to chromophoric (or coloured) dissolved organic matter (CDOM).

Being photosynthetic agents, pigments absorb light very effectively. While the pigments in algae comprise only 1/3000 of the total algal mass, they absorb significantly more light than the cell material, or biomass. Algal biomass, however, scatters light. For example, the phytoplankton *Coccolithophores* is characterised by significant scattering by its cell structure, which is masked in live organisms by pigments. In dead organisms, however, while pigments decay, the cell structure remains optically significant.

To distinguish between the optical impacts of pigments and particulate matter in natural waterbodies, water samples are filtered in order to extract photosynthetic pigments from the particulate matter using organic solvents and, more specifically, the phytoplankton. Accordingly, the term 'particulate matter' is commonly considered to collectively describe inorganic matter, detritus, plus the algal cell material remaining after pigments have been extracted by filtering. For reasons best understood by ocean colour scientists, this group is also referenced as 'non-algal' particles (NAP), although a better term would be 'non-algal pigmented' particles.

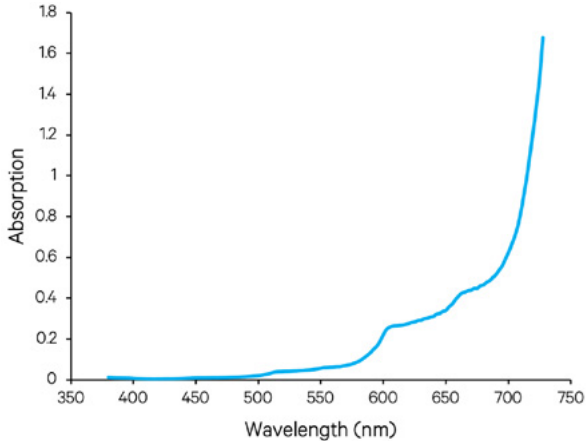
In the following text, optical components will be considered in terms of five discrete groups:

- pure water—optically pure (see Section 8.2.1);
- photosynthetic pigments—from phytoplankton and cyanobacteria (see Section 8.2.2);
- particulate matter—'non-algal' particles (NAP; see Section 8.2.3);
- coloured dissolved organic matter (CDOM)—from hydrocarbon compounds (see Section 8.2.4); and
- coloured dissolved inorganic matter (CDIM)—from mineral compounds (see Section 8.2.5).

8.2.1 Pure water

Molecules of pure liquid water scatter blue wavelengths with rapidly decreased scattering for longer wavelengths. Conversely, pure water absorption of blue wavelengths is very low, but this increases significantly towards NIR wavelengths (see Figure 8.15). Since the least absorption, and some scattering, occurs with blue wavelengths, pure liquid water appears to be coloured blue.

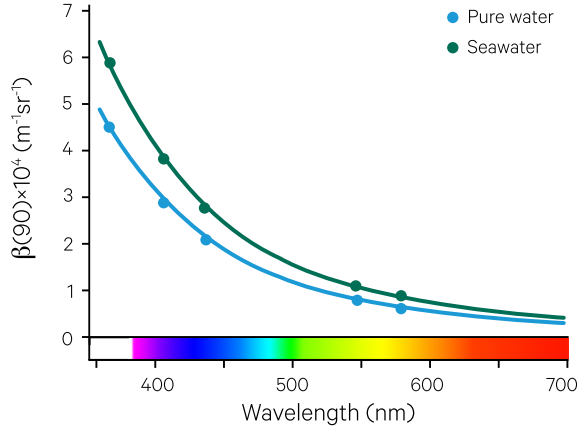
Figure 8.15 Absorption spectrum of pure water



Source: Janet Anstee, CSIRO, using data from Pope and Fry (1997)

Figure 8.16 Effect of salinity on scattering by water

Data from Morel (1968) and Zhang *et al.* (2009) for spectral scattering of water at 20°C. Pure water (shown as solid line) is compared with natural seawater (salinity=3.85%; shown as dashed line). The scattering was measured at five wavelengths, 366 nm, 405 nm, 436 nm, 546 nm and 578 nm (dots), and the scattering is represented with the volume scattering function at 90°, β(90).



Adapted from: Mobley (2020) *https://www.oceanopticsbook.info/view/optical-constituents-of-the-ocean/water*

Natural waters are rarely pure however, and reflectance characteristics can vary slightly with temperature and salinity. Seawater, for example, is 96.5% pure water, with 3.5% salts, plus dissolved and/or suspended substances. The influence of salinity on scattering is evident in Figure 8.16, with a 30% increase in scattering between the freshwater and seawater samples. Zhang *et al.* (2009) report that while the contribution of salinity to the total scattering is minor (less than 10%) in visible wavelengths for very clear ocean waters, it accounts for up to 80% of the total backscattering. By comparison, in the waters of a clear alpine lake a major contribution to the total backscattering (30–60%) comes from the water itself.

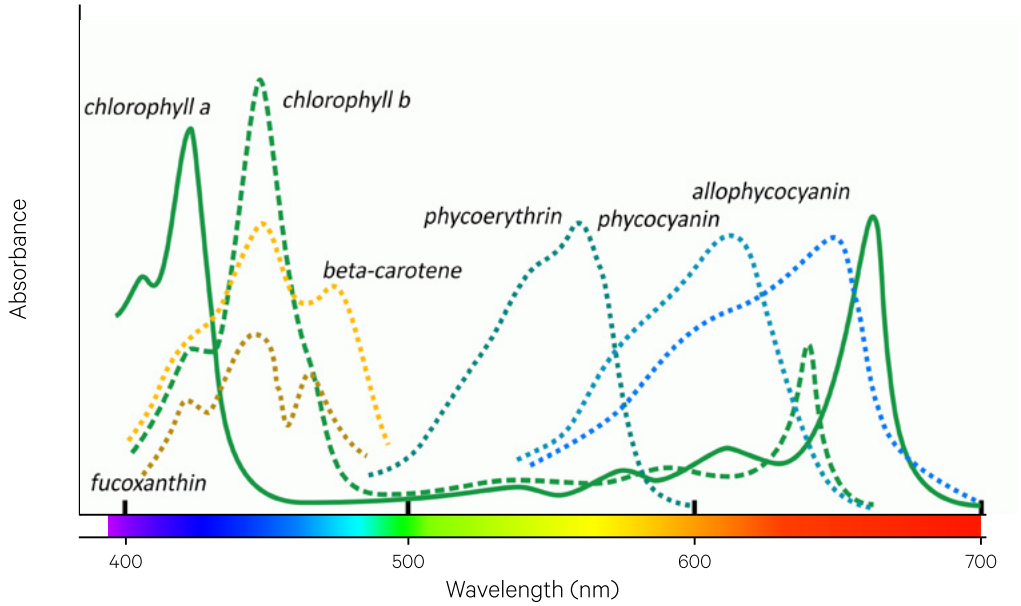
8.2.2 Phytoplankton and cyanobacteria pigments

As introduced in Section 3.3.1, plankton comprise tiny, floating zooplankton (animals) and phytoplankton (plants), some of which are independently mobile. Phytoplankton includes more than 10,000 species, which manifest as a wide range of sizes, shapes, and colours, and occur in inland, coastal, and ocean waters. The composition and concentration of phytoplankton pigments can impact water colour, with the main pigment groups being:

- chlorophylls—which appear as the colour green, due to strongest absorption of blue and red wavelengths;
- carotenoids—which appear to be coloured yellow to red, due to strongest absorption in broad region of blue-green wavelengths; and
- phycobilins—which appear to be predominantly coloured blue, blue-green, and red, due to strongest absorption of yellow to orange wavelengths.

Absorption spectra for these pigments are illustrated in Figure 8.17. To obtain the pigments, the particulate matter, including phytoplankton, that is present after filtering over a 0.45–0.70 μm filter, is flushed with an organic solvent such as ethanol, acetone, or methanol. The filtrate then contains the pure pigments. For cyanobacterial pigments that are water soluble, the cells first need to be destroyed through grinding and heating before the pigments can be flushed out using water.

Figure 8.17 Absorption spectra of algal pigments



Adapted from: Goodwin and Mercer (1990) by Qiaoyun Xie, University of Technology Sydney. (Original retrieved from *http://biologywiki.apps01.yorku.ca/index.php?title=File:Pigment_spectra.png*)

The most abundant pigment in phytoplankton is chlorophyll a, which has two (*in situ* and *in vivo*) absorption peaks at 438 nm and 676 nm respectively. Cell components and cell walls of phytoplankton also absorb and scatter light. Characteristically, phytoplankton absorption is virtually zero at 720 nm and greater wavelengths. The cyanophycocyanin pigment characterising cyanobacteria (blue-green algae) has a distinctive absorption feature near 620 nm (Simis *et al.*, 2005). Variations in phytoplankton pigments are detailed in Kirk (1994, 2010). Pigments can also be characterised by their fluorescence wavelengths.

Some of the variations in water colour that can result from different species of phytoplankton are shown in Figure 8.18. The absorption spectra for these species are illustrated in Figure 8.17. Two spectra are given for diatoms to indicate the spectral difference resulting from high and low light levels. The major optically active pigments for phytoplankton taxonomic classes are listed in Table 8.8.

Estimates of phytoplankton concentration, derived from bio-optical data, are considered to be indicative of marine primary productivity. Various models have been proposed to relate phytoplankton light absorption to chlorophyll concentration (Bricaud *et al.*, 1995; Brando *et al.*, 2009, 2012; Blondeau-Patissier *et al.*, 2009). These models derive summary parameters, such as the phytoplankton coefficient, which synthesise the absolute cell concentration, composition of the phytoplankton community, and inter-species variations in pigment composition. The total phytoplankton spectrum is obtained as the sum of individual spectra (Mobley, 2020).

Figure 8.18 Water colour variations due to phytoplankton

Phytoplankton species, left to right: diatom, cryptophyte, chorophyte, cyanophyte, premnesiophyte, and dinoflagelate



Source: Mobley (2020) Figure 3. Retrieved from *http://www.oceanopticsbook.info/view/absorption/absorption_by_oceanic_constituents*

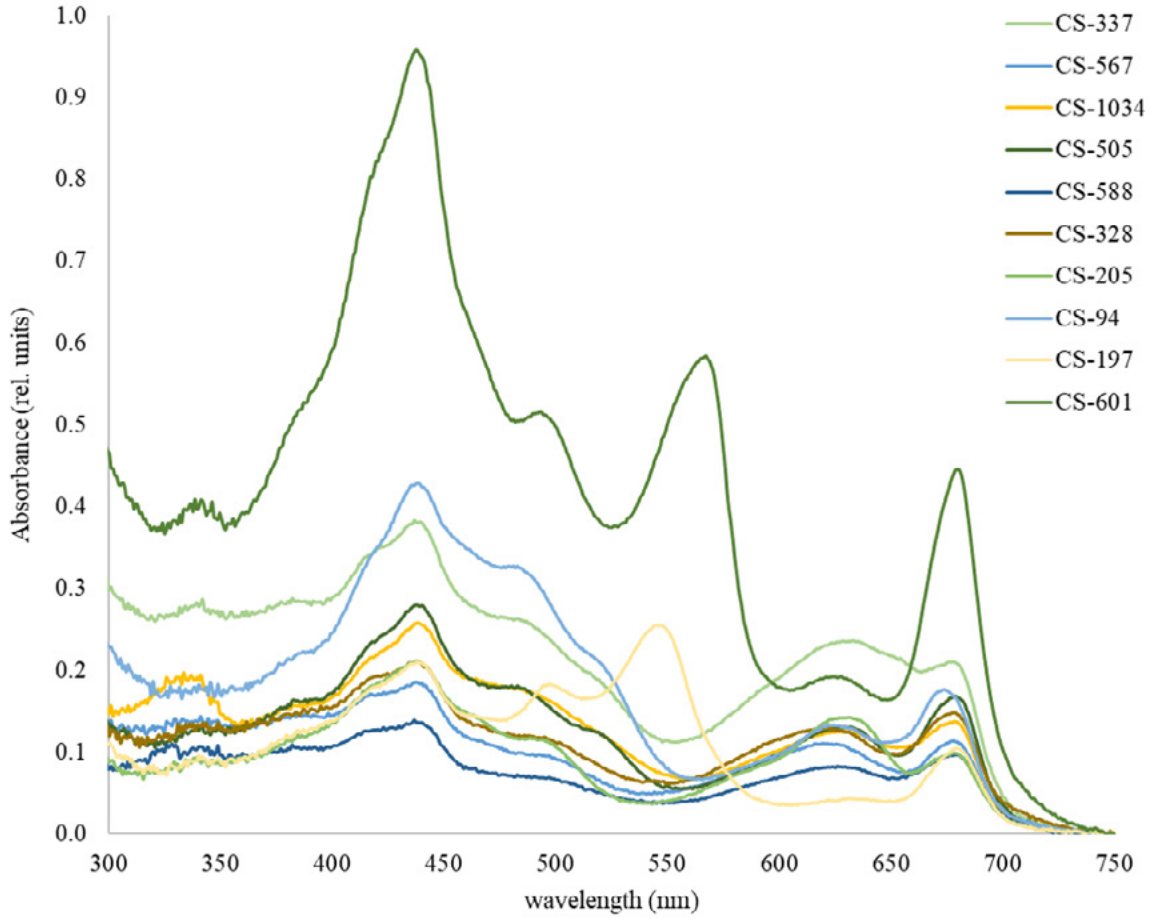
Table 8.8 Major photo pigments for phytoplankton taxonomic classes

Diagnostic pigments	Taxonomic association	Typical cell size (μm)	Phytoplankton class
Fucoxanthin	Diatoms	> 20	Microphytoplankton
Peridinin	Dinoflagellates	> 20	Microphytoplankton
Alloxanthin	Cryptophytes	2–2	Nanophytoplankton
Lutein + chlorophyll b	Chlorophytes	< 2	Picophytoplankton
Zeaxanthin and Lutein	Cyanobacteria	< 2	Picoplankton
Chlorophyll b	Prochlorophytes and flagellates	< 2	Picoplankton
Echinenone	Cyanobacteria	< 2	Picoplankton

Source: Joehnk *et al.* (2018)

Figure 8.19 Absorption spectra for phytoplankton

CS-337: *Dolichospermum circinale* (Burrinjuck Dam, Australia)
CS-567: *Microcystis aeruginosa* (Gippsland Lakes, Australia)
CS-1034: *Chrysosporum ovalisporum* (Brisbane, Australia)
CS-505: *Raphidiopsis raciborskii* (Palm Island, Qld, Australia)
CS-588: *Nodularia spumigena* (Gippsland Lakes, Australia)
CS-328: *Arthrospira maxima* (Lake Chad, Africa)
CS-205: *Synechococcus sp.* (Menai Strait, UK)
CS-94: *Synechococcus sp.* (Queenscliff, NSW, Australia)
CS-197: *Synechococcus sp.* (Sargasso Sea)
CS-601: *Synechococcus sp.* (Ace Lake, Antarctica)



Source: Clementson *et al.* (2021)

8.2.3 Non-algal particles (NAP)

Non-algal particles (NAP) are defined as particulate matter that cannot be extracted by methanol/ethanol/acetone (Kishino *et al.*, 1985). By default, once pigments have been extracted from water samples, NAP is the remaining matter that does not pass through a (0.45–) 0.7 mm filter. This residue can include:

- suspended particulate organic matter (SPOM)—organic particles from bacteria, zooplankton, phytoplankton, including detrital organic matter; and
- suspended particulate inorganic matter (SPIM)—suspended inorganic particles.

All NAP constituents (except iron minerals) mainly absorb UV to blue wavelengths, with absorption reducing exponentially to red to NIR wavelengths (Babin *et al.*, 2003). The proportion of constituents varies with water location, with higher non-organic particle concentrations occurring near rivers and benthic boundary layers. Highest concentrations of NAP occur in inland and coastal waters.

At wavelengths where suspended (undissolved) particles, including algae, in water scatter more radiation than they absorb, the backscattering coefficient will be more than the absorption coefficient, with a consequent increase in the radiance detected by an EO sensor (Kirk, 1994). As such, turbid waters appear brighter in optical wavelengths than clear waters. This characteristic allows EO imagery to be used to map the concentration of NAP in water (see Sections 18.1 and 19). The precise optical properties of suspended sediments vary with their sizes, colours, and concentrations (see Section 5.1.4).

8.2.4 Coloured dissolved organic matter (CDOM)

Rivers and inland waters often contain tannins and other dissolved organic materials that colour their water (Shank *et al.*, 2010). Being dissolved (defined as material passing through a 0.2 μm pore filter[9]; Bricaud *et al.*, 1981), CDOM does not scatter light. Constituents include organic substances, which absorb UV to blue wavelengths with exponential decay towards red wavelengths.

Waters containing high concentrations of CDOM are typically coloured yellow to brown (see Section 5.2.3.1). Highest concentrations occur in inland and coastal waters, and the discharge from inland waters provides a substantial pool of CDOM to coastal waterways. Sources of CDOM in subtropical and tropical coastal waters are primarily derived from leaching or degradation of seagrasses (Otis *et al.*, 2004) or mangrove leaf litter (Maie *et al.*, 2006).

The typical absorption spectrum for CDOM decreases exponentially with wavelength from UV through the visible spectrum (Twardowski *et al.*, 2004). As illustrated in Figure 8.20, the actual slope of the absorption spectrum for each water sample is determined by its CDOM concentration. CDOM absorption spectra are commonly modelled as an exponential decay function of wavelength (Jerlov, 1976):

$$a_{CDOM}(\lambda) = a_{CDOM}(\lambda_0)e^{-S(\lambda_0-\lambda)}$$

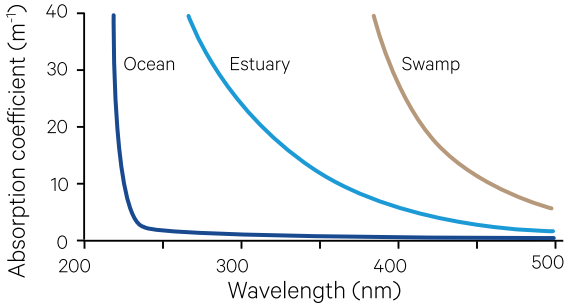
where

$a_{CDOM}(\lambda)$ is the absorption coefficient of wavelength λ;
λ_0 is the reference wavelength (often 440 nm); and
S is the slope of the spectrum within a given wavelength interval (nm^{-1}).

To determine the exponential function for specific CDOM sites, the actual absorptions of filtered samples are measured using a spectrophotometer, typically over the wavelengths 250–800 nm. The CDOM spectral slope is then derived by fitting an exponential curve to the measured absorptions from 300–600 nm (Mannino *et al.*, 2008).

Figure 8.20 CDOM Absorption spectra

Stylised absorption spectra for 0.2 μm filtered water samples indicate the spectral slope changes that occur with decreasing CDOM concentration.



Adapted from: Helms *et al.* (2008) Figure 1a

9 A problem identified by Laanen *et al.* (2011) is that particulate matter is filtered out over 0.7 mm filters (to avoid the filter from clogging up too soon) whereas CDOM is filtered over 0.22 mm filters. This means the 0.22–0.7 mm particulate material is unaccounted for in lab-based bio-optics measurements.

Analysis of over 500 oceanographic field campaigns over a 30 year period in the Global Ocean Carbon Algorithm Database (GOCAD) indicates that the CDOM absorption and spectral slope values are linked to atmospheric and oceanographic processes such as the El Niño Southern Oscillation (ENSO; Aurin *et al*, 2018). For example, exposure of CDOM to sunlight has been shown to increase the spectral absorption slope through photo-bleaching of the CDOM (Del Vecchio and Blough, 2002). In recent studies, it was found that riverine CDOM absorption slopes became very similar to marine CDOM after five days of sunlight exposure (Martin *et al.*, 2018).

8.2.5 Coloured dissolved inorganic matter (CDIM)

The optical absorption characteristics of minerals depends on their colour, which can vary from white to grey, occasionally yellow, brown, or red (and occasionally black in the case of volcanic material). Dissolved inorganic salts have highest absorption in UV wavelengths due to electronic transition bands (see Volume 1—Section 6.3). Scattering by dissolved inorganic salts and/or iron compounds is generally more significant for ocean waters than for freshwater in inland waterbodies.

8.3 Optical Properties of Water

The optical properties of water may be described as either Inherent Optical Properties (IOP; see Table 8.5 and Section 8.3.1) or Apparent Optical Properties (AOP; see Table 8.6 and Section 8.3.2). IOP and AOP are connected via radiative transfer theory (see Section 8.4.1 and Volume 1B—Section 5). Optical properties of the substratum are considered in Section 8.3.3. Systems that classify water colour using IOP and AOP are introduced in Section 18.3.

8.3.1 Inherent Optical Properties

Inherent Optical Properties (IOP) describe the absorption and (back)scattering characteristics of a water sample, including dissolved and suspended components, but not the geometry or magnitude of incoming radiation. As the name implies, IOP describe properties that are *inherent* to the optical behaviour of the water, regardless of lighting conditions. Accordingly, the IOP of a water sample may be measured anywhere, in the field or laboratory, and should yield the same results, assuming no measurement errors are made.

As illustrated in Figure 8.5, when a beam of light enters a volume of water, its energy changes in three ways:

- some is absorbed by the water—absorptance (*A*): proportion of incident light that is absorbed within the volume;
- some is transmitted through the water—transmittance (*T*): proportion of incident light that passes through the volume without interaction; and
- some is scattered out of the beam—scatterance (*B*): proportion of incident light that is scattered out of the beam in all directions.

These three options are represented as fractional components of the incident light beam, such that:

$$A + B + T = 1$$

In pure water, most incident energy is transmitted, rather than scattered or absorbed. Scattering by particles in natural waters, however, extends the path length of light, and thus increases the probability of absorption. It also propagates photons back towards the light source, which is known as backscattering. The precise direction of backscattering depends on the properties of the water.

IOP are defined by illuminating a small volume (thickness Δr) by a narrow, collimated beam of monochromatic light (with spectral radiant power Φ_i). Within the volume, portions of this light are either absorbed (Φ_a), scattered (at angle Ψ within a cone of solid angle $\Delta\Omega$), or transmitted (Φ_t). For a given volume of water, they can be defined as given in Table 8.9.

Shallow waters are generally associated with coasts, currents, and terrigenous inputs, and the optical properties of the water column and the seafloor can vary rapidly in time as well as in space.
(Mazel, 2001)

Table 8.9 Commonly used Inherent Optical Properties

Property	SI units	Symbol	Description
Absorption coefficient	m^{-1}	a	Absorptance per unit distance in the volume, which indicates the distance that a beam of light can penetrate into the volume before it is absorbed. When normalised, this effectively describes the probability of a photon being absorbed by the medium.
Scattering coefficient	m^{-1}	b	Scatterance per unit distance in the volume, which indicates the distance that a beam of light can penetrate into the volume before it is scattered. When normalised this effectively describes the probability of a photon being scattered by the medium.
Backscattering coefficient	m^{-1}	b_b	Indicates the attenuation due to backscattering (90–180° from light source) and computed from the volume scattering function. When normalised this effectively describes the probability of a photon being backscattered.
Forward scattering coefficient	m^{-1}	b_f	Indicates the attenuation due to forward scattering (0–90° from light source) and computed from the volume scattering function. When normalised this effectively describes the probability of a photon being scattered in a forward direction.
Beam attenuation coefficient (or extinction coefficient)	m^{-1}	c	Indicates the distance that a beam of light can penetrate into the volume before it is attenuated (absorbed or scattered). When normalised this effectively describes the probability of a photon being attenuated by the medium.
Volume scattering coefficient	$m^{-1}sr^{-1}$	β	Characterises the intensity of scattering for a given angle. When normalised this effectively describes the probability of a photon being scattered in a particular direction within the medium.
Scattering phase function (or phase function)	sr^{-1}	$\tilde{\beta}$	Indicates the angular distribution of light intensity scattered by a particle at a given wavelength
Single-scattering albedo	n/a	$\tilde{\omega}$ or ω_0	Ratio of the scattering coefficient to the extinction coefficient. This affects radiative transfer and is generally a function of wavelength.

Adapted from: Mobley (2020); AMS (2019)

The two main optical processes in the water column are absorption and elastic scattering (see Section 8.1.1). Absorption is measured in terms of IOP as the absorption coefficient and elastic scattering is quantified by the volume scattering function (see Table 8.4; Dekker *et al.*, 2001). Other IOP can be derived from these primary properties.

The IOP of water vary with its particulate and dissolved materials in terms of:

- composition—type of particulate and dissolved matter;
- morphology—sizes and shapes of particles; and
- concentration—number of particles per unit volume, or particle size distribution.

The magnitude of IOP vary considerably for different water sources, and may be up to several orders of magnitude higher in turbid coastal waters than open ocean water (Mobley, 2020).

8.3.2 Apparent Optical Properties

Since traditionally IOP have not been easy to measure *in situ*, a range of other informative parameters were developed to describe waterbodies (Mobley, 2020). These parameters are known as Apparent Optical Properties (AOP) and provide valuable information about water constituents of waterbodies—their nature and concentrations—from measurements that can be made in the ambient lighting conditions (see Table 8.10). These properties are closer to those measured by EO sensors and can vary if the water is measured at different locations, times, depths, and weather conditions. For example, EO reflectance is an AOP.

As the name implies, AOP are properties that describe how the water *appears* under specific lighting conditions. AOP are relatively stable and are generally consistent with water depth so offer a conduit to describing the optical behaviour of waterbodies. AOP are derived from the relevant IOP and the angular distribution of the ambient lighting conditions. The latter is defined in terms of the geometry of directional radiance vectors, which represents the geometry and magnitude of incident radiation. While IOP are derived from the behaviour of a collimated beam of photons, the AOP are based on the ambient directional radiance, that is, photons heading in a particular range of directions (such as downwards). As such, these parameters are also called diffuse AOP.

Table 8.10 Commonly used Apparent Optical Properties

Remote sensing reflectance (R_{rs}) is a function of wavelength only. K_{PAR} is a function of water depth only. All other AOP are functions of both waterdepth and wavelength.

a. Diffuse attenuation coefficents (K functions)

Property	SI units	Symbol	Definition	Description
Radiance in any direction L	m^{-1}	$K(\theta,\phi)$	$\frac{-d\ln L(\theta,\phi)}{dz}$	EMR energy in all directions
Upwelling radiance L_u	m^{-1}	K_{Lu}	$\frac{-d\ln L_u}{dz}$	Radiance directed upwards
Downwelling irradiance E_d	m^{-1}	K_d	$\frac{-d\ln E_d}{dz}$	Normalised or logarithmic depth derivative of E_d, which indicates the water depth at which downwelling radiation is attenuated.
Upwelling irradiance E_u	m^{-1}	K_u	$\frac{-d\ln E_d}{dz}$	Normalised or logarithmic depth derivative of E_u, which indicates the water depth at which upwelling radiation is attenuated.
Scalar irradiance E_o	m^{-1}	K_o	$\frac{-d\ln E_o}{dz}$	Total number of photons per unit time and area reaching a point from all equally-weighted directions
Photosynthetically active radiation (PAR)	m^{-1}	K_{PAR}	$\frac{-d\ln PAR}{dz}$	EMR in the range 400–700 nm which activates photosynthesis

b. Reflectances

Property	SI units	Symbol	Definition	Description
Irradiance reflectance	n/a	R	$\frac{E_u}{E_d}$	Ratio of upwelling to downwelling plane irradiances, which is more stable than the irradiance measurements alone
Remote sensing reflectance	sr^{-1}	R_{rs}	$\frac{L_w\ (\text{in air})}{E_d\ (\text{in air})}$	Ratio of water-leaving radiance to downwelling irradiance, which is more closely related to EO measurements than R
Subsurface remote sensing reflectance	sr^{-1}	r_{rs}	$\frac{L_u\ (\text{in water})}{E_d\ (\text{in water})}$	Ratio of upwelling radiance (L_u) to downwelling irradiance, just below the water surface

c. Mean cosines

Property	SI units	Symbol	Definition	Description
Of the radiance distribution	n/a	$\overline{\mu}$	$\frac{\left(E_d - E_u\right)}{E_o}$	Summarises range of angular variations in view angle for measured radiance (for given illumination and atmospheric conditions)
Of the downwelling radiance	n/a	$\overline{\mu}_d$	$\frac{E_d}{E_{0d}}$	Uses the Cosine Law to convert the downwelling irradiance E_d (which is intercepted by a surface perpendicular to the incident radiation) to the irradiance that would be intercepted by a horizontal plane, such as the water surface
Of the upwelling radiance	n/a	$\overline{\mu}_u$	$\frac{E_u}{E_{0u}}$	Uses the Cosine Law to convert the upwelling irradiance E_u (which is intercepted by a surface perpendicular to the incident radiation) to the irradiance that would be intercepted by a horizontal plane, such as the water surface

Adapted from: Mobley (2020)

The water-leaving radiance (L_w) is light that has penetrated the water surface, been modified by absorption and scattering, then scattered back to, and through, the surface, such that it may be detected by a sensor located just above the water. Surface radiance (L_r) represents downwelling sunlight and skyglint that is reflected by the water surface, rather than passing through it into the water column. In the case of optically shallow waters, light transmitted to the substratum may be backscattered as well, contributing to the upwelling radiance or irradiance. As illustrated in Figure 8.10, the radiance measured by a sensor positioned above the water surface (L_u) will detect both L_w and L_r and also light scattered and reflected by atmospheric components (L_a). The measured upwelling radiance, however, varies with different illumination positions and intensities, atmospheric composition, and sensor positions. For given illumination and atmospheric conditions, the range of upwelling radiances resulting from angular variations in view angle can be summarised by the upwelling radiance distribution.

Within a sunlit and skylit waterbody, the decrease in irradiance with increasing water depth is approximately exponential for both downwelling and upwelling irradiance. This relationship is conventionally described by the Beer-Lambert equation (see Volume 1A—Section 2.9.2), such that the downwelling plane irradiance at a particular water depth is a function of the:

- downwelling irradiance just below the water surface ($E_d(0)$);
- diffuse attenuation coefficient for downwelling irradiance (K_d); and the
- depth of the overlying water column (z):

$$E_d(z) = E_d(0)^{-K_d z}$$

The diffuse attenuation coefficient of downwelling radiation (K_d) is easily approximated from vertical profiles of spectral irradiance (Zimmerman and Dekker, 2006). Both $E_d(0)$ and K_d are sensitive to changes in water composition (Dekker *et al.*, 2001).

The optical water depth (ζ) is defined as:

$$\zeta = K_d z$$

Table 8.11 Optical depth

Optical depth	Downwelling irradiance (%)	Position in Euphotic Zone
0	100	Upper limit
2.3	10	Mid-point
4.6	1	Lower limit

Data source: Kirk (1994) p 22

The optical depth describes the optical 'penetrability' of a water column rather than the physical attenuation length (τ), or the physical water depth. Optical depth allows the optical nature of different waters to be compared numerically. For example, the same optical depth value will correspond to a much shallower physical depth in coloured, turbid waters, than in clear waters (Kirk, 2010). Being related to the limits of the Euphotic zone, optical depth is particularly relevant to studies of primary productivity (see Table 8.11).

AOP can be measured using *in situ* optical sensors, above-surface spectroradiometers carried on appropriate platforms, and airborne and spaceborne multispectral and hyperspectral scanners (see Section 18).

8.3.3 Optical properties of substratum

In optically shallow water, the substratum may be 'visible' in upwelling radiance due to both the elastic and the inelastic processes (see Section 8.1). As detailed in Section 6, substratum features can vary abruptly and dramatically in terms of space, time, and waterbody depth (Mazel, 2001). The impact of such changes on the optical properties of water can also be dramatic, and the small size of many features requires high spatial resolution measurements. In photosynthetic organisms, pigmentation can also change rapidly in response to illumination variations (Mazel, 2001). This dynamic, three-dimensional tapestry of substratum features presents unique challenges for EO of optically shallow water.

By definition, AOPs, that is the light leaving the substratum at a particular time (see Section 8.3.2), vary with illumination. On the waterbody substratum (or seafloor), lighting conditions change with the:

- time of day;
- season;
- latitude;
- IOPs of water column above;
- tides influencing the height of water column;
- shading by neighbouring features;
- wave focusing;
- shifting of flexible features (such as macrophytes and soft corals) with water movement; and
- fluorescence of organisms and carbonate sediments (Mazel, 2001).

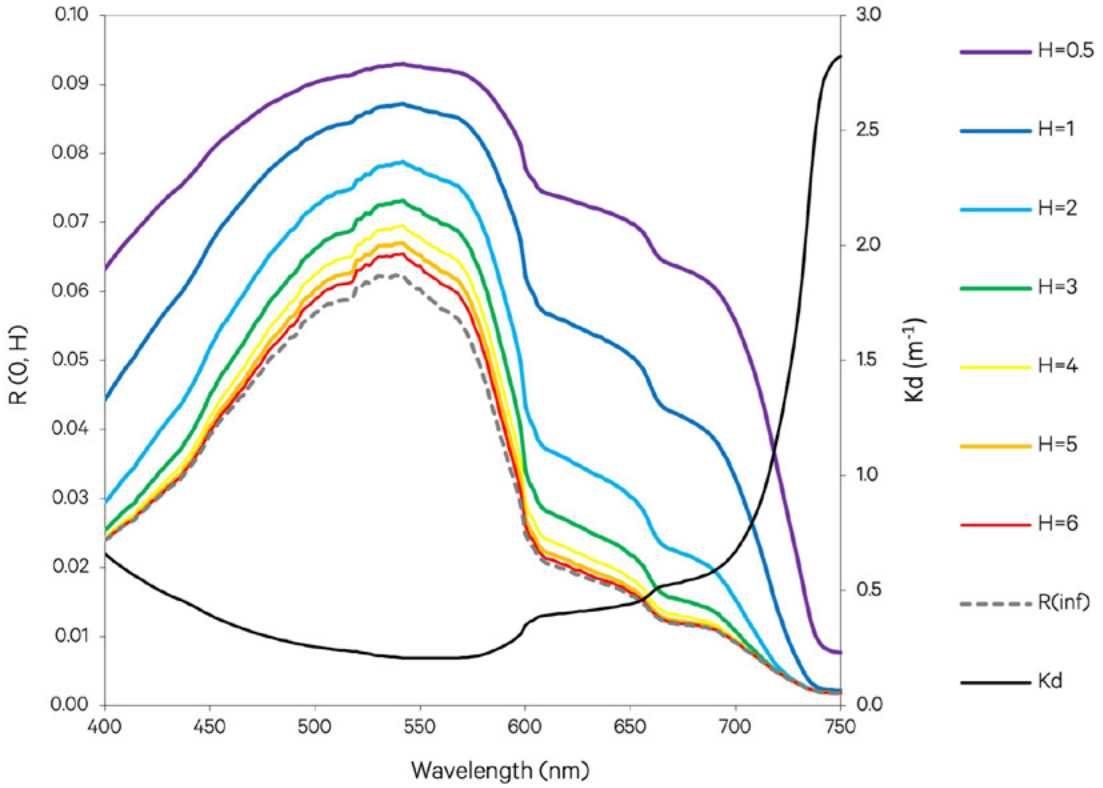
The optical properties of the water play a strong role in determining what biology you will find on the bottom, and the biology of the seafloor plays a dominant role in determining how light interacts with the ocean floor. (Mazel, 2001)

In optically shallow waters, the optical properties of substratum features can modify the shape, symmetry, and/or magnitude of the upwelling radiance distribution (see Section 6; Voss *et al.*, 2003). While traditional EO mapping of substratum features have matched on-site surveys to image values, thus restricting their use to specific sites, more recent research has focused on modelling approaches that encapsulate the optical properties of the three-dimensional nature of the substratum as well as the overlaying water column (Hedley, 2008, 2018).

When reflectance from the substratum contributes to the EO signal, the water is optically shallow, and estimates of bathymetry, water constituents, and substratum type can be derived. Physics-based models have allowed the EO reflectance of specific substratum to be simulated for different water depths (see Figure 8.21). These results highlight the need for high signal-to-noise ratios in EO data to map shallow water features, especially as water depth increases. Understanding the attenuation of reflectance due to depth in different water types is critical for retrieval of substratum information.

Figure 8.21 Simulation of substratum reflectance at different water depths

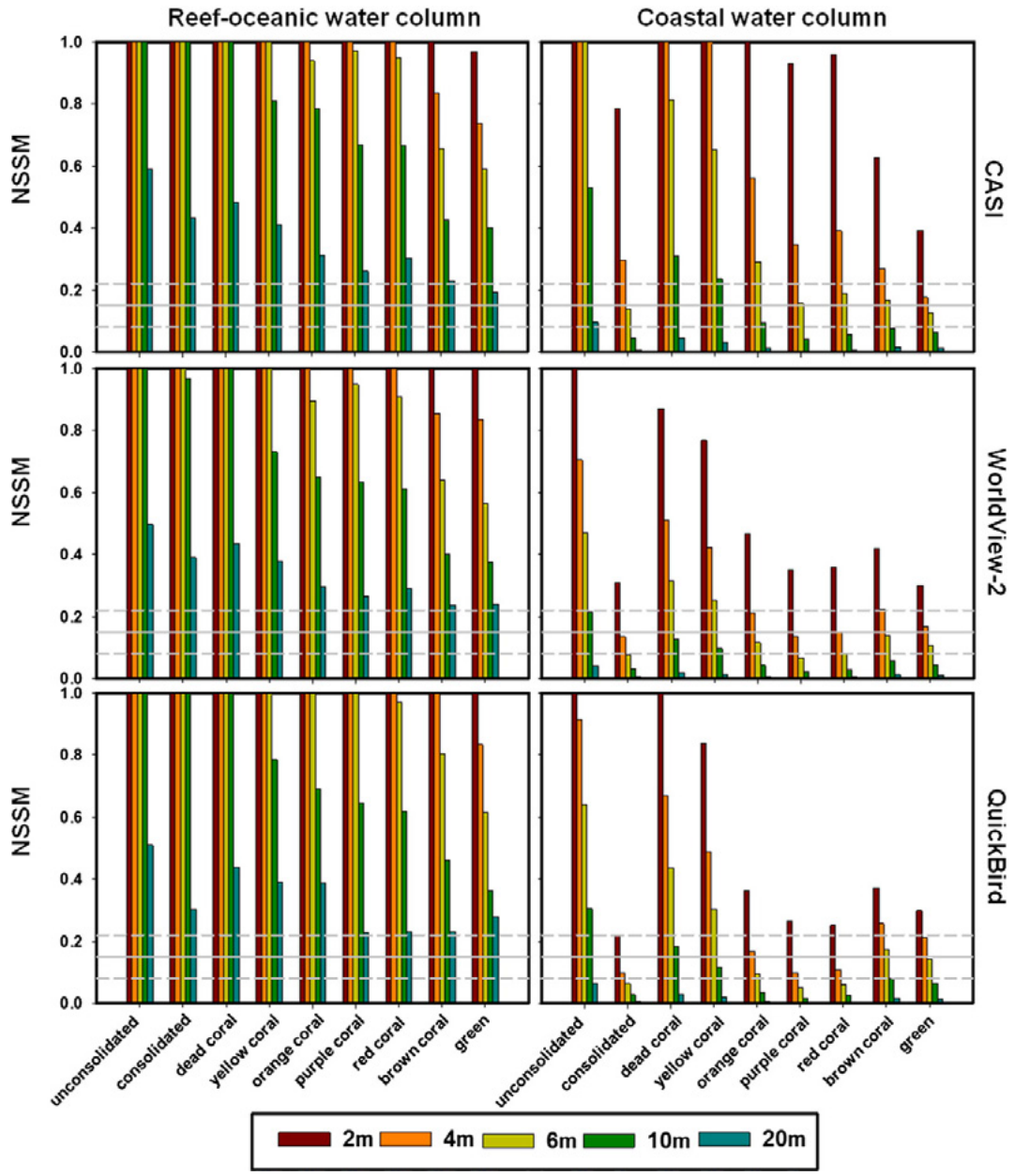
Subsurface irradiance reflectance is modelled for a 10% reflecting substrate (*R* (0, *H*), where 0.10=10% reflectance) through a water column of varying depths (*H*) with 1 μg/l chlorophyll concentration and 2.1 mg/l TSM. Absorption by CDOM at 440 nm is assumed to be 0.2/m. *R* (inf) is an optically deep water column reflectance at surface and K_d for this water type is shown on the second y-axis. For example, with substratum and a water column height of 0.5 m the cyan (top) line shows that the *R* (0, *H*) at the water surface will vary from 0.65 (or 6.5%) at 400 nm to 9.3% at 550 nm, then decrease due to pure water absorption with increasing wavelength. At 6 m water depth the reflectance at the surface of a 10% reflecting substratum is almost invisible as more than 99% of the signal comes from the waterbody.



Source: Dekker *et al.* (2001) Figure 14

Figure 8.22 Modelled subsurface irradiance reflectance

Subsurface irradiance reflectance is modelled through varying water columns by a range of sensors.



Source: Botha *et al.* (2013) Figure 10

The ability to detect a spectral signal from the substratum is dependent on the spectral optical depth of the water column, the brightness and spectral contrast of the substratum, and the sensor design (Dekker *et al.*, 2001). In Botha *et al.* (2013), a simulation method of assessing the spectral separability of various substrates was developed for three EO sensors (an airborne hyperspectral scanner: CASI: and two spaceborne multispectral sensors: WorldView and QuickBird) with different spectral resolutions and densities, but comparable spatial resolutions. This comparison was based on a measure of spectral difference (nSSM; Botha *et al.*, 2013), which combines the spectral angle and a normalized Euclidean distance between the spectra, to quantify both the spectral detectability and separability. The difference was assessed firstly between the substrate and the optically deep water column, then secondly between a pair of different substrates with different brightnesses and colours at varying water depths and optical water types (see Figure 8.22). Of the three sensors, the best substrate separability for shallow water depths over most substrate types in coastal waters was achieved from CASI, which, as a slower airborne sensor, delivered the highest spectral resolution with highest radiometric resolution.

8.4 Optical EO Models

The goal of optical EO models is to define and exploit the relationship between EO measurements (or a model thereof) and the optical properties of a waterbody. In the context of Figure 8.1 above, this model operates between the measurement domain and the attribute domain. For waterbodies, the relationship allows one of these domains to be computed from the other either as a forward or an inverse model (see Figure 8.23 and Table 8.12):

- forward model—computes likely EO measurements from known water properties; and
- inverse model—computes likely waterbody properties from available EO measurements.

In this context, water properties may include water column characteristics, substratum features, or waterbody depth.

Forward models can only be based on semi-analytical, or analytical (RTF-based) models. In the case of optically shallow waters, forward models require simulation of the entire 'EMR transfer chain' from substratum and substratum vegetation cover, up through the water column (including light absorption, volume scattering, inelastic scattering (fluorescence), and transmission), through the air-water interface, and then through the atmosphere (including adjacency effect) to the EO sensor (see Figure 8.10). Semi-analytical inversion methods in general comprise equations that approximate the radiative transfer function method (see Sections 8.1.1 and 8.1.4) with some relationships between IOP and OAC (optically active constituents) estimated statistically (this is the semi-part of 'semi-analytical').

Figure 8.23 Relationship underlying optical EO models

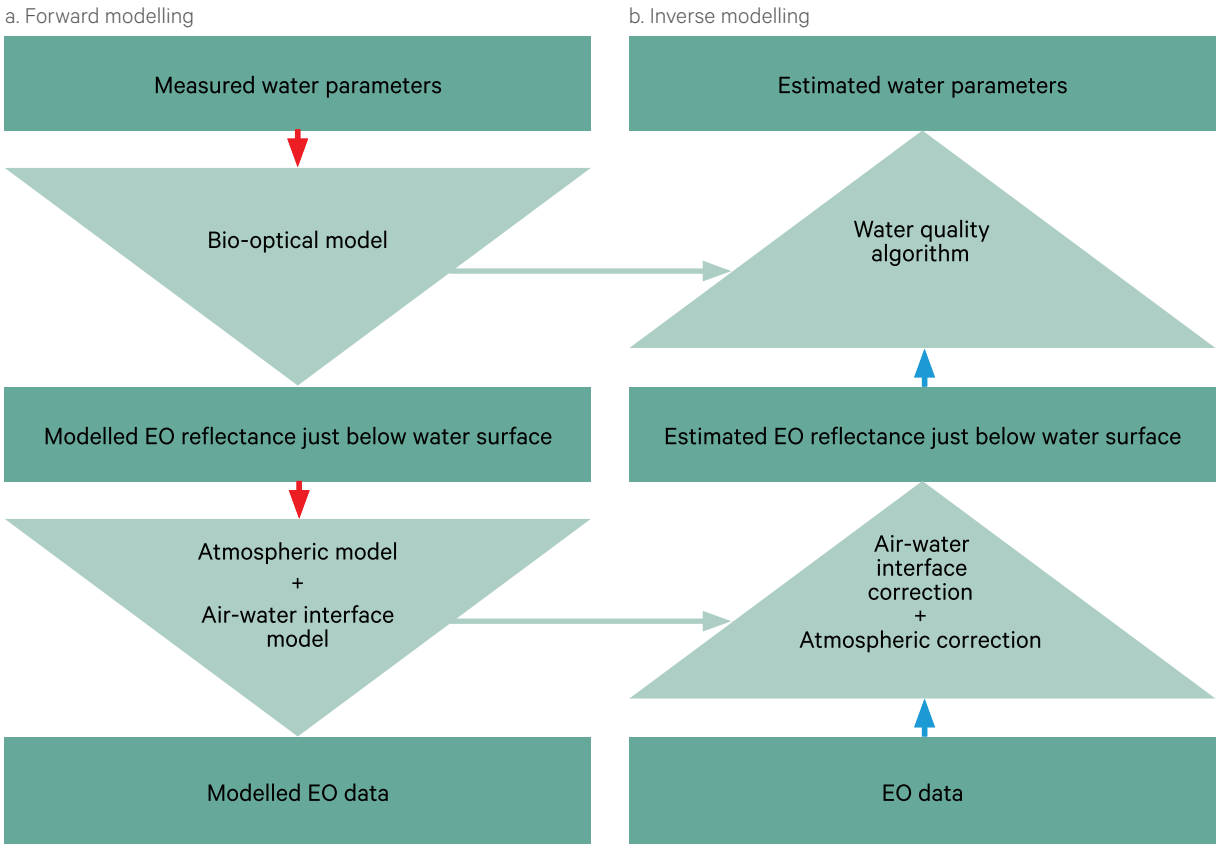


Table 8.12 Forward and inverse models

Model	Possible Inputs	Possible Outputs
Forward	AOP, IOP, concentrations, water depth, substratum (and cover), reflectance library	Just above water or TOA reflectances
Inverse	Just above water reflectances or TOA (EO or *in situ* measurements)	AOP, IOP, concentrations, water depth, substratum (and cover)

Table 8.13 Mathematical inversion models for aquatic ecosystem variables

R: irradiance reflectance; nL_w: near water-leaving radiance; see Table 8.4 for definitions

Inversion Model Type	Empirical	Semi-empirical	Semi-analytical (mostly physics-based)	AI methods
Description	Assume simple stochastic relationship between waterbody properties and EO measurements; uses few spectral bands	Use *a priori* spectral knowledge to determine relationship between water properties and EO measurements; Focuses on bands with relevant spectral information	Use physical laws to model relationship between waterbody/ substratum properties and EO measurements using all spectral bands	Expert at calculating non-linear relationships between waterbody properties and EO measurements using all spectral bands
Essential Inputs	Just above water reflectances or nL_w (EO or *in situ* measurements). A statistically relevant amount and range of variables to be retrieved (OAC, IOP, AOP, transparency, turbidity, etc.) for each image	Just above water reflectances or nL_w (EO or *in situ* measurements); A statistically relevant amount and range of variables to be retrieved (OAC, IOP, AOP, transparency, turbidity, etc.) for each image	Just above water reflectances or nL_w (EO or *in situ* measurements). Relationships between representative IOPS, AOPS with OAC through SIOP and substratum (including cover). Spectral reflectance library	Can be trained empirically, semi-empirically or using semi-analytical or RTFbased models
Preferred Inputs	OAC, IOP, AOP, algal pigments, transparency, turbidity, water depth, substrate optical properties	OAC, IOP, AOP, algal pigments, transparency, turbidity, etc., water depth, substrate optical properties, spectral band selection based on knowledge of absorbing, backscattering and fluorescence effects	SIOP (for all OAC). Substrate spectral reflectance properties	OAC, IOP, AOP, algal pigments, transparency, turbidity, water depth, substrate optical properties
Outputs	For each correlation one of: OAC, IOP, AOP, algal pigments, transparency, turbidity, water depth, substratum type and cover types etc	For each correlation one of OAC, IOP, AOP, algal pigments, transparency, turbidity, water depth, substratum type and cover types etc	Possible in one inversion: OAC, IOP, AOP, algal pigments, transparency, turbidity, water depth, substratum type and cover types etc	Possible in one inversion: OAC, IOP, AOP, algal pigments, transparency, turbidity, water depth, substratum type and cover types etc
Example	Single bands, band ratios, multiple band combinations, simple correlations	Single bands, band ratios, multiple band combinations; causal correlations	Spectral inversion algorithms (iterative inversion, direct inversion, e.g. matrix inversions)	Often requires complex non-linear multiple band combinations
Advantages	Easy to compute for specific waterbody and time provided *in situ* data available; sensitivity can only be estimated for each single waterbody where *in situ* data available	Easy to compute; More accurate than empirical models and faster than semi-analytical inversion methods; Sensitivity and error analysis, intermediate between empirical and semi-analytical methods.	Transferable, flexible, repeatable, most accurate, model based sensitivity can be calculated, model based error analysis estimation built in.	Representative when properly paramaterised, uses all statistically significant spectral bands; Can provide some estimates of sensitivity and error analysis
Disadvantages	Likely to fail when extrapolated temporally or applied to other waters; only makes use of limited amount of spectral data; some empirical relationships may not be causal; band ratios may amplify errors in *R* or nL_w	More transferable than empirical methods but less transferable than semi-analytical methods due to *a priori* spectral knowledge; if properly done relationship is causal	Computationally intensive, requires parameterisation from appropriate input data	Design of AI methods is a 'dark art'; many permutations may be chosen. Once parameterised with representative data very robust. Needs retraining for new water type
Most appropriate for	Optically simple water eg. Chlorophyll concentration in oceans; TSM, also water depth in optically shallow water with homogeneous substratum types and substratum cover	Optically simple and complex waters, e.g. chlorophyll, TSM, CDOM, K_d, also water depth in optically shallow water with homogeneous substratum types and substratum cover	Time series analyses of all water types and optically shallow waters, e.g. coral reef, coastal and inland waterbodies	All water types and optically shallow waters, e.g. coral reef, coastal and inland waterbodies

Inversion models or methods (which are also referred to as algorithms) are designed to estimate waterbody properties (such as OAC, algal species, bathymetry, substratum cover type, and condition) from an EO data source. There are many ways to invert an EO signal (inverse modelling), including:

- empirical models—use simple stochastic relationships, such as regression curves, between input (EO) and output data (see Volume 2A);
- semi-empirical models—use *a priori* spectral band location knowledge (e.g. focusing on the spectral bands adjacent to and in the middle of chlorophyll light absorption bands) to determine a stochastic relationship between input and output data (see Volume 2C);
- semi-analytical models—use knowledge about physical relationships such as IOP, concentration-specific IOP (SIOP) and AOP with the OAC and bathymetry and substratum data, coupled with some statistical approaches for parameterisation (see Volume 2C and Section 18 below);
- machine learning algorithms—use inversion methods such as Artificial Neural Networks (ANN), Maximum Likelihood (ML), or Declarative Machine Learning (DML; see Volume 2E); and
- Object based Image Analysis (OBIA)—mainly used to derive substratum and substratum cover type information over optically shallow waters (see Volume 2A—Section 10).

Note that radiative transfer models cannot be directly inverted so would need one of the above methods for inversion (in which case OBIA is not applicable).

Typically, simpler models are less flexible and transferable than complex and computationally intensive models (see Table 8.13). Sophisticated optical models (such as bio-optical models, Dekker *et al*., 2001; Dekker et al., 2011) now exist which describe the main light processes in both clear and turbid waters, with and without bottom visibility, taking into account highly variable optical conditions in the water column and the substrate, as well as a complex geometry of the incident light field and the viewing angles of an EO sensor.

Semi-analytical models invert the forward bio-optical model, either directly or via iterative methods, to estimate water constituent concentrations and physical properties such as algal pigment concentrations, CDOM, Secchi Disk transparency, vertical attenuation of light, or TSM, and to map substratum type and cover (see Section 18). Radiative transfer models, however, cannot be inverted directly to estimate the same variables. Since OBIA relies on expert knowldege applied to spectral, spatial and textural image information, it is mainly used for mapping substratum type and cover (such as seagrass, macroalgae, corals) in optically shallow waters.

The following subsections describe aspects of optical forward and inverse modelling that are relevant to:

- radiative transfer models (see Section 8.4.1);
- the water column (see Section 8.4.2);
- substratum factors (see Section 8.4.3); and
- integrated models (see Section 8.4.4).

8.4.1 Radiative Transfer Modelling

The Radiative Transfer Equation (RTE) describes the behaviour of radiance passing through a medium, in this case water. Regarding radiance as a beam of photons, six basic interactions between the photons and the medium can occur which modify the beam:

- absorption of beam by medium—photon loss due to conversion to non-radiant energy;
- elastic scattering of beam by medium—photon loss due to scattering the same wavelength in other directions;
- inelastic scattering of beam by medium—photo loss due to scattering in other directions with different wavelength;
- emission of medium—gain of photons by conversion of non-radiant energy into radiant energy;
- elastic scattering of medium—gain of photons by scattering of same wavelength from other directions; and
- inelastic scattering of medium—gain of photons by scattering in other directions with different wavelength.

The optical medium of natural waters has been modelled as a continuous material comprising randomly arranged, single-scattering elements separated by large distances relative to the wavelength of light (Mobley, 1994). Such models have allowed exact solutions to the RTE to be developed (Zimmerman and Dekker, 2006). Relevant model equations and assumptions are detailed in Mobley (2020). Generic methods have been proposed to simplify inversion of RTE models (Hedley *et al*., 2009).

Submerged plant canopies, however, such as seagrass meadows, represent a dense packaging of optically active material. Radiative transfer models for such canopies must rely on more empirical relationships between leaf optical properties and light attenuation by the bulk canopy as well as the water column (see Zimmerman, 2003, 2006; Hedley *et al*., 2017).

Commonly used numerical models include HYDROLIGHT (Mobley and Sundman, 2000) and MOMO (Matrix Operator Method: Fell and Fischer, 2001; Hollstein *et al*., 2010; Hollstein and Fisher, 2012). Such models allow several options for understanding and exploring the optical properties of natural waters, including:

- generating estimates for irradiance at different levels in the water column as a function of selected optical constituents, which can be used to model primary productivity and thermodynamics;
- simulating in-water light fields for different water types from IOP values to determine optimal wavelength bands for EO instruments;
- estimating EO signals that would result from assumed IOP under a range of simulated environmental conditions;
- isolating and removing unwanted parts of EO signals, such as sky radiance;
- varying IOP and boundary conditions to determine the most significant drivers and interrelationships between optical constituents, waterbody features, and environmental conditions;
- simulating optical signatures to develop EO algorithms and evaluate algorithm sensitivity; and
- retrospectively modelling historical water conditions (Mobley, 2020).

Dekker *et al.* (2011) compare five physics-based inversion methods to a semi-empirical method for estimating bathymetry, water column composition, and benthic cover type for a coral reef in the Bahamas and the optically complex Moreton Bay in Australia. The significantly better results from the physics-based inversion methods are particularly pertinent for simple to complex optically shallow waters.

In optically shallow waters, however, best results are obtained from such models when representative SIOPs and spectral reflectances are available. Accurate maps of heterogeneous benthic and substrate features to water depths of 20–25 m have been produced with these approaches (Kutser *et al.*, 2006; Dekker *et al.*, 2011).

8.4.2 Water column

Water column optical inversion models rely directly or indirectly on the optical properties of water introduced in Section 8.3. There is a wide range of forward optical models available for water, from models based on simple analytical solutions developed for specific waters or conditions (see Section 8.4.2.1), to generic radiative transfer models (see Section 8.4.2.4).

Optical properties of the water column that may be estimated from an optical EO signal include:

- suspended matter;
- turbidity;
- vertical attenuation coefficients of downwelling and upwelling light;
- transparency;
- coloured dissolved organic matter (CDOM);
- chlorophyll a content;
- phycobiliprotein pigments (mainly from cyanobacteria); and
- algal blooms, such as red tides and blue-green algal blooms.

If the water column is sufficiently transparent, and the substrate is within the water depth where a sufficient amount of light reaches the bottom and is reflected back out of the water, maps may also be made of seagrasses, macroalgae, sand and sandbanks, coral reefs, and other bottom features (Dekker *et al.*, 2001, 2011; see Section 19).

8.4.2.1 Empirical models

Empirical models assume stochastic relationships between the optical properties of a waterbody and their EO radiance or reflectance measurements. These models typically rely on regression relationships between input and output data, which are implemented using band ratios or simple correlations. This method requires a statistically relevant amount and range for each variable to be retrieved (such as OAC, IOP, AOP, transparency, turbidity) from each image.

Empirical models are easily and rapidly computed for large images, which is a significant advantage given the volume of image data. However, they lack sensitivity to the variations in water composition that can occur in many surface waters, both between waterbodies and over time. As such, empirical relationships are not readily transferable. Moreover, as reflectance or radiance from waterbodies is typically low, slight errors, in for example atmospheric correction, can lead to large errors in an estimated water quality or water substratum variable. When many variables are being retrieved from EO data with only a few broad spectral bands, there will be significant confusion as to what is causing the correlation. These models are most appropriate for studies of optically simple waters and are commonly used to map chlorophyll concentration in oceans. Empirical algorithms for estimating various attributes of inland and transitional waters using EO datasets are reviewed by Matthews (2011).

In optically shallow waters, empirical approaches require *in situ* water depth measurements for parameterisation. These empirical methods work best by assuming homogeneous substrates (and cover types) to water depths of 5–10 m and can be applied to both multispectral and hyperspectral data.

8.4.2.2 Semi-empirical models

Semi-empirical models use *a priori* spectral knowledge to determine the causal relationship between water properties and EO measurements and focus on spectral bands with relevant spectral information. By using *a priori* spectral knowledge to select EO bands for inversion, semi-empirical models are less likely to deliver spurious results than empirical models. This method has more general applicability between similar waterbodies when a statistically relevant amount and range of each variable is to be retrieved from a representative range of waterbodies.

Semi-empirical inversion models also make use of single bands, band ratios, and multiple band combinations and, if done properly, all correlations are causal. As with empirical methods, when many variables are derived from EO data with a few broad spectral bands, there will be significant confusion as to what is causing the correlation. Advantages of these models include:

- the algorithms are easier to compute and more accurate than empirical models;
- they are faster than semi-analytical inversion methods; and
- sensitivity and error analysis is midway between empirical and semi-analytical methods.

8.4.2.3 Semi-analytical models

Mathematical inversion of analytical models often requires some approximations based on modelling or on *in situ* parameterisation, therefore these approaches are often called semi-analytical. Semi-analytical models may involve construction of a forward model for above-water spectral reflectance with several input parameters such as:

- IOPs and AOPs;
- concentrations of water column constituents, such as algal pigments, CDOM and non-algal pigmented particulate and suspended matter, which allow calculation of the SIOP;
- physical descriptive measures of water condition, such as Secchi disk transparency, light attenuation and turbidity;
- water depth; and
- substrate type, which determines the bottom spectral reflectance.

These models are used for both forward and inverse modelling. Such models are more computationally intensive than empirical or semi-empirical models, but faster than physics-based, radiative transfer models (for forward modelling). For complex waters, semi-analytical inversion approaches are preferred over (semi-) empirical algorithms that have become standard in operational applications of EO. These semi-analytical inversion approaches are particularly appropriate for mapping complex optically deep waters and optically shallow waters.

8.4.2.4 Radiative transfer models

Radiative transfer models can be based on Monte Carlo simulation, or simulating the interaction of photons with the atmosphere and the waterbody. The resulting set of modelled photon interactions have allowed mathematical relationships to be established between:

- AOP and IOP of the water column;
- bulk (or composite) IOP and SIOP of the water column;
- radiative transfer from a waterbody to/from the atmosphere; and
- IOP of the water column and the upwelling radiation to the combined concentration of organic and inorganic matter (Bukata, 2005).

In the context of water EO, the RTE (see Section 8.4.1) shows how spectral radiance changes with the optical properties of water. For example, the two-flow model for a homogeneous medium described by Dekker *et al.* (2001) considers three primary changes in downwelling irradiance with increasing water depth:

- decreases with water depth due to absorption of downwelling radiance;
- decreases due to backscattering of downwelling radiance into upwelling radiance; and
- increases due to scattering of upwelling radiance into downwelling radiance.

8.4.3 Substratum factors

In all physics-based EO applications where the substratum is mapped through a water column, an estimate of the water column depth is implicitly or explicitly involved, and vice versa when water depth is mapped there is an implicit assumption about the substratum (and cover) reflectance. In optically shallow waters a measurable signal will be detected from the substratum, or vegetation growing in it, through the water column and through the air-water interface. Water is considered to be optically deep if there is no measurable influence of the benthos on the EO reflectance (Dekker *et al.*, 2001; see Section 18.3.1).

Because of the water column, a given substrate reflectance will be observed to have different reflectance at the water surface for different water depths. Mathematical inversion methods for mapping optically deep and optically shallow waters are summarised in Table 8.13, including their strengths and weaknesses, namely:

- empirical models—use simple stochastic relationships, such as regression curves, between input (EO) and output data (see Volume 2A). In general, these methods cannot deal with variable water column composition, whilst needing a large amount of (difficult to obtain) *in situ* data of substratum type and cover. These methods also require or assume regions of homogenous benthos at varying water depths within the image.
- semi-empirical models—use *a priori* spectral band location knowledge (e.g. focusing on specific spectral bands adjacent to, and in the middle of, pigment bands for substratum cover types, such as seagrasses, macroalgae, or live corals) to determine a stochastic relationship between input and output data (see Volume 2C). As with empirical methods these methods, in general, cannot deal with variable water column composition, and require a large amount of (difficult to obtain) *in situ* data for substratum type and cover.
- semi-analytical models—use knowledge about physical relationships such as IOP, concentration-specific IOP (SIOP), and AOP with the data for OAC, bathymetry and substratum factors, coupled with some statistical approaches for parameterisation (see Volume 2C and Section 18 below). Dekker *et al*. (2011) did a thorough analysis of one empirical and for semi-analytical inversion methods and found the semi-analytical methods were the best performing, and able to deal with both heterogeneous substratum types and varying water column composition.
- machine learning algorithms—use inversion methods such as artificial neural networks (ANN), maximum likelihood (ML), or declarative machine learning (DML). Some of these methods are described in Volume 2E.
- Object based Image Analysis (OBIA)—mostly used for mapping substratum and substratum cover types in optically shallow waters (see Volume 2A—Section 10). The Allen Coral Atlas mapping project (see *https://allencoralatlas.org/*) is using OBIA applied to Sentinel-2 images of all global coral reefs to create a global map of main coral reef features at 10 m spatial resolution. This map does not go down to species level.

The bathymetry and the water column optical properties are thus important to EO in aquatic environments, particularly for seagrass, coral reef, and macroalgal mapping (Dekker *et al*., 2001), since optimal results will be obtained from EO data if the substratum signal (such as from a seagrass canopy) is derived by compensating for the attenuating influence of the water column. Whether a benthic feature, such as seagrass, macroalgae, or coral, can actually be discriminated depends on the spectral optical depth of the water column (and the atmosphere between the sensor and the water surface), the brightness and density of the vegetation, and the spectral contrast between it and the substratum, as well as the spectral, spatial, and radiometric sensitivity of the EO sensor (see Section 20).

EO of optically shallow aquatic environments (seagrass, sand, macroalgae, muds, and coral reefs) requires sensors with a greater signal-to-noise ratio than those required for terrestrial environments (see Section 17.2 below). Coupled with this factor is the number of quantisation levels with which the sensor can record, or its radiometric resolution (see Volume 1B—Section 1.3). This must be high enough to allow a range of brightness levels over which a classification can be performed and sensitive enough to be able to detect the lower water depth of the seagrass beds (Dekker *et al*., 2001).

8.4.4 Integrated models

Other in-water hydrological models that can rely on EO datasets include:

- biogeochemical models—relate primary productivity to water characteristics such as light availability for photosynthesis, temperature, and nutrients. A good biogeochemical model has a good bio-optical model embedded in it; and
- hydrodynamic models—relate circulation within and between waterbodies to water characteristics such as temperature (gradients and stratification), flows, density, salinity, suspended sediment concentration, and bottom roughness and composition. These models can be one-, two- or three-dimensional.

These two types of models can be used in tandem; for example, the hydrodynamic model can be used to parameterise the biogeochemical model for several essential inputs, and results from the biogeochemical model can be used to provide parameters for hydrodynamic models. For example, a combined hydrodynamic and biogeochemical model is essential to model algal growth, and predicting potentially harmful algal blooms. An Australian EO-based, integrated model for surface waters is the eReefs system described in Volume 2D—Excursus 14.4.

8.5 Optical EO sensors

As introduced in Volume 1A—Section 13, the design and management of each EO sensor involves trade-offs between spectral, spatial, radiometric, and temporal resolutions, densities, and extents (see also Volume 1B—Section 1). In the context of complex aquatic ecosystems, essential features of an EO sensor, in order of priority, are defined by CEOS (2018) as:

- spatial resolution—determines the minimum area that can be discriminated so has particular relevance to mapping small waterbodies (although highly detailed imagery will also complicate global mapping studies);
- spectral resolution—spectral wavelengths detected by a sensor determine the aquatic ecosystem variables that can be discerned, both in terms of their amount and accuracy, so specific spectral regions need to be detected. As an example for phytoplankton pigment assessment, two spectral bands are recommended, centred on the wavelengths:
  - 620–624 nm—based on the *in vivo* absorption maximum of cyanophycocyanin for estimating the concentration of cyanobacterial (blue-green) algae; and
  - 676 nm—based on the *in vivo* red absorption maximum of chlorophyll a to determine the overall abundance of algae.

  In order to quantify these absorption features it is also necessary to have two spectral bands adjacent to (but not influenced by) each of these absorption features;
- radiometric resolution—determines the lowest level of radiance detected, and is particularly important for satellite-borne aquatic sensors since the signal leaving a waterbody represents a small proportion of the total signal measured by the sensor (see Volume 1B—Sections 5.2 and 6.4). Landscapes surrounding coastal and inland waterbodies typically exhibit a wide range of radiances, which can be problematic for detecting small differences in dark features; and
- temporal resolution—determines detection of changes, which can vary from hourly (e.g. algal blooms and floods) to days (e.g. pollution events) to weeks (e.g. coral bleaching events) to seasonal or annual (such as floral succession cycles).

A range of archival and current EO sensors provide imagery that is variably suited to mapping water quality, aquatic flora and corals, and shallow water bathymetry (see Table 8.14). In this context, mapped variables for water quality (freshwater, coastal and ocean) include chlorophyll a pigment, cyanophycocyanin, TSM, CDOM, vertical attenuation coefficient for diffuse downwelling irradiance (K_d), and turbidity and/or Secchi Disk transparency (see Sections 18 and 19), and aquatic flora include emergent, floating-leaved and submersed macrophytes, macroalgae, seagrasses, and corals (see Section 20).

A recent development in aquatic EO involves the use of permanent installations of autonomous, near-surface spectroradiometers that effectively emulate an EO signal as measured by an airborne or satellite sensor (albeit atmospherically corrected EO measurements). These above-water *in situ* spectroradiometers:

- provide validation or input to atmospheric correction of satellite images;
- allow application of the same algorithms that are used for EO imagery in combination with their *in situ* sampling programs;
- enable continuous measurements of a waterbody (under daylight conditions);
- can be mounted on any type of superstructure (bridge, tower, buoy, etc); and
- do not suffer from biofouling (but do need cleaning and protecting).

Table 8.14 Optical EO sensors for aquatic mapping

This list provides technical details for various multispectral and hyperspectral sensors carried on previous, current, and future EO missions with spectral bands in the wavelength range 340–1000 nm. Details relate to water mapping applications only. *Names of commercial sensors are italicised.*

Sensor	Dates of Operation	Number of water bands	Spatial resolution (m)	Revisit Frequency	Aquatic mapping suitability		
					Water quality	Flora and corals	Shallow water bathymetry
Hyperion	2000–2017	60	30	16 days (by pointing)	high	high	high
CHRIS-PROBA	2001+	18 or 63	18 or 36	7 days (by pointing)	high	high	high
MERIS	2002–2012	15	260 x 300 coastal; 1150 oceans	2 days (programmable)	high	high	high
HICO	2009–2014	100	90	3–5 days (orbit ±51°)	high	high	high
Sentinel-3	2016+	21	300	daily (with two satellites)	high	high	high
GLIMR	2027	140	300	60 minutes	high	high	high
PRISMA	2019+	66	20	7/25 (by pointing)	high	high	high
EnMap	2021+	90	30	4 days (programmable)	high	high	high
SBG (formerly HysplRI)	?2025+	60	30–45	2–16 days	high	high	high
PACE	2022+	110	1000	daily	high	high	high
ISS HISUI	2019+	60	20 x 30	3–5 days (orbit ±51°)	high	high	high
ISS DESIS	2018+	235	30	3–5 days (orbit ±51°)	high	high	high
OCM-2	2009+	15	300	2–3 days	high	medium	medium
Suomi-VIIRS	2012+	7	740	Daily	mostly high	medium	medium
SGLI	2018+	11	250	2 days	mostly high	medium	medium
GOCI	2010+	8	500	Hourly	mostly high	medium	medium
GOCI-II	2020+	12	250–1000	Hourly	mostly high	medium	medium
Worldview-2	2009+	8	2	1–60 days (programmable)	medium to high	high	medium
Worldview-3	2014+	8	1.24		medium to high	high	medium
IKONOS, QuickBird, SPOT-5/-6 GeoEye etc.	1999+	3–4	2–4	2–3/60 days (programmable)	potential to high	medium	medium
RapidEye	2005+	5	6.5	Daily	potential to high	medium	medium
Sentinel-2	2014	4	10, 20, 60	5 days (with two satellites)	medium to high	medium	medium
Aqua/Terra MODIS	2000+	9	1000	Daily	medium to high	medium	medium
	2000+	2	250, 500		mostly medium	potential	potential
Landsat-4 to -7 MSS	1984–2017	4	30	16 days	medium	medium	medium
Landsat-8 OLI	2013+	5	30	16 days	medium	medium	medium
Himawari-8/-9	2014+	4	500–2000	10 minutes	mostly medium	potential	potential
GOES-R	2017+	4	500–2000	10 minutes	mostly medium	potential	potential
GISAT-1/-2 MSS	2021+	6	42	5–30 minutes	mostly medium	potential	potential
GISAT-1/-2 Hyperspectral	2021+	158	318	5–30 minutes	mostly medium	potential	potential
MSG SEVIRI	2002+	2	1000	96 per day	mostly medium	potential	unsuitable

Adapted from: CEOS (2018) Table 2.7

Ideally a dedicated sensor that was designed for complex aquatic environments would have higher combined spatial and spectral resolutions than are available from current and planned ocean colour sensors (see Table 8.14). It would also include bands that provide information about the biochemistry of inland, estuarine, deltaic, and near-coastal waters, and differentiate macrophytes, macroalgae, seagrasses, and coral reefs (CEOS, 2018). In particular, a comprehensive EO system for observing aquatic ecosystems should:

- estimate algal pigment concentrations of chlorophyll a and cyanobacteria (especially phycoerythrin and phycocyanin) plus accessory pigments, and detect other wavelengths relevant for research into phytoplankton functional types;
- detect algal fluorescence (especially chlorophyll a fluorescence at 684 nm);
- measure suspended matter, possibly split up into organic and mineral matter;
- measure CDOM, and discriminate terrestrial from marine CDOM;
- measure spectral light absorption and backscattering of OAC (see Section 8.2); and
- measure water transparency indicators, such as Secchi disk transparency, vertical attenuation of light and turbidity (see Section 5.1.4);

and in optically shallow waters:

- estimate water column depth (bathymetry); and
- estimate substratum type and cover as well as plants floating at, or just above, the water surface.

For residual sunglint correction (if sunglint mitigation measures are insufficient), and for estimating the atmospheric composition, appropriate spectral bands are required to measure O_3, NO_2, water vapour, and aerosols, as well as NIR and/or SWIR bands for sunglint correction. Thus, for non-oceanic aquatic ecosystems, an appropriate satellite-borne sensor would include (CEOS, 2018):

- approximately 26 bands in the spectral range 380–780 nm for detecting aquatic ecosystem variables (see Table 8.15);
- 15 bands between 360–380 nm and 780–1400 nm to enable removal of atmospheric and air-water interface effects (see Table 8.16);
- spectral resolution: 5 nm (ideal) to 8 nm to achieve an adequate signal-to-noise ratio and Full Width Half Maximum (FWHM; see Volume 1A—Section 13);
- spatial resolution: approximately 17–33 m (which would enable mapping of waterbodies larger than 0.2 ha); and
- radiometric sensitivity: noise-equivalent radiance difference (NEΔL) 0.005 $mWm^{-2}\,sr^{-1}\,nm^{-1}$ (ideal) to 0.010 $mWm^{-2}\,sr^{-1}\,nm^{-1}$;
- radiometric extent: 400 $mWm^{-2}\,sr^{-1}\,nm^{-1}$ in blue wavelengths and 200 $mWm^{-2}\,sr^{-1}\,nm^{-1}$ in red wavelengths for bright targets such as sand; and
- at least one global image every 16 days from Low Earth Orbiting (LEO) satellite (but ideally 1–5 day revisit frequency), preferably in conjunction with Geostationary Earth Orbiting (GEO) satellite imagery at high temporal frequency (see Volume 1A—Section 12).

Table 8.15 Recommended spectral bands for assessing water quality and characterising benthos

FWHM: Full width half maximum (see Volume 1A—Section 13.4); CPC: Cyanophycocyanin; CPE: Cyanophycoerythrin; CDOM: Coloured dissolved organic matter; NAP: non algal pigmented particulate matter; Chl: chlorophyll; PFT: phytoplankton functional type; HAB: harmful algal blooms; FLH: fluorescence line height. NAP, blue and red chlorophyll absorption maxima and related reference bands and HABs detection are ubiquitous in literature. NAP scatters and absorbs light decreasing with increasing wavelength and thus does not need a specific band, although three bands without too much algal pigment or CDOM absorption are useful. The blue chlorophyll absorption band is centered around 438–443 nm *in vivo* and the red chlorophyll band around 676 nm *in vivo*. HABs need Chlorophyll, CPE, and CPC. See Table 8.16 for NAP relevant bands beyond the O_2 absorption feature at 761 nm.

Band number	Waveband centre (mm)	FWHM (mm)	Application
1	+/-380	15	CDOM; NAP; PFT; Mycosporin-like amino acids
2	+/-412	5–8	CDOM; PFT
3	+/-425	5–8	CDOM ; NAP; Blue Chl a absorption reference band; PFT
4	+/-440	5–8	CDOM; Blue Chl a absorption maximum; PFT
5	467	5–8	Band for separating Pheaocystis from diatoms; Blue Chl a absorption band reference band; Accessory pigments
6	+/-475	5–8	Accessory pigments; Blue Chl a absorption band reference band; PFT, NAP
7	+/-490	5–8	Blue Chl band-ratio algorithm; PFT, Accessory pigments
8	+/-510	5–8	Blue Chl band-ratio algorithm; NAP
9	+/-532	5–8	PFT and Carotenoids; NAP
10	+/-542	5–8	NAP
11	555	5–8	NAP; Cyanophycoerythrin reference band; PFT
12	565	5–8	CPE *in vivo* absorption maximum and possibly fluorescence
13	+/-583	5–8	CPE and CPC reference band; Chlorophylls a, b and c ; CPE fluorescence
14	+/-594	5–8	PFT
15	+/-615	5–8	CPC *in vivo* absorption maximum—avoiding Chlorophyll c
16	624	5–8	CPC *in vivo* absorption maximum; suspended sediment, PFT; Chlorophyll c
17	631	5–8	PFT
18	+/-640	5–8	NAP, CPC reference band
19	649	5–8	Chl b *in vivo* absorption maximum
20	665	5–8	FLH baseline
21	676	5–8	Red Chl a *in vivo* absorption maximum
22	683	5	Chlorophyll fluorescence (FLH) band
23	+/-700	5–8	HABs; NAP turbid water; reference band for 2 or 3 band Chl a algorithms
24	+/-710	5–8	FLH baseline; HABs detection; NAP in highly turbid water; reference band for 2 or 3 band Chl a algorithms
25	+/-748	15	NAP in highly turbid water; FLH baseline band
26	+/- 775	15	NAP in highly turbid CDOM rich water
27	+/- 810	15	NAP in highly turbid CDOM rich water

Adapted from: CEOS (2018) Table 2.2

Table 8.16 Recommended spectral bands for atmospheric and air-interface correction

Recommended minimum set of spectral bands for extracting information from EO reflectance spectra of optically deep and shallow waters. * indicates bands covered in Table 8.15. FWHM: Full Width Half Maximum

Waveband centre (mm)	FWHM (mm)	Applications	Band number
+/- 360	8	To constrain the SWIR-based aerosol model over turbid waters	1
+/- 368	8	To constrain the SWIR-based aerosol model over turbid waters	2
+/- 412	8	NO_2	*
+/- 520	8	Aerosol retrieval	3
+/- 575	8	Chappuis band for O_3 absorption	4
+/- 605	8	Chappuis band for O_3 absorption	5
+/- 620	8	Aerosol retrieval	*
+/- 709	8	Aerosol retrieval	*
+/- 740	8	Sunglint removal	*
+/- 761	3	Sunglint removal	6
+/- 775	16	Aerosol retrieval; water vapour reference band	7
+/- 820	16	Water vapour absorption	8
+/- 865	16	Aerosol retrieval; water vapour reference band; sunglint removal	9
+/- 940	16	Water vapour absorption	10
+/-1020	16	water vapour reference band	11
+/-1050	16	water vapour reference band	12
+/-1130	16	Water vapour absorption	13
+/-1135	16	Water vapour reference band	14
+/-1380	16	Cirrus clouds	15

Adapted from: CEOS (2018) Table 2.5

8.6 Further Information

Mobley (2020)

CEOS (2018)

GEBCO: *https://www.gebco.net*

CATDS Ocean Salinity Expert Centre: *http://www.salinityremotesensing.ifremer.fr/home*

8.7 References

AMS (2019). *Meteorology Glossary of American Meteorological Society*: *http://glossary.ametsoc.org/wiki/Main_Page*

Aurin, D., Mannino, A., and Lary, D.J. (2018). Remote Sensing of CDOM, CDOM Spectral Slope, and Dissolved Organic Carbon in the Global Ocean. *Applied Sciences*, 8, 2687. doi:10.3390/app8122687

Babin, M., Stramski, D., Ferrari, G.M., Claustre, H., Bricaud, A., Obolensky, G., and Hoepffner, N. (2003). Variations in the light absorption coefficients of phytoplankton, non-algal particles, and dissolved organic matter in coastal waters around Europe. *Journal of Geophysical Research*, 108(C7), 3211. doi:10.1029/2001JC000882

Blondeau-Patissier, D., Brando, V.E., Oubelkheir, K., Dekker, A.G., Clementson, L.A., Daniel, P. (2009). Bio-optical variability of the absorption and scattering properties of the Queensland inshore and reef waters, Australia. *Journal of Geophysical Research,* 114, C05003.

Botha, E.J., Brando, V.E., Anstee, J.M., Dekker, A.G. and Sagar, S. (2013). Increased spectral resolution enhances coral detection under varying water conditions. *Remote Sensing of Environment,* 131, 247–261.

Botha, E.J., Brando, V.E., and Dekker, A.G. (2016). Effects of Per-Pixel Variability on Uncertainties in Bathymetric Retrievals from High-Resolution Satellite Images. *Remote Sensing*, 8, 459. *https://doi.org/10.3390/rs8060459*

Brando, V.E., Anstee, J.M., Wettle, M., Dekker, A.G., Phinn, S.R., and Roelfsema, C. (2009). A physics based retrieval and quality assessment of bathymetry from suboptimal hyperspectral data. *Remote Sensing of Environment*, 113, 755–770. doi:10.1016/j.rse.2008.12.003.

Brando, V.E., Dekker, A.G., Park, Y.J., and Schroeder, T. (2012). Adaptive semianalytical inversion of ocean color radiometry in optically complex waters. *Applied Optics*, 51, 2808–2833.

Bricaud, A., Babin, M., Morel, A., and Claustre, H. (1995). Variability in the chlorophyll-specific absorption coefficients of natural phytoplankton: Analysis and parameterization. *Journal of Geophysical Research*, 100(C7), 13321–13332.

Bricaud, A., Morel, A., and Prieur, L. (1981). Absorption by dissolved organic matter of the sea (yellow substance) in the UV and visible domains. *Limnology and Oceanography*, 26, 43–53.

Bukata R.P. (2005). *Satellite Monitoring of Inland and Coastal Water Quality*. CRC press, Boka Raton, Florida, USA, 246 p.

CEOS (2018). *Feasibility Study for an Aquatic Ecosystem Earth Observing System*. (Eds: Dekker, A.G., and Pinnel, N.) CSIRO, Canberra.

Clementson, L., Wojtasiewicz, B., and Gunasekera, R. (2021). *Cyanobacterial cultures—absorption spectra, phycocyanin and phycoerythrin concentration for selected cultures*. v1. CSIRO. Data Collection. *https://doi.org/10.25919/9k2k-9n84*

Cox, C., and Munk, W., (1954). Measurement of the Roughness of the Sea Surface from Photographs of the Sun's Glitter. *Journal of the Optical Society of America,* 44, 838–850.

Dekker, A.G. (1993). *Detection of optical water quality parameters for eutrophic waters by high resolution remote sensing*. Ph.D. Thesis. *Earth and Life Sciences*. Vrije Universiteit, Amsterdam. 240 p.

Dekker, A.G., Brando, V.E., Anstee, J.M., Pinnel, N., Kutser, T., Hoogen-boom, J., Peters, S.W.M., Pasterkamp, R., Vos, R.J., Olbert, C., and Malthus, T.J. (2001). Imaging spectrometry of water. Ch 11 in *Imaging Spectrometry: Basic Principles and Prospective Applications*. (Eds: F.D. van der Meer and S.M. de Jong), pp 307–359. Kluwer Academic Publishers, Dordrecht, The Netherlands.

Dekker, A., Byrne, G., Brando, V., and Anstee, J. (2003). *Hyperspectral mapping of intertidal rock platform vegetation as a tool for adaptive management*. CSIRO Land and Water, Canberra, Australia.

Dekker, A.G., Brando, V.E., Anstee, J.M., Fyfe, S., Malthus, T.J.M., and Karpouzli, E.V. (2006). Remote sensing of seagrass ecosystems: use of spaceborne and airborne sensors. Ch. 15 in *Seagrass Biology, Ecology and Conservation*. (Eds: Larkum, A., Orth, R., Duarte, C.). Springer Verlag, Germany, p 347–359.

Dekker, A.G., Phinn, R., Anstee, J., Bissett, P., Brando, V.E., Casey, B., Fearns, P., Hedley, J., Klonowski, W., Lee, Z.P., Lynch, M., Lyons, M., Mobley, C., and Roelfsema, C., (2011). Intercomparison of shallow water bathymetry, hydro-optics, and benthos mapping techniques in Australian and Caribbean coastal environments. *Limnology Oceanography Methods* 9, 396–425.

Del Vecchio, R., and Blough, V. (2002). Photobleaching of chromophoric dissolved organic matter in natural waters: Kinetics and modeling. *Marine Chemistry*, 78, 231–253.

Elachi, C., and van Zyl, J. (2006). *Introduction to the Physics and Techniques of Remote Sensing*, Second Edn. Wiley Interscience, New Jersey.

Estep, L., and Arnone, R.A. (1994). Effect of whitecaps on determination of chlorophyll concentration from satellite data. *Remote Sensing of Environment,* 50, 328–334.

Falkowski, P.G., and Raven, J.A. (2007). *Aquatic photosynthesis*. 2nd edn, Princeton University Press, Princeton, New Jersey.

Fell, F., and J. Fischer. (2001). Numerical simulation of the light field in the atmosphere-ocean system using the matrix-operator method. *Journal of Quantitative Spectroscopy and Radiative Transfer,* 69, 351–388. *doi.org/10.1016/S0022-4073(00)00089-3*

Garaba, S.P., and Zielinski, O. (2013). Methods of reducing surface reflected glint for shipborne above-water remote sensing. *Journal of the European Optical Society—Rapid Publication,* 8, 13058. *http://dx.doi.org/10.2971/jeos.2013.13058*

Goodwin, T.W., and Mercer, E.I. (1990). *Introduction to Plant Biochemistry*. Pergamon Press.

Goyens, C., Jamet, C., and Schroeder, T. (2013). Evaluation of four atmospheric correction algorithms for MODIS-Aqua images over contrasted coastal waters. *Remote Sensing of Environment,* 131, 63–75.

Harrison, B.A., and Jupp, D.L.B. (1989) *Introduction to Remotely Sensed Data: Part ONE of the microBRIAN Resource Manual*. CSIRO, Melbourne. 156 p.

Hedley, J.D. (2008). A three-dimensional radiative transfer model for shallow water environments. *Optics Express*, 16(26), 21887–21021.

Hedley, J.D. (2013). Hyperspectral Applications. Ch 4 in *Coral Reef Remote Sensing*. (Eds: Goodman, J.A., Purkis, S.J., and Phinn, S.R.). Springer, Dordrecht. ISBN 978-90-481-9291-5.

Hedley, J.D. (2018). Influence of Three-Dimensional Coral Structures on Hyperspectral Benthic Reflectance and Water-leaving Reflectance. *Applied Sciences*, 8(12), 2688. doi:10.3390/app8122688

Hedley, J.D., Roelfsema, C., and Phinn, S.R. (2009). Efficient radiative transfer model inversion for remote sensing applications. *Remote Sensing of Environment,* 113, 2527–2532.

Hedley, J.D., Russell, B.J., Randolph, K., Pérez-Castro, M.A., Vasquez-Elizondo, R.M., Enriquez, S., and Dierssen, H.M. (2017). Remote Sensing of Seagrass Leaf Area Index and Species: The Capability of a Model Inversion Method Assessed by Sensitivity Analysis and Hyperspectral Data of Florida Bay. *Frontiers in Marine Science*, 4, 362. doi:10.3389/fmars.2017.00362

Helms, J.R., Stubbins, A., Ritchie, J.D., Minor, E.C., Kieber, D., and Mopper, K. (2008). Absorption spectral slopes and slope ratios as indicators of molecular weight, source, and photobleaching of chromophoric dissolved organic matter. *Limnology and Oceanography*, 53(3), 955–969.

Hollstein, A., and Fischer, J. (2012). Radiative transfer solutions for coupled atmosphere ocean systems using the matrix operator technique, *Journal of Quantitative Spectroscopy and Radiative Transfer*, 113, 536–548. *https://doi.org/10.1016/j.jqsrt.2012.01.010*.

Hollstein, A., von Bismarck, J., Fischer, J., and Preusker, R. (2010). *Description of the Vector Radiative Transfer Model MOMO. ESA support to science project water radiance document* (contract AO 1-5859/08/NL/CT). *Brockmann-consult.de: http://www.brockmann-consult.de/beam-wiki/download/attachments/17563679/momo_model_description.pdf*

Jaffe, J.S., Moore, K.D., McLean, J., and Strand, M.P. (2001). Underwater Optical Imaging: Status and Prospects. *Oceanography,* 14(3), 64–75.

Jerlov, N.G. (1976). *Marine Optics*. Elsevier, New York. 231 p.

Joehnk, K.D., Anstee, J., Ford, P., Botha, H., and Sherman, B. (2018). *Lake Hume blue-green algal risk minimisation*. Report prepared for the Murray-Darling Basin Authority by CSIRO Land and Water, Australia.

Kirk, J.T.O. (1994). *Light and Photosynthesis in Aquatic Ecosystems*, 2nd Edn. Cambridge University Press, Cambridge. 509 p.

Kirk, J.T.O. (2010). *Light and Photosynthesis in Aquatic Ecosystems*, 3rd Edn. Cambridge University Press, Cambridge. 662 p.

Kishino, M., Takahashi, M., Okami, N. and Ichimura, S. (1985). Estimation of the spectral absorption coefficients of phytoplankton in the sea. *Bulletin of Marine Science*, 37(2), 634–642.

Kutser, T., Miller, I., and Jupp, D.L.B. (2006). Mapping coral reef benthic substrates using hyperspectral space-borne images and spectral libraries. *Estuarine, Coastal and Shelf Science,* 70, 449–460.

Laanen, M.L., Peters, S.W.M., Dekker, A.G., and van der Woerd, H.J. (2011). Assessment of the scattering by sub-micron particles in inland waters. *Journal of the European Optical Society,* 6, 11046.

Lindell, T., Pierson, D., Premazzi, G., and Ziliolli, E. (1999). (Eds) *Manual for monitoring European lakes using remote sensing techniques*. Office for official publications of European Communities, Luxembourg. 161 p.

Ma, R., Jiang, G., Duan, H., Bracchini, L., and Loiselle, S. (2011). Effective upwelling irradiance depths in turbid waters: a spectral analysis of origins and fate. *Optics Express,* 19(8), 7128.

Maie, N., Boyer, J.N., Yang, C., and Jaffé, R. (2006). Spatial, geomorphological, and seasonal variability of CDOM in estuaries of the Florida Coastal Everglades, *Hydrobiologia, 569*(1), 135–150.

Mannino, A., Russ, M.E., and Hooker, S.B. (2008), Algorithm development and validation for satellite-derived distributions of DOC and CDOM in the U.S. Middle Atlantic Bight, *Journal of Geophysical Research*, 113, C07051. doi:10.1029/2007JC004493.

Martin, P., Cherukuru, N., Tan, A.S.Y., Sanwlani, N., Mujahid, A., and Müller, M. (2018). Distribution and cycling of terrigenous dissolved organic carbon in peatland-draining rivers and coastal waters of Sarawak, Borneo. *Biogeosciences*, 15, 6847–6865

Matthews, M.W. (2011). A current review of empirical procedures of remote sensing in inland and near-coastal transitional waters. *International Journal of Remote Sensing*, 32(21), 6855–6899. doi:10.1080/01431161.2010.512947

Mazel, C.H. (2001). Optics of the Seafloor. *Oceanography*, 14(3), 54–63.

Mobley, C.D. (1994). *Light and water; Radiative transfer in natural waters*. Academic Press, London, 592 p.

Mobley, C. (2020). *Ocean Optics Web Book*. *http://www.oceanopticsbook.info/view/introduction/overview*

Mobley, C., and Sundman, L.K., (2000). *Hydrolight 4.1 Technical Documentation*, 4.1 edn. Sequoia Scientific Inc., Redmond.

Moses, W.J., Sterckx, S., Montes, M.J., De Keukelaere, L., and Knaeps, E. (2017). Atmospheric Correction for Inland Waters. Ch 3 in *Bio-optical Modeling and Remote Sensing of Inland Waters* (Eds: D.R. Mishra, I. Ogashawara, and A.A. Gitelson), pp 69–100. Elsevier. *https://doi.org/10.1016/B978-0-12-804644-9.00003-3*

Morel, A. (1968). Note au sujet des constantes de diffusion de la lumière pour l'eau et l'eau de mer optiquement pures. *Cahiers Oceanographiques,* 20, 157–162.

Mustard, J., Staid, M., and Fripp, W. (2001). A semianalytical approach to the calibration of AVIRIS data to reflectance over water application in a temperate estuary. *Remote Sensing of Environment*, 75, 335–349.

Ogashawara, I. (2015). Terminology and classification of bio-optical algorithms. *Remote Sensing Letters*, 6(8), 613–617. doi:10.1080/2150704X.2015.1066523

Otis, D.B., Carder, K.L. English, D.C., and Ivey, J.E. (2004). CDOM transport from the Bahamas Banks. *Coral Reefs*, 23(1), 152–160.

Pahlevan, N., Mangin, A., Balasubramanian, S.V., Smith, B., Alikas, K., Arai, K., Barbosa, C., Bélanger, S., Binding, C., Bresciani, M., Giardino, C., Hunter, P., Simis, S., Spyrakos, E., and Tyler, A. (2021). ACIX-Aqua: A global assessment of atmospheric correction methods for Landsat-8 and Sentinel-2 over lakes, rivers, and coastal waters. *Remote Sensing of Environment*, 258, 112366. *https://doi.org/10.1016/j.rse.2021.112366*

Para, J., Coble, P. G., Charriere, B., Tedetti, M., Fontana, C., and Semper, R. (2010). Fluorescence and absorption properties of chromophoric dissolved organic matter CDOM in coastal surface waters of the northwestern Mediterranean Sea, influence of the Rhone River. *Biogeosciences,* 7, 4083–4103.

Parrish, C. (2020). *Index of Refraction of Seawater and Freshwater as a Function of Wavelength and Temperature* webpage, Oregon State University website: *http://research.engr.oregonstate.edu/parrish/index-refraction-seawater-and-freshwater-function-wavelength-and-temperature*

Plass, G.N., and Kattawar, G. (1972). Degree and Direction of Polarization of Multiple Scattered Light 2: Earth's Atmosphere with Aerosols. *Applied Optics*, 11, 2866–2879. doi:10.1364/AO.11.002866.

Pope, R.M., and Fry, E.S. (1997). Absorption spectrum (380–700 nm) of pure water. II. Integrating cavity measurements. *Applied Optics*, 36(33), 8710–8723. *https://doi.org/10.1364/AO.36.008710*

Pozdnyakov, D.V., and Grassl, H. (2003). *Colour of inland and coastal waters: A methodology for its interpretation*. Springer-Praxis, Chichester.

Preisendorfer, R.W. (1976). *Hydrologic optics*. NOAA Tech. Memo. ERL RMEL-67. 90 p.

Shank, G.C., Lee, R., Vähätalo, A., Zepp, R.G., and Bartels, E. (2010). Production of chromophoric dissolved organic matter from mangrove leaf litter and floating Sargassum colonies. *Marine Chemistry*, 119(1–4), 172–181.

Simis, S.G.H., Peters, S.W.M., and Gons, H.J. (2005). Remote sensing of the cyanobacterial pigment phycocyanin in turbid inland water. *Limnology and Oceanography,* 50, 237–245.

Singh, R.K., Shanmugam, P., He, X., and Schroeder, T. (2019). UV-NIR approach with non-zero water-leaving radiance approximation for atmospheric correction of satellite imagery in inland and coastal zones. *Optics Express*, 27(16), 28. *https://doi.org/10.1364/OE.27.0A1118*

Twardowski, M.S., Boss, E., Sullivan, J.M., and Donaghay, P.L. (2004). Modeling the spectral shape of absorbing chromophoric dissolved organic matter. *Marine Chemistry,* 89, 69–88.

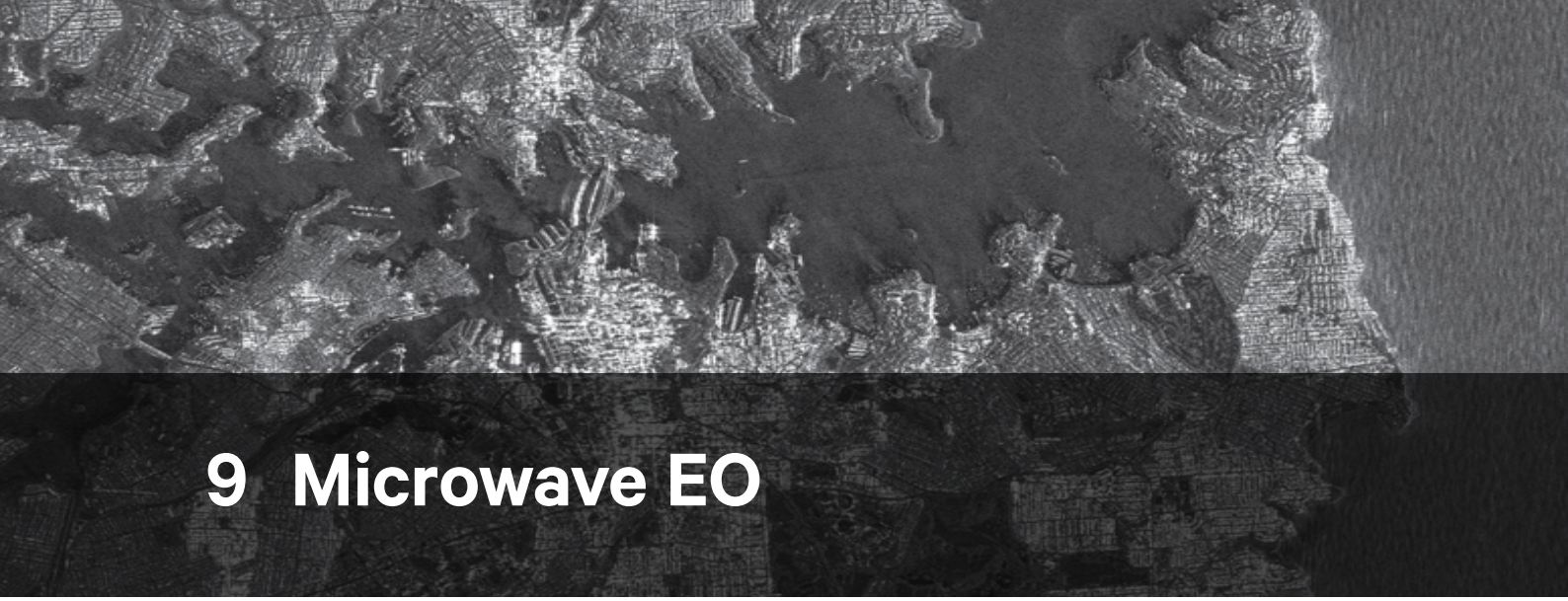
Voss, K.J., Mobely, C.D., Sundman, L.K., Ivey, J.E., and Mazel, C.H. (2003). The spectral upwelling radiance distribution in optically shallow waters. *Limnology and Oceanography,* 48 (1), 364–373.

Zhang, X., Lianbo, H., and He, M-X. (2009). Scattering by pure seawater: Effect of salinity. *Optics Express,* 17, 5698–5710.

Zimmerman, R.C. (2003). A biooptical model of irradience distribution and photosynthesis in seagrass canopies. *Limnology and Oceanography,* 48 (1), 568–585.

Zimmerman, R.C. (2006). Light and photosynthesis in seagrass meadows. Ch 13 in *Seagrasses: biology, ecology and conservation*. (Eds: Larkum, A.W.D., Orth, R.J., and Duarte, C.M.) Springer, Dordrecht. pp. 303–321.

Zimmerman, R.C., and Dekker, A.G. (2006). Aquatic optics: basic concepts for understanding how light affects seagrasses and makes them measurable from space. Ch 12 in *Seagrasses: biology, ecology and conservation*. (Eds: Larkum, A.W.D., Orth, R.J., and Duarte, C.M.) Springer, Dordrecht. pp. 295–301.



9 Microwave EO

Microwave EO is introduced in Volume 1A—Sections 5 and Volume 1B—Section 9. This form of EO offers advantages over optical datasets for some applications, but can also be complementary when used in conjunction with other EO data sources (Richards, 2009, 2012).

As introduced in Section 5.1.4, electromagnetic radiation (EMR) spans a wide range of wavelengths, with microwave radiation being the region with wavelengths between 1 mm and 1 m (see Figure 5.7). Microwave sensors (described in Volume 1A—Sections 13, 14.5, 15.2 and 16) are commonly classified as either:

- passive—detect energy that originates from an independent source and is scattered or reflected by a target; or
- active—radiate a particular form of energy towards a target object or surface and then detect the amount of that energy which is scattered or reflected by it (see Excursus 8.1).

Passive sensors record the microwave energy that is emitted by all materials on Earth with temperatures above 0K (absolute zero—see Volume 1B—Section 8.1). While microwaves are minimally attenuated by atmospheric conditions and can penetrate solids, the emitted energy in this part of the electromagnetic spectrum is low for the average temperature of the Earth's surface (see Figure 9.1).

Microwaves can be generated electronically using an antenna. Active sensors have the advantage of operating independently of solar illumination and most weather conditions. Active microwave EO is based on radar, an acronym for Radio Detection And Ranging (see Excursus 9.1). Both active and passive microwave sensors may also be categorised as imaging or non-imaging (see Table 9.1).

Table 9.1 Spectral regions observed by EO sensors

Note that, in practice, atmospheric windows restrict these ranges for observing Earth's features (see Volume 1A—Table 5.4).

Spectral region	Wavelength	EO sensor			
		Passive		Active	
		Imaging	Non-imaging	Imaging	Non-imaging
Visible	0.38 to 0.7 μm	Passive radiometers Passive spectroradiometers Passive imaging spectrometers		Lidar	Lidar distance only
Near Infrared	0.7 to 1.1 μm				
Short wave Infrared (SWIR)	1.1 to 3.0 μm		Polarimeters		
Middle Infrared (MIR)	3.0 to 8.0 μm	Passive radiometers Polarimeters			
Thermal Infrared (TIR)	8.0 to 15.0 μm		TIR thermometers		
Microwave	1 mm to 1 m	Microwave radiometers Microwave spectrometers		Radar	Polarimeters Scatterometers
Radio	> 10 cm	Passive radiometers	Sounders	Imaging radar	Altimeters Sounders

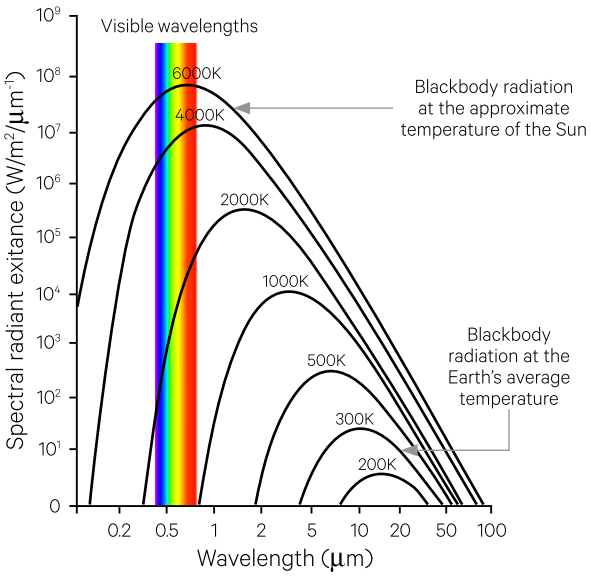
Background image: Synthetic Aperture Radar image (S-band) of Sydney Harbour acquired at night by NovaSAR-1 in 2018 with 6 m resolution. **Source:** SSTL. Retrieved from *https://www.sstl.co.uk/media-hub/images/novasar-1*

In this section we will review the microwave EO framework (see Section 9.1) and detail some specific microwave sensors that are used to observe surface waters, namely:

- passive microwave radiometer—detects emissions of thermal radiation in the wavelength range 1–300 mm (see Section 9.2);
- imaging radar—represents systematically acquired lines of radar returns as an image grid (see Section 9.3);
- Synthetic Aperture Radar (SAR) interferometer—exploits the phase difference between two images acquired for the same scene using two separated antennae (see Section 9.4);
- radar altimeter—measures range or distance from the sensor to specific features (see Section 9.5); and
- microwave scatterometer—measures surface texture (see Section 9.6).

Figure 9.1 Blackbody radiation

The wavelength of peak radiant exitance for a blackbody decreases as its temperature increases (Note: Scales are logarithmic)



Adapted from: NASA/USGS Astrogeology Science Center Radiance Calculator at *http://astrogeology.usgs.gov/tools/thermal-radiance-calculator/*

Excursus 9.1—Radar

Further information: Volume 1B—Section 8

As introduced in Volume 1A—Section 15.2 and Volume 1B—Section 8, radar sensors use actively transmitted radio waves to detect objects and determine their position or 'range'. The principle of operation for these devices is to direct pulses of microwave energy at an object then record the timing of the echo.

Radar images are acquired in a completely different way to centrally-projected images derived in the optical wavelength regions. Radar EO uses microwave EMR, emitted by a rectangular antenna, carried on an aircraft or spacecraft platform, to irradiate the Earth's surface and measure the amount of returning radiation reflected from surfaces (called backscatter) within the resolution elements of the system. The radiation is transmitted in a fan-shaped beam as a series of pulses of very short length. The time taken for each pulse (travelling at the 'speed of light') to be reflected and returned to the antenna determines the distance of that portion of the Earth's surface from the antenna. The radar equation describes the performance of a radar system, and relates the received return power at the antenna to the target parameters and the parameters of the radar:

$$P_R = \frac{P_\tau G_\tau}{4\pi R^2} \sigma \frac{A_R G_R}{4\pi R^2}$$

where

P_R is the received power (W);
P_τ is the transmitted power (W);
G_τ is the gain of the transmitting antenna in the direction of the target;
σ is the radar cross-section or effective backscatter area of the target (m^2);
A_R is the antenna area (m^2);
G_R is the gain of the receiving antenna in the direction of the antenna; and
R is the range (m).

Radar signals may be transmitted at a range of wavelengths/frequencies. The standard wavelengths used and their standard radar frequency letter codes are given in Table 9.2. In general, atmospheric precipitation has minimal effect on radar signals with frequency < 10 GHz, which provides a distinct advantage over passive and active optical sensors for EO when cloud cover is present. Slight attenuation occurs at wavelengths less than 30 mm under clear

atmospheric conditions, with attenuation increasing as wavelength decreases. Heavy precipitation will cause a strong radar echo at wavelengths of 10 mm or less (this principle being used in both ground and aircraft mounted weather detection radar systems).

The radar bands X-, C- and L- are most commonly used for EO (see Figure 9.2). Since penetration depth of a radar signal increases with increasing wavelength, L-band penetrates deeper than C-band, which penetrates deeper than X-band (see Figure 9.3). The interaction between these wavelengths and features on the Earth's surface is partly a function of the scale of the surface 'texture' and its dielectric properties (electrical reflectivity and conductivity; see Volume 1B—Section 8 for details). Scattered signal amplitude and polarisation provides information about scattering properties and structure. Phase measurements of the return pulse are used in interferometry to reconstruct 3D topography.

Table 9.2 Radar bands used for EO

Band code	Wavelength (mm=10^3 μm)	Frequency (GHz=10^9 Hz)	Example of use
K	7.5–25.0	40.0–12.0	Early airborne systems
X	25.0–37.5	8.0–12.0	Military reconnaissance, terrain mapping, surveillance
C	37.5–75.0	4.0–8.0	Sea-ice surveillance (limited penetration of solids or vegetation)
S	75.0–150.0	2.0–4.00	Medium-range meteorological applications, such as rainfall measurement, airport surveillance
L	150.0–300.0	1.0–2.0	Ice sheet monitoring, glacier dynamics, penetrates vegetation
P	300.0–1000.0	0.3–1.0	Experimental—penetrates vegetation, sea ice, soil, glaciers

Figure 9.2 Radar wavelengths

The radar wavelengths that are commonly used for EO are shown at actual size (on an A4 page).

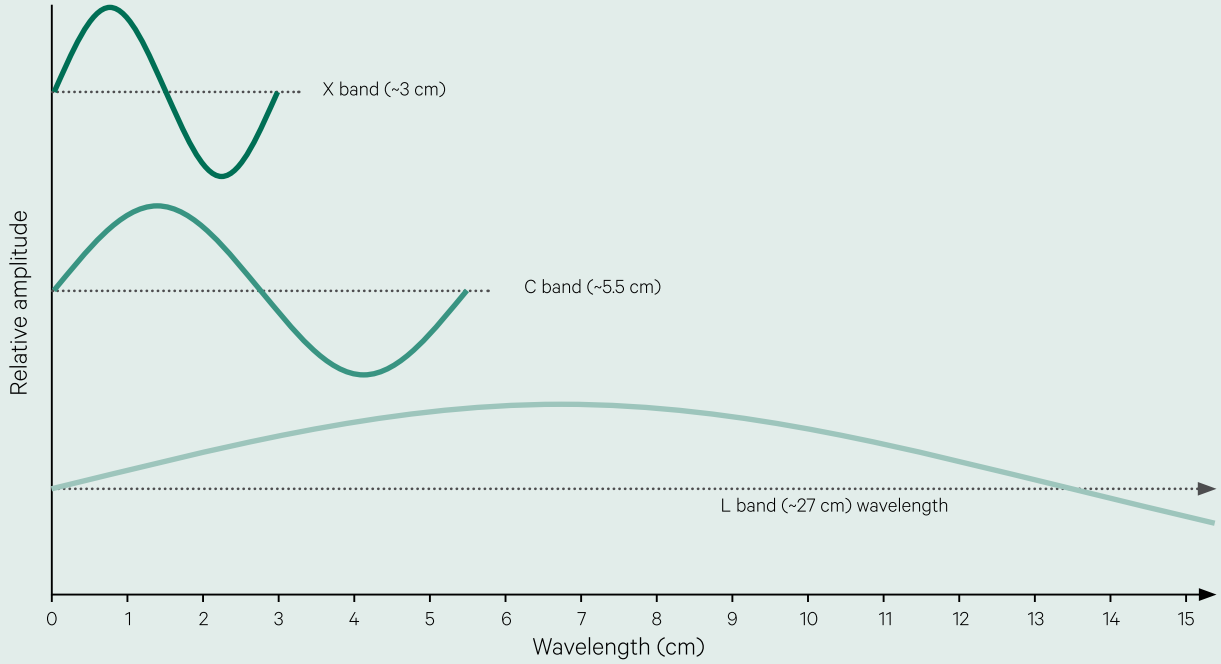
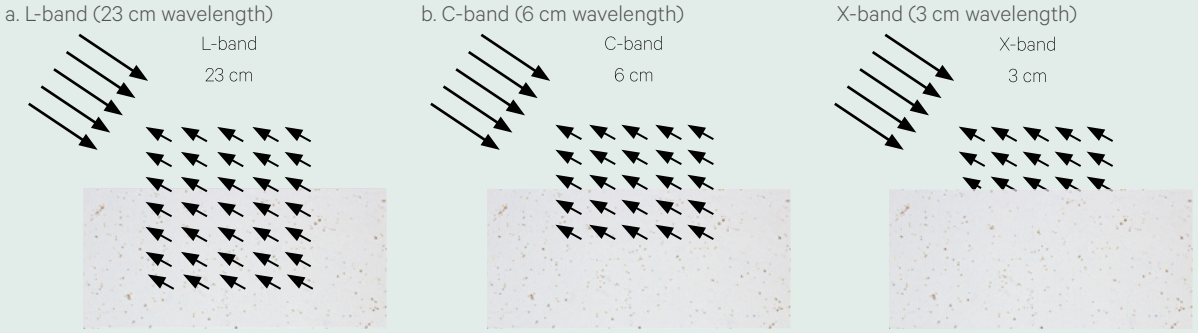


Figure 9.3 Radar penetration in ice/snow cover

While subsurface penetration is possible in the longer L- and C-band radar, it is unlikely from the shorter X-band.



Source: Bruce Forster and Linlin Ge, Course Notes, UNSW

9.1 Microwave EO Framework

The basic physics of EMR is introduced in Volume 1, and in this section we will summarise foundational information that is most relevant to microwave EO. A detailed description of microwave EO can be found in Volume 1B—Section 8.

9.1.1 Review of microwave EMR

EMR is described as having dual natures, comprising both waves and elementary particles, called photons. Newtonian physics views EMR as a wave, which can experience interference and diffraction when propagated through space (see Volume 1A—Section 2.5.2). The quantum view of a beam of EMR, however, is that the energy is not strictly continuous, but packaged into discrete units called photons. In this model, the EMR beam is considered as a stream of photons travelling at 3×10^8 m s^{-1} (the speed of light), where the number of photons per unit area is proportional to the power of the beam (Maged, 2020).

While all EMR waves travel at the same speed, the energy they carry varies with both the wavelength/frequency of radiation and its intensity. Microwaves span the wavelength range 1 mm to 1 m and, like optical wavelengths, can be reflected, transmitted, or absorbed by all forms of matter (see Volume 1A—Section 2). Optical wavelengths are smaller than the lenses and sensors that detect them so can be modelled using geometric or ray optics (see Section 8). Unlike optical wavelengths, however, microwave interactions with matter are best described in terms of the Maxwell equations.

Maxwell viewed EMR as transverse waves combining both magnetic and electric force fields (see Figure 9.4 and Volume 1A—Section 2.4), in which a changing electric field induces a magnetic field and conversely a changing magnetic field induces a changing electric field. Maxwell's equations are a set of partial differential equations that interrelate the symbiotic magnetic and electrical fields, and the electrodynamic properties of matter (electric permittivity, magnetic permeability, and electric conductivity; Ulloa *et al.*, 2019). These equations allow the direction and magnitude of one of these fields to be derived from knowledge of the direction and magnitude of the other (Suits, 1983).

The physical mechanisms whereby different wavelengths of EMR interact with, and impact the structure of, matter are summarised in Table 9.3. The precise atomic and molecular interactions vary both with increasing wave energy and the structure of any matter the wave encounters. Resonant effects, such as rotations, vibrations, or displacements of electrons, atoms, and/or molecules primarily result from higher energy waves (gamma rays to MIR), with the actual impact of a wave depending on its energy level(s). Non-resonant effects, such as conduction and scattering, predominantly result from lower energy waves (TIR and microwave).

The quantum energy of microwave photons is in the range of energies that separate the quantum states of molecular rotation and torsion[10] (see Volume 1B—Section 3 for more detail). At a macro-level, these interactions exhibit as rotational processes, thermal emission, scattering, and conduction. Microwave EO sensors essentially quantify the results of these types of interactions, such that chemical and physical properties of surface and atmospheric features are then inferred from this information (see Figure 8.1). Examples of information that can be derived from observations of these wave-matter interactions are given in Table 9.4.

10 Other interactions can lower the energy of excited electrons in atoms and molecules: fluorescence happens when matter instantaneously emits a photon with lower energy and longer wavelength, while phosphorescence occurs when matter can retain the energy of excitation for a period of time then emit that energy gradually.

Figure 9.4 Electromagnetic wave

An EM wave comprises two sinusoidal waves: an electric wave and a magnetic wave. Each component wave is simultaneously oscillating in planes mutually perpendicular to each other, and also to the direction of travel through space. Wavelength (λ) is measured as the distance between successive wave peaks or troughs. Frequency (ν) is measured as the number of cycles per second passing a fixed point.

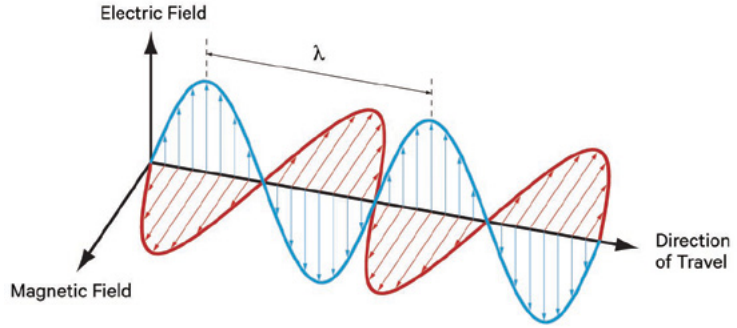


Table 9.3 Effects of EMR on matter

EM Spectral Region	Structural Interactions	Possible Effects
Gamma rays and X-rays	atomic and electronic forces	photoelectric effect, Compton effect, pair production effect
Ultraviolet	electronic excitation and transfer mechanisms	fluorescence, ionisation
Visible and NIR	electronic energy transitions molecular vibrations	molecular vibration, ionic vibration, crystal field effects, charge transfer, electronic conduction
MIR and TIR	molecular vibrations molecular rotations	Si-O stretching vibration, vibrational excitation of atmospheric gases
Microwave	molecular rotations	dielectric heating—primarily by water, oxygen rotational bands

Source: Elachi and van Zyl (2006)

Table 9.4 Wave-matter interactions relevant to EO

EMR Spectral Region	Major Process(es) of Interaction	Information Derived from EO
Gamma rays X-rays	atomic	radioactive material mapping
Ultraviolet	electronic	atmospheric H and He detection
Visible and NIR	electronic molecular vibrations	surface chemical composition
MIR	molecular vibrations and rotations	surface and atmospheric chemical composition
TIR	molecular vibrations and rotations thermal emission	surface constituents surface heat capacity surface and atmospheric temperature
Microwave	molecular rotations thermal emission scattering conduction	surface physical properties surface temperature atmospheric constituents atmospheric precipitation
Radio frequencies	scattering conduction ionospheric effect	surface physical properties subsurface sounding ionospheric sounding

Adapted from: Elachi and van Zyl (2006) Table 2-2

9.1.2 Observing microwave EMR

As introduced in Volume 1A—Section 13, EMR can be observed in terms of:

- amplitude—maximum oscillation of wave from midpoint and proportional to the energy carried;
- energy—as wavelength (the distance travelled in one full wave cycle) or frequency (the number of cycles per unit time), with shorter wavelength at higher frequency carrying more energy;
- polarisation—orientation of electric field of EMR relative to reference vector; and
- coherence—extent to which two waves oscillate in phase; for EM waves, this characteristic describes a relationship in time.

Microwave EO is detailed in Volume 1B—Section 8. Below we review those aspects of EMR observation that are particularly relevant when using microwave datasets for surface water applications.

9.1.2.1 Amplitude

The amplitude, or strength, of the detected microwave signal (either natural emissions for passive sensors, or the echoes of transmitted signals in active sensors) varies with different target materials and their orientations. This is commonly referred to as backscatter. The amount and nature of backscattered EMR can provide information about the size, shape, configuration, and electrical properties of the surfaces and objects irradiated. For example, backscatter is very high when the incoming radiation is at right angles to the object.

The major factors influencing an object's radar return signal intensity are considered to be relief, surface roughness, and electrical properties (see Volume 1B—Section 8.2). Materials differ in terms of their electrical reflectivity and conductivity. One measure of these characteristics is called the 'complex dielectric constant'. For most dry natural materials, the magnitude of this constant has relatively low values (3–8) in the microwave region of the EM spectrum, while water has a value of approximately 80.

The scale of roughness necessary for diffuse reflection decreases with decreasing wavelength and there is a weaker dependence for scattering on the angle of incidence. With decreasing wavelength, the volume scattering component of the backscatter will become more important and, at any given wavelength, the relative contribution of volume scattering increases with increasing angle of incidence (due to the increased slant depth) and will cause the return signal to be depolarised (see Section 9.1.2.3).

9.1.2.2 Energy

The energy carried by EMR is characterised by its wavelength or frequency. As summarised in Table 9.3 and Table 9.4, microwaves interact with matter at the molecular level (see also Volume 1A—Section 15.2 and Volume 1B—Section 8). At these longer wavelengths, the dual electric/magnetic nature of EM waves and their interaction with matter can be modelled by Maxwell's equations (Suits, 1983).

Microwave sensors detect EMR in the wavelength range from 1 mm to 1 m, with different sensors detecting particular wavelengths in this range for specific applications (see Table 9.2). Since this region of the EM spectrum is largely unaffected by the atmosphere, most microwave sensors can operate in all weather conditions.

9.1.2.3 Polarisation

Polarisation, a unique feature of transverse waves, describes the plane in which they oscillate, that is, the orientation of the electric field (or its electric vector) relative to a reference plane. Transverse waves, such as EMR, can be polarised to restrict their vibrations to a single plane relative to the direction of propagation. Microwaves and radio waves are polarised by orienting the antenna to transmit and receive specific wave planes (see Volume 1B—Section 8).

Transmitted signals for imaging radar can be polarised in two orthogonal modes: horizontal (H) and vertical (V), which are typically transmitted separately. These orientations are defined relative to the plane of incidence of EMR, that is, the plane defined by the vertical and the direction of propagation. Horizontal (or plane) polarisation applies when the energy is perpendicular to the wave's plane of incidence. Vertical polarisation, then, is perpendicular to the horizontal polarisation, that is, the electric vector is aligned with both the plane of incidence and the direction of travel.

Interaction with features on the Earth's surface can change the polarisation of the scattered signal, so radar antennae are often designed to receive the H and V signals simultaneously. As a result, polarimetric radar detection systems can measure backscatter amplitude and phase in up to four specific polarisation modes (see Table 9.5). More recently, circular polarisation (the tip of the electric field vector is rotating in a circle as it propagates) is also used, where a circularly polarised wave is transmitted and H and V signals are received. This allows any configuration of transmit and receive to be derived (see Volume 1B—Section 8).

Table 9.5 Polarisation options for radar signals

Transmitted	Received	Code	Type
H	H	HH	Co-polarised
H	V	HV	Cross-polarised
V	H	VH	Cross-polarised
V	V	VV	Co-polarised

Radar system measurements are typically single-polarised (HH or VV or HV or VH), dual-polarised (HH and HV, VV and VH, or HH and VV), or quadrature (quad-) polarised (HH, VV, HV, and VH). A quad-polarised (that is, polarimetric) radar and some dual-polarised systems also measure the signal phase difference between the modes, as well as the signal magnitude, since this is important in polarimetric analysis. Differences in the structure (for example, orientation or shape) of surface features modify the polarisation of reflected microwave energy in varying degrees, with the polarisation mode affecting the scattering intensity 'echo' and thus how the objects appear in the resulting imagery.

9.1.2.4 Coherence

Coherence of a transmitted signal relates to its purity. Two waves with a systematic relationship between their amplitudes are called coherent, that is, they oscillate in phase. In terms of EMR, which comprises two three-dimensional vectors, definition of the underlying physics of coherence is complex, but this characteristic can be simply viewed as their relationship in time. Conversely, waves are 'incoherent' when their amplitudes are randomly related, that is, their waves oscillate out of phase. For example, lasers generate coherent radiation, while sunlight, candles, and incandescent light globes generate incoherent radiation. Since SAR generates coherent radiation, two registered radar images can be differenced to show interference and infer change (see Section 9.4).

9.1.2.5 The Doppler Effect

The Doppler Effect is observed whenever the wave source is moving relative to the observer such that a change in frequency is perceived. For example, when an observer is approaching an energy source, the wave frequency will be observed to be higher than when the observer is moving away. This perception is in fact due to the relative motion of the observer rather than an actual change in the frequency of the wave. This effect can be observed with sound and light waves and is particularly of interest to astronomy for determining the radial velocity of stars and galaxies relative to Earth. Several radar sensors (including traffic speed cameras) are based on the Doppler Effect.

The Doppler effect is used by SAR to effectively increase the length of the physical antenna. By using the flight path of the radar platform, return signals are processed according to their Doppler shifts (that is, a change in wave frequency as a function of the relative velocities of transmitter and receiver). This processing requires that both amplitude and phase information be recorded from objects throughout the time period in which they are within the beam of the moving antenna.

The theoretical increase in the antennae length (the synthetic aperture) allows the computer-processed cross-range or azimuth resolution to be equal to half the real aperture for the whole of the range (near range to far range). Weighted averaging of multiple returns using the platform motion and Doppler shift effects allows the signal that would have been obtained by a longer antenna to be reconstructed. The consequently larger synthetic aperture results in higher spatial resolution imagery that is constant in the along-track (azimuth) and across-track (range) directions (see Volume 1B—Section 8 for details).

9.2 Passive Microwave

Passive microwave radiometers operate in microwave wavelengths from 1 to 300 mm, which are shorter than radar. They rely on detecting the emissions of thermal radiation in the microwave region, which is commonly converted to brightness temperature (see Volume 1B—Section 8.1.1).

In the microwave portion of the spectrum, the two most important properties determining emission levels are the physical temperature (T) of the object and its radiating efficiency or emissivity (ε). Emissivity is the ratio of emitted radiation at a particular wavelength of a real surface to the equivalent radiation from a blackbody at the same temperature and wavelength (see Volume 1A—Section 2.11). In the microwave region, surface materials can have large variations in emissivity. For example, land surfaces can have emissivity of the order of 0.9 while water is of the order of 0.5, although emissivity differences will be less at shorter wavelengths (higher frequencies). Thus, the difference in brightness temperature between land and water at the same kinetic temperature will be largely due to the large difference in their emissivities. It should be noted that ice or snow surfaces and clouds and rain can modify these results (Ferraro *et al.*, 1998).

The intensity of passive microwave radiation emitted by an object depends on its temperature and incident radiation, plus its emittance, reflectance, and transmittance properties. The emitted energy is related to the temperature and moisture content of the emitting object or surface. Surface roughness can also increase the measured radiation from an object or surface because rough texture (such as with ocean waves) increases the surface area of emission per unit area viewed (see Section 16.2.3).

The range of wavelengths detected by microwave radiometers corresponds to the very low energy end of the Earth's energy spectrum (see Volume 1A—Section 5). While all objects emit microwave energy, the amounts are generally very small, so the bandwidth and the spatial resolution of the sensor must be large to allow acquisition of sufficient measurable radiation. A passive microwave sensor detects this naturally emitted microwave energy within the angular field of view of its antenna, which increases with wavelength. Because passive microwave sensors are detecting low energy levels, their imagery has relatively low signal to noise ratio, and the longer wavelengths tend to result in lower spatial resolution. Interpretation of passive microwave imagery is consequently more complex (Ulaby and Long, 2014).

Applications of passive microwave imagery EO include meteorology, hydrology, and oceanography. Oceanographic applications include mapping currents and surface winds (see Sections 16 and 17) and detecting marine pollutants such as oil slicks (see Section 19). There are also detectable differences in microwave emission intensity between water and sea ice (see Section 15), the differentiation of which is important for climatic studies. Other applications include determination of precipitation rates, sea surface temperature (even in cloudy conditions) for global climate studies (see Section 14), and characteristics (including age estimates) for ice and snow cover (see Sections 15.3.4 and 15.4). Non-imaging passive microwave radiometers are used to infer ocean surface wind speed, and atmospheric water content and temperature.

9.3 Imaging Radar

Radar remote sensing is detailed in Volume 1B—Section 8.2 and reviewed in Excursus 9.1 above. The spatial resolution of an imaging radar sensor is determined by its pulse length and beam width. Two types of radar-based systems are commonly used for microwave imaging on aircraft and satellite platforms:

- Side-Looking Airborne Radar (SLAR) or Real Aperture Radar (RAR)—older systems with limited coverage and shorter wavelengths that record amplitude as a function of time; and
- Synthetic Aperture Radar (SAR)—records both amplitude and phase to generate imagery with higher spatial resolution and fewer geometric distortions (see Volume 1A—Section 15.2).

The side-looking nature of imaging radar devices records relief characteristics with higher returns from sensor-facing slopes, and lower or no returns from away-facing slopes or radar shadow areas, in much the same way as an off-nadir Sun position differentially illuminates a landscape with varying relief. Surfaces with local relief variations that are greater than the wavelength of the radar signal will scatter the signal in all directions (diffuse reflectors) and thus return a small, but measurable, portion of the signal to the sensor (see Volume 1A—Section 15). Smooth surfaces, with surface roughness much less than the wavelength of the radar signal, tend to reflect most of the energy away from the sensor (specular reflectors) thus producing a low return signal. While the actual response depends on surface orientation relative to the sensor, more surfaces tend to be specular reflectors for microwave wavelengths than in the optical wavelengths (see Figure 8.6).

Of relevance to surface waters is a scattering mechanism called Bragg Scattering or Bragg Resonance. It has been used to describe scattering from the ocean in terms of resonance with tiny capillary and short gravity waves, even when these waves have a height measured in tenths of a millimetre and ride on waves that are metres high. The short Bragg-scale waves are formed in response to wind stress. If the sea surface is rippled by a light breeze with no long waves present, the radar backscatter is due to the component of the wave spectrum that resonates with the radar wavelength. The Bragg equation defines the ocean wavelengths for Bragg scattering to occur, as a function of radar wavelength (λ_r) and incidence angle (θ; see Figure 9.5):

$$\lambda_s = \frac{\lambda_r}{2\sin\theta}$$

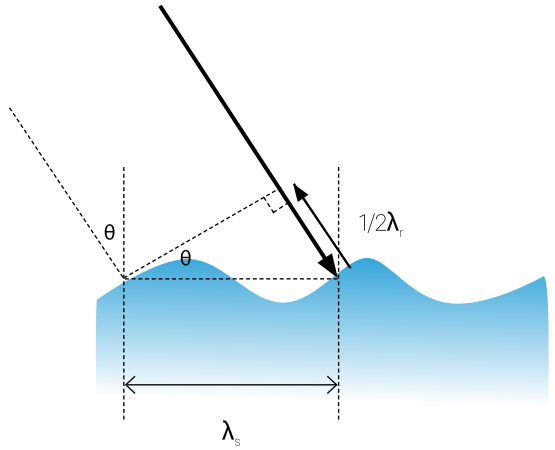
SAR imagery can be acquired as:

- stripmap—the standard acquisition mode with fixed beam direction and no scanning as recorded by SLAR;
- scan—involves moving the antenna in a scan pattern, and is used to capture larger areas with lower spatial resolution; and
- spotlight—used to capture data over small target areas at high spatial resolution, and involves pointing the beam as the platform moves so that the target is in the beam for longer, thus making the synthetic aperture larger.

The roughness of the ocean surface, defined at the scale of a few centimetres, can be detected in SAR imagery, allowing phenomena such as wind, waves, surfactants (e.g. oil), upwelling, boundaries, and bathymetry to be observed (Heron *et al*., 2013). Scattering due to ocean roughness and Bragg scattering are more apparent in VV polarised images (see Figure 9.6). SAR imagery is also used to detect shipping activities (Brusch *et al*., 2011) and track fisheries (Richards, 2012). Different wavelengths and polarisations can be used to monitor a range of surface water features, such as floods and river discharges (see Section 11.4), ice formations (see Section 15), wave heights (Romeiser *et al*., 2004; see Section 16.3.3), and pollution (see Section 19).

Figure 9.5 Bragg scattering

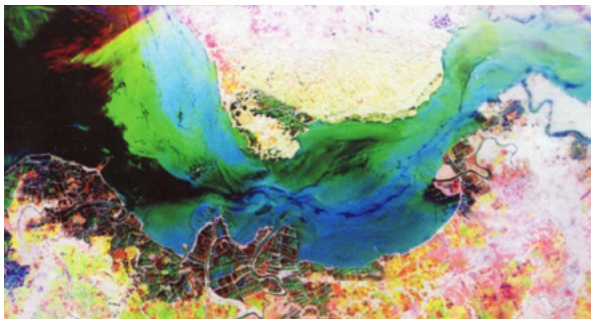
Bragg scattering relationship for an ocean wavelength of λ_s and incoming radiation of λ_r wavelength



Source: Bruce Forster and Linlin Ge, Course Notes, UNSW

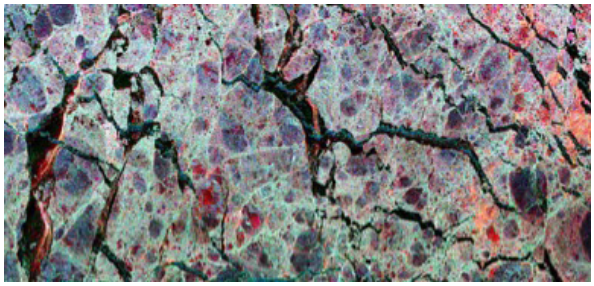
Figure 9.6 SAR composite images

a. Ocean surface roughness for Coastal Panay, Philippines, is highlighted using POLSAR (fully polarised) AIRSAR VV images of increasing wavelength to form a colour composite (C-band as red, L-band as green and P-band as blue)



b. Shuttle SIR-C/X SAR (C-band HH, L-band HV and L-band HH displayed as red, green, blue respectively) for sea ice in Antarctica covering an area 45×18 km. Colours indicate ice thickness, which is related to ice growth stages:

- darker lines of open water and smooth ice (< 0.7 cm thick). Blue lines indicate open water in new fractures while bright red lines indicate new ice growth < 0.5 m thick.
- undeformed floes as blue-grey (~0.7 m thick)
- red-tinged deformed ice pieces (< 2 m thick)



Source: a. NASA JPL; b. CCRS.

9.4 SAR Interferometry

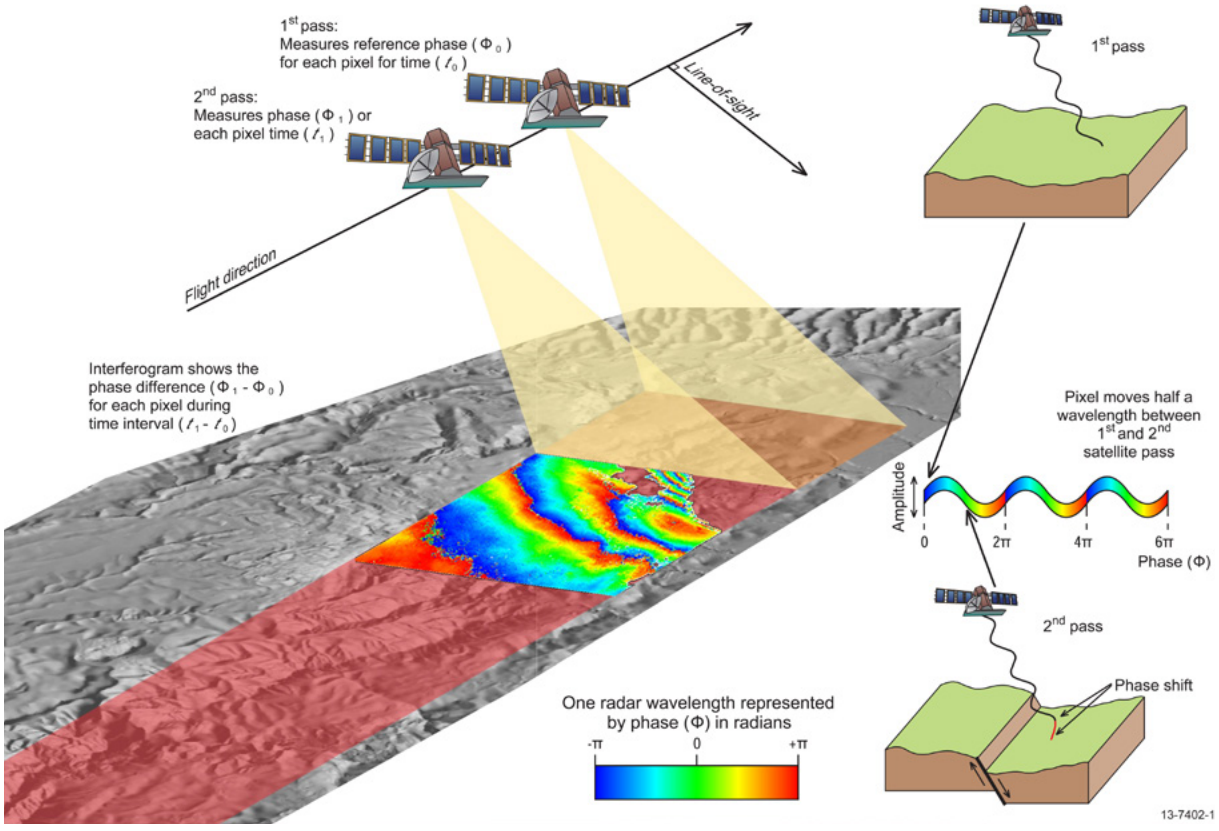
In airborne or spaceborne SAR, radiation is actively transmitted to illuminate the surface, then the backscattered radiation is collected (see Section 9.3). An image of the scene is produced after processing the return signals. Each picture element (pixel) comprises both amplitude and phase information. A conventional SAR image displays the amplitude or power (the square of the amplitude) information.

Interferometric SAR (InSAR), however, exploits the phase information as well as the amplitude. In this technique two images are acquired for the same scene using two separated antennae. After registering the two images and resampling one image to overlay the other, the phases corresponding to each pixel are calculated and differenced, resulting in a phase difference image called an interferogram, which highlights differences in elevation of the imaged surface and changes in position of imaged targets on that surface (see Figure 9.7).

The two antennae may be on the same platform (single-pass InSAR) or the same antenna may be flown twice over the same scene areas (repeat-pass InSAR; see Volume 1B—Section 8.2.7). Along-track interferometry (ATI) uses two antennae, separated in the along-track direction, which detect the same backscattered signals from the Earth's surface, albeit with a very small time lag (Romeiser, 2013). These two datasets are processed to produce two SAR images, the difference of which highlights phase changes and can be used to infer surface velocities (Goldstein and Zebker, 1987).

Figure 9.7 InSAR operation

In this illustration, two SAR images of the same area are acquired at different times. If the surface moves between the two acquisitions a phase shift is recorded. An interferogram maps this phase shift spatially.



Source: Geoscience Australia. Retrieved from *https://www.ga.gov.au/scientific-topics/positioning-navigation/geodesy/geodetic-techniques/interferometric-synthetic-aperture-radar*

Repeat-pass InSAR allows for differential radar interferometry before and after an event. The phase difference between the two dates is related to the height change and measurements of the order of a few millimetres can be detected. If the antennae are separated parallel to the line of flight in the azimuth (along-track) direction, the motion of the sea surface and the radial velocity of the ground moving target can be measured, whereas if the antennae are separated perpendicular to the line of flight in the range (across-track) direction, altitude information can be derived.

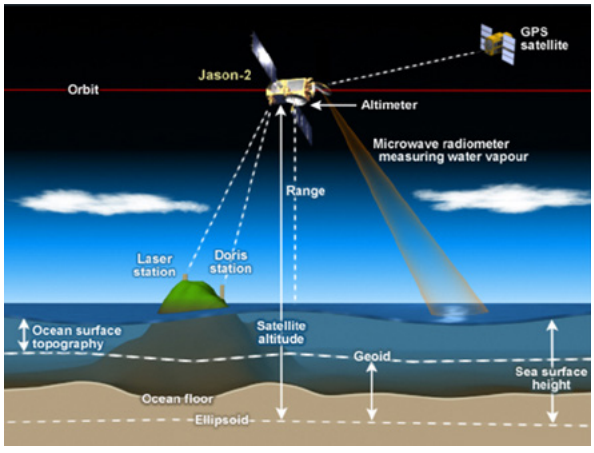
InSAR is being used to measure wave motion (Romeiser, 2013), track ocean currents with greater accuracy than imaging SAR (Romeiser *et al.*, 2004), and monitor the movement of sea ice and ice sheets (see Section 15). It may also prove useful for coastal bathymetric applications (Romeiser, 2013).

9.5 Radar Altimetry

This non-imaging radar detects the microwave backscattering of a surface using a narrow pulse with near normal incidence. Since the basic design of radar devices is to measure distance, by directing the pulse onto the Earth's surface from directly overhead (nadir), the distance being measured is the altitude of the platform above the surface (see Figure 9.8). This relies on accurate knowledge of the platform position with respect to a reference ellipsoid, provided via positioning satellites and ground-based locating systems (see Volume 1A—Section 3).

Figure 9.8 Operation of radar altimeter

Radar altimeters measure the distance between the satellite and the sea surface. The distance between the satellite and the reference ellipsoid is derived by a combination of global positioning satellites, optical laser ranging from ground sites, and radio Doppler ranging from ground sites. Variations in sea surface height, are caused by the combined effect of the geoid and ocean circulation (or dynamic topography).



Source: NASA. Retrieved from *https://sealevel.jpl.nasa.gov/missions/technology/*

Conventional radar altimeters have measured distance from the Earth's surface along the satellite's ground track to generate one-dimensional profiles, which can be interpolated to create a two-dimensional map of surface height. While each profile has relatively high resolution along-track, there are significant gaps between tracks for a single altimeter. Datasets from at least two radar altimeters orbiting simultaneously have been merged to produce two-dimensional, global maps of surface height with moderate spatial resolution (Ducet *et al.*, 2000).

Radar altimeters have been carried on several satellites, starting with Skylab in 1973, and more recently the ERS, Jason, and Cryosat platforms (see Volume 1A—Section 16.1.2). The planned SWOT (Surface Water and Ocean Topography) mission will use radar interferometry (see Section 9.4) to enable wide swath sampling, yielding higher spatial resolution data and denser coverage (Fu and Ubelmann, 2014; see Excursus 12.1).

Routine observation of sea surface topography using satellite radar altimetry has been critical for monitoring sea level changes (see Section 12) and global climatic variations (Hwang *et al.*, 2004). Radar altimeters are also used to determine significant wave height and wind speed, and improve tide models (see Section 16). These applications have produced otherwise unattainable data describing the marine geoid, and the related sea floor topography (Vignudelli *et al.*, 2011; see Section 13.3.1). Other marine applications include identifying types of ice masses, monitoring sea/ice boundaries and modelling ice sheet elevation (Helm *et al.*, 2014; see Section 15). Locally, radar altimetry datasets have also been used to detect oil spills (see Section 19), and infer water circulation patterns (see Excursus 2.2 and Section 17).

9.6 Microwave Scatterometry

This non-imaging device measures the microwave scattering or reflective properties of surfaces and is specifically designed to measure backscattering. This requires that the sensor detect more detailed spectral information than acquired by imaging radar but with reduced spatial resolution and areal coverage. The surface is scanned in two or more directions, usually by multiple sensors using either a series of radar pulses or a continuous signal. The intensity, phase, and polarisation of the backscatter beam can be used to observe changes in the surface of waterbodies.

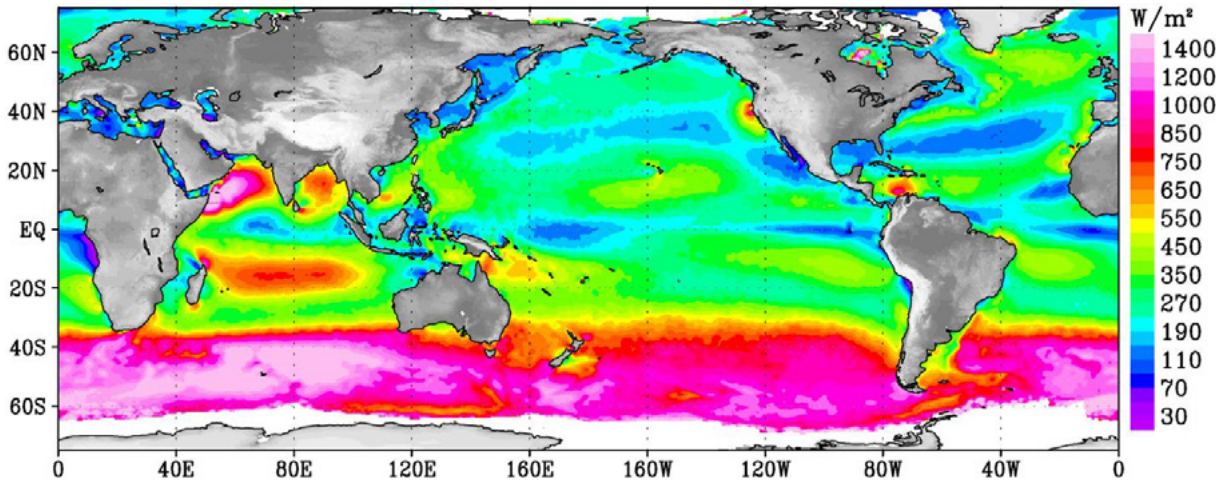
The primary application of microwave scatterometers is to measure wind vectors (that is, speed and direction) over the ocean surface (Barale *et al.*, 2010). This is based on the principle of ocean 'roughness' being caused by wind and resulting in a characteristic surface pattern that may be identified by its scattering properties (see Section 16.2.2). A mathematical model uses the reflectivity data with other sensor characteristics to determine wind speed and direction over the surface. Although radar scatterometers are non-imaging, their data may be used to construct global wind maps when collected over a sufficiently large area.

Spaceborne microwave scatterometers have been carried on several satellite missions, using varying viewing geometries (see Volume 1A—Section 16.1.2.3). Maps of near-surface wind speed and direction are being derived from global scatterometry datasets on a daily basis (Young *et al.*, 2020). These wind vectors provide essential inputs to marine weather and global climate models and are also used with other EO datasets to track severe storm activity and map seasonal trends (see Figure 9.9). Other scatterometry applications of relevance to surface waters include mapping the extent and condition of ice and snow (see Section 15.1).

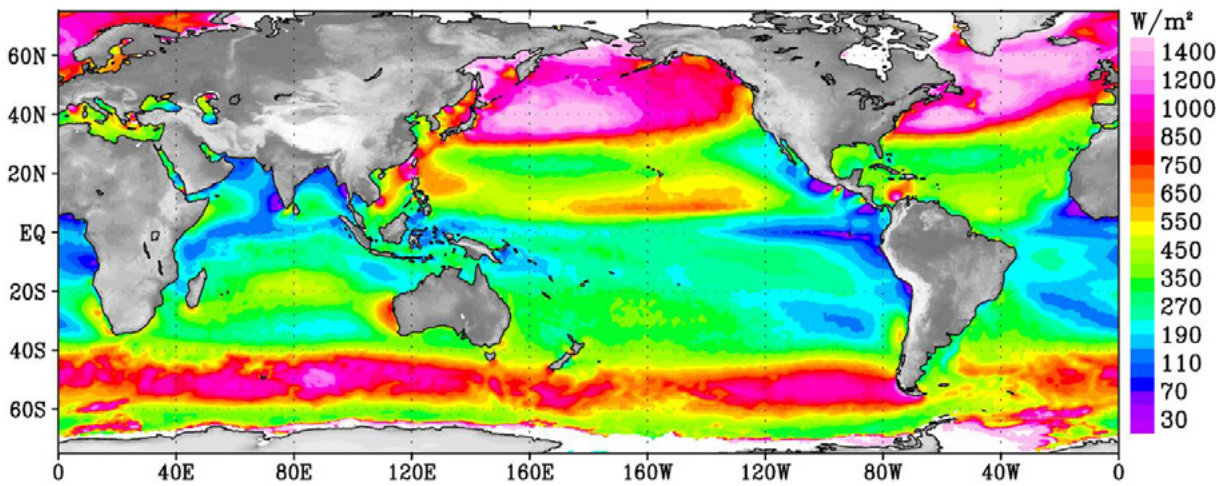
Figure 9.9 Global wind power

QuikScat data showing wind power density over the global oceans for two seasons.

a. Summer in the Northern Hemisphere



b. Winter in the Northern Hemisphere



Source: NASA. Retrieved from *https://winds.jpl.nasa.gov/gallery/quikscatdata/?ImageID=10*

9.7 Further Information

Richards (2009)

Ulaby and Long (2014)

ESA Earth Online: *https://earth.esa.int/eogateway*

ESA Radar Altimetry Tutorial and Toolbox: *http://www.altimetry.info/*

9.8 References

Barale, V., Gower, J.F.R., and Alberotanza, L. (2010). *Oceanography from Space: Revisited* (374 p). *http://dx.doi.org/10.1007/978-90-481-8681-5*

Brusch, S. Lehner, S., Fritz, T., Soccorsi, M., Soloview, A., and van Shie, B. (2011). Ship surveillance with TerraSAR-X. *IEEE Transactions on Geoscience and Remote Sensing*, 49(3), 1092–1103.

Ducet, N., Le Traon, P.Y., and Reverdin, G. (2000). Global high-resolution mapping of ocean circulation from the combination of TOPEX/Poseidon and ERS-1 and -2. *Journal of Geophysical Research*, 105(C8), 19477–19498.

Elachi, C., and van Zyl, J. (2006). *Introduction to the Physics and Techniques of Remote Sensing*, Second Edn. Wiley Interscience, New Jersey.

Ferraro, R.R., Smith, E.A., Berg, W., and Huffman, G.J. (1998). A Screening Methodology for Passive Microwave Precipitation Retrieval Algorithms. *Journal of Atmospheric Sciences*, 55(9), 1583–1600. *https://doi.org/10.1175/1520-0469(1998)055<1583:ASMFPM>2.0.CO;2*

Fu, L.-L., and Ubelmann, C. (2014). On the transition from profile altimeter to swath altimeter for observing global ocean surface topography. *Journal of Atmospheric and Oceanic Technology,* 31(2), 560–568.

Goldstein, R.M., and Zebker, H.A. (1987). Interferometric radar measurement of ocean surface currents. *Nature*, 328, 707–709.

Helm, V., Humbert, A., and Miller, H. (2014). Elevation and elevation change of Greenland and Antarctica derived from CryoSat-2. *Cryosphere*, 8(4), 1539–1559. *http://dx.doi.org/10.5194/tc-8-1539-2014*

Heron, S.F., Heron, M.L., and Pichel, W.G. (2013). Thermal and Radar Overview. Ch 11 in *Coral Reef Remote Sensing*. (Eds: Goodman, J.A., Purkis, S.J., and Phinn, S.R.). Springer, Dordrecht. ISBN 978-90-481-9291-5.

Hwang, C., Shum, C., and Li., J. (2004). *Satellite Altimetry for Geodesy, Geophysics and Oceanography*. Proceedings of: International Workshop on Satellite Altimetry. Berlin Heidelberg: Springer-Verlag.

Maged, M. (2020). *Automatic Detection Algorithms of Oil Spill in Radar Images*. CRC Press, Boca Raton, FL.

Richards, J. (2009). *Remote Sensing with Imaging Radar*. Springer, Heidelberg.

Richards, J. (2012). *Australia and SAR: A Road Map*. CRCSI, Melbourne.

Romeiser, R. (2013). The future of SAR-based oceanography: High-resolution current measurements by along-track interferometry. *Oceanography*, 26(2), 92–99. *https://doi.org/10.5670/oceanog.2013.37*.

Romeiser, R., Ufermann, S., and Kern, S. (2004). Status report on the remote sensing of current features by spacebourne synthetic aperture radar. Proceedings of *Second Workshop on Coastal and Marine Applications of SAR*. March 2003, European Space Agency, pp. 105–124 .

Suits, G.H. (1983). The Nature of Electromagnetic Radiation. Ch 2 in *Manual of Remote Sensing* (Ed: R.N. Colwell), pp. 27–60. ASPRS, Falls Church, Virginia.

Ulaby, F.T., and Long, D.G. (2014). *Microwave, Radar and Radiometric Remote Sensing*. The University of Michigan Press.

Ulloa, R.Z., Santiago, M.G.H., and Rueda, V.L.V. (2019). The interaction of microwaves with materials of different properties. Ch. 6 in *Electromagnetic Fields and Waves* (Ed: Yeap, K.H., and Hirasawa, K.). IntechOpen Ltd. doi:10.5772/intechopen.83675

Vignudelli, S., Kostianoy, A. G., Cipollini, P., and Benveniste, J. (2011*). Coastal Altimetry*. Springer-Verlag, Berlin Heidelberg.

Young, I.R., Kirezci, E., and Ribal, A. (2020). The global wind resource observed by scatterometer. *Remote Sensing*, 12, 2920. doi:10.3390/RS12182920



10 Acoustic EO

Since most of the Earth surface is underwater (see Section 1), extensive areas of the globe are not readily visible to optical sensors (see Section 8). In regions of deeper water, acoustic methods (based on detecting sound waves) can provide valuable information about the submerged surface, including the bathymetry, substrate, and benthos.

Vibrational waves, such as sound waves, are introduced in Volume 1A—Section 9. Vibrational waves are disturbances that transfer energy through different media. Sound is a form of energy that is propagated as longitudinal or compression waves where the particles move in the same plane as the wave (see Figure 10.1).

In a spherical wave, such as a sound wave, energy propagates equally in all directions. As such, the power (P) emitted by the source is distributed evenly over a spherical surface (area = $4\pi r^2$) and, assuming that there is no absorption in the medium, the intensity of the wave is given by the formulae:

$$intensity = \frac{P}{4\pi r^2}$$

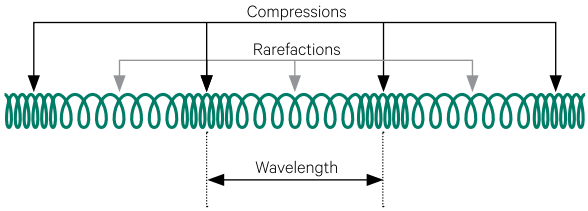
Thus, the intensity of a sound wave (measured as W/m^2) decreases with the square of the distance from the source, since the same amount of energy is being spread over an increasingly larger area. Like other waves, sound waves undergo reflection, refraction, and diffraction (see Section 8.1 and Volume 1A—Section 2.5.2). The reflection of sound waves off surfaces can produce reverberations and echoes. Diffraction occurs when the wavelength of a sound wave is larger than an object it encounters. However, if the wavelength is smaller than the object it tends to reflect off the object rather than diffract around it.

Unlike electromagnetic radiation (EMR), which travels at a constant speed through a medium, and for which frequency and wavelength definitions can be used interchangeably, the speed of sound waves varies considerably with the elastic properties of the medium through which the waves are travelling. In seawater, the speed of sound is a function of water density and compressibility, both of which are dependent on temperature, pressure, and salinity (see Figure 10.2):

- in deep ocean below 1500 m, the speed of sound is governed by pressure, so increases with water depth;
- in upper ocean waters at equatorial and temperate latitudes, there is greater variation in temperature and some variation in salinity, so the speed of sound is more variable, but tends to decrease with temperature; and
- minimum velocity occurs at the thermocline (see Section 5.1.3; Wells, 1986).

Figure 10.1 Longitudinal or compression waves

In a longitudinal wave, energy moves particles of the medium in the direction of wave propagation. This is comparable to pushing a slinky toy at one end, which causes the coils to compress and dilate as the energy moves to the other end.



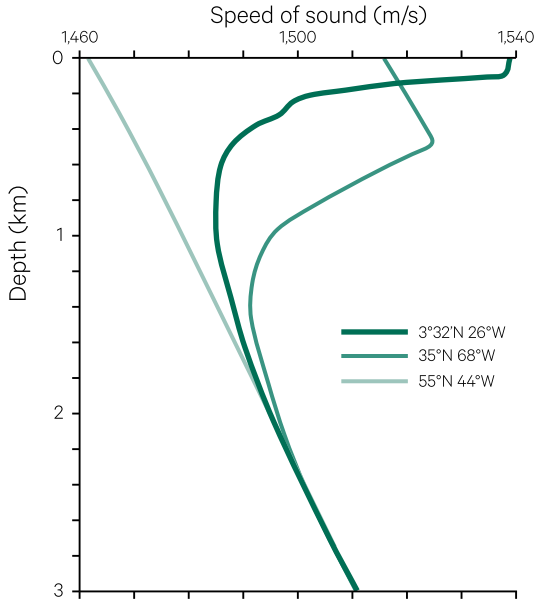
Background image: Multibeam sonar model of Money Shoal, located off the coast of the Northern Territory. This data comes from a marine survey funded by the Marine Biodiversity Hub where Geoscience Australia and the Australian Institute of Marine Science collaborated to map the ocean floor to better understand the biodiversity of the Arafura Marine Park. On this bathymetry image, we see the rich edge of the shoal itself. The top is very rugose highlighting the numerous coral reefs growing on it. This image also shows fields of pockmarks, and a small seafloor crater often created by expulsion of fluid from the subsurface, at the foot of the shoal on either end. The middle of the shoal could not be mapped by ship due to its very shallow nature. Satellite-Derived Bathymetry was later used to complete the mapping of the shoal. **Source:** Geoscience Australia

In ocean water the speed of sound is minimised at water depths in the range 750–1000 m. This zone of minimum speed is known as the Deep Sound Channel (DSC; formerly Sound Fixing and Ranging channel: SOFAR), and enables the guided propagation of undistorted sound for distances up to thousands of kilometres. This channel is commonly used for ocean acoustic tomography and submarine surveillance (DOSITS, 2021).

Light doesn't penetrate beneath the surface of the water, so ocean creatures like whales and dolphins and even 800 species of fish communicate by sound. And a North Atlantic right whale can transmit across hundreds of miles.
(Rose George)

Figure 10.2 Speed of sound varies with water depth

In seawater, the speed of sound is mostly governed by temperature and pressure. From the surface to 1000 m water depth, the effect of temperature dominates. At water depths greater than 1000 m, the effect of pressure is more dominant.



Adapted from: Wells (1986) Figure 2.4

10.1 Acoustic EO Framework

Since sound waves are strongly reflected by the water surface, both active and passive acoustic sensors need to be in contact with the water (Churnside, 2013). Echosounding involves the use of active sonar (SOund NAvigation and Radar) sensors, which transmit short sound pulses (or 'pings') towards the seafloor and measure various characteristics of its echo (reflected sound), including time and strength. While the time between sending the signal and receiving its acoustic return provides a measurement of waterbody depth, or bathymetry data, the strength of the returning signal provides a measurement of seafloor reflectivity. Bathymetric measurements based on sonar echoes have been used to map seafloor topography since the early 1920s (Dierssen and Theberge, 2014).

The proportion of acoustic energy reflected back from the seabed is determined by the impedance contrast (or 'hardness') and the apparent roughness (relative to the acoustic wavelength) of the reflecting surface. In practical terms, the intensity or strength of the return signal, or backscatter intensity, is related to:

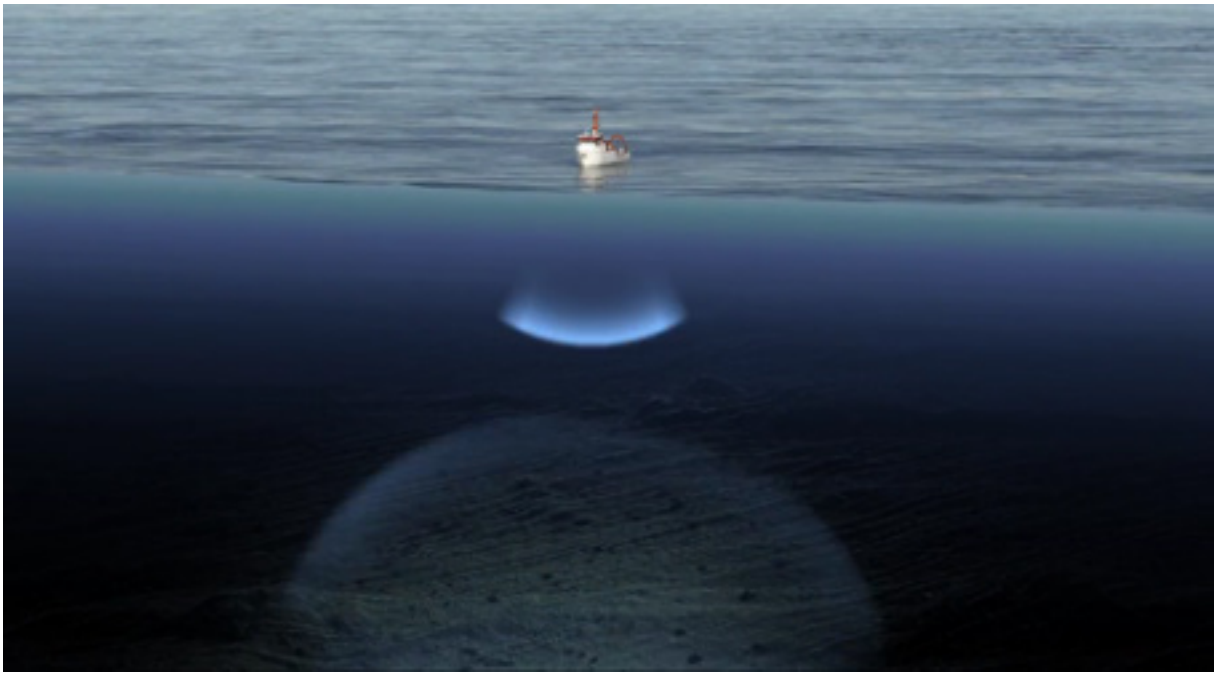
- the heterogenity of the seabed material—sizes of sediment grains, bioturbation, and geological layering; and
- the surface roughness—such as seabed substrate, microtopography, and landforms (Lamarche and Lurton, 2018).

In general, since softer materials absorb some of the sound energy, backscatter intensity increases with surface roughness or hardness. Thus, backscatter information can be used to determine bottom type and differentiate between different types of seafloor, such as hard rock or soft sediment, and, by association, benthic habitat and biodiversity (Lamarche *et al*., 2016).

While sonar-based bathymetric measurements relying on timing of echoes are relatively simple in terms of acoustic physics, backscatter measurements involve consideration of more complex acoustic and geophysical processes in both the water and the seabed (Lamarche and Lurton, 2018). Seabed backscatter is defined as the amount of acoustic energy being received by the sonar after a complex interaction with the seabed. This is measured as the surface scattering coefficient, a dimensionless quantity that accounts for the intensity (power) ratio of the incident and scattered waves, determined per unit area at a reference distance of 1 m. When expressed in decibels (dB), this quantity is commonly called the backscatter strength (Lurton, 2010). The intensity of the backscatter received by the sonar depends on the transmitted source level, transmission loss (absorption in the water column and geometrical spreading), and target strength.

Figure 10.3 Hull-mounted sonar system

The sonar system mounted on the hull of a vessel sends out sound waves that bounce off the seafloor and return to the ship.



Source: Geoscience Australia

Echosounders use different sound frequencies depending on the application they are used for, the water depth being targeted, and data resolution required. For example:

- measurement of water depth employs frequencies ranging from around 12 kHz to 400 kHz;
- detection of sediment layers below the seafloor uses lower frequencies (generally < 3.5 kHz); and
- identification of pelagic organisms uses higher frequencies (200 kHz; DOSITS, 2021).

Considering that frequency is positively correlated with energy dissipation, higher frequencies (> 200 kHz) are used to map the seafloor in shallow water (< 400 m), and lower frequencies (< 30 kHz) are generally used for deep water (> 2000 m). Frequency also influences data resolution, as does water depth. While frequency mainly controls vertical resolution (for example, better definition of subsurface sediment layers or more precise seafloor depth detection), water depth controls horizontal resolution. In the case of multibeam echosounders (MBES), this is due to the geometry of the sonar beam (a cone) and the sonar swath, which grows with water depth, so is reflected by a wider footprint at the seafloor (see Figure 10.3).

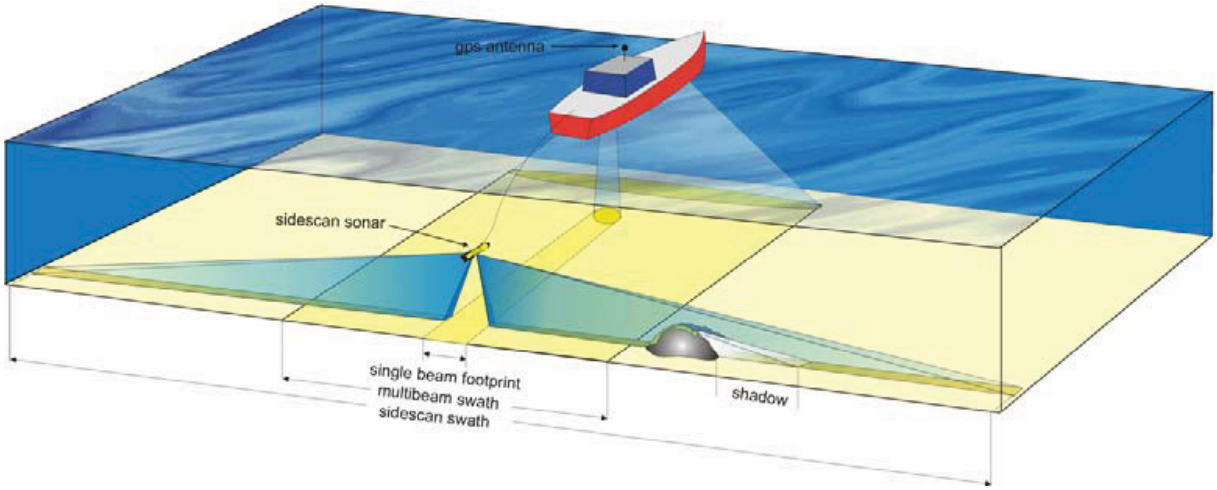
10.2 Echosounders

Echosounders can be grouped in terms of:

- profiling sensors—single beam echosounders that record individual waterbody depth transects or profile lines (see Section 10.2.1); and
- swath sounding systems—use an array of transducers to measure waterbody depth for a strip of the seafloor that is perpendicular to the platform's motion, then combines a sequence of profile lines into a swath:
  - interferometric (also known as bathymetric sidescan; see Section 10.2.2); and
  - beamforming (multibeam echosounders; see Section 10.2.3).

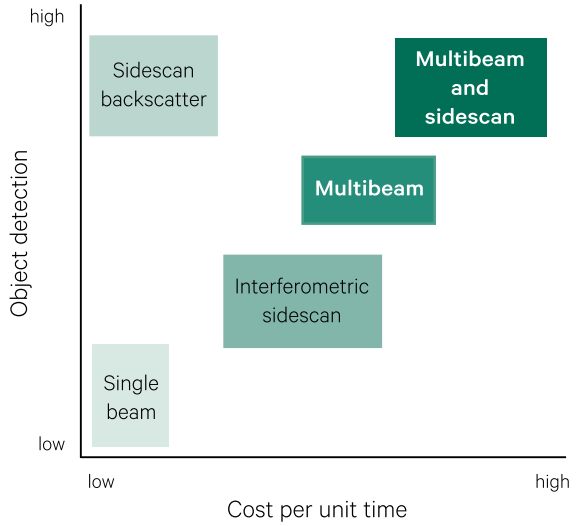
The scanning operations of these three acoustic sensors are illustrated in Figure 10.4. Their ability to detect objects is contrasted with their operating cost in Figure 10.5. Some echosounders operate as dual beam by emitting high frequency and low frequency pulses simultaneously.

Figure 10.4 Beam patterns of sonar systems



Source: Penrose *et al.* (2005) Figure 4.1

Figure 10.5 Comparison of sonar systems



Adapted from: Penrose *et al.* (2005) Figure 8.1

10.2.1 Single beam echosounders

Depth sounders or single beam echosounders (SBES) measure the travel time of a short, directional sonar pulse to determine waterbody depth below the survey vessel (see Figure 10.4). As the vessel moves along the water surface, repeated sonar signals are transmitted and received to record a line of waterbody depths below it.

Profiling SBES emit a narrow, conically-shaped beam to generate a single quantitative measurement for each pulse. Imaging SBES use a fan-shaped acoustic beam to scan large areas of the seafloor, mostly for visual interpretation. This traditional form of sonar has been used for more than five decades, but has known limitations in terms of accuracy and repeatibility. Vessel movement make it difficult to ensure a precise beam orientation and spatial coverage is limited.

SBES have also been adapted to image and characterise the subsurface. They are known as sub-bottom profiling systems. Acoustic energy is reflected at the boundary of materials with differing densities, or acoustic impedance. Since the strength of the reflection varies with the impedance contrast of the materials, different acoustic returns are generated from each boundary, the first boundary being the seafloor. These systems produce an acoustic pulse with set frequency, power, and duration, then record the signals reflected both from the substrate and any underlying sedimentary layers. Although the sonar penetration depth and vertical resolution of sub-bottom profilers can vary with substrate hardness, presence of gas deposits, waterbody depth, and sensor design, these systems can deliver valuable information about benthic habitats (Penrose *et al.*, 2005).

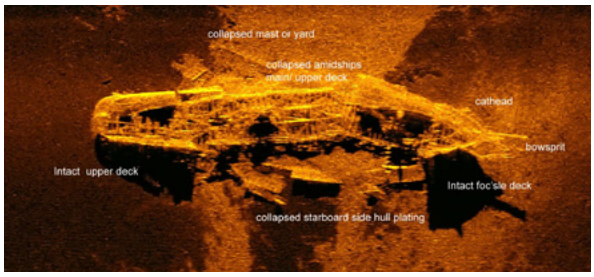
10.2.2 Sidescan sonar

Sidescan sonar (SSS) are imaging SBES that emit one broad beam across a wide angle perpendicular to the path of the platform, and record the intensity or strength of the return signal (also known as backscatter; see Section 10.1 and Figure 10.4). The intensity of consecutive cross-track slices can then be mosaicked to form an image. Traditional SSS do not directly measure waterbody depth, but this can be inferred from the image for specific objects. These images are primarily used for visual detection and recognition of objects (Monahan, 2008). In decreasing importance, the return intensity in sidescan sonars is impacted by sonar frequency, geometry between transducer and target, surface texture, and surface composition and density (Penrose *et al.*, 2005).

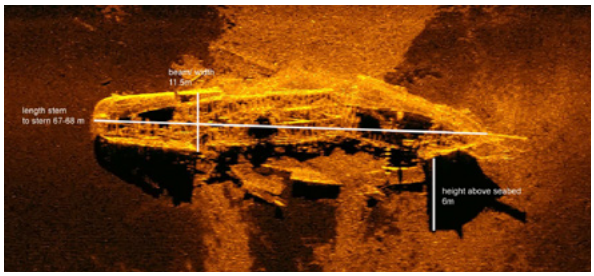
Figure 10.6 Sidescan sonar image of shipwreck

This 19th century merchant vessel (labelled IOS-002) was one of two shipwrecks located on the seafloor of the Indian Ocean during the search for MH370 in December 2015. The vessel was identified as an iron, two-decked sailing ship, with overall length ~75 m and weight 1000–1500 tons, which was probably being used to carry coal from the UK to Australasia (Anderson, 2018).

a. Key features



b. Dimensions



Source: Anderson (2018) Figures 31 and 36. Image source: Fugro/ATSB/WA Museum.

Sidescan systems provide high resolution data with rapid coverage. As a result, they are used for discriminating small features, although their side-looking perspective detects shadows behind objects that protrude from the seafloor (see Figure 10.6). These sidescan datasets can be used to:

- delineate naturally occurring and man-made seafloor features (reefs, sand waves, rocky outcrops, submarine infrastructures, wrecks, pipelines);
- assess environmental issues for marine geology resource management, including the location of ore and aggregate deposits;
- target areas of development suitability (such as the feasibility of undersea cable placement), where identification of seafloor type and geohazards may have considerable impact on the development;
- establish baseline data to support environmental monitoring and habitat mapping;
- detect mines; and
- estimate size of shipwrecks.

Interferometric sidescan sonar (ISSS; also known as Phase Differencing Bathymetric Sonar: PDBS, or bathymetric sidescan) exploit the interference patterns from SSS to model the angle of the echo's return path (Sewada *et al.*, 2018). These systems comprise two (or more) parallel arrays of transducers (or staves), separated by a prescribed distance. By assuming that the arrays receive identical echoes from a given target, the measured time delay (or the phase lag of the two echoes) can be used to determine the incident angle of the acoustic return (Nishimura, 1997). These measurements are then modelled to derive the three-dimensional positions of the sounding points (Kolough, 1984). Compared with MBES, ISSS enable greater coverage of the seafloor, but with reduced accuracy.

10.2.3 Multibeam echosounders

Multibeam echosounders (MBES; also known as multibeam sonar systems) are viewed as the most advanced type of acoustic sensor for observing the seafloor. With high spatial resolution and accuracy, MBES concurrently generate:

- a bathymetry map—indicating seafloor depth and complexity; and
- a backscatter image—indicating surface hardness.

These products can be analysed together to derive an accurate seafloor classification. Generally, the MBES transducer is mounted rigidly to the hull of the survey vessel and its position can be calculated very accurately. However, on a small embarcation, the MBES can be mounted on poles which hang on the side of the ship or at the bow. Other parts of the multibeam system include auxilliary sensors to ensure accurate positioning, motion sensing, and sound speed measurement.

Table 10.1 MBES footprint

The beam footprint for MBES at nadir (m) are given below for selected pairs of beam width and water depth. The MBES footprint increases in outer (off-nadir) beams.

Water depth (m)	Beam width (degrees)					
	0.5	0.7	1	2	3	4
10	0.09	0.12	0.17	0.35	0.52	0.70
25	0.22	0.31	0.44	0.87	1.31	1.74
50	0.44	0.61	0.87	1.74	2.62	3.49
75	0.65	0.92	1.31	2.62	3.92	5.23
100	0.87	1.22	1.75	3.49	5.23	6.97
250	2.18	3.03	4.36	8.72	13.08	
500	4.36	6.11	8.73	17.45		
1000	8.73	12.22	17.45			
1500	13.09	18.33				
2500	21.82					

Source: Picard *et al.* (2020) Table 7

MBES use an array of sonar projectors or transducers pointing in different directions on either side of the platform. Each transducer ensonifies at slightly different times so that all echoes are returned simultaneously as a single strong pulse. Beamforming (a signal processing technique) is then used to derive individual bearings. This results in a beam pattern known as swath that is:

- wide in the across-track direction, which means it covers the area immediately under the vessel and on either side of the vessel; and
- narrow along-track, which means it does not cover the area in front or behind the vessel (see Figure 10.4 and Figure 10.7).

Since the beam footprint is a function of beam width and depth, water depth dictates acoustic data resolution and survey efficiency for MBES (see Table 10.1).

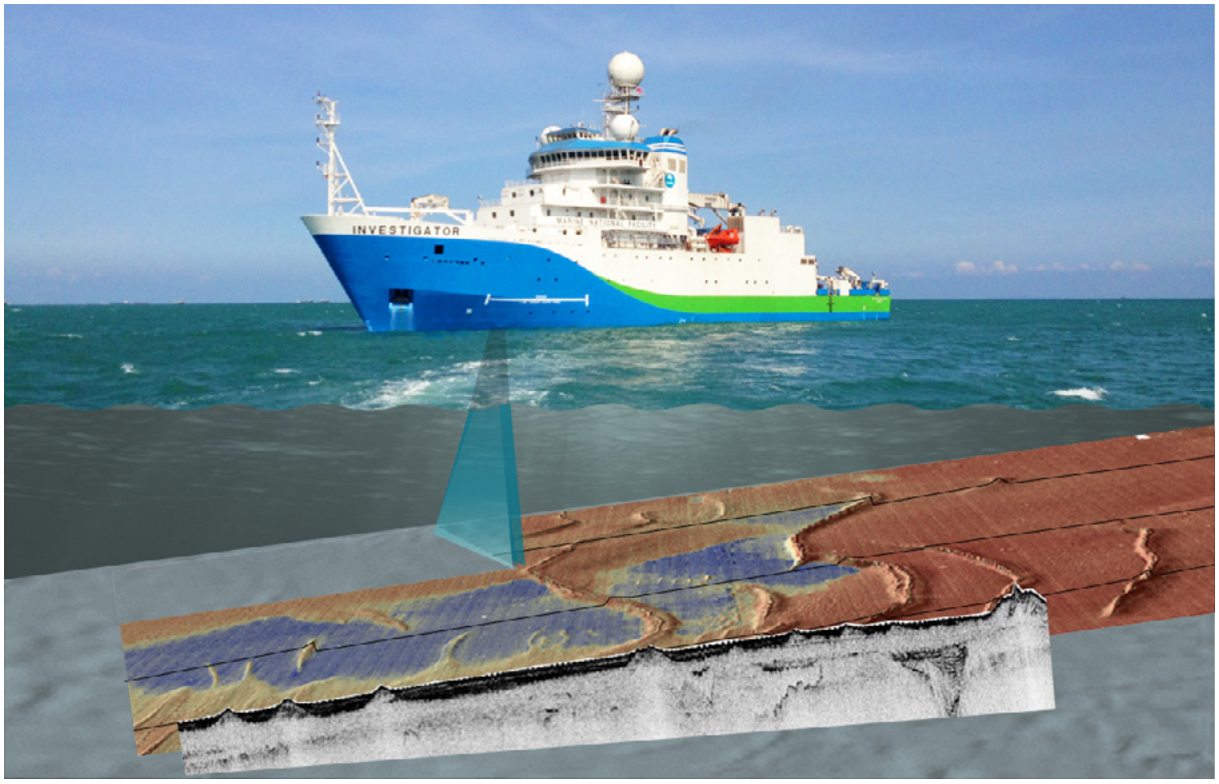
MBES systems generally offer two types of seabed backscatter data, namely:

- 'one-per-beam' backscatter (either beam average or maximum intensity); and
- 'time series' backscatter, similar to sidescan technology (Lamarche and Lurton, 2018).

Recent MBES can also record water column backscatter, resulting from the sonar time series for each beam. Water column data can be used for direct mapping of fish and marine mammals (see Figure 20.15), the mapping of plumes and vents, the location of mid-water targets, and a wide range of physical oceanographic processes (Picard *et al.*, 2020).

Figure 10.7 Multibeam mapping

In this image we see a combination of outputs from multibeam mapping, that is, depth overlaid by backscatter information. In general, red indicates a 'harder' seabed and blue softer. This softness can be witness to the third element of information shown, namely a sub-bottom profile, which provides a cross-section of the seabed subsurface. In this case, the dark layers between the bedforms represent the 'soft' or muddy material accumulated between the hardened and relict bedforms.



Source: Kim Picard, GA

10.3 Acoustic Surveys and Platforms

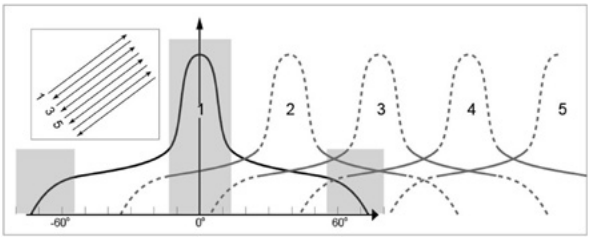
Whether the purpose of a marine survey is to identify, delineate, or map biogenic, anthropogenic, or geological features, or produce a navigation chart, survey planning is essential for maximising the value of each survey and delivering consistent datasets that can be integrated and shared quantitatively. Standard procedures for calibration, acquisition, processing, validation, and reporting have been (or are being) developed for MBES nationally and globally (Lamarche and Lurton, 2018; Picard *et al.*, 2020) and other aspects of marine survey (IHO, 2019; Przeslawski and Foster, 2018).

Specific planning tools that are available for MBES surveys in Australia are detailed in Picard *et al.* (2020), including access to national bathymetric holdings as listed in Section 10.5. Picard *et al.* (2020) distinguish between:

- baseline, or exploratory, surveys—which map the distribution of defined marine feature(s) at a particular scale and acquire information needed for more focused surveys; versus
- monitorings surveys—which acquire higher resolution data for specific features at relevant revisit intervals, with greater positional accuracy.

Figure 10.8 Swath overlap for backscatter data

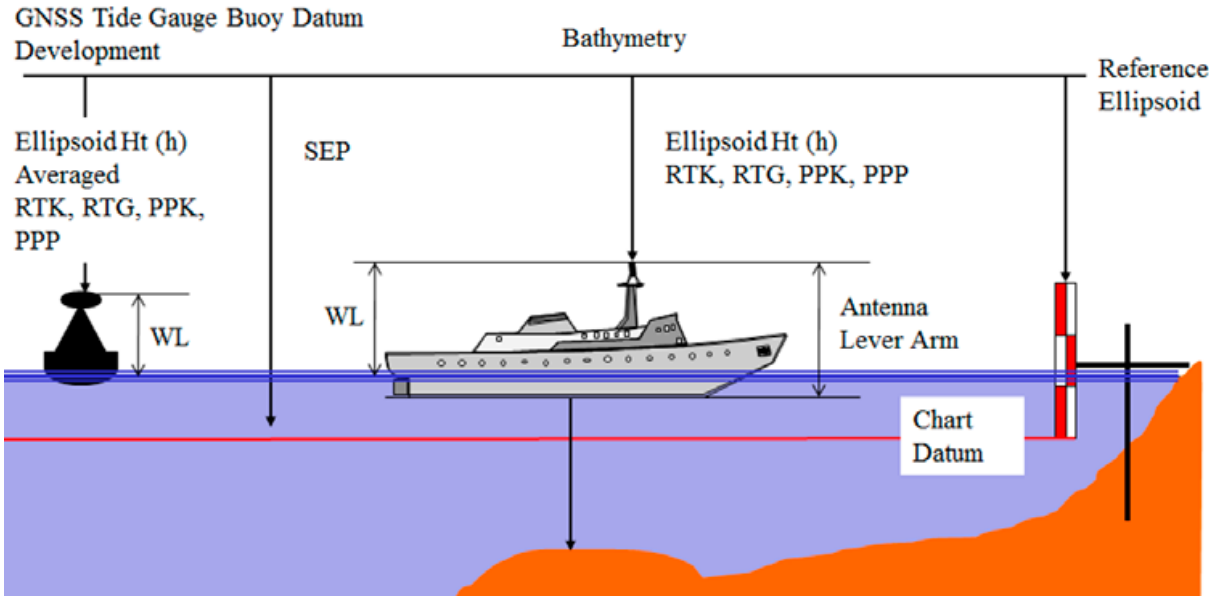
Backscatter data quality is greatest for intermediate incidence angles (shown as unshaded regions below) and reduced near the edges of a swath and near the centre of the swath (shown as shaded regions).



Source: Lamarche and Lurton (2018) Figure 4

Figure 10.9 Relationship between reference ellipsoid, antenna, water line, and chart datum

The most common datums used for seafloor mapping surveys are the ellipsoidal or tidal datum. WL: Water line; RTK: Real Time Kinematic (fixed or float solution); RTG: Real Time GIPSY (real time PPP); PPK: Post Processed Kinematic (fixed or float solution); PPP: Precise Point Positioning; SEP: separation model for datum-to-ellipsoid relationship



Source: Mills and Dodd (2014) Figure 2

All acoustic surveys require careful planning to ensure that survey lines provide optimal coverage of the seabed for a given area or sampling frame (Foster *et al*., 2018). Ideally, survey planning ensures that each survey line is parallel to the seabed contour direction, spaced appropriately to accommodate waterbody depth and swath width, and overlaps adjacent lines by at least 30% (Picard *et al*., 2020). Overlapping survey lines increase confidence in the data's accuracy and help address any gaps in the data caused by factors such as bad weather. Since the quality of backscatter data is lower near the edges of swaths, and also in the centre due to specular reflection (see Figure 10.8), to avoid using this data requires considerable overlap of swaths (Lamarche and Lurton, 2018). Crosslines or checklines running perpendicular to the main survey lines are also recommended to determine the quality of soundings before survey lines are acquired.

Sonar systems can be towed by a vessel in a 'towfish' container, or mounted on the hull of a manned vessel or on the body of an Autonomous Underwater Vehicle (AUV; see Excursus 5.1). A towed sensor has the advantage of accessing greater waterbody depths but the disadvantage of being more susceptible to rough sea conditions. For mounted systems, the attitude of the platform (in terms of pitch, roll, and yaw—see Volume 2B—Section 2) needs to be carefully tracked to avoid distortions in the resulting acoustic data. The positional instability of most platforms used for underwater sensing necessitates accurate referencing to official ellipsoidal or tidal datums (see Figure 10.9 and Volume 1A—Section 3).

10.4 Acoustic Data Processing

The quality of acoustic data is impacted by various ambient factors during acquisition. For example, platform speed directly impacts sounding density and echo quality, and water column aeration (determined by sea state and survey direction and speed relative to wave action) diminishes the quality and strength of the echo. Longer acoustic pulses increase signal penetration through the water column but reduce vertical resolution (Picard *et al*., 2020).

Specific calibration procedures for MBES are provided by Picard *et al*. (2020) and for seafloor backscatter by Lamarche and Lurton (2018). When processing multibeam bathymetry data, corrections need to be made to allow for factors such as water salinity, sea temperature, and ocean depth, as these affect how quickly sonar signals travel through the water. To calibrate acoustic readings relative to the characteristics of the water column, requires sound velocity profiling (SVP). This measures the speed of sound in water at different vertical levels in the water column for defined frequencies at specific locations in a sampling frame (Lucieer *et al*., 2018). SVP accounts for variations in the temperature and salinity profile of a water column and impacts both the accuracy and uncertainty of each sounding position, horizontally and vertically, especially nearer the edges of each swath (Picard *et al*., 2020).

Thus, all acoustic soundings require processing before they can be used in the form of a raster dataset. Processing includes a set of corrections from all auxillary systems, including ship motion, navigation, sound velocity, and vertical datum. Once these corrections have been applied, it is possible to apply filters to remove outliers and, for bathymetry data, to proceed to creating a surface or digital elevation model (DEM).

Table 10.2 Examples of sounding accuracy and TPU

In this example, TPU (total propagated uncertainty) is computed to 1σ using the Combined Uncertainty Bathymetric Estimator (CUBE).

Depth band (m)	0–5	5–20	20–50	50–100	100–200
Position accuracy					
IHO Standard	5.25	5.50	6.00	6.50	7.25
TPU Estimate	0.27	0.27	0.30	0.34	0.42
Depth accuracy					
IHO Standard	0.38	0.39	0.44	0.50	0.63
TPU Estimate	0.27	0.27	0.28	0.31	0.35

Source: Picard *et al*. (2020) Table 10

The horizontal spatial resolution of acoustic data is determined by the distance between pings along the survey track (which in turn is a function of the platform travel speed and the pulse repetition frequency, PRF; Lucieer *et al.*, 2018). The total propagated uncertainty (TPU) quantifies the survey quality by considering all potential sources of horizontal and vertical error for each measurement (Hare *et al.*, 1995). Sounding measurements, their metadata, and sonar calibration data, are used to estimate TPU, which enables outliers to be identified and removed, and an overall uncertainty surface to be generated for the survey (Lucieer *et al.*, 2018). Examples of IHO accuracy standards and TPU are given in Table 10.2.

10.5 Further Information

International Hydrographic Organisation (IHO)

https://iho.int

AusSeabed

http://www.ausseabed.gov.au/

Visualisations of Seafloor Terrain

Geoscience Australia produces 3D animations and other visualisation products, allowing viewers to 'fly through' the seafloor terrain:

Bathymetry of the Australian Margin: *https://www.ga.gov.au/about/projects/marine/northern-australia-bathymetry*

Bathymetry of Casey Station, Australian Antarctic Region: *https://www.youtube.com/watch?v=ywr6vAC7x1Y*

Bathymetry of Gifford Guyot (2019); *https://atlas.parksaustralia.gov.au/amps?featureId=AMP_TE_GIF*

Bathymetry of the MH370 Search Area: *https://www.youtube.com/watch?v=EDCYGOpNhLI*

Bathymetry of the Western Margins Of Western Australia: *https://www.youtube.com/watch?v=9-3dl8prWRc*

Sonar

DOSITS (2021)

General Bathymetric Chart of the Oceans (GEBCO)

https://www.gebco.net

Archive of seafloor charts: *https://www.gebco.net/data_and_products/historical_gebco_charts/*

International Association of Oil and Gas Producers (IOGP)

Seabed Survey Data Model: *https://www.iogp.org/Geomatics/*

MBES

https://www.hydro-international.com/content/article/state-of-the-art-in-multibeam-echosounders

NOAA

Introduction to Sonar and Multibeam Mapping: *https://oceanexplorer.noaa.gov/okeanos/edu/collection/media/hdwe-MMBkgnd.pdf*

Office of Coast Survey Hydrographic Survey Equipment: *https://nauticalcharts.noaa.gov/learn/hydrographic-survey-equipment.html*

10.6 References

Anderson, R. (2018). *Maritime archaeological analysis of two historic shipwrecks located during the MH370 aircraft search*. Report No. 322, Department of Maritime Archaeology Western Australian Museum.

Churnside, J.H. (2013). Review of profiling oceanographic lidar. *Optical Engineering*, 53(5), 051405. *https://doi.org/10.1117/1.OE.53.5.051405*

Dierssen, H.M., and Theberge, A.E. (2014). Bathymetry: History of Seafloor Mapping. In *Encyclopedia of Natural Resources*, Taylor and Francis. doi:10.1081/E-ENRW-120047531

DOSITS (2021). *Discovery of Sound in the Sea* website, University of Rhode Island: *https://dosits.org/*

Foster, S.D., Monk, J., Lawrence, E., Hayes, K.R., Hosack, G.R., and Przeslawski, R. (2018). Statistical considerations for monitoring and sampling. In *Field Manuals for Marine Sampling to Monitor Australian Waters*, (Eds: Przeslawski, R., Foster, S.). National Environmental Science Programme (NESP). pp 23–41.

Hare, R.M. (1995). Depth and position error budgets for multi-beam echosounding. International Hydrographic Review, 72(1), 35.

IHO (2019). *IHO Standards for Hydrographic Surveys*. 6th edn. International Hydrographic Organisation, Monaco. *https://iho.int/uploads/user/pubs/Drafts/S-44_Edition_6_draft_1_7_1.pdf*

Kolough, D. (1984). Interferometric Side-Scan Sonar A Topographic Sea-Floor Mapping System. International *Hydrographic Review*, 56(2), 35–49.

Lamarche, G., Orpin, A., Mitchell, J., and Pallentin, A. (2016). Benthic habitat mapping. Ch 5 in *Biological sampling in the deep sea*. (Eds: Clark, M.R., Consalvey, M., Rowden, A.A.). Wiley-Blackwell, Hoboken. pp 80–102.

Lamarche G., and Lurton X. (2018). Recommendations for improved and coherent acquisition and processing of backscatter data from seafloor-mapping sonars. *Marine Geophysical Research*, 39, 5–22. doi:10.1007/s11001-017-9315-6. *https://link.springer.com/article/10.1007/s11001-017-9315-6*

Lucieer, V., Picard, K., Siwabessy, J., Jordan, A., Tran, M., and Monk, J. (2018). Seafloor mapping field manual for multibeam sonar. In *Field Manuals for Marine Sampling to Monitor Australian Waters* (Eds: Przeslawski, R., and Foster, S.). National Environmental Science Programme (NESP). pp 42–64.

Lurton, X. (2010). *An introduction to underwater acoustics. Principles and applications*. 2nd edn. Springer Praxis Books, Oxford. ISBN 978 3 540 78480 7

Mills, J., and Dodd, D. (2014). *Ellipsoidally Referenced Surveying for Hydrography*, FIG. Publication No. 62, FIG Commission 4. *http://www.fig.net/resources/publications/figpub/pub62/figpub62.asp*

Monahan, D. (2008). Bathymetry. In *Encyclopedia of Ocean Sciences* 2nd edn (Eds: J.H. Steele, S. Thorpe, and K. Turekian). Elsevier. pp 297–304.

Nishimura, C.E. (1997). *Fundamentals of Acoustic Backscatter Imagery*. Naval Research Laboratory, NRL/FR/7420–97-9848, Washington. *https://apps.dtic.mil/dtic/tr/fulltext/u2/a333800.pdf*

Penrose, J.D., Siwabessy, P.J.W., Gavrilov, A., Parnum, I., Hamilton, L.J., Bickers, A., Brooke, B., Ryan, D.A., and Kennedy, P. (2005). *Acoustic Techniques for Seabed Classification*. Technical Report 32, CRC for Coastal Zone Estuary and Waterway Management.

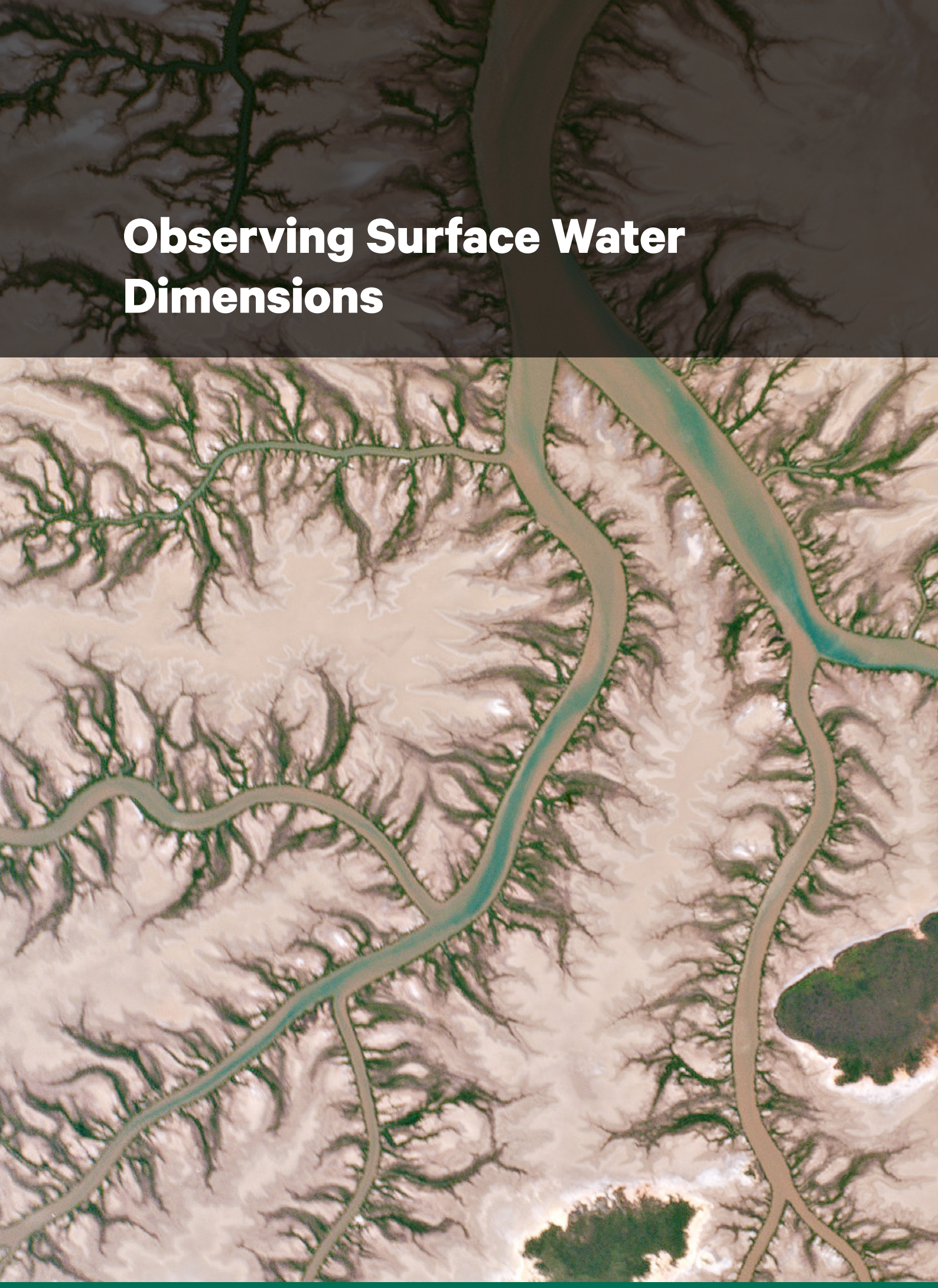
Picard, K., Leplastrier, A., Austine, K., Bergersen, N., Cullen, R., Dando, N., Donohue, D., Edwards, S., Ingleton, T., Jordan, A., Lucieer, V., Parnum, I., Siwabessy, J., Spinoccia, M., Talbot-Smith, R., Waterson, C., Barrett, N., Beaman, R., Bergersen, D., Boyd, M., Brace, B., Brooke, B., Cantrill, O., Case, M., Dunne, S., Fellows, M., Harris, U., Ierodiaconou, D., Johnstone, E., Kennedy, P., Leplastrier, A., Lewis, A., Lytton, S., Mackay, K., McLennan, S., Mitchell, C., Nichol, S., Post, A., Price, A., Przeslawski, R., Pugsley, L., Quadros, N., Smith, J., Stewart, W., Sullivan J., Tran, M., and Whiteway, T. (2020). *Australian Multibeam Guidelines 2020*. Version 2.0. Record 2018/19. Geoscience Australia, Canberra. *http://dx.doi.org/10.11636/Record.2018.019*

Przeslawski, R., and Foster, S. (Eds). (2018). *Field Manuals for Marine Sampling to Monitor Australian Waters, Version 1*. Report to the National Environmental Science Programme, Marine Biodiversity Hub. 212 p. *http://dx.doi.org/10.11636/9781925297669*

Sewada, J.S., Ioana, C., Geen, M., and Jerome Mars, J. (2018). Wideband signals for Phase Differencing Sonar Systems. *OCEANS'18 MTS/IEEE*, May 2018, Kobe, Japan. Hal-01982962

Wells, N. (1986). *The Atmosphere and Ocean. A Physical Introduction*. Taylor and Francis, London.

Observing Surface Water Dimensions



The following three sections detail EO-based analyses that can be used to map and monitor the dimensions of surface waters:

- extent—presents ways to use EO data to map and monitor water extent, including delineating shorelines, monitoring floods, and differentiating permanent and ephemeral waterbodies (see Section 11);
- level—describes EO approaches to measuring and monitoring sea level (see Section 12); and
- bathymetry—discusses EO approaches to mapping waterbody depth and geomorphology in coastal and ocean regions (see Section 13).

Contents

11 Extent 181

12 Level 197

13 Bathymetry 223

Background image on previous page: This image of mangroves bordering tidal flats near the Keep River inlet, Queensland, was acquired on 15 March 2015. **Source:** Planet Labs Inc. (CC BY SA 4.0). Retrieved from *https://www.planet.com/gallery/#!/post/keep-river-mangroves*



11 Extent

Norman Mueller

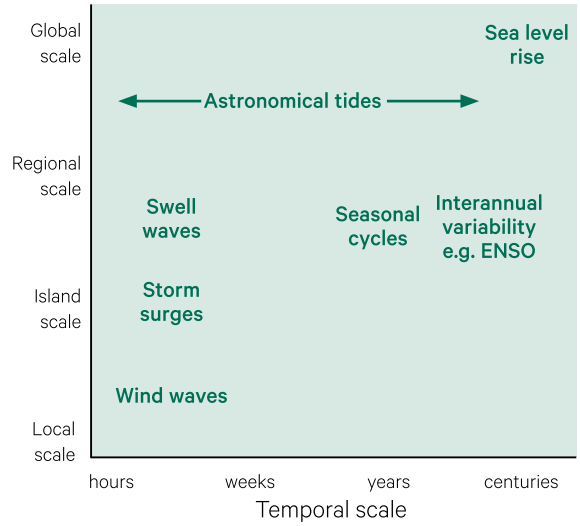
One of the most readily discernable changes in a waterbody is its extent, which is closely tied to the prevailing meteorological conditions (see Section 7.2). The extent of inland waterbodies impacts nearby human residents and other biota, with both expansion during floods and contraction during drought conditions resulting in changes in water availability and amenity. In coastal areas, floods and storms can dramatically disrupt settlements, services, and aquatic ecosystems.

A number of scales come into play when observing changes in the extent of global surface waters. As illustrated in Figure 11.1, localised water disturbances, such as wind waves, occur at one extreme of spatial and temporal scales, and changes to sea level occur at the other extreme. Nonetheless, EO datasets have proved to be invaluable for monitoring these changes, and differentiating cyclic patterns from longer term variations.

After an overview of the coverage and topographic characteristics of Australian waters (see Section 11.1) and a summary of suitable EO sensors for delineating water extent (see Section 11.2), the use of EO datasets are described in terms of:

- delineating shorelines (see Section 11.3);
- mapping and monitoring floods (see Section 11.4); and
- differentiating permanent and temporary inland waterbodies (see Section 11.5).

Figure 11.1 Scales of observing ocean changes



Adapted from: CSIRO (2018)

Background image: Astronaut photograph of flooding in Brisbane, Queensland, taken from the International Space Station on 13 January 2011, when around 20,000 homes were inundated. Brown, sediment-laden floodwaters contrast with rooftops and vegetation, with low-lying suburbs in the northwest being significantly impacted. Source: NASA Earth Observatory ISS026-E-17421. Retrieved from *https://earthobservatory.nasa.gov/images/48625/flooding-in-brisbane-suburbs*

Recommended Chapter Citation: Mueller, N. (2021). Extent. Ch 11 in *Earth Observation: Data, Processing and Applications. Volume 3B—Surface Waters.* CRCSI, Melbourne. pp. 181–195. ISBN 978-0-6482278-5-4

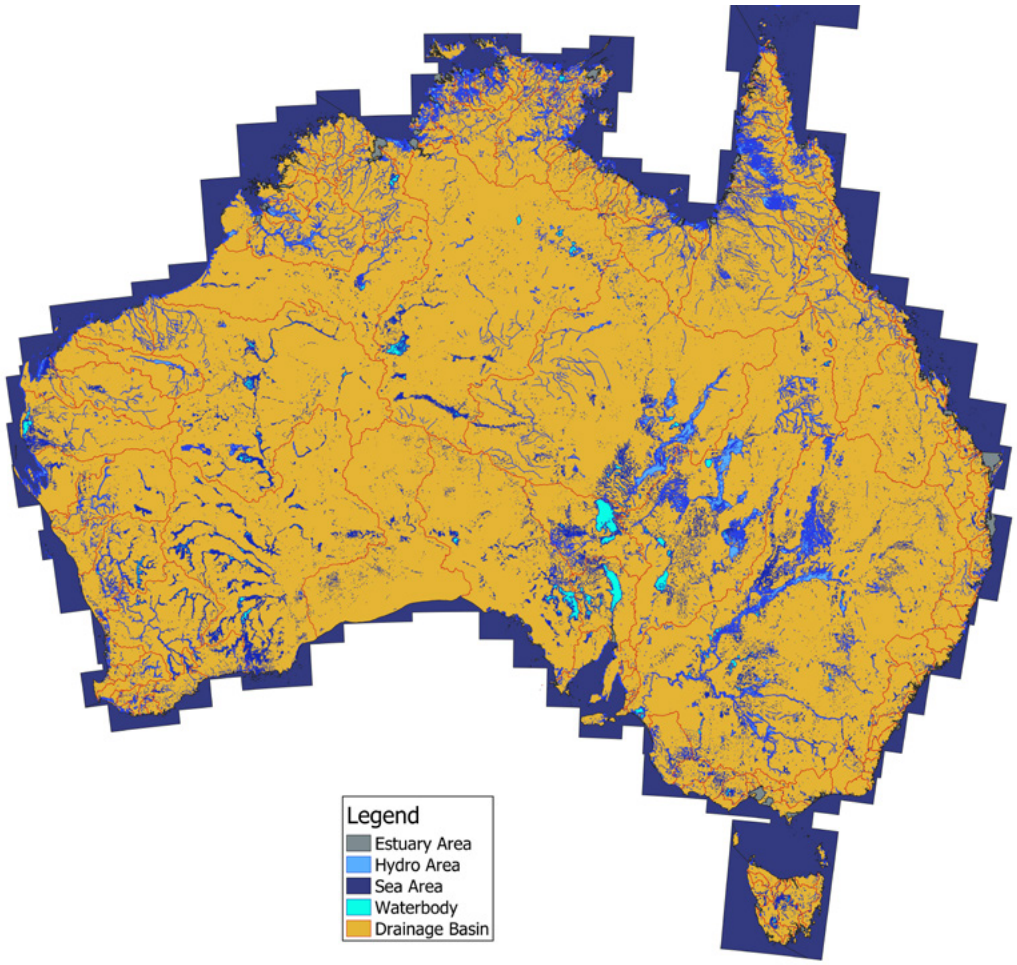
11.1 Extent of Australian Surface Waters

The extent of Australia's vast marine jurisdiction is detailed in Section 2.1. Its inland waterbodies, however, are limited in terms of their abundance, capacity, and permanence.

Australia is the driest continent in the world (see Volume 3A), apart from Antarctica (see Section 2.5). Approximately 35% of the continent is desert, and 70% of the mainland receives less than 500 mm of rainfall per year (GA, 2019). Approximately 12% of rainfall reaches Australia's rivers. By comparison, in Europe 39% of rainfall reaches rivers, and in North America 52% reaches rivers (Parliament of Australia, 2013). Inland surface water is relatively scarce, and Australia is dominated by ephemeral waterbodies, fed by monsoonal summers in the north, and winter rainfall in the south. In contrast to Europe, Australian rivers frequently lack defined channels, are often formed by 'chains of ponds', can cease to flow for long periods, and can experience severe flooding (Finlayson, 2010). As a result, mapping the extent of Australia's surface water from EO can be challenging.

In Australia, the Bureau of Meteorology (BoM) maintains inland water information, providing information on dam levels, river flows, and many other features of the water balance (see *http://www.bom.gov.au/water/*). One aspect of this information is the topographic mapping of Australia's surface water networks, consolidated into the Australian Hydrological Geospatial Fabric (or Geofabric; Atkinson *et al.*, 2008; see Volume 2D—Excursus 13.2). The Geofabric provides information on the location and shape of hydrologic features such as rivers, lakes, wetlands, and catchments, and is a valuable resource when attempting to analyse EO data for water features. Figure 11.2 shows a collection of Australia's water resources as provided by the Geofabric. However, while the Geofabric provides the official distribution of hydrologic features of Australia, it does not provide information on their varying extent resulting from changes in rainfall or water usage. EO datasets provide a valuable addition to surface water data in this regard.

Figure 11.2 A selection of hydrologic features of Australia from the Geofabric



Source: BoM (2019). Map data retrieved from *http://www.bom.gov.au/water/geofabric/download.shtml*

11.2 EO Sensors for Water Extent

Many sensors are able to provide information on water extent. Each type of sensor has advantages and disadvantages and, for each type, many methods have been developed to provide the required output, over the required area, in the required time frame. A range of EO sensors is introduced in Volume 1A—Sections 14 to 16. Interpretation of optical and microwave imagery is considered in Volume 1B—Sections 6 to 8. Both active and passive sensors are used to detect electromagnetic radiation (EMR; see Section 8 and 9), with the most commonly used EO sensors being passive optical and active microwave, with one complementing the other. Table 11.1 describes the general categories of EO sensors which can be used to delineate the extent of surface waters.

The analysis of surface water extent from passive optical sensor data exploits the physical property that water absorbs longer wavelength light far more than shorter wavelength light (see Sections 5.1.4 and 8). This can be observed as the loss of colour in greater water depths when SCUBA diving (everything tends to look more and more bluish, with red wavelengths being absorbed). Similarly, in the analysis of water extent, the shorter wavelengths of blue and green light are reflected far more strongly than the longer near infrared (NIR) and shortwave infrared (SWIR) wavelengths. SWIR is almost totally absorbed by water, with little or no reflection. Hence clear surface water appears extremely dark or black in the shortwave region of the EM spectrum. However as water turbidity increases, reflectance increases as well, which can cause errors in water extent analyses (see Section 18).

A major issue with passive optical data is the occurrence of clouds, which prevent optical sensors from observing the ground beneath them. Clouds also cast shadows, which reduce the reflectance of light from the ground. As a result cloud shadows (and terrain shadows) can be easily mistaken for water. In general the analysis of passive optical imagery for surface water requires good cloud and shadow masking to avoid misclassification errors (see Volume 2). As surface water is associated with rainfall, and hence cloudy conditions, this is a significant disadvantage for the analysis of surface water using passive optical sensors. An example of the response of a passive optical sensor to a land area that includes a variety of water turbidity conditions and mixtures of water, soil and vegetation is demonstrated in Figure 11.3.

Most tribal groups on the coast 18,000 years ago must have slowly lost their entire territory [...] a succession of retreats must have occurred. The slow exodus of refugees, the sorting out of peoples and the struggle for territories probably led to many deaths as well as new alliances.
(Geoffrey Blainey[11])

Table 11.1 EO sensors relevant to water extent

TIR: Thermal infrared; SAR: Synthetic Aperture Radar

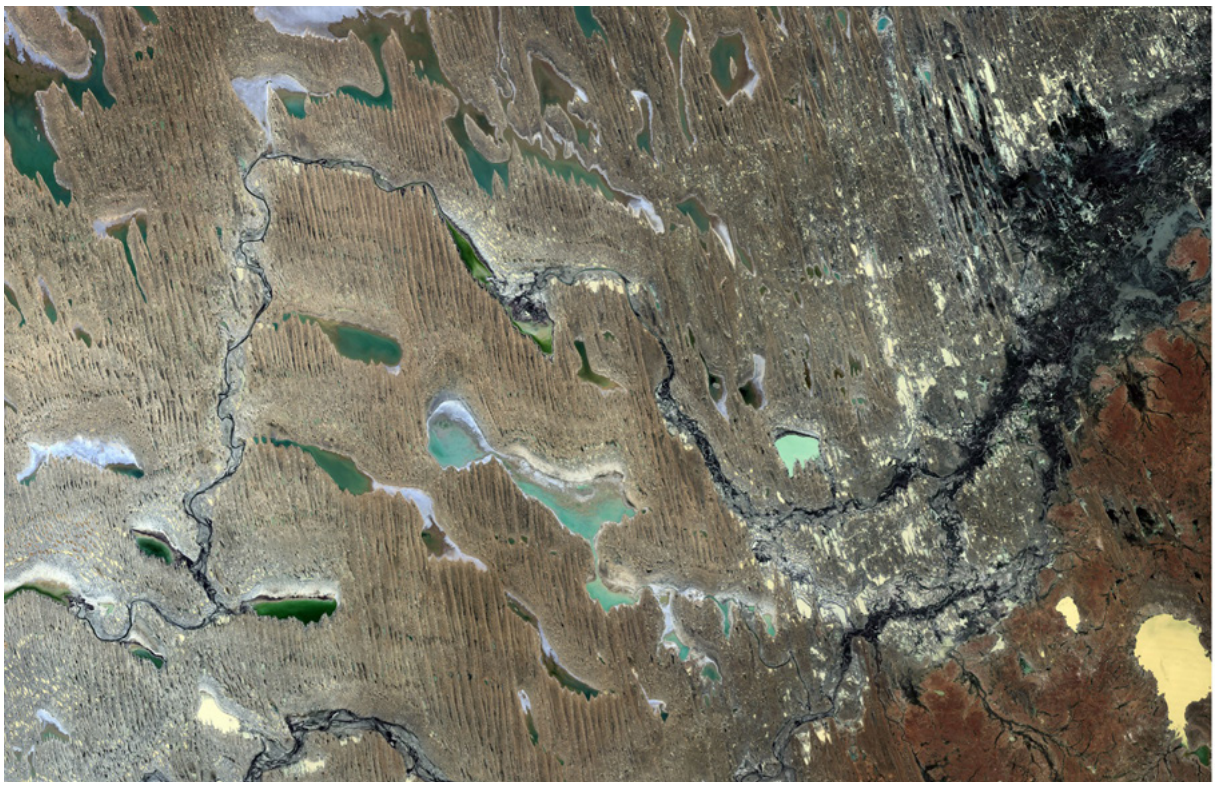
Type	Sensor	Platform	Relevance	Advantages	Disadvantages
Passive optical	Multispectral radiometer	Satellite or airborne	Nature, extent, and change in water extent and turbidity	Availability of regularly acquired imagery over very large acquisition areas, spectral discrimination of environmental features, time series	Clouds, high resolution can be expensive, few spectral bands provide little information on quality
	Hyperspectral radiometer	Satellite or airborne	Nature, extent, and change in water extent and turbidity	Multiple spectral measurement bands, best for optical water quality measurement	Clouds, cost, data complexity
	TIR radiometer	Satellite or airborne	Water temperature and extent	Possible to detect water at night	Clouds, low resolution
Active microwave	SAR	Satellite or airborne	Nature, extent, and drift of water and ice; Floods	Cloud penetrating, able to acquire at night	Generally high cost, specialised processing

11 Blainey, G. (1975). *Triumph of the Nomads: A History of Aboriginal Australia.* Macmillan, Melbourne. 285 p.

Figure 11.3 Region north of Lake Eyre during flooding

These images were acquired by Landsat-5 over a region north of Lake Eyre on 28 March 2011 during a flood.

a. True colour image, with the red, green and blue data channels displayed as RGB. This demonstrates a variety of water colours, due to turbidity and salinity, and the difficulty in clearly discriminating the water area from emergent vegetation in the right side of the image.



b. The same image shown in false colour, with SWIR, NIR and green displayed as RGB. This strongly highlights water in shades of blue and vegetation in shades of green, enabling easier visual delineation of water extent. The variation in the blue colouring is due to turbidity.

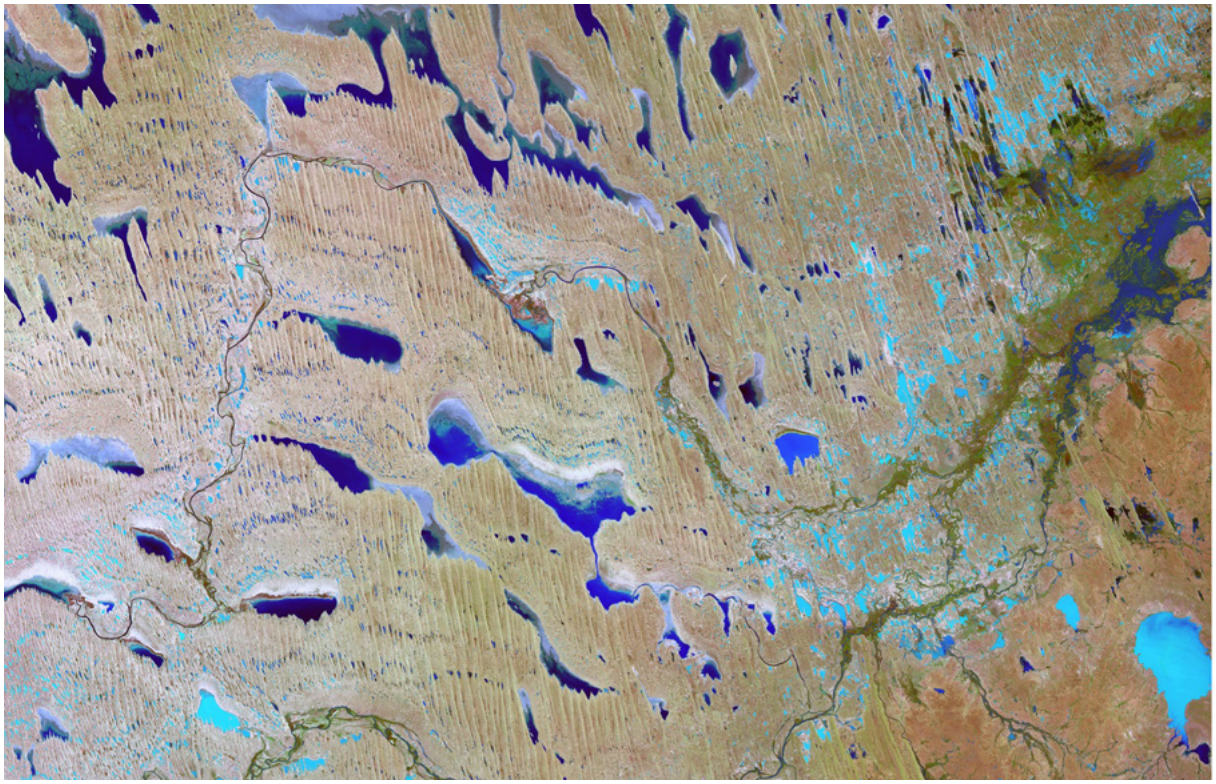


Figure 11.4 Sentinel-1a SAR image of Lake Sorrell in Tasmania, acquired on the 7 May 2015

The waterbody shows a high degree of variation across its area due to wind-induced wave action. Given this variation in backscatter, a simple threshold approach to determining water extent would either underestimate the water in the lake or generate many false positives elsewhere in the image.



Active microwave sensors have the advantage that the wavelengths used are generally able to penetrate clouds, and hence overcome the cloud and shadow challenges that occur with passive optical sensors (see Section 9). In active microwave sensing, a signal is sent to the ground at an angle to the side of the platform (see Volume 1A—Section 15.2 and Volume 1B—Section 8). The signal then interacts with targets on the ground before a portion of the signal is reflected back to the sensor, with the reflected portion depending on the relative size of the ground targets compared to the wavelength of the signal. Where the target is smaller than the wavelength, little or no signal is reflected back to the sensor and most scatters away, while where the target is larger than the wavelength, much of the signal is reflected back to the sensor. Accordingly, targets that have little surface 'roughness', such as surface water, return little information to the sensor so will appear as dark shades in an EO image, while 'rough' targets will appear brighter. However variations can occur where surface water:

- is adjacent to flat, smooth terrain; or
- contains objects such as large rocks, vegetation, debris; or
- wind creates waves on the water surface, subsequently altering the roughness.

As a result, surface water can be misclassified as dry terrain and vice versa, depending on the mixture of targets in an area. The use of multiple images in a time series, and techniques such as coherence (see Section 9.1.2.4), can help in such cases. An example of the response of an active microwave sensor (in this case Synthetic Aperture Radar, SAR) to the variety of features in and adjacent to water is shown in Figure 11.4.

11.3 Delineating Shorelines

The basic issue in determining water extent is that every pixel along a shoreline contains a mixture of terrestrial and water features, and the resulting EO measurement, represented as an image pixel, will be dominated by the feature with the most signal. In open water each pixel comprises a mixture of pure water, turbidity factors, wave action, algae content, etc. At the shoreline, however, these water factors are mixed with vegetation, soil, infrastructure, plus the potential that the sensor might not be able to get a clear observation of the surface due to the other factors blocking its view. For instance, a tall building or dense forest canopy could easily obscure a nearby waterbody from the viewing position of the sensor (see Volume 1B—Section 3). The delineated shoreline is thus the best solution found when determining what the pixel mostly represents from the mixture of features within it. Mapping surface water extent from satellite imagery continues to be a challenge, with many new methods being published each year. The DEA Coastlines product defines shorelines annually since 1988, and their rates of change, for the entire Australian coastline (Bishop-Taylor *et al.*, 2019a).

11.3.1 Passive optical analysis

The absorption of SWIR and NIR wavelengths by water allows some basic water extents to be created from optical imagery with appropriate spectral bands. The approach of a simple threshold applied to a single band is very limited as misclassification can occur with dark, non-water features such as dense, dark forests, dark soil, and mud. In addition, water quality has a large impact on NIR reflection, especially if algae is present in the water (see Section 19).

Better results can be obtained by exploiting the broader spectral response of water, through the use of ratios and normalised difference indices (see Volume 2C—Section 10). Typically these concentrate on comparing an IR band with a visible band, such as NIR and visible green. However these methods generally require fine tuning of thresholds that then do not transfer well between images, and require a lot of manual refinement to provide repeatable results. Of the various forms available for the Normalised Difference Water Index (NDWI) the most popular ones were proposed by McFeeters (1996) and Gao (1996) respectively:

$$\frac{\rho_{green} - \rho_{NIR}}{\rho_{green} + \rho_{NIR}}$$

$$\frac{\rho_{NIR} - \rho_{SWIR}}{\rho_{NIR} + \rho_{SWIR}}$$

A further development substituted the longer SWIR band for the NIR band to create the Modified Normalised Difference Water Index (MNDWI; Xu, 2006):

$$\frac{\rho_{SWIR} - \rho_{green}}{\rho_{SWIR} + \rho_{green}}$$

The applicability of each normalised difference index depends on the situation, and many further developments have been made to create indices that are more robust to other features in imagery such as urban structures and vegetation. In general however the McFeeters (1996) NDWI tends to be useful in coastal applications, while the Xu (2006) MNDWI is more robust to variations in water quality and tends to be useful in freshwater applications. The Gao (1996) NDWI was originally intended as a vegetation water content index, so is used less frequently in open water. For example the European Commission (EC) Joint Research Centre (JRC) employed the Gao (1996) NDWI for broad regional area understanding of vegetation stress (JRC, 2011).

More advanced indices have also been developed. For example an in-depth review of seven index methods was conducted by Fisher *et al.* (2016). The result of this study is a set of high accuracy water indices that are more useful for analyses across multiple images and locations.

Some very large scale surface water products derived from passive optical data have been developed by combining multiple bands and indices using machine learning to create algorithms that are more robust, and applicable across mutliple scenes and time series. The Water Observations from Space (WOfS; Mueller *et al.*, 2016) algorithm used spectral bands and normalised difference indices in a single decision tree produced using machine learning to create a 30-year, continent-wide, surface water product that is automatically updated for each new Landsat image across Australia (see Volume 1A—Excursus 5.1). The resulting data provides an ongoing measure of water extent for Australia. Tulbure *et al.* (2016) employed a random forest machine learning algorithm to examine the 30-year dynamics of surface water in the Murray-Darling Basin from Landsat imagery. The result provides a very high accuracy understanding of surface water for the basin.

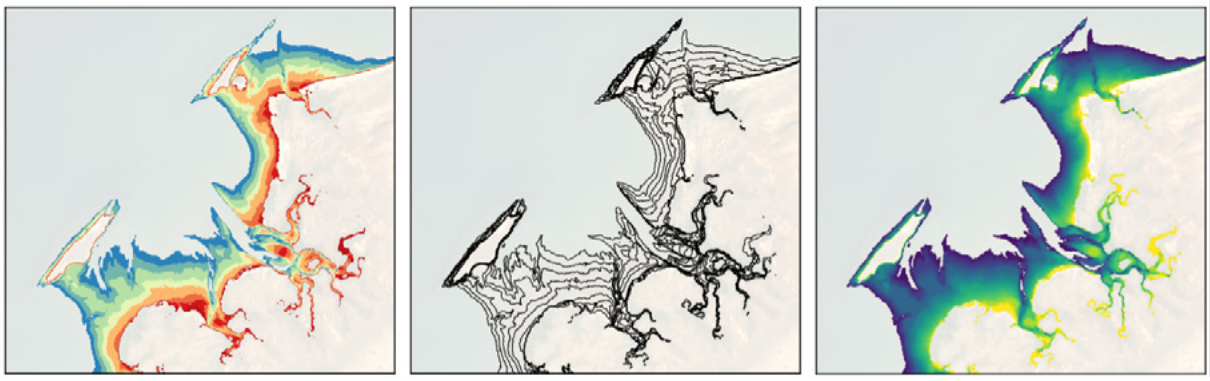
Figure 11.5 NIDEM process

The National Intertidal Digital Elevation Model (NIDEM) uses three decades of Landsat imagery to extract and interpolate shoreline contours.

a. 10% intervals of the tidal range mapped from DEA Landsat imagery (colour spectrum from blue to red shows inundated pixels at increasing high tide)

b. Waterline contours extracted and assigned median tidal heights for each 10% interval

c. Interpolated elevation relative to mean sea level from < 2.5 m (blue) to > 1.5 m (yellow)



Source: Bishop-Taylor *et al.* (2019b) Figure 17

The National Intertidal Digital Elevation Model (NIDEM; an enhanced version of the Intertidal Extents Model, ITEM)—see Volume 2A—Excursus 2.1), uses EO time series imagery from the Digital Earth Australia (DEA) platform (see Volume 2D—Section 11.2) to map Australia's intertidal zone at continental scale. The intertidal zone is highly significant for migratory shorebirds and marine biodiversity but extremely difficult to map and survey at ground level. As illustrated in Figure 11.5, NIDEM allows changes in our shorelines to be monitored and modelled (Bishop-Taylor *et al.*, 2019b).

At the global scale, Pekel *et al.* (2016) employed expert systems, visual analytics, and evidential reasoning to build a surface water product for the world based on Landsat data from 1984 to 2015. The broad applicability of this product has led to its adoption by the United Nations as an underpinning dataset for understanding surface water change in relation to droughts and population increase, and as a key dataset in measuring surface water change against the Sustainable Development Goals (UN, 2019a; see Volume 3A—Section 20). Excursus 11.1 presents one of the global methods by Verpooter *et al.* (2014) in detail.

These methods for determining surface water extent from optical imagery, all share Landsat as their source data, primarily due to its regular coverage of the globe over the last few decades. Into the future the recent successful launches of the Copernicus satellites in the Sentinel-1 and Sentinel-2 series, will provide similar capacity but at higher spatial and temporal resolution, and also from their SAR sensor, which will be advantageous in cloudy conditions or at night.

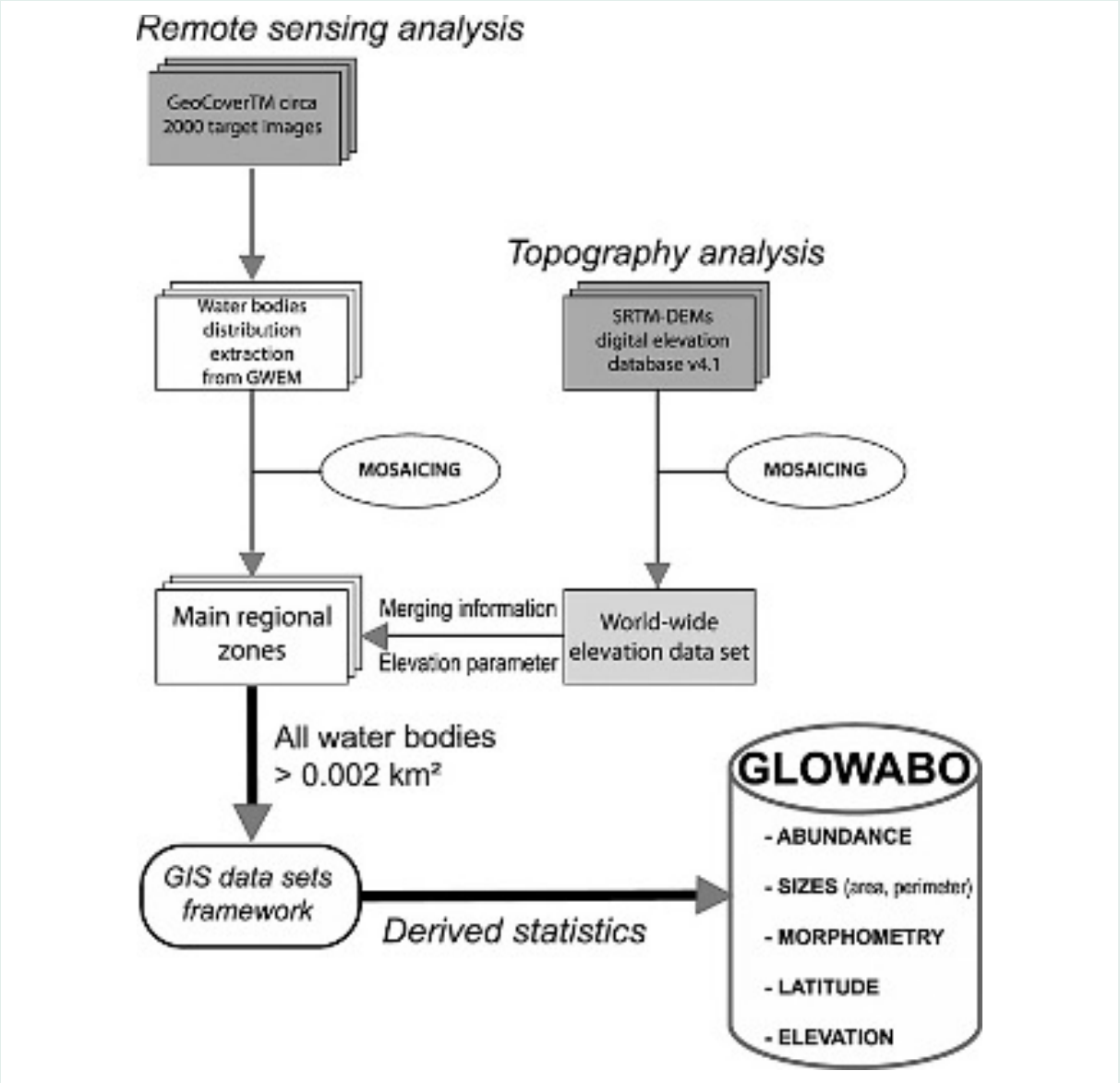
Excursus 11.1—GLOWABO

Source: Verpooter *et al.* (2014)
Further Information: Verpooter *et al.* (2012)

A GLObal WaterBodies database (GLOWABO) was compiled from high resolution satellite imagery to enable assessment of global limnological conditions, and quantify the contribution of lakes to global biogeochemical processes (Verpooter *et al.*, 2014). GLOWABO was generated using an automated method for extracting lakes from satellite imagery called GWEM (GeoCover™ Waterbodies Extraction Method; Verpoorter *et al.*, 2012). This method used a global set of regional Landsat GeoCover mosaics comprising 882 nearly cloud-free, pan-sharpened tiles with 14.25 m spatial resolution. These mosaic tiles were created from 8,500 Landsat ETM+ scenes acquired between 1997 and 2003 using ETM bands 2 (green), 4 (NIR), and 7 (SWIR). Elevation data was based on Shuttle Radar Topography Mission digital elevation model (SRTM-DEM) database 4.1 (Jarvis *et al.*, 2008) for all lakes between 60°N and 56°S (excluding the Capsian Sea).

Figure 11.6 GLOWABO overview

Inputs are shown as grey boxes and outputs as white boxes.



Source: Verpoorter *et al.* (2014) Figure 1

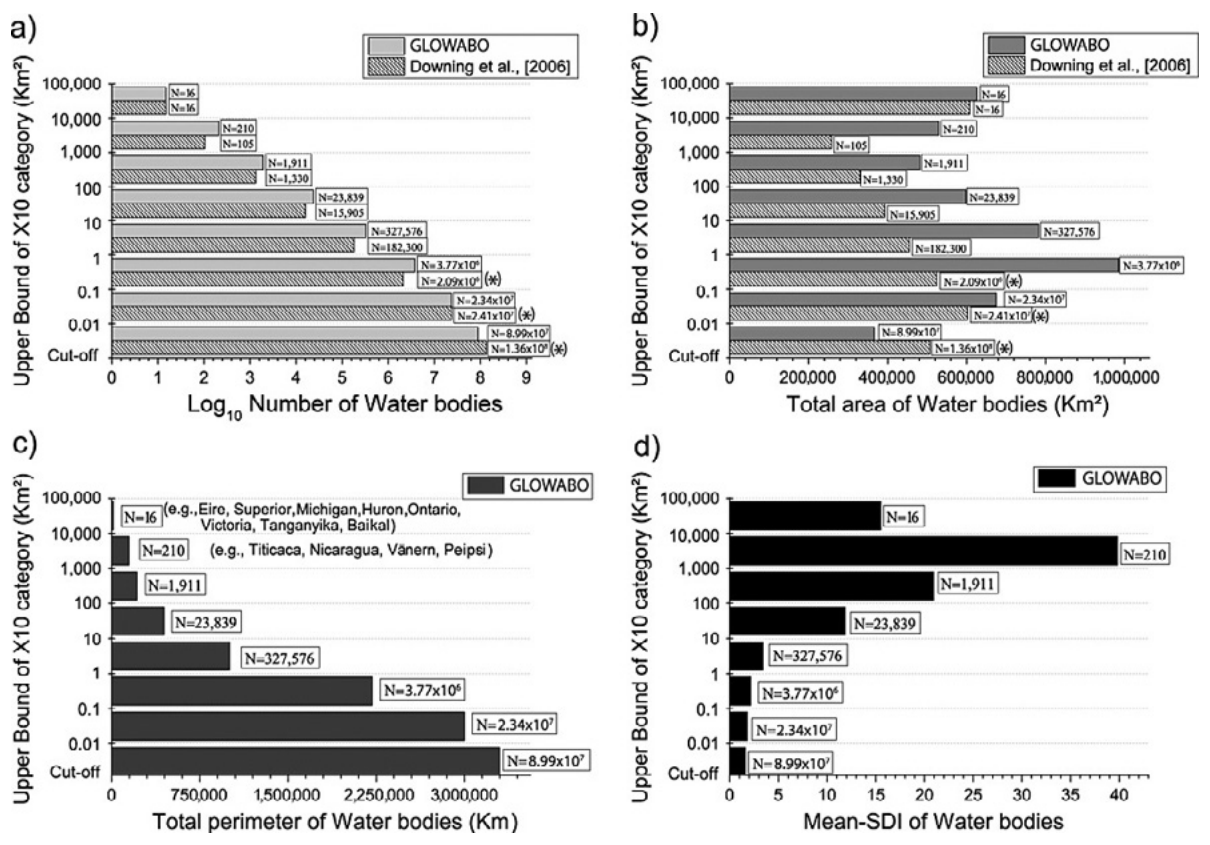
Lake measurements extracted using this method included count, area, perimeter, geographic distribution, elevation, and shape (indicated by shoreline development index: SDI; see Figure 11.6). This inventory concluded that:

- around 117 million lakes of size greater than 0.002 km^2 exist globally compared with a previous estimate of 163 milllion (Downing *et al.*, 2006);
- these lakes cover 3.7% of the non-glaciated land area;
- previous estimates based on map compilations (such as the Global Lake and Wetland Database: GLWD; Lehner and Döll, 2004) underrepresented small lakes, and statistical extrapolations based on size-abundance relationships (such as Downing *et al.*, 2006) overestimated them (see Figure 11.7);
- the greatest abundance, area, and perimeter of waterbodies exist between 45°N and 75°N (see Figure 11.8); and
- 85% of lakes, 50% of lake area and 50% of total lake area occur at elevations below 500 m (see Figure 11.8).

These results are significant for global and regional analyses of hydrologic and biogeochemical processes, including emission of carbon dioxide and methane, sediment burial of carbon and other elements, and primary production (Wetzel, 1992). As high resolution time series datasets become available, it will also be feasible to globally monitor the dynamics of lake abundance, size and distribution.

Figure 11.7 GLOWABO estimates

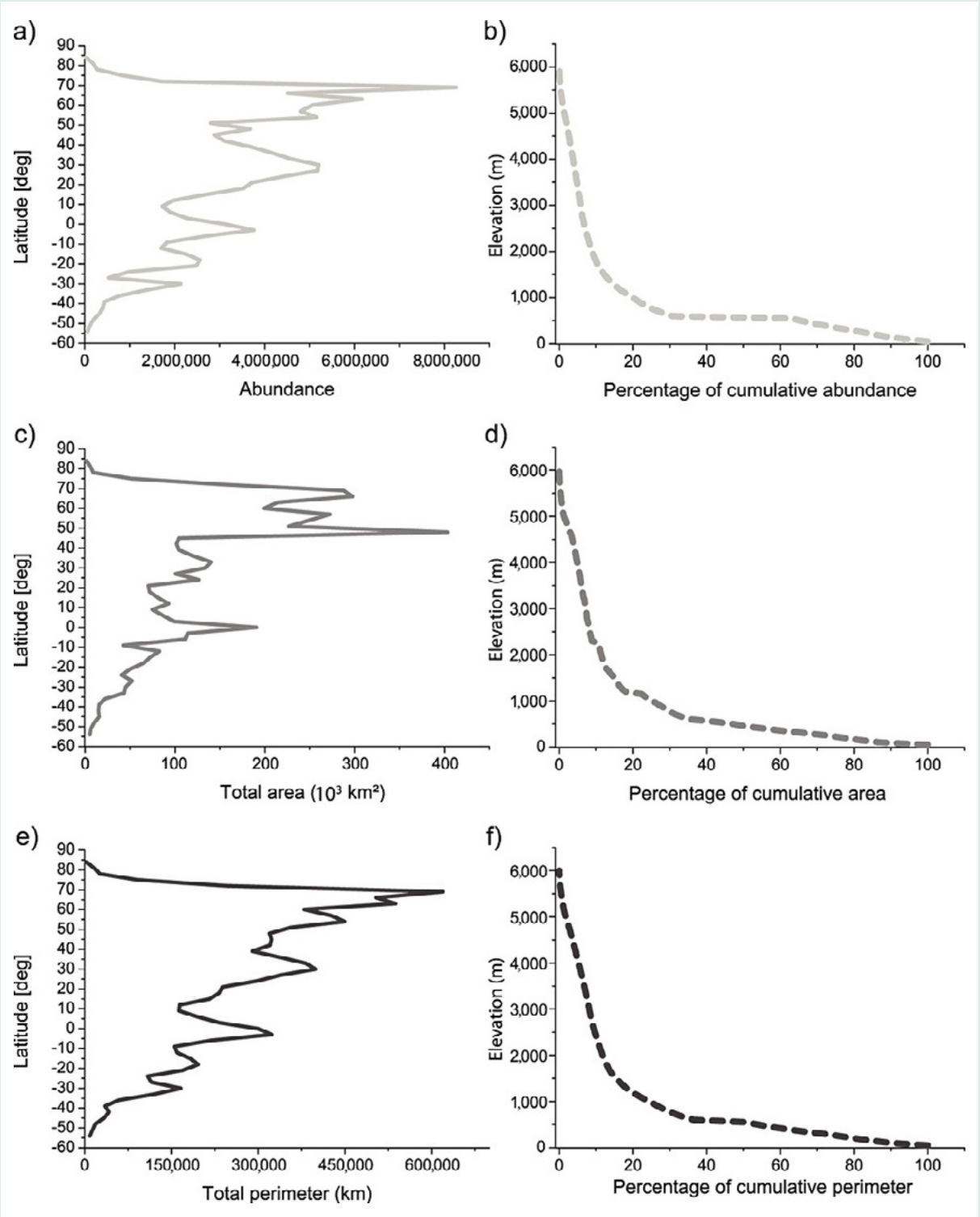
a. Abundance
b. Total area—global areal extent of lakes is dominated by medium and large lakes
c. Total perimeter
d. Shape (mean SDI)—smaller lakes tend to be rounder.



Source: Verpoorter *et al.* (2014) Figure 2

Figure 11.8 Distribution of lakes by latitude and elevation

a. Abundance relative to latitude
b. % cumulative abundance relative to elevation
c. Total area relative to latitude
d. % cumulative area relative to elevation
e. Total perimeter relative to latitude
f. % total perimeter relative to elevation



Source: Verpoorter *et al.* (2014) Figure 3

11.3.2 Synthetic Aperture Radar

As described in Section 11.2, the analysis of SAR data presents many advantages and disadvantages for mapping surface water extent. To date, few SAR analysis methods have provided consistent regional and temporal outputs, with most methods being suitable for one general location at a time. However, the growing time series of SAR imagery is presenting new opportunities for estimating water extent in lakes (Vickers *et al*., 2019).

The most basic method for determining water extent from SAR follows a similar concept to passive optical (see Section 11.3.1), employing a threshold on the backscatter to separate the darker, smoother water areas from the brighter, rougher terrestrial areas. However such thresholding normally requires manual tuning by the analyst. A further complication arises from the fact that SAR data is acquired at an angle to the side of the sensor platform, meaning that there will be brightness variation across the track of the SAR image from the changing incident angle of the microwave radiation.

One method to automate the measurement of water extent from SAR for flood mapping has been developed by Twele *et al*. (2016) using high speed analysis of Sentinel-1 SAR. The method employs an automated histogram splitting system to determine a suitable backscatter threshold to find areas that have the highest likelihood of being water. In addition, elevation data is used to constrain a 'growing' algorithm, which broadens areas with high likelihood of being water into adjacent areas so long as the elevation is constrained. This helps to minimise false positives in areas where the backscatter is impacted by non-water features, such as occurs with flooded vegetation and buildings.

11.4 Monitoring Floods

While *in situ* mapping of the extent of a flood can be quite dangerous, as areas impacted by floods are often waterlogged and being quickly eroded, the ability to delineate the area of impact can help determine safe zones for people and livestock, and identify infrastructure and environment at risk of damage. The method for measuring flood extent from EO data is essentially the same as for the more usual water extent mapping, however, responding to any form of natural disaster with EO requires as short a period as possible from image capture to extent provision. Accordingly, it is common to use less accurate methods in order to create a product that is both useful and delivered quickly. In addition, the emergency service agencies that use flood extent datasets often do not have the facilities to analyse imagery themselves, so these datasets are usually simplified for rapid integration into GIS, rather than for extensive scientific use. Typically a flood extent analyst will:

- apply simple thresholding on a NDWI or SAR backscatter channel to produce a base product;
- manually edit the output to remove false classifications due to clouds and shadows, and add areas that the base analysis missed; then
- extract a simplified vector polygon (or set of polygons) from the analysis before either direct delivery to the end user or incorporation into a map product in GIS software.

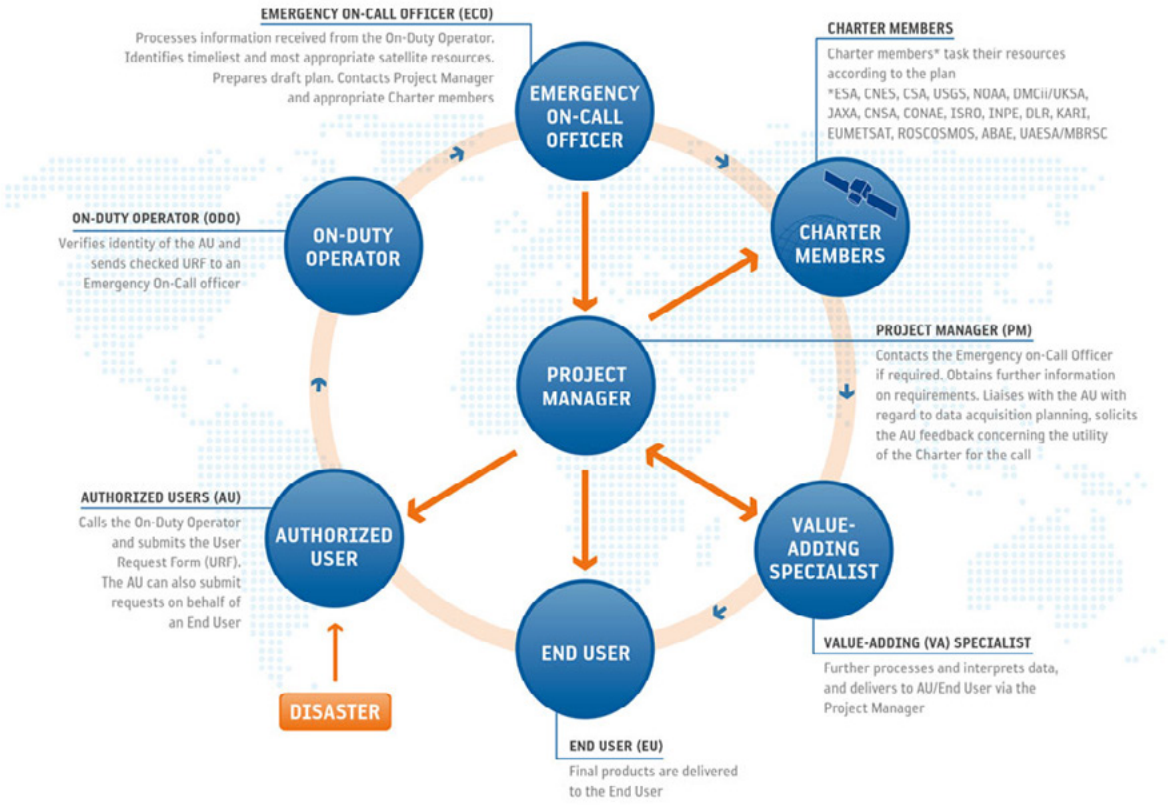
Some more automated methods have also been developed for flood response. In Australia the Landgate Floodmap service (Landgate, 2019) provides national coverage of flooding in Australia using high frequency, moderate resolution imagery such as from the MODIS satellites Terra and Aqua. The frequent national coverage of these satellites, and their low latency from data acquisition to availability, permits flood information to be produced quickly and regularly (for example, see Volume 1B—Excursus 7.1).

Internationally the Dartmouth Flood Observatory (DFO, 2019) has provided a world-wide flood mapping service since 1993. Using a combination of moderate resolution optical and SAR imagery, this system automatically produces flood extent maps for major flood events around the world.

11.4.1 The International Charter for Space and Major Disasters

The International Charter for Space and Major Disasters (ICSMD) is an international agreement amongst satellite imagery providers to supply their data in times of natural disaster for the purpose of providing assistance with the disaster response (ICSMD, 2020). A wide range of EO imagery providers have volunteered to supply data, whether public good or commercial, at no charge for disaster response.

Figure 11.9 Charter Activation



Source: ICSMD (2020)

This data is coordinated through a nominated Project Manager and delivered to a Value Added Provider, who creates extent and impact products for delivery to the end user (see Figure 11.9). Many types of data become available in this way, including very high resolution optical and SAR products.

One example of the use of this Charter for flood mapping in Australia occurred in October 2016 (Disasters Charter, 2016), when the New South Wales State Emergency Service (NSW SES) requested assistance following a long period of heavy rain throughout central NSW. The success of this response to the flooding was due to excellent organisation on the part of NSW SES in understanding the predicted movement of peak flood through the river systems, allowing image capture to be organised to coincide with the peak as closely as possible. Many hundred of images were supplied and analysed, using methods from manual image thresholding, to automated machine learning, to provide regular, ongoing disaster response information to NSW SES.

11.4.2 The Copernicus Emergency Management Service

The Copernicus Emergency Management Service (CEMS) is another facility for the provision of EO data for disaster response. Unlike the Charter, CEMS sources data through the Copernicus programme of the European Commission (EC), then acts as its own Value Added Provider to create mapping products, which it provides directly to the end user. The advantage of this arrangement is that data need not be downloaded from one part of the Earth to another, speeding up map delivery substantially. In addition, CEMS is a dedicated emergency management service responding frequently to disasters around the world, and so has developed considerable skills for providing highly useful disaster response products very quickly. During the 2016 floods in NSW, CEMS was used as a Value Added Provider for the Charter, helping to provide mapping information to the NSW SES (EC, 2019) from both CEMS and the Charter in a coordinated effort.

11.5 Permanent/Temporary water

The UN FAO has defined water seasonality in its Land Cover Classification System (LCCS; UN, 2019b; see Volume 3A—Section 3) according to the number of months per year that surface water is present at a location. Where water exists for over three months the waterbody is considered (semi-) permanent, and where it exists for less than three months the body is considered temporary or seasonal.

From the repeat observations of a waterbody in an EO time series dataset, water perenniality or hydroperiod can be computed from the time series of extracted water extents. This is especially useful for remote waterbodies where *in situ* mapping would have only observed a waterbody in one state of fill, and thus unable to provide information on its permanence. The Water Observations from Space (WOfS) product was originally designed to provide information on areas at risk of flooding, by examining the frequency of water observed in any location and deriving the percentage of time that water was classified as present in the location (see Volume 1A—Excursus 5.1). This subsequently led to the water perenniality information being incorporated into the BoM Geofabric dataset for all of Australia. However since WOfS is derived from passive optical sensors in the Landsat series of satellites, clouds often impact the image, and the time series of water observation is often interrupted. Hence the outputs of WOfS miss waterbodies that are obscured by clouds, and do not provide absolute certainty of the perenniality, or of how continuously water actually has existed in any waterbody. One potential future solution to this problem is to supplement the optical analysis with SAR-derived water extents that can fill in these data gaps.

11.6 Further Information

International Charter for Space and Major Disasters (ICSMD)

https://disasterscharter.org/web/guest/home

Bureau of Meteorology

Information on dam levels, river flows, and many other features of the water balance: *http://www.bom.gov.au/water/*

Water Observations from Space (WOfS)/ DEA Water Observations

https://cmi.ga.gov.au/data-products/dea/613/dea-water-observations-landsat

Floodmap

https://floodmap.landgate.wa.gov.au/

DEA Coastlines

https://cmi.ga.gov.au/data-products/dea/581/dea-coastlines

European Union Science Hub

Monitoring our Blue Planet: First SDG indicator platform launched by Google, the JRC and UN Environment: *https://ec.europa.eu/jrc/en/science-update/monitoring-our-blue-planet-first-sdg-indicator-platform-launched-google-jrc-and-un-environment*

Dartmouth Flood Observatory

https://floodobservatory.colorado.edu/

11.7 References

Atkinson, R., Power, R., Lemon, D., O'Hagan, R., Dovey, D., and Kinny, D., (2008). *The Australian hydrological geospatial fabric—Development methodology and conceptual architecture*. Water for a Healthy Country, CSIRO.

Bishop-Taylor, R., Sagar, S., Lymburner, L., Alam, I., and Sixsmith, J. (2019a). Sub-pixel waterline extraction: Characterising accuracy and sensitivity to indices and spectra. *Remote Sensing*, 11(24), 2984. *https://www.mdpi.com/2072-4292/11/24/2984*

Bishop-Taylor, R., Sagar, S., Lymburner, L., and Beaman, R.J. (2019b). Between the tides: Modelling the elevation of Australia's exposed intertidal zone at continental scale. *Estuarine, Coastal and Shelf Science*, 23, 115–128. *https://doi.org/10.1016/j.ecss.2019.03.006*

Blainey, G. (1975). *Triumph of the Nomads: A History of Aboriginal Australia*. Macmillan, Melbourne. 285 p

BoM (2019). *Australian Hydrological Geospatial Fabric (Geofabric)* website: *http://www.bom.gov.au/water/geofabric/index.shtml*

CSIRO (2018). *Causes of extreme sea levels* webpage, Commonwealth Scientific and Industrial Research Organisation website: *https://research.csiro.au/slrwavescoast/extremes/causes-extreme-sea-levels/*

DFO (2019). *Dartmouth Flood Observatory* website: *http://floodobservatory.colorado.edu/*

Disasters Charter (2016). *Flood in Australia* webpage, International Charter Space and Major Disasters website: *https://disasterscharter.org/web/guest/activations/-/article/flood-in-austral-2*

Downing, J.A., Prairie, Y.T., Cole, J.J., Duarte, C.M., Tranvik, L.J., Striegl, R.G., McDowell, W.H., Kortelainen, P., Caraco, N.F., Melack, J.M., and Middelburg, J.J. (2006). The global abundance and size distribution of lakes, ponds, and impoundments, *Limnology and Oceanography*, 51, 2388–2397. doi:10.4319/lo.2006.51.5.2388

EC (2019). *Copernicus Emergency Management Service*. *https://emergency.copernicus.eu/*

Finlayson, B. (2010). Rivers in Australia. *Frontiers of Earth Science in China*, 4(4), 375–385. *https://doi.org/10.1007/s11707-010-0129-y*

Fisher, A., Flood, N., and Danaher, T. (2016). Comparing Landsat Water Index Methods for Automated Water Classification in Eastern Australia. *Remote Sensing of Environment*, 175, 167–182. doi:10.1016/j.rse.2015.12.055

Gao, B.C., (1996). NDWI—A normalized difference water index for remote sensing of vegetation liquid water from space. *Remote Sensing of Environment*, 58(3), 257–266.

GA (2019). *Deserts* webpage on Geoscience Australia website: *http://www.ga.gov.au/scientific-topics/national-location-information/landforms/deserts*

ICSMD (2020). *International Charter for Space and Major Disasters* website: *https://disasterscharter.org/web/guest/home*

Jarvis, A., Reuter, H.I., Nelson, A., and Guevara, E. (2008). *Hole-filled seamless SRTM data V4*. International Centre for Tropical Agriculture (CIAT). *http://srtm.csi.cgiar.org*

JRC (2011). *NDWI: Normalised Difference Water Index* Product Fact Sheet, European Union Joint Research Centre. *https://edo.jrc.ec.europa.eu/documents/factsheets/factsheet_ndwi.pdf*

Landgate (2019). *Floodmap* webpage, Landgate website: *https://floodmap.landgate.wa.gov.au/*

Lehner, B., and Döll, P. (2004). Development and validation of a global database of lakes, reservoirs and wetlands, *Journal of Hydrology*, 296, 1–22. doi:10.1016/j.jhydrol.2004.03.028

McFeeters, S.K., (1996). The use of the Normalized Difference Water Index (NDWI) in the delineation of open water features. *International Journal of Remote Sensing*, 17(7), 1425–1432. doi:10.1080/01431169608948714

Mueller, N., Lewis, A., Roberts, D., Ring, S., Melrose, R., Sixsmith, J., Lymburner, L., McIntyre, A., Tan, P., Curnow, S., and Ip, A. (2016). Water observations from space: Mapping surface water from 25 years of Landsat imagery across Australia. *Remote Sensing of Environment*, 174, 341–352. *https://doi.org/10.1016/j.rse.2015.11.003*.

Parliament of Australia (2013). *Water* webpage APH website: *https://www.aph.gov.au/About_Parliament/Parliamentary_Departments/Parliamentary_Library/pubs/BriefingBook44p/Water*

Pekel, J.F., Cottam, A., Gorelick, N., and Belward, A.S. (2016). High-resolution mapping of global surface water and its long term changes. *Nature*, 540, 418–422. doi:10.1038/nature20584

Tulbure, M.G., Broich, M., Stehman, S.V., and Kommareddy, A. (2016). Surface water extent dynamics from three decades of seasonally continuous Landsat time series at subcontinental scale in a semi-arid region. *Remote Sensing of Environment*, 178, 142–157. doi:10.1016/j.rse.2016.02.034

Twele, A., Cao, W., Plank, S., and Martinis, S., (2016). Sentinel-1-based flood mapping: a fully automated processing chain. *International Journal of Remote Sensing*, 37(13), 2990–3004. doi:10.1080/01431161.2016.1192304

UN (2019a). The Sustainable Development Goals Report. UN, Rome. *https://unstats.un.org/sdgs/report/2019/*; *https://unstats.un.org/sdgs/report/2019/The-Sustainable-Development-Goals-Report-2019.pd*f

UN (2019b). *Land Cover Classification System v2*, UN Food and Agriculture Organisation. *http://www.fao.org/3/y7220e/y7220e06.htm*

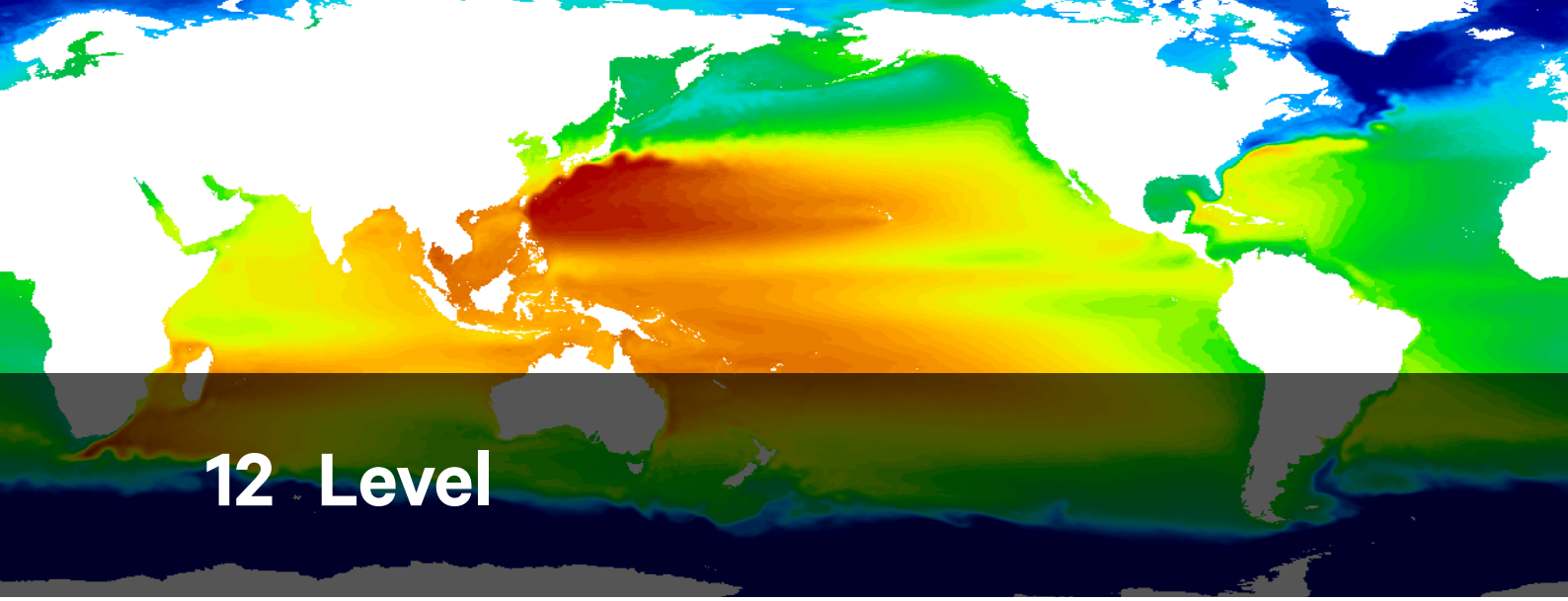
Verpoorter, C., Kutser, T., and Tranvik, L. (2012). Automated mapping of water bodies using Landsat multispectral data. *Limnological and Oceanographic Methods*, 10, 1037–1050. doi:10.4319/lom.2012.10.1037

Verpooter, C., Kutser, T., Seekell, D.A., and Tranvik, L.J. (2014). A global inventory of lakes based on high-resolution satellite imagery. *Geophysical Research Letters*, 41, 6396–6402. doi:10.1002/2014GL060641

Vickers, H., Malnes, E., and Høgda, K.-A. (2019). Long-Term Water Surface Area Monitoring and Derived Water Level Using Synthetic Aperture Radar (SAR) at Altevatn, a Medium-Sized Arctic Lake. *Remote Sensing*, 11, 2780. *https://doi.org/10.3390/rs11232780*

Wetzel, R.W. (1992). Gradient-dominated ecosystems—Sources and regulatory functions of dissolved organic matter in freshwater ecosystems, *Hydrobiologia,* 229, 181–198. doi:10.1007/BF00007000

Xu, H., (2006) Modification of normalised difference water index (NDWI) to enhance open water features in remotely sensed imagery. *International Journal of Remote Sensing*, 27(14), 3025–3033. doi:10.1080/01431160600589179



12 Level

Edward King

The level (or height) of the sea surface is a familiar concept to anyone with experience of the coast (see Sections 4.1 and 7.2). It is societally relevant on a day-to-day basis, if not hour by hour, to recreation, port operations, shipping, and other commercial uses of the coastal ocean, such as fishing, aquaculture, and energy generation. Accurate information about the long term change in sea level and the frequency of extreme events is also vitally important to the design and placement of coastal infrastructure, including roads and buildings. For example, a new bridge with a 100 year lifetime and a minimum specified clearance for shipping needs to be constructed to accommodate future sea level rise.

Although sea level is a straightforward concept in an everyday sense, it is important to be clear about how it is measured and with respect to which reference frame (see Volume 1A—Excursus 3.2). The sea surface closely follows the geoid which is determined in turn by the mass distribution in the crust. Measurements made relative to the crust (at tide gauge stations) or to a version of the geoid (followed by a satellite) are made comparable by transfer to a reference ellipsoid. The normal practice in surveying is to refer all measurements to an idealised geocentric reference ellipsoid, aligned with the axis of Earth's rotation (see Volume 2B—Section 1). The sea surface height then is the distance between this reference ellipsoid and the sea surface (see Figure 12.1). All measurements include the astronomical tides but this periodic feature may be removed from consideration over time scales of more than a day.

In a static world the sea surface would lie on an equipotential of the Earth's gravity field, the Geoid (see Volume 1A—Section 3.3). The geoid is an irregular surface, varying by hundreds of metres, depending on the geology, topography (including subsurface ocean trenches and seamounts), and even the presence of water, either in the ocean or as ice (see Volume 1A—Section 8). The presence of various dynamic forcings—including wind, heating and cooling, currents, and changes in salinity—perturb the sea surface away from the geoid giving rise to a dynamic topography of the sea surface, by amounts typically in the range ±1.5 m. Ocean tides also displace the sea surface by several metres. Although they are not spatially uniform they are regular and predictable, so it is usual to consider them separately from dynamic topography.

Tide gauge stations measure the sea surface height relative to the local land surface (see Section 12.4.2). For comparison with other observations, including from other stations, the position of the station relative to the ellipsoid must be accounted for. Over longer periods this position must be monitored as, for example, the foundations of the station could subside, or the local crust can move relative to the ellipsoid due to continental drift and isostatic adjustment (see Volume 1A—Section 3.2).

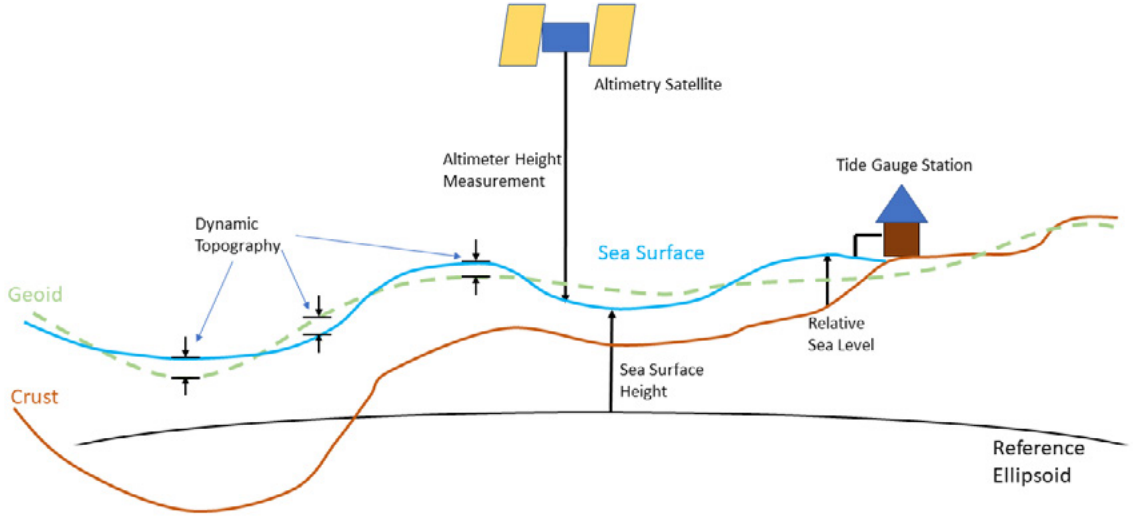
In the subsections below, we firstly describe sea level variations in Australian waters (see Section 12.1). Next we describe EO sensors that acquire data relevant to monitoring sea level (see Section 12.2), then consider the causes of short and long term changes in sea level (see Section 12.3). Various methods that are used to measure sea level are reviewed in Section 12.4, monitoring approaches used to quantify past sea level changes are discussed in Section 12.5, and projections of future sea level change are presented in Section 12.6.

Background image: The Mean Dynamic Topography MDT-CNES-CLS18 is an estimate of the mean over the 1993–2012 period of sea surface height above the geoid (bias subtracted 0.47 m), with height ranging through the colour spectrum from -1 m (blue) to 1 m (red). Source: AVISO/CNES. Plot derived from data located at *https://www.aviso.altimetry.fr/en/data/products/auxiliary-products/mdt.html*

Recommended Chapter Citation: King, E.A. (2021). Level. Ch 12 in *Earth Observation: Data, Processing and Applications. Volume 3B—Surface Waters.* CRCSI, Melbourne. pp. 197–221. ISBN 978-0-6482278-5-4

Figure 12.1 Reference frames and measurements for sea level observation

The sea surface closely follows the geoid, which is determined in turn by the mass distribution in the Earth's crust. Measurements that are made relative to the crust (at tide gauge stations) or to a version of the geoid (followed by a satellite) are made comparable by transfer to a reference ellipsoid. All measurements include the astronomical tides but this periodic feature is removed for consideration over timescales of more than a day.



Source: Edward King, CSIRO

12.1 Level of Australian Surface Waters

The factors affecting the sea level on Earth range from local through regional to global, and even solar system scales. These factors include atmospheric forcing (pressure and wind) and their interactions with the seabed and coasts, ocean temperature and salinity (freshwater inflow and evaporation), tectonic plate movement, ice melt, and tidal forces. The time scales of these forcings vary from sub-daily for tides and weather through seasonal to decadal for climate, and even longer for geodetic changes.

The Australian coast experiences the impacts of all of these factors across a range of spatial scales and time frames. Tides range from almost zero in some locations to 6 m or 7 m in parts of the north and northwest. Tropical cyclones can raise storm surges of 5 m or more, and suitably exposed parts of the coast experience enhanced sea levels through wave action. Warm and cold eddies in the East Australian Current result in undulations of the sea surface in the range of 1 m. Changes in global climate will result in long term change to Australian sea levels—a mean increase of around 1 m by 2100 is entirely plausible from current projections (see Section 12.6), and significantly greater change is possible over subsequent centuries. Changes in the ocean circulation and distribution of the mass of water on the Earth's surface (as polar ice melts) mean that these changes in sea level will not necessarily be uniformly distributed around Australia.

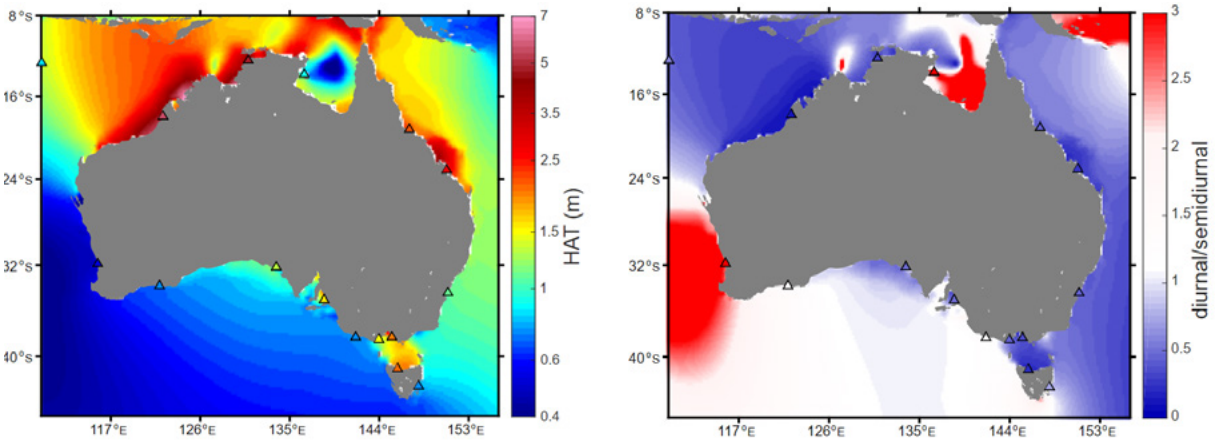
As introduced in Excursus 4.1, Earth's tides arise from the response of the oceans to the gravitational attraction of astronomical bodies, primarily the Moon and the Sun. The combinations of lunar and solar gravitational attraction, coupled with regional and local coastline and bathymetry, give rise to a range of different daily tidal height patterns: diurnal, with one high and low per day; semidiurnal, with two equal high and two equal low tides per day; and mixed semidiurnal, with two differing high and two differing low tides per day (Figure 4.6 and Figure 4.7). For further details see, for example, Townsend, 2012, Chapter 6.

The tides are dramatically modified by interaction with the seabed on the continental shelves and near the coast, particularly in embayments and straits that constrain tidal flows. The resulting patterns in sea level can be complex and are often unique to individual locations. The variability of tide height and the types of tide around Australia is shown in Figure 12.2. Despite the complex patterns, once the local characteristics are determined through observation, tides are essentially periodic and predictable because they arise from the known motions of astronomical bodies.

Figure 12.2 Variability of Australian tides

a. Highest astronomical tide (HAT) on a logarithmic colour scale

b. Tide type indicated by the ratio of principal diurnal constituents to the semidiurnal constituents.



Source: McInnes *et al.* (2016) Figure 2b and 2c

12.2 EO Sensors for Sea Level

The interconnectedness of the oceans means that global scale forcing is relevant even locally, so global observations of sea level are necessary to build a holistic understanding that can explain and, importantly, predict changes into the future. Spaceborne radar altimeters provide such a global observation system.

Multiple radar altimetry instruments have provided a continuous record of global sea level since 1993 with unprecedented precision (see Section 12.2.1). This comprehensive and accurate record has led to the detection, and subsequent characterisation, of many physical phenomena. The improved understanding of the response of the ocean and cryosphere to global climate change, the processes of mesoscale oceanography, and even tides, has been nothing less than a revolution driven by this branch of Earth Observation (EO). Even as it becomes a tool for routine monitoring of sea level, with further improvements in accuracy and coverage and the advent of imaging altimeters such as the imminent SWOT mission (launch due in 2022; see Excursus 12.1), the discovery phase of the satellite altimetry era is far from over.

Gravity measuring satellites, such as the pair that make up the GRACE mission (see Excursus 1.1), also provide important information on the distribution of water between the ocean, the cryosphere, and terrestrial storages (see Table 12.1).

Table 12.1 EO sensors relevant to water level

Type	Sensor	Platform	Relevance	Advantages	Disadvantages
Active microwave	Radar altimeter	Satellite	Sea level change (tidal and non-tidal), Surface wind speed, Topography of ice sheets	All weather, highly precise	Not an imaging system, so measurements are only along infrequently repeated tracks (10–30 days)
Gravity	GRACE mission (see Excursus 1.1)	Satellite	Monitoring changes in distribution of water between the ocean, the cryosphere, and terrestrial storages	Global coverage	Low spatial resolution

12.2.1 Radar altimetry

The satellite altimeter operates by measuring the travel time of a transmitted radio pulse reflected from the sea surface (see Section 9.5 and Figure 12.1). Several adjustments are made to account for delays due to atmospheric and ionospheric effects, also for spreading of the return pulse resulting from reflection over a finite area of the sea surface. Satellite orbits are generally elliptical but are also perturbed by the Earth's gravity field, so the satellite altitude above the reference ellipsoid is not constant. Precision orbit determination, via a range of techniques, is required to translate the measurement into a sea surface height relative to the reference ellipsoid. Determination and monitoring of the geoid (relative to the reference ellipsoid) is, in turn, necessary to derive the dynamic topography (see Volume 1A—Section 3.3). Satellite altimetry is therefore a sophisticated measurement technique, which demands constant attention to detail. This emphasises the immense value of being able to measure the sea surface height globally and repeatedly, capturing not only the dynamic topography at a range of spatial and temporal scales, but also the change in the mean state over the longer term.

Radar altimetry from space has been trialled since the Skylab mission in 1973, and on various other missions through the 1970s and 1980s, including the European ERS missions (1991 and 1995) and the US Navy Geosat and Geosat Follow-On (GFO) satellites. The first high quality altimeter for oceanography was flown on TOPEX/Poseidon, launched in 1992. Since then, there has been a series of missions that have delivered a continuous time series of sea level measurements (see Table 12.2). Of particular note are the series comprising TOPEX/Poseidon, Jason-1/-2/-3 and Sentinel-6, that focused on providing a consistent record of sea surface height from essentially the same orbit over nearly three decades (see Section 12.7).

Table 12.2 Satellite missions providing data from a radar altimeter instrument

Mission	Operational dates	Orbital altitude (km)	Revisit frequency (days)	Goals
Geosat	1985/03–1990/01	800	First 18 months: non-repeating, then 17	Determination of marine geoid
ERS-1	1991/07-2000/03	785	Variously 3, 168 and 35	Atmosphere and ocean observations (multiple payloads)
TOPEX/Poseidon	1992/09-2005/10	1336	9.9	Sea surface height
ERS-2	1995/04–2011/07	785	35	Atmosphere and ocean observations (multiple payloads)
GFO	1998/02–2008/11	800	17	Real time ocean topography
Jason-1	2001/12–2013/06	1336	9.9	Sea surface height
Envisat	2002/03–2012/04	782–799	30–35	Atmosphere and ocean observations (multiple payloads)
OSTM/Jason-2	2008/06–2019/10	1336	9.9	Sea surface height
Cryosat-2	2010/04–present	717	369	Polar ice and sea surface height
Saral	2013/02–present	800	35 day until 2016/07 then non-repeating	Sea surface height
Jason-3	2016/01–present	1336	9.9	Sea surface height
Sentinel-3A	2016/02–present	814	27	Operational monitoring of environment (multiple payloads)
Sentinel-3B	2018/04–present	814	27	Operational monitoring of environment (multiple payloads)
Sentinel-6	2020/11–present	1336	10	Sea surface height

Excursus 12.1—Surface Water and Ocean Topography (SWOT)

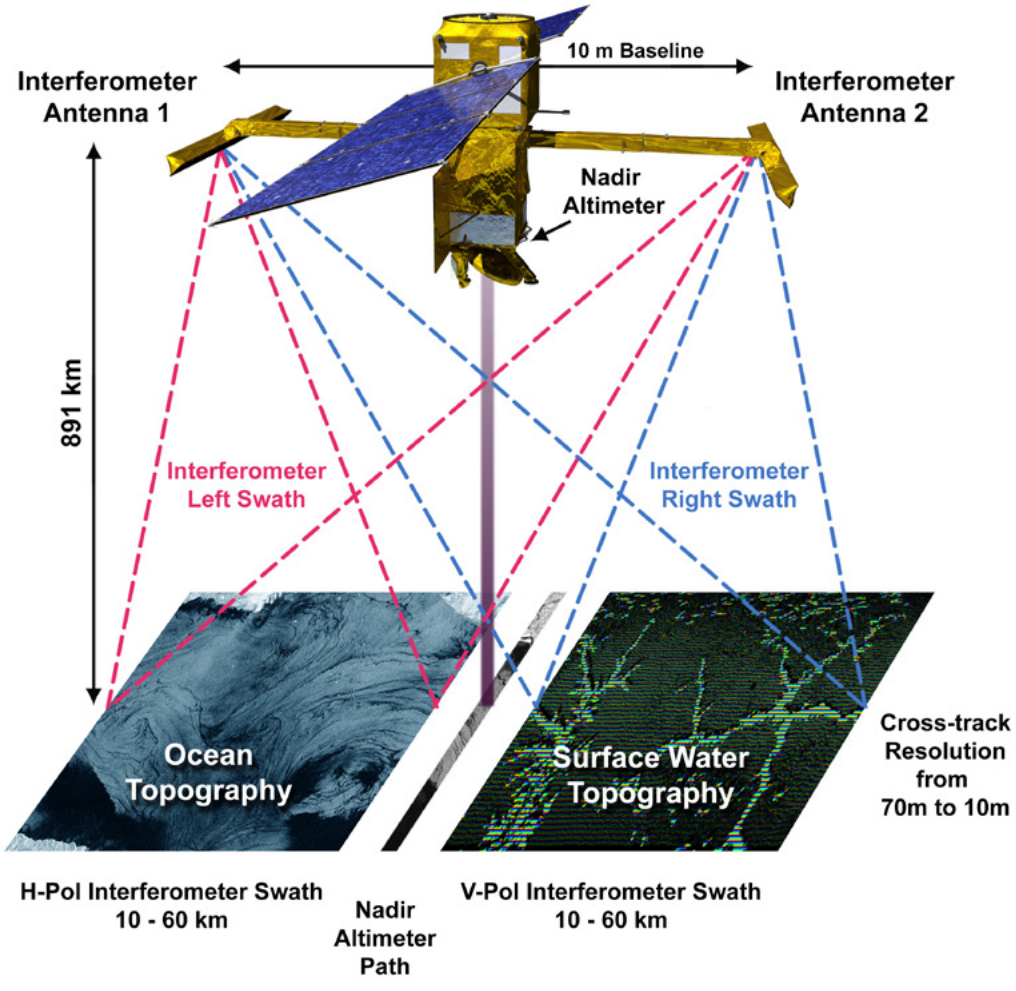
Source: Edward King
Further Information: *https://swot.jpl.nasa.gov/*

The Surface Water and Ocean Topography (SWOT) satellite mission is a joint project between NASA and CNES space agencies to fly a new experimental altimetry instrument in 2022. This mission aims to "make the first global survey of Earth's surface water, observe the fine details of the ocean's surface topography, and measure how waterbodies change over time" (NASA, 2021).

The sensor utilises SAR interferometry (see Section 9.4) to produce a map of sea surface height across a swath approximately 120 km in width (see Figure 12.3). SWOT represents a radical step forward from traditional, nadir-sampling altimeters, to more readily provide two-dimensional maps of sea surface topography that characterise significant mesoscale ocean features at a scale that has not previously been possible (see Figure 12.4). The high spatial resolution will also permit altimetry measurements much closer to the coast.

Figure 12.3 Operation of SWOT

The SWOT instrument uses SAR interferometry to map ocean topography and terrestrial surface water topography in two dimensions with a cross-track dimension of 120 km. This total swath is divided into two parallel swaths that each span 50 km in width, with red lines below showing the transmission paths of radar pulses and blue lines showing the reception paths of the radar echoes. Between these two swaths a conventional altimeter tracks the nadir path, which also provides valuable data for calibration and validation.



Source: NASA. Retrieved from: *https://swot.jpl.nasa.gov/resources/104/diagram-of-swot-data-collection*

The first six months of the SWOT mission will consist of a fast sampling period (one-day repeat) with reduced global spatial coverage (see Figure 12.5). During this phase of the mission, the satellite will overfly the Bass Strait calibration site daily, but neither of the other two calibration sites located in the Northern Hemisphere. A substantial field campaign is under development, with the support of the Integrated Marine Observing System (IMOS) and international partners, to gather high spatial resolution *in situ* observations (using GPS/GNSS buoys) during this period when the critical instrument characterisation and performance assessment work will be undertaken.

The fast sampling phase of this new instrument offers an unprecedented opportunity for ocean and coastal observing. Plans for several other campaigns and observations during the fast sampling phase are well advanced, including at other instrumented sites around Australia and in the Southern Ocean. After six months, the mission orbit will change to a science orbit with a 21-day repeat that will offer near-global surface coverage over the remainder of the planned three-year primary spacecraft mission.

Figure 12.4 Simulated SWOT measurements

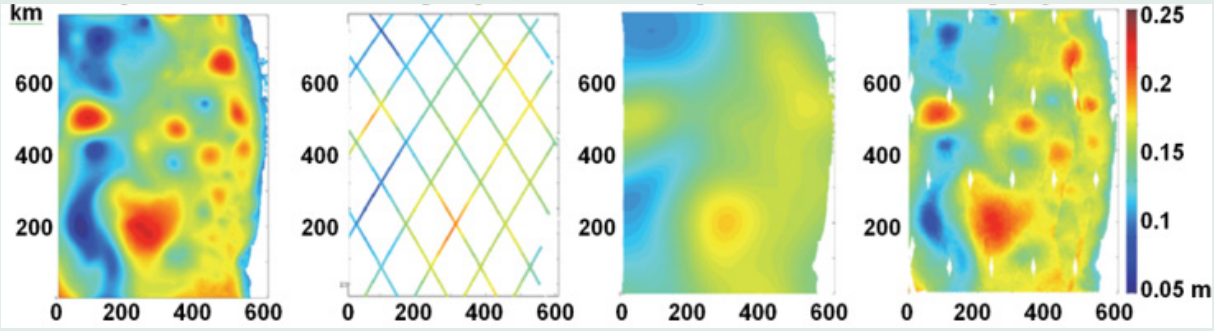
This simulation shows the density of measurements that SWOT will enable, relative to data products previously generated from conventional, nadir-sampling satellite altimeters. Note that the small, white diamonds in Figure 12.4d are gaps between the swath observations.

a. Sea Surface Height (SSH) 'Truth' based on ocean circulation model

b. Jason-1/-2 sampling along ground tracks over one 10-day repeat cycle

c. 2D interpolation of Jason-1/-2 ground tracks

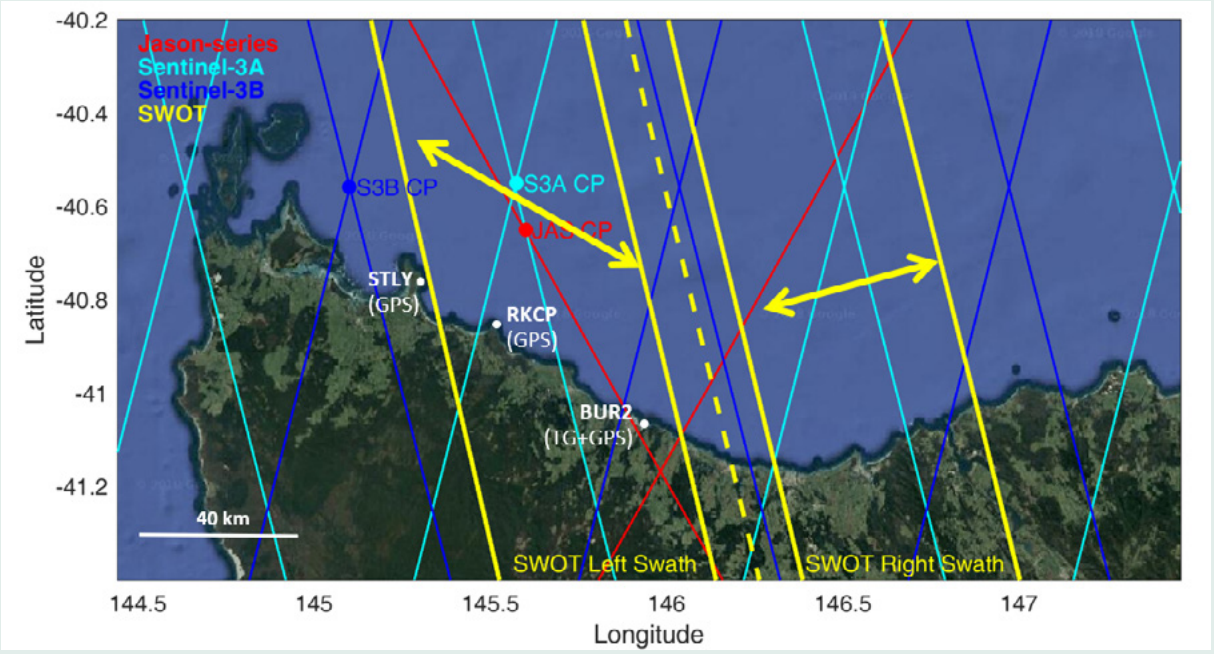
d. Simulated SSH sampled by SWOT swaths over 22-day repeat cycle



Source: Fu and Ubelman (2014)

Figure 12.5 SWOT fast sampling swaths

The location of the SWOT swaths (yellow) during the fast sampling mission phase is shown relative to the Bass Strait altimetry calibration site and the ground tracks of three conventional, nadir-sampling altimeters.



Source: Watson (2018)

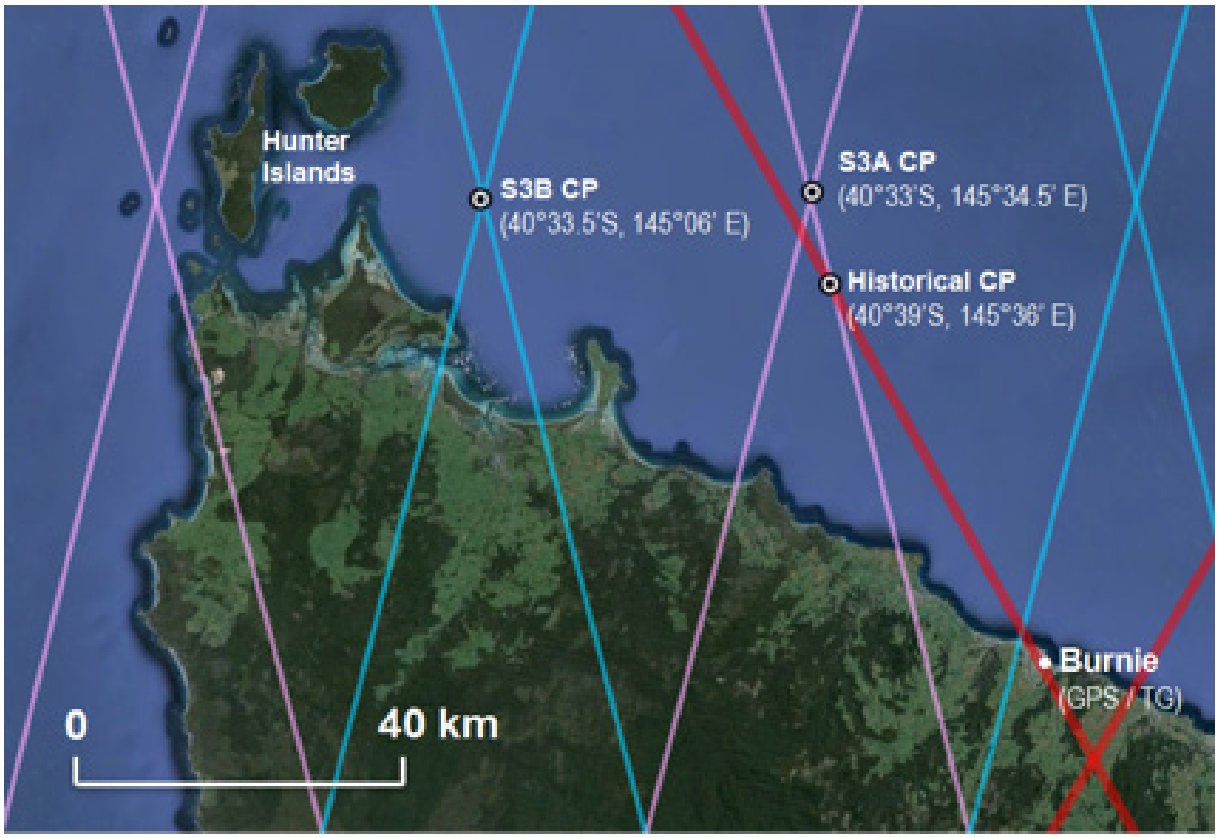
12.2.2 EO sensor calibration

The astonishing accuracy achieved by satellite altimeters is realised not only by excellent instrumentation engineering and precise orbit determination in space (see Section 12.4.3), but also through careful and thorough calibration and validation (cal/val) efforts at the Earth's surface (see Volume 2D). The aim of the *in situ* measurement program is to enable sea level data to be compared directly with observations from satellite altimeter instruments, so that the space-based observations are not only accurate and precise, but also that they can be tied to global reference frames. A series of continuous measurements and short campaigns is necessary to deliver this result.

Australia has played a critical role throughout the modern precision altimetry era via a series of moorings and buoy deployments in Bass Strait (see Figure 12.6). These deployments, which are one of only three such altimetry cal/val sites globally, and the only one in the Southern Hemisphere, have been operated since 1992 by CSIRO, the University of Tasmania and partners and, since 2007, with the support of IMOS (see Volume 2D—Excursus 12.3).

Figure 12.6 *In situ* measurement sites

Mooring deployment sites off northwest Tasmania showing the ground tracks of TOPEX and Jason series missions in red and the Sentinel-3A and -3B ground tracks in pink and blue respectively.

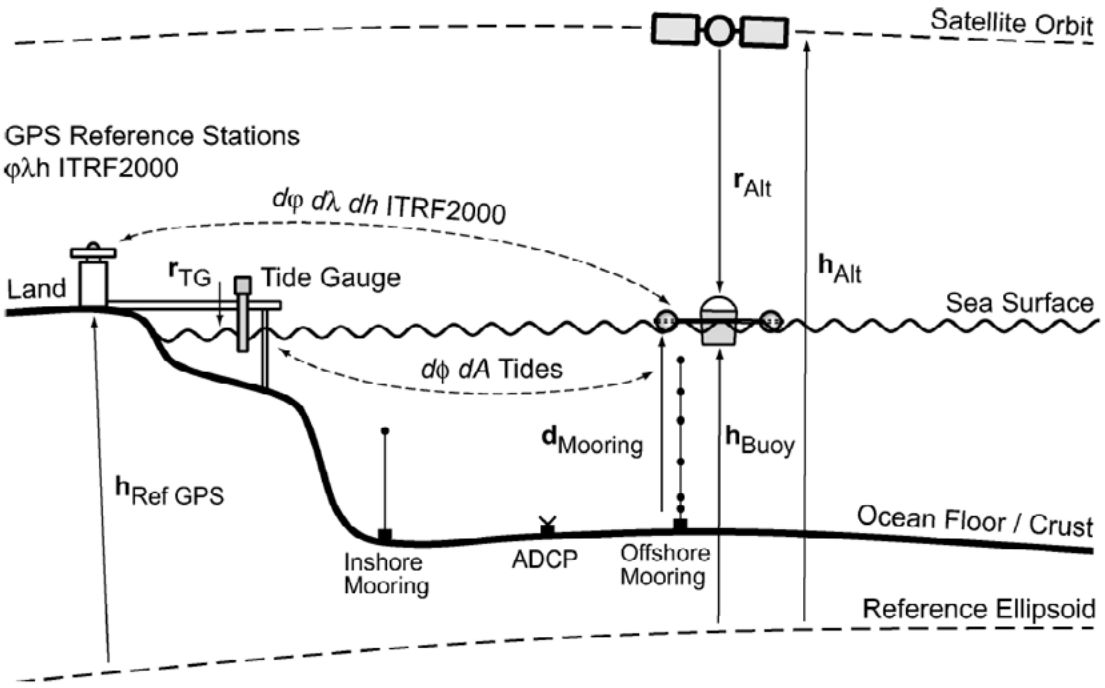


The Bass Strait site was originally located on a descending track of the TOPEX/Poseidon mission, sufficiently far from the coast that the altimeter signal would not be affected by land, but close to the tide gauge located at Burnie port. The water depth is approximately 50 m at this site. This particular ground track also passes close to the satellite laser ranging station at Orroral Valley in the ACT (White *et al.*, 1994). The position and the number of moorings has evolved over the past decade to support the Sentinel-3A and -3B altimeter missions that (because they are flown on satellites with other instruments and missions) have different orbits to the TOPEX/Jason series.

The primary instrumentation used at the calibration site is a high precision pressure sensor at the base of each mooring. Several temperature and salinity instruments are distributed through the water column (see Excursus 5.1). Together, this combination permits an assessment of the water column density, and in turn, measurement of the height of the water column. This represents a measurement of sea level relative to the base of the mooring, where the pressure sensor is located. When the sites are serviced (approximately every six months) collocated GPS buoys are deployed to enable the mooring observations to be tied to the terrestrial reference frame (see Figure 12.7). The coastal tide gauge at Burnie, collocated with a GPS receiver, is transformed (via several corrections) to provide a continuous connection between the mooring and the reference frame in between the periodic GPS buoy deployments (see Figure 12.8). The outcome of this process is the delivery of a record of 'absolute bias' for the satellite altimeter for each overpass, something that has been achieved at this site throughout the modern satellite altimetry era. The absolute bias is a comparison of the satellite altimeter signal with an independent measurement of sea surface height. Monitoring the absolute bias enables estimation of various contributors to the altimeter measurement, such as atmospheric delays and uncertainties in various instrument characteristics, to be understood, and ultimately leads to an improved altimeter data record.

Figure 12.7 Example calibration site

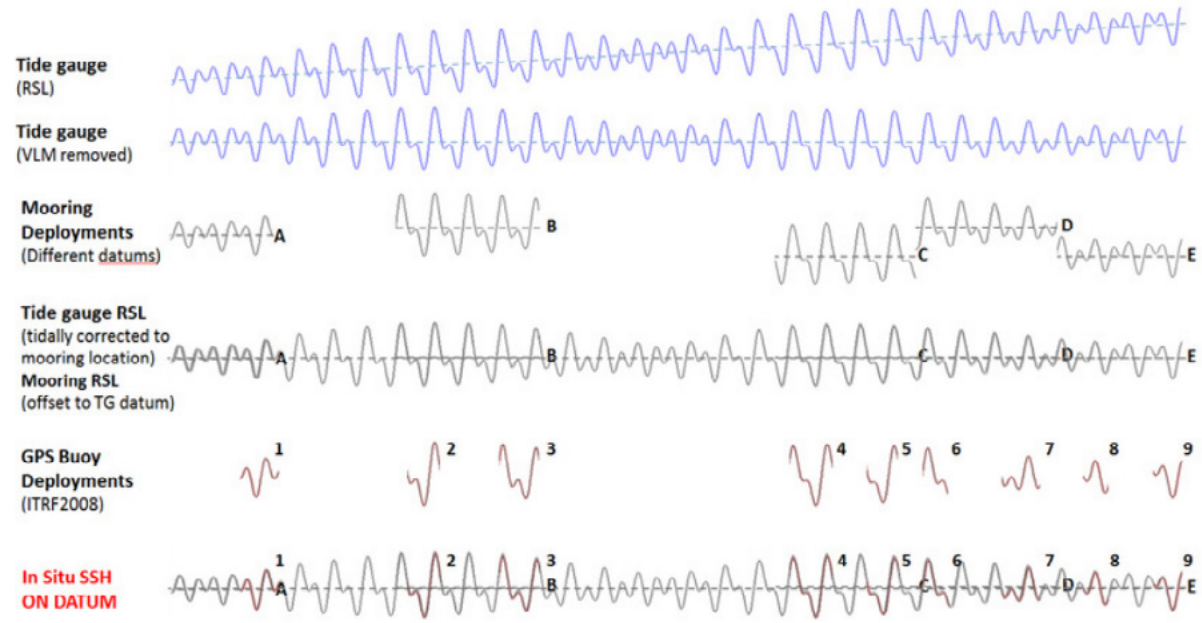
Geometry of the Bass Strait calibration site and associated instrumentation



Source: Watson *et al.* (2004)

Figure 12.8 Converting mooring measurements into datum

Process whereby the tide gauge observations, mooring deployments and periodic GPS buoy deployments are combined to transform the mooring measurements into the datum. RSL: relative sea level, VLM: vertical land motion, TG: tide gauge, ITRF2008: GPS reference frame.

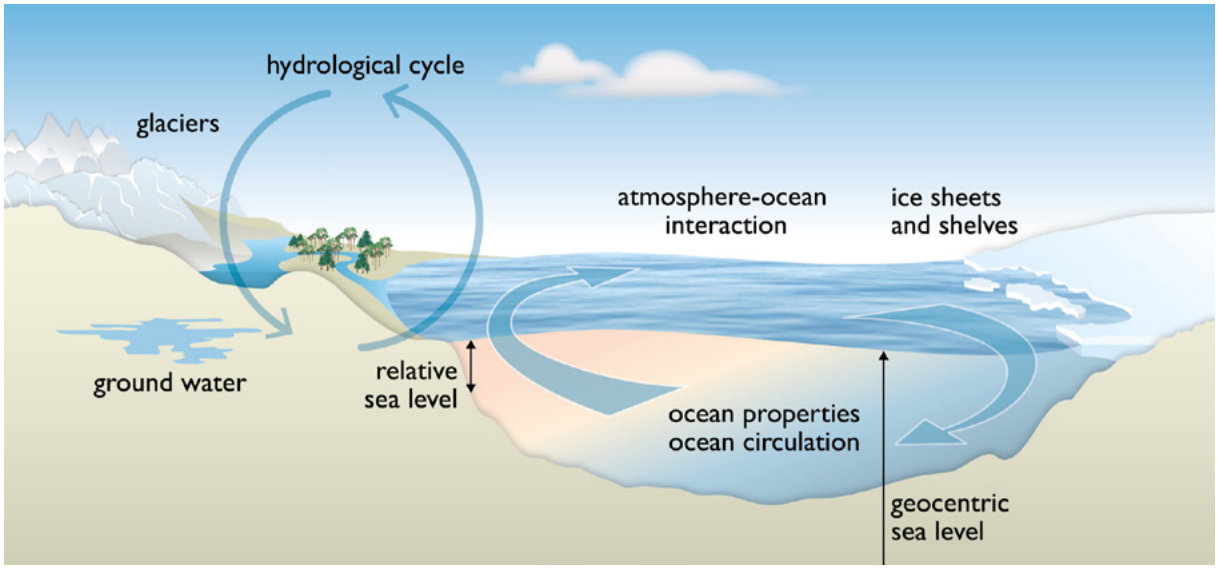


Source: Watson *et al.* (2018)

12.3 Causes of Change in Sea Level

Sea level varies as the volume of water in the oceans of the world changes. This can occur as water is exchanged with other reservoirs including the atmosphere, the cryosphere, and terrestrial storages (see Figure 12.9). Another important cause of volume change—either contraction or expansion—is variation in overall density of the ocean as it stores (or releases) heat. Other changes in sea level arise from localised forcing by the atmosphere, temperature and salinity variation, basin scale circulation, and tides. Relative sea level (measured with respect to land) can change slowly as land is uplifted or subsides over decadal to century time scales, and also abruptly in response to earthquakes.

Figure 12.9 Factors affecting sea level at a range of spatial and temporal scales



Source: IPCC AR5 Report

12.3.1 Short term change

Over periods of hours to days, sea level change is driven primarily by tides, the atmosphere (pressure and wind), and sometimes by geological events such as earthquakes or landslides that involve displacement of the crust resulting in tsunamis. Tides arise predictably from the motions of astronomical bodies (primarily the Moon and Sun) relative to the Earth (see Excursus 4.1 and Section 12.1) .

The sea surface responds to the mass of the atmosphere overlying it. High pressure weather systems depress the sea surface whereas lows permit it to increase. This effect, known as the inverse barometer, is about 1 cm of sea level rise for every 1 hPa decrease in atmospheric pressure. Intense low pressure systems, such as tropical lows and cyclones, can result in sea level increases of the order of 1 m. In the open ocean this is of little consequence but nearer to the coast it can be very significant. In areas without a steep coastal interface (such as modest cliffs) a storm surge coinciding with high tide can easily overtop coastal infrastructure and defences leading to substantial damage from both the force of the water as well as localised flooding inland.

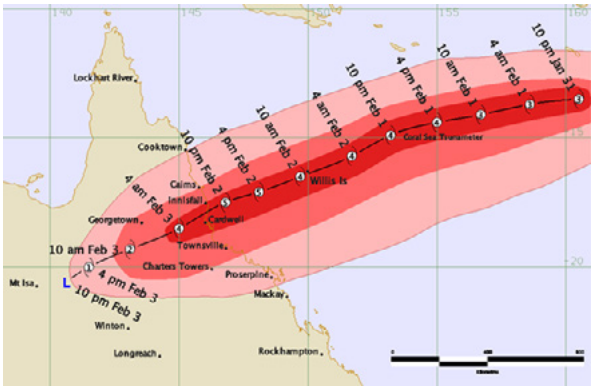
Powerful storms also bring strong winds that induce localised surface currents in shallow water. When directed towards the shoreline this wind stress results in a piling up of water along the coast, known as wind setup, that adds to the storm surge. When this occurs within semi-enclosed embayments that constrain the along-coast flow of the water, the effect can be further amplified. An extreme example of this occurred in northern Queensland when the very powerful Tropical Cyclone Yasi crossed the coast just north of the town of Cardwell. The clockwise rotation of the cyclone, together with the motion of the whole system towards the southwest, led to the strongest onshore winds occurring immediately to the south of the cyclone track (see Figure 12.10). The recorded storm surge was 5 m above the predicted tide, which was falling at the time. Nevertheless the surge amounted to a 2.3 m excess over the highest astronomical tide and caused significant damage.

Away from the equator, when the wind stress is parallel to the coast, the impact of the Coriolis force on the induced currents is important (see Excursus 1.2). The deflection of ocean water towards or away from the coast (depending on current direction and hemisphere) results in a reduction or increase in relative water level at the coast, known as current setup (or setdown).

Figure 12.10 Tropic Cyclone Yasi

In 2011 one of the largest tropical cyclones, TC Yasi, crossed the Queensland coast just north of Cardwell resulting in damage to buildings and the Bruce Highway at the water front.

a. Location of cyclone



b. Waterfront damage

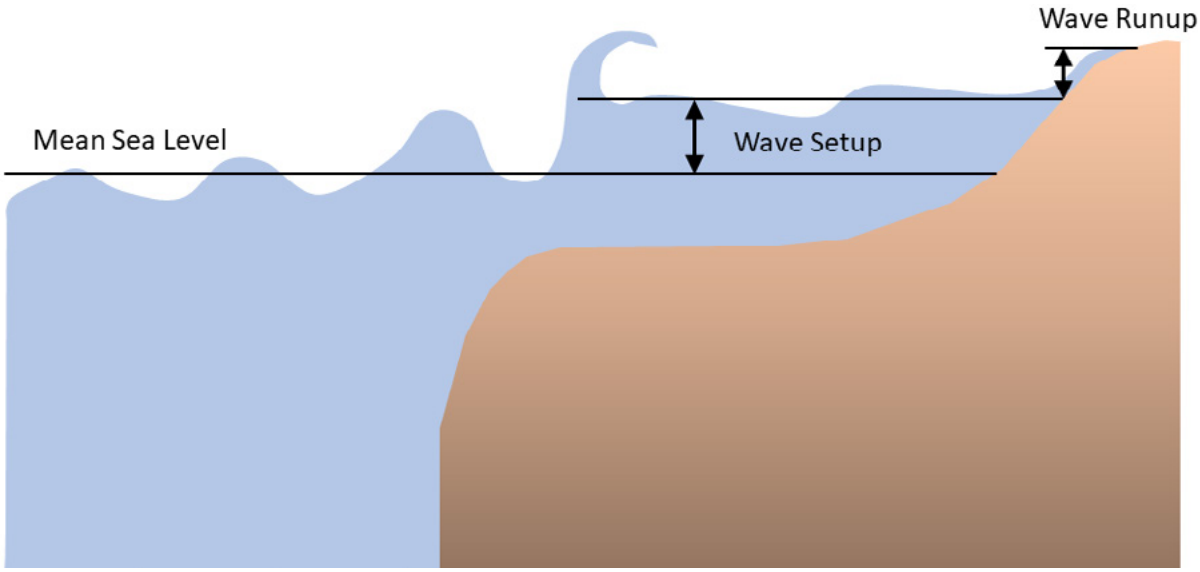


Source: a. Bureau of Meteorology. Retrieved from: *http://www.bom.gov.au/cyclone/history/yasi.shtml*; b. Paul Crock, AFP. Retrieved from: *http://desdemonadespair.net/2011/02/photo-gallery-aftermath-of-cyclone-yasi.html*

Surface waves, whether part of a local storm or arriving as swell from distant storms, also impact coastal sea levels (see Excursus 4.2 and Section 16). Waves steepen and eventually break as they reach shallow water. When the water close to the coast is deep (for example, isolated islands in the open ocean), the energy carried within waves is delivered directly to the shore. In contrast, when coastal waters are shallower (see Figure 12.11), such as in broad continental shelves or fringing reef systems, the wave energy is dissipated further offshore. As the waves break offshore, their energy can be transferred into shoreward momentum of the water at the break, which then increases the sea level closer to the shore. This process, analogous to wind setup but driven by wave energy, is called wave setup. The specific geometry of the actual shoreline (steep or shallow gradient) combines with the incoming waves to determine the reach of the sea inland. This phenomenon is known as wave runup and is superimposed on the underlying sea level (that would be experienced in the absence of waves, for example, due to tide).

Figure 12.11 Wave setup

Wave setup occurs when the energy of waves breaking offshore translates into increased sea levels inshore. Wave runup is the additional sea surface height resulting from individual waves reaching and running up the shore itself.



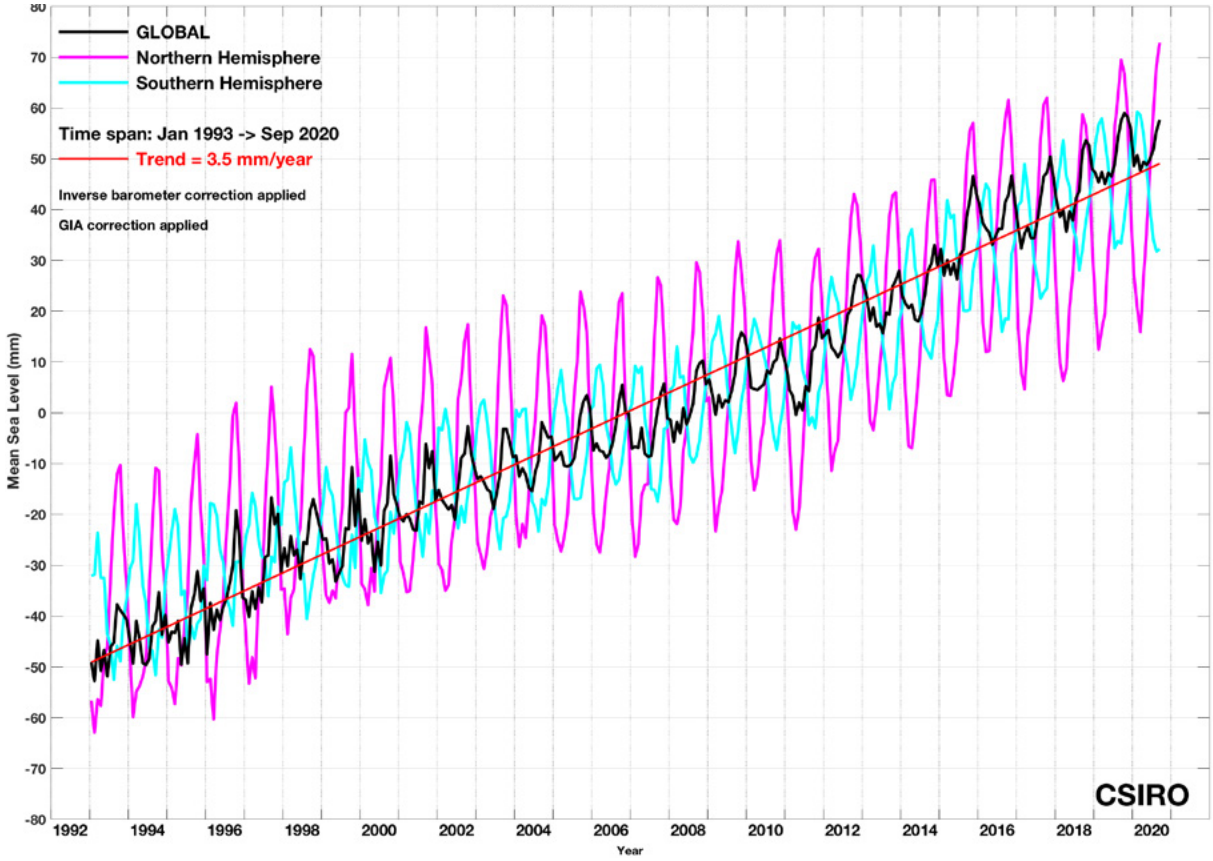
Tsunamis are a special and sometimes extreme case of surface waves impacting sea levels. Some subsea earthquakes result in rapid displacement of the seafloor imparting an impulse into the ocean, which propagates as a long wavelength wave. In the open (deep) ocean, tsunami travel at ~700 km/hr and may be observed as a small vertical displacement (~0.5–1 m). (For example, see the serendipitous satellite altimeter observations of the 2004 Indian Ocean tsunami; Gower, 2005; *https://www.eumetsat.int/satellite-observations-indian-ocean-tsunami*). When the tsunami reaches shallow water it slows to 10–20 km/hr and the crest height increases significantly, up to 10–15 m. In the case of the 2011 Japanese earthquake, flatter areas of the coast were flooded many kilometres inland when the wave overtopped the shoreline. Large tsunamis are immensely destructive—the 2004 Indian Ocean and 2011 Japanese events resulted in estimates of 230,000 and 15,000 deaths respectively. Although tsunamis are usually isolated events, the sea level rise and subsequent return of the water to the sea can last for several hours.

12.3.2 Seasonal to decadal change

The inclination of the Earth's rotational axis to the plane of the orbit around the Sun leads to differential heating in the Northern and Southern Hemispheres over the course of one orbit (see Volume 1A—Section 3.1). This gives rise to the pronounced seasonal weather and climate changes experienced each year. A more subtle impact is on global sea levels. The additional summer heat is absorbed by the ocean in one hemisphere whilst the winter ocean in the opposite hemisphere loses the heat gained in the previous summer. The warmer water is less dense and so occupies a greater volume per unit mass causing a rise in sea level. Consequently the volumes of the Southern and Northern oceans increase and decrease cyclically with opposite phase (see Figure 12.12). However, the effect on sea level is not the same in both hemispheres, with amplitudes of approximately 20 mm in the Southern Hemisphere and 30 mm in the Northern. In the northern winter, the greater land mass results in greater storage of water as ice and snow. This reservoir is released back to the Northern Hemisphere oceans in spring and summer, enhancing the seasonal change in sea levels. As a result, the average sea level across the global ocean contains a small residual seasonal component of 5–10 mm amplitude. Seasonal changes in the atmosphere also result in smaller seasonal changes in sea levels. These include the mean position of the paths of weather features such as low and high pressure systems (affecting sea level via the inverse barometer), and the cyclic strengthening and weakening in surface winds that drive ocean surface currents. These currents transport warm and cold water, so affect ocean density and, in turn, sea level.

Figure 12.12 Mean sea level

Mean sea level in the Northern and Southern Hemispheres over the period 1993–2012 from TOPEX/Poseidon, Jason-1, Jason-2 and Jason-3 satellite altimeter data. The Northern Hemisphere signal is enhanced by the greater storage of water on land as snow and ice during winter. This disparity is visible in the total global sea level as a small residual seasonal variation.



Source: Benoit Legresy, CSIRO

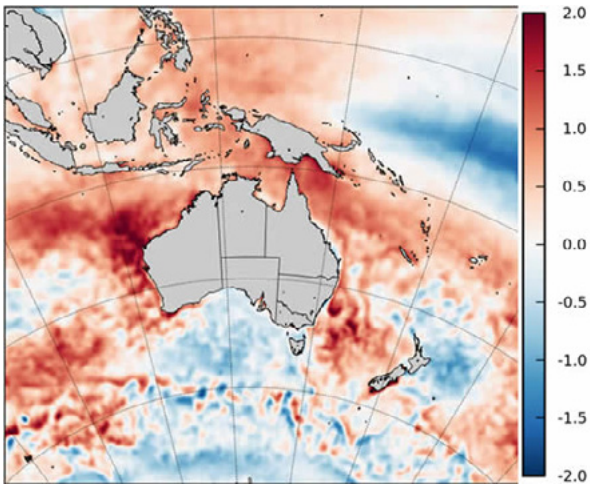
Figure 12.13 Ocean-climate system variability

Examples of sea surface temperature anomalies around Australia

a. Location of the western Pacific warm pool



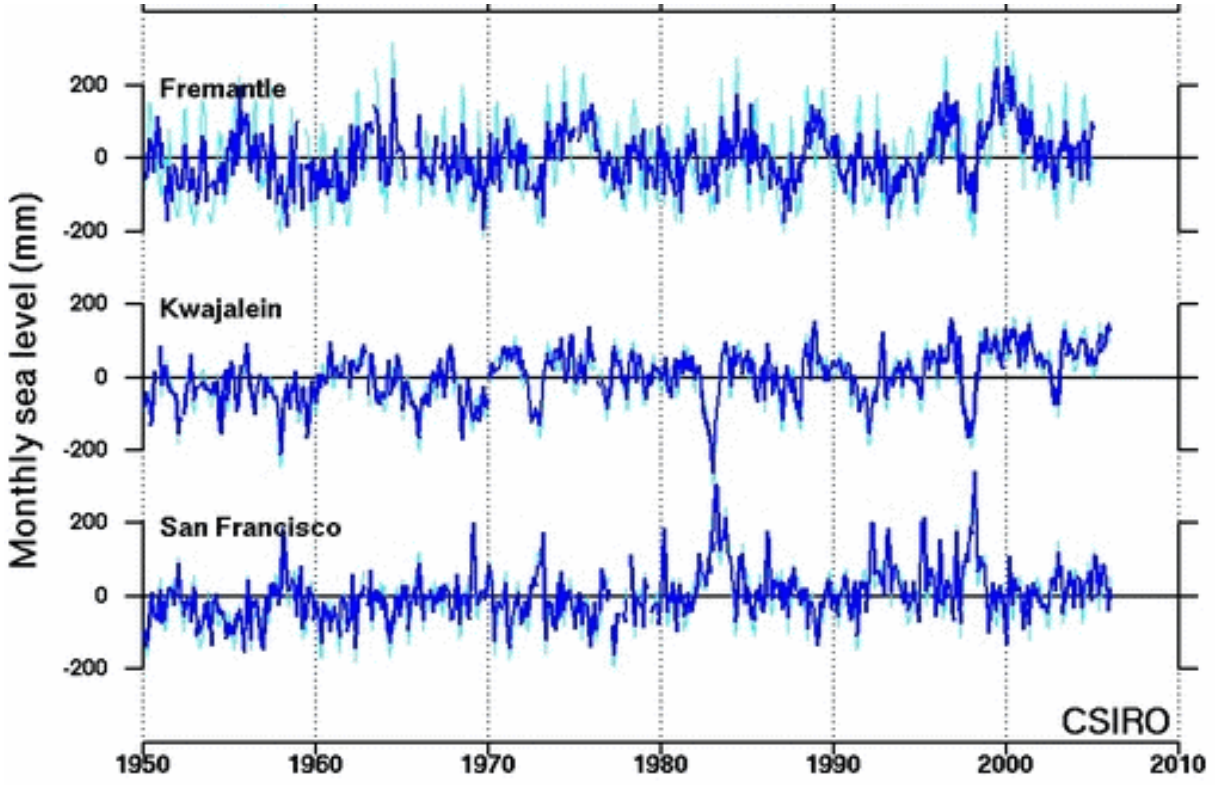
b. Increased sea surface temperature anomalies (°C) across Northern Australia following a strong La Nina event (May 2010–April 2011)



Source: Bureau of Meteorology. Retrieved from a. *http://www.bom.gov.au/climate/enso/history/ln-2010-12/ENSO-what.shtml*; b. *http://www.bom.gov.au/climate/enso/history/ln-2010-12/SST-records.shtml)*

Figure 12.14 Tide gauge records

Monthly (light blue) tide gauge records over 55 years from Fremantle (southwest Western Australia), Kwajalein Atoll (Western Pacific), and San Francisco (Eastern Pacific). The same records with the annual seasonal signal removed are shown in dark blue.



Over periods of years and up to a decade, variability in the ocean-climate system can be detected as sea level change at regional to ocean scales. For example, the El Niño/La Niña oscillation involves changes in the warm pool of surface water in the Western Pacific Ocean over periods of several years (see Figure 12.13a). The size of the pool is strongly affected by the strength of the easterly trade winds in the equatorial Pacific. During strong events there can be sustained changes in ocean surface temperature (see Figure 12.13b) and relative sea level between the Eastern and Western Pacific of the order of 20–30 mm. The tide gauge records shown in Figure 12.14 illustrate this with the strong opposite signals in the San Francisco and Kwajalein records at the time of strong El Niño events in 1983 and 1997. Similar effects can be traced to other long term climate variations such as the Indian Ocean Dipole and Pacific Decadal Oscillation.

12.3.3 Longer term change

Several processes affect global sea levels over much longer periods, from years to decades to centuries. As indicated in Figure 12.9, exchange of water between the ocean, the cryosphere, and the terrestrial hydrosphere is an important factor. Over the longer term, change in the overall heat content of the ocean changes the water density, which is observable as a change in sea level. Change in ocean density due to variation in salinity can also make a very small contribution.

The ocean absorbs 93% of the additional heat trapped in the Earth System by the increased concentrations of greenhouse gases in the atmosphere. The resulting expansion of oceanic water contributes to 1–1.4 mm per year of rise in global sea level. This single factor accounts for a third of global sea level rise observed over the past several decades.

The cryosphere comprises the ice-covered regions of the globe, namely the polar regions (including floating sea ice and terrestrial ice sheets) and the non-polar glaciers (at any latitude but with sufficient altitude for persistent ice; see Section 15). With the Earth in thermal equilibrium, the net quantity of ice stored in the cryosphere is constant over the longer term. The warming of the atmosphere however is leading to erosion of the cryosphere via melting. The contribution of non-polar glacier melt to global sea level rise over the past 40–50 years is 0.6–0.7 mm per year. Direct melting of the Greenland and Antarctic ice sheets has contributed around 0.7 mm per year to global sea level rise in recent decades. Wherever the polar ice is in contact with the ocean, the warmer ocean is also contributing to the melt. Ocean transport of heat from the tropics to the Antarctic ice

sheet, much of which is grounded below sea level, is expected to be an important factor controlling the rate of future sea level rise. The volumes of water stored within the cryosphere are immense, with non-polar glaciers, Greenland, and Antarctica equating to approximately 60 cm, 6 m, and 60 m of potential sea level rise respectively. It is interesting to note that as ice sheets melt and the water runs into the ocean, the decreased mass loading locally allows the underlying crust to rise. This leads to the paradoxical result that, for example, loss of the Antarctic ice sheet will increase relative sea levels less in Antarctica than in locations remote from the source of the additional water.

Other (non-frozen) terrestrial reservoirs exchange water with the oceans via runoff, evaporation, and precipitation (see Section 1.1). Primarily these reservoirs are surface water (rivers, lakes, dam impoundments) and groundwater. Periods of increased dam building in the middle of the 20th century are detectable as a small decease in the rate of Global-Mean Sea Level (GMSL) rise (see Section 4.1). More recently, increased usage of groundwater aquifers for irrigation and other freshwater needs, ultimately delivers terrestrial water to the ocean via runoff (or evaporation and precipitation), contributing to an increase in sea level rise. More information, including a thorough analysis of the quantitative factors involved in these processes, can be found in the Sea Level Change chapter of the IPCFC 5th Assessment report (Church *et al.*, 2013).

12.4 Measuring Sea Level

Contemporary sea level is observed via two primary methods: tide gauges and satellite altimetry. Below we consider two traditional methods used to measure sea level, paleo indicators (see Section 12.4.1) and tide gauges (see Section 12.4.2), then describe the relatively recent option of satellite altimetry (see Section 12.4.3).

12.4.1 Paleo indicators

Before the tide gauge era, knowledge of historical sea levels was derived from paleo indicators, which are markers of past sea levels captured in the natural and human-built environment. Natural markers include geomorphological features such as raised beaches, notches cut by waves, and also fossilised sea life. Of particular value is the record of plants that are known only to exist within a narrow vertical range of the upper limit of the tidal influence in coastal (salt) marshes. The human record comprises buildings originally created at sea level that are now either submerged or elevated, or traces of the impacts of sea action or sea life on historical buildings.

All of these markers are of relative sea level and so apply only locally. This is because they are confounded by uplift and subsidence of the crust over the passage of time. Nevertheless they provide evidence of past sea level change and place some constraints on its likely magnitude.

12.4.2 Tide gauges

Tide gauges are intended to provide a means of observing local short term changes in relative sea level arising from the astronomical tides (see Excursus 4.1), relevant to port operations and other maritime activities. Originally they involved manual recording of high and low tide and their time of occurrence in written form. Progressive automation and improvements in instrumentation have increased the density of the records across the whole of the tide cycle.

Over the longer term, they also provide a record of the sea level range relative to a local reference point. The challenge in using tide gauge records to infer long term sea level change arises in tracking the vertical motion of the reference point relative to a geocentric reference ellipsoid. This motion can arise over a range of time scales from a variety of causes, which can be either gradual or discrete:

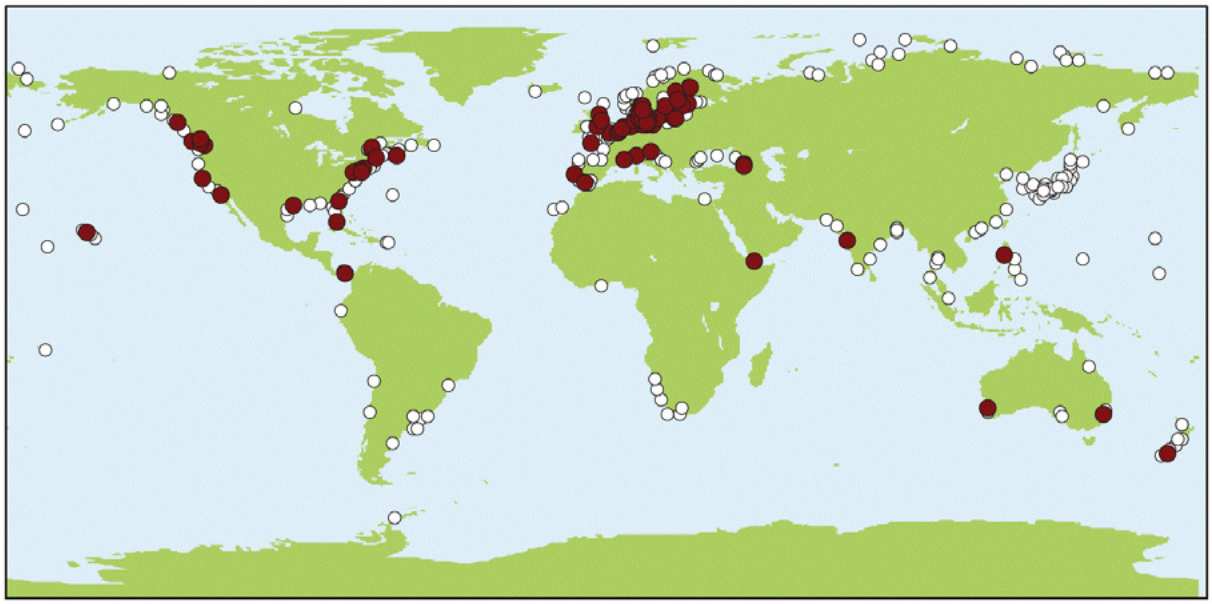
- gradual subsidence of either the structure or land upon which the gauge is mounted;
- differences in mounting point as instrumentation is changed or upgraded;
- rapid movement resulting from earthquakes; or
- rising and falling of the crust as part of slow continental motion.

Improvements in instrumentation over decades, or even centuries, of observation also increase the precision of the observations over time, leading to greater relative uncertainty for the earlier part of long-lived tide gauge stations.

Since 1933 the Permanent Service for MSL (PSMSL, *www.psmsl.org*) has been compiling global tide gauge observations and attempting to account for the various effects enumerated above. Although the longest records are concentrated in the Northern Hemisphere, particularly in Europe (see Figure 12.15), the PSMSL dataset provides a high quality record over the most recent few centuries.

Figure 12.15 PSMSL tide gauge stations

Tide gauge stations within the Permanent Service for MSL dataset. 291 gauges have 50+ year records (shown as white dots) and 74 gauges have 100+ year records (shown as red). The longest records are overwhelmingly in the Northern Hemisphere.

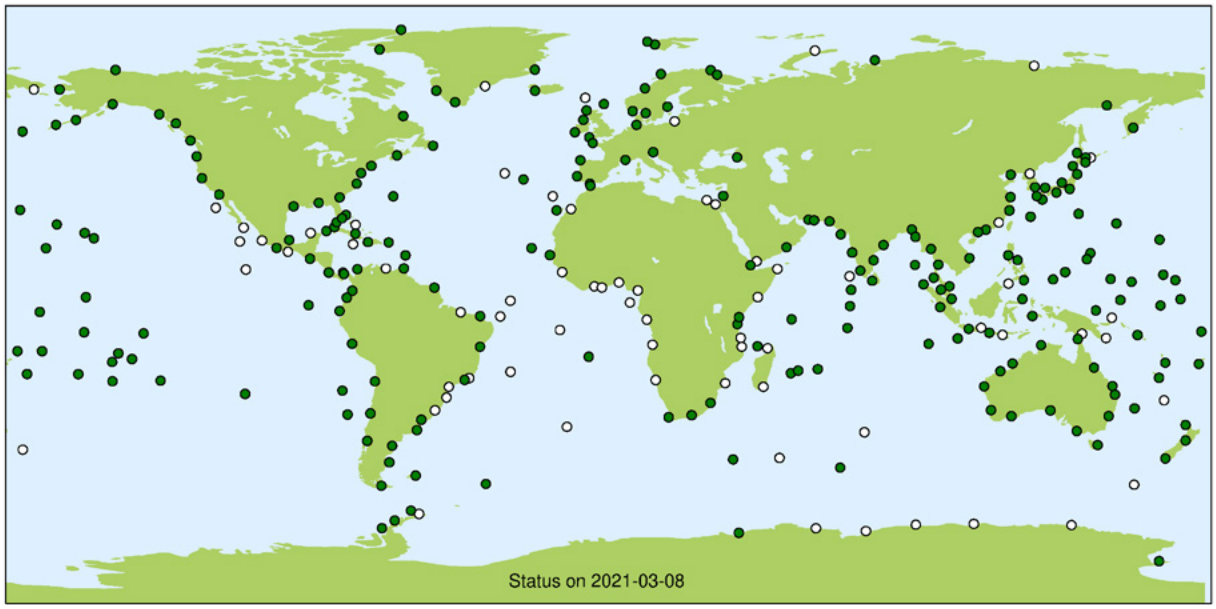


Source: Tamisea *et al.* (2013).

To improve monitoring of sea level over what PSMSL achieved, in 1985 the International Oceanographic Commission (IOC), within the United Nations Educational, Scientific and Cultural Organisation (UNESCO) founded the Global Sea Level Observing System (GLOSS, *https://www.gloss-sealevel.org/*) as a component of the Global Ocean Observing System (GOOS). The GLOSS system provides a means of coordinating tide gauge networks, and standardising quality control. The GLOSS Core Network (GCN; see Figure 12.16) is a set of about 300 stations distributed more uniformly globally. Many are on islands to maximise observations of the open ocean, rather than in coastal and marginal seas where local shelf bathymetry and topographic effects are more pronounced.

Figure 12.16 GLOSS network of tide gauge stations

The 224 active gauges are shown as green dots and 70 inactive gauges are shown as white.



Source: GLOSS. Retrieved from *https://www.gloss-sealevel.org/operational-status*

Modern tide gauge stations record automatically at relatively high frequency (on the order of minutes), so are able to capture observations of short term phenomena such as storm surges and tsunamis. It is worth noting that some modern tide gauges now measure subsurface pressure. This differs from sea level because it includes atmospheric pressure (the inverse barometer effect), which needs to be taken into account to retrieve a measurement of the actual sea surface height measurement. In Australia, the National Tidal Centre at the Bureau of Meteorology (see Excursus 12.2) is the national repository for tide gauge data, including most high frequency observations.

Excursus 12.2—The National Operations Centre (NOC) Tidal Unit

Source: Bureau of Meteorology
Further Information: *http://www.bom.gov.au/oceanography/projects/ntc/ntc.shtml*; *http://www.bom.gov.au/oceanography/projects/abslmp/abslmp.shtml*

The National Operations Centre (NOC) Tidal Unit at the Bureau of Meteorology is the primary source of tide tables, tidal streams, and tidal constituents provided to the Australian Hydrographic Service (AHS). The Tidal Unit also manages the national data archive for sea levels and tides. This unit manages the Australian Baseline Sea Level Monitoring Project (ABSLMP), which is designed to monitor sea level around the coastline of Australia (see Section 12.7). The ultimate goal is to identify long period sea level changes, with particular emphasis on the enhanced greenhouse effect on sea level.

As part of ABSLMP, the Bureau of Meteorology maintains an array of SEAFRAME (SEA-Level Fine Resolution Acoustic Measuring Equipment) stations, which measure sea level very accurately, and record meteorological parameters (water temperature, air temperature, barometric pressure, wind direction, wind gust and wind speed). The array consists of fourteen standard stations distributed around the Australian coast (Darwin, Milner Bay, Thursday Island, Cape Ferguson, Rosslyn Bay, Port Kembla, Burnie, Portland, Port Stanvac, Thevenard, Esperance, Hillarys, and Broome) and on Cocos Keeling Islands, plus two supplementary stations (Lorne and Stony Point). The vertical stability of the gauges is surveyed by State organisations, while Geoscience Australia (GA) maintain earth monitoring installations for geodetic observations at each location, including Global Navigation Satellite System (GNSS) to determine accurate vertical height of the tide gauges. Survey data is archived by GA, with all data being available online.

The Pacific Sea Level and Geodetic Monitoring (PSLGM) project (a continuation of the 20-year South Pacific Sea Level and Climate Monitoring Project, SPSLCMP, which operates under the Climate and Oceans Support Program in the Pacific, COSPPac) provides sea level and meteorological information for 14 countries (Cook Islands, Federated States of Micronesia, Fiji, Kiribati, Marshall Islands, Nauru, Niue, Palau, Papua New Guinea, Samoa, Solomon Islands, Tonga, Tuvalu and Vanuatu), and tide predictions for 17 locations in the Pacific region. Only one of the participating countries (Palau) does not host a permanent tide gauge facility, which provides information on sea levels and tides. This network includes earth monitoring stations for geodetic observations, maintained and implemented by GA. PSLGM provides information about the processes, scale and implications of sea level rise and variability of extreme events on South Pacific communities, and makes sea level data more readily available and usable to support management of coastal infrastructure and industries. It is an important resource for those involved in disaster mitigation and adaptation planning, coastal development, and the shipping, fishing and tourism industries.

12.4.3 Satellite altimetry

The prospect of using spaceborne instrumentation to measure sea level represents a step change, both in spatial coverage and, in the open ocean away from tide gauge stations, in temporal coverage. To determine the range or distance to the sea surface, altimeters use radar, which measures the time a transmitted radio pulse takes to reflect from the ocean surface and return to the spacecraft (see Sections 9.5 and 12.2.1).

The earliest satellite altimeters were flown experimentally during the 1970s, initially on Skylab, Geos-3 and then the short-lived Seasat mission in 1978. Eventually the launch of the joint US/French TOPEX/Poseidon mission in late 1992, initiated the modern era of continuous, high quality, satellite altimetry. This mission has been followed by Jason-1/-2/-3, and in 2021, by the Sentinel-6 missions. Several other satellite altimetry missions have been flown that have complemented this core time series (see Table 12.2). The SWOT mission planned for 2022/23 will carry a novel experimental imaging altimeter (see Excursus 12.1).

12.4.3.1 Instrument operation

Four essential components are required to achieve highly accurate, sea level measurements from a satellite altimeter:

- radar instrumentation that permits a high precision measurement;
- capacity to account for natural factors that affect the observation;
- ability to track the satellite altitude relative to the geocentre with centimetre accuracy; and
- sufficient knowledge of the surface conditions to separate short term and local effects from the underlying persistent sea level.

Several factors affect the choice of radio frequency used for an altimeter. Higher frequencies allow a narrower beam width for a given transmission antenna size (a critical factor for satellite platforms), and permit enough bandwidth to deliver a sharp enough pulse to resolve the distance measurement with precision. As the antenna beamwidth increases, the area illuminated on the sea surface increases and the spatial resolution of the instrument is degraded. An additional constraint is the sensitivity of the signal to perturbation in the atmosphere and ionosphere. Although the atmosphere is transparent at the frequency used, it attenuates and delays the radar pulse depending on its composition and density. The most commonly used frequency is Ku Band (13.6 GHz, 2.2 cm wavelength; see Table 9.2 and Volume 1B—Section 8). Modern altimeters operate a second system at S or C band (3–5 GHz) where there is greater sensitivity to ionospheric delays, enabling a dynamic quantification and correction of the effect.

In addition to the active radar altimeter, a passive microwave radiometer (see Section 9.2) is also usually part of the instrument suite carried on sea surface altimetry missions. The microwave radiometer is used to estimate the water vapour content of the atmosphere along the pulse path, enabling corrections to be applied to the altimeter measurement since water vapour delays the pulse.

A non-smooth sea surface is not uniformly reflective, with wave troughs providing a stronger return than crests. The 'shape' of the returned altimeter pulse allows wind speed and wave height to be estimated, which enables correction of the trough/crest effect. For this reason it is not enough to simply measure the time of return of the leading edge of the pulse—it must also be sampled with sufficient frequency to determine its shape.

Since a satellite altimeter is making a range measurement from a moving platform, any uncertainty in the position of the platform impacts the ultimate value of the range measurement. The task of minimising that uncertainty has given rise to precision orbit determination—a suite of techniques to model and track the satellite path in orbit (see Volume 1A—Excursus 3.2 for a review of Space Geodesy). The satellite tracking system typically has three components based on overlapping, but complementary, methods:

- Satellite global positioning systems (GPS) are used in the same way as GPS receivers on the Earth's surface, by ranging to a constellation of reference satellites that are transmitting positional information (see Volume 1B—Section 10.3). GPS currently provides a three-dimensional positional accuracy of ~3 cm.
- Satellite Laser Ranging (SLR) is a technique in which ground-based lasers reflect from corner reflectors mounted on the satellite (see Volume 1A—Section 16.1.2.1). The light travel time measures the range to the satellite from the laser. The International Laser Ranging Service (ILRS) currently comprises around 40 laser ranging stations around the world to undertake these measurements (ILRS, 2021), yielding a three-dimensional positional accuracy of around 3 cm.
- The French system with the acronym DORIS (Doppler Orbitography and Radiopositioning Integrated by Satellite) consists of about 60 fixed beacons located worldwide (IDS, 2021). A DORIS receiver on the spacecraft detects the doppler shift in these signals (arising from the satellite motion) enabling a precise orbit determination.

All these measurement systems are used to refine knowledge of the satellite orbital model, which itself uses a highly accurate gravity model to describe the motion of the satellite. The gravity model is, like the geoid, a spatially varying field that reflects changes in the distribution and density of the mass of the Earth, although it is smoother than the geoid because of the altitude at which satellites orbit (see Volume 1A—Excursus 3.1). The quality of the gravity model is a limiting factor in the precision of orbit determination. Modern gravity models now incorporate the force exerted by the increased or decreased water from the ocean tides on the satellite (see Excursus 1.1). Although satellite altimeters typically orbit at altitudes of 800–1300 km, there is a non-negligible atmospheric drag effect that needs to be accounted for, as well as a small perturbing force from the solar wind.

Finally, in addition to the range corrections due to the wet and dry path delays, sea state bias, etc, two 'corrections' are often applied to mitigate the problem that altimeter observations are sparse in time (with 10 or more days between revisits), so high frequency variability of the sea surface is badly undersampled. The first 'correction' is to use a tidal model to remove the instantaneous effect of the ocean tides, which creates a 'tideless' sea level. Secondly the local atmospheric pressure is used to correct for the inverse barometer effect, where the sea surface is locally depressed by increasing atmospheric pressure.

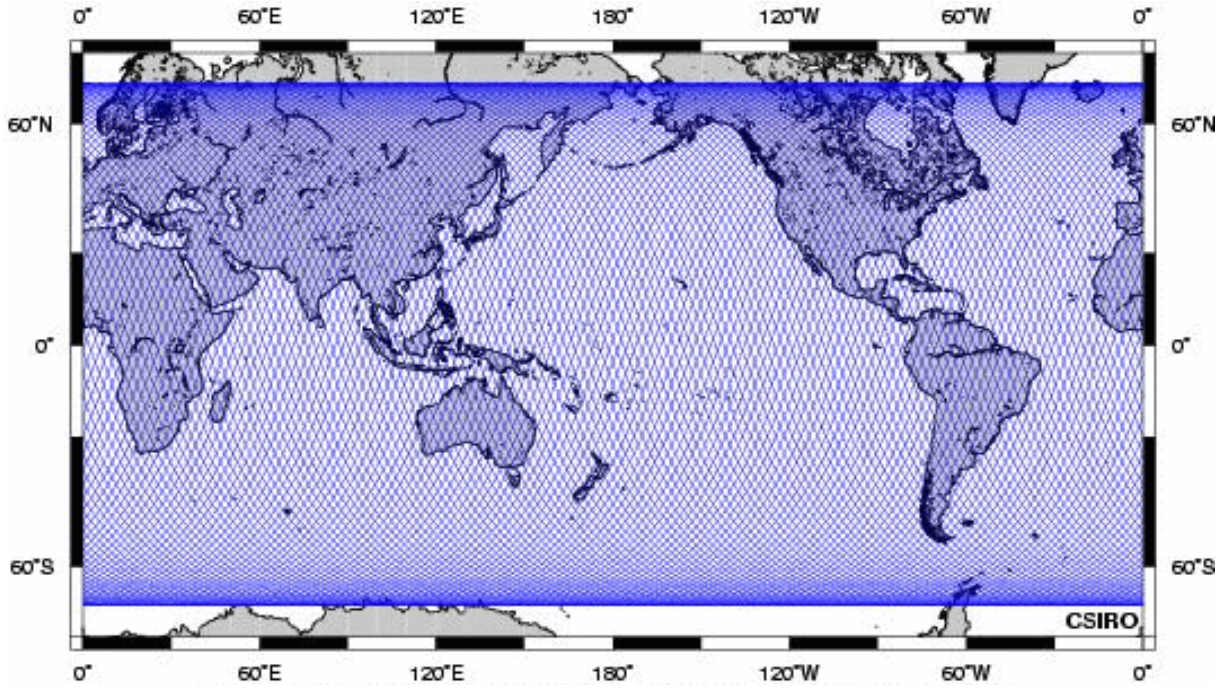
Applying these corrections dealiases the data, but it also changes the way the data is subsequently used. One would not, for example, assimilate the 'fully corrected' altimeter data into an ocean model that simulates coastal inundation.

12.4.3.2 Spatial coverage

The spatial coverage achieved by satellite altimeters depends primarily on the orbit in which they are placed. Each radar pulse illuminates a footprint along the ground track yielding a one-dimensional measurement track across the ocean surface. To derive a two-dimensional coverage, the orbit is arranged so that the ground tracks interleave and cross over many revolutions, ultimately repeating, usually with a 10 day revisit frequency. The spacecraft orbital inclination is usually a compromise to achieve sufficient inclination to cover the majority of the global ocean. To reach the entire ocean surface would require an orbit inclination of 90° (since the North Pole is oceanic), but such an orbit would dramatically decrease the coverage at lower latitudes. The TOPEX/Poseidon orbit was chosen so that it would encompass Drake Passage between South America and Antarctica, but not the polar oceans at latitudes greater than ±66° (see Figure 12.17). In contrast, the Cryosat spacecraft series, which uses a specialised altimeter to measure polar ice caps, is in an orbit that passes within 2° of the Earth's poles.

Figure 12.17 TOPEX/Poseidon altimeter coverage

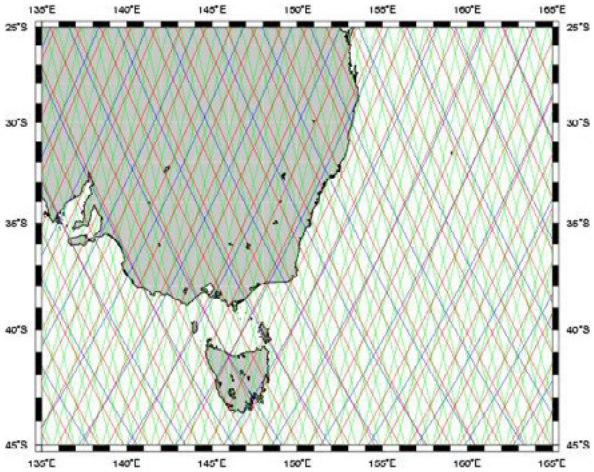
This map shows the ground tracks of a complete 10 day cycle of the TOPEX/Poseidon altimeter mission.



Source: CSIRO

Figure 12.18 Ground tracks of several altimeter missions

Ground tracks of several altimeter missions in southeast Australia are shown: TOPEX/Poseidon and Jason-1 (blue), GEOSAT and GFO (red), and ERS-1/-2 and Envisat (green), with repeat periods of 10, 17 and 35 days respectively.



Source: CSIRO

As illustrated in Figure 12.18, one-dimensional ground tracks never provide complete coverage of the ocean surface. For TOPEX/Poseidon, and the follow-on Jason series, the maximum distance between ground tracks is around 300 km at the equator. Other missions, such as ERS and Envisat-1/-2, reduce this to about 100 km at the equator, but do so at the expense of a much longer revisit cycle (35 compared with 10 days).

12.4.3.3 Tide observations

Historically, most observations of tides have come from tide gauge stations at the coast, or on relatively few isolated islands. Knowledge of tide in the open ocean came almost entirely from hydrodynamic modelling, which was subject to spatially varying uncertainty arising from non-uniform distribution of tide gauge stations and a lack of knowledge about the parameterisation of friction effects. The advent of routine satellite altimetry in 1992 provided the first spatially comprehensive and regular measurements of the tide in the open ocean basins. Although the repeat observation time for any location is typically much longer than the tidal cycle, the predictability of the tidal signal (together with careful choice of satellite orbit) enables its separation from the other oceanographic features affecting the sea level measurement. This in turn has improved our understanding of tidal processes and their modelling. An important result of satellite altimetry therefore has been the reduction in tide estimation errors globally from around 10 cm to the level of 1 cm (see Section 5.3, Cazenave and Fu, 2001; Stammer *et al*., 2014).

12.5 Monitoring Sea Level

The accuracy of sea level monitoring has varied with the advent of modern technologies such as satellite altimetry. Below we review the available trend data from three time spans: geological ages (see Section 12.5.1), recent centuries (see Section 12.5.2), and recent decades (see Section 12.5.3).

12.5.1 In geological ages

Over periods of thousands to tens of thousands of years, our knowledge of sea level comes mostly from geomorphological and fossil evidence (see Section 12.4.1). This knowledge is not only direct but relies also on indicators of the state of the Earth's climate from which the mass balance between the cryosphere and hydrosphere (including the oceans) can be inferred. For example, multiple lines of evidence have established that the Earth underwent a period of substantial glaciation (or ice age) between 115,000 and 11,700 years ago. It is estimated that the release of water from ice at the end of that glaciation led to a rise of global MSL of around 100–120 m.

Similarly there is evidence that during periods in the preceeding 1–3 million years the Earth's temperature was 2–3.5°C higher than during the immediate pre-industrial climate. Accordingly, it is likely that sea levels were substantially higher at times than they are now. The sea level known from the geological record will likely always contain significant inaccuracies since, as a relative sea level indicator, it has been subject to glacial isostatic adjustment and other crustal motion.

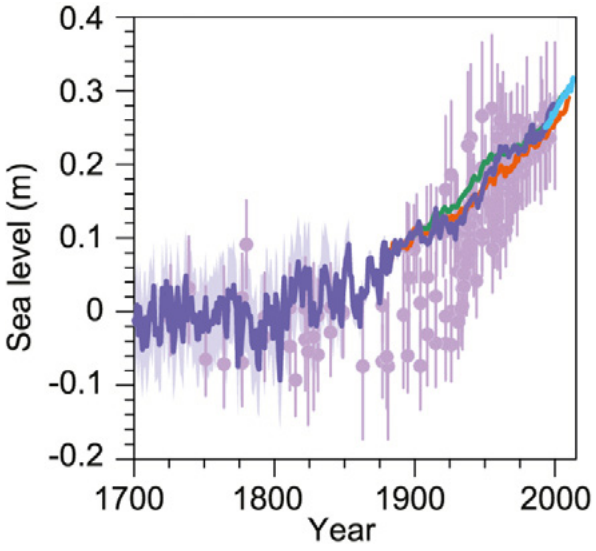
Since the rise at the end of the last glaciation, indicators suggest a stabilisation of global sea levels. In particular, in the 2,000 years up until ~1800, where the evidence also includes human-built structures, there is little indication of change. More details about the reconstruction of the pre-industrial sea level record can be found in Church *et al*. (2013).

12.5.2 In recent centuries

Since around 1700, sea level has been observed and recorded more accurately and consistently (see Figure 12.19). Until the recent advent of routine satellite altimeter measurements, this record comes mainly from tide gauge stations (see Section 12.4.2). Although the uncertainty is greater in the earlier part of the record where fewer stations were operating, it is clear that global sea level began to rise around 1800 and has been increasing steadily since then.

Figure 12.19 The past three centuries of the global sea level record

The dark blue, green, and orange lines show different tide gauge reconstructions. Light blue is the altimeter record, and the purple points are from salt marsh evidence.



Source: Church *et al.* (2013) Figure 13.3e

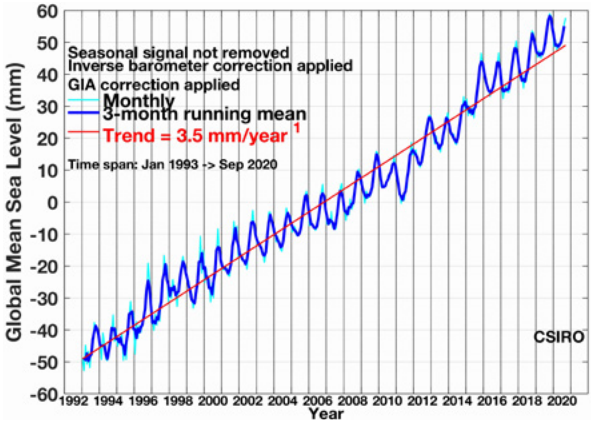
12.5.3 In recent decades

Since 1993, a dense, continuous, spatially extensive and precise record of global sea level has become available from the series of satellite altimeter missions (TOPEX/Poseidon and Jason-1/-2/-3; see Figure 12.20). The robust general trend is an increase of 3.3±0.4 mm/year. There is also evidence for an acceleration in that rise of nearly 0.1 mm/yr/yr (Watson *et al.*, 2015). As the record extends over coming decades (and as the accuracy of altimetry techniques continue to improve), the reality of this acceleration will become more certain.

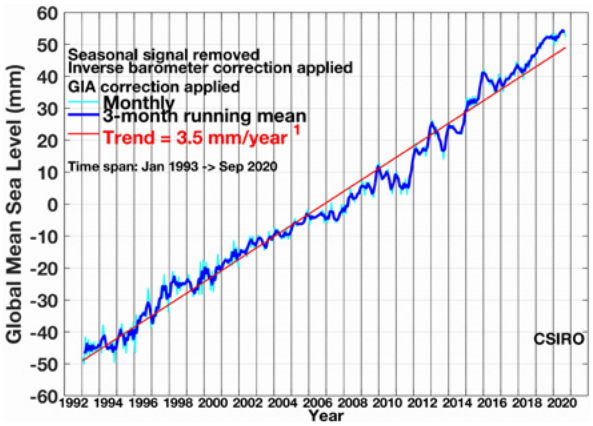
Figure 12.20 The satellite era mean sea level record

Global-Mean Sea Level (GMSL) from TOPEX/Poseidon, Jason-1, Jason-2, and Jason-3 satellite altimeter data

a. Mean sea level record including seasonal signals



b. Mean sea level record excluding seasonal signals



Source: Benoit Legressy, CSIRO. Retrieved from *https://research.csiro.au/slrwavescoast/sea-level/sea-level-changes/*

12.6 Modelling Future Sea Level

Sea level is a function of the volume occupied by ocean waters, which in turn is dependent upon their mass and density (see Section 5.1.2). The state of global climate is therefore a strong mediator of sea level since:

- additional heat trapped within the atmosphere results in ice loss from the cryosphere, increasing the mass of water in the ocean; and
- heat absorbed by the oceans decreases their density, which, for a given mass of water, must increase the volume.

A guide to likely future sea levels can therefore be found in the results of modern climate models, such as those included in the World Climate Research Program Coupled Model Intercomparison Project (WCRP CMIP; *https://www.wcrp-climate.org/wgcm-cmip*). Since a warming climate may also cause increased human reliance on groundwater aquifers for agriculture and other freshwater needs, which ultimately releases more terrestrial water into the ocean, these models need to take account of forcing arising from societal responses.

A significant part of the global effort to understand climate and its evolution occurs within the framework of the Intergovernmental Panel on Climate Change (IPCC), which produces major reports based on the evolving science evidence, typically every 5–8 years. The fifth assessment report (5AR) was completed in 2014 (IPCC, 2014) and the sixth is planned for 2022. An important component of the science underpinning these reports is a comparison of global climate model runs that explore future climates under a range of different greenhouse gas emission scenarios. These scenarios, called Representative Concentration Pathways (RCPs), represent plausible carbon emission trajectories given possible human choices. These are identified by their approximate total radiative forcing in year 2100 relative to 1750, that is, RCP2.6 indicates 2.6 W/m^2. The RCP range from business as usual (rapidly increasing emissions, RCP8.5) through a variety of mitigation approaches including those that reach net-zero emissions at differing rates (see Table 12.3). The agreed emission scenarios serve not only to ease comparison of the performance of the climate models but, since they reflect the consequences of possible interventions, also enable a standardised approach to assessment of the economic and sociological impacts of the choices to be made. IPCC (2013; see Box SPM.1) provides more information on these RCPs.

Table 12.3 Predicted temperature variations

Mean atmospheric temperature changes expected from climate model responses to four of the scenarios in the IPCC AR5 report. Note that temperatures have already increased by nearly 1°C from pre-industrial era when atmospheric CO_2 concentrations were about 270 ppm. Temperature increase is for 2081–2100 relative to 1986–2005.

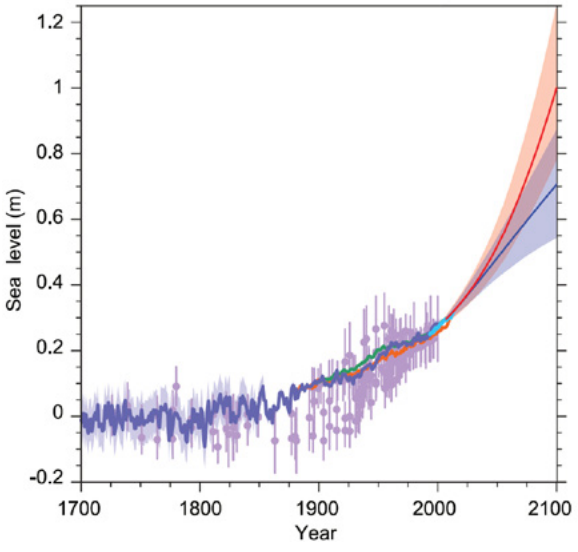
AR5 Scenario	Atmospheric CO_2 equivalent in 2100 (ppm)	Temperature Increase (°C)
RCP8.5	> 1370	3.7 (2.6–4.8)
RCP6.0	850	2.2 (1.4–3.1)
RCP4.5	650	1.8 (1.1–2.6)
RCP2.6	490	1.0 (0.3–1.7)

Source for data: IPCC (2013) Table SPM.2

Projections of future sea levels are informed by modelling using the various RCP scenarios. While climate models differ in detail as to how they incorporate various physical processes, the IPCC future sea level assessment is based on consideration of models that include the three major causes of sea level change: thermal expansion, transfer of water from the cryosphere to the ocean, and transfer from terrestrial stores to the ocean. Over the past several decades, both our understanding of the processes involved, and (by observational measurement) knowledge of the parameters relevant to each, have improved. Consequently the uncertainty surrounding likely future sea levels has been steadily reduced (see Figure 12.21).

Figure 12.21 Historical sea level change

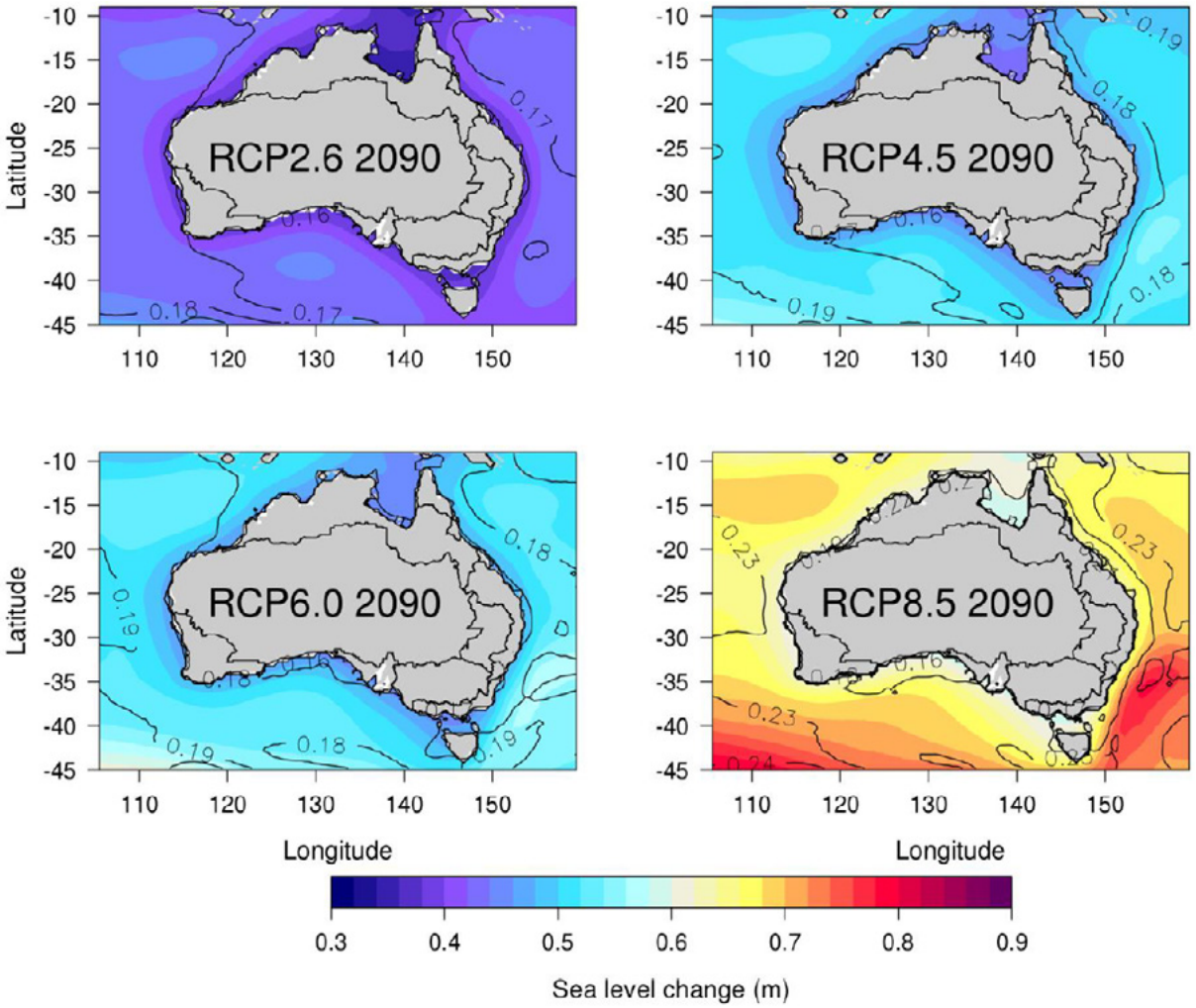
Historical global mean sea level change (colours as in Figure 12.19) extended with IPCC projections from modelling using the RCP8.5 (red) and RCP2.6 (blue) scenarios with uncertainties indicated by the shaded areas.



Source: Stocker *et al.* (2013) Figure TFE.2

Figure 12.22 Projected sea level changes around Australia in 2090

Distribution of sea level changes around Australia in 2090 (relative to 1986–2005) arising from the four different IPCC AR5 scenarios (see Table 12.3). The shading indicates the change and the solid lines the uncertainties.



Source: McInnes *et al.* (2015) Figure 3

The IPCC projections indicate global MSL change by the end of this century of somewhere in the range of 0.5–1.2 m, depending on which emission scenario turns out to be the most realistic. It is important to recognise however that not only is sea level change not spatially uniform, it is the change in relative sea level (measured with respect to local land) that determines the impacts. Two factors are particularly significant in this respect: changes in land elevation and changes in the Earth's gravity field. Long term changes in the elevation of continents as they respond to the loss of ice in the last ice age (Glacial Isostatic Adjustment) will continue, and will also affect Greenland and Antarctica further in the future as more ice is lost. Tilting of continents as a consequence of continental motion will result in opposite effects on relative sea level on opposite sides. Subsidence of land, for example due to increased groundwater extraction, can also increase local relative sea level change. The gravitational field change arises as large amounts of ice are lost from the polar ice caps. The ice sheets are massive in their own right and exert a gravitational pull on the surrounding oceans. As the ice melts, this mass becomes mobile and migrates away from the polar regions and results in a reduction of sea level locally as the ocean responds. The relative sea level rise resulting from the loss of ice sheets is therefore greater further away from the poles.

Taking these factors into account, it is possible to use future global MSL changes to develop regional projections. An example product is shown in Figure 12.22 (from McInnes *et al.*, 2015) for the 21st century. Under all scenarios Australian sea levels are expected to increase. The rate of increase varies with the selected RCP scenario, ranging from 4 mm/year

for RCP2.6 to 12 mm/year by the end of the century for RCP8.5. Extreme sea level events, such as storm surges and wave runup, lead to the most significant impacts of sea level rise via coastal flooding and dissipation of wave energy. For current infrastructure and buildings, existing at fixed heights above the (present) highest tide level, the frequency of such events are expected to increase. These quantitative projections of regional sea level change can be used to estimate the additional height that needs to be incorporated into new infrastructure to keep the frequency of such events from increasing. Such projections indicate that further measures will need to be taken to protect existing Australian coastal infrastructure.

12.7 Further Information

An excellent introductory tutorial to satellite altimetry provided by the European and French Space Agencies can be found on the web at *http://www.altimetry.info/*. A definitive reference is Cazenave and Fu (2001).

Bureau of Meteorology

Australian baseline sea level monitoring project:

http://www.bom.gov.au/oceanography/projects/abslmp/abslmp.shtml

Pacific Sea Level Monitoring Project: *http://www.bom.gov.au/pacific/projects/pslm/index.shtml*

ICSM Permanent Committee on Tides and Mean Sea Level

https://www.icsm.gov.au/what-we-do/permanent-committee-tides-and-mean-sea-level

Accuracy of Tidal Predictions: *https://icsm.gov.au/sites/default/files/2017-05/Port_Tidal_Predictions-V0.4.pdf*

Global Sea Level

Sea Level, Waves and Coastal Extremes: *https://research.csiro.au/slrwavescoast/sea-level/*

Global Sea Level Observing System (GLOSS):

https://www.bodc.ac.uk/resources/inventories/gloss_handbook/

Permanent Service for Mean Sea Level: *http://www.psmsl.org*

Measuring sea level rise

AdaptNSW: *https://climatechange.environment.nsw.gov.au/Impacts-of-climate-change/Coasts-and-sea-level-rise/Measurement-of-sea-level-rise*

Useful websites

CSIRO sea level site: *https://research.csiro.au/slrwavescoast/sea-level/*

NASA/JPL Ocean Surface Topography: *https://sealevel.jpl.nasa.gov/*

CNES AVISO satellite altimetry: *https://www.aviso.altimetry.fr/en/home.html*

University of Colorado: *https://sealevel.colorado.edu/*

NOAA National Ocean Service: *https://oceanservice.noaa.gov/education/sea-level-rise/welcome.html*

ESA/CNES radar altimetry tutorial and toolbox: *http://www.altimetry.info/*

Broadview Radar Altimetry Toolbox: *https://earth.esa.int/web/guest/software-tools/content/-/article/basic-radar-altimetry-toolbox-brat-5040*

Several portals and agency sites provide access to data from radar altimetry missions, including

IMOS Gridded sea level anomaly combines altimetry with tide gauges: *http://oceancurrent.imos.org.au/*

AVISO: *https://www.aviso.altimetry.fr/en/data.html*

NASA: *https://sealevel.jpl.nasa.gov/data/get-data/*

CSIRO: *https://research.csiro.au/slrwavescoast/sea-level/measurements-and-data/sea-level-data/*

Historical and current satellite altimeter missions

https://www.aviso.altimetry.fr/en/missions.html

https://podaac.jpl.nasa.gov/Altimetric_Data_Information/Missions

https://sealevel.jpl.nasa.gov/missions/overview-and-partners/

12.8 References

Church, J.A., Clark, P.U., Cazenave, A., Gregory, J.M., Jevrejeva, S., Levermann, A., Merrifield, M.A., Milne, G.A., Nerem, R.S., Nunn, P.D., Payne, A.J., Pfeffer, W.T., Stammer, D., and Unnikrishnan, A.S. (2013). Sea Level Change. pp 1137–1216, In: *Climate Change 2013: The Physical Science Basis*. Contribution of Working Group I to the Fifth Assessment Report of the Intergovernmental Panel on Climate Change. (Eds: T.F. Stocker, D. Qin, G.-K. Plattner, M. Tignor, S.K. Allen, J. Boschung, A. Nauels, Y. Xia, V. Bex and P.M. Midgley). Cambridge University Press, Cambridge, New York, USA. *doi:10.1017/CBO9781107415324.026* (Available from *https://www.ipcc.ch/report/ar5/wg1/*)

Cazenave, A., and Fu, L.-L. (2001). *Satellite Altimetry and Earth Sciences: A Handbook of Techniques and Applications*. International Geophysics Series, Volume 69. Academic Press.

Fu, L.-L., and Ubelmann, C. (2014). On the transition from profile altimeter to swath altimeter for observing global ocean surface topography. *Journal of Atmospheric and Oceanic Technology,* 31(2), 560–568.

Gower, J. (2005). Jason-1 detects the 26 December 2004 tsunami. *EOS*, 86 (4), 37–38.

IDS (2021). *International DORIS Service* website: *https://ids-doris.org/*

ILRS (2021). *International Laser Ranging Service* website: *https://ilrs.gsfc.nasa.gov/*

IPCC (2013). Summary for Policymakers. In: *Climate Change 2013: The Physical Science Basis*. Contribution of Working Group I to the Fifth Assessment Report of the Intergovernmental Panel on Climate Change (Eds: Stocker, T.F., D. Qin, G.-K. Plattner, M. Tignor, S.K. Allen, J. Boschung, A. Nauels, Y. Xia, V. Bex and P.M. Midgley). Cambridge University Press, Cambridge, New York, USA. *https://www.ipcc.ch/site/assets/uploads/2018/02/WG1AR5_SPM_FINAL.pdf*

IPCC (2014). Climate Change 2014: Synthesis Report. Contribution of Working Groups I, II and III to the Fifth Assessment Report of the Intergovernmental Panel on Climate Change (Eds: R.K. Pachauri and L.A. Meyer). IPCC, Geneva, Switzerland. 151 p.

McInnes, K.L., Church, J., Monselesan, D., Hunter, J.R., O'Grady, J.G., Haigh, I.D., and Zhang, X. (2015). Information for Australian impact and adaptation planning in response to sea-level rise. *Australian Meteorological and Oceanographic Journal*, 65(1), 127–149.

McInnes, K.L., White, C.J., Haigh, I.D., Hemer, M.A., Hoeke, R.K., Holbrook, N.J., Kiem, A.S., Oliver, E.C.J., Ranasinghe, R., Walsh, K.J.E., Westra, S., and Cox, R. (2016). Natural hazards in Australia: sea level and coastal extremes. *Climatic Change*, 139(1), 69–83.

NASA (2021). *SWOT Mission Overview* webpage, Surface Water and Ocean Technology website: *https://swot.jpl.nasa.gov/mission/overview/*

Stammer, D., Ray, R.D., Andersen, O.B., Arbic, B.K., Bosch, W., Carrère, L., Cheng, Y., Chinn, D.S., Dushaw, B.D., Egbert, G.D., Erofeeva, S.Y., Fok, H.S., Green, J.A.M., Griffiths, S., King, M.A., Lapin, V., Lemoine, F.G., Luthcke, S.B., Lyard, F., Morison, J., Müller, M., Padman, L., Richman, J.G., Shriver, J.F., Shum, C.K., Taguchi, E., and Yi, Y. (2014). Accuracy assessment of global barotropic ocean tide models. *Reviews of Geophysics*, 52(3), 243–282.

Stocker, T.F., D. Qin, G.-K. Plattner, L.V. Alexander, S.K. Allen, N.L. Bindoff, F.-M. Bréon, J.A. Church, U. Cubasch, S. Emori, P. Forster, P. Friedlingstein, N. Gillett, J.M. Gregory, D.L. Hartmann, E. Jansen, B. Kirtman, R. Knutti, K. Krishna Kumar, P. Lemke, J. Marotzke, V. Masson-Delmotte, G.A. Meehl, I.I. Mokhov, S. Piao, V. Ramaswamy, D. Randall, M. Rhein, M. Rojas, C. Sabine, D. Shindell, L.D. Talley, D.G. Vaughan and S.-P. Xie. (2013). Technical Summary. In: *Climate Change 2013: The Physical Science Basis*. Contribution of Working Group I to the Fifth Assessment Report of the Intergovernmental Panel on Climate Change. (Eds: Stocker, T.F., D. Qin, G.-K. Plattner, M. Tignor, S.K. Allen, J. Boschung, A. Nauels, Y. Xia, V. Bex and P.M. Midgley). Cambridge University Press, Cambridge, New York, USA. (Available from *https://www.ipcc.ch/site/assets/uploads/2018/02/WG1AR5_TS_FINAL.pdf*)

Tamisiea, M.E., Hughes, C.W., Williams, S.D.P., and Bingley, R.M. (2014). Sea level: measuring the bounding surfaces of the ocean. *Philosophical Transactions of the Royal Society A: Mathematical, Physical and Engineering Sciences*, 372(2025), 20130336. *https://doi.org/10.1098/rsta.2013.0336*

Townsend, D.W. (2012). *Oceanography and marine biology: an introduction to marine science*. Sinauer Associates, Sunderland.

Watson, C., White, N., Coleman, R., Church, J., Morgan, P., and Govind, R. (2004). TOPEX/poseidon and Jason-1: absolute calibration in Bass Strait, Australia. *Marine Geodesy,* 27(1–2), 107–131.

Watson, C.S., White, N.J., Church, J.A., King, M.A., Burgette, R.J., and Legresy, B. (2015). Unabated global mean sea-level rise over the satellite altimeter era. *Nature Climate Change*, 5(6), 565–568.

Watson, C.S., Legresy, B., King, M., Beardsley, J., and Deane, A. (2018). A Review of the Altimeter Validation Facility in Bass Strait, Australia. Oral presentation. *FRM4ALT International Review Workshop*. April 23–26. International Review Workshop on Satellite Altimetry Cal/Val activities and applications. Crete, Greece.

White, N.J., Coleman, R., Church, J.A., Morgan, and P.J., Walker, S.J. (1994). A southern hemisphere verification for the TOPEX/POSEIDON satellite altimeter mission. *Journal of Geophysical Research: Oceans*, 99(C12), 24505–24516.



13 Bathymetry

Kim Picard, Janet Anstee, and Barbara Harrison

Bathymetry is the study or measurement of the depth of water from the surface to the seabed, the solid surface that underlies a waterbody, with depth being measured as the vertical distance from a given vertical datum (see Figure 10.9). Thus, in waterbodies, bathymetry corresponds to mapping topography on land. Bathymetric data is used for a range of marine activities, such as to determine Australia's extended continental shelf, highlight shipping hazards, monitor undersea engineering structures, identify potential deep sea fishing sites, and model tsunami.

Traditionally waterbody depth was measured by sample 'soundings' at selected locations, that is, the length of a lead line that was lowered from a ship until it reached the seabed. For the past century a variety of EO-based methods have been used to estimate waterbody depth. Some of the advances in seafloor mapping since 1903 are illustrated in Figure 13.1.

The initial subsections below provide an overview of waterbody depth mapping around Australia (see Section 13.1) and the EO sensors that can provide useful information for bathymetric studies (see Section 13.2). Subsequent sections consider approaches to EO-based bathymetry that are relevant to Australian surface waters:

- seafloor mapping using acoustic and radar datasets (see Section 13.3); and
- coastal monitoring derived from lidar and satellite imagery (see Section 13.4).

The sea does not belong to despots. Upon its surface men can still exercise unjust laws, fight, tear one another to pieces, and be carried away with terrestrial horrors. But at thirty feet below its level, their reign ceases, their influence is quenched, and their power disappears.
(Jules Verne)

Background image: Adele Island, off the northern WA (Kimberley) coast, was photographed from the International Space Station on 11 June 2015. This pristine cay, which spans just under 3 km in length and 1.6 km in width, is surrounded by extensive sandbanks and coral reefs. It is an important breeding sanctuary for migratory birds, a feeding and breeding ground for humpback whales, and home to rare rollolith habitat. Source: NASA Earth Observatory ISS044-E-903. Retrieved from *https://visibleearth.nasa.gov/images/86331/adele-island*

Recommended Chapter Citation: Picard, K., Anstee, J.M., and Harrison, B.A. (2021). Bathymetry. Ch 13 in *Earth Observation: Data, Processing and Applications. Volume 3B—Surface Waters.* CRCSI, Melbourne. pp. 223–241. ISBN 978-0-6482278-5-4

This chapter is published with the permission of the CEO, Geoscience Australia.

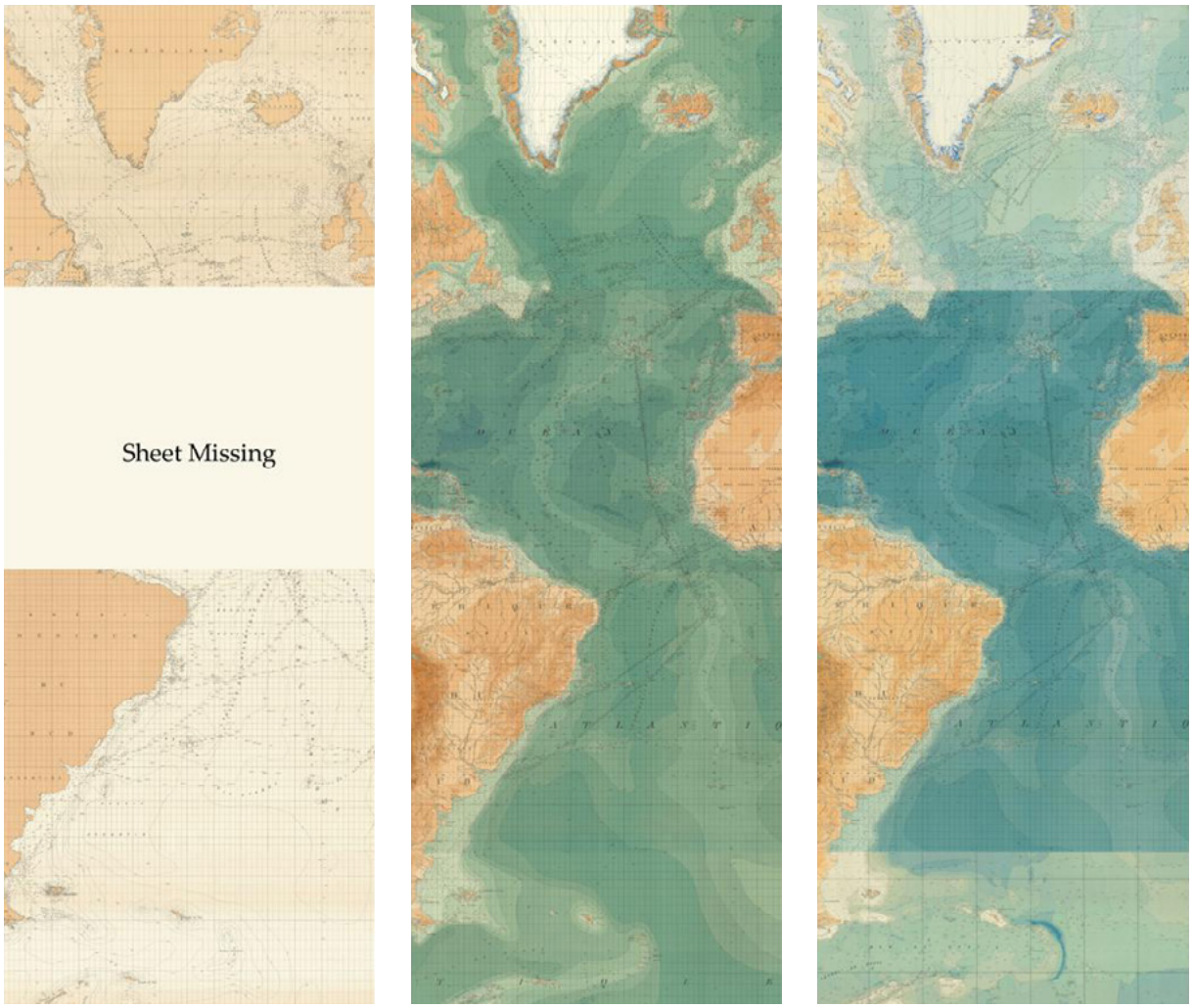
Figure 13.1 Improvements in GEBCO over time

These charts show mapping of the Mid-Atlantic Ridge in the General Bathymetric Chart of the Oceans (GEBCO) since 1903.

1st edition: 1903
(18,000 soundings)

2nd edition: 1912–1930
(> 30,000 soundings)

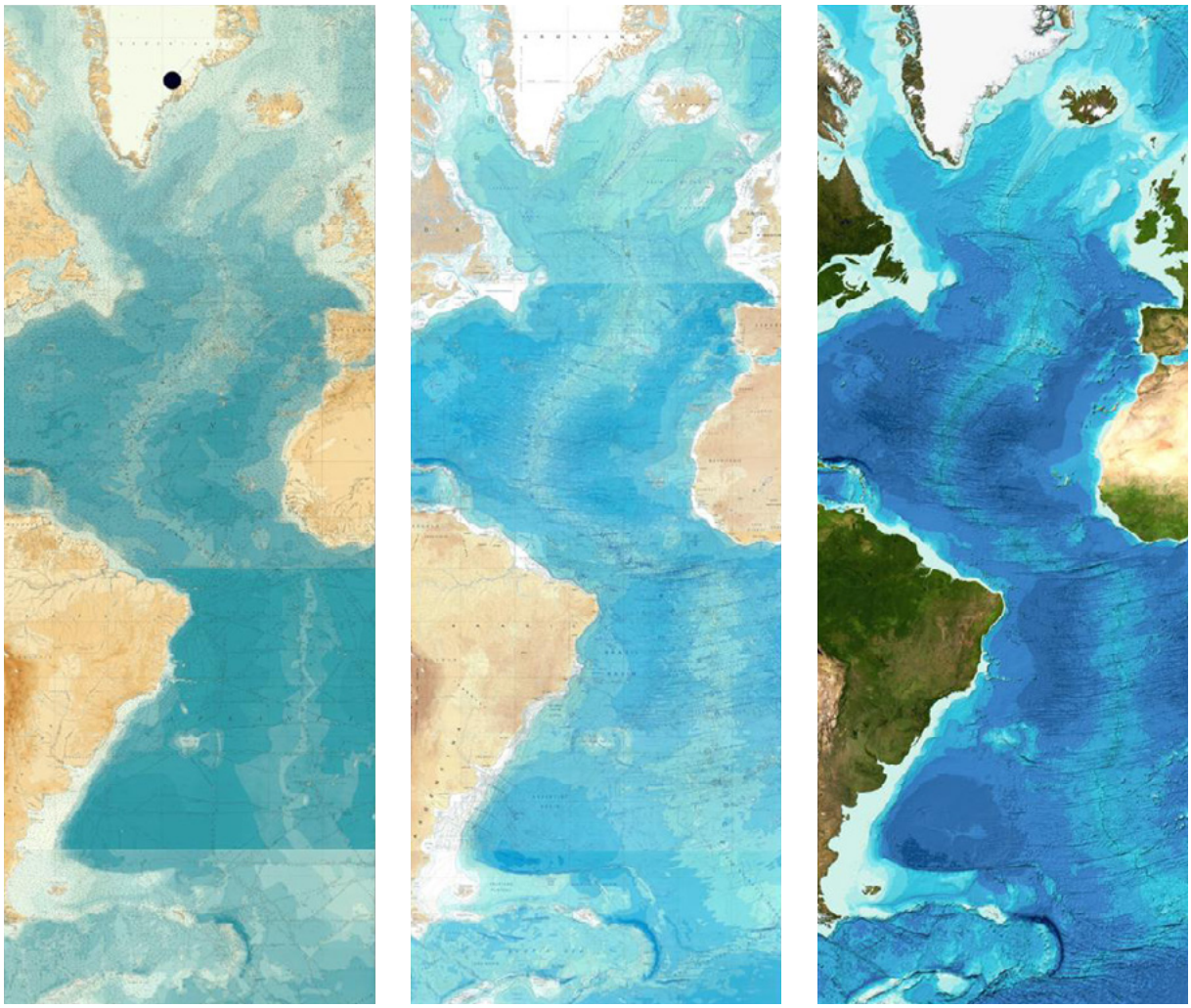
3rd edition; 1932–1966



4th edition: 1958+
(based on echosounders supplying signficantly more bathymetric data)

5th edition: 1972–1984
(using many more soundings)

GEBCO–2014 Grid
(part of global terrain model at 30 arc-second intervals)



Source: Wölfl *et al.* (2019) Figure 6 (courtesy of Anthony Pharaoh, IHO)

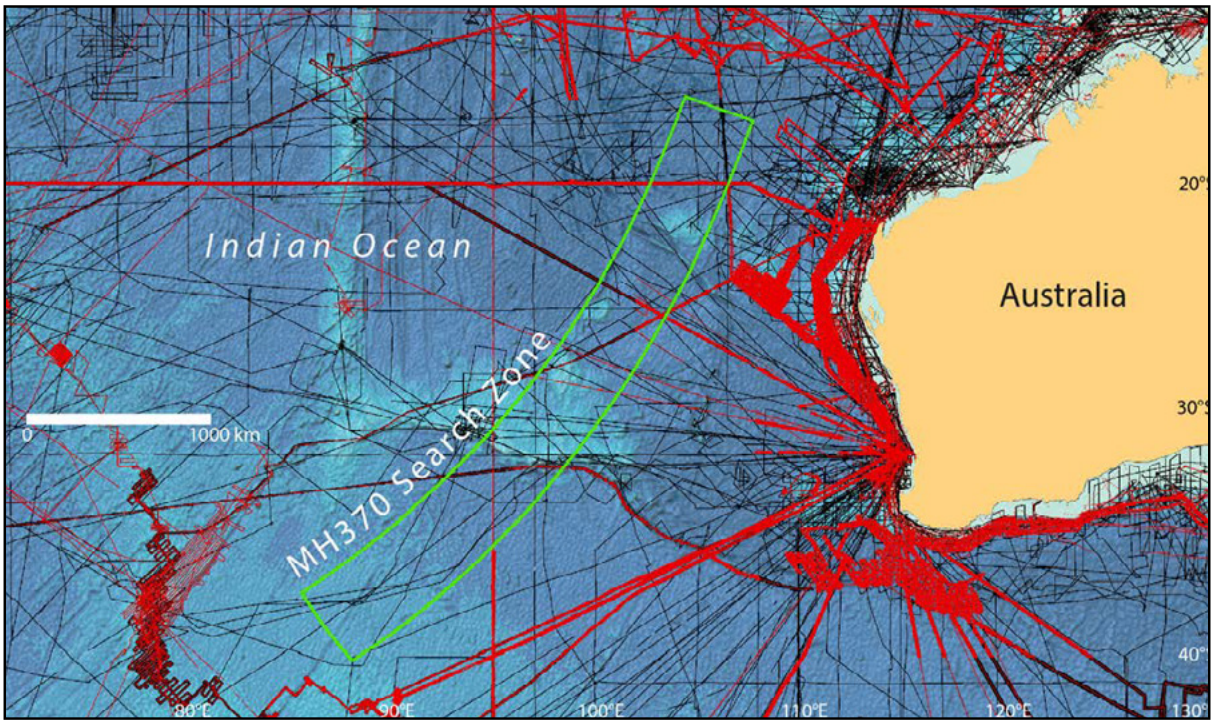
13.1 Bathymetry of Australian Surface Waters

Mapping the shape and composition of the seabed both supports safe navigation and provides data and information for managing Australia's marine estate in a range of scientific applications, including:

- delineating and securing maritime boundaries (see Section 2.1);
- ensuring the safety of life at sea (see Excursus 2.1);
- search and rescue operations (see Figure 13.2);
- monitoring marine conditions (see Excursus 2.2) and flood events (see Section 11.4);
- mapping coastal and nearshore sediments (see Section 6.3);
- understanding geomorphology (see Section 6.2) and geohazards, especially in coastal waters (see Section 20.5);
- conserving marine ecosystems and cultural heritage (see Australasian Underwater Cultural Heritage Database (AUCHD) in Section 13.5);
- assessing alternative energy opportunities (such as offshore wind and wave energy locations; see Section 16.1);
- modelling regional hydrodynamics and global ocean circulation (see Section 17);
- planning aquaculture and monitoring fisheries (see Section 20.7.1);
- deploying and maintaining seafloor installations, such as telecommunication infrastructure; and
- managing oil and gas subsea assets.

Figure 13.2 Search for MH370 relative to available bathymetric datasets

With the disappearance of flight MH370 travelling from Kuala Lumpur to Beijing on 8 March 2014, the lack of high resolution bathymetry hampered the search of parts of the fuselage. In this diagram black lines indicate the available shipborne, single beam echo sounding data, red lines show available multibeam bathymetry, and the green bounding shape highlights the projected search area.



Source: GEBCO (2017) Figure 3-2

The Australian Bathymetric and Topographic Grid provides coverage of (most of) our marine jurisdiction at 250 m horizontal resolution (GA, 2018). The initial bathymetric grid (Harris *et al.*, 2005) enabled the surface area of the seabed and the distribution of defined geomorphic features around the continental margin of Australia to be mapped systematically for the first time, and this was updated with newer datasets in 2009 (see Excursus 13.1 for details). More recently, at a regional level, a few large, high resolution bathymetry models have been compiled, namely the Great Barrier Reef and Coral Sea, the Northern Australia, and the Torres Strait models (Beaman, 2017, 2018, 2020). However, when detailed bathymetric data is needed for operational activities, such as navigating underwater vehicles involved in search and rescue operations in deep ocean areas, the existing resolution and extent of bathymetric data in this region has been found wanting (see Figure 13.2).

In Australia, much of the focus for seabed mapping has involved varying levels of coverage and resolution for the continental shelf and slope waters, resulting in coverage from the upper reaches of estuaries to the abyssal plain for selected locations. This focus derives from the drivers for mapping, vessel and gear availability, and a combination of targeted and opportunistic data collection. Although a significant increase in survey coverage has occurred this century, by 2018 less than 25% of the seafloor in Australia's maritime jurisdiction had been mapped at high resolution (Picard *et al.*, 2018).

While the availability of national bathymetric data varies with the policies of different jurisdictions (Wölfl *et al.*, 2019), national and international efforts are underway to integrate all publicly available data into accessible repositories such as AusSeabed (see Sections 13.3.2 and 13.5) and the General Bathymetric Chart of the Oceans (GEBCO; see Excursus 7.1).

Excursus 13.1—Australian Bathymetric and Topographic Grid

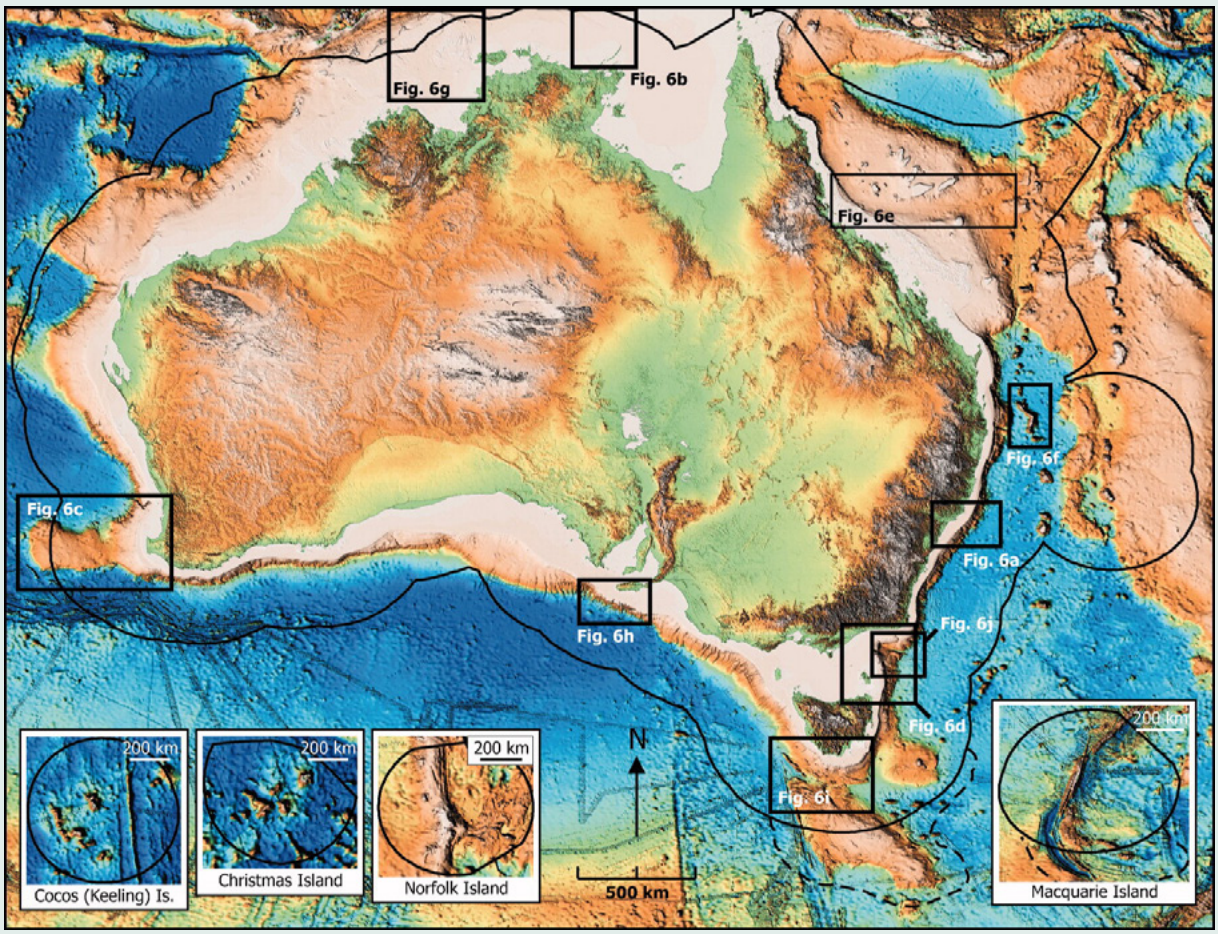
Source: GA (2018): *https://ecat.ga.gov.au/geonetwork/srv/eng/catalog.search?node=srv#/metadata/a05f7892-fae9-7506-e044-00144fdd4fa6*
Further Information: Heap and Harris (2008); Harris *et al.* (2005)

The Australian Bathymetric and Topographic Grid is a consistent, bathymetric data grid, with 250 m resolution, which was created from a range of available datasets (Harris *et al.*, 2005; see Figure 13.3). This grid was produced "specifically to provide regional and local broad scale context for scientific and industry projects, and public education" and "is not suitable for use as an aid to navigation, or to replace any products produced by the Australian Hydrographic Service" (GA, 2018).

The major geomorphic zones, or Primary Bathymetric Units (see Section 6.2), within Australia's marine jurisdiction are the continental shelf, the continental slope, the continental rise, and the abyssal plain (see Figure 13.4 and Table 13.1). These broad categories have been subdivided into bioregions for the National Marine Bioregionalisation (NMB; Keene *et al.*, 2008).

Figure 13.3 Australian Bathymetric and Topographic Grid

Bathymetry is shaded from shallow (white) to deep (blue) for the Australian margin, adjacent seafloor and offshore islands. The subregions indicated are detailed in Heap and Harris (2008).



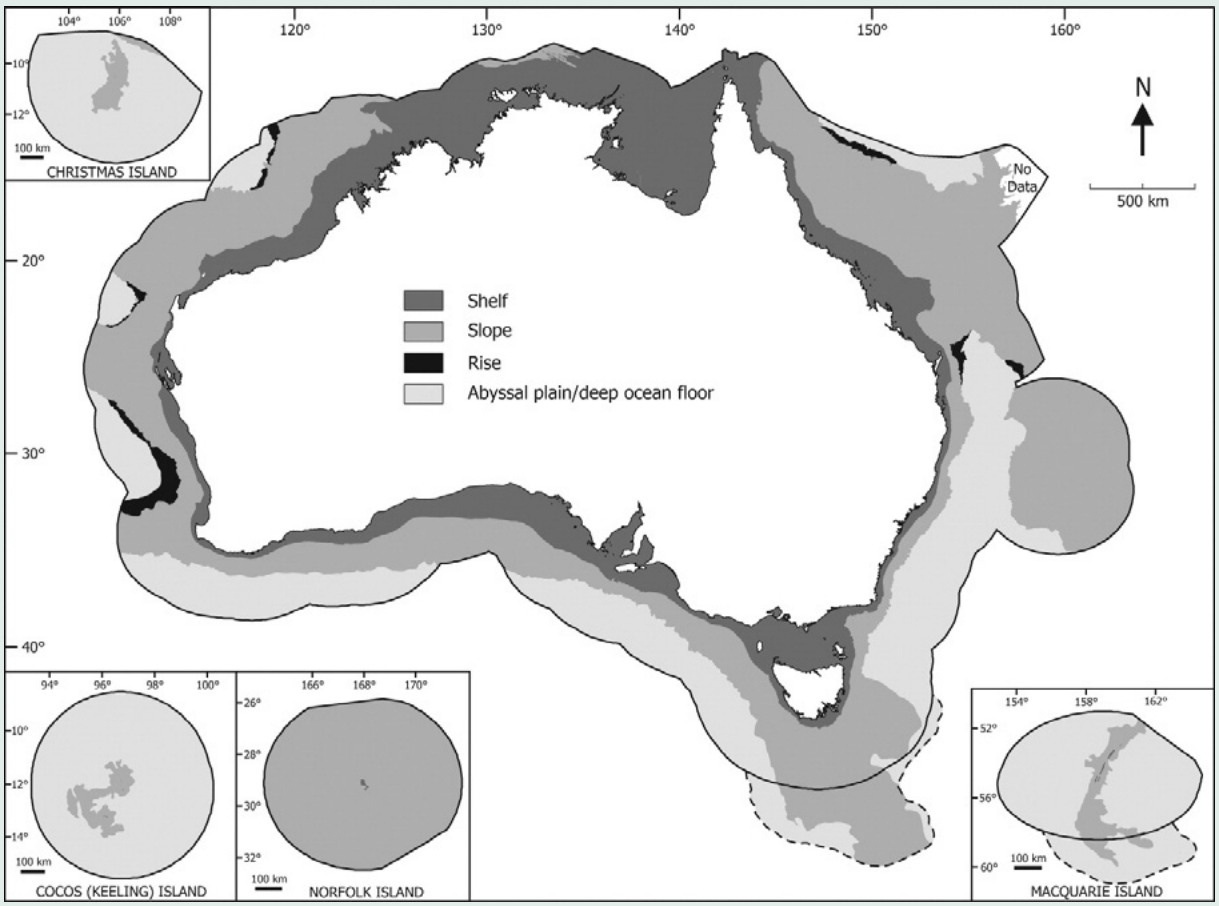
Source: Heap and Harris (2008) Figure 4

Table 13.1 Surface areas of primary bathymetric units

Number	Name	Area (km²)	Area (%)	Distribution
1	Shelf	1,962,030	21.92	Most extensive in northern Australia and connects to Papua New Guinea.
2	Slope	4,011,010	44.8	Continuous around Australian mainland, except in northern Australia.
3	Rise	97,070	1.08	Most well developed in west margin and absent in east margin.
4	Abyssal Plain	2.882,700	32.20	Absent in north and Norfolk Island margins, and most extensive in east and south.
	Total	**8,575,581**	**100**	

Source: Heap and Harris (2008) Table 2

Figure 13.4 Primary bathymetric units

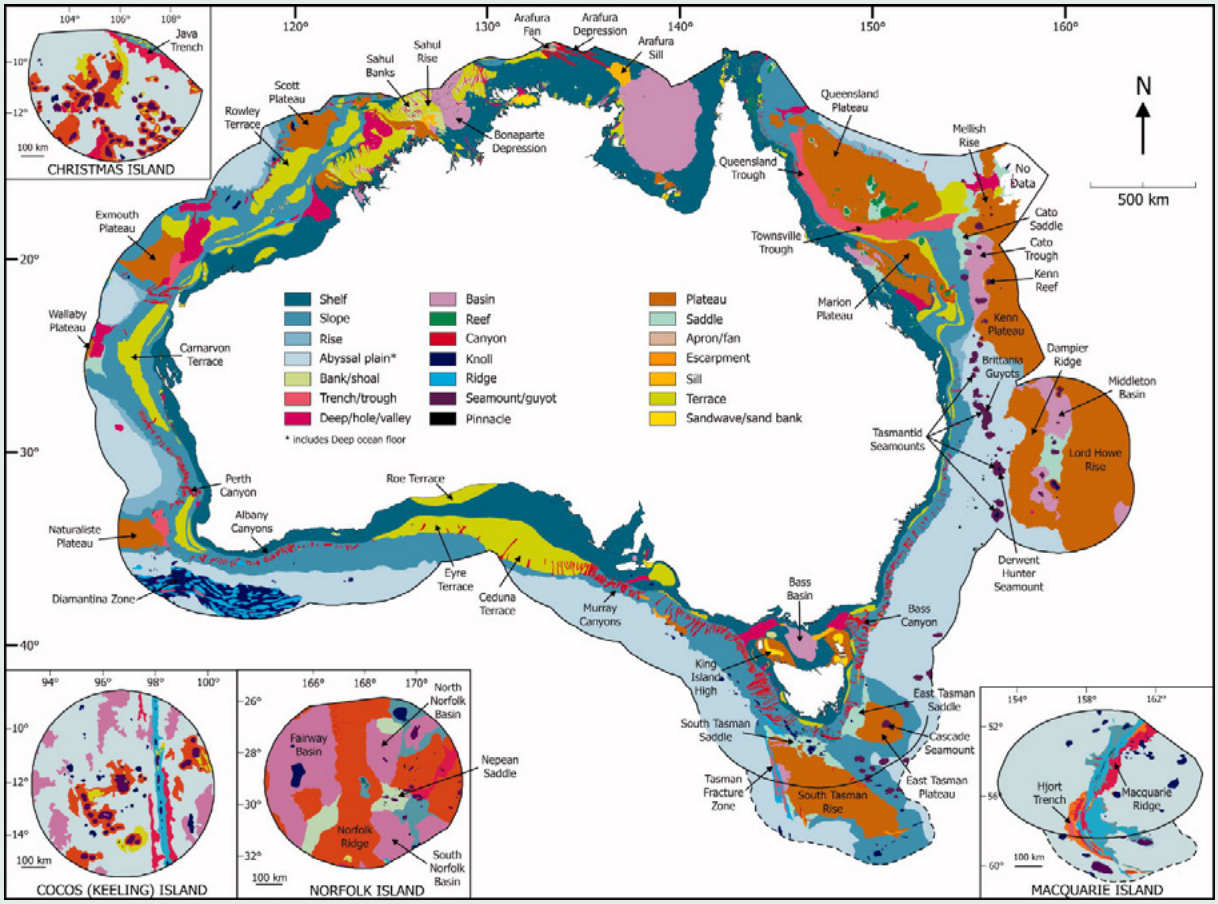


Source: Heap and Harris (2008) Figure 7 (see also: *https://www.environment.gov.au/system/files/resources/36cff669-6183-4ba0-8eab-be8529e78028/files/aspd-bio-2.pdf*)

Drainage maps derived from the Australian Bathymetric and Topographic Grid were also used to identify 21 regional geomorphic features (Heap and Harris, 2008; see Table 13.2). As illustrated in Figure 13.5, the distribution of all features varies regionally. The variety and distribution of these geomorphic features underlie the unique marine environment surrounding Australia. These results have improved our understanding of Australia's continental shelf and slope bathymetry, which is essential for developing regional marine plans and managing our ocean resource, and provided better access to more integrated marine datasets.

Figure 13.5 Distribution of geomorphic features around Australia's continental margin

6,702 individual geomorphic features, covering more than 3.9 million km^2, were identified, leaving 57% of the Australian margin and adjacent seafloor unmapped.



Source: Heap and Harris (2008) Figure 8

Table 13.2 Geomorphic features of Australian continental margin

This set of 21 features was used by Harris *et al.* (2005) to define geomorphic features around the continental margin of Australia, and also to define the global seafloor geomorphic categories shown in Figure 6.2. Features numbered 1 to 20 were derived from IHO (2001) and feature 21 was from Ashley *et al.* (1990).

Number	Name	Definition
1	Shelf	Zone adjacent to a continent (or around an island) and extending from the low water line to a depth at which there is usually a marked increase of slope towards oceanic depths
2	Slope	Slope seaward from the shelf edge to the upper edge of a continental rise or the point where there is a general reduction in slope
3	Rise	Gentle slope rising from the oceanic depths towards the foot of a continental slope
4	Abyssal Plain	Extensive, flat, gently sloping or nearly level region at abyssal depths
5	Bank	Elevation over which the depth of water is relatively shallow but normally sufficient for safe surface navigation
	Shoal	Offshore hazard to surface navigation that is composed of unconsolidated material
6	Deep	In oceanography, an obsolete term which was generally restricted to water depths greater than 6,000 m
	Hole	Local depression, often steep sided, of the seafloor
	Valley	Relatively shallow, wide depression, the bottom of which usually has a continuous gradient. This term is generally not used for features that have canyon-like characteristics for a significant portion of their extent.
7	Trench	Long narrow, characteristically very deep and asymmetrical depression of the seafloor, with relatively steep sides
	Trough	Long depression of the seafloor characteristically flat bottomed and steep sided and normally shallower than a trench
8	Basin	Depression, characteristically in the deep seafloor, more or less equidimensional in plan and of variable extent
9	Reef	Rock lying at or near the sea surface that may constitute a hazard to surface navigation
10	Canyon	A relatively narrow, deep depression with steep sides, the bottom of which generally has a continuous slope, developed characteristically on some continental slopes
11	Knoll	Relatively small isolated elevation of a rounded shape
	Abyssal Hills	Tract, on occasion extensive, of low (100-500 m) elevations on the deep seafloor
	Hill	Small isolated elevation
	Mountains	Large and complex grouping of ridges and seamounts
	Peak	Prominent elevation either pointed or of a very limited extent across the summit
12	Ridge	(a) Long, narrow elevation with steep sides (b) Long, narrow elevation often separating ocean basins (c) Linked major mid-oceanic mountain systems of global extent
13	Seamount	Large isolated elevation, greater than 1000 m in relief above the seafloor, characteristically of conical form
	Guyot	Seamount having a comparatively smooth flat top
14	Pinnacle	High tower or spire-shaped pillar of rock or coral, alone or cresting a summit, which may extend above the surface of the water. It may or may not be a hazard to surface navigation.
15	Plateau	Flat or nearly flat area of considerable extent, dropping off abruptly on one or more sides
16	Saddle	Broad pass, resembling in shape a riding saddle, in a ridge or between contiguous seamounts
17	Apron	Gently dipping featureless surface, underlain primarily by sediment, at the base of any steeper slope
	Fan	Relatively smooth, fan-like, depositional feature normally sloping away from the outer termination of a canyon or canyon system
18	Escarpment	Elongated and comparatively steep slope separating or gently sloping areas
19	Sill	Seafloor barrier of relatively shallow depth restricting water movement between basins
20	Terrace	Relatively flat horizontal or gently inclined surface, sometimes long and narrow, which is bounded by a steeper ascending slope on one side and by a steeper descending slope on the opposite side.
21	Sand Wave	Wave-like bed form made of sand on the seafloor
	Sandbank	Submerged bank of sand in a sea or river that may be exposed at low tide

Source: Harris *et al.* (2005) Tables 2.3 and Heap and Harris (2008) Table 3

13.2 EO Sensors for Bathymetry

The major data sources, platforms, and instruments used for EO are introduced in Volume 1A. Bathymetric and seabed mapping is undertaken using a variety of sensors carried by a range of platforms, including ships, autonomous underwater vehicles (see Excursus 5.1), autonomous surface vehicles, deep-tow equipment, satellites, and fixed wing aircraft (see Table 13.3). The acquired data are used to create products such as bathymetric maps that reveal the topography of the seabed.

Satellite-based radar altimetry provides useful information for regional and global coverage of ocean bathymetry (see Section 13.3.1). Bathymetric maps with higher spatial resolution and accuracy are produced using acoustic data acquired by echosounders (see Sections 10.2.3 and 13.3.2). For coastal bathymetric applications, lidar (see Section 13.4.1) and satellite-based bathymetric methods (see Section 13.4.2) are suitable. Optical sensors that can be used for shallow water bathymetry are listed in Table 8.14.

Table 13.3 EO sensors relevant to bathymetry

Type	Sensor	Platform	Relevance	Advantages	Disadvantages
Passive optical	Multispectral radiometer	Satellite or airborne	Coastal bathymetry	Low cost, large area coverage	Lower vertical accuracy than sonar with direct measurements
Active optical	Bathymetric lidar	Airborne	Coastal bathymetry	High spatial resolution	Small coverage, high cost
Active microwave	Radar altimeter	Satellite	Regional seafloor bathymetry	Global coverage	Low spatial resolution
Sonar	Single beam echosounders	Shipborne	Local seafloor bathymetry	Detailed transects	Small coverage, high cost
	Multibeam echosounders	Shipborne	Detailed seafloor bathymetry	Detailed swath	Small coverage, high cost

13.3 Seafloor Mapping

Generally, very little is known about the seafloor. Although our oceans cover over two-thirds of our planet, only 5% of the global ocean floor has been mapped (Wölfl *et al.*, 2019) and less than 25% of Australia's marine jurisdiction has been mapped in high resolution (see Section 13.1). Existing maps of the seafloor are often low resolution, having been derived from satellite-acquired datasets, and only provide a general indication of waterbody depth.

Bathymetric data for oceans can be collected by:

- satellite altimeters—which use radar instrumentation to measure the height of the ocean surface (see Section 13.3.1); and
- echosounders—which transmit and receive sound waves to determine waterbody depth (see Section 13.3.2).

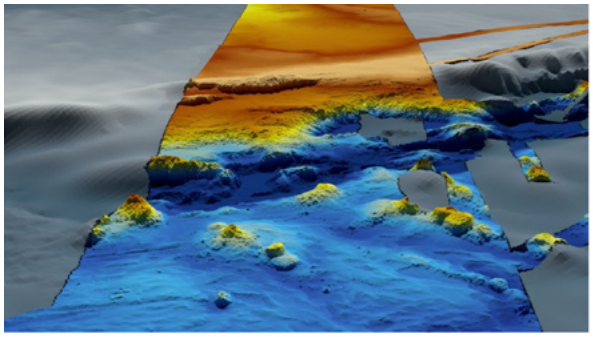
For the same location, Figure 13.6 and Figure 13.7 compare the spatial resolution of seafloor data acquired by these two sensors.

Figure 13.6 Satellite altimetry versus acoustic datasets

a. Image of seafloor acquired by satellite altimetry



b. Multibeam acoustic data overlaid on satellite image



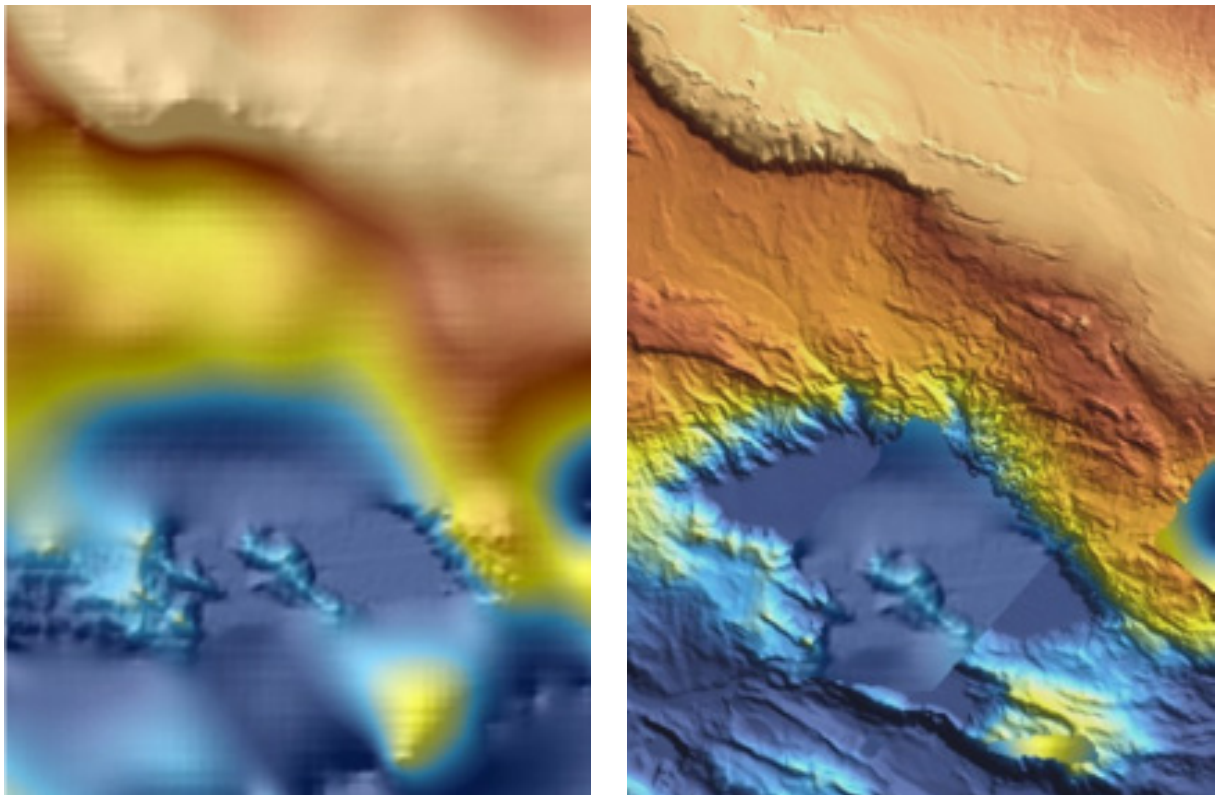
Source: Geoscience Australia

Figure 13.7 Example of bathymetric data improvements

After the disappearance of Malaysia Airlines flight MH370 in 2014, underwater search operations required detailed bathymetric data to be acquired using MBES in the southeast Indian Ocean. The images below compare the level of detail available for Diamantina trench before and after the search. Between these datasets, waterbody depth values differed by more than 100 m in 38% of grid cells, with the maximum difference being 1900 m (Picard *et al.*, 2018).

a. Bathymetric map derived from marine gravity information estimated from satellite altimetry and combined with sonar soundings (Smith and Sandwell, 1997; sourced from SRTM15–PLUS model, Olson *et al.*, 2016).

b. Bathymetric map derived from ship-based MBES data, gridded at 110 m horizontal resolution



Source: Australian Government (2017)

13.3.1 Satellite radar altimetry

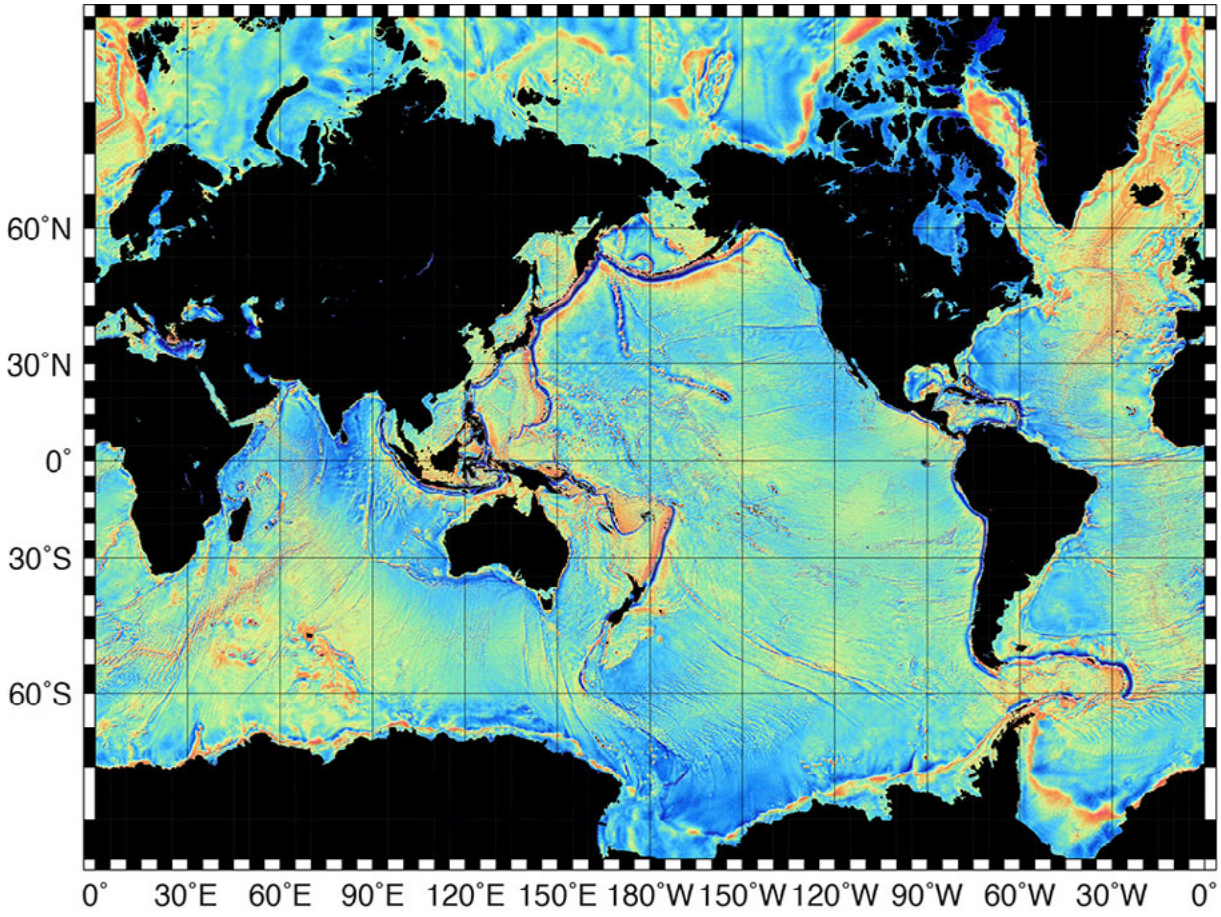
Satellite-borne, radar-based sensors called radar altimeters can be used to measure the height of the ocean surface (see Section 9.5 above and Volume 1A—Section 16). As discussed in Section 12, satellite altimetry measurements can be used to locate seafloor areas that are elevated. Basically, where hills or mountains exist on the seafloor, the gravitational pull around those areas is greater, making the sea surface bulge (Sandwell and Smith, 1997). Low resolution maps of general geomorphic features over a large area can be reliably produced from such datasets.

These datasets have been used to produce regional and global maps of both sea surface and seafloor topography. The first global map showing the topography of ocean basins was developed by Smith and Sandwell (1977) using gravity data from Geosat and satellite altimetry data from ERS-1 with available depth soundings. This revolutionary map provided new insights into the shape of our planet and the boundaries of tectonic plates. The original map has been updated using more recent EO datasets to improve accuracy (Sandwell *et al.*, 2014; see Figure 13.8). Satellite-derived gravity models have become a primary tool for investigating remote ocean basins, mapping tectonic structures, and understanding regional tectonic processes (Sandwell *et al.*, 2014).

Radar altimetry data is also instrumental for monitoring sea level (see Section 12), mapping significant wave heights (see Section 16), and modelling water circulation patterns (see Section 17).

Figure 13.8 Global map of marine gravity

Global Marine Gravity Version 23.1. Colour spectrum shows gravity anomaly from -200 (blue) to 250 (red) mGal.



Source: Sandwell *et al.* (2014). Scripps Instituion of Oceanography, 2 October 2014.

13.3.2 Echosounders

Acoustic sensors, which detect sound waves, are introduced in Volume 1A—Section 9.1 and Section 10 above. Bathymetric data is acquired by both research and commercial surveys from two types of acoustic sensor (see Figure 10.4):

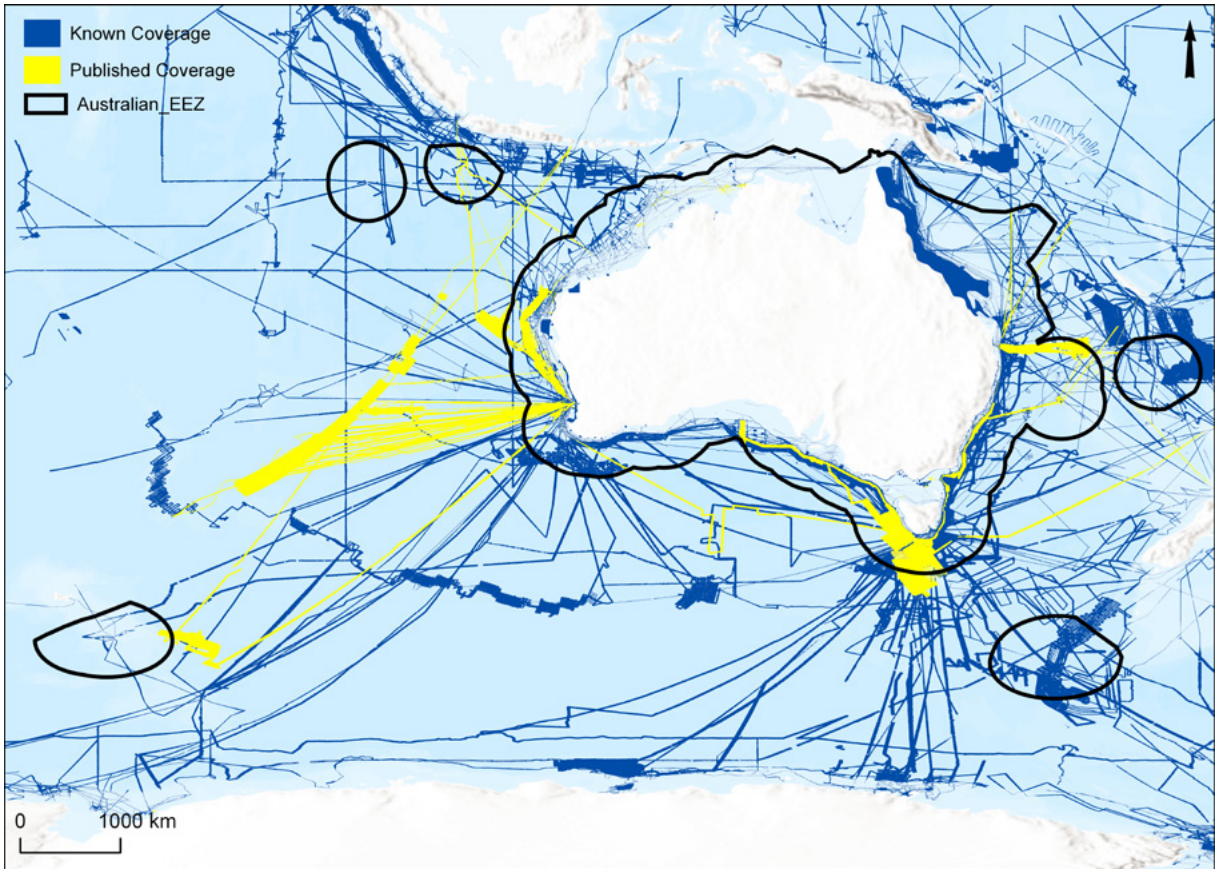
- single beam echosounders (SBES)—which produce a single line of waterbody depth points directly under the sensing platform. These measurements are usually acquired from a moving vessel to identify general seafloor patterns and/or schools of fish (see Section 10.2.1); or
- multibeam echosounders (MBES)—which capture swaths of data by acquiring multiple depth points. These datasets are very high resolution, providing data down to better than 1 m accuracy (see Section 10.2.3). With the capability of covering 100% of the seafloor, MBES are becoming the industry standard for hydrographic and geological applications.

Different acoustic frequencies are used to map different waterbody depths, with higher frequencies being used for shallow water and lower frequencies for deep water (see Section 10.1). Higher frequency, shallow water systems provide greater spatial resolution than lower frequency deep water systems (Picard *et al.*, 2020).

The Australian Hydrographic Office (AHO) retains a copy of every bathymetric survey acquired in Australian waters to be used for charting and navigation purposes. Geoscience Australia (GA) uses datasets acquired both internally and by other agencies and companies to produce a range of products to meet government and scientific needs, including:

- maps of individual surveys;
- a 50 m multibeam dataset of Australia, with a backscatter mosaic and a set of angular backscatter response curves; and
- the Australian Bathymetry and Topography Grid (see Excursus 13.1).

Figure 13.9 AusSeabed bathymetry holdings (by survey) in January 2020



Source: Geoscience Australia

The nationally coordinated program, AusSeabed, is improving the coordination of Australian seabed mapping activities, including collating existing seabed datasets and making them openly accessible, as well as the development of best practice guidelines. The AusSeabed data holdings in January 2020 are illustrated in Figure 13.9. This work contributes to global projects, such as the GEBCO-Nippon Foundation Seabed 2030 project (see Excursus 7.1).

Non-bathymetric applications of acoustic datasets for marine and coastal environments include:

- identification, classification and mapping of benthic habitats (Penrose *et al.*, 2005; see Section 3);
- biomass assessment of pelagic fisheries (see Section 20); and
- engineering and defence investigations of seabed to detect buried munitions, or assess the feasibility of burying cables and pipelines (Austine and Pyne, 2017).

13.4 Coastal Monitoring

While shipborne sensors are appropriate for mapping the seabed in deeper waters, they are not the most appropriate and efficient way to map very shallow waters near land. Bathymetric maps for the narrow coastal margin of the seafloor are best derived from:

- airborne bathymetric lidar systems—which yield datasets with high spatial and vertical resolutions for localised areas (see Section 13.4.1); and
- imagery acquired by spaceborne, optical sensors—which can be used to infer waterbody depth over larger regions (see Section 13.4.2).

13.4.1 Lidar bathymetry

Lidar (LIght Detection And Ranging) instruments can acquire bathymetric data over shallow waters (< 50 m water depth; Volume 1A—Section 15.1). Bathymetric lidar instruments are generally carried by aircraft and traditionally use a 532 nm laser (blue-green). This wavelength offers the most efficient solution in terms of the engineering and physical constraints in lidar instrument design. Lidar can also be used as *in situ* sensors (see Volume 3A—Excursus 5.1). However, the power of lidar must be constrained to comply with eye safety regulations, which limits its potential in some

situations. More recently, oceanographic lidar systems comprise multiple wavelengths. Chen *et al*. (2019) recommend the wavelength range 420–510 nm as optimal for open ocean and 520–580 nm for coastal waters. For 80% of the global ocean a 490 nm laser was shown to be most informative single wavelength (Chen *et al*., 2019).

As with all forms of EMR, some of the laser energy is refracted, backscattered, or absorbed by the water surface, the water column, and the substratum. These factors reduce the lidar signal returned by the substratum and limit the maximum waterbody depth that can be detected. The intense laser signal generated by lidar can penetrate to greater water depths than passive sunlight, and can reach 60 m in clear, coral waters (Purkis and Brock, 2013). The maximum depth penetration of a lidar system depends on its *kd* factor:

$$kd = k \times d$$

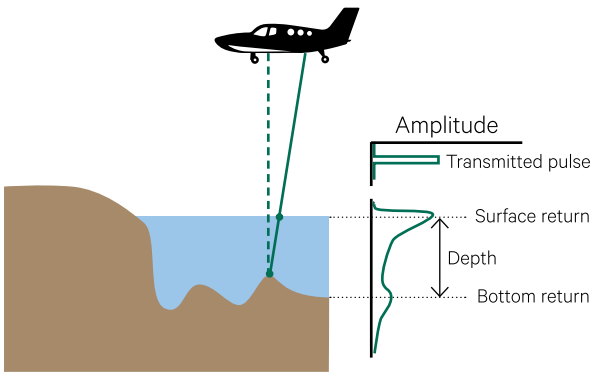
where

k is the attenuation coefficient of the water; and
d is the water depth.

Since high water clarity allows maximum light penetration, lidar acquisition is best timed during periods of minimum turbidity. Bathymetric lidar instruments frequently also carry a near infrared laser to measure the distance to the water surface. The waterbody depth is then determined from the time difference (in picoseconds) between the surface return and the substratum return (see Figure 13.10). It should be noted that the speed of light differs through air and water, so a dual wavelength lidar offers greater ranging accuracy. Lidar systems designed to capture submerged topography, rather than measure water depth, require more accurate aircraft positioning information.

Figure 13.10 Lidar bathymetry

Water depth can be computed from the travel time difference (*t*) between pulse returns from the water surface and the bottom. Depth = *ct*/2, where *c* is velocity of laser light pulse.



Adapted from: Purkis and Brock (2013) Figure 5.1

Like multibeam sonar, lidar sensors generate a 'point cloud' of data. The raw bathymetric lidar dataset comprises discrete sounding measurements, which can subsequently be processed into contour maps, triangulated area networks (TIN), or raster images (see Volume 2D—Section 13). Dark substrates typically give poor lidar returns, so dense meadows of seagrass and algae growing on the seafloor can create problems for this technology. Cloud cover is also a problem for lidar, but most airborne missions can be timed to avoid cloudy conditions.

Profiling oceanographic lidar systems deliver quantitative profiles for optical properties (beam and diffuse attenuation, absorption, volume scattering at 180°, and total backscattering) of the water column to depths of 20–30 m in productive coastal waters and 100 m in open ocean (Churnside, 2013).

Applications of bathymetric and profiling lidar include charting for navigational use, fisheries surveys, studies of coral reef ecosystems and geomorphology, and monitoring of coastal engineering and environmental change (Purkis and Brock, 2013). In particular, lidar is very appropriate for accurate seafloor mapping around coral reefs and flood vulnerability mapping in coastal terrain (Brock and Purkis, 2009).

13.4.2 Satellite-derived bathymetry (SDB)

As introduced in Section 13.3.2, bathymetric measurements have traditionally been derived from data acquired by shipborne echosounders. These vessels are usually subject to the underkeel clearance, which generally precludes their use in shallow water environments. Lidar systems are also used to acquire bathymetric data and are usually deployed on aircraft (see Section 13.4.1). However, the high cost of both deployment methods has led hydrographic organisations to evaluate and, in some cases, to integrate satellite-derived bathymetry (SDB) into operational products (for example, Canadian and UK Hydrographic Offices, Chénier *et al*., 2018a).

The use of SDB is largely driven by the existing gaps in hydrographic surveys (Chénier *et al*., 2018b), but the acceptance of this method is complicated given the need for adherence to minimum standard requirements for hydrographic surveys as defined by the International Hydrographic Organisation (IHO). The recently modified S-44 includes a specification matrix to allow some flexibility for the inclusion of non-traditional bathymetric data sources such as SDB products (IHO, 2020).

Methods were developed to use passive optical sensors to estimate and monitor bathymetry in coastal waters and were particularly useful for the high spatiotemporal assessment of coastal erosion, sea level changes, wave height modelling, and habitat monitoring (Poursanidis *et al.*, 2019; Traganos *et al.*, 2018). For these purposes, SDB methods have the advantage of large area coverage at lower cost and are ideally suited to monitoring dynamic shorelines, particularly in remote locations (Poppenga *et al.*, 2018). However, deriving bathymetry in shallow waters is complex, as these environments are subject to varying conditions for a range of factors including water depth, substrate, and water type, sunglint, surf zones, and anthropogenic impacts.

SDB methods have been based on either empirical or physics-based methods, although method category names vary with different authors (for example, Casal *et al.* (2020) describes them as either empirical, empirically-tuned physics-based, or physics-based inversion models whereas Traganos *et al.* (2018) refer to analytical, semi-analytical, or empirical methods).

A semi-empirical model such as the spectral band ratio technique (see Volume 2C—Section 10), also known as the natural logarithm method (Dierssen *et al.*, 2003; Stumpf *et al.*, 2003; IHO-IOC, 2016) have been applied in relatively clear waters for the retrieval of water column depth. These methods rely on the near exponential variation in light absorption of pure water as water depth increases (see Sections 5.1.1 and 8.2.1). Accordingly, since the bottom radiance of a longer wavelength band (such as visible green) will decay faster than that of a shorter wavelength band (such as visible blue), the ratio of the two bands will maintain a near constant value in a uniformly mixed water column. The logarithm of the band ratio is then taken to represent water depth changes as a linear gradient.

Empirically-tuned physics-based models adjust for the water column properties and variable light conditions through a regression with the satellite data and *in situ* depth data such as lidar or MBES (Casal *et al.*, 2020). The spatiotemporal application of this model to other locations and times, can be limited by water constituents and substratum changes, which will impact the performance of the model.

Non-linear empirical methods, such as neural networks require sufficient training data from *in situ* observations (or forward bio-optical modelling) to link EO reflectances to the full range of possible water column properties.

Machine Learning (ML) methods have also demonstrated improved performance over traditional empirical algorithms, but this approach has generally been implemented in relatively clear waters with few cases of turbid water. Table 13.4 lists recent models that have demonstrated potential for bathymetric retrievals. ML methods are well suited for large scale time series and, although demanding in time to train and stabilise, they may provide potential for operational deployment.

Table 13.4 Examples of neural network and machine learning models

Name	Description	Reference
BathyNET	BathyNet: A Deep Neural Network for Water Depth Mapping from Multispectral Aerial Images using a U-Net Convolution Neural Network (CNN)	Mandlburger *et al.* (2021)
SVR	Support Vector Regression	Agrafiotis *et al.* (2019)
SVM Non linear SVM	Support Vector Machine Non linear Support Vector Machine	Eugenio *et al.* (2015) Misra *et al.* (2018)
ANN RNN DNN	Artificial Neural Network Recurrent Neural Network Deep Neural Network	Makboul *et al.* (2017) Dickens and Armstrong (2019)
GLM	Lyzenga generalised model	Hassan and Nadaoka (2017)
BAG	Ensemble regression tree-fitting algorithm using bagging	Hassan *et al.* (2017)
LSB	Ensemble regression tree fitting algorithm of least squares boosting	Hassan *et al.* (2016)
RF	Random Forest algorithm	Sagawa *et al.* (2019)
MARS	Multi-adaptive Regression Spline	Hassan and Nadaoka (2017)

Adapted from: Ashphaq *et al.* (2021)

To address the issue of changing substratum and water column properties, radiative transfer equations were used to model the optical properties and concentrations of constituents in the water column, the substratum type, and the water depth from the measured bio-optical properties of the water. Lee *et al.*, (1999, 2001) developed a semi-analytical model for EO that expresses the subsurface remote-sensing reflectance r_{rs} as a function of a set of environmental variables, that is, measureable water properties which can be estimated from EO data (see Section 8.3). When the modelled remote sensing reflectance $r_{rs}^{modelled}$ is compared to the measured satellite remote sensing reflectance r_{rs}^{input}, the set of environmental variables that minimises the difference between the model and input reflectance provides the solution.

In Wettle and Brando (2006), Brando *et al.* (2009), and Dekker *et al.* (2011), the Lee *et al.* (2001) algorithm was enhanced and evolved into SAMBUCA, a semi-analytical model for bathymetry unmixing and concentration assessment. SAMBUCA was now able to retrieve simultaneous outputs of:

- the water's optically active constituent concentrations (chlorophyll a, coloured dissolved organic matter (CDOM), and non-algal particulate);
- the percentage substratum cover type (either as homogeneous or mixtures of two different types); water column depth; and
- metrics to assess the reliability of the retrieval.

Inversion methods have been applied to a range of multispectral and hyperspectral imagery, from both airborne and spaceborne sensors (Brando *et al.*, 2009; Hedley *et al.*, 2009; Botha *et al.*, 2013). All input imagery to these models require atmospheric correction (and possibly sunglint and skyglint corrections; Kay *et al.*, 2009) correction to ensure the r_{rs} is radiometrically corrected (see Sections 7.1 and 8.1.3) as inversion model retrievals can be underestimated from glint-affected images (Botha *et al.*, 2013).

A range of semi-analytical models have been developed for substrate and water column retrievals as shown in Table 13.5. In Dekker *et al.* (2011), a number of these models were compared, along with an empirical Lyzenga model. The HOPE, BRUCE and SAMBUCA models match spectra using a non-linear search to retrieve the best match of water column properties, waterbody depth, and substrate type. Several of the models have lookup tables (LUT), which are produced by numerical solutions of the radiative transfer model (RTM), to build large databases of reflectance spectra that correspond to a range of bio-optical conditions. The CRISTAL model's database is used to find a matched spectral reflectance to r_{rs}^{input}, then the database can provide the water column properties, waterbody depth, and substrate type. The ALLUT model uses an adaptive LUT method for IOP parameterisation of the model, which merges both methods.

It was found that the semi-analytical models performed better than the empirical model and they obtained an increased accuracy of retrievals with improved optical characterisation of the study site. An accurate characterisation or parameterisation provides boundary conditions for the retrieval of the environmental variables. The results of the models in Dekker *et al.*, 2011, were produced in relatively clear waters and such results would be less reliable from waters with higher levels of phytoplankton or CDOM (Botha *et al.*, 2013). Fearns *et al.* (2011) used a physics-based inversion method (which explicitly deals with water column constituents and benthic material estimation) with airborne HyMap imagery to retrieve bathymetry over coral reef environments.

Similarly, Collings *et al.* (2018) used World View-2 satellite imagery of a coastal region near Perth, with water depths of 2–20 m, to compare the classical stereo photogrammetric approach to bathymetric mapping with an RTM method (Semi-Analytical Model for Unmixing and Concentration Assessment: SAMBUCA; Botha *et al.*, 2016). When validated against lidar bathymetry and towed video data, the modelling approach gave the most accurate results over sand substrates, while stereo algorithms were most effective when different depth features were well-contrasted. A hybrid method that stratified the study area by substrate type allowed the most appropriate bathymetric algorithm to be used.

Table 13.5 Examples of semi-analytical models

A common architecture for all Sentinel Toolboxes is being jointly developed by Brockmann Consult, SkyWatch, and C-S called the Sentinel Application Platform (SNAP). ESA: European Space Agency; SANP:

NAME	Description	Reference
HOPE	Hyperspectral Optimization Process Exemplar	Lee *et al.* (1999)
SAMBUCA	Semi-Analytical Model for Unmixing and Concentration Assessment	Brando *et al.* (2009)
BRUCE	Bottom Reflectance Un-mixing Computation of the Environment model	Klonowski *et al.* (2007)
SWAM	Shallow WAter inversion Model—ESA's SANP toolbox (*https://step.esa.int/main/toolboxes/snap/*)	Hedley *et al.* (2018)
SWIM	Shallow Water Inversion Model	McKinna *et al.* (2015)
CRISTAL	Comprehensive Reflectance Inversion based on Spectrum matching and Table Lookup)	Mobley and Bissett (2011)
ALLUT	Adaptive Linearized Lookup Trees	Hedley *et al.* (2009)
SMLUT	Spectrum Matching and Look Up Table inversion method	Mobley *et al.* (2005)
BOMBER	Bio-Optical Model Based tool for Estimating water quality and bottom properties from Remote sensing images	Giardino *et al.* (2012)

Adapted from: Ashphaq *et al.* (2021)

13.5 Further Information

Bathymetry

Geoscience Australia: *http://www.ga.gov.au/scientific-topics/marine/survey-techniques/bathymetry*

International Hydrographic Organisation (IHO) Data Centre for Digital Bathymetry (DCDB): *https://www.ngdc.noaa.gov/iho/*

EOMAP: Satellite Derived Bathymetry: *http://www.eomap.com/services/bathymetry/*

Bathymetric data repositories

General Bathymetric Chart of the Oceans (GEBCO): *https://www.gebco.net*

Archive of seafloor charts: *https://www.gebco.net/data_and_products/historical_gebco_charts/*

AusSeabed: *http://www.ausseabed.gov.au*

Seamap Australia

Australian seabed habitat classification scheme and spatial database: *https://seamapaustralia.org*

Australasian Underwater Cultural Heritage Database

https://www.environment.gov.au/heritage/underwater-heritage/auchd

Marine Gravity

Sandwell and Smith (1997)

Exploring Ocean Tectonics from Space: *https://topex.ucsd.edu/grav_outreach/index.html#grav_map*

13.6 References

Agrafiotis, P., Skarlatos, D., Georgopoulos, A., and Karantzalos, K. (2019). Shallow water bathymetry mapping from uav imagery based on machine learning. *International Archives Photogrammetry, Remote Sensing and Spatial Information Sciences*, XLII-2/W10, 9–6. *https://doi.org/10.5194/isprs-archives-XLII-2-W10-9-2019*

Ashley, G.M., Boothroyd, J.C., Bridge, J.S., Clifton, H.E., Dalrymple, R.W., Elliott, T., Flemming, B.W., Harms, J.C., Harris, P.T., Hunter, R.E., Kreisa, R.D., Lancaster, N., Middleton, G.V., Paola, C., Rubin, D.M., Smith, J.D., Southard, J.B., Terwindt, J.H.I., and Twitchell, D.C. (1990). Classification of large-scale subaqueous bedforms: a new look at an old problem. *Journal of Sedimentary Petrology*, 60, 160–172.

Ashphaq, M., Srivastava, P.K., and Mitra, D. (2021). Review of near-shore satellite derived bathymetry: classification and account of five decades of coastal bathymetry research. *Journal of Ocean Engineering and Science*. *https://doi.org/10.1016/j.joes.2021.02.006*

Austine K., and Pyne, A. (2017). Subsea Cable Route Surveying—Planning challenges. *Hydro International*. *https://www.hydro-international.com/content/article/subsea-cable-route-surveying*

Australian Government (2017). *The Data Behind the Search for MH370*. Available at: *https://geoscience-au.maps.arcgis.com/apps/Cascade/index.html?appid=038a72439bfa4d28b3dde81cc6ff3214*

Beaman, R.J. (2017). *High-resolution depth model for the Great Barrier Reef—30 m*. Geoscience Australia, Canberra.

Beaman, R. (2018). *High-resolution depth model for Northern Australia—30 m*. Geoscience Australia, Canberra.

Beaman, R. (2020). *High-resolution depth model for the Great Barrier Reef and Coral Sea—100 m*. Geoscience Australia, Canberra. *https://ecat.ga.gov.au/geonetwork/srv/eng/catalog.search#/metadata/133163*

Botha, E.J., Brando, V.E., Anstee, J.M., Dekker, A.G., and Sagar, S. (2013). Increased spectral resolution enhances coral detection under varying water conditions. *Remote Sensing of Environment*, 131, 247–261.

Botha, E.J., Brando, V., and Dekker, A.J. (2016). Effects of per-pixel variability on uncertainties in bathymetric retrievals from high-resolution satellite images. *Remote Sensing*, 8, 459. *https://doi.org/10.3390/rs8060459*

Brando, V.E., Anstee, J.M., Wettle, M., Dekker, A.G., Phinn, S.R., and Roelfsema, C. (2009). A physics based retrieval and quality assessment of bathymetry from suboptimal hyperspectral data. *Remote Sensing of Environment*, 113, 755–770. doi:10.1016/j.rse.2008.12.003.

Brock, J.C., and Purkis, S.J. (2009). The emerging role of LiDAR remote sensing in coastal research and resource management. *Journal of Coastal Research*, 53, 1–5.

Casal, G., Hedley, J.D., Monteys, X., Harris, P., Cahalane, C., and McCarthy, T. (2020). Satellite-derived bathymetry in optically complex waters using a model inversion approach and Sentinel-2 data, *Estuarine, Coastal and Shelf Science*, 241, 106814. *https://doi.org/10.1016/j.ecss.2020.106814*.

Chen, S., Xue, C., Zhang, T., Hu, L., Chen, G., and Tang, J. (2019). Analysis of the Optimal Wavelength for Oceanographic Lidar at the Global Scale Based on the Inherent Optical Properties of Water. *Remote Sensing*, 11, 2705. doi:10.3390/rs11222705

Chénier, R., Faucher, M.-A., Ahola, R., Shelat, Y., and Sagram, M. (2018a). Bathymetric Photogrammetry to Update CHS Charts: Comparing Conventional 3D Manual and Automatic Approaches. *ISPRS International Journal Geo-Information*, 7(10), 395. *https://doi.org/10.3390/ijgi7100395*

Chénier, R., Faucher, M.-A., and Ahola, R. (2018b). Satellite-derived bathymetry for improving Canadian Hydrographic Service charts. *ISPRS International Journal Geo-Information*, 7, 306. *https://www.mdpi.com/2220-9964/7/8/306*.

Churnside, J.H. (2013). Review of profiling oceanographic lidar. *Optical Engineering*, 53(5), 051405. *https://doi.org/10.1117/1.OE.53.5.051405*

Collings, S., Botha, E.J., Anstee, J., and Campbell, N. (2018). Depth of Satellite Images: Depth Retrieval Using a Stereo and Radiative Transfer-based Hybrid Method. (2018). *Remote Sensing*, 8, 1247. *https://doi.org/10.3390/rs10081247*

Dekker, AG.., Phinn, SR.., Anstee, J., Bissett, P., Brando, V.E., Casey, B., Fearns, P., Hedley, J., Klonowski, W., Lee, Z.P., Lynch, M., Lyons, M., Mobley, C., and Roelfsema, C. (2011). Intercomparison of shallow water bathymetry, hydrooptics, and benthos mapping techniques in Australian and Caribbean coastal environments. *Limnology and Oceanography Methods*, 9, 396–425.

Dickens, K., and Armstrong, A. (2019). Application of machine learning in satellite derived bathymetry and coastline detection. SMU Data Science Review, 2(1). *https://scholar.smu.edu/datasciencereview/vol2/iss1/4*

Dierssen, H.M., Zimmerman, R.C., Leathers, R.A., Downes, T.V., and Davis, C.O. (2003). Ocean color remote sensing of seagrass and bathymetry in the Bahamas Banks by high resolution airborne imagery. *Limnology and Oceanography*, 48(1), 444–455.

Eugenio, F., Marcello, J., and Martin, J. (2015). High-Resolution Maps of Bathymetry and Benthic Habitats in Shallow-Water Environments Using Multispectral Remote Sensing Imagery. *IEEE Transactions on Geoscience and Remote Sensing*, 53(7), 3539–3549. *https://doi.org/10.1109/TGRS.2014.2377300*

Fearns, P.R.C., Klonowski, W., Babcock, R.C., England, P., and Phillips, J. (2011). Shallow water substrate mapping using hyperspectral remote sensing. *Continental Shelf Research* 31, 1249–1259.

GA (2018). *Australian Bathymetry and Topography Grid* webpage, Geoscience Australia website: *https://ecat.ga.gov.au/geonetwork/srv/eng/catalog.search?node=srv#/metadata/a05f7892-fae9-7506-e044-00144fdd4fa6*

GEBCO (2017). *Seabed 2030: Roadmap for Future Ocean Floor Mapping*. The Nippon Foundation/GEBCO (General Bathymetric Chart of the Oceans), June 2017. *https://www.gebco.net/documents/seabed_2030_roadmap_v10_low.pdf*

Giardino, C., Candiani, G., Bresciani, M., Lee, Z., Gagliano, S., and Pepe, M. (2012). BOMBER: A tool for estimating water quality and bottom properties from remote sensing images. *Computers and Geosciences*, 45, 313–318. *https://doi.org/10.1016/j.cageo.2011.11.022*

Harris, P., Heap, A., Passlow, V., Shaffi, L., Fellows, M., Porter-Smith, R., Buchanan, C., and Daniell, J. (2005). *Geomorphic Features of the Continental Margin of Australia*. Geoscience Australia, Canberra.

Hassan, M., Negm, A., Zahran, M., and Saavedra, O. (2016). Bathymetry Determination from High Resolution Satellite Imagery Using Ensemble Learning Algorithms in Shallow Lakes: Case Study El-Burullus Lake. *International Journal of Environmental Science and Development*, 7(4), 295–301. *https://doi.org/10.7763/IJESD.2016.V7.787*

Hassan, M., Salah, M., Nadaoka, K., and Zahran, M. (2017). Assessment of proposed approaches for bathymetry calculations using multispectral satellite images in shallow coastal / lake areas : a comparison of five models. *Arabian Journal of Geosciences*, 10, 42. *https://doi.org/10.1007/s12517-016-2803-1*

Heap, A.D., and Harris, P.T. (2008). Geomorphology of the Australian Margin and Adjacent Seafloor. *Australian Journal of Earth Sciences*, 55(4), 555–585. *http://dx.doi.org/10.1080/08120090801888669*

Hedley, J.D., Roelfsema, C., and Phinn, S.R. (2009). Efficient radiative transfer model inversion for remote sensing applications. *Remote Sensing of Environment,* 113(11), 2527–2532.

Hedley, J.D., Roelfsema, C., Brando, V., Giardino, G., Kutser, T., Phinn, S., Mumby, P.J., Barrilero, O., Laporte, J., and Koetz, B. (2018). Coral reef applications of Sentinel-2: Coverage, characteristics, bathymetry and benthic mapping with comparison to Landsat 8. *Remote Sensing of Environment*, 216, 598–614. *https://doi.org/10.1016/j.rse.2018.07.014*

Hussein, H.M., and Nadaoka, K. (2017). Assessment of machine learning approaches for bathymetry mapping in shallow water environments using multispectral satellite images. *International Journal of GeoInformatics*, 13(2). *https://doi.org/10.52939/ijg.v13i2.1030*

IHO (2001). *Standardization of Undersea Feature Names: Guidelines Proposal form Terminology*. International Hydrographic Organisation and International Oceanographic Commission, Monaco. 40 p.

IHO (2020). *International Hydrographic Organization Standards for Hydrographic Surveys*. International Hydrographic Organisation. *https://iho.int/uploads/user/pubs/standards/s-44/S-44_Edition_6.0.0_EN.pdf*

IHO-IOC (2016). *The IHO-IOC GEBCO cook book*. IHO Publication B–11 (Monaco), IOC Manuals and Guides 63 (France). International Hydrographic Organization, Intergovernmental Oceanographic Commission. *https://www.gebco.net/data_and_products/gebco_cook_book/*

Kay, S., Hedley, J.D., and Lavender, S. (2009). Sun Glint Correction of High and Low Spatial Resolution Images of Aquatic Scenes: a Review of Methods for Visible and Near-Infrared Wavelengths. *Remote Sensing*, 1(4), 697–730. *https://doi.org/10.3390/rs1040697*

Keene, J., Baker, C., Tran, M., and Potter, A. (2008). *Geomorphology and Sedimentology of the East Marine Region of Australia*. Geoscience Australia, Record 2008/10. Geoscience Australia, Canberra. 262 p.

Klonowski, W.M., Fearns, P.R.C.S., and Lynch, M.J. (2007). Retrieving key benthic cover types andbathymetry from hyperspectral imagery. *Journal Applied Remote Sensing*, 1(1), 011505. *https:/doi.org/10.1117/1.2816113*

Lee, Z.P., Carder, K.L., Mobley, C.D., Steward, R.G., and Patch, J.F. (1999). Hyperspectral remote sensing for shallow waters: II. deriving bottom depths and water properties by optimization. *Applied Optics*, 38, 3831–3843, *https://doi.org/10.1364/AO.38.003831*

Lee, L. Kendall, C., Chen, R.F., and Peacock, T.G. (2001). Properties of the water column and bottom derived from Airborne Visible Imaging Spectrometer (AVIRIS) data. J*ournal of Geophysical Research*, 106, 11639–11651.

Lyzenga, D., Malinas, N., and Tanis, F. (2006). Multispectral bathymetry using a simple physically based algorithm. *IEEE Transactions on Geoscience and Remote Sensing,* 44, 2251–2259.

McKinna, L., Fearns, P., Weeks, Werdell, P.J., S., Reichstetter, M., Franz, B., Shea, D.M., and Feldman, G. (2015). A semianalytical ocean color inversion algorithm with explicit water column depth and substrate reflectance parameterization. *Journal of Geophysical Research: Oceans*, 120(3), 1741–1770. *https://doi.org/10.1002/2014JC010224*

Makboul, O., Negm, A., Mesbah, S., and Mohasseb, M. (2017). Performance Assessment of ANN in Estimating Remotely Sensed Extracted Bathymetry. Case Study: Eastern Harbor of Alexandria. *Procedia Engineering*, 181, 912–919. *https://doi.org/10.1016/j.proeng.2017.02.486*

Mandlburger, G., Kölle, M., Nübel, H., and Soergel, U. (2021). BathyNet: A Deep Neural Network for Water Depth Mapping from Multispectral Aerial Images. *PFG—Journal of Photogrammetry, Remote Sensing and Geoinformation Science*, 89, 71–89. *https://doi.org/10.1007/s41064-021-00142-3*

Misra, A., Vojinovic, Z., Ramakrishnan, B., Luijendijk, A., and Ranasinghe, R. (2018). Shallow water bathymetry mapping using Support Vector Machine (SVM) technique and multispectral imagery. *International Journal of Remote Sensing*, 39(13), 4431–4450. *https://doi.org/10.1080/01431161.2017.1421796*

Mobley, C.D., and Bissett, W.P. (2011). *CRISTAL user's guide and technical documentation*. Sequoia Scientific, Inc. 97 p. *https://www.iisd.org/publications/cristal-users-manual-version-5-community-based-risk-screening-tool-adaptation-and*

Mobley, C.D., Sundman, L.K., Davis, C.O., Bowles, J.H., Downes, T.V., Leathers, R.A., Montes, M.J., Bissett, W.P., Kohler, D.D.R., Reid, R.P., Louchard, E.M., and Gleason, A. (2005). Interpretation of hyperspectral remote-sensing imagery by spectrum matching and look-up tables. *Applied Optics*, 44, 3576–3592. *https://doi.org/10.1364/AO.44.003576*

Olson, C.J., Becker, J.J., and Sandwell, D.T. (2016). *SRTM15_PLUS: Data Fusion of Shuttle Radar Topography Mission (SRTM) Land Topography with Measured and Estimated Seafloor Topography (NCEI Accession 0150537)*. Version 1.1. Asheville: NOAA National Centers for Environmental Information.

Penrose, J.D., Siwabessy, P.J.W., Gavrilov, A., Parnum, I., Hamilton, L.J., Bickers, A., Brooke, B., Ryan, D.A., and Kennedy, P. (2005). *Acoustic Techniques for Seabed Classification*. Technical Report 32, CRC for Coastal Zone Estuary and Waterway Management.

Picard, K., Brooke, B.P., Harris, P.T., Siwabessy, P.J.W., Coffin, M.F., Tran, M., Spinoccia, M., Weales, J., Macmillan-Lawler, M., and Sullivan, J. (2018). Malaysia Airlines flight MH370 search data reveal geomorphology and seafloor processes in the remote southeast Indian Ocean. *Marine Geology*, 395, 301–319. *https://doi.org/10.1016/j.margeo.2017.10.014*

Picard, K., Leplastrier, A., Austine, K., Bergersen, N., Cullen, R., Dando, N., Donohue, D., Edwards, S., Ingleton, T., Jordan, A., Lucieer, V., Parnum, I., Siwabessy, J., Spinoccia, M., Talbot-Smith, R., Waterson, C., Barrett, N., Beaman, R., Bergersen, D., Boyd, M., Brace, B., Brooke, B., Cantrill, O., Case, M., Dunne, S., Fellows, M., Harris, U., Ierodiaconou, D., Johnstone, E., Kennedy, P., Leplastrier, A., Lewis, A., Lytton, S., Mackay, K., McLennan, S., Mitchell, C., Nichol, S., Post, A., Price, A., Przeslawski, R., Pugsley, L., Quadros, N., Smith, J., Stewart, W., Sullivan J., Tran, M., and Whiteway, T. (2020). *Australian Multibeam Guidelines 2020*. Version 2.0. Record 2018/19. Geoscience Australia, Canberra. *http://dx.doi.org/10.11636/Record.2018.019*

Poppenga, S.K., Palaseanu-Lovejoy, M., Gesch, D.B., Danielson, J.J., and Tyler, D.J. (2018). *Evaluating the potential for near-shore bathymetry on the Majuro Atoll, Republic of the Marshall Islands, using Landsat 8 and WorldView-3 imagery*. U.S. Geological Survey Scientific Investigations Report 2018–5024. 14 p. *https://doi.org/10.3133/sir20185024*.

Poursanidis, D., Dimosthenis T., Nektarios C., and Peter R. (2019). Cubesats Allow High Spatiotemporal Estimates of Satellite-Derived Bathymetry. *Remote Sensing*, 11(11), 1299. *https://doi.org/10.3390/rs11111299*

Purkis, S.J., and Brock, J.C. (2013). Lidar Overview. Ch 5 in *Coral Reef Remote Sensing*. (Eds: Goodman, J.A., Purkis, S.J., and Phinn, S.R.). Springer, Dordrecht. ISBN 978-90-481-9291-5.

Sagawa, T., Yamashita, Y., Okumura, T., and Yamanokuchi, T. (2019). Satellite Derived Bathymetry Using Machine Learning and Multi-Temporal Satellite Images. *Remote Sensing*, 11(10), 1155. *https://doi.org/10.3390/rs11101155*

Sandwell, D.T., and Smith, W.H.F. (1997). *Exploring the Ocean Basins with Satellite Altimeter Data* webpage: *https://topex.ucsd.edu/marine_grav/explore_grav.html*

Sandwell, D.T., Müller, R.D., Smith, W.H.F., Garcia, E., and Francis, R. (2014). New global marine gravity model from CryoSat-2 and Jason-1 reveals buried tectonic structure. *Science*, 346(6205), 65-67. doi:10.1126/science.1258213

Smith, W.H.F., and Sandwell, D.T. (1997). Global seafloor topography from satellite altimetry and ship depth soundings. *Science*, 277, 1957–1962.

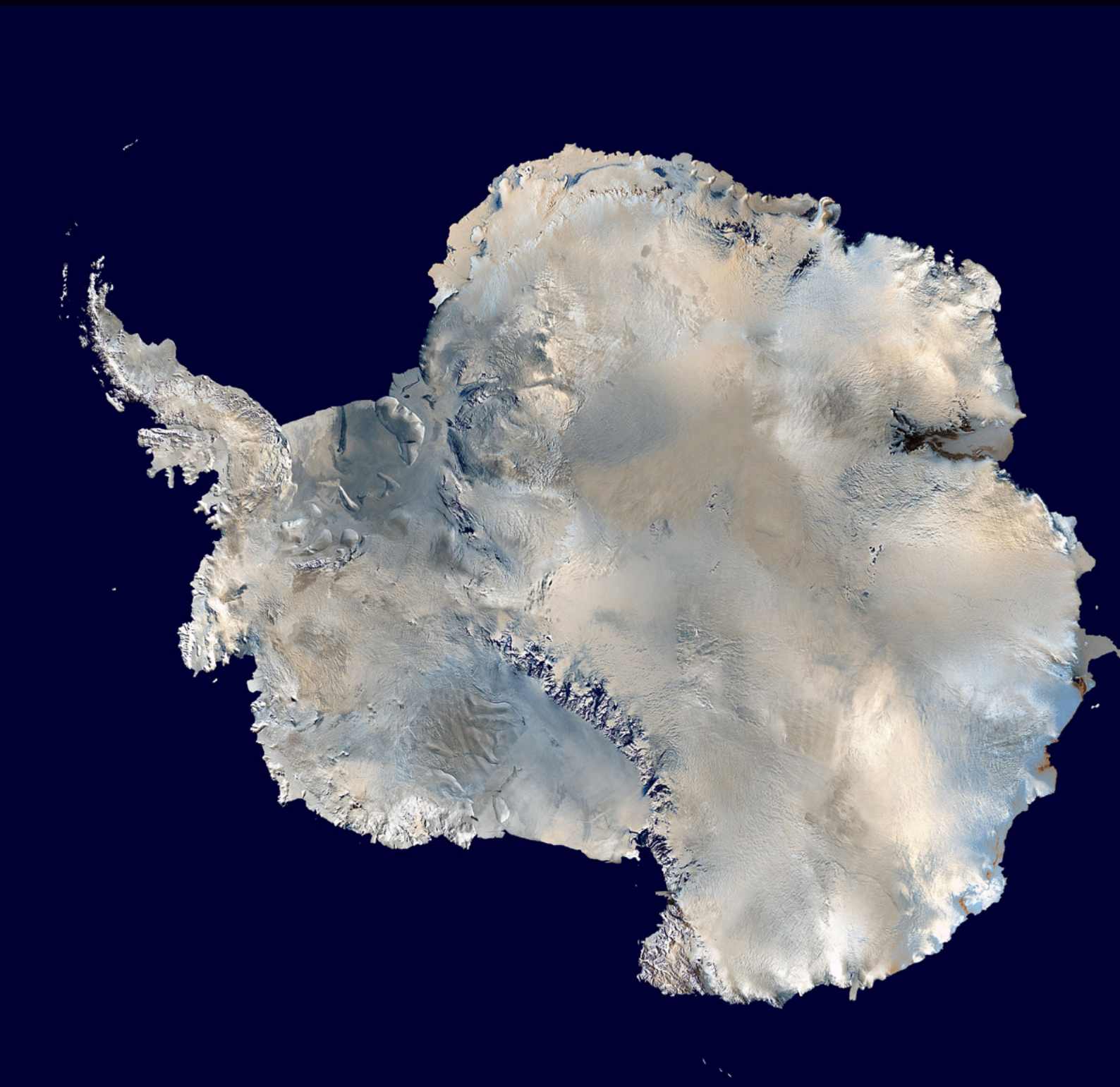
Stumpf, R.P., Holderied, K., and Sinclair, M. (2003). Determination of water depth with high-resolution satellite imagery over variable bottom types. *Limnology and Oceanography,* 48, 547–556.

Traganos, D., Poursanidis, D., Aggarwal, B., Chrysoulakis, N., and Reinartz, P. (2018). Estimating Satellite-Derived Bathymetry (SDB) with the Google Earth Engine and Sentinel-2. *Remote Sensing*; 10(6), 859. *https://doi.org/10.3390/rs10060859*

Wettle, M., and Brando, V.E. (2006). *SAMBUCA—Semi-analytical model for Bathymetry, un-mixing and concentration assessment*. CSIRO Land and Water, Canberra. *https://doi.org/10.4225/08/5866a187b7a3c*

Wölfl, A.-C., Snaith, H., Amirebrahimi, S., Devey, C.W., Dorschel, B., Ferrini, V., Huvenne, V.A.I., Jakobsson, M., Jencks, J., Johnston, G., Lamarche, G., Mayer, L., Millar, D., Pedersen, T.H., Picard, K., Reitz, A., Schmit,t T., Visbeck, M., Weatherall, P., and Wigley, R. (2019). Seafloor Mapping—The Challenge of a Truly Global Ocean Bathymetry. *Frontiers in Marine Science*, 6, 283. *https://doi.org/10.3389/fmars.2019.00283*

Observing Surface Water Energy



The following four sections detail EO-based analyses that can be used to map and monitor the energy in surface waters:

- temperature—details EO methods and datasets used to estimate sea surface temperature and inland water temperature, and detect sea ice (see Section 14);
- ice—considers EO methods to map and monitor both sea ice and ice sheets (see Section 15);
- wind and waves—describe EO methods for mapping and monitoring marine surface waves (see Section 16); and
- circulation—introduces EO techniques that can be used to monitor ocean circulation patterns (see Section 17).

Contents

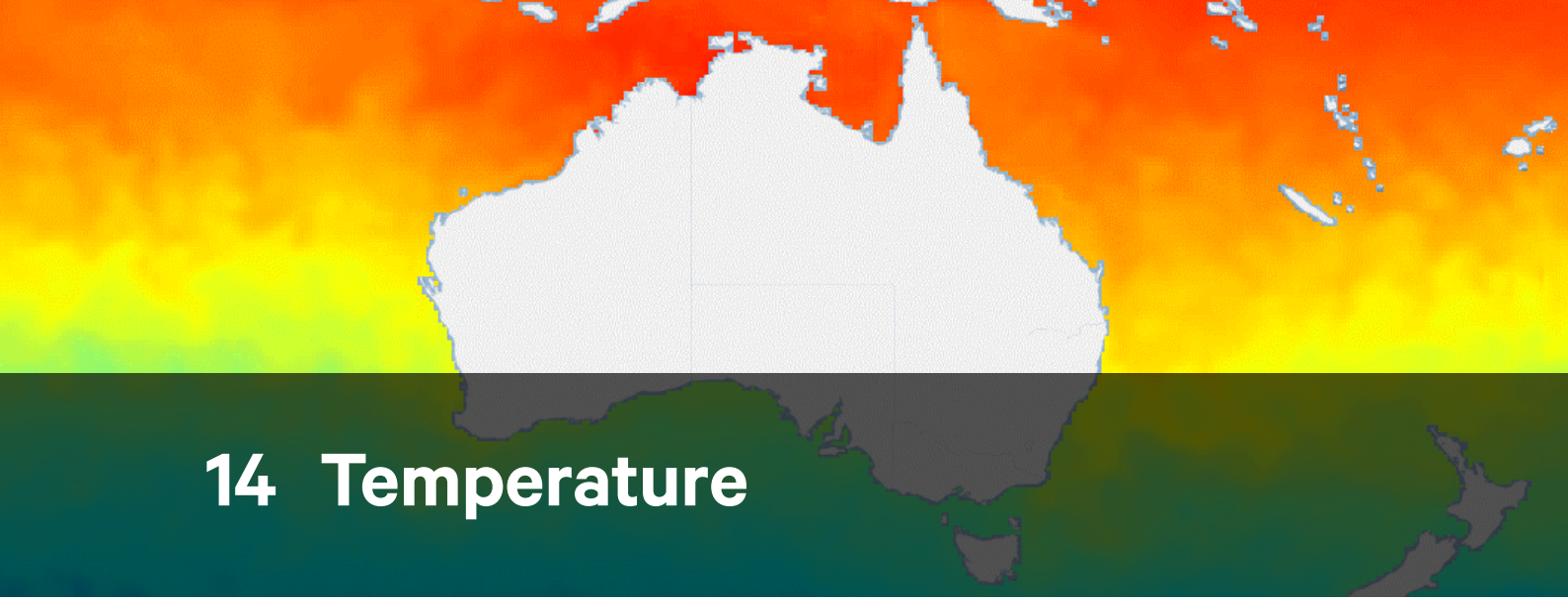
14 Temperature 245

15 Ice 281

16 Winds and Waves 311

17 Circulation 329

Background image on previous page: An orthographic projection of Antarctica from NASA's Blue Marble dataset (1 km resolution global satellite composite) derived from MODIS and AVHRR imagery. **Source:** Davepape, Wikimedia Commons. Retrieved from *https://en.wikipedia.org/wiki/File:Antarctica_6400px_from_Blue_Marble.jpg*



14 Temperature

Helen Beggs

Sea surface temperature (SST) is a vital parameter across a range of marine and climate sciences. Because SST strongly modulates air-sea fluxes it is an essential parameter in weather prediction and atmospheric model simulations. It is also of great importance to the biodiversity and biogeochemistry of the oceans, and marine ecosystem dynamics (Wijffels *et al.,* 2018; see Sections 3, 5, 19, 20, and 21). SST measurements benefit a wide spectrum of operational applications, including ocean, weather, climate and seasonal monitoring/forecasting, military defence operations, validation of atmospheric models, sea turtle tracking, evaluation of coral bleaching, tourism, and commercial fisheries management (Beggs, 2010; O'Carroll *et al.,* 2019; Merchant *et al.,* 2019a). To measure SST, scientists deploy temperature sensors on satellites, drifting and moored buoys, ships, Argo floats, gliders, marine mammals (for example, seals), and ocean reference stations (Merchant *et al.,* 2019a). *In situ* measurements from drifting buoys, moorings, Argo floats, and ships are commonly used to calibrate and validate the satellite-derived SST data (see Section 12.2.2).

In the following sections we introduce temperature variations in Australian surface waters (see Section 14.1) then consider Earth Observation (EO) sensors that are used to map and monitor the temperature of the water surface (see Section 14.2). Methods for retrieving and validating SST from EO imagery are detailed in Section 14.3. Sections 14.4 and 14.5 introduce global and regional satellite products respectively and some sample applications, while Section 14.6 describes the use of EO datasets for observing water temperature of inland waterbodies.

14.1 Temperature of Australian Surface Waters

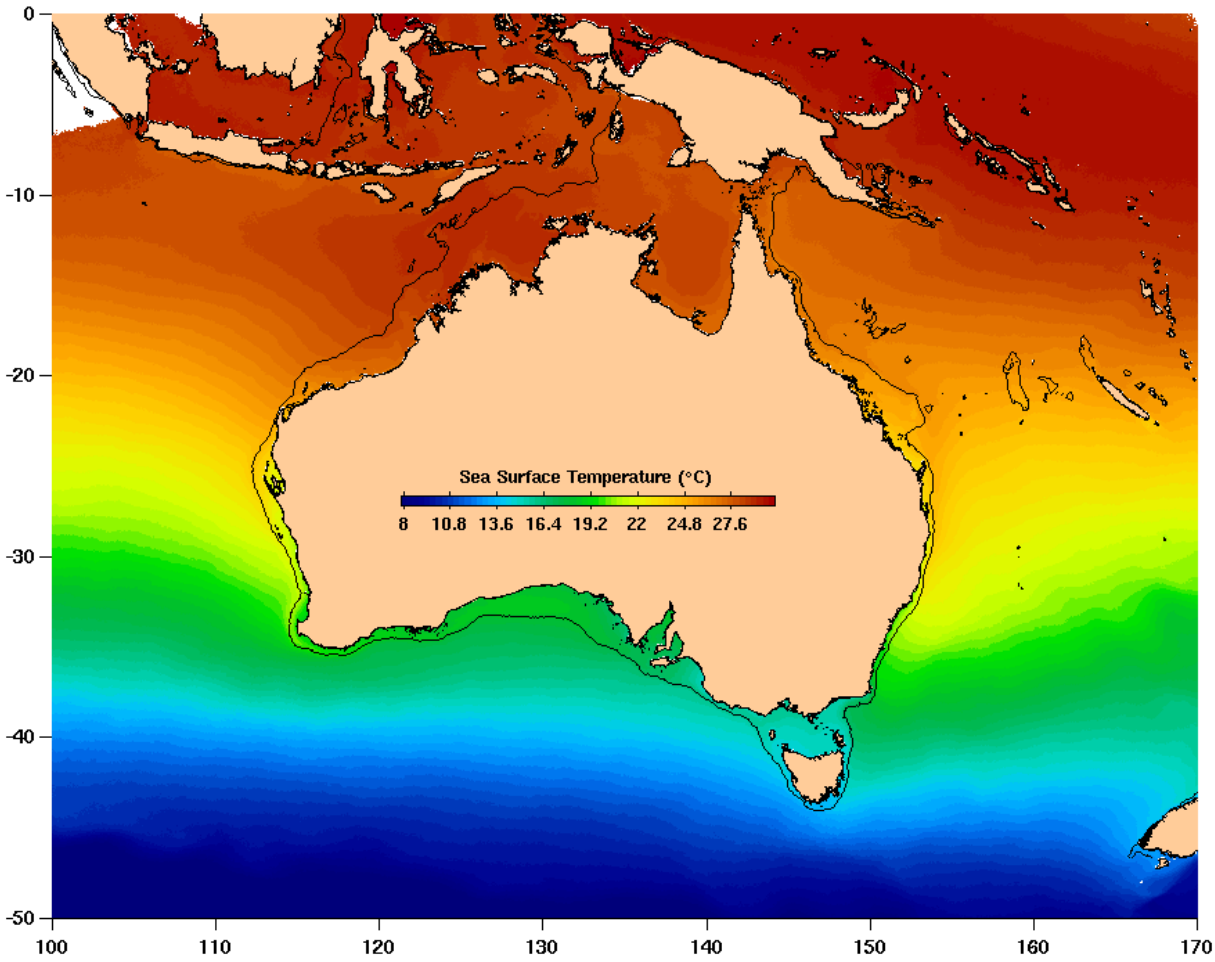
As discussed in Section 1.2 above, the oceans around Australia cover the extremes of the Tropical Warm Pool to the north of Australia, containing the largest area of warmest surface SSTs on the globe, to the Southern Ocean and the 'Roaring Forties' to the south. Indicative water temperatures surrounding the Australian land mass are shown in Figure 14.1, as derived from remotely sensed SST (Wijffels *et al.,* 2018; Griffin *et al.,* 2017).

Background image: Sea surface temperature image for 2 November 2020. Source: Helen Beggs, Bureau of Meteorology, Melbourne.

Recommended Chapter Citation: Beggs, H. (2021). Temperature. Ch 14 in *Earth Observation: Data, Processing and Applications. Volume 3B—Surface Waters.* CRCSI, Melbourne. pp. 245–279. ISBN 978-0-6482278-5-4.

Figure 14.1 Average SST around Australia

This map from the Atlas of Australian Regional Seas (SSTAARS—see Section 14.7) shows mean sea surface temperature (SST) from 1992 to 2016, as derived from AVHRR imagery.



Source: IMOS OceanCurrent (2018). Retrieved from *http://oceancurrent.imos.org.au/monthlymeans.php?link=/30d_MEAN/CLIM_OFAM3_SSTAARS/SST30d/00.gif*

14.2 EO Sensors for Water Temperature

As introduced in Volume 1A—Sections 5.2.2, the thermal radiation of the Earth's surface can be sensed remotely by detecting emissions in the wavelength ranges of:

- middle infrared (MIR: 3–8 μm);
- thermal infrared (TIR: 8–15 μm; see Volume 1A—Section 14.4, and Volume 1B—Section 7); and/or
- microwave (MW: 1–300 mm; see Volume 1A—Section 14.5, and Volume 1B—Section 8.1).

The MIR region is predominantly used for sensing emissions from very hot objects, such as fires and other man-made and natural thermal features on the Earth's surface. Since the TIR radiation range coincides with the peak energy emission of Earth, it is used for monitoring surface water temperature (SWT) and land surface temperature (LST). Passive microwave (PMW) sensors, however, detect emissions of thermal radiation in the microwave region at the very low energy end of the Earth's energy spectrum (see Figure 9.1).

EO sensors used for measuring SWT over the Australian region are listed in Table 14.1, and their essential details are summarised below. For a complete list of satellite sensors that have provided SWTs along with further details, refer to Minnett *et al.* (2019). In the text below, we collectively refer to MIR and TIR sensors as infrared (IR) sensors. Since SST specifically refers to the surface temperature of marine waters, the term SWT is used in this chapter when referring to the surface temperature of both inland and marine waterbodies.

Table 14.1 EO sensors relevant to water temperatures

TIR: Thermal infrared

Type	Sensor	Platform	Spatial Resolution (nadir)	Relevance	Advantages	Disadvantages
Passive optical	TIR wide swath (e.g. AVHRR, MODIS, VIIRS, SGLI)	Polar orbiting satellite (e.g. NOAA-6 to NOAA19, METOPA/B/C, Aqua, Terra, Suomi-NPP, NOAA-20, GCOMC)	0.25–4 km (large off-nadir angles reduce resolution)	SST, Inland water temperatures	Available from 1981, high spatial resolution, good accuracy, good global coverage	Fails over cloud and in presence of atmospheric aerosol, AVHRR on NOAA-6 to NOAA-19 satellites experienced significant orbital drift
	TIR dual-view radiometer (e.g. ATSR-1/2, AATSR, SLSTR)	Polar orbiting satellite (e.g. ERS1/2, Envisat, Sentinel-3a/b)	1–2 km (large off-nadir angles reduce resolution)	SST	Most accurate high resolution satellite SST data source, useful for bias-correcting other satellite SST	Only available from 1991, sparser spatial coverage due to narrower swaths, fails over cloud
	TIR Earth Disc Radiometer (e.g. JAMI, AHI)	Geostationary satellite (e.g. MTSAT-1R, MTSAT-2, Himawari-8/9)	2–10 km (large off-nadir angles reduce resolution)	SST, Inland water temperatures	Frequent update (60 min or 10 min) resolves sub-daily features	Limited field of view with no data at high latitudes, coarser spatial resolution than infrared sensors from polar orbiters, fails over cloud and in presence of atmospheric aerosol
Passive microwave	Microwave radiometer (e.g. AMSR-E, AMSR2, TMI, GMI)	Polar orbiting satellite (e.g. Aqua, GCOM-W, TRMM, GPM)	25–50 km	SST, Snow, Ice	Able to measure SST under non-precipitating cloud and therefore better spatial coverage than infrared	Affected by rain, no useable SST within ~50 km of land

Source for data: Minnett *et al.* (2019)

14.2.1 Infrared sensors

The first instrument to measure SWT from space was the High Resolution Infrared Radiometer (HRIR) in 1964 onboard NASA's sun-synchronous Nimbus-1 satellite (launched in 1964). Since HRIR only had a single infrared (IR) channel (3.5–4.1 μm), it could be used for describing variations in SST in clear-sky regions, but not for quantitative measurements (Allison and Kennedy, 1967).

Accurate EO of SWT became possible with the launch of the multi-channel Advanced Very High Resolution Radiometer (AVHRR) passive IR sensor, which was first carried by the Television Infrared Observation Satellite (TIROS-N) in 1978. The six channels acquired by AVHRR/3 (first carried on NOAA-15 in 1998) are listed in Table 14.2.

Table 14.2 AVHRR/3 channels

The first AVHRR sensor acquired only four channels and AVHRR/2 acquired five channels. Spatial resolution at nadir for all bands in AVHRR/3 is 1.09 km.

Channel number	Wavelength range (μm)	Typical use
1	0.58–0.68	Daytime cloud and surface mapping
2	0.725–1.00	Land-water boundaries
3A	1.58–1.64	Snow and ice detection
3B	3.55–3.93	Night cloud mapping, SST
4	10.30–11.30	Night cloud mapping, SST
5	11.50–12.50	SST

Source: NOAA: *https://www.ospo.noaa.gov/Operations/POES/NOAA19/avhrr.html*

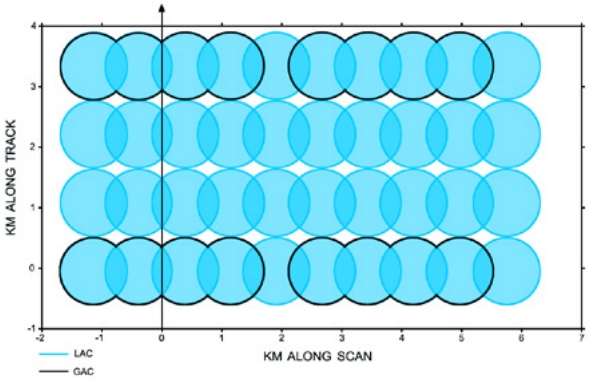
AVHRR sensors have been deployed continuously on the National Oceanic and Atmospheric Administration (NOAA) series of Polar Operational Environmental Satellites (POES), starting with NOAA-6 in 1981 and ending with the launch of NOAA-19 in 2009. NOAA-18 and NOAA-19 are the last in the series of POES satellites to carry AVHRR sensors. Orbital decay of NOAA-18 from 2013, and NOAA-19 from November 2017, has affected the calibration, and therefore accuracy, of AVHRR SST products during some months[12]. Operational AVHRR sensors are also carried on the European Space Agency (ESA) MetOp series of polar orbiters, MetOp-A, -B and –C, starting with the launch of MetOp-A on 19 October 2006. Unlike the POES satellites (whose equatorial crossing times drifted significantly over the lifespan of each satellite since there was no onboard fuel to correct their orbits[13]), the MetOp satellites are sustained in stable 'morning orbits' with equatorial crossing times of 9:30 am and 9:30 pm. However, there will be no AVHRR sensors deployed on future missions, as the Second Generation MetOp satellites (MetOp-SG) will carry different IR sensors. Therefore, after the AVHRR sensor on MetOp-C ceases to operate (expected lifespan out to 2024), there will be no further source of operational AVHRR SWT, ending nearly half a century of continuous global measurements by this remarkably reliable sensor. Courtesy of the AVHRR series of sensors, SSTs provide the longest time series of satellite-derived ocean parameters (Minnett *et al.,* 2019).

With a swath width of ~2700 km, the AVHRRs on POES allowed global daily sampling and produced three types of data:

- Global Area Coverage (GAC) data relies on raw data from these sensors being stored on the satellite and transmitted every few hours to receiving stations on the ground at reduced spatial resolution. The raw data is processed onboard the satellite by subsampling one scan line in three, and averaging every four of five adjacent pixels along each scan line (see Figure 14.2 and Volume 2B).
- Local Area Coverage (LAC) data is recorded onboard at original resolution (1.1 km at nadir) for part of the orbit, then transmitted to a ground station when the satellite is within range.
- High Resolution Picture Transmission (HRPT) data uses real time, direct download to satellite ground stations.

Figure 14.2 AVHRR/3 GAC grid resolution and sampling

Simulated Earth surface footprints for AVHRR/3 showing the relationship between full resolution data (Local Area Coverage, LAC, in blue) and reduced resolution Global Area Coverage (GAC, black outlines).



Source: Eumetsat (2011) Figure 4-1

SWTs derived from GAC data have a spatial resolution of ~4 km at nadir (directly below the satellite) which expands to coarser resolution at the edges of swaths (see Figure 14.3a). HRPT data deliver higher resolution SWT measurements at 1.1 km × 1.1 km resolution at nadir, expanding to 2.3 km × 6.2 km resolution at swath edges, although the spatial coverage is limited to the reception limits of the ground station (Griffin *et al.,* 2017). Another daily AVHRR data type, Full Resolution Area Coverage (FRAC), became available following the launch of MetOp-A in 2006. FRAC provides full global coverage with 1.1 km nadir resolution and swath widths of around 2900 km (Eumetsat, 2011; see Figure 14.3b).

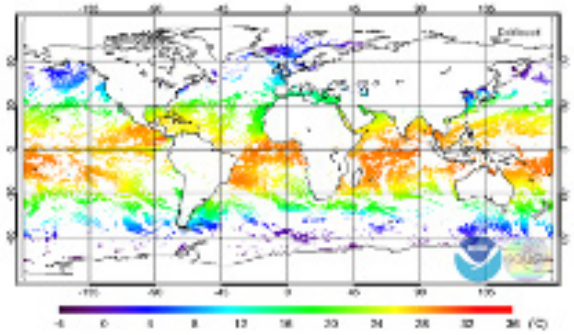
In 2018 NOAA officially replaced the AVHRR sensor program with the Visible Infrared Imaging Radiometer Suite (VIIRS) sensor program, after a long trial beginning with the first VIIRS sensor launched in 2011 onboard the Suomi National Polar orbiting Partnership (NPP) platform, maintained in a stable 'afternoon orbit' with equatorial crossing times of 1:20 am and 1:20 pm. The first of the NOAA Joint Polar Satellite Series (JPSS), NOAA-20 (launched 18 November 2017), carries a VIIRS rather than an AVHRR sensor to measure SWT. The VIIRS sensor provides higher spatial resolution SWT, 0.75 km at nadir expanding out to 1.5 km at swath edge, wider swath width (3060 km), better spatial coverage, and lower noise than the AVHRR (see Figure 14.3c). Importantly, VIIRS delivers higher spectral resolution, density, and extent than the AVHRR sensors (see Volume 1B—Section 1), including 22 channels designed to detect cloud and aerosol properties, ocean colour, ice, and fire, as well as LST and SWT (NASA Earthdata, 2019). The NPP and NOAA-20 also have better orbital stability than the POES satellites.

12 See *http://imos.org.au/facilities/srs/sstproducts/sstdata0/sstdata-validation/*
13 See *https://www.star.nesdis.noaa.gov/smcd/emb/vci/VH/vh_avhrr_ect.php*

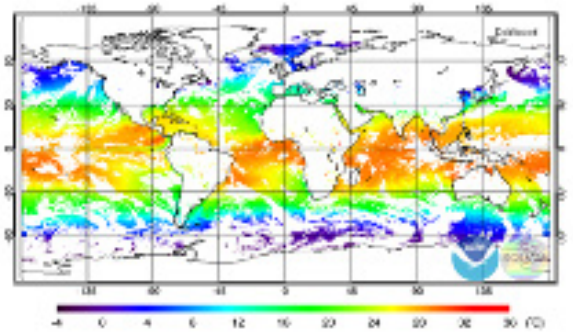
Figure 14.3 Nighttime SST maps

These maps were produced by mapping data from four operational NOAA level 2 (L2P) products on 11 March 2019. GAC: Global Area Coverage; FRAC: Full Resolution Area Coverage; VIIRS: Visible Infrared Imaging Radiometer Suite; AHI: Advanced Himawari Imager

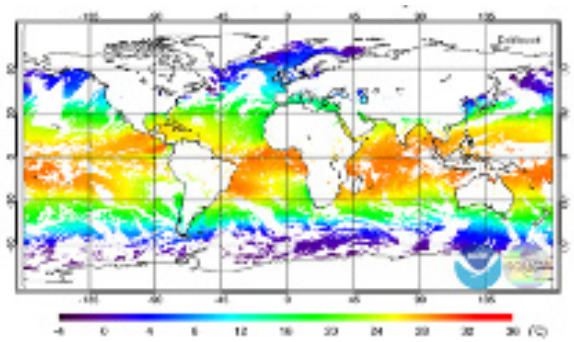
a. 4 km NOAA-19 GAC AVHRR



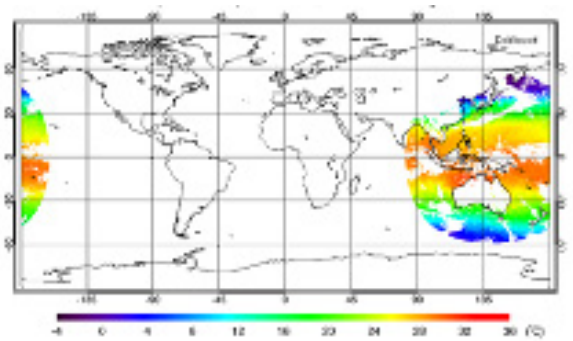
b. 1.1 km MetOp-B FRAC AVHRR



c. 0.75 km NOAA-20 VIIRS



d. 10 minute, 2 km Himawari-8 AHI brightness temperatures



Data are from the NOAA SST Quality Monitor (SQUAM; Dash *et al.*, 2010). Retrieved from *https://www.star.nesdis.noaa.gov/sod/sst/squam*, accessed 16 March 2019.

Recent polar orbiting satellites, such as Suomi NPP, and the JPSS and MetOp series, have had the capability to store the highest resolution IR sensor radiance data onboard, with download to reception stations across the globe every few hours, thus allowing global, daily coverage of around 1 km resolution SWT over cloud-free regions (Figure 14.3b and Figure 14.3c). Even higher spatial resolution SWT (0.25 km at nadir) has been available since 2018 from the Second-generation Global Imager (SGLI) onboard the Japanese Global Change Observation Mission Climate (GCOM-C) polar orbiter (*https://suzaku.eorc.jaxa.jp/GCOM_C/index.html*). The SGLI has a swath width of 1,400 km for SWT, with GCOM-C equatorial crossing times of 10:30 am and 10:30 pm.

Near-global coverage of 1 km resolution SWT was earlier supplied by the Moderate Resolution Imaging Spectroradiometer (MODIS) onboard Terra (launched 18 December 1999) and Aqua (launched 4 May 2002) but, with a swath width of 2330 km (less than AVHRR or VIIRS), the gaps between swaths from one day are filled in on the next.

Although much narrower in swath (~500 km) than the other IR sensors that measure SWT, the dual-view capability of the Along-Track Scanning Radiometer (ATSR) series of IR sensors (ATSR-1, ATSR-2 and AATSR) flown on polar orbiters ERS-1, ERS-2, and EnviSat, from 1991 to 2012, allowed for the accurate determination of atmospheric corrections (such as atmospheric aerosol contamination), which are critical for climate data records (Merchant *et al.,* 2012; Berry *et al.,* 2018). The current generation of dual-view radiometers, the Sea and Land Surface Temperature Radiometer (SLSTR; Donlon *et al.,* 2012; Smith *et al.,* 2014) flying on Sentinel-3a (launched on 4 November 2015) and Sentinel 3b (launched 25 April 2018) has wider swaths than AATSR. All the (A)ATSR and SLSTR sensors flew or fly in morning orbits at around 10 am and 10 pm local equatorial crossing times.

IR sensors on geostationary satellites (from the Himawari series of satellites by the Japanese Meteorological Agency, JMA) have also provided accurate SSTs at high temporal resolution over the Australian region since 2006. While Himawari-6 (also known as MTSAT-1R; Zhang *et al.,* 2016a, 2018) and Himawari-7 (also known as MTSAT-2) provided hourly, 4 km SST observations, the currently operational Himawari-8 (Kurihara *et al.,* 2016; Ditri *et al.,* 2018; Kramar *et al.,* 2016; Griffin and Majewski, 2016; Griffin, 2018) delivers 10 minute, 2 km observations, which, when composited over a number of hours, enables infilling of data gaps due to transient cloud (see Figure 14.3d; Beggs *et al.,* 2018a).

14.2.2 Passive microwave sensors

Unlike IR sensors, passive microwave (PMW) sensors on polar orbiting satellites have the advantage that they can sense SWTs through cloud, but these sensors are impacted by radio frequency interference both from ground-based sources and from geostationary and communication satellites (Gentemann and Hilburn, 2015). PMW SST retrievals also need to be filtered for heavy rain, strong winds, sea ice, sunglint, as well as near land or sea ice, as these retrievals have contributions from emissions that enter through the antenna sidelobes. Due to the microwave frequencies used to measure SST, and limitations of the size of antenna deployable by satellite, PMW sensors are also limited to measuring SST at surface resolutions of several tens of kilometres.

PMW SSTs were retrieved from the Tropical Rainfall Measuring Mission (TRMM) Microwave Imager (TMI) from December 1997 to 2015, although the low inclination orbit only observed up to 40° latitude. The Japanese Advanced Microwave Scanning Radiometer for EOS[14] (AMSR-E) was flown on NASA's Aqua polar orbiter, with spatial resolution of SST retrievals of 74 km × 43 km, 1445 km swath width, and equatorial crossing time of 1:30 am and 1:30 pm (Kawanishi *et al.,* 2003). The AMSR-E was decommissioned in October 2011, when the mechanism to rotate the antenna failed after nine years of valuable global measurements. In the years that followed the failure of AMSR-E, the only source of global PMW SST data was from the WindSat microwave radiometer on the Coriolis polar orbiter (January 2003 to present), with equatorial crossing time of 6 am and 6 pm, and lower accuracy compared with AMSR-E. Fortunately, the second generation Advanced Microwave Scanning Radiometer (AMSR-2) was launched on 17 May 2012, on the Japanese Global Change Observation Mission—Water (GCOM-W; Kachi *et al.,* 2017). As a follow-on to the successful TRMM mission, the Global Precipitation Measurement (GPM) mission was launched on 27 February 2014, with the GPM Microwave Imager (GMI). The GMI's 10.65 GHz channels, have sensitivity to SST variations, but only for warm water, SST > ~13ºC, as at colder temperatures the sensitivity decreases and the noise level increases (Gentemann *et al.,* 2010).

14.3 Sea Surface Temperature

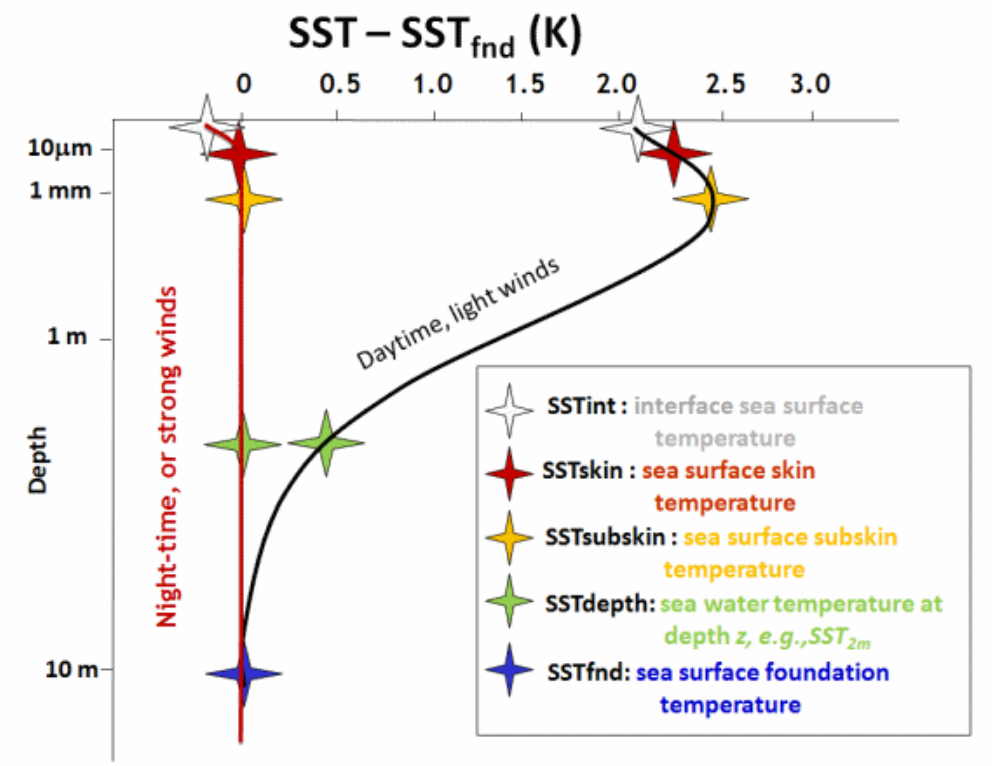
SST is not a single variable but is considered by many to be the temperature within the mixed layer (approximately the upper 10 m) of the ocean. Air-sea fluxes of heat, moisture, and momentum, as well as ocean turbulence, means the temperature variation through the 'mixed layer' can be complex and variable (Minnett *et al.,* 2019). This complexity needs to be considered when comparing or combining measurements of SST from different satellites and *in situ* sensors (Minnett *et al.,* 2019). In order to facilitate these activities, a set of definitions of SST were developed by the international Group for High Resolution SST (GHRSST: *http://www.ghrsst.org*; Donlon *et al.,* 2007), and are now used in all GHRSST-format SST products (GHRSST Science Team, 2012). Figure 14.4 summarises the definition of SST in the upper 10 m of the ocean and provides a framework to understand the differences between complementary SST measurements.

The five different SST definitions are (from Minnett and Kaiser-Weiss, 2012):

- **interface temperature** (SSTint)—the temperature at the air-sea interface on molecular scales (cannot be directly measured);
- **skin sea surface temperature** (SSTskin)—the temperature measured by an IR radiometer typically operating at wavelengths 3.7–12 μm, which represents the temperature within the conductive diffusion-dominated sub-layer at a water depth of ~10–20 μm;
- **subskin sea surface temperature** (SSTsubskin)—the temperature at the base of the conductive laminar sub-layer of the ocean surface, which can be well approximated to the measurement of the surface temperature by a microwave radiometer operating in the 6–11 GHz frequency range (approximately 1 mm water depth);
- **surface temperature at depth** (SSTdepth)—all measurements of water temperature beneath SSTsubskin; and
- **foundation temperature** (SSTfnd)—the temperature free of diurnal temperature variability, that is, the temperature at the first time of the day when the heat gain from the solar radiation absorption exceeds the heat loss at the sea surface (approximately 10 m water depth under calm conditions).

Figure 14.4 Near-surface oceanic temperature gradients

In this schematic, the numbers on the axes are for guidance only and do not represent rigorously derived scales.



Source: Minnett and Kaiser-Weiss (2012)

In most locations and conditions, the ocean surface is warmer than the atmosphere in contact with it, resulting in heat flow from the ocean to the atmosphere (Minnett *et al.,* 2019). The upward flow of heat in the water is accomplished in the top hundred micrometers or so of the water (Wong and Minnett, 2018) by molecular conduction as the air-sea density difference and near-surface viscous layer of the water suppress the turbulent heat transfer (Soloviev and Lukas, 2014). This results in a vertical temperature gradient in the water, just below the interface, leading to decreasing temperature closer to the interface, which is referred to as the 'thermal skin layer' or 'cool skin layer' (see Figure 14.4). The average daytime ocean cool skin amplitude has been measured as ~0.14K[15] and ~0.20K during night, both under well-mixed conditions (surface wind speeds exceeding 6 ms^{-1}; Zhang *et al.,* 2019), with much larger values being seen at very low wind speeds (Donlon *et al.,* 2002; Minnett *et al.,* 2011). Therefore, for applications requiring accuracy to several tenths of a Kelvin (K) the variable thermal skin effect should be taken into account, and retrievals of IR SST should be considered as SSTskin.

At 10 m water depth, between 50% and 90% of sunlight impinging on the surface has typically been absorbed above that depth level, and the temperature at 10 m water depth is relatively stable with respect to direct heating from the daily solar heating cycle (Merchant *et al.,* 2019a). For this reason, the SST at around 10 m water depth is conceptualised as a foundation temperature above which large sub-daily variability is superimposed, particularly under conditions of low to moderate wind speeds and high insolation (Soloviev and Lukas, 1997). This means that the water depth of the foundation temperature at a given location changes from day to day, but not within the day (Merchant *et al.,* 2019a). The 10 m SST is not directly measurable by EO, although a satellite-derived SST observed around local dawn can be used to estimate the foundation SST, because near-surface temperature stratification that develops during daytime is usually eroded by dawn by surface heat loss and wind-driven mixing. Satellite SSTs observed under well-mixed, moderate (for example, 7–12 ms^{-1}) wind conditions are also considered to be reasonable estimates of foundation temperature (Merchant *et al.,* 2019a).

15 The Kelvin (K) temperature scale defines absolute zero and is related to the Celsius temperature scale as 0K = -273.15°C.

During the daytime, and in the absence of sufficiently strong winds to drive vertical mixing of heat, diurnal warming causes a relatively shallow warm layer to be formed (see Figure 14.4). Driven by solar heating, diurnal variability of SST occurs under moderately low wind speeds in all ocean basins and has been observed using both *in situ* and satellite SST observations (Minnett *et al.,* 2019 and references therein). In the Australian region, diurnal warming of several Kelvin has been observed in the Tropical Warm Pool (Zhang *et al.,* 2016a; Zhang *et al.,* 2016b). The abundance of SST retrievals from space and improvements in understanding of the diurnal cycle allowed for numerical simulations to reproduce the diurnal variability of the upper ocean layer. A selection of these models has been inter-compared in various regions, including the Tropical Warm Pool, using hourly-resolution, geostationary satellite SST data (Karagali and Hoyer, 2013; Zhang *et al.,* 2018).

For more comprehensive overviews of SST the reader is referred to Minnett *et al.* (2019) and Merchant *et al.* (2019a). In the following subsections we consider methods to:

- retrieve SST from satellite imagery (see Section 14.3.1);
- validate the derived SST (see Section 14.3.2); and
- refine SST products and coverage (see Section 14.3.3).

Some pointers for selecting the most appropriate SST product for a particular application are provided in Excursus 14.1.

14.3.1 Retrieval of satellite SST

Satellite radiometers collect accurate radiance measurements, from which brightness temperature (T_B) at the top of the atmosphere can be derived. These T_B values are related to, but not the same as, the SST, because of the absorption, emission, and scattering of radiation from the intervening atmosphere, and because the sea surface does not act as an ideal emitter (that is, its emissivity is not 100%; Minnett *et al.,* 2019). The dominant effect (near nadir) in the infrared region is the atmospheric influence; in microwave wavelengths, it is the variability of surface emissivity around relatively low values over the ocean. For more detail, refer to the review by Merchant and Embury (2014).

The first step in deriving accurate SST from a satellite sensor is to navigate the uncalibrated (level 0) data. In the case of the Integrated Marine Observing System (IMOS; see Volume 2D—Excursus 12.3) HRPT AVHRR data from POES satellites, a high precision, CSIRO-developed, satellite orbit model is implemented to automatically geolocate pixels without the need for per scene ground control points (Wijffels *et al.,* 2018).

The next step is to convert the level 0 data from the satellite to T_B values (level 1), by applying a factory calibration. This step is then followed by identification of those pixels that have been affected by:

- land and cloud, in the case of IR retrievals; or
- precipitation or radio frequency interference, in the case of MW retrievals.

Aspects of SST retrieval from infrared (see Section 14.3.1.1) and microwave (see Section 14.3.1.2) sensors are considered separately below. For additional details around satellite SST geolocation, cloud/land masking, and retrievals please refer to Minnett *et al.* (2019) and Merchant *et al.* (2019a).

14.3.1.1 Infrared temperature retrievals

Cloud and land masking is crucial for satellite-based IR temperature retrievals of surface water. Clouds are opaque to TIR radiation, and even a slightly cloud-contaminated signal (subpixel-sized clouds) can result in a considerably colder measurement of the temperature. Also, for land-contaminated pixels, the signal can be biased, as the LST sometimes differs by several degrees from the SWT. Therefore, strict cloud and land masking are necessary to eliminate affected pixels (Lieberherr and Wunderle, 2018).

Historically, identification of clouds in IR measurements from satellites has been driven mainly by binary tests in a decision tree based on T_B uniformity, T_B minima, and comparisons with low resolution gap-free reference fields (Kilpatrick *et al.,* 2015). The accuracy of these tests often decreases near ocean thermal fronts, at cloud edges, in the presence of small cirrus clouds, and low-level, uniform stratus clouds when cloud temperature can be close to that of the sea surface (Minnett *et al.,* 2019). This reliance on stringent uniformity thresholds often results in the misidentification of strong thermal fronts as clouds. An alternative, probabilistic approach to cloud identification in IR imagery based on Bayes' Theorem was developed by Merchant *et al.* (2005). Joint probability distributions of T_B values in two IR channels were derived in clear-sky conditions by radiative transfer simulations, and in cloudy conditions by visual inspection of satellite imagery. Radiative transfer simulations, with weather prediction model output to give the atmospheric state, are used to give an expectation of clear-sky T_B values, which are compared with probability distributions of cloudy measurements. The measured T_B values are then assigned a probability of having been influenced by clouds. This approach has been widely used for several satellite missions including for the (A)ATSR series (Merchant *et al.,* 2012), NOAA GOES satellites (Maturi *et al.,* 2008), OSI-SAF MetOp series and JMA's Himawari-8 satellite (Kurihara *et al.,* 2016).

As the IR radiation from the sea surface propagates through the atmosphere, some is absorbed or scattered out of the path of the radiometer, attenuating the signal. The T_B measured through a clear atmosphere at satellite altitude are cooler than SST. This atmospheric effect (along with surface emissivity effects) must be compensated for to obtain accurate SST (Merchant *et al.,* 2019a). The IR spectral intervals where the atmosphere is relatively transparent are situated between wavelengths 3.5–4.1 μm and 8–12 μm (see Volume 1B—Section 4). The main gas that contributes to the signal attenuation is water vapor, which is very variable in space and time. Other molecules that contribute to the atmospheric effect are quite well-mixed, so cause a relatively constant effect that is simpler to correct. Taking measurements at different spectral intervals in the windows where the water vapor attenuation is different means the measurements contain information about both the surface and the atmospheric state (Merchant *et al.,* 2019a). The spectral intervals being sensed are defined by the designed characteristics of the radiometer, and are usually referred to as 'bands' or 'channels' (see Volume 1A—Section 14). By assuming adequate linearity, a simple SST algorithm takes the form:

$$SST_{ij} = a_0 + a_i T_i + a_j T_j$$

where a_0, a_i and a_j are coefficients that need to be determined by:

- regression analysis of coincident satellite and *in situ* measurements (Kilpatrick *et al.,* 2001);
- regression analysis of offline simulations using radiative transfer modelling (Llewellyn-Jones *et al.,* 1984); or
- 'on-the-fly' using numerical weather prediction (NWP) fields and fast radiative transfer to give a dynamic linearisation point closer to the observed state (Merchant *et al.,* 2008).

The simple algorithm (equation above) has been applied to AVHRR data, where *I* is channel 4 and *j* is channel 5 (see Table 14.2), to retrieve multi-channel SST (MCSST). To correct some of the limitations of the linearity, the simple algorithm has been modified in various forms (such as the Non-Linear SST: NLSST; Walton *et al.,* 1998), to include a reference SST (or first-guess temperature) and a term that includes the satellite zenith angle.

14.3.1.2 Passive microwave temperature retrievals

Two different retrieval algorithms (from JAXA and NASA respectively) are routinely used to produce official JAXA/NASA SSTs from the PMW sensors, AMSR-E and AMSR-2 (Merchant *et al.,* 2019a). The NASA group has also produced SSTs from WindSAT.

The JAXA algorithm produces SST using the 6 GHz channel (Shibata, 2006), whereas the NASA algorithm (adopted by the US-based company Remote Sensing Systems) determines SST and wind speed at the same time using a radiative transfer based two-step algorithm (Wentz and Meissner, 2007). For both products, data that are affected by rain, strong winds, sun glitter, land or sea ice contamination, and radio frequency interference from ground-based sources, geostationary satellites and communication satellites are excluded, but each group has developed their own exclusion criteria (Merchant *et al.,* 2019a).

Both products are widely used in the operational ocean and atmospheric modelling communities, as well as for scientific research and applications. In Australia, AMSR-E and WindSAT SSTs produced by Remote Sensing Systems (see *http://www.remss.com*) were routinely used in operational SST analyses and ocean general circulation models by the Australian Bureau of Meteorology (BoM; Beggs *et al.,* 2011; Andreu-Burillo *et al.,* 2010) and by CSIRO in the Bluelink ocean Reanalysis model (BRAN; Oke *et al.,* 2013; see Excursus 2.2). In recent years, more accurate SST retrievals from AMSR-2, produced by JAXA, have been used for the BoM SST analyses and ocean models (see *http://www.bom.gov.au/oceanography/forecasts*).

14.3.2 Validation of satellite SST

Validation of satellite-derived SSTs is essential to provide confidence in both the derived SST and its associated uncertainty. The traditional approach is to compare the satellite SST to *in situ* surface-based SST measurements by generating a set of coincidences or 'Matchup Data Base' (MDB) within defined spatial and temporal limits (Merchant *et al.,* 2019a). Statistical methods are then applied to the MDB, from which the mean difference and standard deviation are usually calculated. There are five main types of *in situ* measurements available for satellite SST validation:

- drifting buoys;
- Global Tropical Moored Buoy Array (GTMBA);
- SSTdepth sensors on ships;
- Argo floats (see Excursus 5.1); and
- shipborne radiometers.

SST measurements from the first four platform types are routinely available in near real time from the NOAA/NESDIS In Situ Quality Monitor (iQUAM: *https://www.star.nesdis.noaa.gov/socd/sst/iquam/*).

Networks of drifting buoys provide the most prevalent type of *in situ* measurement for SST (Lumpkin *et al.,* 2016), and these have delivered good coverage from the early 2000's across most regions. Near-global coverage can be obtained using measurements from Argo floats (Roemmich *et al.,* 2009), although the temporal sampling is much lower than from drifting buoys (every nine days rather than hourly). The GTMBA (McPhaden *et al.,* 2010) has the advantage of being in open ocean locations and having consistent long term calibrated records at many locations. Measurements from engine room intakes or hull-mounted sensors from Volunteer Observing Ships (Beggs *et al.,* 2011), although not global in nature, are an important source of data for satellite SST validation due to their availability back to the start of the satellite SST era. Hull-mounted temperature sensors, if properly located and insulated from atmospheric effects, have been demonstrated to provide SST observations of similar accuracy to drifting buoys (Beggs *et al.,* 2011). Finally, we have shipborne radiometers (Donlon *et al.,* 2014), which are the only *in situ* data source to provide a temperature at the same water depth (SSTskin) as is detected by IR sensors on satellites.

There are several online systems that provide near real time validation plots of various satellite SST products, with links listed in Section 14.7.

14.3.3 'GHRSST' satellite SST products

Based on the GHRSST (Group for High Resolution SST; Donlon *et al.,* 2007) definitions for SST products (GHRSST Science Team, 2012), numerous global, spatially-mapped SST products are now available for research and operational applications (Beggs, 2010; Donlon *et al.,* 2009). The following labels are used to differentiate four standard levels of product processing:

- Level 1 (L1)—geolocated T_B from individual sensors;
- Level 2 (L2)—geolocated SSTs from individual satellite sensors over a single swath (orbit), granule (section of orbit), or scene (geostationary satellites only);
- Level 3 (L3)—'composite' SST products (see Volume 2D) created by averaging (but not interpolating) L2 data over space and time onto a grid of prescribed latitudes and longitudes (composite products may be produced from a single sensor or multiple sensors over a single orbit to several days); and
- Level 4 (L4)—gap-free SST 'analyses' created by interpolating multiple observation sources onto a pre-defined grid.

Among the ocean surface parameters monitored from satellites, SST is unique in terms of the large volume of concurrent observations, their spatial coverage, and the number of relevant EO sensors and platforms (Minnett *et al.,* 2019). This characteristic allows L3 composites and L4 analyses to achieve more complete spatial coverage than their constituent L2 inputs. In 2000, the Global Ocean Data Assimilation Experiment (GODAE) High Resolution SST Pilot Project (GHRSST-PP; Donlon *et al.,* 2007) was initiated to develop and demonstrate a system that could deliver high resolution, global coverage SST data products operationally in near real time according to GODAE specifications. Various space, meteorological, and oceanographic agencies contributing to GHRSST-PP (now called the Group for High Resolution SST: GHRSST; see *http://www.ghrsst.org*) provide two major types of near real time SST products in prescribed formats (GHRSST Science Team, 2012): L2 preprocessed (L2P) and L4 analysis products.

GHRSST-L2P products are baseline measurement datasets. SST data generated from different sensors are made available to users in a common, self-describing format (netCDF) together with ancillary information to assist with their interpretation and use by data assimilation systems (Donlon *et al.,* 2009). For every L2 input data file, GHRSST produces a matching L2P product that contains identical SST values in the same geographical layout as those in the source L2 product. On a pixel-by-pixel basis, each SST retrieval is augmented with estimates of the bias error and standard deviation error typically derived from statistical databases of *in situ* and satellite data. Other ancillary fields for each pixel are land/lake/river/ice mask, surface wind speed, aerosol optical depth, sea ice concentration, time of measurement, difference from previous reference SST analysis field, and quality control flags, including a quality level flag. A full description of all GHRSST file formats (L2P, L3U, L3C, L3S, and L4) can be found in GHRSST Science Team (2012). The 'Sensor Specific Error Statistics' (SSES) standard deviation errors (given as 'sses_standard_deviation' values in GHRSST files) associated with the highest quality SST observations (denoted by a 'quality_level' value of 5) are typically in the range 0.3°C to 0.5°C for the various satellite IR SST GHRSST-L2P products currently available. One of the particular strengths of the GHRSST L2P, L3U, L3C, and L3S formats is that users can trade off between spatial coverage and accuracy, depending on the requirements of their application, by selecting either a quality_level or sses_standard_deviation threshold. For more information see Beggs (2010).

The design of the GHRSST L2P format was mainly driven by the requirements of the new 'foundation' SST analyses for the 'best' cloud-free SST with sufficient auxiliary data to enable conversion of SST

observations within or immediately below the cool skin to foundation SST (Donlon *et al.,* 2007). The L2P format has proven to be sufficiently universal that GHRSST L2P files from a range of IR and PMW sensors are now used in many operational systems for near real time SST analyses, ocean forecasting, and seasonal prediction (Beggs, 2010). The L2P products provide SST observations at the highest available spatial resolution at the time and location of observation, and are therefore considered most appropriate for input into numerical models. The consistent formats for GHRSST products facilitate addition of new data streams into operational systems.

Although L2P products provide the most timely geolocated SST values, they come with the downside of high data file sizes and computation overheads, which may be a barrier to some users and applications. GHRSST L2P products can be composited on a regular grid (Griffin *et al.,* 2017) to produce L3 products using:

- a single sensor and single swath/scene (L3U);
- single sensor, multiple swaths/scenes (L3C); and
- multiple sensors (L3S).

These composites are popular for various near-coastal applications including fisheries management, protection of endangered species, environmental monitoring and weather forecasting (Beggs, 2010; see *https://coastwatch.noaa.gov/cw/about-coastwatch.html*). For example:

- various L3U products are used in real time maps of SST to advise recreational and commercial fishers (see *https://support.fishtrack.com/hc/en-us/articles/4402098299163-Transitioning-to-our-App*);
- hourly or daily L3C composites of multiple 10-minute, 2 km resolution scenes from Himawari-8 L2P SST can be used to monitor coastal upwelling or diurnal warming (Huang *et al.,* 2018; Beggs *et al.,* 2018a); and
- multi-sensor L3S products (Beggs *et al.,* 2019; see Section 14.4.4) are used to nowcast coral bleaching over the Great Barrier Reef (see *http://www.bom.gov.au/environment/activities/reeftemp/reeftemp.shtml*).

To illustrate the relative spatial coverage and ability of these products to resolve ocean features, examples of SSTs from L3U, L3C, L3S, and L4 products over the seas around Queensland are shown in Figure 14.5.

L3 SST products, unless composited over a very long time period, will contain some grid locations that lack data values. Several applications require a 'gap-free' L4 SST field. L4 analyses of satellite L2 and L3, and *in situ* SST, are produced operationally at various oceanographic and meteorological agencies around the world using the method of optimal interpolation (OI). In OI (or 'statistical' interpolation) systems, voids in observations are generally filled using a weighted combination of the previous analysis and climatology ('background field') and neighbouring observations (Reynolds *et al.,* 2007; Beggs *et al.,* 2011; Brasnett and Surcell Colan, 2016; Maturi *et al.,* 2017). By nature of the statistical interpolation of observations and background field, an L4 SST analysis generally exhibits smoother ocean features than an L3 non-interpolated SST product, composited over one to several days (Beggs *et al.,* 2018b; see Figure 14.5). Several of these SST analyses provide sea surface boundary forcing in atmospheric and ocean models and are used as a constraint to observations in modelling of the upper ocean circulation (Beggs, 2010; O'Carroll *et al.,* 2019; Merchant *et al.,* 2019a). Accurate SST fields are essential in computing different climate variables, such as heat transfer in ocean-atmosphere coupled systems and surface partial pressure of CO_2 (Vinogradova *et al.,* 2009).

Combination of data from IR and PMW sensors from polar orbiting satellites, and IR sensors on geostationary satellites, often with *in situ* measurements from drifting buoys and ships, now results in high-quality, daily SST L4 analyses with high spatial resolution, ranging from 0.25° (NCEI OISST v2.0; Banzon *et al.,* 2016; Reynolds *et al.,* 2007) down to 0.01° (JPL MUR; Chin *et al.,* 2017). Section 14.4 goes into further details regarding global L4 analysis products.

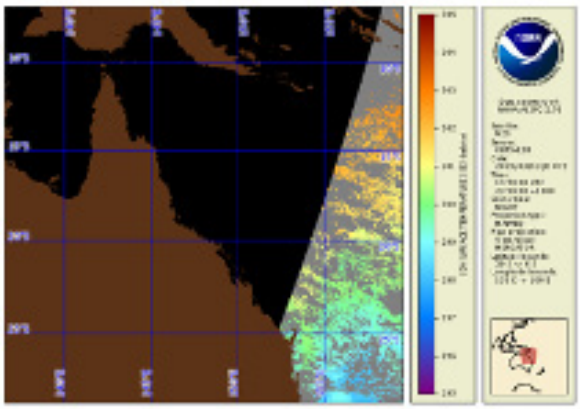
There are now many real time and reprocessed L2, L3, and L4 global satellite SST products provided in GHRSST format, produced by several agencies, available via the GHRSST Data Assembly Centres (see *https://www.ghrsst.org/ghrsst-data-services/services/*). A list of GHRSST products archived by the NOAA National Oceanographic Data Centre can be found at *https://www.nodc.noaa.gov/SatelliteData/ghrsst/accessdata.html*, although this is by no means comprehensive, as additional GHRSST products are freely disseminated by other agencies, such as the Copernicus Marine Environment Monitoring Service (CMEMS: *http://marine.copernicus.eu/services-portfolio/access-to-products/*), the Japan Aerospace Exploration Agency (JAXA: *https://suzaku.eorc.jaxa.jp/GHRSST/*), and the Australian Ocean Data Network (AODN: *http://portal.aodn.org.au*).

More than 100 real time and reprocessed GHRSST L2P/L3 products have been produced from most environmental satellites equipped with SST sensors. In addition, there are more than 30 near real time daily, global (1–25 km resolution) and regional (1–10 km resolution), GHRSST L4 analyses and reanalyses. A selection of those particularly suitable for Australian applications are presented in Section 14.5, including a summary of various features, and their pros and cons.

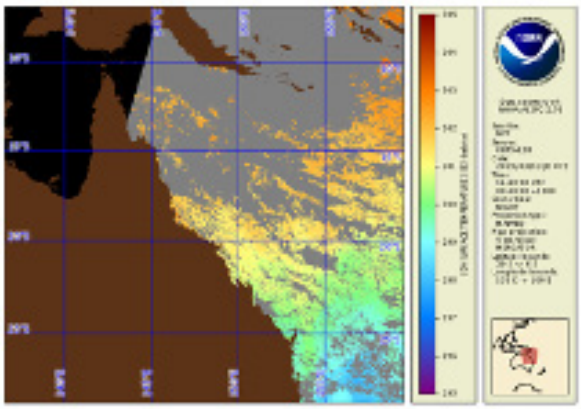
Figure 14.5 Nighttime SST maps for 13 March 2019 over the Queensland region

These maps were produced from imagery acquired by different EO sensors and processed using different methods. All products, except Geo-Polar Blended, are on the same 0.02° x 0.02° rectangular grid. ACSPO: Advanced Clear Sky Processor for Oceans

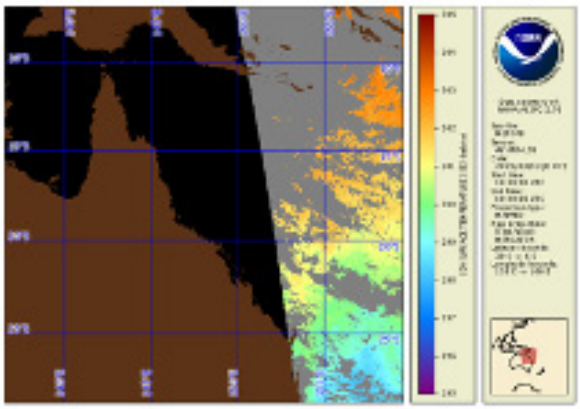
a. 2 km NOAA ACSPO NPP VIIRS L3U



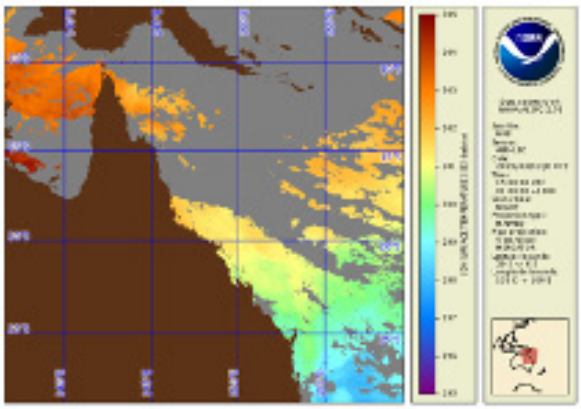
b. 2 km ACSPO NOAA-20 VIIRS L3U



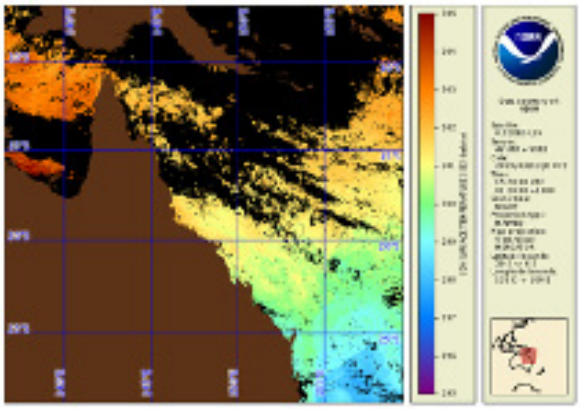
c. 2 km ACSPO METOP-B FRAC AVHRR L3U



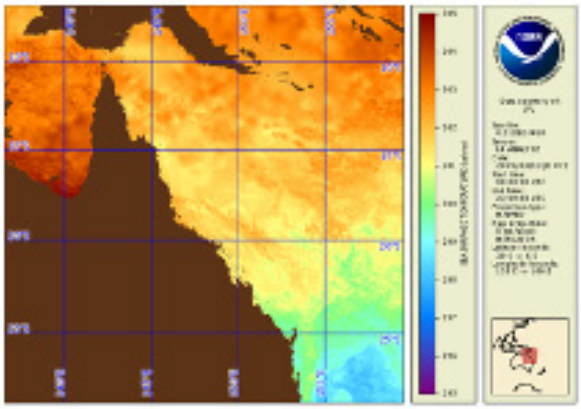
d. 2 km 1-hour Himawari-8 AHI L3C (produced by compositing 2 km 10-min Himawari-8 AHI L3U)



e. 2 km IMOS Multi-sensor L3S (produced by compositing ACSPO NPP VIIRS L3U, ACSPO NOAA-20 VIIRS L3U, 1 km OSI-SAF METOP-B FRAC AVHRR L2P and 2 km IMOS NOAA-18 HRPT AVHRR L2P)



f. 5 km daily Geo-Polar Blended L4 (produced by optimally interpolating nighttime SST from NPP VIIRS L2P, MetOp-B FRAC AVHRR L2P, Himawari-8 AHI L3U over the region)



Data are from the NOAA/NESDIS ACSPO Regional Monitor for SST (ARMS) v2.1. Retrieved from: *https://www.star.nesdis.noaa.gov/sod/sst/arms*, accessed 23 March 2019.

Excursus 14.1—Selecting a Satellite SST Product

Source: Helen Beggs, Bureau of Meteorology (Melbourne)
Further Information: *https://www.ghrsst.org/ghrsst-data-services/products/*; see also Beggs (2010), Dash *et al.* (2012), Fiedler *et al.* (2019a), Beggs *et al.* (2018b), Rayner *et al.* (2019b), and Yang *et al.* (2021)

To select from an increasingly wide array of SST products, users need to consider which of the following parameters are most important for the application and analyses being undertaken:

- depth—skin, subskin, or foundation?
- time—are the dataset duration, local time of measurement, and latency suitable?
- temporal resolution—what is the characteristic time period of the process you wish to measure?
- spatial resolution—what is required for the feature/process of interest?
- spatial coverage—L3S composite versus L4 gap-free?
- do you need microwave data to measure SST under cloud, for example during or after a tropical cyclone?
- quality level (cloud contamination)—what is the minimum acceptable level?
- geolocation accuracy—native projection (L2P) or gridded (L3 or L4)?
- SST accuracy and stability—with respect to what reference?
- stability of sensor and orbit—what deviation is acceptable?

Using satellite SST records to produce coherent climate data records is complicated by the changes that can occur over time in the sensors, satellite orbit, and calibrations (O'Carroll *et al.*, 2019). Different methods have been used to stabilise the SST time series, which may impact subsequent analyses of the resulting datasets. For example:

- The long term satellite SST data record known as 'Pathfinder' (Casey *et al.*, 2010) utilises empirical regression algorithms (Kilpatrick *et al.*, 2001) tuned to drifting buoys to provide a self-consistent approach across the series of AVHRR sensors on the POES satellites from NOAA-7 onwards. Pathfinder is constructed from a single AVHRR sensor at a single time, and the tuning to *in situ* data is primarily to account for the many instrumental issues observed in the series, including errors in calibration (O'Carroll *et al.*, 2019).
- The ATSR Reprocessing for Climate (ARC) Project (Merchant *et al.*, 2012) utilised the ATSR series of sensors, which were designed to provide SST suitable for climate studies. ARC differs from Pathfinder in that it maintains independence from *in situ* measurements, has performed careful harmonisation of the T_B from successive sensors, and employs a physics-based retrieval of SSTskin using a Radiative Transfer Model (RTM; Merchant *et al.*, 2012; 2019b). This allows independent validation of the dataset using *in situ* measurements.
- The ESA SST Climate Change Initiative (CCI) Project Phase II (Merchant *et al.*, 2019b; Rayner *et al.*, 2019a) uses the ATSRs to reduce T_B errors in the AVHRR sensors and in the derived SST values, providing a stabilised dataset of both ATSR and AVHRR for the period they coexist (1991 to 2012), and extends backwards and forwards from the ATSR period using consistent, physically-based retrievals for all AVHRR sensors (O'Carroll *et al.*, 2019).

14.4 Global Sea Surface Temperature Products

A selection of global daily L4 SST analyses, available for periods exceeding 10 years, are listed in Table 14.3 along with their advantages and disadvantages. The OSTIA (Operational Sea Surface Temperature and Sea Ice Analysis), CMC (Canadian Meteorological Centre), GAMSSA (Global Australian Multi-Sensor SST Analysis), MUR (Multi-Scale Ultra High Resolution), and MGDSST (Merged Satellite and In-situ Data Global Daily Sea Surface Temperature) L4 products are referred to as foundation SSTs. These analysis schemes minimise the use of retrievals affected by diurnal variability by employing one or more of the following strategies:

- using only nighttime satellite data;
- using additional daytime data with wind speed above 6 ms^{-1} ; and
- excluding L2 SSTs flagged by the producer as having high diurnal variability (Dash *et al.,* 2012).

Some analyses, such as OSTIA (Donlon *et al.,* 2012; Roberts-Jones *et al.,* 2012), use a combination of an accurate satellite SST reference dataset (in 2018 ACSPO NPP VIIRS L3U) and *in situ* SST data to correct for biases in the other satellite SST data streams. Others use a combination of drifting buoy and ship SST observations to correct for regional and seasonal biases (for example MGDSST, CMC, NCEI[16] 'Reynolds' AVHRR-only OISST[17] v2.0). However, issues remain with the calibration and bias-correction of the IR and PMW SST data streams, particularly at high latitudes north of 50°N and south of 50°S (Reynolds *et al.,* 2009; Dash *et al.,* 2012) where available *in situ* SST observations are still relatively sparse. In addition, some analysis biases have occurred over regions where drifting buoy observations, used for bias-correction of satellite SST data, became sparse due to a format change in data uploaded to the Global Telecommunications System on 2 November 2016, as occurred for the NCEI 'Reynolds' near real time, daily, AVHRR-only OISST v2.0 SST analyses (Liu *et al.*, 2019). The OISST issue was resolved on 16 March 2020 with the operational release of an updated version (v2.1) of the AVHRR-only OISST SST analysis (*https://www.ncdc.noaa.gov/oisst/optimum-interpolation-sea-surface-temperature-oisst-v21*), which now ingests all drifting buoy, mooring, ship, and Argo float SST data available from the Global Telecommunications System (GTS), and has been reprocessed back to 1 January 2016.

Table 14.3 Global, Daily, Multi-Sensor SST analysis products in GHRSST L4 format

Analysis and Citation	Date Period	Spatial resolution; depth	SST and sea ice data inputs	Advantages	Disadvantages	Data Access
CMC0.2deg (Brasnett, 2012; Brasnett, 2008)	1991–2017	0.2°; foundation	Drifting buoys, ships (ICOADS to 2006, GTS thereafter) AQUA/AMSR-E, Coriolis/WindSat, TRMM/TMI, MetOp-A/AVHRR, NOAA-16/AVHRR, NOAA-17/AVHRR, NOAA-18/AVHRR, NOAA-19/AVHRR, ERS-1/ATSR-1, ERS-2/ATSR-2, ENVISAT/AATSR, CMC ice	Highly accurate compared to Argo; good temporal and spatial homogeneity; good feature resolution; includes microwave data	Only from 1991	*https://podaac.jpl.nasa.gov/dataset/CMC0.2deg-CMC-L4-GLOB-v2.0*
CMC0.1deg (Brasnett and Surcell, 2016; Brasnett, 2008)	2016–present	0.1°; foundation	Drifting buoys, moorings, ships (GTS) MetOp-A/AVHRR, MetOp-B/AVHRR, NOAA-18/AVHRR, NOAA-19/AVHRR, NPP/VIIRS, GCOM-W/AMSR-2, CMC ice	Highly accurate compared to Argo; good feature resolution; includes microwave data	Only from 2016, but may be combined with CMC0.2deg to extend record	*https://podaac.jpl.nasa.gov/dataset/CMC0.1deg-CMC-L4-GLOB-v3.0*

16 National Centers for Environmental Information (NOAA)
17 Optimum Interpolation Sea Surface Temperature

Analysis and Citation	Date Period	Spatial resolution; depth	SST and sea ice data inputs	Advantages	Disadvantages	Data Access
ESA SST CCI analysis v2.1 (Rayner *et al.*, 2019a; 2019b; Merchant *et al.*, 2019b)	1981–2016	0.05°; 0.2 m	NOAA-7/AVHRR, NOAA-9/AVHRR, NOAA-11 to 19/AVHRR MetOp-A/AVHRR, ERS-1/ATSR-1, ERS-2/ATSR-2, ENVISAT/AATSR, OSI-SAF ice	Consistently recalibrated and reprocessed (A)ATSR and AVHRR data; second lowest standard deviation wrt Argo (after CMC0.2deg); better feature resolution than other long term analyses (incl. CMC); derived climatology highly consistent with TAO-TRITON moorings in western Pacific and agrees well with near-coral logger temperatures at water depths 3–6 m in Florida Keys and Belize (Rayner ***et al.***, 2019)	Cooler than Argo SST by 0.05–0.1K; a few tenths of degree bias in global mean during Oct 1982 to Sep 1983	*https://cds.climate.copernicus.eu/cdsapp#!/dataset/satellite-sea-surface-temperature?tab=form*
Copernicus Climate Change Service (C3S) v2.0 (Merchant *et al.*, 2019b)	2017 to 28 days behind present	0.05°; 0.2 m	Sentinel-3A/SLSTR, MetOp-A/AVHRR, OSI-SAF ice	Same analysis code as ESA SST CCI v2.1 analysis and designed to extend this analysis up to near real time	Validation not yet publicly available	*https://cds.climate.copernicus.eu/cdsapp#!/dataset/satellite-sea-surface-temperature?tab=form*
CMEMS OSTIA reprocessed analysis (Good et al., 2020)	1981 to six months behind present)	0.05°; foundation	Drifting buoys, moorings, ships (ICOADS), ESA SST CCI v2.1 AVHRR and A(A)TSR data, MetOp-B/AVHRR, OSI-SAF Sentinel-3A/SLSTR, Sentinel-3B/SLSTR, AQUA/AMSR-E, GCOM-W/AMSR2, NPP/VIIRS, NOAA-20/VIIRS, MSG1/SEVIRI, MSG2/SEVIRI, MSG4/SEVIRI, GOES-13/ABI, OSI-SAF ice	Good standard deviation of differences to Argo, includes microwave data; very good feature resolution	Disadvantages not yet identified	*https://resources.marine.copernicus.eu/product-detail/SST_GLO_SST_L4_REP_OBSERVATIONS_010_011/INFORMATION*
UK Met Office OSTIA analysis (Donlon *et al.*, 2012)	2006–present	0.05°; foundation	Drifting buoys, moorings (GTS), JCOM-W/AMSR-2 MetOp-B/AVHRR, NPP/VIIRS, NOAA-20/VIIRS, MSG4/SEVIRI, GOES-13/ABI, OSI-SAF ice	Good standard deviation of differences to Argo, includes microwave data; very good feature resolution after 12 March 2019	Reduced temporal homogeneity, reduced feature sensitivity prior to 12 March 2019. Only extends back to 2006, but may be combined with OSTIA reprocessed analysis to extend record	*https://resources.marine.copernicus.eu/product-detail/SST_GLO_SST_L4_NRT_OBSERVATIONS_010_001/INFORMATION*

Analysis and Citation	Date Period	Spatial resolution; depth	SST and sea ice data inputs	Advantages	Disadvantages	Data Access
JMA MGDSST (Guan and Kawamura 2004; Kurihara *et al.*, 2006)	1982–present	0.25°; foundation	Drifting buoys, moorings, ships (GTS), AQUA/AMSR-E, Coriolis/WindSat, GCOM-W/AMSR-2 Pathfinder V5.0/V5.1 (1982-2006), NOAA-17/AVHRR, NOAA-18/AVHRR, NOAA-19/AVHRR, MetOp-A/AVHRR, MetOp-B/AVHRR, JMA ice	Moderate mean and standard deviations of differences to Argo; moderate temporal and spatial homogeneity; moderate feature sensitivity; includes microwave data	Agrees less closely to Argo than GAMSSA, CMC, CCI v2.1 or OSTIA	*http://www.data.jma.go.jp/gmd/goos/data/pub/JMA-product/mgd_sst_glb_D/*
NOAA AVHRR-only Daily OISST v2.0 and v2.1 (Huang *et al.*, 2021; Banzon *et al.*, 2016; Reynolds *et al.*, 2007)	1981–present	0.25°; ~0.2 m	Drifting buoys, moorings, ships, Argo (GTS), Pathfinder V5.0/V5.1 AVHRR (1981-2005), NOAA-16/AVHRR, NOAA-17/AVHRR NOAA-18/AVHRR, NOAA-19/AVHRR, METOP-A/AVHRR, METOP-B/AVHRR, GSFC NASA NSIDC ice (1981–2004), NCEP ice (2005 to present)	Extends back to 1981 and widely used; moderate feature resolution	Largest mean differences and standard deviations compared with Argo; Reduced spatial homogeneity; Uses all day and night data, so may be affected by diurnal warming; accuracy of OISST v2.0 degraded after 2 November 2016 (Liu et al., 2019), so replaced by OISST v2.1 for 1 Jan 2016 to present.	1981–2015: *https://podaac.jpl.nasa.gov/dataset/AVHRR_OI-NCEI-L4-GLOB-v2.0* 2016-present: *https://podaac.jpl.nasa.gov/dataset/AVHRR_OI-NCEI-L4-GLOB-v2.1*
BoM GAMSSA (Beggs *et al.*, 2020; Zhong and Beggs, 2008)	2008–present	0.25°; foundation	Drifting buoys, moorings, ships (GTS), AQUA/AMSR-E, Coriolis/WindSat, GCOM-W/AMSR-2 NOAA-17/AVHRR, NOAA-18/AVHRR, NOAA-19/AVHRR, MetOp-A/AVHRR, MetOp-B/AVHRR, NPP/VIIRS, NOAA-20/VIIRS, ENVISAT/AATSR, NCEP ice	Moderately accurate compared with Argo; smaller standard deviations than other 0.25° analyses (OISST v2.0 and MGDSST); moderate feature sensitivity. Includes microwave data	Only extends back to 2008	*http://thredds.aodn.org.au/thredds/catalog/IMOS/SRS/SST/ghrsst/L4/GAMSSA/catalog.html*

Analysis and Citation	Date Period	Spatial resolution; depth	SST and sea ice data inputs	Advantages	Disadvantages	Data Access
JPL MUR v4.1 (Chin ***et al.***, 2017)	2002–present	0.01°; foundation	Drifting buoys, Moorings, Ships, Argo (iQuam), AQUA/AMSR-E, GCOM-W/AMSR-2, Coriolis/WindSat, DMSP/SSM/I NOAA-16 to 19/AVHRR, MetOp-A/AVHRR, AQUA/MODIS, TERRA/MODIS, OSI-SAF ice	Moderate standard deviation of differences to Argo; good feature sensitivity	Higher standard deviation to Argo than OSTIA, Geo-Polar Blend or CMC L4	*https://podaac.jpl.nasa.gov/dataset/MUR-JPL-L4-GLOB-v4.1*
NOAA Geo-Polar Blended Night (Maturi ***et al.***, 2017)	2002–present	0.05°; foundation	NOAA-16,17,18,19/AVHRR, MetOp-A,B/AVHRR, NPP/VIIRS, GOES-10,11,12,13,15/Imager, GOES-16/ABI, MTSAT-1R,2/JAMI, Himawari-8,9/AHI, Meteosat-8/SEVIRI, Meteosat-11/SEVIRI,	Good standard deviation of differences to Argo; good feature sensitivity; from 2017 closest agreement with Argo (NOAA/NESDIS/STAR, 2019)	Only extends back to 2002, but may be combined with ESA SST CCI analysis v2.1 to extend record	*https://coastwatch.noaa.gov/cw/satellite-data-products/sea-surface-temperature/sea-surface-temperature-near-real-time-geopolar-blended.html*
Met Office GMPE Median from long term analyses (ESA SST CCI GMPE) (Fiedler ***et al.***, 2019a)	1991–2010	0.25°; no specific depth	1991–2007 (6 products), 2008–2010 (4 products)	Validated in Fiedler *et al.* (2019a); small mean difference and standard deviation of difference to Argo; good spatial homogeneity; moderate temporal homogeneity and feature resolution	Source potentially varies from grid box to grid box	*https://catalogue.ceda.ac.uk/uuid/e0659b01259145c8bfb0de6eb12c2690*
Met Office GMPE Median from near real time analyses (Martin ***et al.***, 2012)	2009–present	0.25°; no specific depth	OSTIA (Met Office, UK), RTG_SST_HR (NCEP, USA), K10 (NAVOCEANO, USA), MGDSST (JMA, Japan), RSS MW (Remote Sensing Systems, USA), RSS MW+IR (Remote Sensing Systems, USA), FNMOC (USA), NOAA AVHRR OI.v2 (NOAA/NCEI, USA), CMC (Canada Meteorological Centre), ODYSSEA (Ifremer, France), GAMSSA (BoM, Australia)	Small mean difference and good standard deviation of differences to Argo, similar to CMC, OSTIA and Geo-Polar Blend	Source potentially varies from grid box to grid box	*https://resources.marine.copernicus.eu/product-detail/SST_GLO_SST_L4_NRT_OBSERVATIONS_010_005/INFORMATION*

Source for data: Fiedler *et al.* (2019a), Martin *et al.* (2012), Dash *et al.* (2012), Rayner *et al.* (2019a), NOAA/NESDIS/STAR (2019) and Met Office (2019)

The NOAA SST Quality Monitor (SQUAM) system (Dash *et al.,* 2012; NOAA/NESDIS/STAR, 2019) provides a tool that reveals differences between several of the operational analyses listed in Table 14.3. Maps, histograms, and time series plots for all combinations of 'L4 minus L4' and 'L4 minus Argo SST', for all available dates, are made available for users at *https://www.star.nesdis.noaa.gov/socd/sst/squam/analysis/l4*. In addition, validation plots of the near real time daily SST analyses in Table 14.3 against independent (not ingested) Argo SST (5 m water depth) observations are available at *https://ghrsst-pp.metoffice.gov.uk/ostia-website/gmpe-argo-stats.html*. Validations of the SST reanalyses listed in Table 14.3 are presented in Fiedler *et al.* (2019a) and Rayner *et al.* (2019a). A comprehensive intercomparison of several of these long term SST analyses (including ESA SST CCI v2.1, CMEMS OSTIA reprocessed, JMA MGDSST, NOAA Daily OISST v2.1 and JPL MUR) has recently assessed their suitability for climate applications (Yang *et al.*, 2021).

None of these L4 analysis products were designed, or able, to suit every possible SST application. When selecting an L4 SST analysis it should be borne in mind that grid resolution does not correspond to feature resolution or 'sensitivity' (see Volume 2D). An analysis may be smoother than the output grid resolution depending on the choice of background error covariance and correlation length scale (Dash *et al.,* 2012). Such a product may be perfectly adequate for its intended application (such as for NWP systems where 'noisy' features cause instabilities in the model) but inadequate for another application (such as monitoring of SST frontal dynamics). Coarse resolution input data cannot resolve fine mesoscale features, and an analysis dominated by, for example, PMW SST at ~50 km resolution, cannot be expected to deliver high resolution output. Thus high resolution SST features within each L4 product are dynamic and are visible only when sufficient SST data are available for input—persistent lack of data results in the analysis system reverting to a smooth background climatological value, until new data are again ingested. An example of this can be seen in the 0.01° JPL MUR SST analysis over the Queensland region (see Figure 14.5f), in which, over the southern Queensland coast there are clear conditions and highly resolved ocean features, whereas to the northeast region there is cloud and less resolved features. The challenge for all analysis systems is to maximize the signal-to-noise ratio for a given output grid resolution while maintaining the highest feature resolution possible through the careful choice of analysis design for a given application (Dash *et al.,* 2012; Banzon *et al.,* 2016).

The following subsections discuss specific applications of selected global SST products.

14.4.1 Numerical Weather Prediction model input

Several of the global L4 products listed in Table 14.3 were specifically designed to be used as the boundary condition for NWP models (CMC, OSTIA, MGDSST and GAMSSA). As such, these provide relatively smooth foundation SST fields with minimum daily bias and standard deviation when compared with independent reliable *in situ* data, such as Argo SST.

14.4.2 Climate monitoring

Other climate products (such as ESA SST CCI v2.1, OSTIA reanalysis, and OISST v2.0) were developed to provide reanalyses of the most accurate and available IR SST observations over long time scales, with maximum stability and minimum bias and standard deviation to independent in situ observations. These have not necessarily been designed for coastal applications or for feature sensitivity, and their accuracy largely depends on both the accuracy of the input satellite SST datasets (GAC AVHRR, and for CCI v2.1 also (A)ATSR SSTs) and their bias correction schemes.

CCI v2.1 and OSTIA reprocessed analyses are the only SST products of this group which use AVHRR data that have been consistently recalibrated from raw counts to T_B (Merchant *et al.*, 2019b), which is particularly important for the earlier AVHRR sensors from the 1980s and 1990s (Jon Mittaz, Uni. Reading, *pers. comm.*). The SST CCI v2.1 analysis has been found to compare well with SST from offshore moorings, but less well with coastal moorings (Rayner *et al.*, 2019a), possibly due to the 4 km resolution GAC AVHRR input data and the existence of higher SST variability close to coasts.

14.4.3 Feature resolution

JPL's 1 km SST analysis on the other hand ingests 1 km resolution MODIS IR SST data, and is designed to resolve small scale ocean features in cloud-free regions where MODIS data are available. It has been demonstrated to be useful for studies of coastal upwelling and fisheries off the Peruvian coast (Vazquez-Cuervo *et al.*, 2013), although not necessarily in all Australian near-coastal upwelling regions (see Section 14.5).

14.4.4 Coral bleaching nowcasting

The 0.05° resolution NOAA Geo-Polar Blended L4 analysis (Maturi *et al.*, 2017; see Figure 14.5f) was developed mainly to provide accurate and high resolution daily SSTs for the NOAA Coral Reef Watch program to derive near real time coral bleaching indices (see *https://coralreefwatch.noaa.gov/*; see Excursus 20.3), although it is also suitable for providing a boundary condition to high resolution NWP models. From 1 January 2017, the Geo-Polar Blended foundation SST analyses exhibit one of the closest global agreement with independent Argo SST (5 m) observations of any of the analyses listed in Table 14.3 (NOAA/NESDIS/STAR, 2019).

14.4.5 Verification

The near real time GHRSST Multi-Product Ensemble (GMPE: Martin *et al.*, 2012) and GMPE reanalyses (Fiedler *et al.*, 2019a; Rayner *et al.*, 2019a) are formed from a median of several daily, high resolution, L4 SST analyses to provide a verification source for other satellite-derived SST products. The near real time GMPE L4 is routinely used to monitor a number of global L4 analyses at *https://ghrsst-pp.metoffice.gov.uk/ostia-website/gmpe-monitoring.html* and *https://www.star.nesdis.noaa.gov/socd/sst/squam/analysis/l4*, and has proven to be invaluable for identifying issues with operational L2P, L3U, and L4 products (for example, Martin *et al.*, 2012; Dash *et al.*, 2012; Liu *et al.*, 2019).

14.5 Regional SST Products

There have been several high resolution, satellite-derived, SST products developed specifically for the Australian region and Australian applications by the BoM and CSIRO. These products are listed in Table 14.4, along with their advantages, disadvantages, and example applications. For comparison, the popular NOAA Pathfinder AVHRR L3C product is also listed. The most widely used of the Australian SST products are described below.

Table 14.4 GHRSST products

GHRSST GDS2 format L2, L3, and L4 products, and climatology, covering the Australian region (70°E to 190°E, 70°S to 20°N), are specifically developed for Australian applications. For comparison, the global NOAA Pathfinder version 5.3 AVHRR L3C product is also included.

Product and Citation	Date Period	Spatial resolution; Temporal resolution; depth	SST data inputs	Advantages and Applications	Disadvantages	Data Access
IMOS AVHRR L2P (Griffin *et al.*, 2017)	1992–present	1.1 km at nadir to ~4 km at swath edges; twice daily; skin	IMOS NOAA-9 to NOAA-19 HRPT AVHRR T_B	Timeliness, well-navigated, consistently calibrated, and bias-corrected using regional buoy SSTs; routinely validated (BoM, 2019); used for ingestion into SST analyses and IMOS OceanCurrent 4-hourly SST composite maps	Formed from IR data so gaps in cloudy regions	Contact *ghrsst@bom.gov.aul* for access
IMOS AVHRR L3U (Griffin *et al.*, 2017)	1992–present	0.02°; twice-daily; skin	IMOS NOAA-9 to NOAA-19 HRPT AVHRR L2P, OSI-SAF MetOp-A/FRAC AVHRR L2P, OSI-SAF MetOp-B/FRAC AVHRR L2P, ACSPO NPP VIIRS L3U, ACSPO NOAA-20 VIIRS L3U	Timeliness, consistently calibrated, and bias-corrected using regional buoy SSTs; routinely validated (BoM, 2019); regular grid; used in RT IMOS OceanCurrent maps and fisheries applications (e.g. *www.fishtrack.com*)	Formed from IR data so gaps in cloudy regions	*http://thredds.aodn.org.au/thredds/catalog/IMOS/SRS/SST/ghrsst/L3U/catalog.html*
IMOS AVHRR L3C (Griffin *et al.*, 2017)	1992–present	0.02°; daily; skin	IMOS NOAA-9 to NOAA-19 HRPT AVHRR L3U	Better spatial coverage than the single swath L3U SSTs; routinely validated (BoM, 2019); used in diurnal variation research (Zhang ***et al.***, 2016b)	Formed from IR data so gaps in cloudy regions	*http://thredds.aodn.org.au/thredds/catalog/IMOS/SRS/SST/ghrsst/L3C-1d/catalog.html*

Product and Citation	Date Period	Spatial resolution; Temporal resolution; depth	SST data inputs	Advantages and Applications	Disadvantages	Data Access
IMOS AVHRR L3S (Griffin *et al.*, 2017; Wijffels *et al.*, 2018)	1992–present	0.02°; 1/3/6 days and 1 month; skin	IMOS NOAA-9 to NOAA-19 HRPT AVHRR L3C	High spatial resolution (2 km) and long time series; Routinely validated (BoM, 2019); used in IMOS OceanCurrent, validation of ocean models, and marine heat wave and biological research	Based on HRPT AVHRR only, so limited in spatial coverage; CAPS-based cloud identification means cloud clearing differs south of 20°S (Wijffels *et al.*, 2018).	*http://thredds.aodn.org.au/thredds/catalog/IMOS/SRS/SST/ghrsst/catalog.html* in the L3S-1d, L3S-3d, L3S-6d and L3S-1m sub-directories
IMOS VIIRS L3U (Griffin *et al.*, 2017)	2012–present	0.02°; twice-daily; skin	ACSPO NPP VIIRS L3U, ACSPO NOAA-20 VIIRS L3U	Greater spatial coverage due to global ACSPO VIIRS L3U coverage. Improved VIIRS SST cloud identification and 0.75–1.5 km pixel resolution. Improved accuracy compared with POES AVHRR SSTs. Routinely validated (BoM, 2019)	Formed from IR data so gaps in cloudy regions	*http://thredds.aodn.org.au/thredds/catalog/IMOS/SRS/SST/ghrsst/L3U/catalog.html*
IMOS VIIRS L3C (Griffin *et al.*, 2017)	2012–present	0.02°; twice-daily; skin	IMOS NPP VIIRS L3U, IMOS NOAA-20 VIIRS L3U	Multiple granules composited, so greater spatial coverage than single granule VIIRS L3U (BoM, 2019).	Formed from IR data so gaps in cloudy regions	*http://thredds.aodn.org.au/thredds/catalog/IMOS/SRS/SST/ghrsst/L3C/catalog.html*
IMOS METOP-AVHRR L3U	2012–present	0.02°; twice-daily; skin	OSI-SAF MetOp-A/FRAC AVHRR L2P, OSI-SAF MetOp-B/FRAC AVHRR L2P	Greater spatial coverage than POES HRPT AVHRR due to global METOP FRAC AVHRR coverage and Bayesian cloud identification; improved accuracy compared with POES AVHRR SSTs. Routinely validated (BoM, 2019)	Formed from IR data so gaps in cloudy regions	Contact *ghrsst@bom.gov.au* Will be supplied to *http://thredds.aodn.org.au/thredds/catalog/IMOS/SRS/SST/ghrsst/L3U/catalog.html*
IMOS METOP-AVHRR L3C	2012–present	0.02°; twice-daily; skin	IMOS MetOp-A,B FRAC AVHRR L3U	Mutliple swaths composited, so greater spatial coverage than METOP AVHRR L3U. Routinely validated (BoM, 2019).	Formed from IR data so gaps in cloudy regions	Contact *ghrsst@bom.gov.au* Will be supplied to *http://thredds.aodn.org.au/thredds/catalog/IMOS/SRS/SST/ghrsst/L3C/catalog.html*
IMOS Multi-sensor L3S (Griffin *et al.*, 2017; Beggs *et al.*, 2019)	2012–present	0.02°; 1/3/6 days and 1 month; skin	IMOS NOAA-15 to 19 HRPT AVHRR L3C, IMOS MetOp-A/FRAC AVHRR L3C, IMOS MetOp-B/FRAC AVHRR L3C, IMOS NPP VIIRS L3C, IMOS NOAA-20 VIIRS L3C	Better spatial coverage and accuracy compared with IMOS AVHRR-only L3S or VIIRS L3C; routinely validated (BoM, 2019); used in IMOS OceanCurrent and coastal upwelling research (Beggs *et al.*, 2018a).	Formed from IR data so gaps in cloudy regions	*http://thredds.aodn.org.au/thredds/catalog/IMOS/SRS/SST/ghrsst/catalog.html* in the L3SM-1d, L3SM-3d, L3SM-6d and L3SM-1m sub-directories
IMOS MTSAT-1R L3U v2 (Zhang *et al.*, 2018)	2006–2010	0.05°; hourly; skin	IMOS MTSAT-1R/JAMI L2P v2	Moderately accurate compared with buoys; used for diurnal variation research	Day/night biases in some regions	*http://rs-data1-mel.csiro.au/thredds/catalog/imos-srs/sst/ghrsst/L3U/mtsat1r/catalog.html*
IMOS MTSAT-1R L3U v3 (Zhang *et al.*, 2016a, 2018)	Jan–Apr 2010	0.05°; hourly; skin	IMOS MTSAT-1R/JAMI L2P v3	Highly accurate over the Tropical Warm Pool compared with buoys; low day/night bias over Tropical Warm Pool makes it ideal for diurnal variation studies (Zhang *et al.*, 2016, 2018)	Only available for four months	*http://dapds00.nci.org.au/thredds/catalog/rr5/satellite/GHRSST/MTSAT-1R/catalog.html*

Product and Citation	Date Period	Spatial resolution; Temporal resolution; depth	SST data inputs	Advantages and Applications	Disadvantages	Data Access
BoM Himawari-8 L2P (Griffin and Majewski, 2016; Griffin, 2018)	Mar 2016–present	2 km at nadir; 10 min; skin	JMA Himawari-8/AHI L1	High temporal resolution; used as input into CSIRO's 4-hourly SST composites for IMOS OceanCurrent.	Some residual cloud contamination	Contact *ghrsst@bom.gov.au*
IMOS Himawari-8 L3C (Beggs *et al.*, 2018a)	Oct 2017–present	0.02°; hourly and daily; skin	BoM Himawari-8/AHI L2P	Routinely validated (BoM, 2019); greater spatial coverage and less cloud contamination than the 10-min Himwari-8 L2P data; useful for studies of coastal upwelling and diurnal warming	Some residual cloud contamination	Contact *ghrsst@bom.gov.au*
BoM RAMSSA L4 (Beggs *et al.*, 2011)	2006–present	(1/12)°; daily; foundation	Drifting buoys, moorings, ships, Argo, XBT, CTD (GTS), REMSS AQUA/AMSR-E L2P, REMSS Coriolis/WindSat L3C, JAXA GCOM-W/AMSR-2 L2P, IMOS NOAA-17 to 19/HRPT AVHRR L2P, NAVO NOAA-17 to 19/GAC AVHRR L2P, NAVO MetOp-A and B/GAC AVHRR L2P, EUMETSAT ENVISAT/AATSR L2P, ACSPO NPP/VIIRS L3U, ACSPO NOAA-20/VIIRS L3U, NCEP ice	Includes microwave so measures SST under cloud; gap-free, daily spatial coverage; moderately accurate compared with independent buoys; used for boundary condition of NWP models, and SST anomaly maps	Only from 2006; lower feature resolution and less accurate than IMOS Multi-sensor L3S	*http://thredds.aodn.org.au/thredds/catalog/IMOS/SRS/SST/ghrsst/L4/RAMSSA/catalog.html*
SSTAARS Climatology (Wijffels *et al.*, 2018)	1992–2016	0.02°; daily; 0.2 m	IMOS night-only 1-day AVHRR L3S SST	Resolves small-scale ocean features in coastal regions; stable and accurate compared with independent *in situ* SST (Wijffels *et al.*, 2018); used in IMOS OceanCurrent for SST anomalies and percentiles	Based on IR only, so fewer observations contributed to climatology in cloudy regions	*http://thredds.aodn.org.au/thredds/catalog/CSIRO/Climatology/SSTAARS/2017/AODN-product/catalog.html*
NOAA Pathfinder AVHRR L3C (Casey *et al.*, 2010)	1981–1983 months behind present	0.04°; twice-daily; skin	NOAA Pathfinder NOAA-7 to 19/GAC AVHRR L2P	Available back to 1981; resolves small-scale ocean features in coastal regions; used for long term SST analyses and ocean models	Less spatial coverage compared with IMOS AVHRR L3C due to narrower swath processed; only one satellite processed at a time unlike IMOS L3C; no error estimates (SSES), unlike IMOS L3C; not routinely validated; not available in real time	*https://data.nodc.noaa.gov/cgi-bin/iso?id=gov.noaa.nodc:AVHRR_Pathfinder-NCEI-L3C-v5.3*

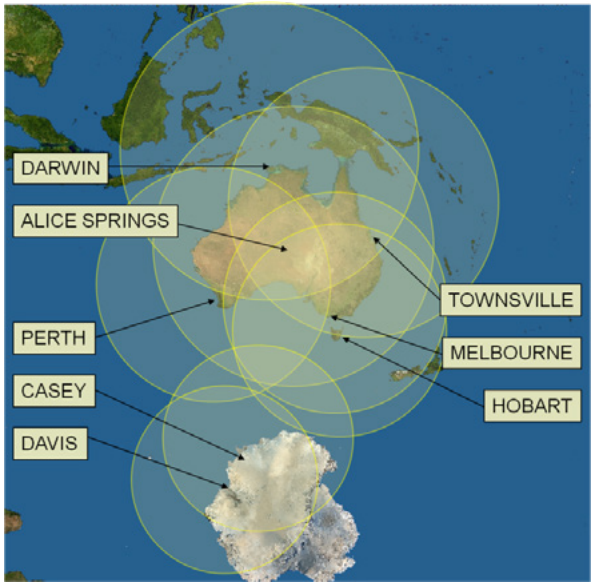
Source for data: Griffin *et al.* (2017), Wijffels *et al.* (2018), Beggs *et al.* (2018b), *http://imos.org.au/facilities/srs/sstproducts/sstdata0/*

14.5.1 IMOS satellite SST products

Starting in the mid-1980's, direct broadcast satellite imagery has been acquired at ground stations located in Australia and Antarctica on a daily basis (see Figure 14.6). Building on the archives and processing expertise of CSIRO and the BoM, the IMOS has made these data available as a consistently processed, calibrated, and formatted archive of SST products for the Australasian region (IMOS, 2018). The collection comprises all HRPT overpasses recorded in the Australian and Antarctic region (see Figure 14.6) from AVHRR onboard all operational POES satellites (NOAA-9 to -19) from January 1992 to the present, 'stitched', and geolocated (King, 2003), and stored with full resolution (1.1 km at nadir).

Figure 14.6 Australian AVHRR ground stations

Location and approximate range of Australian ground stations that receive direct broadcast HRPT AVHRR data from NOAA polar orbiting satellites.



Source: Leon Majewski, Bureau of Meteorology, Melbourne

SST values are derived by regressing the AVHRR T_B to SST observations from drifting and tropical moored buoys in the Australasian region (Griffin *et al*., 2017). The system smoothly and automatically corrects for bias changes in each AVHRR sensor using a running one-year calibration window, adjusted monthly. The data are formatted and flagged according to the GHRSST Data Specification (GDS) 2.0 revision 5 (r5) format specification (GHRSST Science Team, 2012), including time-varying error estimates and quality-level flags for each SST value, calculated using matchups with drifting buoy SST data and proximity to cloud, respectively. The records form a unique 27-year dataset that supplies quality-assured SST values, both at native resolution (L2) and 2 km composites (L3) to within 2 km of coasts (Wijffels *et al*., 2018; see Section 14.3.3 for SST product processing levels and abbreviations). All AVHRR L2P swath data are gridded using a method that weights the pixels by quality level, SSES, and overlap area (Griffin *et al*., 2017), to generate 0.02°×0.02° L3U composites over two domains:

- Australia (70°E to 190°E, 70°S to 20°N); and the
- Southern Ocean (2.5°E to 202.5°E, 77.5°S to 27.5°S).

The highest quality gridded swath SST estimates from multiple passes of the same satellite over the same day for either daytime or nighttime data are averaged to form single sensor L3C composites, then L3S composites formed by combining data from multiple sensors over a fixed time period, such as 1 day, 3 days, 6 days, and 1 month. In order to obtain the most accurate IMOS AVHRR L3U, L3C, or L3S SST estimates at any given grid location, users should choose the highest quality level (5), then subtract the corresponding sses_bias value at that location (Griffin *et al*., 2017; IMOS, 2018). For more details on the IMOS GHRSST products, see IMOS (2018) and references therein.

The VIIRS sensor on NPP and NOAA-20 has now superseded the AVHRR on POES satellites (see Section 14.2.1). To facilitate use of the wider swath and higher resolution VIIRS data (0.75 km compared with 1.1 km for FRAC AVHRR), NOAA produce real time VIIRS L3U SST on the IMOS 0.02° × 0.02° grid (NOAA CoastWatch, 2018). The BoM have composited the NOAA VIIRS L3U data, following the method in Griffin *et al*. (2017), to produce daily day/night L3C composites of VIIRS data on the IMOS grid and domains. The NPP and NOAA-20 VIIRS L3U data are composited, based on quality and uncertainty estimates, with AVHRR SST data from operational POES and MetOp satellites to construct the IMOS 'Multi-sensor L3S' product suite (Griffin *et al*., 2017). This has resulted in improvements to overall quality, accuracy, and coverage of IMOS L3S composites over the IMOS Australian domain (Beggs *et al*., 2019). Figure 14.7 demonstrates the difference in spatial coverage between the AVHRR-only L3S and Multi-sensor L3S. To best use these IMOS L3C and Multi-sensor L3S products, it is recommended that users select data with quality level 4 or higher and subtract sses_bias (Pallavi Govekar, BoM, *pers. comm*. and BoM, 2019).

The IMOS AVHRR and Multi-sensor L3S SSTs are available from the AODN (*http://portal.aodn.org.au*) and SST maps are available for multiple Australian coastal regions from IMOS OceanCurrent (see *http://oceancurrent.imos.org.au*). See Excursus 14.2 for an example of IMOS AVHRR-only L3S SSTs being used in IMOS OceanCurrent. Maps of IMOS Multi-sensor L3S SSTs are also available over some Australian regions from the NOAA ARMS website (see *https://www.star.nesdis.noaa.gov/sod/sst/arms*).

Coastal applications can benefit from the 2 km resolution of the IMOS AVHRR and Multi-sensor L3S products, in contrast to the coarser (4 km), globally-available L3 products (such as NOAA Pathfinder L3C) and statistically-interpolated L4 SST products, which may be unable to provide the required detail. In cloud-free conditions, IMOS Multi-sensor L3S SST products may more accurately reflect near-coastal SST processes, such as coastal upwelling or SST anomalies around reefs, than high resolution, statistically-interpolated, foundation SST analyses such as 1 km resolution JPL MUR L4 (see Figure 14.8 and Beggs *et al*., 2018a) or 5 km NOAA Geo-Polar Blended L4 (see Figure 14.5).

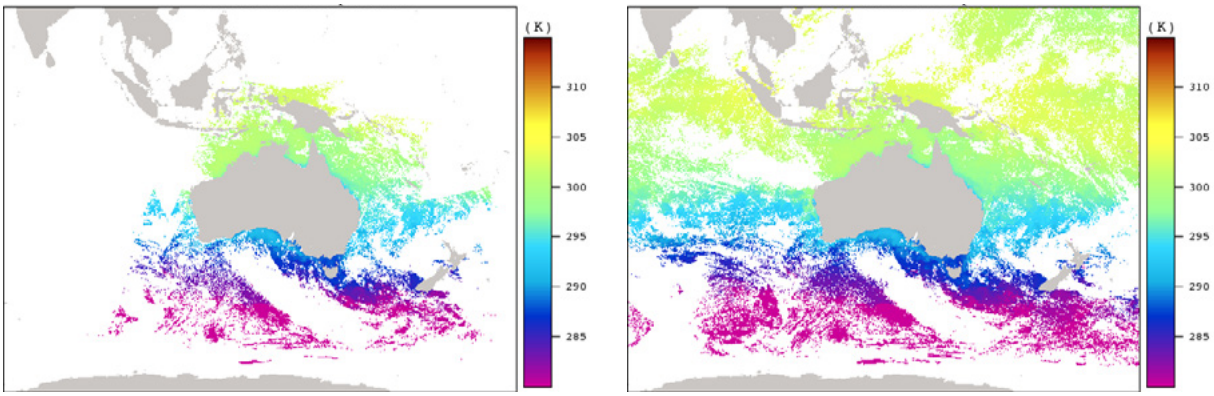
Due to their superior spatial coverage in near-coastal regions, since 21 November 2018 the IMOS multi-sensor, 1-day, nighttime, L3S SSTs have been ingested into the BoM's ReefTemp NextGen coral bleaching nowcasting system (Garde *et al*., 2014; see *http://www.bom.gov.au/environment/activities/reeftemp/reeftemp.shtml*), replacing the IMOS AVHRR-only, 1-day, nighttime, L3S SSTs (Beggs *et al*., 2019). Diurnal warming can also be measured using day-only and night-only IMOS L3C SST products (Zhang *et al*., 2016b), 5 km hourly IMOS MTSAT-1R L3U (Zhang *et al*., 2016a; 2018), or 2 km hourly IMOS Himawari-8 L3C (see Table 14.3; Beggs *et al*., 2018a). For more details on applications of IMOS satellite SST products see Beggs *et al*. (2018b).

Figure 14.7 Skin SST maps

2 km resolution SSTskin maps with quality level 4 and 5 from IMOS data for 10 June 2018 over the IMOS Australian domain (70°E–190°E, 70°S–20°N). For this date, the AVHRR-only L3S was formed using data from NOAA-18 and NOAA-19, and the Multi-sensor L3S included additional data from NPP.

a. AVHRR-only, 1-day, night-only, L3S files

b. Multi-sensor, 1-day, night-only, L3S files

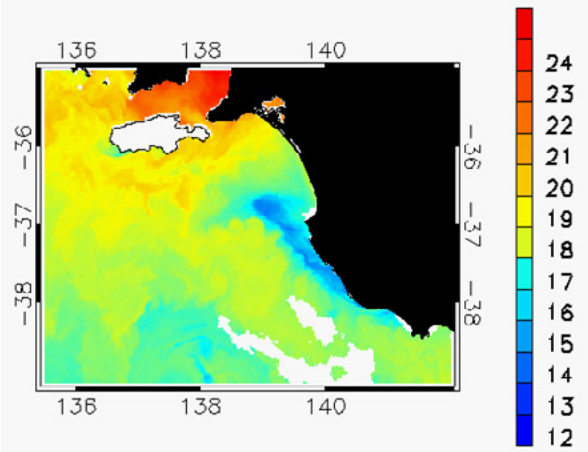


Source: Christopher Griffin, Bureau of Meteorology, Melbourne

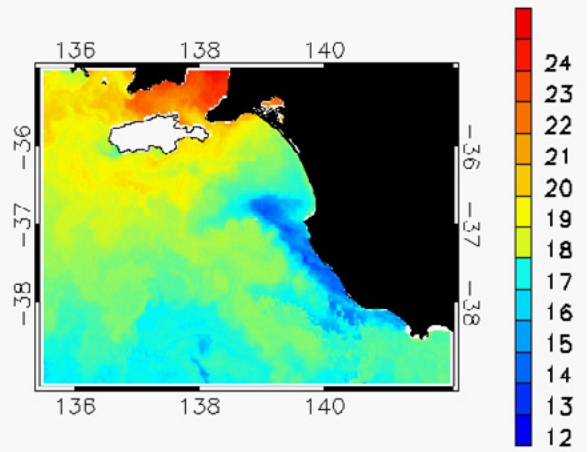
Figure 14.8 SST maps

Maps of SSTs at ~0.2 m water depth for 8 March 2018 over the Bonney Coast, southern Australia, from different EO sensors. Temperature is given in °C. The signature of the cold upwelling is well defined in the L3S product but somewhat less defined in the L4 analysis.

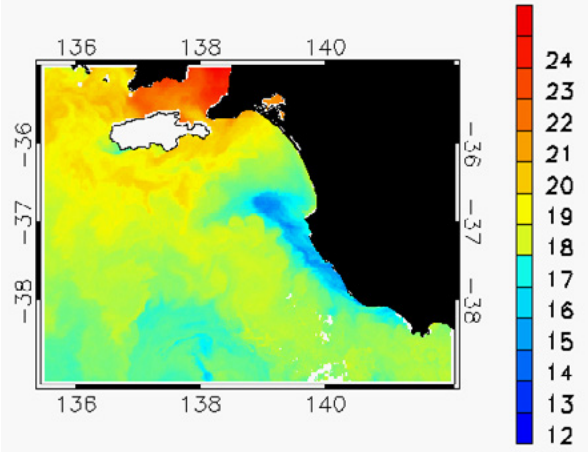
a. 2 km IMOS VIIRS 1-day night-only L3C



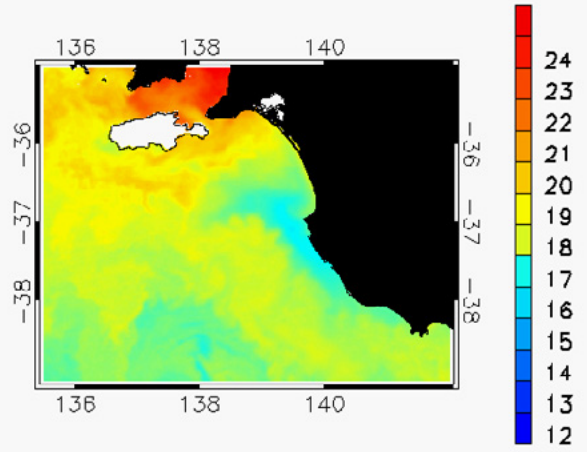
b. 2 km IMOS Himawari-8 1-day night-only L3C



c. 2 km IMOS Multi-sensor 1-day night-only L3S (formed from NOAA-18 and NOAA-19 HRPT AVHRR and NPP VIIRS data)



d. 1 km JPL MUR L4 (formed from AMSR-2, MODIS, and GAC AVHRR data).



Source: Helen Beggs, Bureau of Meteorology, Melbourne

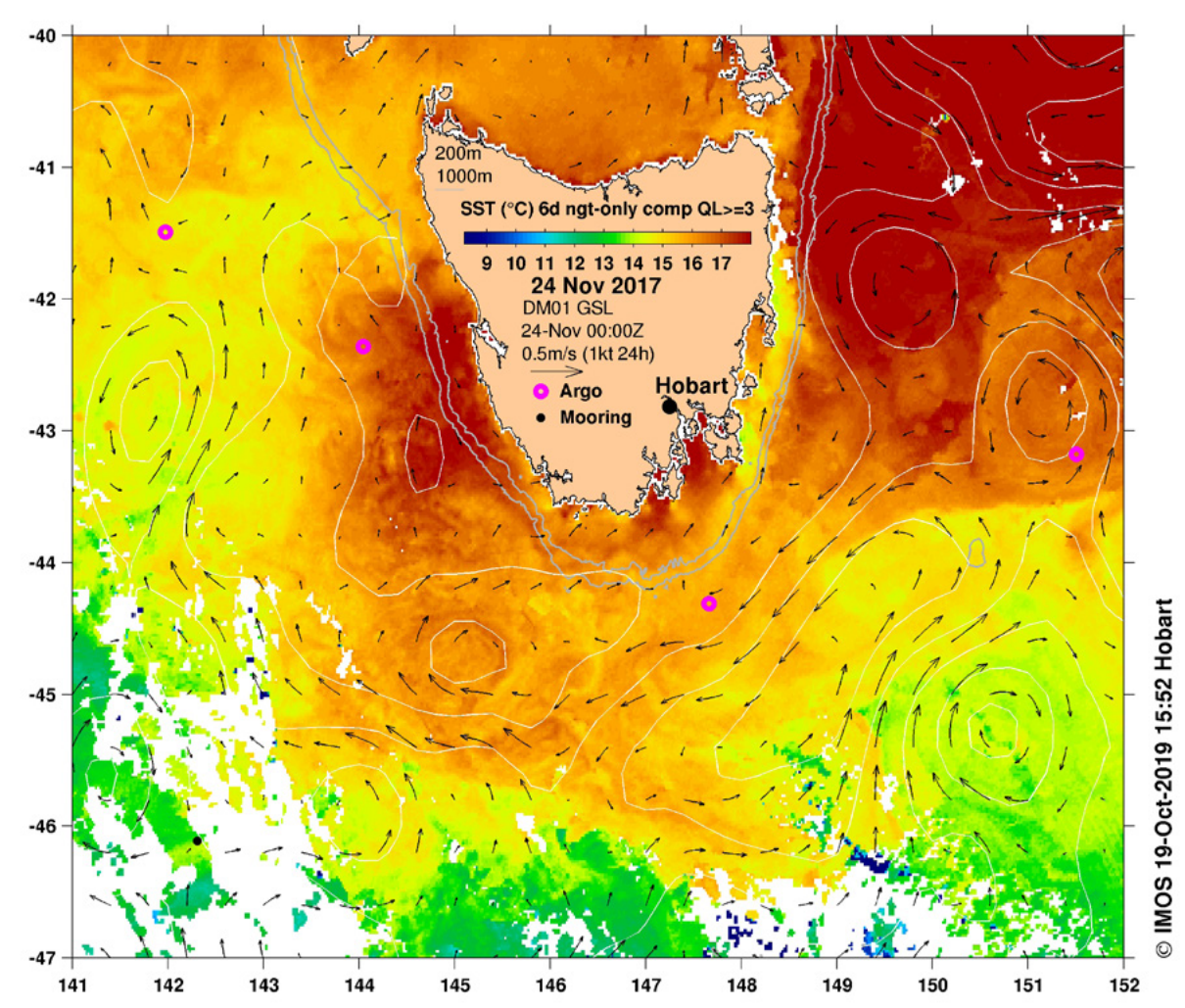
Excursus 14.2—Sea Surface Temperature around Tasmania

Source: Madeleine Cahill, IMOS OceanCurrent
Further Information: OceanCurrent website:
http://oceancurrent.imos.org.au/news.php
http://oceancurrent.imos.org.au/daily.php?link=DR_SST_daily/pctiles/Tas/20171124.gif

In 2017, SST around Tasmania were above the 90th percentile at the end of November, particularly to the west and south. Temperatures were hottest off the northeast coast, associated with a weak Eastern Australian Current (EAC) eddy, but more unusual were the high temperatures off the west coast (see Figure 14.9) that also peaked at over 18°C, which was more than 3–4°C above the November mean. The blocking high in the Tasman Sea that directed northeasterly winds over Tasmania and brought a record six days of temperatures over 26°C also created the conditions for a week or more of cloudless skies. Cloud-free conditions allow maximum solar heating, particularly at this time of year when UV radiation is reaching its peak. SST indicates that off the west coast temperatures increased by up to 4°C over three weeks.

Figure 14.9 IMOS nighttime, 6-day AVHRR L3S SST around Tasmania

This nighttime, 6-day AVHRR L3S SST image around Tasmania was acquired on 24 November 2017. The coincident locations of Argo floats are shown as magenta circles.

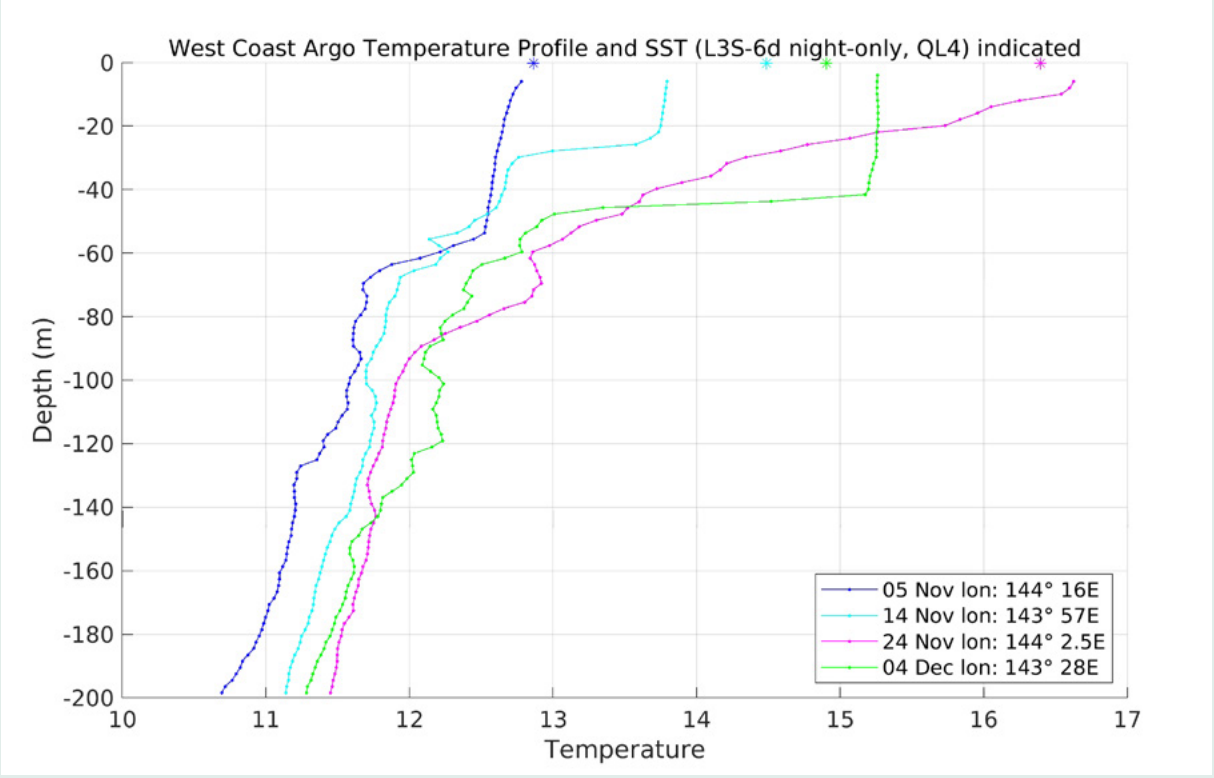


Satellite SST, however, is a measure of only a very thin surface layer (or surface skin) and when winds are very weak there is not much vertical mixing and the SST may only represent a shallow surface layer. Without modelling it is impossible to know how deep this surface layer extends. The unusual weather conditions meant that not only was the sky around Tasmania cloud-free, but the west coast, in the lee of the wind, was almost becalmed as well. The 'hot spot' off the west coast suggests that in this region the heating may only be shallow. The consequence of shallow heating is not only that the extreme temperatures only affect animals and plants near the surface but also that the temperatures will be short-lived and quickly reversed with the next windy day.

Argo floats (shown as magenta circles in Figure 14.9) can provide a window to what is happening beneath the surface. A float off the west coast shelf profiled the water column every ten days through November 2017. The development of a warm mixed-layer throughout the month can be seen in the Argo temperature profiles for that float during November and early December (see Figure 14.10). The closest satellite SST for each profile is also plotted to indicate any discrepancy between the surface and water below. In early November the water was well-mixed down to 60 m and the Argo temperature at 5 m was very close to the mixed layer temperature. For all days that the float profiled, the satellite SST was always within 0.7°C of the temperature at 10 m. After the weather changed, the surface heat was mixed down to 40 m reducing the surface temperature significantly but resulting in an increase of at least 2°C in the mixed layer since the beginning of November.

Based on the SST anomalies, the west coast surface waters were 3–4°C above average for at least 10 days during November. From the Argo profile on November 24, it is clear the low wind speeds allowed the temperatures to be surface intensified at the peak of the event. Unlike the three other profiles, there was no strong thermocline and temperatures at 20 m were about 1°C cooler than at 10 m. So, it is most likely subsurface temperatures, at 10–20 m, would not have reached the 4°C anomaly. In any case, with a 2°C increase in temperature of the top 40 m, the event created a strong injection of heat into surface waters around Tasmania. Unlike the west coast, water temperatures on the east coast, away from sheltered regions, were unaffected by the heating because the atypical northeasterly winds drove an upwelling event that kept the shelf waters cool despite the warm EAC water just offshore.

Figure 14.10 Argo temperature profile and SST



14.5.2 High resolution SST climatologies and extreme events

Quantifying ocean 'extreme' events from SST observations, such as marine heatwaves and cold upwelling, requires a consistent and accurate SST reference, ideally at the same spatial and temporal resolution as the observations and over a period sufficiently long to represent 'typical' ocean conditions. Over the Australian region four high resolution SST climatologies have been compared (Hu *et al.*, 2019) and the following two found to agree most closely over the same time period (1992–2016) and to be most suitable for the study of coastal extreme events.

- The SST Atlas of Australian Regional Seas (SSTAARS: Wijffels *et al.*, 2018; see Figure 14.1 and Table 14.4) was derived from de-biased IMOS 1-day nighttime AVHRR L3S SSTs for the period 1992 to 2016. The SSTAARS 'Atlas' provides the following variables (referenced to middle year, 2005) for each 0.02° × 0.02° pixel:
  - a daily (seasonal fitted) climatological SST (0.2 m);
  - mean SST(0.2 m);
  - decadal trend;
  - monthly seasonal harmonics; and
  - percentiles (all available from the AODN; see *http://portal.aodn.org.au*).
- The SSTAARS Atlas reveals in detail regional oceanographic phenomena, including tidally-driven entrainment cooling over shelves and reef flats, wind-driven upwelling, shelf winter fronts, cold river plumes, and standing mesoscale features in the major offshore currents (Wijffels *et al.*, 2018). SSTAARS daily climatological SSTs are used in conjunction with either IMOS AVHRR L3S or Multi-sensor L3S SSTs to produce maps of SST anomalies and percentiles in IMOS OceanCurrent, which are useful for real time detection of anomalous events (see Excursus 14.2).
- A global, daily, 0.05° resolution, gap-free SST climatology formed from the ESA SST CCI version 2.1 reanalyses for 1981 to 2016 (Merchant *et al.*, 2019b; Rayner *et al.*, 2019a; see Table 14.3) is also highly suitable for use as a high resolution reference for marine heatwave studies over the Australian region, although the feature resolution of the optimally-interpolated SST CCI analysis v2.1 will be significantly coarser than that of the 0.02° composite-based SSTAARS climatology (Hu *et al.*, 2019).

14.6 Inland Water Temperature

Lake surface water temperature (LSWT) is an important parameter with which to assess aquatic ecosystems and the response of various lake characteristics to climate change. Inland waters are warming at highly variable rates that often differ from regional air temperature trends (White *et al.*, 2018). This variable warming is partially attributable to the geographical and morphological characteristics of each individual lake. In very large lakes, significant intra-lake variability in long term warming trends have been observed (White *et al.*, 2018).

Some of the challenges for EO of water temperatures over inland seas, lakes, and the ocean coastal zones include:

- greater atmospheric water vapour, temperature, and aerosol variability than over most of the ocean;
- avoiding land contamination of satellite footprint;
- water surface contaminants; and
- turbidity in interaction with cloud detection (O'Carroll *et al.*, 2019).

Regarding the latter, products are prone to over-masking during the spring-summer warming phase, and to screening of cold, clear water, leading to systematic observation bias (O'Carroll *et al.*, 2019). Problems in satellite-based lake temperature products arise where processing methodologies for cloud detection and temperature retrieval that are optimised for the open ocean (where the atmosphere is usually close to equilibrium with the water surface) are applied. However, inland water-specific methodologies are promising for application of satellite-derived lake temperatures (MacCallum and Merchant, 2012; Crosman *et al.*, 2017; Woolway and Merchant, 2018).

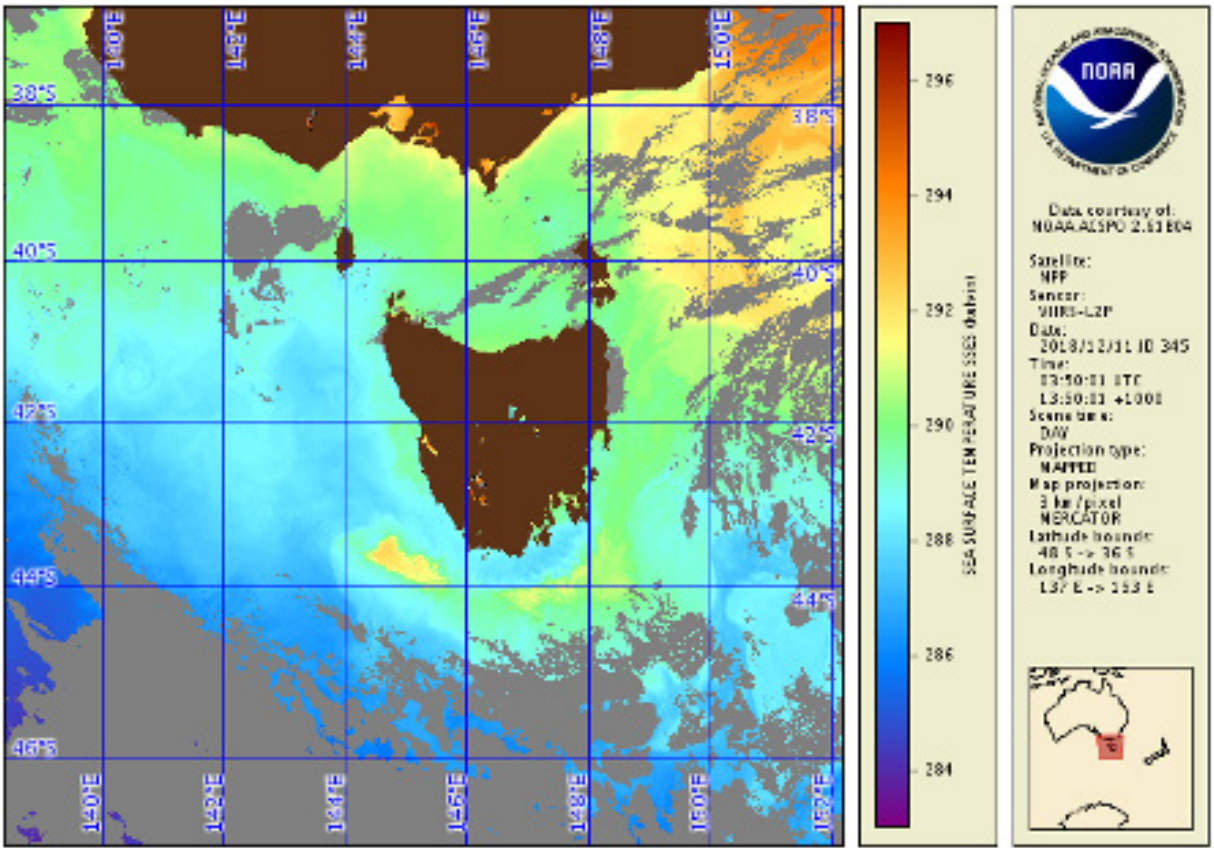
Satellite data for the period 1985 to 2009 was used to measure the surface temperatures of 167 large lakes worldwide (with dimensions of at least 10×10 km pure water area; Schneider and Hook, 2010). Lakes studied were located in North and South America, Europe, Asia, and Africa, but the study excluded Australia, New Guinea, Indonesia, or New Zealand, possibly due to the lack of suitably large lakes. LSWT retrievals derived from 1 km ATSR and 4 km GAC AVHRR Pathfinder version 5 BTs were used. They reported an average warming rate of 0.45°C per decade, with some lakes warming as much as 1°C per decade. The warming trend was global, and the greatest increases were in the mid- to high-latitudes of the Northern Hemisphere (Schneider and Hook, 2010).

To assess climate change and lake dynamics using consistent LSWT data, Lieberherr and Wunderle (2018) used the 1.1 km resolution HRPT AVHRR archive of the University of Bern. To derive such a dataset, challenges such as orbit drift correction, non-water pixel detection, and homogenisation had to be solved. The result was a dataset covering over 35 years of spatial LSWT data for 26 European lakes (Lieberherr and Wunderle, 2018). White *et al.* (2018) had to surmount similar challenges in order to assemble a 0.018° resolution LSWT dataset covering the Laurentian Great Lakes (USA/Canada border), derived from HRPT AVHRR T_B (1986–2016). They subtracted an empirically-determined, mean diurnal cycle to mitigate effects of varying observation times. Adjustments in the georegistration of the images were made to reduce the impact of AVHRR navigational errors on earlier platforms (White *et al.*, 2018). The Australian HRPT archive of well-navigated T_B covering the period 1992 to 2019 (King, 2003; Griffin *et al.*, 2017) offers a similar opportunity to monitor long term trends in Australian inland surface waters, although derivation of LSWT would require sufficient *in situ* LSWT data for either regression or validation.

The IMOS Multi-sensor L3S products (Table 14.4) provide surface water temperatures over most large Australian inland waterbodies. In addition, LSWT data over Australian lakes are available from NOAA (NOAA CoastWatch, 2018) in NPP/NOAA-20 VIIRS L2P/L3U (see Figure 14.11), Aqua/Terra MODIS L2P/L3U, Himawari-8 L3U/L3C SST products, and JPL MUR L4 SST products (see *https://podaac.jpl.nasa.gov*), although the accuracy of the SST values for inland waters would need to be verified using *in situ* water temperature observations. Various federal, state, and municipal environmental and water authorities measure water temperatures in reservoirs, lakes, and rivers. These, and additional targeted temperature datasets, may provide sufficient *in situ* observations to determine the suitability of available satellite-derived SST products for estimates of LSWT in Australia.

Figure 14.11 Daytime SWT map from VIIRS

Daytime surface water temperatures from NPP VIIRS L2P SST files, processed by NOAA/NESDIS/STAR, for 11 December 2018.



Source: NOAA/NESDIS ACSPO Regional Monitor for SST website (*https://www.star.nesdis.noaa.gov/sod/sst/arms*). Retrieved from: *https://www.star.nesdis.noaa.gov/sod/sst/arms/?datatype=none&data_lev=L2P&satt=VIIRS_NPP&daynight=day&variable=sst&date=2018-12-11&region-selected=TM&curr_slide=0&last_slide=1&masked=true&sses=true&front=false&cmp=false&polar_slide=0*

14.7 Further Information

AODN SST Information

https://help.aodn.org.au/satellite-sst-data/

Australian Institute of Marine Science

AIMS contributions to ocean remote sensing: *https://www.aims.gov.au/docs/research/research-highlights/imos*

Bureau of Meteorology

SST Analyses: *http://www.bom.gov.au/marine/sst.shtml*

SST Short-term Forecasts: *http://www.bom.gov.au/oceanography/forecasts/*

SST Seasonal Forecasts: *http://www.bom.gov.au/oceanography/oceantemp/sst-outlook-map.shtml*

Coral Bleaching Nowcasts: *http://www.bom.gov.au/environment/activities/reeftemp/reeftemp.shtml*

Integrated Marine Observing System (IMOS)

SST Webpage: *http://imos.org.au/facilities/srs/sstproducts/*

SST Product Details: *http://imos.org.au/facilities/srs/sstproducts/sstdata0/*

SST Maps in OceanCurrent: *http://oceancurrent.imos.org.au/*

SST Atlas of Australian Regional Seas (SSTAARS): *https://researchdata.ands.org.au/sst-atlas-australian-climatology-fit/1307263*

SST Data Access:

L3C, L3S: *http://portal.aodn.org.au*

L3U, L3C, L3S, L4: *http://thredds.aodn.org.au/thredds/catalog/IMOS/SRS/SST/ghrsst/catalog.html*

CEOS SST videos

http://ceos.org/home-2/satellite-oceanography-user-workshop-videos-available/

ESA SST Climate Change Initiative

http://esa-sst-cci.org

GHRSST

http://www.ghrsst.org

NASA

Sea Surface Temperature: *https://earthobservatory.nasa.gov/global-maps/MYD28M*

State of the Ocean Web Tool: *https://podaac-tools.jpl.nasa.gov/soto*

Access to Satellite-derived Ocean Products (including SST) from the Physical Oceanography Distributed Active Archive Center (PO.DAAC): *https://podaac.jpl.nasa.gov/*

MUR SST Analysis: *https://podaac.jpl.nasa.gov/dataset/MUR-JPL-L4-GLOB-v4.1?search=MUR&provider=POCLOUD*

NOAA

OceanView online visualisation tool: *https://www.star.nesdis.noaa.gov/socd/ov/*

Validation of SST products in near real time

BoM IMOS L2P/L3U/L3C/L3S: *http://imos.org.au/facilities/srs/sstproducts/sstdata0/sstdata-validation*

EUMETSAT L2P: *http://metis.eumetsat.int/sst*

JAXA AMSR-2 L2P: *https://suzaku.eorc.jaxa.jp/cgi-bin/gcomw/validation/gcomw_validation_ssti1.cgi*

NOAA/NESDIS SQUAM L2P/L3U/L4: *http://www.star.nesdis.noaa.gov/sod/sst/squam*

NOAA/NESDIS iQUAM: *https://www.star.nesdis.noaa.gov/socd/sst/iquam/*

UK Met Office: *https://ghrsst-pp.metoffice.gov.uk/ostia-website/gmpe-argo-stats.html*

14.8 References

Allison, L.J., and Kennedy, J.S. (1967). *An Evaluation of Sea Surface Temperature as measured by the Nimbus I High Resolution Infrared Radiometer.* NASA Technical Note, NASA TN D-4078, 26 p., Washington DC, USA: NASA. *https://ntrs.nasa.gov/archive/nasa/casi.ntrs.nasa.gov/19680000754.pdf*

Andreu-Burillo, I., Brassington, G., Oke, P., and Beggs, H. (2010). Including a new data stream in BLUElink Ocean Data Assimilation System. *Australian Meteorological and Oceanographic Journal,* 59, 77–86.

Banzon, V., Smith, T.M., Chin, T.M., Liu, C, and Hankins, W. (2016). A long-term record of blended satellite and in situ sea-surface temperature for climate monitoring, modeling and environmental studies, *Earth System Science Data*, 8, 165–176. *www.earth-syst-sci-data.net/8/165/2016/ doi:10.5194/essd-8-165-2016*

Beggs, H. (2010). Use of TIR from Space in Operational Systems, In: *Oceanography from Space Revisited*. (Eds: V. Barale, J.F.R. Gower and L. Alberotanza). Springer Science+Business Media B.V. pp. 249–271. doi:10.1007/978-90-481-8681-5. *https://www.researchgate.net/publication/259823623_Use_of_TIR_from_Space_in_Operational_Systems*

Beggs, H., Zhong, A., Warren, G., Alves, O., Brassington, G., and Pugh, T. (2011). RAMSSA—An Operational, High-Resolution, Multi-Sensor Sea Surface Temperature Analysis over the Australian Region, *Australian Meteorological and Oceanographic Journal*, 61, 1–22. *http://www.bom.gov.au/jshess/papers.php?year=2011*

Beggs H., Verein, R., Paltoglou, G., Kippo, H., and Underwood, M. (2012). Enhancing ship of opportunity sea surface temperature observations in the Australian region. *Journal of Operational Oceanography*, 5, 59–73.

Beggs, H., Griffin, C., Brassington, G., and Govekar, P. (2018a). *Measuring coastal upwelling using IMOS Himawari-8 and Multi-Sensor SST*. Presented at ACOMO 2018 Workshop, Canberra, Australia, 9–11 October, 2018. *http://imos.org.au/fileadmin/user_upload/shared/SRS/SST/Beggs_ACOMO_Poster_Coastal_Upwelling_20181004.pdf*

Beggs, H., Griffin, C., Govekar, P., Majewski, L., Qi, L., and Zhong, A. (2018b). *Which IMOS GHRST product should I use?* Presented at the IMOS Data Workshop, Adelaide, Australia, 6 July 2018. *http://imos.org.au/fileadmin/user_upload/shared/SRS/SST/IMOS_Data_Workshop-SST-Beggs_08Jul2018.pdf*

Beggs, H., Griffin, C., and Govekar, P. (2019). *New IMOS multi-sensor sea surface temperature composites provide better coverage and accuracy*. IMOS web article, 21 February 2018. *http://imos.org.au/fileadmin/user_upload/shared/SRS/SST/Beggs_2019_IMOS_Multi-sensor_L3S_article_21Feb2018.pdf*

Beggs, H., Qi, L., Govekar, P., and Griffin, C. (2020). Ingesting VIIRS SST into the Bureau of Meteorology's Operational SST Analyses, In *Proceedings of the 2*1st *GHRSST Science Team Meeting, Virtual Meeting hosted by EUMETSAT*, 1–4 June 2020. P. 104–110. *https://www.ghrsst.org/meetings/21st-ghrsst-international-science-team-meeting-g-xxi/*

Berry, D., Corlett, G., Embury, O., and Merchant, C. (2018). Stability assessment of the (A)ATSR Sea Surface Temperature Climate Dataset from the European Space Agency Climate Change Initiative. Remote Sensing, 10, 126.

BoM (2019). *Near real-time fv01 SST Validation* (Webpage for IMOS GHRSST L2P, L3U, L3C and L3S products from POES HRPT AVHRR, NPP VIIRS and Himawari-8 AHI). BOM/IMOS. *http://opendap.bom.gov.au:8080/thredds/fileServer/abom_imos_ghrsst_archive-1/staticweb/sst-nrt-batch/index01.html*

Brasnett, B. (2008). The impact of satellite retrievals in a global sea-surface-temperature analysis. *Quarterly Journal of the Royal Meteorological Society*, 134, 1745–1760. doi:10.1002/qj.319

Brasnett, B. (2012). *A 20-year Reanalysis of Sea Surface Temperature*. Report, CMC. Available on request from the author at *bruce.brasnett@gmail.com*

Brasnett, B., and Surcel Colan, D. (2016). Assimilating Retrievals of Sea Surface Temperature from VIIRS and AMSR2. *Journal of Atmospheric and Oceanic Technology*. *https://doi.org/10.1175/JTECH-D-15-0093.1*

Casey, K.S., Brandon, T.B., Cornillon, P., and Evans, R. (2010). The Past, Present and Future of the AVHRR Pathfinder SST Program. In *Oceanography from Space: Revisited* (Eds: V. Barale, J.F.R. Gower, and L. Alberotanza). Springer. doi:10.1007/978-90-481-8681-5_16. *https://www.nodc.noaa.gov/SatelliteData/pathfinder4km/OFS_21_Cas_09Dec2009.pdf*

Chin, T.M., Vazquez-Cuervo, J., and Armstron, E.M. (2017). A multi-scale high-resolution analysis of global sea surface temperature. *Remote Sensing of Environment*, 200, 154–169. *https://doi.org/10.1016/j.rse.2017.07.029*

Crosman, E., Vazquez-Cuervo, J., and Chin, T.M. (2017). Evaluation of the Multi-Scale Ultra-High Resolution (MUR) Analysis of Lake Surface Temperature. *Remote Sensing*, 9, 723. doi:10.3390/rs9070723.

Dash, P., Ignatov, A., Kihai, Y., and Sapper, J. (2010). The SST Quality Monitor (SQUAM). Journal of Atmospheric and Oceanic Tech*nology*, 27, 1899–1917. doi:10.1175/2010JTECHO756.1

Dash, P., Ignatov, A., Martin, M., Donlon, C., Brasnett, B., Reynolds, R., Banzon, V., Beggs, H., May, D., McKenzie, B., Cayula, J-F., Chao, Y., Grumbine, R., Maturi, E., Harris, A., Mittaz, J., Sapper, J., Chin, T., Vazquez, J., Armstrong, E., Gentemann, C., Cummings, J., Piolle, J-F., Autret, E., Roberts-Jones, J., Ishizaki, S., Hoyer, J., and Poulter, D. (2012). Group for High Resolultion SST (GHRSST) Analysis Fields Inter-Comparisons Part 2. Near real-time web-based Level 4 SST Quality Monitor (L4-SQUAM). *Deep Sea Research II*, 77–80, 31–43.

Ditri, A.L., Minnett, P.J., Liu, Y., Kilpatrick, K., and Kumar, A. (2018). The Accuracies of Himawari-8 and MTSAT-2 Sea-Surface Temperatures in the Tropical Western Pacific Ocean. *Remote Sensing*, 10(2), 212. doi:10.3390/rs10020212

Donlon, C.J., Minnett, P.J., Gentemann, C.L., Nightingale, T.J., Barton, I.J., Ward, B., and Murray, M.J. (2002). Toward improved validation of satellite sea surface skin temperature measurements for climate research. *Journal of Climate*, 15(4), 353–369.

Donlon, C., Robinson, I., Casey, K., Vasquez, J., Armstrong, E., Gentemann, C., May, D., LeBorgne, P., Piolle, J., Barton, I., Beggs, H., Poulter, D. J. S., Merchant, C., Bingham, A., Heinz, S., Harris, A., Wick, G., Emery, B., Stuart-Menteth, A., Minnett, P., Evans, B., Llewellyn-Jones, D., Mutlow, C., Reynolds, R., Kawamura, H., and Rayner, N. (2007). The Global Ocean Data Assimilation Project (GODAE) High Resolution Sea Surface Temperature Pilot Project (GHRSST-PP). *Bulletin of American Meterological Society*, 88, 1197–1213.

Donlon, C., Casey, K., Robinson, I., Gentemann, C., Reynolds, R., Barton, I., Arino, O., Stark, J., Rayner, N., Le Borgne, P., Poulter, D., Vazquez-Cuervo, J., Armstrong, E., Beggs, H., Llewellyn-Jones, D., Minnett, P., Merchant, C., and Evans, R. (2009). The GODAE High-Resolution Sea Surface Temperature Pilot Project. *Oceanography*, 22, 34–45.

Donlon, C.J., Martin, M., Stark, J., Roberts-Jones, J., Fiedler, E., and Wimmer, W. (2012). The Operational Sea Surface Temperature and Sea Ice Analysis (OSTIA) system. *Remote Sensing of Environment*, 116, 140–158. *https://doi.org/10.1016/j.rse.2010.10.017*

Donlon, C.J., Minnett, P.J., Jessup, A., Barton, I., Emery, W., Hook, S., Wimmer, W., Nightingale, T.J., and Zappa, C. (2014). Chapter 3.2—Ship-borne Thermal Infrared Radiometer Systems, *Experimental Methods in the Physical Sciences Vol. 47* (Eds: G. Zibordi, C.J. Donlon, and A.C. Parr). pp 305–404, Academic Press. *http://doi.org/10.1016/B978-0-12-417011-7.00011-8*

Eumetsat (2011). *AVHRR Level 1b Product Guide*. Doc. No. EUM/OPS-EPS/MAN/04/0029 v3A. EUMETSAT, Germany. *https://www-cdn.eumetsat.int/files/2020-04/pdf_avhrr_l1b_product_guide.pdf*

Fiedler, E.K., McLaren, A., Banzon, V., Brasmett, B., Ishizaki, S., Kennedy, J., Rayner, N., Roberts-Jones, J., Corlett, G., Merchant, C.J., and Donlon, C. (2019a). Intercomparison of long-term sea surface temperature analyses using the GHRSST Multi-Product Ensemble (GMPE) system. *Remote Sensing of Environment*, 222, 18–33. *https://doi.org/10.1016/j.rse.2018.12.015*

Fiedler, E.K., Mao, C., Good, S.A., Waters, J., and Martin, M.J. (2019b). Improvements to feature resolution in the OSTIA sea surface temperature analysis using the NEMOVAR assimilation scheme. *Quarterly Journal of the Royal Meteorological Society*, 145(725), 3609–3625. *https://doi.org/10.1002/qj.3644*

Garde, L.A., Spillman, C.M., Heron, S., and Beeden, R. (2014). ReefTemp Next Generation: A New Operational System for Monitoring Reef Thermal Stress. *Journal of Operational Oceanography*, 7, 21–33

Gentemann, C.L., Meissner, T., and Wentz F.J. (2010). Accuracy of Satellite Sea Surface Temperatures at 7 and 11 GHz. *IEEE Transactions on Geoscience and Remote Sensing*, 48, 1009–1018. doi:10.1109/TGRS.2009.2030322

Gentemann, C.L., and Hilburn, K.A. (2015). In situ validation of sea surface temperatures form the GCOM-W1 AMSR2 RSS calibrated brightness temperatures. *Journal of Geophysical Research: Oceans*, 120, 3567–3585. doi:10.1002/2014JC010574

GHRSST Science Team (2012). *The Recommended GHRSST Data Specification (GDS) 2.0*, document revision 5, available from the GHRSST International Project Office, 2012, pp 123. *https://www.ghrsst.org/wp-content/uploads/2016/10/GDS20r5.pdf*

Good, S., Fiedler, E., Mao, C., Martin, M.J., Maycock, A., Reid, R., Roberts-Jones, J., Searle, T., Waters, J., While, J., and Worsfold, M. (2020). The Current Configuration of the OSTIA System for Operational Production of Foundation Sea Surface Temperature and Ice Concentration Analyses. *Remote Sensing*, 12, 720. doi:10.3390/rs12040720

Griffin, C., and Majewski, L. (2016). *GHRSST Himawari-8 SST at Australian Bureau of Meteorology*. Presented at the 17th GHRSST Science Team Meeting, Washington DC, USA, 6–19 June 2016. *http://imos.org.au/facilities/srs/sstproducts/sstdata0/sstdata-references/*

Griffin, C., Beggs, H., and Majewski, L. (2017). *GHRSST compliant AVHRR SST products over the Australian region*, Version 1, Technical Report, Bureau of Meteorology, Melbourne, Australia, 151 p. *http://imos.org.au/fileadmin/user_upload/shared/SRS/SST/GHRSST-DOC-basic-v1.0r1.pdf*

Griffin, C. (2018). *BoM Himawari-8 AHI Cloud/SST/SSES Algorithms*. Presented at NOAA-BoM SST Workshop, College Park, MD, USA, 3–6 April 2018. *http://imos.org.au/facilities/srs/sstproducts/sstdata0/sstdata-references*

Guan, L., and Kawamura, H. (2004). Merging satellite infrared and microwave SSTs: Methodology and evaluation of the new SST. *Journal of Oceanography*, 60(5), 905.

Hu, Y., Beggs, H., and Wang, X.H. (2019). Inter-comparison of high-resolution SST climatology data sets over the Australian region. In: *SST-CCI-Phase-II SST CCI Climate Assessment Report Issue 1*. European Space Agency. 153 pp. *http://www.esa-sst-cci.org/PUG/pdf/SST_CCI-CAR-UKMO-201_Issue_1-signed.pdf*

Huang, Z., Leplastrier, A., Xie, S., and Feng, M. (2018). *Using Himawari-8 geostationary satellite data for the investigation of highly dynamic oceanographic phenomena*, Presented at the ACOMO 2018 Workshop, Canberra, Australia, 9-11 October 2018. *http://imos.org.au/fileadmin/user_upload/shared/IMOS%20General/ACOMO/ACOMO_2018/Powerpoints/Tuesday/Zhi-Huang.pdf*

Huang, B., Liu, C., Banzon, V., Freeman, E., Graham, G., Hankins, W., Smith, T., and Zhang, H.-M. (2021). Improvements of the Daily Optimum Interpolation Sea Surface Temperature (DOISST) Version 2.1. *Journal of Climate*, 34, 2923–2939. *https://doi.org/10.1175/JCLI-D-20-0166.1*

IMOS (2018). *IMOS Satellite Remote Sensing SST Data* webpage: *http://imos.org.au/facilities/srs/sstproducts/sstdata0/*

IMOS OceanCurrent (2018). *IMOS OceanCurrent Surface Currents and Temperature* website: *http://oceancurrent.imos.org.au*

Kachi, M., Maeda, T., Tsutsui, H., Ono, N., Kasahara, M., and Mokuno, M. (2017). Five years observations of global water cycle by GCOM-W/AMSR2. In: *Proceedings of 2017 IEEE International Geoscience and Remote Sensing Symposium (IGARSS)*, 5641–5643. doi:10.1109/IGARSS.2017.812885

Karagali, I., and Hoyer, J.L. (2013). Observations and modelling of the diurnal SST cycle in the North and Baltic Seas. *Journal of Geophysical Research: Oceans*, 118, 4488–4503. doi:10.1002/jgrc.20320

Kawanishi, T., Sezai, T., Ito, Y., Imaoka, K., Takeshima, T., Ishido, Y., Shibata, A., Miura, M., Inahata, H., and Spencer, R.W. (2003). The Advanced Microwave Scanning Radiometer for the Earth Observing System (AMSR-E), NASA's contribution to the EOS for global energy and water cycle studies. *IEEE Transactions on Geoscience and Remote Sensing*, 41(2), 184–194. doi:10.1109/TGRS.2002.808331

Kilpatrick, K.A., Podesta, G.P., and Evans, R.H. (2001). Overview of the NOAA/NASA Pathfinder algorithm for Sea Surface Temperature and associated Matchup Database. *Journal of Geophysical Research*, 106, 9179–9198

Kilpatrick, K.A., Podesta, G., Walsh, S., Williams, E., Halliwell, V., Halliwell, V., Szczodrak, M., Brown, O.B., Minnett, P.J., and Evans, R. (2015). A decade of sea surface temperature from MODIS. *Remote Sensing of Environment*, 165, 27–41. *http://dx.doi.org/10.1016/j.rse.2015.04.023*

King, E. A. (2003). *The Australian AVHRR Data Set at CSIRO/EOC: Origins, Processes, Holdings and Prospects, CSIRO Earth Observation Centre Report 2003/04*. CSIRO, Canberra. *http://www.eoc.csiro.au/tech_reps/2003/tr2003_04.pdf*

Kramar, M., Ignatov, A., Petrenko, B., Kihai, Y., and Dash, P. (2016). Near Real Time SST retrievals from Himawari-8 data with ACSPO at NOAA. *Proceedings of SPIE 9827*, Ocean Sensing and Monitoring VIII, 98270L. doi:10.1117/12.2229771

Kurihara, Y., Sakurai, T., and Kuragano, T. (2006). Global daily sea surface temperature analysis using data from satellite microwave radiometer, satellite infrared radiometer and in-situ observations. *Weather Service Bulletin*, 73, Special issue, s1–s18 (in Japanese).

Kurihara, Y., Murakami, H., and Kachi, M. (2016). Sea surface temperature from the new Japanese geostationary meteorological Himawari-8 satellite. *Geophysical Research Letters*, 43, 1234–1240. doi:10.1002/2015GL067159

Lieberherr, G., and Wunderle, S. (2018). Lake Surface Water Temperature Derived from 35 Years of AVHRR Sensor Data for European Lakes. Remote Sensing, 10, 990. *https://doi.org/10.3390/rs10070990*

Liu, C., Freeman, E., Kent, E.C., Huang, B., Zhang, H.M., Berry, D.I., Worley, S.J., Ouellet, M., Gaboury, I., Ji, Z., and Banzon, V.F. (2019). *ICOADS Drifting Buoy Data Recovery from BUFR and Its Impact on OISST and ERSST*. Presented at American Meteorological Society 99th Annual Meeting, Phoenix, USA, 6–10 January, 2019. *https://ams.confex.com/ams/2019Annual/webprogram/Paper352621.html*

Llewellyn-Jones, D.T., Minnett, P.J., Saunders, R.W., and Zavody, A.M. (1984). Satellite multichannel infrared measurements of sea surface temperature of the N.E. Atlantic Ocean using AVHRR/2. *Quarterly Journal of the Royal Meteorological Society*, 110, 613–631.

Lumpkin, R., Centurioni, L., and Perez, R. (2016). Fulfilling observing system implementation requirements with the Global Drifter Array. Journal of Atmospheric and Oceanic Tech*nology*, 33, 685–695.

MacCallum, S.N., and Merchant, C.J. (2012). Surface water temperature observations of large lakes by optimal estimation. *Canadian Journal of Remote Sensing*, 38. 25–45. *https://doi.org/10.5589/m12-010*.

Martin M., Dash, P., Ignatov, A., Banzon, V., Beggs, H., Brasnett, B., Cayula, J-F., Cummings, J., Donlon, C., Gentemann, C., Grumbine, R., Ishizaki, S., Maturi, E., Reynolds, R., and Roberts_Jones, J. (2012). Group for High Resolution SST (GHRSST) Analysis Fields Intercomparisons: Part 1. A GHRSST Multi-Product Ensemble (GMPE). *Deep Sea Research II*, 77–80, 21–30. *http://dx.doi.org/10.1016/j.dsr2.2012.04.013*

Maturi, E., Harris, A., Merchant, C., Mittaz, J., Potash, B., Meng, W., and Sapper, J. (2008). NOAA's sea surface temperature products from operational geostationary satellites. *Bulletin of the American Meteorological Society*, 89, 1877–1888.

Maturi, E., Harris, A., Mittaz, J., Sapper, J., Wick, G., Zhu, X., Dash, P., and Koner, P. (2017). A New High-Resolution Sea Surface Temperature Blended Analysis. *Bulletin of the American Meteorological Society*, 98(5), 1015–1026. *https://doi.org/10.1175/bams-d-15-00002.1*

McPhaden, M.J., Ando, K., Bourles, B., Freitag, H.P., Lumpkin, R., Masumoto, Y., Murty, V.S.N., Nobre, P., Ravichandran, M., Vialard, J., Vousden, D., and Yu, W. (2010). The global tropical moored buoy array. *Proceedings of OceanObs '09*. *http://www.oceanobs09.net/proceedings/cwp/McPhaden-OceanObs09.cwp.61.pdf*

Merchant, C.J., and Embury, O. (2014). Ch 4.3—Simulation and inversion of satellite thermal measurements. In: Optical radiometry for ocean climate measurements. Experimental methods in the physical sciences, 47 (47). (Eds: Zibordi, G., Donlon, C.J., and Parr, A.C.). Academic Press, pp 489–526. ISBN 9780124170117. *https://doi.org/10.1016/B978-0-12-417011-7.00015-5*

Merchant, C.J., Harris, A.R., Maturi, E., and MacCallum, S. (2005). Probabilistic physically based cloud screening of satellite infrared imagery for operational sea surface temperature retrieval. *Quarterly Journal of the Royal Meteorological Society*, 131, 2735–2755. doi:10.1256/qj.05.15

Merchant, C.J., Le Borgne, P., Marsouin, A., and Roquet, H. (2008). Optimal estimation of sea surface temperature from split-window observations. *Remote Sensing of Environment*, 112, 2469–2484. ISSN 0034-4257 *https://doi.org/10.1016/j.rse.2007.11.011*.

Merchant, C.J., Embury, O., Rayner, N.A., Berry, D.I., Corlett, G.K., Lean, K., Veal, K.L., Kent, E.C., Llewellyn-Jones, D.T., Remedios, J.J., and Saunders, R. (2012). A 20 year independent record of sea surface temperature for climate from Along-Track Scanning Radiometers. *Journal of Geophysical Research*, 117, C12013. doi:10.1029/2012JC008400

Merchant, C.J., Minnett, P.J., Beggs, H., Corlett, G., Gentemann, C., Harris, A.R., Hoyer, J., and Maturi, E.. (2019a). Global Sea Surface Temperature, In: *Taking the Temperature of the Earth. Steps towards integrated understanding of variability and change* (Eds: Glynn Hulley and Darren Ghent). P. 5–55. Elsevier. *https://doi.org/10.1016/B978-0-12-814458-9.00002-2*

Merchant, C.J., Embury, O., Bulgin, C.E., Block, T., Corlett, G., Fiedler, E., Good, S.A., Mittaz, J., Rayner, N.A., Berry, D., Eastwood, S., Taylor, M., Tsushima, Y., Waterfall, A., Wilson, R., and Donlon, C. (2019b). Satellite-based time-series of sea-surface temperature since 1981 for climate applications. *Scientific Data*, 6(223): 1–18. doi:10.1038/s41597-019-0236-x

Met Office (2019). *Validation of GMPE analyses using Argo* webpage, National Centre for Ocean Forecasting. *https://ghrsst-pp.metoffice.gov.uk/ostia-website/gmpe-argo-stats.html*

Minnett, P.J., Smith, M., and Ward, B. (2011). Measurements of the oceanic thermal skin effect. *Deep Sea Research II*, 58, 861–868.

Minnett, P.J., and Kaiser-Weiss, A.K. (2012). *Near-Surface Oceanic Temperature Gradients*. Discussion Document, Group for High Resolution Sea-Surface Temperature. 7 p. *https://www.ghrsst.org/wp-content/uploads/2021/04/SSTDefinitionsDiscussion.pdf*

Minnett, P.J., Alvera-Azcárate, A., Chin, T.M., Corlett, G.K., Gentemann, C.L., Karagali, I., Li, X., Marsouin, A., Marullo, S., Maturi, E., Santoleri, R., Saux Picart, S., Steele, M., and Vazquez-Cuervo, J. (2019). Half a century of satellite remote sensing of sea-surface temperature. *Remote Sensing of Environment*, 233, 111366. *https://doi.org/10.1016/j.rse.2019.111366*.

NASA Earthdata (2019). *Suomi NPP Visible Infrared Imaging Radiometer Suite (VIIRS)* webpage: *https://ladsweb.modaps.eosdis.nasa.gov/missions-and-measurements/viirs/*

NOAA CoastWatch (2018). *ACSPO Global SST from VIIRS* webpage: *https://coastwatch.noaa.gov/cw/satellite-data-products/sea-surface-temperature/acspo-viirs.html*

NOAA/NESDIS/STAR (2019). *SST Quality Monitor v2.1*. *https://www.star.nesdis.noaa.gov/sod/sst/squam*

O'Carroll, A.G., Armstrong, E.M., Beggs, H., Bouali, M., Casey, K.S., Corlett, G.K., Dash, P., Donlon, C.J., Gentemann, C.L., Hoyer, J.L., Ignatov, A., Kabobah, K., Kachi, M., Kurihara, Y., Karagali, I., Maturi, E., Merchant, C.J., Minnett, P., Pennybacker, M. Ramakrishnan, B., Ramsankaran, R., Santoleri, R., Sunder, S., Saux Picart, S., Vazquez-Cuervo, J., and Wimmer, W. (2019). Observational needs of sea surface temperature. *Frontiers in Marine Science*, 6, 420. *https://doi.org/10.3389/fmars.2019.00420*

Oke, P., Sakov, P., Cahill, M. L., Dunn, J. R., Fiedler, R., Griffin, D. A., Mansbridge, J.V., Ridway, K.R., and Schiller, A. (2013). Towards a dynamically balanced eddy-resolving reanalysis: BRAN3. *Ocean Modelling*, 67, 52–70. *https://doi.org/10.1016/j.ocemod.2013.03.008*

Rayner, N., Tsushima, Y., Atkinson, C., Good, S., Roberts, M., Martin, G., Ackerley, D., Titchner, H., Mao, C., Xavier, P., Comer, R., Hu, Y., Beggs, H., Wang, X.H., Margaritis, G., Renshaw, R., Lamas, L., Esteves, R., Almeida, S., de Azevedo, E., Correia, C., Reis, F., and Willén, U. (2019a). *SST-CCI-Phase-II SST CCI Climate Assessment Report Issue 1*. European Space Agency, 153 p. *https://climate.esa.int/media/documents/SST_cci_CAR_v1.pdf*

Rayner, N., Good, S., Block, T., P. Evadzi, P., and Embury, O. (2019b). *SST-CCI-Phase-II SST CCI Product User Guide Issue 2*, European Space Agency, 115 p. *https://climate.esa.int/media/documents/SST_cci_PUG_v2.pdf*

Reynolds, R.W., Smith, T.M., Liu, C., Chelton, D.B., Casey K.S., and Schlax, M.G. (2007). Daily High-resolution Blended Analyses for sea surface temperature. *Journal of Climate*, 20, 5473–5496.

Roberts-Jones, J., Fiedler, E.K., and Martin, M. (2012). Daily, global, high-resolution SST and sea-ice reanalysis for 1985-2007 using the OSTIA system. *Journal of Climate*, 25, 6215–6232

Roemmich, D., Johnson, G.C., Riser, S., Davis, R., Gilson, J., Owens, W.B., Garzoli, S.L., Schmid, C., and Ignaszewski, M. (2009). The Argo Program: observing the global ocean with profiling floats, *Oceanography*, 22, 34–43.

Schneider, P., and Hook, S.J. (2010). Space observations of inland water bodies show rapid surface warming since 1985. *Geophysical Research Letters*, 37 (22), L22405. doi:10.1029/2010GL045059

Shibata, A. (2006). Features of ocean microwave emission changed by wind at 6 GHz. *Journal of Oceanography*, 62, 321–330. doi:10.1007/s10872-006-0057-3.

Smith, D.L., Nightingale, T.J., Middleton, K., Edeson, R., Cox, C.V., Mutlow, C.T., Maddison, B.J., and Coppo, P. (2014). Calibration approach and plan for the sea and land surface temperature radiometer. *Journal of Applied Remote Sensing*, 8(1), 084980. doi:10.1117/1.JRS.8.084980

Soloviev, A., and Lukas, R. (1997). Observation of large diurnal warming events in the near-surface layer of the western equatorial Pacific warm pool. *Deep Sea Research I*, 44, 1055–1076.

Soloviev, A.V., and Lukas, R. (2014). *The near-surface layer of the ocean: Structure, Dynamics and Applications*. 2nd edn. Springer, New York.

Vazquez-Cuervo J., Dewitte B., Chin T.M., Armstrong E.M., Purca S., Alburqueque E. (2013). An analysis of SST gradients off the Peruvian Coast: The impact of going to higher resolution. *Remote Sensing of Environment*, 131, 76–84.

Vinogradova, N.T., Zaccheo, T.S., Alcala, C.M., and Vandemark, D. (2009). Operational high-resolution sea surface temperature product in the Gulf of Maine. *Journal of Operational Oceanography*, 2, 57–66.

Walton, C.C., Pichel, W.G., Sapper, J.F., and May, D.A. (1998). The development and operational application of nonlinear algorithms for the measurement of sea surface temperatures with the NOAA polar-orbiting environmental satellites. *Journal of Geophysical Research*, 103, 27999–28012.

Wentz, F.J., and Meissner, T. (2007). *AMSR-E Ocean Algorithms*, 051707 Report, 6 p. Remote Sensing Systems, Santa Rosa, CA, USA.

White, C.H., Heidinger, A.K., Ackerman, S.A., and McIntyre, P.B. (2018). A Long-Term Fine-Resolution Record of AVHRR Surface Temperatures for the Laurentian Great Lakes. *Remote Sensing*, 10, 1210. *https://doi.org/10.3390/rs10081210*

Wijffels, S.E., Beggs, H., Griffin, C., Middleton, J.F., Cahill, M., King, E., Jones, E., Feng, M., Benthuysen, J.A., Steinberg, C.R., and Sutton, P. (2018). A fine spatial scale sea surface temperature atlas of the Australian regional seas (SSTAARS): seasonal variability and trends around Australasia and New Zealand revisited. *Journal of Marine Systems*, 187, 156–196. *https://doi.org/10.1016/j.jmarsys.2018.07.005*

Wong, E.W., and Minnett, P.J. (2018). The response of the ocean thermal skin layer to variations in incident infrared radiation. *Journal of Geophysical Research: Oceans*, 123, 19. doi:10.1002/2017JC013351

Woolway, R.I., and Merchant, C.J. (2018). Intralake heterogeneity of thermal responses to climate change: a study of large northern hemisphere lakes. *Journal of Geophysical Research: Atmospheres*, 123, 3087–3098. *https://doi.org/10.1002/2017JD027661*

Yang, C., Leonelli, F.E., Marullo, S., Artale, V., Beggs, H., Nardelli, B.B., Chin, T.M., De Toma, V., Good, S., Huang, B., Merchant, C.J., Sakurai, T., Santoleri, R., Vazquez-Cuervo, J., Zhang, H.-M., and Pisano, A. (2021). Sea Surface Temperature intercomparison in the framework of the Copernicus Climate Change Service (C3S). *Journal of Climate*, 33(13), 5257–5283. *https://doi.org/10.1175/JCLI-D-20-0793.1*

Zhang, H., Beggs, H., Majewski, L., Wang, X.H., and Kiss, A.E. (2016a). Investigating Sea Surface Temperature Diurnal Variation over the Tropical Warm Pool Using MTSAT-1R Data. *Remote Sensing of Environment*, 183, 1–12. *http://www.sciencedirect.com/science/article/pii/S003442571630195X*

Zhang, H., Beggs, H., Wang, X.H., Kiss, A.E., and Griffin, C. (2016b). Seasonal patterns of SST diurnal variation over the Tropical Warm Pool region, *Journal of Geophysical Research: Oceans*, 121. doi:10.1002/2016JC012210. *http://onlinelibrary.wiley.com/doi/10.1002/2016JC012210/epdf*

Zhang H., Beggs, H., Wang, X.H., Rodriguez, J., Thorpe, A.L., Brunke, M., Majewski, L., Kiss, A.E., and Gentemann, C. (2018). Comparison of SST Diurnal Variation Models over the Tropical Warm Pool, *Journal of Geophysical Research: Oceans*, 123. *http://dx.doi.org/10.1029/2017JC013517*

Zhang, H., Babanin, A.V., Ignatov, A., and Beggs, H. (2019). *On the differences between daytime and nighttime ocean cool skin signals under well mixed conditions. GHRSST poster, University of Melbourne.* *http://adf5c324e923ecfe4e0a-6a79b2e2bae065313f2de67bbbf078a3.r67.cf1.rackcdn.com/GHRSST%20XX%20-%202019%20Frascati%20-%20Italy/59-Zang_haifeng_GHRSST.pdf*

Zhong, A., and Beggs, H. (2008). *Analysis and Prediction Operations Bulletin No. 77—Operational Implementation of Global Australian Multi-Sensor Sea Surface Temperature Analysis*, Web Document, 2 October 2008. *http://www.bom.gov.au/australia/charts/bulletins/apob77.pdf*



15 Ice

Rob Massom

It is estimated that at least 10% of the Earth's surface is covered in glacial ice, 90% of which is in Antarctica (USGS, 2021). As part of the water cycle, ice caps, glaciers, and permanent snow store 1.7% of the total volume of water on Earth (see Section 1.1).

The following sub-sections describe ice in Australian surface waters (see Section 15.1), relevant EO sensors for mapping and monitoring ice (see Section 15.2), EO of the Antarctic Ice Sheet (see Section 15.3), EO of sea ice (see Section 15.4), and future opportunities and needs in this area (see Section 15.5).

15.1 Ice in Australian Surface Waters

Although geographically isolated by the circumpolar Southern Ocean, Antarctica is connected to the rest of the world through oceanic and atmospheric circulations, and plays a pivotal role in the global climate system (see Section 2.5). Ubiquitous features are a vast ice sheet surrounded by a seasonally-variable cover of sea ice, which together extend over an area of up to ~33 million km^2—or 6% of the Earth's surface—in winter (see Figure 15.1). By virtue of their physical setting and properties, these two immense snow and ice masses interact strongly not only with each other but also with the high-latitude ocean and atmosphere, to significantly modify and affect the ocean-atmosphere system and the processes therein. In this way, Antarctic ice-ocean-atmosphere interactions and processes affect both regional weather and patterns of oceanic and atmospheric variability across the wider Southern Hemisphere and beyond (see Section 1.4). At the same time, the Antarctic cryosphere is not only a highly sensitive indicator of climate change, which is amplified in polar regions, but it also plays an active role in modulating such change. Sea ice also forms an important habitat for a plethora of organisms, from microscopic algae through krill to whales (Thomas, 2017), and either aids or hinders marine operations and other human activities around the continent.

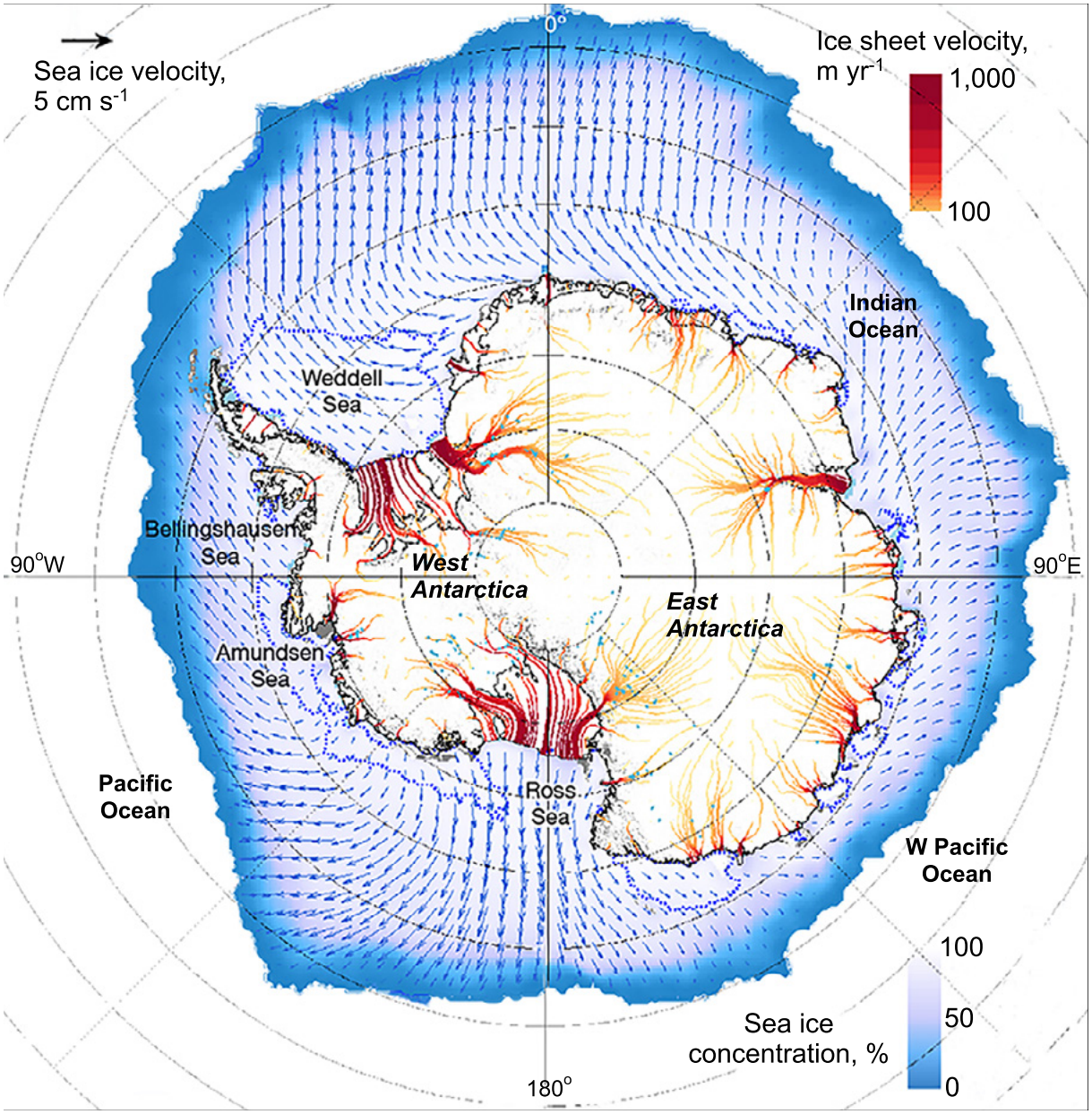
The fundamental role of the Antarctic cryosphere in the Earth system, and its sensitivity to change in the ocean and atmosphere, implies that warming in the region will have wide-ranging consequences for climate, sea level rise, ecosystems, and human activities (including shipping operations). As such, developing improved understanding of the nature, drivers, and impacts of Antarctic sea ice and ice sheet change is a high priority in climate research, leading towards more accurate model prediction of the future trajectory and effects of cryospheric change (Kennicutt *et al.*, 2014). The challenge is great, given the vast scale, remoteness, dynamism, complexity and inhospitable nature of the Antarctic environment, which is also shrouded in darkness for part of the year and extensively cloud covered. Earth Observation from Space (EOS) has a crucially important role to play here, in concert with autonomous sensors and remote sensing systems, process studies, and *in situ* observations (Lubin and Massom, 2006; Massom and Lubin, 2006). The latter provide important additional information that cannot be obtained by EO alone, and are also a crucial means of calibrating and validating key satellite-derived quantities. Timely sea ice and iceberg information is also required in near real time from EO in support of safe shipping and operational activities around Antarctica (COMNAP, 2015; WMO, 2021).

Background image: RS53617 Jade Iceberg near Macey Island. The top of this iceberg is estimated to be around 30 m above ground level. Source: © Peter Layt, Australian Antarctic Division.

Recommended Chapter Citation: Massom, R.A. (2021). Ice. Ch 15 in *Earth Observation: Data, Processing and Applications. Volume 3B—Surface Waters.* CRCSI, Melbourne. pp. 281–310. ISBN 978-0-6482278-5-4.

Figure 15.1 Satellite-derived map of the Antarctic Ice Sheet and surrounding sea ice

Grounded ice sheet and ice shelf motion are derived from multiple satellite interferometric Synthetic Aperture Radar (SAR) images (Rignot *et al.,* 2011) acquired between 2007 and 2009. Ice sheet motion flow lines are superimposed on the MODIS mosaic of Antarctica (Haran *et al.,* 2014). Sea ice motion is the mean of daily gridded Polar Pathfinder radiometry (Tschudi *et al.,* 2016) obtained during winter maximum sea ice extent (September) of each year for the period 1990 to 2016. The motion vectors are superimposed on a map of mean sea ice concentration and extent derived from passive microwave brightness temperatures (Fetterer *et al.,* 2017) for the Septembers of 1990 to 2016. Also shown are the average minimum extent of sea ice recorded between 1990 to 2016 (blue dashed boundaries), the grounded ice sheet and the floating ice shelves (black boundaries), and the bathymetry of the surrounding ocean (Ryan *et al.,* 2009).



Adapted from Shepherd *et al.* (2018). Figure 1

In the following subsection, we provide a brief description of aspects of the Antarctic Ice Sheet and its surrounding sea ice cover that are relevant to, and measurable by, EO. The importance of EO for mapping and monitoring sea ice is highlighted in Excursus 15.1. Detailed information on the geographical setting of Antarctica and high-latitude Southern Ocean, including seafloor bathymetry and large scale ocean current patterns and fronts, is provided by Post *et al.* (2014). For further information on sea ice, see ACE CRC (2014), Thomas (2017) and Weeks (2010), and see ACE CRC (2017) for ice sheet issues. Annual assessments of change/variability in Antarctic sea ice coverage and duration are provided in annual NOAA BAMS State of the Climate Reports (*https://www.ncei.noaa.gov/bams-state-of-climate*). For further information on the relationship of sea ice and oceanography in the Southern Ocean, see Meredith and Brandon (2016).

15.1.1 Antarctic Ice Sheet

Formed from the accumulation and compaction of snowfall over many thousands of years, the Antarctic Ice Sheet covers nearly 14 million km^2 (or > 99%) of the Antarctic continent; this is twice the size of Australia. Of this, the Australian Antarctic Territory comprises the sector between 45°E and 160°E (excluding 136°E–142°E). The ice sheet is more than 4 km thick in places (mean thickness 2.16 km, maximum thickness 4.776 km) and has an average elevation of 2.5 km. Crucially, it holds ~70% of the Earth's freshwater and more than 90% (approximately 26.9 million km^3) of its ice (Fretwell *et al.*, 2013). If melted, this is enough water to raise mean global sea level by nearly 60 m.

The ice sheet is in fact made up of three major components: the East and West Antarctic ice sheets and the Antarctic Peninsula. The distinct differences between the East Antarctic Ice Sheet (EAIS) and the West Antarctic Ice Sheet (WAIS) are depicted in Figure 15.2. The EAIS contains about nine times the ice volume of the WAIS, and is significantly thicker and higher. Moreover, the WAIS largely sits on bedrock up to 2,500 m below sea level in places, and is termed a marine ice sheet. Ice sheet regions that sit resting on bedrock below sea level are thought to be less stable than those that are grounded above sea level, and are therefore more susceptible to climate change. Dynamic instability in the ice sheet response to global warming is potentially the largest unknown in projecting future sea level rise (SLR; Kennicutt *et al.*, 2014).

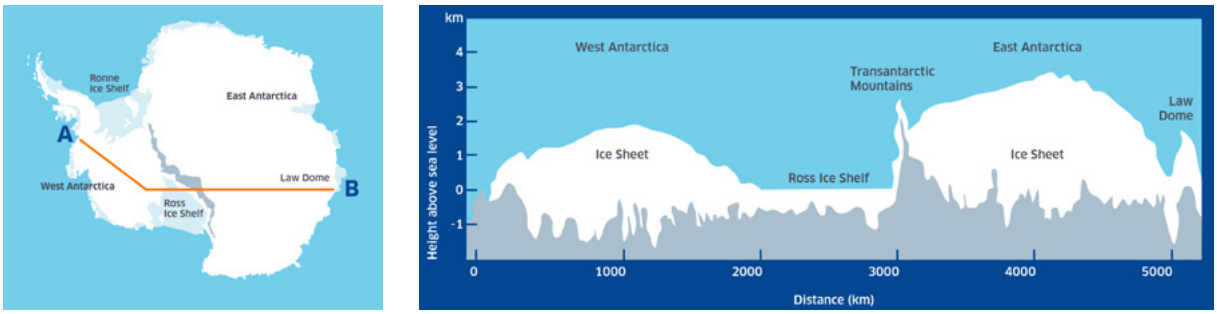
Gravity-driven discharge of ice from the inland ice sheet across the boundary between the grounded and freely-floating parts of the ice sheet (termed the grounding line) and into the Southern Ocean occurs mainly via about 30 major glaciers and ice streams, which each drain extensive catchment regions (Zwally *et al.*, 2012). The rate of ice discharge is determined not only by the ice thickness, surface slope, temperature, basal topography and conditions (Cuffey and Patterson, 2010), but is also affected by the presence of floating glacier tongues and ice shelves that abut 74% (or 39,670 km) of the grounded ice sheet boundary (Bindschadler *et al.*, 2011). As floating seaward extensions of fast-flowing outlet glaciers and ice streams, ice shelves play a crucially important role in buttressing (restraining) the dynamic discharge of grounded ice mass into the ocean—to moderate the ice sheet contribution to SLR (see Figure 15.3).

Figure 15.2 Plan view and cross section profiles across Antarctica

These cross sections show the differences between the West Antarctic Ice Sheet (WAIS) and the East Antarctic Ice Sheet (EAIS).

a. Plan view of the continent from A to B

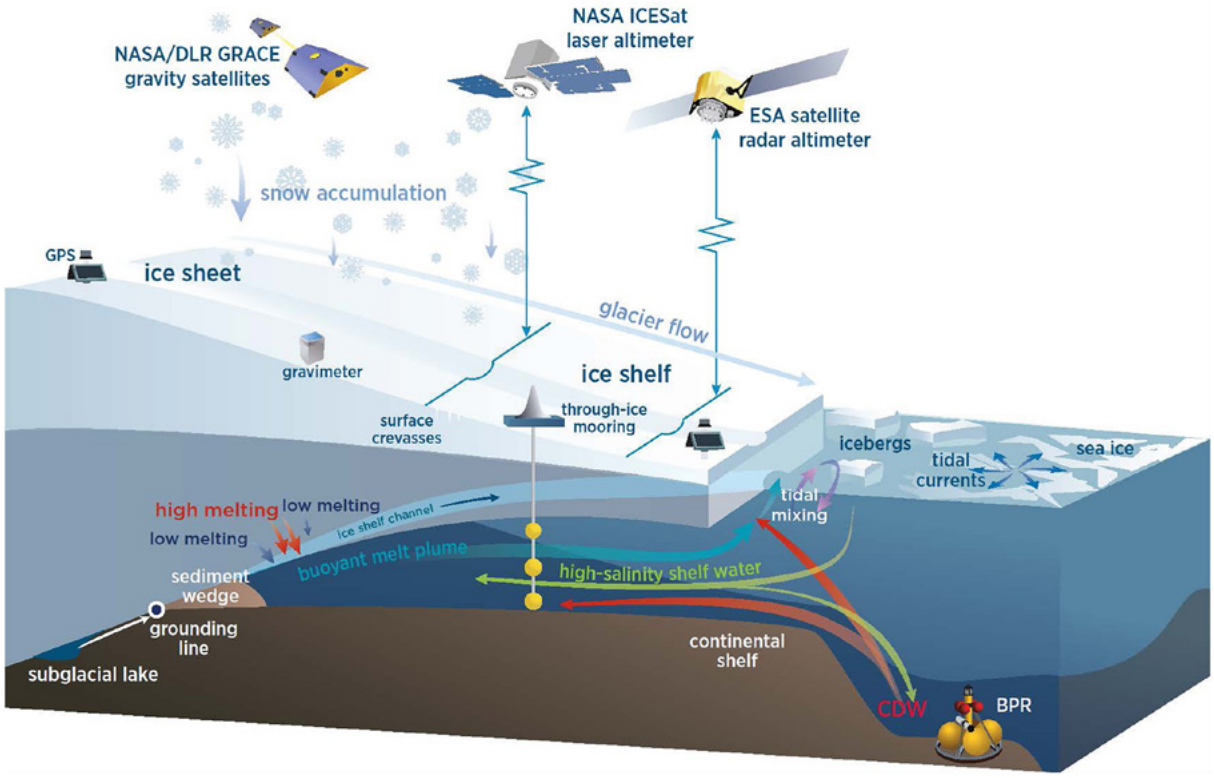
b. Cross section through the continent from A to B



Source: British Antarctic Survey

Figure 15.3 Schematic of an Antarctic ice shelf

The mass budget for an ice shelf is the sum of (i) gains (inputs) from glacier flow across the grounding line and snow accumulation and (ii) losses/outputs by iceberg production and net basal and surface melting.



Source: Padman *et al.* (2018) Figure 3

Given their direct contact with the (warming) atmosphere and ocean, ice shelves are the most vulnerable part of the ice sheet system (ACE CRC, 2017), with EOS showing recent extensive thinning due to basal melting by a warming ocean[18] and (in certain regions) abrupt melt-related, large scale disintegration (see Section 15.3.1). The thinning, weakening, or loss of ice shelves diminishes/removes their buttressing capacity, leading to increased flow of grounded ice into the ocean to contribute to SLR. Clearly this is of great concern, and monitoring the rate of dynamic ice discharge and the 'health' of Antarctic ice shelves—and how, where, and why/whether they are changing—is a high priority in EO. Moreover, increased freshwater input to the Southern Ocean from glacial and iceberg melt has potentially important consequences for ocean stratification properties and circulation, as well as marine ecosystems (Kennicutt *et al.*, 2014).

EOS has a crucial role to play in the measurement and monitoring of the *mass balance* of the ice sheet (Bamber and Payne, 2004), and determination of:

- where, how and why this is changing; and
- its contribution to SLR (in concert with modelling and *in situ* observation).

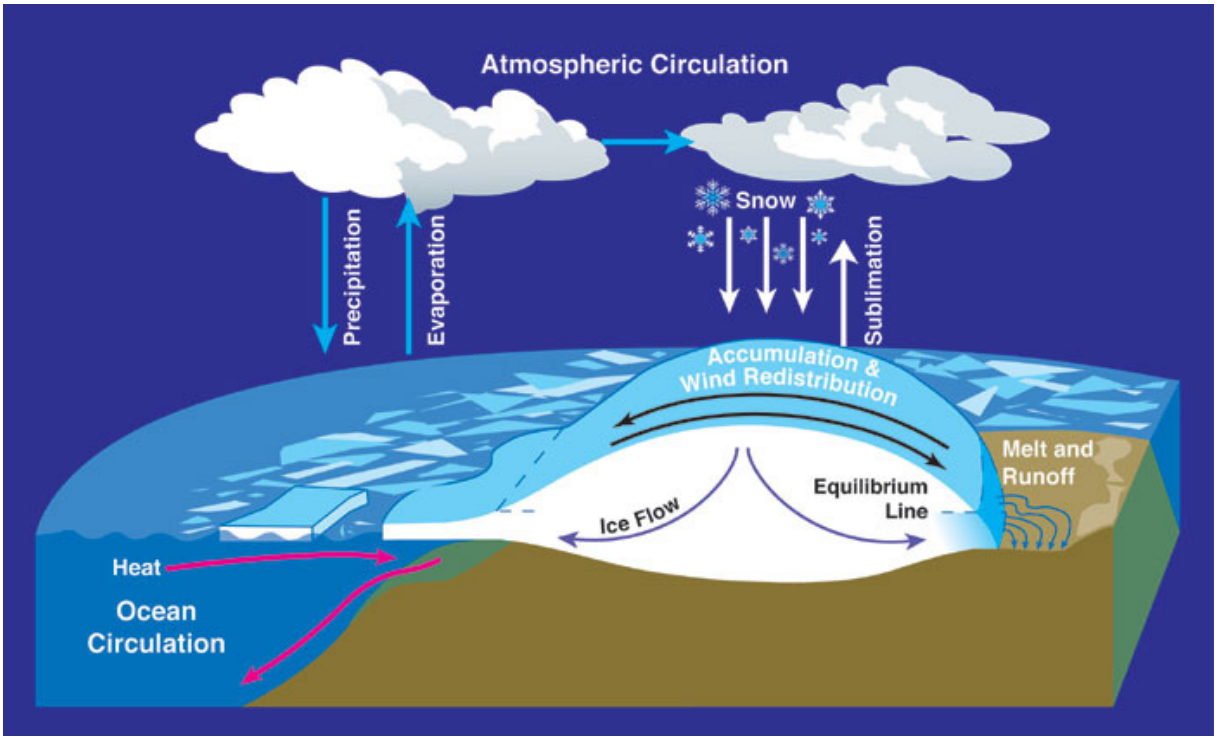
Ice sheet mass balance describes the relationship between:

- total mass gain by snow accumulation; and
- mass loss by a combination of ablation (evaporation), surface melting, basal melting (largely through contact with the ocean), ice discharge, and iceberg calving (Figure 15.4).

The acquisition of regular and reliable repeat measurements of key ice sheet features and properties—and understanding the processes driving observed change—is critical to improving ice sheet models used for the prediction of future ice loss and subsequent SLR (ACE CRC, 2017).

18 Melting of an ice shelf base occurs when water in contact with it is warmer than the freezing point. The freezing point of seawater decreases with water depth, from about -1.9°C at the surface of the ocean to about -4°C at a water depth of 2500 m. As a result, water that is relatively warm, e.g. -0.5°C, will result in strong basal melting of an ice shelf.

Figure 15.4 Schematic of an ice sheet and its individual mass balance components



Source: Abdalati (2006) Figure 1. Retrieved from *https://upload.wikimedia.org/wikipedia/commons/a/a2/Mass_balance_atmospheric_circulation.png*

15.1.2 Antarctic sea ice

In contrast to the ice sheet, its floating margins and icebergs, sea ice is frozen seawater that forms when the ocean cools to the point of freezing (approximately -1.8°C for water with a salinity of 34 psu). From a summer minimum of 3–4 million km^2 (in February), Antarctic sea ice coverage expands to about 19–20 million km^2 at its maximum annual extent in September (about 1.5 times the size of the Antarctic continent itself; see Figure 15.5). This annual advance-retreat cycle—in response to large scale climatological patterns of atmospheric and oceanic temperature and circulation—entails one the greatest seasonal changes on Earth. Crucially, it also substantially modifies the surface properties of the high-latitude Southern Ocean, and its interaction with the overlying atmosphere (see Excursus 15.1 below). At its winter maximum, the latitudinal width of the sea ice zone varies substantially around the continent, from only a few hundred kilometres (such as off East Antarctica at 120°E to 135°E) to ~2200 km in the Weddell Sea sector (where it occupies a deep poleward embayment).

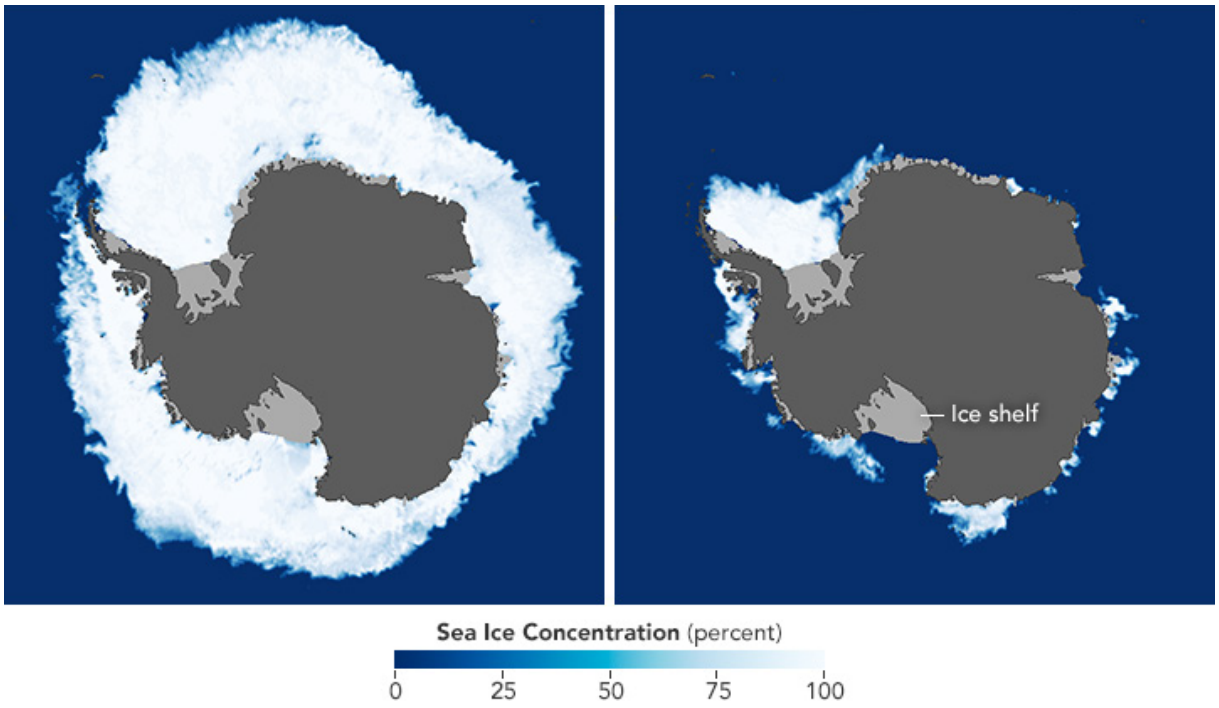
Broadly speaking, sea ice is made up of two main components: 1) ***pack ice***, and 2) the less extensive coastal ***landfast*** or ***fast ice*** (see Figure 15.6). Pack ice comprises a heterogeneous agglomeration of different contiguous pieces of ice (termed ***floes***) of varying age, thickness, and size (sub-metre to kilometre scale) that are constantly moving (up to tens of kilometres a day) in response to winds and ocean currents. Most Antarctic pack ice is seasonal and therefore less than one year old—so-called ***first-year ice***. This type of ice has a thickness range of 0.3–2.0 m (typically), although greater thicknesses (of ~10 m) can occur by ice deformation where ice floes collide (Massom *et al.*, 2006). Perennial sea ice (ice that survives one or more summer melt seasons) is generally thicker than typical first-year ice, but is largely confined to southernmost parts of the Weddell, Amundsen, and eastern Ross seas (see Figure 15.5). The remainder that forms and melts back each year is termed the ***seasonal sea ice zone.***

Figure 15.5 Extent of Antarctic sea ice in 2015/2016

Each year, and on average, Antarctic sea ice coverage peaks in September–October, and attains a minimum in February, when it melts completely back to the continent in places.

a. 2015 maximum (October 6)

b. 2016 minimum (19 February)



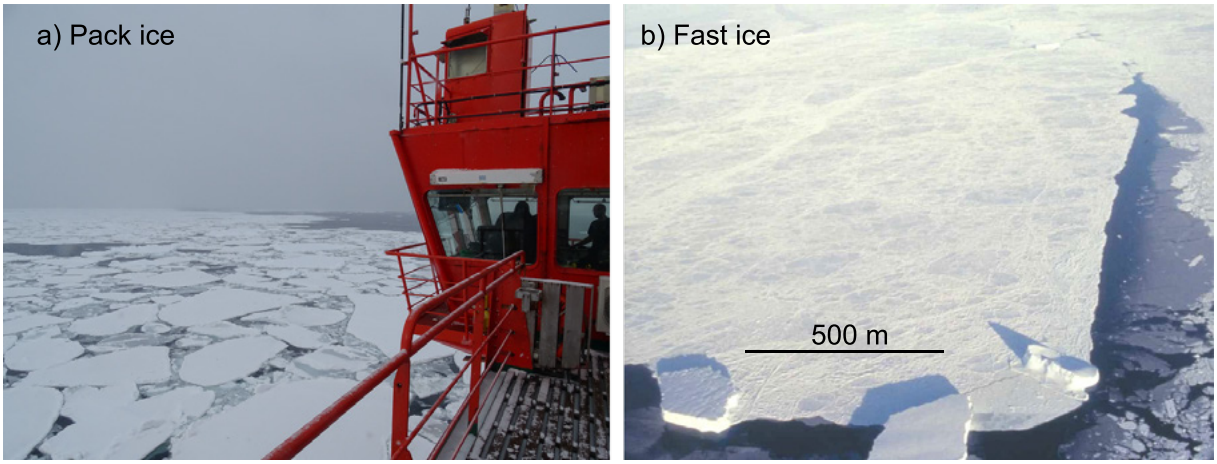
Source: NASA Earth Observatory, based on AMSR2 data supplied by GCOM-W1/JAXA. Retrieved from: *https://earthobservatory.nasa.gov/features/SeaIce/page1.php*

In contrast to pack ice, fast ice is highly-consolidated and stationary sea ice, which is confined to coastal margins, where it is either held in place by myriad grounded icebergs (in waters shallower than about 450 m) and/or by coastal promontories, or occurs in sheltered embayments (Giles *et al.,* 2008a). There, it forms a relatively narrow band from a few kilometres to about 250 km wide in places (Fraser *et al.,* 2012), but plays a key ecological role (Massom *et al.,* 2009) as well as stabilizing ice shelf margins to which it is attached (Massom *et al.,* 2018). Depending on the geographical setting, Antarctic fast ice can be either annual or perennial, and can attain great ages (decades) and thicknesses (of > 10 m) in certain sheltered locations (Massom *et al.,* 2010).

The areal extent of sea ice coverage, its thickness distribution, and patterns of annual advance, retreat, and duration (and their variability) are the product of a complex interplay of both thermodynamic and dynamic processes—the former involving freeze and melt, and the latter involving movement and deformation of the ice driven by winds and ocean currents and interaction with the ice sheet margins and icebergs. At any given time, this complex interplay of processes and the frequent passage of storms creates a highly heterogeneous mixture of ice of different types, ages, and thicknesses. On larger scales, however, the Antarctic sea ice zone is characterised by distinctive large scale components (Massom and Stammerjohn, 2010). The outer part of the pack, called the ***marginal ice zone*** or MIZ, comes into direct contact with the open, high-energy Southern Ocean and is strongly affected by ocean waves that not only generate new ice formation but also break up existing floes. To the south, the more stable mid-pack ice zone (protected by the MIZ) is generally characterised by larger floes and thicker snow cover, but is still affected by a constant passage of storms. Closer to the continent itself, sea ice conditions are strongly affected by interaction with ice sheet margins and grounded icebergs; this is also the realm of fast ice attached to the coast. In the coastal zone, recurrent polynyas (persistent areas of open water bounded by sea ice) play a crucial role as sea ice 'factories' in the freezing season and areas of enhanced melt and biological activity in spring-summer (Barber and Massom, 2007). Polynyas form in the lee of blocking features, such as coastal promontories, and are also maintained by strong katabatic winds cascading seawards from the ice sheet interior.

Figure 15.6 Photographs of Antarctic pack ice and fast ice

Fast ice formation is often associated with grounded icebergs, as shown here.



At the microscale and unlike the freshwater ice sheet, sea ice comprises a heterogeneous matrix of ice with small inclusions (pockets/cells) of brine (Petrich and Eicken, 2017), the characteristics of which are constantly modified by the interaction of physical, chemical, and biological processes that vary over space and time. The ice crystals themselves are either long and thin (***columnar ice*** that grows downwards under calm conditions) or more granular (***frazil ice*** that forms under turbulent conditions); a mix of both is typical for Antarctic sea ice. Sea ice older than a few days also accumulates a snow cover, which acts as an insulative and high-albedo blanket to substantially modify the temperature, thermodynamic growth, and properties of the underlying sea ice (Sturm and Massom, 2017). Snow also strongly modifies the amount and spectral properties of light available for phytoplankton growth within and under the ice (Wongpan *et al*., 2018). Moreover, snow makes an important (though poorly quantified) direct contribution to the overall mass balance of the Antarctic sea ice cover by depressing relatively thin sea ice below sea level. This leads to extensive surface flooding to create slush, which subsequently freezes (depending on season) to form *snow ice* (Massom *et al*., 2001a). The introduction of seawater onto the ice further affects its EO signature, particularly at microwave wavelengths. The wetness, crystal structure, and density of the snow cover change/vary in space and time, to also modify sea ice as an EO target (both in terms of optical and microwave properties), and the retrieval of sea ice thickness estimates from altimeter data (see Section 15.4.4).

Sea ice type is classified (named) and categorised depending on its thickness (related to age/stage of development), and based on established international protocol (see *http://aspect.antarctica.gov.au/home/glossary-and-image-library* for a glossary and image library of sea ice types and terms). Excursus 15.1 summarises the key role of various types of EO for measuring and monitoring Antarctic sea ice.

Excursus 15.1—The Importance of EO for Sea Ice

Source: Rob Massom, Australian Antarctic Division/Australian Antarctic Program Partnership
Further Information: Notz and Bitz (2016); Weeks (2010)

Measuring and monitoring Antarctic sea ice and its snow cover—and determining the nature, drivers and effects of change—are crucially important for a number of reasons, and are key steps towards improved (model) prediction of the likely trajectory and impacts of sea ice change in a future warming world (see Notz and Bitz, 2016, for further information). Sea ice forms a pivotal component of the global climate system and strongly modifies ocean-atmosphere interaction over vast areas of the Southern Ocean (as well as in the Arctic). It significantly increases the ocean-surface albedo—to reduce the amount of incoming solar radiation absorbed at the ocean surface—and also insulates the polar ocean from heat loss to the atmosphere during winter (by up to two orders of magnitude; see

Weeks, 2010, for further information) and heat gain during summer. At the same time, sea ice forms a physical barrier to the atmosphere-ocean exchange of wind energy and climate gases such as water vapour and CO_2. Also, brine (dense salty water) rejected downwards by growing sea ice modifies the ocean density structure, and in places induces deep vertical convection and dense cold Antarctic Bottom Water formation that contributes to global ocean thermohaline (overturning) circulation (see Sections 1.4, 5.1.2, and 16). In this way, the influence of Antarctic sea ice reaches the tropics and the Northern Hemisphere as well as the ocean abyss (Bindoff *et al.,* 2000). Due to its intimate association with the ocean and atmosphere, sea ice is not only a sensitive indicator but also a modulator of climate change and variability—the latter by virtue of its key role within the coupled sea ice/ocean/atmosphere system and due to the ice-albedo feedback mechanism.

Sea ice also dominates the seasonal chemical dynamics of the high-latitude Southern Ocean (Vancoppenolle *et al.*, 2013), and plays a crucial role in marine ecosystem structure and function as a key habitat and food source for a wide range of biota, including krill (Massom and Stammerjohn, 2010; Thomas, 2017). Such is the high biological productivity of the Antarctic seasonal sea ice zone that it also plays an important role in the carbon cycle (see Section 1.5). When the ice melts in spring-summer, it injects a pulse of fresher water that stratifies and stabilises the upper ocean and drives intense blooms of algae following their release from the ice. Such blooms are measured by satellite ocean colour sensors (see Sections 8.5 and 18). From a human perspective, sea ice strongly affects safe shipping, tourism, and other operations in high-latitude Southern Ocean waters, including access to resupply of Australian Antarctic bases, and EOS has a key role in informing such operations in a timely fashion.

In general, the influence of sea ice and the magnitude of its effects depend on a number of fundamentally important characteristics (quantities/variables) that can be measured and monitored from space, and their interrelationships and spatiotemporal characteristics. These are:

- **Concentration**—the percentage coverage of sea ice versus ice-free ocean within a given surface area.
- **Extent**—defined as the total area covered by some amount of ice (including open water between floes).
- **Area**—the part of a given area covered by ice alone (that is, the product of ice extent and concentration).
- **Seasonality**—the timings of annual sea ice advance and retreat for a given Antarctic 'sea ice year' (February to February), and the resultant duration of coverage.
- **Thickness distribution**—the fraction of surface area covered by different ice thickness categories.
- **Thickness and properties of snow cover**—sea ice older than a few days typically accumulates a snow cover. This significantly modifies the physical and chemical properties of the underlying ice, and also affects its growth and melt rates, and its climatic and ecological roles (see Sturm and Massom (2017) for further information). Unfortunately, large scale mapping of snow thickness is not currently possible by satellite, although it can be derived from airborne snow radar (for example, the NASA Ice Bridge Project (Kurtz *et al.,* 2012; see Section 15.6). Issues related to snow in the sea ice system, including the lack of accurate information on precipitation, are outlined by Webster *et al.* (2018).
- **Drift** (movement over space and time), and **dynamics** (including deformation)—principal forces acting on the ice are wind (ice moves at 2% of the wind speed when drifting freely and to the left of the wind direction in the Southern Hemisphere; see Figure 1.10), ocean currents (see Section 17), Coriolis force (see Excursus 1.2), and internal ice stress (involving floe-floe collisions and interaction of the sea ice with the ice sheet margins and icebergs; see Section 1). Divergence of the ice motion field creates ephemeral linear openings (*leads*) that rapidly freeze over in winter, while convergence causes the existing ice to deform and thicken. Around Antarctica, these patterns are cyclical on typical scales of 1–3 days with the constant passage of storms, and dynamic thickening predominates once sea ice grows thermodynamically to ~0.5 m (Worby *et al.,* 1998). Sea ice drift also transports sea ice from regions of formation to regions of melt, to significantly affect the ocean freshwater budget and ocean stratification.

15.2 EO Sensors for Ice

Important EO sensors relevant to ice sheet and sea ice measurement and monitoring (either individually or in combination) are listed in Table 15.1. These include visible through near infrared (NIR) to thermal infrared (TIR) radiometers, Synthetic Aperture Radar (SAR), passive microwave radiometers, radar scatterometers, radar and laser altimeters, and gravity sensors (see Sections 8.5 and 9, also Volume 1A—Sections 14 to 16, and Excursus 1.1). For more information, see Lubin and Massom (2006) and Massom and Lubin (2006).

Table 15.1 EO sensors relevant to ice

TIR: Thermal infrared; SAR: Synthetic Aperture Radar

Type	Sensor	Platform	Relevance	Advantages	Disadvantages
Passive optical	Panchromatic, Multispectral, and Hyperspectral radiometers	Satellite or airborne	Mapping/monitoring of ice sheet margin, glacier surface, iceberg calving events, surface melt, snow surface grain size, Ice sheet surface velocity, Estimating thin sea ice thickness (e.g. coastal polynyas), Sea ice floe size distribution (from high spatial resolution datasets), Sea ice extent (both pack ice and fast ice), Surface albedo, Ocean colour (primary production adjacent to/within the sea ice zone), Iceberg distribution (high resolution)	Time series datasets	Does not penetrate cloud, requires sunlight, sensors with high spatial resolution have limited coverage
	TIR radiometer	Satellite or airborne	Mapping of ice surface 'skin' temperature, and adjacent SST, Detection of thin sea ice and estimation of its thickness, Sea ice extent	Does not require sunlight	Does not penetrate cloud
Active optical	Laser altimeter	Airborne or satellite	Measuring and mapping ice sheet topography, surface roughness and elevation, and monitoring elevation change, Measuring and monitoring sea ice thickness (ice plus snow) and ice surface roughness (also scanning laser), Mapping of ice sheet surface velocity and subsurface structure	Does not require sunlight, higher spatial resolution and accuracy (potentially) than radar altimetry	Does not penetrate cloud
Passive microwave	Passive microwave radiometer	Satellite	Large scale detecting, mapping, and monitoring surface melt on ice sheets, Monitoring extent, concentration, and drift of sea ice, Mapping of polynyas (and estimation of sea-ice production rates—see Tamura *et al.*, 2016)	All weather, long time series, daily circum-Antarctic coverage	Low spatial resolution
Active microwave	SAR	Satellite	High resolution mapping of subsurface structure of ice sheet and glaciers, and surface melt on ice sheets, Grounding line detection and monitoring (SAR interferometry), Detection and tracking of icebergs, Crevasse detection and sea ice surface roughness, Measuring surface velocity of glaciers and ice streams, Sea ice velocity and dynamics, Waves in sea ice, Sea ice type classification	All weather, penetrates snow cover, does not require sunlight, high spatial resolution, reasonably long time series	Relatively poor coverage (relatively narrow swath width), data coverage and availability
	Radar altimeter	Satellite	Measuring and mapping ice sheet surface topography and elevation (change), Monitoring sea ice thickness	All weather, does not require sunlight, time series datasets	Generally less accurate than laser altimetry in steeper ice sheet margins, penetrates the surface
	Scatterometer	Satellite	Large scale mapping of sea ice, snow accumulation, and surface melt on ice sheets, Sea ice velocity, Large scale sea ice type classification, Detection and tracking of large icebergs	More detailed spectral data than imaging radar	Lower spatial resolution than imaging radar
Gravity	GRACE mission	Satellite	Monitoring changes in mass balance of ice sheets	Global coverage	Low spatial resolution

Repeat coverage (ideally regular and systematic) by polar orbiting satellites is invaluable for measuring key ice sheet and sea ice parameters over vast remote regions and in detecting and monitoring change/variability. Important environmental factors affecting the use of optical sensors for EO of the polar ice environment are persistent cloud cover year-round and polar darkness in winter. TIR sensors can 'penetrate' polar darkness but not cloud. Active and passive microwave sensors are crucially important tools for penetrating both polar cloud and darkness. The choice of sensor/combination of sensors for a given application depends on the requisite spatial and temporal (as well as spectral and radiometric) resolutions, amongst other things, taking into account inherent tradeoffs that exist between the various satellite sensor classes (see Volume 1). Airborne, under-ice, and on-ice sensors (see Excursus 5.1) provide important high resolution measurements in key areas of interest, and are also crucial to the calibration and validation of satellite data products. They acquire important measurements at scales intermediate between detailed *in situ* (surface) observations and satellite EO (Newman *et al*., 2019).

Below, we provide a brief summary of the main principles, techniques, and applications of EO relating to first the ice sheet and icebergs (see Section 15.3), then sea ice (see Section 15.4). For more detailed information, refer to Lubin and Massom (2006), Massom and Lubin (2006), Massom (2006; 2009), and Spreen and Kern (2016).

15.3 EO of the Antarctic Ice Sheet

Satellite (in tandem with airborne) EO is crucial for observing, studying, and monitoring ice sheet physical properties and dynamical behaviour, and for extending key *in situ* observations in space and time. Underwater observations (see Excursus 5.1) are also crucial, for example, for determining ocean and ice conditions, properties, and interactive processes under floating ice sheet margins such as ice shelves. Here, we provide a brief assessment of fundamental ice sheet quantities measured by EO.

15.3.1 Ice sheet surface morphology and areal change

Since the 1970s, high resolution imaging using visible through TIR wavelengths acquired by spaceborne sensors (for example, Landsat, SPOT, and ASTER) has been extensively used for fine (decametre) scale mapping and monitoring of the ice sheet margin and glacier surface morphology and features such as surface crevasse patterns (Swithinbank, 1988). Important subtle features not detectable on the ground can be distinguished in such imagery when suitably processed and enhanced. Operating at a resolution of hundreds of metres to kilometre scale, modern wider swath, moderate resolution multispectral radiometers (for example, MODIS and VIIRS) offer more extensive coverage at high radiometric resolution, to reveal an immense amount of surface detail in aid of glaciological research. This includes crevasse propagation over time. Such imagery, when cloud-free, has been composited to produce digital image maps of both the entire ice sheet surface and ice shelves and their surface properties, such as snow surface grain size (Scambos *et al.,* 2007). These again provide a wealth of glaciological information as shown in Figure 15.7 (here at 150 m resolution). 'Mosaic of Antarctica' (MOA) maps and vector datasets with the corresponding coastlines, ice sheet grounding lines, and islands are available from the US National Snow and Ice Data Center (NSIDC; see Section 15.6).

The coastal ice sheet margins of Antarctica are highly dynamic and changeable due to glacier advance and retreat via the calving of icebergs from glacier fronts and ice shelves. Such changes are revealed in time series of cloud-free, moderate resolution NOAA AVHRR and MODIS images of Antarctic ice shelves, which are also available from NSIDC (see Section 15.6). This imagery is readily (routinely) available in near real time, enabling scientists to detect major iceberg calving events as and when they occur. Notable discoveries include the extraordinary rapid disintegration of the Larsen B Ice Shelf in early 2002 to form a plume of thousands of icebergs[19]. So far, ice shelf retreat and collapse has been restricted to the Antarctic Peninsula, where significant regional warming has occurred.

19 For animation, see *https://earthobservatory.nasa.gov/world-of-change/LarsenB*

Satellite SAR is a particularly powerful tool in polar research and operations. It complements optical and TIR sensors by providing high resolution observations of microwave radar backscatter unaffected by cloud and darkness (see Section 9.3 and Volume 1A—Section 15). Selected SAR wavelengths can penetrate metres into the upper snow/firn layer (when dry), to provide additional information on crevasse patterns and upper ice sheet and glacier structure (see Figure 9.3). Multiple, wide swath SAR images acquired during the 1997 RADARSAT-1 Antarctic Mapping Project (RAMP) have been compiled into a high resolution radar mosaic of the southern continent (see Section 15.6). This dataset, which clearly shows the ice sheet drainage basins and other key morphological features, has been used to map the floating ice sheet margin and detect, determine, and monitor changes therein in comparison with earlier and subsequent datasets. The RAMP map is highly complementary to the MOA maps in that it provides key information on subsurface features (given the greater penetration of the radar signal). The MOA map, on the other hand, represents surface features.

Figure 15.7 Portion of Mosaic of Antarctica (MOA) map

Part of the MOA map showing patterns of deformation and crevassing as the ice sheet flows around the stationary Steershead Ice Rise near Siple Dome in the Ross Sea Embayment.



Source: Haran *et al.* (2014). Retrieved from: *https://earthobservatory.nasa.gov/features/MOA*

15.3.2 Icebergs

Satellite EO using high to medium resolution visible to TIR imagery and/or SAR imagery is crucial to the detection of iceberg calving events and the subsequent tracking of the icebergs that calve from the many floating glacier tongues and ice shelves around Antarctica. These icebergs vary in size from tens of metres to many kilometres across, depending on the source. They are encountered all around Antarctica, where they either drift away from their calving sites in ocean currents, or become grounded on banks in waters shallower than ~450 m. Large groups of small grounded icebergs occur in certain near-coastal locations, where they strongly affect sea ice conditions up to 200–300 km offshore (Massom *et al.*, 2001b; for example see Figure 15.6b). Either individually or *en masse*, icebergs can also have an important localised to regional effects on:

- ocean properties and circulation (for example, through input of fresh meltwater);
- sea ice dynamics and the formation of coastal fast ice; and
- biological activity, including primary production (by enhancing stratification and nutrient levels in the upper ocean), while disrupting benthic communities by scouring the seafloor.

The calving and grounding of vast icebergs (tens of kilometres in size) can also have serious negative impacts on ocean primary production, the breeding success of penguins, and human access to bases, by diminishing the size of open water areas in the form of recurrent coastal polynyas (e.g. Arrigo *et al.*, 2002). Drifting icebergs can also be a major hazard to shipping, and can occur far north of the sea ice edge.

While icebergs have been studied using visible and TIR imagery, their systematic detection and tracking for both research and operational purposes necessitates use of active satellite microwave sensors. EO of the many thousands of smaller icebergs (< 1–10 km) requires high resolution SAR imagery. Typically and under cold (freezing) conditions, and by virtue of their relatively high backscatter, icebergs show up as distinctly-shaped, bright objects against an ocean or sea ice background. The breakup of icebergs at low latitudes has also been investigated using satellite laser altimeter (ICESat) data (Scambos *et al.*, 2005).

Larger (vast) icebergs are detectable and trackable in time series datasets of appropriately-processed, operational radar scatterometer data (Budge and Long, 2018). Information on the location of large Antarctic icebergs is given at the:

- US Antarctic Iceberg Tracking Database (*www.scp.byu.edu/data/iceberg*); and at the
- US Navy/NOAA National Ice Center (*https://usicecenter.gov/Products/AntarcIcebergs*).

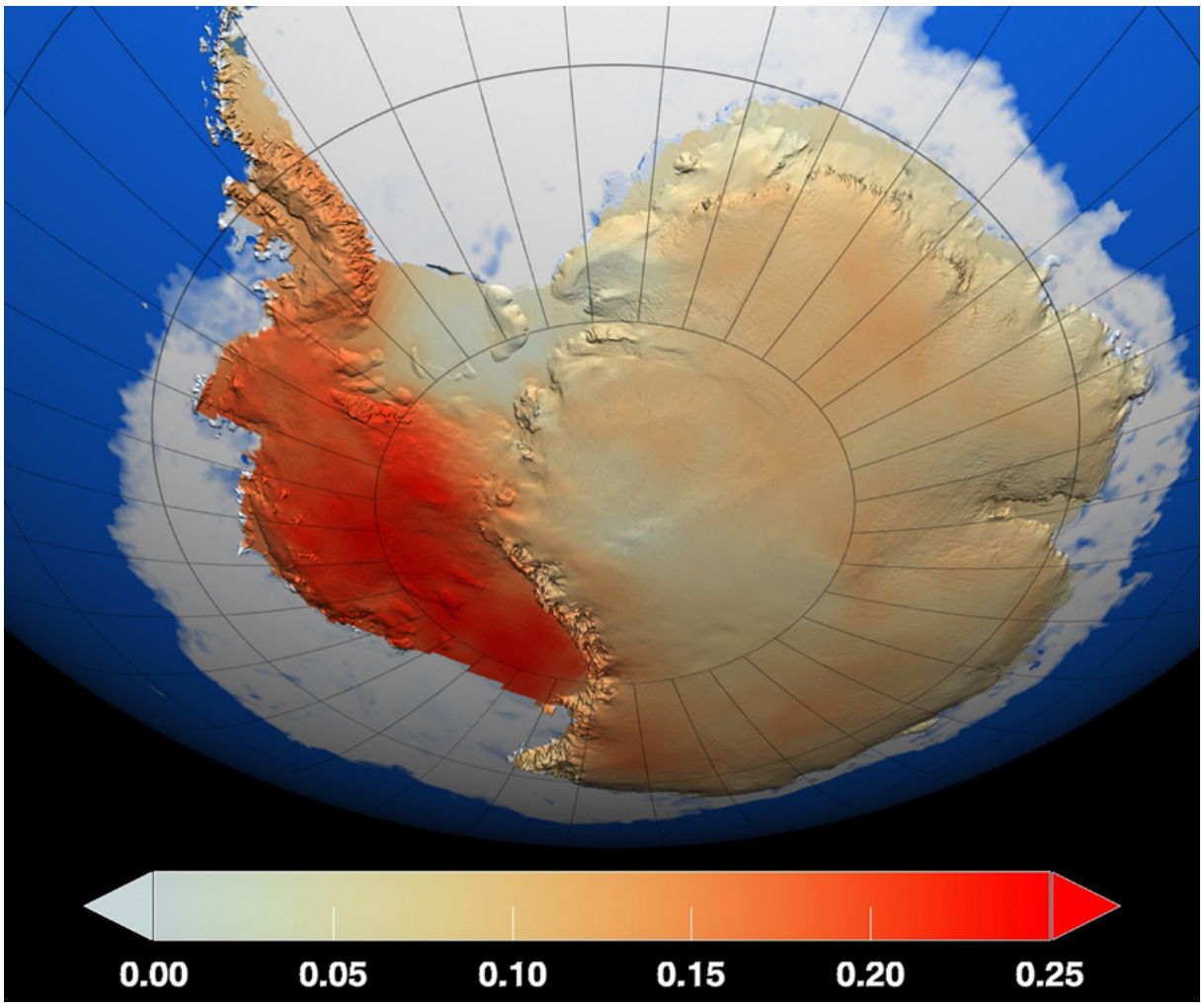
Regarding ice sheet mass balance, it has been estimated from EO that iceberg calving at present accounts for about half of the ice lost from the Antarctic Ice Sheet each year (Depoorter *et al.*, 2013). This amount (proportion) may change in future.

15.3.3 Ice surface temperature

Satellite TIR imaging is the primary tool for monitoring change in ice surface ('skin') temperature (Ts) over large remote regions (see Figure 15.8)—provided cloud cover is not inhibitive and/or can be accurately detected and masked (see Section 14). Cloud masking in EO imagery is typically achieved using multispectral techniques based on differentiating the optical and thermal properties of clouds from a snow/ice background. This is crucial as cloud cover can significantly reduce areal coverage of the surface in daily images. For this reason, large scale maps of Ts are typically composites of cloud-free areas using multiple images acquired over several weeks to months (see Volume 2D). Details of the standard Ts algorithms for the current VIIRS sensor are given in Key *et al.* (2013).

Figure 15.8 Warming trend of Antarctica from 1957 through 2006

Map showing the continent-wide warming trend of Antarctica from 1957 through 2006 (temperature change per decade in °C), based on analysis of cloud-free satellite TIR imagery and weather station data. The underlying (ice sheet) surface colour is based on the Landsat Image Mosaic of Antarctica (LIMA) dataset (*lima.usgs.gov*), while the topography is from a Radarsat-1 SAR-based digital elevation model (*https://nsidc.org/data/NSIDC-0103/versions/2/print*). Sea ice extent in the Southern Ocean surrounding the continent is based on data from the Advanced Microwave Scanning Radiometer for EOS (AMSR-E) acquired on 14 May, 2008 (late austral autumn).



Adapted from: Steig *et al.* (2009). Retrieved from *https://earthobservatory.nasa.gov/images/36736/antarctic-warming-trends*

15.3.4 Surface melt

Closely related to ice sheet surface temperature is surface melt. Melting not only reduces the ice sheet mass, but may in certain areas accelerate ice flow (by meltwater percolating downwards to lubricate the ice sheet base). Pressure from percolating surface meltwater can also enlarge crevasses by a process known as hydrofracture, to reduce ice shelf mechanical integrity (Scambos *et al.,* 2003). Extensive surface ponding was detected and mapped on the Larsen B Ice Shelf prior to its disintegration in 2002 using 250 m resolution MODIS optical imagery. In other regions, meltwater flows across ice shelf surfaces in river systems which drain into the sea (Bell *et al.,* 2017), to locally affect ocean properties (the magnitude of this effect is currently not known). Ocean freshening from increased ice sheet melt may also lead to enhanced sea ice formation, by increasing stratification of the upper ocean and decreasing upward heat entrainment (Bintanja *et al.,* 2013). For these reasons, it is important to not only detect but also monitor surface melt, to determine whether it is changing. Estimation of the magnitude of melt requires coincident surface observations.

Satellite passive microwave radiometry is the primary tool for detecting, mapping, and monitoring the areal extent of large scale (ice sheet-wide) surface melt, its timings of onset and cessation, and its resultant duration (Liu *et al.,* 2006). This is based on the changes in the surface microwave emission characteristics that are observed in microwave brightness temperature observations when snow melts. These date back to 1979 with SMMR then SSM/I. By this method, surface melt patterns can be observed on a daily basis. Annual assessments of Antarctica-wide seasonal melt extent, timings of melt onset and cessation, and resultant duration are provided in annual NOAA BAMS State of the Climate Reports (*https://www.ncei.noaa.gov/bams-state-of-climate*).

Higher resolution, active microwave detection and mapping of surface melt at large scale is also possible using satellite SAR (for example, Luckman *et al.,* 2014) and spaceborne radar scatterometry (for example, the SeaWinds scatterometer flown on QuikSCAT at 5 km resolution (1999–2009) and the MetOp ASCAT at 4.45 km resolution. Such techniques have, for example, revealed change in surface melt duration on Larsen C Ice Shelf (Bevan *et al.,* 2018).

15.3.5 Ice sheet velocity

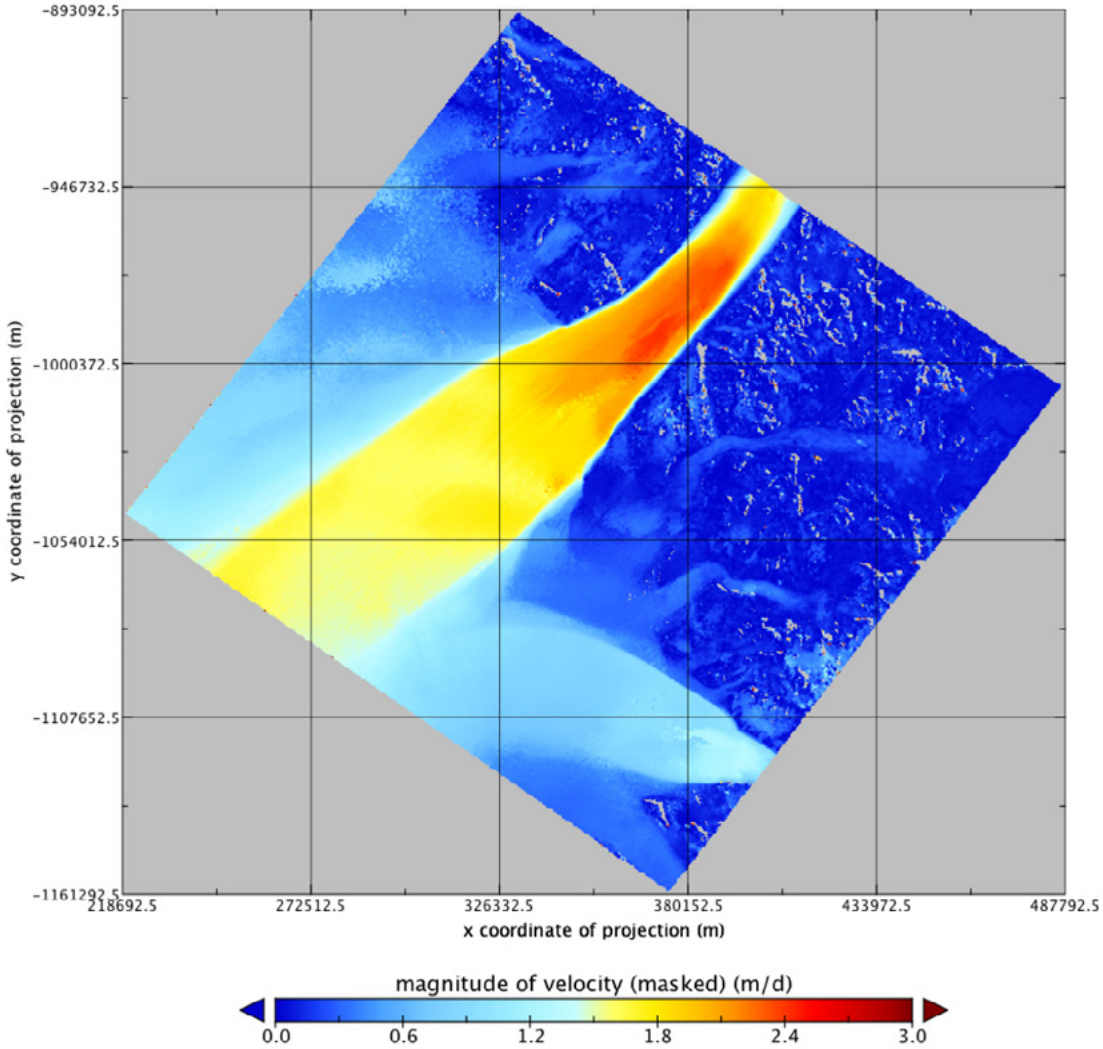
Two main methods are used to measure the surface velocity of Antarctica's glaciers and ice streams. The first involves the tracking (by maximum cross-correlation) of surface features in repeat-pass and high resolution optical imagery (e.g. Scambos *et al.,* 1992) and SAR imagery (e.g. Giles *et al.,* 2009). The NASA-funded Global Land Ice Velocity Extraction from Landsat (GoLIVE) project provides near real time ice velocity data derived from Landsat-8 panchromatic imagery (*https://nsidc.org/support/how/golive-map-application-user-guide*; see Figure 15.9; Fahnestock *et al.,* 2016). Similarly, the Centre for Polar Observation and Modelling Data Portal (*http://www.cpom.ucl.ac.uk/csopr/iv/index.html*) provides frequently updated maps of ice surface velocity in near real time derived from Sentinel-1 SAR imagery, for two key West Antarctic outlet glaciers that are undergoing loss (Pine Island and Thwaites).

The second technique, namely SAR interferometry or InSAR (see Section 9.4 and Volume 1B—Section 8), is particularly powerful in that it can measure ice velocity and strain rate (velocity gradient) to centimetre accuracy (Goldstein *et al.,* 1993; Rignot *et al.,* 2011). This is based on detecting the phase difference between two (or more) different SAR scenes of the same area but from slightly different viewing angles or orbital positions, and acquired at different times (see Massom and Lubin, 2006; see Figure 9.7). Figure 15.1 depicts a map of InSAR-derived mean annual velocity of the Antarctic Ice Sheet and ice shelves, and clearly shows the approximately 30 principal flow units involved in draining grounded ice across the grounding line and into the ocean (Shepherd *et al.,* 2018).

Taken together, these two methods (feature tracking and InSAR) have not only revolutionised our understanding and quantification of patterns of discharge and their change in key individual glaciers/ice streams. They have also led to systematic repeat surveys of Antarctica-wide ice velocity, revealing that the rate of ice discharge has generally increased over the satellite era (for example, Rignot *et al.,* 2008). Satellite velocity observations show that there was a marked speed-up in grounded ice via tributary glaciers immediately following the rapid disintegration of the Larsen B Ice Shelf in 2002, related to removal of the ice shelf buttressing effect (Rignot *et al.,* 2004; Scambos *et al.,* 2004). While ice shelf disintegration/areal loss (or thinning) does not directly contribute to SLR, as the ice area affected is already floating, there is a strong indirect effect.

Figure 15.9 Byrd Glacier velocity

Image showing the Landsat-derived velocity of the relatively fast moving Byrd Glacier (~2.4 m per day, orange and red) and the slower and narrower Mulock Glacier (pale blue), which exit the Transantarctic Mountains and flow into the Ross Ice Shelf.



Source: NASA/GoLIVE. Retrieved from *https://nsidc.org/data/nsidc-0710/versions/1/documentation*

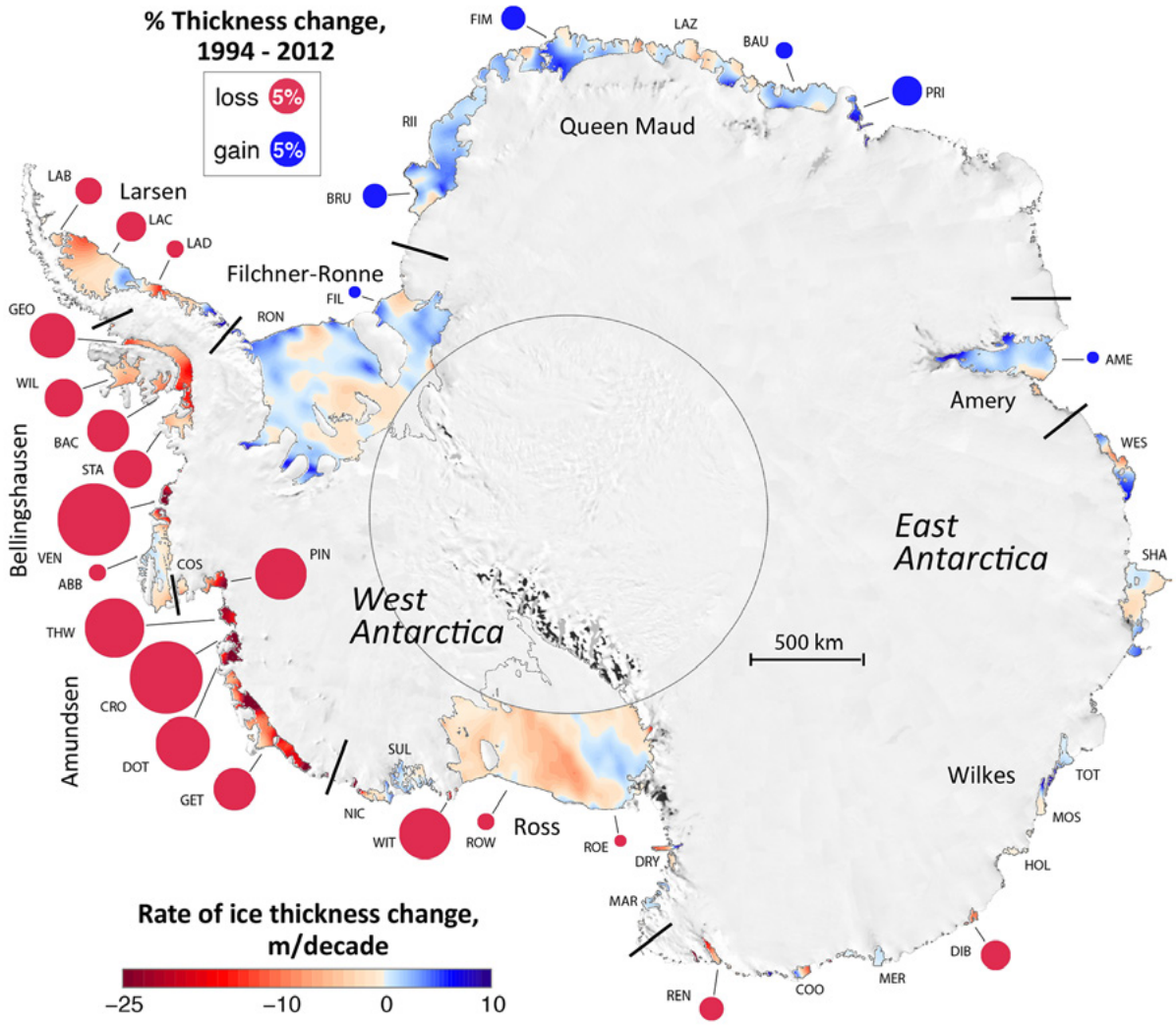
15.3.6 Surface elevation

Spaceborne altimeters (both radar and laser) measure surface elevation at high resolution by transmitting a signal toward the surface and accurately measuring the time interval of its return (see Section 9.5), and are a powerful tool for ice sheet observation (see Rémy and Parouty, 2009, for a review; see also Volume 1A—Section 16). Since their advent in 1992, modern radar altimeters (for example, on ERS, Envisat, CryoSat-2 and Sentinel-3 missions) have been important day/night and all-weather tools for the routine measurement of ice sheet elevation and its change over time (to within tens of centimetres), resolving both detailed patterns in individual catchment areas and large scale, Antarctica-wide change (for example, Pritchard *et al.,* 2009; Gourmelen *et al.,* 2017). Such information is crucial to the assessment of change in ice sheet volume and to help monitor Antarctica's contribution to SLR (see Section 15.3.7).

The multi-decadal records have shown that while the surface elevation of most of Antarctica has changed little over the past 25 years, this is not the case in many coastal sectors. There, the altimeter record has revealed receding surface height thinning (at rates of up to metres per year) on some of Antarctica's fastest-flowing glaciers, notably the Pine Island (a major contributor to recent SLR) and Thwaites glaciers in the west (McMillan *et al.,* 2014) and Totten Glacier in the east. This has been attributed to ice shelf thinning (as shown in Figure 15.10) due to basal melt by a warming ocean and associated increases in ice velocity. Of major concern is the possibility of rapid inland retreat of the grounding line in such regions, leading to increased ice sheet instability (see Joughin *et al.,* 2014; Alley *et al.,* 2015).

Figure 15.10 Antarctic ice shelf thickness changes

Change in Antarctic ice shelf thickness from 1994 to 2012 based on analysis of satellite radar altimeter data. For a description of the ice shelves annotated here, please refer to Paolo *et al.* (2015).



Adapted from Paolo *et al.* (2015) Figure 1

Spaceborne altimeters have revolutionized our understanding of the shape and topographic detail of the Antarctic Ice Sheet, with which to constrain ice dynamics, mass balance estimates (see Section 15.3.7), and models of the ice sheet that are crucial to predicting its likely response to future climatic conditions and contribution to SLR. As an example, a new digital elevation model (DEM) map of Antarctica based on CryoSat-2 altimeter data (Slater *et al.*, 2017) provides the most detailed and accurate three-dimensional view of the full continent to date (see Figure 15.11). Comparison with precise airborne survey data from NASA's Operation IceBridge shows that the new DEM depicts ice elevation to within 9.5 m on average. The model is freely available from the Centre for Polar Observation and Modelling (CPOM) Data Portal (see Section 15.6). Satellite altimetry is also used to map Antarctic sub-glacial lakes and monitor their activity (Siegfried and Fricker, 2018).

Latterly, spaceborne lidar instruments on ICESat (2003–2009) and ICESat-2 (2018+) have provided a more precise means of measuring and monitoring patterns of ice sheet elevation change than radar altimeters (e.g. Smith *et al.*, 2020). This is based upon the relatively small surface illumination area of lasers, which operates better over steeper, craggy Antarctic coastal regions (Markus *et al.*, 2017). The laser return signal also emanates from the surface, whereas radar altimeters can penetrate some depth into the ice sheet surface, depending on both wavelength/frequency and snow/ice conditions (see Figure 9.3). This factor needs to be accounted for in radar-derived estimates of surface elevation change/variability. Being based on an optical instrument, the main disadvantage of laser altimeters is their inability to penetrate cloud cover.

Figure 15.11 DEM of the Antarctic Ice Sheet

This state-of-the-art DEM of the Antarctic Ice Sheet was derived from six years of CryoSat-2 radar altimeter data, with a sampling of the ice sheet surface every kilometre. Gaps that CryoSat could not survey, mostly due to the rugged terrain, are filled in by sophisticated interpolation techniques.



Source: CPOM. Retrieved from: *http://www.cpom.ucl.ac.uk/csopr/icesheets2/dems.php?ais_subject=dem&user_type=normal*

15.3.7 Ice sheet mass balance

Taken together, accurate and sustained EO measurements of changes in ice sheet speed (notably the discharge rate of grounded ice) and surface elevation are (together with ice sheet weight) crucial to the estimation and monitoring of ice sheet mass balance—and therefore the ice sheet stability and contribution to SLR.

There are three main methods for measuring and monitoring ice sheet mass changes, all of which are heavily reliant on EO (ACE CRC, 2018; NSIDC, 2019a). These are the:

- **Volume (elevation) change or geodetic method**—scale monitoring of change in ice surface elevation over time by satellite altimeters (using data available since the early 1990s) has enabled quantitative estimation of the growth or reduction of overall ice volume (e.g. Smith *et al.*, 2020).
- **Mass budget technique**—compares estimates of snow accumulation (input) with ice losses (output) via seaward discharge across flux gates at the ice sheet margins and close to grounding lines from measured ice outflow velocity and thickness change/melt. Major advances in the mapping of glacier ice flow using repeat Landsat optical images (Gardner *et al.,* 2018) and InSAR methods (Mouginot *et al.,* 2014) have greatly facilitated this approach, which still however requires independent information on snow accumulation (currently not well constrained) and an accurate cross-section of each outflowing glacier across its grounding line.
- **Gravimetric approach**—direct 'weighing' of the ice sheet using satellite measurements of gravitational pull as the sensors pass over the ice, that is, detecting changes in the Earth's gravity field over the ice sheet relating to change in ice mass over time due to either accumulation or loss. Key to this was the launch of NASA's Gravity Recovery and Climate Experiment (GRACE) mission in 2003 (see Excursus 5.1). This provided a new means of resolving where the Antarctic Ice Sheet has lost mass, pointing the finger mainly at West Antarctica (Velicogna and Wahr, 2006; Rignot *et al.,* 2011).

Although different, the three methods are complementary and in fact produce similar results at the continental scale—enabling synthesis of the multiple EO-based estimates of ice sheet mass balance. This has revealed that, from 1992 to 2017, Antarctica lost > 2,700 billion tonnes of ice—equivalent to a SLR of 7.6±3.9 mm—with about half of this loss coming since 2012 and mainly from the Antarctic Peninsula and Amundsen Sea sectors (IMBIE Team, 2018). The accelerating mass loss is considered to be largely a response to the thinning of ice shelves due to their contact with warming ocean waters (Pritchard *et al.,* 2012) and, in the case of the Peninsula, rapid wholesale disintegrations of the Larsen A and B ice shelves.

15.4 EO of Sea Ice

Compared to the ice sheet, sea ice represents a more complex, dynamic, and challenging target for EO. It can, however, be readily detected and measured from space by virtue of its distinctive optical and microwave properties compared to open ocean. These are the:

- high reflectance[20] (brightness) of sea ice and snow at optical wavelengths compared to open ocean;
- thermal contrast at TIR wavelengths—the ice/snow surface is generally colder than the non ice-covered ocean, which has a surface temperature approximating -1.8°C during freezing seasons;
- contrast in the passive microwave emissivities[21] of sea ice and ice-free (open) ocean, depending on wavelength/frequency and polarisation[22]; and
- contrast in the microwave (radar) backscatter of sea ice versus open ocean—with sea ice generally being a brighter target, and backscatter depending on the ice thickness, age, and degree of deformation/roughness.

Fundamentally important characteristics of sea ice that can be measured from space are its ***areal extent and seasonality***, ***concentration***, ***motion*** and ***dynamics/deformation***, ***temperature***, ***albedo***, and (potentially) ***thickness*** (also ***snow cover thickness***; see Excursus 15.1). Regular, repeated and sustained basin-scale observations of these parameters are required to:

- understand the large scale dynamic and thermodynamic evolution of the ice cover on seasonal and interannual scales, and change and variability therein;
- detect long term trends in sea ice coverage and properties, including thickness and volume; and
- support safe shipping operations in the high-latitude Southern Ocean.

Taken together, sea ice concentration, thickness distribution and motion are required to determine its mass balance. In the following subsections, we give brief information on key sea ice variables that can be measured and monitored by EO. Massom (2009) and Lubin and Massom (2006) provide further information on error sources, and also on the:

- basic concepts and principles around EO of sea ice;
- applications, strengths, and weaknesses of the different sensor classes for polar ocean research and monitoring; and
- key tradeoffs between them.

Massom (2009) also highlights and discusses key differences between Antarctic and Arctic sea ice as EO targets. This requires different algorithms for extracting key variables from EOS data for each polar region.

15.4.1 Sea ice concentration, extent, and seasonality, and their variability

Spaceborne, wide swath, optical sensors operating at moderate spatial resolution (0.25–1 km; such as MODIS and VIIRS) provide observations of albedo, temperature, and radiative fluxes, and have also been used to derive estimates of thin-ice thickness in coastal polynyas, as well as the interaction of sea ice with ice sheet margins and icebergs. They can also provide information on extent, concentration, and type, based upon the:

- contrasting temperature and albedo of sea ice versus open ocean; and the
- variation of albedo with ice thickness (until the ice becomes snow-covered).

20 Reflectance is the ratio of the intensity of radiation reflected by a target surface to that of the radiation incident upon it.

21 *Emissivity* is the ratio of radiation naturally emitted by a natural surface to that emitted by a *blackbody* (perfect radiator) at the same kinetic temperature.

22 Polarisation describes the direction of orientation in which the electrical field vector of electromagnetic radiation vibrates, and is a key consideration in active and passive microwave EO of sea ice (Long, 2008).

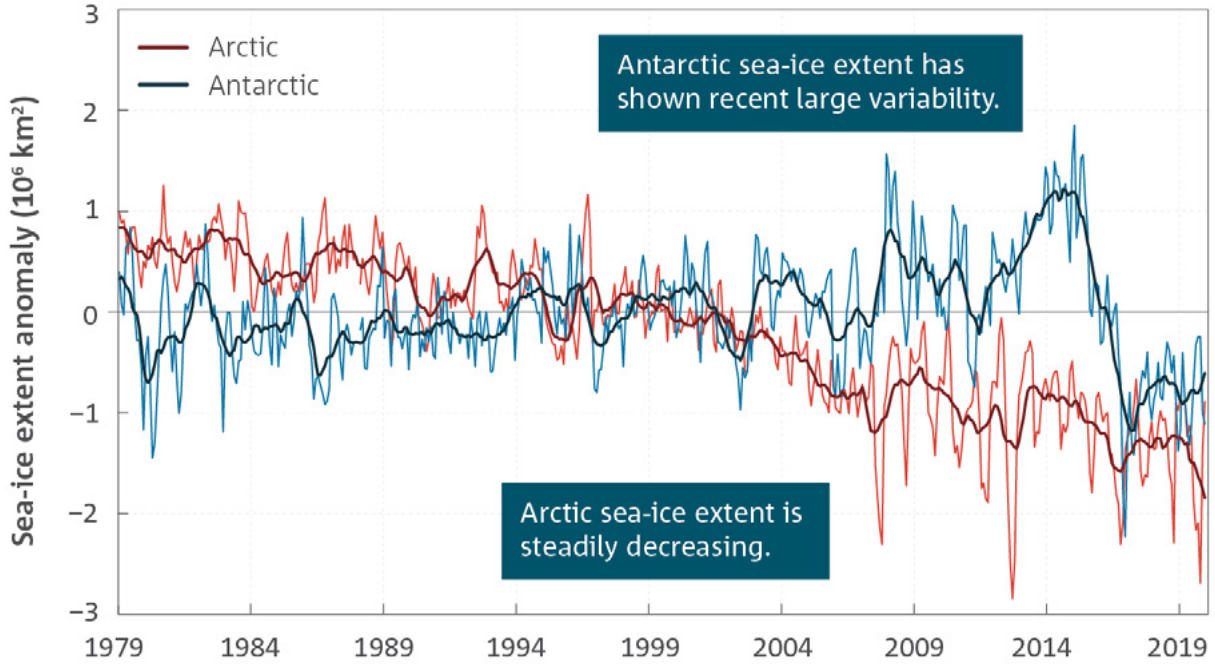
However, persistent cloud cover is an issue (as is polar darkness for optical EO), and cloud masking can be challenging over snow and ice surfaces given their similar optical and thermal properties. For this reason and although it plays a key role in support of shipping and operations due to its ready availability, satellite optical and TIR EO is not the primary source of ice concentration information for monitoring and research purposes. This is more the realm of active and passive microwave EO, which are (largely) unaffected by atmospheric conditions and darkness (see Section 9 and Volume 1A—Section 14).

Satellite-borne, passive microwave sensors (e.g. SMMR, SSM/I, AMSR-E, SSMIS) have provided the most reliable and consistent near real time information on the concentration and extent of the entire Antarctic sea ice cover on a daily/near-daily basis since 1978 and at mapped spatial resolutions ranging from 6.25 km to 25 km. This is based upon the strong frequency-dependent contrast in the microwave emissivities of sea ice and open ocean. Extent is generally defined as the integral sum of all observations with ice concentrations > 15%, while area is the product of ice concentration and extent. A range of sea ice data (including mapped brightness temperatures and derived sea ice concentration) is available from the Scientific Data Search facility managed by the NSIDC (NSIDC, 2019b).

The time series of passive microwave data has been crucial to monitoring change and variability in global sea ice coverage and seasonality (see Figure 15.12). In stark contrast to the Arctic, where sea ice has spiralled since the 1970s, overall Antarctic coverage has paradoxically displayed a slightly increasing trend over the same period (Turner and Comiso, 2017)—of about 1.0±0.5% per decade for 1979–2018 (Parkinson, 2019). In fact, the slight net increase masks strong and contrasting regional contributions, notably a decrease in the Amundsen-Bellingshausen seas sector of –2.5±1.2% per decade for 1979–2018 and increases of up to +2.3±1.2% per decade in other sectors (Parkinson, 2019). Overall and regional trends also show a marked seasonal dependence (Holland, 2014). Moreover, recent years have seen extreme variability, with record maxima in three successive winters (2012, 2013, and 2014; Reid and Massom, 2015) being followed by a record summer minimum in 2017, with below-average overall (net) extent continuing until early 2020 (Reid *et al.*, 2021).

Figure 15.12 Extent of Arctic versus Antarctic sea ice

Plot of the overall extents of Arctic (red) and Antarctic (blue) sea ice for the period January 1979 to December 2019, with the thick lines showing 12-month running means and thin lines showing monthly anomalies. Total area is estimated from satellite image pixels with sea ice concentration of at least 15%. Antarctic sea ice reached a record high in 2014 before decreasing dramatically. The Arctic Ocean's coverage of summertime sea ice has shrunk by about 13% per decade.



Source: BoM (2021). Retrieved from *http://www.bom.gov.au/state-of-the-climate/cryosphere.shtml*

This time series has also revealed strong regional trends in the seasonality (timings of annual advance and retreat and resultant duration) of sea ice coverage around Antarctica (Stammerjohn *et al.*, 2012) that largely reflect the sea ice concentration and extent patterns (Turner *et al.*, 2015). Duration is defined here as the length of time, during each annual Antarctic sea ice cycle (February to February), that a pixel contains sea ice with a concentration of ≥ 15%. West of the Antarctic Peninsula and in the northwestern Weddell Sea, for the period 1979/80 to 2016/17, annual sea ice duration decreased by about 3 months due to a 2-month-later advance and an approximately 1-month-earlier retreat (Stammerjohn and Maksym, 2016). These changes have had impacts on the marine ecosystem, notably on phytoplankton and penguin communities (Massom and Stammerjohn, 2010), and have also been implicated in the timing and nature of breakup events of the Larsen A and B and Wilkins ice shelves (Massom *et al.*, 2018). In contrast and in the western Ross Sea, the annual sea ice season has lengthened substantially—by about three months over 1979/80 to 2016/17 (Stammerjohn *et al.*, 2012). Patterns of change in sea ice advance, retreat, and duration elsewhere are complex, for example, across East Antarctica (Massom *et al.*, 2013).

Although a number of mechanisms have been proposed to explain these changing and/or varying patterns of Antarctic sea ice coverage around Antarctica—including changes in winds, ocean variability, and freshwater input from precipitation and ice shelf melt—considerable uncertainty remains (Hobbs *et al.*, 2016). Indeed, understanding the nature of sea ice change and variability, and the relevant drivers and impacts, is a high priority in climate research (see NAS, 2017).

Systematic, consistent observations of the marine cryosphere are critical for the operational community, whose primary task is to reduce shipping hazards related to iceberg and sea ice tracking. Operational ice services make extensive use of satellite passive microwave ice concentration data (from the DMSP SSM/I and EOS Aqua AMSR-E), ice extent and type data from optical-TIR imagery (e.g. VIIRS and EOS MODIS), SAR, and radar scatterometer data.

Satellite-based annual assessments of Antarctic sea ice concentration, extent, and seasonality are provided in annual NOAA BAMS State of the Climate Reports (*https://www.ncei.noaa.gov/bams-state-of-climate*).

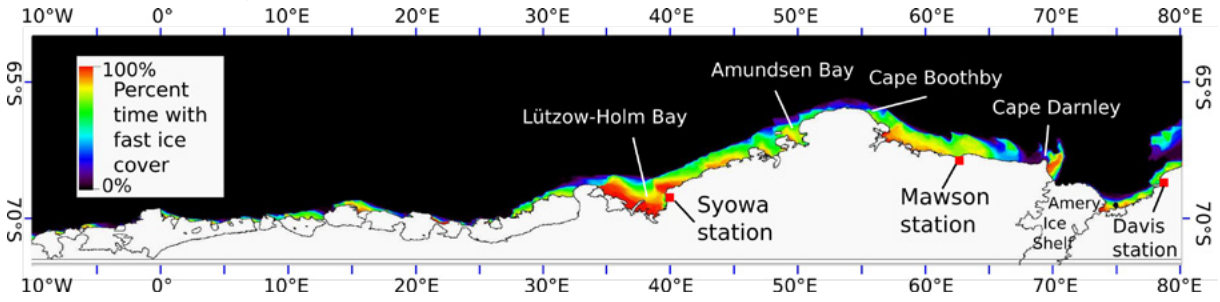
15.4.2 Coastal landfast sea ice (fast ice) distribution

The mapping and monitoring of fast ice from space represents more of a challenge, given that it forms a relatively narrow zone immediately adjacent to the Antarctic coast. This issue has been successfully addressed through use of wide swath MODIS optical imagery, to produce time series maps of fast ice across East Antarctica (from 20°E to 160°E) at 2 km resolution (Fraser *et al.*, 2012; see Figure 15.13). Cloud cover is removed by first applying NASA's standard cloud masking algorithm, then compositing 20 days of imagery to fill in resultant data gaps. In this way, a time series of 20-day composites has been produced for 2000–2009. These show an upturn in coastal fast ice overall, although the shortness of the time series negates trend analysis. Recent extension of the fast ice extent time series to include circumpolar imagery from 2000 to 2018 (Fraser *et al.*, 2020) indicates a marginally significant decrease in overall (circum-Antarctic) fast ice extent of approximately –2.0±1.8% per decade.

Another technique uses maximum cross-correlation of satellite SAR image pairs separated by 1–3 days to provide more detailed maps (at higher spatial and temporal resolution) to detect and map coastal fast ice (Li *et al.*, 2018), by virtue of its stationary nature compared to pack ice. By this method, sea ice that is not moving is classified as fast ice. Coarser resolution mapping is obtained from passive microwave data based on a relationship between horizontally and vertically polarised AMSR-E brightness temperatures at 89 GHz (Nihashi and Ohshima, 2015).

Figure 15.13 Fast ice coverage and persistence

MODIS-derived map of coastal fast ice coverage and persistence in East Antarctica averaged over an 8.8 year period (March 2000 to December 2008), at a spatial resolution of 2 km.



Source: Fraser *et al.* (2012) Figure 2a

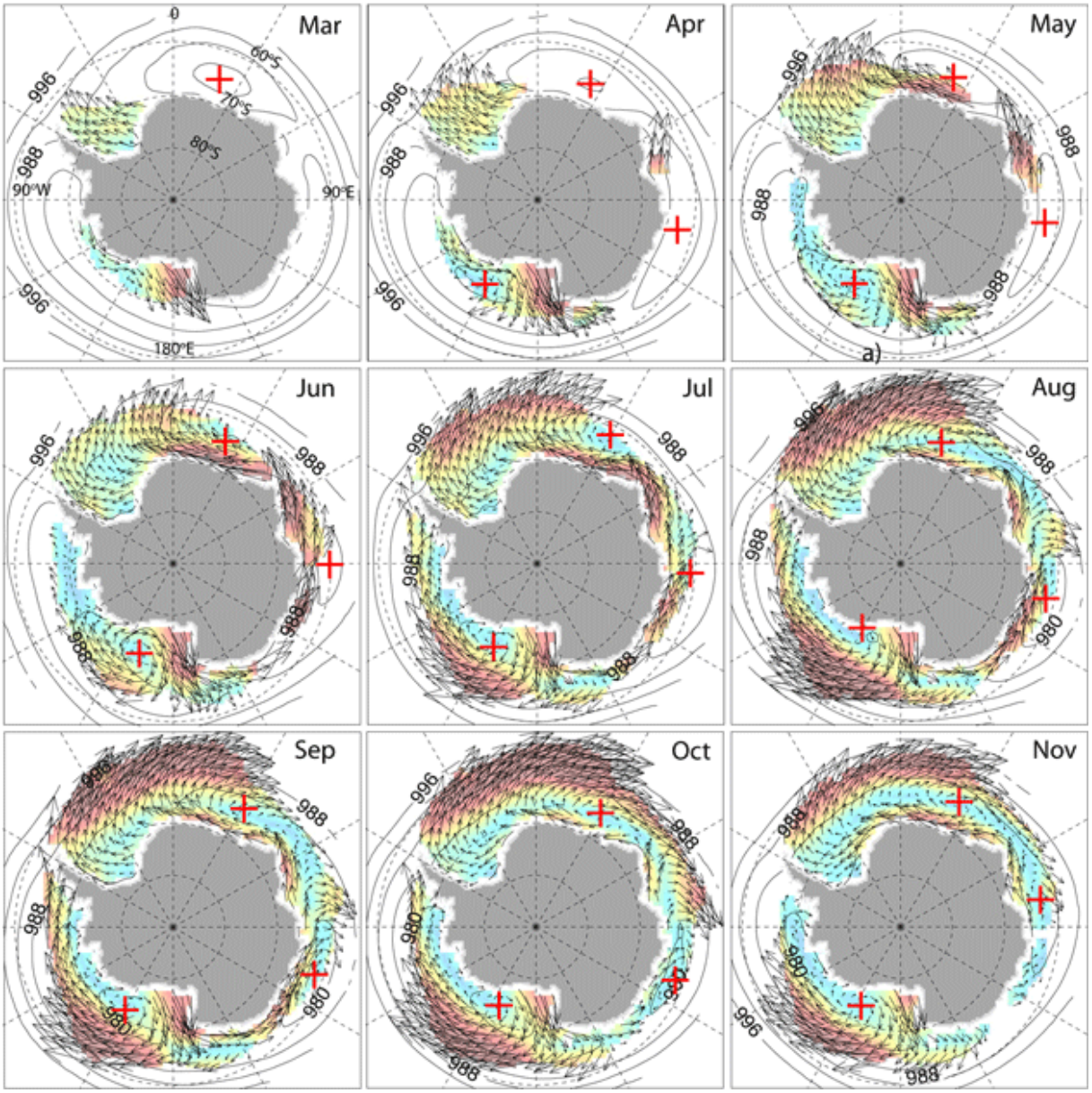
15.4.3 Sea ice motion and dynamics

Identifying and understanding the changes in Antarctic sea ice drift over short to broad time scales is of considerable importance, given the contribution of ice dynamics to ice concentration and extent, seasonality (duration) of coverage, ice deformation and thickening, enhanced ice production and heat loss in open water, and therefore the climate system. Moreover, deformation processes related to differential ice motion significantly impact safe and efficient shipping operations around Antarctica.

Tracking of sea ice motion and dynamics is achieved both at low resolution (using visible–TIR radiometers, passive microwave radiometers, and radar scatterometers) and at high resolution (using SAR imagery), the latter typically in smaller regions of interest. In all cases, the technique is based upon identification and tracking of persistent features/floes within the sea ice field in time sequences of overlapping/repeat images, generally through maximum cross-correlation.

Figure 15.14 Mean monthly (March through November) ice drift for 1982-2015.

Contours are isobars (interval: 4 hPa) from ERA-Interim sea level pressure fields. Drift estimates are shown on a 200 km grid to reduce density of vectors within each plot; every other vector is displayed. Red crosses show the centres of three atmospheric lows in the monthly mean fields. Colour spectrum for motion ranges from 0 km/day (blue) to 10 km/day (red).



Source: Kwok *et al.* (2017) Figure 226-3243-1. Used with permission.

Moderate resolution, ice drift fields derived from satellite passive microwave brightness temperature data (37 GHz and 85 GHz/91 GHz, the latter since 2009) have enabled assessment of large scale drift patterns in Antarctic sea ice over recent decades (Kwok *et al.,* 2017). Although the coarse resolution of the data used leads to uncertainties of several kilometres for individual displacement vectors, this dataset is long and offers complete circumpolar coverage on a daily/near-daily basis by the SMMR, SSM/I and AMSR-E instruments (uninterrupted by cloud and darkness). The climatological pattern of mean sea ice drift around Antarctica is shown in Figure 15.1. It depicts a strong outer zonal band of eastward drifting sea ice at maximum annual extent within the Antarctic Circumpolar Current that is maintained by strong circumpolar westerly winds, and large scale gyres in the Ross and Weddell seas. Around the coastal margin, sea ice drifts predominantly westwards under the influence of strong prevailing easterly winds and within the Antarctic Coastal Current.

The time series of satellite passive microwave data has given great insight into patterns of sea ice drift and their variability and change in response to changing wind forcing. Indeed, it has revealed substantial regional change in patterns of sea ice drift around Antarctica in recent decades (see Figure 15.14). Notably, sea ice drift speed has decreased in the western Weddell Sea in recent decades, in contrast to the eastern Weddell and Ross seas where it has increased (Holland and Kwok, 2012; Kwok *et al.,* 2017). These large and statistically significant changes have been linked to observed changes in surface wind speed and direction associated with change in large scale modes of climate variability, such as the Southern Annular Mode, and a persistent low pressure anomaly in the Amundsen Sea known as the Amundsen Sea Low (Turner *et al.*, 2016).

Improved sea ice motion products are required, and these are potentially obtainable from the merging of results from passive microwave radiometry, radar scatterometry, and drifting ice buoys, for optimal spatial coverage. While the coarser resolution time series are best suited to analyses of large scale sea ice drift patterns, more detailed characterisation of daily and sub-daily ice motion requires use of high resolution SAR and satellite-interrogated buoy data. This, in turn, requires more frequent and extensive (regular and systematic) SAR coverage of the Antarctic sea ice zone.

15.4.4 Sea ice and snow cover thickness

Satellite EO using laser (lidar) and radar altimeters dating back to 1991 (ERS-1), such as those onboard ICESat-1 and -2 and CryoSat-2 respectively, is crucial to the routine large scale estimation and monitoring of Antarctic sea ice thickness and volume. This is based on the accurate measurement of the elevation above sea level of either the:

- ice surface (for radar altimeters); or
- ice plus snow surface (for laser altimeters).

Derivation of ice thickness from these datasets is based on the hydrostatic relationship (Archimedes Principle) between the above- and below-sea level proportions of the ice cover, requiring accurate knowledge of the snow thickness, and the densities of both ice and snow. The following equations are used to determine sea ice thickness (h_i; Kwok, 2010):

$$h_i = \left(\frac{\rho_w}{\rho_w - \rho_i}\right)\boldsymbol{h_f} - \left(\frac{\rho_w - \rho_s}{\rho_w - \rho_i}\right)h_{fs} \quad \text{(lidar)}$$

$$h_i = \left(\frac{\rho_w}{\rho_w - \rho_i}\right)\boldsymbol{h_{fi}} + \left(\frac{\rho_s}{\rho_w - \rho_i}\right)h_{fs} \quad \text{(radar)}$$

where ρ_i, ρ_s, and ρ_w are the densities of sea ice, snow, and seawater respectively. The key observables from laser altimeter/lidar and radar altimeter differ (and are highlighted in bold in the equations above). For laser, h_f is the total freeboard of both ice and snow (where present) above local sea level, that is, assuming that the laser does not penetrate the snow (see Volume 1A—Section 15.1). For radar altimetry, on the other hand, the measured return is assumed to be from the ice surface (see Section 9.5 and Volume 1A—Section 16). Due to the penetration of the radar wave into the snow volume, its return is assumed to be from the sea ice surface and the measured variable h_{fi} is the freeboard of the ice only.

Although promising results have emerged from satellite altimetry, a number of challenges remain that need to be addressed in order to obtain accurate retrievals of circum-Antarctic sea ice thickness. Lack of information on snow depth and density and their variability/evolution introduces considerable uncertainty into estimates of total ice thickness derived from freeboard observations by satellite altimeters. This underlines the need for dedicated validation experiments, using both airborne and autonomous underwater vehicles (AUV; see Excursus 5.1). Such field campaigns are required to identify and quantify errors associated with the conversion of sea ice freeboard to ice thickness. A further obstacle is the complex relationship between ice elevation and thickness around Antarctica (compared to the Arctic). The presence of significant

areas of seawater flooding at the ice surface affects the density of the overlying snow that is used to compute ice thickness from snow elevation, and also the penetration of the signal for radar altimetry. For radar altimetry, the assumption that the return emanates from the snow-ice interface is not always valid (Giles *et al.,* 2008b). An additional critical gap is large scale information about snow depth on sea ice (Webster *et al.*, 2018).

As a result of these factors, our current knowledge of Antarctic sea ice thickness and snow cover thickness is currently limited to compilations of:

- various *in situ* and near-surface remote sensing observations (Worby *et al.,* 2008; Kwok and Maksym, 2014) that are characterised by large spatiotemporal gaps and may be biased towards thinner ice (Maksym *et al.,* 2012); and
- satellite altimeter data that are limited to certain sectors or short time periods (such as Kurtz and Markus, 2012).

As a result, there is inadequate information to determine whether large scale sea ice thickness and volume are changing around Antarctica (Fox-Kemper *et al.*, *in press*), although large scale estimates of Antarctic sea ice and snow cover thickness are emerging (e.g. Kacimi and Kwok, 2020). By contrast and in the Arctic, a combination of extensive satellite altimeter and submarine sonar data has shown a substantial thinning of the ice cover there, which is consistent with the loss of perennial ice (Kwok and Rothrock, 2009).

15.5 Outlook: Future Opportunities and Needs

Major advances in EO have, in recent decades, led to quantum leaps in our understanding of the Antarctic cryosphere, and change and variability therein. Certain key challenges and opportunities remain, however, notably around ensuring continuation of key sensor time series, and adequate data acquisition across the Antarctic Ice Sheet and sea ice cover (Pope *et al.*, 2017).

Of pressing concern is that the Antarctic Ice Sheet is losing ice mass and contributing to global SLR at an accelerating rate (IMBIE Team, 2018). This highlights the critical need to identify and accurately quantify the nature and drivers of the recent change, including ice shelf thinning, weakening, and collapse. This is in turn crucial to reducing current large uncertainties in model predictions of the likely future fate of the ice sheet and its contribution to SLR in response to climate change. An important factor is the need for satellite observations with improved temporal and spatial sampling to more fully understand the processes driving contemporary patterns of ice sheet imbalance (Shepherd *et al.,* 2018).

The accurate synoptic-scale measurement and monitoring of Antarctic sea ice thickness (and overall volume) and snow cover from space also remains a challenge, yet a high priority. New improved estimates may be possible using dual-frequency radar altimeter sensors and by combining coincident measurements from laser and radar altimeters (Kacimi and Kwok, 2020). There is also a pressing need for coordinated and sustained near-surface observations of the sea ice system—as proposed by the Southern Ocean Observing System (SOOS; Newman *et al.*, 2019). These other data sources include sea ice and snow cover measurements from ships (using electromagnetic induction technology) and snow thickness estimates from airborne snow-thickness radars, such as the NASA IceBridge Mission (NASA, 2019; see Section 15.6). Autonomous airborne and underwater vehicles and sensors (see Excursus 5.1) also have a key role to play, not least in the calibration and validation of satellite-derived thickness estimates, and in bridging the scale gap between detailed *in situ* observations (on the floe scale) and large scale satellite measurements (Newman *et al.*, 2019).

By the same token, our understanding of the coupled atmospheric and oceanic drivers of observed sea ice and Southern Ocean change and variability, and the complex interactions and feedbacks involved, remains incomplete (Hobbs *et al.,* 2016; NAS, 2017). This in turn severely limits our ability to confidently and accurately predict the trajectory of future sea ice change and its impacts. Addressing this critical gap involves EO in conjunction with dedicated surface experiments (including process studies) and model improvements. Also crucial is improved information on snow precipitation rates, properties, and thickness as they affect sea ice formation and melt, and how these may be changing (Webster *et al.,* 2018).

As a final comment, field research observations themselves are crucial for satellite validation purposes in general (and to provide information on key parameters that cannot be measured from space). This requires a standardised methodology to ensure consistent acquisition of data in forms that are optimal for the calibration and validation of satellite data algorithms, specific to the geophysical quantities in question.

15.6 Further Information

Antarctica

General information:

https://www.antarctica.gov.au/about-antarctica/ice-and-atmosphere/ice-sheet/

https://www.antarctica.gov.au/about-antarctica/ice-and-atmosphere/sea-ice/

https://www.ga.gov.au/scientific-topics/marine/antarctica

Antarctic Climate and Ecosystems CRC: *https://stors.tas.gov.au/802018*

SOE (2017) *State of Environment Report 2016.* Antarctic Environment: *https://soe.environment.gov.au/theme/antarctic-environment*

Annual assessments of change and variability in the Antarctic ice sheet, sea ice, Southern Ocean and atmosphere, including seasonal changes in melt extent and timing, are given in annual NOAA BAMS State of the Climate Reports: *https://www.ncei.noaa.gov/bams-state-of-climate*

Maps and Images:

Mosaic of Antarctica (MOA) maps and vector datasets with the corresponding coastlines, ice sheet grounding lines and islands are available at: *https://nsidc.org/data/NSIDC-0730/versions/1*

Landsat Image Mosaic of Antarctica (LIMA) dataset: *lima.usgs.gov*

Time series of NOAA AVHRR and MODIS images of Antarctic ice shelves are available at: *https://nsidc.org/data/iceshelves_images/*

Multiple, wide swath SAR imagery acquired during the 1997 RADARSAT-1 Antarctic Mapping Project (RAMP) have been compiled into a high resolution radar mosaic of the southern continent: *https://nsidc.org/data/NSIDC-0103/versions/2/print*

A new DEM model is freely available from the Centre for Polar Observation and Modelling Data Portal (CPOM) at: *http://www.cpom.ucl.ac.uk/csopr/icesheets2/dems.php?ais_subject=dem&user_type=*

Ice sheets

ACE CRC (2017)

NSIDC (2019a)

US Antarctic Iceberg Tracking Database: *www.scp.byu.edu/data/iceberg*

US Navy/NOAA National Ice Center: *https://usicecenter.gov/Products/AntarcIcebergs*

Global Land Ice Velocity Extraction from Landsat (GoLIVE) project provides near real time, ice velocity data derived from Landsat-8 panchromatic imagery: *https://nsidc.org/data/nsidc-0710/versions/1/documentation*

Centre for Polar Observation and Modelling Data Portal provides frequently-updated maps of ice-surface velocity in near real time derived from Sentinel-1 SAR imagery: *http://www.cpom.ucl.ac.uk/csopr/iv/index.html*

Sea Ice

Thomas (2017)

Weeks (2010)

Sea ice type is classified (named) and categorised depending on its thickness (related to age/stage of development), and based on established international protocol. For a glossary and image library of sea ice terms, see: *http://aspect.antarctica.gov.au/home/glossary-and-image-library*

A range of sea ice data (including brightness temperatures and derived sea ice concentration) are available from the Scientific Data Search service of the US National Snow and Ice Data Center (NSIDC): *https://nsidc.org/data/search/#keywords=sea+ice/sortKeys=score,,desc/facetFilters=%257B%257D/pageNumber=1/itemsPerPage=25*

Alfred-Wegener-Institut (AWI): *https://www.awi.de/en/focus/sea-ice.html*

NASA Earth Observatory: *https://earthobservatory.nasa.gov/Features/SeaIce/page1.php* *https://earthobservatory.nasa.gov/Features/SeaIce/page4.php*

National Snow and Ice Data Centre (NSIDC): *https://nsidc.org/cryosphere/seaice/characteristics/polynyas.html*

Polar ice and snow cover

NASA Ice Bridge Project—the largest airborne survey of Earth's polar ice to date: *https://nsidc.org/data/IDCSI2/versions/1*
https://www.nasa.gov/mission_pages/icebridge/index.html

Sea Ice Ecology

Thomas (2017)

Shipping

COMNAP (2015)

WMO (2021)

European Space Agency (ESA)

Cryosat mission: *https://www.esa.int/Applications/Observing_the_Earth/CryoSat/ESA_s_ice_mission*

Integrated Marine Observing System (IMOS)

IMOS Ocean Current: *http://oceancurrent.imos.org.au/*

Bluelink (see Excursus 2.2)

https://www.csiro.au/en/research/natural-environment/oceans/Bluelink

CSIRO (2017)

Southern Ocean Observing System (SOOS)

This international initiative of the Scientific Committee on Antarctic Research (SCAR) and the Scientific Committee on Oceanic Research (SCOR) facilitates the collection and delivery of essential observations on dynamics and change of Southern Ocean systems: *http://www.soos.aq/*

Newman *et al.* (2019)

15.7 References

Abdalati, W. (2006). Recent changes in high-latitude glaciers, ice caps and ice sheets. *Weather*, 61(4), 95–101.

ACE CRC (2014). *Position Analysis: Antarctic Sea Ice and Climate Change 2014*. Antarctic Climate and Ecosystems Cooperative Research Centre, Hobart. *https://wwwace.aappartnership.org.au/publication/antarctic-sea-ice-and-climate-change/*

ACE CRC (2017). *Position Analysis: The Antarctic Ice Sheet and Sea Level*. Antarctic Climate and Ecosystems Cooperative Research Centre, Hobart. *https://wwwace.aappartnership.org.au/publication/the-antarctic-ice-sheet-sea-level/*

Alley, R.B., Anandakrishnan, S., Christianson, S., Horgan, H.J., Muto, A., Parizek, B.R., Pollard, D., and Walker, R.T. (2015). Oceanic forcing of ice-sheet retreat: West Antarctica and more. *Annual Review of Earth and Planetary Sciences*, 43(1), 207–231.

Arrigo, K.R., van Dijken, G.L., Ainley, D.G., Fahnestock, M.A., and Markus,T. (2002). Ecological impact of a large Antarctic iceberg. *Geophysical Research Letters*, 29(7). *https://doi.org/10.1029/2001GL014160*

Bamber, J., and Payne, A. (Eds). (2004). Mass balance of the cryosphere. In *Observations and Modeling of Contemporary and Future Changes*. Cambridge University Press, Cambridge, UK.

Barber, D.G., and Massom, R.A. (2007). The role of sea ice in Arctic and Antarctic polynyas. pp. 1–54 in *Polynyas: Windows to the World, Elsevier Oceanography Series, 74*. (Eds: W.O. Smith and D.G. Barber). Elsevier, Amsterdam.

Bell, R.E., Chu, W., Kingslake, J., Das, I.,Tedesco, M., Tinto, K.J., Zappa, C.J., Frezzotti, M., Boghosian, A. and Lee, W.S. (2017). Antarctic ice shelf potentially stabilized by export of meltwater in surface river. *Nature*, 544(7650), 344–348. *https://doi.org/10.1038/nature22048*

Bevan, S.L., Luckman, A.J., Kuipers Munneke, P., Hubbard, B., Kulessa, B., and Ashmore, D.W. (2018). Decline in surface melt duration on Larsen C Ice Shelf revealed by the advanced scatterometer (ASCAT). *Earth and Space Science*, 5, 578–591. *https://doi.org/10.1029/2018EA000421*

Bindoff, N.L., Rintoul, S.R., and Massom, R. (2000). Polynyas and Bottom Water formation In Adélie Land, Antarctica, *Papers and Proceedings of the Royal Society of Tasmania*, 133(3), 51–56.

Bindschadler, R., Choi, H., Wichlacz, A., Bingham, R., Bohlander, J., Brunt, K., Corr, H., Drews, R., Fricker, H., Hall, M., Hindmarsh, R., Kohler, J., Padman, L., Rack, W., Rotschky, G., Urbini, S., Vornberger, P., and Young, N. (2011). Getting around Antarctica: new high-resolution mappings of the grounded and freely-floating boundaries of the Antarctic ice sheet created for the International Polar Year. *The Cryosphere*, 5, 569–588. *https://doi.org/10.5194/tc-5-569-2011*

Bintanja, R., van Oldenborgh, G., Drijfhout, S., Wouters, B., and Katsman, C.A. (2013). Important role for ocean warming and increased ice-shelf melt in Antarctic sea-ice expansion. *Nature Geoscience*, 6, 376–379. *https://doi.org/10.1038/ngeo1767*

BoM (2021). *State of the Climate 2020*. Bureau of Meteorology, Melbourne. *http://www.bom.gov.au/state-of-the-climate/cryosphere.shtml*

Budge, J.S., and Long, D.G. (2018). A comprehensive database for Antarctic iceberg tracking using scatterometer data. *IEEE Journal of Selected Topics in Applied Earth Observations and Remote Sensing*, 11(2), 434–442. doi:10.1109/JSTARS.2017.2784186

COMNAP (2015). *The COMNAP Sea Ice Challenges Workshop, Hobart, Tasmania. 12–13 May 2015. Workshop Report*, Council of Managers of National Antarctic Programs. *https://www.comnap.aq/symposiums-workshops-reports*

Cuffey, K. and W.S.B. Patterson. (2010). *The Physics of Glaciers*. Academic Press.

Depoorter, M.A., Bamber, J.L., Griggs, J.A., Lenaerts, J.T., Ligtenberg, S.R., van den Broeke, M.R., and Moholdt, G. (2013). Calving fluxes and basal melt rates of Antarctic ice shelves. *Nature,* 502(7469), 89–92.

Fahnestock, M., Scambos, T., Moon, T., Gardner, A., Haran, T., and Klinger, M. (2016). Rapid large-area mapping of ice flow using Landsat 8. *Remote Sensing of Environment*, 185, 84–94, doi.org/10.1016/j.rse.2015.11.023

Fetterer, F., Knowles, K., Meier, W., Savoie, M. and Windnagel, A.K. (2017). *Sea Ice Index*. Version 2 (NSIDC, Boulder, Colorado, USA.

Fox-Kemper, B., Hewitt, H.T., Xiao, C., Aðalgeirsdóttir, G., Drijfhout, S.S., Edwards, T.L., Golledge, N.R., Hemer, M., Kopp, R.E., Krinner, G., Mix, A., Notz, D., Nowicki, S., Nurhati, I.S., Ruiz, L., Sallée, J.-B., Slangen, A.B.A, and Yu, Y. (*in press*). 2021: Ocean, Cryosphere and Sea Level Change. In *Climate Change 2021: The Physical Science Basis. Contribution of Working Group I to the Sixth Assessment Report of the Intergovernmental Panel on Climate Change*. (Eds: MassonDelmotte, V., Zhai, P., Pirani, A., Connors, S.L., Péan, C., Berger, S., Caud, N., Chen, Y., Goldfarb, L., Gomis, M.I., Huang, M., Leitzell, K., Lonnoy, E., Matthews, J.B.R., Maycock, T.K., Waterfield, T., Yelekçi, O., Yu, R., and Zhou, B.). Cambridge University Press.

Fraser, A.D., Massom, R.A., Michael, K.J., Galton-Fenzi, B.K., and Lieser, J.L. (2012). East Antarctic landfast sea-ice distribution and variability, 2000–2008. *Journal of Climate*, 25, 1137–1156.

Fraser, A.D., Massom, R.A., Ohshima, K.I., Willmes, S., Kappes, P.J., Cartwright, J., and Porter-Smith, R. (2020). High-resolution mapping of circum-Antarctic landfast sea ice distribution, 2000–2018. *Earth System Science Data*, 12, 2987–2999. *https://doi.org/10.5194/essd-12-2987-2020*

Fretwell, P., Pritchard, H.D., Vaughan, D.G., Bamber, J.L., Barrand, N.E., Bell, R., Bianchi, C., Bingham, R.G., Blankenship, D.D., Casassa, G., Catania, G., Callens, D., Conway, H., Cook, A.J., Corr, H.F.J., Damaske, D., Damm, V., Ferraccioli, F., Forsberg, R., Fujita, S., Gim, Y., Gogineni, P., Griggs, J.A., Hindmarsh, R.C. A., Holmlund, P., Holt, J.W., Jacobel, R.W., Jenkins, A., Jokat, W., Jordan, T., King, E.C., Kohler, J., Krabill, W., Riger-Kusk, M., Langley, K.A., Leitchenkov, G., Leuschen, C., Luyendyk, B.P., Matsuoka, K., Mouginot, J., Nitsche, F.O., Nogi, Y., Nost, O.A., Popov, S.V., Rignot, E., Rippin, D.M., Rivera, A., Roberts, J., Ross, N., Siegert, M.J., Smith, A.M., Steinhage, D., Studinger, M., Sun, B., Tinto, B.K., Welch, B.C., Wilson, D., Young, D.A., Xiangbin, C., and Zirizzotti, A. (2013). Bedmap2: improved ice bed, surface and thickness datasets for Antarctica. *The Cryosphere*, 7, 375–393. *https://doi.org/10.5194/tc-7-375-2013*

Gardner, A.S., Moholdt, G., Scambos, T., Fahnstock, M., Ligtenberg, S., van den Broeke, M., and Nilsson, J. (2018). Increased West Antarctic and unchanged East Antarctic ice discharge over the last 7 years. *The Cryosphere*, 12, 521–547. *https://doi.org/10.5194/tc-12-521-2018*

Giles, A.B., Massom, R.A., and Lytle, V.I. (2008a). Fast ice distribution in East Antarctica during 1997 and 1999 determined using Radarsat data. *Journal of Geophysical Research*, 113, C02S14. *https://doi.org/10.1029/2007JC004139*

Giles, K.A., Laxon, S.W., and Worby, A.P. (2008b). Antarctic sea ice elevation from satellite radar altimetry. *Geophysical Research Letters*, 35, L03503. *https://doi.org/10.1029/2007GL031572*

Giles, A.B., Massom, R.A., and Warner, R.C. (2009). A method for sub-pixel scale feature-tracking using Radarsat images applied to the Mertz Glacier Tongue, East Antarctica. *Remote Sensing of Environment,* 113, 1691–1699.

Goldstein, R.M., Engelhardt, H., Kamb, B., and Frolich, R.M. (1993). Satellite radar interferometry for monitoring ice sheet motion: Application to an Antarctic ice stream. *Science*, 262(5139), 1525–1530. *https://www.science.org/doi/10.1126/science.262.5139.1525*

Gourmelen, N., Escorihuela, M.J., Shepherd, A., Foresta, L., Muir, A., Garcia-Mondejar, A., Roca, M., Baker, S.G., and Drinkwater, M.R. (2017). CryoSat-2 swath interferometric altimetry for mapping ice elevation and elevation change. *Advances in Space Research*, 62(6), 1226–1242. *https://doi.org/10.1016/j.asr.2017.11.014*

Haran, T., J. Bohlander, T. Scambos, T. Painter, and M. Fahnestock. (2014). *MODIS Mosaic of Antarctica 2008–2009 (MOA2009) Image Map*. National Snow and Ice Data Center, Boulder, Colorado USA. *http://dx.doi.org/10.7265/N5KP8037*

Hobbs W., Massom, R., Stammerjohn, S., Reid, P., Williams, G., and Meier, W. (2016). A Review of recent changes in Southern Ocean sea ice, their drivers and forcings. *Global and Planetary Change*, 143, 228–250. *https://doi.org/10.1016/j.gloplacha.2016.06.008*

Holland, P.R. (2014). The seasonality of Antarctic sea ice trends. *Geophysical Research Letters*, 41(12), 4230–4237. *https://doi.org/10.1002/2014GL060172*

Holland, P.R., and Kwok, R. (2012). Wind-driven trends in Antarctic sea-ice drift. *Nature Geoscience*, 5, 872–875.

IMBIE Team (2018). Mass balance of the Antarctic Ice Sheet from 1992 to 2017. *Nature,* 558, 219–222.

Joughin, I., Smith, B.E., and Medley, B. (2014). Marine ice sheet collapse potentially under way for the Thwaites Glacier Basin, West Antarctica. *Science*, 344(6185), 735–738. *https://doi.org/10.1126/science.1249055*

Kacimi, S., and Kwok, R. (2020). The Antarctic sea ice cover from ICESat-2 and CryoSat-2: freeboard, snow depth and ice thickness. *The Cryosphere*, 14, 4453–4474.

Kennicutt, M., Chown, S.L., Cassano, J., Liggett, D., Massom, R., Peck, L., Rintoul, S., Storey, J., Vaughan, D., Wilson, T., and Sutherland, W.J. (2014). Six priorities for Antarctic science. *Nature*, 512, 23–25. *https://doi.org/10.1038/512023a*

Key, J. R., Mahoney, R., Liu, Y., Romanov, P., Tschudi, M., Appel, I., Maslanik, J., Baldwin, D., Wang, X., and Meade, P. (2013). Snow and ice products from Suomi NPP VIIRS, *Journal of Geophysical Research: Atmospheres*, 118, 12816–12830. *https://doi.org/10.1002/2013JD020459*

Kurtz, N. T., and Markus, T. (2012). Satellite observations of Antarctic sea ice thickness and volume, *Journal of Geophysical Research*, 117, C08025. doi:10.1029/2012JC008141

Kurtz, N., Studinger, M., Harbeck, J., Onana, V., and Farrell, S. (2012, updated 2015). *IceBridge Sea Ice Freeboard, Snow Depth, and Thickness, Version 1*. NASA National Snow and Ice Data Center Distributed Active Archive Center, Boulder, Colorado USA. *https://doi.org/10.5067/7XJ9HRV50O57*

Kwok, R. (2010). Satellite remote sensing of sea-ice thickness and kinematics: A review. *Journal of Glaciology*, 56(200), 1129–1140. *https://doi.org/10.3189/002214311796406167*

Kwok, R., and Maksym, T. (2014). Snow depth of the Weddell and Bellingshausen sea ice covers from IceBridge surveys in 2010 and 2011: An examination. *Journal of Geophysical Research: Oceans*, 119, 4141–4167. *https://doi.org/10.1002/2014JC009943*

Kwok, R., and Rothrock, D.A. (2009). Decline in Arctic sea ice thickness from submarine and ICESat records: 1958–2008, *Geophysical Research Letters*, 36, L15501. doi:10.1029/2009GL039035

Kwok, R., Pang, S.S., and Kacimi, S. (2017). Sea ice drift in the Southern Ocean: regional patterns, variability, and trends. *Elementa: Science of the Anthropocene*, 5, 32. *http://doi.org/10.1525/elementa.226*

Li, X., Ouyang, L., Hui, F., Cheng, X., Shokr, M., and Heil, P. (2018). An Improved Automated Method to Detect Landfast Ice Edge off Zhongshan Station Using SAR Imagery. *IEEE Journal of Selected Topics in Applied Earth Observations and Remote Sensing*, 11, 4737–4746.

Liu, H., Wang, L., and Jezek, K. (2006). Spatio-temporal variations of snow melt zones in Antarctic Ice Sheet derived from satellite SMMR and SSM/I data (1978–2004), *Journal of Geophysical Research*, 111, 1–20, F01003. *https://doi.org/10.1029/2005JF000318*

Long, D.G. (2008). Microwave sensors—Active and passive. In: *Manual of Remote Sensing, Volume 3: Remote Sensing for the Earth Sciences*. (Eds: R.A. Ryerson and A.N. Rencz). John Wiley and Sons, Hoboken, New Jersey, USA.

Lubin, D., and Massom, R.A. (2006). *Polar Remote Sensing. Volume 1: Atmosphere and Polar Oceans*. Praxis/Springer, Chichester, UK, and Berlin, Germany. 756 p.

Luckman, A., Elvidge, A., Jansen, D., Kulessa, B., Kuipers Munneke, P., King, J., and Barrand, N. (2014). Surface melt and ponding on Larsen C Ice Shelf and the impact of föhn winds. *Antarctic Science*, 26(6), 625–635. *https://doi.org/10.1017/S0954102014000339*

McMillan, M., Shepherd, A., Sundal, A., Briggs, K., Muir, A., Ridout, A., Hogg, A., and Wingham, D. (2014). Increased ice losses from Antarctica detected by CryoSat-2. *Geophysical Research Letters,* 41, 3899–3905. *https://doi.org/10.1002/2014GL060111*

Maksym, T., Stammerjohn, S.E., Ackley, S., and Massom, R. (2012). Antarctic sea ice—A polar opposite? *Oceanography*, 25(3), 140–151. *http://dx.doi.org/10.5670/oceanog.2012.88*

Markus, T., Neumann, T., Martino, A., Abdalati, W., Brunt, K., Csatho, B., Farrell, S., Fricker, H., Gardner, A., Harding, D., Jasinski, M., Kwok, R., Magruder, L., Lubin, D., Luthcke, S., Morison, J., Nelson, R., Neuenschwander, A, Palm, S, Popescu, S, Shum., C, K., Schutz, B. E., Smith, B., Yang, Y. K., Zwally, J., (2017). The Ice, Cloud, and land Elevation Satellite-2 (ICESat-2): Science requirements, concept, and implementation. *Remote Sensing of Environment*, 190, 260–273. *https://doi.org/10.1016/j.rse.2016.12.029*

Massom, R.A. (2006). Remote Sensing. In *Encyclopedia of Antarctica Volume 2* (Ed: B. Riffenburgh). Routledge, New York, pp. 790–796.

Massom, R.A. (2009). Principal Uses of Remote Sensing in Sea-Ice Field Research. In *Handbook on Field Techniques in Sea-Ice Research* (Eds: H. Eicken *et al.*,). University of Alaska Press, Fairbanks, USA, pp. 405–466.

Massom, R.A., and Lubin, D. (2006). *Polar Remote Sensing. Volume 2: Ice Sheets*. Praxis/Springer, Chichester, UK, and Berlin, Germany. 426 p.

Massom, R.A. and Stammerjohn, S.E. (2010). Antarctic sea ice change and variability—Physical and ecological implications. *Polar Science*, 4, 149–186.

Massom, R.A., H. Eicken, C. Haas, M.O. Jeffries, M.R. Drinkwater, M. Sturm, A.P. Worby, X. Wu, V.I. Lytle, S. Ushio, K. Morris, P.A. Reid, S. Warren, and I. Allison. (2001a). Snow on Antarctic sea ice. *Reviews of Geophysics*, 39(3), 413–445.

Massom, R.A., Hill, K., Lytle, V.I., Worby, A., and Allison, I. (2001b). Effects of regional fast-ice and iceberg distributions on the behaviour of the Mertz Glacier Polynya, East Antarctica. *Annals of Glaciology*, 33, 391–398.

Massom, R.A., Stammerjohn, S.E., Smith, R.C., Pook, M.J., Iannuzzi, R.A., Adams, N., Martinson, D.G., Vernet, M., Fraser, W.R., Quetin, L.B., Ross, R.M., Massom, Y., and Krouse, H.R. (2006). Extreme anomalous atmospheric circulation in the West Antarctic Peninsula region in austral spring and summer 2001/2, and its profound impact on sea ice and biota. *Journal of Climate*, 19, 3544–3571.

Massom, R.A., Hill, K., Barbraud, C., Adams, N., Ancel, A., Emmerson L., and Pook, M.J. (2009). Fast ice distribution in Adélie Land, East Antarctica: Interannual variability and implications for emperor penguins (*Aptenodytes forsteri*). *Marine Ecology Progress Series*, 374, 243–257.

Massom, R.A., Giles, A.B., Fricker, H.A., Warner, R.C., Legresy, B., Hyland, G., Young, N., and Fraser, A.D. (2010). Examining the interaction between multi-year landfast sea ice and the Mertz Glacier Tongue, East Antarctica: Another factor in ice sheet stability? Journal of Geophysical Research, 115, C12027. *https://doi.org/10.1029/2009JC006083*

Massom, R.A., Reid, P., Stammerjohn, S., Raymond, B., Fraser A., and Ushio, S. (2013). Change and variability in East Antarctic sea ice seasonality, 1979/80–2009/10. *PloS ONE*, 8(5), e64756. *https://doi.org/10.1371/journal.pone.0064756*

Massom, R.A., Scambos, T.A., Bennetts, L.G., Reid, P., Squire, V.A., and Stammerjohn, S.E. (2018). Antarctic ice shelf disintegration triggered by sea ice loss and ocean swell. *Nature,* 558, 383–389.

Meredith, M.P., and Brandon, M.A. (2016). Oceanography and Sea ice In the Southern Ocean. In *Sea Ice*, 3rd edn (Ed: D.N. Thomas). Wiley-Blackwell, New York (USA) and Oxford (UK), pp. 216–238.

Mouginot, J., Rignot, E., and Scheuchl, B. (2014). Sustained increase in ice discharge from the Amundsen Sea Embayment, West Antarctica, from 1973 to 2013. *Geophysical Research Letters*, 41, 1576–1584. *https://doi.org/10.1002/2013GL059069*

NAS (2017). *Antarctic Sea Ice Variability in the Southern Ocean-Climate System: Proc. Of a Workshop*. The National Academies Press, National Academies of Sciences, Engineering, and Medicine, Washington, DC. doi:10.17226/24696. *https://www.nap.edu/catalog/24696/antarctic-sea-ice-variability-in-the-southern-ocean-climate-system*

NASA (2019). *IceBridge Mission* webpage, National Aeronautical and Space Agency: *https://www.nasa.gov/mission_pages/icebridge/index.html*

Newman, L., Heil, P., Trebilco, R., Katsumata, K., Constable, A., van Wijk, E., Assmann, K., Beja, J., Bricher, P., Coleman, R., Costa, D., Diggs, S., Farneti, R., Fawcett, S., Gille, S.T., Hendry, K.R., Henley, S., Hofmann, E., Maksym, T., Mazloff, M., Meijers, A., Meredith, M.M., Moreau, S., Ozsoy, B., Robertson, R., Schloss, I., Schofield, O., Shi, J., Sikes, E., Smith, I.J., Swart, S., Wahlin, A., Williams, G., Williams, M.J.M., Herraiz-Borreguero, L., Kern, S., Lieser, J., Massom, R.A., Melbourne-Thomas, J., Miloslavich, P., and Spreen, G. (2019). Delivering sustained, coordinated and integrated observations of the Southern Ocean for global impact. *Frontiers in Marine Science*, 6. *https://doi.org/10.3389/fmars.2019.00433*

Nihashi, S., and Ohshima, K.I. (2015). Circumpolar mapping of Antarctic coastal polynyas and landfast sea ice: Relationship and variability. *Journal of Climate*, 28, 3650–3670. *https://doi.org/10.1175/JCLI-D-14-00369.1*

Notz, D., and Bitz, C.M. (2016). Sea Ice in Earth System Models. In *Sea Ice*, 3rd edn (Ed: D.N. Thomas). Wiley-Blackwell, New York (USA) and Oxford (UK), pp. 239–260.

NSIDC (2019a). National Snow and Ice Data Center, *SOTC (State of the Cryosphere): Ice Sheets* webpage: *https://nsidc.org/cryosphere/sotc/ice_sheets.html*

NSIDC (2019b). National Snow and Ice Data Center. *Scientific Data Search* webpage: *https://nsidc.org/data/search/#keywords=sea+ice/sortKeys=score,,desc/facetFilters=%257B%257D/pageNumber=1/itemsPerPage=25*

Padman, L., Siegfried, M.R., and Fricker, H.A. (2018). Ocean tide influences on the Antarctic and Greenland Ice Sheets. *Reviews of Geophysics*, 56 (1), 142–184. *doi.org/10.1002/2016RG000546*

Paolo, F.S., Fricker, H.A., and Padman, L. (2015). Volume loss from Antarctic ice shelves is accelerating. *Science*, 348(6232), 327–331.

Parkinson, C.L. (2019). A 40-y record reveals gradual Antarctic sea ice increases followed by decreases at rates far exceeding the rates seen in the Arctic. *Proceedings of National Academy of Science*, 116, 14414–14423. *https://doi.org/10.1073/pnas.1906556116*.

Petrich, S. and Eicken, H. (2017). Overview of Sea Ice Growth and Properties. In *Sea Ice* 3rd edn (Ed: D.N. Thomas). Wiley, doi.org/10.1002/9781118778371.ch1

Pope, A., Wagner, P., Johnson, R., Shutler, J.D., Baeseman, J., and Newman. L. (2017). Community review of Southern Ocean satellite data needs. *Antarctic Science*, 29(2), 97–138. doi:10.1017/S0954102016000390

Post, A.L., Meijers, A.J.S., Fraser, A.D., Meiners, K.M., Ayers, J., Bindoff, N.L., Griffiths, H.J., Van de Putte, A.P., O'Brien, P.E., Swadling, K.M., and Raymond, B. (2014). Environmental Setting. Part 4 In *Biogeographic Atlas of the Southern Ocean*. (Eds: Broyer, C., Koubbi, P., Griffiths, H.J., Raymond, B., Udekem d'Acoz, C. d', Van de Putte, A.P., Danis, B., David, B., Grant, S., Gutt, J., Held, C., Hosie, G., Huettmann, F., Post, A., Ropert-Coudert, Y.) Scientific Committee on Antarctic Research, Cambridge, UK. 510 p. ISBN 978-0-948277-28-3

Pritchard, H.D., Arthern, R.J., Vaughan, D.G. and Edwards, L.A. (2009). Extensive dynamic thinning on the margins of the Greenland and Antarctic ice sheets. Nature, 461, 971–975.

Pritchard, H., Ligtenberg, S., Fricker, H., Vaughan, D.G., van den Broeke, M.R., and Padman, L. (2012). Antarctic ice-sheet loss driven by basal melting of ice shelves. *Nature*, 484, 502–505.

Reid P., and Massom R.A. (2015). Successive Antarctic sea ice extent records during 2012, 2013 and 2014. In: State of the Climate in 2014. *Bulletin of the American Meteorological Society*, 96 (7), S163–S164.

Reid, P., Stammerjohn, S., Massom, R.A., Barreira, S., Scambos, T., and Lieser, J.L. (2021). Sea ice extent, concentration, and seasonality [in *State of the Climate in 2020*]. *Bulletin of American Meteorology Society*, 102(8), S336–S338.

Rémy, F. and Parouty, S. (2009). Antarctice Ice Sheet and radar altimetry: A review. *Remote Sensing*, 1(4), 1212–1239. doi:10.3390/rs1041212. *https://www.mdpi.com/2072-4292/1/4/1212/htm*

Rignot, E., Casassa, G., Gogineni, P., Krabill, W., Rivera, A., and Thomas, R. (2004), Accelerated ice discharge from the Antarctic Peninsula following the collapse of Larsen B ice shelf. *Geophysical Research Letters*, 31, L18401. doi:10.1029/2004GL020697

Rignot, E,, Bamber, J.L., van den Broeke, M.R., Davis, C., Li, Y., van de Berg, W.J., and van Meijgaard, E. (2008). Recent Antarctic ice mass loss from radar interferometry and regional climate modelling. *Nature Geoscience*, 1, 106–110.

Rignot, E., Mouginot, J., and Scheuchl, B. (2011). Ice flow of the Antarctic Ice Sheet. *Science*, 333, 1427–1430.

Ryan, W.B.F., Carbotte, S.M., Coplan, J.O., O'Hara, S., Melkonian, A., Arko, R., Weissel, R.A., Ferrini, V., Goodwillie, A., Nitsche, F., Bonczkowski, J., and Zemsky, R. (2009). Global multi-resolution topography synthesis. Geochemistry, *Geophysics, Geosystems*, 10(3). *https://doi.org/10.1029/2008GC002332*

Scambos, T.A., Dutkiewicz, M.J., Wilson, J.C., and Bindschadler, R.A. (1992). Application of image cross-correlation to the measurement of glacier velocity using satellite image data. *Remote sensing of environment*, 42(3), 177–186.

Scambos, T., Hulbe, C., and Fahnestock, M. (2003). Climate-induced ice shelf disintegration in the Antarctic Peninsula. *Antarctic Research Series,* 79, 79–92. *https://doi.org/10.1029/AR079p0079*

Scambos, T.A., Bohlander, J.A., Shuman, C.A., and Skvarca, P. (2004). Glacier acceleration and thinning after ice shelf collapse in the Larsen B embayment, Antarctica. *Geophysical Research Letters*, 31, L18402. *https://doi.org/10.1029/2004GL020670*

Scambos, T., Sergienko, O., Sargent, A., MacAyeal, D., and Fastook, J. (2005). ICESat profiles of tabular iceberg margins and iceberg breakup at low latitudes. *Geophysical Research Letters*, 32(23). *https://doi.org/10.1029/2005GL023802*

Scambos, T., Haran, T., Fahnestock, M., Painter, T., and Bohlander, J. (2007). MODIS-based Mosaic of Antarctica (MOA) Data Sets: Continent-wide Surface Morphology and Snow Grain Size. *Remote Sensing of Environment* 111(2), 242–257. *http://dx.doi.org/10.1016/j.rse.2006.12.020*

Shepherd, A., Fricker, H.A., and Farrell, S.L. (2018). Trends and connections across the Antarctic cryosphere. *Nature*, 558, 223–232.

Siegfried, M.R., and Fricker, H. (2018). Thirteen years of subglacial lake activity in Antarctica from multi-mission satellite altimetry. *Annals of Glaciology,* 59(76pt1), 42–55. *https://doi.org/10.1017/aog.2017.36*

Slater, T., Shepherd, A., McMillan, M., Muir, A., Gilbert, L., Hogg, A.E., Konrad, H., and Parrinello, T. (2017). A new Digital Elevation Model of Antarctica derived from CryoSat-2 altimetry, *The Cryosphere*, 12(4), 1551–1562. *https://doi.org/10.5194/tc-12-1551-2018*

Smith, B., Fricker, H.A., Gardner, A.S., Medley, B., Nilsson, J., Paolo, F.S., Holschuh, N., Adusumilli, S., Brunt, K., Csatho, B., Harbeck, K., Markus, T., Neumann, T., Siegfried, M.R., and Zwally, H.J. (2020). Pervasive ice sheet mass loss reflects competing ocean and atmosphere processes. *Science*, 368(6496), 1239. *https://doi.org/10.1126/science.aaz5845*

Spreen, G. and Kern, S. (2016). Methods of satellite remote sensing of sea ice. In *Sea Ice*, 3rd edn (Ed: D.N. Thomas). Wiley-Blackwell, New York (USA) and Oxford (UK), pp. 239–260.

Stammerjohn, S., and Maksym, T. (2016). Gaining (and losing) Antarctic sea ice: variability, trends and mechanisms. In *Sea Ice* (Ed: D.N. Thomas). John Wiley and Sons, Ltd. pp. 261–289.

Stammerjohn, S., Massom, R., Rind, D., and Martinson, D. (2012). Regions of rapid sea ice change: An inter-hemispheric seasonal comparison. *Geophysical Research Letters*, 39, L06501. *https://doi.org/10.1029/2012GL050874*

Steig, E., Schneider, D., Rutherford, S., Mann, M., Comiso, J., and Shindell, D. (2009). Warming of the Antarctic ice-sheet surface since the 1957 International Geophysical Year. *Nature*, 457, 459–463. *https://doi.org/10.1038/nature07669*

Sturm, M., and Massom, R.A. (2017). Snow in the Sea Ice System: Friend or Foe? In *Sea Ice*. 3rd edn (Ed: D. Thomas). Wiley-Blackwell, New York (USA) and Oxford (UK), pp. 65–109.

Swithinbank, C.W.M. (1988). Antarctica. In *Satellite Image Atlas of Glaciers of the World*. (Eds: R.S. Williams, Jr and J.G. Ferrigno). United States Geological Survey, Washington DC, USA. B1–B278.

Tamura, T., Ohshima, K. I., Fraser, A. D., and Williams, G. D. (2016). Sea ice production variability in Antarctic coastal polynyas. *Journal of Geophysical Research: Oceans*, 121, 2967–2979. doi:10.1002/2015JC011537

Thomas, D.N. (Ed.) (2017). *Sea Ice*, 3rd edn. Wiley-Blackwell, New York (USA) and Oxford (UK). ISBN: 978-1-118-77838-8. 664 p.

Tschudi, M., Fowler, C.W., Maslanik, J.A., Stewart, J.S., and Meier, W. (2016). *EASE-Grid Sea Ice Age*. Version 3. NASA NSIDC Distributed Active Archive Center, Boulder, Colorado, USA,.

Turner, J., and Comiso, J. (2017). Solve Antarctica's sea-ice puzzle. *Comment in Nature*, 547, 19–21. *https://doi.org/10.1038/547275a*

Turner, J., Hosking, J.S., Bracegirdle, T.J., Marshall, G.J., and Phillips, T. (2015). Recent changes in Antarctic Sea ice. *Philosophical Transactions of the Royal Society of London A: Mathematical, Physical and Engineering Sciences*, 373(2045), 20140163. *https://doi.org/10.1098/rsta.2014.0163*

Turner, J., Hosking, J.S., Marshall, G.J., Phillips, and T., Bracegirdle, T.J. (2016). Antarctic sea ice increase consistent with intrinsic variability of the Amundsen Sea Low. *Climate Dynamics*, 46, 2391–2402. *https://doi.org/10.1007/s00382-015-2708-9*.

USGS (2021). *Ice, Snow, and Glaciers and the Water Cycle* webpage, United States Geological Survey website: *https://www.usgs.gov/special-topic/water-science-school/science/ice-snow-and-glaciers-and-water-cycle?qt-science_center_objects=0#qt-science_center_objects*

Vancoppenolle, M., Meiners, K.M., Michel, C., Bopp, L., Brabant, F., Carnat, G., Delille, B., Lannuzel, D., Madec, G., Moreau, S., Tison, J.-L., and van der Merwe, P. (2013). Role of sea ice in global biogeochemical cycles: emerging views and challenges. *Quaternary Science Reviews*, 79, 207–230.

Velicogna, I., and Wahr, J. (2006). Measurements of time-variable gravity show mass loss in Antarctica. *Science,* 311, 1754–1756.

Webster, M., Gerland, S., Holland, M., Hunke, E., Kwok, R., Lecomte, O., Massom, R., Perovich, D., and Sturm, M. (2018). Snow in the changing sea-ice systems. *Nature Climate Change*, 8, 946–953.

Weeks, W.F. (2010). *On Sea Ice*. University of Alaska Press, Fairbanks, Alaska, USA. 664 p.

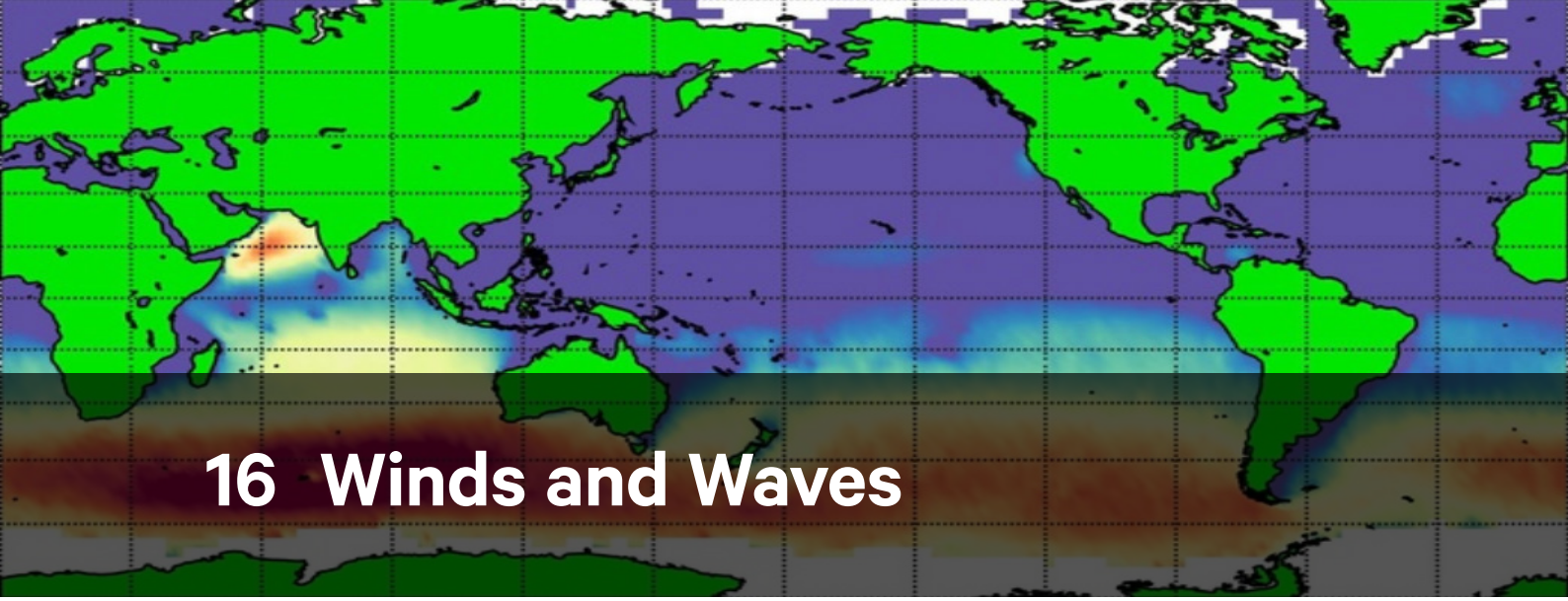
WMO (2021). *Sea-ice Information Services in the World* (WMO-No. 574). World Meteorological Organisation, Geneva, Switzerland. *https://library.wmo.int/index.php?lvl=notice_display&id=7542#.YbFJlL1ByUk*

Wongpan, P., Meiners, K.M., Langhorne, P.J., Heil, P., Smith, I.J., Leonard, G.H., Massom, R.A., Clementson, L.A. and Haskell, T.G. (2018). Estimation of Antarctic land-fast sea ice algal biomass and snow thickness from under-ice radiance spectra in two contrasting areas. *Journal of Geophysical Research—Oceans*, 123(3), 1907–1923.

Worby, A.P., Massom, R. A., Allison, I., Lytle, V. I., and Heil, P. (1998). East Antarctic sea ice: A review of its structure, properties and drift. In *Antarctic Sea Ice Physical Processes, Interactions and Variability*, Antarctic Research Series, 74 (Ed: M.O. Jeffries). pp. 41–68. AGU, Washington D.C.

Worby A., Markus, T., Steer, A., Lytle, V., and Massom, R. (2008). Evaluation of AMSR-E snow depth product over East Antarctic sea ice using in situ measurements and aerial photography. *Journal of Geophysical Research*, 113, C05S94. *https://doi.org/10.1029/2007JC004181*

Zwally, H.J., Giovinetto, M.B., Beckley, M.A., and Saba, J.L. (2012). *Antarctic and Greenland drainage systems* webpage. NASA GSFC Cryospheric Sciences Laboratory, Greenbelt, Maryland, USA. *http://icesat4.gsfc.nasa.gov/cryo_data/ant_grn_drainage_systems.php*



16 Winds and Waves

Mark Hemer and Salman Khan

The marine atmospheric boundary layer is the location of exchanges between the atmosphere and ocean. This exchange occurs in the form of fluxes of energy, momentum, heat, freshwater, gases, and other tracers, and is strongly modulated by interactions between surface winds (on the atmospheric side) and surface waves (on the oceanic side) across the interface (see Excursus 16.1).

Further to these Earth system interactions (see Excursus 7.2), several other marine and coastal sectors need information about marine surface winds and waves. These include sectors requiring near real time data, such as safety at sea and at the coast (see Excursus 2.1), and those requiring long time series data to aid planning and design requirements for marine and coastal Infrastructure. Thus, marine surface winds and waves represent marine data in high demand.

Few *in situ* marine wind datasets exist in the Australian region, and observations are strongly dependent on Earth Observation (EO) data, retrieved from several sensors and platforms. In the Australian region, a loosely coordinated network of *in situ* wave buoys are deployed around the Australian coast, which provide valuable near real time data (see Section 16.3.1). *In situ* buoy data also provide a basis for ground truthing of surface waves measured from satellite platforms, which in turn provide valuable spatial representation of wave fields for broad application.

In the following two sub-sections, we introduce marine winds and waves in Australian surface waters (see Section 16.1), and those EO sensors that are appropriate for observing them (see Sections 16.2 and 16.3).

Background image: Mean monthly global significant wave height for July (southern winter) derived from 33 years of satellite altimeter data (1985–2018). The colours represent wave heights from 2 m (blue) to nearly 5 m (red). This image shows the large wind waves of the Southern Ocean that propagate into the Indian and Pacific oceans as swell. Source: IMOS. Retrieved from *https://imos.org.au/news/newsitem/altimeter-wind-and-wave-database-on-aodn/*

Recommended Chapter Citation: Hemer, M.A., and Khan, S.S. (2021). Waves Ch 16 in *Earth Observation: Data, Processing and Applications. Volume 3B—Surface Waters*. CRCSI, Melbourne. pp. 311–328. ISBN 978-0-6482278-5-4.

Excursus 16.1—Marine Surface Winds and Waves

Surface marine winds are turbulent in nature, with high frequency variability between gusts and relative lulls. Winds are typically represented by average wind speed and direction over a 10-minute period, at some reference level (typically 10 m above sea level). Gusts during the 10-minute period are typically 40% greater than the average wind speed.

The surface wave field at any location can be described by a frequency-directional spectrum (see Excursus 4.2). This spectrum includes peaks of energy representing the:

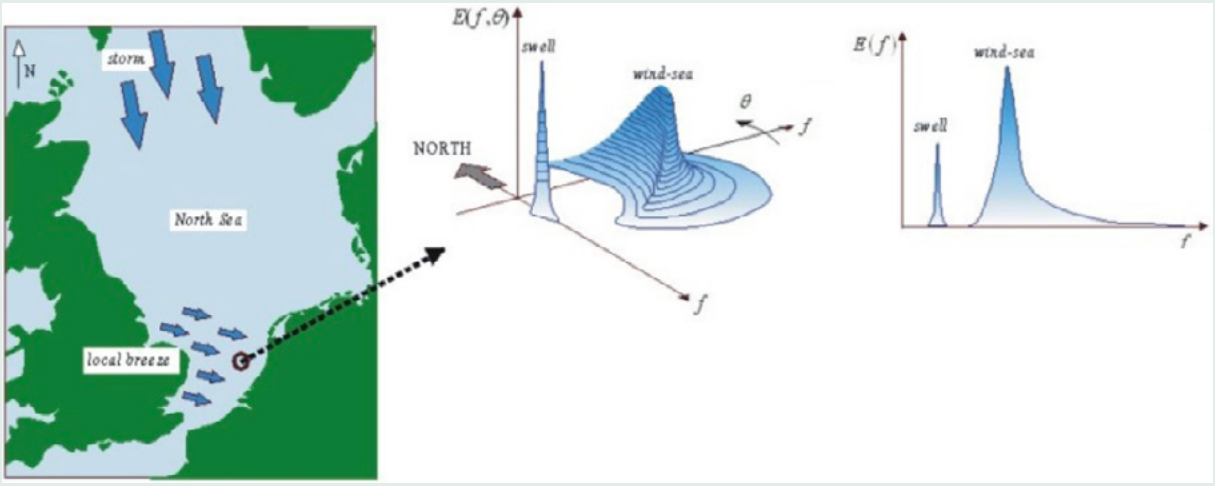
- high frequency (short wavelength) 'wind-sea'—the waves generated locally by the surface winds present at the site; and
- lower frequency (longer wavelength) 'swell'—the waves that have travelled to the site, having been generated by a distant storm (see Figure 16.1).

Multiple swell peaks may exist, if waves are received from different generating systems at the same time. The complexity of such wave fields is typically summarised via several integrated parameters. The parameters include:

- Significant Wave Height (SWH or HS), to represent the energy of the wave field, and is defined as the average wave height, from trough to crest, of the highest one-third of the waves in the field (see Figure 16.2). Significant wave height can be equivalently defined as four times the square root of the zeroth-order moment (area) of the wave spectrum (H_m0).
- Mean and/or peak wave period are often used to represent the period, frequency, or length of waves. The mean wave period I is the mean of all wave periods in a time series representing the sea state, and the peak wave period (T_p), represents the period/frequency at which the spectral peak in energy occurs.
- Directional characteristics of the wave field are represented by the mean or peak wave direction. The mean wave direction (q_m) is the average of all wave directions in the wave spectrum, and peak wave direction (θ_p) is the direction at which the spectral peak in the directional energy spectrum occurs.

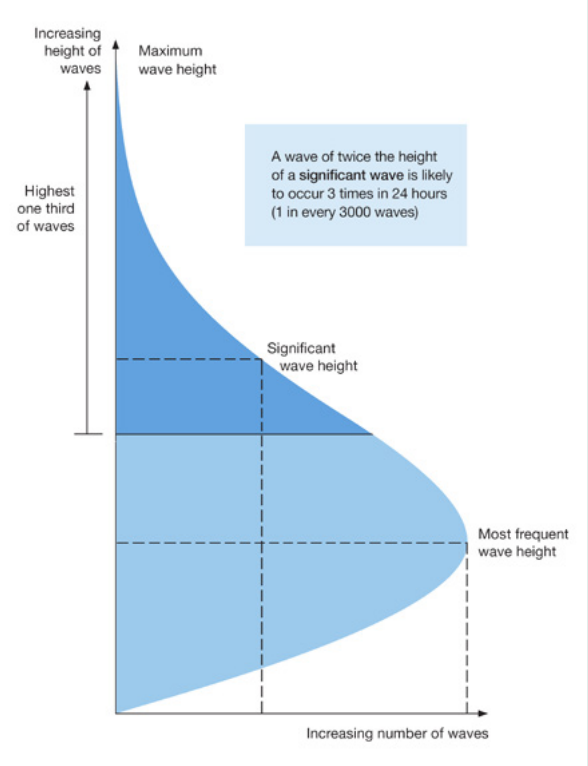
Figure 16.1 Example wave spectrum

This schematic shows one- and two-dimensional wave spectra at the circled location near the coast of Holland, where a long wave swell from the northern North Sea meets a local breeze crossing the southern North Sea. These two forces interact to generate a swell of relatively uniform frequency and direction, and a wind-sea with broader frequency and direction.



Source: ECMWF (2021) (Adapted from: Holthuijsen, 2007, Figure 3.13)

Figure 16.2 Significant wave height



Source: BoM (2021)

For multi-modal seas, neither mean nor peak wave parameters adequately describe the wave field. In these instances, the wave spectrum may be 'partitioned', with integrated parameters defined for individual (wind-sea and swell) peaks in the spectrum.

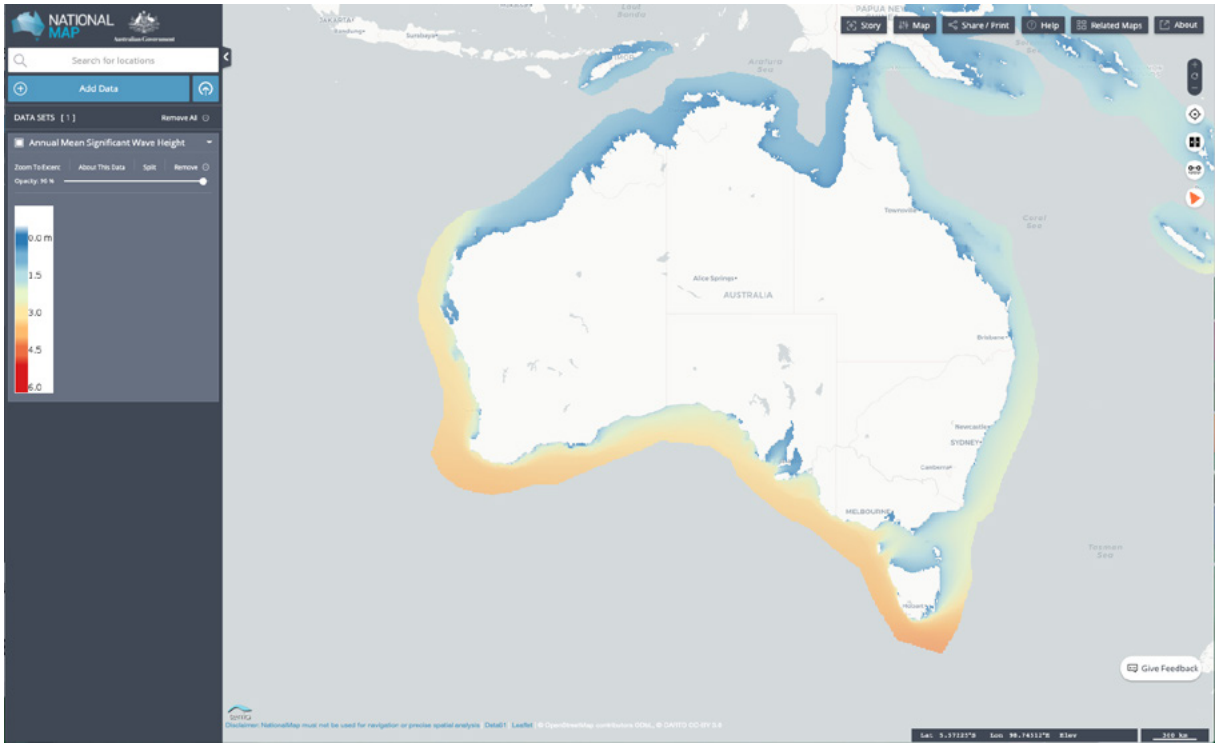
16.1 Winds and Waves in Australian Surface Waters

The wide latitudinal variation covered by Australia's marine jurisdiction spans a broad range of extremes in marine surface winds and waves (see Section 2.1). Surface marine winds range from the strong extratropical winds of the 'Roaring Forties' (and Furious Fifties) south of the continent, through to the tropical belt, with strong seasonal trade wind/monsoon variability, and tropical cyclone (TC) systems. In the mid-latitudes, intense low pressure systems on the east coast (East Coast Lows and Tasman Lows) can drive severe wind and wave hazards along Australia's most populated coasts.

The strong winds of the Southern Ocean generate swell that propagates northwards and dominates the wave field observed on Australia's southern and western coasts (see banner image at start of Section 16). Waves along Australia's east coast are more variable, often with multiple spectral peaks received from a range of generating systems to the south (Southern Ocean and Tasman Sea) and north (Coral Sea). The waves across the north are typically much lower, except during TC events.

Australia's long, southern-facing coastline gives rise to arguably the largest wave energy resource of any country in the world (Hemer *et al.*, 2018). Wind-waves offer advantages as a source of renewable energy given their predictability and consistency, relative to wind and solar, and are being studied for viable energy generation. The Australian Marine Energy Atlas builds on more than 35 years of wind, wave, and tide data to highlight areas with highest potential for energy deployment (see Figure 16.3). Satellite-measured surface marine winds and waves have provided an invaluable validation dataset to assess the spatiotemporal variability of these resources across the Australian region.

Figure 16.3 Australian Marine Energy Atlas



Source: NationalMap. Retrieved from: *https://nationalmap.gov.au/#share=s-daInLA798vii3unPUIMipsuweqi*

16.2 EO Sensors for Winds

A wide variety of EO sensors has been used to map and monitor marine winds (see Table 16.1). Six of these technologies are described in the sub-sections below.

Table 16.1 EO sensors relevant to water waves

SAR: Synthetic Aperture Radar

Type	Sensor	Platform	Relevance	Advantages	Disadvantages
Passive optical	Multispectral radiometer	Satellite	Wave texture, Sunglint	Global coverage, low cost	Low accuracy, coarse scale
Passive microwave	Microwave radiometer	Satellite	Ocean roughness, Surface wind stress	Frequent, global coverage	Impacted by rain
Active microwave	SAR	Satellite or airborne	Surface waves in oceans, wave forecasting, Resolution of directional swell wave spectra	All weather, so useful in tropical regions	High cost, specialised processing, spectral representation limited to long wavelength swell
	Radar altimeter	Satellite	Significant wave height, Surface wind speed,	All weather, so useful in tropical regions	Limited representation of wave field, low frequency sampling
	Scatterometer	Satellite	Surface wind speed and direction,	Frequent, global coverage	Impacted by rain and extreme winds
	Surface Waves Investigation and Monitoring (SWIM) wave scatterometer	CFOSAT	Significant wave height, Directional wave spectrum	Resolution of directional wave spectrum	Single platform (experimental)

16.2.1 *In situ* wind measurements

Few *in situ* marine wind measurements exist in the Australian region, or indeed the Southern Hemisphere. The standard method of marine wind observations is from surface buoys, deployed for weather, navigational, and industrial applications. In Australia, surface marine wind data are predominantly industry owned and operated, and associated with the oil and gas sector (on the North West Shelf, and eastern Bass Strait). In very recent times, industry data also encompasses observations collected for the Star of the South Offshore Wind Project, proposed off the coast of east Gippsland, Victoria. *In situ* surface marine wind observations for which data is openly available is limited to a single meteorological buoy, deployed as part of the Integrated Marine Observing System (IMOS) Southern Ocean Flux Station (SOFS) mooring, in the Sub-Antarctic Zone (46.7°S, 142°E) approximately 350 nautical miles (M) southwest of Tasmania. The SOFS mooring was first deployed in March 2010, and a non-continuous data record spans through to the most recent deployment in April 2021.

This lack of regional *in situ* data has driven high dependency on remotely sensed marine surface winds in studies validating Numerical Weather Prediction (NWP) models for marine surface wind prediction (e.g. Schulz *et al*., 2007). In some such studies, coastal *in situ* observations have been used for this purpose (e.g. Bender, 1996; Alves *et al*., 2002) but these are typically confounded by land effects, and poorly represent the marine winds (Schulz *et al*., 2007). To adequately calibrate and assess the quality of satellite remotely sensed winds, high quality *in situ* buoy data with broad geographic distribution, and of sufficient length, is required. The most used buoy dataset is the US National Data Buoy Centre (NDBC; NDBC, 2009) and is typically considered suitable for the process. The European Centre for Medium Range Weather Forecasts (ECMWF) also manage a buoy database, sourced from several agencies, which has been also used for this purpose (Young *et al*., 2017).

While *in situ* wind measurements for calibration of satellite data are required at a standard reference height of 10 m above sea level, wind anemometers on buoys record measurements at a variety of different heights. These measurements are then translated to 10 m reference height assuming the logarithmic (neutral) boundary layer wind profile (Young *et al*., 2017, 2020; Ribal and Young, 2020). Neutral boundary layer assumptions are made because simultaneous measurements of boundary layer stability (sea surface temperature, air temperature, humidity, etc.) are seldom available. This assumption naturally introduces a calibration error, especially at geographical locations with large stability effects (Young and Donelan, 2018), which should ideally be taken into account (Jang *et al*., 2019). However, when the calibrations are carried out across many different buoys (and locations) and over many years, a broad range of stability conditions is encountered. Hence, on a global scale, it is commonly assumed that such stability effects are averaged out in the calibration (Young *et al*., 2020).

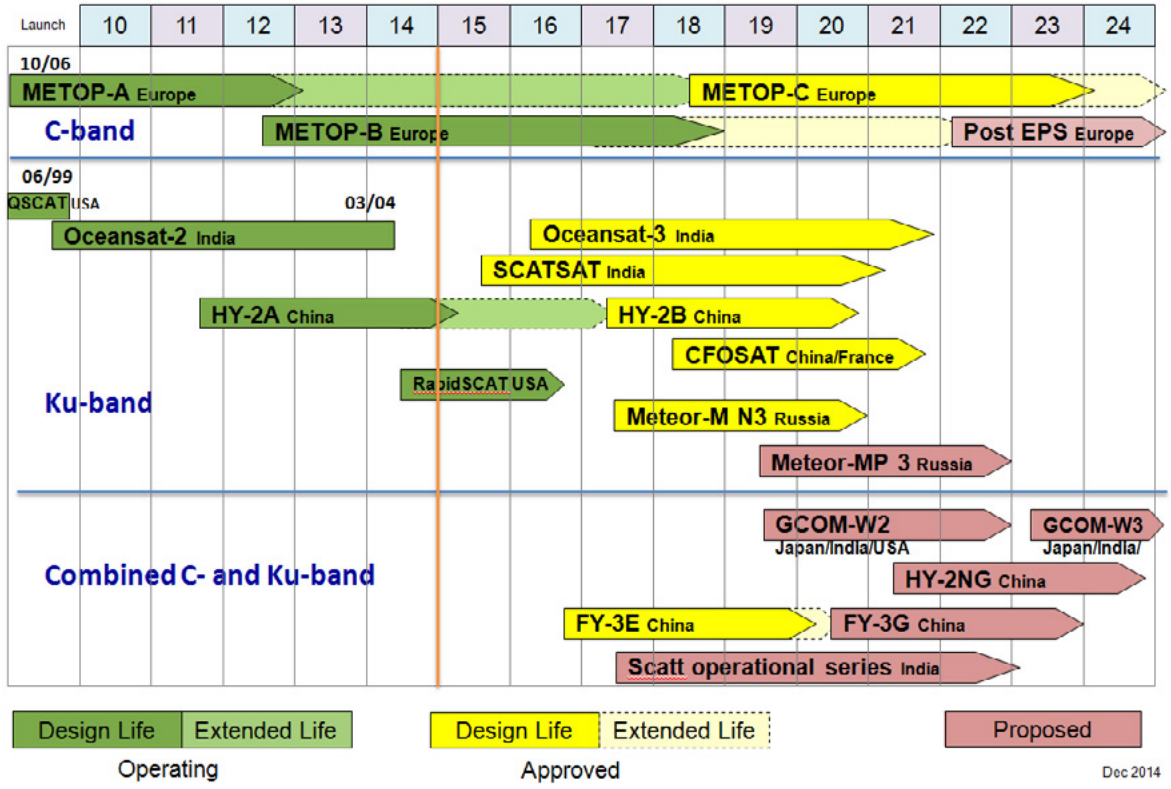
16.2.2 Scatterometers

Satellite scatterometers are active microwave radars with the primary goal of measuring near-surface wind speed and direction over the ocean (see Section 9.6). Scatterometers operate in a side-looking geometry (never observing directly below the satellite) and illuminate the ocean surface at incidence angles typically in the range 20–70°. The electromagnetic wavelength at which these instruments operate varies from 2 cm (Ku-band: NSCAT, QuikSCAT, OSCAT-1, RapidScat, ScatSat) to 5 cm (C-band: ERS, ASCAT). At these viewing geometries and wavelengths, the microwaves are resonant (to the first order) to ocean surface roughness produced by capillary waves, which are the first wave ripples formed due to wind stress on the ocean surface (Wright, 1966). This resonance (often referred to as Bragg scattering) modulates the fraction of energy scattered back towards the radar, and has been experimentally found to be a function of surface wind speed and direction for fixed viewing geometry and instrument properties (Jones and Schroeder, 1978; Stoffelen and Anderson, 1997).

At a given wind direction (relative to the radar look geometry), the backscattered energy increases with wind speed before saturating at a certain level. However, at a given wind speed the backscatter is modulated by the relative wind direction: it has minima at cross-wind directions and maxima at upwind and downwind directions (upwind direction gives slightly stronger backscatter than downwind). Because a single backscatter value can be attributed to a number of wind speed and direction pairs, scatterometers view the ocean surface from several angles to eliminate unlikely wind direction solutions (Stoffelen and Portabella, 2006). Ideally, the solution corresponds to the true wind direction. However, noise in the observations, mostly at low wind speeds and weak backscatter, can affect the quality of fit and thereby result in incorrect directions to be selected. The next best fit is typically in approximately the opposite direction, while the next two minima are in directions roughly perpendicular to the true wind direction.

Figure 16.4 Scatterometer missions

Operating, approved, and planned scatterometer missions, promising an unprecedented amount of ocean observations in the future.



Source: CEOS (2014)

Scatterometers are wide swath instruments (~500–1800 km) with a spatial resolution of 12.5–50 km and rapid global coverage. They are the instrument of choice for global open ocean surface wind vector measurement but become less effective closer to the coast due to contamination of the large scatterometer footprint by land, islands, and other man-made structures. Scatterometer signals are also affected by rain (more in Ku-band than in C-band) and for this reason scatterometer measurements of extreme winds in TC, especially in Ku-band, must be interpreted with caution as a significant portion of the wind field in the storm is generally affected by heavy rain. Moreover, co-polarised (co-pol) scatterometers (HH/VV) lose sensitivity to high winds and start to saturate above wind speeds of ~35 m/s (the strength of Category-1 hurricanes), which makes accurate wind estimates in intense storms difficult. Scatterometers have been widely used for wind data assimilation in NWP models. QuickSCAT (1999–2009), MetOp-A (2007 onwards), MetOp-B (2012 onwards), and ScatSat have all been assimilated in NWP models at various agencies.

Many datasets acquired by satellite scatterometers are available in the public domain:

- QuikSCAT, MetOp-A, OceanSat-2, MetOp-B, and RapidScat data are available from PO.DAAC (*https://podaac.jpl.nasa.gov/*); and
- ERS-1 and ERS-2 data are available from EUMETSAT (*http://archive.eumetsat.int*) and ESA (*https://earth.esa.int*), respectively.

Recently, a multi-mission, calibrated, inter-scatterometer, cross-validated database of scatterometers winds spanning six missions over 27 years (1992–2018) has been developed by the University of Melbourne (Ribal and Young, 2020) and made publicly available through Australia's IMOS ocean data portal, the Australian Ocean Data Network (AODN). These existing databases, and the future prospects with many planned scatterometer missions (see Figure 16.4) will vastly increase the amount of ocean surface wind observations, and represent a revolution in ocean observing.

16.2.3 Passive microwave radiometers

Microwave radiometers are passive instruments that sense the ocean surface brightness temperature, which is related to the emissivity and reflective properties of the ocean surface, explained by the electromagnetic theory of radiative transfer (Ulaby *et al*., 1981; see Sections 9.2 and 14.3.1). The ocean brightness temperature is a function of the ocean roughness (including white capping, wave breaking, and foam) and therefore surface wind stress. Surface wind speed can thus be derived from ocean brightness temperatures typically assuming a neutral boundary layer and a constant value of the drag coefficient. If the radiometer is also fully polarimetric, that is, complete information about the electromagnetic polarisation state (four Stoke's parameters) is available, then the wind direction relative to radiometer look direction can also be derived (Yueh *et al*., 1999). At low wind speed (< ~8 m/s) the directional signal can be noisy, leading to large uncertainties in the wind direction (> ~30°; Bourassa *et al*., 2019).

Radiometers have a wide swath of approximately 1,000–1,400 km and a resolution of about 25–40 km. Because of their wide swath they are typically able to cover most of the Earth within a day or two. However, most traditional radiometers operate in high frequency bands such as X- and K- (SSM/I and SSMIS series, AMSR-2, AMSRE, AMSRJ, GMI, TMI, WindSat), and so are sensitive to rain (Meissner and Wentz, 2012) and also signal saturation at wind speed above ~33 m/s. Resulting daily radiometer measurements have large gaps because of rain, so radiometer-derived winds have been often referred to as fair-weather biased. Traditional radiometers are therefore not very suitable for mapping extreme winds in TC because a large portion of the wind field is also accompanied by heavy rainfall. This limitation is often utilised to derive rain rates (Meissner and Wentz, 2009), which are also delivered as standard products in addition to wind speed by different agencies (e.g. Naval Research Laboratory and Remote Sensing Systems). In some cases, the diversity of frequency bands, coupled with sophisticated geophysical retrieval algorithm design, can be employed to derive all-weather wind speeds as was done for WindSat (Meissner and Wentz, 2009). Alternatively, L-band radiometers, such as the Soil Moisture and Ocean Salinity (SMOS; Cotton *et al*., 2018) and the Soil Moisture Active Passive (SMAP; Meissner *et al*., 2017; see Section 19.7), are virtually unaffected by rain and their signal remains sensitive to wind speed as high as ~70 m/s (strength of Category-5 hurricanes) making them a suitable instrument for monitoring and tracking TC. However, they have lower sensitivity to wind speeds less than 15 m/s and their performance in this regime is worse than scatterometers.

Future missions include:

- NASA JPL's Compact Ocean Wind Vector Radiometer (COWVR) to be mounted on the International Space Station (~2023). It is similar to WindSat, but is more cost-effective and demonstrates new technology for future polarimetric microwave radiometers.
- Weather System Follow-on Microwave (WSF-M) mission is also a continuation of SSMIS and WindSat with similar accuracies to WindSat. The first of the two planned sensors will launch in 2023.
- ESA's Copernicus Imaging Microwave radiometer (CIMR; Donlon, 2019; Meijer, 2019) will have receiving channels in L-, C-, X-, Ku-, and Ka-bands, and a spatial resolution of 5–15 km (55 km at L-band) over a swath of 1920 km. This will be a follow-up of the SMOS and SMAP missions and also provide continuity of AMSR/2 low frequency channels. The prospective launch is 2025 and it is expected to have all-weather ocean wind measurement capability.

16.2.4 Satellite altimeters

The primary goal of satellite radar altimetry is the measurement of the distance between the satellite and the sea surface directly beneath the satellite, which after performing a series of corrections and averaging can be converted into sea surface height anomaly (surface currents) and also the mean sea level with respect to a reference ellipsoid (see Sections 9.5 and 12.2.1). However, opportunistic by-products of significant wave height (see Excursus 16.1) and scalar wind speed can also be derived from radar altimeter measurements.

Satellite altimeters have provided global coverage of wind speed and wave heights for more than three decades onboard polar orbiting satellites (Ribal and Young, 2019). The narrow nadir beam has a cross-track footprint width of ~10 km with typically 1 Hz (relatively high resolution) along-track sampling (every ~7 km). The ground-track separation of up to 400 km can produce considerable gaps in observation for an altimeter, but recently the presence of many altimeters has improved the density of coverage.

Although the instrument of choice for measuring global sea surface wind is a scatterometer, scalar wind speed can also be related to the Normalised Radar Cross Section (NRCS) of the sea surface at normal incidence. Several studies have formalised this relationship and some ground breaking studies were the works of Brown *et al*. (1981), Chelton and McCabe (1985), Chelton and Wentz (1986), Witter and Chelton, (1991), and Abdalla (2012).

The main idea behind deriving altimeter sea surface wind speed is the regression between satellite NRCS and reference wind measurements typically from *in situ* buoys or a NWP model. Generally, wind speed is inversely proportional to the radar backscatter (in dB) at normal incidence: it is the strongest when the sea surface is smooth (lull) and reduces as wind stress roughens the surface. However, overall this relationship is non-linear and only becomes linear as NRCS increases up to a certain threshold (NRCS ~11 dB; Abdalla, 2012; Ribal and Young, 2019), beyond which the relationship is non-linear. A piecewise function has been shown to fit this relationship to a reasonable degree of accuracy for Ku- and Ka-band (only SARAL/Altika) altimeters (Abdalla, 2012; Ribal and Young, 2019), while high wind speeds (> 18 m/s) can be modelled by alternative formulations such as that proposed in Young (1993) and Quilfen *et al.* (2011). There is evidence of the dependence of altimeter wind speed on wave heights in addition to NRCS, but this case is not considered here. Another consideration is the error present in both the altimeter NRCS and reference wind measurements. The NRCS calibration can change over time due to degradation of instrument, satellite drift, etc., while *in situ* measurements have their own errors and NWP models are a simplified version of the real world.

There have been various efforts towards consolidating altimeter databases such as Globwave (*http://cersat.ifremer.fr/about-us/projects/item/102-globwave*), Radar Altimeter Data System (RADS, *http://rads.tudelft.nl*), AVISO (*https://www.aviso.altimetry.fr*), National Satellite Ocean Application Service (NSOAS, *http://www.nsoas.org.cn/*) and National Oceanic and Atmospheric Administration (NOAA) Radar Altimeter Database System (*https://www.star.nesdis.noaa.gov/socd/lsa/RADS.php*). However none of these databases archive all altimeters since 1985. Recently, the University of Melbourne in partnership with IMOS has created a unique database that captures both wind speed and wave height information derived from 13 satellite altimeters, acquired over 33 years. Another initiative is the ESA sea state Climate Change Initiative (CCI) project archive that spans from 1991 to 2018 and captures ten altimeters (Dodet *et al.*, 2020). Such data have been used for many applications, including offshore infrastructure design, calibration/validation of numerical models, climatology, and investigation of long term trends in oceanographic wind speed and wave height (Challenor *et al.*, 1990; Young, 1999; Alves and Young, 2003; Zieger *et al.*, 2009; Young *et al.*, 2011; Young and Ribal, 2019).

16.2.5 Synthetic Aperture Radar

Synthetic Aperture Radar (SAR) is a type of active, side-looking, microwave radar that can take high resolution images of the Earth's surface during day or night and in most weather conditions (see Section 9.3). SAR achieves its high resolution by synthetically increasing the size of the antenna in the satellite orbit direction (azimuth direction) during post-processing, which significantly increases the azimuth spatial resolution. This process utilises the delay-doppler signal, combining many illuminations of a target as it passes through the radar's footprint. The range resolution of a SAR, however, is not improved by the synthetic aperture processing, and in that sense, is similar to a real aperture radar (see Volume 1A—Section 15.2).

Satellite SAR sensors have a wide range of marine applications, including sea ice monitoring and concentration, and deriving surface waves and winds. These datasets can reveal a variety of oceanographic and atmospheric phenomena such as internal waves, oceanographic and atmospheric fronts, atmospheric boundary layer vortices, bathymetric features, rain, and wave-current interactions (Monaldo and Beal, 2004; Brown *et al.*, 1981; Fu and Holt, 1982; Kudryavtsev *et al.*, 2014; Alpers *et al.*, 2016). In this subsection, we will focus on surface winds derived from SAR.

SAR instruments are sensitive to surface wind in a similar way to a scatterometer (Monaldo and Beal, 2004; Jones and Schroeder, 1978). However, unlike a scatterometer, SAR does not look at the same ocean surface from three or more aspect angles, making it necessary to constrain the solution space and invert the correct wind direction. The wind vector inversion from SAR is therefore considered an under-determined problem: one observation of NRCS but two parameters of wind speed and direction to invert. Unless wind direction can be deduced directly from the SAR image as a by-product of other phenomena such as wind streaks, wind rows, or roll vortices (Gerling, 1986), or from doppler information contained in the SAR signal (Mouche *et al.*, 2012), it must be given to the inversion algorithm from an external source such as an NWP model (Portabella *et al.*, 2002) or another matching observation (e.g. *in situ*, scatterometer, radiometer) at a comparable spatial scale. NWP input has the distinct advantage of being available at all locations and times (up to a certain distance and time difference). SAR wind speed and direction retrievals through the scatterometry approach (Portabella *et al.*, 2002) results in ocean wind vector measurements with root mean squared errors of < 2 m/s for wind speed and < 20° for wind direction (Bôas *et al.*, 2019).

Scatterometer and SAR satellite global coverages and spatial resolutions are distinctly different. Scatterometers have a much wider swath compared to SAR satellites and continuously acquire wind speed and direction data over global oceans. SAR satellites primarily map the continents and only some of the SAR satellites (ENVISAT, ERS-1/2, Sentinel-1 A/B, GF-3) have systematically sampled (although not continuously) surface waves in open ocean. Although winds can also be derived from these global records, they are discontinuously sampled every ~100 km or so. Offshore footprints of continental coverage from SAR can be processed to high resolution (as high as tens of metres) wind speed and direction maps. Usually more averaging is done to reduce the effects of speckle noise and also other small scale marine boundary layer phenomena that can manifest in SAR wind retrievals. Nevertheless, these coastal maps can potentially be extremely useful because scatterometer coverage in coastal areas is subject to land contamination due to the much larger footprint and spatial resolution (~12.5–50 km) of a real aperture scatterometer.

C-band SAR platforms are particularly suited for monitoring the ocean surface under a TC because of their high resolution and a reasonably wide swath (up to ~400 km for Sentinel-1). This unique combination makes it possible to characterise the inner core of the storm such as, the eye-wall and radius of maximum wind speed, and rain band locations, as well as more accurate measurements in coastal areas. A shortcoming is the relatively longer repeat cycle time, smaller number of satellite platforms, narrower swath compared to scatterometers, and the planning needed to task existing SAR satellites (with competing priorities) over TC within a few days of their development.

Just like their co-pol scatterometer counterparts, C-band co-pol SAR measurements of TC also lose sensitivity to high winds and saturate above 35 m/s wind speeds. This limitation has been addressed with the proposed dual-pol (co-pol and x-pol) SAR measurements (such as Radarsat-2 and Sentinel-1), where the x-pol component (HV or VH) remains sensitive to high wind speeds as high as 60 m/s (Mouche *et al.*, 2017). These results have attracted a broader audience. For example, EUMETSAT and ESA are now planning to add a cross-polarised channel to the next generation of operational scatterometer missions (that is, the next Polar System Second Generation) dedicated to the ocean surface wind measurement at medium resolution (Stoffelen *et al.*, 2017; Bôas *et al.*, 2019).

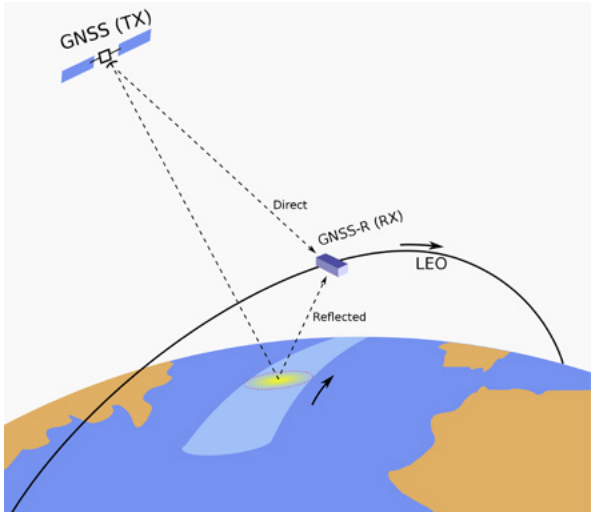
Routine coastal images over Europe and North America from Radarsat-2, Envisat, and Sentinel-1 SAR have enabled the development of high resolution coastal SAR winds databases such as the NOAA SAR winds operational data archive (NOAA Office of Satellite and Product Operations) and wind Atlas for Europe (Hasager *et al.*, 2015), yielding practical applications.

16.2.6 GNSS Reflectometry

Global Navigation Satellite System–Reflectometry (GNSS-R) exploits signals of opportunity from Global Navigation Satellite System (GNSS) constellations (see Volume 1B—Section 10.3), using a bistatic radar method (that is, transmitter and receiver in different locations; see Figure 16.5). This contrasts with monostatic methods like a scatterometer (where the transmitter and receiver are co-located on the same satellite). There are many navigation satellite systems in operation, the most common of which is the global positioning system (GPS). The GNSS-R method sees the navigation signals from these systems forward scattered off the Earth's surface in the bistatic specular direction. Dedicated GNSS-R receivers on land, on airborne platforms, or on separate satellites, detect and cross-correlate the reflected signals with direct signals from the same GNSS transmitter, to provide geophysical information about the reflecting surface (Bôas *et al.*, 2019).

Figure 16.5 GNSS-R system

The receiver satellite in Low Earth Orbit (LEO) obtains a direct signal from the GNSS satellite in its zenith antenna and a reflected one from the Earth's surface in its nadir antenna.



Source: Carlos Molina, Wikimedia Commons. Retrieved from *https://commons.wikimedia.org/wiki/File:GNSS-R_system_diagram.svg*

One of the earliest applications of GNSS-R was observing ocean winds (and waves; e.g. Garrison *et al.*, 1998). There are significant opportunities to exploit this technique, as the passive nature of the receiving hardware enables low power, low mass, and low cost instruments on small satellites, or low payloads on other platforms. However, GNSS-R remains an emerging method for surface marine wind observation. Significant progress has been made internationally in recent years through the UK TechDemoSat-1 (Foti *et al.*, 2017) and the NASA Cyclone Global Navigation Satellite System (CYGNSS) missions (Ruf *et al.*, 2016). Through both missions, retrieval performances are quoted to have RMSEs less than 2 m/s, for wind speeds in the 3–20 m/s range, and able to resolve fine scale structure near the walls of hurricane/cyclone systems (Foti *et al.*, 2017). However, no application of GNSS-R for surface marine wind detection in the Australian region is currently known.

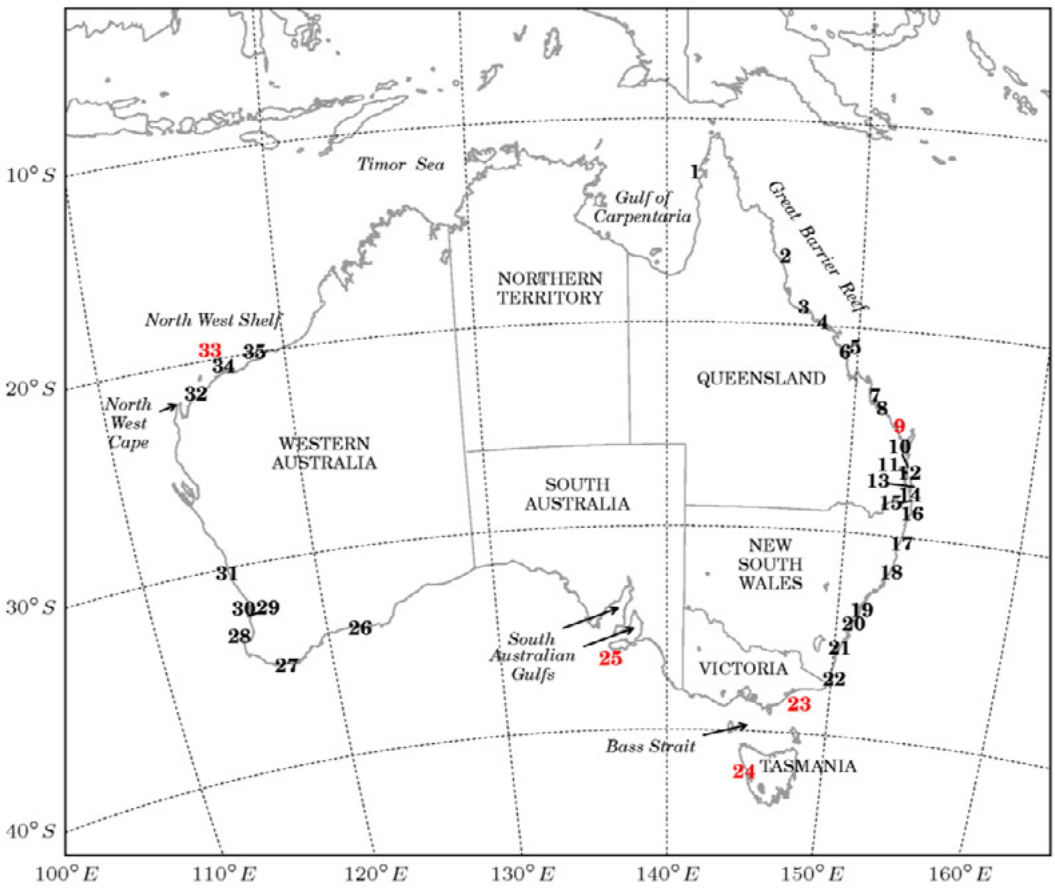
16.3 EO Sensors for Waves

16.3.1 *In situ* wave measurements

The predominant observation platform for *in situ* wave measurements around Australia are moored buoys in the coastal margin (see Section 16.2.1). A semi-coordinated monitoring network of wave measuring buoys is operated by several government agencies from several states, the Commonwealth Bureau of Meteorology, AIMS, IMOS, and in recent years, some university groups (Greenslade *et al.*, 2018; see Figure 16.6). These buoys are almost exclusively located in waters shallower than 100 m water depth, in relatively close (~10 km) proximity to the coast.

While these public facilities provide critical data, their applicability for validation of EO wave data is limited, as the satellite signal is typically contaminated by the coast at these buoy sites. Satellite data processing techniques are being progressively developed to improve the near-shore application, increasing the utility of these observations. It has only been in the past couple of years (since 2018) that this whole network has been made up of directional buoys. Previously, some buoys were not able to collect directional information.

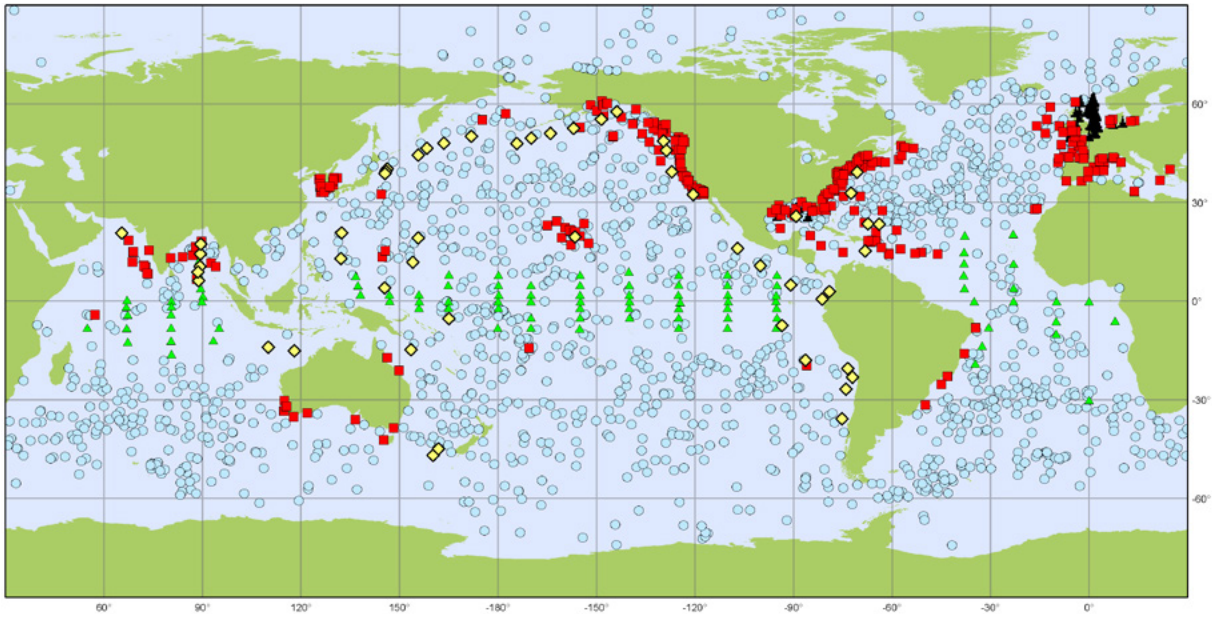
Figure 16.6 Australian wave buoy network



Source: Greenslade *et al.* (2018)

Figure 16.7 Global buoys for March 2016

Global map of *in situ* sensors coordinated by the Data Buoy Cooperation Panel (WMO-IOC) for March 2016. Yellow diamonds: tsunameters (52); red squares: coastal/national marine buoys (310); green triangles: tropical marine buoys (97); black triangles: fixed platforms (103); blue circles: drifting buoys (1,523)



Source: WMO-IOC Data Buoy Cooperation Panel. Retrieved from *https://www.ocean-ops.org/dbcp/network/dbcpmaps.html*

Further to the public sector observation programs, Australia's marine and coastal industries and associated service providers operate a large network of wave observing platforms. These are predominantly moored buoys, but include point measurement benthic moorings (such as Acoustic Doppler Current Profiler, ADCP, and Acoustic Doppler Velocimeter, ADV).

Deep-water wave measurements that are collected sufficiently far offshore to avoid land contamination are also available. These are typically operated by either the US NDBC or Western European nations, with valuable databases coordinated previously via the Joint Technical Commission for Oceanography and Marine Meteorology (JCOMM), and now the UN World Meteorological Organisation (WMO; see Figure 16.7). There are significant global gaps in the spatial distribution of *in situ* measurements, indicating both the value of global satellite derived wave data streams, and also the challenge of verification in some unique wave regimes (such as the Southern Ocean). Ardhuin *et al.* (2019) discuss a range of challenges associated with existing *in situ* wave measurements from moored buoys, recognising that buoys with different physical attributes respond differently, and challenge the notion that moored buoys present a valid 'ground truth'.

In recent years, cost reductions in wave buoy technology has led to the emergence of non-moored, drifting buoy measurements. This blossoming pool of data provides a dataset which is currently untapped for deep-water wave verification of EO products, but introduces further variance in the range of buoy data used as a reference.

16.3.2 Satellite altimeters

EO satellites provide an advantage over *in situ* measurements, by providing a global perspective, which is capable of sampling extreme conditions. Routine sea state measurements from satellite commenced with GEOSAT altimeter measurements in 1985, and an almost continuous record exists since then for altimeter-derived wave conditions. Satellite measurements of wave conditions quickly demonstrated their benefits for resolving global wave conditions, being robust, and sampling through extreme conditions (Young, 1993, 1999; Ardhuin *et al.*, 2019). The limited sampling of satellites however does mean that particular synoptic scale events (such as storms and cyclones) can be easily missed. This limitation is less of an issue when multiple missions are simultaneously operational. The most robust satellite-based measurement of sea state is the significant wave height derived from satellite altimeter wave forms, as a by-product of sea surface height measurements (see Excursus 16.1).

The main oceanographic objective of satellite radar altimetry is to measure the distance between the satellite and the sea surface, by measuring the time for an emitted pulse to reflect off the sea surface at nadir and return to the satellite (see Sections 9.5 and 16.2.4). Echoes reflected back from the wavy surface are registered in time and assembled as radar power signals called waveforms. These waveforms depict the distribution of wave amplitude in the field of view, with a peaked waveform corresponding to low sea state conditions, and a broad waveform corresponding to high sea state conditions. Waveforms are typically averaged, and formed at a rate of 20 Hz. This provides a relatively noisy product, and in order to smooth this noise, HS values are typically averaged to provide a 1 Hz product, which averages data to an approximately 7 km along-track resolution. Although measurements are assigned a longitude/latitude location, the footprint spans over 10 km in diameter, and the resultant HS value is a weighted average over this area.

Altimeters are capable of measuring high extremes, but have difficulty resolving low wave heights below 1 m (Bôas *et al*., 2019). In addition to wave height, altimeters provide a measure of backscatter strength. With calibration, this variable has been used to provide estimates of the mean square slope of the sea surface (Nouguier *et al*., 2016) and wave period (Gommenginger *et al*., 2003).

16.3.3 SAR imagery

Ocean surface waves are one of the features easily visible in SAR images because of the high resolution of SAR compared to the scale of the observed surface waves, and also because the radar signal backscattered toward the radar (due to ocean surface roughness at the scale of capillary waves) is modulated by waves at longer scales (see Section 16.2.5). In fact, longer ocean waves become visible in SAR images because they modulate ocean surface backscatter at Bragg wavelengths. Swells are therefore often well resolved by SAR and are consistent with *in situ* buoy observations (Collard *et al*., 2009) and wave models (Khan *et al*., 2021).

The synthetic aperture post-processing with which a SAR attains a high resolution in azimuth direction (up to a few metres) works well for stationary surfaces (stationary relative to the synthetic aperture integration time of ~0.5 sec) such as land. But, for a moving ocean surface, due to orbital motion of the high frequency surface waves, a similarly high spatial resolution cannot be achieved. This degradation can be up to the order of a couple of hundred metres in the azimuth direction depending on the radar parameters and observation geometry, and varies based on the relative angle between satellite flight direction and wave propagation direction. Generally speaking, SAR cannot image waves shorter than this cut-off wavelength.

SAR can measure directional swell spectra, resolve swell systems, and their associated wave heights, directionalities, and periods, that satellite altimeters are unable to determine. Together these satellite wave data (altimeter and SAR) provide fundamental knowledge of the generation and propagation of waves. Precision of SAR-derived wave spectra is low in environmental conditions with strong distortions from azimuth cut-off effects such as near storms (Ardhuin *et al*., 2019). In the far field, however, emitted swells are well captured by SAR. Nevertheless, SAR-derived swell spectra have been useful in improving the performance of global wave models (Aouf *et al*., 2006; Stopa *et al*., 2016), understanding the propagation of swell systems (Ardhuin *et al*., 2009) and cross-seas (Li, 2016), and are potentially an invaluable source of ocean surface wave measurements for the scientific community.

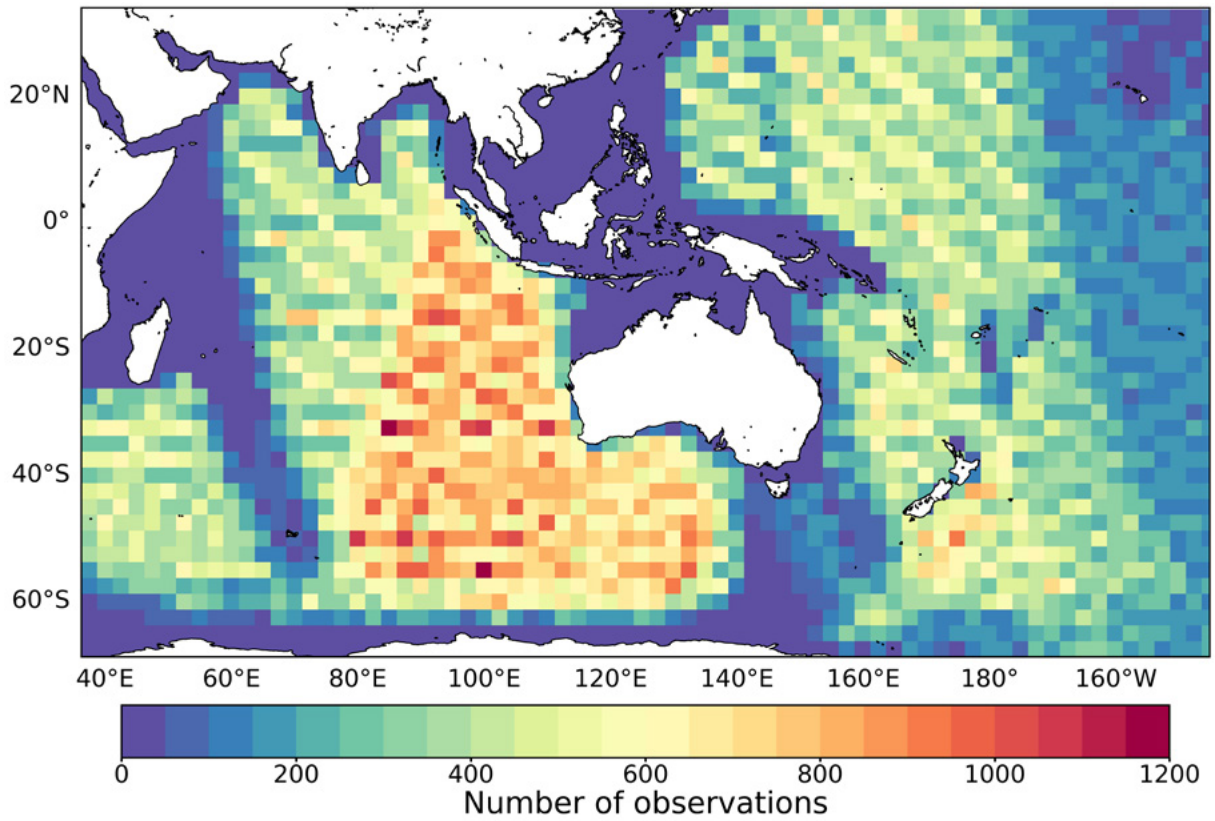
Interested readers are directed to a variety of studies aimed at deriving wave spectra from SAR imagery (Engen and Johnsen, 1995; Johnsen *et al*., 2003), and empirical methods to directly measure HS from SAR images using CWAVE method and its variations (Schulz-Stellenfleth *et al*., 2007; Li, 2016; Stopa and Mouche, 2017) and to estimate other sea state parameters such as wave energy and wave period (Schulz-Stellenfleth *et al*., 2007; Stopa and Mouche, 2017; Li and Huang, 2020), although precision is reduced compared to HS.

SEASAT (operational in 1978) carried both SAR and altimeter sensors and demonstrated global wave measurements for the first time. At present, the continuity of historical C-band SAR satellites (ERS-1, ERS-2, and ENVISAT, 1991–2012), which measured ocean surface waves globally in the wave mode, is ensured by European Copernicus Sentinel-1A and B, and Chinese GaoFen-3 SAR satellites (2014 onward). Sentinel-1 satellites are carrying forward the flagship of ERS-1 and -2 and ENVISAT SAR global wave mode measurements, and have a nominal lifetime of ~7 years. Future continuity is ensured by follow-on Sentinel-1C and -1D platforms (tentative launch after 2022).

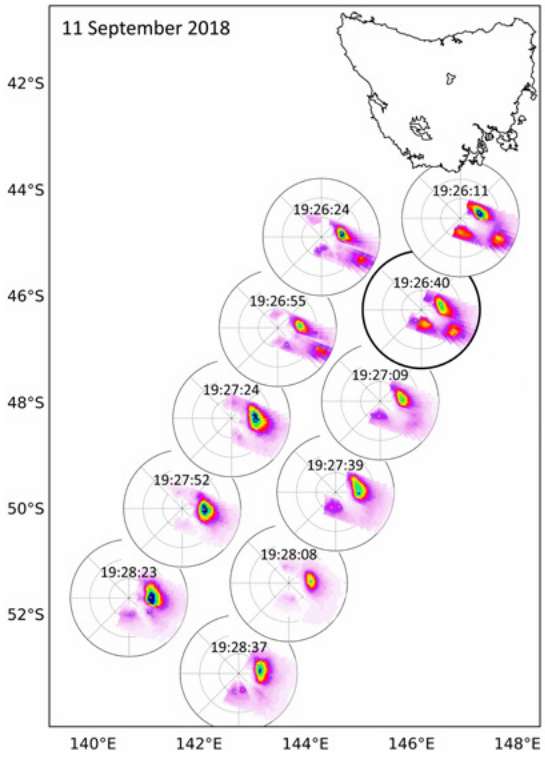
In the Australian context, CSIRO in partnership with IMOS has recently created an Australasian SAR wave spectra database (Khan *et al*., 2021) from Sentinel-1 A and B observations since the start of the respective missions (see Figure 16.8). The aim of this database is to provide an observational source of wave spectra data, which is accurate and easy to use to support research and the scientific community, and to foster uptake of satellite-derived surface wave data.

Figure 16.8 Australasian SAR database

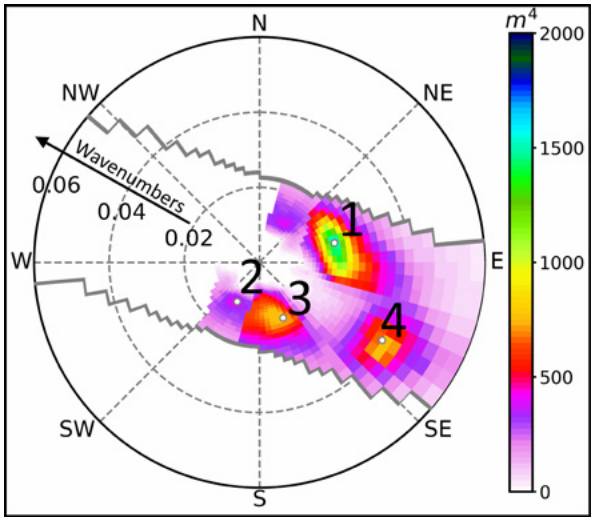
a. Sentinel-1A observations in 2.5°×2.5° bins, acquired between November 2015 and November 2019



b: Sample directional ocean wave spectra at specific times on 11 September 2018. Radial distances indicate wave period and colour contours show power spectral density, a measure of energy from a particular direction.



c. Enlarged wave spectrum at 19:26:40



Source: Salman Khan, CSIRO

In other advancements, wave spectra derived from Sentinel-2 satellites have shown high fidelity (Kudryavtsev *et al.*, 2017), while recent airborne demonstrations by Yurovskaya *et al.* (2018) show that daylight sea state monitoring with drones is already feasible. Such efforts are opening new possibilities to combine different emerging satellite measurements (including SAR and altimeter measurements), and possibly provide validation opportunities for ocean surface processes (Ardhuin *et al.*, 2019).

16.3.4 Emerging platforms

A recent addition, and the first purpose-driven satellite platform launched to measure surface wind waves from space, is the 'wave spectrometer' Surface Waves Investigation and Monitoring (SWIM) instrument onboard the Chinese-French Oceanographic Satellite (CFOSAT; Hauser et al., 2017). CFOSAT was launched in 2018, and is now providing routine level-2 wave spectra data, with a wavelength range of 70–500 m (Hauser *et al.*, 2021). The SWIM instrument is a rotating six-beam radar at small incidence angles operating at 13.575 GHz. The SWIM instrument does not suffer from the same so-called 'azimuth cutoff' problem, being able to resolve a more complete representation of the wave spectrum. Another advantage of the CFOSAT is the availability of a wind scatterometer onboard the same platform, enabling a valuable joint datastream for wind-wave investigations.

Optical imagery has been demonstrated as having value for retrieval of directional wave spectra. Kudryavtsev *et al.* (2017) use the Sentinel-2 Multi-Spectral Instrument (MSI) measurements to demonstrate detection of ocean surface wave spectra by exploiting sunglint (see Sections 4.3 and 8.1.3). Results demonstrate high agreement with *in situ* buoy measurements, but are limited in that they cannot offer full global monitoring due to observation constraints (cloud cover and Sun position; see Volume 1B—Sections 3 and 4), but are unique in their ability to resolve coastal areas covered by Landsat and Sentinel-2 satellites (Bôas *et al.*, 2019).

16.4 Further Information

Waves

Australian Marine Energy Atlas: Hemer *et al.* (2018); accessible via National Map

Marine Science Australia: *https://www.ausmarinescience.com/marine-science-basics/waves/*

WaveFoRCE: *http://waveforce.online/*

Integrated Marine Observing System (IMOS)

Wave Buoys: *https://imos.org.au/facilities/nationalmooringnetwork/wave-buoys*

Surface Waves: *https://imos.org.au/facilities/srs/surface-waves*

Australian Ocean Data Network (AODN): *https://imos.org.au/facilities/aodn*

Ocean Current: *http://oceancurrent.imos.org.au/*

https://imos.org.au/news/newsitem/altimeter-wind-and-wave-database-on-aodn

Bluelink

https://www.csiro.au/en/Research/OandA/Areas/Oceans-and-climate/Bluelink

CSIRO

CSIRO (2017)

Ocean waves: *https://research.csiro.au/slrwavescoast/waves/*

ESA

Seastate CCI: *https://climate.esa.int/en/projects/sea-state/*

eoPortal: *https://earth.esa.int/web/eoportal/home*

CFOSat: *https://earth.esa.int/web/eoportal/satellite-missions/c-missions/cfosat*

NOAA

NOAA National Data Buoy Centre(NDBC): *https://www.ndbc.noaa.gov/*

16.5 References

Abdalla, S. (2012). Ku-Band Radar Altimeter Surface Wind Speed Algorithm. *Marine Geodesy*, 35, 276–298. doi:10.1080/01490419.2012.718676

Alpers, W., Zhang, B., Mouche, A., Zeng, K., and Chan, P.W. (2016). Rain footprints on C-band synthetic aperture radar images of the ocean—Revisited. *Remote Sensing of Environment*, 187, 169–185. doi:10.1016/j.rse.2016.10.015

Alves, J.H.G.M., Greenslade, D.J.M., and Banner, M.L. (2002). Impact of a saturation-dependent dissipation source function on operational hindcasts of wind-waves in the Australian region. *Journal of Atmospheric and Ocean Science*, 8, 239–267. doi:10.1080/10236730290026540

Alves, J.H.G.M., and Young, I.R. (2003). On estimating extreme wave heights using combined Geosat, Topex/Poseidon and ERS-1 altimeter data. *Applied Ocean Research*, 25, 167–186. doi:10.1016/j.apor.2004.01.002.

Aouf, L., Lefèvre, J.M., and Hauser, D. (2006). Assimilation of directional wave spectra in the wave model WAM: An impact study from synthetic observations in preparation for the SWIMSAT Satellite mission. *Journal of Atmospheric and Oceanic Technology*, 23, 448–463. doi:10.1175/JTECH1861.1

Ardhuin, F., Chapron, B., and Collard, F. (2009). Observation of swell dissipation across oceans. *Geophysical Research Letters*, 36, L06607. doi:10.1029/2008GL037030

Ardhuin, F., Stopa, J.E., Chapron, B., Collard, F., Husson, R., Jensen, R.E., Johannessen, J., Mouche, A., Passaro, M., Quartly, G.D., Swail, V., and Young, I. (2019). Observing sea states. *Frontiers in Marine Science*, 6, 124. doi:10.3389/fmars.2019.00124

Bender, L.C. (1996). Modification of the physics and numerics in a third-generation ocean wave model. *Journal of Atmospheric and Oceanic Technology*, 13, 726–750. doi:10.1175/1520-0426(1996)013<0726:MOTPAN>2.0.CO;2

Bôas, A.B.V., Ardhuin, F., Ayet, A., Bourassa, M.A., Brandt, P., Chapron, B., Cornuelle, B.D., Farrar, J.T., Fewings, M.R., Fox-Kemper, B., Gille, S.T., Gommenginger, C., Heimbach, P., Hell, M.C., Li, Q., Mazloff, M.R., Merrifield, S.T., Mouche, A., Rio, M.H., Rodriguez, E., Shutler, J.D., Subramanian, A.C., Terrill, E.J., Tsamados, M., Ubelmann, C., and van Sebille, E. (2019). Integrated observations of global surface winds, currents, and waves: Requirements and challenges for the next decade. *Frontiers in Marine Science*, 6, 425. doi:10.3389/fmars.2019.00425

BoM (2021). *Ruling the waves: How a simple wave height concept can help you judge the size of the sea* webpage, Bureau of Meteorology website: *http://media.bom.gov.au/social/blog/870/ruling-the-waves-how-a-simple-wave-height-concept-can-help-you-judge-the-size-of-the-sea/*

Bourassa, M.A., Meissner, T., Cerovecki, I., Chang, P., Dong, X., De Chiara, G., *et al.* (2019). Remotely sensed winds and wind stresses for marine forecasting and ocean modeling. *Frontiers in Marine Science*, 6, 443. doi:10.3389/fmars.2019.00443

Brown, G. ., Stanley, H.R., and Roy, N.A. (1981). The Wind-Speed Measurement Capability of Spaceborne Radar Altimeters. *IEEE Journal of Oceanic Engineering*, 6, 59–63. doi:10.1109/JOE.1981.1145484

CEOS (2014). *Ocean Surface Vector Wind* webpage, Committee on Earth Observation Satellites website: *https://ceos.org/ourwork/virtual-constellations/osvw/*

Challenor, P.G., Foale, S., and Webb, D.J. (1990). Seasonal changes in the global wave climate measured by the geosat altimeter. *International Journal of Remote Sensing*, 11, 2205–2213. doi:10.1080/01431169008955170

Chelton, D.B., and McCabe, P.J. (1985). A review of satellite altimeter measurement of sea surface wind speed: with a proposed new algorithm. *Journal of Geophysical Research*, 90, 4707–4720. doi:10.1029/JC090iC03p04707

Chelton, D.B., and Wentz, F.J. (1986). Further development of an improved altimeter wind speed algorithm. *Journal of Geophysical Research*, 91, 14250. doi:10.1029/jc091ic12p14250

Collard, F., Ardhuin, F., and Chapron, B. (2009). Monitoring and analysis of ocean swell fields from space: New methods for routine observations. *Journal of Geophysical Research*: *Oceans*, 114, 7023. doi:10.1029/2008JC005215

Cotton, J., Francis, P., Heming, J., Forsythe, M., Reul, N., and Donlon, C. (2018). Assimilation of SMOS L-band wind speeds: impact on Met Office global NWP and tropical cyclone predictions. *Quarterly Journal of the Royal Meteorological Society*, 144, 614–629. doi:10.1002/qj.3237

Dodet, G., Piolle, J.F., Quilfen, Y., Abdalla, S., Accensi, M., Ardhuin, F., et al. (2020). The Sea State CCI dataset v1: Towards a sea state climate data record based on satellite observations. *Earth System Science Data*, 12, 1929–1951. doi:10.5194/essd-12-1929-2020

Donlon, C. (2019). *Copernicus Imaging Microwave Radiometer (CIMR) Mission Requirements Document*. ESA. *https://cimr.eu/sites/cimr.met.no/files/documents/CIMR-MRD-v2.0-20190305-ISSUED_0.pdf*

ECMWF (2021). *The ECMWF Integrated Forecasting System* website: *https://confluence.ecmwf.int/display/FUG/2.2+Ocean+Wave+Model+-+ECWAM*

Engen, G., and Johnsen, H. (1995). SAR-Ocean Wave Inversion Using Image Cross Spectra. *IEEE Transactions on Geoscience and Remote Sensing*, 33, 1047–1056. doi:10.1109/36.406690

Foti, G., Gommenginger, C., and Srokosz, M. (2017). First Spaceborne GNSS-Reflectometry Observations of Hurricanes From the UK TechDemoSat-1 Mission. *Geophysical Research Letters*, 44, 12358–12366. doi:10.1002/2017GL076166

Fu, L.-L., and Holt, B. (1982). *Seasat Views Oceans and Sea Ice With Synthetic-Aperture Radar*. JPL Publication 81-120, NASA. *https://earth.esa.int/documents/10174/1020083/Seasat_views_Oceans_Sea_Ice_with_SAR.pdf*

Garrison, J.L., Katzberg, S.J., and Hill, M.I. (1998). Effect of sea roughness on bistatically scattered range coded signals from the Global Positioning System. *Geophysical Research Letters*, 25(13), 2257–2260. doi:10.1029/98GL51615

Gerling, T.W. (1986). Structure of the surface wind field from the Seasat SAR. *Journal of Geophysical Research*, 91, 2308–2320. doi:10.1029/JC091iC02p02308

Gommenginger, C. P., Srokosz, M.A., Challenor, P.G., and Cotton, P.D. (2003). Measuring ocean wave period with satellite altimeters: A simple empirical model. *Geophysical Research Letters*, 30(22), 02150. doi:10.1029/2003GL017743

Greenslade, D.J.M., Zanca, A., Zieger, S., and Hemer, M.A. (2018). Optimising the Australian wave observation network. *Journal of Southern Hemisphere Earth System Science*, 68, 184–200. doi:10.22499/3.6801.010

Hasager, C.B., Mouche, A., Badger, M., Bingöl, F., Karagali, I., Driesenaar, T., Stoffelen, A., Peña, A., and Longépé, N. (2015). Offshore wind climatology based on synergetic use of Envisat ASAR, ASCAT and QuikSCAT. *Remote Sensing of Environment*, 156, 247–263. doi:10.1016/j.rse.2014.09.030

Hauser, D., Tison, C., Amiot, T., Delaye, L., Corcoral, N., and Castillan, P. (2017). SWIM: The First Spaceborne Wave Scatterometer. *IEEE Transactions on Geoscience and Remote Sensing*, 55, 3000–3014. doi:10.1109/TGRS.2017.2658672

Hauser, D., Tourain, C., Hermozo, L., Alraddawi, D., Aouf, L., Chapron, B., *et al*. (2021). New Observations from the SWIM Radar On-Board CFOSAT: Instrument Validation and Ocean Wave Measurement Assessment. *IEEE Transactions on Geoscience and Remote Sensing*, 59, 5–26. doi:10.1109/TGRS.2020.2994372

Hemer, M.A., Pitman, T., McInnes, K., and Rosebrock, U. (2018) *The Australian Wave Energy Atlas Project Overview and Final Report*. CSIRO Oceans and Atmosphere, Australia. 24 p. *https://arena.gov.au/assets/2014/02/Wave-Atlas-Final-Report.pdf*

Holthuijsen, L.H. (2007). *Waves in oceanic and coastal waters*. Cambridge University Press. doi:10.1017/CBO9780511618536

Jang, J.C., Park, K.A., Mouche, A.A., Chapron, B., and Lee, J.H. (2019). Validation of Sea Surface Wind from Sentinel-1A/B SAR Data in the Coastal Regions of the Korean Peninsula. *IEEE Journal of Selected Topics in Applied Earth Observation Remote Sensing*, 12, 2513–2529. doi:10.1109/JSTARS.2019.2911127

Johnsen, H., Engen, G., Collard, F., Kerbaol, V., and Chapron, B. (2003). *Envisat ASAR Wave Mode Products —Quality Assessment and Algorithm Upgrade*.

Jones, W.L., and Schroeder, L.C. (1978). Radar backscatter from the ocean: Dependence on surface friction velocity. *Boundary-Layer Meteorology*, 13, 133–149. doi:10.1007/BF00913867

Khan, S.S., Echevarria, E.R., and Hemer, M.A. (2021). Ocean Swell Comparisons Between Sentinel-1 and WAVEWATCH III Around Australia. *Journal of Geophysical Research*: *Oceans*, 126, e2020JC016265. doi:10.1029/2020JC016265

Kudryavtsev, V., Kozlov, I., Chapron, B., and Johannessen, J.A. (2014). Quad-polarization SAR features of ocean currents. *Journal of Geophysical Research*: *Oceans*, 119, 6046–6065. doi:10.1002/2014JC010173

Kudryavtsev, V., Yurovskaya, M., Chapron, B., Collard, F., and Donlon, C. (2017). Sun glitter imagery of ocean surface waves. Part 1: Directional spectrum retrieval and validation. *Journal of Geophysical Research*: *Oceans*, 122, 1369–1383. doi:10.1002/2016JC012425

Li, X.M. (2016). A new insight from space into swell propagation and crossing in the global oceans. *Geophysical Research Letters*, 43, 5202–5209. doi:10.1002/2016GL068702

Li, X.M., and Huang, B.Q. (2020). A global sea state dataset from spaceborne synthetic aperture radar wave mode data. *Science Data*, 7, 1–12. doi:10.1038/s41597-020-00601-3

Meijer, Y. (2019). *Copernicus CO_2 Monitoring Mission Requirements Document*. ESA. *ftp://193.17.11.194/pub/EPS/out/lang/TriOpSys/ReferenceDocs/Copernicus%20CO2%20mission%20-%20MRD%20-%20v2.0%20-%20v20190927_final.pdf*

Meissner, T., and Wentz, F.J. (2009). Wind-vector retrievals under rain with passive satellite microwave radiometers. *IEEE Transactions on Geoscience and Remote Sensing*, 47, 3065–3083. *https://ieeexplore.ieee.org/document/5196732*

Meissner, T., and Wentz, F. (2012). The emissivity of the ocean surface between 6–90 GHz over a large range of wind speeds and Earth incidence angles. *IEEE Transactions on Geoscience and Remote Sensing*, 50, 3004–3026. *https://ieeexplore.ieee.org/document/6145646*

Meissner, T., Ricciardulli, L., and Wentz, F.J. (2017). Capability of the SMAP mission to measure ocean surface winds in storms. *Bulletin of American Meteorological Society*, 98, 1660–1677. *https://doi.org/10.1175/BAMS-D-16-0052.1*

Monaldo, F. M., and Beal, R. (2004). Wind Speed and Direction. Ch 13 in *Synthetic Aperture Radar Marine User's Manual* (Eds: Jackson, C.R., and Apel, J.R.). NOAA, Washington. pp. 305–320. *http://www.sarusersmanual.com/*

Mouche, A.A., Collard, F., Chapron, B., Dagestad, K.F., Guitton, G., Johannessen, J.A., Kerbaol, V., and Hansen, M.W. (2012). On the use of doppler shift for sea surface wind retrieval from SAR. *IEEE Transactions on Geoscience and Remote Sensing*, 50, 2901–2909. doi:10.1109/TGRS.2011.2174998

Mouche, A.A., Chapron, B., Zhang, B., and Husson, R. (2017). Combined Co- and Cross-Polarized SAR Measurements under Extreme Wind Conditions. *IEEE Transactions on Geoscience and Remote Sensing*, 55, 6746–6755. doi:10.1109/TGRS.2017.2732508

NDBC (2009). *Handbook of Automated Data Quality Control Checks and Procedures*. National Data Buoy Center, National Oceanic and Atmospheric Administration. *https://www.ndbc.noaa.gov/NDBCHandbookofAutomatedDataQualityControl2009.pdf*

Nouguier, F., Mouche, A., Rascle, N., Chapron, B., and Vandemark, D. (2016). Analysis of Dual-Frequency Ocean Backscatter Measurements at Ku-and Ka-Bands Using Near-Nadir Incidence GPM Radar Data. *IEEE Transactions on Geoscience and Remote Sensing*, 13, 1310–1314. doi:10.1109/LGRS.2016.2583198

Portabella, M., Stoffelen, A., and Johannessen, J.A. (2002). Toward an optimal inversion method for synthetic aperture radar wind retrieval. *Journal of Geophysical Research*: *Oceans*, 107, 1–1. doi:10.1029/2001jc000925

Quilfen, Y., Vandemark, D., Chapron, B., Feng, H., and Sienkiewicz, J. (2011). Estimating gale to hurricane force winds using the satellite altimeter. *Journal of Atmospheric and Oceanic Technology*, 28, 453–458. doi:10.1175/JTECH-D-10-05000.1

Ribal, A., and Young, I.R. (2019). 33 years of globally calibrated wave height and wind speed data based on altimeter observations. *Science Data* 6, 1–15. doi:10.1038/s41597-019-0083-9

Ribal, A., and Young, I.R. (2020). Calibration and cross validation of global ocean wind speed based on scatterometer observations. *Journal of Atmospheric and Oceanic Technology*, 37, 279–297. doi:10.1175/JTECH-D-19-0119.1

Ruf, C.S., Atlas, R., Chang, P.S., Clarizia, M.P., Garrison, J.L., Gleason, S., *et al*. (2016). New ocean winds satellite mission to probe hurricanes and tropical convection. *Bulletin of the American Meteorological Society*, 97, 385–395. doi:10.1175/BAMS-D-14-00218.1

Schulz, E.W., Kepert, J.D., and Greenslade, D.J.M. (2007). An assessment of marine surface winds from the Australian Bureau of Meteorology numerical weather prediction systems. *Weather Forecast*, 22, 613–636. doi:10.1175/WAF996.1

Schulz-Stellenfleth, J., König, T., and Lehner, S. (2007). An empirical approach for the retrieval of integral ocean wave parameters from synthetic aperture radar data. *Journal of Geophysical Research*: *Oceans*, 112, 3019. doi:10.1029/2006JC003970

Stoffelen, A., and Anderson, D. (1997). Scatterometer data interpretation: Estimation and validation of the transfer function CMOD4. *Journal of Geophysical Research*: *Oceans*, 102, 5767–5780. doi:10.1029/96JC02860

Stoffelen, A., and Portabella, M. (2006). On bayesian scatterometer wind inversion. *IEEE Transactions on Geoscience and Remote Sensing*, 44, 1523–1533. doi:10.1109/TGRS.2005.862502

Stoffelen, A., Aaboe, S., Calvet, J.C., Cotton, J., De Chiara, G., Saldaña, J.F., *et al*. (2017). Scientific Developments and the EPS-SG Scatterometer. *IEEE Journal of Selected Topics in Applied Earth Observation Remote Sensing*, 10, 2086–2097. doi:10.1109/JSTARS.2017.2696424

Stopa, J.E., and Mouche, A. (2017). Significant wave heights from Sentinel-1 SAR: Validation and applications. *Journal of Geophysical Research*: *Oceans*, 122, 1827–1848. doi:10.1002/2016JC012364

Stopa, J.E., Ardhuin, F., Babanin, A., and Zieger, S. (2016). Comparison and validation of physical wave parameterizations in spectral wave models. *Ocean Modelling*, 103, 2–17. doi:10.1016/j.ocemod.2015.09.003

Ulaby, F.T., Moore, R.K., and Fung, A.K. (1981). *Microwave remote sensing: Active and passive. Volume 1 – Microwave remote sensing fundamentals and radiometry*. *https://ntrs.nasa.gov/citations/19820039342*

Witter, D.L., and Chelton, D.B. (1991). A Geosat altimeter wind speed algorithm and a method for altimeter wind speed algorithm development. *Journal of Geophysical Research*, 96, 8853–8860. doi:10.1029/91JC00414

Wright, J.W. (1966). Backscattering from Capillary Waves with Application to Sea Clutter. *IEEE Transactions on Antennas Propagation*, 14, 749–754. doi:10.1109/TAP.1966.1138799

Young, I.R. (1993). An estimate of the Geosat altimeter wind speed algorithm at high wind speeds. *Journal of Geophysical Research*, 98, 20275–20285. doi:10.1029/93jc02117

Young, I.R. (1999). Seasonal variability of the global ocean wind and wave climate. *International Journal of Climatology*, 950, 931–950.

Young, I.R., and Donelan, M.A. (2018). On the determination of global ocean wind and wave climate from satellite observations. *Remote Sensing of Environment*, 215, 228–241. doi:10.1016/j.rse.2018.06.006.

Young, I.R., and Ribal, A. (2019). Multiplatform evaluation of global trends in wind speed and wave height. *Science*, 364, 548–552. doi:10.1126/science.aav9527

Young, I.R., Zieger, S., and Babanin, A.V. (2011). Global trends in wind speed and wave height. *Science*, 332, 451–5. doi:10.1126/science.1197219

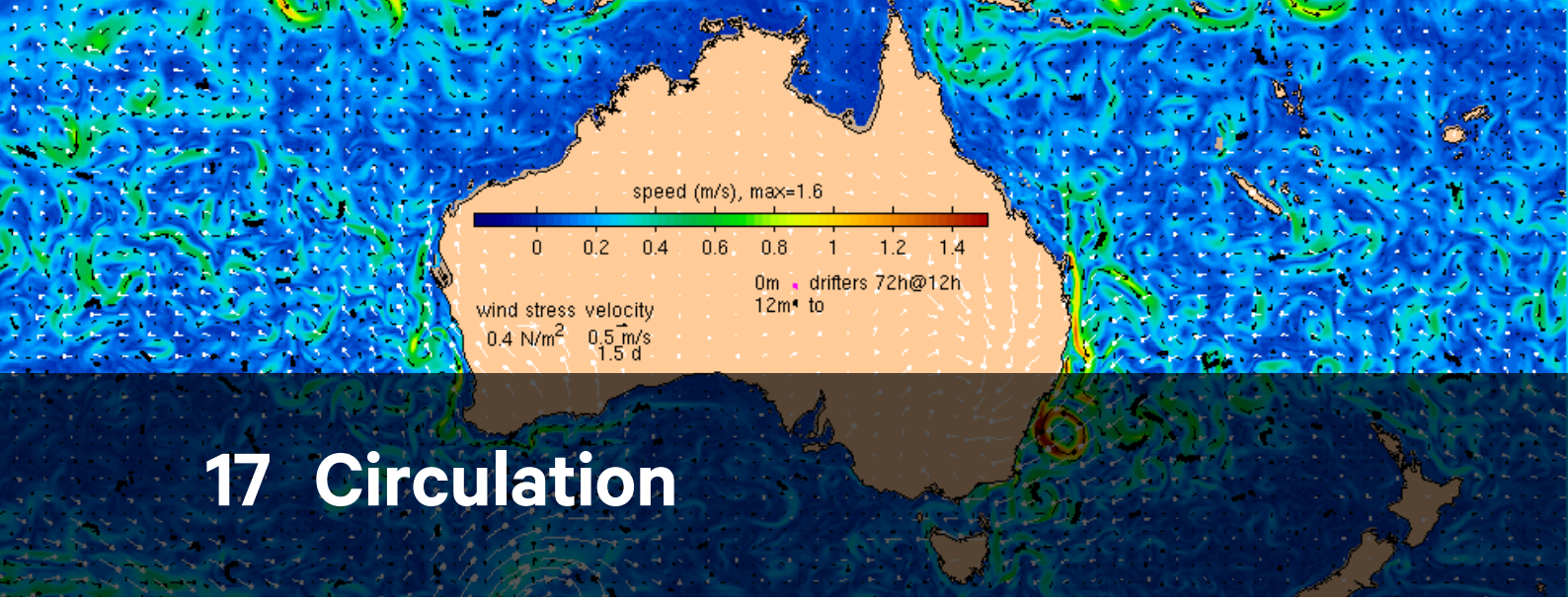
Young, I.R., Sanina, E., and Babanin, A.V. (2017). Calibration and cross validation of a global wind and wave database of altimeter, radiometer, and scatterometer measurements. *Journal of Atmospheric and Oceanic Technology*, 34, 1285–1306. doi:10.1175/JTECH-D-16-0145.1.

Young, I.R., Kirezci, E., and Ribal, A. (2020). The global wind resource observed by scatterometer. *Remote Sensing*, 12, 2920. doi:10.3390/RS12182920

Yueh, S.H., Wilson, W.J., Dinardo, S.J., and Li, F.K. (1999). Polarimetric microwave brightness signatures of ocean wind directions. *IEEE Transactions on Geoscience and Remote Sensing*, 37, 949–959. doi:10.1109/36.752213

Yurovskaya, M., Rascle, N., Kudryavtsev, V., Chapron, B., Marié, L., and Molemaker, J. (2018). Wave spectrum retrieval from airborne sunglitter images. *Remote Sensing of Environment*, 217, 61–71. doi:10.1016/j.rse.2018.07.026

Zieger, S., Vinoth, J., and Young, I.R. (2009). Joint Calibration of Multiplatform Altimeter Measurements of Wind Speed and Wave Height over the Past 20 Years. *Journal of Atmospheric and Oceanic Technology*, 26, 2549–2564. doi:10.1175/2009JTECHA1303.1



17 Circulation

David Griffin

Circulation of near-surface water (defined here as the water either within a few metres of the surface of the ocean, or within the mixed layer) occurs at a range of spatial and temporal scales. Global water circulation is driven by wind and fluxes across the ocean's surface of heat (solar input, evaporative cooling, etc) and freshwater (due to rain or evaporation). Characteristics of these drivers, in combination with the 'topography' of the seafloor, determine the size, shape, speed, and direction of ocean currents. Our current understanding of the global circulation of near-surface water is introduced in Section 1.4 and regional circulation patterns in the Australian region are described in Section 2.3. Terminology used to describe water circulation is summarised in Table 17.1.

The movement of ocean waters around the globe distributes heat and nutrients, regulates weather patterns, and stabilises climatic variations. Given the vast extent of the global ocean and its relative remoteness, it is challenging to map and monitor horizontal and vertical water circulation patterns.

This is one area where the synoptic perspective of EO datasets that have been acquired over several decades have provided insights into both regional and global patterns of water movement, particularly when teamed with automated *in situ* measurements (see Excursus 5.1).

Table 17.1 Water circulation terms

Term	Definition
Convergent	A front is described as convergent when it has two water masses approaching each other, requiring subduction (sinking) of one of these at the surface.
Current	A non-periodic, generally horizontal movement of water due to many causes such as prevalent winds, temperature differential, etc.
Divergent	A divergent front has water diverging at the surface.
Downwelling	The movement of surface waters downward generally occurs when surface waters converge or encounter the coast.
Eddy	A rotating body of water formed where currents or tidal streams pass obstructions. Others form along the edge of a current or stream, or between two adjacent flows (see Section 1.4.3). Larger eddies can be formed by baroclinic instability or barotropic instability, analogously to how weather systems are formed in the atmosphere.
Front	Regions of strong horizontal gradients in water properties (temperature, density, salinity etc).
Geostrophic flow	Balance between Coriolis force (see Excursus 1.2) and pressure gradient associated with elevation of sea level or horizontal gradient of density.
Gyre	Large system of ocean currents resulting from global wind patterns and the Earth's rotation (see Section 1.4.2)
Upwelling	An upward flow of cold, subsurface water, usually a result of divergence. Upwelling regions are typically rich in nutrients and occur near coastlines when the wind drives water away from the coast (which happens when the wind blows with the coast on the right in the Southern Hemisphere) or in the deep ocean when the curl of the wind stress is cyclonic.

Background image: This Australia-wide view of surface circulation on 23 March 2021 shows the daily average speed (see colour bar) and direction (black arrows) of water movement. White vectors show daily average wind stress. **Source:** David Griffin, CSIRO, from OceanMAPS (see Excursus 2.2).

Recommended Chapter Citation: Griffin, D.A. (2021). Circulation. Ch 17 in *Earth Observation: Data, Processing and Applications. Volume 3B—Surface Waters.* CRCSI, Melbourne. pp. 329–342. ISBN 978-0-6482278-5-4.

The 'global conveyor belt' circulates ocean waters slowly by moving warmer surface waters from the equator to the poles and returning denser polar waters to the equator at depth (see Figure 5.4). Density differences between layers in the water column result from differences in temperature and salinity (see Section 5.1.2). Colder, saltier water is denser than warmer, fresher water at any particular depth. Upwelling delivers colder and nutrient-rich water to the surface, while downwelling returns warmer water with lower density to the depths. The resultant gradients of ocean temperature and salinity are in approximate balance with the Coriolis force acting on the velocities (see Figure 5.4). This slow circulation is known as the thermohaline circulation.

Wind-driven gyres also exist at the scale of ocean basins. Their asymmetry—with greater intensity on the western side of the ocean basin—is due to the Earth's rotation. For example, the East Australian Current (EAC) is one of the great western boundary currents of the world (see Section 17.1). Thus, in broad terms, surface waters are circulated globally, regionally, and locally by two mechanisms:

- slower, density-driven, vertical mixing or 'thermohaline' circulation (see Section 5.1.2); and
- faster, wind-driven, surface movements, such as currents or eddies.

A boundary current is a permanent water circulation feature that flows along the coastline of a landmass (see Section 1.4). The dynamics of boundary currents are determined by features of the ocean basin and its adjacent coastline:

- western boundary currents, which flow around the western edge of an ocean basin (eastern side of landmass) towards the poles, are typically narrow, deep, and fast, and often dissipate energy by shedding eddies; and
- eastern boundary currents occur on the eastern side of ocean basins (western coastlines), generally flow towards the equator, are shallower, slower and wider, and frequently involve coastal upwelling.

The boundary between two distinct water (or air) masses is called a front. This means that significant differences exist in their properties, such as temperature or salinity, within a small distance. As masses move towards or away from each other, they generate convergent or divergent fronts respectively. In surface waters, convergent fronts are characterised by downwelling, whereas divergent fronts generate upwelling. Frontal dynamics can complicate the circulation of surface waters, particularly in coastal regions.

The volume of water that is moved by large scale water circulation mechanisms is measured as the volumetric flow rate and commonly expressed using the non-SI unit Sverdup (Sv; Agrawal, 2018). 1 Sv equals the volume transport of 1 million cubic metres (1 km × 1 km × 1 m) per second.

Below we describe the major water circulation patterns around the Australian land mass in terms of seasonal to interannual variability (see Section 17.1 and Excursus 17.1) and then discuss those EO sensors that are relevant to mapping and monitoring these patterns (see Section 17.2). Subsequent subsections introduce EO methods used to observe circulation patterns (see Section 17.3) and ocean fronts (see Section 17.4).

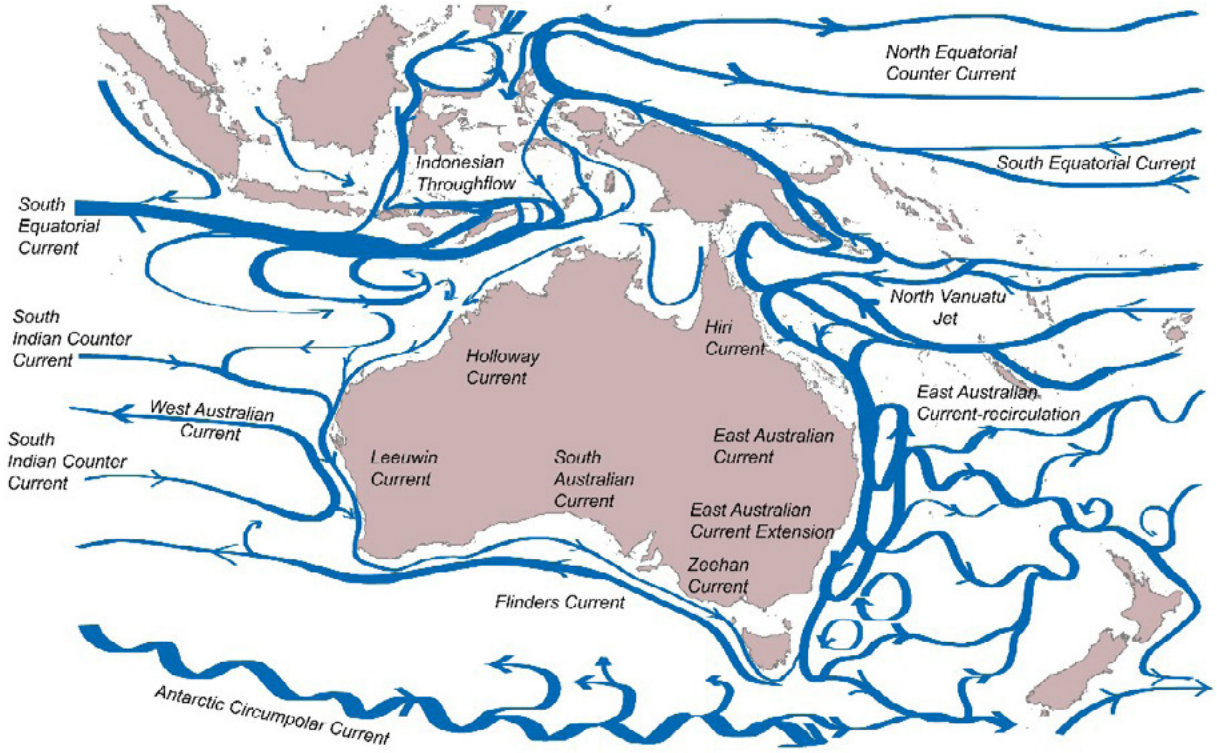
Oceanography is the study of the composition and motion of the water column and the processes which are responsible for that motion. The principal oceanographic processes influencing Australia's continental shelf waters include waves and tides as well as wind-driven and other oceanic currents. (GA, 2021)

17.1 Circulation of Australian Surface Waters

The island continent of Australia is surrounded by surface and subsurface boundary currents that flow along the continental shelf and slope (see Figure 17.1 and Section 2.3). The unique feature of the water circulation around Australia is that along both the east and west coasts, boundary currents transport warm water southward via the East Australian (EAC) and Leeuwin Currents (LC), respectively (Wijeratne *et al.*, 2018). These boundary currents are enhanced through inflows from the south Pacific and south Indian Ocean basins (see Figure 2.1).

Major surface boundary currents around Australia include the Indonesian Throughflow, Holloway, Leeuwin, South Australian, Flinders, Zeehan, East Australian and Hiri currents (see Excursus 17.1). Australia's boundary currents are an important conduit for the poleward heat and mass transport and interocean water exchange in the tropics (Indonesian Throughflow; Sprintall *et al.*, 2009) and the subtropics (Tasman Outflow; Hu *et al.*, 2015; van Sebille *et al.*, 2012).

Figure 17.1 Mean surface currents around Australia



Source: Pattiaratchi and Siji (2018) Figure 1

Excursus 17.1—Major Currents around Australia

Source: Wijeratne *et al.* (2018)

As illustrated in Figure 17.1, there are several currents that transport surface waters around Australia. The names and abbreviations of those discussed in this excursus are summarised in Table 17.2.

Table 17.2 Names and abbreviations of major currents

Name	Abbreviation
Antarctic Circumpolar Current	ACC
East Australian Current	EAC
Flinders Current	FC
Indonesian Throughflow	ITF
Hiri Current	HC
Holloway Current	HLC
Leeuwin Current	LC
North Vanuatu Jet	NVJ
North Caledonia Jet	NCJ
South Australian Current	SAC
South Equatorial Current	SEC
South Indian Counter Current	SICC
West Australian Current	WAC
Zeehan Current	ZC

Indonesian Throughflow

The Indonesian Throughflow (ITF) provides a tropical connection between the Pacific and Indian Oceans and contributes to the South Equatorial Current (SEC), the major westward flow across the Indian Ocean to the eastern Indian Ocean. ITF transports 16.4 Sv (or 10^6 m^3s^{-1}) of water into the Indian Ocean. The ITF is at a maximum during the southeast monsoon (June to August) and its interannual variability is associated with El Niño-Southern Oscillation (ENSO) events with stronger flows during La Niña events (Wijeratne *et al.*, 2018).

Holloway Current

A portion of the ITF flows onto the northwestern Australian continental shelf/slope through the Holloway Current (HLC; Bahmanpour *et al.*, 2016; Wijeratne *et al.*, 2018). The HLC flows to the southwest along the shelf edge of the North West Shelf and contributes to the Leeuwin Current (LC). The HLC extends to depths of 100–200 m and is generally located close to the shelf break. The HLC transport increases towards the southwest with the mean transport of 1.4 Sv at North West Cape. The HLC flows all year round but is subject to seasonal and interannual variability with a maximum in late autumn (April–May) and a minimum in summer (January–February). HLC responds to ENSO events and is stronger during the La Niña and weaker during El Niño events.

South Indian Counter Current

The South Indian Counter Current (SICC) originates in the western Indian Ocean to the south of Madagascar and flows eastward as three branches (southern: sSICC, central: cSICC, and northern: nSICC; Palastanga *et al.*, 2007; Menezes *et al.*, 2014; Wijeratne *et al.*, 2018). While the nSICC is relatively weak, the cSICC (1.4 Sv) and sSICC (6.8 Sv) contribute inflow to the LC at 23°S and 31°S respectively. The combined eastward transport of the cSICC and sSICC is ~8.2 Sv across 100°E with the majority (> 80%) of transport through the sSICC.

West Australian Current

The traditional view of subtropical gyre circulation of the southern Indian Ocean defines the West Australian Current (WAC) as the major eastern boundary current analogue to other ocean basins. However, the presence of the LC modifies this circulation, and the location of the WAC is between the cSICC and sSICC where ~80% of the sSICC flow moves northwards and then offshore.

Leeuwin Current

The Leeuwin Current (LC) is the unique poleward eastern boundary current along the west and south coasts of Australia (Smith *et al.*, 1991; Pattiaratchi and Woo, 2009; Ridgway and Godfrey, 2015). The LC starts at North West Cape, flows along the shelf break (~200 m) to the southern tip of Tasmania, and is described as the longest boundary current in the world (Ridgway and Condie, 2004). The LC follows the curvature of the coastline and turns eastward at Cape Leeuwin and extends along the southern continental shelf/slope as the South Australian Current (SAC). The LC/SAC becomes the Zeehan Current (ZC) and flows around southern Tasmania (Baines *et al.*, 1983; Cresswell, 2000). The southward LC transport increases from north to south with 1.4 Sv through North West Cape to 4.12 Sv at 32.8°S with the increase in transport due to the inflow from sSICC. The maximum LC transport along the western coast

occurs in May–June, with a minimum in October. The transport increases from November to January with a secondary minimum in February. The LC is strongest along the southwest corner of Australia as it flows past Cape Leeuwin into the Southern Ocean. The LC along the south coast has a maximum in June–July, around one month later than along the west coast.

South Australian Current

The South Australian Current (SAC) is the continuation of the LC to the east and has a mean transport of ~1.31 Sv at 136.5°E. The maximum transport occurs in August–September (that is, 4–5 months after the peak of HLC and 2–3 months after the peak in LC along the west coast). The SAC transport is also related to ENSO events with higher transport during La Niña events (Oke *et al*., 2018). The SAC becomes the Zeehan Current (ZC) to the east and is mainly confined to the continental shelf and the upper slope along the west coast of Tasmania with transport 1.9 Sv. The ZC is strongest in September.

Flinders Current

Along the southern coast, offshore of the LC, the Flinders Current (FC) is the dominant flow, extending from the surface to more than 1000 m, flowing westward from Tasmania and past Cape Leeuwin into the Indian Ocean. Along the southern continental slope, the FC is an undercurrent beneath the eastward flowing LC, SAC, and ZC, and a surface current further offshore. The FC gradually intensifies along its pathway from Tasmania to Cape Leeuwin with 6.9 Sv at 122°E increasing to 7.2 Sv at 116.5°E.

South Equatorial, Hiri and East Australian Currents

In the Pacific Ocean, the westward flowing South Equatorial Current (SEC) impinges on the eastern continental shelf slope of Australia (see Figure 16.1). The northern branches of the SEC (North Vanuatu Jet: NVJ, and North Caledonia Jet: NCJ) bifurcate at ~15°S to initiate the Hiri Current (HC), a clockwise circulation that flows into the Gulf of Papua and the southward flowing East Australian Current (EAC) along the Australian coast (Godfrey *et al*., 1980). The HC and EAC have different seasonal cycles—the EAC is at a maximum in December–January whilst the HC peaks in June–July. This indicates that the northern branches of SEC inflow (NVJ and NCJ) contribute more to southward (northward) transport during summer (winter).

NVJ and NCJ contribute a significant component (~11.8 Sv) of the southward EAC transport between 15–22°S. Southward transport of the EAC increased from 11.5 Sv at 20°S to 17.2 Sv at 27°S. To achieve the estimated transport at 27°S of 17.2 Sv, an inflow of ~5.7 Sv is required via the South Caledonia Jet (SCJ). Simulations from ozROMS (a shelf-scale, three-dimensional hydrodynamic model; Wijeratne *et al*., 2018) indicated that inflow from SCJ was mostly confined to the subsurface and transported ~6.4 Sv, in good agreement with the estimate of ~8 Sv by Kessler and Cravatte (2013). Thus SEC inflow to the EAC can be attributed as 65% via NVJ and NCJ and 35% via SCJ.

The EAC recirculation is defined as the northwards flow located further offshore of the main EAC southwards flow (Zilberman *et al*., 2014). The main EAC flow separates from the Australian coast at latitudes 30–34°S and flows eastward as the Tasman Front (TF; Bowen *et al*., 2005; Cetina-Heredia *et al*., 2014, Oke *et al*. 2019). The EAC extension reaches southern Tasmania and flows westward into the eastern Indian Ocean as the Tasman Outflow (TO) or Tasman Leakage (Ridgway and Dunn, 2007; van Sebille *et al*., 2012).

Antarctic Circumpolar Current

The Antarctic Circumpolar Current (ACC) surrounds Antarctica and connects the Indian, Pacific, and Atlantic Oceans. It is the strongest current in the global ocean, transporting 182 Sv from west to east. This current results from strong westerly winds across the Southern Ocean and the significant change in temperature from the equator to the poles. The major fronts in this region are the subantarctic front (SF) and the polar front (PF).

17.2 EO Sensors for Water Circulation

Various EO sensors and their data sources are introduced in Volume 1A, and interpretation of optical, thermal, and microwave imagery is considered in Volume 1B. There is no sensor presently flying that measures water circulation directly, but there are several which, in combination, tell us much about the ocean circulation. These are summarised in Table 17.3.

Table 17.3 EO sensors relevant to water circulation

TIR: Thermal infrared; SAR: Synthetic Aperture Radar

Type	Sensor	Platform	Relevance	Advantages	Disadvantages
Passive optical	Multispectral radiometer	Satellite or airborne	Eddies/currents in coastal zone, Wave texture	Global coverage, low cost	Low accuracy, coarse scale
	Hyperspectral radiometer	Airborne	Eddies/currents in coastal zone	High spectral resolution	High cost, high data volume
	TIR radiometer	Satellite or airborne	Surface water circulation	Possible to detect water movement at night	Clouds, low resolution
Active microwave	SAR	Satellite or airborne	Surface features e.g. ocean fronts, Eddies wakes—detect and track ships	All weather, so useful in tropical regions	High cost, specialised processing
	Radar altimeter	Satellite	Sea level change (tidal and non-tidal), Surface wind speed, Topography of ice sheets	All weather, highly precise	Not an imaging system, so measurements are only along infrequently repeated tracks (10–30 days)
	Scatterometer	Satellite	Surface topography/currents surface wind speed and direction, Sea ice, Snow accumulation	Frequent, global coverage	Impacted by rain and extreme winds
Gravity	Accelerometers	Satellite	Water depth, Mean circulation	Unique global coverage	Relatively coarse resolution

17.2.1 Radar altimeters

The type of mission that comes closest to providing a direct measure of ocean circulation—namely the variations of sea surface height associated with that circulation—is the radar altimeter (see Sections 9.5, 12.2.1 and 16.2.4). As depicted in Figure 12.1, the altimeter measures the distance from the satellite to the surface of the ocean at nadir by measuring the time it takes for an emitted pulse to be returned. Key to its success as a sensor is that it does this with centimetre accuracy at a range of ~1000 km, and that the position of the satellite is also determined with similar precision (using a suite of semi-redundant systems: DORIS, GPS, and laser ranging). As the satellite orbits the Earth it is thus able to acquire a network of lines along which the sea surface height (SSH), relative to a reference ellipsoid, is precisely measured (see Section 12.4.3).

However, oceanographers need to know the sea surface height relative to the geoid, not the reference ellipsoid. This quantity is usually called the dynamic topography (DT) because it is the signal associated with ocean circulation. An estimate of the geoid relative to the reference ellipsoid has been determined from the gravity measurements of the GRACE and GOCE missions, (see Excursus 1.1 and Volume 1A—Section 3.3 and Volume 1A—Figure 8.4), which enables the DT to be estimated (see Figure 12.1). The surface velocity field (V or geostrophic velocity) can be determined in a straightforward manner from the DT (to first order) by geostrophy:

$$V = \frac{\nabla \eta}{f}$$

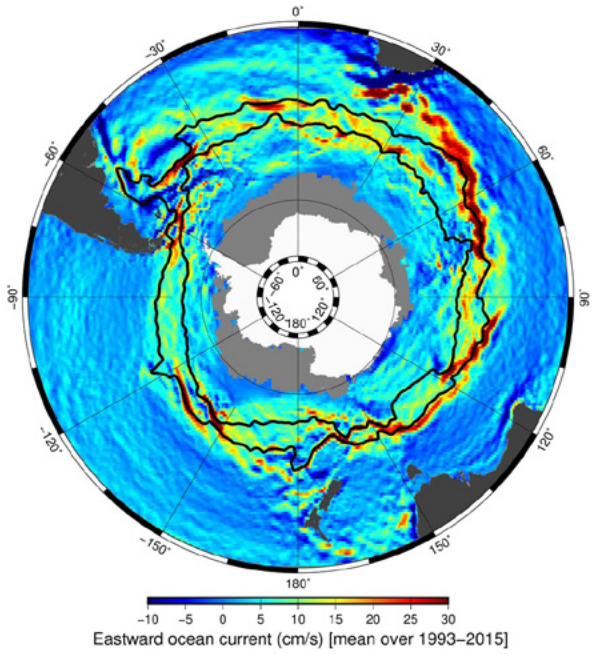
where f is the Coriolis parameter and η is either the DT at a particular time, or its time-mean, known as the mean dynamic topography (MDT). There is, however, a problem. The geoid is not yet known to the same accuracy as the SSH, so the DT and consequently estimates of V derived from it have relatively large errors at mesoscale resolution. Thus, a map like Figure 17.1 cannot yet be made directly from an EO-based estimate of the MDT. A workaround solution exploits the fact that the time-mean of the SSH (the so-called mean sea surface or MSS) is a very accurate measure of the geoid plus the MDT. By subtracting this from SSH we get an accurate estimate of the

sea surface height anomaly (SSHA), or the departure of DT from the mean. This is why altimetry is often described as a technique for measuring the changes (from daily to seasonally and interannually, or the trend) of sea level, rather than sea level in an absolute sense. To complete this workaround solution, an independent estimate of the MDT can be added to the altimetric SSHA to produce estimates of the DT. For this purpose in the IMOS Gridded Sea Level (GSL) product, we use the MDT of the Bluelink global model (see Excursus 2.2).

Archives of satellite imagery are valuable for mapping the speed of surface water movement. For example, in Figure 17.2 the speed of the ACC was modelled using 23 years ocean height observations derived from satellite altimetry.

Figure 17.2 Speed of Antarctic Circumpolar Current

23 years of satellite altimetry data from the European Copernicus Marine Services were used to map the speed of the ACC.



Source: European Copernicus Marine Services. Retrieved from *https://theconversation.com/explainer-how-the-antarctic-circumpolar-current-helps-keep-antarctica-frozen-106164*

17.2.2 Passive optical

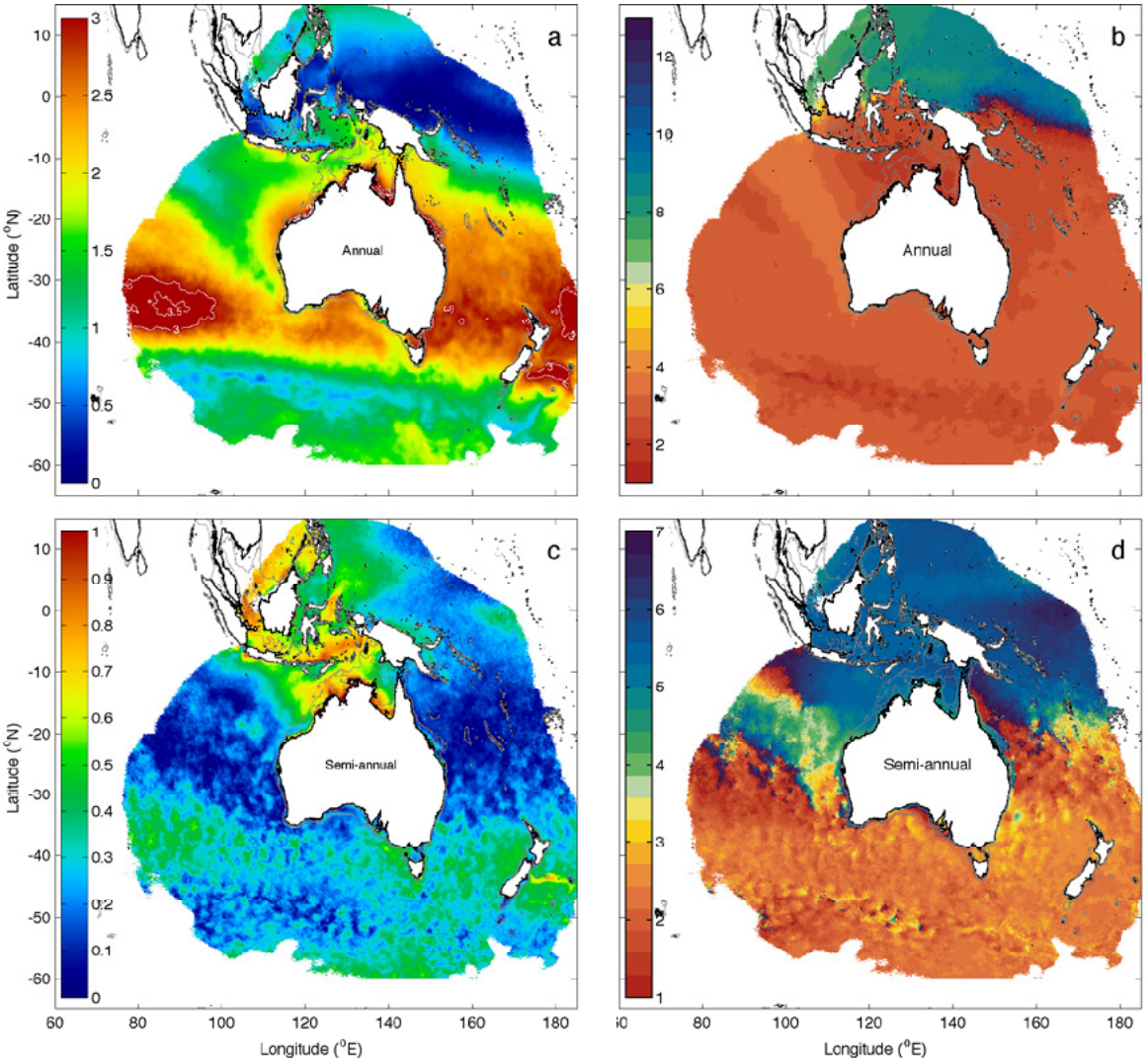
While not providing a direct measure of ocean circulation, passive optical imagery of the ocean (see Section 8) does complement altimetry by yielding stunning images (during periods of clear skies) of the complexities of the flow, as well as the impact of both vertical and horizontal advection (bringing cold water to the surface, or warm tropical waters poleward, respectively). Much can be inferred about the water circulation by analysing the differences (over time or space) in EO optical imagery—but none of these analyses are as straightforward as the radar altimetry equation given in Section 17.2.1. Feature tracking can sometimes be used to infer the advection velocities from sequences of optical images (Bowen *et al.*, 2002).

The main weakness of optical imagery is the impact of clouds. Perhaps the least-impacted application of optical imagery is the determination, from many years of images, of the annual cycle of temperature (see Section 14). But what does this tell us about circulation? This is best explained with reference to an example from the Sea Surface Temperature Atlas of the Australian Regional Seas (SSTAARS, Wijffels *et al.*, 2018). To produce SSTAARS, the annual harmonics of a 25-year (1992–2016) record of daily, high resolution (~2 km), gridded SST observations (see Section 14.5.2 and Wijffels *et al.*, 2018) were analysed (see Figure 17.3). The analysis was done independently for each pixel, yielding a highly detailed map for the whole Australasian region, that revealed fresh insights into many features of the seasonal cycle of Australia's regional circulation. Since a consortium of Australian agencies have downloaded and curated the Large Area Coverage (LAC) data directly from the relevant satellites for several decades, Australia is one of the few countries where this analysis is possible.

If there were no ocean circulation, the amplitude of the annual cycle of sea surface temperature (SST) would be a lot more spatially uniform than the observed amplitude (see Figure 17.3a). Figure 17.4, for example, shows how the amplitude of the annual cycle of temperature is greatly reduced along the path of the LC (see Table 17.2), which brings warm water south in winter. Wijffels *et al.* (2018) provide and discuss more detailed images of temperature variations around the Australasian region.

Figure 17.3 Temperature variations

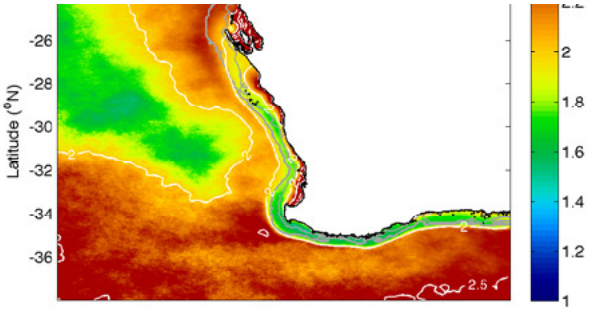
Pixel-wise estimates of (a) the annual harmonic amplitude (°C) and (b) month of the peak temperature. Panels (c) and (d) are as for (a) and (b), but for the semiannual harmonic. Note the change in scale between (a) and (c). Phase is shown in months where '1' relates to January 1 in (a) and January 1/July 1 in (d). As an example, in regions where phase=3 in (b), annual temperatures reach their maximum in March. Grey contours mark the 50 m and 200 m isobaths.



Source: Susan Wijffels, Woods Hole Oceanographic Institution

Figure 17.4 Detailed view of temperature variation

Image shown in Figure 17.3a, with a reduced geographic and temperature range to show more detail.



Source: Susan Wijffels, Woods Hole Oceanographic Institution

17.3 Circulation Patterns

The first images of the ocean acquired by the early thermal imaging sensors revealed something about the ocean that oceanographers and mariners had hitherto only glimpsed from the tracks of becalmed ships or drifting bottles—that the circulation of the ocean is incredibly complex and ever-changing. This conclusion relies on the fact that the temperature of the water is, to an extent, a marker of where it is from, and explains why optical images of the surface properties of the ocean often look like a liquid that has been stirred. At high resolution, the stirring is being done by small eddies (see Section 1.4.3). At larger scales the stirring is generated by currents such as the LC or EAC (see Table 17.2 and Excursus 17.1).

In the EAC for example, eddies are very common and can extend 200–300 km in diameter (see Section 2.3). Excursus 17.2 demonstrates how satellite altimetry and passive optical imagery can be used in combination to follow the changing circulation in this dynamic region for a month in Autumn 2021.

Ever since surface current maps were first produced in the nineteenth century the variability of ocean currents has also been recognized.
(Wells, 1986)

Excursus 17.2—Example Circulation Study

Source: David Griffin, CSIRO
Further Information: *http://oceancurrent.imos.org.au/news.php*

The complexity and variability of ocean circulation are particularly intense off the eastern Australian coast near Sydney. Here the EAC interacts with eddies or forms new ones (Oke *et al.*, 2019), which can aid or frustrate sailors. This example follows the movement of a series of eddies in this region during early Autumn 2021 using a combination of radar altimetry and passive optical imagery (SST and ocean colour).

Figure 17.5 shows a sequence of four images at ~10 day intervals, which correspond to occurrences of clear skies. Figure 17.5a shows that on 4 March 2021 the EAC flowed (as it often does, see Schaeffer *et al.*, 2017, Archer *et al.*, 2017) as a narrow (~25 km) jet of warm water that followed the continental margin southwards. It passed Sydney before leaving the shelf near 34.5°S to flow over and around 'warm-core A', a ~300 km diameter anticyclonic eddy. This process of flowing over and around an existing eddy was described as 'flooding' by Baird *et al.* (2011). Warm-core A was flanked by two cyclonic eddies, cold-core A to the northeast, centred near 33.5°S, 155°E, and cold-core B mostly off-image to the south near 36°S, 154.5E°. Like most cold-core eddies, these are less conspicuous in the SST imagery than the warm-core eddies, but are equally conspicuous in the sea level anomaly field. The geostrophic estimate of velocity associated with cold-core A is in good agreement with the trajectory of a satellite-tracked surface drifter. North and east of cold-core A lies warm-core B, a large ridge continuing off-image to the north while also being partially attached (see the saddle point in the sea level field near 34°S, 158°E) to warm-core C in the south, centered at 35.5°S 158°E. Cold-core C at far southeast, centred near 35°S, 160°E, completes the inventory of meso-scale features in this 6°×11° patch of ocean.

Figure 17.5b (13 March) shows that in some places there has been little change, but much in others. The centre of warm-core A has barely moved, but a slight change of shape takes the EAC closer to Jervis Bay (about 200 km south of Sydney) before peeling offshore. In contrast, cold-core A has all but disappeared, its place taken by warm-core B merging with warm-core C. Cold-core B has come more into view, having moved north, while cold-core C is essentially unchanged.

In Figure 17.5c (24 March) two new features are visible:

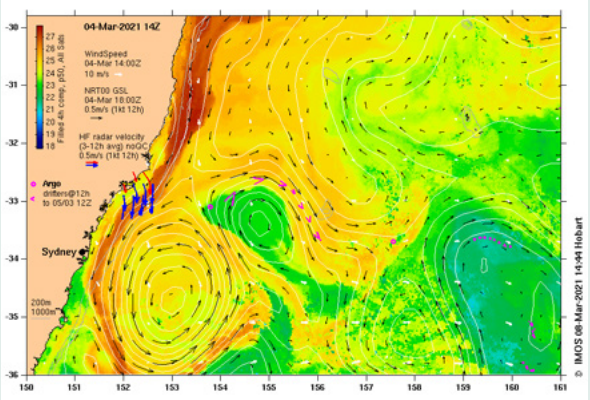
- cold water along much of the coast, probably the result of strong upwelling-favourable winds that blew in the days prior to the image, associated with the record-breaking storms that resulted in widespread flooding; and
- a frontal eddy (Schaeffer *et al.*, 2017) inshore of the EAC at 31°S, 200 km south of where it was 20 days earlier (see *http://oceancurrent.imos.org.au/product.php?product=oceancolour&region=Bris-Syd&date=20210304040000&rtype=DR*). The other features are all still visible, having evolved, including northwest motion of cold-core B, a precursor of what is shown in the next image.

Figure 17.5d (3 April) shows that a critical stage of the EAC eddy-shedding process has been reached. Warm-core A is becoming mostly isolated from the EAC as cold-core B continues to move farther to the northwest. Much of the EAC is evidently flowing east near 33.5°S into and around warm-cores B and C (which seem to be separating again) instead of warm-core A. To further complicate the situation over the upper continental slope near 32.5°S, the frontal eddy has continued its southward motion, and is now centred near 32.2°S, about 1° north of the incipient point of EAC separation.

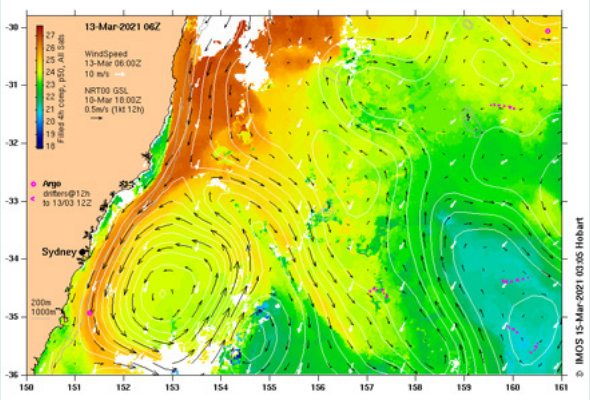
Figure 17.5 Circulation in EAC

This sequence of four images showed water circulation in the EAC from 4 March to 3 April 2021. Colour: sea surface temperature (4 hour composite using all available thermal imagery). White contours: sea level isoheights at 0.1 m intervals. Black vectors: geostrophic velocity calculated from the height field (see key for scale). Other symbols are defined in the legends.

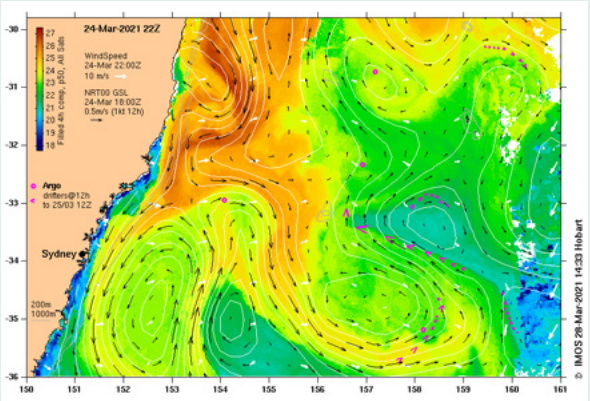
a. 4 March 2021



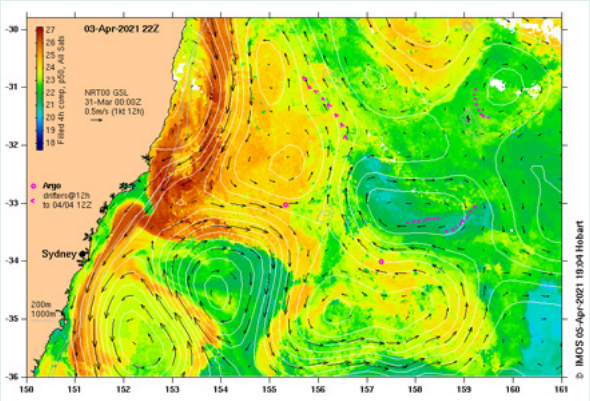
b. 13 March 2021



c. 24 March 2021



d. 3 April 2021



17.4 Ocean Fronts

Fronts are regions where large property changes occur within a small distance. Ocean fronts are defined as regions of large horizontal gradients in water properties (such as temperature and/or salinity). The frontal zone is a region of rapid property change at the surface, and the frontal axis is the location of the largest horizontal property gradient. To avoid strong gradients, both fluids and gases tend to eliminate fronts by turbulent mixing. Since the scale of both ocean and atmospheric fronts depends on the scale of their driving processes, they essentially represent a balance between two or more forces. Accordingly, ocean fronts are associated with convergent flow and vigorous water movement, with greater mixing across larger gradients (Tomczak, 1996).

Ocean fronts are commonly areas of nutrient concentration, thus high primary productivity, with larger fronts serving as fish feeding grounds (see Section 20.7.1). These regions also accumulate floating material, oil, and other forms of pollution. Excursus 17.3 demonstrates the use of EO imagery to monitor the formation and movement of ocean fronts.

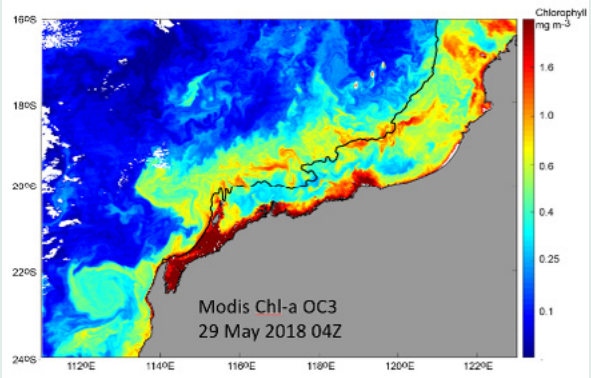
Associations between marine vertebrates and oceanographic fronts vary spatially, temporally and between taxa, influenced by both the biophysical properties of fronts and taxon-specific foraging ecology (Hunt et al. 1999). Despite this variability, there now exists a considerable body of evidence indicating that persistent mesoscale frontal zones are ecologically significant across the oceans (e.g. Polovina et al. 2001; Bost et al. 2009).
(Scales et al., 2014)

Excursus 17.3—Ocean Fronts

Source: Chari Pattiaratchi, University of Western Australia
Further Information: *http://oceancurrent.imos.org.au/news.php*

Ocean fronts, defined as regions of large horizontal gradients in water properties (temperature, salinity etc), are areas of high productivity globally. Satellite imagery from the northwest shelf indicates the existence of two types of fronts extending over 1000 km from North West Cape to Cape Leveque. The nearshore band of high chlorophyll (see Figure 17.6) is associated with a very cold band of water at the coast that usually develops every May, persists throughout winter, and is evident in the SSTAARS climatology (see Section 14.5.2). Water in shallow coastal regions become more saline over summer due to evaporation and, with winter cooling, the water becomes much denser than water further offshore. This cool, dense water then flows offshore along the bottom as a dense, shelf water cascade, which has been observed by ocean glider deployments in the region and other regions of Australia.

Figure 17.6 MODIS Chlorophyll a OC3 29 May 2018



On continental shelves, fronts can also develop just through the reduction of tidal currents with depth, without the influx of different water masses. Simpson and Hunter (1974) showed that a front could develop where mixing due to tidal currents was no longer strong enough to overcome stratification. Many studies undertaken globally have shown that the ratio of the water depth (h) to the cubed value of the nearbed current speed (U) is a good indicator of the location of tidal fronts, in particular where:

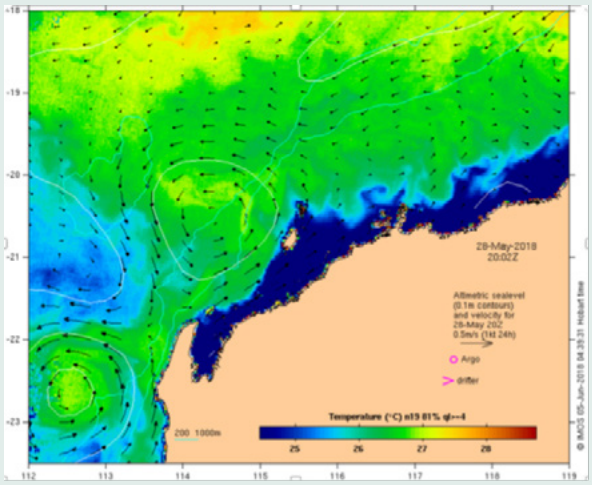
$$\log\left(\frac{h}{|U^3|}\right) = 2.7$$

The band of higher chlorophyll found further offshore, suggesting the presence of a second front, lies in close proximity to the predicted Simpson and Hunter tidal front location (indicated by black line in Figure 17.6).

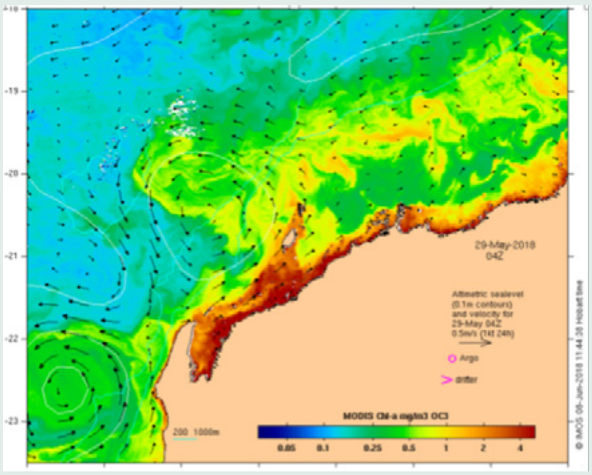
Coastal currents transporting different water masses can also contribute to the existence of fronts and the frontal location could also be related to the location of the Holloway Current that flows towards the southwest. The offshore chlorophyll maximum, although much weaker than in the nearshore front, has affected about 1000 km of the mid-shelf region (see Figure 17.7b). Recent work by Thums *et al.* (2017) demonstrated that flatback turtles (*Natator depressus*) followed the location of the predicted Simpson and Hunter tidal front when migrating along the Kimberley Coast.

Figure 17.7 Frontal systems on Australian northwest shelf

a. Temperature 28 May 2018



b. MODIS chlorophyll a product 29 May 2018



17.5 Further Information

Pattiaratchi, C., Wijeratne, S., and Proctor, R. (2019). A current affair: the movement of ocean waters around Australia. The Conversation. *https://theconversation.com/a-current-affair-the-movement-of-ocean- waters-around-australia-96779*

Pattiaratchi, C.B., and Siji, P. (2020). Variability in ocean currents around Australia. In *State and Trends of Australia's Ocean Report*. (Eds: Richardson, A.J., Eriksen, R., Moltmann, T., Hodgson-Johnston, I., and Wallis, J.R.) Integrated Marine Observing System. *www.imosoceanreport.org.au*

IMOS Ocean Current: *http://oceancurrent.imos.org.au/*

Ocean Current Illustrations:
Diagrams: *https://research.csiro.au/ncmi-idc/information/ocean-circulation/ocean-current-diagrams/*
Animations: *https://research.csiro.au/ncmi-idc/information/ocean-circulation/ocean-current-animations/*

Bluelink:*https://www.csiro.au/en/Research/OandA/Areas/Oceans-and-climate/Bluelink*

Marine Science Australia: *https://www.ausmarinescience.com/marine-science-basics/ocean-currents/*

17.6 References

Agrawal, D.C. (2018). The Sverdrup: The Non-SI Unit of Large-Scale Volume Transport Over the Globe. *The Physics Teacher*, 56, 377. *https://doi.org/10.1119/1.5051151*

Archer, M.R., Roughan, M., Keating, S.R., and Schaeffer, A. (2017). On the variability of the East Australian Current: Jet structure, meandering, and influence on shelf circulation. *Journal of Geophysical Research: Oceans*, 122, 8464–8481. *https://doi.org/10.1002/2017JC013097*.

Bahmanpour, M.H., Pattiaratchi, C., Wijeratne, S., Steinberg, C., and D'adamo, N. (2016). Multi-year observation of the Holloway current along the shelf edge of north-western Australia. *Journal of Coastal Research*, 75, 517–521.

Baird, M.E., Suthers, I.M., Griffin, D.A., Hollings, B., Pattiaratchi, C., Everett, J.D., Roughan, M., Oubelkheir, K., and Doblin, M. (2011). The effect of surface flooding on the physical-biogeochemical dynamics of a warm-core eddy off southeast Australia. *Deep-Sea Research Part II: Topical Studies in Oceanography*, 58, 592–605. doi:10.1016/j.dsr2.2010.10.002

Baines, P.G., Edwards, R.J., and Fandry, C.B. (1983). Observations of a new baroclinic current along the western continental slope of Bass Strait. *Australian Journal of Marine and Freshwater Research*, 34, 155–157.

Bost, C.A., Cotté, C., Bailleul, F., Cherel, Y., Charrassin, J.B., Guinet, C., Ainley, D.G., and Weimerskirch, H. (2009). The importance of oceanographic fronts to marine birds and mammals of the southern oceans. *Journal of Marine Systems*, 78, 363–376.

Bowen, M.M., Emery, W.J., Wilkin, J.L., Tildesley, P.C., Barton, I.J., and Knewtson, R. (2002). Extracting Multiyear Surface Currents from Sequential Thermal Imagery Using the Maximum Cross-Correlation Technique, *Journal of Atmospheric and Oceanic Technology*, 19(10), 1665-1676.

Bowen, M.M., Wilkin, J.L., and Emery, W.J. (2005). Variability and forcing of the East Australian Current. *Journal of Geophysical Research*, 110, C03019. *https://doi.org/10.1029/2004JC002533*

Cetina-Heredia, P., Roughan, M., van Sebille, E., and Coleman, M. (2014). Long-term trends in the East Australian Current separation latitude and eddy driven transport. *Journal of Geophysical Research: Oceans*, 119, 4351–4366. *https://doi.org/10.1002/2014JC010071*

Cresswell, G. (2000). Currents of the continental shelf and upper slope of Tasmania. *Papers and Proceedings of the Royal Society of Tasmania*, 133, 21–30.

GA (2021). *Oceanography* webpage, Geoscience Australia website: https://www.ga.gov.au/scientific-topics/disciplines/oceanography

Godfrey, J.S., Cresswell, G.R., Golding, T.J., and Pearce, A.F. (1980). The separation of the East Australian Current. *Journal of Physical Oceanography*, 10, 430–440.

Hu, D., Wu, L, Cai, W., Gupta, A.S., Ganachaud, A., Qiu, B., Gordon, A.L., Lin, X., Chen, Z., Hu, S., Wang, G., Wang, Q., Sprintall, J., Qu, T., Kashino, Y., Wang, F., and Kessler, W.S. (2015). Pacific western boundary currents and their roles in climate. *Nature*, 522, 299–308. *https://doi.org/10.1038/nature14504*.

Hunt, G. Jr, Mehlum, F., Russell, R., Irons, D., Decker, M., and Becker, P. (1999). Physical processes, prey abundance, and the foraging ecology of seabirds. *Proceedings of 2*2nd *International Ornithological Congress* (Eds N.J. Adams, and R. Slotow), pp. 2040–2056. BirdLife South Africa, Durban, Johannesburg.

Kessler, W.S., and Cravatte, S. (2013). Mean circulation of the Coral Sea. *Journal of Geophysical Research: Oceans*, 118(12), 6385–6410.

Menezes, V.V., Phillips, H.E., Schiller,A., Bindoff, N.L., Domingues, C.M., and Vianna, M.L. (2014). South Indian Countercurrent and associated fronts. *Journal of Geophysical Research: Oceans*, 119, 6763–6791. *https://doi.org/10.1002/2014JC010076*

Oke, P.R., Griffin, D.A., Rykova, T., and De Oliveira, H.B. (2018). Ocean Circulation in the Great Australian Bight in an eddy-resolving ocean reanalysis: the eddy field, seasonal and interannual variability. *Deep Sea Research*, 157–158, 11–26. doi:10.1016/j.dsr2.2018.09.012

Oke, P., Roughan, M., Cetina-Heredia, P.,Pilo, G.,Ridgway, K., Rykova, T., Archer, M.R., Coleman, R.C., Kerry, C.G., Rocha, C., Schaeffer, A., and Vitarelli, E. (2019). Revisiting the circulation of the East Australian Current: its path, separation, and eddy field. *Progress in Oceanography*, 176, 102139. *https://doi.org/10.1016/j.pocean.2019.102139*

Palastanga, V., van Leeuwen, P., Schouten, M., and de Ruijter, W. (2007). Flow structure and variability in the subtropical Indian Ocean: Instability of the South Indian Ocean Countercurrent. *Journal of Geophysical Research*, 112, C01001. *https://doi.org/10.1029/2005JC003395*

Pattiaratchi, C.B, and Siji, P. (2020). Variability in ocean currents around Australia. In *State and Trends of Australia's Ocean Report* (Eds: Richardson, A.J., Eriksen, R., Moltmann, T., Hodgson-Johnston, I., Wallis, J.R.). doi: 10.26198/5e16a2ae49e76

Pattiaratchi, C., and Woo, M. (2009). The mean state of the Leeuwin Current system between North West Cape and Cape Leeuwin. *Journal Royal Society Western Australia*, 92, 221–241.

Polovina, J.J., Howell, E., Kobayashi, D., and Seki, M.P. (2001). The transition zone chlorophyll front, a dynamic global feature defining migration and forage habitat for marine resources. *Progress in Oceanography*, 49, 469–483.

Ridgway, K.R., and Condie, S.A. (2004). The 5500-km-long boundary flow off western and southern Australia. *Journal of Geophysical Research*, 109, C04017. *https://doi.org/10.1029/2003JC001921*

Ridgway, K.R., and Dunn, J.R. (2007). Observational evidence for a Southern Hemisphere oceanic supergyre. *Geophysical Research Letters*, 34, L13612. *https://doi.org/10.1029/2007GL030392*

Ridgway, K.R., and Godfrey, J.S. (2015). The source of the Leeuwin Current seasonality. *Journal of Geophysical Research: Oceans*, 120, 6843–6864. *https://doi.org/10.1002/2015JC011049*

Scales, K.L., Miller, P.I., Hawkes, L.A., Ingram, S.N., Sims, D.W., and Votier, S.C. (2014). On the Front Line: frontal zones as priority at-sea conservation areas for mobile marine vertebrates. *Journal of Applied Ecology*, 51, 1575–1583. doi:10.1111/1365-2664.12330

Schaeffer, A., Gramoulle, A., Roughan, M., and Mantovanelli, A. (2017), Characterizing frontal eddies along the East Australian Current from HF radar observations. *Journal of Geophysical Research: Oceans*, 122, 3964–3980. doi:10.1002/2016JC012171.

Simpson, J.H., and Hunter, J.R. (1974). Fronts in the Irish Sea. *Nature*, 250, 404–406.

Smith, R. L., Huyer, A., Godfrey, J.S., and Church, J. (1991). The Leeuwin current off western Australia, 1986– 1987. *Journal Physical Oceanography*, 21, 323–345.

Sprintall, J., and Revelard, A. (2014). The Indonesian throughflow response to Indo-Pacific climate variability. *Journal of Geophysical Research: Oceans*, 119, 1161–1175. *https://doi.org/10.1002/2013JC009533*

Sprintall, J., Wijffels, S. E., Molcard, R., and Jaya, I. (2009). Direct estimates of the Indonesian throughflow entering the Indian Ocean: 2004–2006. *Journal of Geophysical Research*, 114, C07001. *https://doi.org/10.1029/2008JC005257*

Tomczak, M. (1996). *Fronts in shallow seas and estuaries*. *https://www.mt-oceanography.info/ShelfCoast/notes/chapter09.html*

Thums, M., Waayers, D., Zhi, H., Pattiaratchi, C.B., Bernus, J., and Meekan, M.G. (2017). Environmental predictors of foraging and transit behaviour in flatback turtles (*Natator depressus*). *Endangered Species Research*, 32, 333–349.

van Sebille, E., England, M.H., Zika, J.D., and Sloyan, B.M. (2012). Tasman leakage in a fine resolution ocean model. *Geophysical Research Letters*, 39, L06601. *https://doi.org/10.1029/2012GL051004*

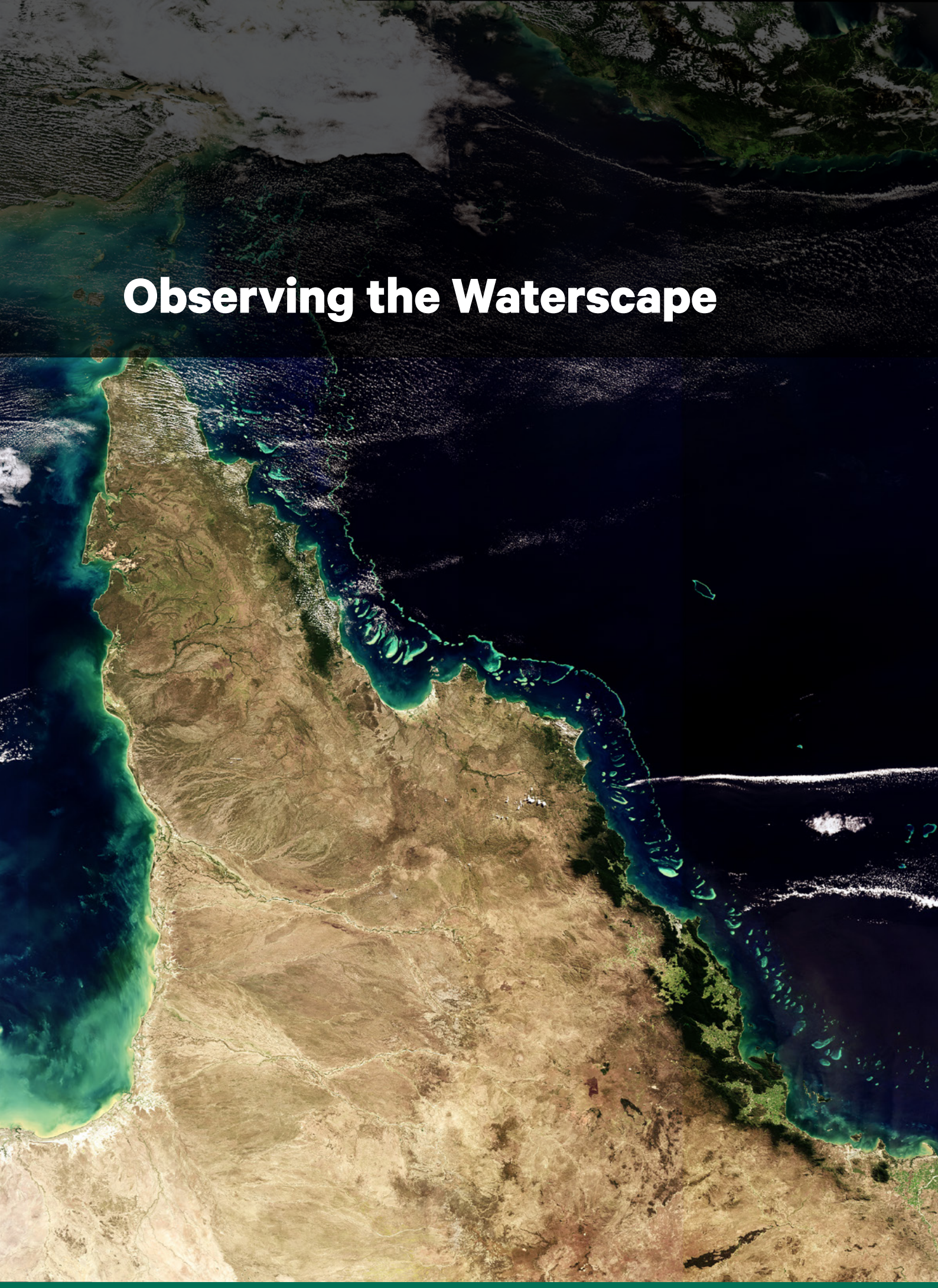
Wells, N. (1986). *The Atmosphere and Ocean. A Physical Introduction*. Taylor and Francis, London.

Wijeratne, S., Pattiaratchi, C., and Proctor, R. (2018). Estimates of Surface and Subsurface Boundary Current Transport Around Australia. *Advancing Earth and Space Science*, 123, 3444–3466. *https://doi.org/10.1029/2017JC013221*

Wijffels, S.E., Beggs, H., Griffin, C., Middleton, J.F., Cahill, M., King, E., Jones, E., Feng, M., Benthuysen, J.A., Steinberg, C.R., and Sutton, P. (2018). A fine spatial scale sea surface temperature atlas of the Australian regional seas (SSTAARS): seasonal variability and trends around Australasia and New Zealand revisited. *Journal of Marine Systems*, 187, 156–196. *https://doi.org/10.1016/j.jmarsys.2018.07.005*

Zilberman, N.V., Roemmich, D.H., and Gille, S.T. (2014). Meridional volume transport in the South Pacific: Mean and SAM-related variability. *Journal of Geophysical Research: Oceans*, 119, 2658–2678. *https://doi.org/10.1002/2013JC009688*

Observing the Waterscape



The following three sections describe specific uses of EO data in a range of applications related to the biogeochemical environment of surface waters in Australia. These applications rely on a variety of EO and other data sources, image processing approaches, and scientific models and, while not exhaustive, they represent the diversity of uses for which EO data is relevant in the Australian surface water environment.

The following three sections detail EO-based analyses of water:

- colour—describes use of optical EO imagery to map and model characteristics of water that are related to its perceived colour, and methods that can be used to determine substratum colour (see Section 18); and
- quality—presents EO data and approaches for determining water quality in marine and inland waters (see Section 19).
- ecology—introduces EO methods for mapping and monitoring coastal and marine aquatic environments, (see Section 20).

Contents

18 Colour 345

19 Quality 367

20 Ecology 395

Background image on previous page: Envisat MERIS image of Great Barrier Reef, Queensland, acquired on 18 May 2008. **Source:** © ESA. Retrieved from *https://www.esa.int/ESA_Multimedia/Images/2009/04/The_Great_Barrier_Reef_Australia*



18 Colour

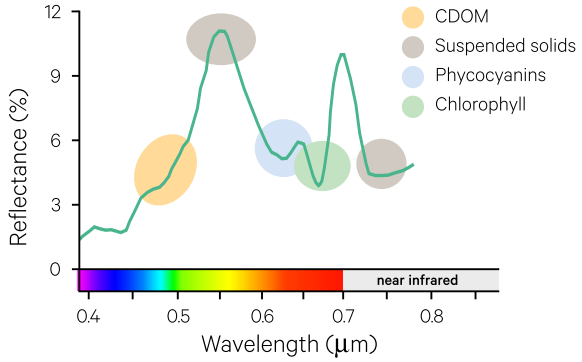
Janet Anstee

Observing water colour is an ancient method for assessing water quality. The surface colour of ocean waters is now considered to be an Essential Climate Variable for biological activity, and can be used to provide information to track long term climate change in aquatic systems (GCOS, 2018).

The colour of waterbodies can be reliably detected using optical EO (see Section 8), and researchers have demonstrated that optical water colour parameters derived from EO datasets can infer water quality (see Section 19). Changes in water colour can be similarly monitored using optical EO datasets by comparing multi-temporal images (see Volume 2D).

Figure 18.1 Characteristic reflectance features of water colour constitutents

Coloured water reflectance components are shown for chlorophyll-rich water. Spectral features are exaggerated in this graph to highlight individual components. Note that the actual reflectance also varies with the density of particles in the water (see Figure 18.2). Note: CDOM = Coloured Dissolved Organic Matter.



Source: Erin Hester, North Carolina State University

The optical constituents of water (introduced in Section 8) that result in its colour are:

- pure water—optically pure (see Section 8.2.1);
- photosynthetic pigments—phytoplankton and cyanobacteria (see Section 8.2.2);
- particulate matter—'non-algal' particles (NAP), both organic and inorganic (see Section 8.2.3):
- coloured dissolved organic matter (CDOM)—from hydrocarbon compounds (see Section 8.2.4); and
- coloured dissolved inorganic matter (CDIM)—from mineral compounds (see Section 8.2.5).

Where the water colour is clearly attributable to the interactions between pure water and one of the other optical constituents, EO data can be used to reliably map and monitor the concentration of that constituent. This situation occurs for the 'optically simple' waters that characterise deep oceans. In these 'Case 1' waters (as defined in Section 8.3.1) the water colour varies with the concentration of phytoplankton and its breakdown products (see Sections 18.5 and 18.6). As such, simple relationships can be established between phytoplankton concentration and the optical reflectance recorded by EO sensors (see Sections 5.2.3.1 and 8.2.2). However, in complex waters multiple optically active constituents occur resulting in characteristic reflectance features for the four water colour constituents shown in Figure 18.1. These are 'case 2' waters (see Section 8.3.1).

Background image: Algal bloom in Westlake Park, Melbourne, during March 2014. Source: © Nearmap

Recommended Chapter Citation: Anstee, J.M. (2021). Colour. Ch 18 in *Earth Observation: Data, Processing and Applications. Volume 3B—Surface Waters.* CRCSI, Melbourne. pp. 345–365. ISBN 978-0-6482278-5-4

In most inland and coastal waters, however, water colour derives from the interactions between multiple optical constituents. These 'Case 2' waters are 'optically complex' and require more sophisticated models based on optical physics to unravel their components (see Section 18.6). In particular, algae can confuse simple mapping techniques as it both contains the pigment of chlorophyll and forms part of suspended matter (Dekker *et al*., 2001).

Optically complex waters involve non-covarying concentrations of several optical constituents (see Section 18.1). Concentrations of these constituents can change rapidly, in both time and space, based on climatic, seismic, and/or anthropogenic 'events', and seasonal, lunar, and diurnal cycles. Optically complex waters can be both:

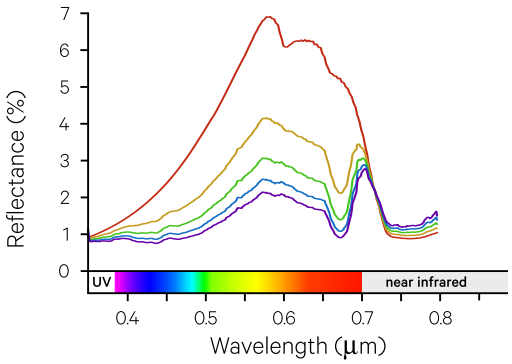
- optically deep (see Section 18.3.1)—the EO signal only derives from the water surface and the water column (plus atmospheric scattering); and
- optically shallow (see Sections 18.3.1 and 18.3.2)—the reflectance from the substratum is also measurable by an EO sensor.

Modelling approaches to the radiative transfer process are introduced in Section 8.4.2.4. When the optical properties of a natural waterbody are known (or can be reasonably assumed), bio-optical models can simulate the optical impact of varying concentrations of different optical constituents and identify those constituents that make greatest contribution to water colour variations (see Figure 18.2).

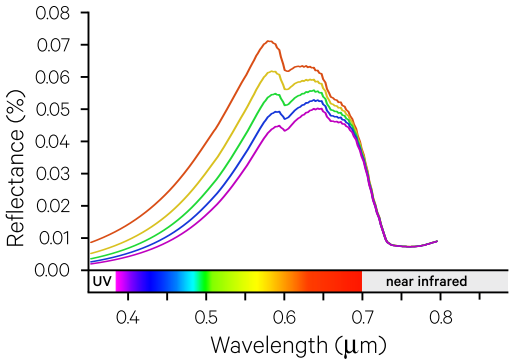
Figure 18.2 Simulations of waterbody reflectance

The Bio-opti model was used to generate reflectance spectra assuming a nadir view of a waterbody with depth 10.5 m over a sand substrate. Concentrations of three water column constitutents have been varied, with lowest concentration shown as violet through to the highest concentration as red. These simulations show the impact of these changed concentrations on reflectance spectra.

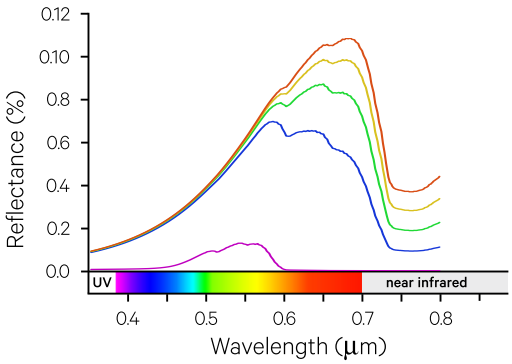
a. Chlorophyll a (CHLA) 0.001–50 μg/l (with CDOM 0.25 m^{-1}, NAP 22.266 mg/l)



b. Coloured dissolved organic matter (CDOM) 0.001–5 m^{-1} (with CHLA 0.001 μg/l, NAP 22.266 mg/l)



c. Non-organic particles (NAP) 0.001–100 mg/l (with CHLA 0.001 μg/l, CDOM 0.25 m^{-1})



Source: Yi Qin, CSIRO

18.1 Colour of Australian Surface Waters

The near pristine marine waters around parts of Australia justify the poetic description of 'jewel-sea'. However, as introduced in Section 7.1, the colour of a waterbody varies with its organic and inorganic content (which can result from both natural and anthropogenic sources), its depth, and its substratum. While clear water is viewed as 'natural', it may not be 'typical' for some aquatic environments. For example, the water in smaller Australian inland waterbodies is frequently stained brown by tannins leached from the foliage and/or bark of local flora and from soil carbon.

Water colour indicates the type and quantity of the optically active constituents in the water column. Algae, suspended sediment, and dissolved organic material can influence the absorption and/or the scattering of the water. These constituents fluctuate in natural waters due to the inflow of rivers and creeks, or inputs of nutrients, pollution, and sediments; additionally currents and wind can cause mixing and resuspension. For example, in Figure 18.3, water colour ranges from blue to aqua to green in coastal waters, and from green to yellow to brown in inland waters, with the colour varying depending on what is in the water:

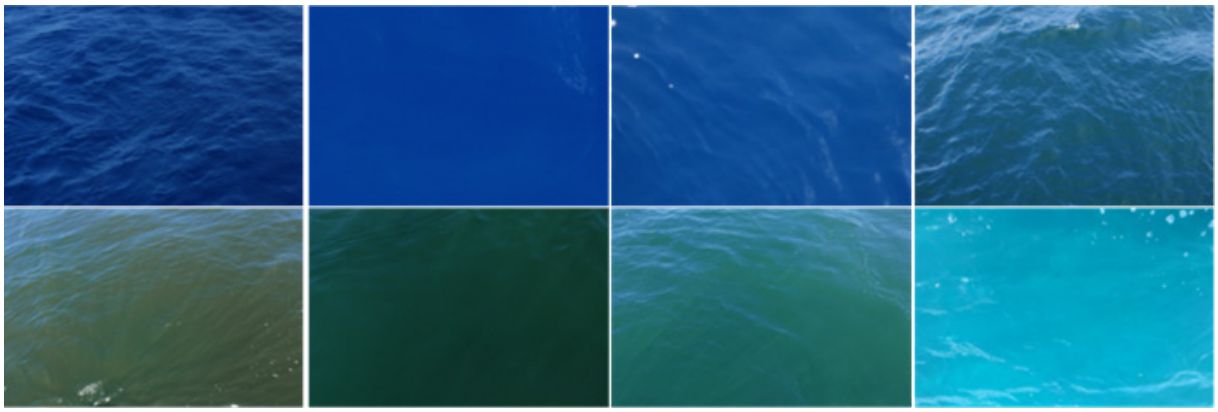
- phytoplankton generally makes the water green;
- non-algal particulates, such as sand, silt, or mud make the water vary from caramel to grey to brown; and
- dissolved organic matter makes the water yellow to orange to dark brown or almost black (like black tea).

I love her far horizons,
I love her jewel-sea,
(Dorothea Mackellar, 'My Country')

Figure 18.3 Variations in surface water colour

In the photos below, the water colour ranges from aqua and green to yellow and brown. The colours vary depending on what is within the water: Phytoplankton generally makes the water green, non-algal particulates, such as sand, silt, or mud, make the water caramel, grey, to brown in colour, while dissolved organic matter makes the water yellowish (like black tea)

a. NSW coastal waters



b. Australian Inland waters

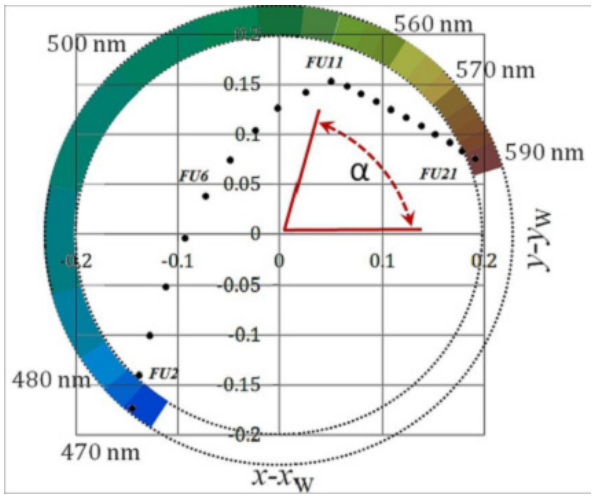


Source: Janet Anstee, CSIRO

An innovative approach to monitoring water colour in Australian surface waters is called 'EyeonWater' (see Volume 2D—Excursus 12.4). This project is part of a global effort to equip citizen scientists with simple tools to accurately record water colour information using the Forel-Ule scale (see Section 18.3). It will also increase the spatial and temporal density of water colour observations in Australia, which will enable scientists to validate local water quality products derived from EO imagery. The scientific challenge is to quantify the link between water colour (from the Forel-Ule colour scale) and the concentrations of algae, sediment, and dissolved organic material in the water. Through a series of experiments (such as van der Woerd and Wernand, 2018, Busch *et al.*, 2016), the citizen science measurements of water colour can be linked to concentrations of constituents (algae, sediments, and organic matter), by converting the satellite image spectrum into three chromaticity coordinates, which are then compressed into a single Hue angle and finally a Forel-Ule value (see Figure 18.4). This means the citizen science data ultimately could be used to validate time series of satellite-derived water colour products.

Figure 18.4 Hue angle conversion

A chromaticity diagram showing the relationship between the Forel-Ule scale and the image hue colour angle (α). The outer ring shows the dominant wavelength (in nm) associated with the Forel-Ule scale.



Source: van der Woerd and Wernand (2015)

18.2 EO Sensors for Water Colour

Characteristics of EO sensors are introduced in Volume 1A. The colours of surface waters are mapped and monitored using passive optical sensors carried on a variety of platforms—spaceborne, airborne, shipborne, and onshore (see Table 18.1). Specific features of optical EO sensors that are desirable for mapping water colour are detailed in Section 8.5.

Table 18.1 EO sensors relevant to water colour

Type	Sensor	Platform	Relevance	Advantages	Disadvantages
Passive optical	Smartphone	Handheld	Water colour	Portable, flexible timing	Not accurately calibrated, small area coverage
	Multispectral radiometer	Satellite	Water colour	Large area, regular coverage	Lower spectral resolution
		Airborne or shipborne	Inland and coastal applications of water colour	Higher spatial resolution	More expensive, smaller area coverage
	Hyperspectral radiometer	Satellite, airborne or shipborne	Inland and coastal water colour	High spectral and temporal resolution	Large data volumes, lower spatial resolution

18.3 Classifications of Water Colour

The colour of water is a complex optical feature (Dekker *et al.*, 2001). Variations in water colour are largely related to water absorption characteristics, whereas variations in intensity of colour are more closely related to backscattering properties (see Section 8.1.1). As introduced in Section 8.3, the optical characteristics of water can be described in terms of their inherent (see Table 8.5 and Table 8.9) or apparent (see Table 8.6 and Table 8.10) properties, where:

- inherent optical properties (IOP) are independent of lighting conditions (see Section 8.3.1); and
- apparent optical properties (AOP) are relative to ambient lighting conditions (see Section 8.3.2).

Figure 18.5 The Forel-Ule colour scale

This colour scale differentiates 21 different water colours.



Source: Wernand (2011)

Various schemes have been proposed to classify water colour. Mobley (2020) lists three methods that are commonly used:

- visual matching of a sample to the Forel-Ule Scale—this colour comparator scale was originally developed by Forel (1890) and extended by Ule (1892) and has been used extensively to classify water colour in rivers, lakes and oceans (Wernand and van der Woerd, 2010, van der Woerd and Wernand, 2018; see Figure 18.5);
- analysis of AOP—to differentiate between waters whose colour is dominated by chlorophyll and those whose colour is dominated by inorganic particles (see Section 18.3.1); and
- analysis of IOP—to determine relative absorption of phytoplankton, non-algal particles, and CDOM (see Section 18.3.2).

The content or constituents of the water can be inferred from the natural water colour to assess water quality issues and monitor long term variations (see also Volume 1B—Section 6.4). For example, the Forel-Ule colour scale has been in use since the late 19th century for the assessment and classification of water quality in oceanography and limnology (Novoa *et al.,* 2014, 2015). This scale defines 21 colours, spanning from indigo blue, through blue-green and yellow to chocolate brown (see Figure 18.5). Since one of the most obvious characteristics of water to the human eye is water colour, to use this scale an observer simply visually compares its sample colours with the colour of the water surface.

This approach offers considerable advantages for assessing historical trends in water colour and chlorophyll concentration at a global scale (Wernand, 2011). For example, global records of Forel-Ule water colour from 1889 to 2000 have been archived (Wernand *et al.,* 2013) and are available for temporal comparison with current conditions. The global project, EyeonWater, collates ongoing observations on water colour based on the Forel-Ule scale.

18.3.1 Classifications based on AOP

Use of AOP spectra (see Section 8.3.2) to classify waterbodies was introduced by Jerlov (1968) and developed by Morel and Prier (1977) to describe two types of oceanographic waters:

- Case 1 waters—chlorophyll concentration is higher than inorganic particle concentration; and
- Case 2 waters—inorganic particle concentration is higher than chlorophyll concentration.

More recently, these meanings have changed to:

- Case 1 waters—where phytoplankton and its breakdown products are the dominant factors in colour; and
- Case 2 waters—where colour is determined by phytoplankton, its breakdown products and many other factors, including CDOM (from terrestrial and *in situ* sources), NAP, CDIM, and, where visible, substratum reflectance.

Dekker *et al.* (2001) differentiate between 'optically shallow' and 'optically deep' waters:

- optically shallow waters—where the substrate signal is detectable through the water column by an EO sensor; and
- optically deep waters—where the substrate signal is not detectable through the water column.

Optically shallow waters are more complex to map and model than optically deep waters. Optically shallow waters typically include coastal (estuarine and coral) and inland waterbodies, as well as shallow, ocean water where the substratum is 'visible' to a sensor above the water surface. Examples of optically shallow waters include submerged macrophytes and sandy bottoms in lakes, seagrass and macro-algae meadows in estuarine and coastal environments, and coral reefs in tropical ocean environments. Maritorena *et al.* (1994) summarise and describe the physics of an optically shallow waterbody where part of the reflectance at the surface is composed of a bottom signal and part results from the water column. Semi-analytical models adequately explain the optical properties of optically shallow waters (see Section 8.4.2.3).

By contrast, in optically deep waters, where the substratum is obscured by the water column, the water colour is only determined by the water surface and the water column. Such waters are either too highly attenuating (turbid) or too deep to allow the substratum to be visible at or above the water surface. Optically deep waters include large inland lakes and reservoirs, coastal and ocean waters, whose vast dimensions are suited to coverage by satellite imagery, but also include shallow inland and coastal waters with high sediment or algal concentrations. The optical properties of oceans are determined by phytoplankton and its breakdown products whereas the other waters may have high concentrations of TSM and CDOM. In oceans as 'optically relatively simple' waters, only a limited number of spectral bands in the blue-green wavelengths suffice to infer chlorophyll concentrations with adequate precision for most oceanographic biological purposes (Dekker *et al.*, 2001). The colour of 'optically complex' waters is determined by optical components other than pure water, phytoplankton, and its breakdown products, and may include a composite of:

- phytoplankton and cyanobacteria pigments;
- particulate matter (NAP) from dead particulate organic matter and particulate inorganic matter;
- CDOM from terrestrial or aquatic origin;
- CDIM; and
- if visible, bottom reflectance influences.

The relatively simple band ratio (empirical) algorithms applicable to clear ocean waters are inappropriate for most inland and coastal waters. They are also inappropriate for some algal bloom situations in ocean waters. For example, to identify the optical properties of cyanobacteria algal blooms using EO would require additional spectral bands detecting green, yellow, and orange wavelengths (see Section 8.5).

18.3.2 Classifications based on IOP

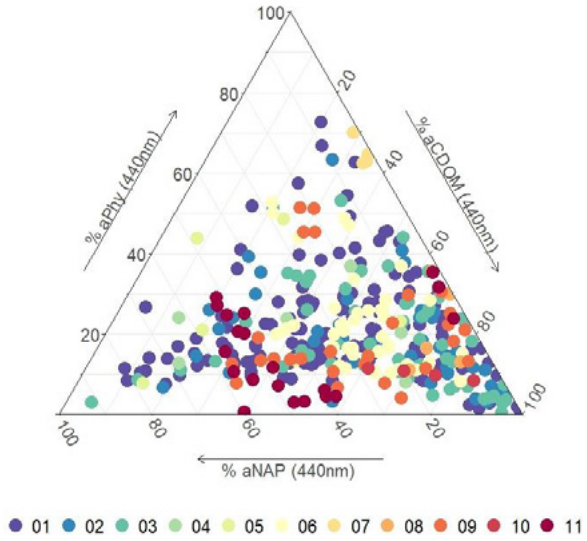
IOP analyses can be represented by ternary diagrams, where the central point indicates equal absorption by the three components (phytoplankton, NAP, and CDOM) and each apex corresponds to water containing a single component (see Figure 18.6).

The variation between water sources visible in Figure 18.6b (Blondeau-Patissier *et al.*, 2009) for reefal waters was similar to that found between Mediterranean, North Sea, and Baltic waters by Babin *et al.* (2003). These two publications clearly illustrate that assuming chlorophyll to be the only optically active substance, and relying on algorithms focusing solely on chlorophyll, will not work in these waters.

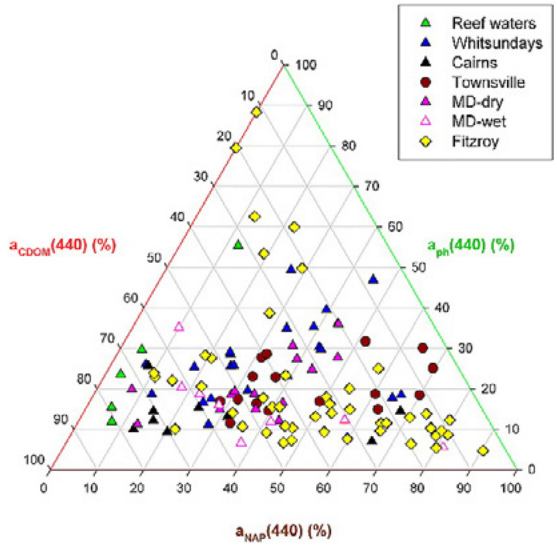
Figure 18.6 Ternary diagrams

CDOM: Colour dissolved organic matter; NAP: Non-algal particles

a. Absorption properties for CDOM, chlorophyll and NAP derived from 11 Australian coastal and inland study site clusters.



b. Ternary plot for waters flowing into the Great Barrier Reef Lagoon (Fitzroy River), the lagoon waters, and ocean reef waters, showing the variation between these sources.



Source: a. Botha *et al.* (2020) Figure 6; b. Blondeau-Patissier *et al.* (2009)

18.3.3 Optical Water Types (OWT)

A recently developed method for characterising optically complex waters is based on classification of Optical Water Type (OWT; Moore *et al.,* 2009, 2014; Vantrepotte *et al.,* 2012). This surge in interest in OWT results from the challenge of trying to develop a single algorithm that applies to multiple types of water, such as from inland to estuarine to coastal to ocean. By initially defining a set of OWT, a locally trained algorithm can then be developed for each water type.

A range of classification methods have been proposed to establish OWT, mostly incorporating some form of cluster analysis to group IOP data based upon differences in the magnitude and shape of reflectance spectra (Spyrakos *et al.,* 2018). For example, rather than discriminating between Case I and Case II waters, Moore *et al.* (2009, 2014) suggested statistically analyzing a range of IOP and AOP, then focusing on the 'shape' of water-leaving reflectance to determine a set of OWT.

OWT can provide information about the concentration of optically significant constituents in each class, proposing a better mechanism for the understanding of biogeochemical and biological variables. OWT classification data has been used to:

- facilitate the empirical retrieval of water column constituents (e.g. McKee and Cunningham, 2006; Melin *et al.,* 2011; Spyrakos *et al.,* 2011);
- train neural networks (e.g. Dzwonkowski and Yan, 2005; Spyrakos *et al.,* 2011);
- parameterize bio optical models, as suggested by Lubac and Loisel (2007) and McKee and Cunningham (2006); and
- understand the role of physical oceanographic processes in complex waters (Cherukuru *et al.,* 2016).

18.4 Transparency

Water transparency is a measure of the clarity of water, and can be estimated by the use of a Secchi disk (a 30 cm white, or black and white, disk), which is lowered into the water column and eventually disappears from view at the secchi depth (see Figure 5.12). The Secchi depth is a measure of the transparency or clarity of the water (Preisendorfer, 1986) or visibility in the vertical direction (Duntley, 1952). Secchi depths have been measured in the world's oceans for over 200 years, enabling large datasets for water transparency to be collated (Wernand, 2011). Measurements of transparency are relevant for the spatiotemporal understanding of water properties, particularly in relation to light availability and fluxes of phytoplankton and suspended sediments. A number of studies have estimated Secchi depth from EO datasets (Phinn *et al.,* 2005; Doron *et al.,* 2011).

Sediments carried by water movement over terrestrial surfaces or shallow substrates can become suspended to create turbid water conditions (see Section 5.1.4). Sources of sediment include river erosion and storm runoff. A healthy aquatic ecosystem will include some turbidity but excessive levels of sediment degrade most aquatic environments, including coral reefs (Pollock *et al.,* 2014). When sediment settles on benthos, it can block light required by aquatic plants for photosynthesis (Fabricius, 2005) and inhibit feeding of organisms. Suspended sediments also attract and transport contaminants, such as nutrients and pesticides, with consequent impact on water quality (see Section 19). As such, sediment load may indicate pollution potential (Ongley, 1996; FAO, 2000). Over time, settling sediments change the hydraulic characteristics of river channels and reduce the storage capacity of reservoirs.

A large turbidity gradient occurs in the first 20 km from many coastlines. Since turbidity results from sediments held in suspension, turbid conditions are maintained by water movement, with sediments settling down out of the water when it is still. Measurements of turbidity can also vary temporally in intertidal and coastal waters, with the concentration of suspended particles potentially changing from near zero to over 100 g/m^3 within one tidal period (Dekker *et al.,* 2001).

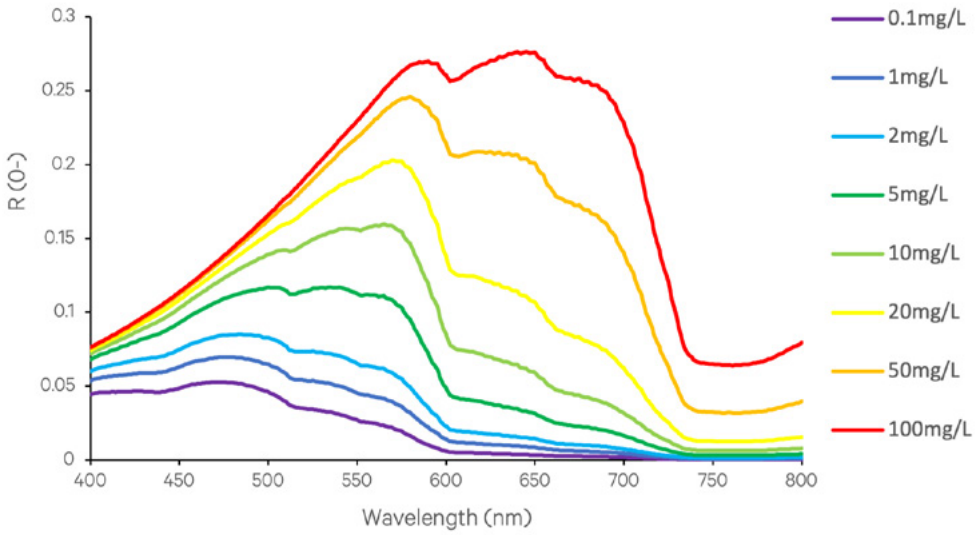
Turbid river plumes are often clearly visible as they travel into coastal waters. The concentration of suspended sediments in tropical river plumes, for example, can vary from a few g/l to a few mg/l (Furnas, 2003). The sediment layer, however, may only span a few metres of water in depth, effectively overlaying clearer waters. While highly visible, such plumes pose less danger to nearshore reefal systems than the lower and more concentrated sediment circulated by wind-driven waves (Furnas, 2003).

The presence of sediments increases water reflectance across all optical wavelengths (see Figure 18.7). The actual shape of the spectral reflectance distribution of suspended sediments varies with properties of the sediment particles, namely their:

- absorption and backscattering properties,
- refractive index;
- mineral composition;
- particle size(s); and
- concentration.

Figure 18.7 Non-algal particulates

Effect of increasing NAP concentrations from 0.001 mg/L to 100 mg/L on spectral reflectance just under the water surface (R(0-)), as modelled by Bio-opti for fixed chlorophyll (1.27 μg/L) and CDOM absorption at 440 nm = 0.199 m^{-1}.



Source: Janet Anstee, CSIRO

There are many different types (e.g. clays, silts, sands) and colours (e.g. white, yellow, red, brown, black) of sediment with different chemical and optical properties (Novo *et al.*, 1989). It should be noted that the observed colour of dry sediment particles changes, in terms of hue, saturation, and intensity, when mixed with water, and also changes with different concentrations of sediment and other water constituents. As the concentration of red loam in clear water increases, for example, the water colour generally changes from yellow to orange then red, whereas in water containing algae with the red loam, the water colour changes from green at low sediment concentrations to orange at high concentrations (Han, 1997). Natural waters, however, generally contain a mixture of different types of sediment.

The particle size of suspended matter in water can also vary markedly between different locations and at different times. Spectral separability and detectably from EO data will be diminished with fewer, less relevant spectral bands (see Figure 18.8, and Sections 8.5 and 18.2).

As illustrated in Figure 18.7, an increased concentration of suspended particles in water tends to strengthen the peak reflectance. This relationship has allowed EO imagery to be used to derive measures of turbidity, often expressed in terms of Total Suspended Solids (TSS) or Suspended Sediment Concentration (SSC; Alfoldi and Munday, 1978; Ritchie and Schiebe, 1986; Curran *et al.*, 1987). As detailed in Volume 2C, processing methods have included:

- correlations with calibration data, using linear (Ritchie *et al.*, 1976;) or logarithmic (Munday and Alfoldi, 1979; Lathrop and Lillesand, 1989) relationships with individual bands;
- correlations with calibration data using linear relationships with combinations of multiple bands (Chen *et al.*, 1992);
- Principal Component Analysis (Blondeau-Patissier *et al.*, 2014); and
- semi-analytical inversion models (see Section 8.4).

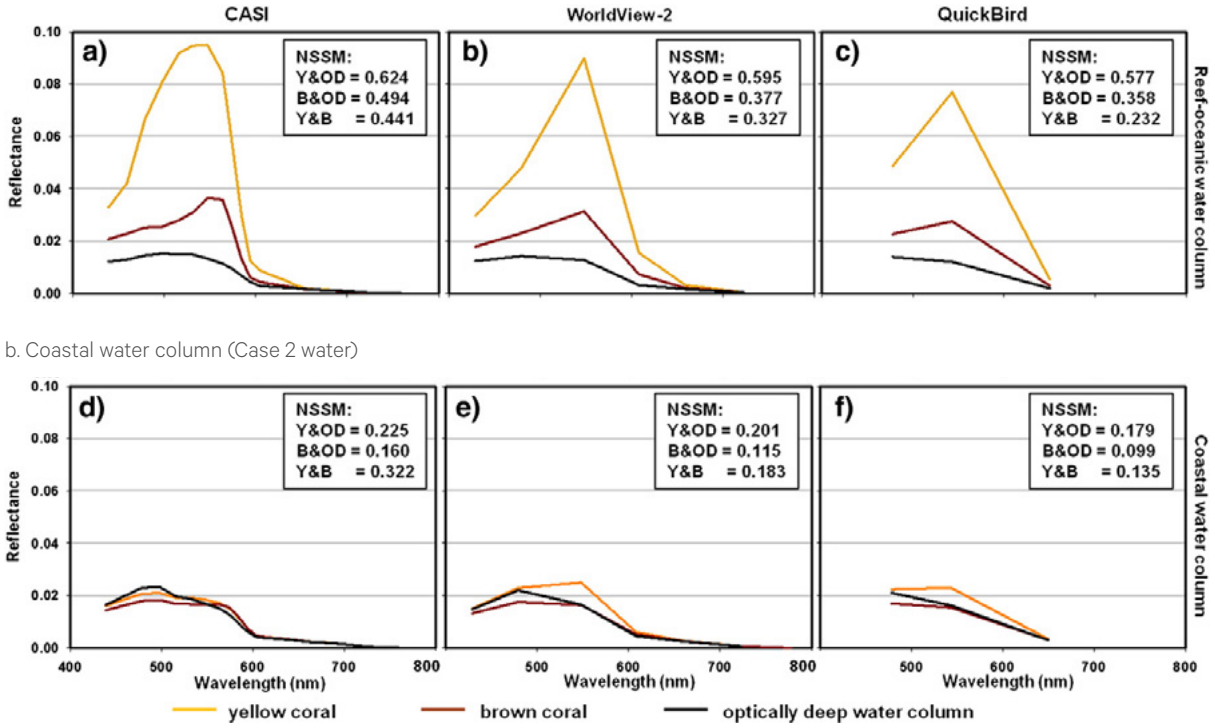
EO-based studies of different waterbodies have generally concluded that the strongest relationship between high sediment concentration and water reflectance is observed in the longer optical wavelength bands, principally red and near infrared (Ritchie and Cooper, 1988, 1991; Schiebe *et al.*, 1992).

Figure 18.8 Simulated EO reflectance for different substrates

In Botha *et al.* (2013), EO reflectance spectra were modelled for three different substrate types at 6 m water depth (Y: yellow coral, B: brown coral and OD: optically deep water column), then resampled to the equivalent spectral bands of the imaging spectrometer CASI and the multispectral sensors, Worldview-2, and QuickBird EO, to demonstrate the effect of spectral resolution and water column constituents on the normalised spectral separability metric (nSSM) of the two substratum types from an optically deep water column and from each other. nSSM has higher values for better separation, and accounts for shape and albedo differences between the two spectra.

a. Reef-oceanic water column (Case 1 water)

b. Coastal water column (Case 2 water)



Source: Botha *et al.* (2013) Figure 8

Various studies have focused on spectral characteristics of different types of sediments and observed that:

- turbidity and reflectance are linearly related for bentonite clay and black cotton soil, and have a curvilinear relationship for kaoline and gray soil (Bhargava and Mariam, 1990);
- have a constant relationship for oxisoil sediment (log-linear 450–700 nm and linear 700–1050 nm; Chen *et al.*, 1991)
- finer sediments raise reflectance faster than coarser sediments for equivalent concentrations (Bhargava and Mariam, 1991; Han and Rundquist, 1996);
- the same concentration of red loam soil resulted in higher reflectance in visible wavelengths (400–700 nm) in clear water than in algae-laden water (Han, 1997);
- algae in water had minimum spectral impact on the relationship between turbidity and reflectance for near infrared (NIR) wavelengths in the range 700–900 nm (Han, 1997); and
- the increase in spectral reflectance with increasing concentration of sediment is reduced when sediment load exceeds 600 mg/l (Lodhi *et al.*, 1998).

Optical measurements of known concentrations of sediment using spectroradiometers have allowed precise relationships between SSC and reflectance to be derived for specific types of sediment (Han, 1997). Such measurements have also been integrated over spectral regions corresponding to EO image bands to calibrate SSC image products (Lodhi *et al.*, 1998).

Since the scattering characteristics of suspended particles are closely related to their size, a universal algorithm to map and model suspended sediments, may be unlikely according to Kirk (1994, 2010). However as particle size affects the slope of the backscattering spectrum it may be possible to estimate particle size from a hyperspectral remote sensing signal, in which case a global suspended matter concentration algorithm may be possible.

In waters with stable levels of other optical constituents, forward optical models have indicated that suspended sediment is the principal contributing factor to changes in radiance in the wavelength range 630–690 nm (Tian *et al.,* 2014). However, in most natural waters, as the concentration of one optical constituent varies, the concentrations of other optical constituents also vary. In many instances, this complexity of factors necessitates more sophisticated modelling approaches to extract the concentrations of individual constituents.

When modelling the particulate backscattering spectrum as a power law function of wavelength, the magnitude and shape of backscattering can be estimated. The slope of the particulate backscattering has been shown to be related to chlorophyll (and thus algal biomass) concentration (Twardowski *et al.,* 2001) and particle size distribution (Reynolds *et al.,* 2001, Kostadinov *et al.,* 2009, Slade and Boss, 2015).

Physics-based models can also be used to understand and parameterise changes in spectral IOP of natural waters with varying concentrations of suspended sediment. For example, Dekker *et al.* (1999) developed a reflectance simulation model to estimate the full range of TSM concentrations that could occur in a dynamic tidal estuary in Kalimantan (Indonesia), then derived algorithms to analytically determine the TSM. Lymburner *et al.* (2016) used bio-optical modelling to develop sensor-specific TSM retrieval algorithms for three different Landsat sensors (TM, ETM+, OLI) over a range of Australian inland waterbodies. While the increased radiometric resolution of Landsat-8 OLI reduced image noise and spectral heterogeneity (Pahlevan *et al.,* 2014), TSM retrievals from all three sensors were comparable and highly correlated with coincident field measurements. These results enabled analysis of the Landsat time series to retrospectively characterise multi-decadal TSM dynamics.

18.5 Dissolved Matter

In the following subsections we will discuss EO methods to determine the concentrations of dissolved matter in surface waters, in the form of CDOM (see Section 18.5.1) and dissolved organic carbon (DOC; see Section 18.5.2).

18.5.1 CDOM

Since CDOM-rich water are typically dark, with little light reflected back to the EO sensor, it is difficult to find reliable methods to estimate CDOM from EO data (Brezonik *et al.,* 2015). A method proposed by Hoge and Lyon (1996), then adapted by Brando *et al.* (2012), retrieved CDOM using a matrix inversion method, which effectively decouples CDOM from the other light absorbing constituents. This approach is strongly driven by an understanding of the relationship between IOP and the water-leaving radiative signal (Tyler *et al.,* 2016; Matthews, 2011). Water quality information is found by inverting the EO signal, given the relationship between the subsurface remote sensing reflectance and coefficients of two IOP (absorption and backscattering; Gordon *et al.*, 1988).

Decreasing sea surface salinity has been previously used to determine freshwater discharge (Molleri *et al.,* 2010). CDOM has been found to be inversely correlated with salinity when compared with *in situ* data. In marine waters, CDOM is generally derived from phytoplankton decay, but in coastal waters, CDOM is predominately from anthropogenic sources transported by rivers and runoff. In Schroeder *et al.* (2012), CDOM was used as a surrogate for freshwater extent rather than backscattering or TSM since it was considered to be more reliable for mapping freshwater plumes, particularly where the particulate material in the freshwater plumes would drop out due to sedimentation.

18.5.2 DOC

Determining DOC in aquatic systems is required for modelling in the global carbon cycle (see Sections 1.5 and 7.4). In coastal environments, 80–90% of the total carbon is represented by DOC (Cao *et al.*, 2018) and EO data has been used to estimate DOC in these regions (Schwarz, 2005; ChunHock *et al.*, 2020).

The ratio between DOC and CDOM absorption at 412 nm allows for the potential to assess DOC distribution in ocean waters (Vantrepotte *et al.,* 2015). The CDOM spectral slope in UV wavelengths ($S_{275–295}$) has demonstrated its potential as a tracer of specific CDOM absorption (e.g. Cao *et al.*, 2018), but as UV reflectance is susceptible to errors in atmospheric correction, this approach has been found to overestimate DOC. While the approach has some limitations in its global applications, particularly for turbid waters, it has potential in less turbid waters.

Nearly all terrestrial ecosystems rest, physically and functionally, on an organic-rich soil foundation. Dissolved organic matter (DOM) is the soil of the sea—a large, biochemically resistant reservoir of organic matter providing a substrate for life, and a source for nutrient regeneration, ion exchange capacity, light and heat absorption, and so on.
Ducklow (2002)

The spectral features of river water are functions of its hydrological, biological, and chemical characteristics (see Section 5). CDOM, DOM, and chlorophyll a can be readily detected by *in situ* and EO optical measurements, and numerical relationships can be developed to relate these measurements to DOC (ChunHock *et al*., 2020), and even primary productivity (Robinson *et al*., 2017). In EO algorithms, CDOM has been used as a proxy for DOC in coastal waters by exploiting the relationship between the optically active CDOM and DOC concentrations at specific wavelengths (Ferrari *et al*., 1996).

For EO algorithms, the accurate retrieval of CDOM is required to derive DOC (Vantrepotte *et al*., 2015). Both empirical (Mannino *et al*., 2008) and semi-analytical (Loisel *et al*., 2014) algorithms have been used to retrieve CDOM accurately and from this, the DOC content is calculated. To derive the full spatiotemporal variability of coastal waters requires the *in situ* parameterisation data to be representative of the seasonal and salinity gradients of the region (Vantrepotte *et al*., 2015), especially where mixing between the freshwater and marine waters occur (Harvey *et al*., 2015).

Excursus 18.1—Blackwater Events

Source: Klaus Joehnk and Tapas Biswas, CSIRO
Further information: Vantrepotte *et al*. (2015); MDBA (2020); King *et al*. (2012)

Blackwater events are natural phenomena where a large increase in the carbon content of a waterbody tints the water colour black (see Figure 18.9). These events typically occur in lowland rivers. The extraction of organic material from dried leaves is a process similar to brewing a cup of tea, where clear water turns brown. The more leaf litter is added, the more decomposed it is, and the longer it is left to brew, the stronger and darker the water becomes. The leaching of organic matter is also strongly dependent on the water temperature.

Figure 18.9 Blackwater plume

Drone image of a blackwater plume entering Lake Victoria, South Australia, in November 2016.



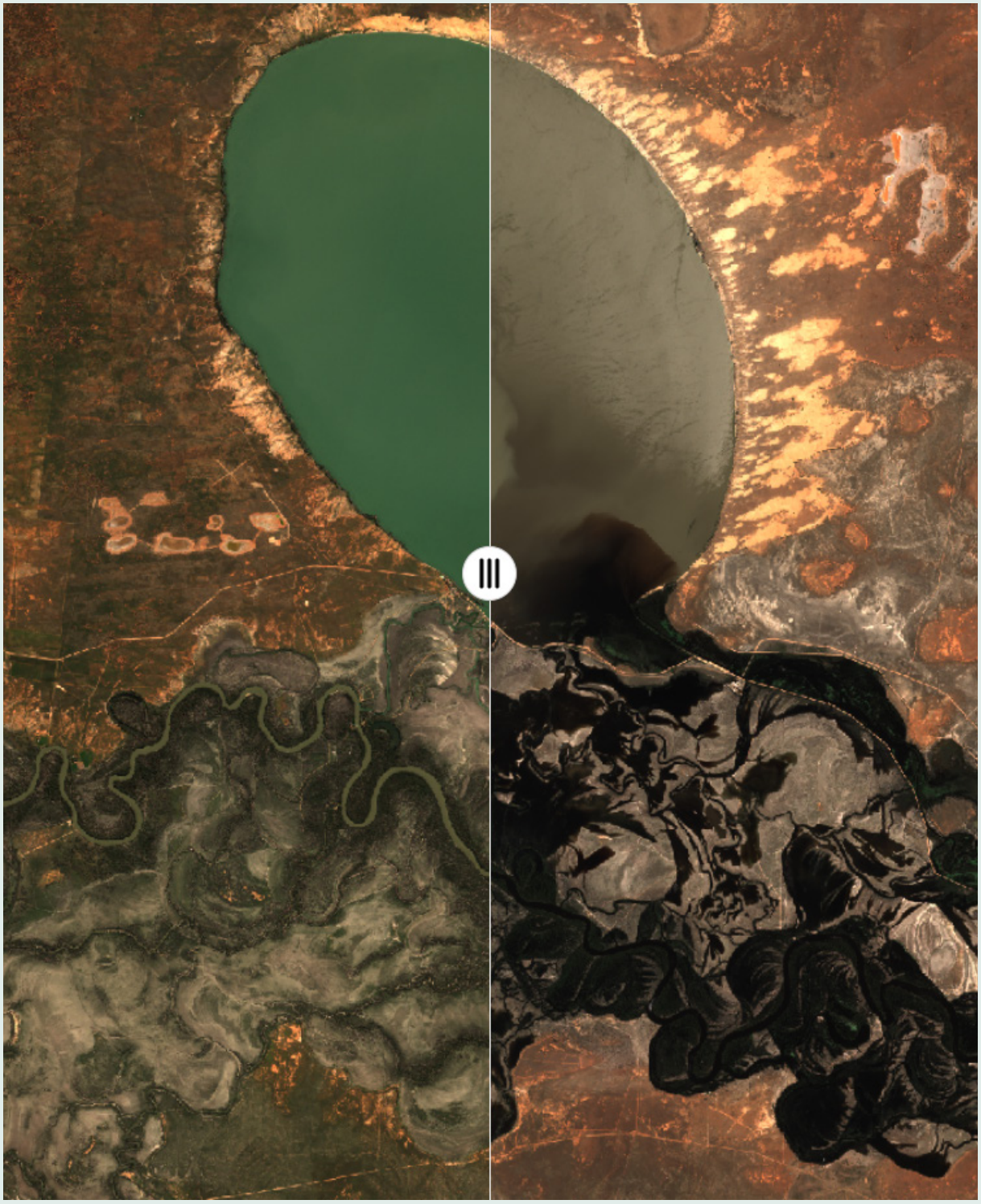
Source: SA Water and Daniel Haines

This phenomenon often occurs in the Australian Murray-Darling Basin, one of the largest river basins in the world, after long drought periods when flooding rains lead to large scale inundation of floodplains. During dry years under non-flood conditions, organic matter (such as leaf litter, grass, or bark) accumulates on the floodplains. Whenever a floodplain that has accumulated a large volume of organic material is inundated, dissolved organic carbon (DOC) is leached, which makes the water appear black, hence the name blackwater.

Although carbon itself is an essential part of a thriving aquatic ecosystem, blackwater events go hand in hand with a decrease in dissolved oxygen (DO), eventually drawing oxygen down to hypoxic conditions leading to fish kills. Adding organic matter under higher temperatures increases microbial decomposition of the organic material, which consumes DO from the water. Whenever this process of consumption is higher than oxygen production (for example, due to photosynthetic algae in the water or re-aeration across the air-water boundary), DO levels drop. As the re-aeration of the stagnant or slowly flowing water on the floodplain is hindered, the water gradually turns black (high carbon content) leading to depleted levels of DO. In the worst case, when DO levels fall below 2 mg/l, fish and invertebrates start to suffocate and eventually die, giving rise to hypoxic blackwater, which finds its way slowly back to the river channel further downstream. While these events are often associated with negative impacts such as fish kills, decreased tourism activity, and additional water treatment costs, they also benefit the the overall ecosystem by delivering carbon into the river, to fuel aquatic food webs and increase river productivity, including fish populations.

Figure 18.10 Blackwater event

Large scale blackwater event around Lake Victoria on 28 November 2016 as seen from Sentinel-2 (right) compared with the natural flow regime on 7 August 2016 (left). The blackwater plume flowing into Lake Victoria shows the different colours of carbon-enriched and natural waters.



Over decades, river regulation in Australia has reduced the frequency of smaller overbank flows during winter and spring, which would steadily wash out carbon from the floodplains. Without these flows there is now a higher chance of litter accumulation, potentially resulting in more intense blackwater events. Under the Murray-Darling Basin Plan, state governments must take blackwater risks into account when planning water resource usage, by identifying potential causes of poor water quality and establishing cost-effective ways to achieve water quality objectives. It is thus necessary to develop options of adapted flow management with the aim of reducing leaf litter accumulation as much as possible to minimise future hypoxic events.

Since blackwater events can affect extensive areas of floodplains and river reaches over hundreds of kilometres, EO imagery provides the opportunity to track these events and provide early warning to undertake regulatory measures (see Figure 18.10). In combination with hydrodynamic modelling, EO can be used to estimate the risk of blackwater conditions as floodwaters progress. Due to their distinctive colour blackwater events are clearly visible from space, but flooding events also coincide with wet periods and a high chance of cloud cover which may obscure ground features.

Additionally, over recent decades, wildfires have increased in frequency and ferocity across Australia, the US, and other countries around the globe, which can result in similar negative effects on water quality as occur with lowland river blackwater events. For example, large plumes of blackwater generated by wildfire were observed during the devastating fires in southeast Australia in 2019/2020. Depending on burn severity in river catchments, rainfall after wildfires can wash out large quantities of ash and charred organic material, which then make their way into streams, reservoirs, and estuaries. This high carbon content tints the water black resulting in negative effects, such as fish kills caused by hypoxic water and smothering of gills.

18.6 Chlorophyll Content

EO of water colour was initially developed for the oceans, as it provides the only feasible method for assessing these vast areas for water quality. Typically, the optical properties of ocean waters are only affected by phytoplankton and its breakdown products. These waters are relatively simple in terms of their optical properties and are commonly referred to as Case 1 waters (see Section 18.3). A few bands in blue/green wavelengths are sufficient to determine chlorophyll concentrations with a precision that is adequate for most oceanographic-biological purposes (Dekker *et al*., 2001).

Chlorophyll a concentration products derived from satelite imagery are often based on ratios of relevant wavelengths. For example, the NASA chlorophyll a algorithm for MODIS (500 m) imagery computes:

$$\frac{\rho_{488}}{\rho_{555}}$$

(in mg/m^3) as illustrated in Figure 18.11a (NASA Earthdata, 2019). This algorithm assumes that the only optically active constituent affecting image reflectance is chlorophyll. While true for most oceanic waters, this assumption may not be true for coastal and inland waters, and near land this algorithm can deliver misleading results. Extensive fieldwork is generally needed in coastal waters to account for local variations in the optical properties of water (see Figure 18.11b). To avoid the impact of cloud, composite imagery is often used to map seasonal and longer term changes in chlorophyll content (see Volume 2D).

In coastal and inland waters, the retrieval of chlorophyll a is often challenging due to the complexity of the optical properties in these waters compared with clear ocean waters. The ocean colour algorithms that are based on chlorophyll a dominating the blue light absorption fail in the coastal and inland waters where there are high concentrations of sediment and CDOM (Gilerson *et al*., 2021).

Physics-based models (such as the MOMO radiative transfer model) have been used to model concentrations of chlorophyll a and suspended matter from multispectral imagery (CASI airborne imagery with six visible bands) over inland waters (Dekker *et al*., 2001; see Volume 1B—Excursus 6.3). Some of the complexities in mapping optically deep waters include:

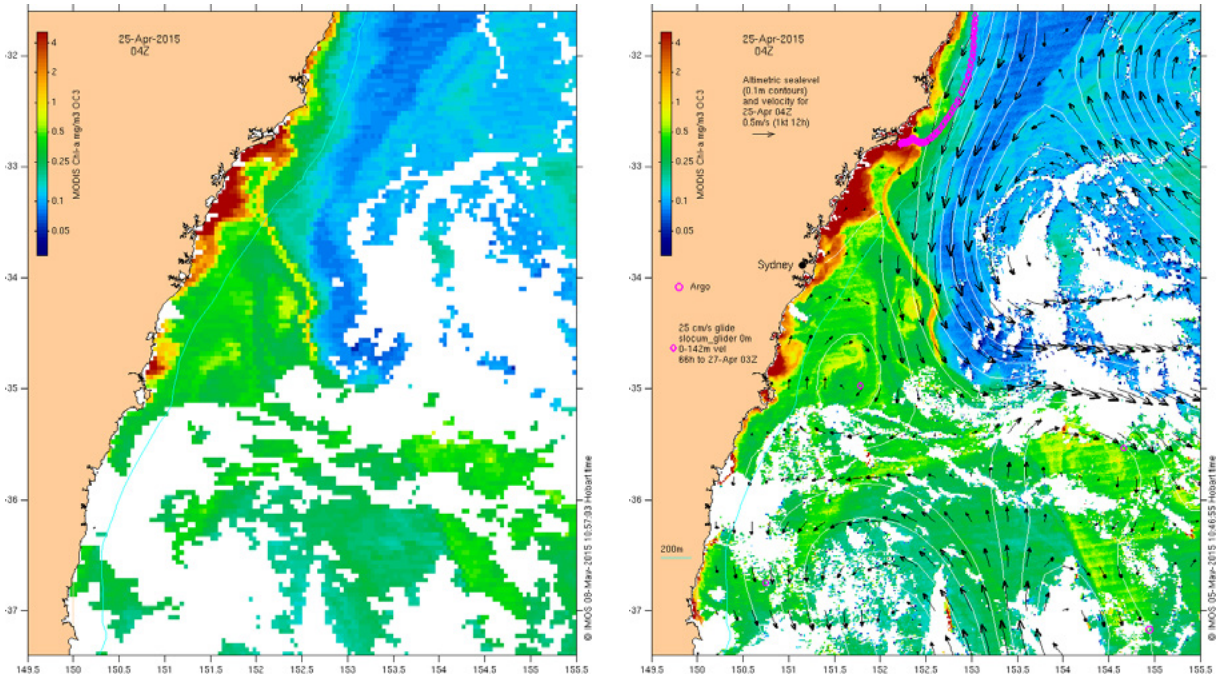
- the spectral characteristics of CDOM, the organic fraction of NAP, and chlorophyll overlap in blue wavelengths, so it is not easy to determine which part of the absorption is due to CDOM;
- microalgae can move vertically in the water column, which means the observed surface concentration may underestimate the total volume of biomass;
- the optically active constituents of algal pigments, NAP, and CDOM, may not necessarily co-vary;
- surface effects such as waves or sunglint can increase the observed EO reflectance; and
- inland waters often are impacted by atmospheric adjacency effects from riparian vegetation, bright sands, or other highly reflective terrain features.

Figure 18.11 MODIS chlorophyll a concentration products

Major storms occurred in the Hunter region, north of Sydney, on 21–22 April 2015. On 25 April, the floodwaters appear as a yellow-orange ribbon near the centre of the images below. These MODIS chlorophyll a products highlight the interaction between floodwater from the Hunter River and both the low chlorophyll waters of the East Australian Current (coloured blue) and the more chlorophyll-rich waters of the Tasman Sea (coloured green). Note that these chlorophyll concentration images may confuse high CDOM levels from the land with high levels of aquatic chlorophyll.

a. Monthly NASA product based on 4 km grid using NASA chlorophyll a algorithm (see Volume 1B—Excursus 6.2) for 25 April 2015 at 04Z

b. The same image processed at 1 km and integrated with other datasets by IMOS OceanCurrent. Contours (at 0.1 m interval) show altimetric sea level and arrows indicate geostrophic current velocity for 25 April 2015.



Source: Edward King, CSIRO © IMOS, based on NASA imagery

18.7 Substratum

The optical properties of substrata can change rapidly in both space and time (Mazel, 2001). For example, while seagrass blades stand vertically in calm water, in moving water the blades bend sideways, thus increasing the area of substratum they appear to cover. Epiphytic growth on seagrass blades can also expand rapidly to significantly restrict the amount of photosynthetically active radiation reaching the blades, with consequent reduction in plant productivity (see Figure 18.12).

As introduced in Sections 6 and 8 above, the reflectance from a waterbody is determined by its water depth, water colour, and substratum colour. The interactions between these factors are important in the interpretation of EO imagery in aquatic environments. Different 'above-water' reflectance values can result from a given substratum at different water depths (see Figure 18.13), or from a given substratum beneath different water colours. As such, EO analyses of substratum extent, and/or the vegetation it supports, require corrections for water depth (see Section 8.4.3).

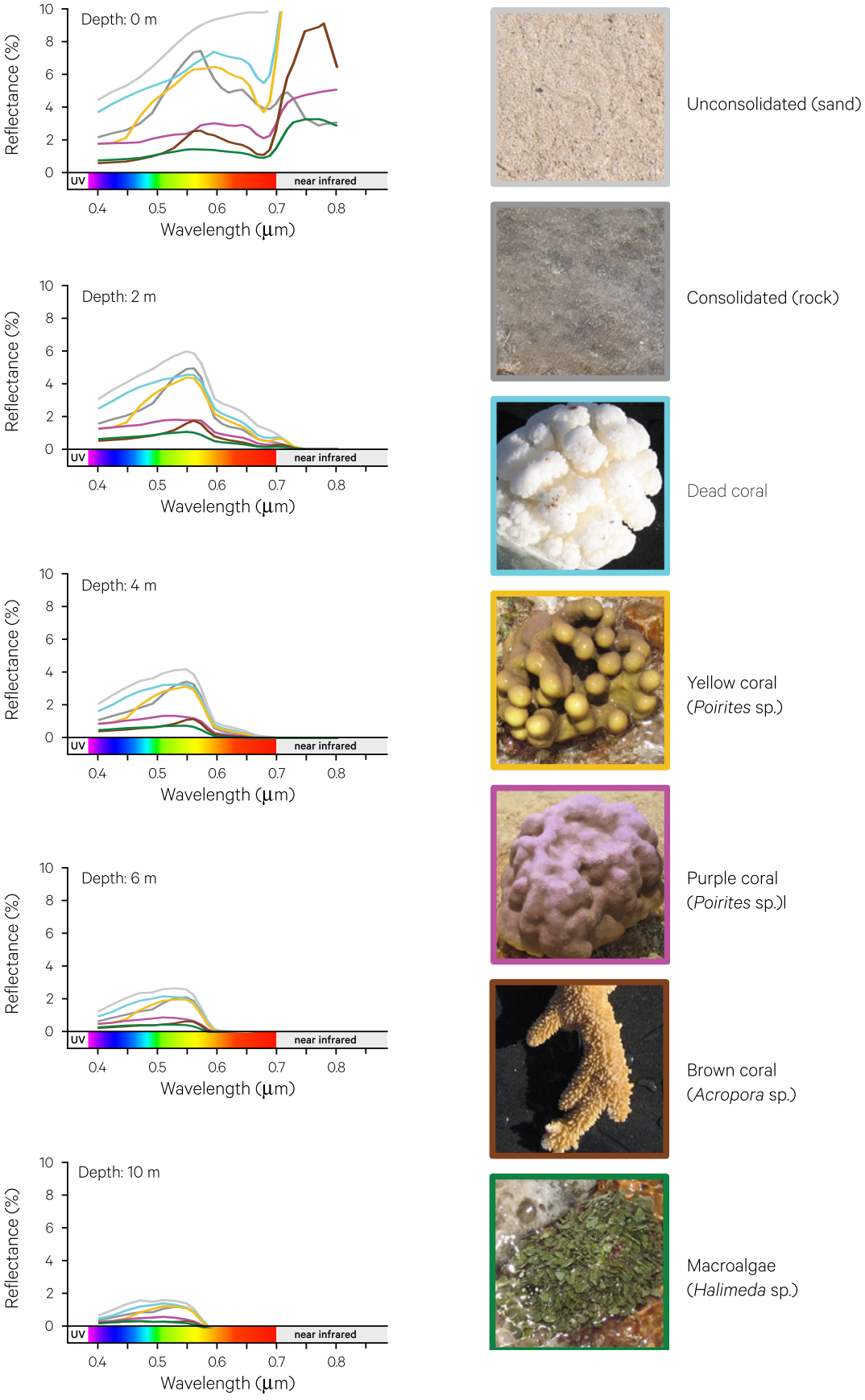
Figure 18.12 Epiphytic growth on seagrass blades



Source: James St John, Wikimedia. Retrieved from: *https://commons.wikimedia.org/wiki/File:Syringodium_filiforme_(manatee_grass)_%26_Thalassia_testudinum_(turtle_grass)_(southeastern_Graham%27s_Harbour,_San_Salvador_Island,_Bahamas)_2_(15860252588).jpg*

Figure 18.13 Impact of water depth on substrate spectra

Reflectance spectra of a range of substrate materials are shown for different water depths. Reflected radiation across all wavelengths is signficantly diminished for all substrates as water depth increases, with the greatest impact occurring in the infrared region.



Adapted from: Botha *et al.* (2013)

18.8 Further Information

NASA

NASA Ocean Colour: *https://oceancolor.gsfc.nasa.gov*

NASA Aeronet-Ocean Colour: *https://data.nasa.gov/Earth-Science/AERONET-OCEAN-COLOR/jhyg-mp9e/data?no_mobile=true*

European Union (EU)

Citizens' Observatory for Coast and Ocean Optical Monitoring (Citclops 2012–2015): *http://www.citclops.eu*

EyeOnWater: *https://www.eyeonwater.org*

Australia

CSIRO Australian-waters EO Phytoplankton-type Products Data Base: *http://aesop.csiro.au/*

OzCoasts: *https://ozcoasts.org.au*

EyeOnWater Australia: *https://research.csiro.au/eyeonwater/*

Western Australian Marine Science Institution: *https://www.wamsi.org.au*

18.9 References

Alfoldi, T.T., and Munday, J.C. (1978). Water quality analysis by digital chromaticity mapping of Landsat data. *Canadian Journal of Remote Sensing,* 4(2), 108–126. doi:10.1080/07038992.1978.10854974

Babin, M., Stramski, D.,Ferrari, G.M., Claustre, H., Bricaud, A., Obolensky, G., and Hoepffner, N. (2003). Variations in the light absorption coefficients of phytoplankton, nonalgal particles, and dissolved organic matter in coastal waters around Europe, *Journal of Geophysical Research*, 108(C7), 3211. doi:10.1029/2001JC000882

Bhargava, D.S., and Mariam, D.W. (1990). Spectral Reflectance Relationships to Turbidity Generated by Different Clay Materials. *Photogrammetric Engineering and Remote Sensing*, 56(2), 225–229.

Bhargava, D.S., and Mariam, D.W. (1991). Effects of suspended particle size and concentration on reflectance measurements. *Photogrammetric Engineering and Remote Sensing*, 57(5), 519–529.

Blondeau-Patissier, D., Brando, V.E., Oubelkheir, K., Dekker, A.G., Clementson, L.A., Daniel, P. (2009). Bio-optical variability of the absorption and scattering properties of the Queensland inshore and reef waters, Australia. *Journal of Geophysical Research,* 114, C05003.

Blondeau-Patissier, D., Gower, J.F.R., Dekker, A.G., Phinn, S.R., and Brando, V.E. (2014). A review of ocean color remote sensing methods and statistical techniques for the detection, mapping and analysis of phytoplankton blooms in coastal and open oceans. *Progress in Oceanography*, 123, 123–144. *https://doi.org/10.1016/j.pocean.2013.12.008*.

Botha, E.J., Brando, V.E., Anstee, J.M., Dekker, A.G., and Sagar, S. (2013). Increased spectral resolution enhances coral detection under varying water conditions. *Remote Sensing of Environment,* 131, 247–261.

Botha, E.J., Anstee, J.M., Sagar, S., Lehmann, E., and Medeiros, T.A.G. (2020). Classification of Australian Waterbodies across a Wide Range of Optical Water Types. *Remote Sensing*, 12, 3018. doi:10.3390/rs12183018

Brando, V.E., Dekker, A.G., Park, Y.J., and Schroeder, T. (2012). Adaptive semianalytical inversion of ocean color radiometry in optically complex waters. *Applied Optics*, 51, 2808–2833.

Brezonik, P.L., Olmanson, L.G., Finlay, J.C., and Bauer, M.E. (2015). Factors affecting the measurement of CDOM by remote sensing of optically complex inland waters. *Remote Sensing of Environment*, 157, 199–215. doi:10.1016/j.rse.2014.04.033

Busch, J.A., Bardaji, R., Ceccaroni, L., Freidrichs, a., Piera, J., Simon, C., Thijsse, P., Wernand, M., van der Woerd, H.J., and Zielinski, O. (2016). Citizen Bio-Optical Observations from Coast- and Ocean and Their Compatibility with Ocean Colour Satellite Measurements. *Remote Sensing*, 8, 879. doi:10.3390/rs8110879

Cao, F., Tzortziou, M., Hu, C., Mannino, A., Fichot, C.G., Del Vecchio, R., Najjar, R.G., and Novak, M. (2018). Remote sensing retrievals of colored dissolved organic matter and dissolved organic carbon dynamics in North American estuaries and their margins, *Remote Sensing of Environment*, 205, 151–165. *https://doi.org/10.1016/j.rse.2017.11.014*

Chen, Z., Hanson, J.D., and Curran, P.J. (1991). The form of the relationship between suspended sediment concentration and spectral reflectance: its implications for the use of Daedalus 1268 data. *International Journal of Remote Sensing,* 12(1), 215–222.

Chen, Z., Curran, P., and Hansom, J. (1992). Derivative reflectance spectroscopy to estimate suspended sediment concentration. *Remote Sensing of Environment*, 40, 67–77. doi:10.1016/0034-4257(92)90127-6.

Cherukuru, N., Davies, P.L., Brando, V.E., Brando, V.E., Anstee, J.M., Baird, M.E., Clementson, L.A., and Doblin, M.A. (2016). Physical oceanographic processes influence bio-optical properties in the Tasman Sea. *Journal of Sea Research*, 110, 1–7. doi:10.1016/j.seares.2016.01.008

ChunHock, S., Cherukuru, N., Mujahid, A., Martin, P., Sanwlani, N., Warneke, T., Rixen, T., Notholt, J., and Müller, M. (2020). A New Remote Sensing Method to Estimate River to Ocean DOC Flux in Peatland Dominated Sarawak Coastal Regions, Borneo. *Remote Sensing*, 12, 3380. *https://doi.org/10.3390/rs12203380*

Curran, P. J., Hansom, J. D., Plummer, S. E., and Pedley, M. I. (1987). Multispectral remote sensing of nearshore suspended sediments: a pilot study. *International Journal of Remote Sensing* 8, 103–112.

Dekker, A.G., Peters, S.W.M., Rijkeboer, M., and Berghuis, H. (1999). Analytical processing of multitemporal SPOT and Landsat images for estuarine management in Kalimantan Indonesia. *18th EARSeL Symposium on Operational Remote Sensing for Sustainable Development* (Eds: G.J.A. Nieuwenhuis, R. Vaughan, and M. Molenaar) pp 315–324. A.A.Balkema, Rotterdam, The Netherlands.

Dekker, A.G., Brando, V.E., Anstee, J.M., Pinnel, N., Kutser, T., Hoogen-boom, J., Peters, S.W.M., Pasterkamp, R., Vos, R.J., Olbert, C., and Malthus, T.J. (2001). Imaging spectrometry of water. Ch 11 in *Imaging Spectrometry: Basic Principles and Prospective Applications*. (Eds: F.D. van der Meer and S.M. de Jong), pp 307–359. Kluwer Academic Publishers, Dordrecht, The Netherlands.

Doron, M., Babin, M., Hembise, O., Mangin, A., and Garnesson, P. (2011). Ocean transparency from space: Validation of algorithms estimating Secchi depth using MERIS, MODIS and SeaWiFS data. *Remote Sensing of Environment*, 115, 2986–3001.

Ducklow, H.W. (2002). Foreword in *Biogeochemistry of marine organic matter*. (Eds: D. Hansell and C. Carlson). Academic Press, San Diego. ISBN: 0-12-323841-2

Duntley, S.Q.(1952). *The Visibility of Submerged Objects*. Visibility Laboratory, Scripps Institution of Oceanography, University of California, San Diego. *https://escholarship.org/uc/item/2mz4d121*

Dzwonkowski, B., and Yan, X.H. (2005). Development and application of a neural network based ocean colour algorithm in coastal waters. *International Journal of Remote Sensing*, 26, 1175–1200.

Fabricius, K. (2005). Effects of terrestrial runoff on the ecology of corals and coral reefs: review and synthesis. *Marine Pollution Bulletin*, 50, 125–146. doi:10.1016/j.marpolbul.2004.11.028

FAO (2000). *Water Quality Management and Control of Water Pollution. Proceedings of a Regional Workshop, Bangkok, Thailand, 26–30 October 1999*. Food and Agriculture Organisation, Rome. *http://www.fao.org/3/a-bl035e.pdf*

Ferrari, G.M., Dowell, M.D., Grossi, S., and Targa, C. (1996). Relationship between the optical properties of chromophoric dissolved organic matter and total concentration of dissolved organic carbon in the southern Baltic Sea region. *Marine Chemistry*, 55, 299–316.

Forel, A. (1890) Une nouvelle forme de la gamme de couleur pour l'étude de l'eau des lacs. *Archives des Sciences Physiques et Naturelles/Société de Physique et d'Histoire Naturelle de Genève*, 6, 25.

Furnas, M. (2003). *Catchments and Corals. Terrestrial Runoff to the Great Barrier Reef*. AIMS, Townsville. 334p.

GCOS (2018). Global Climate Observing System: *https://gcos.wmo.int/en/home*

Gilerson, A., Malinowski, M., Herrera, E., Tomlinson, M., Stumpf, R., and Ondrusek, M. (2021). Estimation of chlorophyll-a concentration in complex coastal waters from satellite imagery. *Proceedings of SPIE 11752, Ocean Sensing and Monitoring XIII, 117520B* (12 April 2021). *https://doi.org/10.1117/12.2588004*

Gordon, H.R., O.B. Brown, R. Evans, J. Brown, R.C. Smith, K.S. Baker, and D.C. Clark (1988) A semianalytical model of ocean colour. *Journal of Geophysical Research*, 93(D9), 10909–10924.

Han, L. (1997). Spectral reflectance with varying suspended sediment concentrations in clear and algae-laden waters. *Photogrammetric Engineering and Remote Sensing,* 63(6), 701–705.

Han, L., and Rundquist, D.C. (1996). Spectra characterization of suspended sediments generated from two texture classes of clay soil. *International Journal of Remote Sensing,* 17, 543–649.

Harvey, E.T., Kratzer, S., and Andersson, A. (2015). Relationships between colored dissolved organic matter and dissolved organic carbon in different coastal gradients of the Baltic Sea. *AMBIO*, 44, 392–401. *https://doi.org/10.1007/s13280-015-0658-4*

Hoge, F.E., and Lyon, P.E. (1996). Satellite retrieval of inherent optical properties by linear matrix inversion of oceanic radiance models—an analysis of model and radiance measurement errors. *Journal of Geophysical Research-Oceans*, 101, 16631–16648.

Jerlov, N.G. (1968). *Optical Oceanography*, Elsevier Oceanography Series 5.

Joehnk, K., Sengupta, A., Biswas, T.K., Mosley, L., and Rees, G. (2020). *Assessment and mitigation options of blackwater risk in the River Murray system*. CSIRO Land and Water, Canberra. 60 p. *https://www.mdba.gov.au/publications/independent-reports/assessment-mitigation-options-blackwater-risk-river-murray-system*

King, A.J., Tonkin, Z, and Lieshcke, J. (2012). Short-term effects of a prolonged blackwater event on aquatic fauna in the Murray River, Australia: considerations for future events. *Marine and Freshwater Research*, 63(7), 576–586. *https://doi.org/10.1071/MF11275*

Kirk, J.T.O. (1994). *Light and Photosynthesis in Aquatic Ecosystems*, 2nd Edn. Cambridge University Press, Cambridge. 509 pp.

Kirk, J.T.O. (2010). *Light and Photosynthesis in Aquatic Ecosystems*, 3rd Edn. Cambridge University Press, Cambridge. 662 pp.

Kostadinov, T.S., Siegel, D.A., and Maritorena, S. (2009). Retrieval of the particle size distribution from satellite ocean color observations. *Journal of Geophys. Research*, 114: C09015. doi:10.1029/2009JC005303

Lathrop, R.G., and Lillesand, T.M. (1989). Monitoring water quality and river plume transport in Green Bay, Lake Michigan with SPOT-1 imagery. *Photogrammetric Engineering and Remote Sensing*, 55(3), 349–354.

Lodhi, M.A., Rundquist, D.C., Han, L., and Kuzila, M.S. (1998). Estimation of suspended sediment concentration in water using integrated surface reflectance. *Geocarto International,* 13(2), 11–15. doi:10.1080/10106049809354637

Loisel, H., Vantrepotte, V., Dessailly, D., and Mériaux, X. (2014). Assessment of the colored dissolved organic matter in coastal waters from ocean color remote sensing. *Optics Express*, 22(11), 13109–13124.

Lubac, B., and Loisel, H. (2007). Variability and classification of remote sensing reflectance spectra in the eastern English Channel and southern North Sea. *Remote Sensing of Environment*, 110, 45–58.

Lymburner, L., Botha, H., Hestir, E., Anstee, J., Sagar, S., Dekker, A., and Malthus, T. (2016). Landsat 8: Providing continuity and increased precision for measuring multi-decadal time series of total suspended matter. *Remote Sensing of Environment*, 185, 108–118. doi:10.1016/j.rse.2016.04.011

Mannino, A., Russ, M.E., and S.B. Hooker (2008). Algorithm development and validation for satellite-derived distributions of DOC and CDOM in the U.S. Middle Atlantic Bight. *Journal of Geophysical Research*, 113, C07051. doi:10.1029/2007JC004493.

Maritorena, S., Morel, A., and Gentili, B. (1994). Diffuse reflectance of oceanic shallow waters: Influence of water depth and bottom albedo. *Limnology and Oceanography,* 39(7), 1689–1703.

Matthews, M.W. (2011). A current review of empirical procedures of remote sensing in inland and near-coastal transitional waters. *International Journal of Remote Sens*ing, 32, 6855–6899.

Mazel, C.H. (2001). Optics of the Seafloor. *Oceanography,* 14(3), 54–63.

McKee, D., and Cunningham, A. (2006). Identification and characterisation of two optical water types in the Irish Sea from in situ inherent optical properties and seawater constituents. *Estuarine, Coastal and Shelf Science*, 68, 305–316.

MDBA (2020). *Blackwater* webpage, Murray-Darling Basin Authority website: *https://www.mdba.gov.au/issues-murray-darling-basin/blackwater*

Melin, F., Vantrepotte, V., Clerici, M., D'Alimonte, D., Zibordi, G., Berthon, J.F., and Canuti, E. (2011). Multi-sensor satellite time series of optical properties and chlorophyll-a concentration in the Adriatic Sea. *Progress in Oceanography*, 91, 229–244.

Mobley, C. (2020). *Ocean Optics Web Book*. *http://www.oceanopticsbook.info/view/introduction/overview*

Molleri, G.S.F., de M. Novo, E.M.L., and Kampel, M. (2010). Space-time variability of the Amazon River plume based on satellite ocean color. *Continental Shelf Research,* 30, 342–352.

Moore, T.S., Campbell, J.W., and Dowell, M.D. (2009). A class-based approach for characterizing the uncertainty of the MODIS chlorophyll product. *Remote Sensing of Environment*, 113, 2424–2430.

Moore, T.S., Dowell, M.D., Bradt, S., and Ruiz Verdud, A. (2014). An optical water type framework for selecting and blending retrievals from bio-optical algorithms in lakes and coastal waters. *Remote Sensing of Environment*, 143, 97–111. doi:10.1016/j.rse.2013.11.021

Morel, A., and Prieur, L. (1977). Analysis of variations in ocean color. *Limnology and Oceanography*, 22(4), 709–722.

Munday, J., and Alfoldi, T.T. (1979). Landsat test of diffuse reflectance models for aquatic suspended solids measurement. *Remote Sensing of Environment,* 8(2), 169–183.

NASA Earthdata (2019). *OceanColour Web*: *https://oceancolor.gsfc.nasa.gov/atbd/chlor_a/#sec_2*

Novo, E., Hansom, J., and Curran, P. (1989). The effect of sediment type on the relationship between reflectance and suspended sediment concentration. *International Journal of Remote Sensing,* 10, 1283–1289. doi:10.1080/01431168908903967.

Novoa, S., Wernand, M.R., and van der Woerd, H.J. (2014). The modern Forel-Ule scale: A 'Do-It-Yourself' colour comparator scale for water monitoring. *Journal of European Optical Society—Rapid Publications*, 9, 14025.

Novoa, S., Wernand, M.R., and van der Woerd, H.J. (2015). WACODI: A generic algorithm to derive the intrinsic color of natural waters from digital images. *Limnology and Oceanography Methods*, 13, 697–711.

Ongley, E.D. (1996). *Control of Water Pollution from Agriculture*. FAO Irrigation and Drainage Paper 55. FAO, Rome.

Pahlevan, N., Lee, Z., Wei, J., Schaaf, C.B., Schott, J. R., and Berk, A. (2014). On-orbit radiometric characterization of OLI (Landsat-8) for applications in aquatic remote sensing. *Remote Sensing of Environment*, 154, 272–284.

Phinn, S.R., Dekker, A.G., Brando, V.E., and Roelfsema, C.M. (2005). Mapping water quality and substrate cover in optically complex coastal and reef waters: an integrated approach. *Marine Pollution Bulletin*, 51(1–4), 459–469.

Pollock, F.J., Lamb, J.B., Field, S.N., Heron, S.F., Schaffelke, B., Shedrawi, G., Bourne, D.G., and Willis, B.L. (2016). Correction: Sediment and Turbidity Associated with Offshore Dredging Increase Coral Disease Prevalence on Nearby Reefs. *PLOS ONE*, 11(11), e0165541.

Preisendorfer, R.W. (1986). Secchi disk science: Visual optics of natural waters. *Limnology and Oceanography*, 31(5), 909–926.

Reynolds, R. A., Stramski, D., and Mitchell, B.G. (2001). A chlorophyll-dependent semianalytical reflectance model derived from field measurements of absorption and backscattering coefficients within the Southern Ocean. *Journal of Geophysical Research*, 106, 7125–7138. doi:10.1029/1999JC000311.

Ritchie, J.C., and Cooper, C.M. (1988). Comparison of Measured Suspended Sediment Concentrations with Suspended Sediment Concentrations Estimated from Landsat MSS Data. *International Journal of Remote Sensing,* 9(3), 379–387.

Ritchie, J.C., and Cooper, C.M. (1991). An algorithm for estimating surface suspended sediment concentrations with Landsat MSS digital data. *Journal of the American Water Resources Association* 27, 373–379. doi:10.1111/j.1752-1688.1991.tb01436.x

Ritchie, J.C., and Schiebe, F.R. (1986). Monitoring suspended sediments with remote sensing techniques. In *Hydrological Applications of Space Technology*, 233–243. IAHS Publ. No. 160.

Ritchie, J.C., Schiebe, F.R., and McHenry, J.R. (1976). Remote sensing of suspended sediments in surface waters. *Photogrammetric Engineering and Remote Sensing,* 42, 1539–1545.

Robinson, C.M., Cherukuru, N., Hardman-Mountford, N.J., Everett, J.D., McLaughlin, M.J., Davies, K.P., Van Dongen-Vogels, V., Ralph, P.J., and Doblin, M.A. (2017). Phytoplankton absorption predicts patterns in primary productivity in Australian coastal shelf waters. *Estuarine, Coastal and Shelf Science*, 192, 1–16. *https://doi.org/10.1016/j.ecss.2017.04.012*

Schiebe, F.R., Harrington, J.A., and Ritchie, J.C. (1992). Remote Sensing of Suspended Sediments: the Lake Chicot, Arkansas Project. *International Journal of Remote Sensing,* 13, 1478–1509.

Schroeder, T, Devlin, M.J., Brando, V.E., Dekker, A.G., Brodie, J.E., Clementson, L.A., and McKinna, L. (2012). Inter-annual variability of wet season freshwater plume extent into the Great Barrier Reef lagoon based on satellite coastal ocean colour observations. *Marine Pollution Bulletin*, 65, 210–223. doi:10.1016/j.marpolbul.2012.02.022

Schwarz, J.N. (2005). Derivation of dissolved organic carbon concentrations from SeaWiFS data. *International Journal of Remote Sensing*, 26(2), 283–293. doi:10.1080/01431160410001723691

Slade, W.H., and Boss, E. (2015). Spectral attenuation and backscattering as indicators of average particle size. *Applied Optics*, 54, 7264–7277. doi:10.1364/AO.54.007264

Spyrakos, E., Vilas, L.G., Palenzuela, J.M.T., and Barton, E.D. (2011). Remote sensing chlorophyll a of optically complex waters (rias Baixas, NW Spain): Application of a regionally specific chlorophyll a algorithm for MERIS full resolution data during an upwelling cycle. *Remote Sensing of Environment*, 115, 2471–2485.

Spyrakos, E., O'Donnell, R., Hunter, P.D., Miller, C., Scott, M., Simis, S.G.H., Neil, C., Barbosa, C.C.F., Binding, C.E., Bradt, S., Bresciani, M., Dall'Olmo, G., Giardino, C., Gitelson, A.A., Kutser, T., Li, L., Matsushita, B., Martinez-Vicente, V., Matthews, M.W., Ogashawara, I., Ruiz-Verdu, A., Schalles, J.F., Tebbs, E., Zhang, Y., and Tyler, A.N. (2018). Optical types of inland and coastal waters. *Limnology and Oceanography*, 63, 846–870.

Tian, L., Wai, O.W.H., Chen, X., Liu, Y., Feng, L., Li, J., and Huang, J. (2014). Assessment of Total Suspended Sediment Distribution under Varying Tidal Conditions in Deep Bay: Initial Results from HJ-1A/1B Satellite CCD Images. *Remote Sensing*, 6(10), 9911–9929. doi:10.3390/rs6109911

Twardowski, M.S., E. Boss, J.B. Macdonald, W.S. Pegau, A.H. Barnard, and J.R. Zaneveld (2001). A model for estimating bulk refractive index from the optical backscattering ratio and the implications for understanding particle composition in case I and case II waters. *Journal of Geophysical Research*, 106, 14129–14142.

Tyler, A.N., Hunter, P.D., Spyrakos, E., Groom, S., Constantinescu, A.M., and Kitchen, J. (2016). Developments in earth observation for the assessment and monitoring of inland, transitional, coastal and shelf-sea waters. *Science of The Total Environment*, 572, 1307–1321.

Ule, W. (1892). *Die bestimmung der Wasserfarbe in den Seen*. Kleinere Mittheilungen. Dr. A. Petermanns Mittheilungen aus Justus Perthes geographischer Anstalt, Gotha: Justus Perthes. pp 70–71.

Van der Woerd, H.J., and Wernand, M.R. (2015). True colour classification of natural waters with medium-spectral resolution satellites: SeaWiFS, MODIS, MERIS and OLCI. *Sensors*, 15, 25663–25680.

Van der Woerd, H.J., and Wernand, M.R. (2018). Hue-Angle Product for Low to Medium Spatial Resolution Optical Satellite Sensors. *Remote Sensing*, 10, 180.

Vantrepotte, V., Loisel, H., Dessailly, D., and Meriaux, X. (2012). Optical classification of contrasted coastal waters. *Remote Sensing of Environment*, 123, 306–323.

Vantrepotte, V., Danhiez, F.-P., Loisel, H., Ouillon, S., Mériaux, X., Cauvin, A., and Dessailly, D. (2015). CDOM-DOC relationship in contrasted coastal waters: implication for DOC retrieval from ocean color remote sensing observation. *Optics Express*, 23, 33–54. *https://doi.org/10.1364/OE.23.000033*

Wernand, M.R. (2011). *Poseidons paintbox, Historical archives of ocean colour in global-change perspective*. Utrecht University, p. 240.

Wernand, M.R., and van der Woerd, H.J. (2010). Spectral analysis of the Forel-Ule Ocean colour comparator scale. *Journal of the European Optical Society—Rapid Publications*, 5, 10014s. doi:10.2971/jeos.2010.10014s.

Wernand, M.R., van der Woerd, and H.J., Gieskes, W.W.C., (2013). Trends in ocean colour and chlorophyll concentration from 1889 to 2000, worldwide. *PloS One*, 8, e63766.



19 Quality

Arnold Dekker, Janet Anstee, Barbara Harrison, and Edward King

Water quality is a subjective descriptor of water that is related to its physical, chemical, and/or biological attributes. It attempts to measure the suitability of water for specific requirements, such as human consumption, agricultural use, recreation, fishing, or ecological sustainability. Attributes of water that are relevant to water quality for most uses of water include:

- physical—temperature, transparency, suspended sediment, and turbidity (see Section 5.1);
- chemical—salinity, pH, nutrients and other chemicals, possibly including various contaminants such as industrial byproducts, pesticides, herbicides, and radioactive substances (see Section 5.2);
- biological—phytoplankton, dissolved organic matter, and microbiota (see Section 5.3).

Inland, coastal, and marine water quality are all impacted by a range of meteorological conditions, including precipitation, evaporation, and temperature. The water quality of inland waterbodies is also a function of runoff within their catchments, which is impacted by the geography surrounding lakes, dams, and rivers, and any disruptive land use practices therein, such as urban development (with consequent production of domestic sewage and industrial pollution). Coastal water quality is also affected by freshwater runoff, particularly after flood events (see Section 11.4). As such, it is directly impacted by both management practices in coastal catchments and aquatic activities in the coastal zone, whereas marine water quality is driven by a range of anthropogenic marine and atmospheric activities, including potential pollution from shipping and infrastructure development, and increased CO_2 levels leading to ocean acidification and temperature rises.

The whole aquatic system can be impacted by pollution. Sources of pollution can be natural, as occur following extreme weather events or tectonic activity, or derived from human activities related to agriculture, industry, mining, or urbanisation. The growing number of new contaminants, such as plastics, cosmetic products and therapeutics, raises particular concerns in terms of their bioavailability, bioaccumulation, and toxicity to aquatic organisms (Galloway and Lewis, 2016; SOE, 2016a). Human litter, which enters coastal waters from populated areas, can be carried long distances by wind and water circulation (Reisser *et al*., 2013; Critchell *et al*., 2015). The vast majority of this type of litter is plastic debris (Rochman *et al*., 2016) and microplastics (Browne, 2015; see Section 19.4.1). Other potential sources of marine pollution include shipping (see Section 19.4.1) and oil spills (see Section 19.4.3).

Pollution, also called environmental pollution, the addition of any substance (solid, liquid, or gas) or any form of energy (such as heat, sound, or radioactivity) to the environment at a rate faster than it can be dispersed, diluted, decomposed, recycled, or stored in some harmless form.
(Encyclopedia Britannica)

Background image: Copernicus satellite image of part of the Phytoplankton Monitoring Network administered by the Murray-Darling Basin Authority. This image is rotated counterclockwise, spanning from Lake Victoria on the left to the Murray River on the right. **Source:** National Environmental Information Infrastructure

Recommended Chapter Citation: Dekker, A.G., Anstee, J.M., Harrison, B.A., and King, E.A. (2021). Quality. Ch 19 in *Earth Observation: Data, Processing and Applications. Volume 3B—Surface Waters.* CRCSI, Melbourne. pp. 367–394. ISBN 978-0-6482278-5-4

19.1 Quality of Australian Surface Waters

The quality of marine, coastal, and inland waters directly impacts the productivity, functioning, and resilience of aquatic ecosystems. Deliberate loading, dumping, and incineration of waste in Australia's marine jurisdiction is regulated by the federal government as part of the International Maritime Organisation's agreement known as the London protocol (IMO, 2020), as are the creation and operation of artificial reefs, dredging operations, and burials at sea (DAWE, 2020).

Many Australian estuaries are considered to be experiencing moderate to strong pollution pressure (SOE, 2016a). The diversion of water for irrigation and regulation also changes the natural flow regimes of inland waterbodies, especially within the Murray-Darling Basin (CSIRO, 2008). The major concerns in terms of coastal and marine water quality in northern Australia, including the Great Barrier Reef (GBR) region, are from:

- levels of sediment, nutrients, and contaminants that originate from agricultural, industrial, or urban land; and
- rising water temperatures and higher acidity levels due to climate variations (AIMS, 2019).

For example, excess nutrient levels in aquatic environments can lead to eutrophication, algal blooms (see Section 19.5), increased turbidity, low-oxygen dead zones, fish kills, disruption in natural microbial processes and biogeochemical cycling and, in tropical areas, crown-of-thorns outbreaks, coral bleaching, and coral disease (Chislock *et al*., 2013). Warmer waters also affect the growth and reproduction of many marine organisms (SOE, 2016a; see Section 19.6 and Excursus 20.3). Global collaborations such as GloboLakes (see Section 19.8) are using EO time series datasets to monitor the response of lakes to environmental changes, including climate, at a range of scales.

Common contaminants found in coastal rivers and estuaries include excess metals, nutrients and organic matter, and industrial chemicals, pesticides, herbicides, terrigenous sediments and debris. SOE (2016a)

19.2 EO Sensors for Water Quality

Various EO data sources and their sensors are introduced in Volume 1A, and interpretation of EO imagery is considered in Volume 1B. As detailed in Section 18, EO methods exist to derive concentrations of chlorophyll, non-algal particles (NAP—or suspended sediments) and coloured dissolved organic matter (CDOM) from optical EO imagery. For example, a range of waterbody features, including a flood plume, are visible in the pseudo true colour composite image shown in Figure 19.1.

While most EO sensors are primarily designed for observing land or ocean, several sensors have been used to map inland and coastal water quality, benthic habitats, or bathymetry (see Table 8.14). The specific water quality variables that can be identified from these datasets are detailed in Table 19.1.

CEOS (2018) recommend detailed specifications for the ideal spaceborne optical sensor for EO of non-oceanic, aquatic environments and the parameters for preferred spectral, spatial, radiometric, and temporal characteristics for mapping water quality (Section 8.5). Minimum spectral requirements include bands that detect cyanophycocyanin (centred on the *in vivo* absorption maximum, 620–624 nm) to estimate blue-green algae concentration and chlorophyll a (centred on *in vivo* red absorption maximum, 676 nm). Additionally, numerous other bands (with appropriate spectral and spatial resolution, and radiometric characteristics) are needed in the range 380–780 nm for detecting aquatic ecosystem variables (see Table 8.15), and in the ranges 360–380 nm and 780–1400 nm for correction of atmospheric and air-water interface effects (see Table 8.16).

To adequately track the continuous variations that occur in complex aquatic ecosystems, such as inland and coastal waterbodies, EO sensors need rapid temporal sampling to monitor changes at appropriate spectral and spatial scales to represent the underlying ecosystem processes. Frequent coverage is important if imagery is to be used to monitor the dynamic nature of aquatic systems, with events such as algal blooms and flooding changing on an hourly basis.

Table 19.1 Suitability of optical EO sensors to map water quality variables

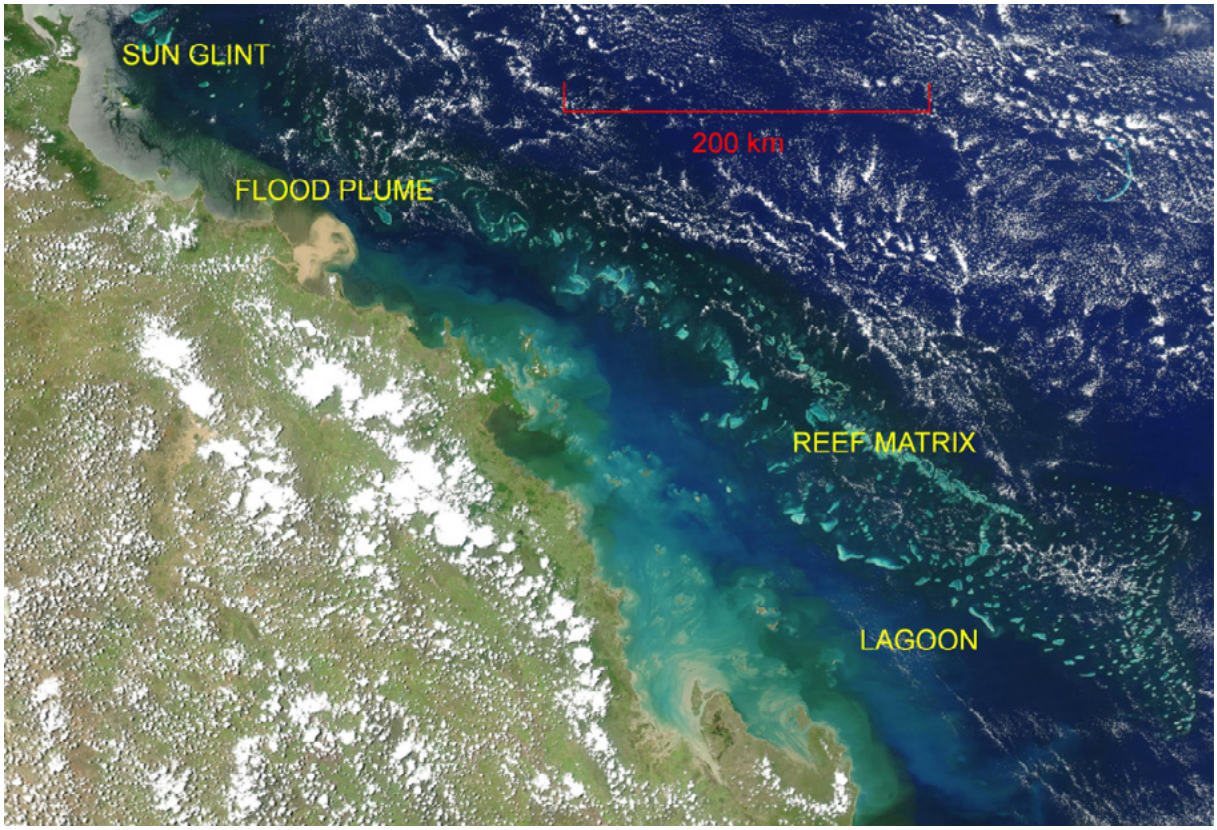
This list includes multispectral and hyperspectral sensors carried on previous, current, and future EO missions with spectral bands in the wavelength range 340–1000 nm. Names of commercial sensors are italicised. TSM: Total Suspended Matter; CDOM: Coloured Dissolved Organic Matter

Sensor	Water-quality variables (freshwater, coastal, and ocean)					
	Chlorophyll a	Cyanophycocyanin	TSM	CDOM	Kd	Turbidity and/or Secchi Disk transparency
Hyperion	high	high	high	high	high	high
CHRIS-PROBA	high	high	high	high	high	high
MERIS	high	high	high	high	high	high
HICO	high	high	high	high	high	high
Sentinel-3 OCLI	high	high	high	high	high	high
GLIMR	high	high	high	high	high	high
PRISMA	high	high	high	high	high	high
EnMap	high	high	high	high	high	high
SBG (formerly HyspIRI)	high	high	high	high	high	high
PACE	high	high	high	high	high	high
ISS HISUI	high	high	high	high	high	high
ISS DESIS	high	high	high	high	high	high
OCM-2	high	high	high	high	high	high
Suomi-VIIRS	medium	potential	high	high	high	high
SGLI	medium	Not suitable	high	high	high	high
GOCI	high	potential	high	medium	high	high
GOCI-II	high	potential	high	medium	high	high
WORLDVIEW-2	medium	medium	high	medium	high	high
WORLDVIEW-3	medium	medium	high	medium	high	high
IKONOS, QuickBird, SPOT-5/-6, GeoEye, Planet, etc.	potential	Surface bloom	high	potential	high	high
RapidEye	potential	Surface bloom	high	potential	high	high
SENTINEL-2	medium	Surface bloom	high	medium	high	high
Aqua/Terra MODIS (1 km)	medium	potential	high	high	high	high
Aqua/Terra MODIS (500 m)	Not suitable	Not suitable	potential	medium	medium	medium
Aqua/Terra MODIS (250 m)						
LANDSAT-4 to -7	potential	Surface bloom	potential	medium	medium	medium
LANDSAT-8/-9	potential	Surface bloom	high	potential	high	high
Himawari-8/-9	potential	Not suitable	high	potential	potential	high
GOES-R	potential	Not suitable	high	potential	potential	high
GISAT-1/-2	potential	potential	high	potential	potential	medium
MSG SEVIRI	potential	Not suitable	medium	Not suitable	potential	medium

Adapted from: CEOS (2018) Table 2.7

Figure 19.1 Great Barrier Reef shown in true colour

Water features, including a flood plume, are clearly visible in this MODIS optical image acquired on 28 February 2008. This image is a composite of 500 m and 1 km bands, produced by CSIRO using data courtesy of NASA.



Source: eReefs. Retrieved from: *https://research.csiro.au/ereefs/remote-sensing/how-it-works/*

Unmanned Aerial Vehicles (UAV) or drones are rapidly developing as viable alternatives to satellites and manned aircraft for monitoring various Earth resources (see Volume 1A—Section 11.2). These flexible platforms have the ability to acquire high frequency data for validating water colour observations, as well as spatially-explicit modelling of suspended sediments and chlorophyll content. Data quality and uncertainty associated with radiometric calibration of the sensor system is paramount when assessing water quality. When instruments carried by drones are well-calibrated, however, the acquired multispectral and hyperspectral images can be used to test the performance (precision and optimal range) of empirical and semi-empirical models for the retrieval of chlorophyll a (Matthews, 2011), or used for semi-analytical inversion methods (see Section 8.4).

Table 19.2 EO sensors relevant to water quality

TIR: Thermal infrared; SAR: Synthetic Aperture Radar

Type	Sensor	Platform	Relevance	Advantages	Disadvantages
Passive optical	Multispectral radiometer	Satellite or airborne	Inland water quality, Marine and coastal pollution, Algal blooms	Indicate sediments and coastal erosion, global coverage, range of spatial resolutions available, low cost	Impacted by cloud cover
	Hyperspectral radiometer	Satellite or airborne	Inland water quality, Marine and coastal pollution, Algal blooms	High spectral resolution	Higher cost for airborne data, large data volume, impacted by cloud cover
	TIR radiometer	Satellite	Marine heatwaves	Global coverage, long time series	Low spatial resolution, impacted by cloud cover
Passive microwave	L-band radiometer (ocean brightness temperature)	Satellite	Marine salinity	All weather so useful in tropical regions	Data availability
Active microwave	SAR	Satellite or airborne	Marine and coastal pollution, Ship detection	All weather and at night	High cost, specialised processing

19.3 Inland Water Quality

Comprehensive information about the water quality of inland waterbodies is lacking in many countries, including Australia (SOE, 2011). Strict controls generally exist for waterbodies supplying drinking water, which result in relatively standard taste, odour, and appearance. However, the quality of waterbodies used for agricultural and recreational purposes tends to be monitored less carefully despite the condition of these waterbodies being significant to environmental health, with uncontrolled degradation in water quality impacting both aquatic ecosystems and the bordering terrestrial ecosystems (see Excursus 19.1).

Most attributes of water quality are dynamic and can vary rapidly in both space and time. An understanding of the dynamics of these attributes is essential to managing inland water resources. There are two primary temporal considerations for inland water quality monitoring:

- sampling designed to represent the dynamics of water quality and the range of conditions that can occur over diurnal, seasonal, and annual cycles; and
- sampling designed to develop a time series dataset (see Volume 2D). Time series are essential for assessing the condition and trends of inland water quality as they relate to the effect of water quality management and climatic variations.

Excursus 19.1—Australian Inland Water Quality

Source: Dekker and Hestir (2012)

In 2011, the National Water Quality Assessment (SOE, 2011) surveyed the water quality status of Australian inland drainage regions and their river basins. Compliance with Australian water quality guidelines for discrete point-based samples were summarised in terms of turbidity, salinity (measured as electrical conductivity), pH, total nitrogen, total phosphorus, cyanobacteria, and microbial quality (faecal coliforms, enterococci, and *E. coli*). At that time, most of these variables were routinely measured in less that half the river basins in Australia, with considerable variation in data consistency, especially for cyanbacteria and microbial quality.

Significant differences were observed between the frequency and type of water quality sampling undertaken in the densely populated parts of Australia compared with more remote locations. In some regions, the ephemeral nature of waterbodies may account for infrequent or inconsistent records. Both poor coordination between agencies, and a lack of consistency in the methods and actual water quality variables measured, have made assessing long term trends difficult.

Many Australian inland waters are exposed to cycles of long periods of relatively low flow or drought conditions, interspersed with intense periods of rainfall, leading to flash floods in high relief terrain or extended and extensive floods in flat terrain. Floods cause large fluxes of suspended sediment, dissolved organic material, salt, nutrients, and contaminants, which can lead to changes in the environmental state in aquatic ecosystems. In the wet tropics higher flows occur throughout the year.

Under stable or drought conditions, salinity and seasonal microbial activity need regular monitoring. More frequent sampling is required when algal blooms are likely to affect water quality. However, during intense rainfall and resulting streamflow events it is most important to estimate changes in the material content of water, such as suspended sediment and organic matter. At such times, algal-related measurements are less relevant, since water turbulence and the resuspension and dissolution of soil materials prevents algal growth. The monitoring of rapid changes in water quality during extreme events is a challenge for any monitoring method, but is necessary to understand the effects of extreme flow events on aquatic ecosystems.

19.3.1 Traditional methods

Traditional monitoring of water quality involves systematic collection and analysis of water samples to provide information and knowledge about a body of water. Such monitoring can be conducted by a wide range of organisations, including government agencies, private utilities, agricultural and industrial water providers, and mining companies, for both privately-owned and public waters. Three basic types of water quality measurement methods are suitable for water quality monitoring:

- *in situ* discrete water sampling for field and laboratory analysis;
- *in situ* continuously deployed, automated physicochemical and bio-optical instruments and samplers; and
- EO-based methods from just above the water surface, through to satellite observations.

While *in situ* sampling, conducted manually or automatically, encompasses a wide range of analyses, and yields precise and replicable results, collection of water samples involves logistical difficulties, particularly given the density of coverage required. Adequate sampling strategies should include vertical profiles to determine variations with water depth, transect measurements to determine spatial variations, and repeated sampling over time to determine temporal changes (Lindell *et al.*, 1999). Further, it is often difficult to accurately georeference the locations of point measurements, and to coordinate the collection of samples to coincide with major changes in water quality. The processing time required for analysis of samples adds another layer of complexity when comparing results. The cost of *in situ* sampling is very high, especially relative the coverage achieved. At present, no legislative standards exist in Australia to define preferred methods for water quality monitoring that could deliver comparable results for different waterbodies.

19.3.2 EO approaches

In recent decades both multispectral and hyperspectral imagery acquired by satellites and aircraft have been used to monitor inland water quality (Durand *et al.*, 1999; Dekker and Hester, 2012; Odermatt *et al.*, 2012; IOCCG, 2018). In particular, the technological advances in sensor design with higher spectral and spatial resolution and selected spectral bands have allowed image data to be tailored to specific situations (see CEOS, 2018, and Section 8.5). These advances have also enabled development of calibrated spectral libraries and models for specific water quality parameters.

As detailed in Section 18, EO datasets can be used to assess surface water concentrations of:

- chlorophyll—an indicator of phytoplankton biomass, trophic and nutrient status and the most widely used index of water quality and nutrient status globally (see Section 18.6).
- cyanophycocyanin (CPC) and cyanophycoerythrin (CPE)—indicators of cyanobacterial biomass, which is common in harmful and toxic algal blooms (see Sections 8.2.2 and 19.5).
- coloured dissolved organic matter (CDOM)—the optically measureable component of dissolved organic matter in the water column sometimes used as an indicator of organic matter and aquatic carbon (see Sections 8.2.4 and 18.5.1).
- total suspended matter (TSM) and non-algal particulate matter (NAP)—important for assessing the quality of drinking water and controlling the light environment of aquatic environments (see Section 18.4).

Additionally, the following conditions can also be estimated from optical imagery:

- vertical light attenuation (Kd—Secchi disk transparency) and turbidity—measurements of the underwater light field that are important for assessing the degree of light limitation, rates of primary production, species composition, and other ecosystem responses (see Section 8).
- emergent and submerged macrophytes—down to the depth of visibility, these are important indicators of wetland and aquatic ecosystem health and function (see Section 20).
- bathymetry—if the substratum of a waterbody reflects a measureable amount of light through the water column to above the surface, then the waterbody depth can be estimated (see Section 13.4.2).

The importance of appropriate spatial resolution data to map inland water quality is discussed in Excursus 19.2. Since many EO sensors routinely offer spatially and temporally comprehensive coverage of all waterbodies at low (or no) cost, the combined information from directly measurable optical properties can be used to derive information about eutrophication, environmental flows, carbon, and primary productivity. Non-optical properties, such as nitrogen, phosphate, dissolved oxygen, and organic and inorganic micro-pollutants can be estimated through inference, proxy relationships, or data assimilation with EO optical properties. However, these relationships are stochastic, may not be causal, and may have a limited validity range (Dekker and Hester, 2012).

Multispectral sensors that include a blue spectral band can be used to detect TSM, Secchi disk transparency, turbidity, and CDOM. While algal pigments may be detectable from multispectral datasets, accuracy will be low, especially when these pigments are present at low concentrations, since broad spectral bands cannot discriminate the narrow pigment spectral absorption features of algal pigments from other absorbing and backscattering materials in the water column. As detailed in Volume 1, the highest spectral resolution for optical EO is offered by hyperspectral sensors or 'imaging spectrometers', where the entire visible and nearby NIR spectrum are measured in narrow (5–20 nm) contiguous bands (see Volume 1A—Section 13 and CEOS, 2018). Specifically designed aquatic sensors with more spectral bands, that are both narrower and suitably positioned, would yield more accurate measurements of chlorophyll than multispectral sensors, and enable phytoplankton pigment types, such as the cyanobacterial pigments to be detected (CEOS, 2018; see Section 8.5). Finer spectral resolution may also enable estimation of the particle size distribution, and fractions of organic and mineral particulate matter.

Two main types of forward optical models are available to map water quality, namely generic radiative transfer models (such as HYDROLIGHT; Mobley and Sundman, 2000) and semi-analytical models (see Section 8.4). These forward models are able to predict the light composition leaving a waterbody based on the water column constituents and, if visible, the benthic reflectance. When the substratum is visible, the SAMBUCA (Semi-analytical Method for Benthic Unmixing and water Column Concentration Assessment; Brando *et al.*, 2009; Dekker *et al.*, 2011) has been applied to inland waterbodies, estuarine waters, coastal tidal lagoons, coastal waters, and coral reefs. An example of applying these models is given in Excursus 19.3.

Excursus 19.2—Assessing Inland Water Quality using Optical EO

Source: Dekker and Hestir (2012)

In order for an EO sensor to effectively measure a waterbody, that body of water must be at least three to four times the size of a pixel to ensure that the pixel comprises 'pure' water, and does not contain any significant signal component from surrounding land and/or vegetation. Thus, to resolve a lake using imagery with 30 m pixel resolution, a minimum of 9 (3×3) 'pure' water pixels, but preferably 16 (4×4) pixels is required. This ground area equates to a waterbody that is at least 120 m wide. Table 19.3 summarises the number of waterbodies in Australia that could be assessed using two commonly available sources of EO imagery with long term archives:

- Landsat (30 m pixel resolution), which would require a waterbody to be at least 120 m wide (> 0.01 km^2); and
- MODIS (250 m pixel resolution) or MERIS (300 m pixel resolution), which would require a waterbody to be at least 1000 m wide (> 1 km^2).

Since 2014, Sentinel-2 imagery has also been available with 10 m pixel resolution.

The effect of changing spatial resolution when discerning waterbodies is illustrated in Figure 19.2. Image spatial resolution has consequences for imaging small waterbodies, such as small or medium width river systems. In these situations high spatial resolution imagery (with pixel sizes of 2–10 m) may be the only option, possibly leading to significant data acquisition costs.

Table 19.3 Size distribution of waterbodies in Australia

Note: These categories are not exclusive, so numbers for medium category includes all large waterbodies.

Category	Size	Number	% of Total	Total Surface Area
Small	< 0.01 km^2	86,000	68	475,423
Medium	> 0.01 km^2	63,000	32	220,000
Large	> 1 km^2	2,300	11	77,500

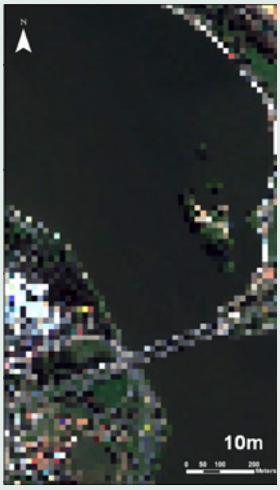
Source: Dekker and Hestir (2012)

Figure 19.2 Effect of spatial resolution on Lake Burley Griffin, Canberra

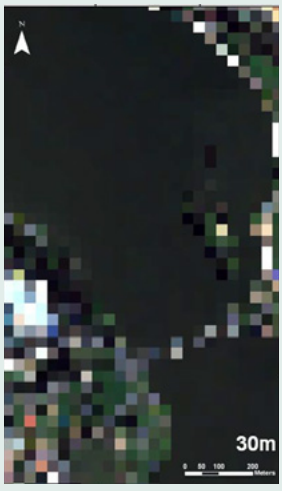
a. 2 m pixel (typical commercial spatial resolution such as QuickBird or WorldView-2)



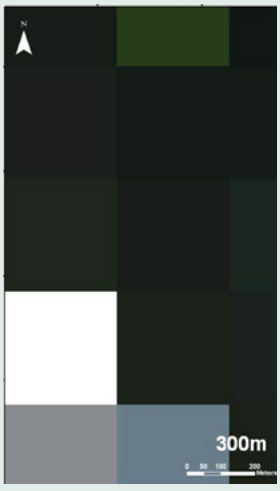
b. 10 m pixel (typical of Sentinel-2)



c. 30 m pixel (Landsat)



d. 300 m pixel (MERIS)



Source: Dekker and Hestir (2012) Figure 3-2

Effective water quality reporting requires a systematic approach that measures the same water quality variables at regular intervals across a wide geographic range. To achieve robust results from optical EO of water quality in Australia, robust methods are required for:

- atmospheric, sunglint and skyglint corrections as appropriate to environmental conditions;
- characterisation of the optical variability of inland waterbodies. This requires collection of a representative spectral library of inland water bio-optical properties to parameterise and validate physics-based inversion algorithms; and
- investigation of scaling effects of *in situ* water quality data versus derived water quality information from EO datasets. This includes investigating the possibility of translating *in situ* algal cell counts to EO-based chlorophyll concentrations, and reconciling point-based measurements with pixel-based measurements.

Dekker and Hestir (2012) recommended a national operational water quality monitoring system based on EO, as summarised in Table 19.4.

Table 19.4 National water quality system based on EO

Water Quality Information	Water Quality Variable
Primary production and eutrophication status	Chlorophyll
	Cyanophycocyanin
	Cyanophycoerythrin
	Surface algal blooms
Aquatic carbon content, carbon fluxes	Coloured dissolved organic matter
Erosion, re-suspension and deposition	Total suspended matter (= sum of chlorophyll – non-algal particles)
Light climate information related to the combined effects of algae, coloured dissolved organic matter and suspended matter	Vertical attenuation of light
	Transparency
	Turbidity
Ecological condition	Emergent macrophytes
	Submerged macrophytes

Source: Dekker and Hestir (2012) Table 5-1

Excursus 19.3—Western Treatment Plant, Werribee

Source: Janet Anstee (CSIRO); Hydraspectra: Tim Malthus and Stephen Gensemer (CSIRO)
Further Information: Joehnk *et al.* (2018); *https://www.melbournewater.com.au/community-and-education/about-our-water/sewerage/western-treatment-plant*; *https://utilitymagazine.com.au/drone-technology-takes-off-at-melbourne-water/*

The Western Treatment Plant (WTP) was established in 1897 to manage human waste from Melbourne's growing suburbs. A network of pipes, sewers, and drains transport sewage 32 km from the city near Port Phillip Bay. The Plant now comprises a network of lagoons, wetlands, and intertidal and shoreline areas that support a diversity of birdlife, including migratory waterfowl from the Northern Hemisphere. In 1982 the facility was declared a Ramsar-listed wetland, and is an important site as it covers 110 km^2, with many shallow lagoons, 1.5–3 m deep.

The Plant operates operates by treating the sewage in Activated Sludge and Nutrient Reduction Plants, and allowing it to flow through anaerobic and aerated aerobic lagoons (a series of ponds). Over a period of about a month, the lagoon bacteria decompose the organic content then solids are settled out of the wastewater in clarifiers. In the process of treating around half of Melbourne's sewage from about 5 million people, a large volume of water is recycled, biogas is generated to run the Plant, and biosolids are available for fertiliser.

Cyanobacteria blooms are a yearly occurrence in WTP's treatment lagoons (see Figure 19.3) where they occasionally interrupt the supply of class A recycled water, which is provided to surrounding market gardens, and reduce the efficiency of lagoon treatment processes. Melbourne Water sought to investigate the potential of EO to resolve the spatial pattern of cyanobacteria blooms and other microalgae and its capacity to detect/quantify surface concentrations. An understanding of bloom spatial patterns at the WTP will facilitate the development of bloom forecasting models (Joehnk *et al.*, 2018) that allow operational and asset management controls (such as desludging targets) to be optimized to avoid and manage nuisance blooms.

Figure 19.3 Cyanobacteria bloom

Sentinel-2A image acquired on 7 March 2018 showing active algal blooms (green) at WTP.

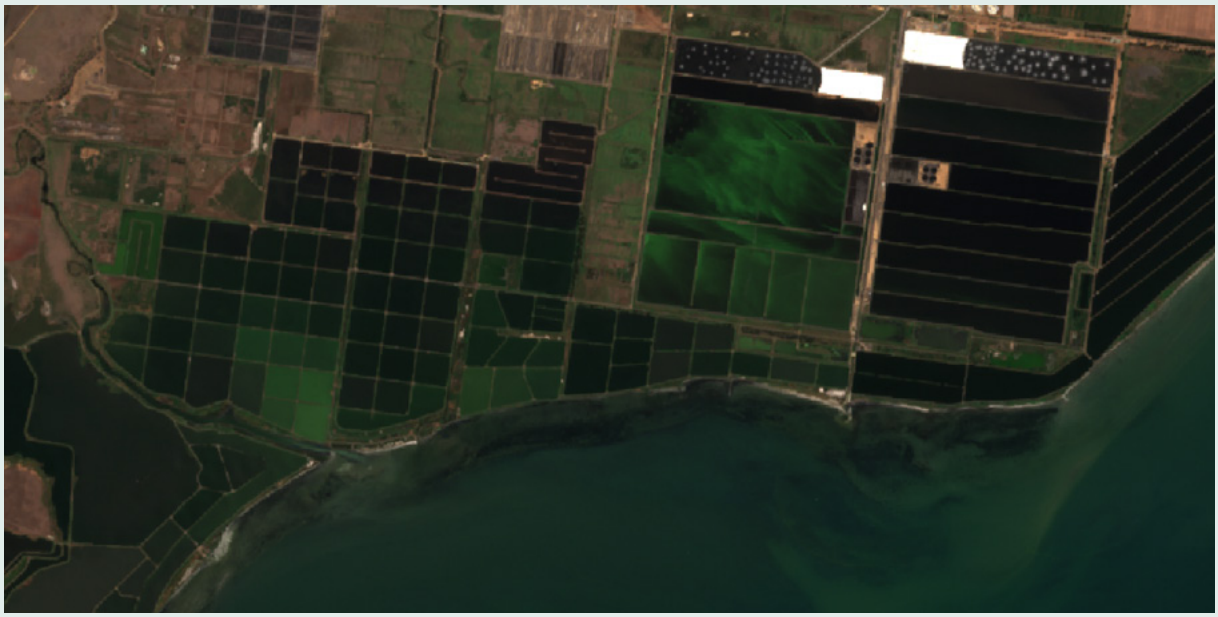


Figure 19.4 *In situ* measurement locations

The field site locations visited during field sampling on 14–15 February 2018.

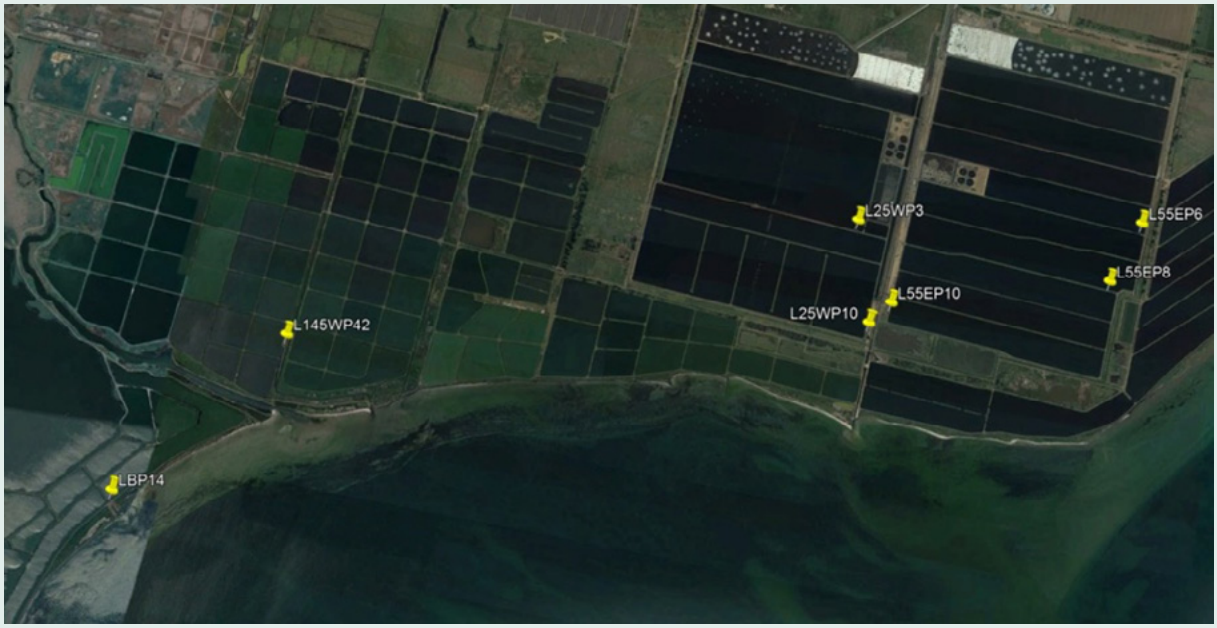


Figure 19.5 HydraSpectra installation

WTP pond L25WP3 on 14 February 2018



Monitoring cyanobacteria blooms remotely requires sensors with high resolution, spectrally, spatially, and temporally, to capture their very dynamic features. While passive optical EO satellite observations often lack the spectral and temporal resolutions required for operational monitoring, and are blocked during periods of cloud cover, these datasets can be complemented by near-surface hyperspectral sensors providing high-frequency images of the water surface. In the case of the WTP, the near-surface sensors can be used to detect scum formation and quantify local cyanobacterial abundance (Malthus *et al.*, 2016). By acquiring EO data, near-surface sensors, together with regular water samples analysis (cell counts, laboratory pigment analysis; Simis *et al.*, 2007), a synoptic overview can be acquired with high frequency monitoring of blooms in problematic areas. The dense data stream will also allow for future data driven, machine learning forecasts.

Initially, a full time series of Digital Earth Australia Landsat data (1987–2016) was used to implement the adaptive linear matrix inversion model (aLMI, Brando *et al.*, 2012) at a selected location to retrieve chlorophyll a as a proxy for cyanobacteria biomass. The aLMI was unable to retrieve data from a number of images in the time series, either due to poor pixel quality (from contamination due to clouds, aerosols, etc) or because the parameterisation inadequately characterised the conditions in the WTP. For the data that was retrieved, the satellite derived data for nearly 30 years were compared with the Melbourne Water *in situ* measurements taken at L55E and L55EP3 (see Figure 19.4).

The database used to parameterise the aLMI model initially was based on an extensive set of inland bio-optical properties collected from NSW and QLD inland reservoirs, dams, rivers, and lakes. This database was amended to include the additional data acquired at the WTP in February 2018. The inclusion of the WTP field data in the parameterisation, generally increased the retrieved value of chlorophyll compared to the previous parameterisation. As the Sentinel-2 imagery is now available on the DEA, its improved capability for chlorophyll a detection, would generate higher temporal frequency of retrievals than Landsat data and be better suited for monitoring the cyanobacteria blooms.

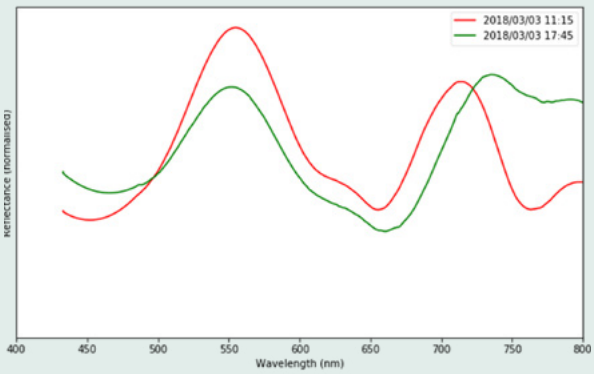
Figure 19.6 HydraSpectra reflectance data

This data was collected at pond L25WP3 in the WTP on 3 March 2018.

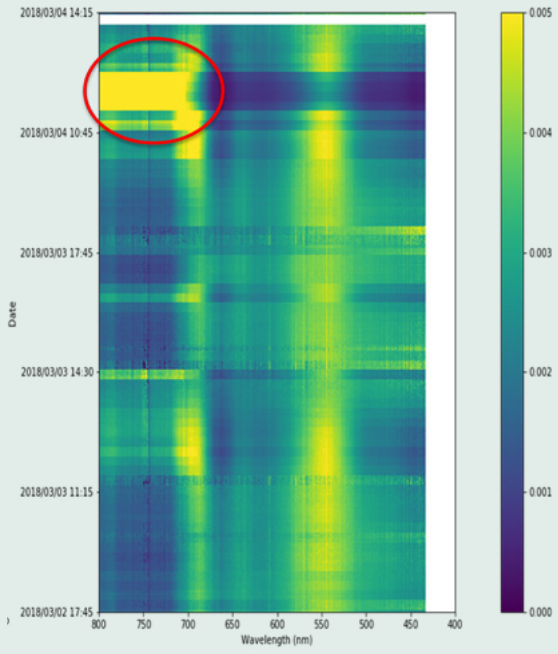
a. Hemispherical photograph of water conditions at 11:15 am



b. Normalised reflectance at 11:15 and 17:45



c. Reflectance colourmap summarising the data obtained over the entire day (with decreasing wavelength from left to right). The red circle indicates a surface scum with high reflectance in near infrared wavelengths.



To assess the potential of a near-surface hyperspectral camera, a single sensor was installed at pond L25WP3 of Melbourne Water's WTP (see Figure 19.5). At installation, the sensor head is oriented at 135° relative to magnetic north to minimises the influence of surface sunglint on the measured water surface reflectance. The system was set up to sample every 15 minutes from 6 am to 6 pm, daily. Data were uploaded once per hour to the FTP server via the Telstra 4G network.

Every 15 minutes, the HydraSpectra delivers a hemispherical photograph of the water surface and sky conditions (see , a normalised spectral plot, a colourmap of surface reflectance. Figure 19.6 shows these results for 3 March 2018, when a *Microcystis* bloom appeared at 11.15 am and disappeared at 12.45 pm due to upcoming wind action mixing the water column. In the colourmap (see Figure 19.6c), the bloom's surface scum is detected by near infrared wavelengths and highlighted by a red circle.

The colourmap (see Figure 19.6c) shows bright green reflectance features in the wavelength range 540–560 nm and a high reflectance feature between 680–710 nm, corresponding to a chlorophyll a reflectance peak near 700 nm. There is also a dark feature corresponding to the phycocyanin absorption between 610–630 nm and a very dark absorption feature between 670–680 nm, correlating with chlorophyll a.

Using the near-surface sensing with satellite derived data provides a better understanding of the bloom spatial patterns. The integration of this information with hydrodynamic modelling is the coming challenge but would greatly enhance the prediction of cyanobacteria blooms.

19.4 Pollution

Pollution of aquatic systems is increasing significantly around the globe, and poses a major threat to both water quality and biodiversity. Growing numbers of marine vessels and infrastructure developments increase the opportunities for marine pollution.

Marine pollution impacts different organisms in different ways. Pollutants can bioaccumulate when an organism is unable to excrete them as quickly as they are ingested, then be transferred to other organisms at higher levels in the food chain (see Section 3.3)

The oil and gas industry has been described as the 'economic backbone' of the the marine sector in Australia (SOE, 2011), with significant reserves being extracted from the sea each year, particularly in northwestern waters (ATC, 2013; Wood Mackenzie, 2020). However, the potential for marine pollution is real in the associated activities of exploration surveys and drilling, development of submarine infrastructure, production operation, and decommissioning. In addition to influencing water quality, these activities can impact the marine environment by disturbing the seabed, introducing underwater noise, adding artificial light, and changing air quality. While the actual impacts of these activities are generally localised, their long term effects are unknown (SOE, 2016b).

EO-based methods are being used to monitor marine areas for different forms of potential pollution, including:

- plastic debris (see Section 19.4.1);
- shipping (see Section 19.4.2); and
- oil spills (see Section 19.4.3).

19.4.1 Plastic debris

Over 300 million tons of plastic are manufactured around the world each year, of which 8 million tons move into the global ocean (IUCN, 2020). Eriksen *et al.* (2014) estimated that 250,000 tons (over 5 trillion pieces) of plastic were floating in coastal and marine waters, mostly originating from land (Jambeck *et al.*, 2015), but more recent estimates for the total volume of marine plastic debris are significantly higher (Agamuthu *et al.*, 2019). Plastics are considered to be the major form of marine debris, amounting to 50–90% of all debris in different regions (Agamuthu *et al.*, 2019).

This growing problem has varied ecological impacts on marine biota and water quality (Rochman *et al.*, 2016). The dynamics of marine plastic litter has been tracked, both globally (van Sebille *et al.*, 2012, 2015) and around Australia (Reisser *et al.*, 2013), to determine its origins, transport pathways, and accumulation zones. Most marine debris finally rests on the ocean floor to disturb, and potentially contaminate, benthic habitats (Maximenko *et al.*, 2019).

Marine debris (or marine litter) is defined as any persistent, manufactured or processed solid material discarded, disposed of or abandoned in the marine and coastal environment (UNEP, 2020).

EO is one option to monitor this problem. A range of approaches have been trialled (Mace, 2012), including identifying spectral features for plastics using airborne hyperspectral imagery (Garaba *et al.*, 2018; Garaba and Dierssen, 2018), and developing a reflectance model that accounts for colour, transparency, reflectivity, and shape of debris (Goddijn-Murphy *et al.*, 2018) that could help to the design appropriate EO sensors (see Section 8.5). Sensor calibration also requires *in situ* data for the various type of debris, especially given that the optical characteristics of floating plastics are likely to change over time (see Section 8.3). Surface wind movements may also hide floating material, so image acquisition is best done in low wind conditions (Goddijn-Murphy *et al.*, 2018).

An Integrated Marine Debris Observing System (IMDOS) has been proposed that will use EO and *in situ* datasets to monitor the risks from marine debris (Maximenko *et al.*, 2019). This global system is envisaged to involve a range of optical and SAR sensors, on a variety of platforms, in conjunction with a network of *in situ* observations for calibration and validation.

19.4.2 Shipping

Tens of thousands of maritime vessels transport over 10,000 million tons of goods around the world each year, with maritime trade (measured in terms of weight per unit distance) doubling during the two decades since 2000 (UNCLAD, 2019). Marine safety and traffic surveillance, as well as tracking illegal fishing activities and oil discharges, increasingly rely on EO-based ship detection methods (see Excursus 2.1).

Australia imports and exports a very high proportion of goods by ship and has been assessed as one of the top shipping nations globally based on cargo volume and distance travelled (Gilbert *et al.*, 2003). Through sensitive environments, such as the GBR, approved shipping lanes have been defined to minimise the risk of environmental damage, either by direct contact with underwater features, such as reefs, or via oil spills (see Section 19.4.3).

In coastal and marine waters, a range of vessels have been detected using EO datasets from both optical and SAR sensors (Crisp, 2004; Kanjir *et al.*, 2018; Bereta *et al.*, 2020), with SAR being most commonly used for ship detection (see Section 9). Since ships comprise many metal components, and typically include sharp edges, they reflect radar signals more strongly than the water surface (see Volume 1B—Section 8). While they appear as bright, geometric shapes on a darker surface when sea conditions are calm, in windy and choppy conditions the characteristic speckle of radar images is enhanced, which reduces the contrast between ships and water, and potentially leads to false detections, especially for small vessels (Sagar *et al.*, 2020).

Accuracy of vessel detection using optical imagery varies with the characteristics of individual sensors and weather conditions, and ship detection algorithms have been developed with varying success (Kanjir *et al.*, 2018). Imagery acquired by nighttime optical sensors has also been used to identify shipborne nightlights (Elvidge *et al.*, 2015; Straka *et al.*, 2015).

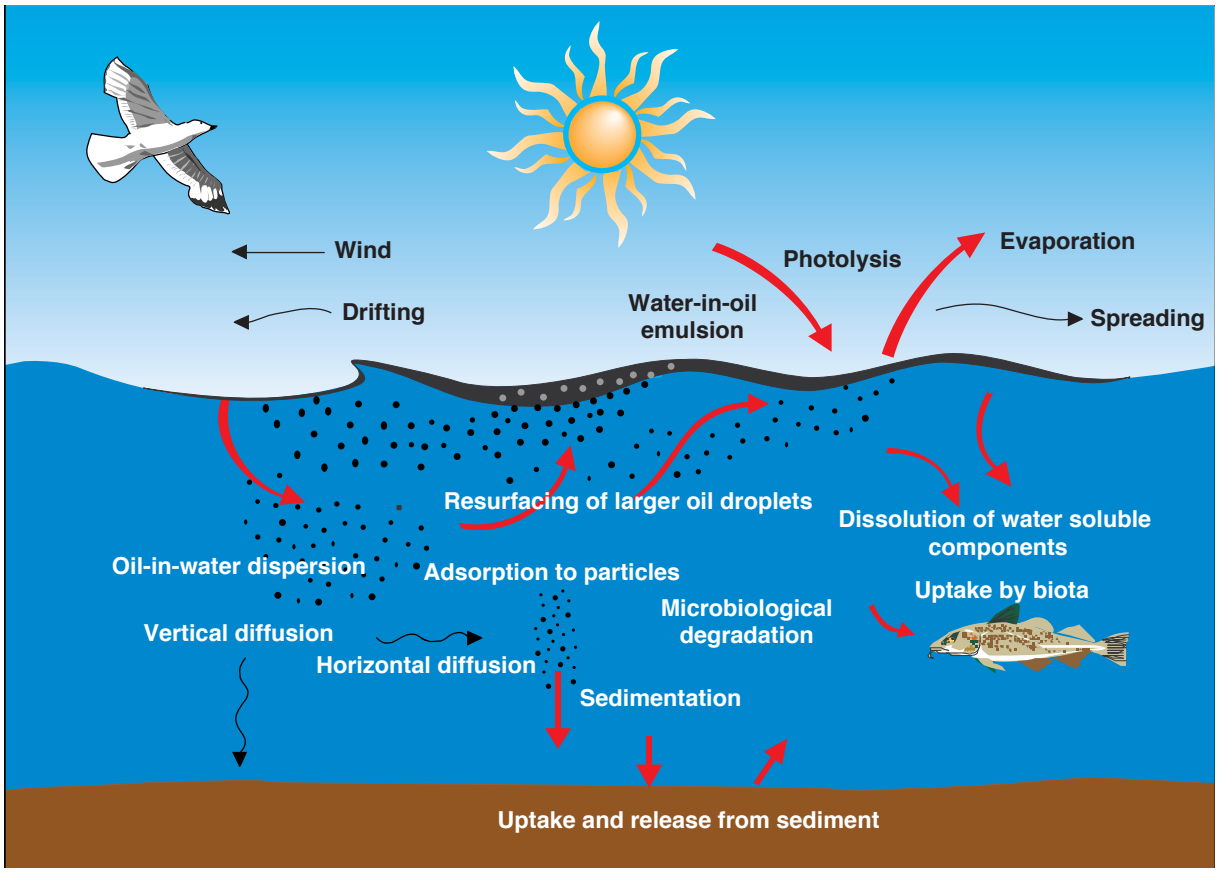
The position, course, and speed of all Commonwealth-endorsed fishing vessels are monitored by the Australian Fisheries Management Authority (AFMA) via International Maritime Satellite (INMARSAT) communications (AFMA, 2020). This system allows AFMA to track illegal fishing and unauthorised entry to Marine Protected Areas (see Excursus 20.2). The Global Fishing Watch, a public, online map of global fishing activity (*globalfishingwatch.org*), has been modified to create an Australian risk report tool to alert marine managers when suspicious vessels are nearby (*https://research.csiro.au/iuu/*; CSIRO, 2017, 2018).

Ninety nine per cent of Australia's trade by volume is carried by sea.
(Scott Morrison, 2019)

19.4.3 Oil spills

Oil is regularly released into the global ocean from a range of sources. Natural seepages from the ocean floor account for nearly half the oil entering the ocean (NOAA, 2020a) and transitting vessels are permitted to release some oil for cleaning purposes (Espedal and Johannessen, 2000). However, large oil spills—whether resulting from drilling platforms, illegal discharges from ships, or accidents—can have major impacts on marine and coastal environments. Oil spills primarily comprise complex mixtures of hydrocarbons, from crude oil to refined products, which have varying chemical and physical characteristics. With exposure to air, light, and microbes, these characteristics change over time as the component chemicals variously evaporate, dissolve, settle, disperse, and/or degrade (Hook *et al.*, 2016; see Figure 19.7). The time required for these processes, however, varies significantly (see Figure 19.8).

Figure 19.7 Weathering processes associated with an oil spill

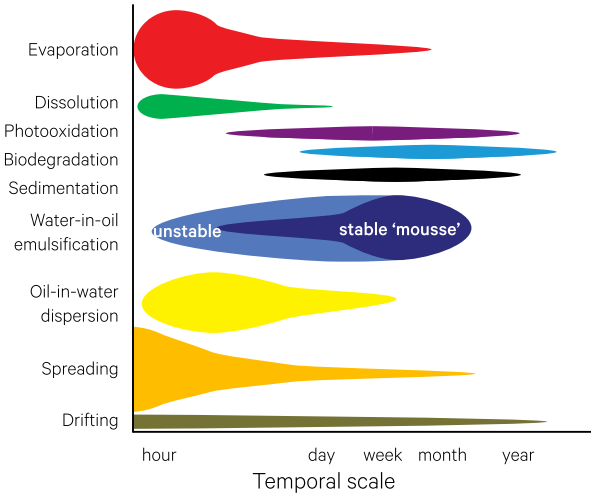


Source: SINTEF (2011) Figure 3.4

Oil spills affect marine life through the direct toxicity of oil, by the smothering effects of the oil on plants and animals, and by coating beaches and rocky shore habitats. The toxicity and physical properties of oil change over time. Chemicals used to disperse oil and increase the rate of breakdown can themselves be toxic to marine life.
(Parliament of Australia, 2018)

Figure 19.8 Duration of oil weathering processes

The relative time scales of different oil weathering processes in the marine environment are compared. The bar thickness indicates relative importance of each process through time, starting from the time of the initial oil spill.



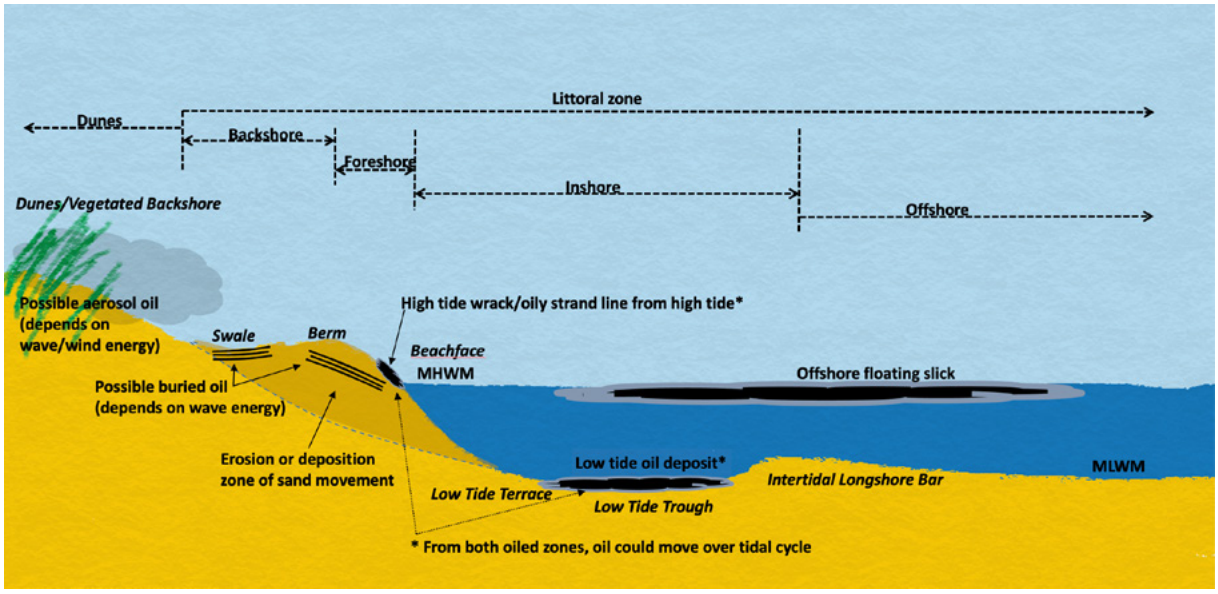
Adapted from: SINTEF (2021) Figure 3.5

Oil spills have differing degrees of toxicity in the marine environment, with refined products generally being considered more toxic (RSC, 2015). Toxicity has been reported to both increase and decrease with time for different organisms in different environments. Oils spills present a particular danger to shorelines, where oil may become concentrated along the high water mark (Hook *et al*., 2016; see Figure 19.9). In terms of marine organisms, oil spills can:

- destroy the insulating ability of furred mammals;
- remove water repellency of bird feathers;
- poison organisms through ingestion;
- reduce the growth in adult fish, including enlarged livers, changes in cardiac and respiration rates, fin erosion, reproduction impairment, and lowered survival of their eggs and larvae (NOAA, 2020b);
- increase photosensitivity; and
- bioaccumulate both in individual organisms and the global food web (RSC, 2015; Hook *et al*., 2016).

As long as there is a global reliance on petroleum products, oil spills will continue to occur.
(Espedal and Johannessen, 2000)

Figure 19.9 Beach profile showing potential oil spill deposits



Source: Paul Irving, AMSA

In particular, the GBR is viewed as a 'high risk' area for oil spills from shipping traffic (Sagar *et al*., 2020). In this context, 'risk' implies both a higher likelihood and more significant consequences. Accordingly, to prevent incidents leading to spills the Australian Marine Safety Authority (AMSA: see Excursus 2.1), the Great Barrier Reef Marine Park Authority (GBRMPA), and the Queensland government have implemented a vessel traffic system, coupled with aerial and satellite observation programs to spot oil on the water. For example, in March 2009, a major oil spill near Cape Moreton coincided with tropical cyclone Hamish and resulted in oil being spread along 80 km of the southeast Queensland coastline (DERM, 2009). Similarly, in April 2010, oil from a merchant vessel that ran aground severely damaged Douglas Shoal and created the longest (3 km) known reef scar in the GBR and a 4 km long oil slick, while multiple small, illegal discharges in July 2015 caused numerous fuel oil slicks and coastal strandings between Townsville and Hinchinbrook Island (AMSA, 2020a).

In Australian waters, AMSA and its state and territory partners under the National Plan for Maritime Environmental Emergencies (AMSA, 2019) are responsible for monitoring—and often responding to—oil spills. AMSA (and its partners through AMSA) operationally relies on a variety of EO data sources to both detect an oil spill event, plan an appropriate response, and assess its overall environmental impact(s) (see Excursus 19.4).

EO datasets can be used to detect oil spills when there is a discernible difference between the reflectance or emission from a 'clean' water surface versus that from water covered by an oil slick. A range of EO sensors can be used for this purpose, although almost all are susceptible to detecting 'false positives'—surface features with the appearance of an oil slick—due to ambient biological, oceanographic, bathymetric, atmospheric, or anthropogenic factors (see Table 19.5). Since each type of sensor detects different EMR wavelengths using different sensing mechanisms, it has different advantages and limitations for this application, all of which can vary with environmental conditions (Table 19.6). Accordingly, integrated systems, which utilise data from multiple EO sensors, have been developed for oil spill response (Hook *et al*., 2016). Spaceborne EO datasets are typically most relevant to offshore oil spills, with aerial surveillance being more appropriate for onshore spills (IOGP, 2016).

Table 19.5 Major EO sensors for oil spill detection

Sensing Mechanism	EO sensor	Operation	Major false positives	Limitations
Passive	UV sensors	Detects sunlight reflected from oil slick, especially thin oil sheens	Wind slicks, sunglints, biogenic matter	Darkness, unclear atmospheric conditions, submerged oil (see Table 19.6)
	Optical sensors	Detects sunlight reflected from oil slick; IR sensors can estimate relative oil thickness	River outflows, algae, sediment, organic matter, shoreline and oceanic fronts, weed and kelp beds	Darkness (especially for visible and NIR wavelengths), unclear atmospheric conditions, submerged oil (see Table 19.6)
	TIR sensors	Detects thermal emissions as differences in surface temperature	Upwellings, water inflows, fronts, man-made heat sources	Unclear atmospheric conditions, submerged oil, low spatial resolution (see Table 19.6)
	Hyperspectral sensor	Identify detailed spectral characteristics of oil slick to determine oil type and thickness	Sunglint, white wave caps, shallow water features	Darkness, unclear atmospheric conditions, submerged oil (see Table 19.6)
Active	Laser fluorosensor	Detects irradiated UV wavelengths from oil slick with high sensitivity; Can also estimate oil slick thickness when combined with water Raman signal	Unknown at present (Fingas and Brown, 2018)	Limited spatial extent, darkness, unclear atmospheric conditions (see Table 19.6)
	SAR	Since oil slicks dampen sea capillary waves, their radar returns are different from those of a 'clean' water surface	Low wind areas sheltered by land, rain cells, organic films, wind fronts, algal blooms, current shear zones, mineral oils, turbulent ship wakes, freshwater plumes	High and low wind speeds, submerged oil (see Table 19.6)

Source: Hook *et al.* (2016) Table 6.2 and IOGP (2016) Table 14

Table 19.6 Environmental limitations on oil spill detection

Environmental conditions	EO sensor wavelengths		
	Optical	TIR	Microwave
Lighting	Sunlight required	Not required	Not required
Cloud/Rain/Fog	Does not penetrate	Does not penetrate	Can penetrate
Sea surface	Imagery impacted by very rough seas	Imagery impacted by very rough seas	Imagery most useful when wind speed 3–12 m/s
Ice	Limited if oil is in or under ice	Limited if oil is in or under ice	Best when ice concentration <30% in open water

Source: IOGP (2016) Table 15

Both optical and SAR imagery are used to detect the locations of oil spills and track the extent of their dispersals (Topouzelis, 2008), including illegal discharges from ships (Brekke and Solberg, 2005), and those originating from offshore oil and gas platforms (Liu *et al.*, 2018). Other EO sensors that are relevant to oil spill response include UV/IR sensors, which can estimate the relative thickness of oil slicks, and laser fluorosensors, which are most selective for separating oil slicks from other features (Fingas and Brown, 2014, 2018), can identify the 'type' of oil involved, and estimate its thickness (Hook *et al.*, 2016).

In optical wavelengths, the reflectance characteristics of an oil spill vary with its chemical composition (Lacava *et al.*, 2017; Wettle *et al.*, 2009). While oil spills cannot be differentiated from seawater using visible wavelengths, sunglint in optical imagery (see Section 8.1.3) may expose smooth oil slicks on the water surface (Sun and Hu, 2016; Hu *et al.*, 2018). Since recent discharges of surface oil are typically warmer than surrounding waters, TIR sensors have also been used to highlight temperature differences (Casciello *et al.*, 2011; Grimaldi *et al.*, 2011; Zhou *et al.*, 2017).

SAR imagery, however, has the advantages of being largely independent of lighting and weather conditions (see Section 9.3). Since a surface oil slick has a dampening effect on sea surface roughness, it appears as an area of low backscattering in SAR imagery (Li *et al.*, 2018; see Volume 1B—Section 8), although the actual appearance depends on the type of oil. High frequency radar (X-band) is more sensitive to small variations in surface geometry than lower frequency bands, but can include more speckle noise (Alpers *et al.*, 2017), and VV-polarised SAR is generally considered most appropriate for marine applications (Li *et al.*, 2018).

Oil spill detection using SAR imagery is complicated by the need to differentiate between oil slicks and false positives, or 'look-alikes', such as natural biofilms, algal slicks, grease, sea ice, low wind speed areas, wind shadows, rain cells, or internal waves (Gens, 2008; Alpers *et al.*, 2017). However, the backscatter and visibility of both oil spills and look-alikes are changed to different extents by wind, such that moderate wind speeds can enhance these differences in their appearance (Solberg *et al.*, 1999; Brekke and Solberg, 2005). In some Australian waters, wind shadows, reef shadows, and upwellings are quite common and can contribute to an increased number of false positives when using SAR-based oil spill detection algorithms. The use of SAR sensors is also limited in very calm or rough seas, or when ice is present (see Table 19.6).

SAR imagery has also been used to detect natural hydrocarbon seepage slicks in Australia's offshore environments, especially where surface oil slicks form (Williams and Lawrence, 2002). Additionally, a range of acoustic datasets (see Section 10) have been used to identify sampling sites to determine natural hydrocarbon seepages (Logan *et al.*, 2008).

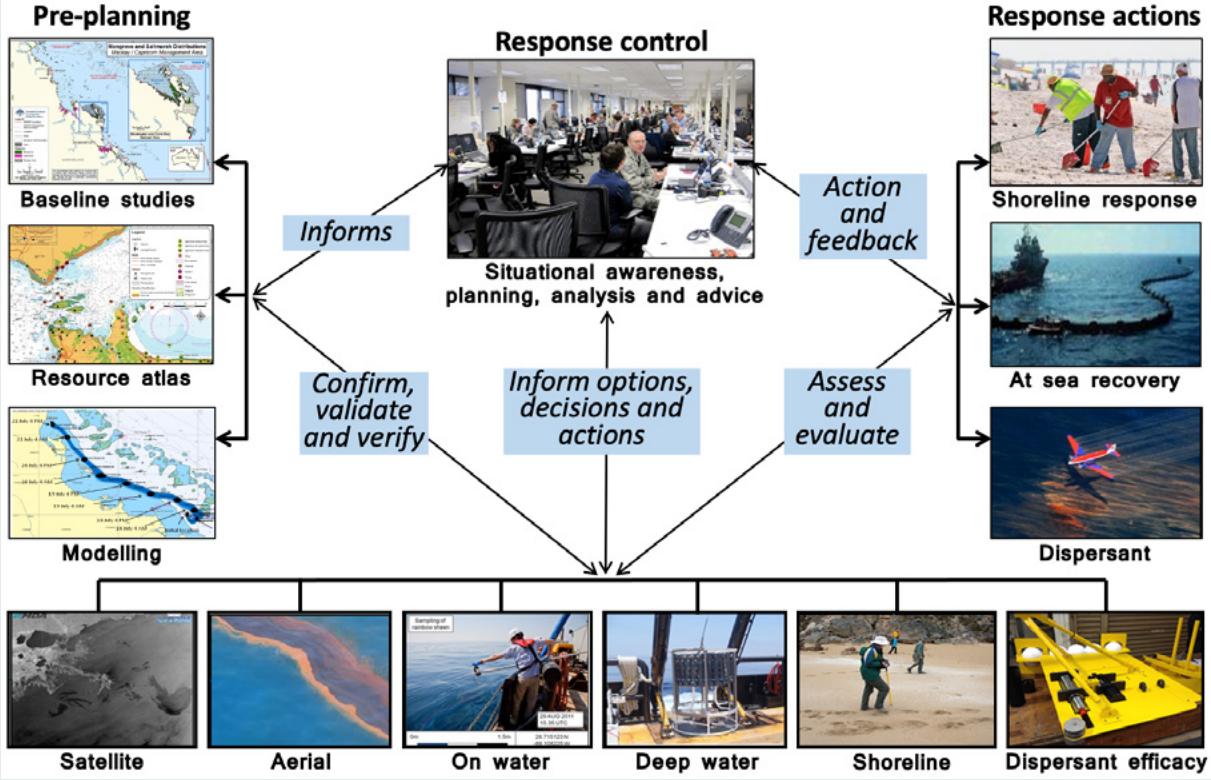
Excursus 19.4—Operational Oil Spill Response

Source: Paul Irving, AMSA
Further Information: Hook *et al.* (2016) Chapter 6

When an oil spill is reported in Australian waters, the Australian Marine and Safety Authority (AMSA: see Excursus 2.1) conducts an initial risk assessment to determine the most appropriate response. Since the goal of any oil spill response is to minimise the ecological and socioeconomic damage, it is essential that the response process offers 'net environmental benefits' (NEB; Davies and Hope, 2015), where NEB is defined as the "gains in value of environmental services or other ecological properties minus the value of adverse environmental effects caused by those actions" (Efroymson *et al.*, 2004). This assessment requires detailed information about the current situation and its likely ramifications (Hook *et al.*, 2016). In the past decade, AMSA and its National Plan partners (see AMSA, 2019) have responded to 41 significant oil spills in Australian waters. Although around double this number of potential oil spills were reported during this time period, many of those reports were not substantiated, or the spills dissipated naturally without warranting intervention.

Figure 19.10 AMSA oil spill response process

This overview of the AMSA response phase monitoring process shows how it can validate existing knowledge, inform situational awareness, and assess and evalutate operational success.



Source: Paul Irving, AMSA

Once it has been determined that a response is appropriate, the response phase needs to be monitored (see Figure 19.10), which requires ongoing detailed information about the current status of the oil spill (Hook *et al.*, 2016). Where available, this information is derived from *in situ* reports, aerial and vessel-based surveillance, oil spill trajectory modelling, and a range of geospatial datasets, including EO. As in any emergency situation, high data quality and rapid processing are needed to ensure that the monitoring information is both current and reliable. With large, frequent coverage and proven data quality, spaceborne EO data has proven to be valuable for locating the extent of the oil slick, mapping its trajectory and ambient conditions, and possibly estimating its thickness. Several operational systems now rely on EO datasets to:

- locate oil slicks that need to be treated with dispersant;
- provide evidence that the dispersant has been applied successfully; and
- dispatch resources to impacted shorelines to remove the stranded oil quickly before it is remobilised by the tide to other sites (Hook *et al.*, 2016).

AMSA have used SAR data for maritime monitoring and marine surveillance since 2013, including detecting oil spills. When looking for spills to initiate a response, or looking for evidence of a spill to initiate a follow-up or prosecution action, AMSA uses a range of remotely sensed evidence, including optical images. Although most incidents have a clear culprit, occasionally a mystery spill occurs, where the culprit needs to be identified. A example of this process is the Pacific Quest oil spill in the Whitsunday Islands in 2002, which used a range of evidence to achieve a conviction. Samples of the spilled oil taken from water were fingerprint-matched to a sample taken from one of six vessels intercepted at their next port of call (Auckland). Satellite location tracking information was used to identify the suspect vessels, and an incidental SPOT image was able to assist by placing the culprit vessel exactly within the footprint of the slick visible to the SPOT sensors (AMSA, 2020b).

19.5 Algal Blooms

An algal or phytoplankton bloom is a temporary biological event involving the rapid growth of microalgae as the natural response to variations in environmental conditions (see Sections 3.3.2.1, 4.6 and 5.3.1.1). As detailed in Sections 8.2.2 and 18.6, algal blooms change the reflectance of surface waters (see Figure 4.11) and this change can be reliably observed using EO (Klemas, 2012; see Figure 19.11).

EO-based methods that have been used to detect phytoplankton blooms in optical imagery include:

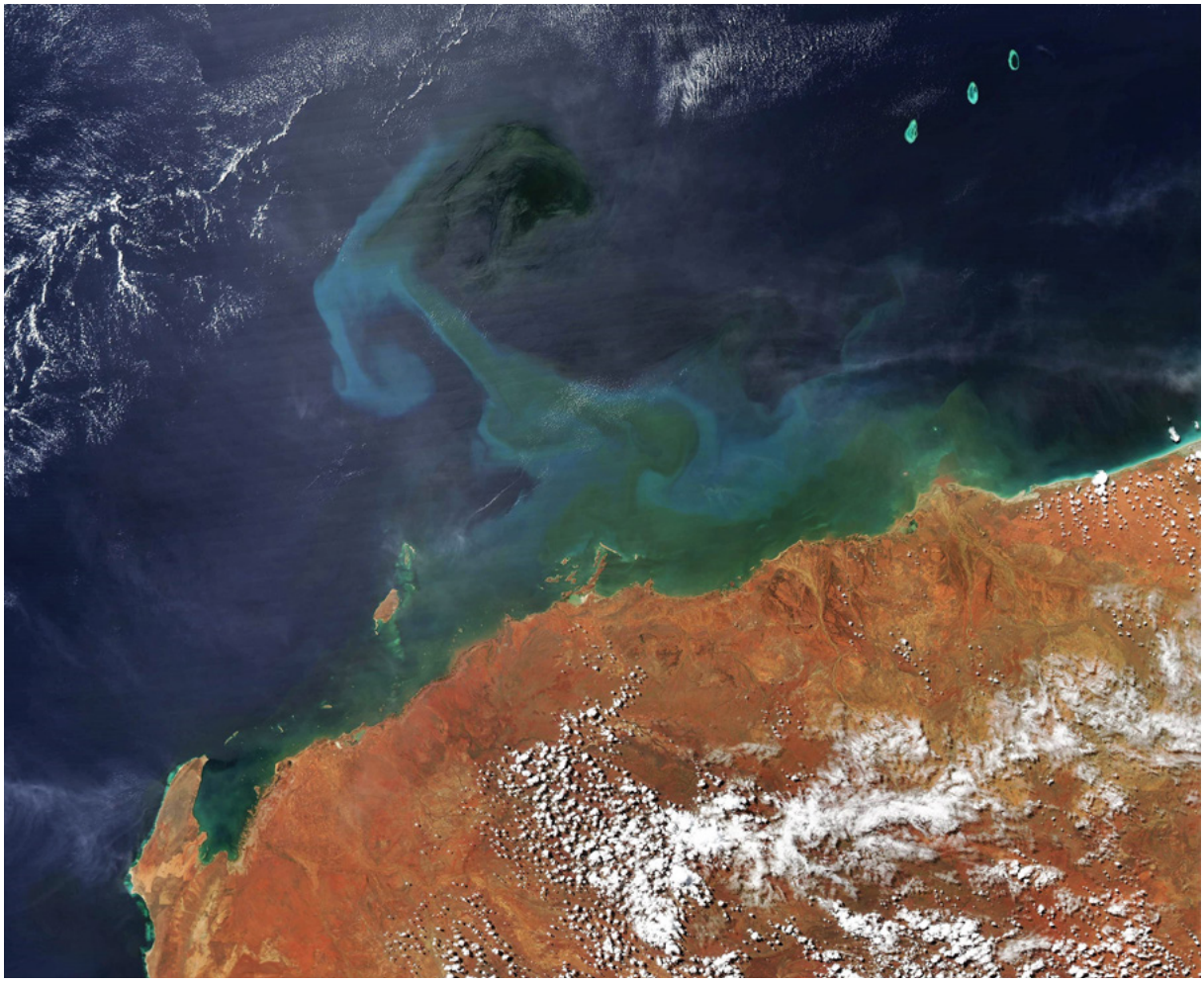
- image classification (see Volume 2E);
- band differences and ratios (see Volume 2C);
- semi-analytical inversion models based on forward bio-optical models (see Section 8.4); and
- neural networks (Blondeau-Patissier *et al.*, 2014).

While band ratios and indices are appropriate for mapping algal blooms in ocean waters, more sophisticated modelling approaches are required in the more complex coastal and inland waters. The availability of hyperspectral datasets is expected to improve current methods (Blondeau-Patissier *et al.*, 2014).

Many inversion algorithms have been developed to map specific taxa, however the more sophisticated spectral inversion algorithms derive better results (Bracher *et al.*, 2017). Monitoring of seasonal, annual, and decadal cycles of phytoplankton growth generally requires the integration of EO datasets and appropriate statistical models (Platt *et al.*, 2009; Song *et al.*, 2010) and/or satellite data climatologies (Park *et al.*, 2010; Miller *et al.*, 2006). An example of monitoring algal blooms using an EO time series dataset is described in Blondeau-Patissier *et al.* (2018).

Figure 19.11 MODIS image of algal bloom

An algal bloom stretched along 750 km of the Pilbara coast, northeast WA, in the wake of Cyclone Veronica. Thls image was acquired by MODIS/Aqua on 29 March 2019.



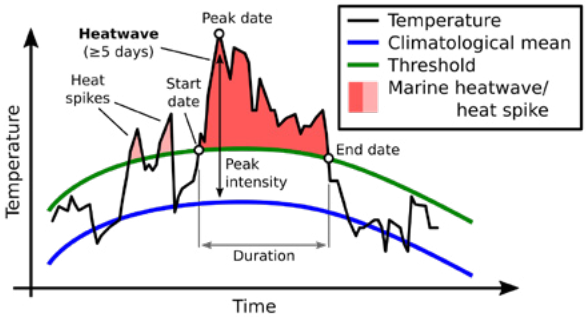
Source: NASA Worldview

19.6 Marine Heatwaves

Just as heatwaves—extended periods of excessively hot weather—happen in the atmosphere, they can occur in the ocean (MHIWG, 2020). Marine heatwaves (MHW) are extreme events, defined as "anomalously warm water events that may last many months and extend over thousands of square kilometres" (Hobday *et al*., 2018). A MHW is defined when the difference between actual water temperature is significantly greater than the expected water temperatures for a given location and season over more than five consecutive days (see Figure 19.12). MHW can occur in any season and have a significant impact on coastal and marine ecosystems, with widespread biological, economic, and political consequences (Mills, 2013; Hobday *et al*., 2016, 2018; Pearce and Feng, 2013; Wernberg *et al*., 2013). In recent years, climatic changes have resulted in a greater frequency of MHW (MHIWG, 2020). One well known consequence of MHW is coral bleaching (Heron *et al*., 2016; McClanahan, 2017; see Excursus 20.3). MHW also impact the distribution of marine species and have resulted in mass mortalities (Sagar *et al*., 2020).

As detailed in Section 14, near real time EO-based estimates of SST are used operationally to monitor the marine environment (see Excursus 14.2), including MHW (Pearce and Feng, 2013; Bond *et al*., 2015; Di Lorenzo and Mantua, 2016). SST time series datasets are being used to analyse the frequency, duration, extent, and intensity of MHW, as well as their spatial and temporal variability, and seasonal character (Sagar *et al*., 2020).

Figure 19.12 Defining marine heatwaves



Source: MHIWG (2021)

19.7 Salinity

Salinity, the dissolved salt content of water, is introduced in Section 5.2.1. Ocean surface salinity varies spatially and temporally, so is indicative of the role of ocean waters in the hydrological cycle (see Section 1.1). With over 85% of global evaporation and over 75% of global precipitation occurring over the ocean, information about changes in ocean surface salinity resulting from these processes, can contribute new information about how Earth's freshwater circulates globally, both within the ocean and between the ocean and atmosphere. Since salinity and temperature determines seawater density (s0ee Figure 5.4 and Section 5.2.1), which drives layering and mixing of ocean waters and the formation of water masses (see Section 17), ocean surface salinity data can also provide valuable information about ocean currents and ocean circulation (NASA, 2017).

Salinity largely determines the distribution of marine and estuarine species, often working in combination with other environmental variables (Smyth and Elliott, 2016). While open oceans are relatively stable and similar in terms of most constituents, including total salinity (with the global ocean only varying between 33‰[23] and 37‰; Srokosz and Banks, 2019), coastal waters are impacted by tides, river flows, evaporation, and anthrogenic factors (Wolanski and Elliott, 2015), which varies their salinity levels in daily, tidal, lunar, and seasonal cycles.

Salinity acts synergistically and antagonistically with other environmental stressors in affecting ecology. Factors such as nutrient availability, temperature, pH, and dissolved oxygen have all been shown potentially to interact to produce a dynamic and changing environment where one factor can exacerbate or negate to some extent the detrimental effects of another. Human activities and anthropogenic effluents can modify local salinity regimes and their effects depend on the assimilative capacity of both the area and the species.
(Smyth and Elliot, 2016)

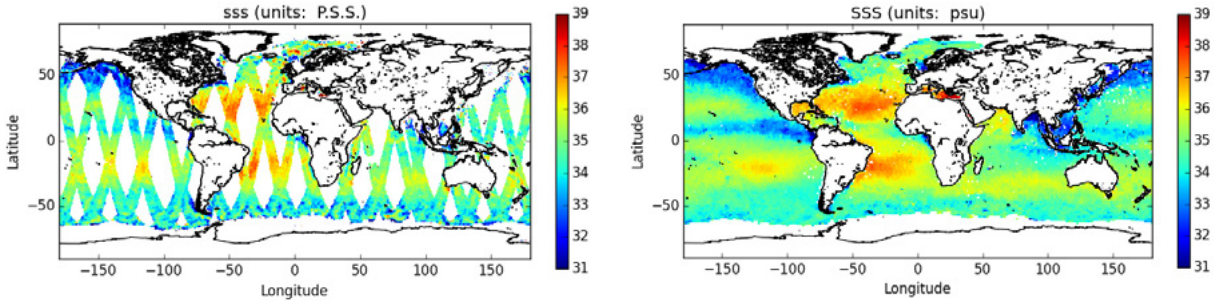
23 ‰: parts per thousand

Figure 19.13 Global salinity image composites

The daily composite SMOS SSS data (0.5° resolution) were obtained from the Ocean Salinity Expertise Center (CECOS) of the CNES-IFREMER Centre Aval de Traitement des Données SMOS (CATDS), at IFREMER, Plouzane (France). The Aquarius data (1° resolution) were furnished through the NASA/CONAE Aquarius/SAC-D Project.

a. Single day sea surface salinity data acquired from SMOS on 15 December 2014.

b. 7 day composite image from Aquarius acquired 10–16 December 2014.



Source: Edward King, CSIRO

As salinity levels of surface waters in oceans change, their dielectric properties at microwave frequencies change slightly (Srokosz and Banks, 2019). On this basis, estimates of sea surface salinity can be derived from carefully calibrated and corrected measurements of 1.4 GHz radiation (L-band) emitted from the ocean surface. These observations are acquired at low spatial resolution (10–100 km) and weekly frequency, but are more difficult in colder waters at high latitudes. Salinity data has been acquired from three satellite missions:

- Soil Moisture and Ocean Salinity (SMOS)—an ESA satellite operating since 2010 (Kerr *et al.*, 2010; Mecklenburg *et al.*, 2016);
- Aquarius—a NASA sensor onboard the Argentine SAC-D spacecraft, which operated from 2011 to mid-2015 (Le Vine *et al.*, 2018); and
- Soil Moisture Active Passive (SMAP)—a NASA mission launched in 2015 to replace Aquarius (Meissner *et al.*, 2019).

These sensors use different techniques to form images but all rely on an accurate measurement of SST (see Section 14) and an estimate of surface wind strength (since surface roughness plays a crucial role in the retrieval algorithm; see Section 16). Products from these missions continue to mature as processing algorithms incorporate advances in instrument understanding, but they are clearly delivering an unprecedented global view of a key ocean variable (see Figure 19.13). Future satellite missions are planned to maintain the continuity of global salinity data.

19.8 Further Information

Inland Water Quality

Dekker and Hestir (2012)

CEOS (2018)

IOCCG: *https://ioccg.org/group/water-quality/*

Water Quality Australia: *https://www.waterquality.gov.au/introduction*

Globolakes (Global Observatory of Lake Responses to Environmental Change)

http://www.globolakes.ac.uk/index.html

Marine Biodiversity Hub

https://www.nespmarine.edu.au/

Marine Heat Wave

http://www.marineheatwaves.org/

NOAA Marine Heatwave Watch: *https://coralreefwatch.noaa.gov/product/marine_heatwave/*

NOAA: *https://research.noaa.gov/article/ArtMID/587/ArticleID/2559/So-what-are-marine-heat-waves*

Maritime Traffic

UNCLAD (2019)

https://www.marinetraffic.com/en/p/company

Australian Marine Water Quality

BOM eReefs Marine Water Quality: *http://www.bom.gov.au/metadata/catalogue/19115/ANZCW0503900427*

IMOS State and Trends of Australia's Ocean Report: 3. Quality: *https://www.imosoceanreport.org.au/time-series/water-quality/*

Department of Environment and Energy (2018). Threat Abatement Plan for the impacts of marine debris on the vertebrate wildlife of Australia's coasts and oceans:

http://www.environment.gov.au/system/files/resources/e3318495-2389-4ffc-b734-164cdd67fe19/files/tap-marine-debris-2018.pdf

Water Quality Guidelines

The Australian and New Zealand Guidelines for Fresh and Marine Water Quality provide authoritative guidance on the management of water quality for natural and semi-natural water resources in Australia and New Zealand. The 2018 revision of the Water Quality Guidelines is presented as an online platform, to improve usability and facilitate updates as new information becomes available:

https://www.waterquality.gov.au/anz-guidelines

GEO AquaWatch

This Group on Earth Observations (GEO) initiative aims to develop and build the global capacity and utility of EO-derived water quality data, products, and information to support water resources management and decision making. In the short term, AquaWatch will develop baseline global water quality monitoring products, and regional and local end-to-end prototype demonstrations:

https://www.geoaquawatch.org

https://earthobservations.org/geoss_wp.php

19.9 References

Agamuthu, P., Mehran, S.B., Norkhairah, A., and Norkhairah, A. (2019). Marine debris: A review of impacts and global initiatives. *Waste Management and Research*, 37(10), 987–1002. *https://doi.org/10.1177/0734242X19845041*

Alpers, W., Holt, B., and Zeng, K. (2017). Oil spill detection by imaging radars: Challenges and pitfalls. *Remote Sensing of Environment*, 201, 133–147.

AFMA (2020). *Satellite Monitoring of fishing boats* webpage, Australian Fisheries Management Authority website: *https://www.afma.gov.au/monitoring-enforcement/satellite-monitoring-fishing-boats*

AIMS (2019). *Water Quality* webpage, Australian Institute of Marine Science website: *https://www.aims.gov.au/water-quality*

AMSA (2019). *National Plan for Maritime Environmental Emergencies*. Australian Maritime Safety Authority. *https://www.amsa.gov.au/marine-environment/national-plan-maritime-environmental-emergencies https://www.amsa.gov.au/sites/default/files/amsa-496-national-plan.pdf*

AMSA (2020a). *Incidents and exercises* webpage, Australian Maritime Safety Authority website: *https://www.amsa.gov.au/marine-environment/incidents-and-exercises*

AMSA (2020b). *Pacific Quest, 25 December 2002* webpage, Australian Maritime Safety Authority website: *https://www.amsa.gov.au/marine-environment/incidents-and-exercises/pacific-quest-25-december-2002*

ATC (2013). *Oil and Gas* webpage, Australian Trade Commission website: *https://www.austrade.gov.au/oil-and-gas/*

Bereta, K., Zissis, D., and Grasso, R. (2020). Automatic Maritime Object Detection Using Satellite Imagery. *IEEE Oceans 2020*. *https://zenodo.org/record/4074827#.X4PMEZMzbUI*

Blondeau-Patissier, D., Gower, J.F., Dekker, A.G., Phinn, S.R., and Brando, V.E. (2014). A review of ocean color remote sensing methods and statistical techniques for the detection, mapping and analysis of phytoplankton blooms in coastal and open oceans. *Progress in Oceanography*, 123, 123–144.

Blondeau-Patissier, D., Brando, V.E., Lønborg, C., Leahy, S.M., and Dekker, A.G. (2018). Phenology of Trichodesmium spp. Blooms in the Great Barrier Reef lagoon, Australia, from the ESA-MERIS 10-year mission. *PLOS ONE*, 13, e0208010. *https://doi.org/10.1371/journal.pone.0208010*

Bond, N.A., Cronin, M.F., Freeland, H., and Mantua, N. (2015). Causes and impacts of the 2014 warm anomaly in the NE Pacific. *Geophysical Research Letters*, 42, 3414–3420.

Bracher, A., Bouman, H.A., Brewin, R.J.W., Bricaud, A., Brotas, V., Ciotti, A.M., Clementson, L., Devred, E., Di Cicco, A., Dutkiewicz, S., Hardman-Mountford, N.J., Hickman, A.E., Hieronymi, M., Hirata, T., Losa, S.N., Mouw, C.B., Organelli, E., Raitsos, D.E., Uitz, J., Vogt, M., and Wolanin, A. (2017). Obtaining Phytoplankton Diversity from Ocean Color: A Scientific Roadmap for Future Development. *Frontiers in Marine Science*, 4. *https://doi.org/10.3389/fmars.2017.00055*

Brando, V.E., Anstee, J.M., Wettle, M., Dekker, A.G., Phinn, S.R., and Roelfsema, C. (2009). A physics based retrieval and quality assessment of bathymetry from suboptimal hyperspectral data. *Remote Sensing of Environment*, 113, 755–770. doi:10.1016/j.rse.2008.12.003.

Brando, V.E., Dekker, A.G., Park, Y.J., and Schroeder, T. (2012). Adaptive semianalytical inversion of ocean color radiometry in optically complex waters. *Applied Optics*, 51, 2808–2833.

Brekke, C., and Solberg, A.H. (2005). Oil spill detection by satellite remote sensing. *Remote Sensing of Environment*, 95, 1–13.

Browne, M.A. (2015). Sources and pathways of microplastic to habitats. In *Marine Anthropogenic Litter* (Eds: Bergmann, M., Gutow, L., and Klages, M.). Springer International Publishing, Switzerland. pp 229–244.

Casciello, D., Lacava, T., Pergola, N., and Tramutoli, V. (2011). Robust Satellite Techniques for oil spill detection and monitoring using AVHRR thermal infrared bands. *International Journal of Remote Sensing*, 32, 4107–4129.

CEOS (2018). *Feasibility Study for an Aquatic Ecosystem Earth Observing System*. (Eds: Dekker, A.G., and Pinnel, N.) CSIRO, Canberra.

Chislock, M.F., Doster, E., Zitomer, R.A., and Wilson, A.E. (2013). Eutrophication: causes, consequences, and controls in aquatic ecosystems. *Nature Education Knowledge*, 4(4), 10.

Crisp, D.J. (2004). *The state-of-the-art in ship detection in synthetic aperture radar imagery*. Defence Science And Technology Organisation Salisbury (Australia) Info Sciences Lab.

Critchell, K., Grech, A., Schlaefer, J., Andutta, F.P., Lambrechts, J., Wolanski, E., and Hamann, M. (2015). Modelling the fate of marine debris along a complex shoreline: lessons from the Great Barrier Reef. *Estuarine, Coastal and Shelf Science*, 167, 414–426.

CSIRO (2008). *Water availability in the Murray–Darling Basin*. A report to the Australian Government from the CSIRO Murray–Darling Basin Sustainable Yields Project, CSIRO, Australia.

CSIRO (2017). *Protecting the world's fisheries. Identifying offending operators and their vessels*. *https://research.csiro.au/iuu/publications/*

CSIRO (2018). *Protecting the world's fisheries. Big data, analytics, and technology to identify offending operators and their vessels*. *https://research.csiro.au/iuu/publications/*.

Davies, A.J., and Hope, M.J. (2015). Bayesian inference-based environmental decision support systems for oil spill response strategy selection. *Marine Pollution Bulletin*, 96, 87–102. doi:10.1016/j.marpolbul.2015.05.041

DAWE (2020). *Sea dumping* webpage, Department of Agriculture, Water and the Environment website: *https://www.environment.gov.au/marine/marine-pollution/sea-dumping*

Dekker, A.G., and Hestir, E.L. (2012). *Evaluating the Feasibility of Systematic Inland Water Quality Monitoring with Satellite Remote Sensing*. Water for a Healthy Country National Research Flagship, CSIRO.

Dekker, AG.., Phinn, SR.., Anstee, J., Bissett, P., Brando, V.E., Casey, B., Fearns, P., Hedley, J., Klonowski, W., Lee, Z.P., Lynch, M., Lyons, M., Mobley, C., and Roelfsema, C. (2011). Intercomparison of shallow water bathymetry, hydrooptics, and benthos mapping techniques in Australian and Caribbean coastal environments. *Limnology and Oceanography Methods*, 9, 396–425.

DERM (2009). *Effect of the March 2009 oil spill on Moreton Bay Ramsar site*. Queensland Department of Environment and Resource Management, Brisbane. *http://www.environment.gov.au/water/topics/wetlands/database/pubs/41-art-3-2-impact-of-march-2009-oil-spill.pdf*

Di Lorenzo, E., and Mantua, N. (2016). Multi-year persistence of the 2014/15 North Pacific marine heatwave. *Nature Climate Change*, 6, 1042–1047. *https://doi.org/10.1038/nclimate3082*

Durand, D., Pozdnyakov, D.V., Sandven, S., Cauneau, F., Wald, L., Jacob, A., Kloster, K., and Miles, M. (1999). *Characterisation of inland and coastal waters with space sensors: final report*. Technical report No. 164, pp. 1–180. Nansen Environmental and Remote Sensing Centre, Bergen.

Efroymson, R.A., Nicolette, J.P., and Suter, G.W. (2004). A framework for Net Environmental Benefit Analysis for remediation or restoration of contaminated sites. *Environmental Management*, 34, 315–331. doi:10.1007/s00267-004-0089-7

Elvidge, C.D., Zhizhin, M., Baugh, K., and Hsu, F.-C. (2015). Automatic boat identification system for VIIRS low light imaging data. *Remote Sensing*, 7, 3020-3036.

Eriksen, M., Lebreton, L.C., Carson, H.S., Thiel, M., Moore, C.J., Borerro, J.C., Galgani, F., Ryan, P.G., and Reisser, J. (2014). Plastic pollution in the world's oceans: more than 5 trillion plastic pieces weighing over 250,000 tons. *PloS ONE*, 9(12), e111913. doi:10.1371/journal.pone.0111913

Espedal, H.A., and Johannessen, O.M. (2000). Cover: Detection of oil spills near offshore installations using synthetic aperture radar (SAR). *International Journal of Remote Sensing*, 21(11), 2141–2144. *http://dx.doi.org/10.1080/014311600500294 68*

Fingas, M., and Brown, C. (2014). Review of oil spill remote sensing. *Marine Pollution Bulletin*, 83, 9–23. doi:10.1016/j.marpolbul.2014.03.059

Fingas, M., and Brown, C.E. (2018). A Review of Oil Spill Remote Sensing. *Sensors*, 18(1), 91. doi:10.3390/s18010091

Galloway, T.S., and Lewis, C.N. (2016). Marine microplastics spell big problems for future generations. *Proceedings of the National Academy of Sciences of the United States of America*, 113(9), 2331–2333.

Garaba, S.P., and Dierssen, H.M. (2018). An airborne remote sensing case study of synthetic hydrocarbon detection using short wave infrared absorption features identified from marine-harvested macro- and microplastics. *Remote Sensing of Environment*, 205, 224–235.

Garaba, S.P., Aitken, J., Slat, B., Dierssen, H.M., Lebreton, L., Zielinski, O., and Reisser, J. (2018). Sensing Ocean Plastics with an Airborne Hyperspectral Shortwave Infrared Imager. *Environmental Science and Technology*, 52, 11699–11707.

Gens, R. (2008). Oceanographic applications of SAR remote sensing. *GIScience and Remote Sensing*, 45, 275–305.

Gilbert, T, Baxter, T., and Spence, A. (2003). The Australian Oil Spill Response Atlas Project. *Proceedings of International Oil Spill Conference, April 2003*. doi:10.7901/2169-3358-2003-1-851

Goddijn-Murphy, L., Peters, S., van Sebille, E., James, N.A., and Gibb, S. (2018). Concept for a hyperspectral remote sensing algorithm for floating marine macro plastics. *Marine Pollution Bulletin*, 126, 255–262. *https://doi.org/10.1016/j.marpolbul.2017.11.011*

Grimaldi, C., Casciello, D., Coviello, I., Lacava, T., Pergola, N., and Tramutoli, V. (2011). An improved RST approach for timely alert and Near Real Time monitoring of oil spill disasters by using AVHRR data. *Natural Hazards and Earth System Sciences*, 11, 1281–1291.

Heron, S.F., Jmaynard, J.A., Van Hooidonk, R., and Eakin, C.M. (2016). Warming trends and bleaching stress of the world's coral reefs 1985–2012. *Scientific reports*, 6, 38402.

Hobday, A.J., Alexander, L.V., Perkins, S.E., Smale, D.A., Straub, S.C., Oliver, E.C.J., Benthuysen, J., Burrows, M.T., Donat, M.G., Feng, M., Holbrook, N.J., Moore, P.J., Scannell, H.A., Gupta, A.S., and Wernberg, T. (2016). A hierarchical approach to defining marine heatwaves. *Progress in Oceanography*, 141, 227–238. *https://doi.org/10.1016/j.pocean.2015.12.014*

Hobday, A.J., Oliver, E.C.J., Sen Gupta, A., Benthuysen, J., Burrows, M.T., Donat, M.G., Holbrook, N.J., Moore, P.J., Thomsen, M.S., Wernberg, T., and Smale, D.A. (2018). Categorizing and naming marine heatwaves. *Oceanography*, 31, 162–173. *https://doi.org/10.5670/oceanog.2018.205*

Hook, S., Batley, G., Holloway, M., Irving, P., and Ross, A. (2016). *Oil Spill Monitoring Handbook*. CSIRO, Clayton South. *https://publications.csiro.au/rpr/download?pid=csiro:EP158596&dsid=DS2*

Hu, C., Feng, L., Holmes, J., Swayze, G. A., Leifer, I., Melton, C., Garcia, O., Macdonald, I., Hess, M., Muller-Karger, F., Graettinger, G., and Green, R. (2018). Remote sensing estimation of surface oil volume during the 2010 Deepwater Horizon oil blowout in the Gulf of Mexico: Scaling up AVIRIS observations with MODIS measurements. *Journal of Applied Remote Sensing*, 12(2), 26008.

IMO (2020). *Convention on the Prevention of Marine Pollution by Dumping of Wastes and Other Matter* webpage, International Maritime Organisation website: *http://www.imo.org/en/OurWork/Environment/LCLP/Pages/default.aspx*

IOCCG (2018). *International Ocean Colour Coordinating Group* website: *https://ioccg.org/*

IOGP (2016). *Satellite remote sensing of oil spills at sea*. IOGP Report 549. International Association of Oil and Gas Producers, London. *https://www.iogp.org/bookstore/product/satellite-remote-sensing-of-oil-spills-at-sea/*

IUCN (2020). *Marine plastics* webpage, Internation Union for Conservation of Nature website: *https://www.iucn.org/resources/issues-briefs/marine-plastics*

Jambeck, J. R., Geyer, R., Wilcox, C., Siegler, T.R., Perryman, M., Andrady, A., Narayan, R., and Law, K.L. (2015). Plastic waste inputs from land into the ocean. *Science*, 347, 768–771.

Joehnk, K.D., Anstee, J., Ford, P., and Robson, B. (2018). *Development of bloom remote sensing capability and cyanobacteria forecasting model for Western Treatment Plant's largest treatment lagoon systems*. Report prepared for Melbourne Water Corporation by CSIRO Land and Water, Australia.

Kanjir, U., Greidanus, H., and Ostir, K. (2018). Vessel detection and classification from spaceborne optical images: A literature survey. *Remote Sensing of Environment*, 207, 1–26.

Kerr, Y., Waldteufel, P., and Wigneron, J.P., Delwart, S., Cabot, F., Boutin, J., Escorihuela, M.-J., Font, J., Reul, N., Gruhier, C., Enach Juglea, S., Drinkwater, M.R., Hahne, A., Martin-Neira, M., Mecklenberg, S. (2010). The SMOS mission: new tool for monitoring key elements of the global water cycle. *Proceedings of the IEEE*, 98, 666–687.

Klemas, V. (2012). Remote Sensing of Algal Blooms: An Overview with Case Studies. *Journal of Coastal Research*, 28, 34–43.

Lacava, T., Ciancia, E., Coviello, I., Di Polito, C.,. Grimaldi, C.S., Pergola, N., Satriano, V., Temimi, M., Zhao, J., and Tramutoli, V. (2017). A MODIS-based Robust Satellite Technique (RST) for timely detection of oil spilled areas. *Remote Sensing*, 9, 128.

Le Vine, D.M., Dinnat, E.P., Meissner, T., Wentz, F.J., Kao, H.-Y., Lagerloef, G., and Lee, T. (2018). Status of Aquarius and Salinity Continuity. *Remote Sensing*, 10, 1585. doi:10.3390/rs10101585

Li, X., Nunziata, F., and Garcia, O. (2018). Oil Spill Detection from Single- and Multipolarization SAR Imagery. *Comprehensive Remote Sensing*, 8, 231–248. *https://doi.org/10.1016/B978-0-12-409548-9.10407-5*

Lindell, T., Pierson, D., Premazzi, G., and Ziliolli, E. (Eds) (1999). *Manual for monitoring European lakes using remote sensing techniques*. Office for official publications of European Communities, Luxembourg. 161pp.

Liu, Y., Hu, C., Sun, C., Zhan, W., Sun, S., Xu, B., and Dong, Y. (2018). Assessment of offshore oil/gas platform status in the northern Gulf of Mexico using multi-source satellite time-series images. *Remote Sensing of Environment*, 208, 63–81.

Logan, G., Jones, A., Ryan, G., Wettle, M., Thankappan, M., Grosjean, E., Rollet, N., and Kennard, J. (2008). *Review of Australian Offshore Natural Hydrocarbon Seepage Studies*. Geoscience Australia Record: 2008/17.

McClanahan, T. (2017). Changes in coral sensitivity to thermal anomalies. *Marine ecology progress series*, 570, 71–85.

Mace, T.H. (2012). At-sea detection of marine debris: Overview of technologies, processes, issues, and options. *Marine Pollution Bulletin*, 65, 23–27.

Malthus, T.J., Botha, E., and Anstee, J. (2016). *Early warning system for harmful algal blooms. Report on Workpackage 2—Rapid Bloom Identification: Satellite sensing*. CSIRO Land and Water, Australia.

Matthews, M.W. (2011). A current review of empirical procedures of remote sensing in inland and near-coastal transitional waters. *International Journal of Remote Sensing*, 32(21), 6855–6899. doi:10.1080/01431161.2010.512947

Maximenko, N., Corradi, P., Law, K.L., van Sebille, E., Garaba, S.P., Lampitt, R.S., Galgani, F., Martinez-Vicente, V., Goddijn-Murphy, L., Veiga, J.M., Thompson, R.C., Maes, C., Moller, D., Löscher, C.R., Addamo, A.M., Lamson, M., Centurioni, L.R., Posth, N., Lumpkin, R., Vinci, M., Martins, A.M., Pieper, C.D., Isobe, A., Hanke, G., Edwards, M., Chubarenko, I.P., Rodriguez, E., Aliani, S., Arias, M., Asner, G.P., Brosich, A., Carlton, J.T., Chao, Y., Cook, A.-M., Cundy, A., Galloway, T.S., Giorgetti, A., Goni, G.J., Guichoux, Y., Hardesty, B.D., Holdsworth, N., Lebreton, L., Leslie, H.A., MacadamSomer, I., Mace, T., Manuel, M., Marsh, R., Martinez, E., Mayor, D., Le Moigne, M., Jack, M.E.M., Mowlem, M.C., Obbard, R.W., Pabortsava, K., Robberson, B., Rotaru, A.-E., Spedicato, M.T., Thiel, M., Turra, A., and Wilcox, C., (2019). Toward the Integrated Marine Debris Observing System. *Frontiers in Marine Science*, 6, 447. *https://doi.org/10.3389/fmars.2019.00447*

Mecklenburg, S., Drusch, M., and Kaleschke, L., Rodriguez-Fernandez, N., Reul, N., Kerr, Y., Font, J., Martin-Neira, M., Oliva, R., Daganzo-Eusebio, E., Grant, J.P., Sabia, R., Macelloni, G., Rautiainen, K., Fauster, J., de Rosnay, P., Munoz-Sabater, J., Verhoest, J., Levens, H., Delwart, S., Crapolicchio, R., de la Fuent, A., and Kornberg, M. (2016). ESA's soil moisture and ocean salinity mission: from science to operational applications. *Remote Sensing of Environment*, 180, 3–18.

Meissner, T., Wentz, F.J., Manaster, A., and Lindsley, R. (2019). *Remote Sensing Systems SMAP Ocean Surface Salinities [Level 2C, Level 3 Running 8-day, Level 3 Monthly], Version 4.0 validated release*. Remote Sensing Systems, Santa Rosa, CA, USA. *www.remss.com/missions/smap. doi:10.5067/SMP40-2SOCS,10.5067/SMP40-3SPCS, 10.5067/SMP40-3SMCS*

MHIWG (2020). *Marine Heatwaves Explained* webpage, Marine Heatwave International Working Group website: *http://www.marineheatwaves.org/all-about-mhws.html*

Miller, P.I., Shutler, J.D., Moore, G.F., and Groom, S.B. (2006). SeaWiFS discrimination of harmful algal bloom evolution. *International Journal of Remote Sensing*, 27, 2287–2301.

Mills, K.E., Apershing, A.J., Brown, C.J., Chen, Y., Chiang, F.-S., Holland, D.S., Lehuta, S., Nye, J.A., Sun, J.C., Thomas, A.C., and Wahle, R.A. (2013). Fisheries Management in a Changing Climate—Lessons from the 2012 Ocean Heat Wave in the Northwest Atlantic. *Oceanography*, 26, 191–195.

Mobley, C., and Sundman, L.K., (2000). *Hydrolight 4.1 Technical Documentation*, 4.1 ed. Sequoia Scientific Inc., Redmond.

Morrison, S. (2019). *National Statement to the United Nations General Assembly*, 25 September 2019, New York. *https://www.pm.gov.au/media/national-statement-united-nations-general-assembly*

NASA (2017). *Aquarius Mission Overview* webpage: *https://www.nasa.gov/mission_pages/aquarius/overview/index.html*

NOAA (2020a). *What is an oil seep?* National Ocean Service, National Oceanic and Atmospheric Administration website: *https://oceanservice.noaa.gov/facts/oilseep.html*

NOAA (2020b). *How does oil impact marine life?* National Ocean Office, National Oceanic and Atmospheric Administration website: *https://oceanservice.noaa.gov/facts/oilimpacts.html*

Odermatt, D., Gitelson, A., Brando, V. E., and Schaepman, M. (2012). Review of constituent retrieval in optically deep and complex waters from satellite imagery. *Remote Sensing of Environment*, 118, 116–126. doi:/10.1016/j.rse.2011.11.013

Parliament of Australia (2018). *Marine Oil Pollution* webpage: *https://www.aph.gov.au/About_Parliament/Parliamentary_Departments/Parliamentary_Library/pubs/BriefingBook43p/marineoilpollution*

Park, Y.J., Ruddick, K., and Lacroix, G. (2010). Detection of algal blooms in European waters based on satellite chlorophyll data from MERIS and MODIS. *International Journal of Remote Sensing*, 31, 6567–6583.

Pearce, A.F., and Feng, M. (2013). The rise and fall of the "marine heat wave" off Western Australia during the summer of 2010/2011. *Journal of Marine Systems*, 111, 139–156.

Platt, T., White, G.N., Zhai, L., Sathyendranath, S., and Roy, S. (2009). The phenology of phytoplankton blooms: ecosystem indicators from remote sensing. *Ecological Modelling*, 220, 3057–3069.

Reisser, J., Shaw, J., Wilcox, C., Hardesty, B.D., Proietti, M., Thums, M., and Pattiaratchi, C. (2013). Marine Plastic Pollution in Waters around Australia: Characteristics, Concentrations, and Pathways. *PloS ONE*, 8(11), e80466. *https://doi.org/10.1371/journal.pone.0080466*

Rochman, C.M., Browne, M.A. Underwood, A., Van Franeker, J.A., Thompson, R.C., and Amaral-Zettler, L.A. (2016). The ecological impacts of marine debris: unraveling the demonstrated evidence from what is perceived. *Ecology*, 97, 302–312.

RSC (2015). *The Behaviour and Environmental Impacts of Crude Oil Released into Aqueous Environments*. Royal Society of Canada, Ottawa, Ontario, Canada. *https://rsc-src.ca/en/behaviour-and-environmental-impacts-crude-oil-released-into-aqueous-environments*

Sagar, S., Falkner, I., Dekker, A., Huang, Z., Blondeau-Patissier, D., Phillips, C., and Przeslawski, R. (2020). *Earth Observation for monitoring of Australian Marine Parks and other off-shore Marine Protected Areas*. Report to the National Environmental Science Program, Marine Biodiversity Hub. Geoscience Australia.

Simis, S.G.H., Ruiz-Verdú, A., Domínguez-Gómez, J.A., Peña-Martinez, R., Peters, S.W.M., and Gons, H.J. (2007). Influence of phytoplankton pigment composition on remote sensing of cyanobacterial biomass. *Remote Sensing of Environment*, 106(4), 414–427.

SINTEF (2011). *Weathering Properties of Bream Crude Oil Related to Oil Spill Response*. SINTEF, Trondheim, Norway.

Smyth, K., and Elliot, M. (2016). Effects of changing salinity on the ecology of the marine environment. In *Stressors in the Marine Environment* (Eds: Solan, M. and Whitely, N.M.). Oxford University Press. doi:10.1093/acprof:oso/9780198718826.003.0009

SOE (2011). *State of Environment Report 2011*. *http://155.187.2.69/soe/2011/report/inland-water/index.html*

SOE (2016a). *Coastal waters* webpage, State of Environment Report 2016: *https://soe.environment.gov.au/theme/coasts/topic/2016/coastal-waters*

SOE (2016b). *Marine oil and gas exploration and production* webpage, State of Environment Report 2016: *https://soe.environment.gov.au/theme/marine-environment/topic/2016/marine-oil-and-gas-exploration-and-production*

Solberg, A.H.S., Storvik, G., Solberg, R., and Volden, E. (1999). Automatic detection of oil spills in ERS SAR images. *IEEE Transactions on Geoscience and Remote Sensing*, 37, 1916–1924.

Song, H., Ji, R., Stock, C., and Wang, Z. (2010). Phenology of phytoplankton blooms in the Nova Scotian shelf-Gulf of Maine region: remote sensing and modeling analysis. *Journal of Plankton Research*, 32, 1485–1499.

Srokosz, M., and Banks, C. (2019). Salinity from space. *Weather*, 74(1), 3–8. doi:10.1002/wea.3161

Straka, W.C., Seaman, C.J., Baugh, K., Cole, K., Stevens, E., and Miller, S.D. (2015). Utilization of the Suomi national polar-orbiting partnership (NPP) visible infrared imaging radiometer suite (VIIRS) day/night band for arctic ship tracking and fisheries management. *Remote Sensing*, 7, 971–989.

Sun, S., and Hu, C. (2016). Sun glint requirement for the remote detection of surface oil films. *Geophysical Research Letters*, 43, 309–316.

Topouzelis, K.N. (2008). Oil Spill Detection by SAR Images: Dark Formation Detection, Feature Extraction and Classification Algorithms. *Sensors*, 8, 6642–6659.

UNCLAD (2019). *Review of Marine Transport 2019*. United Nations Conference on Trade and Development, New York. ISBN 978-92-1-112958-8 *https://unctad.org/system/files/official-document/rmt2019_en.pdf*

UNEP (2020). *Marine Litter* webpage, United Nations Environment Programme website: *https://www.unep.org/explore-topics/oceans-seas/what-we-do/working-regional-seas/marine-litter*

van Sebille, E., England, M.H., and Froyland, G. (2012). Origin, dynamics and evolution of ocean garbage patches from observed surface drifters. *Environmental Research Letters*, 7, 044040.

van Sebille, E., Wilcox, C., Lebreton, L., Maximenko, N., Hardesty, B.D., Van Franeker, J.A., Eriksen, M., Siegel, D., Galgani, F.,and Law, K.L. (2015). A global inventory of small floating plastic debris. *Environmental Research Letters*, 10, 124006.

Wernberg, T., Smale, D.A., Tuya, F., Thomsen, M.S., Langlois, T.J., de Bettignies, T., Bennett, S., and Rousseaux, C.S., (2013). An extreme climatic event alters marine ecosystem structure in a global biodiversity hotspot. *Nature Climate Change*, 3, 78–82.

Wettle, M., Daniel, P.J., Logan, G.A., and Thankappan, M. (2009). Assessing the effect of hydrocarbon oil type and thickness on a remote sensing signal: A sensitivity study based on the optical properties of two different oil types and the HYMAP and Quickbird sensors. *Remote Sensing of Environment*, 113, 2000–2010.

Williams, A., and Lawrence, G. (2002). The role of satellite seep detection in exploring the South Atlantic's ultradeep water, in Surface exploration case histories: Applications of geochemistry, magnetics, and remote sensing. In *AAPG Studies in Geology No. 48 and SEG Geophysical References Series No. 11*, (Eds: Schumacher, D. and LeSchack, L.A.), pp 327–344.

Wolanksi, E., and Elliott, M. (2015). *Estuarine Ecohydrology: An Introduction*, 2nd edn. Elsevier Science, Amsterdam.

Wood Mackenzie (2020). *Australia Oil and Gas Industry Outlook Report*. *https://appea.com.au/wp-content/uploads/2020/06/Australia-Oil-and-Gas-Industry-Outlook-Report.pdf*

Zhou, Y., Jiang, L., Lu, Y.C., Zhan, W.F., Mao, Z.H., Qian, W.X., and Liu, Y.X. (2017). Thermal Infrared Contrast Between Different Types of Oil Slicks on Top of Water Bodies. *IEEE Geoscience and Remote Sensing Letters*, 14, 1042–1045.



20 Ecology

Janet Anstee, Chris Roelfsema, Eva Kovacs, and Stuart Phinn

Ecology is the study of the relationships between living organisms, including humans, and their physical environment; it seeks to understand the vital connections between plants and animals and the world around them. (The Ecological Society of America)

Ecology comprises a range of studies that observe:

- the distribution and abundance of organisms;
- the interactions between organisms; and
- the relationship between individual organisms and their abiotic environment

Aspects of the ecology of aquatic systems are introduced previously in Section 3. As well as marine activities, surface water ecosystems are directly impacted by changes in terrestrial activities and atmospheric variations, including climatic conditions. Given the extent of surface waters on Earth, maintaining their ecological health and balance is paramount for the health of this planet. One measure of this in any environment is its biodiversity (see Excursus 20.1 and Volume 3A—Section 18).

Microscopic phytoplankton organisms are the primary producers in aquatic environments, providing and regulating marine ecosystem services (Tweddle *et al.*, 2018). These organisms generate around half the organic matter on our planet and around half of its atmospheric oxygen (see Section 3.3.2.1), and also function as a CO_2 sink (see Section 1.5). Phytoplankton is the root of the marine food web (see Sections 3 and 5.3), and used as an indicator of marine productivity (IOCCG, 2014). Productivity can also be inferred from geomorphological features (see Section 6.2), with some seafloor features, such as seamounts and submarine canyons which attract pelagic predators for feeding or breeding, being consistent indicators of biodiversity and biomass (Dower *et al.*, 1992; Pollard *et al.*, 2009; Lemos *et al.*, 2018). Other marine features, such as fronts, currents, and upwellings (see Section 17), are more variable in terms of their association with marine biology (Hyrenback *et al.*, 2000).

Phytoplankton community composition, determined by biogeochemical functional groups, has changed over the past century (Dutkiewicz *et al.*, 2019) and phenological studies of phytoplankton taxa indicate that climate variations are impacting a wide range of marine pelagic communities (Edwards and Richardson, 2004). Since deep sea ecosystems depend on production exported from the surface, they are particularly sensitive to environmental change and anthropogenic disturbance, especially the majority of ecosystems that comprise soft sediments (Ashford *et al.*, 2018). Long term phytoplankton monitoring programs (such as Ajani *et al.*, 2016) complement EO time series in establishing trends in phytoplankton diversity and biomass (McClain, 2009), although a longer time series is required to confirm the relationship between phytoplankton trends and climate variations (Henson *et al.*, 2017).

Background image: Suomi-NPP/VIIRS composite acquired on 18 November 2018 showing algal blooms around Tasmania. Source: Ocean Colour Web. Retrieved from *https://oceancolor.gsfc.nasa.gov/gallery/609/?_ga=2.25122042.1316022944.1614576103-2035282742.1614576103*

Recommended Chapter Citation: Anstee, J.M., Roelfsema, C.M., Kovacs, E., and Phinn, S.R. (2021). Ecology. Ch 20 in *Earth Observation: Data, Processing and Applications. Volume 3B—Surface Waters.* CRCSI, Melbourne. pp. 395–436. ISBN 978-0-6482278-5-4

The Millenium Ecosystem Assessment (MEA) was introduced in Volume 3A—Excursus 18.1. The findings of this assessent for coastal and marine ecosystems are summarised in UNEP (2006). Climatic variations, ocean acidification, and commercial pressures are all actively changing ocean habitats, even in the remote Southern Ocean (Constable *et al.*, 2017; Boyd *et al.*, 2019). However, given that the third of the global population living in coastal areas occupy only 4% of the world's land area (UNEP, 2006), the impact of human activities on coastal waters, and their associated intertidal and benthic ecosystems, is paramount. While they are highly productive, their ecosystems are also the most vulnerable to the anthropogenic impacts of:

- degradation—habitat modification and loss leading to biodiversity reduction, and pollution and sedimentation from agricultural, industrial, and urban activities; and
- overexploitation—resulting from unsustainable usage of both biotic and abiotic resources.

Not surprisingly, the consequences of these activities are most severe for island communities. In the cycle of life, degradation and pollution of ecosystems inevitably impact human health and wellbeing, and ultimately become societal problems for both current and future generations all around the globe (see Section 21.4).

This section initially considers surface water ecology in Australia (see Section 20.1) and appropriate EO sensors for water ecology (see Section 20.2), then discusses EO applications to aquatic ecology in terms of:

- wetlands (including seagrass, mangrove, and saltmarsh; see Section 20.3);
- estuarine ecosystems (see Section 20.4);
- coastal waters (see Section 20.5);
- coral reefs (see Section 20.6); and
- marine fauna (see Section 20.7).

Excursus 20.1—Biodiversity

Source: OzCoasts website: *https://ozcoasts.org.au/indicators/coastal-issues/declining_biodiversity/*

The concept of biodiversity refers to the variety of life on three different levels:

- genetic—amount of genetic variability between individuals of a given species;
- species—number of different species (e.g. the species richness) and the 'evenness' (or equitability) with which the different species are distributed; and
- ecosystem—variety of different ecosystems.

In Australia, a comprehensive suite of indicators (pressures on biodiversity, condition of biodiversity, and responses to pressures on biodiversity) were developed as part of the biodiversity theme for the national State of the Environment reporting (*http://www.environment.gov.au/science/soe*). For example, changes in the following biophysical parameters may indicate that a coastal waterway has lost, or is at risk of losing, biodiversity:

- reduced areas of seagrasses, mangroves, salt marshes, intertidal mudflat/sand flats, beaches, and dunes, as well as coral reefs;
- increased frequency of fish kills, algal blooms, or anoxic and hypoxic events;
- reduced diversity of benthic invertebrates, intertidal invertebrates, or fish assemblages;
- water column pH values < 6 or > ~9;
- water column turbidity, chlorophyll a, toxicant or heavy metal levels in excess of ANZECC[24]/ ARMCANZ[25] trigger values;
- sediment heavy metal or toxicant levels in excess of ANZECC/ARMCANZ trigger values;
- widely fluctuating diurnal ranges of pH or dissolved oxygen;
- widely fluctuating seasonal ranges of pH, dissolved oxygen, and salinity; and
- denitrification efficiencies lower then 57%, benthic carbon dioxide fluxes in excess of 12 mmol m^{-2} d^{-1} or sediment ratios of total organic carbon to total sulphur < 5.

24 ANZECC: Australian and New Zealand Environment and Conservation Council
25 ARMCANZ: Agriculture and Resource Management Council of Australia and New Zealand

The oceans cover 70% of the planet's surface area, and marine and coastal environments contain diverse habitats that support an abundance of marine life. Life in our seas produces a third of the oxygen that we breathe, offers a valuable source of protein and moderates global climatic change..
(Convention on Biological Diversity)

20.1 Ecology of Australian Surface Waters

Australia's expansive marine resource is the third largest in the world (see Section 2) and houses a diverse range of mammals, reptiles, fish, invertebrates, flora, and microorganisms, many of which are unique and iconic. Australia is home for this planet's largest coral reef ecosystem, The Great Barrier Reef, which spans 2900 km in length and includes about 3000 individual reefs (see Section 20.6).

Our marine environment is also signficant in terms of global biodiversity, forming part of a migratory network for many marine species. However, it is estimated that less that 25% of the seafloor of our marine estate has been explored (see Section 13.1), with much less than that being described at the habitat level (NMSC, 2015). Marine protected areas (MPA) are important for conserving marine biodiversity, both in coastal and offshore regions (see Excursus 20.2).

While more limited in extent, Australia's inland waters are also critical for a wide variety of biota. Floodplains, for example, are ecosystems with high diversity and productivity which require careful management, particularly in dry landscapes such as Australia (see Excursus 3.1).

In Australia, excluding small offshore islands, the coastline spans around 34,000 km, and includes over 1,000 estuaries (GA, 2020a). Since over half of the growing Australian population lives within seven kilometres of the coast, there are increasing pressures on coastal ecosystems (see Volume 3A—Section 2.5.3). Although the coastal region has major economic, social, and ecological importance, it suffers increasing degradation from a range of anthropogenic activities (Wolanski *et al*., 2008). Degradation can be both direct, such as eutrophication or pollution, or indirect, such as ecosystem decline, and pressures resulting from urbanisation, agriculture, and industry are visibly impacting the biodiversity of coastal waters (see Excursus 20.1).

The term 'coastal zone' generally describes the interface between land and sea, and thus comprises both the portion of land impacted by marine processes, such as tides and waves, and the part of the sea that is impacted by terrestrial processes, such as runoff and erosion. The precise extent of the area denoted as 'coast' and coastal zone varies between jurisdictions and can be justifiably adapted to objectives of policies and management (Harvey and Caton, 2010). For example, while the federal government uses the definition of "the boundaries of the coastal zone extend as far inland and as far seaward as necessary to achieve the policy objectives, with a primary focus on the land/sea interface" (Commonwealth of Australia, 1992), state governments define the term differently, or not all (Harvey and Caton, 2010). Geographically, Australian coasts have been characterised into four regional categories differentiated by humidity (humid and arid) and climate (tropical and warm temperate), such that each category can be described in terms of unique geological, hydrological, meteorological, and biological attributes (see Table 2.2 in Harvey and Caton, 2010).

The coast of Australia displays enormous variety, from tropical rainforest with fringing reefs in the Daintree of North Queensland to the arid sands at Coffin Bay in South Australia; from the hot arid cliffs of the Kimberley coast of northwest Western Australia to the cool, wet, cliffed coast of Western Tasmania; from the alluvial flats and mangroves of the gulf of Carpentaria (Northern Territory) to the saline samphire flats of the Gulf St Vincent (South Australia).
Harvey and Caton (2010)

Excursus 20.2—Marine Protected Areas

Source: Janet Anstee, CSIRO
Further Information: Sagar *et al.* (2020)
Australian Marine Parks Science Atlas: *https://atlas.parksaustralia.gov.au/amps*
Australian Marine Science Program: *https://parksaustralia.gov.au/marine/science/*

Marine parks and aquatic reserves have been established around the world to conserve marine habitats and the various life forms they foster. A network of Marine Protected Areas (MPA) have been declared in both Commonwealth and state/territorial waters to conserve marine biological diversity on a bioregional, ecosystem, habitat, community, and species level (AMP, 2020). This network is designed to be:

- comprehensive—sample the full range of Australia's ecosystems;
- adequate—of appropriate size and configuration to ensure the conservation of marine biodiversity and integrity of ecological processes; and
- representative—reflect the marine life and habitats of the area they are chosen to represent (NHT, undated).

The MPA network was designed using scientific information from:

- detailed surveys of species and habitat at different waterbody depths, only available for a very limited area of Commonwealth waters;
- surrogate information for bathymetry, geomorphology, oceanographic variables, bathomes, Ramsar wetlands, and world heritage areas; and
- models that predict the likely distribution and ecological importance of natural values, such as biota, key ecological features, bioregions, and biologically important areas—based on key ecological features and other biologically significant areas (Sagar *et al.*, 2020).

Using these datasets, 41 bioregions were defined through the Integrated Marine and Coastal Regionalisation of Australia (IMCRA 4.0), with each bioregion representing a large expanse of ocean of broadly similar characteristics (see Section 2.2).

Australia's oldest and most famous marine park is the Great Barrier Reef Marine Park (GBRMP), which spans 14° of latitude (2,300 km) along the Queensland coast and covers 344,400 km^2 of coastal waters (see Figure 20.1). This Park has been managed by the Great Barrier Reef Marine Park Authority (GBRMPA) since 1975 and was declared a world heritage area in 1981. The Great Barrier Reef (GBR) is the longest barrier reef in the world and comprises around 10% of the world's coral reef ecosystems.

In addition to the GBRMP, 3.3 million km^2 of Australia's Commonwealth waters (over 5.5 km from the coast) are protected in a total of 60 marine parks (see Figure 20.2). This constitutes 37% of Australia's oceans and represents the second largest network of marine parks in the world (Parks Australia, 2021). The four IUCN categories that are used to define marine parks shown are listed in Table 20.1. These parks are managed according to six regional management plans, which are shown as different colours in Figure 20.2a: Coral Sea marine park (yellow); temperate (green); southeast (blue); southwest (purple); northwest (magenta); and north (red). Numerous marine parks and aquatic reserves are also managed by state jurisdictions to conserve marine biodiversity in coastal waters. These areas are zoned and managed to ensure that their intrinsic value and sustainability are protected for future generations.

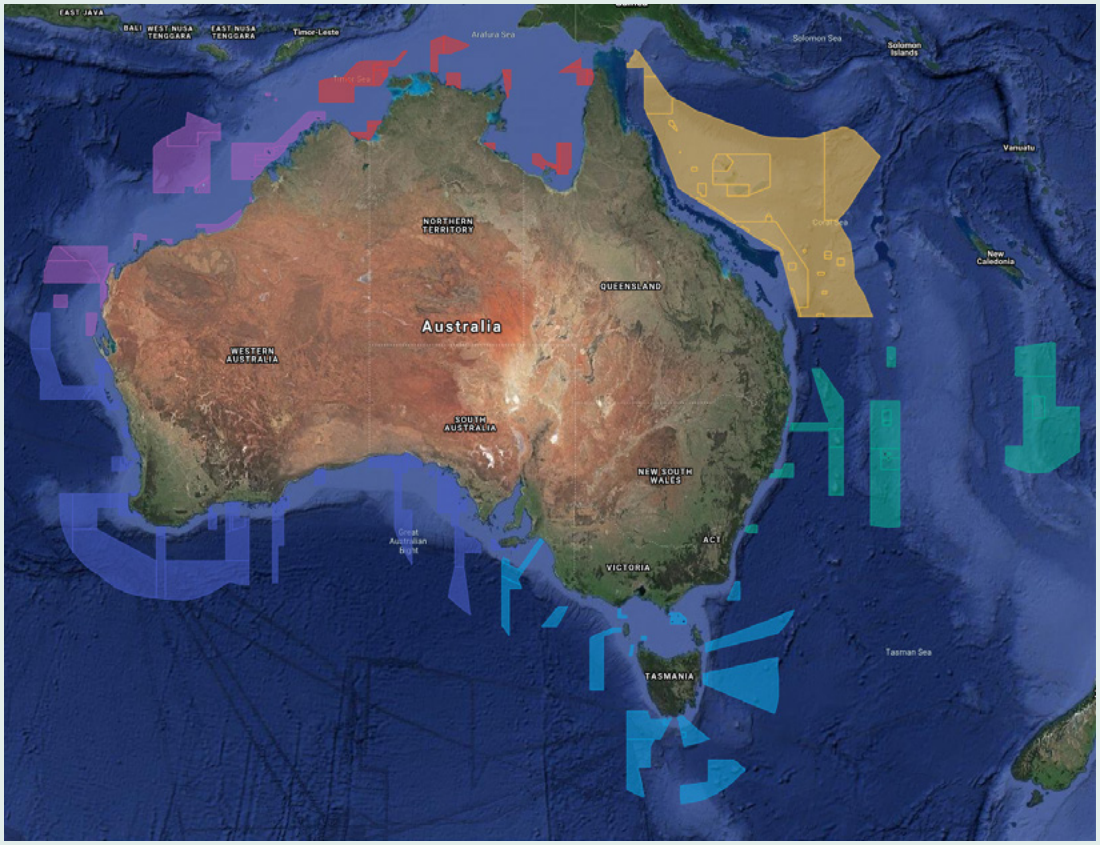
Figure 20.1 Great Barrier Reef Marine Park



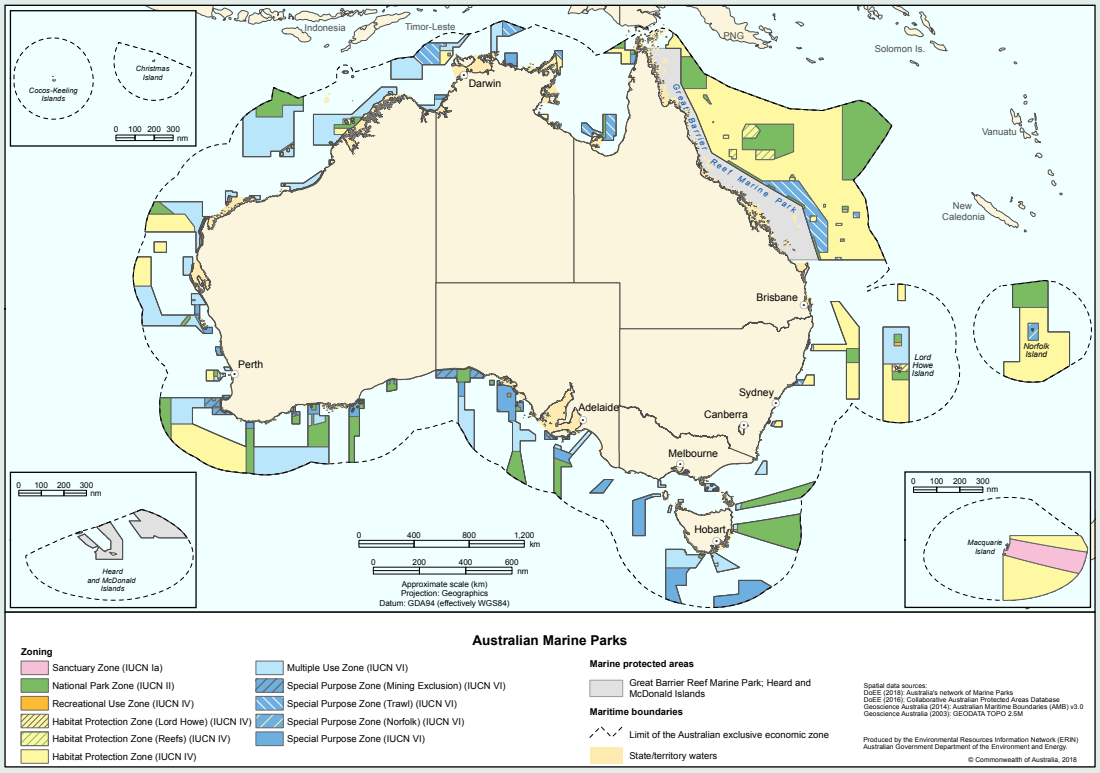
Source: Wikimedia Commons. Retrieved from: *https://commons.wikimedia.org/wiki/File:Great_Barrier_Reef_Marine_Park_locator_map.svg*

Figure 20.2 Australia's other marine parks

a. Geographic zones



b. Functional zones



Source: Parks Australia. Retrieved from a. *https://parksaustralia.gov.au/marine/*; b. *https://parksaustralia.gov.au/marine/pub/maps/National-Full-zoning-incl-SE.pdf*

Table 20.1 Commonwealth Marine Reserves IUCN protected area management categories

IUCN category	IUCN number	Management objective
Strict nature reserve	Ia	Managed primarily for scientific research or environmental monitoring
National park	II	Protected and managed to preserve its natural condition
Habitat/species management area	IV	Managed primarily, including (if necessary) through active intervention, to ensure the maintenance of habitats or to meet the requirements of specific needs
Managed resource protected area	VI	Managed to ensure long term protection and maintenance of biological diversity with a sustainable flow of natural products and services to meet community needs

Source: *http://www.environment.gov.au/topics/marine/marine-reserves/overview/legal-framework*

Australian Marine Parks Science Atlas (see Section 20.8), a platform to promote research within these parks, uses spaceborne EO as one of the primary planning and monitoring tools that is being used to produce a range of maps for each park, including the recent rate of ocean surface warming and ocean productivity hotspots, and inter- and intra-seasonal variations in surface water temperatures and chlorophyll a concentrations. Such maps also provide valuable input to conservation planning software (Tulloch *et al*., 2021).

EO is also used to assess and monitor environmental pressures, such as anthropogenic activities (boating, diving, snorkelling, recreational fishing), marine pollution (such as plastic debris and discharge of oils), illegal commercial fishing (FAO, 2018; Kurekin *et al.,* 2019), and impacts of climate change (such as changes in sea temperature, sea level, currents, phytoplankton composition, and/or benthic communities). Monitoring efforts based on EO datasets also guide management programs and actions for marine parks.

A marine protected area is defined as an area of sea (which may include land, the seabed and subsoil under the sea) established by law for the protection and maintenance of biological diversity and of natural and cultural resources.
(NHT, undated)

20.2 EO Sensors for Water Ecology

EO datasets are used in mapping coastal and estuarine habitats, monitoring coastal ecosystem services, assessing coastal ecosystem risk, and tracking ecological parameters in marine areas (Kachelriess, 2014; Ouellette and Getinet *et al*., 2016; Hedley *et al*., 2016a). Important environmental variables that describe key ecosystem properties in the open ocean can be quantified using various EO datasets, including sea level anomalies (see Section 12), sea surface temperature (SST; see Section 14), water circulation (see Section 16), and chlorophyll a (see Section 18.6). The high spatial and temporal resolutions of EO-based datasets now enable natural events that impact water quality, such as plankton blooms (see Section 19.5) and marine heat waves (see Section 19.6), to be mapped, monitored, and modelled (see Volume 2D—Section 14). Anthropogenic pressures that impact marine biodiversity and ecosystem sustainability, such as marine pollution and illegal fishing, can also be targetted (and in some cases quantified) using EO datasets (see Sections 19.4 and 20.7 respectively).

A range of EO sensors is introduced in Volume 1A, and interpretation of optical and microwave imagery is considered in Volume 1B. The types of EO sensors and platforms that can be used to map and monitor aspects of water ecology are summarised in Table 20.2.

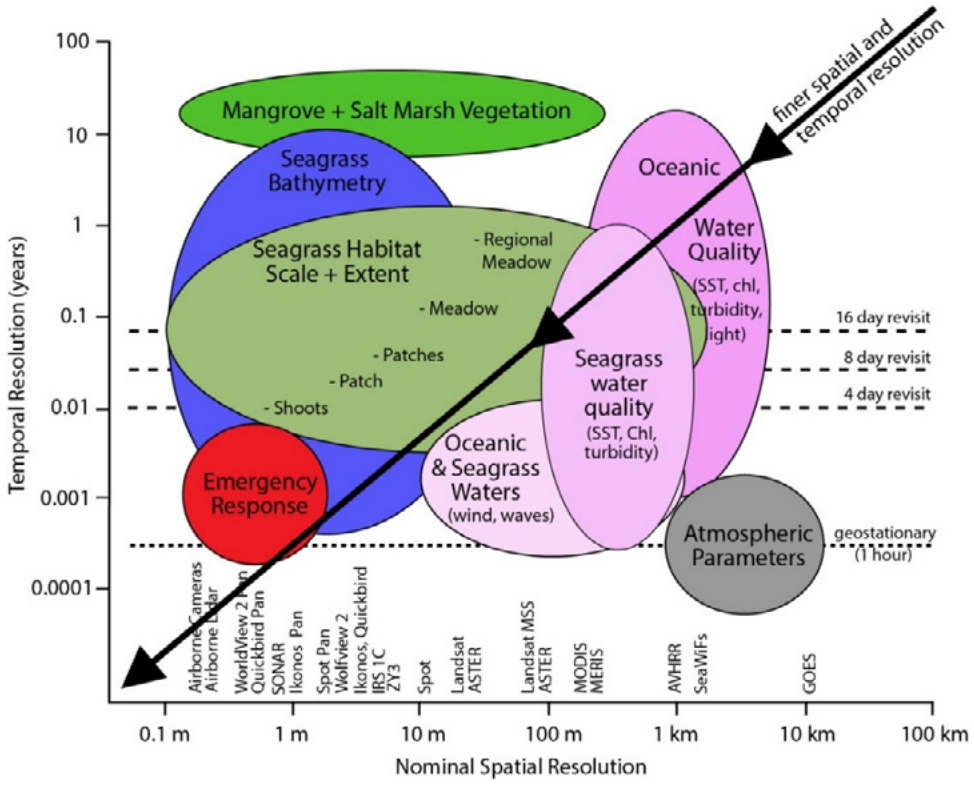
Table 20.2 EO sensors relevant to coastal and marine water ecology

TIR: Thermal infrared; SAR: Synthetic Aperture Radar; UAV: Unmanned aerial vehicle;

Type	Sensor	Platform	Relevance	Advantages	Disadvantages
Passive optical	Multispectral radiometer	Satellite or airborne	Coastal ecology Coral reefs Marine ecology	Global coverage, low cost	Lower spatial resolution in early sensors
	Hyperspectral radiometer	airborne	Coastal ecology Coral reefs	High spectral resolution	High cost, high data volume
	TIR radiometer	Satellite or airborne	Coastal and marine habitats Coral bleaching	Global coverage, low cost	Low spatial resolution
Active optical	Lidar	airborne	Bathymetry Shoreline topography Reef morphology	High spatial resolution	Low coverage
Active microwave	SAR	Satellite or airborne	Mangrove mapping Oil/chemical spills Surface wind and wave fields Sea ice	All weather	High cost, specialised processing
Acoustic	Multibeam Echosounder	UAV or shipborne	Benthic habitats Bathymetry	Waterbody depth coverage	Low coverage

CEOS (2018) recommend detailed specifications for the ideal satellite-borne optical sensor for EO of non-oceanic, aquatic environments. Parameters for the preferred spectral, spatial, radiometric, and temporal characteristics for mapping aquatic ecosystems are summarised in Section 8.5. Optical EO sensors that can map macrophytes, macroalgae, seagrasses, and corals are listed in Table 20.3 (see Table 8.14 for technical details of these sensors). For example, the spatial and temporal resolutions required to map and monitor seagrass and mangrove features in coastal environments is illustrated in Figure 20.3. Various EO datasets and techniques are also being used to classify the pelagic ocean into biomes, provinces, and seascapes to enable effective monitoring, management, and conservation of marine estates (Gohin *et al.*, 2008; Hardman-Mountford *et al.*, 2008; Kavanaugh *et al.*, 2016).

Figure 20.3 EO data resolutions for seagrass and mangrove features in coastal environments



Source: Hedley *et al.* (2016b) Figure 1

While bathymetry derived from multibeam echosounders (MBES) measures ocean depth (see Section 13.3.2), the backscatter intensity can be used as a proxy to understand characteristics of the seafloor, including seafloor hardness and surficial sediment characteristics (see Section 10). These measurements can be used to characterise the environment (or habitat) where marine fauna live, including establishing baseline data to support environmental monitoring and explaining spatial patterns of seafloor biology and biodiversity at continuous scales. Multibeam bathymetry data can be classified by geomorphological analysis to determine the extents of particular habitat types, such as seagrass beds, rocky reef, and sand plains (Lucieer *et al.*, 2018). The biological function of geomorphological features, and their three-dimensional structure into water depths well beyond the reach of EO sensors, has also been explored using satellite-based tracking devices on marine animals (Priede, 2014).

Various configurations of towed underwater camera systems have been used for over a century to obtain images of the seafloor (Bicknell *et al.*, 2016). These platforms are deployed on a cable from a surface vessel and generally use forward-looking oblique and/or downward-looking cameras (Bowden and Jones, 2016, Durden *et al.*, 2016). Towed underwater cameras provide an important non-invasive sampling alternative where extractive methods are either unnecessary or unsuitable, such as in sensitive deep sea habitats (Althaus *et al.*, 2009, Williams *et al.*, 2015, Sherlock *et al.*, 2016), or for repeated sampling in marine reserves (Lawrence *et al.*, 2015). Towed platforms offer cost-effective permanent data capture along transects (up to several kilometres in length) and can traverse highly heterogeneous seafloor topography (Shortis *et al.*, 2007). The quality of imagery acquired by towed systems varies with sea conditions and water clarity, which both vary widely with location, season, and tidal influence. Below 30 m water depth, image quality is also impacted by lighting and camera specifications. A consistent altitude above the seabed is also required to maintain optimal image quality (Carroll *et al.*, 2018).

Table 20.3 Suitability of optical EO sensors for mapping aquatic ecosystem features

This list includes multispectral and hyperspectral sensors carried on previous, current, and future EO missions with spectral bands in the wavelength range 340–1000 nm. Names of commercial sensors are italicised. Note that it focuses on spectral characteristics of sensors rather than spatial resolution and extent, and temporal resolution.

Sensor	Aquatic vegetation type		
	Emergent	Floating-leaved	Submersed
Hyperion	high	high	high
CHRIS-PROBA	high	high	high
MERIS	high	high	high
HICO	high	high	high
Sentinel-3	high	high	high
GLIMR	high	high	high
PRISMA	high	high	high
EnMap	high	high	high
SBG (formerly HyspIRI)	high	high	high
PACE	high	high	high
ISS HISUI	high	high	high
IAA DESIS	high	high	high
OCM-2	medium	medium	medium
Suomi-VIIRS	medium	medium	medium
SGLI	medium	medium	medium
GOCI	medium	medium	medium
GOCI-II	medium	medium	medium
WORLDVIEW-2/-3	high	high	high
IKONOS, QuickBird, SPOT-5,- 6, GeoEye etc.	medium	medium	medium
RapidEye	medium	medium	medium
SENTINEL-2	medium	medium	medium
Aqua/Terra MODIS (1 km)	medium	medium	medium
Aqua/Terra MODIS (500 m)	Not suitable	potential	potential
Aqua/Terra MODIS (250 m)	potential	potential	potential
LANDSAT-4 to -7	medium	potential	potential
LANDSAT-8	medium	medium	medium
Himawari-8/-9	potential	potential	potential
GOES-R	potential	potential	potential
GISAT-1/-2	potential	potential	potential
MSG SEVIRI	potential	potential	potential

Adapted from: CEOS (2018) Table 2.7

20.3 Coastal Wetlands

Wetlands describe areas where water covers the soil continuously or for selected periods of time, which can be naturally occurring or man-made. Examples of wetlands include swamps, marshes, billabongs, lakes, lagoons, saltmarshes, mudflats, mangroves, bogs, fens, and peatlands (see Excursus 3.1). Globally, 54% of wetlands are permanently covered with water and 46% are seasonally inundated (RAMSAR, 2018). These ecosystems include some of the most carbon-rich on Earth and sequester substantially more carbon than forests (Mcleod *et al*., 2011).

RAMSAR (2018) estimate up to 87% of global wetlands have been lost since 1700 and around 35% of wetlands have disappeared since 1970, with the rate of loss increasing this century. These coastal habitats are being degraded by a range of anthropogenic activities, including land reclamation, shoreline infrastructure, rerouting of river systems, domestic grazing, vehicular and pedestrian traffic, rubbish and pollution, and weed invasion (DAWE, 2020). Accordingly, marine species that depend on these habitats are also declining, with 81% of inland wetland species and 36% of coastal and marine species being impacted, 25% of which are at risk of extinction. This decline then reduces water quality and availability, food security, and carbon sequestration.

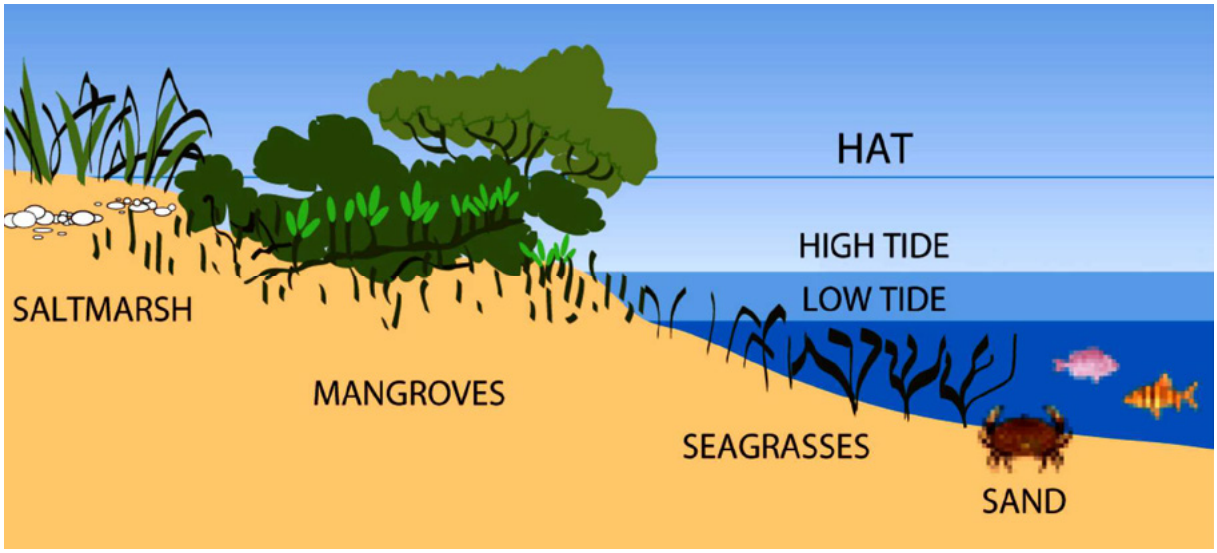
Aquatic vegetation is introduced in Sections 3.3.2 and 6.4. Wetland vegetation traps and stabilises sediments to reduce the impact of waves, tides, and floods on shorelines and rivers (DAWE, 2020). It also filters the transfer of organic matter and nutrients from runoff to maintain water quality (Pennesi *et al*., 2015). Wetlands support a rich array of biodiversity, including providing nurseries for fish and other marine organisms, and feeding and housing birds (especially migratory), mammals, and reptiles (Turner *et al*., 2004). Over two thirds of global fish consumption depends on coastal wetlands (DAWE, 2020).

The vegetation in coastal wetlands, such as melaleuca swamps, varies in density and height. These tend to occur in low-lying ground near estuaries and can include trees and understorey sedges, grasses, and aquatic herbs. Seagrasses, mangroves, and saltmarshes are synergistic, intertidal communities comprising plants that have adapted to saline and waterlogged conditions on the foreshores of coastal lakes and estuaries (see Figure 20.4). The extent of these ecosystems has significantly reduced in Australia since European settlement, and climate change and sea level rise are expected to further modify their distribution and abundance (DAWE, 2020).

Ecological character is the combination of the ecosystem components, processes and benefits/services that characterise the wetland at a given point in time.
(RAMSAR, 2005)

Figure 20.4 Wetland habitat zones

HAT=Highest Astronomical Tide



Source: Daly (2013)

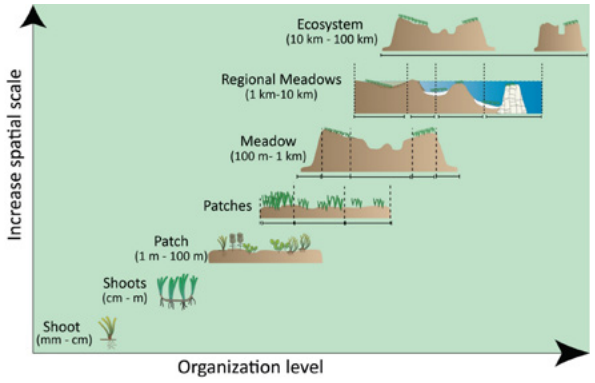
Healthy, functioning natural wetlands are critical to human livelihoods and sustainable development. (RAMSAR, 2018)

EO of aquatic vegetation offers advantages over traditional ground-based surveys but presents some challenges. EO of terrestrial plants makes significant use of the red edge (that is, the difference between their characteristically strong absorption of red wavelengths and strong near infrared (NIR) reflectance—see Volume 3A). However, aquatic plants cannot be recognized by this feature since, in water columns deeper than 1–2 m, wavelengths beyond 680 nm are significantly attenuated by pure water (Kirk, 1994, 2010). Below we will describe EO methods to map and monitor seagrass (see Section 20.3.1), mangroves (see Section 20.3.2), and saltmarshes (see Section 20.3.3). Navarro *et al.* (2021) and Ricart *et al.* (2020) demonstrate the utility of EO for quantitative monitoring of these environments in Australia. An example of wetland monitoring using EO is given in Excursus 19.3.

20.3.1 Seagrass meadows

Australia's coastline nurtures the most abundant and diverse range of seagrasses in the world (Turner *et al.*, 2004; Larkum *et al.*, 2018; Phinn *et al.*, 2018). Seagrasses are productive flowering plants that grow in the soft sediments underlying estuaries and coastal waters (see Figure 20.4). By reducing erosion and water movement, seagrasses help to stabilise the seafloor and improve water clarity. They support benthos and algae and offer breeding grounds for many species of fish. In clear waters, seagrasses can grow at water depths greater than 60 m, but growth may be restricted in intertidal waters where turbidity levels are high. Waters with high levels of nutrients and suspended organic matter also tend to restrict growth (Furnas, 2003), making these plants a good indicator of water quality.

Figure 20.5 Seagrass spatial and organisational scales



Source: Phinn *et al.* (2018) Figure 15.2

The seagrasses are covered by a water column, which attenuates the light that reaches, interacts with, and is reflected from the benthos. In coastal waters, spectral scattering and absorption by phytoplankton, suspended organic and inorganic matter, and dissolved organic substances further restricts the light passing to the benthos (Dekker *et al.*, 2001). Zimmerman (2006) discusses the effects of higher concentrations of optically active materials in the water column on seagrass photosynthesis. Where light penetrates the water column and can be reflected back to the sensor, spectral discrimination between aquatic plant species concentrates on pigment-related spectral features within the visible wavelengths (Fyfe, 2003). Absolute reflectance from submerged species is generally low (< 10%), often lower than the reflectance from a deep water column and, from a visual perspective, seagrass areas generally appear darker than non-vegetated areas, partly due to shading within the canopy (Zimmerman, 2006).

Seagrasses can be observed at a range of spatial scales (see Figure 20.5). They may grow with sparse cover and can be spectrally confused with other benthic features such as areas of macroalgae, detritus, and corals (Mumby *et al.*, 1997a, 1997b). Textural characteristics and associated physical attributes of the environment (for example, it will not grow on a wall or in a high energy zone) could help differentiate seagrasses from other bottom features. While coral is found on hard substrates (see Section 20.6), seagrass tends to grow in unconsolidated substrates of shallow banks or coral reefs. The small size and/or linear shape and patchy nature of many seagrass meadows means that in many cases moderate to high spatial resolution is also required to accurately determine their distribution and abundance.

The spatial extent of seagrass meadows can either increase or decrease rapidly in response to human impacts or natural dynamics. For meadows such changes may occur within a timeframe of weeks to months, whereas spatial changes in corals be much slower. When assessing the dynamics of seagrass meadows, it is important to understand potential human impacts. This understanding is particularly relevant to the timing of EO data that is being acquired to detect changes in seagrass meadows. For example, monitoring seasonal changes in the extent and density of certain seagrass species would require repeated temporal coverage.

Some of the methods that have been used to map seagrass distribution include:

- Principal Components Analysis (PCA; Bajjouk *et al.*, 1998);
- spectral angle mapping (SAM; Dunk and Lewis, 1999; Alberotanza *et al.*, 1999);
- minimum distance classification (Malthus and George, 1997);
- classification with reference to simulated spectral libraries (Louchard *et al.*, 2000);
- radiative transfer modelling (Dekker *et al.,* 2011);
- semi-automated OBIA (Lyons *et al.,* 2012; Roelfsema *et al.,* 2014; Kovacs *et al.,* 2018).

Details of these techniques are provided in Volume 2. Dekker *et al.* (2001) consider a radiative transfer model or semi-analytical model as essential in accounting for water attenuation and multiple backscatter from a reflective substratum (see Section 8.4). Spectral libraries, either generated from *in situ* spectral measurements or simulated by a two-flow model, are needed to reliably differentiate between different types of substrate materials (see Volume 2D—Section 12.3). Airborne hyperspectral imagery has also enabled separation of some algal and seagrass species (Dunk and Lewis, 1999), with green, red, and brown algae being discriminated using visible wavelengths, and brown vegetation, seagrasses, and floating seaweed being separated using infrared wavelengths (Bajjock *et al.*, 1996). Lyons *et al.* (2012) demonstrated long term mapping of seagrass cover and extent using a moderate resolution sensor independently of *in situ* data, via an object-based image analysis (OBIA) approach (see Volume 2A—Section 10). Where species morphologies/colours were distinct, an OBIA methodology that incorporated *in situ* field data and ecological rules (including waves, water depth, and consolidation) has been used to generate maps that distinguish areas of different seagrass species (Roelfsema *et al.,* 2014; Roelfsema *et al.,* 2015; Kovacs *et al.,* 2018). Roelfsema *et al.* (2014) utilised a semi-automated mapping approach that incorporated field data and high resolution imagery to temporally map seagrass cover, species, and biomass. Further, utilising this semi-automated method, Kovacs *et al.* (2018) compared seagrass cover and species map outputs from moderate and high resolution sensors and concluded that all sensors tested were suitable for mapping seagrass in clear shallow waters, but the higher resolution sensors provided more detail and were considered more representative. Recent developments for global mapping of seagrass meadows include the development of machine learning (ML) approaches within the Google Earth Engine using Sentinel-2 imagery (Traganos *et al.,* 2018).

Regardless of which seagrass mapping approach is used however, baseline field data is required for calibration and validation. For approaches based on radiative transfer modelling, this training data comprises a spectral library based on field measurements, and for empirical approaches, the composition of seagrass meadows needs to be directly determined in the field. For validation of either approach, the composition of seagrass meadows in the field is required as reference data for accuracy assessment (Roelfsema *et al.,* 2015).

20.3.2 Mangrove forests

Mangroves are described as woody plants (see Section 3.3.2), which tend to grow at the fringe of the intertidal shallows, so are exposed to both fresh and salty water (DAWE, 2020). They are the most prolific wetland vegetation group globally yet are also one of the most vulnerable ecosystems (Kuenza *et al.*, 2011). Most mangrove forests grow in tropical and subtropical regions (Giri *et al.*, 2011).

Different mangrove species tend to grow in zones parallel to the shoreline, with zones being demarcated by tide levels and soil salinity, oxygen, and nutrients (Stewart and Fairfull, 2008; see Figure 20.4). Mangroves offer erosion protection and act as a sediment trap for runoff. They also house and/or feed a wide range of both terrestrial and marine species (Turner *et al.*, 2004), including migratory birds, and nurture about 75% of coastal fishery catches (MangroveWatch, 2021; IUCN, 2017). Their characteristic growth form with aerial structural roots and exposed breathing roots (pneumatophores) enables them to withstand tidal inundation and oxygen-depleted soil.

Over 90 species of mangroves in 20 families have been identified globally. Mangroves cover around 11,500 km^2 of Australia's coastal region, with greatest concentrations in the north and east (DAWE, 2020). Australia's mangroves comprise 7% of global mangrove coverage, with 41 species, from 19 families, growing along ~22% of the intertidal zone of our tropical, subtropical, and protected temperate coastal rivers, estuaries, and bays (Stewart and Fairfull, 2008).

EO datasets have been used to map mangrove forests for many decades, involving a range of sensors (Kuenzer *et al.*, 2011; Wang *et al.*, 2019). Mangrove communities can be differentiated on the basis of the texture and reflectance properties of their canopy and foliage, particularly in NIR wavelengths (Ramsey and Jensen, 1996), although soil type and intertidal influences can impact spectral characteristics in sparser vegetation (Meza Diaz and Blackburn, 2003). Mangrove backscatter in SAR imagery is somewhat more complicated as summarised in Table 20.4.

Table 20.4 Backscatter from mangroves

Characteristics of the backscatter signal depend on mangrove structural components, biomass, and forest stand.

Frequency	Description	Polarisation		
		VV	HH	HV
C-band	Penetration into the upper part of the canopy, few metres within the crown; Interaction with leaves and small branches; Increase in backscatter is indicative of changing forest structures; Sensitive to crown characteristics (number, density, size, and leaf orientation) and canopy structure (architecture and heterogeneity); Above-ground biomass saturation in SAR response at 50 t DM ha^{-1}	High sensitivity to increasing biomass; Highest correlation with canopy parameters; Highest correlation for tree height and diameter	High sensitivity to increasing biomass; Related to variations in the canopy structure; Highest correlations for tree height and diameter	Significant relationship with LAI (greater at larger incidence angle); High correlation between backscatter coefficient and mean stem height (larger coefficient at smaller incidence angle); High coefficients for determination of mean DBH, tree height, and basal area
L-band	Deeper canopy penetration, involving scattering from trunks and ground surface; Volume scattering predominates by interaction with multiple branches of various sizes; Increase in backscatter is indicative of changing forest structures; Double-bounce scattering between trunks and ground; Sensitive for biomass; Above-ground biomass saturation in SAR response at 100 t DM ha^{-1}	Soil-vegetation interaction and direct backscattering from soil surface; Domination of volume scattering with increasing biomass	Soil-vegetation interaction and direct backscatter from soil; Domination of volume scattering with increasing biomass; Mapping of flooding in forests with high specular backscatter signal of flooded surfaces; Double-bounce trunk-ground term is enhanced by the presence of water; the smaller the incidence angle, the more dominant this term; Canopy volume scattering dominates for stands under non-flooded ground	High correlation with forest parameters (zonation, basal area, height, biomass level, growth stages); Best correlation for biomass; Backscatter coefficient of biomass is greater at smaller incidence angles
P-band	Penetration reaches underlying soil and water surface; Double-bounce effects; High sensitivity to forest parameters; Above-ground biomass saturation in SAR response at 150 t DM ha^{-1}	High interaction with soil surface; Intensity is dependent on soil moisture and roughness, as well as length and sizes of trunks; No correlation with total biomass	High correlation with total biomass	High correlation, with total biomass showing the largest sensitivity; Best correlation for biomass

Source: Kuenza *et al.* (2011) Table 1

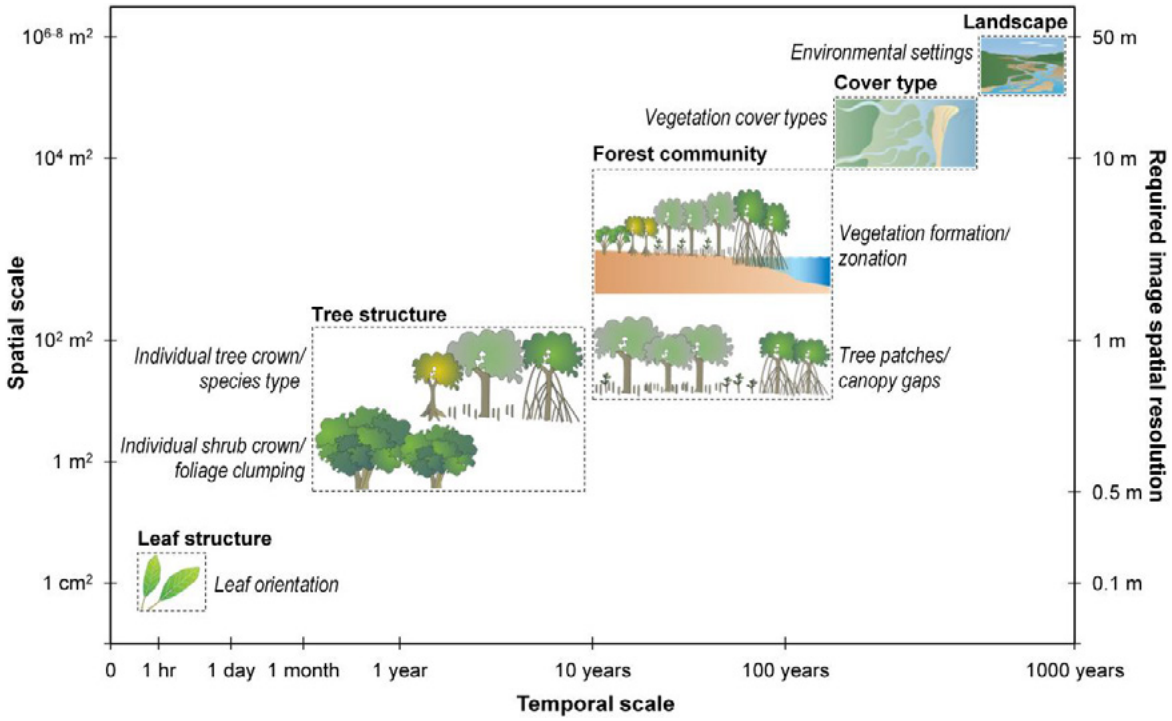
The global distribution and extent of mangroves were mapped by Giri *et al.* (2011), using Landsat imagery and hybrid classification methods. New global inventories are also being derived from multisource EO data, such as lidar and passive optical, and the Google Earth Engine (Yancho *et al.*, 2020).

Classification of satellite-acquired optical imagery has been used for mapping mangrove habitat at regional/national scales, with higher spatial resolution sensors being more appropriate for local scales (Kuenza *et al.*, 2011). The spatial and temporal scales in EO imagery that are required to map mangrove features are summarised in Figure 20.6. Kamal *et al.* (2015) used multi-resolution optical datasets (satellite-acquired) with lidar imagery to derive a hierarchical, object-based classification system for mangrove formation/zonation, canopy structure, and species community. Recent studies have found structural attributes of regenerating mangroves can be characterised from multi-polarised, satellite SAR imagery (Cougo *et al.*, 2015). Lidar datasets have also been used to map mangrove canopy height (Purkis and Brock, 2013).

Until recently, most EO-based mangrove mapping for Australia has been part of global studies (such as the Global Mangrove Watch: Lucas *et al.*, 2014; Thomas *et al.*, 2017; Bunting *et al.*, 2018). 30 years of mangrove dynamics along the entire Australian coastline has now been mapped at 25 m resolution using Digital Earth Australia, a calibrated Landsat archive (see Volume 2D—Section 11.2), with lidar surveys being used to parameterise the canopy cover estimates (Lymburner *et al.*, 2020). These maps allow changes in the extent and density of Australian mangroves to be quantified.

Figure 20.6 Mangrove features versus image resolution

A conceptual temporal and spatial hierarchical organisation of mangroves features identifiable from EO images is shown with the required image pixel resolution for mapping these features.



Source: Kamal *et al.* (2015) Figure 1. Symbols are courtesy of the Integration and Application Network, University of Maryland Center for Environmental Science—*ian.umces.edu/symbols/*

20.3.3 Saltmarshes

Saltmarshes, or tidal marshes, grow in the high tide zone on sheltered foreshores with soft substrates (see Figure 20.4), and comprise vegetation such as sedges, rushes, reeds, grasses, succulent herbs, and shrubs, interspersed with bare patches and/or salt pans. Coastal saltmarshes can occur as narrow fringes on steeper slopes with little species variation, to larger expanses on flatter ground with many species, or extend inland along estuary foreshores. Biodiversity tends to increase in elevated areas that are inundated less frequently. Saltmarshes offer refuges for juvenile fish and migratory wading birds, and provide habitat for birds, bats, mammals, insects, and invertebrates (Daly, 2013).

Many saltmarsh areas in Australia have been resumed for agriculture or urban expansion in the last 200 years. Saltmarshes now extend over 13,500 km^2, mostly along the northern and eastern coastlines, with their distribution being largely determined by elevation, salinity, and inundation frequency (Daly, 2013). This represents around one third of the world's saltmarsh coverage and has been estimated to be storing 212 million tonnes of organic carbon in the first 1 m depth (Macreadie *et al.*, 2017). Landward sites with greatest influence from fluvial flows have been observed to have twice the organic carbon volume as marine sites.

The term 'saltmarsh' is used to describe individual plants, groups of plants and the general estuarine habitat dominated by these plants.
(Daly, 2013)

EO-based multispectral and hyperspectral datasets have been used to identify and map wetland vegetation (Haynes, 2016), and estimate selected biochemical and biophysical parameters, such as water content, biomass, and leaf area index (Adam *et al*., 2010). Airborne hyperspectral imagery has been used to discriminate between different saltmarsh vegetation communities (Silvestri *et al*., 2003). Since saltmarsh vegetation species are reliably correlated with elevation, saltmarsh vegetation maps derived from EO using spectral unmixing methods (see Volume 2E) have been used to infer foreshore elevation with accuracies comparable to laser altimetry. Time series datasets have also been used to study their dynamics at a regional scale (Laengner *et al*., 2019), with global studies now focusing on the carbon budgets of these ecosystems (Alongi, 2020). Lidar data is valuable to define high resolution topography, although it exhibits greater vertical uncertainty in saltmarsh than in other environments (Rogers *et al*., 2016), and has been used for identifying saltmarsh shorelines (Farris *et al*., 2019), monitoring erosion and accretion (Fernandez-Nunez *et al*., 2017), and parameterising tidal creek morphology (Chirol *et al*., 2018). Lidar datasets have been used to estimate the spread of invasive plants (Paynter *et al*., 2019), and integrated with hyperspectral imagery to improve habit classification (Hladik *et al*., 2013) and monitor carbon stores (Kulawardhana *et al*., 2014). SAR data have also been used to map shoreline topography, detect structural changes, and monitor recovery (Ramsey *et al*., 1997, 2009, 2014).

20.4 Estuarine Ecosystems

An estuary is the mouth of a river where freshwater mixes with seawater to create brackish water, creating a transition zone, or ecotone (see Volume 3A), between the river and the sea. These aquatic features are partially enclosed, but still subject to both waves and tides from the sea and fluvial flows from the river. Like their adjoining wetlands, they house unique communities of plants and animals, serve as nurseries for birds, fish and other organisms, and filter runoff. These productive ecosystems are also delicate and being degraded by ongoing erosion, eutrophication, pollution, and excessive harvesting (SOE, 2018). The biodiversity of estuaries can be impacted by a variety of environmental factors including estuary size, supply and retention of nutrients, complexity of water circulation, variety and extent of substrate sediment types, the range of available habitats, and tidal range (OzCoasts, 2020).

Estuaries experience constant change due to tidal and fluvial movement, which result in significant variations in water salinity, temperature, pH, and transparency. Accordingly, their ecosystems are highly variable in both space and time. While estuaries comprise a very small proportion of the world's marine waters, they are highly productive. Since turbidity often limits the growth of phytoplankton in these waters (Monbet, 1992), microphytobenthos (see Section 3.3.2.1) significantly contribute to both primary production (Underwood and Kromkamp, 1999) and chlorophyll a biomass (De Jong and de Jonge, 1995).

Transient biofilms are produced by microphytobenthos at the sediment surface, which help to stabilise intertidal mudflats. Since these patchy substratum features vary in colour with photosynthetic pigments, they can be characterised by reflectance spectra (Paterson *et al*., 1998), and detected by both airborne and spaceborne EO sensors (Méléder *et al*., 2003).

Macroscale distribution of microphytobenthos has been mapped in numerous studies using high resolution imagery (eg. Méléder *et al*., 2003). More recently, image time series have been used to map intrannual (Brito *et al*., 2013) and interannual (Benyoucef *et al*., 2014) variations of microphytobenthos biofilms in European estuaries. Such information furthers our understanding of estuarine ecosystem dynamics, allows separation of short and long term changes, and contributes to the identification of key environmental drivers in this environment.

Biodiversity levels in estuaries are a sensitive measure of their health and balance. Their proximity to human settlements make them particularly vulnerable to the impacts of vegetation clearing in adjacent catchments, urban runoff and the influx of stormwater and wastewater. Each of these flows may contain excessive nutrient loadings that may trigger changes in the distribution and structure of estuarine communities, usually by reducing their complexity.
(OzCoasts website)

20.5 Coastal waters

Coastal waters only represent 15% of the global ocean, but concentrate 90% of commercial fisheries, contribute to 25% of global biological productivity, and represent 80% of the marine biodiversity, while being associated with an intensive tourism-related economy.
(Doxaran et al., 2019)

The Australian national marine boundary definition of coastal waters is "a belt of water between the limits of the Australian States and the Northern Territory and a line 3 M seaward of the territorial sea baseline (TSB)" (GA, 2020b; see Section 2.1.3). However, for optical EO applications, coastal waters are commonly defined as marine areas adjacent to land with water depths less than 30 m (Oullette and Getinet, 2016). This depth represents the limit of solar light penetration through the water column that can be reflected by the substratum and detected by an EO sensor (see Section 8).

Coastal waters are estimated to constitute 8–10% of surface waters, and only 0.5% of their volume (Hoepffner and Zibordi, 2009). Since these waters are the closest to population centres, they are the most directly impacted by anthropogenic activities. In Australia and globally they are being degraded by nutrient and sediment pollution, catchment disturbance, marine debris, water abstraction, dredging, fishing, aquaculture, marine infrastructure, shipping, invasive biota, disease, algal and jellyfish blooms, hypoxic (low oxygen) events, and rising sea temperatures (SOE, 2018; NSW EPA, 2017).

EO datasets provide a reliable basis for observing coastal waters over time. In conjunction with field measurements, the use of unmanned aerial vehicles (UAV) and autonomous underwater vehicles (AUV; see Excursus 5.1) are gaining increasing popularity for monitoring this environment, with both offering high spatial resolution data to verify satellite-acquired observations. Various EO sensors are being used to quantify a range of hydromorphological, physical, chemical, and biological properties of coastal waters (Doxaran *et al.*, 2019), including:

- erosion/storm damage on shorelines and beaches (see Section 11.3);
- extent of flooding (see Section 11.4);
- water temperature (see Section 14);
- productivity (see Sections 18.6; Auricht *et al.*, 2017); and
- water quality (see Section 19).

The acquisition of optical imagery by UAV has also been shown to be a cost-effective alternative to manned aerial surveys of marine mammals, such as humpback whales (Hodgson *et al.*, 2017).

The coastal zone of Australia is a dynamic meeting area of earth (lithosphere) and atmospheric forces (atmosphere), of oceans and rivers (hydrosphere), and of terrestrial and marine life (biosphere). Changes, over a variety of time scales, are a characteristic of all coasts, and are an important driver of coastal management.
(Harvey and Caton, 2010)

20.6 Coral Reefs

...travellers tell us of the vast dimensions of the Pyramids and other great ruins, but how utterly insignificant are the greatest of these, when compared to these mountains of stone accumulated by the agency of various minute and tender animals
(Charles Darwin)

Coral reefs have been called the rainforests of the seas (Oceana, 2021). These structures are both complex and massive—and can survive for thousands of years (see Figure 20.7). Colonies of tiny, stony, coral polyps, mostly 1–3 mm diameter, secrete calcium carbonate, which slowly aggregates into a wide variety of forms and colours. Most corals co-exist with symbiotic algae (zooxanthellae), which photosynthesise and play a critical role in coral health. Highly consolidated reefs occur in clear, saline waters of the euphotic zone where temperatures remain above 18°C for most of the year. As such, their distribution is limited to tropical and subtropical waters. Coral growth can be limited by multiple factors, including sediments, eutrophication, pollution, temperature extremes, wave exposure, low light levels, and predators. Since water depth influences light penetration, temperature, and exposure, it provides a clear indicator for the potential presence of coral. Similarly wave energy partly determines the growth of certain types of coral types. For example, branching corals are often found in the protected areas of the reef, whereas massive and encrusting corals are more present on the exposed areas. Waves can therefore provide an indicator for coral types.

EO can accurately map unconsolidated, bright carbonate sand and, by exclusion, consolidated substrates can also be delineated (see Section 18.7). Since corals generally grow on consolidated substrates, EO mapping reliably predicts coral habitat (see Section 20.6.3).

At least two thirds of the world's coral reefs may collapse ecologically within the lifetime of our grandchildren unless we implement effective management of these ecosystems as an urgent priority.
(Joint Statement from IOC/UNEP/IUCN)

Figure 20.7 Coral diversity

A variety of corals form an outcrop on Flynn Reef, part of the Great Barrier Reef near Cairns, Queensland, Australia, on 24 July 2010.



Source: Toby Hudson (CC-BY-SA 3.0). Retrieved from Wikimedia: *https://commons.wikimedia.org/wiki/File:Coral_Outcrop_Flynn_Reef.jpg*

20.6.1 Structural characteristics

The hierarchical levels at which coral reefs are studied varies from individual polyps to whole reef systems (see Figure 20.8). A four level hierarchy differentiates reefs by the sizes of features present, namely reef/non-reef, reef type, reef geomorphic zone, and reef benthic composition (see Table 20.5). A global implementation of this system for use with EO has been released by Kennedy *et al*. (2021).

Individual coral reefs can be classified into five basic types:

- platform reefs—carbonate structures that have grown on submerged rock;
- fringing reefs—directly border shorelines and islands, and do not have a lagoon;
- barrier reefs—separated from shorelines by a lagoon;
- atoll reefs—barrier or fringing reef surrounding a submerged volcanic island; and
- ribbon reefs—a form of barrier reefs that is long and narrow.

Geomorphic zones within each reef are similar for different reef types. Typically reef topography includes several distinct geomorphologic zones, which are predominantly characterised by their depth and level of consolidation:

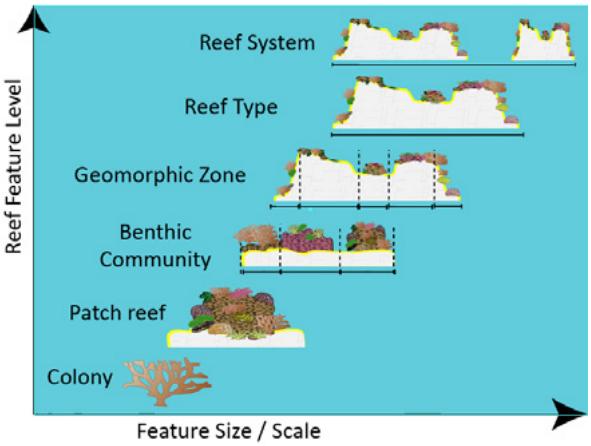
- Reef slope (sheltered and exposed) spans from the low tide mark to deep water, and includes alternating spurs and channels, or 'buttresses', of variable length (up to 300 m) and width (up to several metres). This zone stabilises the structure of the reef, reduces the impact of waves, and drains debris away from the reef. In contrast to the sheltered side, the exposed part of the slope is vulnerable to the impact of prevailing winds and swell. The shallow reef slopes are the most common area for dense hard coral beds.
- Reef Rim is above the low tide mark and this area includes the *Reef Crest*, which is the highest point within a reef system apart from cays (coral islands).
- Outer Reef Flat is generally sheltered by the reef rim, and therefore less exposed to the prevailing winds and sea. It is predominantly consolidated, with sandy areas in between. It may vary from tens to thousands of metres in width, and from centimetres to metres in depth.
- Inner Reef Flat is generally sheltered by a neighbouring higher outer reef flat or reef rim, and therefore less exposed to the prevailing winds and sea. It is predominantly sandy, with some consolidated areas in between, and comprises similar material to the outer reef flat, with comparable extent and depth.
- Lagoon is generally surrounded by the reef flat and/or reef rim, and is protected from wind and waves. Composition is mostly sand with individual patch reefs or coral bommies (outcrops) in between. Depth can vary from several metres to tens of metres.

The rugosity, or topographic roughness, of a reef can vary with many factors and is indicative of habitat complexity and rigour. As in other coastal waters, water depth over these features varies with the tides, so accurate hydrological charts are essential for navigation in reefal waters.

The benthic habitat type of a reef is determined by the composition and abundance of the different benthic and substrate cover types that exist within the reef system. The main benthic cover types include hard and soft coral, macroalgae, turf algae, crustose coralline algae, benthic microalgae, and seagrass. The most common substrate types include rock, rubble, sand, mud, and silt, the mineral composition of which depends on the reef origin.

Hard coral is commonly divided into different morphologies, such as branching, massive, plate, free living, foliose, or sub-massive. Hard and soft coral species vary in morphologies and colour, with soft corals having eight tentacles and hard corals having more or less than this number. Identification of individual species is mostly determined or verified by gene extraction.

Figure 20.8 Coral reef hierarchical scales



Source: Karen Joyce, James Cook University, and Chris Roelfsema, University of Queensland

Table 20.5 Four reef differentiation scales

Feature level	Linear extent (m)	Scale	Minimum mapping unit (ha)	Feature size (m)
Reef System or Region	1,000s–10,000s	< 1:1,000,000	n/a	n/a
Reef Type	100s–1,000s	1:500,000–1,000,000	25	400
Geomorphic Zone	10s–100s	1:100,000–500,000	5-25	75
Benthic Habitat Type	1s–10s	1:25,000–100,000	0.5–5	25

Source: Roelfsema *et al.* (2013).

20.6.2 Optical properties

Reflectance spectra of different living hard corals vary in both shape and value, with dominant features being in the wavelengths between 550 nm and 700 nm (Kutser *et al.*, 2003; Hochberg *et al.*, 2003; Leiper *et al.*, 2012). Most hard coral species exhibit peak reflectance around 610 nm and secondary peaks around 580 nm and 650 nm. Soft corals have similar reflectance characteristics with a minimum in ultraviolet (UV) wavelengths (Kutser *et al.*, 2000; 2001). Dead coral skeletons initially become overgrown with turf algae then macroalgae (usually red and green), with peak reflectance occurring around 600–605 nm and 650 nm. Given the small spectral differences between corals and algae, it is difficult to differentiate between different organisms using optical data alone. Most reefal rock is 'long dead' coral, which may support turf algae or crustose coraline algae, and since the latter provides an ideal surface to promote coral larvae settlements, its identification is important in coral surveys.

As with other shallow water applications, the existence of the water column above the feature of interest presents a further challenge for EO, since a given benthic type displays different observed reflectances at the water surface for differing water depths and water composition (such as chlorophyll and suspended matter; Botha *et al.*, 2013; see Section 6.1). The relevant light attenuation (absorption plus scattering) characteristics of the water column are:

- intensity decreases exponentially with increasing water depth (see Sections 5.1.1 and 8);
- absorption of all NIR wavelengths (> 700 nm), so NIR reflectance can be used to delineate shorelines (see Sections 7.2 and 11.3) as it only penetrates water for several centimetres;
- absorption of visible wavelengths increases with increasing wavelength, such that red wavelengths are absorbed at shallower depths than blue wavelengths (see Figure 5.10). The visible reflectances in EO imagery are the most useful for mapping benthic features, such as coral reefs.

The inherent spatial heterogeneity of coral reefs occurs at all scales. Typical reefal substrates, such as corals, macroalgae, rubble, and sand, may exhibit significantly different spectral and functional characteristics, yet can occur in a variety of mixtures within a square metre (see Figure 18.13). This spatial variation within individual image pixels is a problem for many EO image classification approaches (see Volume 2E). In this context, spatial analysis tools such as OBIA are more appropriate (see Section 20.6.3).

Reefal waters are typically clear due to low concentrations of phytoplankton and sediments, with most attenuation being due to changes in water depth (see Figure 18.13). However, the air-water interface and surface roughness can both significantly influence the spectral signal entering and leaving the water column (see Sections 4.3 and 8.1.3). Lidar can be combined with other sources of EO data, such as hyperspectral or high spatial resolution multispectral imagery, to enhance mapping of coral reefs.

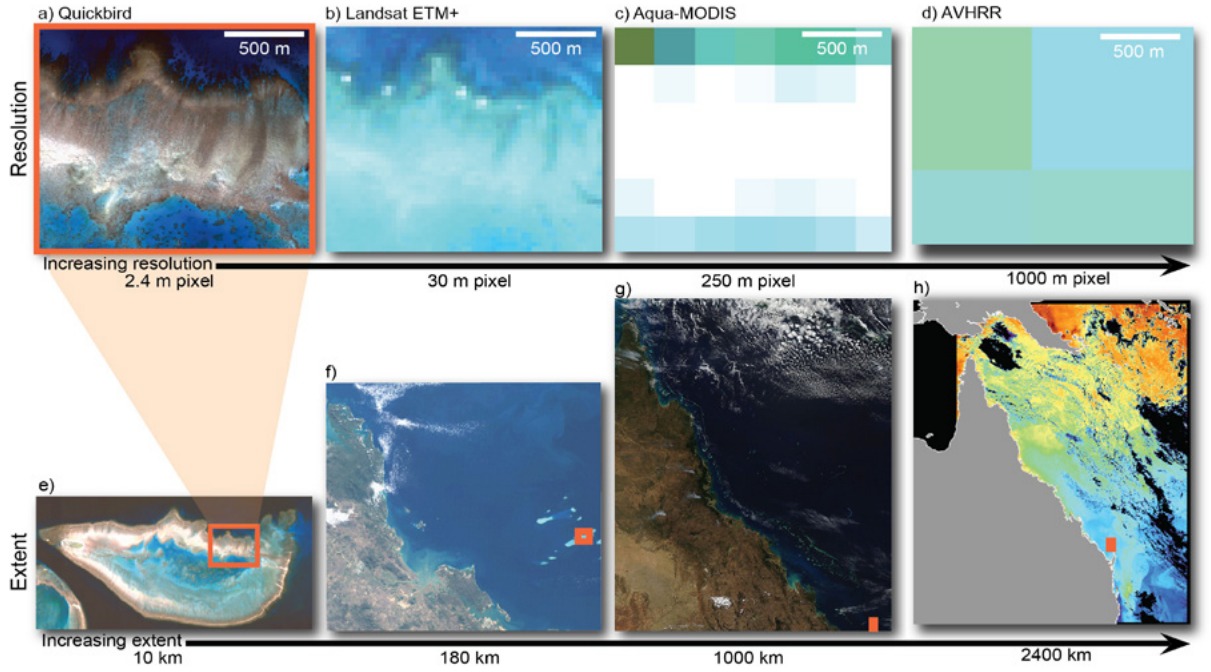
20.6.3 EO datasets and applications

Some of the properties of coral reefs and their aquatic environments that have been mapped using EO data include reef type, extent, geomorphic zonation, benthic habitat type (composition, abundance, sedimentology), shape (bathymetry, rugosity), water quality (chlorophyll concentration, sedimentation; see Section 19), biochemistry (primary production and calcification), sea surface temperature (see Section 14), bleaching (see Excursus 20.3), and exposure to prevailing winds (see Volume 2C— Sections 6.2 and 6.3).

Mapping coral reef features, either by discriminating benthic features or estimating biophysical properties (such as depth and pigment concentration) requires EO data with appropriate spectral and spatial dimensions (see Volume 1B—Section 1). A greater number of benthic and substrate cover types can be mapped from EO imagery as the number of spectral bands is increased and pixel size decreased (see Figure 20.9). This corresponds to the progression in Table 20.5 from mapping reef/non-reef, to mapping geomorphic zones and reef biotope zones, to mapping benthic communities.

Figure 20.9 Comparison of spatial resolution and extent for four EO sensors

The different spatial dimensions of EO image sources (Quickbird, Landsat ETM+, Aqua/MODIS, and AVHRR) are compared using Heron Island reef, in the southern GBR, Queensland. Images (a–d) show the effects of progressively larger pixel sizes for a reef section spanning 1.5 km, while images (e–g) show variations in image extent, ranging from coverage of a single reef to the entire GBR.



Source: Hedley *et al.* (2016b) Figure 2

Similarly, when mapping coral reef biophysical properties (whether in the water column, benthos, or substrate), more detailed and more precise estimations of biophysical properties can be derived by using an increased number of relevant spectral bands (see Section 8.5). Research on hydro-optics in waterbodies and photosystems in corals has established those wavelength regions that are absorbed by specific chemicals and processes. Accordingly, reflectance signatures resolving these features can be used in algorithms to estimate or map them for each pixel. Large numbers of spectral bands with narrow bandwidths also permits specific absorption features or inflection points (produced by photosynthetic or non-photosynthetic pigments) to be resolved (Hochberg and Atkinson, 2000, 2008; Hedley and Mumby, 2002; Hochberg *et al.*, 2003, 2004; Mumby *et al.*, 2004, Hedley *et al.*, 2012).

The most appropriate, simplest, and historically relevant dataset for reefal studies has been aerial photography, which typically covers from local to regional scales (several km^2 to 100s of km^2), with records stretching back as far as the 1930s (Hernandez-Cruz *et al.*, 2006). Multispectral spaceborne systems cover larger areas than aerial photography (10^4–10^6 km^2) and offer significant repeat capacity at spatial resolutions adequate to the reef feature types and levels being mapped. Hyperspectral sensors (both spaceborne and airborne), with additional spectral bands, much narrower bandwidths, and greater ability to identify specific targets, are particularly relevant to reefal studies (Karpouzli *et al.*, 2004; Garcia *et al.*, 2018, Kobryn *et al.*, 2013). Lidar data has proved useful for bathymetric studies (see Section 13.4.1) and reef geomorphological analysis.

The first instance of using multispectral data for coral reef mapping involved Landsat MSS coverage of the GBR in the 1980s (Smith *et al.*, 1975; Jupp *et al.*, 1985), to estimate bathymetry and reef geomorphologic zones. In the 1990s, a systematic classification scheme of benthic features was developed (Mumby and Harborne, 1999), which has continued to be popular for habitat mapping of coral reefs. Low spatial resolution sensors, such as AVHRR and MODIS, are also relevant to reefal studies for observing regional scale, biological variables such as chlorophyll concentration.

Coral reef structure is closely related to exposure to ocean swells (Andréfouët *et al.*, 2001). Spatial variations in the distribution of plant and animal species are usually strongly influenced by the prevailing wind and wave energy regimes in the littoral and sublittoral zones (see Section 20.6.1). Bathymetric datasets can be processed to show the degree of exposure of shallow water features to wave climate

or sunlight. As detailed in Volume 2C—Sections 6.2 and 6.3, the 'exposure' transformation is similar to relief shading with the 'Sun position' effectively on the horizon. Where detailed bathymetry is not available, EO imagery showing visible blue or green wavelengths can be used as a surrogate for water depth. For example, in Figure 20.10 comparable exposure images have been derived from both Landsat MSS imagery (green band) and a sparse grid of water depth samples. Such transformations have proved useful for mapping subsurface morphology, enabling vulnerable areas to be highlighted for early management intervention.

Thermal sensors are also valuable for mapping conditions conducive to coral bleaching (Abram *et al.*, 2003; Maina *et al.*, 2008; see Excursus 20.3). Since bleached corals reflect electromagnetic radiation (EMR) more strongly than healthy corals at all wavelengths (Holden and LeDrew, 1998, 1999; Yamano and Tamura, 2004), their occurrence is likely to be detectable using multispectral EO. The clear and calm waters that typify reefal environments, and the exposure of reefal system at high tide, allow their shorelines to be delineated clearly using NIR bands (see Section 11.3). The varying shorelines of the intertidal region can be regarded as contours, and also used to map topography (Yamano, 2007).

Figure 20.10 Exposure (directional) filtering

Comparable images have been derived for John Brewer Reef, Queensland, by directional filtering of Landsat MSS imagery and measured depth data. Bright areas indicate a higher local slope and aspect to the selected wind direction, and in the prevailing wind direction these areas indicate greater exposure. Darker areas infer sheltered positions relative to that direction. The resulting images highlight reef morphology and show exposure to the prevailing wind direction (southeast).

a. Transect samples of measured water depth formed a sparse grid of points when registered with Landsat MSS imagery. (Note: null pixels are shown as black.) This sparse dataset was interpolated to create a continuous depth image before exposure (directional) filtering.

Measured depth data | Interpolated depth data | Exposure on interpolated depths



b A Landsat MSS4 (green band) image for John Brewer Reef was despiked and smoothed before directional filtering to show exposure to the prevailing wind direction. The exposure image derived from EO data offers an economical approximation to sourcing measured depth data.

Landsat MSS4 image | Preprocessed MSS4 image | Exposure on preprocessed MSS4



Source: Harrison and Jupp (1990) Plate 6

Excursus 20.3—Coral Bleaching

Further information:

https://coralreefwatch.noaa.gov/satellite/index.php
http://www.bom.gov.au/environment/activities/reeftemp/about.shtml
https://www.aims.gov.au/docs/research/climate-change/coral-bleaching/coral-bleaching.html

Coral reefs around the world are being increasingly threatened by coral bleaching. This phenomenon occurs when corals are stressed by changes in environmental conditions, such as temperature, light, or nutrients. They react by expelling the symbiotic algae that live in their tissues, then turn completely white. The symbiotic algae, colloquially called zooxanthellae, are photosynthetic and provide their host coral with food in return for protection. Their presence gives the corals a distinctive brown hue, and the fluorescent pigments produced by the host add the vibrant colours that characterise living corals.

Acute or prolonged stressful environmental conditions cause a breakdown in this symbiotic relationship, first revealing the fluorescent pigments, and then leaving the white calcium carbonate skeleton visible through the coral tissue. Bleached corals can no longer gain energy from photosynthesis, and if bleaching persists for an extended period, corals will starve and die. For those that survive, bleaching can deplete the corals' energy resource to the extent that corals do not reproduce for one or two years. The threat to corals increases as the bleaching events become more frequent because they have no time to recover.

Mass coral bleaching is caused by unusually high water temperatures that stress corals. Continuous monitoring of sea surface temperature at global scales provides researchers and stakeholders with tools to understand and better manage the complex interactions leading to coral bleaching. When bleaching conditions occur, these tools can be used to trigger bleaching response plans and support appropriate management decisions.

Bleaching has been observed on the GBR since 1982, with severe bleaching events occurring in the summers of 1998, 2002, and 2006. Coral mortality appears to increase with the intensity of the bleaching event, which is determined by how much and for how long temperatures remain above the maximum mean summer temperatures.

The NOAA Coral Reef Watch Program (*https://coralreefwatch.noaa.gov*) provides current reef environmental conditions to quickly identify areas at risk for coral bleaching (Strong *et al.*, 2006, 2011). This program uses EO datasets with modelled and *in situ* data to develop and operate a decision support system to monitor stress factors in coral reef ecosystems. The Version 3.1 products use global, daily sea surface temperature (SST; see Section 14.4.4) at 5 km resolution to highlight anomalies and bleaching hotspots through time (Liu *et al.*, 2017). These products offer managers of coral reef systems an opportunity to determine location of heat stress, and incorporate that information into their management strategies of marine jurisdictions.

In Australia, a similar methodology has been used to develop the ReefTemp Next Generation tool (*http://www.bom.gov.au/environment/activities/reeftemp/reeftemp.shtml*; Garde *et al.*, 2013, 2014). This near real time operational tool provides information on coral bleaching risk for the GBR region, using higher resolution (~2 km), daily (with gaps), 14-day composite (near gap-free) nighttime SST data from selected IMOS SST data sources (see Section 14.5.1). Because these SST data have been calibrated to the Australian region, these products are more accurate than their global counterpart.

With the current high spatial and temporal resolution satelites we have the opportunity to assess the presence of coral bleaching. For example, the Allen Coral Atlas monitoring system (see Section 20.8) is using Sentinel-2 time series imagery, acquired while Degree Heating Weeks (DHW) provided by NOAA Coral Watch are low, to create a baseline reflectance image (Hedley *et al.*, 2018). As other time series datasets become available, they can be assessed and compared with this baseline.

20.6.4 Mapping biophysical properties

Geomorphic zonation classes are differentiated by a combination of pixel colour, texture of groups of pixels, water depth, wave action, and neighbourhood relationships (Mumby *et al*., 1997a; Andréfouet *et al*., 2006; Hamylton, 2017; Roelfsema *et al*., 2018, 2020; Andrefouét and Bionaz, 2021). Similarly, to delineate benthic zones the attributes of water depth, consolidation, slope, and waves are most appropriate.

Traditionally, reef classification relied on expert knowledge and detailed field observations to group natural features into relevant, but often inconsistent, classes (see Figure 20.11). Automated classification methods have been developed to both avoid inconsistency of labels and definitions, and assist reef managers to better understand the underlying biophysical attributes (Kennedy *et al*., 2021). Global mapping of geomorphic zones relies on integrating a variety of *in situ* data with high resolution EO datasets using compute-intensive techniques such as ML and OBIA (Lyons *et al*., 2020). For example, the Allen Coral Atlas global reef mapping project called *Reef Cover* combines EO data and geo-ecological information to map coral reefs at a variety of spatial scales (Kennedy *et al*., 2021; see Figure 20.12).

Production of maps quantifying biophysical properties or processes on coral reefs and their surrounding environments can only be done from fully 'corrected'[26] images (see Volume 2), acquired from spaceborne or airborne platforms (see Volume 1A). Several approaches are commonly used to deliver maps of coral reef biophysical properties:

- Unmixing techniques are used to estimate the relative area of each pixel occupied by a set of coral reef benthic cover types (e.g. coral, sand, algae). As detailed in Volumes 2E and 3A, these techniques assume the image pixel is larger than the features to be mapped and are applied to images which have had the influence of the water column removed (Hedley and Mumby, 2003; Hedley *et al*., 2004; Goodman and Ustin, 2007; Lesser and Mobley, 2007). The mathematical solutions required for these techniques become more accurate as the number of uncorrelated input variables (spectral bands in this case) increases; hence hyperspectral image data are used predominantly in this approach (Hedley, 2013).
- Inversion techniques use empirical or analytical mathematical solutions to extract biophysical information from image pixels, including water depth, concentrations of organic and inorganic material in the water column, and benthic/substrate reflectance signatures (see Section 8.4).

Benthic habitats are mostly categorized either using a hierarchy of geomorphological classes or a set of ecological classes (Mumby and Harborne, 1999; Andréfouët, 2011; Kennedy *et al*., 2021). Classification results are enhanced when relevant spectral libraries are available for referencing. Classification approaches may involve spectral and/or textural information as detailed in Volume 2E, and other spatial and neighbourhood relationships (see Volume 2A—Section 10).

Inversion methods can deliver a range of products relating to the model inputs, including bathymetry, benthic type, and concentration of water constituents (Hedley, 2013). Secondary outputs can further be derived from these initial results. Thus, these models allow derivation of bottom reflectance, spectral absorption coefficients for the water column, or relative light conditions in the benthos.

Moderate resolution imagery, in conjunction with benthic field data and other biophysical properties (including water depth, slope, and wave exposure), was used with semi-automated OBIA and ecogeomorphological rules to generate maps of geomorphic zonation and dominant benthic cover (reef top). These input datasets were then used to create an ecological model that predicted dominant coral type (reef slope) for the shallow offshore reefs of the Capricorn Bunker Group in the southern GBR (Roelfsema *et al*., 2018; see Figure 20.13) and central GBR (Roelfsema *et al*., 2020).

The ecological and geomorphological characteristics of geomorphic zones and benthic classes (Kennedy *et al*., 2021) could be used to form ecogeomorphological rules to differentiate them. Examples include:

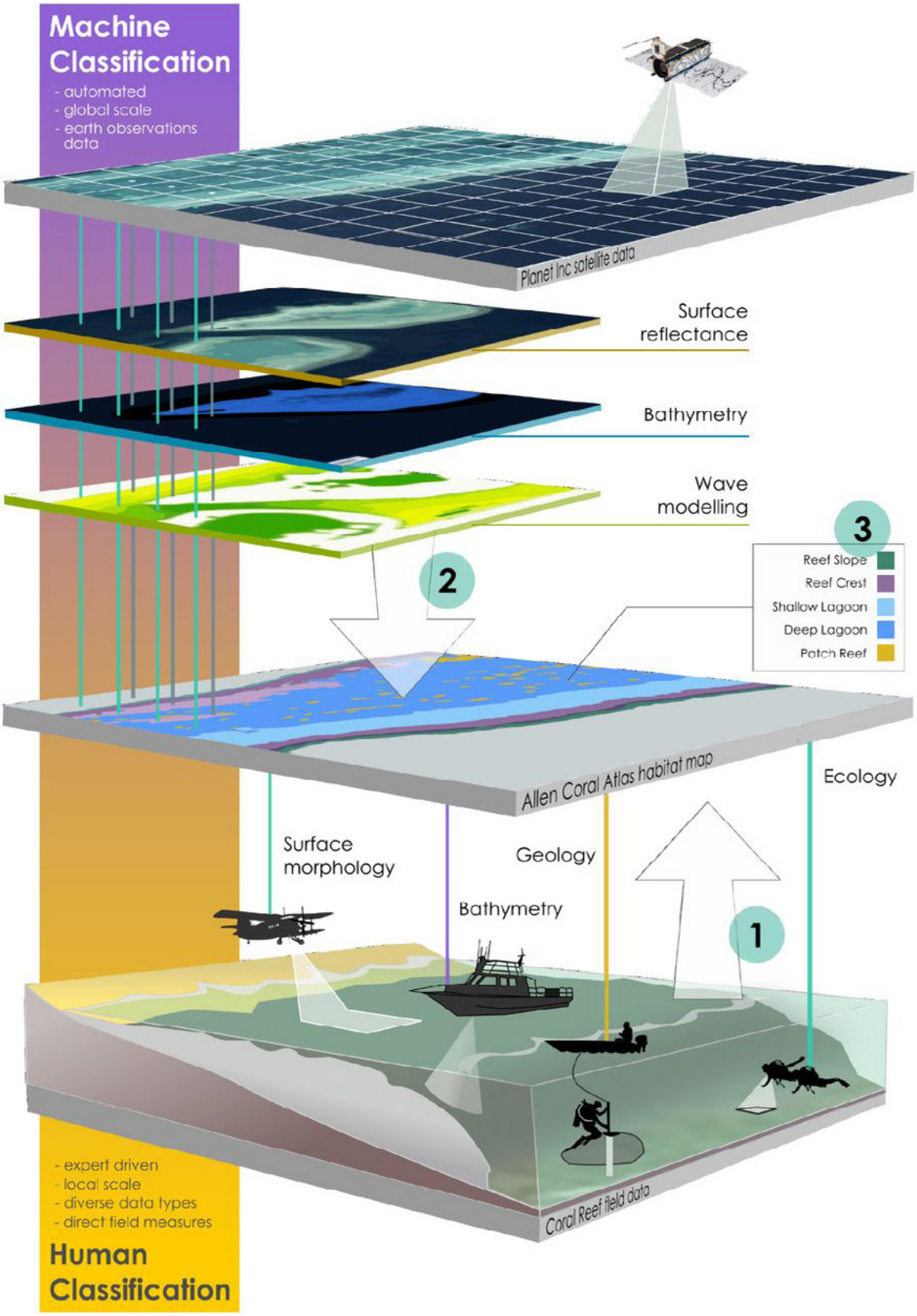
- colour and texture of groups of pixels (objects)—for example, inner reef flat has less texture, with predominantly sand cover and mostly homogenous colour, whereas the outer reef flat has more texture due to a mixture of sand, rock, coral, and algae;
- biophysical attributes such as depth, slope, consolidation, and waves—for example, reef crest is shallow, horizontal, consolidated, with high wave energy, whereas back reef slope, is deep, sloping, partly consolidated, with low wave energy; and
- spatial neighbourhood attributes based on adjacency and enclosing between classes—for example, reef crest is adjacent to outer reef and slope, and could not be enclosed by slope.

As a result of these rules, contextual editing was applied to machine learning based classifications of high and moderate resolutions satellite imagery for mapping of large extent reef systems, such as the full extent of the GBR, and reef systems globally (Roelfsema *et al*., 2021, Lyons *et al*., 2020).

26 Corrections in this context include both geometric and radiometric corrections as detailed in Volume 2.

Figure 20.11 Approaches to reef mapping

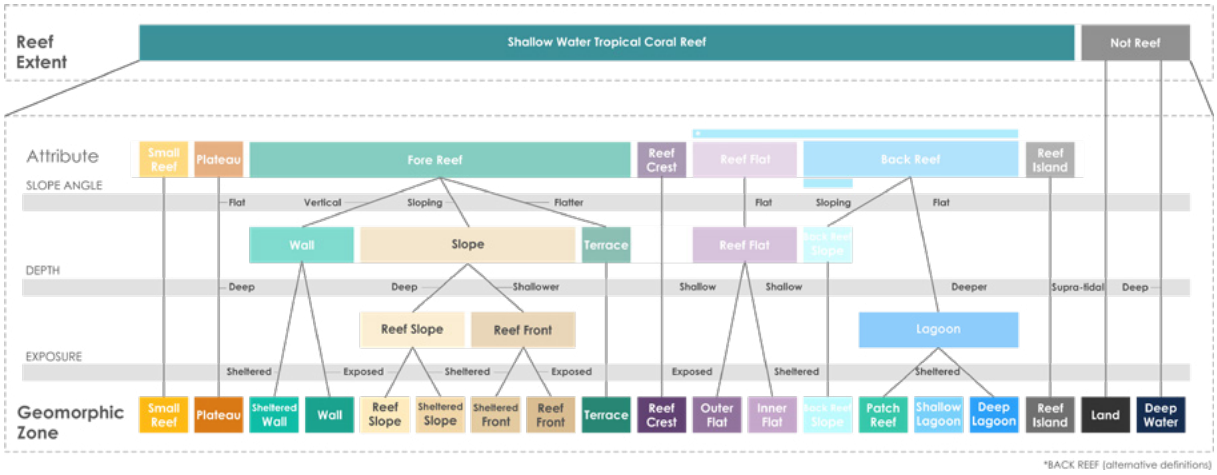
Reef classification has traditionally relied on human interpretation of field data at a local scale. By integrating decades of local scientific knowledge (1) with global EO imagery (2), automated methods, such as Reef Cover, can define consistent classes across of range of spatial scales (3).



Source: Kennedy *et al.* (2021) Figure 1

Figure 20.12 Automated classification of geomorphic zones

Three fundamental characteristics, water depth, slope angle and exposure to waves, can be used to define the underlaying geomorphic structural features of reefs.



Source: Kennedy *et al.* (2021) Figure 2

Monitoring of coral health is also being conducted using fluorescence imaging lidar instruments (Sasano *et al.*, 2012). Most live corals that build reef structures contain fluorescent proteins, which, when excited by UV radiation, fluoresce in blue-green wavelengths (Alieva *et al.*, 2008). Excitation using radiation at 365±5 nm has been shown to produce a fluorescence peak between 450 nm and 550 nm from live coral, but not from dead coral, sand, or marine vegetation. Imaging lidar systems have been deployed on boats to monitor coral health in conjunction with diving patrols and satellite EO (Sasano *et al.*, 2012).

Ongoing research into EO of coral reefs follows three fundamental paths of development:

- Techniques that compensate for water column and atmosphere effects in the EO signal (Lyzenga, 1978, 1985; Gordon and Clark, 1980; Bierwirth *et al.*, 1993; Gordon, 1997; Lee *et al.*, 1999; Louchard *et al.*, 2003; Gao *et al.*, 2009; Dekker *et al.*, 2011). For coral reefs, an important implication from this research is that for passive sensors to be useful, the substratum must be visibly observable in the imagery. Optically deep areas, or areas with high turbidity, cannot be mapped using passive techniques alone, so require active systems (see Sections 8 and 18).
- Higher level products that provide insight into reef status or function (Atkinson and Grigg, 1984; Mumby *et al.*, 1997a; Hochberg and Atkinson, 2000, 2008; Roelfsema *et al.*, 2002; Lesser and Mobley, 2007; Palandro *et al.*, 2008; Purkis *et al.*, 2008). A number of these products are currently used routinely to monitor reef condition.
- Techniques that integrate satellite-based OBIA approaches and physical coral reef attributes (such as depth, slope and waves) with ecogeomorphological properties (Roelfsema *et al.*, 2018, 2020; Lyons *et al.*, 2020).

Products derived from EO data are increasingly being used to monitor changes in reef composition over time. Pressures such as sedimentation, sea level rise, increased storm frequency, ocean acidification, and temperature changes threaten the longevity of coral reefs (Wilkinson, 2008). Managers need to be able to monitor changes using timely and reliable methods (Cochran, 2013), such as analysis of the growing time series of imagery from airborne and satellite borne sensors (Goodman *et al.*, 2013). To ensure high levels of accuracy from such analyses, it is essential that *in situ* data is available for historical imagery. It is also advisable to select imagery acquired during similar diurnal and seasonal conditions (see Volume 2D). For example, while the spectral characteristics of macroalgae are similar to those of corals making these two features difficult to distinguish, the distribution and abundance of macroalgae can change seasonally in contrast to the slower development of coral. An EO-based ecological statistical model was also used to predict coral type along reef slope on the GBR (Roelfsema *et al.*, 2018, 2020).

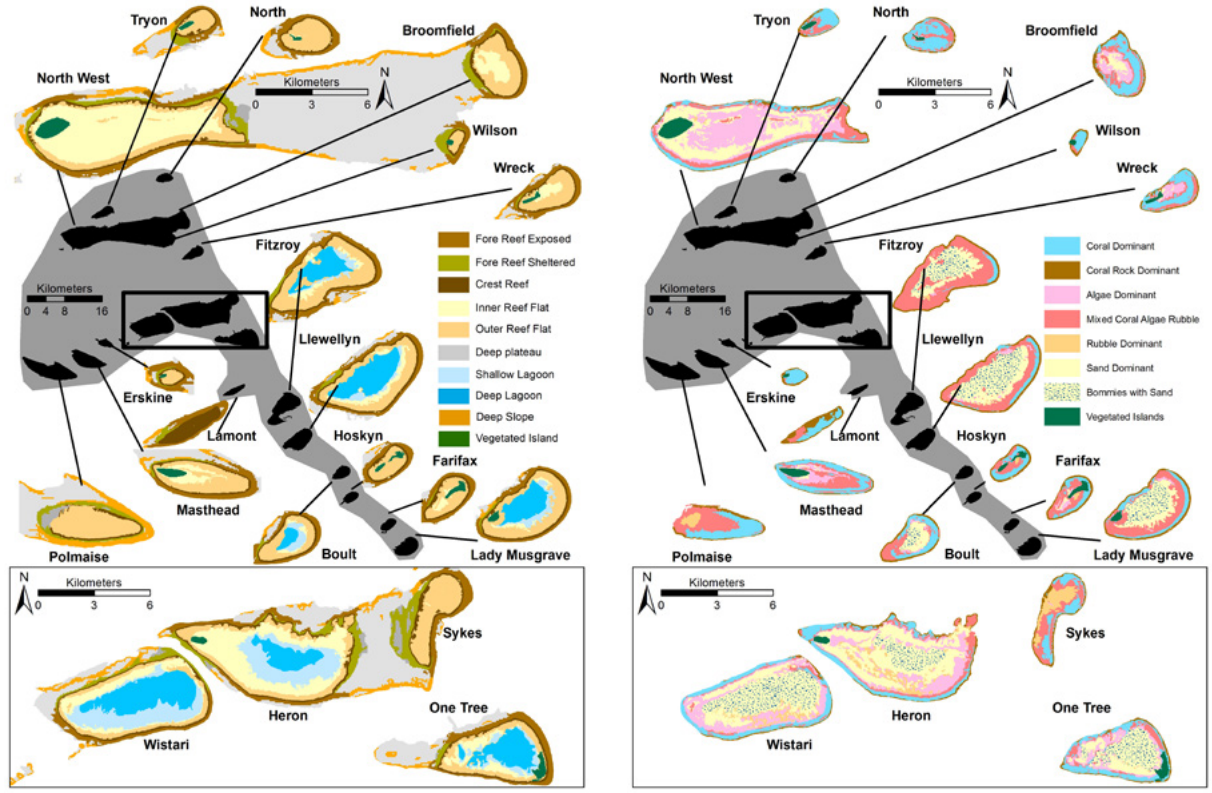
The eReefs platform integrates a suite of process models that simulate hydrodynamic state, sediment transport, water quality, carbon chemistry, and basal ecology (Baird *et al.*, 2021), which enables hindcasting, nowcasting, and forecasting for the GBR lagoon and reef matrix (see Volume 2D—Excursus 14.4). This platform uses EO datasets and *in situ* monitoring to assess risks and management options based on past, current, and projected environmental conditions (see Figure 20.14).

Figure 20.13 Mapping reef biophysical properties

These mapping results for the shallow offshore reefs of the Capricorn Bunker Group in the southern GBR were derived using OBIA of Landsat-8 OLI imagery (acquired on 10 April 2017) in conjunction with ecological modelling of data for field-based benthic composition, reef impact, and wave exposure.

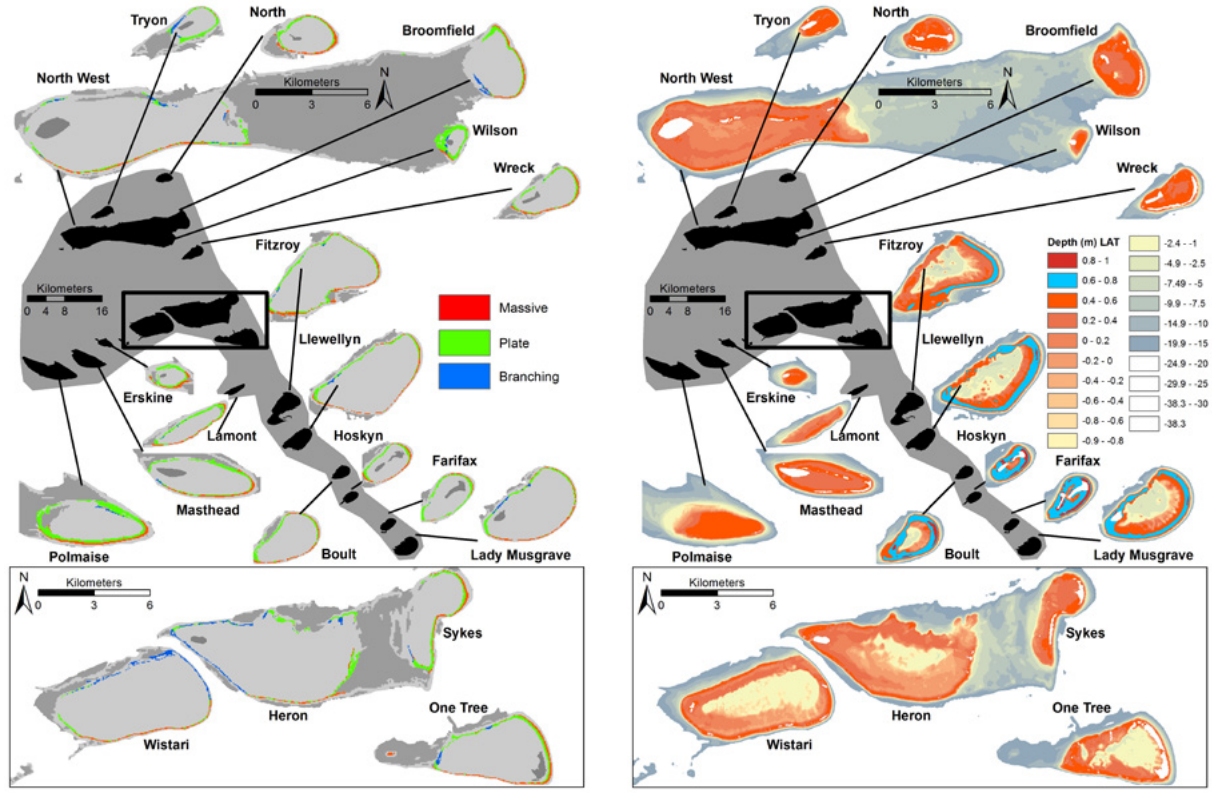
a. Geomorphic zonation

b. Dominant benthic cover, reef top



c. Predicted dominant coral type, reef slope

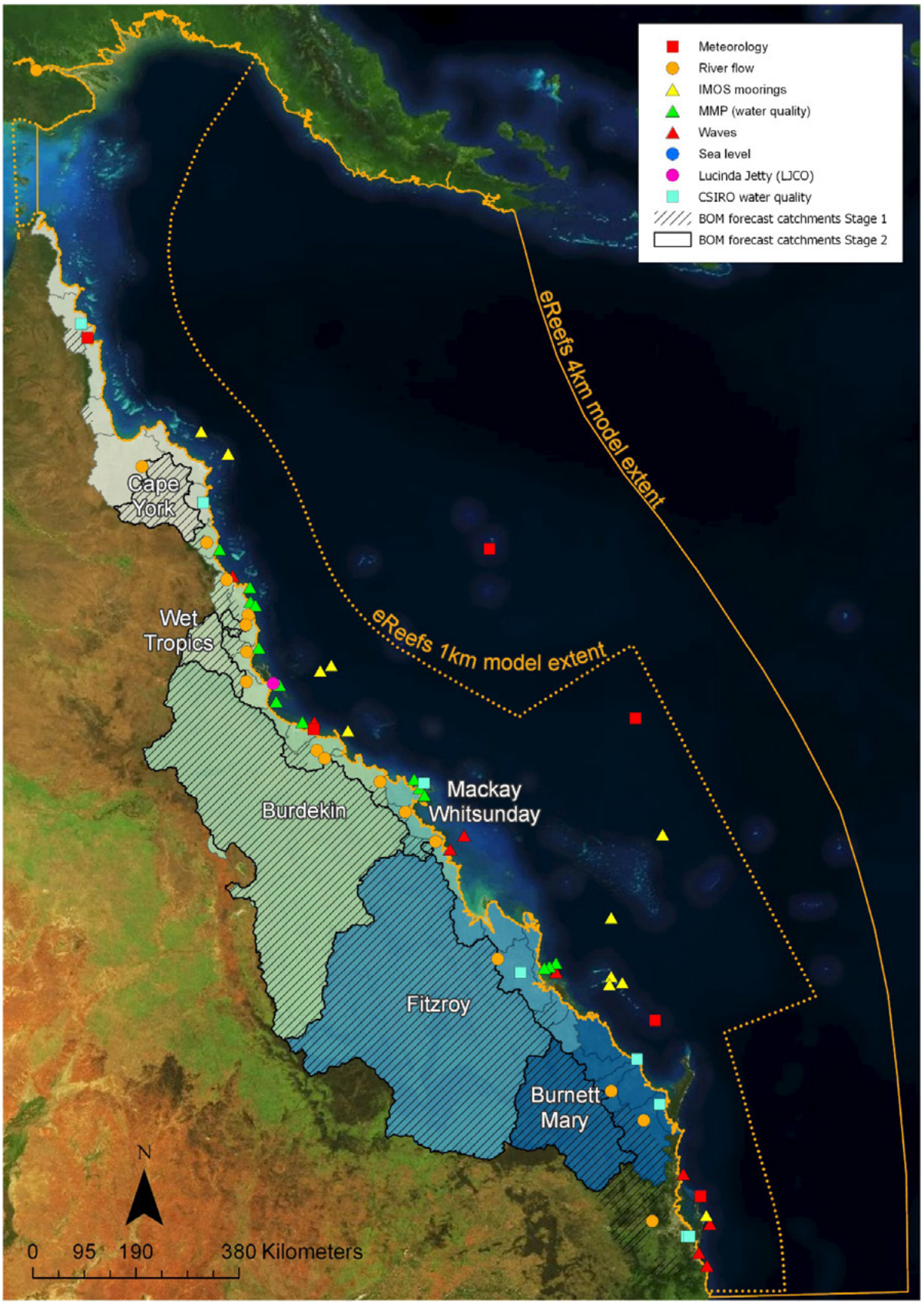
d. Water depth



Source: Chris Roelfsema, University of Queensland

Figure 20.14 eReefs modelling extent

eReefs uses a range of EO-based and *in situ* monitoring datasets to model environmental parameters over the GBR region at 1 km or 4 km resolution.



Source: Steven *et al.* (2019)

In future, it is likely that multispectral and hyperspectral imagery can be used to derive reef properties such as the amount of live coral, algae and sediment cover, structural forms of coral cover, benthic microalgae biomass, and coral and algae light absorption efficiency. These properties provide key links for studies assessing coral productivity, coral reef biochemistry, carbon fluxes, and nutrient dynamics on reefs.

20.7 Marine Fauna

The broad concept of biodiversity is detailed in Volume 3A—Section 18. In recent years both overexploitation and climate variations have modified marine ecosystems (Hazen *et al*., 2018). These factors resulted in variability in fish recruitment and changes in species dominance. This situation has ultimately encouraged an ecosystem-oriented approach to managing fisheries globally (Cury *et al*., 2008), namely "a comprehensive, integrated management of human activities, based on the best available scientific knowledge about the ecosystem and its dynamics, in order to identify and take action on influences which are critical to the health of the marine ecosystem, thereby achieving sustainable use of ecosystem goods and services and maintenance of ecosystem integrity" (IOCCG, 2009).

Since the spatial and temporal variability of phytoplankton directly impacts the distribution of higher order marine organisms (Tweddle *et al*., 2018), marine assessments of biodiversity have focused on monitoring fish populations and the distribution and abundance of specific species (Reynolds *et al*., 2017). Below we consider the role of EO in two aspects of observing marine biodiversity: fishery stock assessment (see Section 20.7.1), and large marine animal counts (see Section 20.7.2). Global monitoring programs for marine biodiversity are considered in Section 21.1.

The assessment of coastal and marine biodiversity using remote sensing is largely based on the correlation of traits of organisms and of species' natural 'tolerance windows' with the habitats in which they live, and then tracking with remote sensing how these habitats change over time.
(Canonico et al., 2019)

20.7.1 Fisheries

Pelagic sampling methods, including catch data, tagging, and baited stereo-videography, are reviewed by Bouchet *et al.* (2018) in terms of their suitability for monitoring within MPA (see Excursus 20.2). Different sampling methods span different spatial and temporal scales, in terms of both data resolutions and extents (see Figure 20.15). Such methods can be integrated with EO-based environmental data to assess fisheries stocks, determine environmental variables driving the distribution of specific species, and/or model species distribution (Enever *et al.*, 2017; Harrison *et al.*, 2017).

A range of EO datasets has been used to monitor different aspects of fisheries, which are also relevant for managing marine habitats (IOCCG, 2009; Chassot *et al.*, 2011; Klemas, 2013; Kacev and Lewison, 2016). These include:

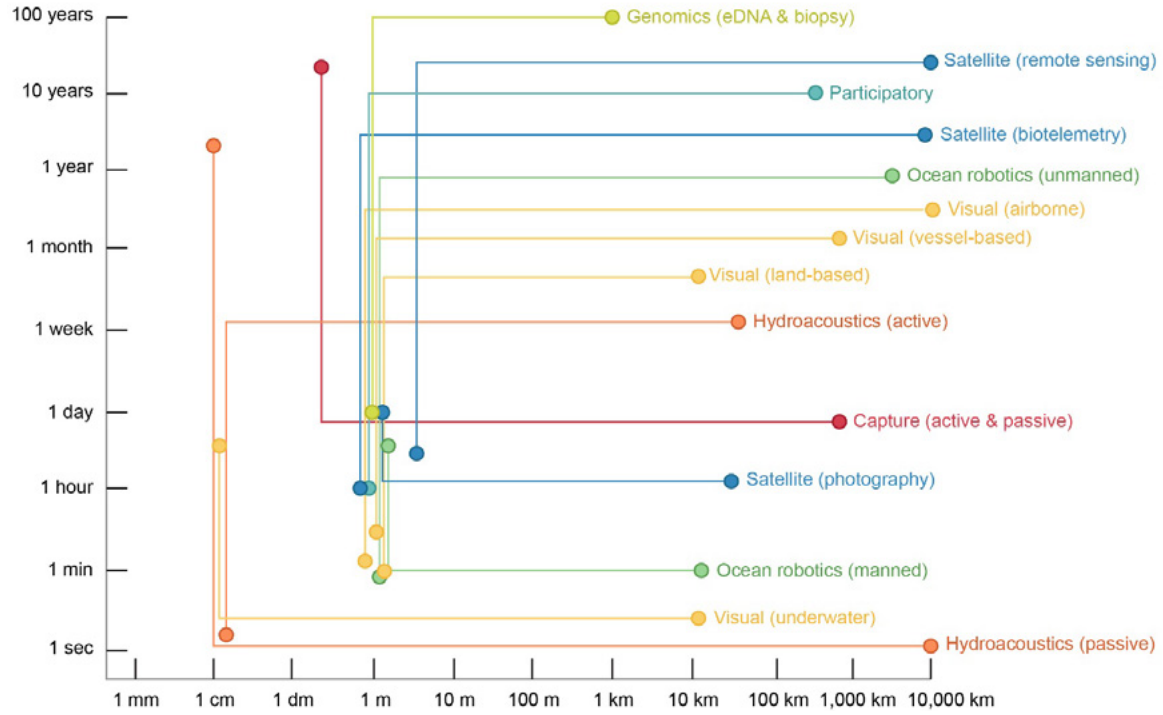
- ocean colour—EO-based chlorophyll a estimates (see Section 18.6) can be used to infer phytoplankton biomass or net primary production (NPP). Thus, algal biomass can be linked with the health of pelagic ecosystems and larval fish survival (Platt *et al.*, 2003);
- sea surface temperature (SST)—is correlated with species diversity for many organisms in coastal and open ocean environments (Tittensor *et al.*, 2010; see Section 14), with thermal fronts being associated with high concentrations of fish and fish food (Bakun, 2006; Reese *et al.*, 2011); and
- water circulation—since locations of some fish (and other migratory) species is associated with circulation features (Scales *et al.*, 2014; see Section 17), these can be used to model species distributions (Rajkumar and Shanmugam, 2018).

For example, Platt and Sathyendranath (2008) identified a number of phytoplankton characteristics using EO-derived ocean colour, including the annual production and loss rates, spatial variance in biomass, initiation, duration, and timing and intensity of the maximum intensity of algal blooms. Since these characteristics are particularly relevant to pelagic ecology, EO time series datasets have been used to analyse ecosystem fluctuations and their interactions with valued fish stocks (Platt *et al.*, 2003). Climatological records are also valuable for validating phenological studies and differentiating anomalies from seasonal variations (Payne *et al.*, 2017). Hobday *et al.* (2010, 2011) highlighted pelagic habitats in Australia's southern and eastern ocean territory to predict the abundance of southern bluefin tuna using EO-based datasets. These forecasts now operationally model habitat preferences and ecological niches to enable sustainable management in two aquatic zones (Payne *et al.*, 2017):

- Great Australian Bight (Eveson *et al.*, 2015; *http://www.cmar.csiro.au/gab-forecasts/*); and
- Southeast Australia (Hobday *et al.*, 2011; *https://www.afma.gov.au/fisheries-services/sbt-zones*).

Figure 20.15 Pelagic sampling methods

Varying temporal and spatial scales of pelagic sampling methods used in marine monitoring are compared.



Source: Bouchet *et al.* (2018) Figure 2.3

Fish provide 20% of the world's protein and are the main source of protein for over a billion people. The extraction and cultivation of fish directly provides around 41 million jobs (FAO, 2007), and indirectly employs 162 million people (UNEP, 2006).
(IOCCG, 2009)

20.7.2 Animal counts

While large marine animals, such as penguins (Fretwell *et al.* 2009, 2012; Lynch *et al.*, 2012) and seals (LaRue *et al.*, 2011; McMahon *et al.*, 2014), have been counted using high resolution satellite imagery, automated processing methods enable frequent counts and simplify the use of time series datasets for trend detection. For example, Fretwell *et al.* (2014) used a simple threshold in the panchromatic and coastal (far blue) bands to count whales. However, such methods only observe animals on or near the ocean surface.

The movement of individual aquatic fauna can be tracked by telemetry, which involves attaching an electronic device to an organism that automatically logs or transmits selected data to a receiver. Relevant data for aquatic organisms would include:

- location—horizontal and vertical;
- water parameters—such as depth, temperature, or salinity; and/or
- physiological attributes—such as digestion, metabolic rate, or respiration.

In recent decades, such telemetric methods have delivered new insights into the dynamics of a range of marine species, including their dietary preferences, migration patterns, habitat characteristics, and interactions between predators and prey. Acoustic telemetry allows smaller tags to be deployed than are required for satellite telemetry so can be used on smaller creatures, but the latter can transmit data in shorter time intervals so deliver more continuous time series (Hussey *et al.*, 2015). Acoustic telemetry also requires detectors to be located within a kilometre from a transmitter so are mostly limited to coastal and freshwater studies. Telemetric datasets are being integrated with oceanographic and isotopic datasets to characterise foraging patterns of selected species (Lowther *et al.*, 2013). More recently, biologging devices, which quantify the fine scale, three-dimensional movements and physiological status of organisms, as well as their environmental context (Lennox *et al.*, 2017), are providing more detailed insights into their foraging behaviour (Andrzejaczek *et al.*, 2019) and other interactions with the marine environment (Lennox *et al.*, 2019).

The distribution of selected species has also been modelled using habitat mapping approaches. Forecasting products to assist in operational monitoring of protected species have been developed using tracking data in combination with EO-based environmental variables (including SST, chlorophyll a concentration, altimetry, wind data, and/or bathymetry; Payne *et al.*, 2017). Bycatch data—marine creatures caught unintentionally during commercial fishing activity—also provide valuable information for habitat mapping. Examples of operational EO-based nowcast and forecast ecological systems include:

- TurtleWatch (*http://www.pifsc.noaa.gov/eod/turtlewatch.php*)—developed by NOAA to identify loggerhead turtle habitats north of the Hawaiian islands, then alert fishermen to areas where they might entangle loggerheads (Howell *et al.*, 2008, 2015); and
- WhaleWatch (*https://www.westcoast.fisheries.noaa.gov/whalewatch/*)—funded by NASA and publicly available from NOAA, provides near real time information on the locations of blue whales along the US west coast with the goal of preventing ship strikes and other threats (Hazen *et al.*, 2017).

A similar project to predict the distribution of the endangered North Atlantic right whale (*Eubalaena glacialis*) is being undertaken by modelling the abundance and timing of its main prey, *Calanus finmarchicus* (IOCCG, 2009). More recently, species distribution models, which use daily EO datasets to track oceanographic conditions in conjunction with satellite telemetry and fisheries observer data, have also been developed to reduce bycatch and thus support a sustainable fishing industry (Hazen *et al.*, 2018).

The abundance and distribution of marine megafauna in coastal waters are being tracked by satellite tags using either GPS transmitters (Marsh *et al.*, 1990; Tomkiewicz *et al.*, 2010; Gredzens *et al.*, 2014) or acoustic tracking systems (Zeh *et al.*, 2015; Dwyer *et al.*, 2015). Bayliss and Hutton (2017) observed a strong correlation between dugong abundance and the extent of seagrass that was mapped using Landsat imagery. Such datasets are being used to identify hotspots in order to sustainably manage indigenous harvesting, and better understand the dynamics of both dugong populations and seagrass habitat.

20.8 Further Information

Biodiversity

Global Ocean Observing System (GOOS): *https://www.goosocean.org/*

Marine Biodiversity Observation Network (MBON): *https://marinebon.org/*

Ocean Biogeographic Information System (OBIS): *https://obis.org/*

GeoHab: Marine Geological and Biological Habitat Mapping: *http://geohab.org*

Butler *et al.* (2010, 2017)

Atlas of Living Australia: *https://www.ala.org.au*

Marine Biodiversity Hub: Research for understanding and managing Australia's marine biodiversity: *https://www.nespmarine.edu.au*

Western Australian Marine Science Institution (WAMSI): *https://www.wamsi.org.au*

eAtlas (Australia's Tropical Lands and Seas): *http://e-atlas.org.au/*

Global Aquatic Ecosystem Assessment

ChloroGIN: *http://www.chlorogin.org/*

Blue Carbon

The Blue Carbon Initiative: *https://www.thebluecarboninitiative.org/*

Intergovernmental Oceanographic Commission: *http://www.unesco.org/new/en/natural-sciences/ioc-oceans/sections-and-programmes/ocean-sciences/ocean-carbon/coastal-blue-carbon/*

Marine Parks

Parks Australia: *https://parksaustralia.gov.au/marine/parks/*

Australian Marine Parks Science Atlas: *https://atlas.parksaustralia.gov.au/amps*

Wetlands

Directory of Important Wetlands in Australia: *https://www.awe.gov.au/water/wetlands/australian-wetlands-database/directory-important-wetlands*

Australian Wetlands Database: *https://www.awe.gov.au/water/wetlands/australian-wetlands-database*

Mangroves

Stewart and Fairfull (2008)

IUCN (2017)

MangroveWatch: *http://mangrovewatch.org.au/?option=com_content&view=section&layout=blog&id=18&Itemid=300032*

Australian Coastal and Marine Territory

Australian Marine Spatial Information System (AMSIS): *http://www.ga.gov.au/scientific-topics/marine/jurisdiction/amsis*

GA (2020)

IMOS State and Trends of Australia's Ocean Report: 2. Biological Productivity: *https://www.imosoceanreport.org.au/time-series/productivity/*

IMOS State and Trends of Australia's Ocean Report: 4. Marine Animals: *https://www.imosoceanreport.org.au/time-series/animals/*

OzCoasts: *https://ozcoasts.org.au*

Fisheries

https://globalfishingwatch.org

Benthic Habitat Classification

National standardised nomenclature for benthic habitat classification is documented by Seamap Australia (Butler *et al.*, 2017): ISBN: 978-1-925646-61-0, *https://vocabs.ardc.edu.au/viewById/129*

CATAMI: Classification Scheme is enabling aggregation, annotation and automated processing of underwater imagery from across Australia (Althaus *et al.*, 2015)

Kennedy *et al.* (2021)

Coral reefs

Corals of the world: *http://www.coralsoftheworld.org/page/home/*

Goodman *et al.* (2013)

Remote Sensing Toolkit: *https://www.rsrc.org.au/rstoolkit*

NASA JPL CORAL mIssion: *https://airbornescience.jpl.nasa.gov/campaign/coral*

NOAA Coral Reef Watch: *https://coralreefwatch.noaa.gov/satellite/publications.php*

Allen Coral Atlas: *https://allencoralatlas.org/atlas/*

Coral Watch—citizen science on the reef: *https://coralwatch.org*

OzCoasts (2020). *Algal blooms* webpage, Australian Online Coastal Information website: *https://ozcoasts.org.au/indicators/coastal-issues/freq_algal_blooms/*

ReefTemp Next Generation: *http://www.bom.gov.au/environment/activities/reeftemp/reeftemp.shtml*,

eReefs: *https://research.csiro.au/ereefs/remote-sensing/*

20.9 References

Abram, N.J., Gagan, M.K., McCulloch, M.T., Chappell, J., and Hantoro, S. (2003). Coral reef death during the 1997 Indian Ocean Dipole linked to Indonesian wildfires. *Science*, 301, 952–955.

Adam, E., Mutanga, O., and Rugege, D. (2010). Multispectral and hyperspectral remote sensing for identification and mapping of wetland vegetation: a review. *Wetlands Ecology and Management*, 18, 281–296. *https://doi.org/10.1007/s11273-009-9169-z*

Ajani, P., Hallegraeff, G., Allen, D., Coughlan, A., Richardson, A., Armand, L., Ingleton, T., and Murray, S. (2016). Establishing baselines: a review of eighty years of phytoplankton diversity and biomass in south-eastern Australia. *Oceanography and Marine Biology: An Annual Review*, 54, 387–412.

Alberotanza, L., Brando, V.E., Ravagnan, G., and Zandonella, A. (1999). Hyperspectral aerial images. A valuable tool for submerged vegetation recognition in the Orbetello Lagoons, Italy. *International Journal of Remote Sensing*, 20, 523–533

Alieva, N.O., Konzen, K.A., Field, S.F., Meleshkevitch, E.A., Hunt, M.E., Beltran-Ramirez, V., Miller, D.J., Wiedenmann, J., Salih, A., and Matz, M.V. (2008). Diversity and evolution of coral fluorescent Proteins. *PloS ONE* 3, e2680

Allen Coral Atlas (2021). *Science & Methods* webpage, Allen Coral Atlas website: *https://allencoralatlas.org/methods/*

Alongi, D.M. (2020). Carbon balance in salt marsh and mangrove ecosystems: A global synthesis. *Journal of Marine Science and Engineering*, 8(10), 767. *https://doi.org/10.3390/jmse8100767*

Althaus, F., Williams, A., Schlacher, T., Kloser, R., Green, M., Barker, B., Bax, N., Brodie, P., and Schlacher-Hoenlinger, M. (2009). Impacts of bottom trawling on deep-coral ecosystems of seamounts are long-lasting. *Marine Ecology Progress Series*, 397, 279–294.

Althaus, F., Hill, N., Ferrari, R., Edwards, L., Przeslawski, R., Schönberg, C.H.L., Stuart-Smith, R., Barrett, N., Edgar, G., Colquhoun, J., Tran, M., Jordan, A., Rees, T., Gowlett-Holmes, K. (2015). A Standardised Vocabulary for Identifying Benthic Biota and Substrata from Underwater Imagery: The CATAMI Classification Scheme. *PloS ONE*, 10(10), e0141039. *https://doi.org/10.1371/journal.pone.0141039*

AMP (2020). *Australian Marine Parks* website: *https://parksaustralia.gov.au/marine/science/science-under-the-surface/*

Andréfouët, S. (2011). Reef typology. In: *Encyclopedia of modern coral reefs—structure form and process* (Ed: Hopley, D.). Springer, Dordrecht

Andréfouët, S., Claereboudt, M., Matsakis, P., Pagès, J., and Dufour, P. (2001). Typology of atolls rims in Tuamotu archipelago (French Polynesia) at landscape scale using SPOT-HRV images. *International Journal of Remote Sensing*, 22, 98–1004.

Andréfouët, S., Muller-Karger, F.E., Robinson, J.A., Kranenburg, C.J., Torres-Pulliza, D., Spraggins, S.A., and Murch, B. (2006). Global assessment of modern coral reef extent and diversity for regional science and management applications: a view from space. In *Proceedings of the 10th International Coral Reef Symposium* (Vol. 2, pp. 1732–1745). ICRS.

Andréfouët, S., and Bionaz, O. (2021). Lessons from a global remote sensing mapping project. A review of the impact of the Millennium Coral Reef Mapping Project for science and management. *Science of the Total Environment*, 776, 145987.

Andrzejaczek, S., Gleiss, A.C., Lear, K.O., Pattiaratchi, C.B., Chapple, T.K., and Meekan, M.G. (2019). Biologging Tags Reveal Links Between Fine-Scale Horizontal and Vertical Movement Behaviors in Tiger Sharks (*Galeocerdo cuvier*). *Frontiers in Marine Science*, 14. *https://doi.org/10.3389/fmars.2019.00229*

Ashford, O.S., A.J. Kenny, C.R.B. Froján, M.B. Bonsall, T. Horton, A. Brandt, G.J. Bird, S. Gerken, and A.D. Rogers. (2018). Phylogenetic and functional evidence suggests that deep-ocean ecosystems are highly sensitive to environmental change and direct human disturbance. *Proceedings of the Royal Society B*, 285, 20180923.

Atkinson, M.J., and Grigg, R.W (1984). Model of coral reef ecosystem. II. Gross and net benthic primary production at French Frigate Shoals, Hawaii. *Coral Reefs*, 3, 13–22

Auricht, H.C.C., Clarke, K.D., Lewis, M.M., and Mosley, L.M. (2017). Have droughts and increased water extraction from the Murray River (Australia) reduced coastal ocean productivity? *Marine and Freshwater Research*, 69(3), 343–356. *https://doi.org/10.1071/MF17226*

Baird, M.E., Mongin, M., Skerratt, J., Margvelashvili, N., Tickell, S., Steven, A.D.L., Robillot, C., Ellis, R., Waters, D., Kaniewska, P., and Brodie, J. (2021). Impact of catchment loads of nutrients and sediments on marine water quality on the Great Barrier Reef: An application of the eReefs marine modelling system. *Marine Pollution Bulletin*, 167, 112297.

Bajjouk, T., Guillaumont, B., and Populus, J. (1996). Application of airborne imaging spectrometry system data to intertidal seaweed classification and mapping. *Hydrobiologia,* 326, 463–471. *https://doi.org/10.1007/BF00047847*

Bajjouk, T., Populus, J., and Guillaumont, B. (1998). Quantification of subpixel cover fractions using principal component analysis and a linear programming method: application to the coastal zone of Roscoff (France). *Remote Sensing of Environment*, 64(2), 153–165.

Bakun, A. (2006). Fronts and eddies as key structures in the habitat of marine fish larvae: Opportunity, adaptive response and competitive advantage. *Scientia Marina*, 70, 105–122.

Bayliss, P., and Hutton, M. (2017). *Integrating Indigenous knowledge and survey techniques to develop a baseline for dugong (Dugong dugon) management in the Kimberley*. Final Report of project 1.2.5 of the Kimberley Marine Research Program Node of the Western Australian Marine Science Institution, WAMSI, Perth, Western Australia, 98 p.

Benyoucef, I., Blandin, E., Lerouxel, A., Jesus, B., Rosa, P., Méléder, V., Launeau, P., Barillé, L. (2014). Microphytobenthos internanual variations in a north-European estuary (Loire estuary, France) detected by visible-infrared multispectral remote sensing. *Estuarine, Coastal and Shelf Science,* 136, 43–52.

Bicknell, A.W.J., B.J. Godley, E.V. Sheehan, S.C. Votier, and M.J. Witt. (2016). Camera technology for monitoring marine biodiversity and human impact. *Frontiers in Ecology and the Environment*, 14, 424–432.

Bierwirth, P.N., Lee, T.J., and Burne, R.V. (1993). Shallow sea-floor reflectance and water depth derived by unmixing multispectral imagery. *Photogrammetric Eng Remote Sensing*. 59, 331–338.

Bouchet, P., Phillips, C., Huang, Z., Meeuwig, J., Foster, S., and Przeslawski, R. (2018). *Comparative assessment of pelagic sampling methods used in marine monitoring*. Report to the National Environmental Science Programme, Marine Biodiversity Hub. 149 p. *https://www.nespmarine.edu.au/system/files/Bouchet%20et%20al%20Comparative%20assessment%20of%20pelgic%20sampling%20methods_Milestone%2015%20RPv3.pdf*

Bowden, D.A., and Jones, D.O.B. (2016). Towed cameras. In *Biological Sampling in the Deep Sea*. (Eds: M.R. Clark, M. Consalvey, and A. Rowden) pp. 260–284. John Wiley and Sons.

Boyd P.W., Kawaguchi, S. Strzepek, R. Meiners, K. Hallegraeff, G. McMinn, A., Swadling, K., and Reilly, D. (2019). *Report Card: Potential Tipping Points for life in the Southern Ocean*. Antarctic Climate and Ecosystems Cooperative Research Centre, Hobart, Australia. *http://dx.doi.org/10.25959/100.00031768*

Brito, A., Benyoucef, I., Jesus, B. Brotas, V., Gernez, P. , Mendes, C., Launeau, P., Dias, M., and Barillé, L. (2013). Seasonality of microphytobenthos revealed by remote-sensing in a South European estuary. *Continental Shelf Research,* 66, 83–91. 10.1016/j.csr.2013.07.004

Bunting, P., Rosenqvist, A., Lucas, R., Rebelo, L.-M., Hilarides, L., Thomas, N., Hardy, A., Itoh, T., Shimada, M., Finlayson, M. (2018). The global mangrove watch—a new 2010 global baseline of mangrove extent. *Remote Sensing*, 10 (10), 1669 doi:10.3390/rs10101669

Butler, A.J., Rees, T., Beesley, P., and Bax, N.J. (2010). Marine biodiversity in the Australian region. *Plos One*, 5(8), e11831.

Butler, C., Lucieer, V., Walsh, P., Flukes, E., and Johnson, C. (2017). *Seamap Australia [Version 1.0] the development of a national benthic marine classification scheme for the Australian continental shelf*. Seamap Australia, University of Tasmania. ISBN: 978-1-925646-61-0

Canonico, G., Buttigieg, P.L., Montes, E., Muller-Karger, F.E., Stepien, C., Wright, D., Benson, A., Helmuth, B., Costello, M., Sousa-Pinto, I., Saeedi, H., Newton, J., Appeltans, W., Bednaršek, N., Bodrossy, L., Best, B.D., Brandt, A., Goodwin, K.D., Iken, K., Marques, A.C., Miloslavich, P., Ostrowski, M., Turner, W., Achterberg, E.P., Barry, T., Defeo, O., Bigatti, G., Henry, L.-A., Ramiro-Sánchez, B., Durán, P., Morato, T., Roberts, J.M., García-Alegre, A., Cuadrado, M.S., and Murton, B. (2019). Global Observational Needs and Resources for Marine Biodiversity. *Frontiers in Marine Science*, 6, 367. doi: 10.3389/fmars.2019.00367

Carroll, A., Althaus, F., Beaman, R., Friedman, A., Ierodiaconou, D., Ingleton, T., Jordan, A., Linklater, M., Monk, J., Post, A., Przeslawski, R., Smith, J., Stowar, M., Tran, M., Tyndall, A. (2018). Marine sampling field manual for towed underwater camera systems. In *Field Manuals for Marine Sampling to Monitor Australian Waters* (Eds: Przeslawski, R., Foster, S.). National Environmental Science Programme (NESP). pp. 131–152.

CEOS (2018). *Feasibility Study for an Aquatic Ecosystem Earth Observing System*. (Eds: Dekker, A.G., and Pinnel, N.) CSIRO, Canberra.

Chassot, E., S. Bonhommeau, G. Reygondeau, K. Nieto, J.J. Polovina, M. Huret, N.K. Dulvy, and H. Demarcq. (2011). Satellite remote sensing for an ecosystem approach to fisheries management. *ICES Journal of Marine Science*, 68, 651–666.

Chirol, C., Haigh, I.D., Pontee, N., Thompson, C.E., and Gallop, S.L. (2018). Parametrizing tidal creek morphology in mature saltmarshes using semi-automated extraction from lidar. *Remote Sensing of Environment*, 209, 291–311. *https://doi.org/10.1016/j.rse.2017.11.012*

Cochran, S.A. (2013). Photography Applications. Ch 2 in *Coral Reef Remote Sensing*. (Eds: Goodman, J.A., Purkis, S.J., and Phinn, S.R.). Springer, Dordrecht. ISBN 978-90-481-9291-5

Commonwealth of Australia (1992). *National Strategy for Ecologically Sustainable Development*. AGPS, Canberra.

Constable, A.J., Melbourne-Thomas, J., Trebilco, R., Press, A.J., and Haward, M. (2017). *Position Analysis: Managing Change in Southern Ocean Ecosystems*. Antarctic Climate and Ecosystems Cooperative Research Centre, Hobart, Australia. 39 p. *http://acecrc.org.au/wp-content/uploads/2017/10/2017-ACECRC-Position-Analysis-Southern-Ocean-Ecosystems.pdf*

Cougo, M.F., Souza-Filho, P.W.M., Silva, A.Q., Fernandes, M.E.B., dos Santos, J.R., Abrew, M.R.S., Nascimento, W.R., and Simard, M. (2015). Radarsat-2 Backscattering for the Modeling of Biophysical Parameters of Regenerating Mangrove Forests. *Remote Sensing*, 7(12), 17097–17112. *https://doi.org/10.3390/rs71215873*

Cury, P.M., Y.-J. Shin, B. Planque, J.M. Durant, J.-M. Fromentin, S. Kramer-Schadt, N.C. Stenseth, M. Travers, and V. Grimm. (2008). Ecosystem oceanography for global change in fisheries. *Trends in ecology and evolution*, 23, 338–346.

Daly, T. (2013). *Coastal saltmarsh*. Primefact 1256. NSW Department of Primary Industry, Sydney. *http://www.dpi.nsw.gov.au/__data/assets/pdf_file/0007/459628/Coastal-Saltmarsh-Primefact.pdf*

DAWE (2020). *Wetlands* webpage, Department of Agriculture, Water and the Environment website: *https://www.environment.gov.au/wetlands*

De Jong, D.J., and de Jonge, V.N. (1995). Dynamics and distribution of microphytobenthic chlorophyll-a in the Western Scheldt estuary (SW Netherlands). *Hydrobiologia,* 311, 21–30.

Dekker, A.G., Brando, V.E., Anstee, J.M., Pinnel, N., Kutser, T., Hoogen-boom, J., Peters, S.W.M., Pasterkamp, R., Vos, R.J., Olbert, C., and Malthus, T.J. (2001). Imaging spectrometry of water. Ch 11 in *Imaging Spectrometry: Basic Principles and Prospective Applications*. (Eds: F.D. van der Meer and S.M. de Jong), pp 307–359. Kluwer Academic Publishers, Dordrecht, The Netherlands.

Dekker, A.G., Phinn, S.R., Anstee, J., Bissett, P., Brando, V.E., Casey, B., Fearns, P., Hedley, J., Klonowski, W., Lee, Z.P., Lynch, M., Lyons, M., Mobley, C., and Roelfsema, C. (2011). Inter-comparison of shallow water bathymetry, hydrooptics, and benthos mapping techniques in Australian and Caribbean coastal environments. *Limnology and Oceanography Methods*, 9, 396–425

Dower, J., Freeland, H., and Juniper, K. (1992). A Strong Biological Response to Oceanic Flow past Cobb Seamount. *Deep-Sea Research Part A-Oceanographic Research Papers*, 39, 1139–1145.

Doxaran, D., Bustamante, J., Dogliotti, A.I., Malthus, T.J., and Senechal, N. (2019). Editorial for the Special Issue "Remote Sensing in Coastal Zone Monitoring and Management—How Can Remote Sensing Challenge the Broad Spectrum of Temporal and Spatial Scales in Coastal Zone Dynamic?" *Remote Sensing*, 11, 1028. doi:10.3390/rs11091028

Dunk, I., and Lewis. M.R. (1999). Seagrass and shallow water feature discrimination using Hymap Imagery. *10*th *Australian Remote Sensing and Photogrammetry Conference*. University of Adelaide., Australia.

Durden, J., T. Schoening, F. Althaus, A. Friedmann, R. Garcia, A. G. Glover, J. Greinert, N. J. Stout, D. O. Jones, and A. Jordt. (2016). Perspectives in visual imaging for marine biology and ecology: from acquisition to understanding. *Oceanography and Marine Biology: An Annual Review*, 54, 1–72. CRC Press, Boca Raton, US. doi:10.1201/9781315368597

Dutkiewicz, S., Hickman, A. E., Jahn, O., Henson, S., Beaulieu C., and Monier, E. (2019). Ocean colour signature of climate change. *Nature Communications*, 10, 578.

Dwyer, R.G., Brooking, C., Brimblecombe, W., Campbell, H.A., Hunter, J., Watts, M., Franklin, C.E. (2015). An open Web based system for the analysis and sharing of animal tracking data. *Animal Biotelemetry*, 3(1), 1–11. doi:10.1186/s40317-014-0021-8.

Edwards, M., and Richardson, A.J. (2004). The impact of climate change on the phenology of the plankton community and trophic mismatch. *Nature*, 430, 881–884.

Enever, R., Lewin, S., Reese, A., and Hooper, T. (2017). Mapping fishing effort: Combining fishermen's knowledge with satellite monitoring data in English waters. *Fisheries Research*, 189, 67–76.

Eveson, J.P., Hobday, A.J., Hartog, J.R., Spillman, C.M., and Rough, K.M. (2015). Seasonal forecasting of tuna habitat in the Great Australian Bight. *Fisheries Research*, 170, 39–49.

FAO (2007). *The State of the World's Fisheries and Aquaculture 2006*. FAO Fisheries and Aquaculture Department, Food and Agriculture Organisation of the United Nations, Rome, 2007. 180 p.

FAO (2018). *Technical guidelines on methodologies and indicators for the estimation of the magnitude and impact of illegal, unreported and unregulated (IUU) fishing. Volume 2—Guiding Principles and Approaches*. Version 1 draft. UN Food and Agriculture Organisation, Rome.

Farris, A.S., Defner, Z., and Ganju, N.K. (2019). Identifying salt marsh shorelines from remotely sensed elevation data and imagery. *Remote Sensing*, 11, 1795. doi:10.3390/rs11151795

Fernandez-Nunez, M., Burningham, H., and Ojeda Zujar, J. (2017). Improving accuracy of LiDAR-derived digital terrain models for saltmarsh management. *Journal of Coastal Conservation*, 21, 209–222. *https://doi.org/10.1007/s11852-016-0492-2*

Fretwell, P.T., and Trathan, P.N. (2009). Penguins from space: faecal stains reveal the location of emperor penguin colonies. *Global Ecology and Biogeography*, 18, 543–552.

Fretwell, P.T., LaRue, M.A., Morin, P., Kooyman, G.L., Wienecke, B., Ratcliffe, N., Fox, A.J., Fleming, A.H., Porter, C., and Trathan, P.N. (2012). An emperor penguin population estimate: the first global, synoptic survey of a species from space. *PloS One*, 7, e33751.

Fretwell, P.T., Staniland, I.J., and Forcada, J. (2014). Whales from space: counting southern right whales by satellite. *PloS One*, 9, e88655.

Furnas, M. (2003). *Catchments and Corals. Terrestrial Runoff to the Great Barrier Reef*. AIMS, Townsville. 334pp.

Fyfe, S.K. (2003). Spatial and temporal variation in spectral reflectance: Are seagrass species spectrally distinct? *Limnology and Oceanography*, 48, 464–479.

GA (2020a). *Australia's Coasts and Estuaries* webpage, Geoscience Australia website: *https://www.ga.gov.au/scientific-topics/marine/coasts-estuaries*

GA (2020b). *Oceans and Seas* webpage, Geoscience Australia website: *http://www.ga.gov.au/scientific-topics/national-location-information/dimensions/oceans-and-seas*

Gao, B.C., Montes, M.J., Davis, C.O., and Goetz, A.F.H. (2009). Atmospheric correction algorithms for hyperspectral remote sensing data of land and ocean. *Remote Sensing of Environment*, 113, S17–S24

Garcia, R.A., Lee, Z., and Hochberg, E.J. (2018). Hyperspectral Shallow-Water Remote Sensing with an Enhanced Benthic Classifier. *Remote Sensing*, 10, 147. doi:10.3390/rs10010147

Garde, L.A., Spillman, C.M., Majewski, L., Griffin, C., Kruger, G., and Beggs, H. (2013), *ReefTemp Next Generation*. Centre for Australian Weather and Climate Research (CAWCR) Technical Report, No 063. 44 p.

Garde, L.A., Spillman, C.M., Heron, S.F., and Beeden, R.J. (2014). Reef Temp Next Generation: A new operational system for monitoring reef thermal stress. *Journal of Operational Oceanography*, 7, 21–33.

Giri, C.. Ochieng, E., Tieszen, L.L., Zhu, Z., Singh, A., Loveland, T., Masek, J., and Duke, N. (2011). Status and distribution of mangrove forests of the world using earth observation satellite data. *Global Ecology and Biogeography*, 20, 154–159. doi:10.1111/j.1466-8238.2010.00584.x

Gohin, F., B. Saulquin, H. Oger-Jeanneret, L. Lozac'h, L. Lampert, A. Lefebvre, P. Riou, and F. Bruchon. (2008). Towards a better assessment of the ecological status of coastal waters using satellite-derived chlorophyll-a concentrations. *Remote Sensing of Environment*, 112, 3329–3340.

Goodman, J., and Ustin, S.L. (2007) Classification of benthic composition in a coral reef environment using spectral unmixing. *Journal of Applied Remote Sensing*, 1(1), 011501.

Goodman, J.A., Purkis, S.J., and Phinn, S.R. (2013). *Coral Reef Remote Sensing: A guide for mapping, monitoring and management*. Springer, Dordrecht. doi:10.1007/978-90-481-9292-2

Gordon, H.R. (1997) Atmospheric correction of ocean color imagery in the Earth observing system era. *Journal of Geophysical Research: Atmosphere*, 102, 17081–17106.

Gordon, H.R., and Clark, D.K. (1980). Atmospheric effects in the remote sensing of phytoplankton pigments. *Boundary-Layer Meteorology*, 18, 299–313.

Gredzens, C., Marsh, H., Fuentes, M.M.P.B., Limpus, C.J., Shimada, T., and Hamann, M. (2014). Satellite Tracking of Sympatric Marine Megafauna Can Inform the Biological Basis for Species Co-Management. *PloS ONE*, 9(6), E98944. *https://doi.org/10.1371/journal.pone.0098944*

Hamylton, S.M. (2017). Mapping coral reef environments: A review of historical methods, recent advances and future opportunities. *Progress in Physical Geography*, 41(6), 803–833.

Hardman-Mountford, N. J., Hirata, T., Richardson, K.A., and Aiken, J. (2008). An objective methodology for the classification of ecological pattern into biomes and provinces for the pelagic ocean. *Remote Sensing of Environment*, 112, 3341–3352.

Harrison, B.A., and Jupp, D.L.B. (1990). *Introduction to Image Processing: Part TWO of the microBRIAN Resource Manual*. CSIRO, Melbourne. 256pp.

Harrison, D.P., Hinton, M.G., Kohin, S., Armstrong, E.M., Snyder, S., O'Brien, F., and Kiefer, D.K. (2017). The pelagic habitat analysis module for ecosystem-based fisheries science and management. *Fisheries Oceanography*, 26, 316–335.

Harvey, N., and Caton, B. (2010). *Coastal Management in Australia*. University of Adelaide Press, Adelaide.

Haynes, T.A. (2016). *Scottish saltmarsh survey national report*. Scottish Natural Heritage Commissioned Report No. 786. ISBN 978-0-9807230-3-8

Hazen, E.L., Palacios, D.M., Forney, K.A., Howell, E.A., Becker, E., Hoover, A.L., Irvine, L., DeAngelis, M., Bograd, S.J., Mate, B.R., and Bailey, H. (2017). WhaleWatch: a dynamic management tool for predicting blue whale density in the California Current. *Journal of Applied Ecology*, 54, 1415–1428.

Hazen, E.L., Scales, K.L., Maxwell, S.M., Briscoe, D.K., Welch, H., Bograd, S.J., Bailey, H., Benson, S.R., Eguchi, T., Dewar, H., Kohin, S., Costa, D.P., Crowder, L.B., and Lewison, R.L. (2018). A dynamic ocean management tool to reduce bycatch and support sustainable fisheries. *Science Advances*, 4(5). *https://doi.org/10.1126/sciadv.aar300*

Hedley, J. (2013). Hyperspectral Applications. Ch 4 in *Coral Reef Remote Sensing*. (Eds: Goodman, J.A., Purkis, S.J., and Phinn, S.R.). Springer, Dordrecht. ISBN 978-90-481-9291-5.

Hedley, J.D., and Mumby, P.J. (2002). Biological and remote sensing perspectives of pigmentation in coral reef organisms. *Advances in Marine Biology*, 43, 277–317.

Hedley, J.D., and Mumby, P.J. (2003). A remote sensing method for resolving depth and subpixel composition of aquatic benthos. *Limnology and Oceanography*, 48, 480–488

Hedley, J.D., Mumby, P.J. Joyce, K.E., and Phinn S.R. (2004). Spectral unmixing of coral reef benthos under ideal conditions. *Coral Reefs*, 23, 60–73.

Hedley, J.D., Roelfsema, C.M., Phinn, S.R., and Mumby, P.J. (2012). Environmental and Sensor Limitations in Optical Remote Sensing of Coral Reefs: Implications for Monitoring and Sensor Design. *Remote Sensing*, 4, 271–302. doi:10.3390/rs4010271

Hedley, J.D., Chollet-Ordaz, I., Harborne, A.R., Roelfsema, C., Skirving, E., Strong, A., Christensen, T., Eakin, Dwight, M., Ticzon, V., Bejarano, S., and Mumby, P.J. (2016a). Current Operational Remote Sensing Technologies For Coral Reef Monitoring And Management: A Review. *Remote Sensing*, 8, 118. doi:10.3390/rs8020118

Hedley, J.D., Roelfsema, C.M., Chollett, I., Harborne, A.R., Heron, S.F., Weeks, S.J., Skirving, W.J., Strong, A.E., Eakin, C.M., Christensen, T.R.L., Ticzon, V., Bejarano, S., and Mumby, P.J. (2016b). Remote Sensing of Coral Reefs for Monitoring and Management: A Review. *Remote Sensing*, 8, 118.

Hedley, J.D., Roelfsema, C., Brando, V., Giardino, G., Kutser, T., Phinn, S., Mumby, P.J., Barrilero, O., Laporte, J., and Koetz, B. (2018). Coral reef applications of Sentinel-2: Coverage, characteristics, bathymetry and benthic mapping with comparison to Landsat 8. *Remote Sensing of Environment*, 216, 598–614. *https://doi.org/10.1016/j.rse.2018.07.014*

Henson, S.A., Cole, H.S., Hopkins, J., Martin, A.P., and Yool, A. (2017). Detection of climate change-driven trends in phytoplankton phenology. Global Change Biology, 24(1), e101–e111. *https://doi.org/10.1111/gcb.13886*

Hernández-Cruz, L.R., Purkis, S.J., and Riegl, B.M. (2006). Documenting decadal spatial changes in seagrass and Acropora palmata cover by aerial photography analysis in Vieques, Puerto Rico: 1937–2000. *Bulletin of Marine Science*, 79(2), 401–404.

Hladik, C., Schalles, J., and Alber, M. (2013). Salt marsh elevation and habitat mapping using hyperspectral and LIDAR data. *Remote Sensing of Environment*, 139, 318–330.

Hobday A.J., Hartog, J.R., Timmiss, T., and Fielding, J. (2010). Dynamic spatial zoning to manage southern bluefin tuna (*Thunnus maccoyii*) capture in a multi-species longline fishery. *Fisheries Oceanography*, 19, 243–253.

Hobday, A., Young, J., Moeseneder, C., and Dambacher, J. (2011). Defining dynamic pelagic habitats in oceanic waters off eastern Australia. *Deep Sea Research Part II: Topical Studies in Oceanography*, 58, 734–745.

Hochberg, E.J., and Atkinson, M.J. (2000). Spectral discrimination of coral reef benthic communities. *Coral Reefs*, 19, 164–171

Hochberg, E.J., and Atkinson, M.J. (2008). Coral reef benthic productivity based on optical absorptance and light-use efficiency. *Coral Reefs*, 27, 49–59.

Hochberg, E.J., Atkinson, M.J., and Andrefouet, S. (2003) Spectral reflectance of coral reef bottom-types worldwide and implications for coral reef remote sensing. *Remote Sensing of Environment*, 85, 159–173.

Hochberg, E.J., Atkinson, M.J., Apprill, A., and Andréfouët, S. (2004). Spectral reflectance of coral. *Coral Reefs*, 23, 84–95.

Hodgson, A., Peel, D., and Kelly, N. (2017). Unmanned aerial vehicles for surveying marine fauna: assessing detection probability. *Ecological Applications*, 27(4), 1253–1267. *https://doi.org/10.1002/eap.1519*

Hoepffner, N., and Zibordi, G. (2009). Remote sensing of Coastal Waters. In *Encyclopedia of Ocean Sciences* (2nd edn), pp. 732–741. Academic Press.

Holden, H., and LeDrew, E. (1998). Spectral discrimination of healthy and non-healthy corals based on cluster analysis, principal components analysis, and derivative spectroscopy. *Remote Sensing of Environment*, 65, 217–224.

Holden, H., and LeDrew, E. (1999). Hyperspectral identification of coral reef features. *International Journal of Remote Sensing*, 13, 2545–2563.

Howell, E.A., Kobayashi, D.R., Parker, D.M., Balazs, G.H., and Polovina, J.J. (2008). TurtleWatch: a tool to aid in the bycatch reduction of loggerhead turtles Caretta caretta in the Hawaii-based pelagic longline fishery. *Endangered Species Research*, 5, 267–278. doi: 10.3354/esr00096

Howell, E.A., Hoover, A., Benson, S.R., Bailey, H., Polovina, J.J., Seminoff, J.A., and Dutton, P.H. (2015). Enhancing the TurtleWatch product for leatherback sea turtles, a dynamic habitat model for ecosystem-based management. *Fisheries Oceanography*, 24(1), 57–68. *https://doi.org/10.1111/fog.12092*

Hussey, N.E., Kessel, S.T., Aarestrup, K., Cooke, S.J., Cowley, P.D., Fisk, A.T., Harcourt, R.G., Holland, K.N., Iverson, S.J., Kocik, J.F., Mills Flemming, J.E., and Whoriskey, F.G. (2015). Aquatic animal telemetry: A panoramic window into the underwater world. *Science*, 348(6240), 1255642. doi:10.1126/science.1255642

Hyrenback, D., Forney, K.A., and Dayton, P. (2000). Marine Protected Areas and ocean basin management. Aquatic Conservation Marine and Freshwater Ecosystems, 10(6), 437–458.

IOCCG (2009). *Remote Sensing in Fisheries and Aquaculture*. (Eds: Forget, M.-H., Stuart, V. and Platt, T.). Reports of the International Ocean-Colour Coordinating Group, No. 8. IOCCG, Dartmouth, Canada. *http://ioccg.org/wp-content/uploads/2015/10/ioccg-report-08.pdf*

IOCCG (2014). *Phytoplankton functional types from space*, Reports of the International Ocean Color Coordinating Group, No. 15,. IOCCG, Dartmouth, NS.

IUCN (2017). *Mangroves: nurseries for the world's seafood supply* webpage, International Union for Conservation of Nature website: *https://www.iucn.org/news/forests/201708/mangroves-nurseries-world%E2%80%99s-seafood-supply*

Jupp, D.L.B., Mayo, K.K., Kuchler, D.A., Claasen, D.V.R., Kenchington, R.A., and Guerin, P.R. (1985). Remote sensing for planning and managing the Great Barrier Reef of Australia. *Photogrammetria,* 40, 21–42.

Kacev, D., and Lewison, R.L. (2016). Satellite remote sensing in support of fisheries management in global oceans. In *Earth Science Satellite Applications*, pp. 207–222. (Ed: Hossain, F.), Springer Remote Sensing/Photogrammetry. Springer. 284 p.

Kachelriess, D., Wegmann, M., Gollock, M., and Pettorelli, N. (2014). The application of remote sensing for marine protected area management. *Ecological Indicators*, 36, 169–177.

Kamal, M., Phinn, S., and Johansen, K. (2015). Object-Based Approach for Multi-Scale Mangrove Composition Mapping Using Multi-Resolution Image Datasets. *Remote Sensing*, 7, 4753–4783. doi:10.3390/rs70404753

Karpouzli, E., Malthus, T.J., and Place, C.J. (2004). Hyperspectral discrimination of coral reef benthic communities in the western Caribbean. *Coral Reefs*, 23, 141–151. doi:10.1007/s00338-003-0363-9

Kavanaugh, M.T., Oliver, M.J., Chavez, F.P., Letelier, R.M., Muller-Karger, F.E., and Doney, S.C. (2016). Seascapes as a new vernacular for pelagic ocean monitoring, management and conservation. *ICES Journal of Marine Science*, 73, 1839–1850.

Kennedy, E.V., Roelfsema, C.M., Lyons, M.B., Kovacs, E.M., Borrego-Acevedo, R., Roe, M., Phinn, S.R., Larsen, K., Murray, N.J., Yuwono, D., and Wolff, J. (2021). Reef Cover, a coral reef classification for global habitat mapping from remote sensing. *Scientific Data*, 8, 196. *https://doi.org/10.1038/s41597-021-00958-z*

Kirk, J.T.O. (1994). *Light and Photosynthesis in Aquatic Ecosystems*, 2nd Edn. Cambridge University Press, Cambridge. 509 p.

Kirk, J.T.O. (2010). *Light and Photosynthesis in Aquatic Ecosystems*, 3rd Edn. Cambridge University Press, Cambridge. 662 p.

Klemas, V. (2013). Fisheries applications of remote sensing: An overview. *Fisheries Research*, 148, 124–136.

Kobryn, H.T., Wouters, K., Beckley, L.E., and Heege, T. (2013). Ningaloo Reef: Shallow Marine Habitats Mapped Using a Hyperspectral Sensor. *PLOS One*, 8(7), e70105. doi:10.1371/journal.pone.0070105

Kovacs, E., Roelfsema, C., Lyons, M., Zhao, S., and Phinn, S. (2018). Seagrass habitat mapping: how do Landsat 8 OLI, Sentinel-2, ZY-3A, and Worldview-3 perform? *Remote Sensing Letters*, 9(7), 686–695. *https://doi.org/10.1080/2150704X.2018.1468101*

Kuenzer, C., Bluemel, A., Gebhardt, S., Vo Quoc, T., and Dech, S. (2011). Remote sensing of mangrove ecosystems: a review. *Remote Sensing*, 3, 878–928. doi:10.3390/rs3050878

Kulawardhana, R.W., Popescu, S.C., and Feagin, R.A. (2014). Fusion of lidar and multispectral data to quantify salt marsh carbon stocks. *Remote Sensing of Environment*, 154, 345–357.

Kurekin, A.A., Loveday, B.R., Clements, O., Quartly, G.D., Miller, P.I., Wiafe, G., and Adu Agyekum, K. (2019). Operational Monitoring of Illegal Fishing in Ghana through Exploitation of Satellite Earth Observation and AIS Data. *Remote Sensing*, 11, 293.

Kutser, T., Parslow, J., Clementson, L., Skirving, W., Done, T., Wakeford, M., and Miller, I. (2000). Hyperspectral detection of coral reef bottom types. *Ocean Optics XV*. Monaco.

Kutser, T., Herlevi, A., Kallio, K., and Arst, H. (2001). A hyperspectral model for interpretation of passive optical remote sensing data from turbid lakes. *The Science of the Total Environment*, 268(1–3), 47–58.

Kutser, T., Dekker, A.G., and Skirving, W. (2003). Modeling spectral discrimination of Great Barrier Reef benthic communities by remote sensing instruments. *Limnology and Oceanography*, 48, 497–510.

Laengner, M.L., Siteur, K., and van der Wal, D. (2019). Trends in the Seaward Extent of Saltmarshes across Europe from Long-Term Satellite Data. *Remote Sensing*, 11, 1653. doi:10.3390/rs11141653

LaRue, M.A., Rotella, J.J., Garrott, R.A., Siniff, D.B., Ainley, D.G., Stauffer, G.E., Porter, C.C., and Morin, P.J. (2011). Satellite imagery can be used to detect variation in abundance of Weddell seals (*Leptonychotes weddellii*) in Erebus Bay, Antarctica. *Polar Biology*, 34, 1727.

Larkum, A.W., Kendrick, G.A. and Ralph, P.J. (Eds.) (2018). *Seagrasses of Australia: structure, ecology and conservation*. Springer.

Lawrence, E., Hayes, K., Lucieer, V., Nichol, S., Dambacher, J., and Hill, N. (2015). Mapping Habitats and Developing Baselines in Offshore Marine Reserves with Little Prior Knowledge: A Critical Evaluation of a New Approach. *PloS ONE*, 10, e0141051.

Lee, Z., Carder, K.L., Mobley, C.D., Steward, R.G., and Patch, J.S. (1999). Hyperspectral remote sensing for shallow waters. 2. Deriving bottom depths and water properties by optimization. *Applied Optics*, 38, 3831–3843

Leiper, I., Phinn, S., and Dekker, A.G. (2012). Spectral reflectance of coral reef benthos and substrate assemblages on Heron Reef, Australia. *International Journal of Remote Sensing*, 33(12), 3946–3965. doi: 10.1080/01431161.2011.637675

Lemos, A.T., Ghisolfi, R.D.R., and Mazzini, P.L.F. (2018). Annual phytoplankton blooming using satellite-derived chlorophyll-a data around the Vitoria-Trindade Chain, Southeastern Brazil. *Deep-Sea Research Part I-Oceanographic Research Papers*, 136, 62–71.

Lennox, R.J., Aarestrup K., Cooke S.J., Cowley P.D., Deng Z.D., and Fisk A.T. (2017). Envisioning the future of aquatic animal tracking: Technology, science, and application. *BioScience*, 67(10), 884–896.

Lennox, R.J., Engler-Palma, C., Kowarski, K., Filous, A., Whitlock, R., Cooke, S.J., and Auger-Méthé, M. (2019). Optimizing marine spatial plans with animal tracking data. *Canadian Journal of Fisheries and Aquatic Science*, 76(3), 497–509. *https://doi.org/10.1139/cjfas-2017-0495*

Lesser, M.P., and Mobley, C.D. (2007). Bathymetry, water optical properties, and benthic classification of coral reefs using hyperspectral remote sensing imagery. *Coral Reefs*, 26(4), 819–829.

Liu, G., Skirving, W.J., Geiger, E.F., De La Cour, J.L., Marsh, B.L., Heron, S.F., Tirak, K.V., Strong, A.E., and Eakin, C.M. (2017). NOAA Coral Reef Watch's 5km Satellite Coral Bleaching Heat Stress Monitoring Product Suite Version 3 and Four-Month Outlook Version 4. *Reef Encounter*, 32(1), 39–45.

Louchard, E.M., Reid, P., Stephens, C., Davis, C.O., Leathers, R.A., and Downes, V. (2003). Optical remote sensing of habitats and bathymetry in coastal environments at Lee Stocking Island, Bahamas. A comparative spectral classification approach. *Limnology and Oceanography*, 48, 511–521.

Louchard, E.M., Reid, R.P., and Stephens, C.F. (2000). Classification of sediment types and estimation of water depth using spectral libraries. *Ocean Optics XV*. Monaco.

Lowther, A.D., Harcourt, R.G., Page, B., and Goldsworthy, S.D. (2013). Steady as He Goes: At-Sea Movement of Adult Male Australian Sea Lions in a Dynamic Marine Environment. *PloS ONE*, 8(9), e74348. doi:10.1371/journal.pone.0074348

Lucas, R., Rebelo, L.-M., Fatoyinbo, L., Rosenqvist, A., Itoh, T., Shimada, M., Simard, M., Souza-Filho, P.W., Thomas, N., Trettin, C., Accad, A., Carreiras, J., and Hilarides, L. (2014). Contribution of L-band SAR to systematic global mangrove monitoring. *Marine and Freshwater Research*, 65, 589–603. doi:10.1071/MF13177

Lucieer, V., Picard, K., Siwabessy, J., Jordan, A., Tran, M., and Monk, J. (2018). Seafloor mapping field manual for multibeam sonar. In *Field Manuals for Marine Sampling to Monitor Australian Waters* (Eds: Przeslawski, R., and Foster, S.), pp 42–64. National Environmental Science Programme (NESP).

Lymburner, L., Bunting, P., Lucas, R., Scarth, P., Alam, I., Phillips, C., Ticehurst, C., and Held, A. (2020). Mapping the multi-decadal mangrove dynamics of the Australian coastline. *Remote Sensing of Environment*, 238, 111185. *https://doi.org/10.1016/j.rse.2019.05.004*

Lynch, H.J., White, R., Black, A.D., and Naveen, R. (2012). Detection, differentiation, and abundance estimation of penguin species by high-resolution satellite imagery. *Polar Biology*, 35, 963–968.

Lyons, M.B., Phinn, S.R., and Roelfsema, C.M. (2012). Long term land cover and seagrass mapping using Landsat and object-based image analysis from 1972 to 2010 in the coastal environment of South East Queensland, Australia. *ISPRS Journal of Photogrammetry and Remote Sensing*, 71, 34–46. doi: 10.1016/j.isprsjprs.2012.05.002

Lyons, M., Roelfsema, C.M., Kennedy, E.V., Kovacs, E.M., Borrego-Acevedo, R., Markey, K., Roe, M., Yuwono, D.M., Harris, D.L., Phinn, S.R., Asner, G., Li, J., Knapp, D.E., Fabina, N.S., Larsen, K., Traganos, D., and Murray, N.J. (2020). Mapping the world's coral reefs using a global multiscale earth observation framework. *Frontiers in Ecology and the Environment*, 6(4), 557–568. *https://doi.org/10.1002/rse2.157*

Lyzenga, D.R. (1978) Passive remote sensing techniques for mapping water depth and bottom features. *Applied Optics*, 17, 379–383.

Lyzenga, D.R. (1985), Shallow-water bathymetry using combined lidar and passive multispectral scanner data. *International Journal of Remote Sensing*, 6, 115–125.

Macreadie, P., Ollivier, Q., Kelleway, J., Kelleway, J.J., Serrano, O., Carnell, P.E., Ewers Lewis, C.J., Atwood, T.B., Sanderman, J., Baldock, J., Connolly, R.M., Duarte, C.M., Lavery, P.S., Steven, A., and Lovelock, C.E. (2017). Carbon sequestration by Australian tidal marshes. *Scientific Reports*, 7, 44071. *https://doi.org/10.1038/srep44071*

Maina, J., Venus, V., McClanahan, T.R., and Ateweberhan, M. (2008). Modelling susceptibility of coral reefs to environmental stress using remote sensing data and GIS models. *Ecological Modeling*, 212, 180–199.

Malthus, T.J., and George, D.G. (1997). Airborne remote sensing of macrophytes in Cefni Reservoir, Anglesey, UK. Aquatic Botany, 58, 317–332

MangroveWatch (2021). *Mangrove Watch* website: *http://mangrovewatch.org.au/*

Marsh, H., and Rathbun, G.B. (1990). Development and Application of Conventional and Satellite Radio Tracking Techniques for Studying Dugong Movements and Habitat Use. *Australian Wildlife Research* 17, 83–100.

McClain, C.R. (2009). A decade of satellite ocean color observations. *Annual Review of Marine Science*, 1, 19-42.

Mcleod, E., Chmura, G.L., Bouillon, S., Salm, R., Björk, M., Duarte, C.M., Lovelock, C.E., Schlesinger, W.H., and Silliman, B.R. (2011). A blueprint for blue carbon: toward an improved understanding of the role of vegetated coastal habitats in sequestering CO_2. *Frontiers in Ecology and the Environment*, 9, 552–560. doi:10.1890/110004

McMahon, C.R., Howe, H., van den Hoff, J., Alderman, R., Brolsma, H., and Hindell, M.A. (2014). Satellites, the all-seeing eyes in the sky: counting elephant seals from space. *PloS One*, 9, e92613.

Méléder, V., Barille, L., Launeau, P., Carrere, V., and Rince, Y. (2003). Spectrometric constraint in analysis of benthic diatom biomass using monospecific cultures 10.1016/j.rse.2003.08.009. *Remote Sensing of Environment*, 88(4), 386–400.

Meza Diaz, B., and Blackburn, G.A. (2003). Remote sensing of mangrove biophysical properties: Evidence from a laboratory simulation of the possible effects of background variation on spectral vegetation indices. *International Journal of Remote Sensing*, 24, 53–73.

Monbet, Y. (1992). Control of Phytoplankton Biomass in Estuaries: A comparative analysis of microtidal and macrotidal estuaries. *Estuaries,* 15(4), 563–571.

Mumby, P.J., and Harborne, A.R. (1999). Development of a systematic classification scheme of marine habitats to facilitate regional management and mapping of Caribbean coral reefs. *Biological Conservation*, 88, 155–163.

Mumby, P.J., Green, E.P., Edwards, A.J., and Clark, C.D. (1997a). Coral reef habitat-mapping: how much detail can remote sensing provide? *Marine Biology*, 130, 193–202.

Mumby, P.J., Green, E.P., Edwards, A.J., and Clark, C.D. (1997b). Measurement of seagrass standing crop using satellite and digital airborne remote sensing. *Marine Ecology Progress Series*, 159, 51–60.

Mumby, P.J., Edwards, A.J., Arias-Gonzalez, J.E., Lindeman, K.C., Blackwell, P.G., Gall, A., Gorczynska, M.I., Harborne, A.R., Pescod, C.L., Renken, H., Wabnitz, C.C.C., and Llewellyn, G. (2004). Mangroves enhance the biomass of coral reef fish communities in the Caribbean. *Nature*, 427, 533–536.

Navarro, A., Young, M., Macreadie, P.I., Nicholson, E., and Ierodiaconou, D. (2021). Mangrove and Saltmarsh Distribution Mapping and Land Cover Change Assessment for South-Eastern Australia from 1991 to 2015. *Remote Sensing*, 13(8), 1450. *https://doi.org/10.3390/rs13081450*

NHT (undated). *Australia's Marine Protected Areas: Protecting our coasts and oceans*. Brochure published by National Heritage Trust: *https://parksaustralia.gov.au/marine/pub/scientific-publications/archive/nrsmpa-protect.pdf*

NMSC (2015). *National Marine Science Plan 2015–2025: Driving the development of Australia's blue economy. National Marine Science Committee*. ISBN 978-1-925012-02-6. *https://www.marinescience.net.au/wp-content/uploads/2018/06/National-Marine-Science-Plan.pdf*

NSW EPA (2017). *Coastal, estuarine and marine ecosystems, State of the Environment 2015* webpage, NSW Environmental Protection Agency website: *https://www.epa.nsw.gov.au/about-us/publications-and-reports/state-of-the-environment/state-of-the-environment-2015/20-coastal-estuarine-marine-ecosystems*

Oceana (2021). *Marine science and Ecosystems Coral Reef* webpage, Oceana website: *https://oceana.org/marine-life/marine-science-and-ecosystems/coral-reef*

Ouellette, W., and Getinet, W. (2016). Remote sensing for Marine Spatial Planning and Integrated Coastal Areas Management: Achievements, challenges, opportunities and future prospects. *Remote Sensing Applications: Society and Environment*, 4, 138–157.

OzCoasts (2020). *Changes in biodiversity* webpage, Australian Online Coastal Information website: *https://ozcoasts.org.au/indicators/coastal-issues/declining_biodiversity/*

Palandro, D.A., Andréfouët, S., Hu, C., Hallock, P., Muller-Karger, F.E., Dustan, P., Callahan, M.K., Kranenburg, C., and Beaver, C.R. (2008). Quantification of two decades of shallow-water coral reef habitat decline in the Florida Keys National Marine Sanctuary using Landsat data (1984–2002). *Remote Sensing of Environment*, 112, 3388–3399

Parks Australia (2021). *Australian Marine Parks* webpage, Parks Australia website: *https://parksaustralia.gov.au/marine/parks/*

Paterson, D.M., Doerffer, R., Kromkamp, J., Morgan, G., and Gieske, W., (1998). Assessing the biological and physical dynamics of intertidal sediment ecosystems: a remote sensing approach. In *Proceedings of Third European Marine Science and Technology Conference (MAST Conference)*, Lisbon, 23–27 May 1998 (Eds: Barthel *et al.*), Project Synopses vol. I, pp. 377–390.

Payne, M.R., Hobday, A.J., MacKenzie, B.R., Tommasi, D., Dempsey, D.P., Fässler, S.M., Haynie, A.C., Ji, R., Liu, G., and Lynch, P.D. (2017). Lessons from the first generation of marine ecological forecast products. *Frontiers in Marine Science*, 4, 289.

Paynter, I., Schaaf, C., Bowen, J.L., Deegan, L., Peri, F., and Cook, B. (2019). Characterizing a New England Saltmarsh with NASA G-LiHT Airborne Lidar. *Remote Sensing*, 11(5), 509. *https://doi.org/10.3390/rs11050509*

Pennesi, C., Rindi, F., Totti, C., and Beolchini, F. (2015). Marine Macrophytes: Biosorbents. In: *Springer Handbook of Marine Biotechnology*. (Ed: Kim, S.K.) Springer Handbooks. Springer, Berlin, Heidelberg.

Phinn, S., Roelfsema, C., Kovacs, E., Canto, R., Lyons, M., Saunders, M., and Maxwell, P. (2018). Mapping, Monitoring and Modelling Seagrass Using Remote Sensing. Ch 15 in *Seagrasses of Australia* (Ed: Larkum, A.W.D. *et al.*) Springer International Publishing. https://doi.org/10.1007/978-3-319-71354-0_15

Platt, T., and Sathyendranath, S. (2008). Ecological indicators for the pelagic zone of the ocean from remote sensing. *Remote Sensing of Environment*, 112, 3426–3436.

Platt, T., Fuentes-Yaco, C., and Frank, K.T. (2003). Marine ecology: spring algal bloom and larval fish survival. *Nature*, 423, 398.

Pollard, R.T., I. Salter, R.J. Sanders, M.I. Lucas, C.M. Moore, R.A. Mills, P.J. Statham, J.T. Allen, A.R. Baker, D.C. E. Bakker, M.A. Charette, S. Fielding, G.R. Fones, M. French, A.E. Hickman, R.J. Holland, J.A. Hughes, T.D. Jickells, R.S. Lampitt, P.J. Morris, F.H. Nédélec, M. Nielsdóttir, H. Planquette, E.E. Popova, A.J. Poulton, J.F. Read, S. Seeyave, T. Smith, M. Stinchcombe, S. Taylor, S. Thomalla, H.J. Venables, R. Williamson, and M.V. Zubkov. (2009). Southern Ocean deep-water carbon export enhanced by natural iron fertilization. *Nature*, 457, 577.

Priede, I.G. (2014). Biogeography of the Oceans: a Review of Development of Knowledge of Currents, Fronts and Regional Boundaries from Sailing Ships in the Sixteenth Century to Satellite Remote Sensing. *Pure and Applied Geophysics*, 171, 1013–1027.

Purkis, S.J., and Brock, J.C. (2013). Lidar Overview. Ch 5 in *Coral Reef Remote Sensing*. (Eds: Goodman, J.A., Purkis, S.J., and Phinn, S.R.). Springer, Dordrecht. ISBN 978-90-481-9291-5.

Purkis, S.J., Graham, N.A.J., and Riegl, B.M. (2008). Predictability of reef fish diversity and abundance using remote sensing data in Diego Garcia (Chagos Archipelago). *Coral Reefs*, 27(1), 167–178.

Rajkumar, K.S.P., and Shanmugam, R.S. (2018). Satellite derived extraction of spatiotemporal variability of upwelling and its influence on marine fishery resources. *Journal of Marine Science and Technology—Taiwan*, 26, 92–101.

RAMSAR (2005). *A Conceptual Framework for the wise use of wetlands and the maintenance of their ecological character*. Resolution IX.1 Annex A, Item 15. *https://www.ramsar.org/sites/default/files/documents/pdf/res/key_res_ix_01_annexa_e.pdf*

RAMSAR (2018). *The Global Wetland Outlook—Status and Trends 2018*. The RAMSAR Convention Secretariat, Switzerland. *https://www.global-wetland-outlook.ramsar.org*

Ramsey, E.W., III, and Jensen, J.R. (1996). Remote sensing of mangrove wetlands: Relating canopy spectra to site-specific data. *Photogrammetric Engineering and Remote Sensing*, 62, 939–948.

Ramsey, E.W., III., Nelson, G.A., Laine, S.C., Kirkman, R.G., and Topham, W. (1997). Generation of coastal marsh topography with radar and ground-based measurements. *Journal of Coastal Research*, 13(4), 1335–1341.

Ramsey, E., Rangoonwala, A., Middleton, B., and Lu, Z. (2009). Satellite optical and radar data used to track wetland forest impact and short-term recovery from Hurricane Katrina. *Wetlands*, 29, 66.

Ramsey, E., III., Rangoonwala, A., Chi, Z., Jones, C.E., and Bannister, T. (2014). Marsh dieback, loss, and recovery mapped with satellite optical, airborne polarimetric radar, and field data. *Remote Sensing Environment*, 152, 364–374.

Reese, D.C., O'Malley, R.T., Brodeur, R., and Churnside, J.H. (2011). Epipelagic fish distributions in relation to thermal fronts in a coastal upwelling system using high-resolution remote-sensing techniques. *ICES Journal of Marine Science*, 68(9), 1865–1874. doi:10.1093/icesjms/fsr107

Reynolds, S.D., Norman, B.M., Beger, M., Franklin, C.E., and Dwyer, R.G. (2017). Movement, distribution and marine reserve use by an endangered migratory giant. *Diversity and Distributions*, 23, 1268–1279.

Ricart, A.M., York, P.H., Bryant, C.V., Rasheed, M.A., Ierodiaconou, D., and Macreadie, P.I. (2020). High variability of Blue Carbon storage in seagrass meadows at the estuary scale. *Scientific Reports*, 10(1), 5865. doi:10.1038/s41598-020-62639-y

Roelfsema, C.M., Dennison, W.C., and Phinn, S.R. (2002). Spatial distribution of benthic microalgae on coral reefs determined by remote sensing. *Coral Reefs*, 21(3), 264–274.

Roelfsema, C., Phinn, S., Jupiter, S., Comley, J., and Albert, S. (2013). Mapping coral reefs at reef to reef-system scales, 10s–1000s km^2, using object-based image analysis. *International Journal of Remote Sensing*, 34(18), 6367–6388. doi:10.1080/01431161.2013.800660

Roelfsema, C., Lyons, M., Kovacs, E.M., Maxwell, P., Saunders, M.I., Samper-Villarreal, J., and Phinn, S. (2014). Multi-temporal mapping of seagrass cover, species and biomass: A semi-automated object based image analysis approach. *Remote Sensing of Environment*, 150, 172–186. *https://doi.org/10.1016/j.rse.2014.05.001*

Roelfsema, C., Lyons, M., Dunbabin, M., Kovacs, E.M., and Phinn, S. (2015). Integrating Field Survey Data with Satellite Image Data to Improve Shallow Water Seagrass Maps: The Role of AUV and Snorkeller Surveys? *Remote Sensing Letters*, 6(2), 135–144. doi:10.1080/2150704x.2015.1013643

Roelfsema, C., Kovacs, E., Ortiz, J.C., Wolff, N.H., Callaghan, D., Wettle, M., Ronan, M., Hamylton, S.M., Mumby, P.J., and Phinn, S. (2018). Coral reef habitat mapping: A combination of object-based image analysis and ecological modelling. *Remote Sensing of Environment*, 208, 27–41. *https://doi.org/10.1016/j.rse.2018.02.005*

Roelfsema, C., Lyons, M., Kovacs, E., Kennedy, E., Markey, K., Borrego, R., Tudman, P., Roe, M., Gonzalez-Rivero, M., Callaghan, D., Murray, N., and Phinn, S. (2020). Habitat maps to enhance monitoring and management of the Great Barrier Reef. *Coral Reefs*, 39, 1039–1054. *https://doi.org/10.1007/s00338-020-01929-3*

Roelfsema, C.M., Lyons, M.B., Castro-Sanguino, C., Kovacs, E.M., Callaghan, D., Wettle, M., Markey, K., Borrego-Acevedo, R., Tudman, P., Roe, M., Kennedy, E.V., Gonzalez-Rivero, M., Murray, N., and Phinn, S.R. (2021). How Much Shallow Coral Habitat Is There on the Great Barrier Reef? *Remote Sensing*, 13, 4343. *https://doi.org/10.3390/rs13214343*

Rogers, J., Parrish, C.E., Ward, L.G., and Burdick, D.M. (2016). Assessment of elevation uncertainty in salt marsh environments using discrete-return and full-waveform lidar. *Journal of Coastal Research*, SI 76, 107–122. doi:10.2112/SI76-010

Sagar, S., Falkner, I., Dekker, A., Huang, Z., Blondeau-Patissier, D., Phillips, C., Przeslawski, R. (2020). *Earth Observation for monitoring of Australian Marine Parks and other off-shore Marine Protected Areas*. Report to the National Environmental Science Program, Marine Biodiversity Hub. Geoscience Australia.

Sasano, M., Yamanouchi, H., Matsumoto, A., Kiriya, N., Hitomi, K., and Tamura, K. (2012). Development of boat-based fluorescence imaging lidar for coral monitoring. *Proceedings of 12th International Coral Reef Symposium*, 9–13 July 2012, Cairns, Australia.

Scales, K.L., Miller, P.I., Hawkes, L.A., Ingram, S.N., Sims, D.W., and Votier, S.C. (2014). On the Front Line: frontal zones as priority at-sea conservation areas for mobile marine vertebrates. *Journal of Applied Ecology*, 51, 1575–1583.

Sherlock, M., Marouchos, A., Williams, A., and Tyndall, A. (2016). A vessel towed platform for deepwater high resolution benthic imaging. pp 1–6 in *OCEANS 2016-Shanghai*. IEEE, Shanghi. doi:10.1109/OCEANSAP.2016.7485396.

Shortis, M., Seager, J., Williams, A., Barker, B., and Sherlock, M. (2007). A towed body stereo-video system for deep water benthic habitat surveys. *Proceedings of Eighth Conference on Optical 3-D Measurement Techniques*, Volume II (Eds: A. Grun and H. Kahmen), pp 150–157. ETH Zurich, Switzerland. ISBN 3- 906467-67-8

Silvestri, S., Marani, M., and Marani, A. (2003). Hyperspectral remote sensing of salt marsh vegetation, morphology and soil topography. *Physics and Chemistry of the Earth (Parts A/B/C)*, 28 (1–3), 15–25. *https://www.sciencedirect.com/science/article/pii/S1474706503000044*

Smith, E.V., Rogers, R.H., and Reed, L.E. (1975). Automated mapping and inventory of Great Barrier Reef zonation with Landsat data. In *IEEE Ocean '75*, 1, 775–780.

SOE (2018). *Coastal waters* webpage. State of Environment website: *https://soe.environment.gov.au/theme/coasts/topic/2016/coastal-waters*

Steven, A.D.L., Baird, M.E., Brinkman, R., Car, N.J., Cox, S.J., Herzfeld, M., Hodge, J., Jones, E., King, E., Margvelashvili, N., Robillot, C., Robson, B., Schroeder, T., Skerratt, J., Tickell, S., Tuteja, N., Wild-Allen, K., Yu, J. (2019). eReefs: An operational information system for managing the Great Barrier Reef. *Journal of Operational Oceanography*, 12, 1–17. *https://doi.org/10.1080/1755876X.2019.1650589*

Stewart, M., and Fairfull, S. (2008). *Mangroves*. Primefact 746. NSW Department of Primary Industry, Sydney. *http://www.dpi.nsw.gov.au/__data/assets/pdf_file/0020/236234/mangroves.pdf*

Strong, A.E., Arzayus, F., Skirving, W., and Heron, S.F. (2006). Identifying coral bleaching remotely via Coral Reef Watch—improved integration and implications for climate change. Ch 9 in *Coral Reefs and Climate Change: Science and Management* (Eds: J.T. Phinney, O. Hoegh-Guldberg, J. Kleypas, W. Skirving, and A.E. Strong). American Geophysical Union.

Strong, A.E., Liu, G., Skirving, W., and Eakin, C.M. (2011). NOAA's Coral Reef Watch program from satellite observations. *Annals of GIS*, 17(2), 83–92. *https://doi.org/10.1080/19475683.2011.576266*

Thomas, N., Lucas, R., Bunting, P., Hardy, A., Rosenqvist, A., and Simard, M. (2017). Distribution and drivers of global mangrove forest change, 1996–2010. *Plos One*, 12, e0179302. doi:10.1371/journal.pone.0179302

Tittensor, D.P., Mora, C., Jetz, W., Lotze, H.K., Ricard, D., Berghe, E.V., and Worm, B. (2010). Global patterns and predictors of marine biodiversity across taxa. *Nature*, 466, 1098.

Tomkiewicz, S.M., Fuller, M.R., Kie, J.G., and Bates, K.K. (2010). Global positioning system and associated technologies in animal behaviour and ecological research. *Philosophical Transactions of the Royal Society B,* 365, 2163–2176. doi:10.1098/rstb.2010.0090

Traganos, D., Aggarwal, B., Poursanidis, D., Topouzelis, K., Chrysoulakis, N., and Reinartz, P. (2018). Towards Global-Scale Seagrass Mapping and Monitoring Using Sentinel-2 on Google Earth Engine: The Case Study of the Aegean and Ionian Seas. *Remote Sensing*, 10(8), 1227. *https://doi.org/10.3390/rs10081227*

Tulloch, V.J., Atkinson, S., Possingham, H.P., Peterson, N., Linke, S., Allan, J.R., Kaiye, A., Keako, M., Sabi, J., Suruman, B., and Adams, V.M. (2021). Minimizing cross-realm threats from land-use change: A national-scale conservation framework connecting land, freshwater and marine systems. *Biological Conservation*, 254, 108954.

Turner, L., Tracy, D., Tilden, J., and Dennison, W.C. (2004). *Where river meets sea: Exploring Australia's estuaries*. CRC for Coastal Zone Estuary and Waterway Management, Brisbane.

Tweddle, J. F., Gubbins, M., and Scott, B.E. (2018). Should phytoplankton be a key consideration for marine management? *Marine Policy*, 97, 1–9.

Underwood, G., and Kromkamp, J., (1999). Primary production by phytoplankton and microphytobenthos in estuaries. *Advances in Ecological Research*, 29, 93–153.

UNEP (2006). *Marine and Coastal Ecosystems and Human Well-being: A synthesis report based on the findings of the Millenium Ecosystem Assessment*. United Nations Environmental Programme. 76 p.

Wang, L., Jia, M., Yin, D., and Tian, J. (2019). A review of remote sensing of mangrove forests: 1956–2018. *Remote Sensing of Environment*, 231, 111223. *https://doi.org/10.1016/j.rse.2019.111223*

Wilkinson, C. (2008). *Status of coral reefs of the world*. GCRMN, Townsville.

Williams, A., Althaus, F., and Schlacher, T.A. (2015). Towed camera imagery and benthic sled catches provide different views of seamount benthic diversity. *Limnology and Oceanography: Methods*, 13, 62–73.

Wolanksi, E., Newton, A., Rabalais, N., and Legrand, C. (2008). Coastal Zone Management. In *Encyclopedia of Ecology*, pp. 630–637. Elsevier.

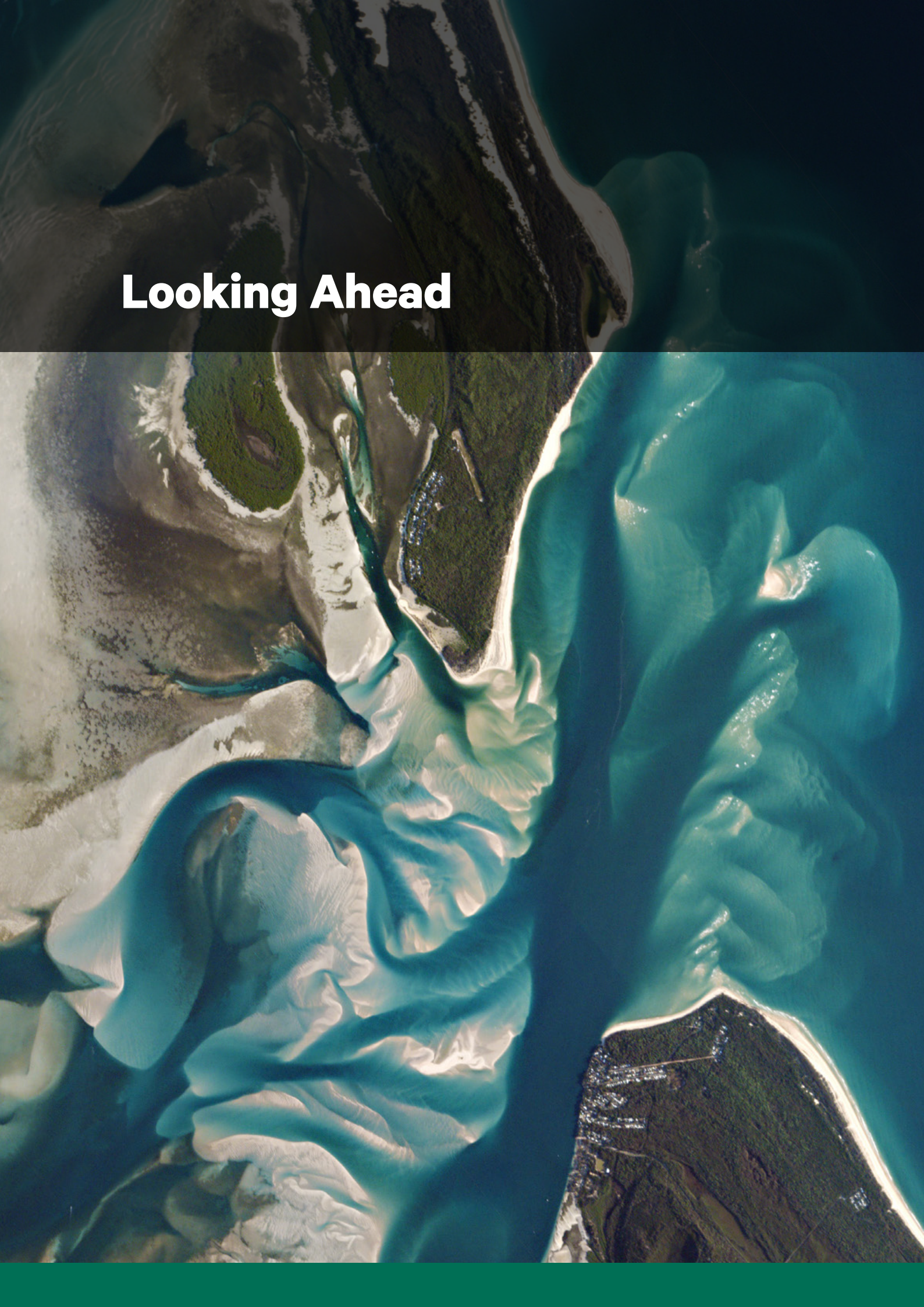
Yamano, H. (2007). The use of multi-temporal satellite images to estimate intertidal reef-flat topography. *Journal of Spatial Science*, 52, 73–79.

Yamano, H., and Tamura, M. (2004). Detection limits of coral reef bleaching by satellite remote sensing: simulation and data analysis. *Remote Sensing of Environment*, 90, 86–103.

Yancho, J.M.M., Jones, T.G., Gandhi, S.R., Ferster, C., Lin, A., and Glass, L. (2020). The Google Earth Engine Mangrove Mapping Methodology (GEEMMM). *Remote Sensing*, 12, 3758.

Zeh, D.R., Heupel, M.R., Limpus, C.J., Hamann, M., Fuentes, M.M.P.B., Babcock, R.C., Pillans, R.D., Townsend, K.A., and Marsh, H. (2015). Is acoustic tracking appropriate for air-breathing marine animals? Dugongs as a case study. *Journal of Experimental Marine Biology and Ecology*, 464, 1–10.

Zimmerman, R.C. (2006). Light and photosynthesis in seagrass meadows. Ch 13 in *Seagrasses: biology, ecology and conservation*. (Eds: Larkum, A.W.D., Orth, R.J., and Duarte, C.M.). Springer, Dordrecht. pp. 303–321.



Looking Ahead

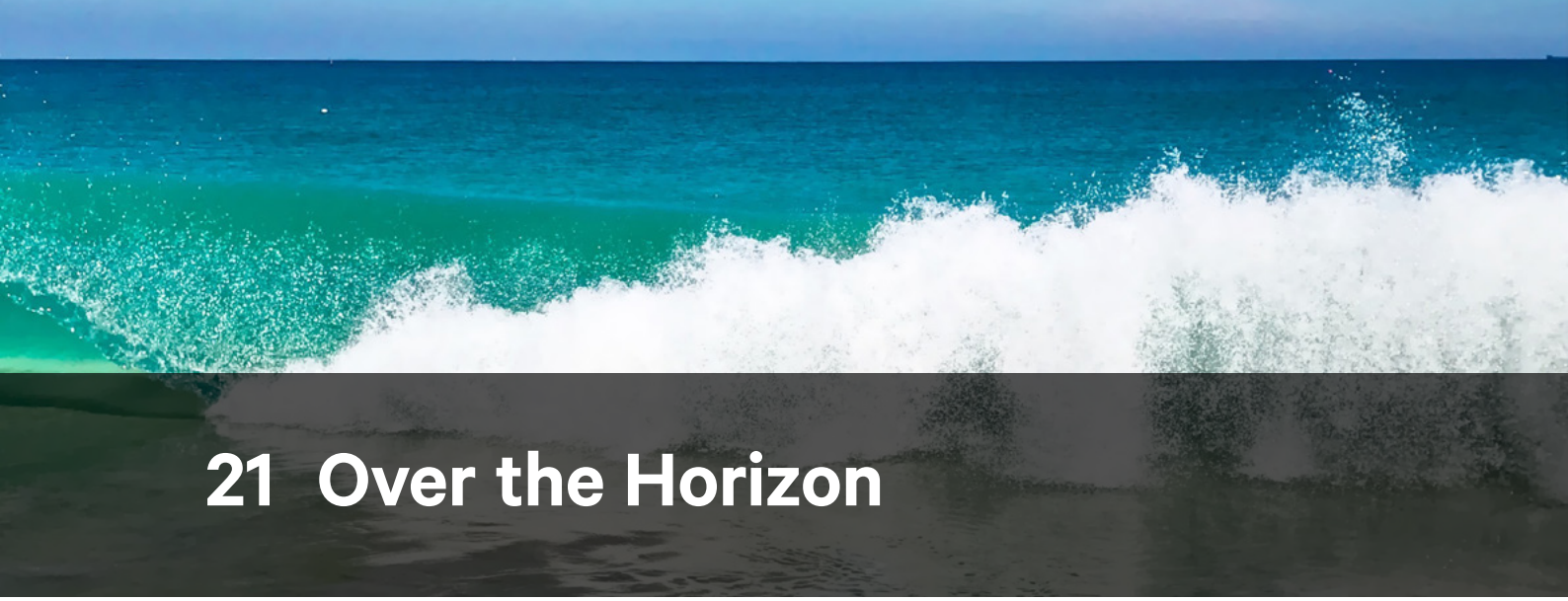
We conclude this sub-volume by looking ahead to new technologies and new methods for integrating EO and other datasets in surface water environments, and review the expanded range of aquatic challenges they can address.

Contents

21 Over the Horizon 439

22 Glossary 449

Background image on previous page: South Passage between Moreton and North Stradbroke Islands, Great Barrier Reef, Queensland, acquired on 1 October 2015. **Source:** Planet Labs Inc. (CC BY SA 4.0). Retrieved from *https://www.planet.com/gallery/#!/post/amity-point*



21 Over the Horizon

Barbara Harrison, Edward King, Arnold Dekker, David Hudson, and Stuart Phinn

Despite covering most of the globe and for the most part being remote from human settlements, our surface waters are increasingly being threatened by anthropogenic activities. Trends in human population growth and their impact on terrestrial vegetation are detailed in Volume 3A—Section 19. The major threats to terrestrial biodiversity—namely habitat changes, overexploitation, invasive species, climatic variations and pollution (see Volume 3A—Section 18)—also apply to aquatic environments, whether inland, coastal, or marine. In order to leave our planet in reasonable shape for future generations, a greater emphasis needs to be placed on sustainability—a balance between consumption and production—in all environments, including surface waters (see Volume 3A—Section 19). In this context, the following subsections consider:

- global coverage of current EO sensors in terms of temporal frequency and spatial extent, and the increased spectral resolution and density of future sensors (see Section 21.1);
- processing advances to interpret and integrate large datasets more rapidly (see Section 21.2);
- smart solutions for using EO resources to manage our water resources more sustainably (see Section 21.3); and
- human impacts on the aquatic environment (see Section 21.4).

I would feel more optimistic about a bright future for man if he spent less time proving he can outwit Nature and more time tasting her sweetness and respecting her seniority.
(E.B. White)

21.1 The Global Picture

Broadscale coverage observation of the ocean by satellite has typically been provided at 1–2 km resolution at roughly daily frequency. Geostationary satellites have generated imagery at hourly frequency, but by dint of their much larger orbit, at even lower spatial resolution. This is now changing as a series of polar orbiting, optical sensors with ~300 m resolution are operational, and geostationary sensor technology advances. In the latter case, 10 minute full-disk imagery at 500 m spatial resolution in the optical spectrum, and 2 km in the infrared, are becoming routine (e.g. Schmit *et al.,* 2005; Da, 2015). These innovations will deliver more useful data for coastal and inland waters where high spatial resolution is needed. The benefits of increased observation frequency are two-fold:

- improved coverage through (moving) broken cloud; and
- an ability to probe aquatic processes at sub-daily (even sub-hourly) time scales.

Background image: City Beach, Perth, photographed in February 2017. **Source:** Akbys, Wikimedia Commons. Retrieved from: *https://commons.wikimedia.org/wiki/File:City_Beach,_Perth,_Australia_(February_2017)_(33389330432).jpg*

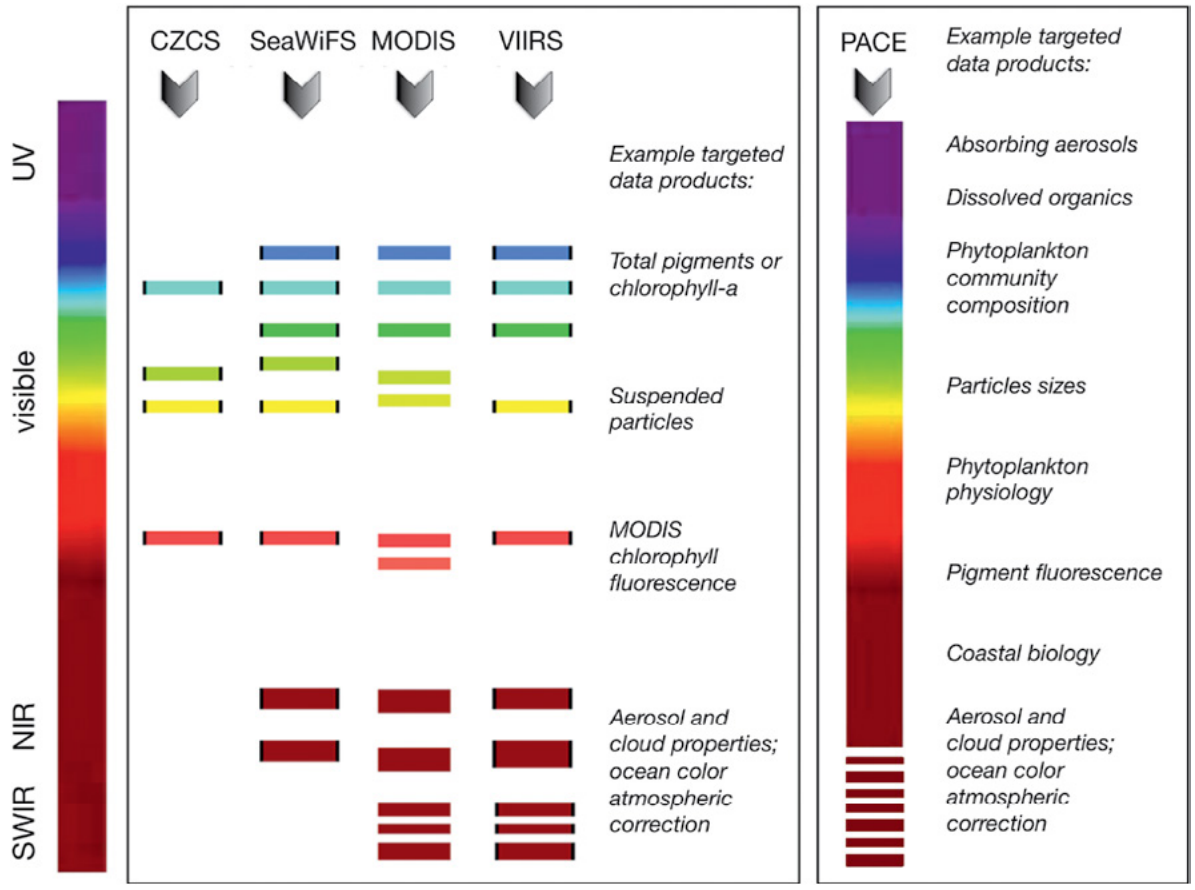
Recommended Chapter Citation: Harrison, B.A., King, E.A., Dekker, A.G., Hudson, D., and Phinn, S.R. (2021). Over the Horizon. Ch 21 in *Earth Observation: Data, Processing and Applications. Volume 3B—Surface Waters.* CRCSI, Melbourne. pp. 439–448. ISBN 978-0-6482278-5-4.

Measurements of the status and trends of key indicators for the ocean and marine life are required to inform policy and management in the context of growing human uses of marine resources, coastal development, and climate change.
(Muller-Karger, 2020)

In addition to these large satellites, nanosatellites—miniature satellites carrying multispectral sensors that are often networked into constellations—offer rapid revisit capability at high spatial resolution (see Volume 1A—Section 1.3.3 and Volume 1B—Section 10.6.2). This increased frequency of coverage with good spatial detail is particularly useful for monitoring aquatic events that change rapidly, such as floods (see Section 11.4) and oil spills (see Section 19.4.3).

As well as improvements in spatial and temporal resolution, new types and combinations of satellite sensors are yielding different insights. In particular, the joint US/Argentinian Aquarius (Le Vine *et al.*, 2007) and the European SMOS (Font *et al.*, 2004) missions have delivered, for the first time, near-global maps of sea surface salinity, representing a quantum leap in our understanding of this key physical ocean variable (see Section 19.7). The SWOT mission (see Excursus 12.1) will provide an experimental imaging altimeter while the (currently unfunded) SKIM mission proposed a similar instrument to SWIM that was flown on CFOSAT, but with Doppler capability to retrieve ocean surface currents for the first time. Both of these missions, utilising novel sensor technology, have the capacity and potential to revolutionise sub-mesoscale oceanography. There is a trend also to fly multiple instruments on satellites in close formation (for example, the A-Train, Stephens *et al.*, 2002) so that multi-faceted and complementary observations are made of both aquatic environments and the atmosphere.

Figure 21.1 Spectral characteristics of hyperspectral PACE OCI compared with heritage spaceborne ocean colour sensors



Source: Werdell *et al.* (2019) Figure 2

Protecting our oceans is also one of the world's more pressing environmental challenges.
(Scott Morrison, 2019)

Knowledge of the atmosphere is key to correcting and adjusting the satellite surface imagery, but also these atmospheric processes have direct impact on the sea surface. Contemporaneous observations of different aspects of the ocean surface (for example colour, temperature, salinity, wind stress, and surface height) provide a progressively richer view of the process complexities. Within the next decade, imaging altimeters providing broad rather than narrow-track sea surface height (Guijarro *et al.*, 2003), and hyperspectral optical sensors that enable a far more nuanced interpretation of coastal-ocean biology and sediment transport in coastal regions, will continue to transform our understanding of coastal waters and oceans.

In particular, the PACE mission, which is due for launch in 2023, carries the Ocean Colour Instrument (OCI) and two multi-angle polarimeters (Werdell *et al.*, 2019). OCI has a spatial resolution of 1 km and a temporal frequency of 1–2 days, but most importantly provides full hyperspectral resolution from ultraviolet (UV) to shortwave infrared (SWIR) wavelengths, thus enabling more detailed analyses than were possible with earlier sensors (see Figure 21.1). Together these sensors will improve our understanding of water colour in large inland water bodies, estuaries, coasts and oceans, and also of atmospheric parameters (Sagar *et al.*, 2020; Cawse-Nicholson *et al.*, 2021).

For global studies, a set of common, agreed variables is necessary to enable disparate *in situ* datasets to be exchanged and integrated. Essential Ocean Variables (EOV) have been defined in recent years to this end (Miloslavich *et al.*, 2018; see Excursus 7.2 and Excursus 21.1) and are also linked to components of the UN Sustainable Development Goals (SDG; see Volume 3A—Section 20). EOV are closely related to Essential Biodiversity Variables (EBV; see Volume 3A—Section 19.3) with both being indicative of the status of ecosystem components and ecosystem health (GOOS, 2021). These essential variables define a baseline against which anthropogenic pressures and fundamental environmental changes in the global marine environment can be quantified (see Section 21.4). Given the breadth, depth, and interconnectedness of the world ocean, a global approach is the only feasible way to understand and monitor its complexity and share the cost of acquiring this essential data (Canonico *et al.*, 2019).

Table 21.1 Global monitoring systems

System	Goal	Website
Global Ocean Observing System (GOOS)	Sustained collaborative system of ocean observations, encompassing *in situ* networks, satellite systems, governments, UN agencies, and individual scientists	*https://www.goosocean.org/*
Marine Biodiversity Observation Network (MBON)	Global community of practice within GEO BON (Group on Earth Observations Biodiversity Observation Network) for the sustained collection, curation, and analysis of marine biodiversity data	*https://marinebon.org/*
Ocean Biogeographic Information System (OBIS)	Global open access data and information clearing-house on marine biodiversity for science, conservation, and sustainable development	*https://obis.org/*
Ocean Best Practices System (OBPS)	Global, sustained system comprising technological solutions and community approaches to enhance management of methods as well as support the development of ocean best practices	*https://www.oceanbestpractices.org/*
GEO AquaWatch	Develop and build the global capacity and utility of Earth Observation-derived water quality data, products and information to support water resources management and decision making.	*https://www.geoaquawatch.org/*
GEO Blue Planet (see Greb *et al.*, 2018)	Advance and exploit synergies among the many observational programs devoted to ocean and coastal waters Improve engagement with a variety of users for enhancing the timeliness, quality, and range of services delivered Raise awareness of the societal benefits of ocean observations at the public and policy levels	*https://geoblueplanet.org/*
GeoGLOWS	Provide relevant, actionable water information to promote the use of EO in the decision-making process while promoting the strengthening of observational networks.	*https://www.geoglows.org/*
Integrated Marine Biosphere Research (IMBeR)	Global research project focusing on ocean sustainability in the context of global change	*http://imber.info/*

For freshwater environments, Essential Climate Variables (ECV) have been defined for lakes, and Essential Water Variables (EWV) are in the process of being defined. For coasts there are many related activities around CEOS-Coasts and GEO Blue Planet. A signification development is the adoption of the UN Sustainable Development Goals (SDG) for oceans, inland waters, and wetlands (SDG 14, 6, and 15 respectively), that will require a global effort in monitoring and assessing progress against these SDG goals (see Volume 3A—Section 20.4). The recent global adoption of SEEA (System of Economic Environmental Accounting; see Volume 3A—Section 20.5) will also require systematic monitoring and assessment of our natural resources and thus will be another driver for operational EO applications.

In addition to biodiversity data repositories such as the Global Biodiversity Information Facility (GBIF), a number of global, EO-based systems specifically monitor surface waters with a focus on biodiversity (see Table 21.1). These global monitoring programs are providing the foundation of baseline observations that will be essential to guide efforts and measure progress in conserving biodiversity and improving sustainability in the inland, coastal, and marine environments (see Section 21.4).

Excursus 21.1—Essential Ocean Variables

Source: GOOS: *https://www.goosocean.org/index.php?option=com_content&view=article&id=170&Itemid=114*
Further Information: Lindstrom *et al*., (2012); Muller-Karger *et al*. (2018); Moltmann *et al*. (2019)

Given the vast extent and remoteness of the ocean, *in situ* observations can be both costly and dangerous to acquire. To maximise the value of any data collected, a framework of Essential Ocean Variables (EOV; see Excursus 7.2) has been designed by the Global Ocean Observing System (GOOS; in collaboration with many other global monitoring consortia—see Section 7.5 above) based on the criteria of being:

- relevant—to the GOOS themes of climate, operational ocean services, and ocean health;
- feasible—using established, scientifically understood methods; and
- cost-effective—generates and archives affordable data, primarily by using coordinated, established observing systems and historical datasets.

EOV describe the key physical, biogeochemical, and biological attributes of oceans (see Table 21.2) and are closely related to Essential Biodiversity Variables (EBV; see Volume 3A—Section 18; Muller-Karger *et al*., 2018). Development of EOV was based on the drivers-pressures-state-impact-response (DPSIR) model (Volume 3A—Section 11.3). A review of 24 international conventions or agreements, that were deemed to be relevant to global ocean biology, identified key anthropogenic pressures and societal drivers in the marine environment (see Figure 21.2).

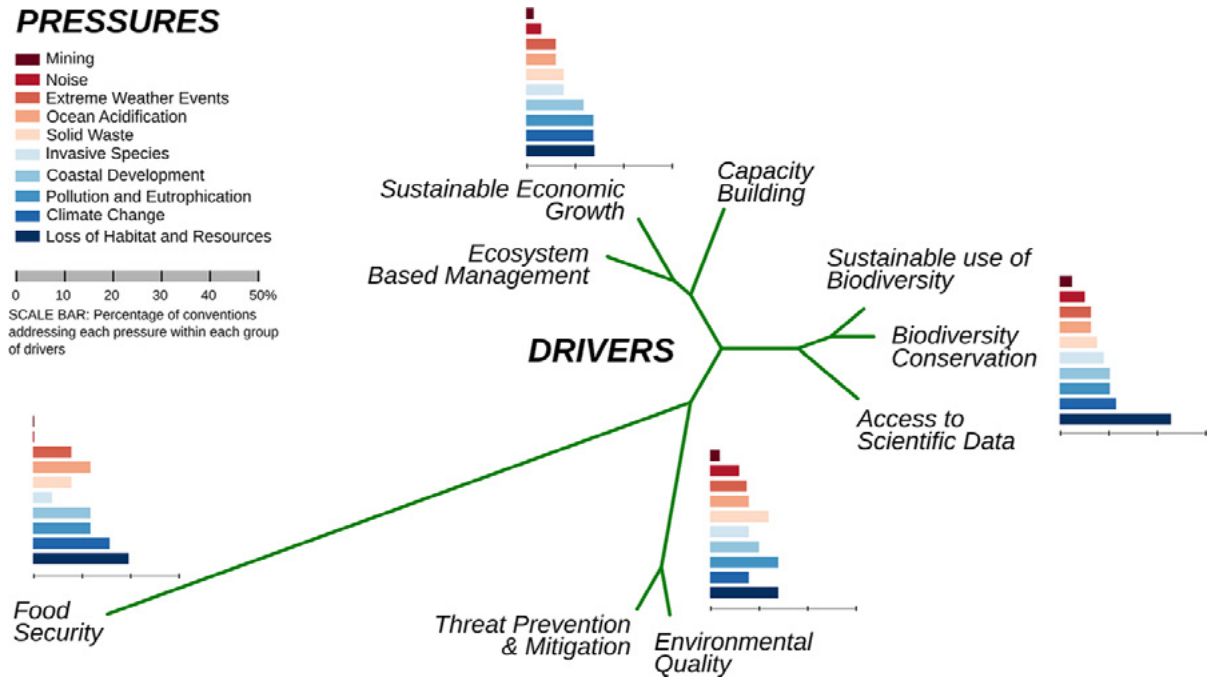
Table 21.2 Essential Ocean Variables

Physics	Biogeochemistry	Biology and Ecosystems	Cross-disciplinary
Sea state	Oxygen	Phytoplankton biomass and diversity	Ocean colour
Ocean surface stress	Nutrients	Zooplankton biomass and diversity	Ocean Sound
Sea ice	Inorganic carbon	Fish abundance and distribution	
Sea surface height	Transient tracers	Marine turtles, birds, mammals abundance and distribution	
Sea surface temperature	Particulate matter	Hard coral cover and composition	
Subsurface temperature	Nitrous oxide	Seagrass cover and composition	
Surface currents	Stable carbon isotopes	Macroalgal canopy cover and composition	
Subsurface currents	Dissolved organic carbon	Mangrove cover and composition	
Sea surface salinity		Microbe biomass and diversity (emerging)	
Subsurface salinity		Invertebrate abundance and distribution (emerging)	
Ocean surface heat flux			

Source: GOOS (2021)

Figure 21.2 Pressures and drivers on global ocean biology

The length of lines between drivers indicates similarity and horizontal bars represent pressures.



Source: Miloslavich *et al.* (2018) Figure 2

21.2 From Data to Information

In this sub-volume we have presented the state of the art in optical, thermal, microwave, and acoustic EO as they relate to surface waters. However, the many potential synergies between the information from different EO sensors have not yet been realised. As with most technologies, each dataset needs to reach a level of maturity—be sufficiently reliable and understood—before it can be routinely integrated with other datasets (see Volume 2D).

EO has, since its inception, been hamstrung by the ability to produce data volumes that exceed analysis capacity. Without a doubt, the rapid commodification of computing (globally) in the past two decades is reversing this trend by making it possible to handle more observations efficiently and without compromise through averaging or approximation (see Volume 2D). The more detailed knowledge and simultaneous observations of the atmosphere permit a thorough and accurate accounting for its effect in imagery, leading to higher quality biogeophysical products. Enhanced computing capacity also enables more complex retrieval algorithms to use more data to be better able to account for the complexity present within the imaged scene.

Another variation on this theme is sensor-sensor fusion, where similar sensors on different platforms with different revisit times, spatial or spectral resolution are combined (see Volume 2D). For example combining high frequency but low spatial resolution observations from geostationary satellites with the lower frequency higher spatial resolution from low earth orbit, could yield a product that is more useful than either of its constituents. Similar approaches could be used with multispectral and hyperspectral instruments. The recent development of high-altitude drones (so-called pseudo-satellites) that are solar powered and can linger on station at stratospheric altitudes (~20 km) for months at a time offer the prospect of a powerful opportunity to use sensor-sensor fusion to bridge across scales between traditional satellite observations and ground (or near-ground) measurements. All these would benefit from the dramatic improvements in data management and computing capacity that is emerging today.

Lastly, the use of EO data in a model-data fusion (or data assimilating) paradigm, in which theoretical behaviour is dynamically constrained by data, is already having a dramatic impact on understanding of all aspects of terrestrial, freshwater, coastal, and ocean processes. This impact is now extending from physical oceanography into improved biological modelling in the eReefs system (see Section 20.6.4 and Volume 2D—Excursus 14.4), including assessing how changes in catchment management practices impact the waters of the Great Barrier Reef. Improved processing and data handling capacity offers, by far, the greatest prospect for yielding the full potential of satellite data to the study of surface waters on Earth.

While EO datasets have always been huge, rapid developments, from autonomous *in situ* sensors and data collection based on citizen science (see Volume 2D—Section 12), to sensors somewhere in the atmosphere, to sophisticated satellites (singles and swarms), will create an even greater data deluge that will need to be harnessed into meaningful information. Smart data analytics will become core, and it is likely that a paradigm shift in the conversion of data into information will be required (Sudmanns *et al*., 2019). Extremely large datasets have become known as 'big data', where big generally implies five 'v' attributes:

- volume—extremely high;
- variety—wide range of forms;
- velocity—high speed processing required;
- veracity—data uncertainty needs to be addressed; and
- value—goal of data analysis (Sudmanns *et al*., 2019).

EO is one example of 'big Earth data', which Sudmanns *et al*. (2019) define in terms of four characteristics:

- "non-repeatability—observations of physical objects and processes are unique in space and time and generally cannot be repeated;
- uncertainty—big data involves different approaches to observation and recording, as well as indirect observation and sampling;
- multidimensionality—a wide range of data sources and complex analysis methods including cross-scale modelling lead to a wide range of dimensionality and often multidimensionality; and
- computational complexity—combining the first three issues results in a high degree of computational complexity in data analysis."

Some of the challenges involved in maximising the value of this data source for a given area of interest are summarised in Table 21.3. Sudmanns *et al*. (2019) propose that new norms, standards, and guidelines will be required to store, process, and access these massive EO datasets, and integrated web-based workflows will be required to 'bring the user to the data, not the data to the user'. Visualisation is also a key challenge with all types of big data, to ensure they realise their potential.

We are currently on a path to removing the existing bottlenecks in instrumentation, sensors, communication, and computer processing power. A key development during the decade 2010–20 has been the realisation of Analysis Ready Data (ARD) applications, which are opening up archives comprising myriad images into accessible data from which quantitative information can be extracted (see Volume 2D—Sections 3.2 and 11). The next step will be to provide 'Interpretation Ready Data' to end users so they can make informed decisions for managing and taking care of our aquatic ecosystems, resulting in the final end product of decision ready data.

Table 21.3 Big Earth data challenges

Technological challenges	Technological, computational challenges of distributed, highly scalable systems
	Multiple data sources require consistency of definitions of phenomena and measurement parameters
	Data curation and stewardship
Methodological challenges	Provision of Analysis Ready Data (ARD)
	Uncertainty analysis and characterisation
	Model/data validation and quality assurance
Social challenges	Complex interrelated systems and processes at the energy-water-food-climate nexus
	Lack of data regarding some human-centred aspects and 'soft' parameters
	Multiple scales across spatial and temporal processes

Source: Sudmanns *et al*. (2019) Figure 2

21.3 Smart Management of Surface Water Resources

Water underpins all life on Earth. The requirement for spatially and temporally comprehensive information on our ocean, coral reef, coastal, and inland water ecosystems will only increase. Easily accessible, trusted, quantitative, validated information products from EO will enable human society to understand and manage these ecosystems more sustainably. Adaptive management requires:

- long term data trends;
- near real time monitoring of extreme events; as well as
- predictive capability.

These three requirements have consequences for information acquired from EO sensors:

- long term data trends require careful calibration and intercalibration of generations of sensors;
- near real time monitoring requires very fast processing pipelines to get data to decision makers with minimal delays; and
- predictions require combinations of *in situ* and EO-based information with biogeochemical and hydrodynamic models.

Volume 1B—Section 10 and Volume 3A—Section 20 summarise various aspects of the 'smart' environment that directly impact our understanding of planet Earth, including:

- the rapidly maturing Internet of Things (IoT)—a global network of devices, people, processes, and data (see Volume 1B—Section 10.2 and Volume 3A—Section 20.1), including aquatic sensors (see Excursus 5.1);
- the importance of locational accuracy—both in terms of positioning devices, integrated location-based services, and the National Positioning Infrastructure (see Volume 1B—Section 10.3 and Volume 2B), which is particularly critical in remote inland, coastal, coral reef, and marine environments;
- increasing data volumes from a wide range of sources—including EO platforms and sensors, open datasets, and crowdsourced/citizen science contributions (see Volume 1A—Section 1.3.1, Volume 1B—Sections 10.4 and 10.6, and Volume 2D—Section 12); and
- the growth of integrated 'smart' systems—such as ARD and virtual worlds (see Volume 1B—Sections 10.5 and Volume 2D—Sections 3.2 and 11).

In the context of Surface Waters applications of EO, each of these technological aspects of the smart paradigm have already contributed to a greater appreciation of the complexity and fragility of the aquatic environment. Within the smart environment framework, the emphasis in EO is likely to shift from raw data processing and algorithms to how we intelligently harmonise all data streams in a mutually synergistic manner (most likely through sophisticated data assimilation methods) to provide accessible, easily comprehensible, timely, management-relevant information in such a way that it is conducive to good decision-making and will benefit our aquatic environments globally.

21.4 The Human Factor

As detailed in the preceding sections, spaceborne EO methods, together with *in situ* and airborne data, are already making our lives—and those of our fauna and flora—better globally. Some of the current benefits that society now derives from EO of surface waters include:

- mass balance applications for estimating regional and global freshwater availability (see Excursus 1.1);
- monitoring coastal zone integrity, flooding, and potential erosion factors (see Section 11);
- accurate monitoring of sea level and the impact of sea level changes to settlement safety, estuarine health, and storm potential (see Section 12);
- detailed bathymetric mapping for surveillance, search and rescue, and pollution control (see Section 13);
- mapping and monitoring sea surface temperature for ocean, weather, climate, and ecological forecasting and modelling (see Section 14);
- mapping and monitoring conditions in Antarctica and the Southern Ocean for intelligent conservation and climate change impacts (see Section 15);
- monitoring and modelling ocean and coastal water circulation, including waves, to prepare for storms (e.g. Waveforce) and utilise natural energy potential (see Sections 16 and 17);
- monitoring and modelling water quality (both marine and inland) to ensure water security for both social and environmental benefits (see Sections 18 and 19); and
- managing inland, coastal, and marine ecology to ensure sustainable use of resources and protect biodiversity from various sources of pollution and other anthropogenic pressures (see Section 20).

Table 21.4 Target variables for pressures and drivers in the aquatic biological environment

Factor		Target variables
Drivers	Scientific knowledge and data access	Patterns of biodiversity (location of biodiversity hotspots and their relationship to the location of high levels of ecosystem services), primary productivity (photosynthetic activity), harmful algal blooms, zooplankton biomass, fish abundance (catch/captures), levels of bycatch, discards, and waste, population size and trends of threatened species, geographic range and habitat needs of threatened species, key life-history parameters of selected indicator species (leading to detect changes), changes in breeding and nursery areas, reproduction and survival (under eutrophication conditions), noise, species structure of highly productive sea areas
	Sustainable use of biodiversity and resources	Condition of depleted fishing stocks, population size and trends of threatened species, geographic range and habitat needs of threatened species
	Conservation of biodiversity and ecosystems	Trends in abundance, distribution and extinction risks of species, cover condition, representativeness, effectiveness of protected areas, trends in genetic diversity, trends in extent condition and vulnerability of ecosystems (for example to degradation by pollutants, bycatch, invasive species), biomes, habitats (e.g. coral reefs), control of harmful invasive species (e.g. in ballast waters), condition of migratory species and corridors, and areas critical for sensitive life stages (e.g. for Arctic species)
	Improve management: use of integrated ecosystem approach	Assessments on biodiversity and ecosystem services
	Development through sustainable economic growth	Fisheries, economic benefits, access to marine resources and markets
	Capacity building	Taxonomy (biodiversity), technology, implementation of effective conservation and management of straddling and highly migratory fish stocks, develop research capacity, strengthen national data systems, strengthen statistical capacities, improve data accessibility, quality and synthesis
	Threat prevention and impact mitigation	Integrated assessments, sustainability of long term socioeconomic benefits, assessment of transportation corridors
	Environmental quality and health	Oil pollution, chemical pollution, sewage, garbage and debris, air pollution, control of harmful antifouling systems, harmful algal blooms, nutrient enrichment and eutrophication, acidification, biotoxins, pathology, emerging diseases, health indices, sound (noise), marine renewable energy developments
	Food security	Abundance and quality of fisheries stocks, control of harmful algal blooms
Pressures	Loss of resources: habitats/biodiversity (including overfishing)	Species presence/absence and distribution (from microbes to marine mammals), status of populations (e.g. abundance of commercially important, migratory, and "iconic" species), fisheries production, captures and by-catch, extent (cover) of living benthic habitats (coral reefs, seagrasses, mangroves)
	Climate change	Primary productivity, harmful algal blooms, coral bleaching (extent)
	Pollution / eutrophication	Phytoplankton diversity and biomass, presence of toxic, waterborne pathogens, harmful algal blooms
	Coastal development	Extent (cover) of living benthic habitats (coral reefs, seagrasses, mangroves)
	Invasive species	Range (presence) and abundance of invasive species
	Solid wastes	Volume and/or weight marine debris
	Ocean acidification	Calcareous phytoplankton abundance, coral skeletal density
	Extreme weather events	Extent (cover) of living benthic habitats (coral reefs, seagrasses, mangroves) susceptible to storms, hurricanes, extreme rainfall and sedimentation
	Noise	Movement of marine mammals (cetaceans)
	Mining	Diversity of deep sea benthic species

Source: Miloslavich *et al.* (2018) Tables S4 and S5

At some level in monitoring and marine ecology more generally, we have to turn the argument around so that we are monitoring recovery and restoration, or even resilience in the face of increasing threats—as well as the many ongoing declines. Monitoring is but a small and necessary cost to sustain or increase the value of the benefits we get from nature.
(Nicholas Bax)

Many of these benefits use the word 'sustainable'. The concept of sustainability is discussed in detail in Volume 3A—Section 20, including international agreements and initiatives designed to achieve this end, the most relevant of which are the UN SDG. At a global scale, EO offers the only practical approach to monitoring sustainability in both terrestrial and aquatic environments.

To ensure a sustainable future, however, perhaps the fundamental question relating to any application of EO becomes "how can EO be used to both reduce pressures on the environment and improve benefits to society?". The major societal pressures and drivers that have been identified in the marine environment are illustrated in Figure 21.2 and their target variables are defined in Table 21.4. These drivers and pressures are now being tracked using EOV (see Excursus 21.1) within a number of global marine monitoring programs (see Table 21.1). Similar activities are now taking place in coastal and inland water ecosystems globally.

Other examples of a sustainable focus in EO applications are the various activities coordinated by the Group on Earth Observation (GEO; see Volume 3A—Section 20.1), including its Societal Benefit Areas (SBA; see Volume 3A—Section 20.3). In particular, the GEO Blue Planet initiative aims to link coastal and ocean information with society, which has direct implications for transportation, maritime safety, water quality, marine biodiversity, sustainable resource usage, and disaster management, and for inland waters GEO AquaWatch is developing a global EO-based monitoring and modelling system (Greb *et al.*, 2018). EO products are already addressing the global problem of water security, both in terms of monitoring water quality (see Section 19) and the extreme conditions of floods and droughts (Chawla *et al.*, 2020).

In future, we hope that advances in EO data acquisition, integration, and delivery will provide the rich information that humans will use to understand the choices that they can make to protect and enhance the societal benefits, and improve the sustainable use of all aquatic resources.

21.5 Further Information

Essential Ocean Variables

GOOS: *https://www.goosocean.org/index.php?option=com_content&view=article&id=170&Itemid=114*

CSIRO (2017)

21.6 References

Canonico, G., Buttigieg, P.L., Montes, E., Muller-Karger, F.E., Stepien, C., Wright, D., Benson, A., Helmuth. B., Costello, M., Sousa-Pinto, I., Saeedi, H., Newton, J., Appeltans, W., Bednaršek, N., Bodrossy, L., Best, B.D., Brandt, A., Goodwin, K.D., Iken, K., Marques, A.C., Miloslavich, P., Ostrowski, M., Turner, W., Achterberg, E.P., Barry, T., Defeo, O., Bigatti, G., Henry,. L.-A., Ramiro-Sánchez, B., Durán, P., Morato, T., Roberts, J.M., García-Alegre, A., Cuadrado, M.S., and Murton, B. (2019). Global Observational Needs and Resources for Marine Biodiversity. *Frontiers in Marine Science*, 6, 367. doi:10.3389/fmars.2019.00367

Cawse-Nicholson, K., Townsend, P.A., Schimel, D., Assiri, A.M., Blake, P.L., Buongiorno, M.F., Campbell, P., Carmon, N., Casey, K.A., Correa-Pabón, R.E., and Dahlin, K.M. (2021). NASA's surface biology and geology designated observable: A perspective on surface imaging algorithms. *Remote Sensing of Environment*, 257, 112349. *https://doi.org/10.1016/j.rse.2021.112349*

Chawla, I., Karthikeyan, L., and Mishra, A.K. (2020). A review of remote sensing applications for water security: Quantity, quality, and extremes. *Journal of Hydrology*, 585, 124826.

CSIRO (2017). *Oceans: Science and Solutions for Australia*. (Ed: Mapstone, B.D.). CSIRO, Melbourne. *https://bluepeteraustralia.files.wordpress.com/2017/12/oceans-csiro-research.pdf*

Da, C. (2015). Preliminary assessment of the Advanced Himawari Imager (AHI) measurement onboard Himawari-8 geostationary satellite. *Remote Sensing Letters*, 6(8), 637–646. doi:10.1080/2150704X.2015.1066522

Font J., Lagerloef, G.S.E., Le Vine, D.M., Camps, A., and Zanifé, O.-Z. (2004). The Determination of Surface Salinity With the European SMOS Space Mission. *IEEE Transactions on Geoscience and Remote Sensing*, 42(10), 2196–2205.

GOOS (2021). *Essential Ocean Variables* webpage, The Global Ocean Observing System website: *https://www.goosocean.org/index.php?option=com_content&view=article&id=170&Itemid=114*

Greb, S., Dekker, A.G., and Binding, C. (Eds) (2018). *Earth Observations in Support of Global Water Quality Monitoring*. IOCCG Report Series, No. 17, International Ocean Colour Coordinating Group, Dartmouth, Canada.

Guijarro, J., Santoleri, R.. Nardelli, B.B., Borgarelli, L., Croci, R., Venturini, R., Alberti, G., Caramagno, A., and Pirondini, F. (2003). Innovative radar altimeter concepts, *Proceedings of IGARSS '03, IEEE International*, 2, 1080–1082.

Le Vine, D.M., Lagerloef, G.S.E., Colomb, F.R., Yueh, S.H., and Pellerano, F.A. (2007). Aquarius: An instrument to monitor sea surface salinity from Space. *IEEE Transactions on Geoscience and Remote Sensing*, 45(7), 2040–2050.

Lindstrom, E., Gunn, J., Fischer, A., McCurdy, A., and Glover, L.K. (2012). *A Framework for Ocean Observing*. By the Task Team for an Integrated Framework for Sustained Ocean Observing, UNESCO IOC/INF-1284 revision. doi:10.5270/OceanObs09-FOO

Miloslavich, P., Bax, N., Simmons, S. E., Klein, E., Appeltans, W., Aburto-Oropeza, O., Garcia, M.A., Batten, S.D., Benedetti-Cecchi, L., Checkley, *D.M.Jr.*, Chiba, S., Duffy, J.E., Dunn, D.C., Fischer, A., Gunn, J., Kudela, R., Marsac, F., Muller-Karger, F.E., Obura, D., and Shin, Y.-J. (2018). Essential Ocean Variables for sustained observations of marine biodiversity and ecosystems. *Global Change Biology*, 24, 2416–2433. doi:10.1111/gcb.14108

Moltmann T., Turton, J., Zhang, H.-M., Nolan, G., Gouldman, C., Griesbauer, L., Willis, Z., Piniella, Á.M., Barrell, S., Andersson, E., Gallage, C., Charpentier, E., Belbeoch, M., Poli, P.l, Rea, A., Burger, E.F., Legler, D.M., Lumpkin, R., Meinig, C., O'Brien, K., Saha, K., Sutton, A., Zhang, D., and Zhang, Y. (2019). Global Ocean Observing System (GOOS), Delivered Through Enhanced Collaboration Across Regions, Communities, and New Technologies. *Frontiers in Marine Science*, 6, 291. doi:10.3389/fmars.2019.00291

Morrison, S. (2019). *National Statement to the United Nations General Assembly*, 25 September 2019, New York. *https://www.pm.gov.au/media/national-statement-united-nations-general-assembly*

Muller-Karger, F.E., Miloslavich, P., Bax, N.J., Simmons, S., Costello, M.J., Sousa, P.I., Canonico, G., Turner, W., Gill, M., Montes, E., Best, B.D., Pearlman, J., Halpin, P., Dunn, D., Benson, A., Martin, C.S., Weatherdon, L.V., Appeltans, W., Provoost, P., Klein, E., Kelble, C.R., Miller, R.J., Chavez, F.P., Iken, K., Chiba, S., Obura, D., Navarro, L.M., Pereira, H.M., Allain, V., Batten, S., Benedetti-Checchi, L., Duffy, J. E., Kudela, R.M., Rebelo, L.-M., Shin, Y., and Geller, Gary. (2018). Advancing Marine Biological Observations and Data Requirements of the Complementary Essential Ocean Variables (EOVs) and Essential Biodiversity Variables (EBVs) Frameworks. *Frontiers in Marine Science*, 5, 211. doi:10.3389/fmars.2018.00211

Sagar, S., Falkner, I., Dekker, A., Huang, Z., Blondeau-Patissier, D., Phillips, C., Przeslawski, R. (2020). *Earth Observation for monitoring of Australian Marine Parks and other off-shore Marine Protected Areas*. Report to the National Environmental Science Program, Marine Biodiversity Hub. Geoscience Australia.

Schmit, T.J., Gunshor, M.M., Menzel, W.P., Gurka, J.J., Li, J., and Bachmeier, A.S. (2005). Introducing the next-generation advanced baseline imager on GOES-R. *Bulletin of American Meteorological Society*, 86, 1079–1096. *http://dx.doi.org/10.1175/BAMS-86-8-1079*

Stephens, G.L., Vane, D.G., Boain, R.J., Mace, G.G., Sassen, K., Wang, Z., Illingworth, A.J., O'Connor, E.J., Rossow, W.B., Durden, S.L., Miller, S.D., Austin, R.T., Benedetti, A., Mitrescu, C., and The CloudSat Science Team (2002). The Cloudsat Mission and the A-Train. *Bulletin of American Meteorological Society*, 83, 1771–1790. *http://dx.doi.org/10.1175/BAMS-83-12-1771*

Sudmanns, M., Tiede, D., Lang, S., Bergstedt, H., Trost, G., Augustin, H., Baraldi, A., and Blaschke, T. (2019). Big Earth data: disruptive changes in Earth observation data management and analysis? *International Journal of Digital Earth*, 13(7), 832–850. *https://doi.org/10.1080/17538947.2019.1585976*

Werdell, P.J., Behrenfeld, M.J., Bontempi, P.S., Boss, E., Cairns, B., Davis, G.T., Franz, B.A., Gliese, U.B., Gorman, E.T., Hasekamp, O., Knobelspiesse, K.D., Mannino, A., Martins, J.V., McClain, C.R., Meister, G., and Remer, L.A. (2019). The Plankton, Aerosol, Cloud, Ocean Ecosystem Mission: Status, Science, Advances. *Bulletin of the American Meteorological Society*, 100(9), 1775–1794.

Glossary

Sources include glossaries from Australian Hydrographic Office, International Hydrographic Office, and Geoscience Australia.

Term	Definition
AAPP	Australian Antarctic Program Partnership
AAT	Australian Antarctic Territory
AATSR	Advanced Along-Track Scanning Radiometer
ABSLMP	Australian Baseline Sea Level Monitoring Project
ACSPO	Advanced Clear Sky Processor for Oceans
AHI	Advanced Himawari Imager
AHO	Australian Hydrographic Office
AMSA	Australian Marine Safety Authority
AMSR-E	Advanced Microwave Scanning Radiometer for EOS
AMSR2	Advanced Microwave Scanning Radiometer 2
AODN	Australian Ocean Data Network
AOP	Apparent Optical Properties
Aphotic Zone	The Aphotic Zone (or midnight zone) refers to the darker, deeper waters below 1000 m in which light levels are too low for photosynthesis. This zone is also called Deep Sea in oceans and the Profundal Zone in lakes. The Aphotic Zone comprises 90% of the total area of oceans on Earth.
Aquifer	Saturated, subterranean zone below the Water Table. Groundwater is often extracted from aquifers artificially by installing a well or bore. Unconfined aquifers require a pump to raise groundwater to the surface from a bore. Confined aquifers, however, exist above layers of relatively impermeable rock such that natural internal pressures spontaneously eject the groundwater to (or above) the surface. Such waters are called artesian waters.
Artesian Waters	Confine aquifer from which groundwater is spontaneously released to the surface.
ATSB	Australian Transport Safety Bureau
AVHRR	Advanced Very High Resolution Radiometer
Benthic Zone	The lowest level of any aquatic ecosystem which extends from the shoreline to deep water. This zone consists of rock, sand and sediment on the floor of an ocean, sea, lake or river. As such, the conditions of the benthic zone can vary significantly between shallow coastal waters and deep ocean. It supports a wide range of benthic organisms, or 'benthos', depending on local conditions such as the amount of light that reaches it, the ambient temperature and available nutrients.
Benthos	Plants and animals that live on the seafloor. These include immobile sponges and corals, creeping crabs and snails, burrowing worms, crustaceans and bivalves, as well as barnacles, seaweeds, and sea squirts.
BRAN	Bluelink Reanalysis
BoM	Bureau of Meteorology
CARS	CSIRO Atlas of Regional Seas
CASI	Compact Airborne Spectrographic Imager
Catchment	The area of land draining into a river is referred to as its catchment or watershed.
CCI	Climate Change Initiative
CDIM	Coloured dissolved inorganic matter
CDOM	Coloured dissolved organic matter
CMC	Canadian Meteorological Centre
CMEMS	Copernicus Marine Environment Monitoring Service
Coastal Waters	Shallower marine waters within 3M of the Territorial Sea Baseline (TSB). These include estuaries, beaches, salt marshes, mudflats and mangrove swamps, as well as the shallow waters on the fringe of oceans, which contain coral reefs and lagoons, seagrass meadows, and kelp forests.
CoM	Commonwealth of Australia
Confidence Level	Probability that the true value of a measurement will lie within the specified uncertainty from the measured value.

Term	Definition
Contiguous Zone	Belt of water extending 24M from TSB within which Australia may exercise control related to customs, immigration, pollution, and quarantine.
Coriolis force	A composite centrifugal force, due to rotation of the Earth, acting on objects (including air and water) moving in relation to the Earth. It causes deflection of such moving objects to the left in the Southern Hemisphere, and to the right in the Northern Hemisphere.
Correction	Compensation applied to data to adjust for an estimated systematic effect.
CSIRO	Commonwealth Scientific and Industrial Research Organisation
Current	A non-periodical, generally horizontal movement of water (or other fluid) due to many causes such as prevalent winds, temperature differential etc., but not to gravitational forces of the Moon and Sun (see tidal stream)
Cryosphere	The frozen water part of the Earth system, comprising sea ice, ice caps and ice sheets, glaciers, snow cover, icebergs, lake and river ice, and frozen ground.
C3S	Copernicus Climate Change Service
Datum	1. Any numerical or geometrical quantity which may serve as a reference or base for other quantities. In marine applications, a base elevation or plane used as a reference from which to reckon heights or depths, plural: datums. 2. A single piece of information, plural: data.
Deep Sea	Aphotic Zone in Oceans.
Delta	A Delta result from settling river sediment and can occur where one river meets another, a river meets a lake or reservoir, or a river meets an open sea that has weak tidal currents. The formation of deltas gradually slows down flow of rivers.
Demersal Zone	The Demersal Zone includes water near the seabed, but below the pelagic zone.
DIC	Dissolved inorganic carbon
DOC	Dissolved organic carbon
Dysphotic Zone	Lower division of Photic Zone which receives only 1% of the photosynthetically active radiation (PAR) that is intercepted by the water surface.
Ebb (or Ebb Stream)	The horizontal movement of water associated with falling tide, usually setting seaward or in the direction opposite to tide progression. Also known as ebb current or outgoing stream.
Eddy	A circular movement of water, usually formed where currents or tidal streams pass obstructions, along the edge of a current or stream, or between two adjacent flows.
EMR	Electromagnetic radiation
ENSO	El Niño-Southern Oscillation
EO	Earth Observation
EOS	Earth Observation from Space
EOV	Essential Ocean Variable
Error	Difference between a measured value and the correct or true value. Errors can be categorised as systematic or random errors.
Estuary	An estuary is a semi-enclosed waterbody at the river mouth where river flow and tides mix fresh and salt water. These areas are typically turbid and provide a valuable habitat for marine and bird life.
Euphotic Zone	Upper division of Photic Zone, this zone extends from the water surface to that water depth at which only 1% of surface photosynthetically active radiation (PAR) is detected. It includes shallow, coastal waters and the upper part of deeper, ocean waters down to 200 m (in clear water). The Euphotic zone supports phytoplankton, microscopic algae and cyanobacteria as well as water plants and zooplankton, and the vast majority of marine life. It is estimated that 70% of the all photosynthesis on Earth occurs in the Euphotic Zone.
Exclusive Economic Zone (EEZ)	Area within 200 M of TSB, in which Australia has sovereign rights over waters, seabed and subsoil.
Feature	Any object, whether natural or manmade, which is distinct from the surrounding area.
Feature Detection	Ability of a system to detect features of a defined size.
Flow	1. The motion characteristic of a fluid. 2. Combination of tidal stream and current, also known in US as total current.
Freshwater	Inland waterbodies contain no (or low) salt levels.
FWHM	Full Width Half Maximum
GA	Geoscience Australia
GAMSSA	Global Australian Multi-Sensor SST Analysis
GCOM-C	Copernicus Climate Change Service - Climate

Term	Definition
GCOM-W	Copernicus Climate Change Service - Water
GEBCO	General Bathymetric Chart of the Oceans
GEO	Geostationary Earth Orbiting
Geoid	An equipotential surface (i.e. Having the same potential gravity at each point) that would be assumed by the sea level in the absence of tides, currents, water density variations and atmospheric effects. It is the surface of reference for astronomical observations and geodetic levelling.
Geostrophic current	A steady flow where the Coriolis force balances exactly the horizontal pressure gradient.
GFO	Geosat Follow-On
GHRSST	Group for High Resolution SST
GLOSS	Global Sea Level Observing System
GMPE	GHRSST Multi-Product Ensemble
GNSS	Global Navigation Satellite Systems
GOOS	Global Ocean Observing System
GRACE	Gravity Recovery and Climate Experiment
HAB	Harmful algal bloom
HAT	Highest Astronomical Tide
HS	Significant wave height
Hydrosphere	The hydrosphere comprises all the water on the Earth's surface, inside the Earth and in its atmosphere.
Hydrographic survey	A survey of a body of water to determine several classes of data pertaining to it, such as depth, configuration and nature of the bottom, direction and force of the currents, heights and times of tides, location of fixed objects for navigation purposes, etc. These data form the basis for a navigational chart.
ICSMD	International Charter for Space and Major Disasters
IHO	International Hydrographic Office
IMCRA	Interim Marine and Coastal Regionalisation of Australia
IMOS	Integrated Marine Observing System
Inland Waters	Freshwater rivers and lakes located within the Territorial Sea Baseline (TSB). These generally have low levels of dissolved salt. Ponds, dams and lakes feature standing water while rivers and streams have flowing water.
Intertidal Zone	Spanning from the high to low tide marks, this zone describes the coastal land that is exposed to changing tides, and thus impacted by waves at high tide, and Sun and wind at low tide.
IOC	International Oceanographic Commission
IOP	Inherent Optical Properties
IPCC	Intergovernmental Panel on Climate Change
JAXA	Japan Aerospace Exploration Agency
JMA	Japan Meteorological Agency
LAT	Lowest Astronomical Tide
LEO	Low Earth Orbiting
Limnetic Zone	In lakes, that water which is close enough to the surface to admit sufficient light for photosynthesis.
Littoral Zone	The Littoral Zone extends from the high tide mark to the continental shelf and thus includes the intertidal and neritic zones defined above.
LST	Land Surface Temperature
Marine Waters	Salty waterbodies external to land masses.
MBON	Marine Biodiversity Observation Network
Mean Sea Level (MSL)	A tidal datum; the arithmetic mean of hourly heights of the sea at the tidal station observed over a period of time (preferably 19 years).
Metadata	Data describing a dataset and its usage.
MGDSST	Merged Satellite and *in situ* Data Global Daily Sea Surface Temperature
ML	Machine learning
MPA	Marine Protected Areas
MUR	Multi-Scale Ultra High Resolution

Term	Definition
NAP	Non-algal particles
Nautical Mile (M)	Unit of distance equalling 1,852 m, which approximates 1 minute of latitude.
NDBC	National Data Buoy Centre
Nekton	Swimming animals including fish, serpents, and whales.
Neritic Zone	This occurs along coastlines between the low tide mark and the continental shelf. Since some sunlight reaches the bottom of this relatively shallow zone, it fosters photosynthetic organisms, such as phytoplankton and seaweeds. Most coral reefs occur in this zone. Organisms such as mollusks, sponges, crustaceans, and worms can live on the seafloor of this zone.
NMB	National Marine Bioregionalisation
NOAA	National Oceanic and Atmospheric Administration
OAC	Optically active constituents
OBIA	Object based Image Analysis
OBIS	Ocean Biogeographic Information System
OBPS	Ocean Best Practices System
Ocean	Deeper marine waters at least 3 M away from the Territorial Sea Baseline (TSB). These large waterbodies are saline and subject to tidal variations.
Oceanic Zone	The water spanning between continental shelves of different land masses.
OISST	Optimum Interpolation Sea Surface Temperature
OSTIA	Operational Sea Surface Temperature and Sea Ice Analysis
Pelagic Zone	The Pelagic Zone describes open water in oceans that is both away from the coast and above the seafloor, and includes both photic and aphotic waters.
Photic Zone	This zone refers to water that is close enough to the surface to admit sufficient light for photosynthesis. In lakes, this region is referred to as the Limnetic Zone. The Photic Zone can be further divided into the Euphotic, or sunlit, zone and the Dysphotic, or twilight, zone (see Figure 2.9).
Phytoplankton	Microscopic marine plants.
Plankton	Minute animals called zooplankton and microscopic plants called phytoplankton, most of which do not have the ability to move themselves around so tend to drift and float with water movement.
Profundal Zone	Aphotic Zone in lakes
RAMSSA	Regional Australian Multi-Sensor SST Analysis
Riparian Zone	The Riparian zone occurs along the edges of rivers or streams and includes the river bed, banks and floodplains.
RTE	Radiative Transfer Equation
SAR	Synthetic Aperture Radar
SDB	Satellite Derived Bathymetry
Seabed/seafloor	The solid surface that underlies a waterbody.
SEAFRAME	SEA-Level Fine Resolution Acoustic Measuring Equipment
SIOP	Concentration-specific IOP
SLR	Sea level rise
SGLI	Second-Generation Global Imager
SLSTR	Sea and Land Surface Temperature Radiometer
SPIM	Suspended particulate inorganic matter
SPOM	Suspended particulate organic matter
Spring	A spring occurs when groundwater naturally overflows onto the land surface.
SST	Sea Surface Temperature
SSTAARS	Sea Surface Temperature Atlas of the Australian Regional Seas
SSTdepth	Surface sea surface temperature at depth: all measurements of water temperature beneath SSTsubskin.
SSTfnd	Foundation sea surface temperature: the temperature free of diurnal temperature variability, that is, the temperature at the first time of the day when the heat gain from the solar radiation absorption exceeds the heat loss at the sea surface (approximately 10 m water depth under calm conditions).

Term	Definition
SSTint	Interface sea surface temperature: the temperature at the air-sea interface on molecular scales (cannot be directly measured).
SSTskin	Skin sea surface temperature: the temperature measured by an IR radiometer typically operating at wavelengths 3.7–12 μm, which represents the temperature within the conductive diffusion-dominated sublayer at a water depth of ~10–20 μm.
SSTsubskin	Subskin sea surface temperature: the temperature at the base of the conductive laminar sublayer of the ocean surface, which can be well approximated to the measurement of the surface temperature by a microwave radiometer operating in the 6–11 GHz frequency range (approximately 1 mm water depth).
Substratum	This layer rests on the seabed (or lithosphere) and may comprise sand, silt, mud, rocks, and live and/or dead coral.
Systematic Error	Component of measurement error that remains constant or varies in a predictable manner.
Territorial Sea	Belt of Australian water less or equal to 12 M from the Territorial Sea Baseline (TSB), over which Australia has sovereign rights to the water, seabed and subsoil, plus the airspace above.
Territorial Sea Baseline (TSB)	Reference boundary delimiting land and sea, which is used to define Australia's Maritime Zones.
Thermocline	A layer in a body of water in which the temperature decreases with depth at an appreciably greater rate than above and below, also such a gradient of temperature. Also called discontinuity or thermal layer.
Total Horizontal Uncertainty (THU)	Component of total propagated uncertainty (TPU) calculated in the horizontal dimension. THU is a two-dimensional quantity with all contributing horizontal measurement uncertainties included.
Total Propagated Uncertainty (TPU)	Three-dimensional uncertainty with all contributing measurement uncertainties included.
Total Vertical Uncertainty (TVU)	Component of total propagated uncertainty (TPU) calculated in the vertical dimension. TVU is a one-dimensional quantity with all contributing vertical measurement uncertainties included.
TSM	Total suspended matter
Tsunami	A wave generated by seismic activity. Also called seismic sea wave, or, inaccurately, a tidal wave. Barely discernible in the open ocean, their amplitude may increase to several metres in the shallow coastal regions. Most common in the Pacific.
UN	United Nations
Uncertainty	Estimate characterising the range of values within which the true value of a measurement is expected to lie as defined within a particular confidence level. It is expressed as a positive value.
UNCLOS	United Nations Convention on the Law of the Sea
Underkeel Clearance	Distance between the lowest point of the ship's hull and the seabed, riverbed, etc.
UNESCO	United Nations Educational, Scientific and Cultural Organisation
Upwelling	An upward flow of subsurface water, usually a result of divergence, offshore currents, winds, and wind drift transport.
VIIRS	Visible Infrared Imaging Radiometer Suite
Watershed	The area of land draining into a river is referred to as its catchment or watershed.
Water Table	Upper boundary of aquifer.
Wave	1. A periodic disturbance which moves through or over the surface of the medium (eg. water) with speed dependent upon the properties of the medium. It is characterised by frequency, length, and amplitude. 2. A ridge-like deformation, or undulation of a liquid or solid surface.
WST	Water Surface Temperature
WMO	World Meteorological Organisation (UN)
Zooplankton	Minute marine animals.


crc·si

CSIRO

Australian Government
Geoscience Australia

bushfire&natural
HAZARDSCRC

FRONTIER SI